

Transactions of the ASME®

Journal of Applied Mechanics

Technical Editor, **LEWIS T. WHEELER** (1997)

Department of Mechanical Engineering,
University of Houston,
Houston, TX 77204-4792

APPLIED MECHANICS DIVISION

Chairman, **T. A. CRUSE**
Secretary, **A. NEEDLEMAN**
Associate Technical Editors,
R. ABAYARATNE (1997)
T. R. AKYLAS (1997)
D. M. BARNETT (1996)
R. BECKER (1998)
S. A. BERGER (1997)
I. M. DANIEL (1996)
W. J. DRUGAN (1997)
J. T. JENKINS (1996)
J. W. JU (1998)
S. KYRIAKIDES (1997)
S. LICHTER (1998)
W. K. LIU (1996)
X. MARKENSCOFF (1997)
M. ORTIZ (1998)
J. N. REDDY (1998)
W. N. SHARPE, JR. (1996)
S. W. SHAW (1997)
M. SHINOZUKA (1997)
M. TAYA (1996)

BOARD ON COMMUNICATIONS

Chairman and Vice-President
R. MATES

Members-at-Large
T. BARLOW, N. H. CHAO, A. ERDMAN,
G. JOHNSON, L. KEER,
E. M. PATTON, S. PATULSKI,
S. ROHDE, R. SHAH, F. WHITE,
J. WHITEHEAD, K. T. YANG

OFFICERS OF THE ASME

President, **D. T. KOENIG**
Executive Director, **D. L. BELDEN**
Treasurer, **R. A. BENNETT**

PUBLISHING STAFF

Managing Director, Engineering
CHARLES W. BEARDSLEY
Director, Technical Publishing
JANET M. WEINRIB
Managing Editor, Technical Publishing
CYNTHIA B. CLARK
Managing Editor, Transactions
CORNELIA MONAHAN
Production Editor
JUDITH SIERANT
Production Assistant
MARISOL ANDINO

Transactions of the ASME, Journal of Applied Mechanics
(ISSN 0021-8936) is published quarterly (Mar., June, Sept.,
Dec.) for \$210.00 per year by The American Society of
Mechanical Engineers, 345 East 47th Street, New York,
NY 10017.

Second class postage paid at New York, NY and additional
mailing office. POSTMASTER: Send address changes to
Transactions of the ASME, Journal of Applied Mechanics, c/o
THE AMERICAN SOCIETY OF MECHANICAL ENGINEERS,
22 Law Drive, Box 2300, Fairfield, NJ 07007-2300.
CHANGES OF ADDRESS must be received at Society
headquarters seven weeks before they are to be effective.
Please send old label and new address. PRICES: To
members, \$40.00, annually; to nonmembers, \$210.00. Add
\$30.00 for postage to countries outside the United States
and Canada.

STATEMENT from By-Laws. The Society shall not be
responsible for statements or opinions advanced in papers or
... printed in its publications (B7.1, Para. 3). COPYRIGHT ©
1995 by The American Society of Mechanical Engineers.
Authorization to photocopy material for internal or personal
use under circumstances not falling within the fair use
provisions of the Copyright Act is granted by ASME to
libraries and other users registered with the Copyright
Clearance Center (CCC). Transactional Reporting Service
provided that the base fee of \$3.00 per article is paid directly
to CCC, Inc., 222 Rosewood Drive, Danvers, MA 01923.
Request for special permission or bulk copying should be
addressed to Reprints/Permission Department. INDEXED by
Applied Mechanics Reviews and Engineering Information, Inc.
Canadian Goods & Services Tax Registration #126148048.

Published Quarterly by The American Society of Mechanical Engineers

VOLUME 62 • NUMBER 3 • SEPTEMBER 1995

555 List of Reviewers

TECHNICAL PAPERS

557 Elastic Fields Resulting From Concentrated Loading on a Three-Dimensional Incompressible Wedge

M. T. Hanson

566 A Generalized Self-Consistent Mechanics Method for Solids Containing Elliptical Inclusions

Y. Huang and K. X. Hu

573 Green's Function for Elastic Medium With General Anisotropy

Ching S. Chang and Yang Chang

579 The Elastic Field Caused by a Circular Cylindrical Inclusion—Part I: Inside the Region $x_1^2 + x_2^2 < a^2$, $-\infty < x_3 < \infty$ Where the Circular Cylindrical Inclusion is Expressed by $x_1^2 + x_2^2 \leq a^2$, $-h \leq x_3 \leq h$

Linshi Wu and Shanyi Du

585 The Elastic Field Caused by a Circular Cylindrical Inclusion—Part II: Inside the Region $x_1^2 + x_2^2 > a^2$, $-\infty < x_3 < \infty$ Where the Circular Cylindrical Inclusion is Expressed by $x_1^2 + x_2^2 \leq a^2$, $-h \leq x_3 \leq h$

Linshi Wu and Shanyi Du

590 Development of Generalized Plane-Strain Tensors for the Concentric Cylinder

N. Chandra and Zhiyuan Xie

595 Buckling and Post-buckling Behavior of a Pipe Subjected to Internal Pressure

D. M. Tang, M. A. Ilgamov, and E. H. Dowell

601 Crack Propagation in Homogeneous and Bimaterial Sheets Under General In-Plane Loading: Nonlinear Analysis

P. H. Geubelle and W. G. Knauss

607 Strip Element Method to Analyze Wave Scattering by Cracks in Anisotropic Laminated Plates

G. R. Liu and J. D. Achenbach

614 A Crack Very Close to a Bimaterial Interface

A. Romeo and R. Ballarini

620 Buckling Instability of Straight Edge Cracks

H. M. Jensen and M. D. Thouless

626 Some Observations on Yield Surfaces for 304 Stainless Steel at Large Prestrain

H. C. Wu, J. K. Lu, and W. F. Pan

633 Inertial Effects on Void Growth in Porous Viscoplastic Materials

W. Tong and G. Ravichandran

640 Damage-Coupled Creep Mechanics and its Structural Analysis Principle

Pan Zeng and X. F. Sun

646 Measurement of Cyclic Biaxial Elastoplastic Stresses at Notch Roots

C. H. Yang and W. N. Sharpe

654 Diffusion Rate for Stress in Orthotropic Materials

S. A. Matemilola, W. J. Stronge, and D. Durban

662 Rotation of a Cylinder in a Casing at Zero Reynolds Number

C. Y. Wang

667 Three-Dimensional Viscous Flows Between Concentric Cylinders Executing Axially Variable Oscillations: A Hybrid Spectral/Finite Difference Solution

D. Mateescu, M. P. Paidoussis, and W.-G. Sim

674 Thermohydrodynamic Analysis of Process-Liquid Hydrostatic Journal Bearings in Turbulent Regime, Part I: The Model and Perturbation Analysis

Zhou Yang, L. San Andres, and D. W. Childs

679 Thermohydrodynamic Analysis of Process-Liquid Hydrostatic Journal Bearings in Turbulent Regime, Part II: Numerical Solution and Results

Zhou Yang, L. San Andres, and D. W. Childs

685 Analysis of Linear Nonconservative Vibrations

F. Ma and T. K. Caughey

692 On the Inverse Problem of Rectangular Plates Subjected to Elastic Impact, Part I: Method Development and Numerical Verification

Ching-Shih Yeh and Enboa Wu

(Contents continued on Outside Back Cover)

CONTENTS (CONTINUED)

- 699 On the Inverse Problem of Rectangular Plates Subjected to Elastic Impact, Part II: Experimental Verification and Further Applications
Ching-Shih Yen and Enboa Wu
- 706 Free Vibration of a Class of Homogeneous Isotropic Solids
P. G. Young and S. M. Dickinson
- 709 Toeplitz Jacobian Matrix for Nonlinear Periodic Vibration
A. Y. T. Leung and T. Ge
- 718 Vibration of Stress-Free Hollow Cylinders of Arbitrary Cross Section
K. M. Liew, K. C. Hung, and M. K. Lim
- 725 Three-Dimensional Rigid-Body Collisions With Multiple Contact Points
D. B. Marghitu and Y. Hurmuzlu
- 733 A Finite Elastoplastic Constitutive Formulation With New Co-rotational Stress-Rate and Strain-Hardening Rule
Z. Xia and F. Ellyin
- 740 Partitioning the Parameter Space According to Different Behaviors During Three-Dimensional Impacts (95-APM-8)
V. Bhatt and J. Koechling
- 747 A General Formulation of the Theory of Wire Ropes
Wei Jiang
- 756 Dynamic Formulation for Geometrically Exact Sandwich Beams and One-Dimensional Plates
Loc Vu-Quoc and I. K. Ebcioğlu
- 764 On the Instability Mechanisms of a Disk Rotating Close to a Rigid Surface (95-APM-9)
F. Y. Huang and C. D. Mote
- 772 Equilibrium Displacement and Stress Distribution in a Two-Dimensional, Axially Moving Web Under Transverse Loading
C. C. Lin and C. D. Mote, Jr.
- 780 Anisotropic Yield Surfaces Based on Elastic Projection Operators
H. L. Schreyer and Q. H. Zuo
- 786 Analytical Expressions for the Relaxation Moduli of Linear Viscoelastic Composites With Periodic Microstructure (95-APM-10)
R. Luciano and E. J. Barbero
- 794 The Role of Temperature in the Entanglement Kinetics of a Polymer Melt
R. S. Jeyaseelan and A. J. Giacomin
- 802 Tension of Conductor Under Concentrated Loads
P. Yu, P. S. Wong, and F. Kaempffer

BRIEF NOTES

- Thermal Stresses in a Multilayered Anisotropic Medium With Interface Thermal Resistance
T. C. Chen and H. I. Jang 810
- Packing Characterization of Granular Composite Media in Two Dimensions
G. J. Filatovs 811
- Elastic Buckling of a Circular Disk due to Internal Membrane Forces
W.-Y. Shih, L. Kudryavtsev, and K. K. Wang 813
- A Numerical Investigation of the Elastothermodynamic Damping of Fiber-Reinforced Metal-Matrix Composites
K. B. Milligan and V. K. Kinra 816
- Vibrations of Solid Cylinders Revisited
J. R. Hutchinson 818
- On Young's Modulus for Anisotropic Media
P. Boulanger and M. Hayes 819
- On Kinematical Conditions for Steady Motions of Strings and Rods
T. R. Nordenholz and O. M. O'Reilly 820
- The Shear Center Problem for Nonlinear Material Behavior
E. Reissner 822

BOOK REVIEW

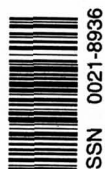
- 824 *Pressure Vessel Design: Concepts and Principles*, edited by J. Spence and A. S. Tooth . . .
Reviewed by C. W. Bert

ERRATA

- 705 Antiplane Elastic Wave Scattering From a Curved Randomly Rough Crack, by A. Bostrom, P.-A. Jansson, and P. Olsson and published in the Dec. 1994 issue of the *Journal of Applied Mechanics*

ANNOUNCEMENTS AND SPECIAL NOTES

- 572 Change of Address form
- 600 Call for Proposals to Host a IUTAM Symposium in 1998 or 1999
- 613 Symposium on Recent Developments in Elasticity—Announcement
- 691 Third International Conference on Vibration Problems—Announcement
- 698 19th International Congress of Theoretical and Applied Mechanics—Announcement
- 724 19th International Congress of Theoretical and Applied Mechanics—Call for U.S. Papers
- 793 3rd EUROMECH Solid Mechanics Conference—Announcement
- 825 Worldwide Mechanics Meetings Conference Listing
- inside back cover Information for Authors



ISSN 0021-8936



JOURNAL CODE JE



ISSUE CODE 9503

Elastic Fields Resulting From Concentrated Loading on a Three-Dimensional Incompressible Wedge

M. T. Hanson

Department of Engineering Mechanics,
University of Kentucky,
Lexington, KY 40506-0046
Mem. ASME

This paper considers point force or point moment loading applied to the surface of a three-dimensional wedge. The wedge is two-dimensional in geometry but the loading may vary in a direction parallel to the wedge apex, thus creating a three-dimensional problem within the realm of linear elasticity. The wedge is homogeneous, isotropic, and the assumption of incompressibility is taken in order for solutions to be obtained. The loading cases considered presently are as follows: point normal loading on the wedge face, point moment loading on the wedge face, and an arbitrarily directed force or moment applied at a point on the apex of the wedge. The solutions given here are closed-form expressions. For point force or point moment loading on the wedge face, the elastic field is given in terms of a single integral containing associated Legendre functions. When the point force or moment is at the wedge tip, closed-form (nonintegral) expressions are obtained in terms of elementary functions. An interesting result of the present research indicates that the wedge paradox in two-dimensional elasticity also exists in the three-dimensional case for a concentrated moment at the wedge apex applied in one direction, but that it does not exist for a moment applied in the other two directions.

1 Introduction

A considerable amount of research in the field of elasticity has been directed at determining fundamental solutions for concentrated loading. The search for these solutions has been particularly fruitful in the case of point forces. In three-dimensions the classic solutions found by Kelvin for point force loading in an isotropic full space and Boussinesq and Cerruti for point loading on an isotropic half-space are milestones which have proven invaluable in the application of linear elasticity to problems of practical interest. Subsequent investigations have found point force solutions for even more complicated problems. Mindlin (1936) presented the solution for buried loading in a half-space. Rongved (1955) evaluated the solution for a point force in one of two bonded dissimilar elastic, isotropic half-spaces. Dundurs and Hetenyi (1965) solved the analogous problem when the interface was frictionless. Pan and Chou (1976) have evaluated the solution for arbitrary point loading in a transversely isotropic full space.

The solutions for point force loading, so-called Green's functions, are valuable for several reasons. Obviously, they can be used to model material response to concentrated loading. More importantly, however, the solution for any loading condition can be obtained from the point force solutions by quadrature. Furthermore, solutions for other nuclei of strain such as center of dilatation, concentrated moments and force doublets become readily available. Even infinitesimal dislocation loops can be obtained from the Green's functions by certain combinations of force doublets (Mura, 1982).

Contributed by the Applied Mechanics Division of THE AMERICAN SOCIETY OF MECHANICAL ENGINEERS for publication in the ASME JOURNAL OF APPLIED MECHANICS.

Discussion on this paper should be addressed to the Technical Editor, Prof. Lewis T. Wheeler, Department of Mechanical Engineering, University of Houston, Houston, TX 77204-4792, and will be accepted until four months after final publication of the paper itself in the ASME JOURNAL OF APPLIED MECHANICS.

Manuscript received by the ASME Applied Mechanics Division, June 18, 1993; final revision, May 5, 1994. Associate Technical Editor: X. Markenscoff.

Although Green's functions for a half-space geometry have received the most attention, point force solutions for other three-dimensional geometric regions have also been obtained. As a noninclusive illustration of this point we mention the solutions for point loading at the tip of a solid cone reviewed by Love (1927), the hollow cone solution given by Knops (1958) and Lure (1964), the transversely isotropic cone given in Lekhnitskii (1963) and Chen (1965) (these are not general Green's functions since the force is applied at the cone tip only), and the general Green's functions for a point force in an elastic, isotropic layer derived by Benitez and Rosakis (1987). Analytical point force solutions for another three-dimensional geometry of great interest presently, here denoted as the three-dimensional wedge, have received minimal attention in past literature. Until recently, the only consideration of this geometry was in the Russian literature, mainly available through the translation of the classic book by Uflyand (1965). The Papkovitch-Neuber potential function formulation for cylindrical coordinates is outlined there along with the application of the Kontorovich-Lebedev integral transform developed in Russia for this geometry. Uflyand presents solutions for the potential functions in the special case of point force loading applied to the surface of a three-dimensional wedge, with wedge angle such that the problem is equivalent to a full space with a half-plane slit. The papers by Babeshko and Berkovich (1972) and Berkovich (1974) discuss contact problems for a three-dimensional wedge but no results are given. Although concentration is directed at analytical solutions, the analytical/numerical analysis presented by Hetenyi (1970), Keer et al. (1983, 1984) and Hanson and Keer (1990) for loading on a quarter space are deserving of mention since a quarter space is a special case of a three-dimensional wedge with a 90 degree total wedge angle. The analytical solution for arbitrary point force loading in a general three-dimensional wedge region is still an unsolved problem in linear elasticity.

Recent research by the author has made some progress towards finding Green's functions for this geometry. This interest

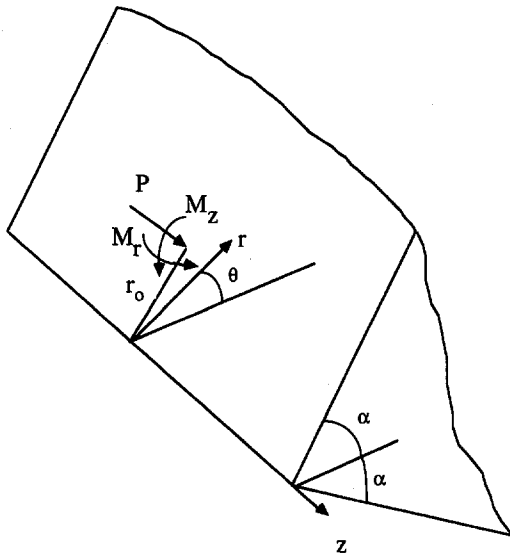


Fig. 1 Geometry and coordinate system for a three-dimensional wedge of angle 2α . A point normal force P or moments M_r , or M_θ are applied at the point $r = r_0$, $\theta = \alpha$, $z = 0$.

stems from the application of a wedge geometry in performing stress analysis of cutting tools and in rail-wheel contact. In a recent paper (Hanson and Keer, 1991), the potential functions for point normal loading on the face of a three-dimensional wedge with arbitrary wedge angle were evaluated. The solution was obtainable though only for the case of an incompressible material. Since this analysis was directed at contact problems for a wedge region, the elastic field was not evaluated. Subsequent to the publication of this paper, the authors have discovered a similar evaluation of the potential functions for this problem by Efimov and Efimov (1986), but in a slightly different form. The extension of this research to include point tangential loading on the surface of a three-dimensional incompressible wedge and internal point loading (for a special direction of the point force) was completed by Hanson et al. (1994). Again only the potential functions were evaluated.

The present analysis derives closed-form expressions for the entire elastic field when point force loading is applied on the surface of a three-dimensional incompressible wedge. The solution is obtained through differentiation of the potential functions. The elastic field is given in terms of a single integral containing associated Legendre functions. The solution for the point force is utilized to obtain the elastic field for concentrated couples applied to the wedge face. A limiting case is also considered where the concentrated action (force or moment) moves to the wedge apex. The solution in this case is given explicitly in terms of elementary functions. It is well known in the field of plane-strain linear elasticity that a paradoxical solution exists when a concentrated couple is applied at the apex of a two-dimensional wedge, which was apparently first investigated by Sternberg and Koiter (1958). In particular, the solution for the elastic field becomes infinite at a particular value of the wedge angle. The present analysis reveals the elastic field for the three-dimensional analog to this problem. It is shown that for a point couple applied to the tip of the wedge, the elastic field exhibits the same paradox if the couple vector is directed parallel to the wedge apex. No such paradox exists for a couple with a vector contained in a plane perpendicular to the wedge apex.

2 Elastic Field for Concentrated Normal Force Loading

The problem under consideration is shown in Fig. 1. Cylindrical coordinates r , θ , z are employed and the three-dimensional

wedge occupies the region $0 < r < \infty$, $-\infty < z < \infty$, $-\alpha < \theta < \alpha$, where the z -axis falls along the apex of the wedge. Thus the three-dimensional wedge actually has a two-dimensional geometry but the problem is three-dimensional since the loading will vary in both the r and z directions. In this section the loading is a point normal compressive force of magnitude P ($M_r = M_\theta = 0$) located at $r = r_0$, $z = 0$, $\theta = \alpha$ and all other stresses on the wedge faces being taken as zero.

The Papkovitch-Neuber potential function formulation is used in the solution procedure. The radial, tangential and axial displacements as well as the stresses are written in terms of the four potential functions Φ_0 , Φ_1 , Φ_2 , Φ_3 as (Uflyand, 1965)

$$\begin{aligned} 2\mu u &= -\frac{\partial F}{\partial r} + 4(1-\nu)\{\cos(\theta)\Phi_1 + \sin(\theta)\Phi_2\} \\ 2\mu v &= -\frac{1}{r}\frac{\partial F}{\partial \theta} + 4(1-\nu)\{\cos(\theta)\Phi_2 - \sin(\theta)\Phi_1\} \\ 2\mu w &= -\frac{\partial F}{\partial z} + 4(1-\nu)\Phi_3 \end{aligned} \quad (1)$$

where F is the following combination of potentials:

$$F = \Phi_0 + r \cos(\theta)\Phi_1 + r \sin(\theta)\Phi_2 + z\Phi_3 \quad (2)$$

with μ as the shear modulus and ν is Poisson's ratio. The stresses follow suit as

$$\begin{aligned} \sigma_{rr} &= -\frac{\partial^2 \Phi_0}{\partial r^2} + 2(1-\nu)\left\{\cos(\theta)\frac{\partial \Phi_1}{\partial r} + \sin(\theta)\frac{\partial \Phi_2}{\partial r}\right\} \\ &\quad - r \cos(\theta)\frac{\partial^2 \Phi_1}{\partial r^2} - r \sin(\theta)\frac{\partial^2 \Phi_2}{\partial r^2} \\ &\quad + \frac{2\nu}{r}\left\{\cos(\theta)\frac{\partial \Phi_2}{\partial \theta} - \sin(\theta)\frac{\partial \Phi_1}{\partial \theta}\right\} \\ &\quad + 2\nu\frac{\partial \Phi_3}{\partial z} - z\frac{\partial^2 \Phi_3}{\partial r^2} \end{aligned} \quad (3)$$

$$\begin{aligned} \sigma_{\theta\theta} &= \left(\frac{\partial^2}{\partial r^2} + \frac{\partial^2}{\partial z^2}\right)\Phi_0 \\ &\quad - (1-2\nu)\frac{\partial}{\partial r}\{\cos(\theta)\Phi_1 + \sin(\theta)\Phi_2\} \\ &\quad + \frac{2(1-\nu)}{r}\left\{\cos(\theta)\frac{\partial \Phi_2}{\partial \theta} - \sin(\theta)\frac{\partial \Phi_1}{\partial \theta}\right\} \\ &\quad - \frac{1}{r}\left\{\cos(\theta)\frac{\partial^2 \Phi_1}{\partial \theta^2} + \sin(\theta)\frac{\partial^2 \Phi_2}{\partial \theta^2}\right\} \\ &\quad + 2\nu\frac{\partial \Phi_3}{\partial z} + z\left(\frac{\partial^2}{\partial r^2} + \frac{\partial^2}{\partial z^2}\right)\Phi_3 \end{aligned} \quad (4)$$

$$\begin{aligned} \sigma_{zz} &= -\frac{\partial^2}{\partial z^2}\{\Phi_0 + r \cos(\theta)\Phi_1 + r \sin(\theta)\Phi_2\} - z\frac{\partial^2 \Phi_3}{\partial z^2} \\ &\quad + 2(1-\nu)\frac{\partial \Phi_3}{\partial z} + 2\nu\left\{\cos(\theta)\frac{\partial \Phi_1}{\partial r} + \sin(\theta)\frac{\partial \Phi_2}{\partial r}\right. \\ &\quad \left. + \frac{1}{r}\left(\cos(\theta)\frac{\partial \Phi_2}{\partial \theta} - \sin(\theta)\frac{\partial \Phi_1}{\partial \theta}\right)\right\} \end{aligned} \quad (5)$$

$$\tau_{rz} = -\frac{\partial^2 F}{\partial z \partial r} + 2(1-\nu) \left\{ \cos(\theta) \frac{\partial \Phi_1}{\partial z} + \sin(\theta) \frac{\partial \Phi_2}{\partial z} + \frac{\partial \Phi_3}{\partial r} \right\} \quad (6)$$

$$\tau_{r\theta} = \frac{\partial \Phi}{\partial r} + \frac{2(1-\nu)}{r} \left\{ \cos(\theta) \frac{\partial \Phi_1}{\partial \theta} + \sin(\theta) \frac{\partial \Phi_2}{\partial \theta} \right\} \quad (7)$$

$$\tau_{z\theta} = \frac{\partial \Phi}{\partial z} + \frac{2(1-\nu)}{r} \frac{\partial \Phi_3}{\partial \theta} \quad (8)$$

where Φ in Eqs. (7), (8) is given as

$$\Phi = -\frac{1}{r} \frac{\partial \Phi_0}{\partial \theta} - \frac{z}{r} \frac{\partial \Phi_3}{\partial \theta} - \left\{ \cos(\theta) \frac{\partial \Phi_1}{\partial \theta} + \sin(\theta) \frac{\partial \Phi_2}{\partial \theta} \right\} + (1-2\nu) \{ \cos(\theta) \Phi_2 - \sin(\theta) \Phi_1 \}. \quad (9)$$

For point normal loading on the upper face (all other surface tractions zero) the potentials were derived by Hanson and Keer (1991) for an incompressible wedge ($\nu = 0.5$). The results can be put in the following form:

$$\Phi_0 = \Phi_3 = 0$$

$$\Phi_1 = \frac{P}{2\pi R} + \frac{P}{2\pi(rr_0)^{1/2}} \int_0^\infty A(\tau, \theta) P_{ir-1/2}(\cosh(\beta)) d\tau$$

$$\Phi_2 = \frac{P}{2\pi(rr_0)^{1/2}} \int_0^\infty B(\tau, \theta) P_{ir-1/2}(\cosh(\beta)) d\tau \quad (10)$$

where $R = (r^2 + r_0^2 + z^2 - 2rr_0 \sin(\theta))^{1/2}$ and the functions $A(\tau, \theta)$ and $B(\tau, \theta)$ are given as

$$A(\tau, \theta) = \frac{1}{D(\tau) \cosh(\pi\tau)} \times \left\{ r_1(\tau) \tau \sinh(\pi\tau) \sinh[\tau(\theta + \alpha)] - r_2(\tau) \tau \sinh(\pi\tau) \sinh[\tau(\theta - \alpha)] - D(\tau) \cosh \left[\tau \left(\theta + \frac{\pi}{2} \right) \right] \right\}$$

$$B(\tau, \theta) = \frac{\tau \tanh(\pi\tau)}{D(\tau)} \{ q_1(\tau) \sinh[\tau(\theta + \alpha)] - q_2(\tau) \sinh[\tau(\theta - \alpha)] \}. \quad (11)$$

In Eqs. (10) for the potentials, the first term for Φ_1 is the solution for an incompressible half-space while the integral terms are the wedge effect, $P_{ir-1/2}(\cosh(\beta))$ is a Legendre function of the first kind and β is defined by the relation

$$\cosh(\beta) = \frac{r^2 + r_0^2 + z^2}{2rr_0}. \quad (12)$$

The functions $r_1(\tau)$, $r_2(\tau)$, $q_1(\tau)$, $q_2(\tau)$, and $D(\tau)$ in Eqs. (11) are given in Hanson and Keer (1991).

Knowing the potentials allows the elastic field to be evaluated by differentiation. Using the results above allows the elastic field to be given as ($\nu = 0.5$)

$$2\mu u = \frac{P \cos(\theta)}{2\pi} \left\{ \frac{1}{R} + \frac{r(r - r_0 \sin(\theta))}{R^3} \right\} + \frac{3P}{4\pi(rr_0)^{1/2}} \int_0^\infty F_1(\tau, \theta) P_{ir-1/2}(\cosh(\beta)) d\tau$$

$$- \frac{P(r^2 - r_0^2 - z^2)}{4\pi(rr_0)^{3/2} \sinh(\beta)} \int_0^\infty F_1(\tau, \theta) \times P_{ir-1/2}(\cosh(\beta)) d\tau \quad (13)$$

$$2\mu v = -\frac{P}{2\pi} \left\{ \frac{\sin(\theta)}{R} + \frac{rr_0 \cos^2(\theta)}{R^3} \right\} + \frac{P}{2\pi(rr_0)^{1/2}} \int_0^\infty F_2(\tau, \theta) P_{ir-1/2}(\cosh(\beta)) d\tau \quad (14)$$

$$2\mu w = \frac{P}{2\pi} \frac{zr \cos(\theta)}{R^3} - \frac{Pz}{2\pi(rr_0)^{1/2} r_0 \sinh(\beta)} \times \int_0^\infty F_1(\tau, \theta) P_{ir-1/2}(\cosh(\beta)) d\tau \quad (15)$$

$$\sigma_{rr} = -\frac{3P}{2\pi} \frac{r \cos(\theta)(r - r_0 \sin(\theta))^2}{R^5} - \frac{P}{8\pi r(rr_0)^{1/2}} \int_0^\infty F_3(\tau, \theta) P_{ir-1/2}(\cosh(\beta)) d\tau + \frac{P(r^2 - 2r_0^2 - 2z^2)}{2\pi(rr_0)^{3/2} r \sinh(\beta)} \int_0^\infty F_1(\tau, \theta) \times P_{ir-1/2}(\cosh(\beta)) d\tau - \frac{P(r^2 - r_0^2 - z^2)^2}{8\pi(rr_0)^{5/2} r \sinh^2(\beta)} \int_0^\infty F_1(\tau, \theta) \times P_{ir-1/2}(\cosh(\beta)) d\tau \quad (16)$$

$$\sigma_{\theta\theta} = -\frac{P}{2\pi} \frac{3rr_0^2 \cos^3(\theta)}{R^5} + \frac{P}{2\pi r(rr_0)^{1/2}} \int_0^\infty F_4(\tau, \theta) P_{ir-1/2}(\cosh(\beta)) d\tau \quad (17)$$

$$\sigma_{zz} = -\frac{3P}{2\pi} \frac{rz^2 \cos(\theta)}{R^5} + \frac{P}{4\pi r(rr_0)^{1/2}} \int_0^\infty F_5(\tau, \theta) P_{ir-1/2}(\cosh(\beta)) d\tau - \frac{P \coth(\beta)}{2\pi r(rr_0)^{1/2}} \int_0^\infty F_1(\tau, \theta) P_{ir-1/2}(\cosh(\beta)) d\tau - \frac{Pz^2}{2\pi(rr_0)^{3/2} r_0 \sinh^2(\beta)} \int_0^\infty F_1(\tau, \theta) \times P_{ir-1/2}(\cosh(\beta)) d\tau \quad (18)$$

$$\tau_{rz} = -\frac{3P}{2\pi} \frac{rz \cos(\theta)(r - r_0 \sin(\theta))}{R^5} + \frac{3Pz}{4\pi(rr_0)^{3/2} \sinh(\beta)} \int_0^\infty F_1(\tau, \theta) \times P_{ir-1/2}(\cosh(\beta)) d\tau - \frac{Pz(r^2 - r_0^2 - z^2)}{4\pi(rr_0)^{5/2} \sinh^2(\beta)} \int_0^\infty F_1(\tau, \theta) \times P_{ir-1/2}(\cosh(\beta)) d\tau \quad (19)$$

$$\tau_{r\theta} = \frac{3P}{2\pi} \frac{rr_0 \cos^2(\theta)(r - r_0 \sin(\theta))}{R^5} + \frac{3P}{4\pi r(rr_0)^{1/2}} \int_0^\infty F_6(\tau, \theta) P_{ir-1/2}(\cosh(\beta)) d\tau - \frac{P(r^2 - r_0^2 - z^2)}{4\pi(rr_0)^{3/2} r \sinh(\beta)} \int_0^\infty F_6(\tau, \theta) \times P_{ir-1/2}(\cosh(\beta)) d\tau \quad (20)$$

$$\tau_{z\theta} = \frac{3P}{2\pi} \frac{rr_0z \cos^2(\theta)}{R^5} - \frac{Pz}{2\pi(rr_0)^{3/2} \sinh(\beta)} \times \int_0^\infty F_6(\tau, \theta) P_{ir-1/2}^1(\cosh(\beta)) d\tau \quad (21)$$

where the functions $F_i(\tau, \theta)$ ($i = 1, \dots, 6$) are given in Appendix A and the Legendre functions are defined by the integral representation (where the zero superscript is suppressed above, $P_{ir-1/2}^0(\cosh(\beta)) = P_{ir-1/2}(\cosh(\beta))$).

$$P_{ir-1/2}^m(\cosh(\beta)) = (-1)^{m/2} 2^{1/2} \pi^{-3/2} \cosh(\pi\tau) \sinh^m(\beta) \times \int_0^\infty t^{m-1/2} e^{-t \cosh(\beta)} K_{ir}(t) dt \quad (22)$$

Some differential relations used to derive the above expressions are given in Appendix B. It is easy to verify that the closed-form term in each of these expressions represents a point force on an incompressible half-space. The integral terms are the alterations caused by the effect of the wedge which vanish for $\alpha = \pi/2$.

3 Elastic Field for Point Loading at the Edge

In this section point force loading at the wedge tip is considered. Efimov and Efimov (1986) also analyzed this case but their solution was not general since point force loading parallel to the edge was not included and the present choice of coordinates effects a simpler solution algebraically.

A first consideration might be to let $r_0 \rightarrow 0$ in the above solution. Using the result (which can be established by using Eq. (30) from Hanson and Keer (1991))

$$\lim_{r_0 \rightarrow 0} \frac{1}{(rr_0)^{1/2}} P_{ir-1/2}(\cosh(\beta)) = \frac{\cosh(\pi\tau) \delta(\tau)}{(r^2 + z^2)^{1/2}} \quad (23)$$

where $\delta(\tau)$ is the Dirac delta function, the potentials can be obtained in closed form as

$$\Phi_1 = \frac{P \sin(\alpha)}{2(\sin(2\alpha) + 2\alpha)(r^2 + z^2)^{1/2}},$$

$$\Phi_2 = \frac{P \cos(\alpha)}{2(\sin(2\alpha) - 2\alpha)(r^2 + z^2)^{1/2}}. \quad (24)$$

In this case the force is applied at the wedge tip but its direction is perpendicular to the upper wedge face and hence not a general solution.

To obtain a general solution, based on the form of the potentials above, the potentials are taken as

$$\Phi_0 = 0, \quad \Phi_i = \frac{C_i}{(r^2 + z^2)^{1/2}}, \quad i = 1, 2, 3. \quad (25)$$

This satisfies the condition that the potentials must be harmonic, have a singularity only at the origin and leads to traction-free wedge faces as seen below. The elastic field for these potentials is easily found to be ($\nu = 0.5$)

$$2\mu u = \{[C_1 \cos(\theta) + C_2 \sin(\theta)](2r^2 + z^2) + C_3 z r\} \frac{1}{(r^2 + z^2)^{3/2}} \quad (26)$$

$$2\mu v = [C_2 \cos(\theta) - C_1 \sin(\theta)] \frac{1}{(r^2 + z^2)^{1/2}} \quad (27)$$

$$2\mu w = \{[C_1 \cos(\theta) + C_2 \sin(\theta)] r z + C_3(r^2 + 2z^2)\} \frac{1}{(r^2 + z^2)^{3/2}} \quad (28)$$

$$\sigma_{\theta\theta} = \tau_{r\theta} = \tau_{z\theta} = 0 \quad (29)$$

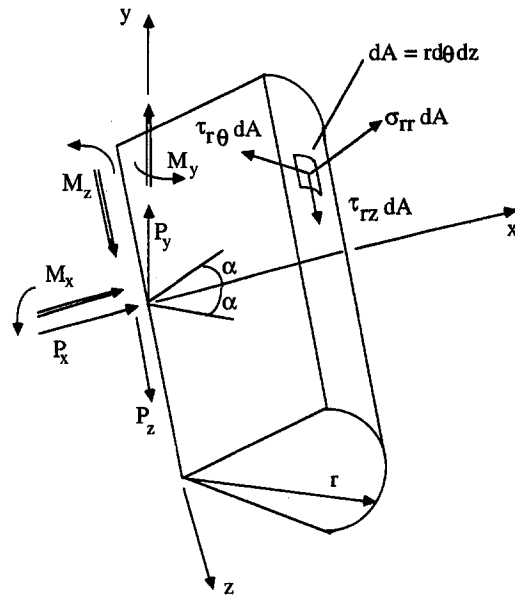


Fig. 2 Wedge section used for equilibrium loaded by point forces and moments at the origin

$$\sigma_{rr} = -3\{[C_1 \cos(\theta) + C_2 \sin(\theta)] r^3 + C_3 z r^2\} \frac{1}{(r^2 + z^2)^{5/2}} \quad (30)$$

$$\sigma_{zz} = -\{[C_1 \cos(\theta) + C_2 \sin(\theta)](2r^3 + 3rz^2) + 3C_3 z^3\} \frac{1}{(r^2 + z^2)^{5/2}} \quad (31)$$

$$\tau_{rz} = -3\{[C_1 \cos(\theta) + C_2 \sin(\theta)] r^2 z + C_3 r z^2\} \frac{1}{(r^2 + z^2)^{5/2}}. \quad (32)$$

In order to determine the constants C_1, C_2, C_3 , equilibrium of a portion of the wedge tip with radius r shown in Fig. 2 is considered. Point forces are applied at the origin in the positive x, y , and z directions, where the x -axis is located in the midplane of the wedge. Force equilibrium of this element leads to the relations

$$P_x = -\int_{-\infty}^{\infty} \int_{-\alpha}^{\alpha} [\cos(\theta) \sigma_{rr} - \sin(\theta) \tau_{r\theta}] r d\theta dz \quad (33)$$

$$P_y = -\int_{-\infty}^{\infty} \int_{-\alpha}^{\alpha} [\sin(\theta) \sigma_{rr} + \cos(\theta) \tau_{r\theta}] r d\theta dz \quad (34)$$

$$P_z = -\int_{-\infty}^{\infty} \int_{-\alpha}^{\alpha} \tau_{rz} r d\theta dz. \quad (35)$$

Substituting the stress field into the above integrals leads to the following values for the constants:

$$C_1 = \frac{P_x}{2(2\alpha + \sin(2\alpha))}, \quad C_2 = \frac{P_y}{2(2\alpha - \sin(2\alpha))},$$

$$C_3 = \frac{P_z}{12\alpha}. \quad (36)$$

It can also be shown by using Eqs. (66)–(68) below that the above stress fields give no net moment on the element of the wedge shown in Fig. 2 ($M_x = M_y = M_z = 0$). The above solutions for point force loading are valid for any wedge angle since the denominators in Eq. (36) are never zero (except when $\alpha = 0$).

4 Elastic Field for Concentrated Moment Loading

In this section the elastic field is derived for the case when a concentrated moment is applied on the upper surface of the wedge, all other surface stresses taken to be zero. The moments to be considered are shown in Fig. 1 ($P = 0$). The moments M_r and M_z are applied at the point $r = r_0, z = 0, \theta = \alpha$ with moment vectors pointing in the positive r and z directions, respectively.

The solution for M_z can be obtained by differentiating with respect to r_0 the solution in Section 2 for a point normal force and replacing P with $-M_z$. Using this procedure leads to the following results:

$$2\mu u = \frac{M_z \cos(\theta)}{2\pi} \left\{ \frac{r_0}{R^3} + \frac{3r(r - r_0 \sin(\theta))(r_0 - r \sin(\theta))}{R^5} \right\} + \frac{3M_z}{8\pi r_0 (r r_0)^{1/2}} \int_0^\infty F_1(\tau, \theta) P_{ir-1/2}(\cosh(\beta)) d\tau + \frac{M_z(3z^2 - 2r_0^2)}{4\pi (r r_0)^{3/2} r_0 \sinh(\beta)} \int_0^\infty F_1(\tau, \theta) \times P_{ir-1/2}^1(\cosh(\beta)) d\tau - \frac{M_z(r^2 - r_0^2)^2}{8\pi (r r_0)^{5/2} r_0 \sinh^2(\beta)} \int_0^\infty F_1(\tau, \theta) \times P_{ir-1/2}^2(\cosh(\beta)) d\tau \quad (37)$$

$$2\mu v = \frac{M_z}{2\pi} \left\{ \frac{(r - r_0 \sin(\theta))}{R^3} - \frac{3rr_0 \cos^2(\theta)(r_0 - r \sin(\theta))}{R^5} \right\} + \frac{M_z}{4\pi r_0 (r r_0)^{1/2}} \int_0^\infty F_2(\tau, \theta) P_{ir-1/2}(\cosh(\beta)) d\tau - \frac{M_z(r_0^2 - r^2 - z^2)}{4\pi (r r_0)^{3/2} r_0 \sinh(\beta)} \int_0^\infty F_2(\tau, \theta) \times P_{ir-1/2}^1(\cosh(\beta)) d\tau \quad (38)$$

$$2\mu w = \frac{3M_z z r \cos(\theta)(r_0 - r \sin(\theta))}{2\pi R^5} - \frac{3M_z z}{4\pi (r r_0)^{1/2} r_0^2 \sinh(\beta)} \int_0^\infty F_1(\tau, \theta) \times P_{ir-1/2}^1(\cosh(\beta)) d\tau + \frac{M_z z (r_0^2 - r^2 - z^2)}{4\pi (r r_0)^{3/2} r_0^2 \sinh^2(\beta)} \int_0^\infty F_1(\tau, \theta) \times P_{ir-1/2}^2(\cosh(\beta)) d\tau \quad (39)$$

$$\sigma_{rr} = -\frac{3M_z r \cos(\theta)(r - r_0 \sin(\theta))}{2\pi} \times \left\{ \frac{2 \sin(\theta)}{R^5} + \frac{5(r - r_0 \sin(\theta))(r_0 - r \sin(\theta))}{R^7} \right\} - \frac{M_z}{16\pi (r r_0)^{3/2}} \int_0^\infty F_3(\tau, \theta) P_{ir-1/2}(\cosh(\beta)) d\tau + \frac{M_z(r_0^2 - r^2 - z^2)}{16\pi (r r_0)^{5/2} \sinh(\beta)} \int_0^\infty F_3(\tau, \theta) \times P_{ir-1/2}^1(\cosh(\beta)) d\tau - \frac{M_z(6z^2 - 3r^2 - 2r_0^2)}{4\pi (r r_0)^{5/2} \sinh(\beta)} \int_0^\infty F_1(\tau, \theta) \times P_{ir-1/2}^1(\cosh(\beta)) d\tau$$

$$+ \frac{M_z(11r_0^4 - 9r^4 - 13z^4 + 6r^2z^2 - 2z^2r_0^2 - 10r^2r_0^2)}{16\pi (r r_0)^{7/2} \sinh^2(\beta)} \times \int_0^\infty F_1(\tau, \theta) P_{ir-1/2}^2(\cosh(\beta)) d\tau + \frac{M_z(r^2 - r_0^2 - z^2)^2(r_0^2 - r^2 - z^2)}{16\pi (r r_0)^{9/2} \sinh^3(\beta)} \times \int_0^\infty F_1(\tau, \theta) P_{ir-1/2}^3(\cosh(\beta)) d\tau \quad (40)$$

$$\sigma_{\theta\theta} = \frac{3M_z r r_0 \cos^3(\theta)}{2\pi} \left\{ \frac{2}{R^5} - \frac{5r_0(r_0 - r \sin(\theta))}{R^7} \right\} + \frac{M_z}{4\pi (r r_0)^{3/2}} \int_0^\infty F_4(\tau, \theta) P_{ir-1/2}(\cosh(\beta)) d\tau - \frac{M_z(r_0^2 - r^2 - z^2)}{4\pi (r r_0)^{5/2} \sinh(\beta)} \int_0^\infty F_4(\tau, \theta) \times P_{ir-1/2}^1(\cosh(\beta)) d\tau \quad (41)$$

$$\sigma_{zz} = -\frac{15M_z r z^2 \cos(\theta)(r_0 - r \sin(\theta))}{2\pi R^7} + \frac{M_z}{8\pi (r r_0)^{3/2}} \int_0^\infty F_5(\tau, \theta) P_{ir-1/2}(\cosh(\beta)) d\tau - \frac{M_z(r_0^2 - r^2 - z^2)}{8\pi (r r_0)^{5/2} \sinh(\beta)} \int_0^\infty F_5(\tau, \theta) \times P_{ir-1/2}^1(\cosh(\beta)) d\tau + \frac{M_z(r_0^2 - 3r^2 - 3z^2)}{8\pi (r r_0)^{5/2} \sinh(\beta)} \int_0^\infty F_1(\tau, \theta) \times P_{ir-1/2}^1(\cosh(\beta)) d\tau + \frac{M_z(r_0^3 - r_0r^2 - r_0z^2 - 5rz^2)}{4\pi (r r_0)^{5/2} r_0 \sinh^2(\beta)} \times \int_0^\infty F_1(\tau, \theta) P_{ir-1/2}^2(\cosh(\beta)) d\tau + \frac{M_z z^2 (r_0^2 - r^2 - z^2)}{4\pi (r r_0)^{5/2} r_0^2 \sinh^3(\beta)} \int_0^\infty F_1(\tau, \theta) \times P_{ir-1/2}^3(\cosh(\beta)) d\tau \quad (42)$$

$$\tau_{rz} = \frac{3M_z r z \cos(\theta)}{2\pi} \times \left\{ -\frac{\sin(\theta)}{R^5} - \frac{5(r - r_0 \sin(\theta))(r_0 - r \sin(\theta))}{R^7} \right\} + \frac{9M_z z}{8\pi (r r_0)^{3/2} r_0 \sinh(\beta)} \int_0^\infty F_1(\tau, \theta) \times P_{ir-1/2}^1(\cosh(\beta)) d\tau + \frac{M_z z (4z^2 - r^2 - r_0^2)}{4\pi (r r_0)^{5/2} r_0 \sinh^2(\beta)} \int_0^\infty F_1(\tau, \theta) \times P_{ir-1/2}^2(\cosh(\beta)) d\tau + \frac{M_z z (r^2 - r_0^2 - z^2)(r_0^2 - r^2 - z^2)}{8\pi (r r_0)^{7/2} r_0 \sinh^3(\beta)} \times \int_0^\infty F_1(\tau, \theta) P_{ir-1/2}^3(\cosh(\beta)) d\tau \quad (43)$$

$$\begin{aligned} \tau_{r\theta} = & -\frac{3M_z r \cos^2(\theta)}{2\pi} \left\{ \frac{r - 2r_0 \sin(\theta)}{R^5} \right. \\ & \left. - \frac{5r_0(r - r_0 \sin(\theta))(r_0 - r \sin(\theta))}{R^7} \right\} \\ & + \frac{3M_z}{8\pi(rr_0)^{3/2}} \int_0^\infty F_6(\tau, \theta) P_{ir-1/2}(\cosh(\beta)) d\tau \\ & + \frac{M_z(3z^2 - 2r_0^2)}{4\pi(rr_0)^{5/2} \sinh(\beta)} \int_0^\infty F_6(\tau, \theta) \\ & \times P_{ir-1/2}^1(\cosh(\beta)) d\tau \\ & + \frac{M_z(r^2 - r_0^2 - z^2)(r_0^2 - r^2 - z^2)}{8\pi(rr_0)^{7/2} \sinh^2(\beta)} \\ & \times \int_0^\infty F_6(\tau, \theta) P_{ir-1/2}^2(\cosh(\beta)) d\tau \quad (44) \end{aligned}$$

$$\begin{aligned} \tau_{z\theta} = & -\frac{3M_z r \cos^2(\theta)}{2\pi} \left\{ \frac{1}{R^5} - \frac{5r_0(r_0 - r \sin(\theta))}{R^7} \right\} \\ & - \frac{3M_z z}{4\pi(rr_0)^{3/2} r_0 \sinh(\beta)} \int_0^\infty F_6(\tau, \theta) \\ & \times P_{ir-1/2}^1(\cosh(\beta)) d\tau \\ & + \frac{M_z z(r_0^2 - r^2 - z^2)}{4\pi(rr_0)^{5/2} r_0 \sinh^2(\beta)} \int_0^\infty F_6(\tau, \theta) \\ & \times P_{ir-1/2}^2(\cosh(\beta)) d\tau \quad (45) \end{aligned}$$

The solution for M_r can be obtained by differentiating with respect to z the solution in Section 2 for a point normal force and replacing P with $-M_r$. This leads to the following results:

$$\begin{aligned} 2\mu u = & \frac{M_r z \cos(\theta)}{2\pi} \left\{ \frac{1}{R^3} + \frac{3r(r - r_0 \sin(\theta))}{R^5} \right\} \\ & - \frac{5zM_r}{4\pi(rr_0)^{3/2} \sinh(\beta)} \int_0^\infty F_1(\tau, \theta) \\ & \times P_{ir-1/2}^1(\cosh(\beta)) d\tau \\ & + \frac{M_r z(r^2 - r_0^2 - z^2)}{4\pi(rr_0)^{5/2} \sinh^2(\beta)} \int_0^\infty F_1(\tau, \theta) \\ & \times P_{ir-1/2}^2(\cosh(\beta)) d\tau \quad (46) \end{aligned}$$

$$\begin{aligned} 2\mu v = & -\frac{M_r z}{2\pi} \left\{ \frac{\sin(\theta)}{R^3} + \frac{3rr_0 \cos^2(\theta)}{R^5} \right\} \\ & - \frac{M_r z}{2\pi(rr_0)^{3/2} \sinh(\beta)} \int_0^\infty F_2(\tau, \theta) \\ & \times P_{ir-1/2}^1(\cosh(\beta)) d\tau \quad (47) \end{aligned}$$

$$\begin{aligned} 2\mu w = & -\frac{M_r r \cos(\theta)}{2\pi} \left\{ \frac{1}{R^3} - \frac{3z^2}{R^5} \right\} \\ & + \frac{M_r}{2\pi(rr_0)^{1/2} r_0 \sinh(\beta)} \int_0^\infty F_1(\tau, \theta) \\ & \times P_{ir-1/2}^1(\cosh(\beta)) d\tau \\ & + \frac{M_r z^2}{2\pi(rr_0)^{3/2} r_0 \sinh^2(\beta)} \int_0^\infty F_1(\tau, \theta) \\ & \times P_{ir-1/2}^2(\cosh(\beta)) d\tau \quad (48) \end{aligned}$$

$$\begin{aligned} \sigma_{rr} = & -\frac{15M_r z r \cos(\theta)(r - r_0 \sin(\theta))^2}{2\pi R^7} \\ & + \frac{M_r z}{8\pi r(rr_0)^{3/2} \sinh(\beta)} \int_0^\infty F_8(\tau, \theta) \\ & \times P_{ir-1/2}^1(\cosh(\beta)) d\tau \\ & - \frac{M_r z(2r^2 - 3z^2 - 3r_0^2)}{2\pi r(rr_0)^{5/2} \sinh^2(\beta)} \int_0^\infty F_1(\tau, \theta) \\ & \times P_{ir-1/2}^2(\cosh(\beta)) d\tau \\ & + \frac{M_r z(r^2 - r_0^2 - z^2)^2}{8\pi r(rr_0)^{7/2} \sinh^3(\beta)} \int_0^\infty F_1(\tau, \theta) \\ & \times P_{ir-1/2}^3(\cosh(\beta)) d\tau \quad (49) \end{aligned}$$

$$\begin{aligned} \sigma_{\theta\theta} = & -\frac{15M_r z r r_0^2 \cos^3(\theta)}{2\pi R^7} \\ & - \frac{M_r z}{2\pi r(rr_0)^{3/2} \sinh(\beta)} \int_0^\infty F_4(\tau, \theta) \\ & \times P_{ir-1/2}^1(\cosh(\beta)) d\tau \quad (50) \end{aligned}$$

$$\begin{aligned} \sigma_{zz} = & \frac{3M_z r \cos(\theta)}{2\pi} \left\{ \frac{2}{R^5} - \frac{5z^2}{R^7} \right\} \\ & + \frac{M_r z}{4\pi r(rr_0)^{3/2} \sinh(\beta)} \int_0^\infty F_7(\tau, \theta) \\ & \times P_{ir-1/2}^1(\cosh(\beta)) d\tau \\ & + \frac{M_r z(r_0^2 + 5r^2 + z^2)}{4\pi r(rr_0)^{5/2} \sinh^2(\beta)} \int_0^\infty F_1(\tau, \theta) \\ & \times P_{ir-1/2}^2(\cosh(\beta)) d\tau \\ & + \frac{M_r z^3}{2\pi(rr_0)^{5/2} r_0 \sinh^3(\beta)} \int_0^\infty F_1(\tau, \theta) \\ & \times P_{ir-1/2}^3(\cosh(\beta)) d\tau \quad (51) \end{aligned}$$

$$\begin{aligned} \tau_{rz} = & \frac{3M_r r \cos(\theta)(r - r_0 \sin(\theta))}{2\pi} \left\{ \frac{1}{R^5} - \frac{5z^2}{R^7} \right\} \\ & - \frac{3M_r}{4\pi(rr_0)^{3/2} \sinh(\beta)} \int_0^\infty F_1(\tau, \theta) \\ & \times P_{ir-1/2}^1(\cosh(\beta)) d\tau \\ & + \frac{M_r(r^2 - r_0^2 - 6z^2)}{4\pi(rr_0)^{5/2} \sinh^2(\beta)} \int_0^\infty F_1(\tau, \theta) \\ & \times P_{ir-1/2}^2(\cosh(\beta)) d\tau \\ & + \frac{M_r z^2(r^2 - r_0^2 - z^2)}{4\pi(rr_0)^{7/2} \sinh^3(\beta)} \int_0^\infty F_1(\tau, \theta) \\ & \times P_{ir-1/2}^3(\cosh(\beta)) d\tau \quad (52) \end{aligned}$$

$$\begin{aligned} \tau_{r\theta} = & \frac{15M_r z r r_0 \cos^2(\theta)(r - r_0 \sin(\theta))}{2\pi R^7} \\ & - \frac{5M_r z}{4\pi r(rr_0)^{3/2} \sinh(\beta)} \int_0^\infty F_6(\tau, \theta) \\ & \times P_{ir-1/2}^1(\cosh(\beta)) d\tau \\ & + \frac{M_r z(r^2 - r_0^2 - z^2)}{4\pi r(rr_0)^{5/2} \sinh^2(\beta)} \int_0^\infty F_6(\tau, \theta) \\ & \times P_{ir-1/2}^2(\cosh(\beta)) d\tau \quad (53) \end{aligned}$$

$$\begin{aligned} \tau_{z\theta} = & -\frac{3M_r r r_0 \cos^2(\theta)}{2\pi} \left\{ \frac{1}{R^5} - \frac{5z^2}{R^7} \right\} \\ & + \frac{M_r}{2\pi(r r_0)^{3/2} \sinh(\beta)} \int_0^\infty F_6(\tau, \theta) \\ & \times P_{ir-1/2}^1(\cosh(\beta)) d\tau \\ & + \frac{M_r z^2}{2\pi(r r_0)^{5/2} \sinh^2(\beta)} \int_0^\infty F_6(\tau, \theta) \\ & \times P_{ir-1/2}^2(\cosh(\beta)) d\tau. \quad (54) \end{aligned}$$

5 Elastic Field for Point Couples at the Edge

The solution for concentrated couples applied at a point on the edge of the wedge is now considered. Taking a limit of the above equations would provide a solution but not a general one. To get a general solution for the moments M_x , M_y , and M_z applied at the origin as shown in Fig. 2 ($P_x = P_y = P_z = 0$), we proceed as in Section 3. The potentials are now taken as

$$\begin{aligned} \Phi_0 = \Phi_3 = 0 \\ \Phi_1 = \frac{C_1 r \sin(\theta) + D_1 z}{(r^2 + z^2)^{3/2}}, \quad \Phi_2 = \frac{C_2 r \cos(\theta) + D_2 z}{(r^2 + z^2)^{3/2}}. \quad (55) \end{aligned}$$

This choice of harmonic functions leads to the elastic field

$$2\mu u = \frac{3[C_1 + C_2]r^3 \cos(\theta) \sin(\theta) + [D_1 \cos(\theta) + D_2 \sin(\theta)]z(4r^2 + z^2)}{(r^2 + z^2)^{5/2}} \quad (56)$$

$$2\mu v = \frac{[C_2 - C_1]r + [D_2 \cos(\theta) - D_1 \sin(\theta)]z}{(r^2 + z^2)^{3/2}} \quad (57)$$

$$2\mu w = \frac{3[C_1 + C_2]r^2 z \cos(\theta) \sin(\theta) + [D_1 \cos(\theta) + D_2 \sin(\theta)]r(2z^2 - r^2)}{(r^2 + z^2)^{5/2}} \quad (58)$$

$$\sigma_{\theta\theta} = 0 \quad (59)$$

$$\tau_{r\theta} = \frac{3[C_1 \cos^2(\theta) - C_2 \sin^2(\theta)]r^2}{(r^2 + z^2)^{5/2}} \quad (60)$$

$$\tau_{z\theta} = \frac{3[C_1 \cos^2(\theta) - C_2 \sin^2(\theta)]zr}{(r^2 + z^2)^{5/2}} \quad (61)$$

$$\sigma_{rr} = \frac{3[C_1 + C_2]r^2 \cos(\theta) \sin(\theta)(2z^2 - 3r^2) - 15[D_1 \cos(\theta) + D_2 \sin(\theta)]zr^3}{(r^2 + z^2)^{7/2}} \quad (62)$$

$$\sigma_{zz} = \frac{-15[C_1 + C_2]r^2 z^2 \cos(\theta) \sin(\theta) + 3[D_1 \cos(\theta) + D_2 \sin(\theta)]zr(2r^2 - 3z^2)}{(r^2 + z^2)^{7/2}} \quad (63)$$

$$\tau_{rz} = \frac{-3[C_1 + C_2]rz \cos(\theta) \sin(\theta)(4r^2 - z^2) + 3[D_1 \cos(\theta) + D_2 \sin(\theta)]r^2(r^2 - 4z^2)}{(r^2 + z^2)^{7/2}} \quad (64)$$

From Eqs. (59)–(61) it is apparent that the wedge surfaces are stress free if

$$C_1 \cos^2(\alpha) = C_2 \sin^2(\alpha). \quad (65)$$

If the stress field above is substituted into Eqs. (33)–(35) and use is made of Eq. (65), it is easily shown that the net force resulting from the above stresses is zero. The unknown constants can be found from the moment relations resulting from equilibrium of Fig. 2 as

$$M_x = -\int_{-\infty}^{\infty} \int_{-\alpha}^{\alpha} [r \sin(\theta) \tau_{rz} - z \sigma_{rr} \sin(\theta) - z \tau_{r\theta} \cos(\theta)] r d\theta dz \quad (66)$$

$$M_y = -\int_{-\infty}^{\infty} \int_{-\alpha}^{\alpha} [z \cos(\theta) \sigma_{rr} - z \sin(\theta) \tau_{r\theta} - r \cos(\theta) \tau_{rz}] r d\theta dz \quad (67)$$

$$M_z = -\int_{-\infty}^{\infty} \int_{-\alpha}^{\alpha} r \tau_{r\theta} r d\theta dz \quad (68)$$

Substituting the stress field into the above equations and using Eq. (65) determines the constants as

$$C_1 = \frac{M_z \sin^2(\alpha)}{2[2\alpha \cos(2\alpha) - \sin(2\alpha)]},$$

$$C_2 = \frac{M_z \cos^2(\alpha)}{2[2\alpha \cos(2\alpha) - \sin(2\alpha)]} \quad (69)$$

$$D_1 = \frac{M_y}{2[2\alpha + \sin(2\alpha)]},$$

$$D_2 = -\frac{M_x}{2[2\alpha - \sin(2\alpha)]} \quad (70)$$

It was pointed out by Dundurs that Eqs. (66)–(68) may not be a strong enough requirement to eliminate other second-order (self-equilibrated) singularities such as a center of dilatation or a force dipole without moment. Indeed, the presence of an additional self-equilibrated singularity of this type might be a possibility since the procedure in this section was to guess a form of the potentials and only the net force and net moment equilibrium conditions were enforced to evaluate the unknown constants. In order to make a definitive statement on this matter, the solution in Section 4 is again considered. In this section the elastic field for two concentrated moments M_r and M_z applied to the upper wedge face were evaluated. These solutions were obtained by taking a single force doublet and thus can not contain any other second-order self-equilibrated singularities. The nonintegral closed-form terms in these expressions correspond to the incompressible half-space result for each couple. The integral terms all vanish for $\alpha = \pi/2$. If one lets $r_0 \rightarrow 0$ in these half-space expressions the solutions for M_r and M_z applied at the origin are obtained. This half-space result is in exact agreement with the solution in this section for M_z when $\alpha = \pi/2$ in Eq. (69). Furthermore, the half-space solution for M_r at the origin in the previous section agrees with the solution for M_r above with $\alpha = \pi/2$ in Eq. (70).

After a further consideration of this matter it was also recognized that the solution for the couple M_y positioned at the edge for an arbitrary wedge angle could be obtained by differentiating the solution for P_x in Section 3 with respect to z and replacing P_x with $-M_y$. This leads directly to the solution for M_y above. Similarly, taking the solution for P_y in Section 3, differentiating with respect to z and replacing P_y with M_x also leads to the general solution for M_x above. The solution for M_z can not be obtained in this way. In light of the above comments, it is most probable that additional self-equilibrated second-order singularities are not present in the solution of this section.

6 Discussion and Conclusions

The results derived in this paper present the closed-form expressions to various concentrated loadings applied to an incompressible wedge. In most cases the solutions are well behaved, exhibiting a displacement or stress singularity only at the location of the concentrated action (force or moment). However, in some situations an additional singularity will arise. If the wedge angle is larger than 90 deg (half-space) there will

be an additional singularity at the apex of the wedge. In this case the wedge resembles a notch, and a power singularity in the stress field should result. If the wedge angle takes on the value $\alpha = \pi$, the wedge becomes a full space with a half-plane crack. In this case the stress field should exhibit the well-known square root singularity as the crack front is approached.

The solution derived in Section 5, for concentrated couples at the edge, also exhibits a singularity in addition to that noted above. From Eq. (69) for the concentrated moment M_z , the denominator contains the quantity $2\alpha \cos(2\alpha) - \sin(2\alpha)$. This is identical to the denominator in the Airy stress function for the plane-strain problem. This term, and hence the denominator in the displacement and stress fields becomes zero at an angle of $\alpha = .715\pi$. Thus, the solution for the entire elastic field becomes infinite as this wedge angle is approached. It was this pathological behavior in the two-dimensional solution which motivated, in part, the present three-dimensional investigation. The two-dimensional plane-strain solution is a line couple uniformly distributed along the edge and hence the total moment applied to the wedge is infinite. It was questioned whether the three-dimensional counterpart to this problem would display analogous behavior when there is only a point couple along the edge, the total moment being finite. The present three-dimensional solution as noted above displays identical behavior, at least for the incompressible wedge. In retrospect this is not so surprising since three-dimensional incompressible solutions in elasticity behave very similar to their two-dimensional counterparts.

However, there is another very interesting result in the present analysis which has not been previously reported in the literature. The solution in Section 5 also considers the concentrated couples M_x and M_y . It is apparent that the solution for each of these moments is not singular for any wedge angle greater than zero. The reason as to why these solutions do not behave pathologically and the solution for M_z does puzzled the author. It was not until consideration was given to the possibility of other second-order self-equilibrated singularities as mentioned above that the reason for this was revealed. At the end of Section 5 it was pointed out that the solutions for the moments M_x and M_y , applied at the edge could be obtained by differentiation with respect to z the solutions in Section 3 for P_x and P_y . Hence the denominator in the solution for M_y is identical to the denominator in the solution for P_x . Similarly, the denominator in the solution for M_x is identical to the denominator in the solution for P_y . Therefore, the well behaved point force solutions in the x and y directions dictate that these two concentrated couple solutions must also be well behaved. Since a similar procedure can not be applied to obtain the solution for M_z at the edge, a restriction on the behavior of this solution can not be inferred.

In conclusion, the only anomalous behavior occurs for the moment with the M_z orientation. A detailed investigation into the cause of this behavior for the moment M_z has been conducted by Sternberg and Koiter (1958), Dempsey (1981), Ting (1984, 1985), and Dundurs and Markenscoff (1989) as well as the references mentioned therein.

Acknowledgment

Partial support during the course of this investigation is gratefully acknowledged from the National Science Foundation under grant number MSS-9210531. The author is also grateful to Prof. John Dundurs for his thought provoking comments on the possibility of self-equilibrated second-order singularities existing in the solutions derived in Section 5.

References

Babeshko, V. A., and Berkovich, V. N., 1972, "On the Theory of Mixed Problems for the Three-Dimensional Wedge," *PMM*, Vol. 36, pp. 892-896.
Benitez, F. G., and Rosakis, A. J., 1987, "Three-Dimensional Elastostatics of a Layer and a Layered Medium," *Journal of Elasticity*, Vol. 18, pp. 3-50.

Berkovich, V. N., 1974, "Some Contact Problems for a Three-Dimensional Wedge with a Finite Number of Contact Regions," *PMM*, Vol. 38, pp. 344-350.
Chen, W. T., 1965, "Stresses in a Transversely Isotropic Elastic Cone Under an Asymmetric Force at its Vertex," *ZAMP*, Vol. 16, pp. 337-344.
Dempsey, J. P., 1981, "The Wedge Subjected to Tractions: A Paradox Resolved," *J. Elasticity*, Vol. 11, pp. 1-10.
Dundurs, J., 1994, personal communication.
Dundurs, J., and Markenscoff, X., 1989, "The Sternberg-Koiter Conclusion and Other Anomalies of the Concentrated Couple," *ASME JOURNAL OF APPLIED MECHANICS*, Vol. 56, pp. 240-245.
Dundurs, J., and Hetenyi, M., 1965, "Transmission of Force Between Two Semi-Infinite Solids," *ASME JOURNAL OF APPLIED MECHANICS*, Vol. 32, pp. 377-386.
Efimov, A. B., and Efimov, D. G., 1986, "Concentrated Actions Applied to an Elastic Incompressible Wedge," *Mechanics of Solids*, Vol. 21, No. 6, pp. 83-86.
Hanson, M. T., and Keer, L. M., 1990, "A Simplified Analysis for an Elastic Quarter Space," *Quarterly Journal of Mechanics and Applied Mathematics*, Vol. 43, pp. 561-587.
Hanson, M. T., and Keer, L. M., 1991, "Analysis of Edge Effects on Rail-Wheel Contact," *Wear*, Vol. 144, pp. 39-55.
Hanson, M. T., Xu, Y., and Keer, L. M., 1994, "Stress Analysis for a Three-Dimensional Incompressible Wedge Under Body Force or Surface Loading," *Quarterly Journal of Mechanics and Applied Mathematics*, Vol. 47, pp. 141-158.
Hetenyi, M., 1970, "A General Solution for the Elastic Quarter Space," *ASME JOURNAL OF APPLIED MECHANICS*, Vol. 37, pp. 70-76.
Keer, L. M., Lee, J. C., and Mura, T., 1983, "Hetenyi's Elastic Quarter Space Problem Revisited," *Int. J. Solids Structures*, Vol. 19, pp. 497-508.
Keer, L. M., Lee, J. C., and Mura, T., 1984, "A Contact Problem for the Elastic Quarter Space," *Int. J. Solids Structures*, Vol. 20, pp. 513-524.
Knops, R. J., 1958, "On the Variation of Poisson's Ratio in the Solution of Elastic Problems," *Quarterly Journal of Mechanics and Applied Mathematics*, Vol. 11, pp. 326-350.
Lekhnitskii, S. G., 1963, *Theory of Elasticity of an Anisotropic Body*, Holden-Day, pp. 383-389.
Love, A. E. H., 1927, *A Treatise on the Mathematical Theory of Elasticity*, Dover, pp. 201-203.
Lure, A. I., 1964, *Three-Dimensional Problems of the Theory of Elasticity*, Interscience Publishers, pp. 137-144.
Mindlin, R. D., 1936, "Force at a Point in the Interior of a Semi-Infinite Solid," *Physica*, Vol. 7, pp. 195-202.
Mura, T., 1982, *Micromechanics of Defects in Solids*, 1st ed., Martinus Nijhoff, pp. 37-46.
Pan, Y. C., and Chou, T. W., 1976, "Point Force Solution for an Infinite Transversely Isotropic Solid," *ASME JOURNAL OF APPLIED MECHANICS*, Vol. 43, pp. 608-612.
Rongved, L., 1955, "Force Interior to One of Two Joined Semi-Infinite Solids," *Proceedings of the 2nd Midwestern Conference on Solid Mechanics*, pp. 1-13.
Sternberg, E., and Koiter, W. T., 1958, "The Wedge Under a Concentrated Couple: A Paradox in the Two-Dimensional Theory of Elasticity," *ASME JOURNAL OF APPLIED MECHANICS*, Vol. 25, pp. 575-581.
Ting, T. C. T., 1984, "The Wedge Subjected to Tractions: a Paradox Re-examined," *J. Elasticity*, Vol. 14, pp. 235-247.
Ting, T. C. T., 1985, "A Paradox on the Elastic Wedge Subjected to a Concentrated Couple and on the Jeffery-Hammal Viscous Flow Problem," *Zeit. Ang. Math. Mech.*, Vol. 65, pp. 188-190.
Uflyand, Y. S., 1965, *Survey of Articles on the Applications of Integral Transforms in the Theory of Elasticity*, North Carolina State University, Applied Mathematics Research Group, File No. PSR-24/6, pp. 342-383.

APPENDIX A

The functions $F_i(\tau, \theta)$ ($i = 1, \dots, 8$) are defined as

$$F_1(\tau, \theta) = \cos(\theta)A(\tau, \theta) + \sin(\theta)B(\tau, \theta) \quad (A1)$$

$$F_2(\tau, \theta) = \cos(\theta)B(\tau, \theta) - \sin(\theta)A(\tau, \theta) - \cos(\theta) \frac{\partial A(\tau, \theta)}{\partial \theta} - \sin(\theta) \frac{\partial B(\tau, \theta)}{\partial \theta} \quad (A2)$$

$$F_3(\tau, \theta) = 5 \cos(\theta)A(\tau, \theta) + 5 \sin(\theta)B(\tau, \theta) + 4 \sin(\theta) \frac{\partial A(\tau, \theta)}{\partial \theta} - 4 \cos(\theta) \frac{\partial B(\tau, \theta)}{\partial \theta} \quad (A3)$$

$$F_4(\tau, \theta) = \cos(\theta) \frac{\partial B(\tau, \theta)}{\partial \theta} - \sin(\theta) \frac{\partial A(\tau, \theta)}{\partial \theta} - \cos(\theta)\tau^2 A(\tau, \theta) - \sin(\theta)\tau^2 B(\tau, \theta) \quad (A4)$$

$$F_5(\tau, \theta) = 2 \cos(\theta) \frac{\partial B(\tau, \theta)}{\partial \theta} - 2 \sin(\theta) \frac{\partial A(\tau, \theta)}{\partial \theta} - \cos(\theta)A(\tau, \theta) - \sin(\theta)B(\tau, \theta) \quad (A5)$$

$$F_6(\tau, \theta) = \cos(\theta) \frac{\partial A(\tau, \theta)}{\partial \theta} + \sin(\theta) \frac{\partial B(\tau, \theta)}{\partial \theta} \quad (\text{A6})$$

$$F_7(\tau, \theta) = 3 \cos(\theta) A(\tau, \theta) + 3 \sin(\theta) B(\tau, \theta) - 2 \cos(\theta) \frac{\partial B(\tau, \theta)}{\partial \theta} + 2 \sin(\theta) \frac{\partial A(\tau, \theta)}{\partial \theta} \quad (\text{A7})$$

$$F_8(\tau, \theta) = 21 \cos(\theta) A(\tau, \theta) + 21 \sin(\theta) B(\tau, \theta) + 4 \sin(\theta) \frac{\partial A(\tau, \theta)}{\partial \theta} - 4 \cos(\theta) \frac{\partial B(\tau, \theta)}{\partial \theta} \quad (\text{A8})$$

where $A(\tau, \theta)$ and $B(\tau, \theta)$ are defined in Eq. (11) and their derivatives are

$$\begin{aligned} \frac{\partial A(\tau, \theta)}{\partial \theta} &= \frac{\tau}{D(\tau) \cosh(\pi\tau)} \\ &\times \left\{ r_1(\tau) \tau \sinh(\pi\tau) \cosh[\tau(\theta + \alpha)] \right. \\ &\quad \left. - r_2(\tau) \tau \sinh(\pi\tau) \cosh[\tau(\theta - \alpha)] \right. \\ &\quad \left. - D(\tau) \sinh\left[\tau\left(\theta + \frac{\pi}{2}\right)\right] \right\} \quad (\text{A9}) \end{aligned}$$

$$\begin{aligned} \frac{\partial B(\tau, \theta)}{\partial \theta} &= \frac{\tau^2 \tanh(\pi\tau)}{D(\tau)} \{ q_1(\tau) \cosh[\tau(\theta + \alpha)] \\ &\quad - q_2(\tau) \cosh[\tau(\theta - \alpha)] \}. \quad (\text{A10}) \end{aligned}$$

APPENDIX B

Some useful differential relationships for the Legendre functions used here can be obtained from Eq. (22). For example it is easy to show that

$$\frac{\partial}{\partial \beta} P_{ir-1/2}(\cosh(\beta)) = P_{ir-1/2}^1(\cosh(\beta)) \quad (\text{B1})$$

$$\begin{aligned} \frac{\partial}{\partial \beta} P_{ir-1/2}^1(\cosh(\beta)) \\ = \coth(\beta) P_{ir-1/2}^1(\cosh(\beta)) + P_{ir-1/2}^2(\cosh(\beta)). \quad (\text{B2}) \end{aligned}$$

Using these results, the chain rule and the definition for β in Eq. (12) the following derivatives can be obtained:

$$\frac{\partial}{\partial r} P_{ir-1/2}(\cosh(\beta)) = P_{ir-1/2}^1(\cosh(\beta)) \frac{\partial \beta}{\partial r} \quad (\text{B3})$$

$$\frac{\partial}{\partial z} P_{ir-1/2}(\cosh(\beta)) = P_{ir-1/2}^1(\cosh(\beta)) \frac{\partial \beta}{\partial z} \quad (\text{B4})$$

$$\frac{\partial \beta}{\partial r} = \frac{r^2 - r_0^2 - z^2}{2r^2 r_0 \sinh(\beta)}, \quad \frac{\partial \beta}{\partial z} = \frac{z}{r r_0 \sinh(\beta)}. \quad (\text{B5})$$

In a similar manner the second derivatives can be obtained as

$$\begin{aligned} \frac{\partial^2}{\partial r^2} P_{ir-1/2}(\cosh(\beta)) &= \frac{r_0^2 + z^2}{r^3 r_0 \sinh(\beta)} P_{ir-1/2}^1(\cosh(\beta)) \\ &\quad + \frac{(r^2 - r_0^2 - z^2)^2}{4r^4 r_0^2 \sinh^2(\beta)} P_{ir-1/2}^2(\cosh(\beta)) \quad (\text{B6}) \end{aligned}$$

$$\begin{aligned} \frac{\partial^2}{\partial z^2} P_{ir-1/2}(\cosh(\beta)) &= \frac{1}{r r_0 \sinh(\beta)} P_{ir-1/2}^1(\cosh(\beta)) \\ &\quad + \frac{z^2}{r^2 r_0^2 \sinh^2(\beta)} P_{ir-1/2}^2(\cosh(\beta)) \quad (\text{B7}) \end{aligned}$$

$$\begin{aligned} \frac{\partial^2}{\partial r \partial z} P_{ir-1/2}(\cosh(\beta)) &= -\frac{z}{r^2 r_0 \sinh(\beta)} P_{ir-1/2}^1(\cosh(\beta)) \\ &\quad + \frac{z(r^2 - r_0^2 - z^2)}{2r^3 r_0^2 \sinh^2(\beta)} P_{ir-1/2}^2(\cosh(\beta)). \quad (\text{B8}) \end{aligned}$$

Some other useful relations are

$$\begin{aligned} \frac{\partial}{\partial r} \left\{ \frac{1}{\sinh(\beta)} P_{ir-1/2}^1(\cosh(\beta)) \right\} \\ = \frac{1}{\sinh(\beta)} P_{ir-1/2}^2(\cosh(\beta)) \frac{\partial \beta}{\partial r} \quad (\text{B9}) \end{aligned}$$

$$\begin{aligned} \frac{\partial}{\partial r} \left\{ \frac{1}{\sinh^2(\beta)} P_{ir-1/2}^2(\cosh(\beta)) \right\} \\ = \frac{1}{\sinh^2(\beta)} P_{ir-1/2}^3(\cosh(\beta)) \frac{\partial \beta}{\partial r} \quad (\text{B10}) \end{aligned}$$

where these also apply with r replaced by z .

A Generalized Self-Consistent Mechanics Method for Solids Containing Elliptical Inclusions

Y. Huang

Department of Mechanical Engineering-
Engineering Mechanics,
Michigan Technological University,
Houghton, MI 49931

K. X. HU

Corporate Manufacturing Research Center,
Motorola,
Schaumburg, IL 60196

The determination of the effective moduli for a material containing elliptical inclusions is the objective of this paper. This is done by incorporating an inclusion/matrix/composite model into a general energy equivalence framework. Through the evaluation of the average strain in each individual inclusion, the current approach can handle the inclusion's orientation dependency in a straightforward manner. The case of an in-plane isotropic distribution of elliptical inclusions is addressed in detail. For the case of reinforcements, or hard inclusions, the effect of the inclusion aspect ratio on in-plane effective moduli is small if the aspect ratio is larger than 0.5. For aspect ratios less than 0.3, the effective moduli increase dramatically, which implies that flat reinforcements are much more effective than traditional cylindrical reinforcements. It is also established that the generalized self-consistent method predicts a stronger dependence of effective moduli on the inclusion aspect ratio than does the Mori-Tanaka method, especially for shear moduli.

1 Introduction

There are several approaches that can be used to estimate the effective moduli of composite materials. The Mori-Tanaka method (Taya and Chou, 1981; Weng, 1984, 1990; Benveniste, 1987) has many diverse applications in that it can accommodate elliptical inclusions, thereby accounting for a wide range of variations in inclusion shapes (Zhao et al., 1989; Zhao and Weng, 1990). Another method, the inclusion/matrix/composite model (also referred to as the generalized self-consistent method; Christensen and Lo, 1979; Luo and Weng, 1987, 1989; Christensen, 1990) provides accurate predictions that are well suited for extreme types of inclusions (i.e., voids and rigid inclusions), and the method also gives the correct asymptotic behavior of composites as the inclusion volume fraction approaches 1 (fully packed). Moreover, Cherkaev et al. (1992), Day et al. (1992), and Thorpe and Jasiuk (1992) established, from both a general formulation and a numerical solution, that the effective Young's modulus for a two-dimensional isotropic matrix containing voids, E_{2D} is independent of the Poisson's ratio, ν , for the matrix material. Christensen (1993) pointed out that the inclusion/matrix/composite model meets this criterion. Recently, Huang et al. (1994) showed that the solution for a composite material containing single-phase inclusions obtained by the inclusion/matrix/composite model can be equivalently addressed within the general energy balance framework proposed by Budiansky (1965). Huang et al. (1994) extended the applicability of the inclusion/matrix/composite model to multiphase composite materials. The predictions for multiphase composites and for a material containing voids (an extreme type of inclusion) show excellent agreement with experimental data and with exact numerical solutions, even at high inclusion volume fractions. The inclusion/matrix/composite model, however, can currently accommodate only cylindrical and spherical inclusions. A solution for elliptical inclusions, which can ac-

count for a wide range of shape variations, is highly desirable so that a full comparison to the Mori-Tanaka method can be made. It should be noted that the approach of Christensen and Lo (1979) for the inclusion/matrix/composite model has difficulty in accommodating the elliptical inclusions for two reasons: (1) the inclusion's orientation dependency, which is not an issue for cylindrical or spherical inclusions, cannot be handled in a trivial fashion and (2) for a material containing elliptical inclusions, the effective shear modulus in the eigenvalue equations will not decouple from other effective elastic constants, for example, the effective Poisson's ratio. Therefore, a remote shear loading cannot, in general, lead to the solution of the shear modulus.

Benveniste (1985) described an approach using the inclusion/matrix/composite model for composite materials, and Miloh and Benveniste (1988) applied it to composite conductivity. This paper presents a solution to the effective moduli of a material containing elliptical inclusions within a general energy framework incorporating the inclusion/matrix/composite model. Through the evaluation of the average strain in each individual inclusion, the current approach can handle the inclusion's orientation dependency in a straightforward manner. The case of in-plane isotropic distribution of elliptical inclusions is addressed in detail. The effects of the aspect ratio of an elliptical inclusion on the effective in-plane moduli are examined for extreme types of inclusions, i.e., voids and rigid inclusions.

2 The Energy Equivalence Framework and the Inclusion/Matrix/Composite Model

We consider a large cube of a multiphase composite made of a coherent mixture of several isotropic elastic materials with elliptical shapes. The spatial distributions of the phases are assumed to be such that the composite material is homogeneous. There are a total of $N-1$ phases of elliptical inclusions embedded in the matrix material. The elastic modulus and Poisson's ratio of the matrix are E and ν , and the elastic modulus, Poisson's ratio, and volume concentration of the I th individual phase are E_I , ν_I , and c_I ($I = 1, 2, \dots, N-1$), respectively. In general, the composite material is anisotropic, due to geometrical shapes and spatial orientations of inclusions, and is characterized by the following general stress-strain relation:

Contributed by the Applied Mechanics Division of THE AMERICAN SOCIETY OF MECHANICAL ENGINEERS for publication in the ASME JOURNAL OF APPLIED MECHANICS.

Discussion on this paper should be addressed to the Technical Editor, Prof. Lewis T. Wheeler, Department of Mechanical Engineering, University of Houston, Houston, TX 77204-4792, and will be accepted until four months after final publication of the paper itself in the ASME JOURNAL OF APPLIED MECHANICS.

Manuscript received by the ASME Applied Mechanics Division, Apr. 15, 1993; final revision, June 1, 1994. Associate Technical Editor: G. J. Dvorak.

$$\sigma_{ij} = C_{ijkl} \epsilon_{kl} \quad \text{or} \quad \epsilon_{ij} = C_{ijkl}^{-1} \sigma_{kl}, \quad (1)$$

where C_{ijkl} is the elastic moduli tensor of the composite material. To determine C_{ijkl} or its inverse (tensor of elastic constants), apply a uniform stress, $\sigma_{ij} = \sigma_{ij}^0$, to the surface of the cube of composite material. The strain energy of the composite material is given exactly as

$$U = \frac{1}{2} C_{ijkl}^{-1} \sigma_{ij}^0 \sigma_{kl}^0 V, \quad (2)$$

where V is the total volume of the composite material. Also, in terms of the stress, strain, and moduli of each individual phase (Budiansky, 1965),

$$U = \frac{1}{2} \int_V \sigma_{ij} \epsilon_{ij} dV = \frac{1}{2} \left\{ \frac{1+\nu}{E} \sigma_{ij}^0 \sigma_{ij}^0 - \frac{\nu}{E} \sigma_{ii}^0 \sigma_{jj}^0 + \sum_{l=1}^{N-1} c_l \left[\left(1 - \frac{1+\nu}{1+\nu_l} \frac{E_l}{E} \right) \sigma_{ij}^0 \bar{\epsilon}_{ij}^l + \frac{\nu - \nu_l}{(1-2\nu_l)(1+\nu_l)} \frac{E_l}{E} \sigma_{ii}^0 \bar{\epsilon}_{jj}^l \right] \right\} V, \quad (3)$$

where $\bar{\epsilon}_{ij}^l = 1/V_l \int_{V_l} \epsilon_{ij} dV$ is the average strain in the l th phase and $V_l = c_l V$ is the volume of the l th phase. Equations (2) and (3) lead to

$$C_{ijkl}^{-1} \sigma_{ij}^0 \sigma_{kl}^0 = \frac{1+\nu}{E} \sigma_{ij}^0 \sigma_{ij}^0 - \frac{\nu}{E} \sigma_{ii}^0 \sigma_{jj}^0 + \sum_{l=1}^{N-1} c_l \left[\left(1 - \frac{1+\nu}{1+\nu_l} \frac{E_l}{E} \right) \sigma_{ij}^0 \bar{\epsilon}_{ij}^l + \frac{\nu - \nu_l}{(1-2\nu_l)(1+\nu_l)} \frac{E_l}{E} \sigma_{ii}^0 \bar{\epsilon}_{jj}^l \right]. \quad (4)$$

Equation (4) can be interpreted as an energy equivalence between two different views of the composite: one regards the composite as an overall effective medium, and the other goes into the details of the individual phases. Within the framework of linear elasticity, the average strain in inclusions is proportional to the remote stress. Therefore, Eq. (4) is quadratic with respect to remote stress, σ_{ij}^0 , and comparison of the coefficients on the left and right-hand sides of Eq. (4) leads to the equations that govern the effective moduli of the composite, C_{ijkl} (or C_{ijkl}^{-1}).

In order to illustrate the procedure for the determination of the effective moduli of composite materials, we consider a material containing single-phased, unidirectionally aligned elliptical inclusions. The matrix and the inclusions are isotropic, with elastic moduli, E and E_l , Poisson's ratios, ν and ν_l , and inclusion volume concentration, c . It is assumed that these unidirectionally aligned inclusions are parallel to the x_3 -axis and are randomly distributed in the x_1 - x_2 plane such that the composite possesses transverse isotropy and is characterized by an in-plane isotropic stress-strain relation

$$\sigma_{\alpha\beta} = 2\bar{G}\epsilon_{\alpha\beta} + (\bar{B} - \bar{G})\epsilon_{\gamma\gamma}\delta_{\alpha\beta} \quad \alpha, \beta = 1, 2 \quad (5)$$

where \bar{G} is the in-plane shear modulus and \bar{B} is the in-plane bulk modulus, i.e., $\epsilon_{\alpha\alpha} = \sigma_{\alpha\alpha}/(2\bar{B})$. Assuming that a biaxial tension ($\sigma_{11} = \sigma_{22} = \sigma_0$) and a biaxial tension/compression ($\sigma_{11} = -\tau_0, \sigma_{22} = \tau_0$) are applied separately to the composite, the energy equivalence, Eq. (4), gives

$$\frac{1}{\bar{B}} = \frac{1}{B} + c \left(1 - \frac{B_l}{B} \right) \frac{\bar{\epsilon}_{11}^{(1)} + \bar{\epsilon}_{22}^{(1)}}{\sigma_0} \quad (6)$$

$$\frac{1}{\bar{G}} = \frac{1}{G} + c \left(1 - \frac{G_l}{G} \right) \frac{\bar{\epsilon}_{22}^{(2)} - \bar{\epsilon}_{11}^{(2)}}{\tau_0}, \quad (7)$$

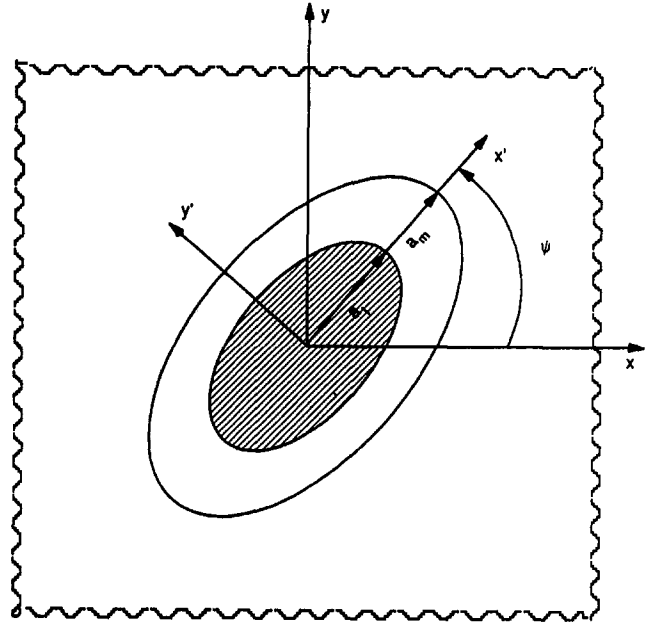


Fig. 1 Schematic diagram of an inclusion/matrix/composite model

where $B = E/[2(1+\nu)(1-2\nu)]$ and $G = E/[2(1+\nu)]$; $B_l = E_l/[2(1+\nu_l)(1-2\nu_l)]$ and $G_l = E_l/[2(1+\nu_l)]$ are the in-plane bulk and shear moduli, respectively, for the matrix and inclusions; and $\bar{\epsilon}_{11}^{(1)} + \bar{\epsilon}_{22}^{(1)}$ and $\bar{\epsilon}_{22}^{(2)} - \bar{\epsilon}_{11}^{(2)}$ are the average strains in the inclusions due to biaxial tension, $\sigma_{11} = \sigma_{22} = \sigma_0$, and biaxial tension/compression, $\sigma_{11} = -\sigma_{22} = -\tau_0$, respectively.

It should be emphasized here that Eqs. (6) and (7) (or their parental form, Eq. (4)) are exact presentations of energy equivalence. The approximation nature of various approaches comes solely from the evaluation of the average strains for inclusions. The dilute approximation evaluates $\bar{\epsilon}_{ij}^l$ by the strain that would occur in an isolated inclusion embedded in the matrix material, and the self-consistent approximation by the strain that would occur in an isolated inclusion embedded in the composite. Obviously, the dilute solution neglects the inclusion interaction, while the self-consistent solution overestimates it.

Huang et al. (1994) proposed an evaluation of the average strain based on the inclusion/matrix/composite model, i.e., an inclusion is embedded in a finite matrix that, in turn, is embedded in an infinite composite. Their estimation of composite moduli is in excellent agreement with experimental data and accurate numerical calculations. We will use the inclusion/matrix/composite model to evaluate $\bar{\epsilon}_{11}^{(1)} + \bar{\epsilon}_{22}^{(1)}$ and $\bar{\epsilon}_{22}^{(2)} - \bar{\epsilon}_{11}^{(2)}$, i.e., the average strain of all inclusions is approximated by the average strain in a single inclusion surrounded by a finite matrix that is embedded in an infinite medium that has the as-yet-unknown moduli of composite materials. An elliptical inclusion and a surrounding elliptical ring of the matrix with coinciding major axes are placed at an arbitrary angle ψ with the x_1 -axis of the composite (Fig. 1). The surrounding elliptical ring shares the same aspect ratio as the elliptical inclusion. For two-dimensional cases, the aspect ratio of the inclusion can be taken as $0 \leq \lambda \leq 1$ without loss of generality. The lengths, a_l and a_m , of the major axes of the inclusion and the matrix ring are chosen so as to preserve the inclusion volume fraction of the composite, that is,

$$c = \left(\frac{a_l}{a_m} \right)^2. \quad (8)$$

Averaging of the strains should be taken over the volume of the elliptical inclusion, as well over as the orientation ψ . Obviously, it is the averaging over the orientation ψ that accounts

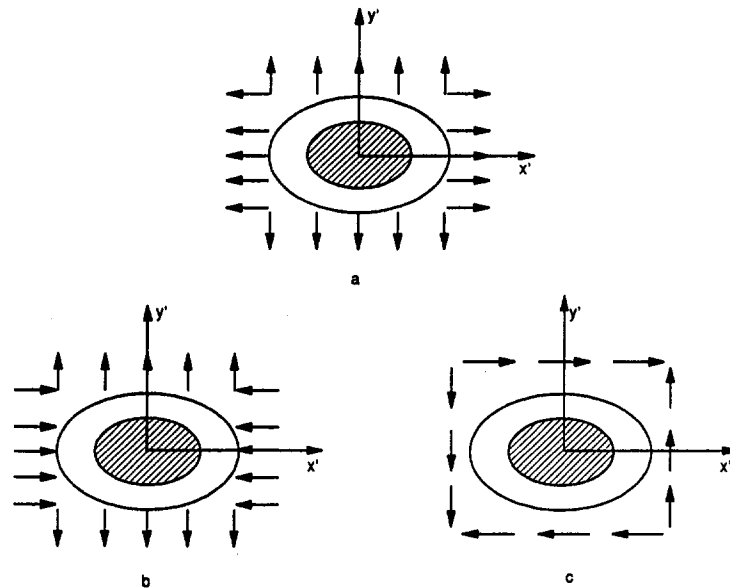


Fig. 2 Fundamental problems: (a) remote biaxial tension in the direction of major axes of the elliptical inclusion; (b) remote biaxial tension/compression; (c) remote shear

for the randomness of the distribution of elliptical inclusions in a statistical sense.

For the biaxial tension $\sigma_{11} = \sigma_{22} = \sigma_0$, the remote stresses in the local $x' - y'$ coordinate system (Fig. 1; x' -axis coincides with the principal axis of the inclusion) are

$$\sigma'_{xx} = \sigma'_{yy} = \sigma_0, \quad \tau'_{xy} = 0 \quad (9)$$

and the strain in the inclusion in terms of local strains is

$$\epsilon_{11}^{(1)} + \epsilon_{22}^{(1)} = \epsilon'_{xx} + \epsilon'_{yy} \quad (10)$$

Let ϵ'_{xx1} , ϵ'_{yy1} , and ϵ'_{xy1} denote the strains, in the local $x' - y'$ coordinate system, of the inclusion subject to a unit biaxial remote loading $\sigma'_{xx} = \sigma'_{yy} = 1$, as shown in Fig. 2(a). This fundamental solution is established in the next section. Obviously,

$$\frac{\bar{\epsilon}_{11}^{(1)} + \bar{\epsilon}_{22}^{(1)}}{\sigma_0} = \bar{\epsilon}'_{xx1} + \bar{\epsilon}'_{yy1} \quad (11)$$

where $\bar{\epsilon}'_{xx1}$ and $\bar{\epsilon}'_{yy1}$ are the average of ϵ'_{xx1} and ϵ'_{yy1} over the inclusion (refer to Fig. 2(a)).

For the biaxial tension/compression $\sigma_{11} = -\sigma_{22} = -\tau_0$, we have remote stresses in the local coordinates of the elliptical inclusion,

$$\sigma_{x'x'} = -\sigma_{y'y'} = -\tau_0 \cos 2\psi, \quad \sigma_{x'y'} = \tau_0 \sin 2\psi \quad (12)$$

and $\epsilon_{22}^{(2)} - \epsilon_{11}^{(2)}$ in the inclusion in terms of local strains,

$$\epsilon_{22}^{(2)} - \epsilon_{11}^{(2)} = (\epsilon'_{yy} - \epsilon'_{xx}) \cos 2\psi + 2\epsilon'_{xy} \sin 2\psi \quad (13)$$

Let ϵ'_{xx2} , ϵ'_{yy2} , and ϵ'_{xy2} denote the strains of the inclusion subject to a unit remote tension/compression $\sigma'_{xx} = -\sigma'_{yy} = -1$, as shown in Fig. 2(b), and ϵ'_{xx3} , ϵ'_{yy3} , ϵ'_{xy3} denote the strains of the inclusion subject to a unit remote shearing $\sigma'_{xy} = 1$, as shown in Fig. 2(c). These two fundamental solutions are also given in the next section. Therefore,

$$\begin{aligned} \epsilon'_{yy} - \epsilon'_{xx} &= \tau_0 \cos 2\psi (\epsilon'_{yy2} - \epsilon'_{xx2}) + \tau_0 \sin 2\psi (\epsilon'_{yy3} - \epsilon'_{xx3}) \quad (14) \\ \epsilon'_{xy} &= \tau_0 \cos 2\psi \epsilon'_{xy2} + \tau_0 \sin 2\psi \epsilon'_{xy3} \quad (15) \end{aligned}$$

It is important to note that $\epsilon'_{\alpha\beta 2}$ and $\epsilon'_{\alpha\beta 3}$ are independent of the inclusion orientation ψ (refer to Figs. 2(b)–(c)), so averaging over the inclusion and over the orientation ψ can be carried out separately. First, averaging over the inclusion, we have

$$\bar{\epsilon}'_{yy} - \bar{\epsilon}'_{xx} = \tau_0 \cos 2\psi (\bar{\epsilon}'_{yy2} - \bar{\epsilon}'_{xx2}) \quad (16)$$

$$\bar{\epsilon}'_{xy} = \tau_0 \sin 2\psi \bar{\epsilon}'_{xy3} \quad (17)$$

In arriving at Eqs. (16) and (17), use is made of the fact that ϵ'_{xx3} , ϵ'_{yy3} , and ϵ'_{xy2} are asymmetric about the x' -axis, thus the average of these quantities over the inclusion is zero.

Using Eqs. (16) and (17) and averaging Eq. (13) over the inclusion and the inclusion orientation, ψ ($0 < \psi < \pi$), we have

$$\frac{\bar{\epsilon}_{22}^{(2)} - \bar{\epsilon}_{11}^{(2)}}{\tau_0} = \frac{1}{2} (\bar{\epsilon}'_{yy2} - \bar{\epsilon}'_{xx2}) + \bar{\epsilon}'_{xy3} \quad (18)$$

where the fact that the average of $\cos^2 2\psi$ or $\sin^2 2\psi$ is $\frac{1}{2}$ has been used.

With Eqs. (11) and (18) in mind, the solution to in-plane bulk and shear moduli through Eqs. (6) and (7) then boils down to obtaining the average inclusion strain quantities of the three fundamental problems shown in Figures 2(a)–(c). This will be treated in the next section.

3 Fundamental Solutions

The fundamental solutions needed in Section 2 are the average strains in an elliptic inclusion embedded in an elliptic matrix, which in turn is embedded in an infinite composite. The inclusions and matrix have the same aspect ratio. The composite is subject to three sets of unit remote stress (Fig. 2),

- (I) remote biaxial tension: $\sigma'_{xx} = \sigma'_{yy} = 1$
- (II) remote biaxial tension/compression: $\sigma'_{xx} = -1, \sigma'_{yy} = 1$
- (III) remote pure shear: $\sigma'_{xy} = 1$.

where x' and y' are the major axes of the ellipse, as shown in Fig. 1.

The Airy stress function, ϕ , for a plane-strain problem symmetric about axes x' and y' (e.g., subject to sets I and II), has the following general structure:

$$\phi = A_0 r^2 + B_0 \ln r + \sum_{n=2,4,6,\dots} \cos n\theta (A_n r^{n+2} + B_n r^n + C_n r^{2-n} + D_n r^{-n}), \quad (19)$$

where (r, θ) are the polar coordinates for axes x' and y' . The corresponding stress components are

$$\begin{aligned} \sigma_{rr} = & \frac{1}{r} \frac{\partial \phi}{\partial r} + \frac{1}{r^2} \frac{\partial^2 \phi}{\partial \theta^2} = 2A_0 + B_0 r^{-2} \\ & + \sum_{n=2,4,6,\dots} \cos n\theta [(2-n)(1+n)A_n r^n \\ & + n(1-n)B_n r^{n-2} + (2+n)(1-n)C_n r^{-n} \\ & - n(1+n)D_n r^{-n-2}] \quad (20) \end{aligned}$$

$$\begin{aligned} \sigma_{\theta\theta} = & \frac{\partial^2 \phi}{\partial r^2} = 2A_0 - B_0 r^{-2} \\ & + \sum_{n=2,4,6,\dots} \cos n\theta [(2+n)(1+n)A_n r^n \\ & - n(1-n)B_n r^{n-2} + (2-n)(1-n)C_n r^{-n} \\ & + n(1+n)D_n r^{-n-2}] \quad (21) \end{aligned}$$

$$\begin{aligned} \sigma_{r\theta} = & -\frac{\partial}{\partial r} \left(\frac{1}{r} \frac{\partial \phi}{\partial \theta} \right) = \sum_{n=2,4,6,\dots} \sin n\theta [n(1+n)A_n r^n \\ & - n(1-n)B_n r^{n-2} + n(1-n)C_n r^{-n} \\ & - n(1+n)D_n r^{-n-2}]. \quad (22) \end{aligned}$$

The corresponding displacements are

$$\begin{aligned} u_r = & A_{11} \{ 2A_0 r - B_0 r^{-1} + \sum_{n=2,4,6,\dots} \cos n\theta [(2-n)A_n r^{n+1} \\ & - nB_n r^{n-1} + (2+n)C_n r^{1-n} + nD_n r^{-n-1}] \} \\ & + A_{12} \{ 2A_0 r + B_0 r^{-1} + \sum_{n=2,4,6,\dots} \cos n\theta [(2+n)A_n r^{n+1} \\ & + nB_n r^{n-1} + (2-n)C_n r^{1-n} - nD_n r^{-n-1}] \} \quad (23) \end{aligned}$$

$$\begin{aligned} u_\theta = & A_{11} \sum_{n=2,4,6,\dots} \sin n\theta [(n+4)A_n r^{n+1} + nB_n r^{n-1} \\ & + (n-4)C_n r^{1-n} + nD_n r^{-n-1}] \\ & - A_{12} \sum_{n=2,4,6,\dots} n \sin n\theta [A_n r^{n+1} + B_n r^{n-1} \\ & + C_n r^{1-n} + D_n r^{-n-1}] \quad (24) \end{aligned}$$

where the rigid-body rotation is neglected since the loading is symmetric about axes x' and y' , and the elastic compliances, A_{11} and A_{12} , are related to the shear and bulk moduli, G and B , by

$$2(A_{11} + A_{12}) = \frac{1}{B} \quad \text{and} \quad 2(A_{11} - A_{12}) = \frac{1}{G}. \quad (25)$$

For the inclusion, the stress must be finite at the origin, which requires $B_0 = 0, C_n = D_n = 0$ ($n = 2, 4, 6, \dots$), and A_0, A_n , and B_n to be replaced by A_0^i, A_n^i , and B_n^i ($n = 2, 4, 6, \dots$), where the superscript stands for the inclusion. The elastic moduli B and G are substituted by the corresponding moduli of the

inclusion, B_i and G_i , respectively. For the matrix, the constants to be determined are $A_0^m, B_0^m, A_n^m, B_n^m, C_n^m$, and D_n^m ($n = 2, 4, 6, \dots$) and the moduli are replaced by the corresponding moduli in the matrix, B and G . For the composite, the stress in the remote field must also be finite, which requires $A_2 = 0$ and $A_n = B_n = 0$ ($n = 4, 6, \dots$). Thus, the nonzero constants to be determined are $A_0^c, B_0^c, B_2^c, C_n^c$, and D_n^c ($n = 2, 4, 6, \dots$). The corresponding moduli in the composite are \bar{B} and \bar{G} , respectively. The constants A_0^c and B_2^c are directly determined by the remote applied stress. For loading set I, $A_0^c = \frac{1}{2}$ and $B_2^c = 0$. For loading set II, $A_0^c = 0$ and $B_2^c = \frac{1}{2}$. Other constants are determined by the continuity conditions across the inclusion/matrix and matrix/composite interfaces. The normal and shear stress components at the interfaces are

$$\sigma_{mn} = (n_r, n_\theta) \begin{pmatrix} \sigma_{rr} & \sigma_{r\theta} \\ \sigma_{r\theta} & \sigma_{\theta\theta} \end{pmatrix} \begin{pmatrix} n_r \\ n_\theta \end{pmatrix} \quad (26)$$

$$\sigma_{ns} = (n_r, n_\theta) \begin{pmatrix} \sigma_{rr} & \sigma_{r\theta} \\ \sigma_{r\theta} & \sigma_{\theta\theta} \end{pmatrix} \begin{pmatrix} -n_\theta \\ n_r \end{pmatrix} \quad (27)$$

where n_r and n_θ are the directional cosines of a unit normal at the interfaces in polar coordinates, given by

$$n_r = \cos \alpha, \quad n_\theta = \sin \alpha,$$

$$\alpha = \tan^{-1} \frac{(1 - \lambda^2) \sin \theta \cos \theta}{\lambda^2 \cos^2 \theta + \sin^2 \theta} \quad (28)$$

for an ellipse with aspect ratio λ . Without loss of generality, the length of a major axis of the elliptical inclusion can be taken as 1 (one). Thus, the elliptical inclusion is characterized by the following equation in polar coordinates:

$$r = \rho_0(\theta) \equiv \frac{\lambda}{(\lambda^2 \cos^2 \theta + \sin^2 \theta)^{1/2}}. \quad (29)$$

The continuity conditions at the inclusion/matrix interface are

$$[\sigma_{mn}] = 0, \quad [\sigma_{ns}] = 0, \quad [u_r] = 0, \quad [u_\theta] = 0, \quad (30)$$

where $[\cdot]$ stands for the difference in the argument across the interface, and the radial coordinate r in the expressions of σ_{mn} , σ_{ns} , u_r , and u_θ is substituted by $\rho_0(\theta)$ at the inclusion/matrix interface. It is emphasized that the moduli in the expressions of u_r and u_θ must be used for the corresponding regions. The continuity conditions at the matrix/composite interface are the same as for equation (30), except that $\rho_0(\theta)/\sqrt{c}$ is substituted for the radial coordinate r .

Equation (30) at two interfaces forms the governing equations to determine the unknowns $A_0^i, A_0^m, B_0^m, B_0^c, A_n^i, B_n^i, A_n^m, B_n^m, C_n^m, D_n^m, C_n^c$, and D_n^c ($n = 2, 4, 6, \dots$). Equation (30) is solved by the standard collocation method for converged truncation in the number of expansions of unknowns.

The average strain for loading set I is given by

$$\begin{aligned} \bar{\epsilon}'_{xx1} + \bar{\epsilon}'_{yy1} &= \frac{1}{2B_i} (\bar{\sigma}'_{xx1} + \bar{\sigma}'_{yy1}) \\ &= \frac{1}{2B_i} \cdot \frac{1}{\pi \lambda} \int_0^{2\pi} d\theta \int_0^{\rho_0(\theta)} (\sigma'_{xx1} + \sigma'_{yy1}) r dr, \quad (31) \end{aligned}$$

where

$$\sigma'_{xx1} + \sigma'_{yy1} = \sigma'_{rr1} + \sigma'_{\theta\theta1}. \quad (32)$$

The average strain for loading set II is

$$\bar{\epsilon}'_{yy2} - \bar{\epsilon}'_{xx2} = \frac{1}{2G_i} \cdot \frac{1}{\pi\lambda} \int_0^{2\pi} d\theta \int_0^{\rho_0(\theta)} (\sigma'_{yy2} - \sigma'_{xx2}) r dr, \quad (33)$$

where

$$\sigma'_{yy2} - \sigma'_{xx2} = (\sigma'_{\theta\theta 2} - \sigma'_{rr2}) \cos 2\theta + 2\sigma'_{r\theta 2} \sin 2\theta. \quad (34)$$

For a stress distribution antisymmetric about axis x' , such as loading set III, the Airy stress function in Eq. (19) needs to be modified as follows:

$$\phi = A_0\theta + B_0r \sin \theta + \sum_{n=2,4,6,\dots} \sin n\theta [A_n r^{n+2} + B_n r^n + C_n r^{2-n} + D_n r^{-n}], \quad (35)$$

where $A_0\theta$ corresponds to pure shear; $B_0r \sin \theta$ is the rigid-body rotation, which is important in matching displacement across interfaces because the loading is asymmetric; and the terms in summation are similar to those in Eq. (19) except that $\cos n\theta$ is changed to $\sin n\theta$. The above procedure to determine unknowns holds, except that $A_0^i = 0$, $B_0^i = 0$, and $B_2^i = -\frac{1}{2}$. The average strain is

$$\bar{\epsilon}'_{xy3} = \frac{1}{2G_i} \bar{\sigma}'_{xy3} = \frac{1}{2G_i} \cdot \frac{1}{\pi\lambda} \int_0^{2\pi} d\theta \int_0^{\rho_0(\theta)} \sigma'_{xy3} r dr, \quad (36)$$

where

$$\sigma'_{xy3} = (\sigma'_{rr3} - \sigma'_{\theta\theta 3}) \sin \theta \cos \theta + \sigma'_{r\theta 3} \cos 2\theta. \quad (37)$$

It is noted that the series solution can warrant the convergence

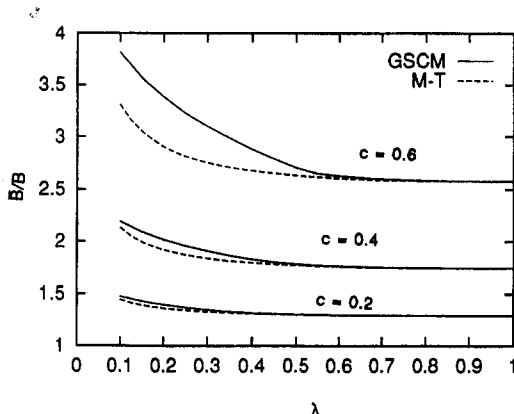


Fig. 3(a)

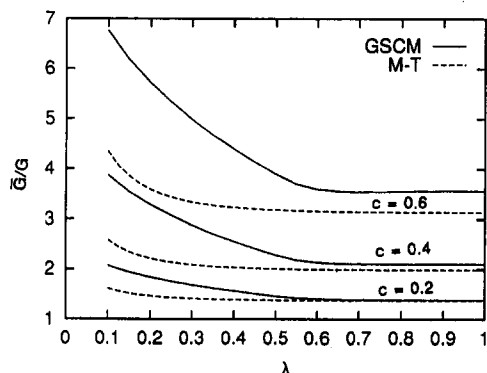


Fig. 3(b)

Fig. 3 Variation of moduli with aspect ratio λ for glass-epoxy composites: $E_i = 72.4$ GPa, $E = 2.76$ GPa, $\nu_i = 0.2$, and $\nu = 0.35$; (a) in-plane bulk modulus; (b) in-plane shear modulus

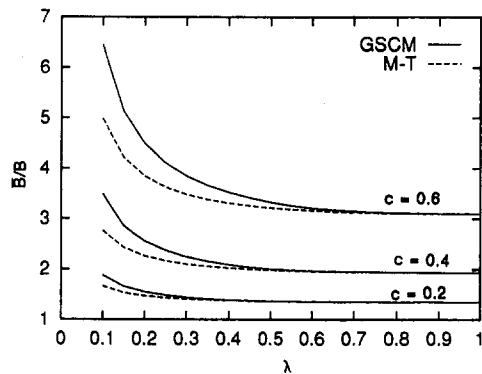


Fig. 4(a)

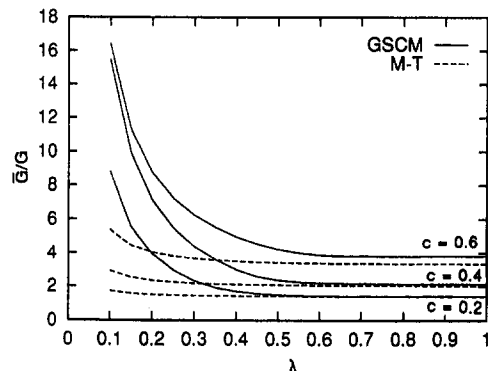


Fig. 4(b)

Fig. 4 Variation of moduli with aspect ratio λ for rigid inclusions: $E_i/E = \infty$ and $\nu = 0.3$; (a) in-plane bulk modulus; (b) in-plane shear modulus

for λ greater than 0.1. For $\lambda < 0.1$, oscillation occurs as the number of terms increases.

4 Results and Conclusions

The in-plane bulk and shear moduli for various types of inclusions are presented in this section. Of primary interest here are the effects of aspect ratio on effective moduli. Two extremes of inclusions—voids and rigid particles—will be addressed in order to cover commonly encountered inclusions ranging from defects to reinforcements. (For voids and rigid particles, the analysis in Sections 2 and 3 must be modified. See the Appendix for details.)

Variation of the in-plane bulk modulus and of the shear modulus with the inclusion aspect ratio is shown in Figs. 3(a) and 3(b) for glass-epoxy composites with three different inclusion volume fractions, $c = 0.2, 0.4$, and 0.6 . The epoxy matrix has the properties $E = 2.76$ GPa and $\nu = 0.35$, and the glass fibers have $E_i = 72.4$ GPa and $\nu_i = 0.2$. The moduli estimated by the Mori-Tanaka method (Zhao and Weng, 1990) are also shown in Figs. 3(a) and 3(b) for comparison. It is clearly seen that the inclusion/matrix/composite model exhibits a stronger dependence on the inclusion aspect ratio than does the Mori-Tanaka method. In particular, aspect ratio has little effect on the effective moduli if the aspect ratio is greater than 0.5. In an attempt to confirm this conclusion for a wide range of reinforcements, we consider an extreme case: a material containing rigid elliptical inclusions. Figures 4(a) and 4(b) show the variation of effective in-plane bulk and shear moduli with the aspect ratio of rigid inclusions for inclusion volume fractions $c = 0.2, 0.4$, and 0.6 (matrix Poisson's ratio $\nu = 0.3$) for both methods. It is affirmed that the aspect ratio, or shape, of the inclusion has little effect on the effective moduli if the aspect ratio is

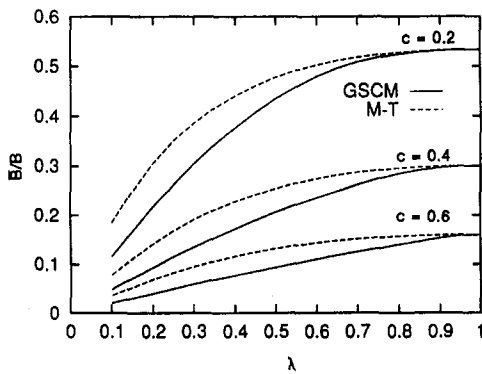


Fig. 5(a)

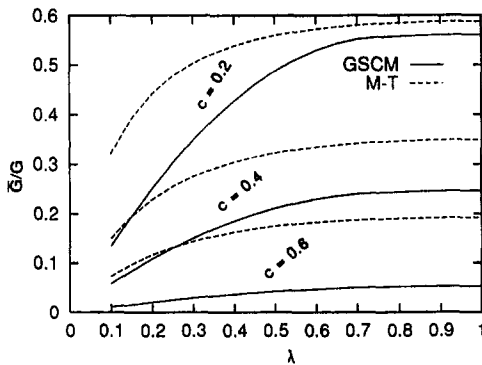


Fig. 5(b)

Fig. 5 Variation of moduli with aspect ratio λ for voids: $E_i/E = 0$ and $\nu = 0.3$: (a) in-plane bulk modulus; (b) in-plane shear modulus

greater than 0.5. The effective moduli, however, can be sharply enhanced by reducing the aspect ratio to a value of less than 0.3. For example, the shear modulus at aspect ratio $\lambda = 0.1$ is more than seven times larger than that for cylindrical rigid inclusions ($\lambda = 1$) for rigid inclusion volume fraction $c = 0.4$. This observation is similar to that discovered by Zhao and Weng (1990) and implies that relatively flat reinforcements are much more effective than traditional cylindrical reinforcements. However, it is observed that the inclusion/matrix/composite model and the Mori-Tanaka method give the same in-plane bulk modulus for cylindrical inclusions ($\lambda = 1$) and the effect of aspect ratio on the composite bulk modulus is much smaller. The bulk modulus at $\lambda = 0.1$ is less than twice that at $\lambda = 1$ for $c = 0.4$. It is noted that all the results we present here are within the Hashin-Shtrikman (1963) bounds.

A material containing unidirectional elliptical voids is considered in Figs. 5(a) and 5(b) in order to examine the effect of damage on effective moduli. Contrary to what is observed for rigid inclusions, aspect ratio does affect the effective moduli at the full range. It is also seen that the effect of aspect ratio on composite moduli estimated by the inclusion/matrix/composite model is larger than that predicted by the Mori-Tanaka method.

Zhao and Weng (1990) established that the Hill (1963) and Hashin-Shtrikman (1963) bounds are identical to the prediction by the Mori-Tanaka method for the two limits of aspect ratios, $\lambda = 0$ and $\lambda = 1$. It is observed that the present results do not violate the bounds. Based on the results presented above for material containing randomly distributed, unidirectional elliptical inclusions, we can conclude the following:

1 For the case of reinforcements, or hard inclusions, the effect of inclusion aspect ratio on in-plane effective moduli is very limited for aspect ratios between 0.5 and 1.0. However,

as the aspect ratio decreases to less than 0.3, the effect of aspect ratio increases rapidly.

2 For the case of damage, or voids, the void aspect ratio has a significant effect on the effective moduli at the full range.

3 The inclusion/matrix/composite model, all known as the generalized self-consistent method, predicts a stronger dependence of composite moduli on the inclusion aspect ratio than does the Mori-Tanaka method. The previous conclusion that the difference between the two methods is small was established for spherical or cylindrical inclusions only. Through variation of inclusion shapes, the current analysis shows that the differences between the two methods can become quite significant. The difference between the two methods for the shear modulus is larger than the difference for the in-plane bulk modulus.

4 The shear modulus exhibits a stronger dependence on the inclusion shapes than does the in-plane bulk modulus.

The current approach can be extended to study the behavior of materials containing extremely shaped inclusions, such as cracks and ribbon types of reinforcements. Such an extension will, however, require a redefinition of the physical model and a reformulation of some fundamental solutions.

References

- Benveniste, Y., 1985, "The Effective Mechanical Behavior of Composite Materials with Imperfect Contact Between the Constituents," *Mechanics of Materials*, Vol. 4, pp. 197–208.
- Benveniste, Y., 1987, "A New Approach to the Application of Mori-Tanaka's Theory in Composite Materials," *Mechanics of Materials*, Vol. 6, pp. 147–157.
- Budiansky, B., 1965, "On the Elastic Moduli of Some Heterogeneous Material," *Journal of the Mechanics and Physics of Solids*, Vol. 13, pp. 223–227.
- Cherkaev, A., Lurie, K., and Milton, G. W., 1992, "Invariant Properties of Stress in Plane Elasticity and Equivalence Classes of Composites," *Proceedings of the Royal Society of London*, Vol. A438, pp. 519–529.
- Christensen, R. M., 1990, "A Critical Evaluation for a Class of Micro-Mechanics Models," *Journal of the Mechanics and Physics of Solids*, Vol. 38, pp. 379–404.
- Christensen, R. M., 1993, "Effective Properties of Composite Materials Containing Voids," *Proceedings of the Royal Society of London*, Vol. A440, pp. 461–473.
- Christensen, R. M., and Lo, K. H., 1979, "Solutions for Effective Shear Properties in Three Phase Sphere and Cylinder Models," *Journal of the Mechanics and Physics of Solids*, Vol. 27, pp. 315–330.
- Day, A. R., Snyder, K. A., Garboczi, E. J., and Thorpe, M. F., 1992, "The Elastic Moduli of a Sheet Containing Circular Holes," *Journal of the Mechanics and Physics of Solids*, Vol. 40, pp. 1031–1051.
- Hashin, Z., and Shtrikman, S., 1963, "A Variational Approach to the Theory of the Elastic Behavior of Multi-Phase Materials," *Journal of the Mechanics and Physics of Solids*, Vol. 11, pp. 127–140.
- Hill, R., 1963, "Elastic Properties of Reinforced Solids: Some Theoretical Principles," *Journal of the Mechanics and Physics of Solids*, Vol. 11, pp. 357–372.
- Huang, Y., Hu, K. X., Wei, X., and Chandra, A., 1994, "A Generalized Self-Consistent Mechanics Method for Composite Materials with Multiphase Inclusions," *Journal of the Mechanics and Physics of Solids*, Vol. 42, pp. 491–504.
- Luo, H. A., and Weng, G. J., 1987, "On Eshelby's Inclusion Problem in a Three-Phase Spherically Concentric Solid, and a Modification of Mori-Tanaka's Method," *Mechanics of Materials*, Vol. 6, pp. 347–361.
- Luo, H. A., and Weng, G. J., 1989, "On Eshelby's S-Tensor in a Three-Phase Cylindrically Concentrated Solid, and the Elastic Moduli of Fiber-Reinforced Composites," *Mechanics of Materials*, Vol. 8, pp. 77–88.
- Miloh, T., and Benveniste, Y., 1988, "A Generalized Self-Consistent Method for Effective Conductivity of Composites with Ellipsoidal Inclusions and Cracked Bodies," *Journal of Applied Physics*, Vol. 63, pp. 789–796.
- Taya, M., and Chou, T.-W., 1981, "On Two Kinds of Ellipsoidal Inhomogeneities in an Infinite Elastic Body: An Application to a Hybrid Composite," *International Journal of Solids and Structures*, Vol. 17, pp. 553–563.
- Thorpe, M. F., and Jasiuk, I., 1992, "New Results in the Theory of Elasticity for Two-Dimensional Composites," *Proceedings of the Royal Society of London*, Vol. A438, pp. 531–544.
- Weng, G. J., 1984, "Some Elastic Properties of Reinforced Solids, with Special Reference to Isotropic Containing Spherical Inclusions," *International Journal of Engineering Science*, Vol. 22, pp. 845–856.
- Weng, G. J., 1990, "The Theoretical Connection Between Mori-Tanaka's Theory and the Hashin-Shtrikman-Walpole Bounds," *International Journal of Engineering Science*, Vol. 28, pp. 1111–1120.
- Zhao, Y. H., Tandon, G. P., and Weng, G. J., 1989, "Elastic Moduli of a Class of Porous Materials," *Acta Mechanica*, Vol. 76, pp. 105–130.
- Zhao, Y. H., and Weng, G. J., 1990, "Effective Elastic Moduli of Ribbon-Reinforced Composites," *ASME JOURNAL OF APPLIED MECHANICS*, Vol. 57, pp. 158–167.

APPENDIX

For a solid containing voids or rigid inclusions, it is difficult to evaluate the average inclusion strain in the voids or rigid inclusions. Equation (4) needs to be reformulated to a form suitable for voids or rigid inclusions.

For voids, Eq. (4) can be rearranged to

$$C_{ijkl}^{-1} \sigma_{ij}^0 \sigma_{kl}^0 = \frac{1 + \nu}{E} \sigma_{ij}^0 \sigma_{ij}^0 - \frac{\nu}{E} \sigma_{ii}^0 \sigma_{jj}^0 + \sigma_{ij}^0 \sum_{\text{voids}} \frac{\int_{s_v} u_i n_j ds}{V}, \quad (38)$$

where V is the total volume of the composite, s_v is the surface of a void, and u_i and n_j are the components of displacement (due to applied stress σ_{ij}^0) and are unit normal (pointing into the matrix) at void surfaces. The corresponding equation for rigid inclusions is

$$C_{ijkl}^{-1} \sigma_{ij}^0 \sigma_{kl}^0 = \left(\frac{1 + \nu}{E} \sigma_{ij}^0 - \frac{\nu}{E} \sigma_{kk}^0 \delta_{ij} \right) \times \left(\sigma_{ij}^0 - \sum_{\text{rigid inclusions}} \frac{\int_{s_r} \sigma_{ik} n_k x_j ds}{V} \right), \quad (39)$$

where V is the total volume of the composite, s_r is the surface of a rigid inclusion, $\sigma_{ik} n_k$ is the traction on the boundary of rigid inclusions (n_k is the component of a unit normal pointing into the matrix), and x_j is the Cartesian coordinate. The ratios of the surface integral over total volume in Eqs. (38) and (39) are related to the volume concentration of voids and rigid inclusions. The fundamental solutions in Section 3 need to be changed accordingly. For voids, the continuity at the inclusion/matrix interface, Eq. (30), is changed to zero traction conditions. For rigid inclusions, Eq. (30) at the inclusion/matrix interface is changed to zero displacement requirements.

Ching S. Chang
Professor.

Yang Chang
Research Assistant.

Department of Civil Engineering,
University of Massachusetts,
Amherst, MA 01003

Green's Function for Elastic Medium With General Anisotropy

It is difficult to obtain explicit expressions of Green's function for elastic medium with general anisotropy. The difficulty is associated with an integration of functions with high degrees of singularity. In this paper, we propose a method employing extend functions. This method avoids the difficulty of singularities and renders an explicit series expression of Green's function for general anisotropic conditions. Analytical expression of the coefficients in the series are provided. Numerical examples are given to evaluate the applicability of this method.

1 Introduction

Green's function has been an important topic in both applied and theoretical studies of continuum mechanics. As a fundamental solution, Green's function has been widely applied to general boundary value problems for both homogeneous media and inhomogeneous media (Bregbia et al., 1984). Green's function also plays an important role in homogenization methods in micromechanics (Eshelby, 1959; Mura, 1987).

For isotropic elastic solids, Green's function of a point load applied in an infinite medium was first obtained by Kelvin (Sir Thompson, 1848). For transversely isotropic materials, many attempts have been made to obtain the Green's function (Elliott, 1948; Kroner, 1953; Woo and Shield, 1962; Willis, 1965; Sveklo, 1969; Lejcek, 1969). However, for some "degenerational" cases, these solutions do not exist due to problems of singularity. Pan and Chou (1976) provide solution for the degenerated conditions.

For general anisotropic materials, an integral form of the Green's function can be expressed. However, as to date, explicit analytical expression of Green's function for general three-dimensional anisotropic materials are not available. The difficulty arises mathematically from an integration of a singular function in the process of obtaining the Green's function.

Considerable efforts have been made to derive approximate solutions of Green's function for general anisotropic materials. Walpole (1967) proposed an approximate solution based on the method of perturbation. As discussed by Mura and Kinoshita (1971), reliability of the approximation is questionable since a high degree of singularity appears in the kernel of his integral equation. Kroner (1953) took another approach to obtain the Green's function by expanding the Fourier's transformation of Green's function into a series. A similar approach was also employed by Mura and Kinoshita (1971) and by Kinoshita and Mura (1971).

However, the method by Kinoshita and Mura (1971) is based on the premise that the transformed Green's function in a Fourier space can be expanded into a series of homogeneous polynomials of even order. This premise is not true for general anisotropic materials.

Along the approach of series expansion, a method employing extend functions is proposed which makes it possible to derive an explicit series expression of Green's function for general

anisotropic conditions. Analytical expressions of the coefficients in the series are provided. Numerical examples of the derived Green's function are given for transversely isotropic materials. The results are compared with the Green's function derived by Pan and Chou (1976) to evaluate the applicability of this method.

2 Problem Definition

Green's Function $G_{it}(\mathbf{x})$ represents the displacement u_i at point " \mathbf{x} " due to a unit force t_i in an infinite homogeneous medium, such that

$$C_{ijkl}G_{it,ki}(\mathbf{x}) + \delta_{ji}\delta(\mathbf{x}) = 0 \quad (1)$$

where $\delta(\mathbf{x})$ is the Dirac-delta function; δ_{ji} is the Kronecker delta; and C_{ijkl} is the stiffness tensor, defined by

$$\sigma_{ij} = C_{ijkl}u_{l,k} \quad (2)$$

in which σ_{ij} is the Cauchy stress and $u_{l,k}$ is the displacement gradient. The fourth-rank tensor C_{ijkl} with 81 independent constants completely describes the material property of an anisotropic medium.

3 Green's Function in Integral Form

The most elegant method for obtaining Green's function is the technique of the Fourier transformation. The pair of Green's function in Fourier transformation, $\bar{G}_{it}(\xi)$ and $G_{it}(\mathbf{x})$, are related in the following manner:

$$\bar{G}_{it}(\xi) = \int_{-\infty}^{+\infty} G_{it}(\mathbf{x}) \exp(i\mathbf{x} \cdot \xi) d\mathbf{x} \quad (3)$$

$$G_{it}(\mathbf{x}) = \left(\frac{1}{2\pi}\right)^3 \int_{-\infty}^{+\infty} \bar{G}_{it}(\xi) \exp(i\xi \cdot \mathbf{x}) d\xi. \quad (4)$$

From the Fourier transformation of Eq. (1) we obtain

$$K_{jt}\bar{G}_{it}(\xi) = \delta_{jt} \quad (5)$$

where

$$K_{jt} = C_{ijkl}\xi_k\xi_l. \quad (6)$$

Multiplying Eq. (5) by K_{jt}^{-1} leads to

$$\bar{G}_{it}(\xi) = \delta_{jt}K_{jt}^{-1} = K_{it}^{-1}. \quad (7)$$

The inversion of K_{it} can be expressed in terms of the adjoint tensor S_{it} and the determinant T , given by

$$\bar{G}_{it}(\xi) = K_{it}^{-1} = \frac{S_{it}}{T} \quad (8)$$

Contributed by the Applied Mechanics Division of THE AMERICAN SOCIETY OF MECHANICAL ENGINEERS for publication in the ASME JOURNAL OF APPLIED MECHANICS.

Discussion on this paper should be addressed to the Technical Editor, Professor Lewis T. Wheeler, Department of Mechanical Engineering, University of Houston, Houston, TX 77204-4792, and will be accepted until four months after final publication of the paper itself in the ASME JOURNAL OF APPLIED MECHANICS.

Manuscript received by the ASME Applied Mechanics Division, Jan. 13, 1993; final revision, Apr. 18, 1994. Associate Technical Editor: F. Y. M. Wan.

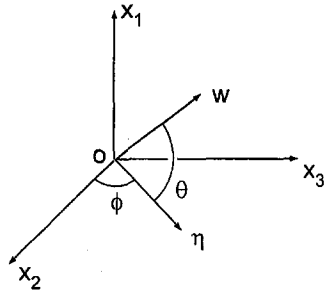


Fig. 1 Transformation of coordinate systems

where the adjoint tensor of K_{lt} is a fourth-order polynomial;

$$S_{lt} = \epsilon_{ikm} \epsilon_{ijn} C_{kjis} C_{muv} \xi_j \xi_s \xi_u \xi_v, \quad (9)$$

and the determinant of K_{lt} is a sixth-order polynomial;

$$T = 2\epsilon_{pqr} C_{pk1m} C_{qr2s} C_{rh3g} \xi_k \xi_m \xi_s \xi_t \xi_g, \quad (10)$$

with the permutation tensor $\epsilon_{ikm} = 0.5(l-k)(k-m)(m-l)$.

Our objective is to evaluate the integral in Eq. (4) for obtaining the Green's function $G_{lt}(\mathbf{x})$. It is straightforward that the volume integral in Eq. (4) can be reduced to a surface integral by performing a spherical coordinate transformation. A brief description of the spherical coordinate transformation is given here. Let

$$\xi = R\eta; \quad \mathbf{x} = r\mathbf{w} \quad (11)$$

$$R = (\xi_i \xi_i)^{1/2}; \quad r = (x_i x_i)^{1/2} \quad (12)$$

where η and \mathbf{w} are unit vectors. R and r are the lengths of ξ and \mathbf{x} , respectively. The infinitesimal volume element $d\xi$ is given by

$$d\xi = R^2 dR dS(\eta) \quad (13)$$

where $dS(\eta)$ is a surface element on the unit sphere S^2 in a ξ -space, centered at the origin of the coordinates ξ_k . Substituting Eqs. (11) and (13) into Eq. (4) leads to

$$G_{lt}(\mathbf{x}) = \left(\frac{1}{2\pi}\right)^3 \int_{S^2} \int_0^\infty \exp(iRr\eta \cdot \mathbf{w}) R^2 \bar{G}_{lt}(R\eta) dR dS(\eta) \quad (14)$$

where $S^2 = \{\eta | \eta_i \eta_i = 1\}$.

Note that the function $\bar{G}_{lt}(\xi)$, referred to Eqs. (8)-(10), has homogeneous sixth-order terms on the denominator and homogeneous fourth-order terms on the numerator. Therefore, the following relationship holds:

$$\bar{G}_{lt}(\eta) = R^2 \bar{G}_{lt}(R\eta) = R^2 \bar{G}_{lt}(\xi). \quad (15)$$

By the definition of Dirac delta (Friedman, 1956),

$$\delta(r\eta \cdot \mathbf{w}) = \frac{1}{2\pi} \int_{-\infty}^{\infty} \exp(iRr\eta \cdot \mathbf{w}) dR. \quad (16)$$

Using Eqs. (15) and (16), Eq. (14) becomes

$$G_{lt}(\mathbf{x}) = \frac{1}{8\pi^2} \int_{S^2} \delta(r\eta \cdot \mathbf{w}) \bar{G}_{lt}(\eta) dS(\eta). \quad (17)$$

The surface integration in Eq. (17) can be further converted to a line integral. Note that η is a unit vector in the $\xi_1 - \xi_2 - \xi_3$ space and \mathbf{w} is a unit vector in the $x_1 - x_2 - x_3$ space. Select the coordinate system $x_1 - x_2 - x_3$ in such a way that η is on the plane of $x_2 - x_3$ perpendicular to the x_1 -axis. Let θ be the angle between η and \mathbf{w} (see Fig. 1), and ϕ be the angle between the x_2 -axis and η . Then $\eta \cdot \mathbf{w} = \cos \theta$.

Using the variables, θ and ϕ , the surface element in Eq. (17) is expressed by

$$dS(\eta) = \sin \theta d\theta d\phi = -d(\eta \cdot \mathbf{w}) d\phi. \quad (18)$$

Thus Eq. (17) becomes

$$G_{lt}(\mathbf{x}) = \frac{1}{8\pi^2} \int_{-1}^1 \delta(r\eta \cdot \mathbf{w}) \int_0^{2\pi} \bar{G}_{lt}(\eta) d\phi d(\eta \cdot \mathbf{w}). \quad (19)$$

Integrating Eq. (19) with respect to $(\eta \cdot \mathbf{w})$ leads to

$$G_{lt}(\mathbf{x}) = \frac{1}{8r\pi^2} \int_0^{2\pi} \bar{G}_{lt}(\eta) d\phi. \quad (20)$$

We can now evaluate Green's function $G_{lt}(\mathbf{x})$ using Eq. (20), provided that the function $\bar{G}_{lt}(\eta)$ has no singular point on the surface of the unit sphere S^2 . According to Eqs. (8) and (6), the presence of singularities in the function $\bar{G}_{lt}(\eta)$ implies that

$$\det |C_{ijkl} \eta_k \eta_l| = 0. \quad (21)$$

It is interesting to note that Eq. (21) can be interpreted as the condition given by Hill and Hutchinson (1975) for strain localization. It also can be interpreted as the condition given by Hill (1962) that a shear wave is unable to transmit through the medium.

4 Series Expression of $\bar{G}_{lt}(\eta)$

We now seek an explicit expression for the integration in Eq. (20). As defined in Eq. (8), the function $\bar{G}_{lt}(\eta)$ is a ratio of two polynomials: the adjoint tensor $S_{ij}(\eta)$ and the determinant $T(\eta)$, given by

$$\bar{G}_{lt}(\eta) = \frac{S_{lt}(\eta)}{T(\eta)}. \quad (22)$$

For convenience, the sixth-order polynomial $T(\eta)$ and the fourth-order polynomial $S_{ij}(\eta)$ are expressed in alternative forms different from those in Eqs. (9) and (10), given by

$$T(\eta) = \sum_{i+m+n=6} a_{imn} \eta_1^i \eta_2^m \eta_3^n \quad (23)$$

$$S_{lt}(\eta) = \sum_{i+m+n=4} b_{imnl} \eta_1^i \eta_2^m \eta_3^n \quad (24)$$

where i , m , and n are non-negative integers. Because the polynomials are homogeneous, they must be summed up to six for $T(\eta)$ and four for $S_{lt}(\eta)$. The constants a_{imn} and b_{imnl} are dependent on the constitutive tensor C_{ijkl} as shown in Eqs. (9) and (10). The expanded form of Eqs. (23) and (24) are as follows:

$$T(\eta) = a_{600} \eta_1^6 + a_{060} \eta_2^6 + a_{006} \eta_3^6 + a_{510} \eta_1^5 \eta_2 + a_{501} \eta_1^5 \eta_3 + a_{150} \eta_1 \eta_2^5 + a_{105} \eta_1 \eta_3^5 + \dots \quad (25)$$

$$S_{lt}(\eta) = b_{400l} \eta_1^4 + b_{040l} \eta_2^4 + b_{004l} \eta_3^4 + b_{310l} \eta_1^3 \eta_2 + b_{301l} \eta_1^3 \eta_3 + b_{103l} \eta_1 \eta_2^3 + b_{130l} \eta_1 \eta_3^3 + \dots \quad (26)$$

Since the function $\bar{G}_{lt}(\eta)$ is rational of two even-order polynomials, Eq. (20) is most appropriate to be integrated employing the method of residues. However, the method of residues requires to find roots of the sixth-order polynomial $T(\eta)$. Unfortunately, no analytical solution exists for obtaining the roots of a general sixth-order polynomial. Therefore the integration can only be carried out by numerical methods, accuracy of which is moot.

To seek for an analytical expression of this integral (Eq. (20)), other than the method of residues, one can take the approach of expanding the function $\bar{G}_{ij}(\eta)$ into a series. Kroner (1953) expanded the function $\bar{G}_{ij}(\eta)$ into a series in which each term involves an integral of a product of Legendre polynomials and $\bar{G}_{ij}(\eta)$. These integrals are difficult to perform for obtaining an explicit solution.

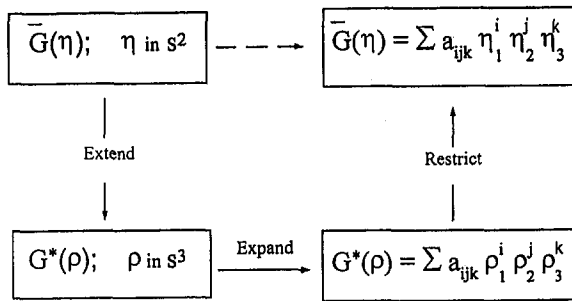


Fig. 2 Schematic illustration of the proposed method

Kinoshita and Mura (1971) suggested a method based on the assumption that the rational function $\bar{G}_{ij}(\eta)$ can be expanded into a series containing only even-order terms of $\{\eta_1, \eta_2, \eta_3\}$. With this method, the integration in Eq. (20) can be elegantly replaced by a series of derivatives of functions. These derivatives can then be carried out to obtain an explicit solution. Unfortunately, this interesting method cannot be used because, in contrary to the premise, there is always a presence of odd-order terms of η_i when $\bar{G}_{ij}(\eta)$ is expanded into a series.

4.1 Proposed Approach. Following this approach, we now attempt to seek a series expression for the function $\bar{G}_{ij}(\eta)$, leading to an explicit solution. To this end, we propose the following method:

We introduce an extend function $G_{ij}^*(\rho_k)$ by extending the domain of $\bar{G}_{ij}(\eta_k)$ from the surface s^2 to the volume s^3 of a unit sphere. By definition, the extend function $G_{ij}^*(\rho_k)$ can take any form as long as the two functions, $G_{ij}^*(\rho_k)$ and $\bar{G}_{ij}(\eta_k)$, are identical on the surface s^2 . Conversely, the restrict function of $G_{ij}^*(\rho_k)$ by restricting the domain from s^3 to s^2 is equal to the function $\bar{G}_{ij}(\eta_k)$, given by

$$G_{ij}^*(\rho_k)|_{s^3 \rightarrow s^2} = \bar{G}_{ij}(\eta_k). \quad (27)$$

Thus, one can express the extend function $G_{ij}^*(\rho_k)$ into a series. Then, by restricting the domain of this series from s^3 to s^2 , a series expression for the function $\bar{G}_{ij}(\eta_k)$ is indirectly obtained.

It is noted that the extend function $G_{ij}^*(\rho_k)$, defined in a domain larger than s^2 , does not necessarily take the same form as $\bar{G}_{ij}(\eta_k)$. Therefore, the method allows freedom regarding not only the selection of an appropriate extend function but also the selection of an appropriate point at which the function can be conveniently expanded. The procedure is schematically show in Fig. 2.

4.2 Selection of the Extended Function $G_{ij}^*(\rho)$. Among all points in the domain s^3 , it is most desirable to expand the function $G_{ij}^*(\rho_k)$ into a series with respect to the point of origin, which gives the simplest form of the series. Therefore, the domain of the selected function G_{ij}^* should include the point of origin. This excludes the possibility of selecting extend function $G_{ij}^*(\rho_k)$ to take the same form as $\bar{G}(\eta_k)$ due to its singularity at the point of origin. Therefore, we must search for an altered form which is not singular at point of origin.

For this purpose, we construct the extend function $G_{ij}^*(\rho_k)$ in the following procedure: First, replace η in $\bar{G}_{ij}(\eta)$ by ρ to obtain a function $\mathbf{F}(\rho)$. Then replace ρ_3^2 with $1 - \rho_1^2 - \rho_2^2$, ρ_3^4 with $(1 - \rho_1^2 - \rho_2^2)^2$ and ρ_3^6 with $(1 - \rho_1^2 - \rho_2^2)^3$ in $\mathbf{F}(\rho)$ to obtain $G^*(\rho)$. It is obvious that this altered function satisfies the requirement in Eq. (27) and is nonsingular at point of origin. The function $G_{ij}^*(\rho_k)$ is given by

$$G_{ij}^*(\rho_k) = \frac{S_{ij}^*(\rho)}{T^*(\rho)} \quad (28)$$

where

$$T^*(\rho) = \sum_{\substack{i+m+n=6 \\ n=1}} a_{imn}^* \rho_1^i \rho_2^m \rho_3^n \quad (29)$$

$$S_{ij}^*(\rho) = \sum_{\substack{i+m+n=4 \\ n=1}} b_{imnj}^* \rho_1^i \rho_2^m \rho_3^n. \quad (30)$$

The values of i, m, n are non-negative integers. The power $(i + m + n)$ equals to 0, 2, 4 or 6 for $T^*(\rho)$ and to 0, 2, or 4 for $S_{ij}^*(\rho)$. Note that after the substitution of ρ_3^{2m} with $(1 - \rho_1^2 - \rho_2^2)^m$, $m = 1, 2, 3$, the two polynomials are no longer homogeneous; the order n of ρ_3 is equal to either 0 or 1. The relationships of the constants a_{imn}^* and b_{imnj}^* in Eqs. (29)–(30) and the constants a_{imn} and b_{imnj} in Eqs. (23)–(24) are given in the Appendix.

The nonsingularity of $G_{ij}^*(\rho)$ at the point of origin can be observed from the polynomial series $T^*(\rho)$. For example, the expanded form of Eq. (29) is given as follows:

$$T^*(\rho) = a_{000}^* + a_{200}^* \rho_1^2 + a_{020}^* \rho_2^2 + a_{110}^* \rho_1 \rho_2 + a_{101}^* \rho_1 \rho_3 + a_{011}^* \rho_2 \rho_3 + \dots \quad (31)$$

Note that $a_{000}^* \neq 0$, thus $T^*(\mathbf{0})$ is not equal to zero.

4.3 Series Expression of $\bar{G}_{ij}(\eta)$. Since $\rho_1 \rho_2 \rho_3$ are the three independent variables in $G_{ij}^*(\rho)$, Taylor's expansion of $G_{ij}^*(\rho)$ at the point of origin can now be expressed as

$$G_{ij}^*(\rho) = \sum_{n=0}^{\infty} \frac{1}{n!} \left(\rho_1 \frac{\partial}{\partial \rho_1} + \rho_2 \frac{\partial}{\partial \rho_2} + \rho_3 \frac{\partial}{\partial \rho_3} \right)^n G_{ij}^*(\mathbf{0}) \quad (32)$$

Using the identity

$$(a + b + c)^n = \sum_{p+q+s=n} \frac{n!}{p!q!s!} a^p b^q c^s, \quad (33)$$

Taylor's expansion in Eq. (32) can be expressed as follows:

$$G_{ij}^*(\rho) = \sum_{n=0}^{\infty} \sum_{p+q+s=n} \frac{1}{n!p!q!s!} \frac{\partial^n G_{ij}^*(\mathbf{0})}{\partial \rho_1^p \partial \rho_2^q \partial \rho_3^s} \rho_1^p \rho_2^q \rho_3^s \quad (34)$$

where p, q, s , are non-negative integers. The order of n must be even; the odd-order derivatives vanish. The expansion in Eq. (34) will have one term for $n = 0$; 6 terms for $n = 2$; 15 terms for $n = 4$; and 28 terms for $n = 6$. For higher order of n , the number of terms increased rapidly (e.g., 45 terms for $n = 8$).

Now we restrict function of $G_{ij}^*(\rho)$ from domain s^3 to s^2 (i.e., from ρ_k to η_k) for obtaining the series expression of $\bar{G}_{ij}(\eta)$, given by

$$\bar{G}_{ij}(\eta) = \sum_{n=0}^{\infty} \sum_{p+q+s=n} \frac{1}{n!p!q!s!} \frac{\partial^n G_{ij}^*(\mathbf{0})}{\partial \rho_1^p \partial \rho_2^q \partial \rho_3^s} \eta_1^p \eta_2^q \eta_3^s. \quad (35)$$

5 Series Function for Green's Function

Substituting Eq. (35) into Eq. (20), one can obtain the Green's function

$$G_{ij}(\mathbf{x}) = \frac{1}{8\pi^2 r} \sum_{n=0}^{\infty} \sum_{p+q+s=n} \frac{1}{p!q!s!} \frac{\partial^n G_{ij}^*(\mathbf{0})}{\partial \rho_1^p \partial \rho_2^q \partial \rho_3^s} J_{pqs} \quad (36)$$

where p, q, s are non-negative integers.

$$J_{pqs} = \int_0^{2\pi} \int_0^\pi \eta_1^p \eta_2^q \eta_3^s d\phi \quad (37)$$

The expanded terms of Eq. (36) are illustrated in the following equation:

Table 1 Transverse isotropic elastic constants for materials A and B in (a) conventional notation and (b) contracted notation

(a)	A	B
E_x (kPa)	2,933	6,333
E_y (kPa)	9,565	9,500
μ_{xy} (kPa)	800	2,000
μ_{zx} (kPa)	4,000	4,000
ν_{xy}	0.83	0.58
ν_{xy}	0.11	0.13

(Transverse Isotropic on X-Y Plane)

(b)	A	B
C_{11} (kPa)	10,000	10,000
C_{33} (kPa)	10,000	10,000
C_{13} (kPa)	2,000	2,000
C_{44} (kPa)	4,000	4,000
C_{66} (kPa)	800	2,000

(C_{ij} is in Contracted Notation)

Table 1; 6/95 JAM; Chang and Chang; Green's Function for Elastic Medium With General Anisotropy

$$G_{ij}(\mathbf{x}) = \frac{1}{8\pi^2 r} (G_{ij}^0 J_{000} + G_{ij,12}^0 J_{110} + G_{ij,13}^0 J_{101} + G_{ij,23}^0 J_{011} + \frac{1}{2} G_{ij,11}^0 J_{200} + \frac{1}{2} G_{ij,22}^0 J_{020} + \frac{1}{2} G_{ij,33}^0 J_{002} + \frac{1}{6} G_{ij,1222}^0 J_{130} + \frac{1}{6} G_{ij,1333}^0 J_{103} + \frac{1}{6} G_{ij,1113}^0 J_{301} + \frac{1}{6} G_{ij,1112}^0 J_{310} + \frac{1}{6} G_{ij,2333}^0 J_{013} + \frac{1}{6} G_{ij,2223}^0 J_{031} + \frac{1}{4} G_{ij,1122}^0 J_{220} + \dots) \quad (38)$$

where we denote the derivatives, $[\partial^n G_{ij}^*(\mathbf{0})]/(\partial \rho_1^n \partial \rho_2^n \partial \rho_3^n)$, by

$$G_{ij,mnkl}^0 = \frac{\partial^n G_{ij}^*(\mathbf{0})}{\partial \rho_u \partial \rho_v \partial \rho_k \partial \rho_l \dots} \quad (39)$$

Note that the constants G_{ij}^0 , $G_{ij,uv}^0$, $G_{ij,mnkl}^0$ are functions of coefficients C_{ijkl} only. The integrals denoted by J_{pqrs} are functions of the position vector x_i . For purpose of illustration, explicit expressions of these constants and integrals are given in the Appendix for the first few orders.

6 Examples

The described method is intended for deriving the Green's function of a general anisotropic material. Herein, an example is first given to show that the present formulation deduces the solution for an isotropic material. Examples are also given for the anisotropic material to evaluate applicability of the method.

6.1 Isotropic Material. For an isotropic material the stiffness tensor is given by

$$C_{ijkl} = \lambda \delta_{ij} \delta_{kl} + \mu (\delta_{ik} \delta_{jl} + \delta_{il} \delta_{jk}). \quad (40)$$

$\bar{G}_{ki}(\boldsymbol{\eta})$ in Eq. (20) is obtained from Eq. (8), i.e.,

$$\bar{G}_{ki}(\boldsymbol{\eta}) = \frac{S_{ki}(\boldsymbol{\eta})}{T(\boldsymbol{\eta})} \quad (41)$$

where $S_{ki}(\boldsymbol{\eta})$ and $T(\boldsymbol{\eta})$ are given in Eqs. (9) and (10),

$$S_{ki}(\boldsymbol{\eta}) = 2\delta_{ki}(1 - \nu)\eta_m \eta_m - \eta_k \eta_i \quad (42)$$

$$T(\boldsymbol{\eta}) = 2\mu(1 - \nu)\eta_m \eta_m \eta_j \eta_j. \quad (43)$$

Based on the proposed method, the selected extend function $G^*(\rho)$ is given by

$$G_{ki}^*(\rho) = \frac{S_{ki}^*(\rho)}{T^*(\rho)} \quad (44)$$

where

$$S_{ki}^* = \begin{cases} 2(1 - \nu)\delta_{ki} - \rho_k \rho_i; & (\text{except for } k = i = 3) \\ 2(1 - \nu) - (1 - \rho_1^2 - \rho_2^2); & (\text{for } k = i = 3) \end{cases} \quad (45)$$

$$T^* = 2\mu(1 - \nu). \quad (46)$$

The second derivatives, $S_{gh,ik}^*$ and $T_{,ik}^*$, are given by

$$S_{gh,ik}^* = \begin{cases} 2(\delta_{1i}\delta_{1k} + \delta_{2i}\delta_{2k}); & (\text{for } g = h = 3) \\ -(\delta_{gk}\delta_{hi} + \delta_{gi}\delta_{hk}); & (\text{except for } g = h = 3) \end{cases} \quad (47)$$

$$T_{,ik}^* = 0. \quad (48)$$

For an isotropic material, the expansion of $\bar{G}_{ij}(\boldsymbol{\eta})$ is up to the second-order terms; higher-order terms are zero. Therefore the series expression of the Green's function according to Eq. (36) is given by

$$G_{ij}(\mathbf{x}) = \frac{1}{8\pi^2 r} (G_{ij}^0 J_{000} + G_{ij,12}^0 J_{110} + G_{ij,13}^0 J_{101} + G_{ij,23}^0 J_{011} + \frac{1}{2} G_{ij,11}^0 J_{200} + \frac{1}{2} G_{ij,22}^0 J_{020} + \frac{1}{2} G_{ij,33}^0 J_{000}). \quad (49)$$

The values of G_{ij}^0 and $G_{gh,ik}^0$ are obtained from the formula (A5), (A6), (A1), and (A2) in the Appendix, given by

$$G_{gh}^0 = \begin{cases} 2(1 - \nu)\delta_{gh}; & (\text{except for } g = h = 3) \\ 2(1 - \nu) - 1; & (\text{for } g = h = 3) \end{cases} \quad (50)$$

$$G_{gh}^0 = \begin{cases} \delta_{1i}\delta_{1k} + \delta_{2i}\delta_{2k}; & (\text{for } g = h = 3) \\ \mu(1 - \nu) \\ -\delta_{gk}\delta_{hi} - \delta_{gi}\delta_{hk}; & (\text{except for } g = h = 3). \\ 2\mu(1 - \nu) \end{cases} \quad (51)$$

The expression of J_{ijk} are obtained from formulae (A13) and (A14) in the Appendix.

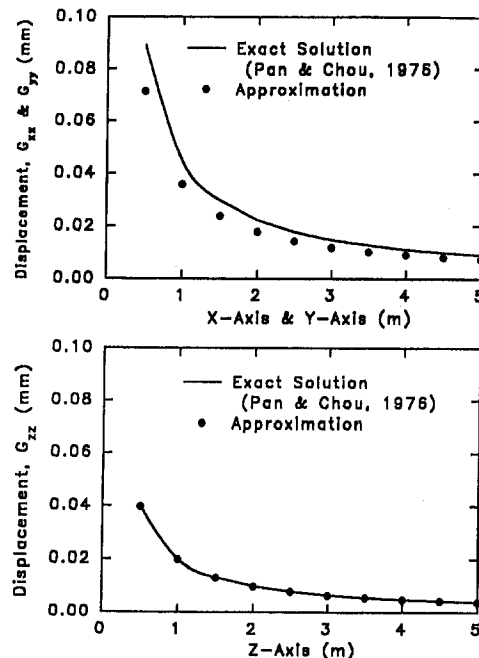


Fig. 3 Approximate Green's function obtained from the present formulation for material A

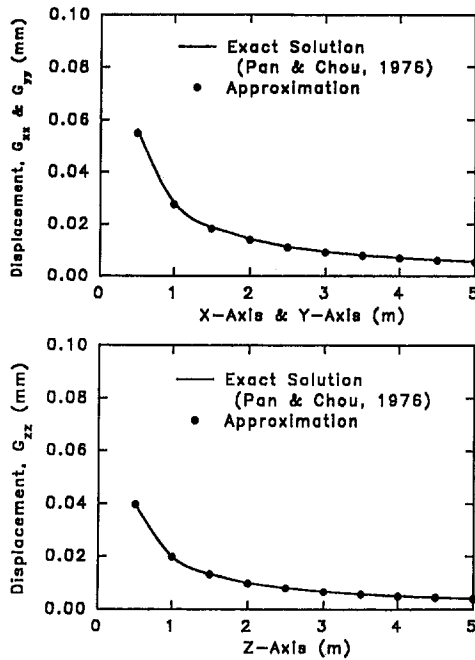


Fig. 4 Approximate Green's function obtained from the present formulation for material B

The Green's function is thus obtained by introducing Eqs. (50)–(51), (A13), (A14) into Eq. (49), given by

$$G_{ki}(\mathbf{x}) = \frac{1}{16\pi\mu r} \left\{ (3 - 4\nu)\delta_{ki} + \frac{x_k x_i}{r^2} \right\}. \quad (52)$$

It is noted that, for an isotropic material, the present method leads to an analytical form identical to the exact solution.

6.2 Anisotropic Material. The present method is applicable to materials with general anisotropy. The following is an illustration of the present formulation for the case of transverse isotropic. The computed Green's functions using the present method are truncated after the sixth-order terms of the series. The computed Green's functions are compared with solutions from Pan and Chou (1976) to evaluate the accuracy of the present sixth-order solution.

Material properties for this case (same in the directions x and y) is given in Table 1 for material types A and B. Material A is more anisotropic than material B. In Figs. 3 and 4, G_{xx} represents the displacements at various locations along the direction of the x -axis due to a unit force (1 kN) applied at the point of origin in the x direction. G_{yy} and G_{zz} carry similar meaning for direction y and direction z , respectively. For material B in Fig. 4, the present formulation with up to sixth-order terms yields results very close to the exact solution. However, for the more anisotropic material A in Fig. 3, there are small degree of discrepancies. To achieve a greater accuracy, higher-order terms need to be considered.

7 Concluding Remarks

A method of employing extend function has been used to avoid the difficulties of singularities, leading to an explicit analytical solution of Green's function for general anisotropic materials in the form of a series. Explicit expressions of the coefficients in the series are derived and tabulated in the Appendix up to fourth-order terms. The present method deduces exact solution for isotropic material. Numerical examples have shown that the present formulation with sixth-order terms yields results reasonably close to the exact solution. However, to achieve greater accuracy for materials

with higher degree of anisotropy, higher-order terms in the series expansion need to be considered.

References

- Brebbia, C. A., Telles, J. C. F., and Wrobel, L. C., 1984, *Boundary Element Techniques*, Springer-Verlag, Berlin.
- Elliott, H. A., 1948, "Three-dimensional stress distribution in hexagonal aeotropic crystals," *Proceedings, Cambridge Philosophical Society*, Vol. 44, pp. 522–533.
- Eshelby, J. D., 1959, "The elastic field outside an ellipsoidal inclusion," *Proceedings of Royal Society, London*, Vol. A252, 561–569.
- Friedman, B., 1956, *Principles and Techniques of Applied Mathematics*, John Wiley and Sons, New York.
- Hill, R., 1962, "Acceleration waves in Solids," *Journal of Mechanics and Physics of Solids*, Vol. 10, pp. 1–16.
- Hill, R., and Hutchinson, J. W., 1975, "Bifurcation phenomena in the plane tension test," *Journal of Mechanics and Physics of Solids*, Vol. 23, pp. 239–264.
- Kinoshita, N., and Mura, T., 1971, "Elastic Fields of inclusions in anisotropic media," *Physica Status Solidi (a)*, Vol. 5, pp. 759–768.
- Kroner, E., 1953, "Das fundamentalintegral der anisotropen elastischen differentialgleichungene," *Zeitschrift fur Physik*, Vol. 136, pp. 402–410.
- Lejcek, L., 1969, "The Green function of the theory of elasticity in an anisotropic hexagonal medium," *Czech. Journal of Physics, Series B*, Vol. 19, pp. 799–803.
- Mura, T., 1971, "Displacement and Plastic Distortion Fields Produced by Dislocations in Anisotropic Media," *ASME JOURNAL OF APPLIED MECHANICS*, Vol. 38, pp. 865–868.
- Mura, T., and Kinoshita, N., 1971, "Green's functions for anisotropic elasticity," *Physica status solidi (b)*, Vol. 47, pp. 607–618.
- Mura, T., 1987, *Micromechanics of Defects in Solids*, Martinus Nijhoff Publishers, Dordrecht, The Netherlands.
- Pan, Y. C., and Chou, T. W., 1976, Point Force Solution for an Infinite Transversely Isotropic Solid," *ASME JOURNAL OF APPLIED MECHANICS*, Vol. 43, pp. 608–612.
- Sveklo, V. A., 1969, "Concentrated force in a transversely isotropic half-space and in a composite space," *Journal of Applied Mathematics and Mechanics*, Vol. 33, pp. 517–523.
- Thompson, Sir W. (Lord Kelvin), 1848, "Note on the integration of the equation of equilibrium of an elastic solid," *Cambridge and Dublin Mathematical Journal*, pp. 76–99.
- Vogel, S. M., and Rizzo, F. J., 1973, "An integral equation formulation of three dimensional anisotropic elastostatic boundary value problems," *Journal of Elasticity*, Vol. 3, Sept.
- Walpole, L. J., 1967, "The elastic field of an inclusion in an anisotropic medium," *Proceedings of Royal Society, London*, Vol. A300, pp. 270–289.
- Woo, T. C., and Shield, R. T., 1962, "Fundamental solutions for small deformations superposed on finite biaxial extension of an elastic body," *Archive for Rational Mechanics and Analysis*, Vol. 9, pp. 196–224.
- Willis, J. R., 1965, "The elastic interaction energy of dislocation loops in anisotropic media," *Quarterly Journal of Mechanics and Applied Mathematics*, Vol. 18, pp. 419–433.

APPENDIX

1 Evaluation of Constants a_{ijk}^* and b_{ijkmn}^*

The following expressions given the relationships between the constants a_{ijk}^* and b_{ijkmn}^* (in Eqs. (29) and (30)) and the constants a_{pqrs} and b_{pqrst} (in Eqs. (23) and (24)).

$$\underline{i + j + k = 0}: a_{000}^* = a_{004}$$

$$\underline{i + j + k = 2}: a_{000}^* = a_{202} - 2a_{004} \quad a_{101}^* = a_{103}, \quad \text{etc.}$$

$$\underline{i + j + k = 4}: a_{400}^* = a_{400} - a_{202} + a_{004}$$

$$a_{310}^* = a_{310} - a_{112}, \quad \text{etc.}$$

$$\underline{i + j + k = 0}: b_{000}^* = b_{006}$$

$$\underline{i + j + k = 2}: b_{200}^* = b_{204} - 3b_{006} \quad b_{110}^* = b_{114}, \quad \text{etc.}$$

$$\underline{i + j + k = 4}: b_{400}^* = b_{402} - 2b_{204} + 3b_{006}$$

$$b_{310}^* = b_{312} - 2b_{114}, \quad \text{etc.}$$

$$\underline{i + j + k = 6}: b_{600}^* = b_{600} - b_{402} + b_{204} -$$

$$b_{006} \quad b_{510}^* = b_{510} - b_{312} + b_{114}, \quad \text{etc.}$$

2 Evaluation of Constants g_{gh}^0 , $G_{ij,uv}^0$, $G_{ij,uvkl}^0$, and $G_{ij,uvklmn}^0$

For convenience, abbreviations are defined for the adjoint matrix tensor, determinant, and their derivatives as follows:

$$S = S_{gh}^*(0); \quad T = T^*(0) \quad (A1)$$

$$S_{ij} = S_{gh,ij}^*(0); \quad T_{ij} = T_{ij}^*(0) \quad (A2)$$

$$S_{ijkl} = S_{gh,ijkl}^*(0); \quad T_{ijkl} = T_{ijkl}^*(0) \quad (A3)$$

$$T_{ij\dots} = T_{ij\dots}^*(0). \quad (A4)$$

The explicit expressions of constants g_{gh}^0 , $G_{ij,uv}^0$, $G_{ij,uvkl}^0$, and $G_{ij,uvklmn}^0$ of Eq. (38) are given in the following for the order of n equals to 0, 2, 4:

$$n = 0: \quad G_{gh}^0 = \frac{S}{T} \quad (A5)$$

$$n = 2: \quad G_{gh,ik} = \frac{TS_{ik} - ST_{ik}}{T^2} \quad (A6)$$

$$n = 4: \quad G_{gh,ijkl} = \frac{V_{21}}{T^2} + \frac{V_{31}}{T^3} \quad (A7)$$

where

$$\begin{aligned} V_{21} &= T_{jl}S_{ik} + TS_{ikjl} + S_{ij}T_{kl} + S_{il}T_{kj} \\ &\quad - (S_{kl}T_{il} + S_{kl}T_{ij} + S_{jl}T_{ik} + ST_{ikjl}) \\ V_{31} &= 2(-TS_{ik}T_{jl} + ST_{ik}T_{jl} - TS_{ij}T_{kl} - TS_{il}T_{kj} \\ &\quad + ST_{ij}T_{kl} + ST_{il}T_{kj}). \quad (A8) \end{aligned}$$

3 Evaluation of Integration J_{pqrs}

The explicit expressions of J_{pqrs} are given in the following for the orders of 0, 2, 4, and 6. J_{pqrs} in Eq. (37) can be transformed in terms of α_{ij} by using the following equation:

$$\eta_i = \alpha_{i2} \cos \phi + \alpha_{i3} \sin \phi \quad (A9)$$

where $\alpha_{i2} = \cos(\eta_i, x_2)$, $\alpha_{i3} = \cos(\eta_i, x_3)$ as shown in Fig. 1.

The integrals J_{pqrs} can now be performed using the following two equations:

$$\begin{aligned} &\int_0^{2\pi} \cos^m \phi \sin^n \phi d\phi \\ &= \begin{cases} \frac{(m-1)!!(n-1)!!}{(m+n)!!} 2\pi & (m \wedge n \geq 0 \text{ even}) \\ 0 & (m \vee n \geq 0 \text{ odd}) \end{cases} \quad (A10) \end{aligned}$$

$$\begin{aligned} \int_0^{2\pi} \sin^n \phi d\phi &= \int_0^{2\pi} \cos^n \phi d\phi \\ &= \begin{cases} \frac{(n-1)!!}{n!!} 2\pi & (n \geq 0 \text{ even}) \\ 0 & (n \geq 0 \text{ odd}). \end{cases} \quad (A11) \end{aligned}$$

Further, using the property of orthogonality for α_{ij} , given by

$$\frac{x_i x_j}{r^2} + \alpha_{i2} \alpha_{j2} + \alpha_{i3} \alpha_{j3} = \delta_{ij} \quad (A12)$$

where $r^2 = x_1^2 + x_2^2 + x_3^2$, J_{pqrs} can thus be expressed as functions of x_i as follows:

$$J_{000} = 2\pi \quad (A13)$$

$$J_{200} = \pi \left(1 - \frac{x_1^2}{r^2} \right), \quad J_{110} = -\pi \frac{x_1 x_2}{r^2} \quad (A14)$$

$$J_{400} = \frac{3\pi}{4} \left(1 - \frac{x_1^2}{r^2} \right)^2, \quad J_{310} = \frac{3\pi}{4} \frac{x_1^2 x_1 x_2}{r^2 r^2}$$

$$J_{220} = \frac{\pi}{4} \left(1 - \frac{2x_2^2}{r^2} + 3 \frac{x_1^2 x_2^2}{r^4} \right),$$

$$J_{211} = \frac{\pi}{4} \left(\frac{3x_1^2}{r^2} - 1 \right) \frac{x_2 x_3}{r^2} \quad (A15)$$

$$J_{510} = -\frac{5\pi}{8} \left(1 - \frac{x_1^2}{r^2} \right)^2 \frac{x_1 x_2}{r^2},$$

$$J_{330} = \frac{\pi}{8} \left(-3 + 3 \frac{(x_1^2 + x_2^2)}{r^2} - 5 \frac{x_1^2 x_2^2}{r^4} \right) \frac{x_1 x_2}{r^2}$$

$$J_{600} = \frac{5\pi}{8} \left(1 - \frac{x_1^2}{r^2} \right)^3,$$

$$J_{321} = \frac{\pi}{8} \left(-1 + \frac{(x_1^2 + 3x_2^2)}{r^2} - 5 \frac{x_1^2 x_2^2}{r^4} \right) \frac{x_1 x_3}{r^2}$$

$$J_{411} = \frac{\pi}{8} \frac{x_2 x_3}{r^2} \left(-1 + \frac{x_1^2}{r^2} - 5x_1^5 \right),$$

$$J_{420} = \frac{\pi}{8} \left(1 - \frac{2x_1^2 + x_2^2}{r^2} + \frac{6x_1^2 x_2^2 + x_1^4}{r^4} - 5x_1^4 x_2^2 \right). \quad (A16)$$

The other components of J_{ijk} can be easily obtained by rotating $x_1 \rightarrow x_2 \rightarrow x_3 \rightarrow x_1$, i.e., $J_{ijk} = J_{ijk}(x_1 \leftrightarrow x_2)$, $J_{kji} = J_{ijk}(x_1 \leftrightarrow x_3)$, $J_{kij} = J_{kji}(x_2 \leftrightarrow x_3)$, etc.

The Elastic Field Caused by a Circular Cylindrical Inclusion— Part I: Inside the Region $x_1^2 + x_2^2 < a^2$, $-\infty < x_3 < \infty$ Where the Circular Cylindrical Inclusion is Expressed by $x_1^2 + x_2^2 \leq a^2$, $-h \leq x_3 \leq h$

Linzhi Wu

Shanyi Du

Research Laboratory of Composite
Materials,
School of Astronautics,
Harbin Institute of Technology,
Harbin, 150006, P. R. China

The displacement and stress fields caused by uniform eigenstrains in a circular cylindrical inclusion are analyzed inside the region $x_1^2 + x_2^2 < a^2$, $-\infty < x_3 < \infty$ and are given in terms of nonsingular surface integrals. Analytical solutions can be expressed as functions of the complete elliptic integrals of the first, second and third kind. The corresponding elastic fields in the region $x_1^2 + x_2^2 > a^2$, $-\infty < x_3 < \infty$ are solved by using the same technique (by Green's functions) in the companion paper (Part II).

1 Introduction

Eshelby (1957, 1959, 1961) has outlined a general method of calculating the elastic strain field caused by an ellipsoidal inclusion in an infinite homogeneous isotropic elastic medium, when the inclusion undergoes a change of shape which in the absence of the surrounding material would be an arbitrary uniform strain. Since then, the inclusion problem has greatly been developed, as pointed out by the extensive reviews of Mura (1987, 1988). A number of techniques have been used to deal with the class of problems. However, many results at present are not expressed in explicit form but are in the form of numerical solutions.

Chiu (1977, 1978) has solved the stress field due to uniform eigenstrains in a cuboidal inclusion surrounded by an infinite elastic space and a half one, respectively, but most of the works have been done for ellipsoidal inclusions, for example, Seo and Mura (1979) have solved the elastic field in a half-space due to an ellipsoidal inclusion with uniform eigenstrains; Castles and Mura (1985) have shown the analysis of eigenstrains outside of an ellipsoidal inclusion, etc. Takao et al. (1981) have investigated the problem of a cylindrical inclusion with uniform axial eigenstrain, but they have only obtained the closed-form solution for the stress and strain fields along the cylindrical axis. Hasegawa et al. (1992) have also obtained the closed-form solutions for a solid or hollow circular cylindrical inclusion with uniform eigenstrain prescribed in an isotropic infinite solid, but their elastic fields are limited to the axisymmetric case.

The present paper derives expressions using the technique of Green's function to obtain the displacement and stress fields in

an infinite isotropic elastic medium having a circular cylindrical domain (of the same material) within which arbitrary uniform eigenstrains are given. Analytical solutions in the region $x_1^2 + x_2^2 < a^2$, $-\infty < x_3 < \infty$ show that displacement and stress fields can be expressed as functions of the complete elliptic integrals of the first, second and third kind. In the subsequent paper, Part II, we following the same technique will give the corresponding results for the region $x_1^2 + x_2^2 > a^2$, $-\infty < x_3 < \infty$.

In what follows, the summation convention over repeated Latin indices is adopted from 1-3. Furthermore, a comma indicates partial differentiation, thus $f_{,i}$ means $\partial f / \partial x_i$. In cases where differentiations are made with respect to x'_i , they are written in full notation.

2 Statement of the Problem

In the theory of micromechanics of materials (Mura, 1987), when an eigenstrain is prescribed in a finite region in a homogeneous material, the finite region is called an inclusion. The elastic moduli of the inclusion are assumed to be the same as the matrix. If the finite region has elastic moduli different from those of the matrix, the region is called an inhomogeneity.

We consider a circular cylindrical inclusion Ω with length $2h$ and radius a in an infinite isotropic medium D as shown Fig. 1. From Mura (1987), the induced displacement field $u_i(\mathbf{x})$ due to eigenstrains $\epsilon_{ij}^*(\mathbf{x})$ is given by

$$u_i(\mathbf{x}) = - \int_{\Omega} \int_{\Omega} \int_{\Omega} C_{jlmn} \epsilon_{mn}^*(\mathbf{x}') G_{ij,l}(\mathbf{x} - \mathbf{x}') d\mathbf{x}' \quad (1)$$

where C_{jlmn} are the elastic moduli of material and $G_{ij}(\mathbf{x} - \mathbf{x}')$ are the elastic Green's functions for the infinite medium. For the isotropic case, Green's functions $G_{ij}(\mathbf{x} - \mathbf{x}')$ following Mura (1987) can be expressed in the form

$$G_{ij}(\mathbf{x} - \mathbf{x}') = \frac{1}{16\pi\mu(1-\nu)} \left[\frac{(3-4\nu)\delta_{ij}}{|\mathbf{x} - \mathbf{x}'|} + \frac{(x_i - x'_i)(x_j - x'_j)}{|\mathbf{x} - \mathbf{x}'|^3} \right], \quad (2)$$

Contributed by the Applied Mechanics Division of THE AMERICAN SOCIETY OF MECHANICAL ENGINEERS for publication in the ASME JOURNAL OF APPLIED MECHANICS.

Discussion on this paper should be addressed to the Technical Editor, Prof. Lewis T. Wheeler, Department of Mechanical Engineering, University of Houston, Houston, TX 77204-4792, and will be accepted until four months after final publication of the paper itself in the ASME JOURNAL OF APPLIED MECHANICS.

Manuscript received by the ASME Applied Mechanics Division, Sept. 13, 1993; final revision, Mar. 17, 1994. Associate Technical Editor: D. M. Barnett.

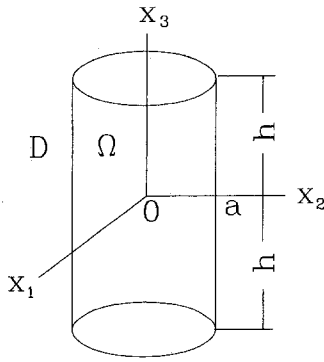


Fig. 1 The geometry of a circular cylindrical inclusion

where μ and ν are the shear modulus and Poisson's ratio of medium, respectively, and $|\mathbf{x} - \mathbf{x}'| = [(x_i - x'_i)(x_i - x'_i)]^{1/2}$. When $\epsilon_{mn}^*(\mathbf{x}')$ are uniform in Ω , Eq. (1) by integration by parts can be written as

$$u_i(\mathbf{x}) = C_{j3mn}\epsilon_{mn}^* \left[\int_{\Omega_1} \int G_{ij}(\mathbf{x} - \mathbf{x}') dx'_1 dx'_2 \right] \Big|_{x'_3=-h}^h + C_{jlmn}\epsilon_{mn}^* \int_0^h \int_{-h}^h G_{ij}(\mathbf{x} - \mathbf{x}') n_l ad\theta dx'_3 \quad (3)$$

where Ω_1 is the area of the base of circular cylinder, n_i is the outward unit normal to cylindrical surface, and (r, θ, x_3) are cylindrical coordinates, namely there are relations $x'_1 = a \cos \theta$, $x'_2 = a \sin \theta$ on the cylindrical surface.

Taking into account the symmetry in directions x_1, x_2 , we only need to solve the following kinds of integrals:

$$I(x_1, x_2, z) = \int_{\Omega_1} \int \frac{dx'_1 dx'_2}{|\mathbf{x} - \mathbf{x}'|} I_{ij}(x_1, x_2, z) = \int_{\Omega_1} \int \frac{(x_i - x'_i)(x_j - x'_j) dx'_1 dx'_2}{|\mathbf{x} - \mathbf{x}'|^3} \quad (i = 1, 3, \quad j = 1, 2, 3, \quad i \leq j) \quad (4)$$

and

$$J^c(x_1, x_2, x_3) = a \int_0^{2\pi} \int_{-h}^h \frac{\cos \theta d\theta dx'_3}{|\mathbf{x} - \mathbf{x}'|} J_{ij}^c(x_1, x_2, x_3) = a \int_0^{2\pi} \int_{-h}^h \frac{\cos \theta (x_i - x'_i)(x_j - x'_j) d\theta dx'_3}{|\mathbf{x} - \mathbf{x}'|^3} \quad (i, j = 1, 2, 3, \quad i \leq j) \quad (5)$$

where $z = x_3 - x'_3$.

3 Solution of Eqs. (4) and (5)

We first consider the integrals in (4). When point $\mathbf{x} = (x_1, x_2, x_3)$ satisfies the conditions $x_1^2 + x_2^2 < a^2$, $-\infty < x_3 < \infty$, the integrals are explicitly performed. As shown in Fig. 2, the area element $dx'_1 dx'_2$ in (4) can be written as

$$dx'_1 dx'_2 = r dr d\varphi \quad (6)$$

where $r = |\mathbf{x} - \mathbf{x}'|$ and $d\varphi$ is an arc element of a unit circle centered at point \mathbf{x} . Upon integration with respect to r , we obtain

$$I(x_1, x_2, z) = \int_0^{2\pi} \sqrt{r^2(\varphi) + z^2} d\varphi - 2\pi|z| I_{11}(x_1, x_2, z) = \int_0^{2\pi} \cos^2 \varphi \sqrt{r^2(\varphi) + z^2} d\varphi + z^2 \int_0^{2\pi} \frac{\cos^2 \varphi d\varphi}{\sqrt{r^2(\varphi) + z^2}} - 2\pi|z|$$

$$I_{33}(x_1, x_2, z) = -z^2 \int_0^{2\pi} \frac{d\varphi}{\sqrt{r^2(\varphi) + z^2}} + 2\pi|z|$$

$$I_{12}(x_1, x_2, z) = \int_0^{2\pi} \sin \varphi \cos \varphi \sqrt{r^2(\varphi) + z^2} d\varphi + z^2 \int_0^{2\pi} \frac{\sin \varphi \cos \varphi d\varphi}{\sqrt{r^2(\varphi) + z^2}}$$

$$I_{13}(x_1, x_2, z) = z \int_0^{2\pi} \frac{\cos \varphi r(\varphi) d\varphi}{\sqrt{r^2(\varphi) + z^2}} - z \int_0^{2\pi} \cos \varphi \ln [r(\varphi) + \sqrt{r^2(\varphi) + z^2}] d\varphi \quad (7)$$

where $r(\varphi)$ is the positive root of

$$(x_1 + r \cos \varphi)^2 + (x_2 + r \sin \varphi)^2 = a^2, \quad (8)$$

which is

$$r(\varphi) = -\sqrt{x_1^2 + x_2^2} \cos(\varphi - \phi) + \sqrt{(x_1^2 + x_2^2) \cos^2(\varphi - \phi) + a^2 - x_1^2 - x_2^2} \quad (9)$$

where $\cos \phi = x_1 / \sqrt{x_1^2 + x_2^2}$, $\sin \phi = x_2 / \sqrt{x_1^2 + x_2^2}$.

According to the properties of trigonometric function, we can obtain, after some manipulation,

$$I(x_1, x_2, z) = 2 \int_0^\pi \sqrt{r_1^2(\varphi) + z^2} d\varphi - 2\pi|z| I_{11}(x_1, x_2, z) = 2 \sin^2 \phi \int_0^\pi \sqrt{r_1^2(\varphi) + z^2} d\varphi + 2 \cos 2\phi \int_0^\pi \cos^2 \varphi \sqrt{r_1^2(\varphi) + z^2} d\varphi + 2z^2 \sin^2 \phi \int_0^\pi \frac{d\varphi}{\sqrt{r_1^2(\varphi) + z^2}} + 2z^2 \cos 2\phi \int_0^\pi \frac{\cos^2 \varphi d\varphi}{\sqrt{r_1^2(\varphi) + z^2}} - 2\pi|z| I_{33}(x_1, x_2, z) = 2\pi|z| - 2z^2 \int_0^\pi \frac{d\varphi}{\sqrt{r_1^2(\varphi) + z^2}} I_{12}(x_1, x_2, z) = -\sin 2\phi \left\{ \int_0^\pi \sqrt{r_1^2(\varphi) + z^2} d\varphi - 2 \int_0^\pi \cos^2 \varphi \sqrt{r_1^2(\varphi) + z^2} d\varphi + z^2 \int_0^\pi \frac{d\varphi}{\sqrt{r_1^2(\varphi) + z^2}} - 2z^2 \int_0^\pi \frac{\cos^2 \varphi d\varphi}{\sqrt{r_1^2(\varphi) + z^2}} \right\}$$

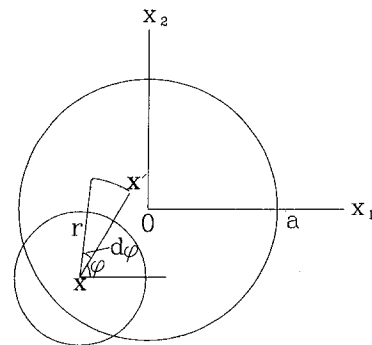


Fig. 2 The projection of Fig. 1 in ox_1x_2

$$I_{13}(x_1, x_2, z) = 2z \cos \phi \left\{ \int_0^\pi \frac{\cos \varphi r_1(\varphi) d\varphi}{\sqrt{r_1^2(\varphi) + z^2}} - \int_0^\pi \cos \varphi \ln [r_1(\varphi) + \sqrt{r_1^2(\varphi) + z^2}] d\varphi \right\}, \quad (10)$$

where

$$r_1(\varphi) = -\sqrt{x_1^2 + x_2^2} \cos \varphi + \sqrt{(x_1^2 + x_2^2) \cos^2 \varphi + a^2 - x_1^2 - x_2^2}. \quad (11)$$

Letting $r_1(\varphi) = \sqrt{t}$, we have

$$\cos \varphi = \frac{a^2 - x_1^2 - x_2^2 - t}{2\sqrt{x_1^2 + x_2^2}\sqrt{t}} \quad (12)$$

$$d\varphi = \frac{a^2 - x_1^2 - x_2^2 + t}{2t\sqrt{(t - t_1)(t_2 - t)}} dt, \quad (13)$$

where

$$t_1 = r_1^2(0) = (a - \sqrt{x_1^2 + x_2^2})^2, \\ t_2 = r_1^2(\pi) = (a + \sqrt{x_1^2 + x_2^2})^2. \quad (14)$$

Thus, Eq. (10), in terms of Appendix A, can further be expressed in the form

$$I(x_1, x_2, z) = I^1(x_1, x_2, z) + (a^2 - x_1^2 - x_2^2 + z^2)I^2(x_1, x_2, z) + (a^2 - x_1^2 - x_2^2)z^2I^3(x_1, x_2, z, 0) - 2\pi|z|$$

$$I_{33}(x_1, x_2, z) = 2\pi|z| - z^2I^2(x_1, x_2, z) - (a^2 - x_1^2 - x_2^2)z^2I^3(x_1, x_2, z, 0)$$

$$I_{11}(x_1, x_2, z) = \frac{x_2^2}{x_1^2 + x_2^2} \{ I^1(x_1, x_2, z) + (a^2 - x_1^2 - x_2^2 + 2z^2)I^2(x_1, x_2, z) + 2(a^2 - x_1^2 - x_2^2)z^2I^3(x_1, x_2, z, 0) \} - 2\pi|z| + \frac{x_1^2 - x_2^2}{12(x_1^2 + x_2^2)^2} \{ [a^2 + 4z^2 + 7(x_1^2 + x_2^2)]I^1(x_1, x_2, z)$$

$$+ 4[(2x_1^2 + 2x_2^2 - a^2)z^2 - (a^2 - x_1^2 - x_2^2)^2]I^2(x_1, x_2, z) + 3(a^2 - x_1^2 - x_2^2)^2(a^2 - x_1^2 - x_2^2 - 2z^2)I^3(x_1, x_2, z, 0) + 6(a^2 - x_1^2 - x_2^2)^3z^2I^4(x_1, x_2, z) \}$$

$$I_{12}(x_1, x_2, z) = -\frac{x_1x_2}{x_1^2 + x_2^2} \{ I^1(x_1, x_2, z) + (a^2 - x_1^2 - x_2^2 + 2z^2)I^2(x_1, x_2, z) + 2(a^2 - x_1^2 - x_2^2)z^2I^3(x_1, x_2, z, 0) \} + \frac{x_1x_2}{6(x_1^2 + x_2^2)^2} \{ [a^2 + 4z^2 + 7(x_1^2 + x_2^2)]I^1(x_1, x_2, z) + 4[(2x_1^2 + 2x_2^2 - a^2)z^2 - (a^2 - x_1^2 - x_2^2)^2]I^2(x_1, x_2, z) + 3(a^2 - x_1^2 - x_2^2)^2(a^2 - x_1^2 - x_2^2 - 2z^2)I^3(x_1, x_2, z, 0) + 6(a^2 - x_1^2 - x_2^2)^3z^2I^4(x_1, x_2, z) \} \\ I_{13}(x_1, x_2, z) = \frac{x_1z}{x_1^2 + x_2^2} [(a^2 + x_1^2 + x_2^2)I^2(x_1, x_2, z) - I^1(x_1, x_2, z)]. \quad (15)$$

It should be pointed out that integration by parts for the derivation of $I_{13}(x_1, x_2, z)$ in (10) is used. Evidently, the remaining components are obtained by the following formulae:

$$I_{ij}(x_1, x_2, z) = I_{ji}(x_1, x_2, z) \\ I_{22}(x_1, x_2, z) = I_{11}(x_2, x_1, z) \\ I_{23}(x_1, x_2, z) = I_{13}(x_2, x_1, z). \quad (16)$$

Subsequently, let us consider the integrals in (5). Integrating (5) with respect to x_3' and taking into account properties of trigonometric function, we can obtain

$$J^c(x_1, x_2, x_3) = 2a \cos \phi \int_0^\pi \cos \theta \ln [-z + f(x_1, x_2, z, \theta)] d\theta \Big|_{x_3=-h}^h \\ J_{11}^c(x_1, x_2, x_3) = -2az \times \int_0^\pi \left\{ \frac{-2ax_1 \sin^2 \phi + (x_1^2 + 3a^2 \sin^2 \phi) \cos \phi \cos \theta}{[f^2(x_1, x_2, z, \theta) - z^2]f(x_1, x_2, z, \theta)} + \frac{-2ax_1 \cos 2\phi \cos^2 \theta + a^2 \cos 3\phi \cos^3 \theta}{[f^2(x_1, x_2, z, \theta) - z^2]f(x_1, x_2, z, \theta)} \right\} d\theta \Big|_{x_3=-h}^h$$

$$J_{22}^c(x_1, x_2, x_3) = -2az \int_0^\pi \left\{ \frac{ax_2 \sin 2\phi + [x_2^2 + a^2(1 - 3 \sin^2 \phi)] \cos \phi \cos \theta}{[f^2(x_1, x_2, z, \theta) - z^2]f(x_1, x_2, z, \theta)} + \frac{-2ax_2 \sin 2\phi \cos^2 \theta - a^2 \cos 3\phi \cos^3 \theta}{[f^2(x_1, x_2, z, \theta) - z^2]f(x_1, x_2, z, \theta)} \right\} d\theta \Big|_{x_3=-h}^h$$

$$J_{33}^c(x_1, x_2, x_3) = 2az \cos \phi \int_0^\pi \frac{\cos \theta d\theta}{f(x_1, x_2, z, \theta)} \Big|_{x_3=-h}^h + J^c(x_1, x_2, x_3)$$

$$J_{12}^c(x_1, x_2, x_3) = -2az \int_0^\pi \left\{ \frac{a(x_1 \cos \phi - x_2 \sin \phi) \sin \phi - a(x_1 \sin 2\phi + x_2 \cos 2\phi) \cos^2 \theta}{[f^2(x_1, x_2, z, \theta) - z^2]f(x_1, x_2, z, \theta)} + \frac{[x_1x_2 \cos \phi + a^2(1 - 3 \cos^2 \phi) \sin \phi] \cos \theta + a^2 \sin 3\phi \cos^3 \theta}{[f^2(x_1, x_2, z, \theta) - z^2]f(x_1, x_2, z, \theta)} \right\} d\theta \Big|_{x_3=-h}^h$$

$$J_{13}^c(x_1, x_2, x_3) = 2a \int_0^\pi \frac{-a \sin^2 \phi + x_1 \cos \phi \cos \theta - a \cos 2\phi \cos^2 \theta}{f(x_1, x_2, z, \theta)} d\theta \Big|_{x_3=-h}^h$$

$$J_{23}^c(x_1, x_2, x_3) = 2a \int_0^\pi \frac{a \sin \phi \cos \phi + x_2 \cos \phi \cos \theta - a \sin 2\phi \cos^2 \theta}{f(x_1, x_2, z, \theta)} d\theta \Big|_{x_3=-h}^h \quad (17)$$

where

$$f(x_1, x_2, z, \theta) = [a^2 + x_1^2 + x_2^2 - 2a\sqrt{x_1^2 + x_2^2} \cos \theta + z^2]^{1/2}.$$

Letting $\sqrt{a^2 + x_1^2 + x_2^2 - 2a\sqrt{x_1^2 + x_2^2} \cos \theta + z^2} = t$, we, after some manipulation, can obtain

$$\cos \theta = \frac{a^2 + x_1^2 + x_2^2 + z^2 - t^2}{2a\sqrt{x_1^2 + x_2^2}} \quad (18)$$

$$d\theta = \frac{2t}{\sqrt{(t^2 - t_1^2)(t_2^2 - t^2)}} dt \quad (19)$$

where

$$t_1 = \sqrt{(a - \sqrt{x_1^2 + x_2^2})^2 + z^2},$$

$$t_2 = \sqrt{(a + \sqrt{x_1^2 + x_2^2})^2 + z^2}. \quad (20)$$

Thus, Eq. (17) following Appendix B can be written as

$$J^c(x_1, x_2, x_3) = -\frac{x_1}{x_1^2 + x_2^2} \left[\frac{\pi}{2} (a^2 + x_1^2 + x_2^2) - zJ^1(x_1, x_2, z) + z(2a^2 + 2x_1^2 + 2x_2^2 + z^2)J^2(x_1, x_2, z) - (a^2 - x_1^2 - x_2^2)^2 J^3(x_1, x_2, z, z) \right] \Big|_{x_3=-h}^h$$

$$J_{33}^c(x_1, x_2, x_3) = -\frac{x_1}{x_1^2 + x_2^2} \left[\frac{\pi}{2} (a^2 + x_1^2 + x_2^2) + zJ^1(x_1, x_2, z) - z^3 J^2(x_1, x_2, z) - (a^2 - x_1^2 - x_2^2)^2 J^3(x_1, x_2, z, z) \right] \Big|_{x_3=-h}^h$$

$$J_{11}^c(x_1, x_2, x_3) = \frac{4ax_1z}{x_1^2 + x_2^2} \left[2ax_2^2 J^4(x_1, x_2, z) - \frac{x_1^4 + x_1^2x_2^2 + 3a^2x_2^2}{\sqrt{x_1^2 + x_2^2}} J^5(x_1, x_2, z) + 2a(x_1^2 - x_2^2) J^6(x_1, x_2, z) - \frac{a^2(x_1^2 - 3x_2^2)}{\sqrt{x_1^2 + x_2^2}} J^7(x_1, x_2, z) \right] \Big|_{x_3=-h}^h$$

$$J_{22}^c(x_1, x_2, x_3) = \frac{4ax_1z}{x_1^2 + x_2^2} \left[-2ax_2^2 J^4(x_1, x_2, z) - \frac{x_1^2x_2^2 + x_2^4 + a^2(x_1^2 - 2x_2^2)}{\sqrt{x_1^2 + x_2^2}} J^5(x_1, x_2, z) + 4ax_2^2 J^6(x_1, x_2, z) - \frac{a^2(3x_2^2 - x_1^2)}{\sqrt{x_1^2 + x_2^2}} J^7(x_1, x_2, z) \right] \Big|_{x_3=-h}^h$$

$$J_{12}^c(x_1, x_2, x_3) = \frac{-4ax_2z}{x_1^2 + x_2^2} \left[a(x_1^2 - x_2^2) J^4(x_1, x_2, z) + \frac{x_1^4 + x_1^2x_2^2 + a^2(x_2^2 - 2x_1^2)}{\sqrt{x_1^2 + x_2^2}} J^5(x_1, x_2, z) + a(x_2^2 - 3x_1^2) J^6(x_1, x_2, z) + \frac{a^2(3x_1^2 - x_2^2)}{\sqrt{x_1^2 + x_2^2}} J^7(x_1, x_2, z) \right] \Big|_{x_3=-h}^h$$

$$J_{13}^c(x_1, x_2, x_3) = \frac{4a}{\sqrt{x_1^2 + x_2^2}} \left[-\frac{ax_2^2}{\sqrt{x_1^2 + x_2^2}} J^2(x_1, x_2, z) + x_1^2 J^8(x_1, x_2, z) - \frac{a(x_1^2 - x_2^2)}{\sqrt{x_1^2 + x_2^2}} J^9(x_1, x_2, z) \right] \Big|_{x_3=-h}^h$$

$$J_{23}^c(x_1, x_2, x_3) = \frac{4ax_1x_2}{\sqrt{x_1^2 + x_2^2}} \left[\frac{a}{\sqrt{x_1^2 + x_2^2}} J^2(x_1, x_2, z) + J^8(x_1, x_2, z) - \frac{2a}{\sqrt{x_1^2 + x_2^2}} J^9(x_1, x_2, z) \right] \Big|_{x_3=-h}^h. \quad (21)$$

It should be noted that the relations $\cos \phi = x_1/\sqrt{x_1^2 + x_2^2}$, $\sin \phi = x_2/\sqrt{x_1^2 + x_2^2}$ in the derivation of (21) are used. Obviously, if variable $\cos \theta$ in (5) is replaced by $\sin \theta$ and the corresponding integrals are expressed by $J_{ij}^s(x_1, x_2, x_3)$, all the other components related to displacement field are given by the following relations:

$$J_{ij}^c(x_1, x_2, x_3) = J_{ji}^c(x_1, x_2, x_3)$$

$$J^s(x_1, x_2, x_3) = J^c(x_2, x_1, x_3)$$

$$J_{11}^s(x_1, x_2, x_3) = J_{22}^c(x_2, x_1, x_3)$$

$$J_{22}^s(x_1, x_2, x_3) = J_{11}^c(x_2, x_1, x_3)$$

$$J_{12}^s(x_1, x_2, x_3) = J_{12}^c(x_2, x_1, x_3)$$

$$J_{33}^s(x_1, x_2, x_3) = J_{33}^c(x_2, x_1, x_3)$$

$$J_{13}^s(x_1, x_2, x_3) = J_{23}^c(x_2, x_1, x_3)$$

$$J_{23}^s(x_1, x_2, x_3) = J_{13}^c(x_2, x_1, x_3)$$

$$J_{ij}^s(x_1, x_2, x_3) = J_{ji}^s(x_1, x_2, x_3). \quad (22)$$

4 The Corresponding Displacement and Stress Fields

Following (2)–(5), the induced displacement field within the region $x_1^2 + x_2^2 < a^2$, $-\infty < x_3 < \infty$ can be expressed as

$$u_i(\mathbf{x}) = \frac{1}{16\pi\mu(1-\nu)} [(\lambda\delta_{i3}\epsilon_{mm}^* + 2\mu\epsilon_{i3}^*) \times (3 - 4\nu)I(x_1, x_2, z)|_{x_3=-h}^h + (\lambda\delta_{j3}\epsilon_{mm}^* + 2\mu\epsilon_{j3}^*)I_{ij}(x_1, x_2, z)|_{x_3=-h}^h + (\lambda\delta_{i1}\epsilon_{mm}^* + 2\mu\epsilon_{i1}^*)(3 - 4\nu)J^c(x_1, x_2, x_3) + (\lambda\delta_{j1}\epsilon_{mm}^* + 2\mu\epsilon_{j1}^*)J_{ij}^c(x_1, x_2, x_3) + (\lambda\delta_{i2}\epsilon_{mm}^* + 2\mu\epsilon_{i2}^*)(3 - 4\nu)J^s(x_1, x_2, x_3) + (\lambda\delta_{j2}\epsilon_{mm}^* + 2\mu\epsilon_{j2}^*)J_{ij}^s(x_1, x_2, x_3)]. \quad (23)$$

From Appendixes A and B, the displacement field can be expressed as functions of the complete elliptic integrals of the first, second, and third kind. To determine the stress field, we only need to solve the first partial derivative of the three complete elliptic integrals with respect to variable x_i in terms of Hooke's law.

After some manipulation, we have

$$\frac{\partial F(k)}{\partial x_i} = \frac{E(k) - (1 - k^2)F(k)}{k(1 - k^2)} k_{,i}$$

$$\frac{\partial E(k)}{\partial x_i} = \frac{E(k) - F(k)}{k} k_{,i}$$

$$\frac{\partial \Pi(h, k)}{\partial x_i} = \frac{kk_{,i}}{k^2 + h} \left[\frac{E(k)}{1 - k^2} - \Pi(h, k) \right] + \frac{h_{,i}}{2(1 + h)h(k^2 + h)} [hE(k) - (k^2 + h)F(k) + (k^2 - h^2)\Pi(h, k)] \quad (24)$$

where $F(k)$, $E(k)$, and $\Pi(h, k)$ are the complete elliptic integrals of the first, second, and third kind, respectively.

Following (23) and (24), the stress field within the corresponding region can be obtained in terms of Hooke's law. Evidently, it still is functions of the complete elliptic integrals of the first, second, and third kind. Because of the complexity of stress field, we here do not give the concrete expressions.

5 Conclusions

Analytical expressions for the displacement and stress fields caused by arbitrary uniform eigenstrains in a circular cylindrical inclusion are derived and given by using the technique of Green's function. It should be pointed out that the present solutions only correspond to the region $x_1^2 + x_2^2 < a^2$, $-\infty < x_3 < \infty$. In Part II of this paper, we shall derive and give the expressions for displacement and stress fields inside the region $x_1^2 + x_2^2 > a^2$, $-\infty < x_3 < \infty$. There we will investigate the limit case of infinite cylindrical inclusion. From Section 4, the displacement and stress fields within the region $x_1^2 + x_2^2 < a^2$, $-\infty < x_3 < \infty$ can be expressed as functions of the complete elliptic integrals of the first, second, and third kind, so numerical solutions of the elastic field due to arbitrary uniform eigenstrains in a circular cylindrical inclusion can easily and numerically be obtained.

Acknowledgment

This research was supported by National Education Foundation for Doctoral Degrees.

References

- Castles, R. R., and Mura, T., 1985, "The Analysis of Eigenstrains Outside of an Ellipsoidal Inclusion," *Journal of Elasticity*, Vol. 15, pp. 27-34.
- Chiu, Y. P., 1977, "On the Stress Field Due to Initial Strains in a Cuboid Surrounded by an Infinite Elastic Space," *ASME JOURNAL OF APPLIED MECHANICS*, Vol. 44, pp. 587-590.
- Chiu, Y. P., 1978, "On the Stress Field and Surface Deformation in a Half Space With a Cuboidal Zone in Which Initial Strains Are Uniform," *ASME JOURNAL OF APPLIED MECHANICS*, Vol. 45, pp. 302-306.
- Eshelby, J. D., 1957, "The Determination of the Elastic Field of an Ellipsoidal Inclusion and Related Problems," *Proceedings of the Royal Society, London*, Vol. A241, pp. 376-396.
- Eshelby, J. D., 1959, "The Elastic Field Outside an Elastic Inclusion," *Proceedings of the Royal Society, London*, Vol. A252, pp. 561-569.
- Eshelby, J. D., 1961, "Elastic Inclusions and Inhomogeneities," *Progress in Solid Mechanics*, Vol. 2, I. N. Sneddon and R. Hill, eds., North-Holland, Amsterdam, pp. 89-140.
- Hasegawa, H., Lee, V. G., and Mura, T., 1992, "The Stress Fields Caused by a Circular Cylindrical Inclusion," *ASME JOURNAL OF APPLIED MECHANICS*, Vol. 59, pp. S107-S114.
- Mura, T., 1987, *Micromechanics of Defects in Solids*, Martinus Nijhoff.
- Mura, T., 1988, "Inclusion Problem," *ASME Applied Mechanics Review*, Vol. 41, pp. 15-20.
- Seo, K., and Mura, T., 1979, "The Elastic Field in a Half Space Due to Ellipsoidal Inclusions With Uniform Dilatational Eigenstrains," *ASME JOURNAL OF APPLIED MECHANICS*, Vol. 46, pp. 568-572.
- Takao, Y., Taya, M., and Chou, T. W., 1981, "Stress Field Due to a Cylindrical Inclusion with Constant Axial Eigenstrain in an Infinite Elastic Body," *ASME JOURNAL OF APPLIED MECHANICS*, Vol. 48, pp. 853-858.

APPENDIX A

1 Evaluation of the Integrals $I^1(x_1, x_2, z)$ and $I^2(x_1, x_2, z)$

Letting $\xi = \sqrt{(t-t_1)/(t_2-t_1)}$, we have

$$I^1(x_1, x_2, z) = \int_{t_1}^{t_2} \frac{tdt}{\sqrt{(t+z^2)(t-t_1)(t_2-t)}}$$

$$= 2\sqrt{t_2+z^2}E\left(\sqrt{\frac{t_2-t_1}{t_2+z^2}}\right) - \frac{2z^2}{\sqrt{t_2+z^2}}F\left(\sqrt{\frac{t_2-t_1}{t_2+z^2}}\right) \quad (A1)$$

$$I^2(x_1, x_2, z) = \int_{t_1}^{t_2} \frac{dt}{\sqrt{(t+z^2)(t-t_1)(t_2-t)}} = \frac{2}{\sqrt{t_2+z^2}}F\left(\sqrt{\frac{t_2-t_1}{t_2+z^2}}\right) \quad (A2)$$

where $F(k)$ and $E(k)$ are the complete elliptic integrals of the first and second kind, respectively.

2 Evaluation of the Integral $I^3(x_1, x_2, z, s)$

Letting $\xi = \sqrt{(t_2-t)/(t_2-t_1)}$, we can obtain

$$I^3(x_1, x_2, z, s) = \int_{t_1}^{t_2} \frac{dt}{(t-s)\sqrt{(t+z^2)(t-t_1)(t_2-t)}} = \frac{2}{(t_2-s)\sqrt{t_2+z^2}}\Pi\left(\frac{t_1-t_2}{t_2-s}, \sqrt{\frac{t_2-t_1}{t_2+z^2}}\right) \quad (A3)$$

where $\Pi(h, k)$ is the complete elliptic integral of the third kind.

3 Evaluation of the Integral $I^4(x_1, x_2, z)$

Following the formula

$$\int \frac{f(x)dx}{x^2\sqrt{ax^2+bx+c}} = -\frac{\sqrt{ax^2+bx+c}}{cx}f(x) - \frac{b}{2c} \int \frac{f(x)dx}{x\sqrt{ax^2+bx+c}} + \int \frac{\sqrt{ax^2+bx+c}df(x)}{cx}dx, \quad (A4)$$

we can obtain

$$I^4(x_1, x_2, z) = \int_{t_1}^{t_2} \frac{dt}{t^2\sqrt{(t+z^2)(t-t_1)(t_2-t)}} = \left(\frac{t_1+t_2}{2t_1t_2} - \frac{1}{2z^2}\right)I^3(x_1, x_2, z, 0) - \frac{1}{2t_1t_2}I^2(x_1, x_2, z) + \frac{(t_1+z^2)(t_2+z^2)}{2t_1t_2z^2}I^3(x_1, x_2, z, -z^2) \quad (A5)$$

where

$$t_1 = (a - \sqrt{x_1^2 + x_2^2})^2, \quad t_2 = (a + \sqrt{x_1^2 + x_2^2})^2. \quad (A6)$$

APPENDIX B

1 Evaluation of the Integrals $J^1(x_1, x_2, z)$ and $J^2(x_1, x_2, z)$

Letting $\xi = t^{-1}$, we have

$$J^1(x_1, x_2, z) = \int_{t_1}^{t_2} \frac{t^2dt}{\sqrt{(t_2^2-t^2)(t^2-t_1^2)}} = t_2E\left(\frac{\sqrt{t_2^2-t_1^2}}{t_2}\right) \quad (B1)$$

$$J^2(x_1, x_2, z) = \int_{t_1}^{t_2} \frac{dt}{\sqrt{(t_2^2 - t^2)(t^2 - t_1^2)}} = \frac{1}{t_2} F\left(\frac{\sqrt{t_2^2 - t_1^2}}{t_2}\right) \quad (\text{B2})$$

2 Evaluation of the Integral $J^0(x_1, x_2, z)$

According to the formula

$$\int \frac{f(x)x}{\sqrt{ax^2 + bx + c}} dx = \frac{\sqrt{ax^2 + bx + c}}{a} f(x) - \frac{b}{2a} \int \frac{f(x)}{\sqrt{ax^2 + bx + c}} dx - \frac{1}{a} \int \sqrt{ax^2 + bx + c} \frac{df(x)}{dx} dx, \quad (\text{B3})$$

we can get

$$J^0(x_1, x_2, z) = \int_{t_1}^{t_2} \frac{t^4 dt}{\sqrt{(t_2^2 - t^2)(t^2 - t_1^2)}} = (t_1^2 + t_2^2)J^1(x_1, x_2, z) - \frac{1}{2} J^0(x_1, x_2, z) - \frac{t_1^2 t_2^2}{2} J^2(x_1, x_2, z). \quad (\text{B4})$$

Then,

$$J^0(x_1, x_2, z) = \frac{2(t_1^2 + t_2^2)}{3} J^1(x_1, x_2, z) - \frac{t_1^2 t_2^2}{3} J^2(x_1, x_2, z). \quad (\text{B5})$$

3 Evaluation of the Integrals $J^3(x_1, x_2, z, s)$ and $J^i(x_1, x_2, z)$ ($i = 4, 5, \dots, 9$)

Letting

$$\eta = \left[\frac{2t_1}{t_1 + t_2} \left(\frac{t_2 - t_1}{t - t_1} + \frac{t_2 - t_1}{2t_1} \right) \right]^{-1/2},$$

one can obtain

$$J^3(x_1, x_2, z, s) = \int_{t_1}^{t_2} \frac{dt}{(t-s)\sqrt{(t_2^2 - t^2)(t^2 - t_1^2)}} = \frac{4t_1}{(t_1 + t_2)(t_1^2 - s^2)} \Pi\left(\frac{(t_2 - t_1)(t_1 + s)}{(t_1 + t_2)(t_1 - s)}, \frac{t_2 - t_1}{t_1 + t_2}\right) - \frac{2}{(t_1 + t_2)(t_1 + s)} F\left(\frac{t_2 - t_1}{t_1 + t_2}\right) \quad (\text{B6})$$

$$J^4(x_1, x_2, z) = \int_{t_1}^{t_2} \frac{dt}{(t^2 - z^2)\sqrt{(t_2^2 - t^2)(t^2 - t_1^2)}} = \frac{1}{2z} [J^3(x_1, x_2, z, z) - J^3(x_1, x_2, z, -z)] \quad (\text{B7})$$

$$J^5(x_1, x_2, z) = -\frac{1}{2a\sqrt{x_1^2 + x_2^2}} \int_{t_1}^{t_2} \frac{t^2 - a^2 - x_1^2 - x_2^2 - z^2}{(t^2 - z^2)\sqrt{(t_2^2 - t^2)(t^2 - t_1^2)}} dt = \frac{a^2 + x_1^2 + x_2^2}{2a\sqrt{x_1^2 + x_2^2}} J^4(x_1, x_2, z) - \frac{J^2(x_1, x_2, z)}{2a\sqrt{x_1^2 + x_2^2}} \quad (\text{B8})$$

$$J^6(x_1, x_2, z) = \frac{1}{4a^2(x_1^2 + x_2^2)} \int_{t_1}^{t_2} \frac{(t^2 - a^2 - x_1^2 - x_2^2 - z^2)^2}{(t^2 - z^2)\sqrt{(t_2^2 - t^2)(t^2 - t_1^2)}} dt = \frac{(a^2 + x_1^2 + x_2^2)^2}{4a^2(x_1^2 + x_2^2)} J^4(x_1, x_2, z) - \frac{2a^2 + 2x_1^2 + 2x_2^2 + z^2}{4a^2(x_1^2 + x_2^2)} J^2(x_1, x_2, z) + \frac{1}{4a^2(x_1^2 + x_2^2)} J^1(x_1, x_2, z) \quad (\text{B9})$$

$$J^7(x_1, x_2, z) = -\frac{1}{8a^3(x_1^2 + x_2^2)^{3/2}} \int_{t_1}^{t_2} \frac{(t^2 - a^2 - x_1^2 - x_2^2 - z^2)^3}{(t^2 - z^2)\sqrt{(t_2^2 - t^2)(t^2 - t_1^2)}} dt = \frac{1}{8a^3(x_1^2 + x_2^2)^{3/2}} \{ (a^2 + x_1^2 + x_2^2)^3 J^4(x_1, x_2, z) - [z^4 + 3(a^2 + x_1^2 + x_2^2)^2 + 3(a^2 + x_1^2 + x_2^2)z^2] \times J^2(x_1, x_2, z) + [3(a^2 + x_1^2 + x_2^2) + 2z^2] J^1(x_1, x_2, z) - J^0(x_1, x_2, z) \} \quad (\text{B10})$$

$$J^8(x_1, x_2, z) = -\frac{1}{2a\sqrt{x_1^2 + x_2^2}} \int_{t_1}^{t_2} \frac{t^2 - a^2 - x_1^2 - x_2^2 - z^2}{\sqrt{(t_2^2 - t^2)(t^2 - t_1^2)}} dt = \frac{-1}{2a\sqrt{x_1^2 + x_2^2}} J^1(x_1, x_2, z) + \frac{a^2 + x_1^2 + x_2^2 + z^2}{2a\sqrt{x_1^2 + x_2^2}} J^2(x_1, x_2, z) \quad (\text{B11})$$

$$J^9(x_1, x_2, z) = \frac{1}{4a^2(x_1^2 + x_2^2)} \int_{t_1}^{t_2} \frac{(t^2 - a^2 - x_1^2 - x_2^2 - z^2)^2}{\sqrt{(t_2^2 - t^2)(t^2 - t_1^2)}} dt = \frac{1}{4a^2(x_1^2 + x_2^2)} [J^0(x_1, x_2, z) - 2(a^2 + x_1^2 + x_2^2 + z^2) J^1(x_1, x_2, z) + (a^2 + x_1^2 + x_2^2 + z^2)^2 J^2(x_1, x_2, z)] \quad (\text{B12})$$

where

$$t_1 = \sqrt{(a - \sqrt{x_1^2 + x_2^2})^2 + z^2}, \quad t_2 = \sqrt{(a + \sqrt{x_1^2 + x_2^2})^2 + z^2}. \quad (\text{B13})$$

The Elastic Field Caused by a Circular Cylindrical Inclusion— Part II: Inside the Region

$$x_1^2 + x_2^2 > a^2, \quad -\infty < x_3 < \infty$$

Where the Circular Cylindrical Inclusion is Expressed by

$$x_1^2 + x_2^2 \leq a^2, \quad -h \leq x_3 \leq h$$

Linzhi Wu

Shanyi Y. Du

Research Laboratory of Composite
Materials,
School of Astronautics,
Harbin Institute of Technology,
Harbin, 150006, P. R. China

Analytical solutions are presented for the displacement and stress fields caused by a circular cylindrical inclusion with arbitrary uniform eigenstrains in an infinite elastic medium. The expressions obtained and those presented in Part I constitute the solutions of the whole elastic field, $-\infty < x_1, x_2, x_3 < \infty$. In the present paper, it is found that the analytical solutions within the region $x_1^2 + x_2^2 > a^2, -\infty < x_3 < \infty$ can also be expressed as functions of the complete elliptic integrals of the first, second, and third kind. When the length of inclusion tends towards the limit (infinity), the present solutions agree with Eshelby's results. Finally, numerical results are shown for the stress field.

1 Introduction

The theory of inclusions has been successfully applied to composite materials including fiber, precipitate, and martensite problems. An extensive review of inclusion problems has been given by Mura (1987, 1988). However, many results cannot be expressed in analytical form, but are in the form of numerical solutions.

Eshelby (1957, 1959) developed a method of solution for the problem of an isotropic ellipsoidal inclusion which undergoes a uniform eigenstrain in the absence of a surrounding isotropic matrix. Since then, the inclusion problem has greatly been developed. A number of techniques have been used to deal with this class of problems. Sankaran and Laird (1976) applied Eshelby's method to deformation field of a misfitting inclusion and calculated radial stress component when the length of cylindrical inclusion tends to the limit case. Using a method which employs the Galerkin vector Chiu (1977) has obtained the explicit form of stress field due to initial strains in a cuboid surrounded by an infinite elastic space. Other applications in this respect have been performed by Seo and Mura (1979) for numerical calculations of elastic field when an ellipsoidal inclusion with a uniform dilatational eigenstrain is located near the surface of a half-space, and by Karihaloo and Viswanathan (1988) for the elastic field of a partially debonded ellipsoidal inclusion and by Lee et al. (1992) for the stress field of a sliding circular inclusion.

Takao et al. (1981) and Hasegawa et al. (1992) have also investigated the problem of cylindrical inclusion due to uniform

axial eigenstrain, but they have obtained the closed-form solution only for the axisymmetric case. Using the technique of Green's function, this paper obtains analytical solutions for the displacement and stress fields caused by arbitrary uniform eigenstrains in a circular cylindrical inclusion. These solutions can be expressed as functions of the complete elliptic integrals of the first, second, and third kind. The present results are compared with previous studies. Finally, numerical results are shown for the stress field.

In what follows, the summation convention over repeated Latin indices is adopted from 1-3. And a comma indicates partial differentiation, thus $f_{,i}$ means $\partial f / \partial x_i$. In cases where differentiations are made with respect to x'_i , they are written in full notation.

2 Solution of Eq. (4) in Part I

As shown in Fig. 1, when point $\mathbf{x} = (x_1, x_2, x_3)$ is located within the region $x_1^2 + x_2^2 > a^2, -\infty < x_3 < \infty$, the area element $dx'_1 dx'_2$ in (4) of Part I can still be expressed as

$$dx'_1 dx'_2 = r dr d\varphi \quad (1)$$

where $r = |\mathbf{x} - \mathbf{x}'|$ and $d\varphi$ is an arc element of a unit circle centered at point \mathbf{x} . To differentiate from the symbols of Part I, we herein use the symbols $\bar{I}(x_1, x_2, z)$ and $\bar{I}_{ij}(x_1, x_2, z)$ to replace $I(x_1, x_2, z)$ and $I_{ij}(x_1, x_2, z)$ of Eq. (4) in Part I. Upon integration with respect to r , we have

$$\bar{I}(x_1, x_2, z) = \int_{\varphi_1}^{\varphi_2} \sqrt{r^2 + z^2} \Big|_{r=r_1(\varphi)}^{r_2(\varphi)} d\varphi$$

$$\bar{I}_{11}(x_1, x_2, z)$$

$$= \int_{\varphi_1}^{\varphi_2} \cos^2 \varphi \sqrt{r^2 + z^2} \Big|_{r=r_1(\varphi)}^{r_2(\varphi)} d\varphi + z^2 \int_{\varphi_1}^{\varphi_2} \frac{\cos^2 \varphi}{\sqrt{r^2 + z^2}} \Big|_{r=r_1(\varphi)}^{r_2(\varphi)} d\varphi$$

$$\bar{I}_{33}(x_1, x_2, z) = -z^2 \int_{\varphi_1}^{\varphi_2} \frac{1}{\sqrt{r^2 + z^2}} \Big|_{r=r_1(\varphi)}^{r_2(\varphi)} d\varphi$$

Contributed by the Applied Mechanics Division of THE AMERICAN SOCIETY OF MECHANICAL ENGINEERS for publication in the ASME JOURNAL OF APPLIED MECHANICS.

Discussion on this paper should be addressed to the Technical Editor, Prof. Lewis T. Wheeler, Department of Mechanical Engineering, University of Houston, Houston, TX 77204-4792, and will be accepted until four months after final publication of the paper itself in the ASME JOURNAL OF APPLIED MECHANICS.

Manuscript received by the ASME Applied Mechanics Division, Sept. 13, 1993; final revision, Mar. 17, 1994. Associate Technical Editor: D. M. Barnett.

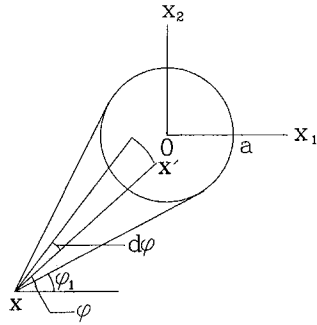


Fig. 1 The projection of Fig. 1 in Part I on plane ox_1x_2 when point x is located within $x_1^2 + x_2^2 > a^2$, $-\infty < x_3 < \infty$

$$\begin{aligned} \bar{I}_{12}(x_1, x_2, z) &= \int_{\varphi_1}^{\varphi_2} \sin \varphi \cos \varphi \sqrt{r^2 + z^2} \Big|_{r=r_1(\varphi)}^{r_2(\varphi)} d\varphi \\ &\quad + z^2 \int_{\varphi_1}^{\varphi_2} \frac{\sin \varphi \cos \varphi}{\sqrt{r^2 + z^2}} \Big|_{r=r_1(\varphi)}^{r_2(\varphi)} d\varphi \\ \bar{I}_{13}(x_1, x_2, z) &= z \int_{\varphi_1}^{\varphi_2} \frac{r \cos \varphi}{\sqrt{r^2 + z^2}} \Big|_{r=r_1(\varphi)}^{r_2(\varphi)} d\varphi \\ &\quad - z \int_{\varphi_1}^{\varphi_2} \cos \varphi \ln (r + \sqrt{r^2 + z^2}) \Big|_{r=r_1(\varphi)}^{r_2(\varphi)} d\varphi \quad (2) \end{aligned}$$

where $z = x_3 - x'_3$ and $r_1(\varphi)$ and $r_2(\varphi)$ are two roots of equation

$$(x_1 + r \cos \varphi)^2 + (x_2 + r \sin \varphi)^2 = a^2 \quad (3)$$

which are

$$\begin{aligned} r_{1,2}(\varphi) &= -\sqrt{x_1^2 + x_2^2} \cos(\varphi - \phi) \\ &\quad \mp \sqrt{(x_1^2 + x_2^2) \cos^2(\varphi - \phi) + a^2 - x_1^2 - x_2^2} \quad (4) \end{aligned}$$

where $\cos \phi = x_1/\sqrt{x_1^2 + x_2^2}$, $\sin \phi = x_2/\sqrt{x_1^2 + x_2^2}$. It should be noted that the lower and upper limits φ_1 and φ_2 of integrals in (2) are the angles between the axis x_1 and two tangents of coordinates (x_1, x_2) relative to the circle, respectively (as shown in Fig. 1), and the incremental direction of variable φ is defined as the counterclockwise one.

Next, let us determine the lower and upper limits φ_1 and φ_2 of integrals in (2). According to the knowledge of analytic geometry, we have

$$\begin{aligned} \tan \varphi_1 &= \frac{\sqrt{x_1^2 + x_2^2 - a^2} x_2 - a x_1}{\sqrt{x_1^2 + x_2^2 - a^2} x_1 + a x_2}, \\ \tan \varphi_2 &= \frac{\sqrt{x_1^2 + x_2^2 - a^2} x_2 + a x_1}{\sqrt{x_1^2 + x_2^2 - a^2} x_1 - a x_2} \quad (5) \end{aligned}$$

where $\varphi_2 - \varphi_1$ satisfies the relation $0 < \varphi_2 - \varphi_1 < \pi$.

To solve the integrals of (2), we introduce the variable transformation $\varphi - \phi = \theta$. Hence, Eq. (2) can further be expressed in the form

$$\begin{aligned} \bar{I}(x_1, x_2, z) &= \int_{\varphi_1 - \phi}^{\varphi_2 - \phi} \sqrt{r^2 + z^2} \Big|_{r=r_1(\theta)}^{r_2(\theta)} d\theta \\ \bar{I}_{11}(x_1, x_2, z) &= \sin^2 \phi \int_{\varphi_1 - \phi}^{\varphi_2 - \phi} \sqrt{r^2 + z^2} \Big|_{r=r_1(\theta)}^{r_2(\theta)} d\theta \\ &\quad + \cos 2\phi \int_{\varphi_1 - \phi}^{\varphi_2 - \phi} \cos^2 \theta \sqrt{r^2 + z^2} \Big|_{r=r_1(\theta)}^{r_2(\theta)} d\theta \\ &\quad - \sin 2\phi \int_{\varphi_1 - \phi}^{\varphi_2 - \phi} \sin \theta \cos \theta \sqrt{r^2 + z^2} \Big|_{r=r_1(\theta)}^{r_2(\theta)} d\theta \end{aligned}$$

$$\begin{aligned} &+ z^2 \sin^2 \phi \int_{\varphi_1 - \phi}^{\varphi_2 - \phi} \frac{1}{\sqrt{r^2 + z^2}} \Big|_{r=r_1(\theta)}^{r_2(\theta)} d\theta \\ &+ z^2 \cos 2\phi \int_{\varphi_1 - \phi}^{\varphi_2 - \phi} \frac{\cos^2 \theta}{\sqrt{r^2 + z^2}} \Big|_{r=r_1(\theta)}^{r_2(\theta)} d\theta \\ &- z^2 \sin 2\phi \int_{\varphi_1 - \phi}^{\varphi_2 - \phi} \frac{\sin \theta \cos \theta}{\sqrt{r^2 + z^2}} \Big|_{r=r_1(\theta)}^{r_2(\theta)} d\theta \end{aligned}$$

$$\bar{I}_{33}(x_1, x_2, z) = -z^2 \int_{\varphi_1 - \phi}^{\varphi_2 - \phi} \frac{1}{\sqrt{r^2 + z^2}} \Big|_{r=r_1(\theta)}^{r_2(\theta)} d\theta$$

$$\begin{aligned} \bar{I}_{12}(x_1, x_2, z) &= -\sin \phi \cos \phi \left[\int_{\varphi_1 - \phi}^{\varphi_2 - \phi} \sqrt{r^2 + z^2} \Big|_{r=r_1(\theta)}^{r_2(\theta)} d\theta \right. \\ &\quad \left. + z^2 \int_{\varphi_1 - \phi}^{\varphi_2 - \phi} \frac{1}{\sqrt{r^2 + z^2}} \Big|_{r=r_1(\theta)}^{r_2(\theta)} d\theta \right] \\ &\quad + \sin 2\phi \int_{\varphi_1 - \phi}^{\varphi_2 - \phi} \cos^2 \theta \sqrt{r^2 + z^2} \Big|_{r=r_1(\theta)}^{r_2(\theta)} d\theta \\ &\quad + z^2 \sin 2\phi \int_{\varphi_1 - \phi}^{\varphi_2 - \phi} \frac{\cos^2 \theta}{\sqrt{r^2 + z^2}} \Big|_{r=r_1(\theta)}^{r_2(\theta)} d\theta \\ &\quad + \cos 2\phi \int_{\varphi_1 - \phi}^{\varphi_2 - \phi} \sin \theta \cos \theta \sqrt{r^2 + z^2} \Big|_{r=r_1(\theta)}^{r_2(\theta)} d\theta \\ &\quad + z^2 \cos 2\phi \int_{\varphi_1 - \phi}^{\varphi_2 - \phi} \frac{\sin \theta \cos \theta}{\sqrt{r^2 + z^2}} \Big|_{r=r_1(\theta)}^{r_2(\theta)} d\theta \end{aligned}$$

$$\begin{aligned} \bar{I}_{13}(x_1, x_2, z) &= z \cos \phi \left[\int_{\varphi_1 - \phi}^{\varphi_2 - \phi} \frac{r \cos \theta}{\sqrt{r^2 + z^2}} \Big|_{r=r_1(\theta)}^{r_2(\theta)} d\theta \right. \\ &\quad \left. - \int_{\varphi_1 - \phi}^{\varphi_2 - \phi} \cos \theta \ln (r + \sqrt{r^2 + z^2}) \Big|_{r=r_1(\theta)}^{r_2(\theta)} d\theta \right] \\ &\quad - z \sin \phi \left[\int_{\varphi_1 - \phi}^{\varphi_2 - \phi} \frac{r \sin \theta}{\sqrt{r^2 + z^2}} \Big|_{r=r_1(\theta)}^{r_2(\theta)} d\theta \right. \\ &\quad \left. - \int_{\varphi_1 - \phi}^{\varphi_2 - \phi} \sin \theta \ln (r + \sqrt{r^2 + z^2}) \Big|_{r=r_1(\theta)}^{r_2(\theta)} d\theta \right] \quad (6) \end{aligned}$$

where

$$\begin{aligned} r_{1,2}(\theta) &= -\sqrt{x_1^2 + x_2^2} \cos \theta \\ &\quad \mp \sqrt{(x_1^2 + x_2^2) \cos^2 \theta + a^2 - x_1^2 - x_2^2} \quad (7) \end{aligned}$$

To guarantee the one-to-one correspondence between coordinates (x_1, x_2) and angles ϕ , φ_1 , and φ_2 , we define the ranges of angles ϕ and φ_1 as

$$\begin{aligned} -\frac{\pi}{2} < \varphi_1 < \pi \quad \text{when} \quad -\pi \leq \phi < 0, \\ \frac{\pi}{2} < \varphi_1 < 2\pi \quad \text{when} \quad 0 \leq \phi < \pi. \end{aligned} \quad (8)$$

Following the knowledge of analytic geometry, we easily prove

$$\frac{\pi}{2} < \varphi_1 - \phi < \pi < \varphi_2 - \phi < \frac{3\pi}{2}. \quad (9)$$

Letting $\bar{r}_{1,2}(\theta) = \sqrt{t}$, respectively, we have

$$\cos \theta = \frac{a^2 - x_1^2 - x_2^2 - t}{2\sqrt{x_1^2 + x_2^2} \sqrt{t}} \quad (10)$$

$$d\theta = \pm \frac{a^2 - x_1^2 - x_2^2 + t}{2t\sqrt{(t-t_1)(t_2-t)}} dt, \quad (11)$$

where

$$t_1 = (a - \sqrt{x_1^2 + x_2^2})^2, \quad t_2 = (a + \sqrt{x_1^2 + x_2^2})^2. \quad (12)$$

Clearly, (11) takes a positive sign when $(\pi/2) < \theta < \pi$, but it is negative when $\pi < \theta < (3\pi/2)$. Thus, (6) can be rewritten as

$$\bar{I}(x_1, x_2, z) = \int_{\Sigma_1} \frac{t^2 + (a^2 - x_1^2 - x_2^2 + z^2)t + (a^2 - x_1^2 - x_2^2)z^2}{2t\sqrt{(t+z^2)(t-t_1)(t_2-t)}} dt$$

$$\bar{I}_{33}(x_1, x_2, z) = -z^2 \int_{\Sigma_1} \frac{t + a^2 - x_1^2 - x_2^2}{2t\sqrt{(t+z^2)(t-t_1)(t_2-t)}} dt$$

$$\begin{aligned} \bar{I}_{11}(x_1, x_2, z) &= \sin^2 \phi [\bar{I}(x_1, x_2, z) - \bar{I}_{33}(x_1, x_2, z)] \\ &+ \frac{\sin 2\phi}{8(x_1^2 + x_2^2)} \int_{\Sigma_2} \frac{g(t)dt}{t^2\sqrt{t+z^2}} \\ &+ \frac{\cos 2\phi}{8(x_1^2 + x_2^2)} \int_{\Sigma_1} \frac{f(t)dt}{t^2\sqrt{(t+z^2)(t-t_1)(t_2-t)}} \end{aligned}$$

$$\begin{aligned} \bar{I}_{12}(x_1, x_2, z) &= \sin \phi \cos \phi [\bar{I}_{33}(x_1, x_2, z) - \bar{I}(x_1, x_2, z)] \\ &- \frac{\cos 2\phi}{8(x_1^2 + x_2^2)} \int_{\Sigma_2} \frac{g(t)dt}{t^2\sqrt{t+z^2}} \\ &+ \frac{\sin 2\phi}{8(x_1^2 + x_2^2)} \int_{\Sigma_1} \frac{f(t)dt}{t^2\sqrt{(t+z^2)(t-t_1)(t_2-t)}} \end{aligned}$$

$$\begin{aligned} \bar{I}_{13}(x_1, x_2, z) &= \frac{z}{2\sqrt{x_1^2 + x_2^2}} \\ &\times \left[\cos \phi \int_{\Sigma_1} \frac{a^2 + x_1^2 + x_2^2 - t}{\sqrt{(t+z^2)(t-t_1)(t_2-t)}} dt \right. \\ &\left. - \sin \phi \int_{\Sigma_2} \frac{dt}{\sqrt{t+z^2}} \right] - z \ln(r + \sqrt{r^2 + z^2}) \\ &\times \cos(\phi - \theta) \Big|_{r=\bar{r}_{1,2}(\theta)}^{\bar{r}_{1,2}(\theta)} \Big|_{\theta=\bar{\theta}_{1,2}(\phi)}^{\bar{\theta}_{1,2}(\phi)} \quad (13) \end{aligned}$$

where

$$\begin{aligned} f(t) &= t^4 + (x_1^2 + x_2^2 - a^2 + 2z^2)t^3 \\ &- (a^2 - x_1^2 - x_2^2)(a^2 - x_1^2 - x_2^2 + 2z^2)t^2 \\ &+ (a^2 - x_1^2 - x_2^2)^2(a^2 - x_1^2 - x_2^2 - 2z^2)t \\ &+ 2(a^2 - x_1^2 - x_2^2)^3z^2 \end{aligned}$$

$$g(t) = t^3 + 2z^2t^2 - (x_1^2 + x_2^2 - a^2)^2t - 2(x_1^2 + x_2^2 - a^2)^2z^2 \quad (14)$$

$$\int_{\Sigma_1} F(t)dt = \int_{\bar{r}_1}^{r_2} F(t)dt + \int_{\bar{r}_2}^{r_1} F(t)dt + \int_{\bar{r}_1}^{r_3} F(t)dt + \int_{\bar{r}_4}^{r_1} F(t)dt$$

$$\int_{\Sigma_2} G(t)dt = \int_{\bar{r}_1}^{r_2} G(t)dt - \int_{\bar{r}_2}^{r_1} G(t)dt + \int_{\bar{r}_1}^{r_4} G(t)dt - \int_{\bar{r}_3}^{r_1} G(t)dt \quad (15)$$

and

$$\begin{aligned} \bar{r}_{1,2} &= [-\sqrt{x_1^2 + x_2^2} \cos(\varphi_{1,2} - \phi) \\ &+ \sqrt{(x_1^2 + x_2^2) \cos^2(\varphi_{1,2} - \phi) + a^2 - x_1^2 - x_2^2}]^2 \\ \bar{r}_{3,4} &= [-\sqrt{x_1^2 + x_2^2} \cos(\varphi_{2,1} - \phi) \\ &- \sqrt{(x_1^2 + x_2^2) \cos^2(\varphi_{2,1} - \phi) + a^2 - x_1^2 - x_2^2}]^2. \quad (16) \end{aligned}$$

Following (5) and the relations $\cos \phi = x_1/\sqrt{x_1^2 + x_2^2}$, $\sin \phi = x_2/\sqrt{x_1^2 + x_2^2}$, we can prove that $\bar{r}_1 = \bar{r}_2 = \bar{r}_3 = \bar{r}_4 = x_1^2 + x_2^2 - a^2$. Thus, one easily finds that $\bar{I}(x_1, x_2, z)$ and $\bar{I}_{ij}(x_1, x_2, z)$ in Eq. (13) can be expressed by $I(x_1, x_2, z)$ and $I_{ij}(x_1, x_2, z)$ in Part I. Their concrete relations are as follows:

$$\bar{I}(x_1, x_2, z) = I(x_1, x_2, z) + 2\pi|z| = I^1(x_1, x_2, z) + (a^2 - x_1^2 - x_2^2 + z^2)I^2(x_1, x_2, z) + (a^2 - x_1^2 - x_2^2)z^2I^3(x_1, x_2, z, 0)$$

$$\bar{I}_{33}(x_1, x_2, z) = I_{33}(x_1, x_2, z) - 2\pi|z| = -z^2I^2(x_1, x_2, z) - (a^2 - x_1^2 - x_2^2)z^2I^3(x_1, x_2, z, 0)$$

$$\begin{aligned} \bar{I}_{11}(x_1, x_2, z) &= I_{11}(x_1, x_2, z) + 2\pi|z| = \frac{x_1^2}{x_1^2 + x_2^2} \\ &\times [\bar{I}(x_1, x_2, z) - \bar{I}_{33}(x_1, x_2, z)] \\ &+ \frac{x_1^2 - x_2^2}{12(x_1^2 + x_2^2)^2} \{ [a^2 + 4z^2 + 7(x_1^2 + x_2^2)]I^1(x_1, x_2, z) \\ &+ 4[(2x_1^2 + 2x_2^2 - a^2)z^2 - (a^2 - x_1^2 - x_2^2)^2]I^2(x_1, x_2, z) \\ &+ 3(a^2 - x_1^2 - x_2^2)^2(a^2 - x_1^2 - x_2^2 - 2z^2)I^3(x_1, x_2, z, 0) \\ &+ 6(a^2 - x_1^2 - x_2^2)^3z^2I^4(x_1, x_2, z) \} \end{aligned}$$

$$\begin{aligned} \bar{I}_{12}(x_1, x_2, z) &= I_{12}(x_1, x_2, z) = \frac{x_1x_2}{x_1^2 + x_2^2} \\ &\times [\bar{I}_{33}(x_1, x_2, z) - \bar{I}(x_1, x_2, z)] \\ &+ \frac{x_1x_2}{6(x_1^2 + x_2^2)^2} \{ [a^2 + 4z^2 + 7(x_1^2 + x_2^2)]I^1(x_1, x_2, z) \\ &+ 4[(2x_1^2 + 2x_2^2 - a^2)z^2 - (a^2 - x_1^2 - x_2^2)^2]I^2(x_1, x_2, z) \\ &+ 3(a^2 - x_1^2 - x_2^2)^2(a^2 - x_1^2 - x_2^2 - 2z^2)I^3(x_1, x_2, z, 0) \\ &+ 6(a^2 - x_1^2 - x_2^2)^3z^2I^4(x_1, x_2, z) \} \end{aligned}$$

$$\begin{aligned} \bar{I}_{13}(x_1, x_2, z) &= I_{13}(x_1, x_2, z) = \frac{x_1z}{x_1^2 + x_2^2} \\ &\times [(a^2 + x_1^2 + x_2^2)I^2(x_1, x_2, z) - I^1(x_1, x_2, z)] \quad (17) \end{aligned}$$

where $I^1(x_1, x_2, z)$, $I^2(x_1, x_2, z)$, $I^3(x_1, x_2, z, s)$ and $I^4(x_1, x_2, z)$ have already been given in Appendix A of Part I. The remaining components can be obtained by the following formulae:

$$\begin{aligned} \bar{I}_{ij}(x_1, x_2, z) &= \bar{I}_{ji}(x_1, x_2, z) \\ \bar{I}_{22}(x_1, x_2, z) &= \bar{I}_{11}(x_2, x_1, z) \\ \bar{I}_{23}(x_1, x_2, z) &= \bar{I}_{13}(x_2, x_1, z). \quad (18) \end{aligned}$$

Thus, Eqs. (4) in Part I are entirely determined. According to Part I we find that the integrals of Eq. (5) are not related to the position of point \mathbf{x} . Hence, when point \mathbf{x} is located within the region $x_1^2 + x_2^2 > a^2$, $-\infty < x_3 < \infty$, the corresponding integrals of (5) can still be expressed as (20) and (21) in Part I.

3 The Displacement and Stress Fields

Following Eqs. (2) and (3) in Part I, the induced displacement field within the region $x_1^2 + x_2^2 > a^2$, $-\infty < x_3 < \infty$ can be expressed in the following form:

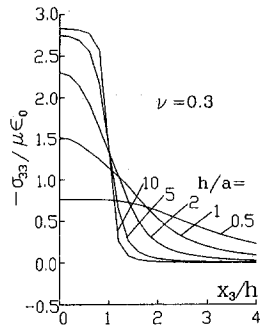


Fig. 2 Variation of normal stress σ_{33} along the x_3 -axis under the condition $\epsilon_{33} = \epsilon_0$, $\epsilon_{11} = \epsilon_{22} = \epsilon_{12} = \epsilon_{13} = \epsilon_{23} = 0$

$$u_i(\mathbf{x}) = \frac{1}{16\pi\mu(1-\nu)} \times [(\lambda\delta_{13}\epsilon_{mm}^* + 2\mu\epsilon_{13}^*)(3-4\nu)\bar{I}(x_1, x_2, z)|_{x_3=-h}^h + (\lambda\delta_{j3}\epsilon_{mm}^* + 2\mu\epsilon_{j3}^*)\bar{I}_{ij}(x_1, x_2, z)|_{x_3=-h}^h + (\lambda\delta_{i1}\epsilon_{mm}^* + 2\mu\epsilon_{i1}^*)(3-4\nu)J^c(x_1, x_2, x_3) + (\lambda\delta_{j1}\epsilon_{mm}^* + 2\mu\epsilon_{j1}^*)J_{ij}^c(x_1, x_2, x_3) + (\lambda\delta_{i2}\epsilon_{mm}^* + 2\mu\epsilon_{i2}^*)(3-4\nu)J^s(x_1, x_2, x_3) + (\lambda\delta_{j2}\epsilon_{mm}^* + 2\mu\epsilon_{j2}^*)J_{ij}^s(x_1, x_2, x_3)]. \quad (19)$$

Since the first partial derivative of the complete elliptic integrals of the first, second, and third kind are obtained (see Eq. (24) in Part I), the corresponding stress field is in reality expressed by explicit formulae. Due to the complexity of the stress field, we here do not give its concrete expressions.

4 An Infinite Cylindrical Inclusion

To obtain the solution of the displacement and stress fields for an infinite cylindrical inclusion ($h \rightarrow \infty$), we first give the series expansions of the complete elliptic integrals of the first, second, and third kind as

$$F(k) = \frac{\pi}{2} \left[1 + \left(\frac{1}{2}\right)^2 k^2 + \left(\frac{1 \cdot 3}{2 \cdot 4}\right)^2 k^4 + \dots \right]$$

$$E(k) = \frac{\pi}{2} \left[1 - \left(\frac{1}{2}\right)^2 k^2 - \left(\frac{1 \cdot 3}{2 \cdot 4}\right)^2 \frac{k^4}{3} - \dots \right]$$

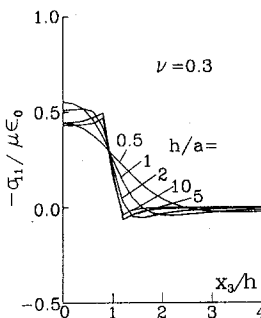


Fig. 3 Variation of normal stress σ_{11} along the x_3 -axis under the condition $\epsilon_{33} = \epsilon_0$, $\epsilon_{11} = \epsilon_{22} = \epsilon_{12} = \epsilon_{13} = \epsilon_{23} = 0$

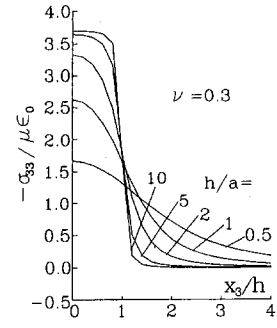


Fig. 4 Variation of normal stress σ_{33} along the x_3 -axis under the condition $\epsilon_{11} = \epsilon_{22} = \epsilon_{33} = \epsilon_0$, $\epsilon_{12} = \epsilon_{13} = \epsilon_{23} = 0$

$$\Pi(h_1, k) = \frac{\pi}{2} \left[\frac{1}{\sqrt{1+h_1}} + \frac{k^2}{2h_1} \left(1 - \frac{1}{\sqrt{1+h_1}} \right) + \frac{3k^4}{8h_1^2} \left(\frac{h_1}{2} - 1 + \frac{1}{\sqrt{1+h_1}} \right) + \dots \right]$$

$$\Pi(-k^2, k) = \frac{\pi}{2} \left[1 + \frac{3}{4}k^2 + \dots \right] \quad (20)$$

where h_1 is a constant. From the results in Part I and Eqs. (17) and (20), we can determine the displacement and stress fields for an infinite cylindrical inclusion. When $h \rightarrow \infty$, we, after some manipulation, have the following formulae:

(i) For the interior points,

$$I(x_1, x_2, z)|_{x_3=-\infty}^{\infty} = 0, \quad I_{ij}(x_1, x_2, z)|_{x_3=-\infty}^{\infty} = 0$$

$$J^c(x_1, x_2, x_3) = J_{33}^c(x_1, x_2, x_3) = 2\pi x_1$$

$$J_{11}^c(x_1, x_2, x_3) = -J_{22}^c(x_1, x_2, x_3) = -\pi x_1$$

$$J_{12}^c(x_1, x_2, x_3) = -\pi x_2$$

$$J_{13}^c(x_1, x_2, x_3) = J_{23}^c(x_1, x_2, x_3) = 0 \quad (21)$$

$$u_1(\mathbf{x}) = \frac{2(1-2\nu)\lambda\epsilon_{mm}^* + (5-8\nu)\mu\epsilon_{11}^* - \mu\epsilon_{22}^*}{8\mu(1-\nu)} x_1 + \frac{(3-4\nu)\epsilon_{12}^*}{4(1-\nu)} x_2$$

$$u_3(\mathbf{x}) = \epsilon_{13}^* x_1 + \epsilon_{23}^* x_2 \quad (22)$$

$$\sigma_{11}(\mathbf{x}) = -\frac{3\mu}{4(1-\nu)} \epsilon_{11}^* - \frac{\mu}{4(1-\nu)} \epsilon_{22}^* - \frac{\mu\nu}{1-\nu} \epsilon_{33}^*$$

$$\sigma_{33}(\mathbf{x}) = -\frac{\mu\nu}{1-\nu} (\epsilon_{11}^* + \epsilon_{22}^*) - \frac{2\mu}{1-\nu} \epsilon_{33}^*$$

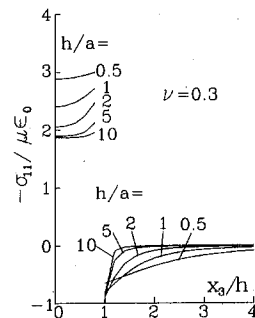


Fig. 5 Variation of normal stress σ_{11} along the x_3 -axis under the condition $\epsilon_{11} = \epsilon_{22} = \epsilon_{33} = \epsilon_0$, $\epsilon_{12} = \epsilon_{13} = \epsilon_{23} = 0$

$$\sigma_{12}(\mathbf{x}) = -\frac{\mu}{2(1-\nu)} \epsilon_{12}^* \quad (23)$$

$$\sigma_{13}(\mathbf{x}) = -\mu \epsilon_{13}^*,$$

and other components $u_2(\mathbf{x})$, $\sigma_{22}(\mathbf{x})$, and $\sigma_{23}(\mathbf{x})$ are obtained by the corresponding exchanges of (x_1, x_2) , $(\epsilon_{11}^*, \epsilon_{22}^*)$, and $(\epsilon_{13}^*, \epsilon_{23}^*)$.

(ii) For the exterior points,

$$\bar{I}(x_1, x_2, z)|_{x_3=-\infty}^{\infty} = 0, \quad \bar{I}_y(x_1, x_2, z)|_{x_3=-\infty}^{\infty} = 0$$

$$J^c(x_1, x_2, x_3) = J_{33}^c(x_1, x_2, x_3) = \frac{2a^2 x_1 \pi}{x_1^2 + x_2^2}$$

$$J_{11}^c(x_1, x_2, x_3) = -J_{22}^c(x_1, x_2, x_3) = \pi A(x_1, x_2)$$

$$J_{12}^c(x_1, x_2, x_3) = \pi B(x_1, x_2)$$

$$J_{13}^c(x_1, x_2, x_3) = J_{23}^c(x_1, x_2, x_3) = 0 \quad (24)$$

$$u_1(\mathbf{x}) = \frac{1}{8(1-\nu)(1-2\nu)} \left[\frac{2(1-\nu)(3-4\nu)a^2 x_1}{x_1^2 + x_2^2} + (1-\nu)A(x_1, x_2) + \nu B(x_2, x_1) \right] \epsilon_{11}^*$$

$$+ \frac{1}{8(1-\nu)(1-2\nu)} \left[\frac{2\nu(3-4\nu)a^2 x_1}{x_1^2 + x_2^2} + \nu A(x_1, x_2) + (1-\nu)B(x_2, x_1) \right] \epsilon_{22}^* + \frac{\nu}{8(1-\nu)(1-2\nu)}$$

$$\times \left[\frac{2(3-4\nu)a^2 x_1}{x_1^2 + x_2^2} + A(x_1, x_2) + B(x_2, x_1) \right] \epsilon_{33}^* + \frac{1}{8(1-\nu)}$$

$$\times \left[B(x_1, x_2) + \frac{2(3-4\nu)a^2 x_2}{x_1^2 + x_2^2} - A(x_2, x_1) \right] \epsilon_{23}^*$$

$$u_3(\mathbf{x}) = \frac{a^2 x_1}{x_1^2 + x_2^2} \epsilon_{13}^* + \frac{a^2 x_2}{x_1^2 + x_2^2} \epsilon_{23}^* \quad (25)$$

where

$$A(u, v) = \frac{-4a^2 u}{a^2 - u^2 - v^2} \left[\frac{4a^2 v^2 - a^2 u^2 - u^2 v^2 - v^4}{(u^2 + v^2)^2} + \frac{a^2(u^2 - 3v^2)(a^2 + 3u^2 + 3v^2)}{4(u^2 + v^2)^3} \right]$$

$$B(u, v) = \frac{-4a^2 v}{a^2 - u^2 - v^2} \left[\frac{3a^2 v^2 - 7a^2 u^2 - v^4 + u^4}{2(u^2 + v^2)^2} - \frac{a^2(v^2 - 3u^2)(a^2 + 3u^2 + 3v^2)}{4(u^2 + v^2)^3} \right]$$

The component $u_2(\mathbf{x})$ can as well be obtained by the exchanges of (x_1, x_2) and $(\epsilon_{11}^*, \epsilon_{22}^*)$. Because the expressions of the stress field are very complex, we do not give its concrete form. From (22) and (23) we find that the present results coincide with Eshelby's solutions.

5 Discussions and Conclusions

(i) In comparison with the solutions of Takao et al. (1981) and Hasegawa et al. (1992), the analytical expressions of the present paper have generality, since the problem which is con-

sidered by the present work can be nonsymmetric and eigenstrains in the circular cylindrical inclusion can be arbitrary constants.

(ii) From the solutions shown above and Part I, we can find that the whole elastic field is expressed by the complete elliptic integrals of the first, second, and third kind. When $h \rightarrow \infty$, the stress field within the circular cylindrical inclusion is uniform and the stress components outside one only are some elementary functions.

(iii) From Appendixes A and B in Part I and the corresponding formulae ((15) and (21) in Part I and (17)), we can conclude the following: (a) when $x_3 \rightarrow \pm h$, $\sqrt{x_1^2 + x_2^2} \neq a$ or $\sqrt{x_1^2 + x_2^2} \rightarrow a$, $x_3 \neq \pm h$, there is not singularity for the elastic field; (b) when $x_3 \rightarrow \pm h$, $\sqrt{x_1^2 + x_2^2} \rightarrow a$, we, after some manipulation, can find that the elastic field has logarithmic singularities.

(iv) As an interesting particular example, we calculate the stress fields in two kinds of cases of which eigenstrains ϵ_{ij}^* are $\epsilon_{33}^* = \epsilon_{01}^* = \epsilon_{11}^* = \epsilon_{22}^* = \epsilon_{12}^* = \epsilon_{13}^* = \epsilon_{23}^* = 0$ and $\epsilon_{11}^* = \epsilon_{22}^* = \epsilon_{33}^* = \epsilon_{01}^*, \epsilon_{12}^* = \epsilon_{13}^* = \epsilon_{23}^* = 0$, respectively. Figures 2-5 show the distributions of stresses σ_{33} and σ_{11} caused by the circular cylindrical inclusion. The figures are sketched in nondimensional form for Poisson's ratio $\nu = 0.3$. From Figs. 2 and 4, one can see the variations of stress σ_{33} due to the relative positions x_3/h under the condition of $h/a = 0.5, 1, 2, 5$, and 10. It can be observed that the stress component σ_{33} have the largest values at $x_3/h = 0$ and decrease as x_3/h becomes larger. In addition, we can also find that the larger h/a , the faster the decreasing of stress σ_{33} .

(v) Figure 3 shows the variations of stress σ_{11} due to eigenstrains $\epsilon_{33}^* = \epsilon_{01}^*, \epsilon_{11}^* = \epsilon_{22}^* = \epsilon_{12}^* = \epsilon_{13}^* = \epsilon_{23}^* = 0$ under the condition of $h/a = 0.5, 1, 2, 5$ and 10. It can be found that the stress σ_{11} is still continuous at $x_3/h = 1$ and when $h/a = 5$ and 10, the variations of σ_{11} are not the monotone decreasing. From Fig. 5, it can be observed that when eigenstrains ϵ_{11}^* and ϵ_{22}^* are not zero, the normal stress σ_{11} at $x_3/h = 1$ are not continuous.

Acknowledgment

This research was supported by National Education Foundation for Doctoral Degrees.

References

- Chiu, Y. P., 1977, "On the Stress Field Due to Initial Strains in a Cuboid Surrounded by an Infinite Elastic Space," *ASME JOURNAL OF APPLIED MECHANICS*, Vol. 44, pp. 587-590.
- Eshelby, J. D., 1957, "The Determination of the Elastic Field of an Ellipsoidal Inclusion and Related Problems," *Proceedings of the Royal Society, London*, Vol. A241, pp. 376-396.
- Eshelby, J. D., 1959, "The Elastic Field Outside an Elastic Inclusion," *Proceedings of the Royal Society, London*, Vol. A252, pp. 561-569.
- Hasegawa, H., Lee, V. G., and Mura, T., 1992, "The Stress Fields Caused by a Circular Cylindrical Inclusion," *ASME JOURNAL OF APPLIED MECHANICS*, Vol. 59, pp. S107-S114.
- Karihaloo, B. L., and Viswanathan, K., 1988, "A Partially Debonded Ellipsoidal Inclusion in an Elastic Medium. Part 1: Stress and Displacement fields," *Mechanics of Materials*, Vol. 7, pp. 191-197.
- Lee Mikyoung, Jasiuk, I., and Tsuchida, E., 1992, "The Sliding Circular Inclusion in an Elastic Half-Plane," *ASME JOURNAL OF APPLIED MECHANICS*, Vol. 59, pp. S57-S64.
- Mura, T., 1987, *Micromechanics of Defects in Solids*, Martinus Nijhoff.
- Mura, T., 1988, "Inclusion Problem," *ASME Applied Mechanics Review*, Vol. 41, pp. 15-20.
- Sankaran, R., and Laird, C., 1976, "Deformation Field of a Misfitting Inclusion," *Journal of the Mechanics and Physics Solids*, Vol. 24, pp. 251-262.
- Seo, K., and Mura, T., 1979, "The Elastic Field in a Half Space Due to Ellipsoidal Inclusions With Uniform Dilatational Eigenstrains," *ASME JOURNAL OF APPLIED MECHANICS*, Vol. 46, pp. 568-572.
- Takao, Y., Taya, M., and Chou, T. W., 1981, "Stress Field Due to a Cylindrical Inclusion with Constant Axial Eigenstrain in an Infinite Elastic Body," *ASME JOURNAL OF APPLIED MECHANICS*, Vol. 48, pp. 853-858.

Development of Generalized Plane-Strain Tensors for the Concentric Cylinder

N. Chandra
Assoc. Mem. ASME.

Zhiyum Xie

Department of Mechanical Engineering,
Florida A&M University/Florida State
University College of Engineering,
Tallahassee, FL 32316-2175

A pair of two new tensors called GPS tensors \mathbf{S} and \mathbf{D} is proposed for the concentric cylindrical inclusion problem. GPS tensor \mathbf{S} relates the strain in the inclusion constrained by the matrix of finite radius to the uniform transformation strain (eigenstrain), whereas tensor \mathbf{D} relates the strain in the matrix to the same eigenstrain. When the cylindrical matrix is of infinite radius, tensor \mathbf{S} reduces to the appropriate Eshelby's tensor. Explicit expressions to evaluate thermal residual stresses σ_r , σ_θ and σ_z in the matrix and the fiber using tensor \mathbf{D} and tensor \mathbf{S} , respectively, are developed. Since the geometry of the present problem is of finite radius, the effect of fiber volume fraction on the stress distribution can be easily studied. Results for the thermal residual stress distributions are compared with Eshelby's infinite domain solution and finite element results for a specified fiber volume fraction.

1 Introduction

Eshelby (1957) proposed a tensor in his celebrated paper which relates the strain in an ellipsoidal inclusion constrained within an infinite domain to the strain when the same inclusion is placed outside of the matrix without any constraint (eigenstrain). For the case of elastic isotropic inclusion of ellipsoidal shape with uniform eigenstrain, Eshelby tensor can be expressed in terms of geometry and elastic properties of the fiber. In this case, the inclusion is embedded in an infinite domain. In this paper, we consider an infinitely long circular cylindrical inclusion embedded in a coaxial cylindrical matrix of finite dimension. For this problem, we propose a pair of new tensors called Generalized Plane Strain (GPS) tensors, \mathbf{S} and \mathbf{D} . The tensor \mathbf{S} , relates the strain in the inclusion constrained by the matrix to the eigenstrain, and the tensor \mathbf{D} relates the same eigenstrain to the strain in the matrix. When the cylindrical matrix is of infinite radius, the \mathbf{S} tensor reduces to the appropriate Eshelby tensor. Since GPS tensors are derived for the cylindrical inclusion problem they can be easily applied to inhomogeneous inclusion problems for finite elastic body using the equivalent inclusion method. One such application to inhomogeneous inclusion problem is the evaluation of spatial distribution of thermal residual stress/strain in the fiber and the matrix in unidirectional fiber-reinforced composites. Such an analysis is needed in the study of damage in the interfacial regions of composites.

Eshelby tensor has been used to evaluate the effective elastic properties using self-consistent methods (Hershey, 1954; Kroner, 1958; Kerner, 1956; Hill, 1965; Budiansky, 1965). The method was extended to a three-phase generalized self-consistent scheme by Christensen and Lo (1979). Nemat-Nasser (1981) and Weng (1987) used the Mori-Tanaka approach to evaluate the elastic properties of nondilute composite systems. Luo and Weng (1989) later proposed a new tensor by considering the three-phase model of fiber, matrix, and effective composite. In all the above research works (except the latter) the Eshelby tensor was used. They evaluated the effective properties

of composites with finite fiber volume fraction, hence finite matrix radius, which is not consistent with the assumption of infinite matrix in the Eshelby's approach. The proposed GPS tensor can be used in the determination of effective stiffness properties of the composites using self-consistent methods. Since the GPS tensor has been developed for finite radius, it can replace the Eshelby tensor in the evaluation of bounds and effective properties of composites.

2 Formulation of the Problem

Let us consider two concentric circular cylinders of radius r_0 and R as shown in Fig. 1. The inner cylinder represents the inclusion and the outer cylinder represents the matrix. We consider a cylindrical coordinate system (r, θ, z) with origin at O as shown in the Fig. 1. The inclusion Ω is subjected to axisymmetric eigenstrain $\epsilon_{ij}^*(r)$, given by

$$\epsilon_{ij}^*(r) = \delta_{ij} \{ \epsilon_T^*(r) + (\epsilon_L^*(r) - \epsilon_T^*(r)) \delta_{i3} \}$$

where the subscript T refers to the transverse direction and L the longitudinal direction. Both inclusion and matrix are assumed to be elastic isotropic materials. Since the composite is infinitely long, the problem is generalized plane strain in nature. Let the radial, tangential, and longitudinal displacement components be u , v , and w respectively. Due to the axisymmetric nature of the problem, u is a function of r only, v is zero, and w is a function of z only, that is,

$$u = u(r), \quad v = 0, \quad w = w(z).$$

Since this is a generalized plane strain (GPS) problem, we may set

$$w = w(z) = \epsilon_o z,$$

where ϵ_o is an unknown constant. The strain components in the cylindrical coordinate system in terms of displacements are

$$\epsilon_{rr} = \frac{du(r)}{dr}, \quad \epsilon_{\theta\theta} = \frac{u(r)}{r}, \quad \epsilon_{zz} = \frac{dw}{dz} = \epsilon_o. \quad (1)$$

Since all the shear components are zero, the stress and strain components σ_{rr} , $\sigma_{\theta\theta}$, σ_{zz} , and ϵ_{rr} , $\epsilon_{\theta\theta}$, ϵ_{zz} are denoted by σ_r , σ_θ , σ_z , and ϵ_r , ϵ_θ , ϵ_z , respectively, for the sake of simplicity.

Contributed by the Applied Mechanics Division of THE AMERICAN SOCIETY OF MECHANICAL ENGINEERS for publication in the ASME JOURNAL OF APPLIED MECHANICS.

Discussion on this paper should be addressed to the Technical Editor, Prof. Lewis T. Wheeler, Department of Mechanical Engineering, University of Houston, Houston, TX 77204-4792, and will be accepted until four months after final publication of the paper itself in the ASME JOURNAL OF APPLIED MECHANICS.

Manuscript received by the ASME Applied Mechanics Division, Jan. 3, 1994; final revision, June 6, 1994. Associate Technical Editor: J. N. Reddy.

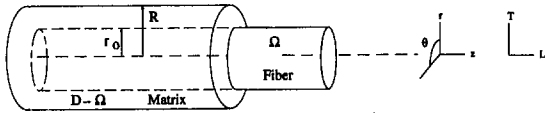


Fig. 1 Schematic illustration of the composite

The stress-strain relations are

$$\sigma_i = 2\mu(\epsilon_i - \epsilon_i^*) + \lambda(\epsilon_r + \epsilon_\theta + \epsilon_z - 2\epsilon_r^* - \epsilon_L^*) \quad (2)$$

for $i = r, \theta, z$, where λ and μ are Lamé constants.

The stress equilibrium equation in a cylindrical coordinate system is

$$\frac{d\sigma_r}{dr} + \frac{\sigma_r - \sigma_\theta}{r} = 0, \quad (3)$$

subject to the boundary condition

$$\sigma_r = 0, \quad \text{for } r = R, \quad (4)$$

and longitudinal equilibrium condition

$$\int_0^R \sigma_z r dr = 0. \quad (5)$$

Substituting (2) and (1) into equilibrium Eq. (3) yields

$$\frac{d^2 u}{dr^2} + \frac{1}{r} \frac{du}{dr} - \frac{u}{r^2} = F(r), \quad (6)$$

where

$$F(r) = \frac{1}{1-\nu} \frac{d}{dr} [\epsilon_r^*(r) + \nu \epsilon_L^*(r)] \quad (7)$$

Thus, Eqs. (6) and (7) are the governing field equations for the generalized plane-strain inclusion problem in terms of radial displacements u with $\epsilon_r^*(r)$ and $\epsilon_L^*(r)$ as the specified eigenstrains in the transverse and longitudinal directions. The solution to the above ODE can be obtained using the Green function solution method as follows:

$$u(r) = br + \frac{1}{1-\nu} \int_0^R \{\epsilon_r^* + \nu \epsilon_L^*\} \frac{\xi}{r} (r-\xi)_+^0 d\xi, \quad (8)$$

where b is an unknown constant and will be determined by the boundary condition (4), and $(r-\xi)_+^0$ is the Heaviside step function

$$(r-\xi)_+^0 = \begin{cases} 1, & \text{if } \xi < r, \\ 0, & \text{if } \xi > r. \end{cases}$$

The strain components ϵ_r and ϵ_θ can be obtained from (1) and (8)

$$\epsilon_r = b + \frac{\epsilon_r^* + \nu \epsilon_L^*}{1-\nu} - \int_0^R \left\{ \frac{\epsilon_r^* + \nu \epsilon_L^*}{1-\nu} \right\} \frac{\xi}{r^2} (r-\xi)_+^0 d\xi, \quad (9)$$

$$\epsilon_\theta = b + \int_0^R \left\{ \frac{\epsilon_r^* + \nu \epsilon_L^*}{1-\nu} \right\} \frac{\xi}{r^2} (r-\xi)_+^0 d\xi. \quad (10)$$

From the stress-strain relation (2), the boundary condition (4) and the longitudinal equilibrium condition (5), b and ϵ_o can be determined as

$$b = \frac{1}{1-\nu} \frac{1}{R^2} \int_0^R \{(1-2\nu)\epsilon_r^*(\xi) - \nu \epsilon_L^*(\xi)\} \xi d\xi,$$

$$\epsilon_o = \frac{2}{R^2} \int_0^R \epsilon_L^*(\xi) \xi d\xi.$$

Substituting the constants into (9), (10), and (1), a general expression for the strain ϵ_i , $i = r, \theta$ can be written as

$$\epsilon_i(r) = \int_0^R G_{iT}(r, \xi) \epsilon_T^*(\xi) + \int_0^R G_{iL}(r, \xi) \epsilon_L^*(\xi) d\xi \quad (11)$$

with

$$G_{rT}(r, \xi) = \left(\frac{1-2\nu}{1-\nu} \right) \frac{\xi}{R^2} - \frac{\xi(r-\xi)_+^0}{(1-\nu)r^2} + \frac{\xi \delta(r-\xi)}{(1-\nu)r},$$

$$G_{rL}(r, \xi) = \left(\frac{-\nu}{1-\nu} \right) \frac{\xi}{R^2} - \frac{\nu \xi (r-\xi)_+^0}{(1-\nu)r^2} + \frac{\nu \xi \delta(r-\xi)}{(1-\nu)r},$$

$$G_{\theta T}(r, \xi) = \left(\frac{1-2\nu}{1-\nu} \right) \frac{\xi}{R^2} + \frac{\xi(r-\xi)_+^0}{(1-\nu)r^2},$$

$$G_{\theta L}(r, \xi) = \left(\frac{-\nu}{1-\nu} \right) \frac{\xi}{R^2} + \frac{\nu \xi (r-\xi)_+^0}{(1-\nu)r^2},$$

$$G_{zT}(r, \xi) = 0, \quad G_{zL}(r, \xi) = \frac{2}{R^2} \xi, \quad (12)$$

where $\delta(\cdot)$ is the Dirac delta function. Equation (11) describes the solution to the generalized plane-strain inclusion problem. At this stage the eigenstrain in the inclusion can be a function of the radius. For this case, the stress components are found to be

$$\sigma_r(r) = \frac{2\mu}{1-\nu} \int_0^R \left(\frac{1}{R^2} - \frac{(r-\xi)_+^0}{r^2} \right) \{\epsilon_r^*(\xi) + \nu \epsilon_L^*(\xi)\} \xi d\xi,$$

$$\sigma_\theta(r) = \frac{2\mu}{1-\nu} \int_0^R \left(\frac{1}{R^2} + \frac{(r-\xi)_+^0}{r^2} - \frac{\delta(r-\xi)}{\xi} \right) \times \{\epsilon_r^*(\xi) + \nu \epsilon_L^*(\xi)\} \xi d\xi,$$

$$\sigma_z(r) = \frac{4\mu}{1-\nu} \int_0^R \left(\frac{1}{R^2} - \frac{\delta(r-\xi)}{2\xi} \right) \times \{\nu \epsilon_r^*(\xi) + \epsilon_L^*(\xi)\} \xi d\xi. \quad (13)$$

3 Development of GPS Tensor

If the eigenstrains ϵ_r^* and ϵ_L^* are assumed to be uniform (constant) in the inclusion Ω and zero in the matrix $D - \Omega$, then (11) reduces to

$$\epsilon_i(r) = \int_0^R G_{iT}(r, \xi) \epsilon_T^* d\xi + \int_0^R G_{iL}(r, \xi) \epsilon_L^* d\xi$$

$$= \epsilon_T^* \int_0^{r_0} G_{iT}(r, \xi) d\xi + \epsilon_L^* \int_0^{r_0} G_{iL}(r, \xi) d\xi.$$

The above equations can be rewritten by defining a pair of new tensors, called Generalized Plane Strain (GPS) tensors, \mathbf{D} and \mathbf{S} . \mathbf{D} is defined in the matrix ($R > r \geq r_0$)

$$D_{ij} = \int_0^{r_0} G_{ij}(r, \xi) d\xi.$$

In the inclusion, $r \leq r_0$, we define the tensor \mathbf{S} as

$$S_{ij} = \int_0^{r_0} G_{ij}(r, \xi) d\xi.$$

We note that in the domain of the definition of \mathbf{D} , $G_{ij}(r, \xi)$ is in the matrix and in the definition of \mathbf{S} , $G_{ij}(r, \xi)$ is restricted to the inclusion. We calculate each component of GPS tensor in detail,

$$D_{rT} = \frac{1-2\nu}{2(1-\nu)} \left(\frac{r_o}{R}\right)^2 + \frac{1}{2(1-\nu)} \times \left\{ 1 - \left[\left(\frac{r_o}{r}\right)^2 + 1 \right] (r - r_o)_+^0 \right\},$$

$$D_{rL} = \frac{-\nu}{2(1-\nu)} \left(\frac{r_o}{R}\right)^2 + \frac{\nu}{2(1-\nu)} \times \left\{ 1 - \left[\left(\frac{r_o}{r}\right)^2 + 1 \right] (r - r_o)_+^0 \right\},$$

$$D_{\theta T} = \frac{1-2\nu}{2(1-\nu)} \left(\frac{r_o}{R}\right)^2 + \frac{1}{2(1-\nu)} \times \left\{ 1 + \left[\left(\frac{r_o}{r}\right)^2 - 1 \right] (r - r_o)_+^0 \right\},$$

$$D_{\theta L} = \frac{-\nu}{2(1-\nu)} \left(\frac{r_o}{R}\right)^2 + \frac{\nu}{2(1-\nu)} \times \left\{ 1 + \left[\left(\frac{r_o}{r}\right)^2 - 1 \right] (r - r_o)_+^0 \right\},$$

$$D_{zT} = 0, \quad D_{zL} = \left(\frac{r_o}{R}\right)^2. \quad (14)$$

$$S_{rT} = \frac{1}{2(1-\nu)} + \left(\frac{r_o}{R}\right)^2 \frac{1-2\nu}{2(1-\nu)},$$

$$S_{rL} = \frac{\nu}{2(1-\nu)} - \left(\frac{r_o}{R}\right)^2 \frac{\nu}{2(1-\nu)},$$

$$S_{\theta T} = \frac{1}{2(1-\nu)} + \left(\frac{r_o}{R}\right)^2 \frac{1-2\nu}{2(1-\nu)},$$

$$S_{\theta L} = \frac{\nu}{2(1-\nu)} - \left(\frac{r_o}{R}\right)^2 \frac{\nu}{2(1-\nu)},$$

$$S_{zT}(r_o) = 0, \quad S_{zL}(r_o) = \left(\frac{r_o}{R}\right)^2. \quad (15)$$

It should be noted that the **D** tensor defined in the matrix varies with r , i.e., $D_{ij} = D_{ij}(r)$, however the **S** tensor is constant. In summary, for the inclusion problem with uniform (constant) eigenstrains ϵ_T^* and ϵ_L^* in the inclusion Ω , the corresponding total strains are given by

$$\epsilon_i = S_{iT}(r_o)\epsilon_T^* + S_{iL}(r_o)\epsilon_L^*, \quad \text{in the inclusion } \Omega, \quad (16)$$

$$\epsilon_i = D_{iT}\epsilon_T^* + D_{iL}\epsilon_L^* \quad \text{in the matrix } D - \Omega. \quad (17)$$

Using GPS tensors we can obtain explicit expressions for the displacement and the stress components in both the inclusion and matrix:

In the inclusion $\Omega = \{(r, \theta, z) : r \leq r_o\}$:

$$u(r) = \left[\frac{1}{2(1-\nu)} + \left(\frac{r_o}{R}\right)^2 \frac{1-2\nu}{2(1-\nu)} \right] r \epsilon_T^* + \left[\frac{\nu}{2(1-\nu)} - \left(\frac{r_o}{R}\right)^2 \frac{\nu}{2(1-\nu)} \right] r \epsilon_L^*, \quad (18)$$

$$\sigma_r = \sigma_\theta = \frac{\mu}{1-\nu} \left[\left(\frac{r_o}{R}\right)^2 - 1 \right] (\epsilon_T^* + \nu \epsilon_L^*),$$

$$\sigma_z = \frac{2\mu}{1-\nu} \left[\left(\frac{r_o}{R}\right)^2 - 1 \right] (\nu \epsilon_T^* + \epsilon_L^*). \quad (19)$$

In the matrix $D - \Omega = \{(r, \theta, z) : r_o < r \leq R\}$:

$$u(r) = \left(\frac{1-2\nu}{2(1-\nu)} \epsilon_T^* - \frac{\nu}{2(1-\nu)} \epsilon_L^* \right) \times \left(\frac{r_o}{R} \right)^2 r + \left(\frac{r_o}{r} \right)^2 \frac{\epsilon_T^* + \nu \epsilon_L^*}{2(1-\nu)}, \quad (20)$$

$$\sigma_r = \frac{\mu}{1-\nu} \left[\left(\frac{r_o}{R}\right)^2 - \left(\frac{r_o}{r}\right)^2 \right] (\epsilon_T^* + \nu \epsilon_L^*),$$

$$\sigma_\theta = \frac{\mu}{1-\nu} \left[\left(\frac{r_o}{R}\right)^2 + \left(\frac{r_o}{r}\right)^2 \right] (\epsilon_T^* + \nu \epsilon_L^*),$$

$$\sigma_z = \frac{2\mu}{1-\nu} \left(\frac{r_o}{R}\right)^2 (\nu \epsilon_T^* + \epsilon_L^*). \quad (21)$$

4 Application of GPS Tensors to Thermal Residual Stress

GPS tensors **S** and **D** have been developed for an infinite long circular cylindrical inclusion problem. **S** relates the prescribed eigenstrain ϵ_{ij}^* to the total strain ϵ_i in the inclusion (fiber) whereas **D** relates the same eigenstrain with the total strain in the surrounding matrix. Consider the composite material **D** with fiber Ω and matrix $D - \Omega$ as shown in Fig. 1. We assume both fiber and matrix are elastically isotropic and transversely isotropic in thermal property. Let the Young's modulus and Poisson's ratio of fiber and matrix be E^f, ν^f and E^m, ν^m , respectively. The transverse and longitudinal coefficients of thermal expansion of fiber and matrix are denoted by α_T^f, α_L^f and α_T^m, α_L^m , respectively. High residual stresses can develop when the composite material is cooled from a processing temperature, say T_o , to room temperature due to the coefficient of thermal expansion mismatch between the fiber and the matrix. The thermal eigenstrains in the fiber at any temperature T are

$$\epsilon_r^{\text{th}} = \epsilon_\theta^{\text{th}} = \epsilon_T^{\text{th}} = \Delta\alpha_T(T - T_o) = \Delta\alpha_T\Delta T, \quad (22)$$

and

$$\epsilon_z^{\text{th}} = \epsilon_L^{\text{th}} = \Delta\alpha_L(T - T_o) = \Delta\alpha_L\Delta T, \quad (23)$$

where $\Delta\alpha_T = \alpha_T^f - \alpha_T^m$, $\Delta\alpha_L = \alpha_L^f - \alpha_L^m$, $\Delta T = T - T_o$. Then the stress-strain relations are

$$\sigma_i = 2\mu^f(\epsilon_i - \epsilon_i^{\text{th}}) + \lambda^f(\epsilon_r + \epsilon_\theta + \epsilon_z - 2\epsilon_T^{\text{th}} - \epsilon_L^{\text{th}}) \quad \text{in the fiber } \Omega, \quad (24)$$

for $i = r, \theta, z$. By introducing fictitious uniform eigenstrains ϵ_r^* and ϵ_L^* in the fiber Ω ($\epsilon_r^* = \epsilon_\theta^* = \epsilon_T^*$, $\epsilon_z^* = \epsilon_L^*$), Eq. (24) can be rewritten as

$$\sigma_i = 2\mu^m(\epsilon_i - \epsilon_i^* - \epsilon_i^{\text{th}}) + \lambda^m(\epsilon_j - \epsilon_j^* - \epsilon_j^{\text{th}})\delta_{ij} \quad \text{in the fiber } \Omega \quad (25)$$

for $i = r, \theta, z$. Here the index J takes on the same number as j but is not summed.

Now the total eigenstrains in the inclusion Ω are

$$\epsilon_T^{**} = \epsilon_T^* + \epsilon_T^{\text{th}}, \quad \epsilon_L^{**} = \epsilon_L^* + \epsilon_L^{\text{th}}.$$

The total strains in the fiber Ω are given by

$$\epsilon_r = \epsilon_\theta = S_{rT}\epsilon_T^{**} + S_{rL}\epsilon_L^{**}, \quad \epsilon_z = S_{zT}\epsilon_T^{**} + S_{zL}\epsilon_L^{**},$$

where $S_{ij}(i = r, \theta, z; j = T, L)$ is the GPS tensor. The elastic constants of the matrix are used to calculate each components of the GPS tensor S .

Substituting the above equalities into (24), (25), and equating the expressions for σ_r and σ_z , respectively, we get

$$[2(\Delta\mu + \Delta\lambda)S_{rT} + 2(\mu^m + \lambda^m)]\epsilon_T^{**} + [2(\Delta\mu + \Delta\lambda)S_{rL} + \Delta\lambda S_{zL} + \lambda^m]\epsilon_L^{**} = 2(\mu^f + \lambda^f)\epsilon_T^h + \lambda^f\epsilon_L^h, \quad (26)$$

$$[2\Delta\lambda S_{rT} + 2\lambda^m]\epsilon_T^{**} + [(2\Delta\mu + \Delta\lambda)S_{zL} + 2\Delta\lambda S_{rL} + (2\mu^m + \lambda^m)]\epsilon_L^{**} = 2\lambda^f\epsilon_T^h + (2\mu^f + \lambda^f)\epsilon_L^h, \quad (27)$$

where $\Delta\mu = \mu^f - \mu^m$, $\Delta\lambda = \lambda^f - \lambda^m$. The determinant of the coefficient matrix of the above system of equations is

$$\begin{aligned} Det &= 2\Delta\mu(2\Delta\mu + 3\Delta\lambda)S_{rT}S_{zL} \\ &+ 2\Delta\mu[2\mu^m(S_{rT} + S_{zL}) + \lambda^m(S_{rT} + 2S_{zL} - 2S_{rL})] \\ &+ 2\Delta\lambda\mu^m(2S_{rT} + 2S_{rL} + S_{zL}) + 2\mu^m(2\mu^m + 3\lambda^m). \end{aligned} \quad (28)$$

Solving (26) and (27) for ϵ_T^{**} and ϵ_L^{**} , we get

$$\begin{aligned} \epsilon_T^{**} &= \frac{2}{Det} [\Delta\mu(S_{zL} - S_{rL}) + \mu^m][2(\mu^f + \lambda^f)\Delta\alpha_T \\ &+ \lambda^f\Delta\alpha_L]\Delta T - \frac{2\mu^f}{Det} [2\Delta\mu S_{rL} + \Delta\lambda(2S_{rL} + S_{zL}) \\ &+ \lambda^m](\Delta\alpha_L - \Delta\alpha_T)\Delta T, \end{aligned} \quad (29)$$

$$\begin{aligned} \epsilon_L^{**} &= \frac{2}{Det} [\Delta\mu S_{rT} + \mu^m][2(\mu^f + \lambda^f)\Delta\alpha_T + \lambda^f\Delta\alpha_L]\Delta T \\ &+ \frac{4\mu^f}{Det} [(\Delta\mu + \Delta\lambda)S_{rT} + (\mu^m + \lambda^m)] \\ &\times (\Delta\alpha_L - \Delta\alpha_T)\Delta T. \end{aligned} \quad (30)$$

Then the stress components, from (19) (21), are found to be the following.

In Ω :

$$\begin{aligned} \sigma_r = \sigma_\theta &= \frac{\mu^m}{1 - \nu^m} \left[\left(\frac{r_o}{R} \right)^2 - 1 \right] (\epsilon_T^{**} + \nu^m \epsilon_L^{**}), \\ \sigma_z &= \frac{2\mu^m}{1 - \nu^m} \left[\left(\frac{r_o}{R} \right)^2 - 1 \right] (\nu^m \epsilon_T^{**} + \epsilon_L^{**}). \end{aligned} \quad (31)$$

In $D - \Omega$:

$$\begin{aligned} \sigma_r &= \frac{\mu^m}{1 - \nu^m} \left[\left(\frac{r_o}{R} \right)^2 - \left(\frac{r_o}{r} \right)^2 \right] (\epsilon_T^{**} + \nu^m \epsilon_L^{**}), \\ \sigma_\theta &= \frac{\mu^m}{1 - \nu^m} \left[\left(\frac{r_o}{R} \right)^2 + \left(\frac{r_o}{r} \right)^2 \right] (\epsilon_T^{**} + \nu^m \epsilon_L^{**}), \\ \sigma_z &= \frac{2\mu^m}{1 - \nu^m} \left(\frac{r_o}{R} \right)^2 (\nu^m \epsilon_T^{**} + \epsilon_L^{**}). \end{aligned} \quad (32)$$

If we consider the special case where the thermal property is isotropic, i.e., $\alpha_L = \alpha_T = \alpha$, then the stresses in the fiber Ω are

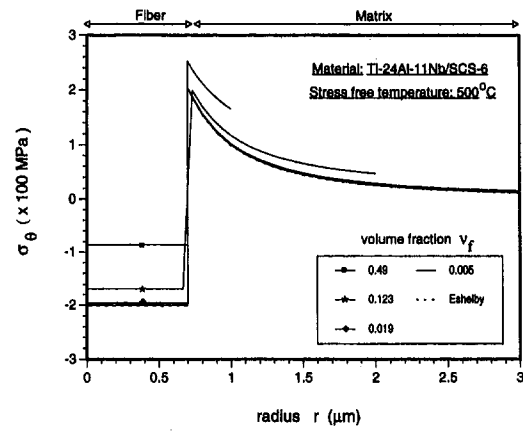


Fig. 2 Tangential stress distribution with different volume fraction of fiber

$$\begin{aligned} \sigma_r = \sigma_\theta &= \frac{E^m r_o^2}{(1 - \nu^m) \cdot Det} \left(\frac{1}{R^2} - \frac{1}{r_o^2} \right) \left[\Delta\mu \left(\frac{r_o}{R} \right)^2 + \mu^m \right] \\ &\times (2\mu^f + 3\lambda^f)(\alpha^f - \alpha^m)\Delta T, \\ \sigma_z &= \frac{E^m r_o^2}{(1 - \nu^m) \cdot Det} \left(\frac{1}{R^2} - \frac{1}{r_o^2} \right) \left[\Delta\mu \left(\frac{r_o}{R} \right)^2 + \mu^m + \mu^f \right] \\ &\times (2\mu^f + 3\lambda^f)(\alpha^f - \alpha^m)\Delta T. \end{aligned}$$

In the matrix $D - \Omega$

$$\begin{aligned} \sigma_r &= \frac{E^m r_o^2}{(1 - \nu^m) \cdot Det} \left(\frac{1}{R^2} - \frac{1}{r^2} \right) \left[\Delta\mu \left(\frac{r_o}{R} \right)^2 + \mu^m \right] \\ &\times (2\mu^f + 3\lambda^f)(\alpha^f - \alpha^m)\Delta T, \\ \sigma_\theta &= \frac{E^m r_o^2}{(1 - \nu^m) \cdot Det} \left(\frac{1}{R^2} + \frac{1}{r^2} \right) \left[\Delta\mu \left(\frac{r_o}{R} \right)^2 + \mu^m \right] \\ &\times (2\mu^f + 3\lambda^f)(\alpha^f - \alpha^m)\Delta T, \\ \sigma_z &= \frac{E^m}{(1 - \nu^m) \cdot Det} \left(\frac{r_o}{R} \right)^2 \left[\Delta\mu \left(\frac{r_o}{R} \right)^2 + \mu^m + \mu^f \right] \\ &\times (2\mu^f + 3\lambda^f)(\alpha^f - \alpha^m)\Delta T, \end{aligned}$$

where Det is given by (28).

5 Some Results

We can demonstrate the application of GPS tensor concept to the evaluation of residual stress in unidirectional fiber-reinforced composites. The process-induced residual stress distribution in the case of intermetallic matrix composite Ti-24Al-11Nb/SCS-6 system has been computed using the S and D tensors. Figure 2 shows the spatial distribution of tangential residual stress σ_θ as a function of various fiber volume fraction $V_f = (r_o/R)^2$. The results are also compared with FEM solutions (Chandra et al., 1994) for the case of $V_f = 0.11$ which show good agreement. We should note that $V_f = 0$ ($R = \infty$) corresponds to the infinite domain Eshelby solution, which has a lower peak stress at the interface compared to higher fiber volume fractions. Also the magnitude of the residual compressive stress in the fiber decreases when the volume fraction is increased. Thus there is an upward shift in the tangential stress profile when the fiber volume fraction is increased, i.e., R is reduced. Also we can observe that σ_θ does not vanish at the outer surface of the composite. Similar results for the radial

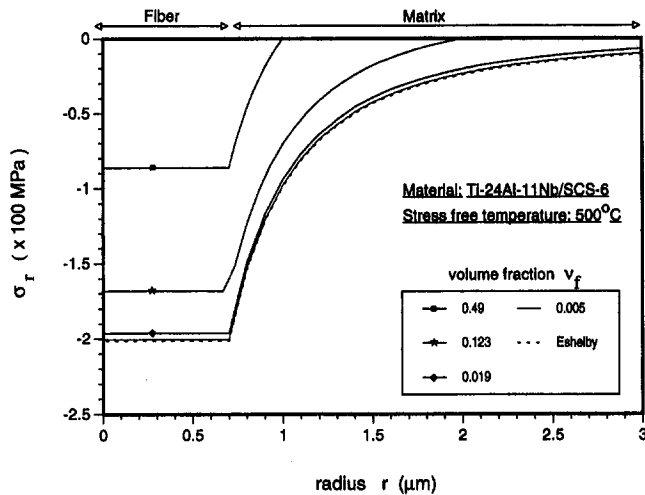


Fig. 3 Radial stress distribution with different volume fraction of fiber

stress distribution are shown in Fig. 3. Here also we observe an upward shift in the profile, and the rate of change of σ_r with radius ($d\sigma_r/dr$) increases with the volume fraction. It is found that within the fiber the tangential stress and radial stress coincide and remain constant. This can be easily explained from the fact the S tensor is a constant within the fiber and the thermal eigenstrain is uniform in the transverse plane.

6 Summary

In this paper we have proposed a pair of two new tensors, GPS tensors S and D , for the concentric cylindrical inclusion problem. Explicit expressions to evaluate σ_r , σ_θ , and σ_z in the matrix and the fiber using tensor D and tensor S , respectively, have been developed. Since the geometry of the present problem is finite, the effect of volume fraction on the stress distribution can be easily studied using $V_f = (r_o/R)^2$. Results for the stress

distributions have been compared with Eshelby's infinite domain solution and finite element results for a specified fiber volume fraction. Since a finite domain cylindrical inclusion problem has been solved using GPS tensors, the tensors can be used to replace the Eshelby tensor in the evaluation of bounds and effective properties of composites in self-consistent methods.

Acknowledgment

The authors wish to acknowledge the financial support provided by National Aeronautics and Space Administration, and discussion with Prof. George Weng.

References

- Budiansky, B., 1965, "On the elastic moduli of some heterogeneous materials," *Journal of the Mechanics and Physics of Solids*, Vol. 13, pp. 223–227.
- Chandra, N., Ananth, C. R., and Garmestani, H., 1994, "Micromechanical modeling of process-induced residual stresses in Ti-24Al-11Nb/SCS-6 composite," *Journal of Composites Technology and Research*, Vol. 16, pp. 37–46.
- Christensen, R. M., and Lo, K. H., 1979, "For effective shear properties in three phase sphere and cylinder models," *Journal of the Mechanics and Physics of Solids*, Vol. 27, pp. 315–330.
- Eshelby, J. D., 1957, "The determination of the elastic field of an ellipsoidal inclusion, and related problems," *Proceeding Roy. Soc., London*, Vol. A241, pp. 376–396.
- Hershey, A. V., 1954, "The Elasticity of an Isotropic Aggregate of Anisotropic Cubic Crystals," *ASME JOURNAL OF APPLIED MECHANICS*, Vol. 21, p. 236.
- Hill, R., 1965, "A self-consistent mechanics of composite materials," *Journal of the Mechanics and Physics of Solids*, Vol. 13, pp. 213–222.
- Kerner, E. H., 1956, "The elastic and thermalelastic properties of composite media," *Proc. Phys. Soc.*, Vol. 69, p. 808.
- Kroner, E., 1958, "Berechnung der elastischen konstanten des vielkristalls aus den konstanten des einkristalls," *Z. Phys.*, Vol. 151, p. 504.
- Luo, H. A., and Weng, G. J., 1987, "On Eshelby's inclusion problem in a three-phase spherically concentric solid, and a modification of Mori-Tanaka's method," *Mechanics of Materials*, Vol. 6, pp. 347–361.
- Luo, H. A., and Weng, G. J., 1989, "On Eshelby's S-tensor in a three-phase cylindrically concentric solid, and the elastic moduli of fiber-reinforced composite," *Mechanics of Materials*, Vol. 8, pp. 77–88.
- Mori, T., and Tanaka, K., 1973, "Average Stress in Matrix and Average Elastic Energy of Materials with Misfitting Inclusions," *Acta Metallurgica*, Vol. 21, pp. 571–574.
- Nemant-Nasser, S., and Taya, M., 1981, "On effective moduli of an elastic body containing periodically distributed voids," *Quart. Appl. Math.*, Vol. 39, pp. 43–59.

Buckling and Post-buckling Behavior of a Pipe Subjected to Internal Pressure

D. M. Tang

Research Associate,
Department of Mechanical Engineering and
Materials Science,
Duke University,
Durham, NC 27706

M. A. Ilgamov

Director, Institute of Mechanics at Kazan,
The Russian Academy of Sciences

E. H. Dowell

Dean, School of Engineering,
Duke University,
Durham, NC 27706
Fellow ASME

It is well known that a thin elastic shell under external pressure may undergo buckling and collapse. Less well known is that a hollow beam under internal pressure may buckle as an Euler column. This is the subject of the present study. The buckled deflection and natural frequency about the buckled configuration of a vertical pipe with clamped (y -axis) and hinged (z -axis) boundary conditions at the lower support location, considering the influence of internal pressure and initial (manufactured) curvature, has been studied analytically and experimentally. The buckling and post-buckling behavior of the pipe beam with an initial static deflection depends upon the nonlinear coupling due to deflection in the two directions including the anisotropic boundary condition at the one support location. The coupling effects increase as the internal pressure and the initial static deflection increase. When the initial static deflection is zero, the coupling effect disappears. The theoretical results agree reasonably well with the experiments.

1 Introduction

It is well known that a thin elastic shell under *external* pressure may undergo buckling and collapse. Less well known is that a hollow beam under *internal* pressure may buckle as an Euler column. This is the subject of the present study.

The linear and nonlinear dynamical behaviour of pipes conveying fluid has been studied theoretically and experimentally by many authors in the last several years. Recently, increasing attention has been devoted to the nonlinear aspects of the dynamical behaviour of this system. Substantial contributions were made by Holmes (1977), Lundgren et al. (1979), Rousselet and Herrmann (1981), Bajaj et al. (1980), and Paidoussis (1991). From these studies, it is found that this system is capable of displaying chaotic motion and other interesting dynamical behaviour.

Two particularly interesting experiments by Tang and Dowell (1988) and by Paidoussis and Moon (1988) present the first closely correlated theoretical-experimental results for the chaotic dynamics of this system. Tang and Dowell (1988) considered a cantilevered pipe with an inset steel strip and equispaced magnets on either side which permitted buckling of the pipe. Once the flow velocity is sufficiently above the threshold for flutter about the buckled state, chaotic motions were possible. Both forced response and self-excited response were considered. Paidoussis and Moon (1988) considered motion-limiting restraints on which the cantilevered pipe would impact, once the flutter motion becomes sufficiently large as the flow velocity is increased. It was shown that chaotic oscillations occur at sufficiently high flow velocity. However, neither of these investigations considered the influence of internal fluid pressure and nozzle discharge.

A more general model of the lateral internal forces in a vertical cantilevered pipe conveying incompressible fluid has been developed by Ilgamov et al. (1994) including the influence of

internal pressure and nozzle discharge. Based upon this improved model, theoretical results are in better agreement with the experimental data by Tang and Dowell (1988) for the minimum excitation force required for generating chaotic response. This suggests the desirability of considering a more basic and elementary physical configuration to further understand these interesting results as described below.

In this paper, following Ilgamov et al. (1994), we discuss buckling and post-buckling behavior of a closed pipe due to an internal fluid pressure. The pipe is clamped at the upper end in both the y - and z -directions, and hinged and clamped at the lower end in the z and y directions, respectively. The axial displacement (x -axis) of these supports is zero. A distinct difference from earlier studies in the literature is that the boundary conditions in the y and z directions are not identical (see Fig. 1).

Here the two-dimensional static instability problem for the buckled pipe beam has been studied analytically and experimentally as well as natural oscillations about the buckled configuration. The experimental results including correlation with theory give a clearer understanding of the influence of the internal pressure and initial static deflection of the pipe on buckling and post-buckling behavior.

Earlier related work has considered the nonlinear vibration of an unbuckled beam by Watzky (1992) and the onset of buckling in a linear, elastic beam by Faupel (1964, 1981) and Clodfelter (1975).

2 Equations of Motion

The system under consideration consists of a pipe beam of length, L , inside radius, r , wall thickness, h , mass per unit length, m , flexural rigidity, EI , and coefficient of Kelvin-Voigt damping, α , containing a fluid of density, ρ . The pipe beam is clamped in both the y and z directions at its upper end, connected to vessel A with pressure p_0 , and hinged (z -axis) and clamped (y -axis) at its lower immovable end (in the x direction). The pipe is assumed to have an initial (manufactured) curvature in a three-dimensional oriented Euclidean space, defined by a vector of $w_0(x, y, z)$, and a buckled deflection, $w(x, y, z, t)$, of the pipe along the x -axis.

The compression force in the pipe is

Contributed by the Applied Mechanics Division of THE AMERICAN SOCIETY OF MECHANICAL ENGINEERS for publication in the ASME JOURNAL OF APPLIED MECHANICS.

Discussion on this paper should be addressed to the Technical Editor, Prof. Lewis T. Wheeler, Department of Mechanical Engineering, University of Houston, Houston, TX 77204-4792, and will be accepted until four months after final publication of the paper itself in the ASME JOURNAL OF APPLIED MECHANICS.

Manuscript received by the ASME Applied Mechanics Division, Nov. 6, 1992; final revision, May 6, 1994. Associate Technical Editor: A. K. Noor.

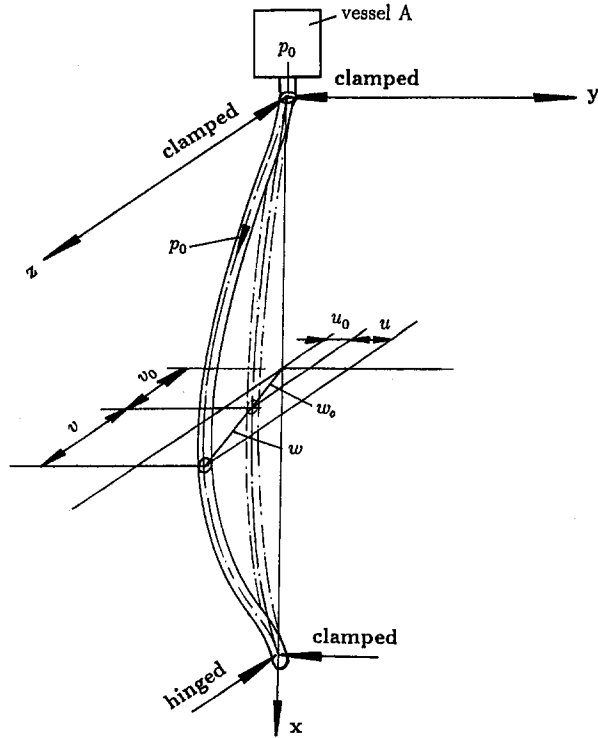


Fig. 1 Physical representation of a vertical pipe-fluid system

$$N_1 = 2\pi r h p_0.$$

The distributed lateral force along the x -axis due to bending of the pipe is (see Ilgamov, 1994),

$$N_2 = -\pi r^2 p_0 \frac{\partial^2(\mathbf{w} + \mathbf{w}_0)}{\partial x^2}.$$

The distributed force vector in the rectangular Cartesian coordinate system, taking into account the liquid static pressure, is represented as

$$\mathbf{N}_p = -\pi r^2 \rho \frac{\partial^2 \mathbf{w}}{\partial t^2} - (\pi r^2 p_0 + 2\pi r h p_0) \frac{\partial^2(\mathbf{w} + \mathbf{w}_0)}{\partial x^2}.$$

The nonlinear equation of bending motion in the three-dimensional oriented Euclidean space can be given by

$$EI \left(\frac{\partial^4 \mathbf{w}}{\partial x^4} + \alpha \frac{\partial^5 \mathbf{w}}{\partial x^4 \partial t} \right) - C \frac{\partial^2(\mathbf{w} + \mathbf{w}_0)}{\partial x^2} \int_0^L \left| \left(\frac{\partial(\mathbf{w} + \mathbf{w}_0)}{\partial x} \right)^2 - \left(\frac{\partial \mathbf{w}_0}{\partial x} \right)^2 \right| dx + (m + \pi r^2 \rho) \frac{\partial^2 \mathbf{w}}{\partial t^2} + (m + \pi r^2 \rho) g \left[\frac{\partial(\mathbf{w} + \mathbf{w}_0)}{\partial x} - (L - x) \frac{\partial^2(\mathbf{w} + \mathbf{w}_0)}{\partial x^2} \right] + P \frac{\partial^2(\mathbf{w} + \mathbf{w}_0)}{\partial x^2} = 0 \quad (1)$$

where $C = \pi r h E / L$ and $P = \pi r^2 (1 + 2\frac{h}{r}) p_0$. For a detailed derivation of this equation, see Watzky (1992). Here we have generalized the equation to include an initial (manufactured) curvature and the effect of an internal pressure after Ilgamov (1994).

The transverse displacement vectors, \mathbf{w} and \mathbf{w}_0 may be represented as

$$\mathbf{w} = u\mathbf{j} + v\mathbf{k}$$

$$\mathbf{w}_0 = u_0\mathbf{j} + v_0\mathbf{k}$$

where \mathbf{j} , \mathbf{k} are unit base vectors associated with the y and z -axes in the reference Cartesian coordinate system.

Substituting this representation into (1), we obtain two coupled nonlinear equations in the xoy and xoz -planes, respectively. They are

$$(m + \pi r^2 \rho) \ddot{u} + EI(u'''' + \alpha \dot{u}''''') - C(u'' + u_0'') \int_0^L (u'^2 + v'^2 + 2u'u_0' + 2v'v_0') dx + (m + \pi r^2 \rho) g [u' + u_0' - (L - x)(u'' + u_0'')] + P(u'' + u_0'') = 0 \quad (2)$$

$$(m + \pi r^2 \rho) \ddot{v} + EI(v'''' + \alpha \dot{v}''''') - C(v'' + v_0'') \int_0^L (u'^2 + v'^2 + 2u'u_0' + 2v'v_0') dx + (m + \pi r^2 \rho) g [v' + v_0' - (L - x)(v'' + v_0'')] + P(v'' + v_0'') = 0 \quad (3)$$

where $(\dot{\quad}) = \partial/\partial t$ and $(\quad)' = \partial/\partial x$.

Boundary conditions are, at $x = 0$,

$$u(0) = u'(0) = 0, \quad v(0) = v'(0) = 0,$$

and at $x = L$,

$$u(L) = u'(L) = 0, \quad v(L) = v''(L) = 0.$$

Let

$$u_0 = \sum_{s=0}^M du_s \bar{x}^s$$

$$v_0 = \sum_{s=0}^M dv_s \bar{x}^s \quad (4)$$

$$u = \sum_{i=1}^N p_i \phi_i$$

$$v = \sum_{i=1}^N q_i \psi_i \quad (5)$$

where ϕ_i and ψ_i are the i th normal mode of the associated linear problem without internal pressure. Note that the ψ_i , ϕ_i , $i = 1, 2, \dots, N$, satisfy the boundary conditions and the orthonormal conditions of the clamped-clamped and clamped-hinged pipe-beam, respectively.

In (4), u_0 and v_0 are determined by measurement, and du_s , dv_s are obtained using a curve fitting method.

Substituting (4), (5) into (2), (3), and using Galerkin's method, one obtains a finite set of second-order ordinary differential equations for the modal amplitudes, $p_n(t)$ and $q_n(t)$, ($n = 1, 2, \dots, N$), as follows:

$$\ddot{p}_n + 2\xi_{un}\omega_{un}\dot{p}_n + \omega_{un}^2 p_n + \sum_{k=1}^N C_{kn}^p p_k + \sum_{k=1}^N C_{kn}^q q_k + \sum_{i,j=1}^N (B_{ijn}^p p_i p_j + B_{ijn}^{pq} p_i q_j + B_{ijn}^q q_i q_j) + \sum_{i,j,k=1}^N (A_{ijkn}^p p_i p_j p_k + A_{ijkn}^{pq} p_i p_k q_j) + \sum_{k=1}^N \eta_k = 0 \quad (6)$$

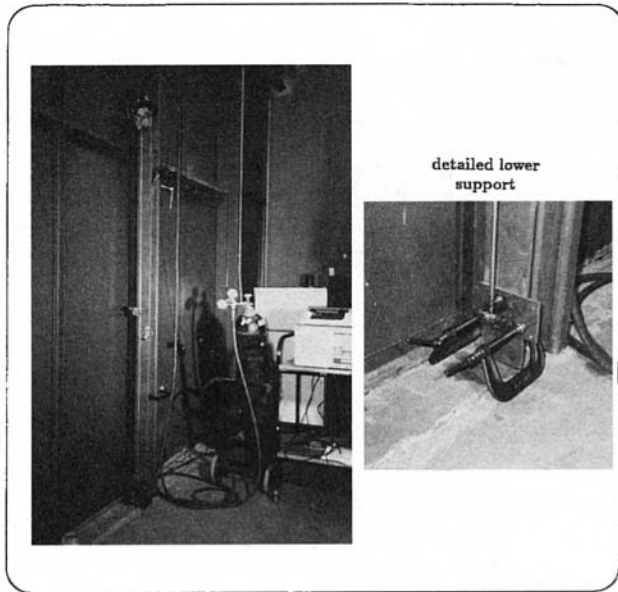


Fig. 2 Experimental apparatus

$$\begin{aligned} \ddot{q}_n + 2\xi_{vn}\omega_{vn}\dot{q}_n + \omega_{vn}^2 q_n + \sum_{k=1}^N \bar{C}_{kn}^q q_k + \sum_{k=1}^N \bar{C}_{kn}^p p_k \\ + \sum_{i,j=1}^N (\bar{B}_{ijn}^q q_i q_j + \bar{B}_{ijn}^{qp} q_i p_j + \bar{B}_{ijn}^p p_i p_j) \\ + \sum_{i,j,k=1}^N (\bar{A}_{ijkn}^q q_i q_j q_k + \bar{A}_{ijkn}^{qp} p_i p_j q_k) + \sum_{k=1}^N \bar{\eta}_k = 0 \quad (7) \end{aligned}$$

where the generalized static force is due to the initial curvature of the pipe. The system is always asymmetrical even if $\eta_k = 0$, $\bar{\eta}_k = 0$. For the coefficients $A_{ijkn}^p, \bar{A}_{ijkn}^q, \dots$, see Appendix A.

Now, consider the buckling deflection and natural frequency of this coupled pipe-beam with the prescribed boundary conditions and an initial static deflection in the y and z directions. The static buckling deflection, u, v , can be obtained from (6), (7) when the time derivatives are set to zero. By taking N modes, Eqs. (6) and (7) serve to reduce the system to a set of $2N$ third-order nonlinear algebraic equation. The solution of the equations can be obtained by iteration using the Newton-Raphson method, for example.

Assume p_{bn}, q_{bn} are the generalized coordinates of the buckled equilibrium position calculated from (6) and (7). Then let

$$p_n = p_{bn} + \hat{p}_n \quad (8)$$

and

$$q_n = q_{bn} + \hat{q}_n$$

where \hat{p}_n and \hat{q}_n are the small dynamic perturbations of the post-buckled pipe beam. Substituting (8) into (6) and (7), and neglecting higher order perturbation values, we can obtain a set of $2N$ second-order perturbation differential equations. The coupled buckling natural frequencies may be determined by a numerical eigenvalue extraction procedure.

3 Numerical Results and Correlation With Experiment

Results obtained from numerical simulation and experiment are based on the following parameters. The dimensions of the steel pipe beam are a length of 177.2 (cm), 0.95 (cm) in outside diameter and 0.0254 (cm) wall thickness. The flexural rigidity EI is found by measuring the frequency of the pipe beam in its

fundamental mode. The pipe mass per unit length is 7.662×10^{-7} (kg·sec²/cm²).

The experimental system with the pipe beam containing air is shown in Fig. 2. The air pressure is provided by a high pressure tank with a regulator (the measurement range is 0–28.12 kg/cm²). The displacements at 89 (cm) from the clamped end for u and 106.7 (cm) for v are measured by two RVDT transducers, respectively. The signals from these transducers were amplified and recorded on a signal analyzer, SD 380.

The initial static deflection is measured and then the coefficients, du_i , and dv_i , are determined using a curve fitting method. It is determined that

$$\begin{aligned} du_0 &= -0.0051328, & du_1 &= .504378, \\ du_2 &= -.489224, & du_3 &= -.00176842 \\ dv_0 &= -.001026, & dv_1 &= .10087, \\ dv_2 &= -.097834, & dv_3 &= -.00354385. \end{aligned}$$

The theoretical results were obtained initially by taking two modes each for u and v . The first mode is dominant however, with the second mode amplitude less than five percent of the first mode amplitude. Therefore taking $N = 1$ or one mode each for u and v and neglecting the damping, the coupled buckling frequencies can be determined from (6), (7), and (8) by

$$\omega^4 - (s_{11} + s_{22})\omega^2 + s_{11}s_{22} - s_{12}s_{21} = 0 \quad (9)$$

where

$$\begin{aligned} s_{11} &= \omega_{u1}^2 + C_{11}^p + 2B_{111}^p p_{b1} + B_{111}^{pq} q_{b1} \\ &\quad + 3A_{1111}^p p_{b1}^2 + A_{1111}^{pq} q_{b1}^2 \\ s_{12} &= C_{11}^q + 2B_{111}^q q_{b1} + B_{111}^{pq} q_{b1} + 2A_{1111}^{pq} p_{b1} q_{b1} \\ s_{21} &= \bar{C}_{11}^p + 2\bar{B}_{111}^p + \bar{B}_{111}^{qp} q_{b1} + 2\bar{A}_{1111}^{qp} p_{b1} q_{b1} \\ s_{22} &= \omega_{v1}^2 + \bar{C}_{11}^q + 2\bar{B}_{111}^q + \bar{B}_{111}^{qp} p_{b1} + 3\bar{A}_{1111}^q q_{b1}^2 + \bar{A}_{1111}^{qp} p_{b1}^2 \end{aligned}$$

and p_{b1} and q_{b1} are the buckled equilibrium positions.

The buckled natural frequencies in the y - and z -directions may be given even more simply and analytically using a one mode, uncoupled approximation and the linear stiffness terms of these perturbation equations, such that $\omega_{bu1} = \sqrt{s_{11}}$ and $\omega_{bv1} = \sqrt{s_{22}}$. However, this uncoupled approximation may have a large error as compared to the coupled buckling frequency from (9) when the internal pressure increases. Results shown in Fig. 3 are for a comparison of the buckled frequencies with and without coupling versus internal pressure for a pipe beam with

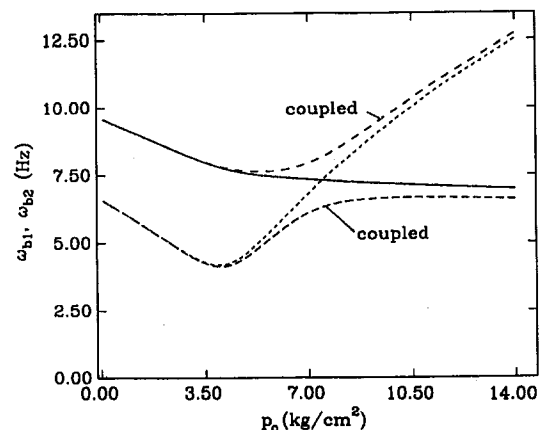


Fig. 3 Comparison of the buckled frequencies with and without coupling versus internal pressure for a sine-initial curvature pipe-beam ($u_0(L/2) = 0.1$ (cm), $v_0(L/2) = 0.05$ (cm), (—), ω_{bu1} , (---), ω_{bv1} for without coupling; (— —), ω_{b1} , (---), ω_{b2} , for with coupling

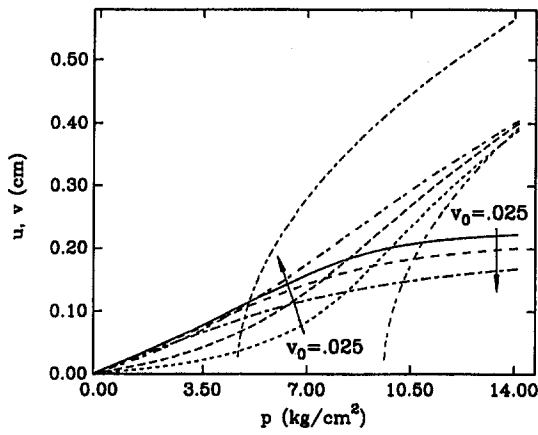


Fig. 4(a)

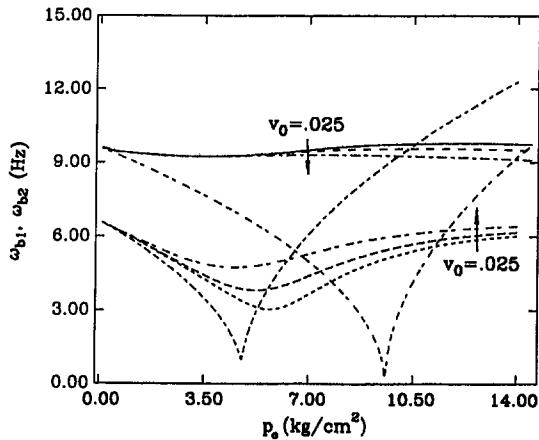


Fig. 4(b)

Fig. 4 Effects of the initial static deflection on the buckling behavior for $u_0 = 0.254$ (cm) and several v_0 : (—), for $u_0 = 0.025$ (cm); (---), for $u_0, v_0 = 0.05$ (cm); (- -), for $u_0, v_0 = 0.1$ (cm); (- · - ·), for $v_0 = 0.025$ (cm); (- · - ·), for $v_0 = 0.05$ (cm); (- · - ·), for $v_0 = 0.1$ (cm); (- -), for $u_0, v_0 = u_0 = 0$; (- · - ·), for $v_0, v_0 = u_0 = 0$; (a) for buckled deflection, (b) for buckled frequency

sine-initial curvature ($u_0(L/2) = 0.1$ (cm), $v_0(L/2) = 0.05$ (cm)). Note $p_0 = 4.85$ (kg/cm^2) is the critical buckling pressure for the isolated z -direction deflection. The results obtained by the uncoupled approximation agree reasonably well with the coupled solution except when the two frequencies are near each other. As p_0 increases from the nominal critical pressure to 9.56 (kg/cm^2), ($p_0 = 9.56$ (kg/cm^2) is the critical buckling pressure for the isolated y -direction deflection), the error of the approximate method increases, but in the higher pressure range, the error decreases again. This error pattern appears to be related to a coupled mode or veering phenomenon.

When the pipe beam is a straight beam ($u_0 = v_0 = 0$), and one mode is considered, we obtain a set of static buckled equilibrium Eqs. from (6), (7), and (8) as

$$\begin{bmatrix} A_{1111}^p & A_{1111}^{pq} \\ \bar{A}_{1111}^{qp} & \bar{A}_{1111}^q \end{bmatrix} \begin{Bmatrix} p_{b1}^2 \\ q_{b1}^2 \end{Bmatrix} = - \begin{Bmatrix} \omega_{u1}^2 + C_{11}^p \\ \omega_{v1}^2 + \bar{C}_{11}^q \end{Bmatrix}. \quad (10)$$

In Eq. (10), A_{1111}^p , A_{1111}^{pq} , \bar{A}_{1111}^q , and \bar{A}_{1111}^{qp} are greater than zero, and

$$|\Delta| = \begin{vmatrix} A_{1111}^p & A_{1111}^{pq} \\ \bar{A}_{1111}^{qp} & \bar{A}_{1111}^q \end{vmatrix} = 0.$$

Thus there is no physically meaningful solution for q_{b1}^2 and

p_{b1}^2 both nonzero. Therefore, for a straight pipe beam with anisotropic boundary condition at one support, there is no coupling influence. That is, only $p_{b1} \neq 0$ and $q_{b1} \equiv 0$ or $p_{b1} \equiv 0$ and $q_{b1} \neq 0$ are possible solutions. This is true when higher modes are included as well.

Figure 4 shows the effects of the initial static deflection on the buckled deflection and first buckled natural frequency versus p_0 . The initial static deflection is assumed to have the first mode

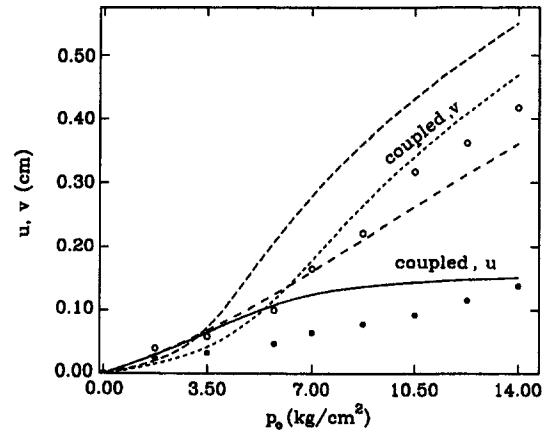


Fig. 5(a)

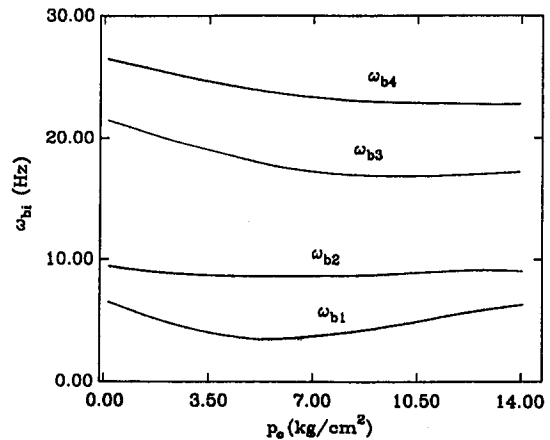


Fig. 5(b)

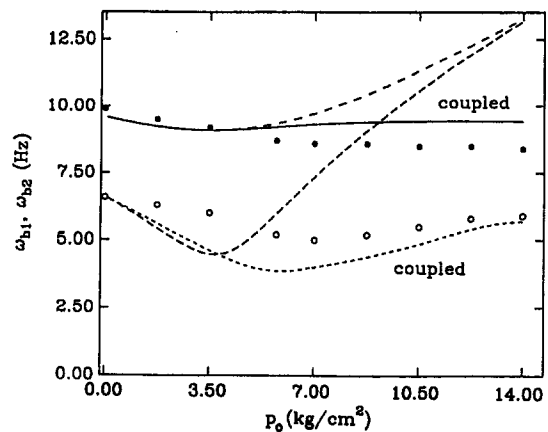


Fig. 5(c)

Fig. 5 Theoretical and experimental results of coupled and uncoupled buckling deflection and frequency versus p_0 , (---), for u and uncoupling, (—), for u and coupling, (- -), for v and uncoupling, (- · - ·), for v and coupling, (●) for u test, (O) for v test, (a) for buckled deflection, (b) and (c) for buckled frequency

shape of the clamped-clamped beam. The middle displacements are 0.254 (cm) for the y -direction and 0.025, 0.05 and .1 (cm), respectively, for the z -direction. It is found that u decreases and v increases as v_0 increases when p_0 increases as shown in Fig. 4(a). The coupled first buckled frequencies ω_{b1} (called ω_{yb1}) increases and the second one ω_{b2} (called ω_{zb1}) decreases as v_0 increases as shown in Fig. 4(b). The pressure corresponding to the minimum frequency for ω_{b1} decreases as v_0 increases. The results for a straight pipe beam are also plotted in Fig. 4(a) and Fig. 4(b). The influence of the initial curvature is quite evident. It is well known from the perturbation equations that the buckled frequency significantly depends upon the initial static deflection shape. When the initial static deflection shape coincides with the first natural mode shape, the second mode components for both the y - and z -directions are almost zero. The higher order mode buckled frequencies are nearly equal to the unbuckled higher order natural frequencies, and the first two modal buckled frequencies have the largest change.

Figure 5 shows the theoretical results for coupled and uncoupled buckling deflections and buckled frequencies versus p_0 for the measured initial static deflection. For the buckling deflections, the buckled deflections u , v , increase and the uncoupled response is larger than the coupled one as p_0 increases as shown in Fig. 5(a). For the buckled frequencies, the first four calculated coupled buckling frequencies ω_{b1} , ω_{b2} , ω_{b3} , and ω_{b4} are shown in Fig. 5(b). Figure 5(c) shows the first two coupled buckling frequencies and the uncoupled frequencies versus p_0 . It is found that the coupled ω_{b1} , ω_{b2} have smaller changes compared to the uncoupled frequencies as p_0 increases, and the coupled frequencies are lower than the uncoupled ones in the higher pressure range. In the lower pressure range, the buckled frequencies decrease as p_0 increases and the difference between the coupled and uncoupled frequencies is small.

For comparison with the theoretical results, the measured data are also plotted in Fig. 5(a) and Fig. 5(c) as indicated by the symbol (●) for u and ω_{b2} and the symbol (○) for v and ω_{b1} . The agreement between theory and experiment is substantially improved by using the nonlinear coupled buckling theory as compared to the uncoupled buckling theory, especially for the z -direction deflection and the buckled frequency. The poorer agreement in the y -direction is due to the larger initial static curvature in the same direction. The measured static curvature looks like a half sine-wave with the maximum deflection 0.317 (cm) in the y -direction and 0.1 (cm) in the z -direction.

4 Concluding Remarks

The buckling and post-buckling behavior of a vertical pipe with different boundary conditions at the lower end in the y - and z -directions, and considering the influence of internal pressure and initial static deflection, has been studied. It was shown that the buckling deflection and buckled frequency of the vertical pipe beam with an initial static deflection depend upon the nonlinear coupling due to deflection in two directions including the different boundary conditions in the two different directions at the same support location. The coupling effects increase as the internal pressure and the initial static deflection increase. When the initial static deflection is zero, the coupling effect disappears. The theoretical results agree reasonably well with the experiments.

Acknowledgments

This work was supported by the Army Research Office under Grant DAAL03-87-K-0023; Dr. Gary Anderson is the technical monitor. All numerical simulations were done on the supercomputer, Cray Y-MP, in the North Carolina Supercomputing Center (NCSC).

References

- Bajaj, A. K., Sethna, P. R., and Lundgren, T. S., 1980, "Hopf Bifurcation Phenomena in Tubes Carrying a Fluid," *SIAM Journal of Applied Mathematics*, Vol. 39, pp. 213-230.
- Clodfelter, G. A., 1975, "Development of the Filament-Wound Composite Launch Tubes for SMAWT Program," AD-A012 150, Army, Missile Research, Development and Engineering Laboratory, Redstone Arsenal, AL.
- Faupel, J. H., 1964, *Engineering Design*, John Wiley and Sons, New York, pp. 536-538.
- Faupel, J. H., and Fisher, F. E., 1981, *Engineering Design*, John Wiley and Sons, New York, pp. 614-616.
- Holmes, P. J., 1977, "Bifurcations to Divergence and Flutter in Flow-Induced Oscillations: a Finite-dimensional Analysis," *Journal of Sound and Vibration*, Vol. 53, pp. 471-503.
- Ilgamov, M. A., Tang, D. M., and Dowell, E. H., 1994, "Flutter and Forced Response of a Cantilevered Pipe: the Influence of Internal Pressure and Nozzle Discharge," *J. of Fluids and Structures*, Vol. 8, pp. 139-156.
- Lundgren, T. S., Sethna, P. R., and Bajaj, A. K., 1979, "Stability Boundaries for Flow-Induced Motions of Tubes with an Inclined Terminal Nozzle," *Journal of Sound and Vibration*, Vol. 64, pp. 553-571.
- Paidoussis, M. P., 1991, "Pipes Conveying Fluid: a Model Dynamical Problem," in *Proceedings of Canadian Congress of Applied Mechanics*, 1-33, Winnipeg, Manitoba, Canada.
- Paidoussis, M. P., and Moon, F. C., 1988, "Nonlinear and Chaotic Fluidelastic Vibration of a Flexible Pipe Conveying Fluid," *J. of Fluids and Structures*, Vol. 2, pp. 567-591.
- Rousselet, J., and Herrmann, G., 1981, "Dynamic Behavior of Continuous Cantilevered Pipes Conveying Fluid near Critical Velocities," *ASME JOURNAL OF APPLIED MECHANICS*, Vol. 43, pp. 945-947.
- Tang, D. M., and Dowell, E. H., 1988, "Chaotic Oscillations of a Cantilevered Pipe Conveying Fluid," *J. of Fluids and Structures*, Vol. 2, pp. 263-283.
- Watzky, A., 1992, "Non-linear Three-Dimensional Large-Amplitude Damped Free Vibration of A Stiff Elastic Stretched String," *Journal of Sound and Vibration*, Vol. 153, No. 1, pp. 125-142.

APPENDIX A

$$A_{ijkn}^p = c_0 G_{ij} G_{kn}$$

$$A_{ijkn}^{pq} = c_0 \bar{G}_{ij} G_{kn}$$

$$B_{ijn}^p = -c_0 \left[2G_{jn} \int_0^L u_0' \phi_i' dx - G_{ij} \int_0^L u_0'' \phi_n dx \right]$$

$$B_{ijn}^{pq} = -2c_0 G_{jn} \int_0^L v_0' \psi_i' dx$$

$$B_{ijn}^q = -c_0 \bar{G}_{ij} \int_0^L u_0'' \phi_n dx$$

$$C_{kn}^p = -2c_0 \int_0^L u_0'' \phi_n dx \int_0^L u_0' \phi_k' dx + \left(\frac{2g}{L} \right) H_{kn} + R_0 G_{kn}$$

$$C_{kn}^q = -2c_0 \int_0^L u_0'' \phi_n dx \int_0^L v_0' \psi_k' dx$$

$$\eta_k = \left(\frac{2g}{L} \right) \left[\int_0^L u_0' \phi_k dx + \int_0^L (x-L) u_0'' \phi_k dx \right] + R_0 \int_0^L u_0'' \phi_k dx$$

$$\bar{A}_{ijkn}^q = c_0 \bar{G}_{ij} \bar{G}_{kn}$$

$$\bar{A}^{qp} = c_0 \bar{G}_{kn} G_{ij}$$

$$\bar{B}_{ijn}^q = -c_0 \left[2\bar{G}_{jn} \int_0^L v_0' \psi_i' dx - \bar{G}_{ij} \int_0^L v_0'' \psi_n dx \right]$$

$$\bar{B}_{ijn}^{qp} = -2c_0 \bar{G}_{jn} \int_0^L u_0' \phi_i' dx$$

$$\bar{B}_{ijn}^p = -c_0 \bar{G}_{ij} \int_0^L v_0'' \psi_n dx$$

$$\bar{C}_{kn}^q = -2c_0 \int_0^L v_0'' \psi_n dx \int_0^L v_0' \psi_k' dx + \left(\frac{2g}{L}\right) \bar{H}_{kn} + R_0 \bar{G}_{kn} \quad \text{and}$$

$$\bar{C}_{kn}^p = -2c_0 \int_0^L v_0'' \psi_n dx \int_0^L u_0' \phi_k' dx$$

$$\bar{\eta}_k = \frac{2g}{L} \left[\int_0^L v_0' \psi_k dx + \int_0^L (x-L) v_0'' \psi_k dx \right] + R_0 \int_0^L v_0'' \psi_k dx$$

where

$$c_0 = 2C/(m + \pi r^2 \rho)L, \quad R_0 = 2P/(m + \pi r^2 \rho)L$$

$$G_{ij} = \int_0^L \phi_i'' \phi_j dx = - \int_0^L \phi_i' \phi_j' dx$$

$$\bar{G}_{ij} = \int_0^L \psi_i'' \psi_j dx = - \int_0^L \psi_i' \psi_j' dx$$

$$H_{ij} = \int_0^L \phi_i' \phi_j dx + \int_0^L (x-L) \phi_i'' \phi_j dx$$

$$\bar{H}_{ij} = \int_0^L \psi_i' \psi_j dx + \int_0^L (x-L) \psi_i'' \psi_j dx$$

Crack Propagation in Homogeneous and Bimaterial Sheets Under General In-Plane Loading: Nonlinear Analysis

P. H. Geubelle

Post Doctoral Researcher,
Harvard University,
Cambridge, MA 02138
Mem. ASME

W. G. Knauss

Professor of Aeronautics and
Applied Mechanics,
California Institute of Technology,
Pasadena, CA 91125
Mem. ASME

The problem of non-coplanar crack propagation in homogeneous and bimaterial sheets is investigated within the framework of the nonlinear theory of plane stress and for the Generalized Neo-Hookean class of hyperelastic solids. The analysis is performed numerically using a boundary layer approach and the maximum energy release rate criterion. The influence of the large deformation effect on the limiting process associated with the concept of "infinitesimal virtual crack extension" is examined, together with the possible relation between the size of the nonlinear zone and the additional length parameter appearing in the linearized analysis of the interfacial crack propagation problem. As the virtual crack extension is gradually shortened to a size comparable to that of the nonlinear zone, a transition is observed between the nonunique value of the kink angle predicted by the linearized theory and a single "nonlinear" value, which is independent of the crack extension length but also independent of the far-field loading conditions. In the limit of homogeneous properties this angle is zero and is corroborated by experiments on natural rubber undergoing large deformations.

1 Introduction

The propagation path taken by a crack subjected to loading that is not symmetric with respect to the crack plane has been investigated extensively since the early work by Erdogan and Sih (1963) in two-dimensional geometries. Various criteria have been proposed to determine the kink angle of the crack: some, such as the maximum (opening) stress criterion, suggest that the fracture process be dictated by the conditions existing at the crack-tip prior to its propagation; others, such as the criterion of local symmetry and the maximum energy release rate criterion (Palaniswamy and Knauss, 1978; Wu, 1978; Lo, 1978; Hayashi and Nemat-Nasser, 1981a; Karahaloo, 1982), require the knowledge of the near-tip conditions during crack propagation. The latter criterion is a generalization of the Griffith energy-balance argument to the non-coplanar situation and consists in comparing the energy stored in the solid before and after the kinking process, for a vanishingly small "virtual" extension of the crack. The pre-

dicted propagation angle corresponds thus to that which maximizes the reduction in potential energy between the two states. Due to its attractive relationship to the fundamental minimum potential energy principle, the maximum energy release rate criterion is today the most commonly used principle. Various investigation methods have been proposed in combination with this criterion such as the use of Muskhelishvili's complex potentials and conformal mapping (Palaniswamy and Knauss, 1978; Wu, 1978) or dislocation (Green's) method (Lo, 1978; Hayashi and Nemat-Nasser, 1981a). More recently, Maiti (1990) examined the crack kinking problem numerically using the finite element method.

As pointed out by Shih (1991), mode mixity is one of the main characteristics of the near-tip stress and deformation fields for an interfacial crack. It is therefore natural that the issue of crack kinking away from an interface has received special attention in the past few years as substantial progress was made in the mechanics of bimaterial interface fracture. Almost all investigations (Hayashi and Nemat-Nasser, 1981b; He and Hutchinson, 1989; Mukai et al., 1990; Wang et al., 1992) involve the dislocation method employed successfully in the homogeneous case under the precepts of linear elasticity theory. However, as was underlined in Geubelle and Knauss (1993), the bimaterial situation presents a major difficulty absent in the homogeneous situation: While, in the monolithic case, it is possible to compute the energetically most favorable kink angle as the length of the extension tends to zero, such a limiting process is not possible in

Contributed by the Applied Mechanics Division of THE AMERICAN SOCIETY OF MECHANICAL ENGINEERS for publication in the ASME JOURNAL OF APPLIED MECHANICS.

Discussion on this paper should be addressed to the Technical Editor, Professor Lewis T. Wheeler, Department of Mechanical Engineering, University of Houston, Houston, TX 77204-4792, and will be accepted until four months after final publication of the paper itself in the ASME JOURNAL OF APPLIED MECHANICS.

Manuscript received and accepted by the ASME Applied Mechanics Division, Mar. 30, 1990; final revision, Feb. 10, 1994. Associate Technical Editor: C. F. Shih.

general within the linearized theory for bimaterial cases, and a unique kink angle cannot be computed. In order to resolve the nonuniqueness issue, an additional length parameter corresponding to the length of the extension has to be introduced. Note once again that such a length scale does not appear in the homogeneous case. It has been suggested that the additional length scale is associated with physical size scales present in the components of the bimaterial specimen such as the size of the microstructure or of the fracture process domain. This approach does not seem, however, compatible with the experimentally deduced additional length parameter¹ obtained for the particular material combination used in Geubelle and Knauss (1993).

In the present paper, we examine whether the length parameter can be somehow associated with the size of the nonlinear large deformation zone present around the crack tip. We thus investigate how the limiting process mentioned above is affected by relinquishing the assumption of infinitesimal strains and allowing for large deformations and rotations along with nonlinear constitutive behavior. The motivation behind the present analysis comes from the fact that the length parameter appearing in the linearized bimaterial situation has been shown to be associated with the inconsistencies inherent in the linear analysis of the interface crack problem (contact and overlapping of the crack faces, oscillatory near-tip fields, ...). However, as was first shown by Knowles and Sternberg (1983), these difficulties disappear if finite strain effects are taken into account. We show here that, even in the homogeneous situation, the size of the large deformation zone introduces a length scale which restricts the limiting process associated with the maximum energy release rate criterion.

The analysis is conducted within the framework of the nonlinearly elastic theory of plane stress. Material and geometrical nonlinearities are combined through the use of the Generalized Neo-Hookean model. Due to the complexity of the field equations and of the problem geometry, the analysis is performed numerically with the aid of the finite element method. The details of the computational analysis are described in the next section. Then, the results corresponding to the homogeneous case are discussed in Section 3 while Section 4 is dedicated to a survey of the bimaterial situation.

2 Numerical Investigation

We present next the details of the numerical analysis, within the nonlinear theory of elasticity, of the maximum energy release rate criterion, and, in particular, of the spatial discretization and the computation of the energy release rate.

Finite Element Mesh. Throughout the present numerical investigation, we are concerned with the boundary value problem symbolically represented in Fig. 1. It consists of a circular domain of radius l , along the outer boundary of which displacement boundary conditions corresponding to a "linear K -field" are applied. The crack, initially of length l , is extended by an amount Δl in a direction ω relative to the crack axis². The ratio of the crack extension length to the original length is varied between 10^{-6} and 10^{-2} . The lower limit is justified by the numerical imprecision associated with very high gradients close to the crack-tip while a ratio of 10^{-2} is the maximum allowable value to keep the "boundary layer" approach meaningful. The latter approach has been chosen instead of the more conventional "global problem," such as, for example, the centered crack problem, for the following three reasons: first, it has been shown to provide

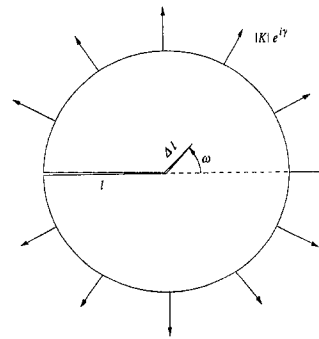


Fig. 1 Geometry of the boundary layer analysis of the crack propagation problem

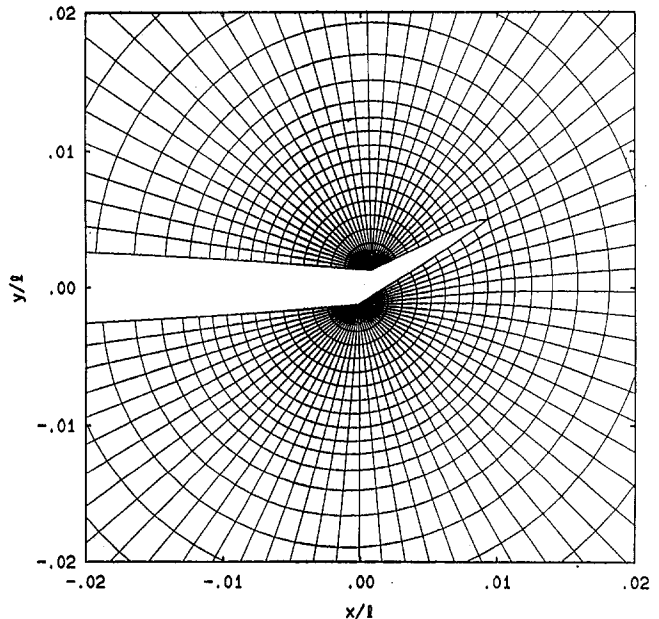


Fig. 2 Details of the deformed finite element mesh after crack extension in the case $\Delta l/l = 10^{-2}$

similar results as long as the length of the crack extension Δl is small compared to the original length l ; second, because it allows a direct control through the applied K -field boundary conditions over the loading conditions prevailing at the crack-tip before its extension; and finally, because the more compact geometry associated with such a boundary layer approach allows for a better spatial discretization than the global approach for an equivalent computational cost.

As pointed out by Maiti (1990), the design of the finite element mesh is of prime importance, especially in the crack-corner and branch-tip region, to ensure precision of the predicted energetically most favorable kink angle. It was suggested there to use a doubly focused mesh (i.e., focused at the kink corner and at the branch tip) in order to capture the interaction between the two singularities arising in the post-extension problem. Since the analysis of the bimaterial situation, for which such a discretization is not possible for most kink angles, constitutes one of the main objectives of the present investigation, we have opted for a simpler mesh focused at the original crack tip only, as described in Fig. 2. Numerical precision has, however, been achieved by increasing the mesh refinement: the crack extension is represented by ten equally spaced elements and the inner annuli are divided into 72 5-degree-sectors. Outside of the inner circle of radius Δl , 25 to 35 elements are distributed geometrically along a radial line, with the progression factor chosen such

¹See discussion in Section 4 of (Geubelle and Knauss, 1993).

²Note that, throughout the present analysis, dimensions and angles are defined with respect to the undeformed coordinates.

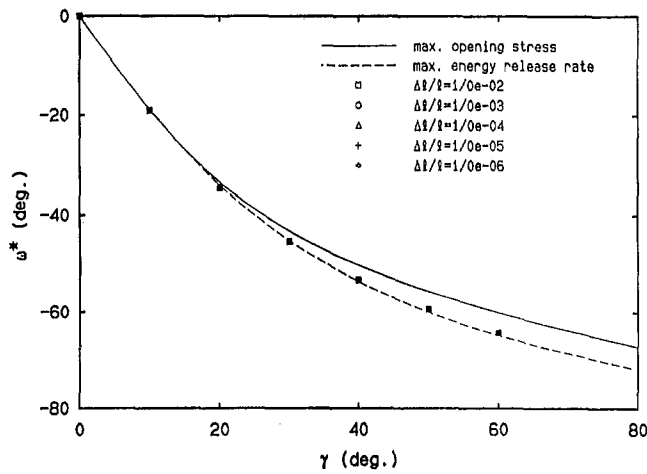


Fig. 3 Results of the preliminary linear analysis of the homogeneous situation: variation of the energetically most favorable kink angle ω^* with respect to the mode-mixity parameter γ for various values of the ratio $\Delta l/l$

that the first “outside” element has a size similar to that of the ten “inner” ones. The total number of four-node bilinear elements was thus 3240 for $\Delta l/l = 10^{-6}$ and 2520 for $\Delta l/l = 10^{-2}$.

The precision of the numerical scheme was assessed by performing a preliminary linearly elastic analysis of the homogeneous situation for which generally accepted results exist. The results are shown in Fig. 3 which presents the variation of the kink angle ω^* as predicted by the maximum energy release rate criterion with respect to the phase angle γ characterizing the local mode mixity at the unextended crack tip, defined by

$$\gamma = \tan^{-1} (K_2/K_1). \quad (2.1)$$

The numerical values, denoted by symbols and corresponding to five values of $\Delta l/l$, are compared with the analytical solution (dashed curve). Also shown is the prediction corresponding to the maximum opening stress criterion which, in the homogeneous case, gives results very similar to those of the energy-based criterion, especially for small values of γ . The agreement between the numerical and analytical results is quite satisfactory, differing in all cases by at most 1.0 deg.

Computation of the Energy Release Rate. As mentioned before, the nonlinear analysis of the crack propagation problem is performed within the framework of the finite strain theory of plane stress, the main relations of which have been summarized by Knowles and Sternberg (1983). The material model used throughout the present investigation is the so-called Generalized Neo-Hookean (GNH) model described in detail by Geubelle and Knauss (1994a). It is characterized by three parameters μ , b , and n which determine, respectively, the linearly elastic, “yielding” and “hardening” behaviors of the incompressible hyperelastic material through the plane stress elastic potential

$$U(I, J) = \frac{\mu}{2b} \left\{ \left[1 + \frac{b}{n} (I + J^{-2} - 3) \right]^n - 1 \right\}, \quad (2.2)$$

with I and J being the two scalar invariants associated with the two-dimensional deformation.³ The GNH model has been implemented, together with a fully Lagrangian scheme, in a modified version of the finite element program FEAP (Taylor, 1977). The initial crack problem is first solved by

applying nodal tractions along the crack extension to keep it closed. Then, these tractions are progressively relaxed until the stress-free kink is fully open and the associated unloading work is computed. This process is repeated for various crack extensions to obtain the variation of the energy release rate with respect to the kink angle, and, thereby, to compute the energetically most favorable crack path.

As mentioned by Geubelle and Knauss (1993), two methods are used to calculate the energy release rate G : the first one is based on the potential energy definition

$$G_w = - \lim_{\Delta l \rightarrow 0} \frac{\Delta \Pi}{\Delta l}, \quad (2.3)$$

where Π is the potential energy contained in the body and, in the present case, is the integral over the domain of the strain energy density $U(I, J)$ defined in (2.2). For hyperelastic solids, the energy release rate can be equivalently determined by computing the closure work of the extended crack

$$G_{cc} = \lim_{\Delta l \rightarrow 0} \frac{1}{\Delta l} \int_0^{\Delta l} \int_0^{\Delta n} \mathbf{T} \cdot d\Delta \mathbf{u} ds, \quad (2.4)$$

where \mathbf{T} and $\Delta \mathbf{u}$ denote the traction and displacement jump vectors along the crack extension, respectively. By monitoring the modal tractions and displacements of the M nodes distributed along the kink during the N unloading steps of the extension process, and using a simple trapezoidal integration rule, (2.4) is approximated by

$$G_{cc} \approx \frac{1}{2\Delta l} \sum_{I=1}^M \sum_{J=1}^N \sum_{\alpha=1}^2 (T_{\alpha}^{I,J-1} + T_{\alpha}^{I,J}) (\Delta u_{\alpha}^{I,J} - \Delta u_{\alpha}^{I,J-1}), \quad (2.5)$$

with $T_{\alpha}^{I,J}$ and $\Delta u_{\alpha}^{I,J}$ representing the α -component at node I and unloading step J of the tractions and displacements, respectively. The two approaches yield very similar results (within 0.1 percent) if a sufficient number of unloading steps are used (5 to 50, depending on the load level).

3 Homogeneous Case

Confident of the precision of the numerical scheme, we first investigate the homogeneous Neo-Hookean situation for which the hardening parameter of the hyperelastic sheet is unity. Seven values of the local mixity parameter have been considered ($\gamma = 0, 10, 20, 30, 40, 50$, and 60). The amplitude of the far-field loading has also been varied as $\bar{K} = |K|/\mu\sqrt{l} = 10^{-4}, 10^{-3}, 10^{-2}, 10^{-1}$ and 1 , where $|K| = \sqrt{K_1^2 + K_2^2}$, μ is the shear modulus, and l is the radius of the circular domain on which the boundary layer analysis is performed. For each far-field loading condition five values of the crack extension length Δl have been investigated, as mentioned earlier ($\Delta l/l = 10^{-6}, 10^{-5}, 10^{-4}, 10^{-3}$ and 10^{-2}). The results of the 175 cases thus defined are summarized in Fig. 4 which presents the variation, with respect to $\Delta l/l$, of the ratio ω^*/ω_L^* , where ω^* and ω_L^* are the kink angles predicted by the nonlinear and linear theory respectively.⁴ It is observed that, except in the particular case $\gamma = 0$ deg (mode I) for which, by symmetry, the maximum energy release rate criterion always predicts a coplanar crack growth, the nonlinear analysis suggests a dependence of the energetically most favorable kink angle ω^* on the length of the extension Δl . As the size of the nonlinear zone increases with \bar{K} , a transition is observed between the γ -dependent linear value ω^* and a unique γ -independent value $\omega^* = 0$ deg.

³See Section 2 of (Geubelle and Knauss, 1994a) for more details.

⁴Recall that, as shown in Fig. 3, ω_L^* is independent of the crack extension length Δl .

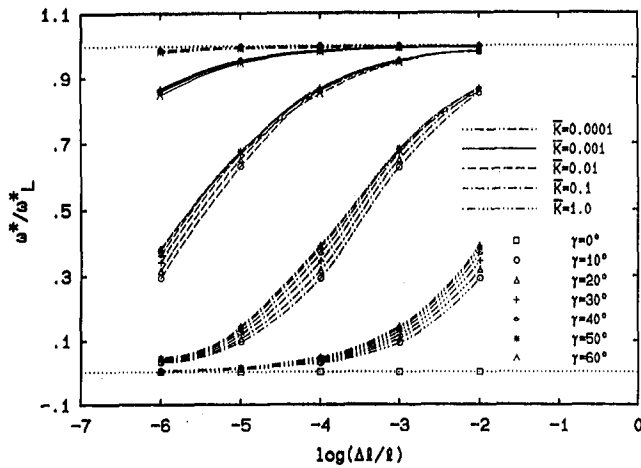


Fig. 4 Ratio of the "nonlinear" to the "linear" predicted kink angle versus $\Delta l/l$ for various values of the mode-mixity parameter γ and amplitude K characterizing the crack-tip loading conditions before the extension

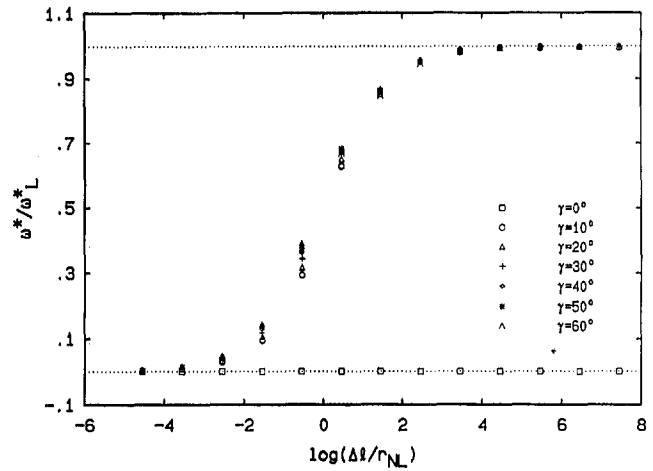


Fig. 6 Variation of ω^* (normalized by the linear value ω_L^*) with respect to the crack extension length Δl (normalized by the size of the nonlinear zone r_{NL})

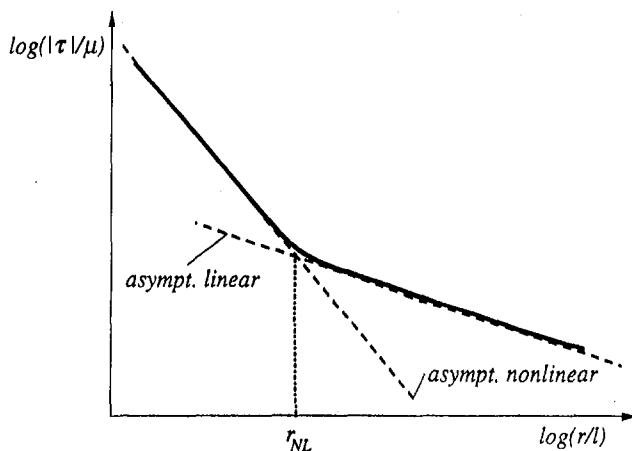


Fig. 5 Radial variation of the norm of the true (Cauchy) stress tensor and determination of the size of the zone of dominance of the nonlinear effects by comparison with the linear and nonlinear asymptotic predictions

One can better visualize the transition process by comparing the length of the extension Δl with a "measure" of the size of nonlinear zone. The length scale characterizing the zone of dominance of the nonlinear effects that is adopted here is derived from the results of an asymptotic analysis of the near-tip stress and deformation fields for a crack in a homogeneous sheet of GNH material under general (mixed-mode) loading conditions (Geubelle and Knauss, 1994a). It was shown there that, in the large deformation region, the stress singularity is stronger than that predicted by the linearized theory (the norm of the Cauchy stress tensor varies as the inverse of the distance to the crack-tip instead of the inverse square root singularity suggested by the linearized theory), and that, under "small-scale nonlinear yielding" conditions such as those considered in the present boundary-layer type analysis, a fairly sharp transition is observed between the two asymptotic behaviors, as symbolically represented in Fig. 5. The size r_{NL} of the nonlinear zone has been shown (Geubelle and Knauss, 1994a) to be

$$\frac{r_{NL}}{l} = \frac{1}{3\pi n^2} \frac{I}{\mu l}, \quad (3.1)$$

where I is the value of the conservation integral. It is interesting to note that if the individual curves in Fig. 4 are

shifted by normalizing the crack extension length Δl with respect to the nonlinear zone size r_{NL} , one obtains the single set of transition curves presented in Fig. 6. It seems therefore that the load-dependent measure (3.1) of the nonlinear zone size, which is, in the present analysis, the only length scale characterizing the large deformation effects on the near-tip fields, unifies all the transition curves surprisingly well despite its relative simplicity.

Although the transition curves are slightly different for each value of the local mixity parameter γ , the six "mixed-mode" curves ($\gamma \neq 0$ deg) show a fairly sharp transition between the two limiting values ($\omega^* = 0$ deg and $\omega^* = \omega_L^*$). This somewhat surprising result can be explained by the structure of the large deformation strain and stress fields existing near the crack-tip under nonsymmetric loading conditions. It has been shown, through the asymptotic analysis summarized by Geubelle and Knauss (1994a), that, within the nonlinear theory of plane stress and for the GNH class of hyperelastic materials, the near-tip fields corresponding to mixed-mode cases consist of mere rotations of the symmetric (mode I) approximations, the rotation depending on the "linear mixity parameter" γ through a one-to-one relation which is itself a function of the "hardening" exponent n . It is therefore natural that, when the length of the crack extension is chosen well within the zone of dominance of the nonlinear effects, the predicted kink angle ω^* , which is "measured" in terms of the undeformed coordinates, tends to zero for all mixity ratios.

Within the framework of the linearized theory, the size of the nonlinear zone may thus become a "geometrical lower bound" to the concept of virtual crack extension inherent in the maximum energy release rate criterion: the limit $\Delta l \rightarrow 0$ appearing in the definitions (2.3) and (2.4) of G exists even if the nonlinear effects are taken into account but the value of the predicted path angle corresponding to such a limiting process seems at variance with experimental observations (see, e.g., Palaniswamy and Knauss, 1978). But most test results available to date have been obtained in situations in which finite strain effects are not dominant. Recent experiments on natural rubber (Hodowany and Montilla, 1993) have shown that when large deformations are allowed to develop prior to crack propagation, the results summarized in the present analysis are corroborated.

The case $n = 0.7$ has also been investigated for $\gamma = 40$

⁵See Fig. 19 in (Geubelle and Knauss, 1994a).

deg, showing a very similar transition curve (Fig. 6). Although the analysis has been performed within the framework of the nonlinearity elastic theory of plane stress for the particular class of GNH materials, we believe that such a behavior should also occur for other classes of materials, as well as under plane strain conditions where the rotation property of the near-tip fields has been shown to be valid, too (Le, 1992).

4 Interface Crack Problem

We turn next to the large deformation investigation of the interface crack propagation problem. Let $(\mu^{(1)}, b^{(1)}, n^{(1)})$ and $(\mu^{(2)}, b^{(2)}, n^{(2)})$ be the material parameters characterizing the upper and lower Generalized Neo-Hookean sheets, respectively. Detailed asymptotic analyses of various bimaterial problems (Geubelle and Knauss, 1994b, 1994c) have shown that, as was the case in the homogeneous situation, the deformation fields existing near the tip of an interface crack between two sheets of GNH materials consist in the rotation of a "canonical bimaterial field," the rotation being a function of the far-field conditions and the geometrical and mechanical characteristics of the bimaterial specimen. For example, in the particular case where both components have similar "hardening" behaviors (i.e., $n^{(1)} = n^{(2)} = n$), the near-tip field is given by (Geubelle and Knauss, 1994b)

$$\mathbf{y} = \mathbf{Q}\mathbf{y}^*, \quad (4.1)$$

where \mathbf{y} is the deformed coordinate vector field, \mathbf{Q} is an orthonormal tensor and \mathbf{y}^* is the "canonical" deformation field

$$\begin{cases} y_1^* \sim cr^p g(\theta; n), \\ y_2^* \sim ar^m j(\theta) f(\theta; n) + kr^t l(\theta, n) + dr^q j(\theta) h(\theta; n), \end{cases} \quad (4.2)$$

in which the asymptotic exponents m , p , t , and θ are a function of n and have been given in Fig. 2 of (Geubelle and Knauss, 1994b); the angular functions $f(\theta; n)$, $g(\theta; n)$, $h(\theta, n)$, and $l(\theta; n)$ are continuous on $[-\pi, \pi]$; a , c , d , and k are scalars and $j(\theta)$ is the step function characterizing the concentration of the deformations in the weaker component as

$$j(\theta) = \begin{cases} 1 & (0 \leq \theta \leq \pi), \\ \xi = \left[\frac{\mu^{(1)}}{\mu^{(2)}} \left(\frac{b^{(1)}}{b^{(2)}} \right)^{n-1} \right]^{1/(2n-1)} & (-\pi \leq \theta \leq 0). \end{cases} \quad (4.3)$$

It is therefore expected that, due to the structure (4.1)–(4.3) of the near-tip fields, the nonlinear analysis of the maximum energy release rate criterion yields results similar to the homogeneous situation: when the crack extension length Δl is chosen within the zone where the near-tip approximation is valid, one obtains an energetically most favorable kink angle which does not depend on Δl but also not on the far-field loading conditions. In the "boundary layer" analysis adopted here, the latter are characterized by the complex stress intensity factor $K = K_1 + iK_2$ associated with the linearized bimaterial asymptotic solution.⁶

The numerical investigation described in Section 3 for the homogeneous case has been repeated for exemplary purposes in the bimaterial situation with $\mu^{(1)}/\mu^{(2)} = 2$, $b^{(1)}/b^{(2)}$

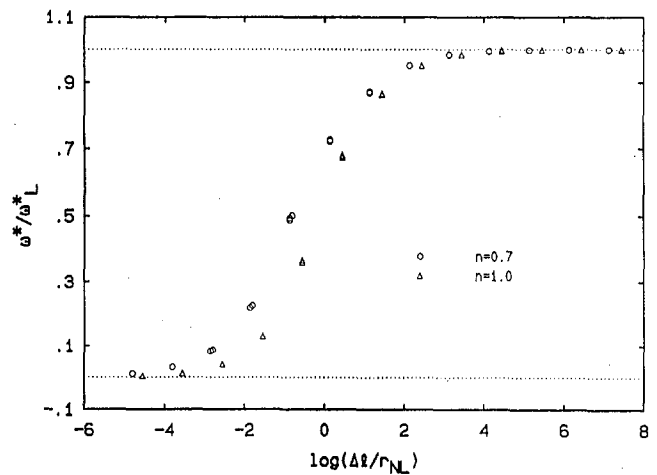


Fig. 7 Kink angle ω^* versus $\Delta l/r_{NL}$ for $\gamma = 40$ deg and for two values of the "hardening" exponent $n = 0.7$ and 1.0

$= 1$ and $n^{(1)} = n^{(2)} = n = 0.8$. The corresponding values of the "linear" moduli mismatch parameters⁷ are $\alpha = 0.333$, $\beta = 0.083$, and $\epsilon = -0.027$. The nonlinear mismatch parameter ξ introduced in (4.3) is equal to 3.175. Ten loading conditions have been considered ($\bar{K} = |K|/\mu^{(2)}\sqrt{l} = 10^{-4}$, 10^{-3} , 10^{-2} , 10^{-1} and 1, and $\gamma = 0$ deg and -30 deg) with, for each case, the same values of $\Delta l/l$ as in Section 3. The results are summarized in Figs. 8(a) (for $\gamma = -30$ deg) and 8(b) (for $\gamma = 0$ deg), showing, as was the case in the monolithic situation, a transition between the linear values of ω^* (obtained for small \bar{K}) and the unique nonlinear value⁸ which is found to be $\omega^* \approx -30$ deg. Note that since the value predicted by the linear theory depends on Δl , a transition curve similar to that presented in Figs. 6 and 7 does not exist. Although the "unique kink angle" associated with the large deformation zone depends on the material combination, the trend observed in the present problem is applicable to other bimaterial situations because of the aforementioned "rotation property" of the near-tip fields.

The nonlinear analysis of the crack extension problem thus seems to restrict the limiting process ($\Delta l \rightarrow 0$) which, in the linearized analysis, did not provide a unique value of the energetically most favorable kink angle. But the independence of the (large deformation) kink angle on the far-field loading conditions seems to indicate also that conditions prevailing outside of the nonlinear zone might provide an indication for the additional length scale necessary to obtain an agreement between analytical and experimental results, for situations where the large deformation effects are not negligible. The values deduced from the experimental observations described in Section 4 of (Geubelle and Knauss, 1993) do not contradict this possibility.

Acknowledgments

This work has been sponsored by AFOSR (contract F044611-88-K-0024) under the technical monitoring of Dr. C. T. Liu. Additional support has been provided by ONR (grant N00014-91-J-1427) under the patronage of Dr. Peter Schmidt.

⁶The definition of the bimaterial stress intensity factor used here is similar to that described in Section 1 of (Geubelle and Knauss, 1993): the length scale that needs to be introduced in order to determine the phase angle γ has been chosen as the radius l of the circular domain represented in Fig. 1.

⁷See Section 1 of (Geubelle and Knauss, 1993).

⁸Note that, in the case $\Delta l/l = 10^{-2}$, the size of the nonlinear zone corresponding to the largest value of \bar{K} is of the order of the length of the crack extension. This explains why the transition between the "linear" and the "nonlinear" values of ω^* is not completely shown in Figs. 8(a) and 8(b).

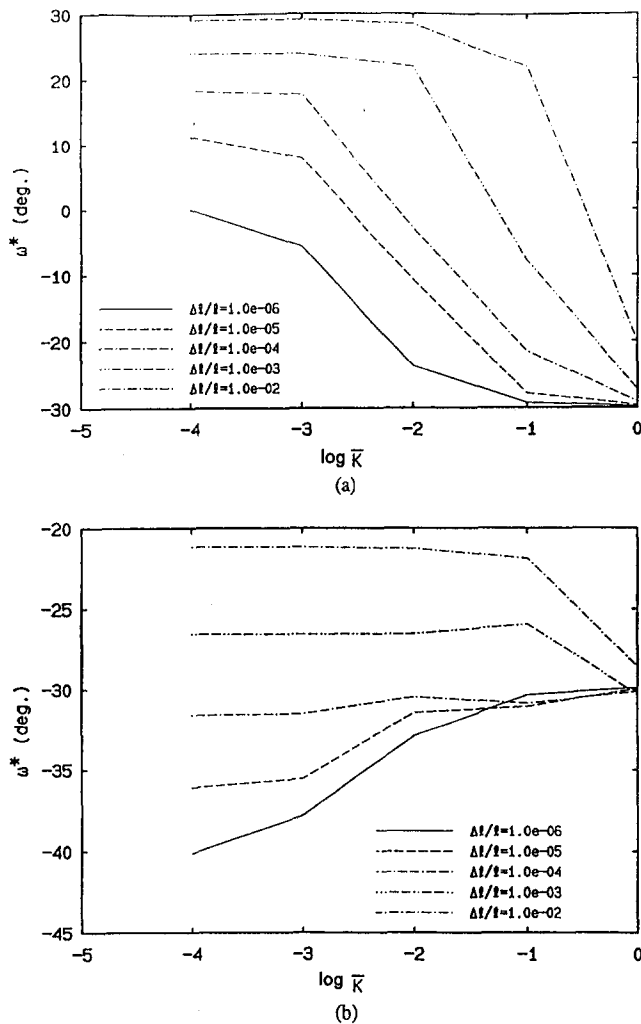


Fig. 8 Variation of ω^* with respect to the amplitude \bar{K} of the applied far-field loading for various values of the crack extension length $\Delta l/l$ showing a transition between the "linear" value (obtained for $\bar{K} \leq 10^{-4}$) and the unique "nonlinear" value which is independent of γ : (a) $\gamma = -30$ deg, (b) $\gamma = 0$ deg.

The access to the Cray YMP of the San Diego Super-computing Center was made possible through a grant by the National Science Foundation.

References

- Erdogan, F., and Sih, G. C., 1963, "On the Crack Extension in Plates under Plane Loading and Transverse Shear," *J. Basic Engng.*, Vol. 85, pp. 519-527.
- Geubelle, P. H., and Knauss, W. G., 1993, "Crack Propagation at and Near Bimaterial Interfaces: Linear Analysis," Galcit SM Report 91-16, Caltech, ASME JOURNAL OF APPLIED MECHANICS, Vol. 61, pp. 560-566.
- Geubelle, P. H., and Knauss, W. G., 1994a, "Finite Strains at the Tip of a Crack in a Sheet of Hyperelastic Material: I. Homogeneous Case," Galcit SM Report 92-42, Caltech, *J. Elasticity*, Vol. 35, pp. 61-98.
- Geubelle, P. H., and Knauss, W. G., 1994b, "Finite Strains at the Tip of a Crack in a Sheet of Hyperelastic Material: II. Special Bimaterial Cases," Galcit SM Report 92-43, Caltech, *J. Elasticity*, Vol. 35, pp. 99-137.
- Geubelle, P. H., and Knauss, W. G., 1994c, "Finite Strains at the Tip of a Crack in a Sheet of Hyperelastic Material: III. General Bimaterial Case," Galcit SM Report 92-44, Caltech, *J. Elasticity*, Vol. 35, pp. 139-174.
- Hayashi, K., and Nemat-Nasser, S., 1981a, "Energy Release Rate and Crack Kinking Under Combined Loading," ASME JOURNAL OF APPLIED MECHANICS, Vol. 48, pp. 520-524.
- Hayashi, K., and Nemat-Nasser, S., 1981b, "On Branched Interface Cracks," ASME JOURNAL OF APPLIED MECHANICS, Vol. 48, pp. 529-533.
- He, M.-Y., and Hutchinson, J. W., 1989, "Kinking of a Crack out of an Interface," ASME JOURNAL OF APPLIED MECHANICS, Vol. 56, pp. 270-278.
- Hodowany, J., and Montilla, K., 1993, "Crack Propagation in a Non-linear Elastic Thin Sheet," Ae104c Project Report, Graduate Aeronautical Laboratories, California Institute of Technology, Pasadena, CA.
- Karihaloo, B. L., 1982, "On Crack Kinking and Curving," *Mech. of Materials*, Vol. 1, pp. 189-201.
- Knowles, J. K., and Sternberg, E., 1983, "Large Deformations Near the Tip of an Interface Crack between Two Neo-Hookean Sheets," *J. Elasticity*, Vol. 13, pp. 257-293.
- Le, K. C., 1992, "On the Singular Elastostatic Field Induced by a Crack in a Hadamard Material," *Q. J. Mech. Appl. Math.*, Vol. 45, No. 1, pp. 101-117.
- Lo, K. K., 1978, "Analysis of Branched Cracks," ASME JOURNAL OF APPLIED MECHANICS, Vol. 45, pp. 797-802.
- Maiti, S. K., 1990, "Finite Element Computation of the Strain Energy Release Rate for Kinking of a Crack," *Int. J. Fract. Mech.*, Vol. 43, pp. 161-170.
- Mukai, D. J., Ballarini, R., and Miller, G. R., 1990, "Analysis of Branched Interface Cracks," ASME JOURNAL OF APPLIED MECHANICS, Vol. 57, pp. 887-893.
- Palaniswamy, K., and Knauss, W. G., 1978, "On the Problem of Crack Extension in Brittle Solids under General Loading," *Mechanics Today*, S. Nemat-Nasser, ed., Pergamon Press, pp. 87-148.
- Shih, C. F., 1991, "Cracks on Bimaterial Interfaces: Elasticity and Plasticity Aspects," *Mat. Sc. Engng. A*, Vol. 143, pp. 77-90.
- Taylor, R. L., 1977, "Computer Procedures for Finite Element Analysis," *The Finite Element Method*, 3rd ed., O. C. Zienkiewicz, ed., McGraw-Hill, Chapter 24.
- Wang, T. C., Shih, C. F., and Suo, Z., 1992, "Crack Extension and Kinking in Laminates and Bicrystals," *Int. J. Solids Struct.*, Vol. 39, No. 3, pp. 327-344.
- Wu, C. H., 1978, "Maximum Energy Release Rate Criterion Applied to a Tension-Compression Specimen with Crack," *J. Elast.*, Vol. 8, pp. 235-257.

Strip Element Method to Analyze Wave Scattering by Cracks in Anisotropic Laminated Plates

G. R. Liu¹

J. D. Achenbach
Fellow ASME.

Center for Quality Engineering
and Failure Prevention,
Northwestern University,
Evanston, IL 60208-3020

The strip element method (SEM) has been extended to investigate wave scattering by cracks in anisotropic laminated plates. The cracked plates are divided into domains in which the extended SEM is applied. For each domain a set of SEM equations is obtained which gives a relationship between the traction and displacement vectors on the vertical boundaries. These equations are solved by using the conditions at the junctures of the domains. To obtain the time domain response a Fourier transform technique is used, and an exponential window method is introduced to avoid singularities in the Fourier integration. For composite plates with horizontal and vertical cracks, scattered wave fields in both the time and frequency domains are computed, and discussed in comparison with results for uncracked plates. A technique for determining the length of a crack in a plate is also presented. It is shown that the SEM is an efficient technique for the calculation of elastodynamic fields in cracked anisotropic laminated plates.

1 Introduction

Ultrasonic waves can be used to characterize mechanical properties and to detect cracks and delaminations in laminates. To use the ultrasonic method, it is necessary to clearly understand wave propagation in anisotropic laminated plates with and without cracks.

An exact solution for waves in anisotropic laminated plates has been given by Liu et al. (1990). These authors discussed effects of fiber orientation and stacking sequence of layers on the phase velocities and strain energy distributions in the thickness direction of laminated plates. Finite element methods have been used by Dong et al. (1972, 1985), Nelson et al. (1973), Kausel (1986), and Datta et al. (1988) to investigate the dispersion of waves in laminated media. Liu et al. (1991a) presented an assembly of six characteristic wave surfaces to explain the anisotropic and dispersion properties of Lamb waves in anisotropic laminated plates. The characteristic wave surfaces were obtained by using the finite element method (FEM).

A matrix formulation for anisotropic laminates under spatially periodic time-harmonic surface loads was presented by Mal (1988). Liu et al. (1991b) proposed a hybrid numerical method which combines the FEM and FFT techniques to obtain the transient response of anisotropic laminated plates. However, this method cannot be used for calculating the response in the frequency domain due to the presence of singularities in the integral for the inverse Fourier transform. To deal with these kinds of integrations Xu and Mal (1985, 1987) have presented a technique in which the kernel is represented by a series of Chebyshev polynomials to calculate two-dimensional Green's functions for a layered isotropic viscoelastic solid. Kundu and Mal (1985) modified the work of Xu and Mal (1987) by removing poles from the real wave number axis. Waas (1972) and

Kausel (1981) proposed a semi-numerical method (SNM) for the solution of two-dimensional Green's functions for a layered isotropic stratum. In this method, the stratum is divided into elements, the displacement field is linearized in the elements, and the expression for the Green's function in the wave number domain becomes a simple function containing poles only. The Green's functions can subsequently be obtained by using Cauchy's theorem. The advantage of the SNM is that numerical integration of a Fourier integral has been avoided. Its disadvantage is that the higher the frequency the more elements are needed to obtain good results. Hence the SNM is not efficient at high frequencies. The SNM was extended to transversely isotropic layers by Seale et al. (1989). For cases in which the locations of poles are difficult to obtain for a given frequency, such as for wave propagation in piezoelectric plates where the elastic and electric fields are coupled, Liu et al. (1994) have presented an alternative method for calculating responses in the frequency domain by introducing a complex integral path to avoid singularities and rapid changes of the integrals in the inverse Fourier integration. Recently, Liu and Achenbach (1994) presented a strip element method (SEM) for stress analysis of anisotropic linearly elastic solids. The SEM can easily be used to calculate responses of anisotropic media in the frequency domain. A major advantage of the SEM is that it requires much smaller storage than the FEM. However, in the original version of the SEM the external loads are acting only on boundaries perpendicular to the elongated direction of the strip elements.

Recently, scattering of waves in an elastic layer has been investigated by Al-Nassar et al. (1991) and Karunasena et al. (1991), who used a combined finite element and Lamb wave modal expansion method. Dispersion equations for Lamb waves were obtained by an exact method. The Lamb modes were analyzed by using Müller's method, a numerically complex roots search procedure which calculates the wave number for a given frequency. Karim et al. (1992) presented a similar technique which combines the finite element method and guided wave mode expansions to calculate scattering of Lamb waves by cracks or inclusions. In this method the finite element boundary has to be far enough from the loads and inclusions, because only Lamb waves with real wave numbers have been used in the exterior regions. The use of these Lamb waves is equivalent to an absorbing boundary attached to the finite element regions.

¹ Current address: Department of Mechanical and Production Engineering, National University of Singapore, Ten Kent Ridge Crescent, S 0511, Singapore.

Contributed by the Applied Mechanics Division of THE AMERICAN SOCIETY OF MECHANICAL ENGINEERS for publication in the ASME JOURNAL OF APPLIED MECHANICS.

Discussion on this paper should be addressed to the Technical Editor, Prof. Lewis T. Wheeler, Department of Mechanical Engineering, University of Houston, Houston, TX 77204-4792, and will be accepted until four months after final publication of the paper itself in the ASME JOURNAL OF APPLIED MECHANICS.

Manuscript received by the ASME Applied Mechanics Division, May 24, 1993; final revision, Mar. 7, 1994. Associate Technical Editor: S. K. Datta.

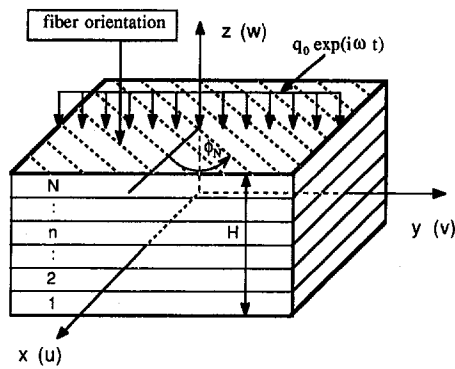


Fig. 1 An anisotropic laminated plate and its coordinate system

The boundary element method (BEM) has been used to investigate scattered waves in a half-space and in finite depth strata (Von Estorff et al. 1990), where the SNM was used to calculate Green's functions. Another efficient way to investigate scattering of Lamb waves, presented by S. W. Liu et al. (1991) and Datta et al. (1992), combines the BEM and FEM, where the FEM is used in the interior region and the BEM is used for the exterior region. Green's functions for the BEM were obtained by using an integration technique given by Xu and Mal (1987).

In this paper, the SEM is extended to investigate scattering of waves by cracks in anisotropic laminated plates. First the SNM is extended to obtain the solution in the frequency domain for uncracked anisotropic laminated plates subjected to an external loading. Then, a general SEM solution for a loaded laminated plate with boundaries perpendicular to the plane of the plate (vertical boundaries) is given by combining the SNM solution (a particular solution of the governing differential equations) and the fundamental SEM solution (the complementary solution of the associated homogeneous form of the governing differential equations). A set of general SEM equations which gives the relationship between the traction and displacement vectors at node points on the vertical boundaries is obtained from the general SEM solution. For a plate with a crack, the plate is divided into several domains. A general SEM equation is obtained for each domain. By assembling all the equations, a set of algebraic equations is obtained, which is solved by using the conditions on the vertical boundaries between the domains. To obtain the response of a plate in the time domain, a Fourier transformation technique is used and an exponential window method (EWM) is introduced to avoid singularities of the integrand in the Fourier integration. For composite plates with horizontal and vertical cracks, scattered wave fields in the frequency and time domains have been computed. The results are discussed in comparison with results for uncracked plates. A technique for determining the length of a crack is also presented.

2 Approximate Governing Differential Equations

Consider a laminated plate with any number of anisotropic layers. The thickness of the plate is denoted by H , as shown in Fig. 1. The plate is divided into N strip elements. The thickness, the elastic coefficient matrix, the fiber orientation, and the density of the n th element are defined by h_n , c_n , ϕ_n , and ρ_n . Two-dimensional problems are considered in this paper. The excitation and the resulting wave fields are independent of y . Boundary conditions are separated into two categories. There are boundary conditions on horizontal planes (HBCs) for boundaries that are parallel to the plane of the plate, and on vertical planes (VBCs) for boundaries that are perpendicular to that plane.

In each element, the displacement vector $\mathbf{U}_e^T(x, z) = \{u(x, z) \ v(x, z) \ w(x, z)\}$ is assumed to be of the form.

$$\mathbf{U}_e(x, z) = \mathbf{N}(z)\mathbf{V}_e(x) \exp(i\omega t), \quad (1)$$

where $i = \sqrt{-1}$. The variables t and ω are time and angular frequency, respectively. The matrix \mathbf{N} and the vector \mathbf{V}_e are given by

$$\mathbf{N} = \left[\left(1 - 3\frac{z}{h} + 2\frac{z^2}{h^2} \right) \mathbf{I} \ 4\left(\frac{z}{h} - \frac{z^2}{h^2} \right) \mathbf{I} \ \left(-\frac{z}{h} + 2\frac{z^2}{h^2} \right) \mathbf{I} \right], \quad (2)$$

$$\mathbf{V}_e^T = \{ \mathbf{V}_L^T \ \mathbf{V}_M^T \ \mathbf{V}_U^T \}. \quad (3)$$

In Eq. (2), h is the thickness of the element, and \mathbf{I} is a 3 by 3 identity matrix. In Eq. (3), \mathbf{V}_L , \mathbf{V}_M , and \mathbf{V}_U , which denote the displacement amplitude vectors on the lower, middle, and upper node lines of the element, are functions of x . By applying the principle of virtual work to each element, a set of approximate differential equations can be obtained for each element. Assembling all the elements and using the HBCs, a system of approximate governing differential equations for the total plate can finally be obtained (details can be found in Liu and Achenbach, 1994):

$$\bar{\mathbf{q}} = \left[-\mathbf{A}_{2r} \frac{\partial^2 \mathbf{V}}{\partial x^2} + \mathbf{A}_{1r} \frac{\partial \mathbf{V}}{\partial x} + \mathbf{A}_{0r} \mathbf{V} - \omega^2 \mathbf{M}_r \mathbf{V} \right], \quad (4)$$

where the matrices \mathbf{A}_i ($i = 0, 1, 2$), \mathbf{M}_r and the vector \mathbf{V} can be obtained by assembling the corresponding matrices \mathbf{A}_i , \mathbf{M} and vector \mathbf{V}_e of adjacent elements just as is done in the FEM. The matrices \mathbf{A}_i and \mathbf{M} for an element can be found in the Appendix of Liu and Achenbach (1994) for monoclinic materials, and Liu et al. (1991b) for general anisotropic materials and two-dimensional and three-dimensional problems. The vector $\bar{\mathbf{q}}$ is related to the traction vector \mathbf{q} applied to the horizontal nodal lines of the plate by

$$\mathbf{q} = \bar{\mathbf{q}} \exp(i\omega t). \quad (5)$$

For a plate with vertical boundaries, the general solution of Eq. (4) consists of two parts, namely, a particular solution which satisfies Eq. (4), and the complementary solution which satisfies the associated homogeneous equation of Eq. (4). The complementary solution has been given by Liu and Achenbach (1994). A particular solution for a transversely isotropic half-space has been given by Seale and Kausel (1989). The latter is an extension of the solution for isotropic layered media given by Waas (1972) and Kausel (1981). In the sequel we give a compact formulation for a particular solution for general anisotropic laminated plates.

3 A Particular Solution for Infinite Anisotropic Laminated Plates

We introduce the Fourier transformation with respect to the horizontal coordinates x as follows:

$$\tilde{\mathbf{V}}_p(k) = \int_{-\infty}^{\infty} \mathbf{V}_p(x) e^{ikx} dx, \quad (6)$$

where k is the wave number, and the subscript p indicates the particular solution. Application of the Fourier transform to Eq. (4) leads to the following equation in the transform domain:

$$\tilde{\mathbf{q}} = [k^2 \mathbf{A}_{2r} - ik \mathbf{A}_{1r} + \mathbf{A}_{0r} - \omega^2 \mathbf{M}_r] \tilde{\mathbf{V}}_p. \quad (7)$$

This equation can be rewritten in the form

$$\mathbf{p} = [\mathbf{A} - k\mathbf{B}] \mathbf{d}, \quad (8)$$

where

$$\mathbf{A} = \begin{bmatrix} \mathbf{0} & \mathbf{I} \\ \omega^2 \mathbf{M}_r - \mathbf{A}_{0r} & i \mathbf{A}_{1r} \end{bmatrix}, \quad \mathbf{B} = \begin{bmatrix} \mathbf{I} & \mathbf{0} \\ \mathbf{0} & \mathbf{A}_{2r} \end{bmatrix}, \quad (9)$$

and

$$\mathbf{p}^T = \{\mathbf{0} \quad -\tilde{\mathbf{q}}^T\}, \quad \mathbf{d}^T = \{\tilde{\mathbf{V}}_p^T \quad k\tilde{\mathbf{V}}_p^T\}. \quad (10)$$

Applying the modal analysis technique (see, e.g., Liu et al., 1991b) to Eq. (8), we find

$$\mathbf{d} = \sum_{m=1}^{2M} \frac{\varphi_m^L \mathbf{P} \varphi_m^R}{(k - k_m) B_m}, \quad (11)$$

where $M = 3(2N + 1)$ is the number of rows of the square matrices \mathbf{A}_i (or \mathbf{M}_i) and

$$B_m = \varphi_m^L \mathbf{B} \varphi_m^R. \quad (12)$$

In Eqs. (11) and (12), k_m , φ_m^L and, φ_m^R are, respectively, the eigenvalues and the left and right eigenvectors obtained from the following eigenvalue equations:

$$\mathbf{0} = [\mathbf{A} - k_m \mathbf{B}] \varphi_m^R, \quad \mathbf{0} = \varphi_m^L [\mathbf{A} - k_m \mathbf{B}]. \quad (13)$$

The eigenvectors φ_m^L and φ_m^R can be written as

$$\varphi_m^L = \{\varphi_{m_1}^L, \varphi_{m_2}^L\}, \quad \varphi_m^R = \begin{Bmatrix} \varphi_{m_1}^R \\ \varphi_{m_2}^R \end{Bmatrix}, \quad (14)$$

where $\varphi_{m_1}^L$, $\varphi_{m_2}^L$, $\varphi_{m_1}^R$, and $\varphi_{m_2}^R$ have the same dimension. From Eqs. (10), (11), and (14) we obtain

$$\tilde{\mathbf{V}}_p = \sum_{m=1}^{2M} \frac{\varphi_m^L \tilde{\mathbf{q}} \varphi_m^R}{(k - k_m) B_m}. \quad (15)$$

If we specialize the spatial variation of the load to that of a line load acting at $x = x_0$, we may write

$$\tilde{\mathbf{q}} = \mathbf{q}_0 \delta(x - x_0) \quad (16)$$

where δ is the Dirac delta function and \mathbf{q}_0 is a constant vector representing the amplitude of the external force. In this case, the Fourier transform of the external force, $\tilde{\mathbf{q}}$, becomes $\mathbf{q}_0 e^{ikx_0}$. Hence, Eq. (15) reduces to

$$\tilde{\mathbf{V}}_p = \sum_{m=1}^{2M} \frac{\varphi_m^L \mathbf{q}_0 \varphi_m^R}{(k - k_m) B_m} e^{ikx_0}. \quad (17)$$

Applying the inverse Fourier transformation to Eq. (17), the displacement in the spatial domain can be expressed by

$$\mathbf{V}_p = \frac{1}{2\pi} \int_{-\infty}^{\infty} \sum_{m=1}^{2M} \frac{\varphi_m^L \mathbf{q}_0 \varphi_m^R}{(k - k_m) B_m} e^{-ik(x-x_0)} dk. \quad (18)$$

It is noted that in Eq. (18), φ_m^L , φ_m^R , \mathbf{q}_0 , and B_m are independent of k . Considering k complex, as shown in Fig. 2, the integral in Eq. (18) is an analytic function of k , except at $2M$ poles ($k = k_m$) in the complex k -plane. Hence, the integration in Eq. (18) can be carried out by using Cauchy's theorem.

$$\mathbf{V}_p = \begin{cases} -i \sum_{m=1}^M \frac{\varphi_m^{+L} \mathbf{q}_0 \varphi_m^{+R}}{B_m^+} e^{-ik_m^+(x-x_0)}, & \text{for } x \geq x_0 \\ i \sum_{m=1}^M \frac{\varphi_m^{-L} \mathbf{q}_0 \varphi_m^{-R}}{B_m^-} e^{-ik_m^-(x-x_0)}, & \text{for } x < x_0 \end{cases}, \quad (19)$$

where “+” denotes variables evaluated at the poles corresponding to waves propagating in the positive x direction (leftward) included by the lower semicircular loop (dashed line in Fig. 2), while “-” denotes variables evaluated at poles corresponding to waves propagating in the negative x direction (rightward) included by the upper semicircular loop (solid line in Fig. 2).

It may be noted that Eq. (19) gives a two-dimensional Green's function for the displacement for anisotropic laminated plates. The Green's function for stresses can be obtained by using Eq. (19). If the external force is distributed in the x direction, the solution can be obtained in the form of a superposition integral over \mathbf{V}_p .

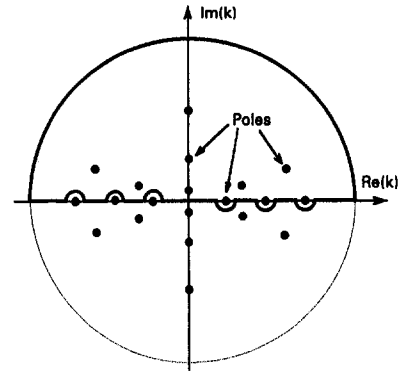


Fig. 2 Contours for evaluating Eq. (18)

4 The General Solution for an Anisotropic Laminated Plate

The complementary solution of the associated homogeneous equation of Eq. (4) can be expressed by superposition of the right eigenvectors obtained from the first equation in Eq. (13) (see Liu and Achenbach, 1994):

$$\mathbf{V}_c = \sum_{j=1}^{2M} C_j \varphi_j^R \exp(ik_j x) = \mathbf{G}(x) \mathbf{C}, \quad (20)$$

where the subscript c denotes the complementary solution. The constant vector \mathbf{C} can be determined by using VBCs. The general solution of Eq. (4) is

$$\mathbf{V}_g = \mathbf{V}_c + \mathbf{V}_p = \mathbf{G}(x) \mathbf{C} + \mathbf{V}_p, \quad (21)$$

where the subscript g denotes the general solution. Using VBCs of the plate, and following the process given by Liu and Achenbach (1994), a relationship between the tractions and the displacements on the vertical boundaries is obtained as

$$\mathbf{R}_b = \mathbf{K} \mathbf{V}_b + \mathbf{S}_p, \quad (22)$$

where

$$\mathbf{R}_b = \{\mathbf{R}_b^L \quad \mathbf{R}_b^R\}^T, \quad \mathbf{V}_b = \{\mathbf{V}_b^L \quad \mathbf{V}_b^R\}^T, \quad (23)$$

are the external traction and displacement vectors on the vertical boundaries. The matrix \mathbf{K} in Eq. (22) is the stiffness matrix given by

$$\mathbf{K} = \begin{bmatrix} \mathbf{R}_{1l} & \mathbf{0} \\ \mathbf{0} & \mathbf{R}_{1r} \end{bmatrix} + \begin{bmatrix} \mathbf{R}_{2l} \mathbf{G}_L' \mathbf{G}_d^{-1} \\ \mathbf{R}_{2r} \mathbf{G}_R' \mathbf{G}_d^{-1} \end{bmatrix}, \quad (24)$$

and the vector \mathbf{S}_p is the equivalent external force acting on the vertical boundaries:

$$\mathbf{S}_p = \begin{bmatrix} \mathbf{R}_{1l} & \mathbf{0} \\ \mathbf{0} & \mathbf{R}_{1r} \end{bmatrix} \begin{Bmatrix} \mathbf{V}_p^{L'} \\ \mathbf{V}_p^{R'} \end{Bmatrix} - \begin{bmatrix} \mathbf{R}_{2l} \mathbf{G}_L' \mathbf{G}_d^{-1} \\ \mathbf{R}_{2r} \mathbf{G}_R' \mathbf{G}_d^{-1} \end{bmatrix} \begin{Bmatrix} \mathbf{V}_p^L \\ \mathbf{V}_p^R \end{Bmatrix}. \quad (25)$$

In Eqs. (24) and (25) the prime indicates differentiation with respect to x , and the matrix \mathbf{G}_d is given by

$$\mathbf{G}_d = \begin{bmatrix} \mathbf{G}_L \\ \mathbf{G}_R \end{bmatrix}. \quad (26)$$

The matrices \mathbf{R}_{1l} and \mathbf{R}_{2l} are obtained by combining \mathbf{R}_l and \mathbf{R}_2 for all elements. The matrices \mathbf{R}_1 and \mathbf{R}_2 for an element can be found in the Appendix of Liu and Achenbach (1994) for monoclinic materials, and in the Appendix of this paper for general anisotropic materials. The superscripts or subscripts L and R in Eqs. (23)–(26) indicate that the matrix or vector has been evaluated on the left and right vertical boundaries. For cases that the plate has only one boundary on the left or right,

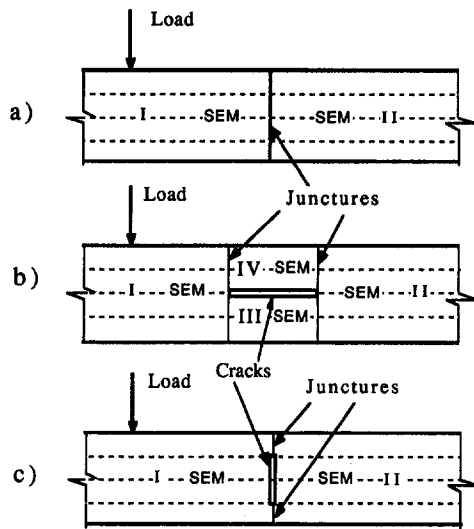


Fig. 3 Division of plates into domains in which the SEM can be applied. (a) an uncracked plate is divided into left and right domains; (b) a plate with a horizontal crack is divided into four domains; (c) a plate with a vertical crack is divided into two domains.

the condition at infinity on the x -axis has to be used, and the size of the system given by Eq. (22) will be reduced by half (see Liu and Achenbach, 1994).

5 Application of the SEM to an Anisotropic Laminated Plate

To apply the SEM to a plate which contains cracks, the plate has to be divided into domains in which the SEM is applicable. To illustrate the procedure we consider first an infinite uncracked plate, which is divided into left and right domains. The SEM is applied to the two domains. For each domain, Eq. (22), which gives a relationship between the tractions and displacements on the juncture, can be obtained. By assembling the equations for the two domains, a relationship between the displacement and the traction acting on the juncture can be obtained. The boundary conditions on the juncture subsequently yield the displacement. The constant vector \mathbf{C} in Eq. (21) follows as

$$\mathbf{C} = \mathbf{G}_d^{-1}(\mathbf{V}_g - \mathbf{V}_p), \quad (27)$$

and the complete displacement field can be obtained by using Eqs. (21) and (27). It is noted that for an uncracked plate, it is not necessary to use the SEM. However, this is a good test of the SEM program, because the results obtained by the SEM can be compared with the particular solution given in Section 3. For an infinite plate with a horizontal or a vertical crack, the regions of applicability of the SEM are shown in Fig. 3(b) and Fig. 3(c).

6 Solution in the Time Domain

To obtain the solution in the time domain, Fourier superposition will be applied:

$$u_i(t) = \frac{1}{2\pi} \int_{-\infty}^{\infty} u(\omega) F(\omega) e^{i\omega t} d\omega, \quad (28)$$

where $u(\omega)$ is a solution in the frequency domain obtained in Sections 3 and 5, while $F(\omega)$ is the Fourier transform of the time dependence of the external force, $f(t)$, acting on the plate. The subscript i in Eq. (28) indicates that the variable is in the time domain. The integration of Eq. (28) usually has to be carried out numerically. For an infinite plate difficulties with the integration result from singularities of $u(\omega)$ at $\omega = 0$ and

at the cut-off frequencies ($k = 0$), as discussed by Vasudevan and Mal (1985). To overcome these difficulties, an exponential window method (EWM) is employed here. The EWM has been used by Vasudevan and Mal (1985) to calculate the transient response of an elastic plate and by Kausel et al. (1992) to obtain the transient response for damped and undamped vibrating structures. By using the EWM, the integration path in Eq. (28) can be shifted downward in the complex ω -plane by an arbitrary amount η without changing the results. Hence, Eq. (28) can equivalently be written as

$$u_i(t) = \frac{e^{\eta t}}{2\pi} \int_{-\infty}^{\infty} u(\omega - i\eta) F(\omega - i\eta) e^{i\omega t} d\omega, \quad (29)$$

where

$$F(\omega - i\eta) = \int_0^{t_d} e^{-\eta t} f(t) e^{-i\omega t} dt, \quad (30)$$

in which t_d is the duration of the external force. By using Eq. (29) instead of Eq. (28), the singularity of $u(\omega)$ at $\omega = 0$ is avoided, since $u(\omega - i\eta)$ is well behaved for $-\infty < \omega < \infty$. The displacement in the time domain can, therefore, be obtained.

7 Numerical Examples

An SNM and an SEM program written in FORTRAN 77 have been run on an HP workstation. The SNM program is used for uncracked plates, and the SEM program is used for plates with cracks. Computations have been carried out for three plates denoted by [C90/G0]_s, [C0/G90]_s, and [C90/G45/G-45]_s. In this notation, the letters C and G stand, respectively, for carbon/epoxy and glass/epoxy layers, while the numbers following the letters indicate the angle ϕ of the fiber orientation with respect to the x -axis (see, Fig. 1). The subscript s indicates that the plate is symmetrically stacked. Material constants of carbon/epoxy and glass/epoxy can be found in Liu et al. (1991b). To use dimensionless variables, c_{44} has been chosen as a reference elastic constant and $c_s = \sqrt{c_{44}}/\rho$ as the reference velocity, where ρ is the density of the material. For hybrid composite plates, c_{44} for $\phi = 0$ and ρ of the carbon/epoxy material have been chosen as the reference constants.

7.1 Response in the Frequency Domain. To check the programs, displacement responses of an isotropic plate with a Poisson's ratio of 1/3 subjected to a time-harmonic line load have been computed by the SNM and SEM programs. The results are shown in Fig. 4. Sixteen elements were used in both programs. The juncture (see Fig. 3(a) for the SEM) is at $x = 4H$. Excellent agreement is observed. The convergence of the results has also been checked. For both programs there is no significant difference between the results obtained by using 8

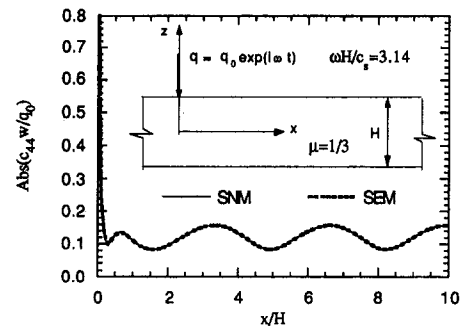


Fig. 4 Displacements on the upper surface of an isotropic plate subjected to a time-harmonic line load. Comparison of the results according to the semi-numerical method (SNM) and the strip element method (SEM).

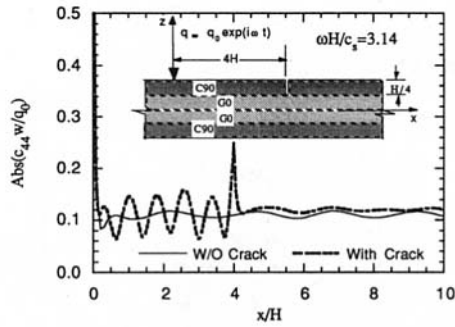


Fig. 5 Displacements on the upper surface of a laminated plate subjected to a time-harmonic line load. Comparison of the results obtained by the SEM for an uncracked plate and for a plate with a vertical surface-breaking crack.

elements and 16 elements. This example has also been solved by using the original SEM (Liu and Achenbach, 1994), in which the plate is divided into elements in the vertical direction and a viscoelastic nonreflecting boundary is used at the end of the regular elements. Without showing a figure, we state that very good agreement was observed.

Displacement responses of a cracked isotropic plate have also been calculated. For a plate with a horizontal crack over $4H \leq x \leq 5H$ in the midplane of the plate, additional peaks in the spectrum are observed as compared with the uncracked plate. These peaks have been observed and discussed by Datta et al. (1992) and Karim et al. (1992). We consider the absolute value of the displacement on the plate surfaces. Oscillations appear between the load and the crack, because reflections of waves from the crack interact with the incident field.

For plate [C90/G0]_s, the effect of a vertical surface-breaking crack in the upper C90 layer has been calculated. For a time-harmonic load which acts at a distance of $4H$ from the crack, the displacement w on the upper surface of plate [C90/G0]_s is shown in Fig. 5, together with the results for the uncracked plate. The displacement is discontinuous at $x = 4H$, even though this is not visible in the figure. The presence of the crack only slightly affects the solution in the far field. As expected, an oscillation of the absolute value of the displacement between the load point and the crack is observed. From Fig. 5, the position of the crack is obvious. It is also found that the amplitude of the additional oscillation is related to the depth of the crack.

For plate [C0/G90]_s, the effect of an interior vertical crack assumed in the G90 layers has been investigated. Figure 6 shows the displacement responses for plate [C0/G90]_s without and with a crack. A oscillation of the absolute value of the displacement between the load point and the crack is observed. The effects of the crack are smaller than for a surface breaking crack

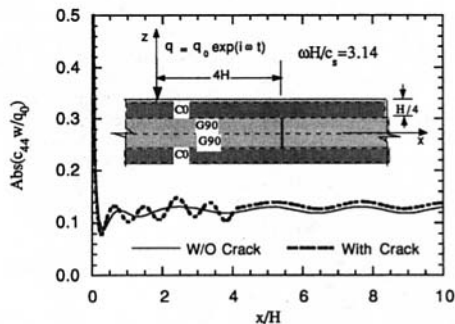


Fig. 6 Displacements on the upper surface of a laminated plate subjected to a time-harmonic line load. Comparison of the results obtained by the SEM for an uncracked plate and for a plate with a vertical interior crack.

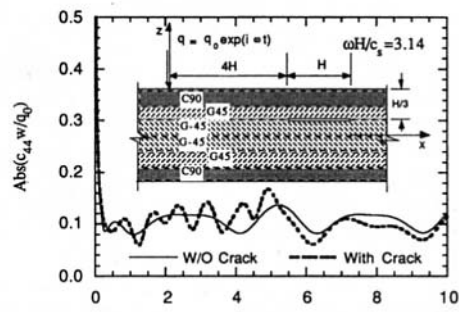


Fig. 7 Displacements on the upper surface of a laminated plate subjected to a time-harmonic line load. Comparison of the results obtained by the SEM for an uncracked plate and for a plate with a horizontal crack.

in plate [C90/G0]_s. For the subsurface crack the displacement is continuous, but the position of crack is still distinguishable.

For plate [C90/G45/-45]_s, the effect of a delamination between the G45 and G-45 layers has been studied. Figure 7 shows the scattered displacement field in comparison with the uncracked plate. Again a superimposed oscillation is observed between the load and the crack. It is noted that the superimposed oscillation ends at the right crack tip. A crack tip functions as a wave source which emits waves in all directions. Hence, at any observation point left of the right crack tip, there are waves moving to the right generated by the load and waves moving to the right generated by the right crack tip. The interference of these waves generates phase changes of the displacement responses, which appear as the additional oscillations in the absolute values of the displacement. On the other hand, at any observation point right of the right crack tip, there are only waves moving to the right, because all sources in the plate (the load, the left and right crack tips) are located to the left of the observation points. In principle, this difference in the nature of the displacement responses makes it possible to distinguish a horizontal crack from a vertical crack and to determine the length of the crack, by following two steps. First, by obtaining Fig. 7, we can determine the approximate position of the right crack tip. Then, applying the load on the other side of the crack, we can also determine the position of the left crack tip. The depth of the horizontal crack is related to the peaks of the response spectrum, as has been discussed by Datta et al., (1992).

7.2 Response in the Time Domain. A Gaussian modulated sinusoid is used as the time history of the applied load:

$$f(t) = \frac{2}{\sigma\sqrt{2\pi}} e^{-(t-t_0)^2/(2\sigma^2)} \sin(\omega_c t), \quad 0 \leq t < t_d, \quad (31)$$

where t is time, σ is a parameter which controls the duration of the pulse, t_0 determines the time delay of the pulse, and ω_c is the center angular frequency of the pulse. The time history of the applied load used in this paper is shown in Fig. 8. The Fourier transform of the applied load is

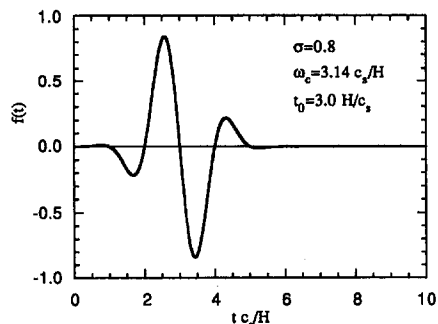


Fig. 8 Time history of the applied load

$$F(\omega) = \int_0^d f(t)e^{-i\omega t} dt. \quad (32)$$

A numerical evaluation of $F(\omega)$ shows that the absolute value of $F(\omega)$ has peak amplitudes at two values of ω and approaches zero rapidly as $|\omega|$ increases. Hence high frequency responses are not generated.

Responses of a plate excited by a pulsed line load given by Eq. (31) can be obtained from Eq. (29), which is obtained by introducing the exponential window method (EWM). To check the validity of the EWM, displacement responses of an isotropic plate with a Poisson's ratio of 1/3 have been computed by the SEM and a hybrid numerical methods (Liu et al., 1991b), and the results are shown in Fig. 9. Sixteen elements were used in both methods. Excellent agreement is observed.

It should be noted that the shifting constant η in Eqs. (29) and (30) has to be chosen appropriately (see Kausel et al., 1992). Various η were tested and it was found that a larger η will introduce severe numerical precision loss in the long time responses. A small η (say, $\eta = 0.1H/c_s$) is enough to avoid the singularity of $u(\omega)$ at $\omega = 0$ and the rapid changes at the cut-off frequencies.

Figure 10 shows the scattered displacement field on the surface of the plate [C90/G45/-45]_s with and without a horizontal crack. The observation point is at $x = 10H$. It is seen that significant differences are observed when $tc_s/H > 12$.

8 Comments on the SEM

The major advantage of the SEM is that much less computer memory is needed as compared to the FEM. The dimension of matrix \mathbf{K} in Eq. (24) depends only on the number of nodal points on the junctures. For a specific example the memory requirements of the FEM, BEM, and SEM have been compared by Liu and Achenbach (1994). The SEM is very efficient for calculating the response in the frequency domain. The computation time is mainly spent on solving Eq. (13) to obtain the eigenvalues and eigenvectors. It is noted that these eigenvalues and eigenvectors are independent of the crack length, and the position and distribution of the external loads. Hence in many cases, Eq. (13) only needs to be solved once. Liu and Achenbach (1994) have discussed in some detail various ways of maintaining accuracy and making the computation efficient.

In this study no singular crack-tip elements were used. However, to deal with the singularities of the fields at the crack tips, the thicknesses of elements near the tips have been taken very small (about one eighth of the thickness of the regular elements). It has been found that the results computed on the surface of the plates (sufficiently far from the crack tips) are not significantly affected by a further reduction of the size of the elements near the crack tips.

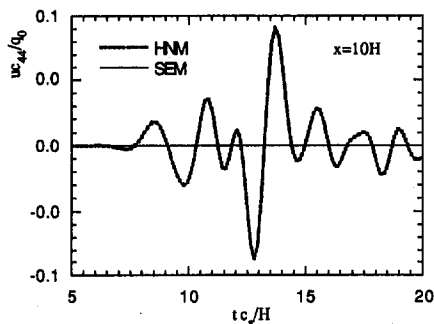


Fig. 9 Time-domain displacement response on the upper surface of an isotropic plate. Comparison of the hybrid numerical method (HNM) and the strip element method (SEM).

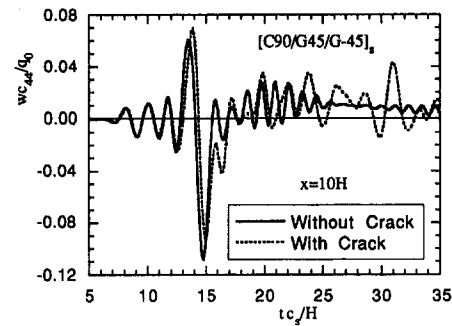


Fig. 10 Time-domain displacement response on the upper surface of a laminated plate. Comparison of the results obtained by the SEM for an uncracked plate and for a plate with a horizontal crack.

9 Conclusions

In this paper, the SEM has been extended to investigate the scattering of waves generated by a line load applied to an anisotropic laminated plate containing a crack. From the computed results, it is possible to detect the presence and determine the position of the crack, and to estimate its size, by examining the absolute value of the displacement responses. More quantitative characterizations of the crack will require more detailed investigations. It has been shown that the SEM is a powerful tool for such investigations.

Acknowledgment

The work represented in this paper was partially supported by the Science and Technology Agency of Japan and by the U.S. Office of Naval Research under Contract N00014-89-J-13621P10.

References

- Al-Nassar, Y. N., Datta, S. K., and Shah, A. H., 1991, "Scattering of Lamb Waves by a Normal Rectangular Strip Weldment," *Ultrasonics*, Vol. 29, pp. 125-132.
- Datta, S. K., Shah, A. H., Bratton, R. L., and Chakraborty, T., 1988, "Wave Propagation in Laminated Composite Plates," *Journal of the Acoustical Society of America*, Vol. 83, No. 6, pp. 2020-2026.
- Datta, S. K., Ju, T. H., and Shah, A. H., 1992, "Scattering of an Impact Wave by a Crack in a Composite Plate," *ASME JOURNAL OF APPLIED MECHANICS*, Vol. 59, pp. 596-603.
- Dong, S. B., and Huang, K. H., 1985, "Edge Vibrations in Laminated Composite Plates," *ASME JOURNAL OF APPLIED MECHANICS*, Vol. 52, pp. 433-438.
- Dong, S. B., and Nelson, R. B., 1972, "On Natural Vibrations and Waves in Laminated Orthotropic Plates," *ASME JOURNAL OF APPLIED MECHANICS*, Vol. 39, pp. 739-745.
- Karim, M. R., Awal, M. A., and Kundu, T., 1992, "Elastic Wave scattering by Cracks and Inclusions in Plates: In-Plane case," *International Journal of Solids and Structures*, Vol. 29, No. 19, pp. 2355-2367.
- Karunasena, W. M., Shah, A. H., and Datta, S. K., 1991, "Plane-Strain-Wave Scattering by Cracks in Laminated Composite Plates," *ASCE Journal of Engineering Mechanics*, Vol. 117, No. 8, pp. 1738-1754.
- Kausel, E., 1981, "An Explicit Solution for the Green's Functions for Dynamic Loads in Layered Media," Technical Report R81-13, Department of Civil Engineering, M.I.T., Cambridge, MA.
- Kausel, E., 1986, "Wave Propagation in Anisotropic Layered Media," *International Journal for Numerical Methods in Engineering*, Vol. 23, pp. 1567-1578.
- Kausel, E., and Roësset, J. M., 1992, "Frequency Domain Analysis of Undamped Systems," *ASCE Journal of Engineering Mechanics*, Vol. 118, No. 4, pp. 721-734.
- Kundu, T., and Mal, A. K., 1985, "Elastic Waves in a Multilayered Solid due to a Dislocation Source," *Wave Motion*, Vol. 7, pp. 459-471.
- Liu, G. R., Achenbach, J. D., 1994, "A strip Element Method for Stress Analysis of Anisotropic Linearly Elastic Solids," *ASME JOURNAL OF APPLIED MECHANICS*, Vol. 61, pp. 270-277.
- Liu, G. R., Tani, J., 1993, "Surface Waves in Functionally Gradient Piezoelectric Plates," *ASME Journal of Vibration and Acoustics*, to appear.
- Liu, G. R., Tani, J., Ohyoshi, T., and Watanabe, K., 1991a, "Characteristic Wave Surfaces in Anisotropic Laminated Plates," *ASME Journal of Vibration and Acoustics*, Vol. 113, pp. 279-285.
- Liu, G. R., Tani, J., Ohyoshi, T., and Watanabe, K., 1991b, "Transient Waves in Anisotropic Laminated Plates," Part 1: Theory; Part 2: Application, *ASME Journal of Vibration and Acoustics*, Vol. 113, pp. 230-239.

Liu, G. R., Tani, J., Watanabe, K., and Ohyoshi, T., 1990, "Lamb Wave Propagation in Anisotropic Laminates," *ASME Journal of Applied Mechanics*, Vol. 57, No. 2, pp. 923-929.

Liu, S. W., Datta, S. K., and Ju, T. H., 1991, "Transient Scattering of Rayleigh-Lamb waves by a Surface-Breaking Crack: Comparison of Numerical Simulation and Experiment," *Journal of Nondestructive Evaluation*, Vol. 10, No. 3, pp. 111-126.

Mal, A. K., 1988, "Wave Propagation in Layered Composite Laminates under Periodic Surface Loads," *Wave Motion*, Vol. 10, pp. 257-266.

Nelson, R. B., and Dong, S. B., 1973, "High Frequency Vibrations and Waves in Laminated Orthotropic Plates," *Journal of Sound and Vibration*, Vol. 30, pp. 33-44.

Seale, S. H., and Kausel, E., 1989, "Point Loads in Cross-Anisotropic, Layered Halfspaces," *ASCE Journal of Engineering Mechanics*, Vol. 115, No. 3, pp. 509-524.

Vasudevan, N., and Mal, A. K., 1985, "Response of an Elastic Plate to Localized Transient Sources," *ASME JOURNAL OF APPLIED MECHANICS*, Vol. 52, pp. 356-362.

Von Estorff, O., Pais, A. L., and Kausel, E., 1990, "Some Observations on Time Domain and Frequency Domain Boundary Elements," *International Journal for Numerical Methods in Engineering*, Vol. 29, pp. 785-800.

Waas, G., 1972, "Linear two-dimensional analysis of soil dynamics problems in semi-infinite layer media," Ph.D. Thesis, University of California, Berkeley, CA.

Xu, P. C., and Mal, A. K., 1985, "An Adaptive Integration Scheme for Irregularly Oscillatory Functions," *Wave Motion*, Vol. 7, pp. 235-243.

Xu, P. C., and Mal, A. K., 1987, "Calculation of the Inplane Green's Functions for a Layered Viscoelastic Solid," *Bulletin of the Seismological Society of America*, Vol. 77, No. 5, pp. 1823-1837.

APPENDIX

Matrices used in Eqs. (24) and (25):

$$\mathbf{R}_1 = \frac{1}{h} \begin{bmatrix} -3\mathbf{D}_{xz} & 4\mathbf{D}_{xz} & -\mathbf{D}_{xz} \\ -\mathbf{D}_{xz} & \mathbf{0} & \mathbf{D}_{xz} \\ \mathbf{D}_{xz} & -4\mathbf{D}_{xz} & 3\mathbf{D}_{xz} \end{bmatrix}, \quad \mathbf{R}_2 = \begin{bmatrix} \mathbf{D}_{xx} & \mathbf{0} & \mathbf{0} \\ \mathbf{0} & \mathbf{D}_{xx} & \mathbf{0} \\ \mathbf{0} & \mathbf{0} & \mathbf{D}_{xx} \end{bmatrix}$$

where

$$\mathbf{D}_{xx} = \begin{bmatrix} c_{11} & c_{16} & c_{15} \\ c_{61} & c_{66} & c_{65} \\ c_{51} & c_{56} & c_{55} \end{bmatrix}, \quad \mathbf{D}_{xz} = \begin{bmatrix} c_{15} & c_{14} & c_{13} \\ c_{65} & c_{64} & c_{63} \\ c_{55} & c_{54} & c_{53} \end{bmatrix}.$$

A Crack Very Close to a Bimaterial Interface

A. Romeo
Graduate Student.

R. Ballarini
Associate Professor.

Department of Civil Engineering,
Case Western Reserve University,
Cleveland, OH 44106-7201

This paper presents the plane elastostatics analysis of a semi-infinite crack perpendicular to a perfectly bonded bimaterial interface. Both cases of the crack approaching the interface and penetrating the interface are addressed. The distance from the tip of the crack to the interface is δ . A singular integral equation approach is used to calculate the stress intensity factor, K_I , and the crack-opening displacement at the interface, η , as functions of δ , the Dundurs parameters α and β , and the stress intensity factor k_I associated with the same crack terminating at the interface (the case $\delta = 0$). The results are presented as $K_I = k_I \delta^{1/2-\lambda} f(\alpha, \beta)$ and $\eta = C k_I \delta^{1-\lambda} \tilde{\eta}(\alpha, \beta)$ where λ is the strength of the stress singularity associated with $\delta = 0$, f and $\tilde{\eta}$ are functions calculated numerically and C is a material constant. These results can be used to determine the stress intensity factor and crack opening displacement of cracks of finite length $2a$ with one tip at a distance δ from the interface for $\delta/a \ll 1$. The selected results presented for a crack loaded by a uniform far-field tension in each half-plane show that the stress intensity factors approach their limits at a relatively slow rate.

1 Introduction

Consider the plane elastostatics problem shown in Fig. 1(a). A Mode I crack of length $2a$ is perpendicular to the perfectly bonded interface between two isotropic half-planes with shear moduli μ_i and Poisson's ratios ν_i , $i = 1, 2$. The distance from the left tip of the crack to the interface is δ . Because of its relevance to fracture of composite materials, the problem of calculating the stress intensity factors for this configuration has been addressed by several authors (Erdogan et al., 1973; Atkinson, 1975). It is well known that this elasticity problem can be formulated using the Green's function for the stress produced along the crack line by an edge dislocation. This procedure leads to the following singular integral equation and uniqueness condition:

$$\frac{2\mu_1}{\pi(\kappa_1 + 1)} \int_{\delta}^{\delta+2a} b(\xi) \left[\frac{1}{y-\xi} + \frac{\alpha + \beta^2}{1 - \beta^2} \frac{1}{y + \xi} + \frac{2(\alpha - \beta)}{1 + \beta} \frac{\xi(y - \xi)}{(y + \xi)^3} \right] d\xi = -\sigma_{xx}(y)$$

$$\int_{\delta}^{\delta+2a} b(\xi) d\xi = 0 \quad \delta \leq y, \xi \leq \delta + 2a \quad (1)$$

where σ_{xx} is the stress along the crack line induced by the remote loading in the uncracked body, α and β are the Dundurs parameters (Dundurs, 1969)

$$\alpha = \frac{\mu_2(\kappa_1 + 1) - \mu_1(\kappa_2 + 1)}{\mu_2(\kappa_1 + 1) + \mu_1(\kappa_2 + 1)}$$

$$\beta = \frac{\mu_2(\kappa_1 - 1) - \mu_1(\kappa_2 - 1)}{\mu_2(\kappa_1 + 1) + \mu_1(\kappa_2 + 1)}$$

Contributed by the Applied Mechanics Division of THE AMERICAN SOCIETY OF MECHANICAL ENGINEERS for publication in the ASME JOURNAL OF APPLIED MECHANICS.

Discussion on this paper should be addressed to the Technical Editor, Prof. Lewis T. Wheeler, Department of Mechanical Engineering, University of Houston, Houston, TX 77204-4792, and will be accepted until four months after final publication of the paper itself in the ASME JOURNAL OF APPLIED MECHANICS.

Manuscript received by the ASME Applied Mechanics Division, July 2, 1993; final revision, May 3, 1994. Associate Technical Editor: D. M. Parks.

$\kappa_i = 3 - 4\nu_i$ for plane strain and $\kappa_i = (3 - \nu_i)/(1 + \nu_i)$ for plane stress. The unknown dislocation density $b(\xi)$ is defined in terms of the crack opening displacement $[u_x(\xi)]$ as

$$b(\xi) \equiv -\frac{\partial}{\partial \xi} [u_x]. \quad (2)$$

The first equation in (1) represents the zero traction condition along the crack surfaces, while the second enforces single-valued displacements (both crack tips are closed). In the following, the loading is taken as uniform remote tension in each half-plane, $\sigma^{(1)}$ and $\sigma^{(2)}$, such that

$$\sigma^{(2)} = \frac{1 + \alpha}{1 - \alpha} \sigma^{(1)} \quad (3)$$

and therefore $\sigma_{xx} = \sigma^{(1)}$ in Eq. (1).

The ratio $\delta/2a$ enters in the kernel of the singular integral Eq. (1) in such a way that stress intensity factor values calculated using a direct numerical solution inevitably lose accuracy for $\delta/2a \ll 1$. Indeed, the smallest ratio for which Erdogan et al. (1973) present results is $\delta/2a = 0.05$. Their results showed that as $\delta \rightarrow 0$ the stress intensity factor of the crack tip closest to the interface approaches zero when $\mu_2 > \mu_1$ and infinity when $\mu_1 > \mu_2$. These limits result from the discontinuous change in the order of the stress singularity as δ becomes equal to zero. As will be explained in the next section, for $\delta = 0$ and $\mu_2 > \mu_1$ the stress ahead of the crack tip is of the order $k_I r^{-\lambda}$ with $\lambda < \frac{1}{2}$. This weaker singularity in effect reduces to zero, as $\delta \rightarrow 0$, the amplitude K_I of the square root singularity associated with $\delta \neq 0$. For $\mu_1 > \mu_2$, $\lambda > \frac{1}{2}$, and similar arguments explain why K_I increases to infinity as $\delta \rightarrow 0$. Assuming linear elastic fracture mechanics these limits imply that the crack reaches the interface at infinite load for $\mu_2 > \mu_1$ and zero load for $\mu_1 > \mu_2$.

As a first step toward the development of physically sound propagation criteria for interface cracks, this paper is concerned with determining, as functions of the elastic mismatch, the rate at which the square root singularity approaches the limits discussed above. To this end the problem is formulated asymptotically in terms of a semi-infinite crack in which the only length parameter is δ .

The approach used is essentially the same as that used by Hutchinson et al. (1987) to study a crack very close to and parallel to a bimaterial interface. It relies on some relevant well-

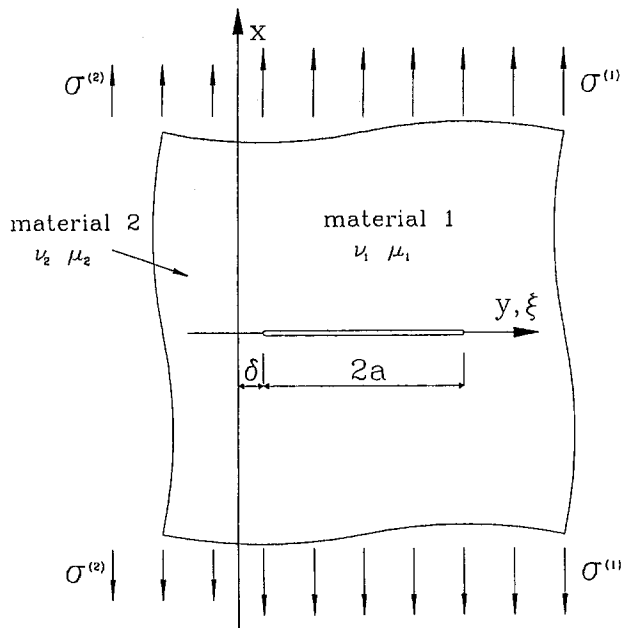


Fig. 1(a)

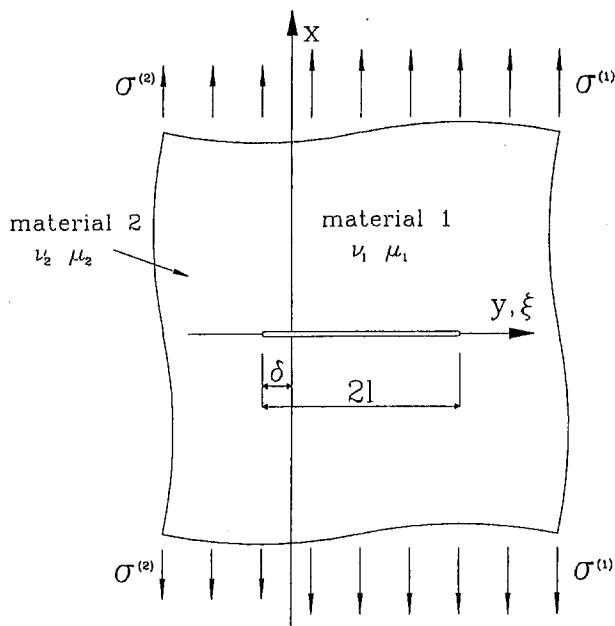


Fig. 1(b)

Fig. 1 Finite length crack (a) approaching and (b) penetrating a bimaterial interface

known results for the asymptotic behavior of the stresses and crack-opening displacements in the vicinity of the tip of a crack impinging on a bimaterial interface. These are reviewed briefly in the next section. The solution of the semi-infinite crack problem is discussed in the third section and an example of how the asymptotic analysis can be applied to the problem of Fig. 1(a) is provided in the 4th section. The last section extends the method to the case of a finite crack that penetrates a distance δ through the interface, Fig. 1(b).

2 Finite Crack Terminating at the Interface

The results of the Williams technique analysis for a crack terminating at the interface ($\delta = 0$ in Fig. 1(a)) show that the

traction ahead of the crack tip is characterized by

$$\lim_{y \rightarrow 0^-} \{\sigma_{xx}^{(2)}(y)\} = \frac{k_I}{\sqrt{2\pi}} (-y)^{-\lambda} \quad (4)$$

where superscript (i) denotes "in material (i)," k_I is the stress intensity factor, and λ ($0 \leq \lambda < 1$) is the root of the equation derived by Zak and Williams (1963)

$$\cos(\lambda\pi) = \frac{2(\beta - \alpha)}{(1 + \beta)} (1 - \lambda)^2 + \frac{\alpha + \beta^2}{1 - \beta^2} \quad (5)$$

The loci of constant λ in the α - β plane are shown in Fig. 2(a). As pointed out by Dundurs (1970), this figure clearly illustrates that for $\alpha \rightarrow 1$ the quantity λ is more sensitive to the mismatch in the Poisson's ratios, while for $\alpha \rightarrow -1$ it is more sensitive to the mismatch in the shear moduli.

Another important result from the Williams analysis relates the crack-opening displacement (COD), $[u_x^{(1)}(y)]$, to the stress ahead of the crack, i.e.,

$$\begin{aligned} \lim_{y \rightarrow 0^+} \{\sigma_{xx}^{(2)}(-y)\} &= \lim_{y \rightarrow 0^+} \left\{ -\psi \frac{\partial}{\partial y} [u_x^{(1)}(y)] \right\} \\ &= \lim_{y \rightarrow 0^+} \{\psi b(y)\} \end{aligned} \quad (6)$$

where the bimaterial parameter ψ is defined as

$$\psi \equiv \frac{2\mu_1}{(\kappa_1 + 1) \sin(\lambda\pi)} \frac{1}{(1 - \beta^2)} [1 - 2\beta(\lambda - 1)] \quad (7)$$

Equation (6) allows the determination of the stress intensity factor of a crack of length $2a$ in terms of the dislocation density as

$$k_I = \lim_{y \rightarrow 0^+} \{\psi \sqrt{\pi a} \tilde{b}(y)\} \quad (8)$$

in which

$$\tilde{b}(y) = a^{-(\lambda+1/2)} b(y) y^\lambda (2a - y)^{1/2}$$

is the regular part of the dislocation density $b(y)$.

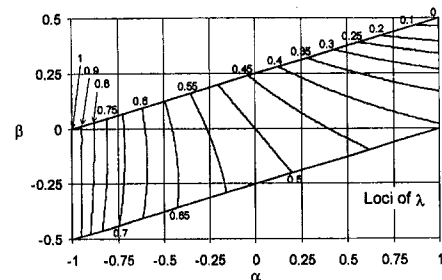


Fig. 2(a)

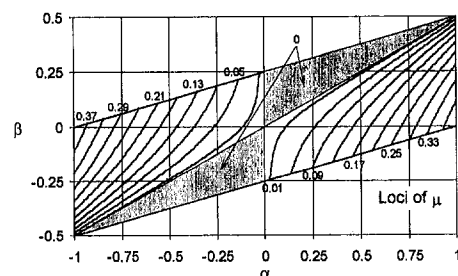


Fig. 2(b)

Fig. 2 Loci of (a) constant λ and (b) constant μ in the α - β plane

It is worth noting that (8) could also be derived by studying the behavior near the crack tip of the generalized Cauchy-type integral that represents the stress $\sigma_{xx}^{(2)}$.

3 Semi-infinite Crack Analysis

Consider a semi-infinite crack perpendicular to the interface and terminating at a distance δ from it. The COD at a point $r = y - \delta$ very close to the crack tip ($r/\delta \ll 1$) is given by $[u_x] \propto K_I r^{1/2}$, where K_I is the stress intensity factor. For $r/\delta \gg 1$ the COD approaches the one associated with the crack tip impinging on the interface ($\delta = 0$), i.e., $[u_x] \propto k_I r^{1-\lambda}$. The physical meaning is that since δ is very small the COD in the far-field is indistinguishable from the COD of the same crack impinging on the interface.

Linearity and dimensional considerations (δ is the only characteristic length) demand that

$$\frac{K_I}{k_I \delta^{1/2-\lambda}} = f(\alpha, \beta) \quad (9)$$

where f is a function of the Dundurs parameters only. This type of argument was employed by Hutchinson et al. (1987) and He and Hutchinson (1989).

It should be noted that this last result was derived by Atkinson (1975) by applying the Mellin transform to the integral equation

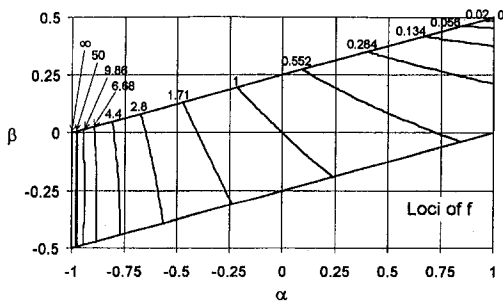


Fig. 3(a)

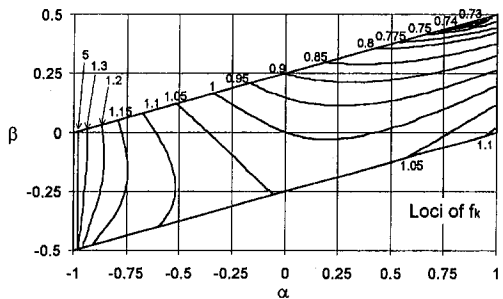


Fig. 3(b)

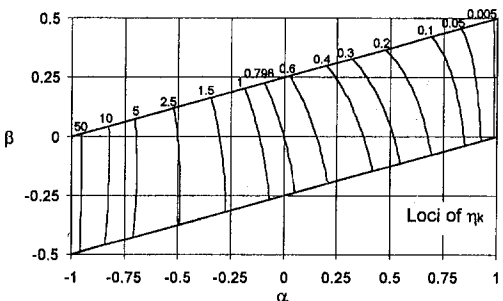


Fig. 3(c)

Fig. 3 Loci of (a) constant f , (b) constant f^* , and (c) constant η_k in the α - β plane

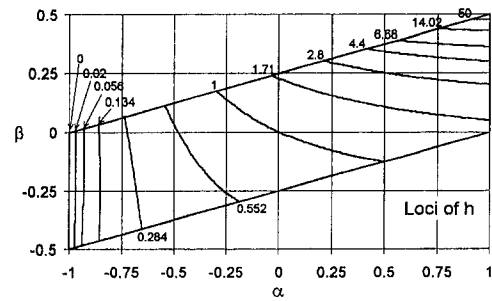


Fig. 4 Loci of constant h in the α , β -plane

and using the Wiener-Hopf technique. He showed that the stresses ahead of the crack are given by (using the notation in his paper)

$$\sigma_{xx} \approx \epsilon^{1/2} r^{-1/2} \left\{ \sum_{k=1}^N A_k \epsilon^{s_k^* - 2} + O(\epsilon^{3s_1^* - 4}) \right\} \quad (10)$$

where the A_k are constants independent of ϵ , α_1 and β are material constants (not to be confused with the Dundurs parameters), and s_k^* are the N real roots ($\text{Re}(s) > 1$) of the equation

$$\cos(\pi s) + \alpha_1 - \beta(s-1)^2 = 0. \quad (11)$$

It can be easily shown that the dominant term of the stress given by (10) corresponds to that produced by the stress intensity factor defined by relation (9), the constants A_k being identified with the values of $k_I f(\alpha, \beta)$, and $s_1^* = 2 - \lambda$. Atkinson developed his solution for a constant pressure loading, but did not present numerical results for coefficients A_k . The main contribution of the present paper is that it presents complete results for these universal functions.

As will be described in the next section, (9) provides a powerful tool for the asymptotic analysis of finite length cracks approaching a bimaterial interface. The values of the function $f(\alpha, \beta)$ were calculated by integrating numerically (1) for $2a = \infty$. The details of the solution procedure are given in the Appendix.

The loci of constant f in the α - β plane are shown in Fig. 3(a). It is interesting to note that the sensitivity of f to changes in shear moduli and Poisson ratios is qualitatively the same as that of the singularity coefficient λ .

4 Finite Crack Very Close to the Interface

The numerical scheme used for solving the singular integral equation for the finite crack depicted in Fig. 1(a) becomes unstable when the ratio $\delta/2a$ assumes very small values. For these cases, an indirect method based on asymptotical analysis is recommended for computing the stress intensity factor. This approach relies on the combination of (9) and the stress intensity factor k_I associated with the finite crack terminating at the interface ($\delta = 0$).

As an example, consider the case of a crack acted upon by a uniform remote tension field in the two connected half-planes according to (3). As shown in the Appendix the stress intensity factor k_I can be represented as

$$\frac{k_I}{\sigma \sqrt{\pi a^\lambda}} = h(\alpha, \beta). \quad (12)$$

The loci of constant h in the α - β plane are shown in Fig. 4. It is observed that the stress intensity factor for this problem is yet another parameter that is more sensitive to the mismatch in the Poisson's ratios for $\alpha \rightarrow 1$, while for $\alpha \rightarrow -1$ it is more sensitive to the mismatch in the shear moduli. Combining (9) and (12) leads to the following expression for the stress intensity factor of a crack of length $2a$ at a distance δ from the interface:

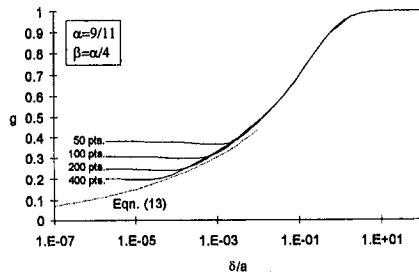


Fig. 5(a)

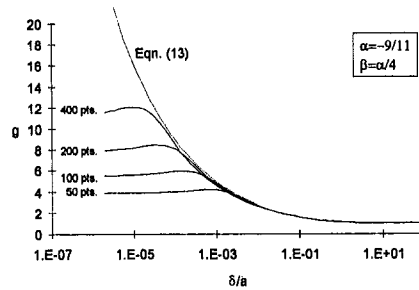


Fig. 5(b)

Fig. 5 Numerical instability and transition to the asymptotical solution of g for small δ/a ratios for (a) $\alpha = 4\beta = \frac{9}{11}$ and (b) $\alpha = 4\beta = -\frac{9}{11}$

$$\frac{K_I}{\sigma\sqrt{\pi a}^{1/2}} = g(\alpha, \beta) = \left(\frac{\delta}{a}\right)^{1/2-\lambda} f(\alpha, \beta)h(\alpha, \beta); \quad \delta/a \rightarrow 0. \quad (13)$$

Selected results for the asymptotic value of the stress intensity factor as calculated using (13) are presented in Figs. 5(a) and 5(b) for $\alpha = 4\beta = \pm\frac{9}{11}$; these values of the Dundurs parameters include $\nu_1 = \nu_2$ and $\mu_2/\mu_1 = 10$ or $\mu_1/\mu_2 = 10$. The solid lines in these plots are the values of the stress intensity factor calculated through a direct numerical solution of (1) along the finite interval. The procedure used for these calculations is outlined in the Appendix. As expected the direct solution for a given number of integration points breaks down as the distance from the crack tip to the interface assumes relatively small values. The asymptotic solution approaches the envelope defined by the value of δ/a at which the direct numerical solution, for a given value of integration points, becomes unstable.

The most interesting results of this analysis is that the stress intensity factor approaches the aforementioned limits at relatively slow rates. For significant elastic mismatch, $\alpha = 4\beta = \frac{9}{11}$, the stress intensity factor for $\delta/a = 0.001$ is approximately 30 percent of the nominal value associated with no interface. These results suggest that although the stress intensity factor for $\mu_2 > \mu_1$ approaches zero, this limit is associated with distances δ much smaller than the plastic zone that inevitably surrounds the crack tip. The leading edge of the plastic zone will thus reach the interface at a finite load. Perhaps more importantly, cracks in typical engineering materials will have extremely small δ values that will invalidate a continuum mechanics formulation.

5 Finite Crack Extending Through the Interface

The asymptotical technique described in the previous sections can be easily extended to other interface crack problems. The natural extension of the previous formulation is to a finite crack of length $2l = 2(a + b)$ that has extended beyond the interface a distance $\delta = 2b \ll l$ (Fig. 1(b)). This problem can be reduced to a set of coupled singular integral equations using the same Green's function approach that is used to derive (1) (Erdogan

and Biricikoglu, 1973). These equations are written symbolically in terms of the dislocation densities $b^{(i)}(\xi)$ ($i = 1, 2$):

$$A_1 \int_0^{2a} b^{(1)}(\xi) K_{1i} d\xi + A_2 \int_{-2b}^0 b^{(2)}(\xi) K_{2i} d\xi = -\sigma^{(i)} \quad (i = 1, 2)$$

$$\int_0^{2a} b^{(1)}(\xi) d\xi + \int_{-2b}^0 b^{(2)}(\xi) d\xi = 0 \quad (14)$$

where K_{ij} ($i, j = 1, 2$) are Cauchy-type kernels. The first two Eqs. (14) represent the traction boundary conditions, while the third enforces single-valued displacements. The condition on the dislocation density required to insure compatibility at the interface is given by

$$\lim_{y \rightarrow 0^+} b^{(2)}(y)/b^{(1)}(-y) = F(\alpha, \beta, \mu) \quad (15)$$

where

$$F(\alpha, \beta, \mu) = \frac{(1 + \alpha)\beta + (\alpha - \beta) \times (1 - \beta)(-1 + 4\mu - 2\mu^2) - (1 - \beta^2) \cos(\mu\pi)}{(1 + \alpha)(-1 + 2\beta - 2\beta\mu)} \quad (16)$$

and μ is the power of the stress singularity, which satisfies the characteristic equation

$$(1 - \beta^2)(1 + \cos^2 \mu\pi) + 2[2\alpha\beta - 1 - (2\alpha\beta - \beta^2) \cos \mu\pi] + 4\mu(2 - \mu) [(\alpha - \beta)^2(1 - \mu)^2 - \alpha\beta + \beta(\alpha - \beta) \cos \mu\pi] = 0.$$

The loci of constant μ are plotted in Fig. 2(b).

Again a direct solution of Eqs. (14) is inadequate for very small b/a ratios and an alternative approach is furnished by the asymptotical analysis. The reference problem is still the finite crack of length $2l$ terminating at the interface. The semi-infinite analysis on the other hand has to be redefined, since the crack tip is now located beyond the interface at a distance δ from it. As before, the far-field COD has to approach the one associated with no penetration, $[u_x] \propto kr^{1-\lambda}$, and in the vicinity of the crack tip the COD is given by $[u_x] \propto Kr^{1/2}$. However, an additional requirement is that the COD at the interface be of the order $r^{1-\mu}$. Equation (9) still applies with $f(\alpha, \beta)$ replaced by the new function $f^*(\alpha, \beta)$ whose values are computed by solving numerically the proper set of integral equations (see Appendix); the loci of this function in the α - β plane are plotted in Fig. 3(b).

Combining (9) and (12) leads to the asymptotical expression of the stress intensity factor of a finite crack of length $2l$ the has penetrated in material 2 by the distance $\delta = 2b \ll l$

$$\frac{K_I}{\sigma^{(1)}\sqrt{\pi l}^{1/2}} = g^*(\alpha, \beta) = \left(\frac{2c}{1+c}\right)^{1/2-\lambda} f^*(\alpha, \beta)h(\alpha, \beta) \quad (17)$$

where

$$c = b/a.$$

The predictions of Eq. (17) are valid in the limit $\delta/l \rightarrow 0$. Figures 6 and 7 show the convergence of the nondimensional stress intensity factor values found by direct numerical integration to the asymptotic solution given by (17) for the two material combinations already used in the previous sections, $\alpha = \pm\frac{9}{11} = 4\beta$. Note that the for the case $\alpha = +\frac{9}{11} = 4\beta$, which corresponds to $\lambda = 0.347$, the rate of convergence is much slower than for $\alpha = -\frac{9}{11} = 4\beta$ ($\lambda = 0.755$).

Note that the asymptotic analysis can be used to compute not only stress intensity factors but also other quantities such as the

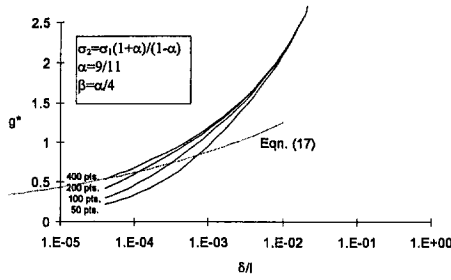


Fig. 6 Numerical instability and transition to the asymptotical solution of g^* for small δ/a ratios for $\alpha = 4\beta = \frac{9}{11}$

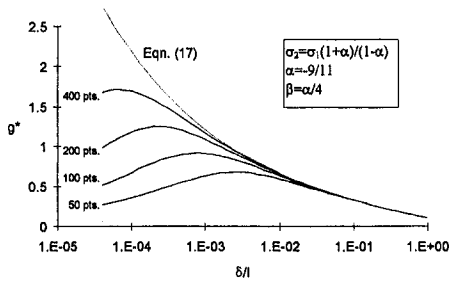


Fig. 7 Numerical instability and transition to the asymptotical solution of g^* for small δ/a ratios for $\alpha = 4\beta = -\frac{9}{11}$

crack-opening displacement at the interface. In fact, for a semi-infinite crack the COD at the interface, η , is given by

$$\eta = \frac{1 + \kappa_1}{2\mu_1} k_f \delta^{1-\lambda} \tilde{\eta}(\alpha, \beta) \quad (18)$$

where $\tilde{\eta}$ is a function of the Dundurs parameters whose loci are shown in Fig. 3(b). The asymptotic expression of the crack-opening displacement at the interface for the finite crack in Fig. 1(b) is then given by

$$\eta_f = -\sqrt{\pi} \phi_1 \delta \left(\frac{l}{\delta}\right)^\lambda h(\alpha, \beta) \tilde{\eta}(\alpha, \beta) \quad \delta/l \rightarrow 0 \quad (19)$$

where

$$\phi_1 = -\frac{\sigma^{(1)}(\kappa_1 + 1)}{2\mu_1}$$

6 Conclusions

The numerical schemes that are used to solve integral equations describing the elastostatics problems of finite length cracks close to a bimaterial interface are not accurate when the relative distance δ from the crack tip to the interface becomes very small. An asymptotic analysis has been developed that provides accurate stress intensity factors for such problems and gives insight into their rate of change as $\delta \rightarrow 0$. For the case of a crack approaching or penetrating a bimaterial interface, it has been shown that the stress intensity factor at the leading crack tip approaches its limiting value at a slow rate. These results suggest that propagation criteria for such problems are associated with nonlinear processes. The technique presented in this paper can be used to solve a class of problems in which a small parameter leads to an unstable direct numerical solution of the governing equations.

Acknowledgment

This work was supported by the Lewis Research Center under Grant NAG3-856.

References

- Atkinson, C., 1975, "On the Stress Intensity Factors Associated with Cracks Interacting with an Interface Between Two Elastic Media," *International Journal of Engineering Science*, Vol. 13, pp. 489–504.
- Dundurs, J., 1969, "Elastic Interaction of Dislocations with Inhomogeneities," *Mathematical Theory of Dislocations*, T. Mura, ed., ASME, New York, pp. 70–114.
- Dundurs, J., and Lee, S., 1970, "Stress Concentrations Due to Edge Dislocation Pile-ups in Two-phase Materials," *Scripta Metallurgica*, Vol. 4, pp. 313–314.
- Erdogan, F., and Biricikoglu, V., 1973, "Two Bonded Half Planes with a Crack Going Through the Interface," *International Journal of Engineering Science*, Vol. 11, pp. 745–766.
- Erdogan, F., Gupta, G. D., and Cook, T. S., 1973, "Numerical Solution of Singular Integral Equations," *Mechanics of Fracture*, Vol. 1, G. C. Sih, ed., Noordhoff International Publishing, pp. 368–425.
- He, M. Y., and Hutchinson, J. W., 1989, "Crack Deflection at an Interface Between Dissimilar Elastic Materials," *International Journal Solids Structures*, Vol. 25, No. 9, pp. 1053–1067.
- Hutchinson, J. W., Mear, M. E., and Rice, J. R., 1987, "Crack Paralleling an Interface Between Dissimilar Materials," *ASME JOURNAL OF APPLIED MECHANICS*, Vol. 54, No. 4, pp. 828–832.
- Miller, G. R., and Keer, L. M., 1985, "A Numerical Technique for the Solution of Singular Integral Equations of the Second Kind," *Quarterly of Applied Mathematics*, Vol. 42, pp. 455–465.
- Rubinstein, A. A., 1992, "Stability of the Numerical Procedure for Solution of Singular Integral Equations on Semi-Infinite Interval. Application to Fracture Mechanics," *Computers & Structures*, Vol. 44, No. 1/2, pp. 71–74.
- Zak, A. R., and Williams, M. L., 1963, "Crack Point Stress Singularities at a Bi-Material Interface," *ASME JOURNAL OF APPLIED MECHANICS*, Vol. 30, pp. 142–143.

APPENDIX

Let

$$A_i = \frac{2\mu_i}{\pi(1 + \kappa_i)} \quad (i = 1, 2)$$

$$M = \frac{\alpha + \beta^2}{1 - \beta^2}; \quad N = \frac{2(\alpha - \beta)}{1 + \beta}; \quad S = \frac{1 + \alpha}{1 - \beta^2};$$

$$P = \frac{\alpha - \beta^2}{1 - \beta^2}; \quad Q = \frac{2(\alpha - \beta)}{1 - \beta}; \quad T = \frac{1 - \alpha}{1 - \beta^2};$$

$$K_{11}(\xi, y) = \frac{1}{y - \xi} + \frac{M}{y + \xi} + \frac{\xi(y - \xi)N}{(y + \xi)^3};$$

$$K_{12}(\xi, y) = S \left[\frac{1}{y - \xi} - 2\beta \frac{\xi}{(y - \xi)^2} \right];$$

$$K_{21}(\xi, y) = T \left[\frac{1}{y - \xi} + 2\beta \frac{\xi}{(y - \xi)^2} \right];$$

$$K_{22}(\xi, y) = \frac{1}{y - \xi} - \frac{P}{y + \xi} - \frac{\xi(y - \xi)Q}{(y + \xi)^3}. \quad (A1)$$

The following procedures were used to solve the integral equations numerically.

Crack of Length $2a$ at Distance δ From the Interface ($\delta \geq 0$)

The integral equations for this case are

$$A_1 \int_{\delta}^{\delta+2a} b(\xi) K_{11}(\xi, y) d\xi = -\sigma^{(1)}$$

$$\int_{\delta}^{\delta+2a} b(\xi) d\xi = 0 \quad \delta \leq y, \xi \leq \delta + 2a$$

The case $\delta = 0$ corresponds to a crack impinging on the interface. For the numerical computation these equations are rendered in nondimensional form and normalized in the interval $[-1, 1]$ by means of the transformations

$$t = \frac{\xi - (a + \delta)}{a}; \quad \zeta = \frac{y - (a + \delta)}{a};$$

$$\phi = -\frac{\sigma^{(1)}(\kappa_1 + 1)}{2\mu_1}.$$

The nondimensional stress intensity factor at the crack tip closest to the interface is given by

$$h(\alpha, \beta) = \frac{k_I}{\sigma^{(1)}\sqrt{\pi a^\lambda}} = \frac{\kappa_1 + 1}{2\mu_1} \psi \tilde{b}(-1); \quad \delta = 0 \quad (\text{A3})$$

$$g(\alpha, \beta) = \frac{K_I}{\sigma^{(1)}\sqrt{\pi a^{1/2}}} = \tilde{b}(-1); \quad \delta > 0 \quad (\text{A4})$$

where

$$\psi = \frac{2\mu_1}{\kappa_1 + 1} \frac{1}{\sin(\lambda\pi)} \frac{1 + \alpha}{1 - \beta^2} [1 - 2\beta(\lambda - 1)]$$

and

$$\tilde{b}(t) = b(t)(1 + t)^\lambda (1 - t)^{1/2}$$

is the regular part of the dislocation density ($\lambda = \frac{1}{2}$ when $\delta > 0$). For the numerical solution of (A1), two methods were compared. $\tilde{b}(t)$ in the first method is represented as a truncated series of Jacobi polynomials (Erdogan et al., 1973), while in the second method it is expressed in terms of piecewise quadratic polynomials (Miller and Keer, 1985). The results shown a faster convergence for the latter method for which 64 integration points were necessary to capture three significant figures, versus 400 integration points necessary for the first method.

Semi-infinite Crack Whose Tip is at Distance δ From the Interface

The singular integral equation is the same as the first (A2) except that the upper limit $2a$ is replaced with ∞ . The unknown dislocation density is represented in real coordinates as

$$b(\xi) = \frac{k_I}{\sqrt{2\pi}} \frac{\xi^{1/2}}{(\xi - \delta)^{1/2} \xi^\lambda} \left[\frac{\kappa_1 + 1}{2\mu_1} \tilde{b}(\xi) + w(\xi) \psi^{-1} \right] \quad (\text{A5})$$

with the additional condition $\lim_{\xi \rightarrow \infty} \tilde{b}(\xi) = 0$ replacing the crack closure condition that appears in the second Eq. (A2). As discussed by Rubinstein (1992), this representation stabilizes the singular integral equation. $w(\xi)$ is a function of the type

$$w(\xi) = \sin^2 \left[\frac{\pi}{2} \left(1 - \frac{\delta}{\xi} \right) \right]. \quad (\text{A6})$$

With the change of variables $\xi = 2\delta/(1 - t)$, $y = 2\delta/(1 - \zeta)$ (A4) is normalized in the interval $[-1, 1]$.

By extracting the dominant term of the singularity of the resulting equation, the nondimensional ratio of the local and far-field stress intensity factors is determined as

$$f(\alpha, \beta) = \frac{K_I}{k_I} \delta^{\lambda-1/2} = \tilde{b}(-1). \quad (\text{A7})$$

Crack of Length $2a$ Extending Through the Interface by δ ($\delta \geq 0$)

The set of coupled singular integral equations is given in (14) with A_i and K_{ij} defined in (A1). The compatibility condition at the interface is given in (15). The normalized nondimensional

form of (14) and (15) is attained by means of the transformations

$$t_1 = \frac{\xi - a}{a}; \quad \zeta_1 = \frac{y - a}{a}; \quad \phi_1 = -\frac{\sigma^{(1)}(1 + \kappa_1)}{2\mu_1};$$

$$t_2 = -\frac{\xi + b}{b}; \quad \zeta_2 = -\frac{y + b}{b}; \quad \phi_2 = -\frac{\sigma^{(2)}(1 + \kappa_2)}{2\mu_2};$$

that lead to the following representation of the dislocation densities:

$$b^{(1)}(t_1) = \tilde{b}^{(1)}(t_1)(1 - t_1)^{-1/2}(1 + t_1)^\mu;$$

$$b^{(2)}(t_2) = \tilde{b}^{(2)}(t_2)(1 - t_2)^{-1/2}(1 + t_2)^\mu \quad (\text{A8})$$

where

$$c = b/a.$$

The nondimensional stress intensity factor at the crack tip closer to the interface is then given by

$$g^*(\alpha, \beta) = \frac{K_I}{\sigma^{(1)}\sqrt{\pi l}}$$

$$= -\frac{1}{2^\mu \phi_1} \sqrt{\frac{2c}{1+c}} \frac{1+\alpha}{1-\alpha} \tilde{b}^{(2)}(1). \quad (\text{A9})$$

Semi-infinite Crack Whose Tip is at Distance δ Beyond the Interface

The equations for this case are similar to the first two Eqs. (14) with the upper limit $2a$ replaced with ∞ , and Eq. (15). The third Eq. (14) is replaced by the following condition that stabilizes the integral equations and insures uniqueness of the solution:

$$\lim_{\xi \rightarrow \infty} \tilde{b}^{(1)}(\xi) = 0.$$

The dislocation density functions have the form

$$b^{(1)}(\xi) = \frac{k_I}{\sqrt{2\pi}} \frac{1}{(\xi + \delta)^{\lambda-\mu} \xi^\mu} \left[\frac{\kappa_1 + 1}{2\mu_1} \tilde{b}^{(1)}(\xi) + w_1(\xi) \psi^{-1} \right]$$

$$b^{(2)}(\xi) = \frac{k_I}{\sqrt{2\pi}} \frac{\kappa_2 + 1}{2\mu_2} \frac{\tilde{b}^{(2)}(\xi)}{(-\xi)^\mu (\delta + \xi)^{1/2}} \delta^{1/2+\mu-\lambda} \quad (\text{A10})$$

where $w_1(\xi)$ is a function of the type

$$w_1(\xi) = \sin^2 \left[\frac{\pi}{2} \frac{\xi + 1}{\xi} \right]. \quad (\text{A11})$$

The normalized form of the set of equations is attained through the change of variables

$$t_1 = \frac{\xi - \delta}{\xi + \delta}; \quad \zeta_1 = \frac{y - \delta}{y + \delta}; \quad t_2 = \frac{2\xi + \delta}{\delta}; \quad \zeta_2 = \frac{2y + \delta}{\delta}.$$

By extracting the dominant term of the crack-tip singularity, the nondimensional ratio of the local and far-field stress intensity factor is then given by

$$f^*(\alpha, \beta) = \frac{K_I}{k_I} \delta^{\lambda-1/2} = \tilde{b}^{(2)}(1). \quad (\text{A12})$$

The crack-opening displacement at the interface is given by

$$\eta = -\int_{-\delta}^0 B_2(\xi) d\xi = \frac{\delta}{2} \int_{-1}^1 B_2(t_2) dt_2$$

$$= \frac{1 + \kappa_1}{2\mu_1} k_I \delta^{1-\lambda} \tilde{\eta}(\alpha, \beta) \quad (\text{A13})$$

H. M. Jensen
 Department of Solid Mechanics,
 Building 404,
 Technical University of Denmark,
 DK-2800 Lyngby, Denmark

M. D. Thouless¹
 IBM Research Division,
 T. J. Watson Center,
 Yorktown Heights, NY 10598
 Mem. ASME

Buckling Instability of Straight Edge Cracks

A buckling instability in a system where a straight edge crack lies at the interface between a thin elastic film and a substrate is analysed theoretically and experimentally. The buckling, which can occur also under remote tensile loads, may result in crack growth before the conventional criterion for fracture is met on the straight crack front by enhancing the mode adjusted crack driving force. If crack growth occurs, buckling will cause a wavy crack front to develop.

1 Introduction

If the stress within a film, coating or laminate attached to a substrate has a compressive component, then delamination can occur by a mechanism of buckling-assisted crack growth (Chai et al., 1981; Evans and Hutchinson, 1984). In this process, buckling of the film over an interfacial flaw provides a driving force for crack propagation along the interface. This mechanism has been analysed by a number of authors for the case in which the flaw is situated away from the edge of the laminated system. In practical cases though, the most likely location for a flaw is at the edge of the film. Such flaws may be introduced by handling, contact stresses along the edge of the substrate, or by dicing when a large coated system is cut into smaller components. It is the purpose of this paper to discuss some aspects of the initiation of delamination from this type of flaw.

The geometry considered is sketched in Fig. 1. A crack lies at the interface between an isotropic, elastic film and substrate. The crack front is assumed to be initially parallel to a stress-free edge, and when the crack propagates it runs away from the free edge. Furthermore, it is assumed that the interface has a sufficiently low toughness compared to the surrounding materials that the crack always remains at the interface. Two distinct regions can be identified: a bonded and a debonded zone with the crack front at the boundary between these two zones. If it is assumed that the width of the system is large compared to the crack length, a , which in turn is large compared to the film thickness, h , and it is assumed that a homogeneous, biaxial stress state (σ_{xx} , σ_{yy}) exists in the bonded film, and friction between the cracks faces can be neglected, then the stress state in the debonded film can be shown to be

$$\begin{aligned}\sigma_{yy}^* &= 0 \\ \sigma_{xx}^* &\equiv -\sigma^* = \sigma_{xx} - \nu\sigma_{yy}\end{aligned}\quad (1)$$

where ν is Poisson's ratio of the film. When the crack length is much larger than the thickness of the film, the energy release rate, G_0 , for the crack exhibits a steady-state value which is independent of a . This steady-state energy release rate can be calculated from the difference in the strain energies ahead and behind the crack front:

$$G_0 = \frac{1 - \nu^2}{2E} h\sigma_{yy}^2 \quad (2)$$

¹ Present address: Department of Mechanical Engineering and Applied Mechanics, University of Michigan, Ann Arbor, MI 48109.

Contributed by the Applied Mechanics Division of THE AMERICAN SOCIETY OF MECHANICAL ENGINEERS for publication in the ASME JOURNAL OF APPLIED MECHANICS.

Discussion on this paper should be addressed to the Technical Editor, Prof. Lewis T. Wheeler, Department of Mechanical Engineering, University of Houston, Houston, TX 77204-4792, and will be accepted until four months after final publication of the paper itself in the ASME JOURNAL OF APPLIED MECHANICS.

Manuscript received by the ASME Applied Mechanics Division, Nov. 1, 1993; final revision, June 3, 1994. Associate Technical Editor: W. K. Liu.

where E is the Young's modulus of the film. It should be noted that G_0 is independent of the elastic properties of the substrate and the stress components in the x -direction. The condition for crack propagation along the length of the debonded zone is

$$\frac{1 - \nu^2}{2E} h\sigma_{yy}^2 = \Gamma \quad (3)$$

where Γ is the toughness of the interface under the appropriate stress state. The condition given by Eq. (3) is the same irrespective of whether σ_{yy} is compressive or tensile. However, the value of Γ may change; typically, it is much larger when σ_{yy} is compressive. A detailed analysis of the crack-tip stress field shows that under these conditions the crack surfaces near the tip are forced into contact, and frictional effects can be expected to increase the toughness (Stringfellow and Freund, 1993; Thouless et al., 1992).

The sequence of photographs in Fig. 2 show experimental results for the apparent shape of an edge flaw in a model system consisting of a mica film bonded to an aluminium substrate. The compressive stress in the mica is constant for all three micrographs, but the size of the flaw is different. Details of the experimental procedure are given below, but it can be seen that an edge flaw develops a characteristic wavy shape at some critical size. The instability is caused by an out-of-plane buckling of the film from a compressive stress in the delaminated region. It will be seen that an important consequence of the buckling is that it causes a nonhomogeneous stress state to develop at the crack front, resulting in regions for which there is an enhanced tendency for delamination.

2 Buckling Analysis

The assumption that the crack length is large compared to the film thickness allows the delaminated region to be treated as a thin plate clamped to the substrate at the crack front. In the following, nonlinear von Kármán plate theory is employed.

2.1 Classical Buckling. If σ_{xx}^* is compressive, buckling of the film may occur at sufficiently large crack lengths. The shape of the buckling mode for a wide plate, neglecting effects of contact between the film and the substrate, is $w(x, y) = w(y) \cos(2\pi x/L)$, where L is the wavelength. The governing equation for the normal deflection $w(y)$ in nondimensional form (introducing $\bar{y} = y/a$ and $\bar{w} = w/h$) becomes

$$\bar{w}'''' - 2\bar{k}^2\bar{w}'' + \bar{k}^4\bar{w} = \frac{12(1 - \nu^2)a^2\sigma^*}{Eh^2} \bar{k}^2\bar{w} \quad (4)$$

where $(\quad)' = d(\quad)/d\bar{y}$ and $\bar{k} = 2\pi a/L$. The clamped/free boundary conditions consistent with the assumption $a \gg h$ are

$$\bar{w}'' - \nu\bar{k}^2\bar{w} = 0, \quad \bar{w}''' - (2 - \nu)\bar{k}^2\bar{w}' = 0 \quad \text{at free edge} \quad (5a)$$

$$\bar{w} = 0, \quad \bar{w}' = 0 \quad \text{at crack front.} \quad (5b)$$

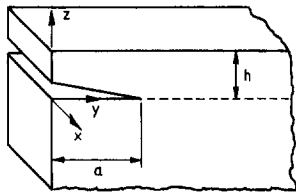


Fig. 1 Geometry for the plane-strain edge crack

The solution to the eigenvalue problem in σ^* described by (4) and (5) is a function of normalized wavelength and Poisson's ratio only, i.e.,

$$\frac{\sigma^*}{\sigma_c} = f\left(\frac{L}{a}, \nu\right), \quad \sigma_c = \frac{E\pi^2}{12(1-\nu^2)} \left(\frac{h}{a}\right)^2 \quad (6)$$

The variation of σ^*/σ_c with L/a is shown in Fig. 3 for three values of ν . The minimum buckling stress occurs at a finite wavelength which agrees with the observations in Fig. 2. From Fig. 3 using the value $\nu = \frac{1}{3}$, buckling of the film will occur if the normalized stress in the delaminated film exceeds the minimum buckling stress, which is

$$\sigma^*/\sigma_c \cong 1.24 \quad \text{at } L/a \cong 3.3. \quad (7)$$

2.2 Buckling and Post-buckling Under Contact. The results in the previous section neglect the unilateral constraint from the substrate. To investigate this effect and to predict the post-buckling behavior, a full nonlinear numerical analysis was carried out taking contact into account.

The basis for the numerical method is the principle of virtual work in incremental form for the plate of area A :

$$\iint_A [\Delta \dot{N}_{\alpha\beta} \delta E_{\alpha\beta} + \Delta N_{\alpha\beta} \dot{w}_{,\alpha} \delta w_{,\beta} + N_{\alpha\beta}^0 \dot{w}_{,\alpha} \delta w_{,\beta} + \dot{M}_{\alpha\beta} \delta K_{\alpha\beta}] dA = - \iint_A [\dot{N}_{\alpha\beta}^0 \delta E_{\alpha\beta} + N_{\alpha\beta} \delta E_{\alpha\beta} + M_{\alpha\beta} \delta K_{\alpha\beta}] dA \quad (8)$$

where $(\dot{\quad})$ denotes an increment, $N_{\alpha\beta}$ are the effective membrane stresses, and $\Delta N_{\alpha\beta}$ denotes changes relative to the prestressed state, $N_{\alpha\beta}^0$, (i.e., $N_{\alpha\beta} = N_{\alpha\beta}^0 + \Delta N_{\alpha\beta}$). Furthermore, in (8), $M_{\alpha\beta}$ are the bending moments. The strain measures, $E_{\alpha\beta}$ and $K_{\alpha\beta}$, are related to the plate displacements by

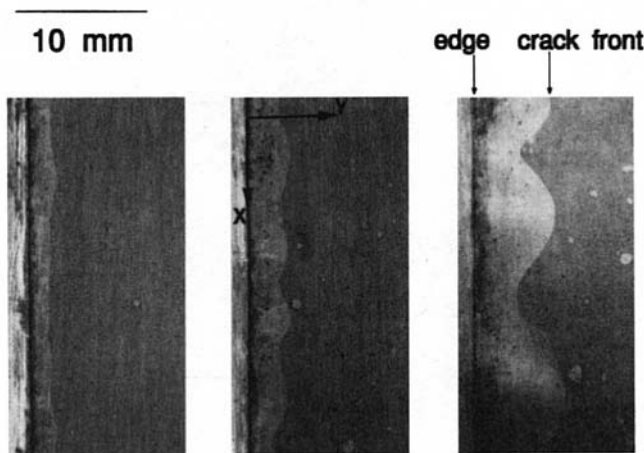


Fig. 2 Sequence of micrographs showing the shape of edge flaws of increasing size in a mica/aluminium system ($h \approx 36 \mu\text{m}$, $\sigma \approx 97 \text{ MPa}$)

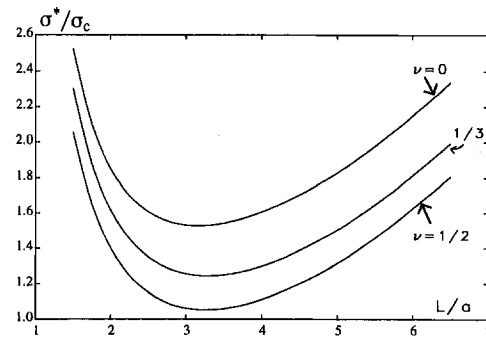


Fig. 3 Variation of normalized buckling stress with wavelength for three values of Poisson's ratio for the film

$$E_{\alpha\beta} = \frac{1}{2}(v_{\alpha,\beta} + v_{\beta,\alpha} + w_{,\alpha}w_{,\beta})$$

$$K_{\alpha\beta} = w_{,\alpha\beta} \quad (9)$$

where v_α are the in-plane displacements in the x and y -directions, respectively. In the numerical procedure, (8) is discretized by a FEM/Rayleigh-Ritz method of the type described in Jensen (1988). Some of the details involved in the analysis are described in Appendix B.

In Fig. 4 a comparison of the classical buckling stress with the numerical prediction obtained when the effects of contact are included is shown for $\nu = \frac{1}{3}$. This indicates that buckling of the film will occur if the normalized stress exceeds a critical value given by

$$\sigma^*/\sigma_c \cong 1.67 \quad \text{at } L/a \cong 2.6. \quad (10)$$

This is approximately a 35 percent correction to the results of Eq. (7).

The changes in the membrane stress $\Delta N = \Delta N_{yy} - h\sigma_{yy}$ and the bending moment $M = M_{yy}$ along the crack front can also be obtained from the numerical calculations for the post-buckling regime. The energy release rate and the phase angle of loading at the interface crack tip is then given by (Suo and Hutchinson, 1990)

$$G = \frac{6(1-\nu^2)}{Eh^3} \left[\frac{h^2}{12} \Delta N^2 + M^2 \right] \quad (11a)$$

$$\tan \psi = \frac{\tan \omega + \sqrt{12} M/(h\Delta N)}{1 - \tan \omega \sqrt{12} M/(h\Delta N)} \quad (11b)$$

where ω has been tabulated by numerical methods in Suo and Hutchinson (1990) as a function of the elastic mismatch for the bimaterial system. The ratio $M/(h\Delta N)$ determines the phase angle of the crack-tip loading; if $M/(h\Delta N) < 1/(\sqrt{12} \tan \omega)$

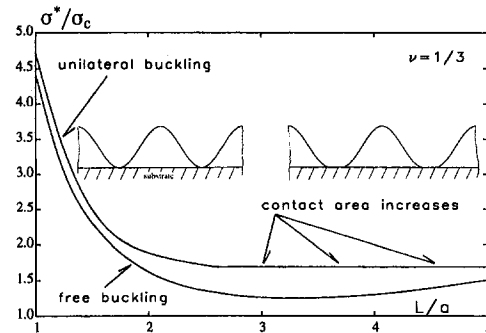


Fig. 4 Comparison of the buckling stress including effects of contact and the classical buckling stress. Typical variations with x for fixed y of the normal deflection are indicated.

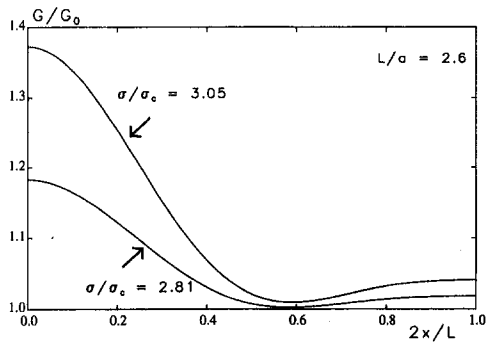


Fig. 5(a)

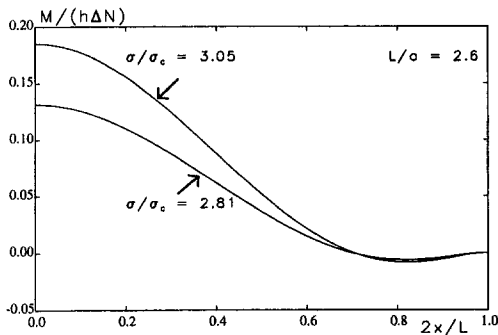


Fig. 5(b)

Fig. 5 Variation along the crack front of (a) normalized energy release rate and (b) ratio of effective crack-tip loads. Symmetry conditions are specified at $x = 0$ and $x = L/2$ and the stress state is equi-biaxial compression.

with $M > 0$ and $\Delta N > 0$, the crack sides are in contact over distances comparable to the film thickness. Contact of the crack faces within a film thickness from the tip due to the oscillations of the near-tip fields cannot be treated with the proposed numerical method. It is seen that the stress state in the bonded zone has to be specified in order to calculate the crack-tip quantities (11). In the following, equi-biaxial compression is assumed ($\sigma_{xx} = -\sigma$, $\sigma_{yy} = -\sigma$) and Poisson's ratio of the film is set to $\nu = \frac{1}{3}$.

Figures 5(a) and 5(b) show the variation of G/G_0 and $M/h\Delta N$ along the crack front at two values of stress in the post-buckling regime. The variations are shown over the half wavelength analysed (with symmetry conditions specified at $x = 0$ and $x = L/2$). The maximum values of G/G_0 and $M/h\Delta N$ along the crack front are shown in Figs. 6(a) and 6(b) as functions of σ/σ_c for three values of L/a . The significance of the buckling instability is clearly demonstrated by Fig. 6; at the stress $\sigma/\sigma_c = 3.05$ which is only 20 percent above the buckling stress for $L/a = 2.6$, the energy release rate has already increased 37 percent compared to the plane strain value (2). Furthermore, the ratio $M/h\Delta N$ has increased from 0 to 0.19, and experimental results in Thouless et al. (1992) show that a such increase in $M/h\Delta N$ may result in a decrease of the toughness Γ in (3) by as much as a factor 0.5.

3 Experiments

Three distinct sets of experiments were conducted; the first examined buckling in the absence of contact between the film and the substrate, the second examined the effect of substrate contact on buckling, and the third examined the mechanisms of delamination from an edge flaw. The system for all these experiments consisted of a thin sheet of mica bonded to a relatively thick block of aluminium by a thermosetting resin. Owing to the thermal-expansion mismatch between mica and alumin-

ium, an equi-biaxial, compressive stress ($\sigma_{xx} = -\sigma$, $\sigma_{yy} = -\sigma$) was induced in the bonded portion of the mica by cooling from the bonding temperature. The magnitude of this compressive stress was determined by measuring the curvature of a system consisting of mica bonded to a thin substrate by the same resin (Hutchinson et al., 1992). Mica is a particularly suitable material for the film in these model systems as it is transparent, elastic, relatively tough in a direction normal to the plane of the film, and it can be obtained in large sheets of very uniform thickness.

In the first set of experiments, a portion of the mica overhung the substrate by a distance a . When a was large this cantilevered portion buckled as shown in Fig. 7 upon cooling to room temperature. The wavelength of the buckling was measured optically for the different thicknesses of mica and for various values of a . The results are plotted in Fig. 8, which show the conditions required for the onset of buckling and the variation of the wavelength with σ^*/σ_c . Included in the figure is the prediction from Section 2.1 since there was no contact with the substrate.

In the second set of experiments, the mica did not overhang the substrate. Instead, a region of delamination was introduced up to a predetermined distance a by means of a razor blade inserted into the resin (Fig. 1). The sense of the mode II component drives such a crack to the mica-resin interface. Micrographs of the delaminated system after the razor blade had been withdrawn are shown in Fig. 2. It should be emphasized that no delamination took place in these experiments except for that introduced by the razor blade. The delamination front was approximately straight when introduced; other than some possible healing, it is still straight in all the micrographs in Fig. 2, and is located approximately at the maximum extent of the wavy profiles. The apparent waviness at the two largest crack lengths in this figure is caused by the crack faces being forced into contact over a portion of the delaminated region owing to extensive buckling. When buckling occurred, the profile could be examined by running a stylus over the surface of the mica, and a typical example of the profile is shown in Fig. 9. The wave-

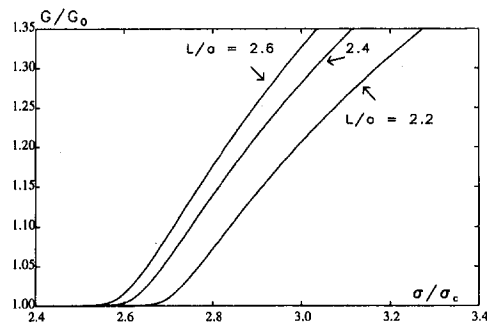


Fig. 6(a)

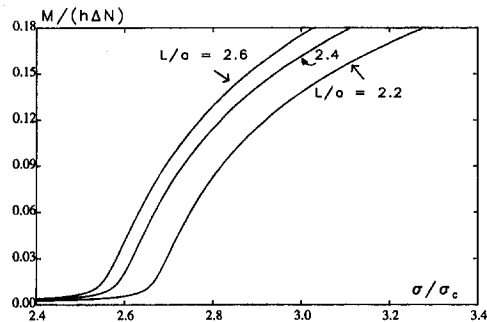


Fig. 6(b)

Fig. 6 Variation with compressive equi-biaxial stress of maximum values obtained along the crack front of (a) normalized energy release rate and (b) ratio of effective crack-tip loads

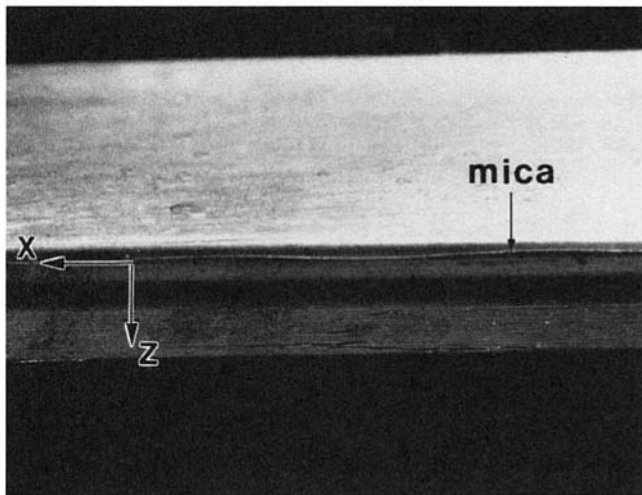


Fig. 7 Micrograph showing buckling of the mica film due to compression. There is no contact between the film and the substrate. The system is viewed edge on ($h \approx 28 \mu\text{m}$, $\sigma \approx 97 \text{ MPa}$, $a \approx 2.5 \text{ mm}$).

length of the buckling was measured optically and the results are plotted in Fig. 10. It should be noted that the criterion for the onset of buckling agrees very well with that predicted by the theory of Section 2.2. The initial wavelength, $L = 2.6a$, is also in excellent agreement with the experiments.

A final set of experiments examined the growth of an edge delamination under conditions of a gradually increasing equi-biaxial, compressive stress. Two distinct types of behavior were observed dependent on which of the conditions (3) or (10) was met first. When the initial delamination was small, crack propagation occurred simultaneously over the entire front. When the initial delamination was larger, the front did not move but, instead, tunnels of delamination developed at isolated portions along the front. The measurements made of the stress required to propagate the edge flaw are published in a companion paper (Thouless et al., 1994), but they show that there are circumstances under which delamination along the entire crack front can occur before the condition for buckling is met. This type of failure appears to be one of pure mode II crack growth with crack-tip closure. In contrast to this mechanism, delamination can occur at much lower stress levels if the buckling criterion is met before crack growth occurs.

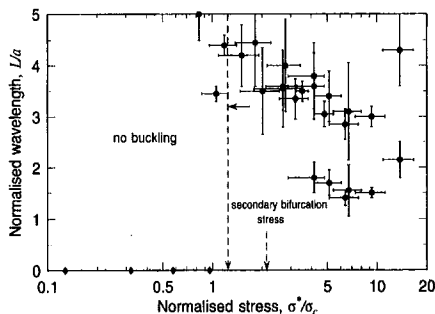


Fig. 8 Measured wavelength as a function of equi-biaxial compressive stress in the absence of contact between film and substrate. The lower set of data corresponds to what were clearly identifiable as higher-order buckling instabilities. The points marked with diamonds correspond to cases where buckling was not observed.

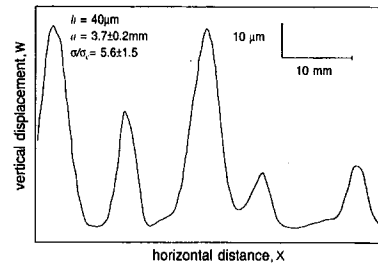


Fig. 9 Typical buckling profile of the mica film under the influence of contact between the film and substrate

4 Discussion

An edge flaw in a film which is subjected to either tension or compression can propagate when the energy-release rate equals the appropriate interfacial toughness (Eq. (3)). This is a very well-known result for a tensile film, and edge delamination has long been recognised as an important failure mechanism. That the same mechanism can also operate when the film is under a compressive stress is less well appreciated, owing to the fact that a mechanics analysis indicates that the crack tip is closed under such conditions. This crack-tip closure means that the crack is subjected to a pure mode II deformation with extensive frictional effects at the tip which can be expected to increase the apparent interfacial toughness dramatically. However, if the geometry is such that the buckling condition (10) is met before crack propagation occurs, then a transition in the failure mechanism can result in a lower delamination stress.

Once buckling has occurred, not only is the crack-driving force enhanced over portions of the crack front (Fig. 5(a)), but there are local regions where the film is lifted from the substrate resulting in the crack tip being open rather than closed (Fig. 5(b)). These perturbations in the stress state are responsible for the development of local areas of delamination after buckling which can eventually grow to cause failure of the coated system (Thouless et al., 1994). Edge crack buckling was apparently observed in Campbell (1990) in a system where sapphire was coated with SiC. Associated crack growth was not reported.

From Figs. 8 and 10, the experiments indicate that the value of L/a decreases at very high values of σ^*/σ_c . This decrease is probably caused by the onset of higher order instabilities that are beyond the scope of the analysis. From Fig. 6 it is seen that for relatively moderate post-buckling stresses there is no tendency for shorter wavelengths than $L/a = 2.6$ to release more energy at the interface crack tip, and thus they are not more likely to be observed. A post-buckling analysis, however, based on the numerical method described in Appendix B, in which a search for solutions not satisfying symmetry conditions

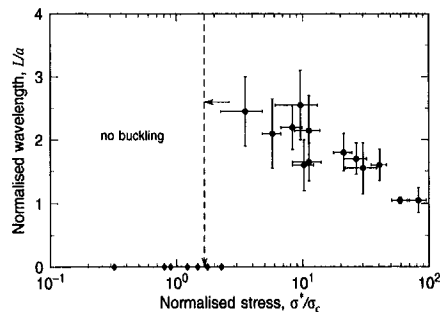


Fig. 10 Measured wavelength as a function of equi-biaxial compressive stress under the influence of contact between the film and substrate. The points marked with diamonds correspond to cases where buckling was not observed.

at $x = 0$ or $x = L/2$ was performed, showed such secondary bifurcations at stress levels 72 percent higher than the first bifurcation stress in the absence of contact. This result is included in Fig. 8 showing good agreement with experiments. It should also be noted that including into the numerical calculations some residual component of σ_{yy}^* in the delaminated region, due to friction between the film and the substrate, had a tendency to increase the critical stress (10) while decreasing the L/a ratio at buckling.

The discussion of the previous paragraphs has been devoted to delamination under an equi-biaxial stress state, as is appropriate for applications involving thin films. However, similar issues are pertinent for the delamination of composites which may be subjected to applied loads in addition to any residual stresses that may be present. In particular, Eq. (1) shows that buckling may be involved even if the remote stress components are tensile; i.e., buckling above an edge defect must be considered if $\sigma_{xx} < \nu\sigma_{yy}$. Similar failure mechanisms to those in Section 3 were observed experimentally for the same model system subject to combinations of residual stress and plane-strain bending for which $\sigma_{xx} < \nu\sigma_{yy}$, but it was not studied systematically, since it appeared to be similar in detail to the equi-biaxial results.

The nonstraight crack growth resulting from the buckling instability is studied in detail in Thouless et al. (1994) where it is seen that it has visual similarities with the Taylor instability which can occur in an adhesive interlayer (McEwan and Taylor, 1966, Fields and Ashby, 1976 and Conley et al., 1992). However, the mechanisms causing these two instabilities are entirely different and, since they can occur in identical systems, caution should be taken not to mistake them. This holds especially for cases where buckling is induced by remote tensile loads.

Finally, it is noted that the condition (10) is independent of whether the edge crack lies at an interface; buckling—and from this the enhancement of the energy release rate (Fig. 5(a))—should be considered also for edge cracks in homogeneous materials.

Acknowledgments

The contributions of E. G. Liniger to the experimental measurements are gratefully acknowledged.

References

- Campbell, G. H., 1990, "The Role of Interfaces in Whisker Toughening of Ceramics," Ph.D. thesis, University of California, Santa Barbara, CA.
- Chai, H., Babcock, C. D., and Knauss, W. G., 1981, "One Dimensional Modeling of Failure in Laminated Plates by Delamination Buckling," *International Journal of Solids and Structures*, Vol. 17, pp. 1069–1083.
- Conley, K. M., Gu, W., Ritter, J. E., and Lardner, T. J., 1992, "Observations on Finger-like Crack Growth at a Urethane Acrylate/Glass Interface," *Journal of Adhesion*, Vol. 39, pp. 173–184.
- Evans, A. G., and Hutchinson, J. W., 1984, "On the Mechanics of Delamination and Spalling in Compressed Films," *International Journal of Solids and Structures*, Vol. 20, pp. 455–466.
- Fields, R. J., and Ashby, M. F., 1976, "Finger-like Crack Growth in Solids and Liquids," *Philosophical Magazine*, Vol. 33, pp. 33–48.
- Hutchinson, J. W., Thouless, M. D., and Liniger, E. G., 1992, "Growth and Configurational Stability of Circular, Buckling-driven Thin Film Delaminations," *Acta Metallurgica et Materialia*, Vol. 40, pp. 295–308.
- Jensen, H. M., 1988, "Collapse of Hydrostatically Loaded Cylindrical Shells," *International Journal of Solids and Structures*, Vol. 24, pp. 51–64.
- Jensen, H. M., 1993, "Energy Release Rates and Stability of Straight-sided, Thin-film Delaminations," *Acta Metallurgica et Materialia*, Vol. 41, pp. 601–607.
- McEwan, A. D., and Taylor, G. I., 1966, "The Peeling of a Flexible Strip Attached by a Viscous Adhesive," *Journal of Fluid Mechanics*, Vol. 26, pp. 1–15.
- Nilsson, K.-F., Thesken, J. C., Sindelar, P., Giannakopoulos, A. E., and Storåkers, B., 1993, "A Theoretical and Experimental Investigation of Buckling Induced Delamination Growth," *Journal of the Mechanics and Physics of Solids*, Vol. 41, pp. 749–782.
- Stringfellow, R. G., and Freund, L. B., 1993, "The Effect of Interfacial Friction on the Buckle-driven Spontaneous Delamination of a Compressed Thin Film," *International Journal of Solids and Structures*, Vol. 30, pp. 1379–1395.

Suo, Z., and Hutchinson, J. W., 1990, "Interface Crack between Two Elastic Layers," *International Journal of Fracture*, Vol. 43, pp. 1–18.

Thouless, M. D., Hutchinson, J. W., and Liniger, E. G., 1992, "Plane-strain, Buckling-driven Delamination of Thin Films: Model Experiments and Mode-II Fracture," *Acta Metallurgica et Materialia*, Vol. 40, pp. 1281–1286.

Thouless, M. D., Jensen, H. M., and Liniger, E. G., 1994, "Delamination from Edge Flaws," *Proceedings of the Royal Society of London*, Vol. A447, pp. 271–279.

APPENDIX A

In-Plane Crack Perturbation Analysis

For completeness, a perturbation analysis of the straight edge crack is given in this appendix to verify that buckling is the only mechanism causing the observed instabilities. As stated earlier, the interface is assumed to have a sufficiently low toughness that the crack remains at the interface. Assume no buckling has occurred, and that the crack front is perturbed by

$$y^p(x) = a \left[1 + \epsilon \cos \left(\frac{2\pi x}{L} \right) \right] \quad (A1)$$

where ϵ ($\epsilon \ll 1$) is the perturbation amplitude, and $()^p$ refers to state variables in the perturbed region. The in-plane equilibrium equations and the clamped/free boundary conditions consistent with $h \ll a$ are (Jensen, 1993)

$$\sigma_{\alpha\beta,\beta}^p = 0 \quad (A2a)$$

$$\sigma_{yy}^p = \sigma_{xy}^p = 0 \quad \text{at free edge } (y = 0) \quad (A2b)$$

$$v_x^p = 0, v_y^p = -a\epsilon_{yy}^0 \quad \text{at crack front } (y = a) \quad (A2c)$$

where ϵ_{yy}^0 is the strain in the unperturbed delaminated region. The solution to (A2) can be obtained in closed form and the energy release rate along the perturbed crack front is calculated from (11a) and is given by

$$G^p = G_0 \left[1 + \epsilon g \cos \left(\frac{2\pi x}{L} \right) \right]$$

$$g = \frac{2\eta(e^{2\eta} - 1 - 2\eta e^\eta)}{(1 + \nu)(\nu - 3)(1 + e^{2\eta}) - e^\eta[10 - 4\nu + 2\nu^2 + \eta^2(1 + \nu)^2]} \quad (A3)$$

where $\eta = \pi a/L$. The in-plane perturbation introduces no bending moment at the crack front and thus no change in the phase angle of loading to lowest order in ϵ . The stable mode is therefore given by the value of η which releases the most energy at the crack tip. Inspection of g in Eq. (A3) shows that $g < 0$ for $\eta > 0$, and $g = 0$ for $\eta = 0$ for all ν where $0 \leq \nu \leq \frac{1}{2}$. The lowest order contribution to G_0 is therefore always negative for any perturbation of the straight crack front that advances ahead of this front, and the straight-sided shape of the crack front must always be stable prior to buckling (assuming linear elastic material behavior).

APPENDIX B

Numerical Formulation

In the numerical procedure, the incremental form of the principle of virtual work, (8), is formulated using displacements as free variables. By a combination of (9) and Hookes law, (8) is discretized in displacement space. The variation with x of all the displacements is represented by four Hermitian cubics $H_i(s)$ ($0 \leq s \leq 1$) in N (typically 20) subelements. Only a half-buckling wavelength is analysed, i.e., $0 \leq x \leq L/2$, and symmetry conditions at $x = 0$ and $x = L/2$ are specified. The variation of displacements in the y -direction is represented by J (typically seven) Chebyshev polynomials $T_j(t)$ ($-1 \leq t \leq 1$) modified

to meet the clamped-free boundary conditions at $t = 1$ and $t = -1$, respectively. This means that in each subelement

$$\begin{Bmatrix} v_\alpha \\ w \end{Bmatrix} = \sum_{i=1}^4 \sum_{j=0}^J \begin{Bmatrix} v_\alpha^{ij} \\ w^{ij} \end{Bmatrix} T_j(t) H_i(s) (1-t) \begin{Bmatrix} 1 \\ 1-t \end{Bmatrix}. \quad (\text{B1})$$

The integrations in (8) are performed numerically with four Gauss integration points in the s -direction in each element and, typically, 16 Gauss integration points in the interval $-1 \leq t \leq 1$.

In (8), the terms on the left-hand side contribute to the FEM-stiffness matrix and the right-hand side gives the loads. The last two terms on the right-hand side of (8) are equilibrium correction terms. It is seen that the prestresses, $N_{\alpha\beta}^0$, result in a symmetric contribution to the stiffness matrix and, additionally, a load term.

Contact between the film and substrate is modelled by treating the substrate as an elastic foundation acting only if the film deformations are negative (penetration into the substrate). The stiffness is chosen to be sufficiently high that the negative deformations of the film are negligible compared to outwards deflections. Frictionless sliding between the film and substrate is assumed to occur in the contact zone.

The bifurcation stress is found for a given value of L/a by initially adding a small imperfection to the system. Increments of either stress or displacement are then specified until the bifurcation point has been passed. The imperfection is then removed, and the sign of the specified increment is reversed. In this way, the bifurcation point is approached via the post-buckling path, as shown schematically in Fig. B1. For the case of a vanishing substrate stiffness, the numerical results are in very close agreement with the analytical results of Section 2.1.

This procedure for finding the bifurcation stress is repeated for different L/a ratios until the stress reaches a minimum value (at $L/a = 2.6$ for $\nu = \frac{1}{3}$ cf. Fig. 4). As indicated in Fig. 4 larger values of L/a increases the contact area without affecting the bifurcation stress or the deformation in the film which has lifted off the substrate. In practice, this part of the curve would not

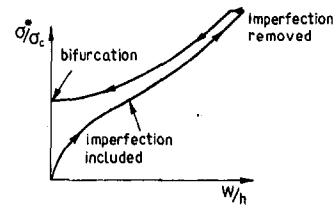


Fig. B1 Illustration of the numerical method used to find the bifurcation stress for a geometrically constrained problem.

be observed because the flat parts of the film will be critically stable in the sense that any small imperfection would trigger a new buckle.

The algorithm for finding the bifurcation stress differs from that suggested by Nilsson et al. (1993) where an iterative procedure is formulated starting with the buckling mode in the absence of contact. An attempt to compare the two algorithms has not been made.

The numerical calculation of the secondary bifurcation stresses discussed in Section 4 and shown in Fig. 8 are carried out for the case of buckling without contact between the film and the substrate, only. This means that only one quarter of a buckling wavelength needs to be considered under the boundary conditions

$$\begin{aligned} \dot{v}_1 = \dot{v}_{2,x} = \dot{w}_x &= 0 \quad \text{at } x = 0 \\ \dot{v}_1 = \dot{v}_{2,x} = \dot{w} &= 0 \quad \text{at } x = L/4. \end{aligned} \quad (\text{B2})$$

At each step in the incremental loading procedure, the sign of the determinant of the FEM-stiffness matrix is checked under nonsymmetric boundary conditions. For $\nu = \frac{1}{3}$ and $L/a = 3.3$, initial bifurcation occurs at $\sigma^*/\sigma_c = 1.24$ (Eq. 7) and secondary bifurcation occurs at $\sigma^*/\sigma_c = 2.13$ in a mode satisfying the following boundary conditions:

$$\begin{aligned} \dot{v}_{1,x} = \dot{v}_2 = \dot{w} &= 0 \quad \text{at } x = 0 \\ \dot{v}_{1,x} = \dot{v}_2 = \dot{w}_x &= 0 \quad \text{at } x = L/4. \end{aligned} \quad (\text{B3})$$

H. C. Wu
Professor,
Fellow ASME.

J. K. Lu¹
Graduate Student.

W. F. Pan²
Graduate Assistant.

Department of Civil Engineering,
The University of Iowa,
Iowa City, IA 52242

Some Observations on Yield Surfaces for 304 Stainless Steel at Large Prestrain

Experiments to study the yield surface of 304 stainless steel with either 20 percent tension or 20 percent shear prestrain have been conducted. Explicit transformation equations have also been derived to convert the experimentally determined first Piola-Kirchhoff stress components into the Cauchy stresses and the second Piola-Kirchhoff stresses for combined axial-torsional experiments. It has been found that, in the phenomenological approach, the stress measure and the definition of yield have significant effect on the degree of anisotropy of strain-hardening. In particular, the strain-hardening rule is extremely complicated if the second Piola-Kirchhoff stress is used. Also, the equivalent stress-strain curves have been investigated by means of different stress measures.

1 Introduction

The yield condition is one of the most important properties in the study of elastic-plastic deformation. This condition presents itself in the form of yield surface in the stress space. Previous investigators have shown that the yield surface translates and distorts from the initial state when it is subjected to preloading histories. Typical experiments to determine the yield surfaces are reported in Ivey (1961), Mair and Pugh (1964), Phillips and his co-workers (1972, 1973, 1974, 1984), Marjanovic and Szczepinski (1975), Shiratori et al. (1976), and Wu and Yeh (1991). Because of the small strain range and the small proof strain (or deviation from linearity) definition of yield, almost no cross effect was found in the cited experiments under axial, shear, or combined axial shear prestrain histories. The amount of translation and the degree of distortion of yield surface is determined by the loading path and the extent of loading.

In the finite deformation range, even though the strain hardening and anisotropy during plastic deformation are determined uniquely by the dislocation and texture development of the material, there are two major factors affecting the size, shape, and translation of yield surface, if the yield surface is being determined by use of the phenomenological concept as it has been done in the aforementioned experiments in the small strain range. The first factor is the stress measure. When the axial strain is large and the cross-sectional area changes, the differences among stress measures (the Cauchy, the first Piola-Kirchhoff, and the second Piola-Kirchhoff stresses) are then significant. The second factor is the definition of yield. Methods (Lode extrapolation, proof strain, and proportional limit) for determining the yield point and the magnitude of proof strain for judging the occurrence of yield may also strongly influence the shape and size of the yield surface. This point is of interest, since in the case of large strain, the elastic strain is usually negligible. And, in this case, question arises as to whether a proof strain

of five microstrain ($\mu\epsilon = 10^{-6}$) should be used to define yield as in the case of small deformation or should a larger amount of proof strain be used? Both factors affect the evolution rules for isotropic and kinematic hardening from the phenomenological view point.

In this paper, we investigate the translation and distortion of yield surface either subjected to a 20 percent axial or 20 percent engineering shear prestrain for 304 stainless steel. Based on the transformation equations among stress measures to be presented, the experimental data of Wu and Yeh (1991) and some new experimental data by us, we present the initial and subsequent yield surfaces in the stress space of different stress measures. We shall refer to these yield surfaces as the Cauchy yield surface, the first Piola-Kirchhoff (or 1st P-K for short) yield surface and the second Piola-Kirchhoff (or 2nd P-K for short) yield surface. Based on the transformation equations, it is found that significant differences in the yield surface of different stress measures exist even when the axial prestrain is only of a moderate amount of 20 percent. These differences increase with the increasing amount of prestrain. Furthermore, we found a rotation in the 2nd P-K yield surface in the case of pure shear prestrain. This effect is not generally known and may have significant consequences in the quest for a hardening rule for yield surface.

Even though the physics of plastic deformation is independent of the stress measure, the use of different stress measures to provide different representations of the same phenomenon do call for consistent descriptions for all aspects of the constitutive equation, i.e., the hardening rule of yield surface and the flow rule may depend on the stress measure as well. These problems should be further investigated.

The equivalent stress of each stress measure for tension or pure torsion has also been determined and used to demonstrate the anisotropic rate of strain hardening, i.e., the rate of strain hardening with axial prestrain is different than that with shear prestrain. Different amounts of proof strain used to define yield have also been shown to significantly affect the extent of isotropic and kinematic hardening.

2 Relations Among Stress Measures for Thin-Walled Tubes

In this section, we establish relations among the stress measures which will be used in the discussions related to the determination of yield surfaces by use of thin-walled tubular specimens. The following relations among the 1st P-K stress π , the

¹ Currently Associate Professor, Department of Civil Engineering, National Pingtung Polytechnic Institute, Taiwan.

² Currently Associate Professor, Department of Engineering Science, National Cheng Kung University, Taiwan.

Contributed by the Applied Mechanics Division of THE AMERICAN SOCIETY OF MECHANICAL ENGINEERS for publication in the ASME JOURNAL OF APPLIED MECHANICS.

Discussion on this paper should be addressed to the Technical Editor, Prof. Lewis T. Wheeler, Department of Mechanical Engineering, University of Houston, Houston, TX 77204-4792, and will be accepted until four months after final publication of the paper itself in the ASME JOURNAL OF APPLIED MECHANICS.

Manuscript received by the ASME Applied Mechanics Division, June 29, 1990; final revision, May 10, 1994. Associate Technical Editor: R. M. McMeeking.

2nd P-K stress \mathbf{P} , and the Cauchy stress $\boldsymbol{\sigma}$ are usually found in the literature:

$$\boldsymbol{\sigma} = J^{-1} \mathbf{F} \cdot \boldsymbol{\pi} \quad (1)$$

$$\mathbf{P} = \boldsymbol{\pi} \cdot (\mathbf{F}^{-1})^T \quad (2)$$

where J is the Jacobian and \mathbf{F} is the deformation gradient of the transformation that describes the deformation of the continuum. Notation $(\)^T$ denotes the transpose of a tensor. From Eqs. (1) and (2), we note that the deformation gradient \mathbf{F} plays a major part and will be first determined.

Considering the axial-torsion of a thin-walled tube, we use two sets of cylindrical coordinates $(X^1, X^2, X^3) = (R, \Theta, Z)$ and $(x^1, x^2, x^3) = (r, \theta, z)$ to describe the undeformed and deformed status, respectively. The two sets of coordinates are related by

$$\begin{aligned} r &= \beta_m R_m - \beta_2 (R_m - R) = (\beta_m - \beta_2) R_m + \beta_2 R \\ \theta &= \Theta + \varphi \beta_3 Z \\ z &= \beta_3 Z \end{aligned} \quad (3)$$

in the range of $R_1 \geq R \geq R_0$, where R_1 and R_0 are the undeformed outer and inner radii, respectively; and $r_1 \geq r \geq r_0$, where r_1 and r_0 are the deformed outer and inner radius, respectively; $\beta_m = (r_m/R_m)$ describes the stretch ratio of the mean radii which are denoted by R_m and r_m in the undeformed and deformed status, respectively; $\beta_2 = (h/H)$ describes the stretch ratio of the wall thicknesses, which are denoted by H and h in the undeformed and deformed status, respectively; $\beta_3 = (z/Z)$ describes the deformation in the axial direction, which is denoted by Z and z in the undeformed and deformed status, respectively; and φ is the angle of twist per unit deformed length and is related to the shear strain 2η by

$$2\eta = r\varphi. \quad (4)$$

We note that if the value of β_i ($i = m, 2, 3$) is greater than one, then it implies stretching; if it is equal to one, then there is no length change; and there is contraction when this value is less than one. Taylor and Quinney (1932) found that the hoop and radial strains are not equal for a thin-walled tube under combined tension-torsional loading condition. According to Taylor and Quinney, the values of β_m and β_2 are the same for the tension only condition but are different and depend on the constitutive equations used for the combined tension-torsional loading condition. Usually, the stresses in the experimental data are the physical components in the cylindrical-coordinates system, so that all stress components have the same unit.

The physical components of deformation gradient \mathbf{F} is found from (3) as

$$\mathbf{F} = \begin{bmatrix} \beta_2 & 0 & 0 \\ 0 & \frac{r}{R} & \varphi \beta_3 r \\ 0 & 0 & \beta_3 \end{bmatrix} = \begin{bmatrix} \beta_2 & 0 & 0 \\ 0 & \beta_m & 2\eta \beta_3 \\ 0 & 0 & \beta_3 \end{bmatrix}. \quad (5)$$

The last expression of Eq. (5) is found by considering the mean radius of the tube, where $R = R_m$, $r = r_m = \beta_m R_m$ and $2\eta = r_m \varphi$. It may be shown that Eq. (5) is same as that obtain by McMeeking (1982). The inverse of the above matrix is

$$\mathbf{F}^{-1} = \begin{bmatrix} \beta_2^{-1} & 0 & 0 \\ 0 & \beta_m^{-1} & -R_m \varphi \\ 0 & 0 & \beta_3^{-1} \end{bmatrix}. \quad (6)$$

When the material is incompressible, which is a reasonable assumption for metallic materials undergoing large plastic deformation, the Jacobian is

$$J = \beta_2 \beta_3 \beta_m = 1. \quad (7)$$

We now proceed to find the relations among the components of $\boldsymbol{\sigma}$, $\boldsymbol{\pi}$, and \mathbf{P} . For the case of thin-walled tube under axial-torsional loading condition, the stress states of $\boldsymbol{\sigma}$, $\boldsymbol{\pi}$, and \mathbf{P} are given by their respective physical components as

$$\begin{aligned} \boldsymbol{\sigma} &= \begin{bmatrix} 0 & 0 & 0 \\ 0 & 0 & \tau \\ 0 & \tau & \sigma \end{bmatrix} & \boldsymbol{\pi} &= \begin{bmatrix} 0 & 0 & 0 \\ 0 & \pi^{\theta\theta} & \pi^{\theta z} \\ 0 & \pi^{z\theta} & \pi^{zz} \end{bmatrix} \\ \text{and } \mathbf{P} &= \begin{bmatrix} 0 & 0 & 0 \\ 0 & P^{\theta\theta} & P^{\theta z} \\ 0 & P^{z\theta} & P^{zz} \end{bmatrix} \end{aligned} \quad (8)$$

in which $\sigma^{zz} = \sigma$ is the axial stress, which is equal to the axial force divided by $2\pi r_m h$; $\sigma^{\theta z} = \sigma^{z\theta} = \tau$ is the shear stress, which is equal to the torque divided by $2\pi r_m^2 h$; $\sigma^{\theta\theta} = 0$ due to symmetry and $\sigma^{rr} = 0$ due to no surface tractions on both the inner and outer lateral surfaces of the tube. The last condition is an approximation, but it is justifiable when the wall is thin. Substituting Eqs. (5), (6), and (8) into (1) and (2), we obtain

$$\boldsymbol{\sigma} = \begin{bmatrix} 0 & 0 & 0 \\ 0 & \beta_m \pi^{\theta\theta} + \varphi R_m \beta_m \beta_3 \pi^{z\theta} & \beta_m \pi^{\theta z} + \varphi R_m \beta_m \beta_3 \pi^{zz} \\ 0 & \beta_3 \pi^{z\theta} & \beta_3 \pi^{zz} \end{bmatrix} \quad (9)$$

$$\boldsymbol{\pi} = \begin{bmatrix} 0 & 0 & 0 \\ 0 & -\tau R_m \varphi & \frac{1}{\beta_m} (\tau - \varphi R_m \beta_m \sigma) \\ 0 & \frac{\tau}{\beta_3} & \frac{\sigma}{\beta_3} \end{bmatrix} \quad (10)$$

and

$$\mathbf{P} = \begin{bmatrix} 0 & 0 & 0 \\ 0 & \frac{1}{\beta_m} (\pi^{\theta\theta} - \varphi R_m \beta_m \pi^{\theta z}) & \frac{\pi^{\theta z}}{\beta_3} \\ 0 & \frac{1}{\beta_m} (\pi^{z\theta} - \varphi R_m \beta_m \pi^{zz}) & \frac{\pi^{zz}}{\beta_3} \end{bmatrix}. \quad (11)$$

The component $\pi^{z\theta}$, which equals the torque divided by $2\pi R_m H r_m$, and the component π^{zz} , which equals the axial force divided by $2\pi R_m H$, are known quantities from experiment, where R_m is the mean radius of the tube in the undeformed configuration and an approximated r_m may be obtained by measuring the deformed outer radius r_1 and then subtracting $H/2$ from it. For convenience, most experimental results in the literatures are presented in terms of the 1st P-K stress components π^{zz} and $\pi^{z\theta}$. However, this is only of an approximated nature since r_m is not measured in most experiments. The current wall thickness h is very difficult to measure.

The other components of $\boldsymbol{\pi}$ cannot be readily determined experimentally in the case considered. However, they may be expressed in terms of π^{zz} and $\pi^{z\theta}$. To this end, we obtain, from (8) and (9), the following relations:

$$\sigma^{\theta\theta} = 0 = \beta_m \pi^{\theta\theta} + \varphi R_m \beta_m \beta_3 \pi^{z\theta} \quad (12)$$

$$\sigma^{\theta z} = \tau = \beta_m \pi^{\theta z} + \varphi R_m \beta_m \beta_3 \pi^{zz} \quad (13)$$

$$\sigma^{z\theta} = \tau = \beta_3 \pi^{z\theta} \quad (14)$$

$$\sigma^{zz} = \sigma = \beta_3 \pi^{zz}. \quad (15)$$

Equation (12) leads to

$$\pi^{\theta\theta} = -\varphi R_m \beta_3 \pi^{z\theta}. \quad (16)$$

By substituting Eq. (14) into (13), we obtain

$$\pi^{tz} = \frac{1}{\beta_m} (\beta_3 \pi^{z\theta} - \varphi R_m \beta_m \beta_3 \pi^{zz}). \quad (17)$$

Thus, all components of the 1st P-K stress may be determined.

By using Eqs. (14) and (15), Cauchy stress components may be calculated. In view of Eq. (8), the state of Cauchy stress can be completely determined. It is seen that when the axial strain is equal to zero, i.e., $\beta_3 = 1$, we have $\sigma^{z\theta} = \pi^{z\theta}$ and $\sigma^{zz} = \pi^{zz}$. But if the axial strain is large, then the difference between the two measures can be large. These transformation equations are used in the next section where we compare theoretical predictions of yield surfaces with experimental data.

For the axial prestrain only condition, we have β_m equaling β_2 (Taylor and Quinney (1932)). From Eq. (7), we then obtain the relations among β_i as

$$\beta_m = \beta_2 = \sqrt{\frac{1}{\beta_3}}. \quad (18)$$

For the torsional prestrain only condition, all values of β_i 's may be approximated by one. This may be estimated by use of experimental results of Wu and Xu (1989) for pure torsion of 304 stainless steel. It has been found that for an angle of relative grip rotation of 32.5 deg, φ is 12.76 rad/m and the corresponding engineering shear strain is 10.3 percent, which gives rise to an axial strain ϵ of 0.23 percent. By using Eq. (3), we found that $\beta_3 = 1.0023$, which may be approximated by one in this case. Since the diameter of the thin-walled tube undergoes a small amount of change during pure torsion, we obtain the following approximated relations among β_i :

$$\beta_m \cong \beta_2 \cong \beta_3 \cong 1. \quad (19)$$

These relations will be used in the next section and will be further discussed.

3 Experimental Determination of Yield Surfaces

Experiments were conducted, by use of a computer-controlled, axial-torsional, closed-looped, electrohydraulic MTS materials test system. The same batch of annealed 304 stainless steel specimens as in Wu and Yeh (1991) was used in this investigation. Tubular specimens were machined from annealed 25 mm (1 in.) round bars in an as-received condition. The specimens have a uniform gage section with enlarged ends. The gage section has a nominal dimension of 15 mm (0.6 in.) in the outside diameter and 1.3 mm (0.05 in.) wall thickness. More detailed information about the material and specimens may be found in Wu and Yeh (1991).

Strain was measured by rosette strain gages applied on the exterior surface in the middle section of the specimens. All tests to determine the yield surfaces were strain-controlled at a constant strain rate of 5×10^{-6} per second.

We used the proof strain method to determine yield points. Yield is defined to occur when axial and torsional stress-strain curves deviate from the elastic line by a specified amount of proof strain $\Delta\hat{\epsilon}$ which is defined as

$$\Delta\hat{\epsilon} = \sqrt{\Delta\epsilon^2 + \frac{4}{3}\Delta\eta^2} \quad (20)$$

where $\Delta\epsilon$ is the axial and $2\Delta\eta$ is the engineering shear strain increment. We used $\Delta\hat{\epsilon} = 5$ microstrains which was a very small strain and was sensitive to factors such as elastic moduli, the zero offset strain, the elastic domain, and the probing path as discussed in Wu and Yeh (1991). The probing of yield surfaces followed the procedures described in that paper even though in the present case the prestrains were finite.

Experiments were conducted for two loading paths. For each path, the initial and a subsequent yield surface were determined. These two paths are further described as follows:

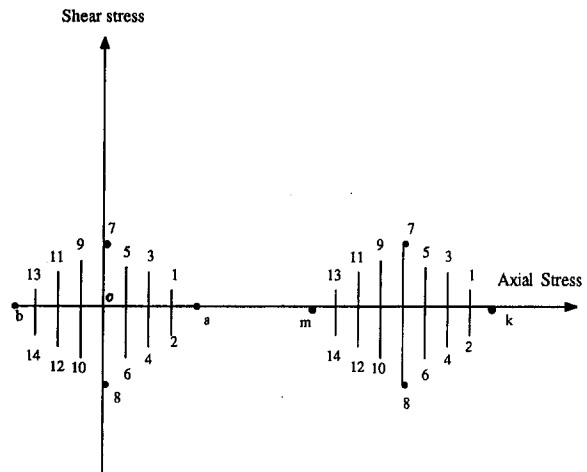


Fig. 1(a) Probing paths for Path 1 loading

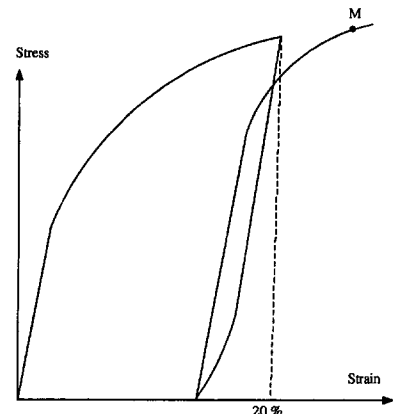


Fig. 1(b) A schematic axial stress-strain curve

Path 1. Loading in the axial direction. The initial yield surface was first determined. The probing paths in the axial-shear stress space for the initial and subsequent yield surfaces for this path are shown in Fig. 1(a). The numbers in the figure denote the sequence of yield point probing.

After completed the determination of the initial yield surface, we switched the control mode of test machine from "strain" to "stroke." The specimen was then stretched to 20 percent axial strain in stroke control, and subsequently unloaded to zero axial load (zero nominal stress). We then removed the specimen from the test machine and installed a new strain gage on it. The specimen was then reset on the machine and loaded gradually to move the stress-strain curve back to merge with the original stress-strain curve by checking the stress magnitude. Figure 1(b) shows schematically the specimen strained to 20 percent, unloaded to zero stress, and then restrained to point *M* which had the same stress as the previous high before unstraining. At this amount of prestrain we determined the corresponding subsequent yield surface. The probing path of this yield surface is shown in the right side figure of Fig. 1(a) as previously mentioned. Note that point *k* in Fig. 1(a) corresponds to the stress represented by point *M* in Fig. 1(b).

Path 2. Loading in the shear direction. The initial and subsequent yield surfaces were determined by a similar procedure as in Path 1. However, the directions of probing paths were different. They were parallel to the axial stress direction. The determination of the subsequent yield surface following a 20 percent shear prestrain also required a procedure that included the unloading and removal of the specimen and the installation of a new strain gage on the specimen before the probing for yield points.

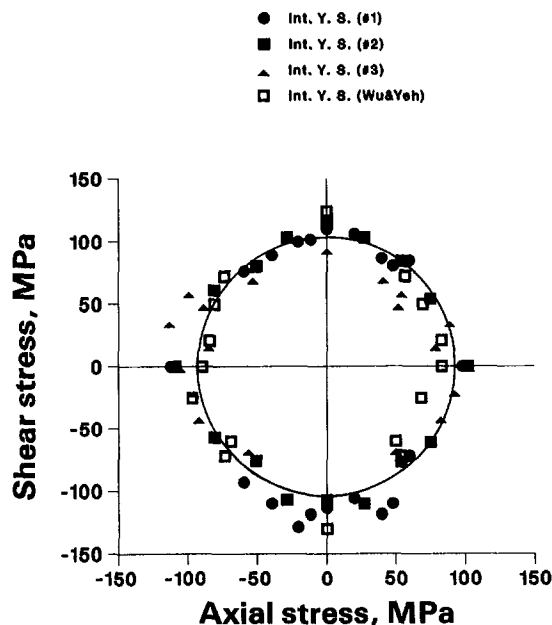


Fig. 2 The initial yield surface

Three specimens of annealed 304 stainless steel were tested. Specimens #1 and #2 were tested with Path 1 loading history and the results of these two specimens agree closely. Specimen #3 had Path 2 loading history. Figure 2 shows the experimental data of the initial yield surface for the three specimens tested together with the results obtained by Wu and Yeh (1991) for the same material. This figure is drawn in the 1st P-K stress space by using the axial stress divided by $\sqrt{3}$ as the horizontal axis and the shear stress as the vertical axis. It is seen that the initial yield surface may well be approximated by the Mises yield criterion (a circle). Deviation of some data points from the circle might be caused by the machining effect of specimens, since the specimens have not been heat treated after machining. However, the machining effect does not pose any problem for the subsequent yield surfaces. Figure 3 shows both the initial Mises yield surface (the circle) and subsequent yield surfaces (curves with data points) of specimens #1, #2, and #3 in the 1st P-K stress space. The figure is again drawn by using the axial stress divided by $\sqrt{3}$ as the horizontal axis and the shear stress as the vertical axis. The results obtained by Wu and Yeh (1991) for small deformation (with less than one percent prestrain) are also shown by solid curves without data points to illustrate the differences in the translation and distortion of yield surface at two different prestrain levels. It can be seen that the characteristics and the magnitude of translation and distortion of the yield surface depend significantly on the loading path and the pre-strain level.

The subsequent yield surfaces can be separated into the forward and rear parts by a hyperplane which passes through the center of the yield surface and is perpendicular to the loading path (Phillips and Weng, 1975). It is seen from Fig. 3 that both the forward and rear parts deflate as the loading proceeds. This observation contradicts with what is known at the small strain level, where the forward part inflates. Another observation which also deviates from the general understanding at the small prestrain level is that, for a prestrain of only 20 percent, the cross effect is very significant for the material tested. Specifically, for a prestrain of 20 percent in the axial direction, the maximum magnitude of shear stress on the subsequent yield surface has a significant reduction compared to the corresponding stress magnitude on the initial yield surface; and, in the case of shear prestrain of 20 percent, the axial stress on the subsequent yield surface is increased. This cross effect was not apparent in the

work of Wu and Yeh (1991) for the same material at small strain level, and was also absent in the works of Phillips and co-workers (1972, 1973, 1974, 1984) for 1100-0 aluminum in the small strain range.

It is of interest to compare the present result with those of Helling et al. (1986) who tested 1100 aluminum, 70:30 brass and 2024 aluminum alloy with prestrains in shear in the range of 1.2 ~ 32 percent. These authors observed the distortion of the subsequent yield surface, but with well rounded forward part. Furthermore, they observed a large expansion in the size of the yield surface for 1100 aluminum, a little expansion for 70:30 brass and a little contraction for 2024 aluminum alloy. Some of these differences as compared to the present results could be due to the different materials used and could also be due to different methods used in the determination of yield surfaces. Although the proof strain was also $5\mu\epsilon$, Helling et al. (1986) had radial probing paths versus the paths of the present investigation shown in Fig. 1(a). Furthermore, while the present probing was strain controlled, the probing of Helling et al. (1986) was load and torque controlled.

The magnified unloading stress-strain curve of specimen #1 is shown in Fig. 4(a). The intersections of the unloading curve with parallel straight lines that have the slope equal to Young's modulus indicate the different yield points defined by different amounts of proof strain (P.S.). Figure 4(b) shows the experimental results with data points of the subsequent yield surface defined by a $5\mu\epsilon$ proof strain and the projected subsequent yield surfaces (dashed lines) for various proof strains. These projected surfaces are drawn based on only two yield points marked on the axial stress axis and experimentally determined by different proof strains shown in Fig. 4(a). It is seen that with different amounts of proof strain, significantly different features in the yield surfaces may be observed, both qualitatively and quantitatively. With a large proof strain, the distortion of yield surface becomes less apparent.

After the subsequent yield surface was found, the specimen was removed from the test machine and cut through the cross section in the middle of the gage section. By measuring the change of the cross-sectional area, it was found that the reduction of the cross-sectional area was 17 percent for specimens #1 and #2 and no observable area change was found for specimen #3.

We now investigate the effect of stress measure on the shape, size, and translation of the yield surface. Figure 5 shows, in the middle of the figure, the subsequent yield surface for specimen #1 using the 1st P-K stress components. These stress components are determined from the experimental data. The experimental results for specimen #2 agree very closely with those of specimen #1, but are not shown in the figure. Also shown in the figure are the theoretical yield surfaces of the Cauchy

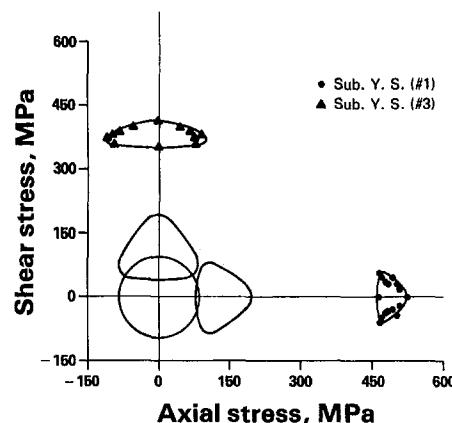


Fig. 3 Initial and subsequent yield surfaces

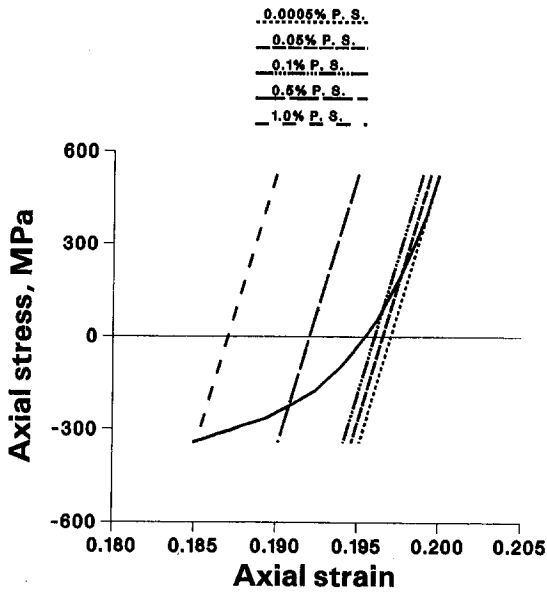


Fig. 4(a) Determination of yield point by different proof strains

- 0.0005% P. S.
- 0.05% P. S.
- ▲ 0.1% P. S.
- 0.5% P. S.
- 1.0% P. S.

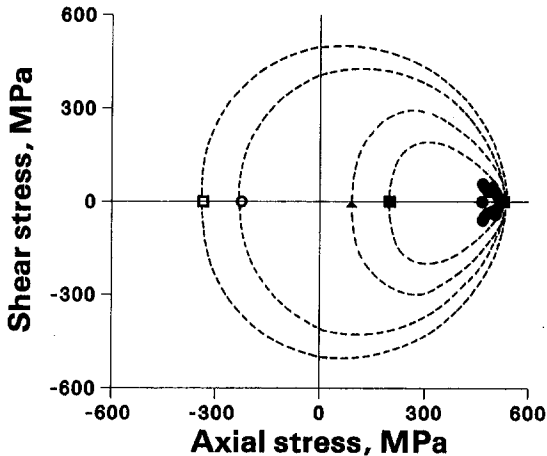


Fig. 4(b) Projected yield surfaces for different proof strains

stress components determined from Eqs. (8), (14), and (15) and the 2nd P-K stress components obtained by Eq. (11). As an independent verification, the Cauchy yield surface is again determined from the experimental Cauchy stress components which was obtained based on the measured deformed area. The agreement between the two Cauchy yield surfaces is generally good. However, it may be observed from the figure that the amount of axial strain affects the size of the Cauchy yield surface. In fact, from (14) and (15), $\sigma = \beta_3 \pi^{zz}$ and $\tau = \beta_3 \pi^{z\theta}$ and the Cauchy yield surface is an isotropic expansion of the 1st P-K yield surface with β_3 being the factor of expansion. For an axial prestrain of 20 percent, the size of the Cauchy yield surface is about 20 percent larger than that of the corresponding 1st P-K yield surface. We also note that the translation (the back stress) of the former yield surface is 20 percent more than that of the latter. In the case of the 2nd P-K stress, we have $P^{z\theta} \cong (\pi^{z\theta}/\beta_m)$ and $P^{zz} = (\pi^{zz}/\beta_3)$ from Eq. (11) for φ approximately equal to zero (φ is zero during axial prestrain and is very small and negligible during the probing of yield surface).

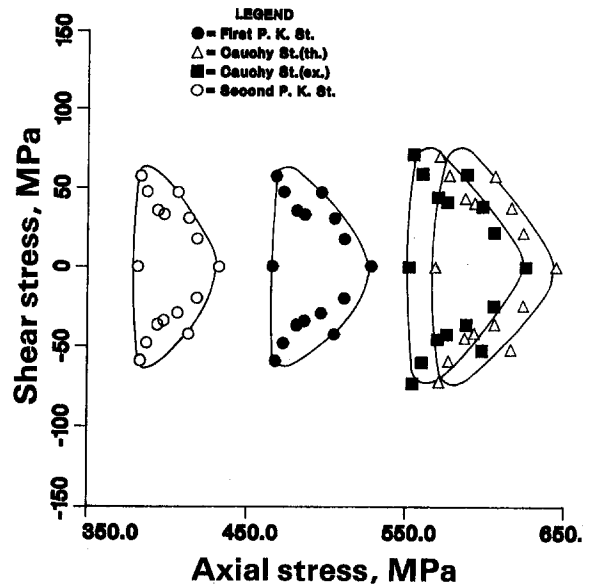


Fig. 5 The Cauchy, the first and second Piola-Kirchhoff yield surfaces for loading Path 1

The 2nd P-K yield surface is about 9.5 percent larger than that of the 1st P-K yield surface in the shear direction but is about 17 percent smaller in the axial direction. The back stress of the former is 17 percent less than that of the latter. These results have suggested that the evolution rules for both isotropic and kinematic hardening are stress measure dependent.

Figure 6 shows the subsequent yield surfaces determined by each stress measure for the case of prestrain in shear. It can be seen that due to no observable area change, the Cauchy stress σ and τ are almost identical to the 1st P-K stress components π^{zz} and $\pi^{z\theta}$ from Eqs. (14) and (15). Therefore, the Cauchy and the 1st P-K yield surfaces are indistinguishable in the figure. However, the components of the 2nd P-K stress are different than those of the Cauchy stress. It is seen, from Eqs. (11) and (19), that $P^{z\theta} \cong \pi^{z\theta} - \varphi R_m \pi^{zz}$ and $P^{zz} \cong \pi^{zz}$, i.e., the component $P^{z\theta}$ depends on the twist angle per unit length φ . This leads to a rotation of the 2nd P-K surface, with the angle of rotation

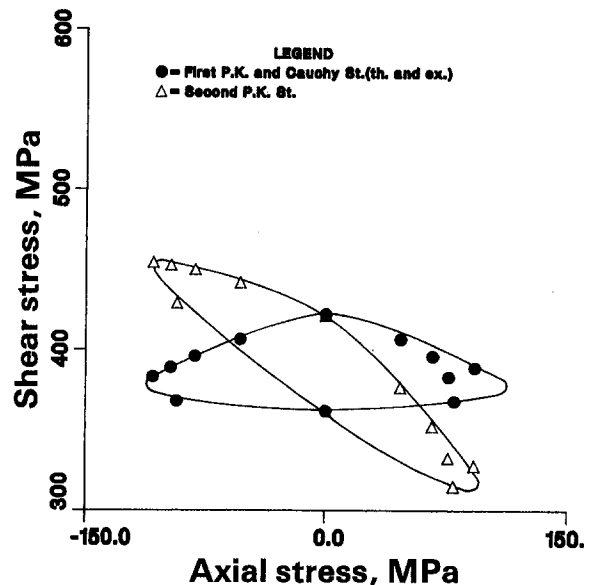


Fig. 6 The Cauchy, the first and second Piola-Kirchhoff yield surfaces for loading Path 2

increasing with the shear strain. It also leads to a further distortion of the 2nd P-K surface in that the yield surface is not symmetric with respect to the shear stress axis. These results complicate the hardening rule of the 2nd P-K yield surfaces.

In the aforementioned example, the theoretical results in the case of pretorsion is calculated based on the approximation of (19). Without this approximation, the axial strain exists but is very small. It is less than 0.3 percent for a prestrain in torsion of 20 percent. In this case, $1.003 > \beta_3 > 1$ and, from Wu et al. (1995) where the circumferential strain was investigated, we obtain $0.9973 < \beta_m < 1$. Thus, the effect of this approximation is very small. Also, we emphasize that the rotation and distortion of the 2nd P-K surface is independent of this approximation.

In the Appendix, the Mises yield criterion in the Cauchy stress space is transformed into the stress spaces of other stress measures. The results show similar features as those described in this section concerning the size, distortion, and location of the yield surfaces.

4 The Equivalent Stress-Strain Curves

It has been assumed for sometime in the literatures that the equivalent stress versus the equivalent strain curve describes the strain-hardening behavior of a material. Recently, there are discussions (Jonas et al., 1981; Wu and Yeh, 1987), to indicate that this curve for axial tension would be different than that for pure torsion. This difference in fact exposes the nonisotropic nature of strain hardening for an initially isotropic material.

We now proceed to investigate the effect of stress measure on the equivalent stress versus the equivalent strain curve. By using the second invariant of the deviatoric stress tensor, the equivalent stress of each stress measure (the equivalent Cauchy stress $\hat{\sigma}$, the equivalent 1st P-K stress $\hat{\pi}$ and the equivalent 2nd P-K stress \hat{P}) is defined by

$$\begin{aligned}\hat{\sigma} &= [3(\frac{1}{2}s_{ij}s_{ij})]^{1/2} = (\sigma^2 + 3\tau^2)^{1/2} \\ \hat{\pi} &= [3(\frac{1}{2}\pi_{ij}^d\pi_{ij}^d)]^{1/2} \\ &= [(\pi^{\theta\theta})^2 + (\pi^{zz})^2 - \pi^{zz}\pi^{\theta\theta} + 3\pi^{z\theta}\pi^{\theta z}]^{1/2} \\ \hat{P} &= [3(\frac{1}{2}P_{ij}^dP_{ij}^d)]^{1/2} \\ &= [(P^{\theta\theta})^2 + (P^{zz})^2 - P^{zz}P^{\theta\theta} + 3(P^{z\theta})^2]^{1/2}\end{aligned}\quad (21)$$

where s_{ij} , π_{ij}^d , and P_{ij}^d are deviators of σ_{ij} , π_{ij} , and P_{ij} , respectively. The equivalent strain is defined as

$$\hat{\epsilon} = [\epsilon^2 + \frac{4}{3}\eta^2]^{1/2}\quad (22)$$

where ϵ is the axial strain. Explicit forms of these relations can be obtained for each stress measure for the following two cases.

A Uniaxial Tension. In the uniaxial case, $\varphi = 0$, $2\eta = 0$, and $\tau = 0$. By considering the true strain, we have

$$\hat{\epsilon} = \frac{z}{z} = \frac{\beta_3}{\beta_3}\quad (23)$$

Thus, $\epsilon = \ln(\beta_3)$ or $\beta_3 = e^\epsilon$. Hence, ϵ is the logarithmic strain. Then, by use of (10) and (11), Eqs. (21) and (22) become

$$\begin{aligned}\hat{\sigma} &= \sigma \\ \hat{\pi} &= \frac{\sigma}{\beta_3} = e^{-\epsilon}\hat{\sigma} \\ \hat{P} &= e^{-2\epsilon}\hat{\sigma} \\ \hat{\epsilon} &= \epsilon.\end{aligned}\quad (24)$$

B Pure Torsion. In the case of pure torsion, $\sigma = 0$. Equations (21) and (22) can be reduced, through Eqs. (10) and (11) and the approximation of (19), to

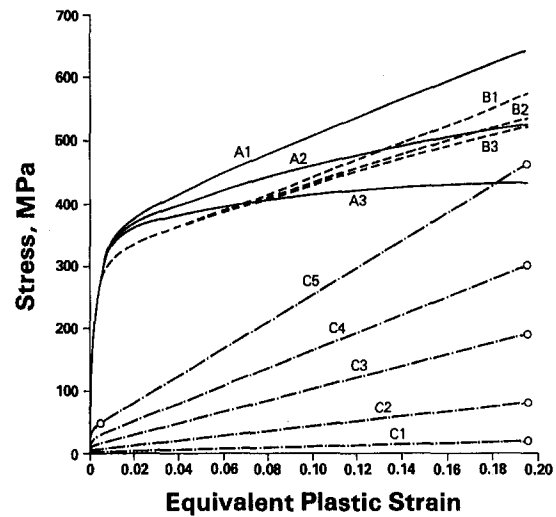


Fig. 7 Equivalent stresses and back stresses versus equivalent strain

$$\begin{aligned}\hat{\sigma} &= \sqrt{3}\tau \\ \hat{\pi} &= \hat{\sigma}\sqrt{\frac{2}{3}\eta^2 + 1} \\ \hat{P} &= \hat{\sigma}\sqrt{\frac{16}{3}\eta^2 + 1} \\ \hat{\epsilon} &= \frac{2\eta}{\sqrt{3}}.\end{aligned}\quad (25)$$

Figure 7 shows the equivalent stress $\hat{\sigma}$, $\hat{\pi}$, \hat{P} versus the equivalent strain $\hat{\epsilon}$ curves for uniaxial tension and pure torsion. (A1: $\hat{\sigma}$ for tension, A2: $\hat{\pi}$ for tension, A3: \hat{P} for tension; B1: $\hat{\sigma}$ for torsion, B2: $\hat{\pi}$ for torsion, B3: \hat{P} for torsion). The curves for torsion are plotted from experiment data for $\hat{\epsilon}$ less than 0.112. By extending the experimental data using the same trend of the curve, all the three curves have been calculated and extended to $\hat{\epsilon} = 0.2$. It is seen that the difference between equivalent stresses for tension and torsion becomes appreciable when the strain becomes large. We note that the curves for tension and torsion of the equivalent Cauchy stress are almost parallel when the strain is large. But, the curves of the equivalent 1st P-K stress cross each other at $\hat{\epsilon} = 0.18$ and those of the equivalent 2nd P-K stress intersect each other quite early, at $\hat{\epsilon}$ of only 0.07. The projected back stresses for the case of uniaxial tension are also shown in Fig. 7. (C1: 1.0 percent proof strain (P.S.), C2: 0.5 percent P.S., C3: 0.1 percent P.S., C4: 0.05 percent P.S., C5: 0.005 percent P.S.). The back stresses, which have been obtained from Fig. 4(b) by use of different amounts of proof strain, represent only a rough estimation. Nevertheless, they show the trend of change for the back stresses. The data points which include a point from Wu and Yeh (1991) at small strain level are shown by circles in the figure.

This figure shows that the extent of anisotropic hardening is greatly influenced by the stress measure if the phenomenological approach is used. The uneven tension and torsion curves shown in the figure further confirm the idea of anisotropic rate of strain hardening previously discussed by Wu and Yeh (1987). We note that the previous observation was from test results in the small strain range, whereas the present results provide data in the large strain range. The figure also shows that the definition of yield has a significant effect on the extent of isotropic or kinematic hardening. Therefore, in the discussion of deformation induced anisotropy, the effect of stress measure and the definition of yield are both important.

5 Concluding Remarks

Due to difficulties associated with the measurement of the deforming cross-sectional area of a thin-wall specimen, the first

Piola-Kirchhoff stress components are usually used for reporting experimental results. Explicit transformation equations have been derived to convert the stress components into the Cauchy stress or the second Piola-Kirchhoff stress for combined axial-torsional experiments.

Experiments have been conducted to investigate the yield behavior of annealed 304 stainless steel under 20 percent axial or 20 percent engineering shear prestrain. It is seen that the direction of the prestraining path strongly influences the distortion of the yield surface. A significant decrease in the size of yield surface (a strong cross effect) was found in the case of axial prestrain, and an increase in size with strong distortion was observed in the case with shear prestrain. It has been shown that the differences among the 1st P-K, the 2nd P-K, and the Cauchy stresses increase when the axial strain increases. Also, the evolution rules for both isotropic and kinematic hardening are stress measure and definition of yield dependent.

The transformation equations derived in this paper have been shown to predict the Cauchy yield surface well, when compared with an independently determined experimental, subsequent Cauchy Yield surface based on the measured, deformed cross-sectional area. Many existing theories have been formulated in terms of the Cauchy stress. The present results seem to indicate that Cauchy stress is a reasonable stress measure to use in engineering analysis involving finite deformation. While the 1st P-K stress can also be a meaningful stress measure to use, it suffers the disadvantage of nonsymmetry. We suggest, however, that cautions be exercised when the 2nd P-K stress is used. Even though the 2nd P-K stress has an advantage of being symmetric, its physical meaning is not clear and, in particular, it leads to a strain-hardening rule much more complicated than usual and needs to be further investigated. Finally, we note that, for this simple stress state of axial-torsion, the Cauchy stress has only two nonzero components (σ , τ), while the other two stress measures have additional nonzero components. Therefore, the first and second P-K yield surfaces shown in Figs. 5 and 6 do not fully represent the stress state if these two stress measures are used.

References

- Helling, D. E., Miller, A. K., and Stout, M. G., 1986, "An Experiment Investigation of the Yield Loci of 1100-0 Aluminum, 70:30 Brass and an Overaged 2040 Aluminum Alloy after Various Prestrains," *ASME J. Eng. Mat. Tech.*, Vol. 108, pp. 313-320.
- Ivey, H. J., 1961, "Plastic Stress-Strain Relations and Yield Surfaces for Aluminum Alloy," *J. Mech. Eng. Sci.*, Vol. 3, No. 1, pp. 15-31.
- Jonas, J. J., Canova, G. R., Shrivastava, S. C., and Christodoulou, N., 1981, "Sources of the Discrepancy Between the Flow Curves Determined in Torsion and in Axisymmetric Tension and Compression Testing," *Plasticity of Materials at Finite Strain*, E. H. Lee and R. C. Mallett, eds., pp. 206-222.
- Mair, W. M., and Pugh, H. L. D., 1964, "Effect of Prestrain on Yield Surface in Copper," *J. Mech. Eng. Sci.*, Vol. 6, pp. 150-163.
- Marjanovic, R., and Szczepinski, W., 1975, "On the Effect of Biaxial Cyclic Loading on the Yield Surface of M-63 Brass," *Acta Mech.*, No. 23, pp. 65-74.
- McMeeking, R. M., 1982, "The Finite Strain Tension-Torsion Test of a Thin-Walled Tube of Elastic-Plastic Material," *Int. J. Solid Structures*, Vol. 18, pp. 166-223.
- Phillips, A., and Kasper, R., 1973, "On the Foundations of Thermoplasticity: An Experimental Investigation," *ASME JOURNAL OF APPLIED MECHANICS*, Vol. 40, pp. 891-896.
- Phillips, A., and Lu, W. Y., 1984, "An Experiment Investigation of Yield Surfaces and Loading Surfaces of Pure Aluminum with Stress-Controlled and Strain-Controlled Path of Loading," *ASME J. Eng. Mat. Tech.*, Vol. 106, pp. 349-354.

- Phillips, A., and Tang, J. L., 1972, "The Effect of Loading Path on the Yield Surface at Elevated Temperatures," *Int. J. Solid and Structures*, Vol. 8, p. 463.
- Phillips, A., and Weng, G. J., 1975, "An Analysis Study of An Experimentally Verified Hardening Law," *ASME JOURNAL OF APPLIED MECHANICS*, Vol. 42, p. 375.
- Phillips, A., Tang, J. L., and Ricciuti, M., 1974, "Some New Observations on Yield Surface," *Acta Mechanica*, Vol. 20, p. 23.
- Shiratori, E., Ikegami, K., Yoshida, F., Kaneko, K., and Koike, S., 1976, "The Subsequent Yield Surface after Preloading under Combined Axial Load and Torsion," *Bulletin JSME*, Vol. 19, pp. 877-883.
- Taylor, G. I., and Quinney, H., 1932, "The Plastic Distortion of Metal," *Phil. Trans. Roy. Soc., Lond.*, Vol. A230, pp. 323-362.
- Wu, H. C., and Xu, Z. Y., 1989, "An Extensometer Investigation of the Axial Effect During Tension," *Proc. Int. Conf. on Constitutive Laws for Eng. Material* J. Fan, and S. Murakami, eds., Chongqing, China, pp. 232-238.
- Wu, H. C., and Yeh, W. C., 1987, "Some Considerations in the Endochronic Description of Anisotropic Hardening," *Acta Mechanica*, Vol. 69, p. 59.
- Wu, H. C., and Yeh, W. C., 1991, "On the Experimental Determination of Yield Surfaces and Some Results of Annealed 304 Stainless Steel," *Int. J. Plasticity*, Vol. 7, No. 8, pp. 803-826.
- Wu, H. C., Lu, J. K., and Pan, W. F., 1995, "Endochronic Equations for Finite Plastic Deformation and Application to Metal Tube Under Torsion," *Int. J. Solids Structures*, Vol. 32, pp. 1079-1097.

APPENDIX

The Mises yield surface in the Cauchy stress space is

$$(\sigma - r_\sigma)^2 + 3(\tau - r_\tau)^2 = k^2 \quad (A1)$$

where r_σ and r_τ are, respectively, the axial and shear components of the back stress. k is the shear yield stress and is assumed to be constant in this discussion. By use of Eqs. (14) and (15), Eq. (A1) is transformed into

$$\left(\pi^{zz} - \frac{r_\sigma}{\beta_3}\right)^2 + 3\left(\pi^{z\theta} - \frac{r_\tau}{\beta_3}\right)^2 = \left(\frac{k}{\beta_3}\right)^2 \quad (A2)$$

Using (11), Eq. (A2) is further transformed into an equation in the $P^{z\theta}$ versus P^{zz} stress space.

In the case of axial prestrain only, $\varphi \cong 0$ and $r_\tau = 0$; and by use of Eq. (18), the yield function in the $P^{z\theta}$ versus P^{zz} stress space may be written as

$$\frac{\left(P^{zz} - \frac{r_\sigma}{\beta_3}\right)^2}{\left(\frac{k}{\beta_3}\right)^2} + \frac{(P^{z\theta})^2}{\left(\frac{k}{\sqrt{3}\beta_3}\right)^2} = 1 \quad (A3)$$

By comparing Eqs. (A1), (A2), and (A3), we see that the semi-major axes (in the axial stress direction) of the ellipses are k for the Cauchy yield surface, k/β_3 for the 1st P-K surface, and k/β_3^2 for the 2nd P-K surface. The semi-minor axes (in the shear stress direction) are, respectively, $k/\sqrt{3}$, $k/\sqrt{3}\beta_3$, and $k/\sqrt{3}\beta_3$. The back stress for the three yield surfaces are, respectively, r_σ , r_σ/β_3 , and r_σ/β_3^2 . It is seen that the size, shape, and the back stress of the yield surfaces are all influenced by the deformation of the material element when different stress measures are used.

In the case of torsion only prestrain, $r_\sigma = 0$. If we use the approximation of Eq. (19), then the yield surface in the 2nd P-K stress space is governed by the equation

$$(P^{zz})^2 + 3[(P^{z\theta} + \varphi R_m P^{zz}) - r_\tau]^2 = k^2 \quad (A4)$$

This equation contains a $6\varphi R_m P^{z\theta} P^{zz}$ term, and a rotation in the ellipse has occurred.

Inertial Effects on Void Growth in Porous Viscoplastic Materials

W. Tong

Assoc. Mem. ASME.

G. Ravichandran

Assoc. Mem. ASME.

Graduate Aeronautical Laboratories,
Division of Engineering and
Applied Science,
California Institute of Technology,
Pasadena, CA 91125

The present work examines the inertial effects on void growth in viscoplastic materials which have been largely neglected in analyses of dynamic crack growth and spallation phenomena using existing continuum porous material models. The dynamic void growth in porous materials is investigated by analyzing the finite deformation of an elastic/viscoplastic spherical shell under intense hydrostatic tensile loading. Under typical dynamic loading conditions, inertia is found to have a strong stabilizing effect on void growth process and consequently to delay coalescence even when the high rate-sensitivity of materials at very high strain rates is taken into account. Effects of strain hardening and thermal softening are found to be relatively small. Approximate relations are suggested to incorporate inertial effects and rate sensitivity of matrix materials into the porous viscoplastic material constitutive models for dynamic ductile fracture analyses for certain loading conditions.

1 Introduction

Dynamic fracture and spallation are important aspects of material behavior under high stress and loading rates. The major micromechanism that leads to ductile fracture in many structural materials is void growth and coalescence (McClintock, 1968; Rice and Tracey, 1969; Curran et al., 1987; Freund, 1990). Microvoids as internal defects exist practically in all structural materials fabricated by current material synthesizing and processing methods. Nucleation of voids may occur during deformation processes such as extrusion, forging and rolling, and pores may not be eliminated completely in materials produced via powder-metallurgy routes (Spitzig et al., 1988). Although such voids have little effect on the overall elastic-plastic deformation of structural materials under normal loading conditions, the growth of those voids under high tensile stress is the key micromechanism that controls the formation and propagation of cracks during dynamic ductile fracture and spallation processes (Godse et al., 1989). The cracking of compacts that occurs during the shock wave consolidation of metallic and composite powders is also related to the void nucleation and growth under tensile loading upon the reflection of compaction waves (Linse, 1983; Thadhani, 1988; Tong et al., 1993).

The deformation of a single hole or cavity in an infinite medium or a thick-walled shell containing a void has been extensively studied. Early investigations were mainly quasi-static analyses of a void in a rate-independent, perfectly plastic matrix material (McClintock, 1968; Rice and Tracey, 1969) and later in viscoplastic and/or strain-hardening matrix material (e.g., Wilkinson and Ashby, 1975; Nemat-Nasser and Hori, 1987; Haghi and Anand, 1991). The inclusion of the dynamic (inertial) effects was first introduced by Carroll and Holt (1972) in their study of the collapse of a hollow sphere in a rate-independent perfectly plastic material. Johnson (1981) extended the results of Carroll and Holt to the growth of a void in a viscoplastic solid described by a simple linear overstress model. An outcome of his analysis is the negligible effect of inertia (in comparison with viscosity) on the dynamic void

growth process in copper under loading conditions that were considered. Klocker and Monthelet (1988) analyzed the dynamic growth of a void in an infinite medium using the same viscoplastic model for copper and concluded that inertial effects have a stabilizing influence for strain rates greater than 10^3 per second associated with void radii larger than $10 \mu\text{m}$. Glennie (1972) modified the void growth calculations of Rice and Tracey (1969) to include the effect of inertia which was shown to play an important part in limiting the rate of void growth in a rate-independent, perfectly plastic medium. Luk et al. (1991) developed models for the dynamic expansion of spherical cavities at constant velocity for elastic-plastic, rate-independent materials with powder-law strain hardening. More recently, Ortiz and Molinari (1992) examined the effect of strain hardening and rate sensitivity on the dynamic expansion of a cavity in an infinite medium and showed that whereas the early stages of cavity expansion are dominated by viscous effects, inertia tends to dominate the long-term response of the cavity for weakly rate-dependent materials (they set the rate sensitivity parameter to 0.01 in their calculations). Cortes (1992a) applied the same approach of Carroll and Holt (1972) and Johnson (1981) to some simple viscoplastic materials with strong rate sensitivity (a rate sensitivity parameter of 0.5 was used) and linear strain hardening or thermal softening and concluded that both material viscosity and strain hardening may have an important influence on the tensile strength of ductile materials against void growth at high strain rates while thermal softening by itself has a negligible effect. Inertial effects on dynamic void growth were however not explicitly examined.

The deformation and damage of voided materials has also been extensively modeled using phenomenological theories of dilatational plasticity (Hutchinson, 1987). Gurson (1977) proposed such a theory which consists of a yield condition, a flow law, and a nucleation and evolution law of voids in terms of the volume fraction of voids and his theory is widely used in analyzing ductile fracture and localization failure problems (e.g., Tvergaard, 1982; Needleman and Tvergaard, 1991). There is an increasing trend of applying continuum porous material models such as the Gurson-Tvergaard-Needleman (GTN) theory and others to analyze dynamic crack growth and spallation phenomena (Perzyna, 1986; Needleman and Tvergaard, 1991; Eftis and Nemes, 1992). The present work examines the inertial (dynamic) effects on microvoid growth in viscoplastic materials which have been largely neglected in these phenomenological porous material models. The dynamic void growth in porous materials is investigated by analyzing the void expansion under intense hydrostatic tensile loading. Under high loading

Contributed by the Applied Mechanics Division of THE AMERICAN SOCIETY OF MECHANICAL ENGINEERS for publication in the ASME JOURNAL OF APPLIED MECHANICS.

Discussion on this paper should be addressed to the Technical Editor, Prof. Lewis T. Wheeler, Department of Mechanical Engineering, University of Houston, Houston, TX 77204-4792, and will be accepted until four months after final publication of the paper itself in the ASME JOURNAL OF APPLIED MECHANICS.

Manuscript received by the ASME Applied Mechanics Division, Aug. 9, 1993; final revision, Mar. 1, 1994. Associate Technical Editor: C. F. Shih.

rates such as the ones generated by strong plane shock waves, the hydrostatic tension is the dominant stress state in ductile failure (Perzyna, 1986; Curran et al., 1987). The complication of the effects of triaxiality on void growth is excluded and hence inertial effects on void growth can be brought into forefront in our current analysis. The finite deformation formulation for stress wave propagation in elastic/viscoplastic materials applied to the spherical shell is adopted in our analysis. Such a formulation has recently been given by Tong and Ravichandran (1993a) in their study of dynamic pore collapse of viscoplastic materials. The matrix material is modeled as rate dependent with both strain hardening and thermal softening. Under a typical dynamic loading condition, inertia is found to have a strong stabilizing effect on void growth process that leads to coalescence even when the high rate sensitivity of materials in the very high strain rate range is taken into account. Effects of strain hardening and thermal softening are found to be small in comparison to both inertia and rate-sensitivity of materials.

In the following section, formulations are presented for both static and dynamic void growth in viscoplastic materials under hydrostatic tensile loading. Those formulations are then applied to pure aluminum and results of static and dynamic void growth analyses are given in Section 3. The inertial effects on void growth are discussed in terms of dynamic loading rate, void size, initial porosity, and matrix material properties. Approximate relations are suggested to incorporate inertial effects and/or strong rate sensitivity into the current porous viscoplastic material constitutive models for dynamic ductile fracture analyses. Finally, some conclusions from our present study are summarized in Section 4.

2 Void Growth: Continuum and Micromechanical Models

2.1 Gurson-Tvergaard-Needleman Model. A brief summary of the Gurson-Tvergaard-Needleman porous material model (Gurson, 1977; Tvergaard, 1982; Needleman and Tvergaard, 1991) is given here and an expression of void growth under hydrostatic tension is derived in the following section for a viscoplastic matrix material. A central issue in analyzing the plastic deformation of such porous materials is to define a yield condition or a flow potential which provides the rate of plastic deformation tensor and subsequently the evolution relation of porosity as a function of external loading, and matrix properties. As one of the simplest forms, the flow potential Φ can be written as

$$\Phi = \Phi(\boldsymbol{\sigma}, f, \bar{\sigma}), \quad (1)$$

where $\boldsymbol{\sigma}$ is the applied Cauchy stress tensor, f is the void volume fraction (porosity), and $\bar{\sigma}$ is the average strength of the matrix material which can in general be a function of strain rate, strain, and temperature. The plastic part of the rate of deformation, \mathbf{D}^p , is taken to be in a direction normal to the flow potential,

$$\mathbf{D}^p = \dot{\Lambda} \frac{\partial \Phi}{\partial \boldsymbol{\sigma}}, \quad (2)$$

where $\dot{\Lambda}$ is the plastic flow proportionality factor.

The focus of current study is to understand void growth and coalescence, and hence the relations pertinent to nucleation of new voids is not included in the following discussions. The evolution equation in terms of porosity due to the growth of existing voids is determined from the condition that the matrix material is plastically incompressible,

$$\dot{f} = (1 - f)\mathbf{D}^p : \mathbf{I}. \quad (3)$$

The specific flow potential for porous materials introduced

first by Gurson (1977) and then modified by Tvergaard (1982) is

$$\Phi = \frac{\sigma_e^2}{\bar{\sigma}^2} + 2q_1 f \cosh\left(\frac{3}{2} q_2 \frac{\sigma_h}{\bar{\sigma}}\right) - 1 - q_1^2 f^2 = 0, \quad (4)$$

where $\sigma_e = \sqrt{\frac{3}{2} \boldsymbol{\sigma}' : \boldsymbol{\sigma}'}$, $\sigma_h = \frac{1}{3} \boldsymbol{\sigma} : \mathbf{I}$, $\boldsymbol{\sigma}' = \boldsymbol{\sigma} - \sigma_h \mathbf{I}$, and q_1 and q_2 are dimensionless constants of the order of 1. The matrix material is characterized as a power-law viscoplastic solid with both strain hardening and thermal softening. The average matrix plastic strain rate is given by

$$\dot{\bar{\epsilon}} = \dot{\epsilon}_0 \left(\frac{\bar{\sigma}}{g}\right)^{1/m}, \quad (5)$$

and the function g is prescribed in terms of the average plastic strain $\bar{\epsilon}$ and temperature $\bar{\theta}$ of the matrix material as

$$g(\bar{\epsilon}, \bar{\theta}) = \sigma_0 \left(1 + \frac{\bar{\epsilon}}{\epsilon_0}\right)^n \left(\frac{\bar{\theta}}{\theta_0}\right)^\nu, \quad (6)$$

where $\dot{\epsilon}_0$, σ_0 , ϵ_0 , θ_0 , m , n , ν are viscoplastic constants of the matrix material. The form of the function g in Eq. (6) is very similar to that used by Klopp et al. (1985). The treatment of strain hardening is modified here to give a better description of plastic deformation in the small strain range. Viscoplastic parameters for aluminum at high strain rates are (Klopp et al., 1985): $m = 0.254$, $n = 0.04$, $\nu = -0.4$, $\sigma_0 = 216.5$ MPa, $\dot{\epsilon}_0 = 8.83 \times 10^4$ s⁻¹, $\epsilon_0 = 0.03$, $\theta_0 = 295$ K.

The heating due to plastic dissipation is accounted for and adiabatic conditions are assumed under dynamic loading so that balance of energy leads to

$$\dot{\bar{\theta}} = \frac{\beta \bar{\sigma} \dot{\bar{\epsilon}}}{\rho_0 c_p}, \quad (7)$$

where ρ_0 is the density of the matrix material in the reference configuration, c_p is the heat capacity, and parameter β is the fraction of the plastic work converted to heat. For aluminum, $\rho_0 = 2700$ kg/m³, $c_p = 893$ J/kg/K, and $\beta = 0.9$.

For comparison with results of the following analysis of dynamic void growth, only hydrostatic tension loading will be considered, i.e., $\boldsymbol{\sigma}' = 0$, $\sigma_e = 0$. The evolution equation for f for a given loading $\sigma_h(t)$ can be written following Eqs. (3)-(5):

$$\dot{f} = \dot{\epsilon}_0 (1 - f)^2 \times \left[\frac{3q_2}{2} \frac{1}{\cosh^{-1}\left(\frac{1 + q_1^2 f^2}{2q_1 f}\right)} \right]^{1+m/m} \left(\frac{\sigma_h}{g}\right)^{1/m}. \quad (8)$$

2.2 Dynamic Void Growth Analysis. The form of the flow potential proposed by Gurson (1977) itself is the result of a static analysis of the expansion of a spherical shell of perfectly plastic rate-independent materials. Following such an approach, we study the dynamic void growth in viscoplastic matrix materials by considering the expansion of a spherical shell under a given dynamic tensile loading $\sigma_h(t)$. The current inner and outer radii r of the spherical shell are a and b , respectively, at time $t > 0$. The initial inner and outer radii R are a_0 and b_0 , respectively (i.e., $t = 0$). The initial (f_0) and current (f) void volume fractions of the porous material are thus given by

$$f_0 = \left(\frac{a_0}{b_0}\right)^3, f = \left(\frac{a}{b}\right)^3, 0 \leq f_0 \leq 1, 0 \leq f \leq 1. \quad (9)$$

The finite deformation formulation for stress wave propagation in elastic/viscoplastic materials applied to the spherical shell has recently been given by Tong and Ravichandran (1993a) in their study of dynamic pore collapse of viscoplastic

materials. The resulting system of quasi-linear hyperbolic partial differential equations can be written in terms of relations along characteristics (for details, see Tong and Ravichandran, 1993a)

$$\left\{ \begin{array}{l} dT_R = \pm \rho_0 c du - B_1 dt \mp \frac{2}{R} (T_R - T_\theta) c dt, \\ \frac{dR}{dt} = \pm c = \pm \sqrt{\frac{A_1}{\rho_0}}, \\ dT_\theta = \frac{A_2}{A_1} (dT_R + B_1 dt) - B_2 dt, \frac{dR}{dt} = 0, \\ d\eta = \frac{r^2}{R^2 A_1} (dT_R + B_1 dt) + \frac{2\eta u}{r} dt, \frac{dR}{dt} = 0. \end{array} \right. \quad (10)$$

This system of characteristic relations written in the form of a finite difference equations is solved by using a second-order accurate integration method, except, where large oscillations exist, a first-order accurate scheme is used (Ranganath and Clifton, 1972; Tong et al., 1992). For aluminum, the elastic Young's modulus and shear modulus are set to 70 GPa and 26 GPa, respectively.

As a final note, the *quasi-static* analysis of a thick spherical shell under hydrostatic loading has been given by Wilkinson and Ashby (1975) for rigid power-law viscoplastic materials without either strain hardening or thermal softening ($g \equiv \sigma_0$, see Eq. (6)). Their results for current comparison purposes can be summarized as

$$\dot{f} = \dot{\epsilon}_0 m^{1/m} \left(\frac{3}{2} \right)^{1+m/m} \frac{(1-f)f}{(1-f^m)^{1/m}} \left(\frac{\sigma_h}{\sigma_0} \right)^{1/m}. \quad (11)$$

The above result of Wilkinson and Ashby (1975) is an exact *quasi-static* solution (neglecting elastic deformation) of the problem considered in our *dynamic* analysis while the GTN model (Eq. 8) provides an *approximate* quasi-static one (with $n = \nu = 0$ in Eq. (6)).

3 Numerical Results

We present here a series of numerical analyses of static and dynamic void growth in aluminum as formulated in the previous section. The viscoplastic material parameters for aluminum have been experimentally determined for strain rates of 10^5 s^{-1} and higher and the rate sensitivity of pure aluminum is among the highest ones at this very high strain rate range (Klopp et al., 1985; Tong et al., 1992). Thus, effects of rate sensitivity on void growth are expected to be strong and the importance of inertia on dynamic void growth can be critically assessed. The relative importance of dynamic effects as compared with other viscoplastic material properties are also examined in terms of initial porosity, void size, strain hardening, thermal softening, and loading rate.

It is well known experimentally that coalescence of voids occurs when the porosity f in the materials reaches about 0.1-0.3 (Perzyna, 1986; Needleman and Tvergaard, 1991; Cortes, 1992). To fix ideas, an empirical measure of the material resistance against void growth and coalescence under a given *constant* loading rate, the *critical tensile strength* of the porous matrix material, can be defined as the applied hydrostatic stress level when $f = 0.3$ (Cortes, 1992). Although being introduced just to facilitate discussions in the following, the critical tensile strength is somewhat related to the spallation strength of a material as determined in a plate-impact spallation experiment (Johnson, 1981; Perzyna, 1986). The tensile loading in such an experiment increases monotonically but in general not linearly. The percentage of the difference between dynamic and static critical tensile strengths (σ_{dc} and σ_{sc}) will be used as a

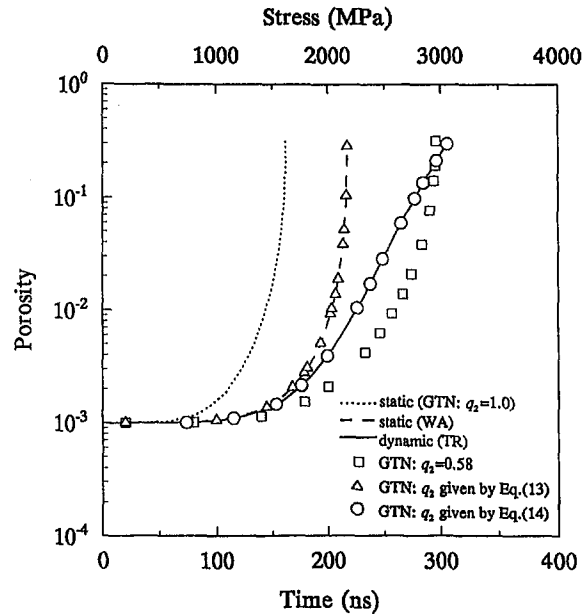


Fig. 1 Comparison of void growth by both static and dynamic analyses ($a_0 = 10 \mu\text{m}$, $\sigma_h = 10 \text{ MPa/ns}$, $q_1 = 1.0$, $f_0 = 10^{-3}$). The legends used throughout the paper are: GTN—results given by Eq. (8); TR—results given by Eq. (10); WA—results given by Eq. (11).

parameter in our following assessment of inertial effects on void growth, namely:

$$\delta = \frac{\sigma_{dc} - \sigma_{sc}}{\sigma_{sc}}. \quad (12)$$

Results of static analyses given by the GTN model, Eq. (8), and by Wilkinson and Ashby (1975), Eq. (11), in which inertia is neglected altogether provide a description of effects of the viscosity on void growth, while results of our dynamic analyses in comparison with those of static analyses should show clearly the inertial effects on void growth in both rate-independent and rate-dependent materials. Figure 1 shows results of both static and dynamic void growth analyses in a rate-dependent material for a typical dynamic loading rate, initial porosity, and void size. At the early stage up to 150 ns, results of both analyses are nearly identical which indicates that inertial effects are minimal and the void growth is dominated by the viscosity so far. However, the dynamic void growth becomes much slower later and the dynamic critical tensile strength is about 41 percent higher than the static one for the highly rate-sensitive material ($m = 0.254$). Thus, inertia overtakes the viscosity and dominates the later stage of the void growth. The prediction of the critical tensile strength by the GTN model is even lower if values of the two adjustable parameters q_1 and q_2 are set to be 1.25 and 1.0, respectively, as suggested by Needleman and Tvergaard (1991). By trial and error, the result by the GTN model is found to be able to match that of Wilkinson and Ashby (1975) fairly well if $q_1 = 1.0$ and $q_2 = 0.8$. Thus, parameters q_1 and especially q_2 in the GTN model seem to be dependent on the rate-sensitivity parameter m of the matrix material (note that the rate sensitivity is 0.01 in the analysis of Needleman and Tvergaard (1991)).

As a parametric study of the effect of rate sensitivity on void growth, the rate sensitivity parameter m is allowed to change in the range of 0 to 1 which simulates materials from rate independent to very strongly rate dependent. These results shown in Fig. 2 indicate the strong effects of rate sensitivity on *both* static and dynamic void growth. For a given loading rate, void size, and porosity, the dynamic effect is more dominant in a more weakly rate-dependent material ($\delta = 125$ percent, 41

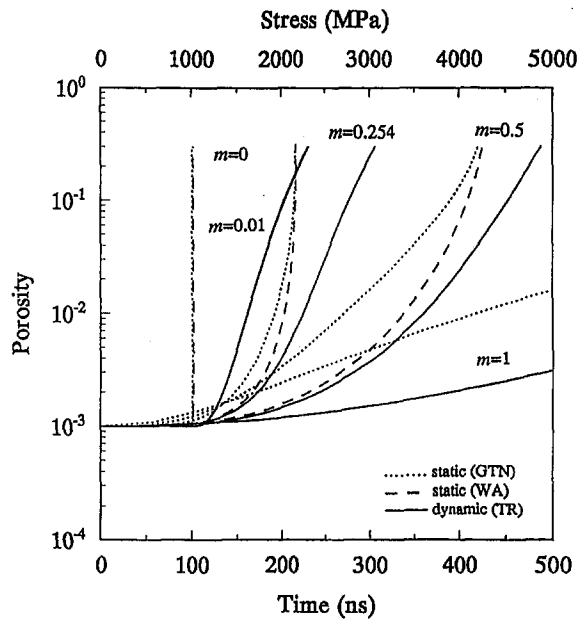


Fig. 2 Effects of rate sensitivity of the matrix material on both static and dynamic void growth ($a_0 = 10 \mu\text{m}$, $\sigma_n = 10 \text{ MPa/ns}$, $f_0 = 10^{-3}$, $m = 0, 0.01, 0.254, 0.5, \text{ and } 1.0$, $q_1 = 1.0$, and $q_2 = 1.0, 1.0, 0.8, 0.73, \text{ and } 0.61$, respectively)

percent, 15 percent, and 0 percent for $m = 0.01, 0.254, 0.5,$ and 1.0 , respectively). Again, parameter q_2 in the GTN model are shown to depend strongly on the rate-sensitivity parameter m of the matrix material and the results of the GTN model do not compare well with those of Wilkinson and Ashby (1975) for large m (0.5-1.0). For both static and dynamic void growth analyses, there is no major difference between $m = 0$ and $m = 0.01$. Our results confirm the conclusions of Glennie (1972) and Ortiz and Molinari (1992) that inertial effects are important in stabilizing dynamic void growth when $m = 0$ or 0.01 . Our results also indicate that inertial effects could be neglected for very strongly rate-sensitive material ($m \approx 1.0$) in void growth analysis under certain loading rates. However, the estimate by Johnson (1981) itself only proved that the dominance of the viscous effect in the initial stage of void growth which is also true for weakly rate-dependent materials (Ortiz and Molinari, 1992). Relevant to the dynamic fracture and spallation is the relative importance of viscosity and inertia on void growth over a long period up to a porosity of 0.1-0.3. Using the parameters used in the analysis of Johnson (1981), we find that the inertia is dominant at later stages of void growth (Tong and Ravichandran, 1993b). Furthermore, recent experimental evidence does not support the description of material behavior with a linear or near linear viscous relation at very high strain rates, even for pure metals (Klopp et al., 1985; Follansbee and Kocks, 1988; Tong et al., 1992). At room temperature, the rate sensitivity of pure copper at fixed structure is found to be only about 0.05 and the total rate sensitivity of copper is at most 0.15-0.20 (Tong et al., 1992) and the highest rate sensitivity was found to be only about 0.254 for pure aluminum (Klopp et al., 1985). Thus, analyses by Perzyna (1986), Klocker and Monthelet (1991), Cortes (1992a), and Nemes and Eftis (1992) using a rate sensitivity of 0.5-1.0 for copper would not be realistic and could greatly overestimate the viscous effects on void growth. The conditions under which inertial effects can be important on void growth would be highly overestimated using these analyses.

Effects of initial porosity, void size, and dynamic loading rate on void growth are also examined (Tong and Ravichandran, 1993b). A smaller initial porosity in the material gives a higher critical tensile strength in both static and dynamic analyses.

The dynamic effect becomes more dominant with lower initial porosity: the dynamic critical tensile strength is found to be 25 percent, 41 percent, and 67 percent higher than the corresponding static one for the initial porosity of $10^{-2}, 10^{-3},$ and 10^{-4} . For the given moderate loading rate $\dot{p} = 10 \text{ MPa/ns}$, the parameter δ is found to be 6 percent, 41 percent, and 89 percent for void radii of 1, 10, and 25 μm , respectively. Due to the strong rate sensitivity ($m = 0.254$), the static critical tensile strength increases significantly with increasing loading rate. The dynamic effect on void growth also increases with increasing loading rates ($\delta = 11$ percent, 41 percent, and 157 percent for $\dot{p} = 1, 10,$ and 100 MPa/ns , respectively).

Finally, we examine the effects of strain hardening and thermal softening of matrix materials on both static and dynamic void growth. Figure 3 shows the results predicted by the GTN model for various matrix strain-hardening and thermal softening behavior. As expected, strain hardening increases the static critical tensile strength while thermal softening reduces the strength. The change of the critical tensile strength due to either strain hardening or thermal softening is small in comparison with that due to inertial effects (see Fig. 1), unless a very large strain-hardening exponent is assumed (say, $n \geq 0.15$). The results from our dynamic void growth analysis are shown in Fig. 4 for the same sets of viscoplastic parameters. The effects (both in trend and magnitude) of strain hardening and thermal softening on void growth are similar in both static and dynamic cases. Thermal effects seem somewhat less significant than that of strain hardening on void growth even for $\nu = -1.0$ (linear temperature dependence) (see Figs. 3 and 4). One of the reasons for this is that the adiabatic heating is very much localized around the inner radius of the void during void growth. Heat conduction and melting are not included in our analysis which also tend to under estimate the thermal effects. Nevertheless, because of the degree of localization of heating the thermal effects are expected to be no stronger than those of strain hardening. In both static and dynamic void growth analyses the results of a matrix material with $n = 0$ and $\nu = 0$ are virtually identical to that of a matrix material with $n = 0.04$ and $\nu = -0.4$ which have been suggested by Klopp et al. (1985). Thus, the effect of strain hardening appears to annul the effect of thermal softening in both static and dynamic void growth in

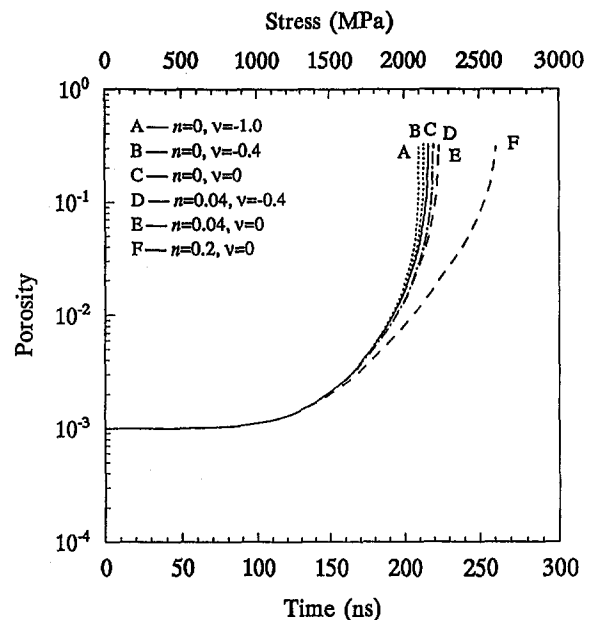


Fig. 3 Effects of strain hardening and thermal softening of the matrix material on the static void growth given by the GTN model ($q_1 = 1.0, q_2 = 0.8, \sigma_n = 10 \text{ MPa/ns}, f_0 = 10^{-3}$)

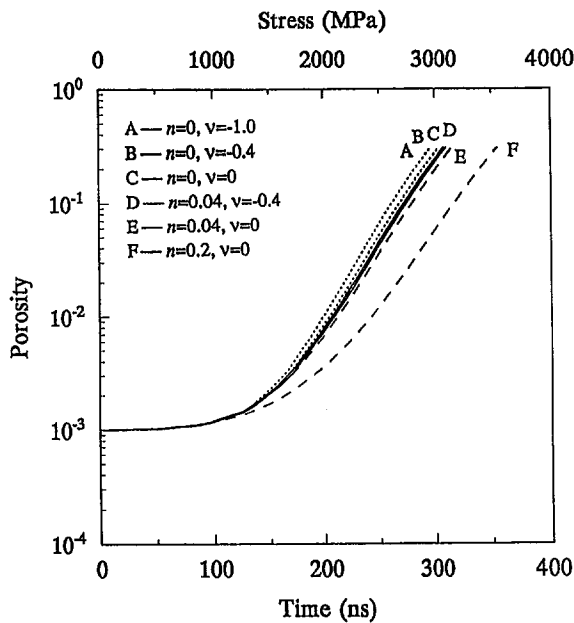


Fig. 4 Effects of strain hardening and thermal softening of the matrix material on the dynamic void growth ($a_0 = 10 \mu\text{m}$, $\dot{\sigma}_h = 10 \text{ MPa/ns}$, $f_0 = 10^{-3}$)

aluminum. The dynamic effects (as measured by the parameter δ) are, however, almost unaffected by the inclusion of both strain hardening and thermal softening.

4 Discussions and Conclusions

In examining the results of static and dynamic void growth presented in the semi-logarithmic scale in Figs. 1-4, the most striking difference is that the static analysis predicts an exponential void growth at a later stage while the dynamic analysis predicts a nearly linear void growth. Thus, inertia has a strong stabilizing effect on void growth under a typical dynamic loading condition. Strong rate sensitivity of materials at high strain-rate range also increases significantly the resistance of matrix materials to void growth under both static and dynamic loadings. Both inertia and a stronger rate sensitivity should be incorporated into the analysis and modeling of damage and failure of ductile materials. We have demonstrated here that the strong rate sensitivity (say, $m = 0.1-0.25$) of matrix materials can be approximately incorporated into the GTN model by adjusting the parameter q_2 to be a different constant. The parameter q_1 in the GTN model seems to be very weakly dependent on the rate sensitivity of matrix materials (Sun and Huang, 1992). Furthermore, for material models without strain hardening and thermal softening, the parameter q_2 can be determined explicitly for the given m and f by comparing Eqs. (8) and (11), namely

$$q_2(m, f) = \left(\frac{m}{1-f^m} \right)^{1/1+m} \left(\frac{f}{1-f} \right)^{m/1+m} \times \cosh^{-1} \left(\frac{1+q_1^2 f^2}{2q_1 f} \right). \quad (13)$$

Naturally, the prediction by the GTN model on void growth using Eqs. (8) and (13) matches that by Wilkinson and Ashby (1975) using Eq. (11), as shown in Fig. 1.

As pointed out by Carroll and Holt (1972), a dynamic void growth relation becomes quite complex even for perfectly plastic and rate-independent materials (a second-order ordinary differential equation). Inclusion of such a relation may not be feasible in the current modeling of dynamic failure using finite

element analysis. An approximate method is thus sought to incorporate inertia into the framework of the phenomenological GTN theory for porous viscoplastic materials at least under some simple loading conditions. The parameter q_1 in the GTN model is again assumed to be very weakly dependent on the inertial effects when the hydrostatic tension is the dominant stress state in controlling void growth. Further adjustment of the parameter q_2 in the GTN model is found to be not satisfactory in incorporating the inertial effects into the GTN flow potential. Although the GTN model predicts correctly the dynamic critical tensile strength against void growth in aluminum as shown in Fig. 1 when q_2 is set to 0.58, the characteristic of the void growth is still exponential instead of a nearly linear in terms of the semi-logarithmic scale. For a given dynamic void growth history $f(t)$ such as those shown in Fig. 2, the parameter q_2 can be estimated from Eq. (8) and the results are shown in Fig. 5 in solid lines for different rate sensitivities for $q_1 = 1.0$. Results given by Eq. (13) are also shown in Fig. 5 in dashed lines which represent the effects of only rate sensitivity on the parameter q_2 . In the original GTN model, the parameter q_2 equals to a constant of 1.0 which corresponds to the static void growth in a rate-independent matrix material. Under the dynamic loading, q_2 is found to be strongly dependent on both strain-rate sensitivity and inertia and is a function of the current porosity of the porous viscoplastic material. Initially the parameter q_2 is much less than 1.0 and increases gradually towards 1.0 which indicates the strong effect of the rate sensitivity of the matrix materials (especially for $m = 0.5-1.0$) while inertial effects are negligible. The large decrease in q_2 at later stages reflects the dominance of inertial effects over rate dependence on void growth (especially for $m = 0-0.5$). For $m = 0.01$, inertia dominates the void growth very early in terms of increase in porosity while for $m = 1.0$, inertia is not significant from early stages. In addition to rate sensitivity, the transition point, at which dynamic void growth process which is dominated by rate dependence changes to one that is dominated by inertia, is also clearly affected by the initial porosity of the material, loading rate, and void size.

The above procedure can be adopted in general to estimate the inertial effects on dynamic void growth in viscoplastic materials. For any dynamic loading, the dynamic void growth curve $f(t)$ can be obtained by using the dynamic analysis of spherical shell presented in this study. The dependence of parameter q_2 in the GTN model on f is then computed using Eq. (8). For

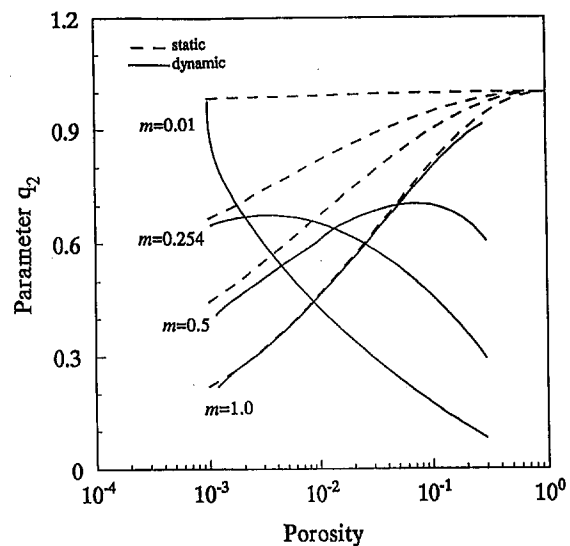


Fig. 5 Effects of rate sensitivity of the matrix material and inertia on the parametric function $q_2(f)$ in dynamic void growth process ($a_0 = 10 \mu\text{m}$, $\dot{\sigma}_h = 10 \text{ MPa/ns}$, $f_0 = 10^{-3}$, $q_1 = 1.0$, $m = 0.01, 0.254, 0.5$, and 1.0)

strong rate dependence and/or inertial effects (i.e., q_2 is far from constant), the function $q_2(f)$ can be obtained by curve fitting. The GTN model with q_1 and $q_2(f)$ can then be used in finite element analysis to model the deformation and failure of porous viscoplastic materials under the similar dynamic loading. For example, the curve fitting of the dynamic void growth shown in Fig. 1 gives

$$q_2(f) \approx h_2 \log^2(f) + h_1 \log(f) + h_0, f \geq f_0, \quad (14)$$

where $h_0 = 0.0646$, $h_1 = -0.494$, and $h_2 = -0.10$. The prediction on the dynamic void growth using such a $q_2(f)$ function and $q_1 = 1.0$ in the GTN model is also shown in Fig. 1, which is in excellent agreement with results of the current complete dynamic analysis. The initial porosity, void size, and dynamic loading rate will undoubtedly affect the curve-fitting results of $q_2(f)$, as discussed earlier, those factors have been shown to influence the dynamic void growth process for a given material (Tong and Ravichandran, 1993b). For example, for the case considered in Fig. 1, if $f_0 = 10^{-2}$, then $h_0 = 0.0086$, $h_1 = -0.801$, and $h_2 = -0.21$; if $f_0 = 10^{-4}$, then $h_0 = -0.003$, $h_1 = -0.355$, and $h_2 = -0.058$.

In a typical void growth induced failure process, the initial porosity f_0 in the material is commonly of the order of 10^{-4} to 10^{-2} . The porosity f defined in our spherical unit cell model (Eq. (9)) is related to the inner pore radius a through (neglecting volume change)

$$\frac{f}{f_0} \approx \left(\frac{a}{a_0}\right)^3, \text{ for, say, } 1 \leq \left(\frac{a}{a_0}\right) \leq 4. \quad (15)$$

For example, consider the case in which $f_0 = 10^{-3}$, one can verify that when $f/f_0 = 7.9444$ then $a/a_0 = 2$, and when $f/f_0 = 60.2$ then $a/a_0 = 4$. That is, f/f_0 is directly related to a length-scale parameter a/a_0 in the early stage of void growth. As shown in Fig. 1 in our paper that inertia clearly begins to overtake the effect of viscosity when $f/f_0 \approx 2$. In other words, when $a/a_0 \geq 1.26$, microinertia effects become significant in that particular case considered which is consistent with the statement by Ortiz and Molinari (1992). They stated that microinertia effects are particularly significant for voids which are larger than a characteristic dimension which depends on both the mechanical properties of the solid and the rate of expansion. However, we prefer the porosity f to the void radius a as a parameter characterizing void growth: in analyzing the growth and coalescence of voids that leads to fragmentation process, the criterion for ductile failure of materials is commonly related not to the size of voids but rather to the volume fraction of voids (f). Void size is not a micromechanical parameter or state variable in phenomenological ductile failure models such as the ones proposed by Perzyna (1986) and Needleman and Tvergaard (1991). Thus a parameter such as δ defined by Eq. (12) is a better measure of inertia on overall void growth and coalescence. There exists a possibility that in some cases microinertia effects will eventually become significant only after $f > 0.3$ (which may not be relevant to dynamic failure analysis anymore).

Other issues such as nucleation, interaction, size variation, and spatial distribution of voids are also important aspects of ductile failure processes and have yet to be addressed. Non-spherical symmetry of the loading and deformations on void growth are not considered in our analysis of a spherical shell. Analyses of void growth under combined hydrostatic and deviatoric dynamic loading are scarce and effects of deviatoric loading on dynamic void growth remain unclear. It appears that void growth may be affected by the presence of a field of deviatoric strain rates (Cortes, 1992b). The curve fitting of $q_2(f)$ requires that the loading history at each material point or element is to be known a priori. Even with those limitations, there are some potential applications of our analysis. Dynamic ductile failure dominated by hydrostatic loading is one class of important problems encountered in shock wave phenomena. For

example, although there is a relatively large deviatoric stress initially under a plane shock-wave loading, the inertial effects are expected to be small anyway during this very early stage of loading. Due to plastic flow, a hydrostatic stress state exists immediately behind a plane shock-wave front while inertia effects on void growth begin to dominate. Our analysis can be used as a tool to estimate the relative importance of inertia and material viscosity in ductile failure processes. In a dynamic structural analysis, the loading history of the actual or possible ductile failure sites can be estimated either by experiment or by the finite element analysis using models such as the GTN theory. Calculations using the GTN theory and our analysis can then be carried out for the microvoid growth at those sites. A comparison between those two results can be used to determine the necessity of including inertia in the analysis. Furthermore, there are some important dynamic ductile failure phenomena and experiments in which the overall loading condition is simple and is known a priori, for example, the spallation of materials in normal plate-impact experiments (Johnson, 1981; Perzyna, 1986). Our analysis combined with the GTN model can be readily applied to such an experiment.

In the light of increasing accuracy in determining viscoplastic properties of materials, the exclusion of inertial effects would become one of the leading causes for errors in analyzing damage and failure in ductile materials under dynamic loading. From a series of numerical analyses of both static and dynamic void growth in aluminum, a clear view of the inertial effects on void growth has emerged. The inertia tends to dominate for lower initial porosity, larger void size, higher loading rate, and less rate-sensitive and less strain-hardening matrix (such as structural steels and alloys) at a later stage of void growth. The dynamic void growth analysis presented here can be extended easily to other more sophisticated viscoplastic models for matrix materials (e.g., Follansbee and Kocks, 1988; Tong et al., 1992) and effects of loading histories and strain-rate histories on dynamic void growth can readily be assessed. The role of heat conduction and melting can also be studied using the current formulation.

In summary, the dynamic analysis of the expansion of a spherical shell can be used to compute the dynamic void growth curve $f(t)$ for a given loading condition. Such a void growth curve can then be used in conjunction with continuum porous viscoplasticity theories such as the Gurson-Tvergaard-Needleman (GTN) constitutive model to determine the relative importance of inertia and viscoplastic properties of the matrix (especially the rate dependence) on void growth process by examining the characteristics of the function $q_2(f)$. The inclusion of such a function into the GTN model is found to be able to provide an approximate dynamic void growth curve when inertia is dominant and/or material is strongly rate sensitive.

Acknowledgments

The authors would like to acknowledge the support of this research by the Division of Materials Research of the National Science Foundation through grant No. DMR-9396132. G.R. acknowledges the support of an NSF Presidential Young Investigator award, grant No. MSS-9157846. The computations were performed on a Cray Y-MP at the Jet Propulsion Laboratory (JPL) Supercomputer Center which was made possible through a grant provided by Cray Research, Inc., to the California Institute of Technology.

References

- Carroll, M. M., and Holt, A. C., 1972, "Static and Dynamic Pore-Collapse Relations for Ductile Porous Materials," *Journal of Applied Physics*, Vol. 43, pp. 1626-1636.
- Cortes, R., 1992a, "The Growth of Microvoid Under Intense Dynamic Loading," *International Journal of Solids and Structures*, Vol. 29, pp. 1339-1350.

- Cortes, R., 1992b, "Dynamic Growth of Microvoids Under Combined Hydrostatic and Deviatoric Stresses," *International Journal of Solids and Structures*, Vol. 29, pp. 1637–1645.
- Curran, D. R., Seaman, L., and Shockey, D. A., 1987, "Dynamic Failure of Solids," *Physics Reports*, Vol. 147, pp. 253–388.
- Follansbee, P. S., and Kocks, U. F., 1988, "A Constitutive Description of the Deformation of Copper Based on the Use of the mechanical Threshold Stress as an Internal State Variable," *Acta Metallurgica*, Vol. 36, pp. 81–93.
- Freund, B., 1990, *Dynamic Fracture*, Cambridge University Press, New York.
- Glennie, E. B., 1972, "The Dynamic Growth of a Void in a Plastic Material and An Application to Fracture," *Journal of the Mechanics and Physics of Solids*, Vol. 20, pp. 415–429.
- Godse, R., Ravichandran, G., and Clifton, R. J., 1989, "Micromechanisms of Dynamic Crack Propagation in an AISI 4340 Steel," *Materials Science & Engineering*, Vol. A122, pp. 79–88.
- Gurson, A. L., 1977, "Continuum Theory of Ductile Rupture by Void Nucleation and Growth: Part I—Yield Criterion and Flow Rules for Porous Ductile Media," *ASME Journal of Engineering Materials and Technology*, Vol. 99, pp. 2–15.
- Haghi, M., and Anand, L., 1991, "Analysis of Strain-Hardening Viscoplastic Thick-Walled Sphere and Cylinder Under External Pressure," *International Journal of Plasticity*, Vol. 7, pp. 123–140.
- Hutchinson, J. W., 1987, *Micro-Mechanics of Damage in Deformation and Fracture*, Department of Solid Mechanics, The Technical University of Denmark, Lyngby, Denmark.
- Johnson, J. N., 1981, "Dynamic Fracture and Spallation in Ductile Solids," *Journal of Applied Physics*, Vol. 52, pp. 2812–2825.
- Klocker, H., and Monthellet, F., 1991, "Influence of Flow Rule and Inertia on Void Growth in a Rate Sensitive Material," *Journal de Physique IV*, Vol. C3, pp. 733–738.
- Klopp, R. W., Clifton, R. J., and Shawki, T. G., 1985, "Pressure-Shear Impact and the Dynamic Viscoplastic Response of Metals," *Mechanics & Materials*, Vol. 4, pp. 375–385.
- Linse, V. D., 1983, *Dynamic Compaction of Metal and Ceramic Powders*, NMAB-394, National Academy Press, Washington, D.C.
- Luk, V. K., Forrestal, M. J., and Amos, D. E., 1991, "Dynamic Spherical Cavity-Expansion of Strain-Hardening Materials," *ASME JOURNAL OF APPLIED MECHANICS*, Vol. 58, pp. 1–6.
- McClintock, F. A., 1968, "A Criterion for Ductile Fracture by Growth of Holes," *ASME JOURNAL OF APPLIED MECHANICS*, Vol. 35, pp. 363–370.
- Needleman, A., and Tvergaard, V., 1991, "An Analysis of Dynamic, Ductile Crack Growth in a Double Edge Cracked Specimen," *International Journal of Fracture*, Vol. 49, pp. 41–67.
- Nemat-Nasser, S., and Hori, M., 1987, "Void Collapse and Void Growth in Crystalline Solids," *Journal of Applied Physics*, Vol. 62, pp. 2746–2757.
- Nemes, J. A., and Eftis, 1992, "Pressure-Shear Waves and Spall Fracture Described by a Viscoplastic-Damage Constitutive Model," *International Journal of Plasticity*, Vol. 8, pp. 185–207.
- Ortiz, M., and Molinari, A., 1992, "Effect of Strain Hardening and Rate Sensitivity on the Dynamic Growth of a Void in a Plastic Material," *ASME JOURNAL OF APPLIED MECHANICS*, Vol. 59, pp. 48–53.
- Perzyna, P., 1986, "Internal State Variable Description of Dynamic Fracture of Ductile Solids," *International Journal of Solids and Structures*, Vol. 22, pp. 797–818.
- Ranganath, S., and Clifton, R. J., 1972, "A Second-Order Accurate Difference Method for Systems of Hyperbolic Partial Differential Equations," *Computer Methods in Mechanics and Engineering*, Vol. 1, pp. 173–188.
- Rice, J. R., and Tracey, D. M., 1969, "On the Ductile Enlargement of Voids in Triaxial Stress Fields," *Journal of the Mechanics and Physics of Solids*, Vol. 17, pp. 201–217.
- Spitzig, W. A., Smelser, R. E., and Richmond, O., 1988, "The Evolution of Damage and Fracture in Iron Compacts with Various Initial Porosities," *Acta Metallurgica*, Vol. 36, pp. 1201–1211.
- Sun, L., and Huang, Z., 1992, "Dynamic Void Growth in Rate-Sensitive Plastic Solids," *International Journal of Plasticity*, Vol. 8, pp. 903–924.
- Thadhani, N. N., 1988, "Shock Compression Processing of Powders," *Advances in Materials & Manufacturing Processes*, Vol. 3, pp. 493–549.
- Tong, W., Clifton, R. J., and Huang, S., 1992, "Pressure-Shear Impact Investigation of Strain Rate History Effects in Oxygen-Free High-Conductivity Copper," *Journal of the Mechanics and Physics of Solids*, Vol. 40, pp. 1251–1294.
- Tong, W., and Ravichandran, G., 1993a, "Dynamic Pore Collapse in Viscoplastic Materials," *Journal of Applied Physics*, Vol. 74, pp. 2425–2435.
- Tong, W., and Ravichandran, G., 1993b, "Inertial Effects on Void Growth in Porous Viscoplastic Materials," GALCIT Technical Report SM93-18, California Institute of Technology, Pasadena, CA.
- Tong, W., Ravichandran, G., Christman, T., and Vreeland, T., Jr., 1993, "Processing SiC Particulate Reinforced Titanium Metal Matrix Composites by Shock Wave Consolidation," *Acta Metallurgica et Materials*, submitted for publication.
- Tvergaard, V., 1982, "On Localization in Ductile Materials Containing Spherical Voids," *International Journal of Fracture*, Vol. 18, pp. 237–252.
- Wilkinson, D. S., and Ashby, M. F., 1975, "Pressure Sintering by Power Law Creep," *Acta Metallurgica*, Vol. 23, pp. 1277–1285.

Damage-Coupled Creep Mechanics and its Structural Analysis Principle

Pan Zeng¹

Professor,
Department of Mechanical Engineering,
Tsinghua University,
100084 Beijing, P.R. China

X. F. Sun

Professor,
Institute of Applied Mechanics,
Southwest Jiaotong University,
610031 Chengdu, Sichuan, P.R. China

Continuum damage mechanics (CDM) is considered as a general method to treat the progressive deterioration of materials and structures in the framework of continuum mechanics. The damage-coupled creep mechanics based on CDM is discussed in the paper first, including the description of effective stress concept and the expression of all field equations in creep. The general formulation of a constitutive relation is presented after simplifying treatment for the sake of the modeling of creep damage problem in computational mechanics. The parametric variational principle (PVP) developed from the idea of optimal theory is introduced to establish the numerical principle of structural analysis for damage-coupled creep mechanics, including both the associated potential variational principle and the corresponding FEM formulations. The possibility of applying the principle presented by this paper to the life and damage prediction of structural components is finally illustrated by some examples on creep experiments for three kinds of materials.

1 Introduction

The present computational possibilities should allow structural analysis in which the material degradation and its corresponding strength decrease be taken into account during the whole calculation, but unfortunately there is no suitable method to deal with the complete coupling effect between the constitutive equation and damage in structural analysis. In the classical method of prediction of failure by CDM this coupling is usually neglected. In many circumstances, especially in the prediction of macrocrack growth, this coupling should not be neglected because the influence of the damage on the state of stress in the neighborhood of the crack is of primary importance (Lemaitre, 1985). Therefore, the modern way to calculate the rupture condition should be to simultaneously calculate the stress, strain, and damage field histories with coupled constitutive equations.

Saanouni (1985, 1988) and Chaboche (1989) introduced a correction term in the stiffness matrix of a common finite element model to take into account the damage coupling. It can be found that this approach actually is an approximate one based on the classical variational principle, not a complete coupling method. The difficulties associated with the corresponding numerical method are, perhaps, the complexity and nonlinearity of constitutive equations.

It is well known that creep is an important field studied by CDM (Ashby, 1984; Hayhurst, 1972, 1975; Murakami, 1980), so this paper first discusses the framework of damage-coupled creep mechanics on the basis of CDM for structural analysis, which covers the descriptions of damage-coupled constitutive equations, equilibrium equations, strain-displacement relations, and boundary and initial conditions. Then the complete coupling structural analysis principle is proposed, and the corresponding implementations based on numerical technique are given. Fi-

nally, several applications to high-temperature creep are discussed in detail.

2 Damage-Coupled Creep Mechanics

2.1 Effective Stress Concept. The effective stress is defined by

$$\bar{\sigma}_{ij} = \frac{\sigma_{ij}}{1 - \omega} \quad (1)$$

where σ_{ij} is the nominal stress, ω is an isotropic damage variable (here, is a scalar). And the incremental form of effective stress is

$$d\bar{\sigma}_{ij} = \frac{d\sigma_{ij}}{(1 - \omega)} + \frac{\sigma_{ij}^0}{(1 - \omega^0)^2} d\omega. \quad (2)$$

Similarly, the damage-coupled constitutive equation can also be expressed as follows:

$$\begin{aligned} d\sigma_{ij} &= (1 - \omega^0) D_{ijkl} d\epsilon_{kl}^e - \frac{\sigma_{ij}^0}{(1 - \omega)} d\omega \\ &= \bar{D}_{ijkl} d\epsilon_{kl}^e - \frac{\sigma_{ij}^0}{(1 - \omega^0)} d\omega \end{aligned} \quad (3)$$

where

$$\bar{D}_{ijkl} = (1 - \omega^0) D_{ijkl} \quad (4)$$

is called the damage-coupled elasticity tensor.

2.2 All Field Equations. The purpose here is to give an overall description of damage-coupled creep problems which will be used as a basis of structural analysis. Now, all associated equations based on CDM during loading are listed as follows in terms of incremental quantity:

(a) equilibrium equations

$$d\sigma_{ij,j} + db_i = 0 \quad \text{in } \Omega \quad (5)$$

(b) strain-displacement relations

$$2d\epsilon_{ij} = du_{i,j} + du_{j,i} \quad \text{in } \Omega \quad (6)$$

(c) constitutive relations

¹ Research Fellowship (1994–1995) of Alexander von Humboldt Foundation, Institute B of Mechanics, University of Stuttgart, 70550 Stuttgart, Germany.

Contributed by the Applied Mechanics Division of THE AMERICAN SOCIETY OF MECHANICAL ENGINEERS for publication in the ASME JOURNAL OF APPLIED MECHANICS.

Discussion on the paper should be addressed to the Technical Editor, Professor Lewis T. Wheeler, Department of Mechanical Engineering, University of Houston, Houston, TX 77204-4792, and will be accepted until four months after final publication of the paper itself in the ASME JOURNAL OF APPLIED MECHANICS.

Manuscript received by the ASME Applied Mechanics Division, Mar. 17, 1992; final revision, Sept. 6, 1993. Associate Technical Editor: R. M. McMeeking.

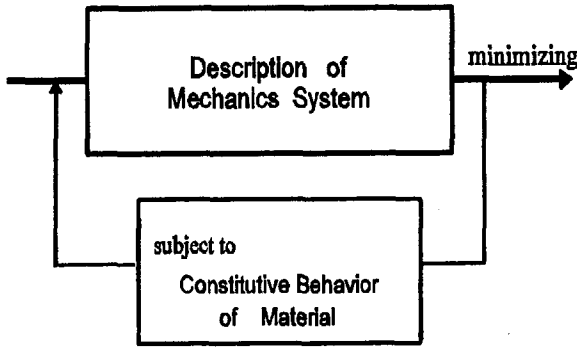


Fig. 1 The parametric variational principle from optimal theory

$$d\epsilon_{ij} = d\epsilon_{ij}^e + d\epsilon_{ij}^p + d\epsilon_{ij}^c \quad (7)$$

$$d\sigma_{ij} = \bar{D}_{ijkl} d\epsilon_{kl} - \frac{\sigma_{ij}^0}{(1 - \omega^0)} d\omega \quad (8)$$

$$d\epsilon_{ij}^p = \lambda^p \frac{\partial g}{\partial \sigma_{ij}} \quad (9)$$

$$f(\bar{\sigma}_{ij}, \epsilon_{ij}^p) \leq 0 \quad (10)$$

$$\lambda^p \begin{cases} > 0 & \text{when } f = 0 \text{ for plastic loading} \\ = 0 & \text{when } f < 0 \text{ for elastic loading or unloading} \end{cases}$$

$$(11)$$

$$\dot{\epsilon}_{ij}^c = q_{ij}(\bar{\sigma}_{kl}, \omega) \quad (12)$$

$$\dot{\omega} = - \frac{\partial x^*}{\partial Y} \quad (13)$$

(d) boundary and initial conditions

$$d\sigma_{ij} \cdot n_j = d\bar{p}_i \quad \text{on } S_p \quad (14)$$

$$du_i = d\pi_i \quad \text{on } S_u \quad (15)$$

$$\epsilon_{ij}^c|_{t=0} = 0 \quad (16)$$

$$\omega|_{t=0} = 0 \quad (17)$$

in which $d\epsilon_{ij}$, $d\epsilon_{ij}^e$, $d\epsilon_{ij}^p$, and $d\epsilon_{ij}^c$ are, respectively, the total, elastic, plastic, and creep components of the strain tensor; the superposed mark '.' denotes the time derivative; f is the yielding function; g is the plastic potential function; λ^p is the plastic flow factor; q is the creep function; x^* is the dissipation potential function of CDM, Y is the damage energy lease rate.

3 Basic Framework of Parametric Variational Principle

3.1 Fundational of Optimal Theory. The fundamental strategy of the parametric variational principle draws the concepts from the optimal theory. It can be found that there are mainly two aspects: the description of the mechanical system and the constraint of constitutive relations (see Fig. 1).

3.2 On Complex Constitutive Relations. The expressions of all constitutive relations in CDM are very irregular, complex, and nonlinear, so it is difficult to directly apply them to deal with practical problems. In the parametric variational principle, all constitutive relations are considered as the constraints to act on the mechanical system, which should be generalized in order to obtain a group of linear constraint equations.

In general, after the mathematical treatment of the original constitutive relations, the corresponding constraint equations can be expressed as follows:

$$\psi(d\epsilon, du, \lambda) = 0 \quad (18)$$

where ψ indicates the vector function, $d\epsilon$ or du is the argument function, and λ is the parameter variable, which as an argument does not participate in the variation.

3.3 Parametric Variational Principle. The variational principle is an important basis of the numerical method. The parametric variational principle is a modern variational method coming from the optimal theory to solve the nonlinear unspecified boundary problems in continuum mechanics, which has been successfully applied in many fields, e.g., elastoplasticity, geomechanics, frictional contact problem, and viscoplasticity, etc.

First, as a description of mechanical system, the generalized potential energy functional is constructed as

$$\begin{aligned} \Pi(d\epsilon, du, \lambda) = & \int_{\Omega} [A(d\epsilon, du, \lambda)] d\Omega \\ & - \left[\int_{\Omega} dbdud\Omega + \int_{S_p} d\bar{p}du dS \right] \quad (19) \end{aligned}$$

where $A(d\epsilon, du, \lambda)$ is the generalized strain energy functional and $d\bar{p}$ is the boundary force.

After the above preparation of the constraint equations and generalized strain energy functional, the parametric variational principle can be expressed as follows:

find $d\epsilon$ or du

$$\text{minimize } \Pi(d\epsilon, du, \lambda)$$

$$\text{subject to } \psi(d\epsilon, du, \lambda) = 0. \quad (20)$$

4 General Expression of Constitutive Relations

The constitutive relations of damage-coupled creep are very complex and nonlinear. In this paper, the all constitutive relations are considered as the constraint conditions to act on the mechanical system, which should be generalized, aiming at obtaining a group of linear equations.

First, the loading consistent conditions (10) and (11) are mathematically treated. Then, substitution of relations (3), (7), (9) into the function $f = f^0 + df$ leads to the following relation:

$$\begin{aligned} f &= f^0 + \frac{\partial f}{\partial \bar{\sigma}_{ij}} d\bar{\sigma}_{ij} + \frac{\partial f}{\partial \epsilon_{ij}^p} d\epsilon_{ij}^p \\ &= f^0 + \frac{\partial f}{\partial \bar{\sigma}_{ij}} D_{ijkl} d\epsilon_{kl}^e + \lambda^p \frac{\partial f}{\partial \epsilon_{ij}^p} d\epsilon_{ij}^p \\ &= \zeta_{ij}^{(f)} d\epsilon_{ij} + I^{(f)} \lambda^p + \rho_{ij}^{(f)} \lambda_{ij}^c + \xi^{(f)} \quad (21) \end{aligned}$$

where

$$\zeta_{ij}^{(f)} = D_{ijkl} \frac{\partial f}{\partial \bar{\sigma}_{kl}} \quad (22)$$

$$I^{(f)} = \frac{\partial f}{\partial \epsilon_{ij}^p} \frac{\partial g}{\partial \sigma_{ij}} - D_{ijkl} \frac{\partial f}{\partial \bar{\sigma}_{ij}} \frac{\partial g}{\partial \sigma_{kl}} \quad (23)$$

$$\rho_{ij}^{(f)} = -D_{ijkl} \frac{\partial f}{\partial \bar{\sigma}_{kl}} \quad (24)$$

$$\xi^{(f)} = f^0 \quad (25)$$

$$\lambda_{ij}^c = d\epsilon_{ij}^c. \quad (26)$$

By introducing a positive complementary factor ν into the loading consistent condition, (10) and (11) could lead to

$$f + \nu = 0 \quad (27)$$

$$\lambda^p \nu = 0, \quad \lambda^p \geq 0, \quad \nu \geq 0. \quad (28)$$

Define the function $\psi^{(f)}(d\epsilon_{ij}, \lambda^p, \lambda_{ij}^c, \nu)$ as

$$\begin{aligned} \psi^{(f)}(d\epsilon_{ij}, \lambda^p, \lambda_{ij}^c, \nu) &= f + \nu \\ &= \zeta_{ij}^{(f)} d\epsilon_{ij} + I^{(f)} \lambda^p + \rho_{ij}^{(f)} \lambda_{ij}^c + \xi^{(f)} + \nu \end{aligned} \quad (29)$$

so Eqs. (27) and (28) could be rewritten as

$$\psi^{(f)}(d\epsilon_{ij}, \lambda^p, \lambda_{ij}^c, \nu) = 0 \quad (30)$$

$$\lambda^p \nu = 0, \quad \lambda^p \geq 0, \quad \nu \geq 0. \quad (31)$$

Similar treatment of the creep Eq. (12) gives the following expression:

$$\begin{aligned} \psi_{ij}^{(c)}(d\epsilon_{kl}, d\omega, \lambda^p, \lambda_{kl}^c) \\ = \zeta_{ijkl}^{(c)} d\epsilon_{kl} + \eta_{ij}^{(c)} d\omega + I_{ij}^{(c)} \lambda^p + \rho_{ijkl}^{(c)} \lambda_{kl}^c + \xi_{ij}^{(c)} = 0 \end{aligned} \quad (32)$$

where

$$\zeta_{ijkl}^{(c)} = D_{mnlk} \frac{\partial q_{ij}}{\partial \bar{\sigma}_{mn}} dt \quad (33)$$

$$\eta_{ij}^{(c)} = \frac{\partial q_{ij}}{\partial \omega} dt \quad (34)$$

$$I_{ij}^{(c)} = -D_{mnlk} \frac{\partial q_{ij}}{\partial \bar{\sigma}_{mn}} \frac{\partial g}{\partial \sigma_{kl}} dt \quad (35)$$

$$\rho_{ijkl}^{(c)} = -D_{mnlk} \frac{\partial q_{ij}}{\partial \bar{\sigma}_{mn}} dt - \delta_{ij} \delta_{kl} \quad (36)$$

$$\xi_{ij}^{(c)} = q_{ij}^0 dt. \quad (37)$$

Furthermore, the damage Eq. (13) could also be expressed as

$$\begin{aligned} \psi^{(d)}(d\epsilon_{ij}, d\omega, \lambda^p, \lambda_{ij}^c) \\ = \zeta_{ij}^{(d)} d\epsilon_{ij} + \eta^{(d)} d\omega + I^{(d)} \lambda^p + \rho_{ij}^{(d)} \lambda_{ij}^c + \xi^{(d)} = 0 \end{aligned} \quad (38)$$

where

$$\zeta_{ij}^{(d)} = D_{ijkl} \frac{\partial h}{\partial \bar{\sigma}_{kl}} dt \quad (39)$$

$$\eta^{(d)} = \frac{\partial h}{\partial \omega} dt - 1 \quad (40)$$

$$I^{(d)} = -D_{ijkl} \frac{\partial h}{\partial \bar{\sigma}_{ij}} \frac{\partial g}{\partial \sigma_{kl}} dt \quad (41)$$

$$\rho_{ij}^{(d)} = -D_{ijkl} \frac{\partial h}{\partial \bar{\sigma}_{kl}} dt \quad (42)$$

$$\xi^{(d)} = h^0 dt. \quad (43)$$

The above expressions on constitutive relations could be summarized as follows:

$$\psi^{(f)}(d\epsilon_{ij}, \lambda^p, \lambda_{ij}^c, \nu) = 0 \quad (44)$$

$$\psi_{ij}^{(c)}(d\epsilon_{kl}, d\omega, \lambda^p, \lambda_{kl}^c) = 0 \quad (45)$$

$$\psi^{(d)}(d\epsilon_{ij}, d\omega, \lambda^p, \lambda_{ij}^c) = 0 \quad (46)$$

$$\lambda^p \nu = 0, \quad \lambda^p \geq 0, \quad \nu \geq 0 \quad (47)$$

which give the overall descriptions of constraint equations for elastoplastic creep damage problem together with the initial conditions (16) and (17). It can be found that Eqs. (44), (45), and (46) are all linear equations in terms of variables $d\epsilon_{ij}$, λ^p , λ_{ij}^c , $d\omega$, ν , and the nonlinear item is only in the positive complementary Eq. (47).

5 PVP for Damage-Coupled Creep Mechanics

According to the basic framework of the parametric variational principle discussed above, a potential energy functional for the damage-coupled creep problem is actually constructed as follows:

$$\begin{aligned} \Pi(d\epsilon_{ij}, du_i, d\omega, \lambda^p, \lambda_{ij}^c) \\ = \int_{\Omega} \left\{ \frac{1}{2} \bar{D}_{ijkl} d\epsilon_{ij} d\epsilon_{kl} - \lambda^p \bar{D}_{ijkl} \frac{\partial g}{\partial \sigma_{ij}} d\epsilon_{kl} \right. \\ \left. - \lambda_{ij}^c \bar{D}_{ijkl} d\epsilon_{kl} - \frac{d\omega}{(1-\omega^0)} \sigma_{ij}^0 d\epsilon_{ij} \right\} d\Omega \\ - \left[\int_{\Omega} db_i du_i d\Omega + \int_{S_p} d\bar{p}_i du_i dS \right]. \end{aligned} \quad (48)$$

Now the structural analysis principle for the damage-coupled creep problem could be stated as follows: in the range of any time $[t, t + dt]$, among admissible solutions which satisfy the strain-displacement relation (6) and geometric boundary condition (15), the exact solution renders the functional Π a minimum under the constraint conditions of Eqs. (44)–(47) together with the initial conditions (16) and (17), where du_i (or $d\epsilon_{ij}$) is the argument function, $d\omega$, λ_{ij}^c , λ^p are the parameters representing the incremental quantities of damage, creep and the plastic flow factor, respectively, which as arguments do not participate in the variation (Zhong et al., 1988; Zeng, 1991). For related proof please see the paper of Zeng (1992).

6 Corresponding FEM Formulation

The finite element method (FEM) is a numerical approach which can be used for obtaining an accurate or approximate solution of complex engineering problems. Now, based on the above variational principle, the finite element analysis is interpreted as an approximate means for solving the damage-coupled creep problem. The procedure includes the discretization of the domain or structure, and the introduction of interpolation polynomial functions, i.e.,

$$d\mathbf{u} = \mathbf{N}_u \delta \quad (49)$$

$$d\boldsymbol{\epsilon} = \mathbf{B}_\epsilon \delta \quad (50)$$

$$d\omega = \mathbf{N}_\omega \alpha \quad (51)$$

$$\boldsymbol{\lambda}^c = \mathbf{B}_\kappa \boldsymbol{\kappa} \quad (52)$$

where δ , α , and $\boldsymbol{\kappa}$ are the incremental vectors of nodal displacement, damage, and creep strain, respectively, \mathbf{N}_u , \mathbf{B}_ϵ , \mathbf{N}_ω , and \mathbf{B}_κ are the matrices of interpolation functions (shape function) of displacement, strain, damage, and creep strain, respectively.

Substitution of Eqs. (49)–(52) into Eq. (48) yields the matrix formulae of potential energy of mechanical system, and also substitution of Eqs. (49)–(52) into Eqs. (44)–(47) gives the matrix formulae of constraint equations, they are listed as follows:

$$\Pi(\delta) = \frac{1}{2} \delta^T \mathbf{K} \delta - \delta^T [\Phi_1 \boldsymbol{\lambda}^p + \Phi_2 \alpha + \Phi_3 \boldsymbol{\kappa} + \mathbf{q}] \quad (53)$$

subject to

$$\mathbf{C}_1 \delta + \mathbf{U}_1 \alpha + \mathbf{V}_1 \boldsymbol{\lambda}^p + \mathbf{W}_1 \boldsymbol{\kappa} + \mathbf{d}_1 = 0 \quad (54)$$

$$\mathbf{C}_2 \delta + \mathbf{U}_2 \alpha + \mathbf{V}_2 \boldsymbol{\lambda}^p + \mathbf{W}_2 \boldsymbol{\kappa} + \mathbf{d}_2 = 0 \quad (55)$$

$$\mathbf{C}_3 \delta + \mathbf{V}_3 \boldsymbol{\lambda}^p + \mathbf{W}_3 \boldsymbol{\kappa} + \mathbf{d}_3 + \nu = 0 \quad (56)$$

$$\boldsymbol{\nu}^T \boldsymbol{\lambda}^p = 0, \quad \boldsymbol{\nu}^T \geq 0, \quad \boldsymbol{\lambda}^p \geq 0 \quad (57)$$

with

$$\begin{aligned}\bar{\mathbf{K}} &= \sum_{e=1}^n \int_{\Omega^e} (\mathbf{B}_e^T \bar{\mathbf{D}} \mathbf{B}_e) d\Omega \\ &= (1 - \omega^0) \sum_{e=1}^n \int_{\Omega^e} (\mathbf{B}_e^T \mathbf{D} \mathbf{B}_e) d\Omega\end{aligned}\quad (58)$$

$$\Phi_1 = \sum_{e=1}^{n_1} \int_{\Omega^e} \left[\mathbf{B}_e^T \bar{\mathbf{D}} \left(\frac{\partial g}{\partial \boldsymbol{\sigma}} \right) \right] d\Omega \quad (59)$$

$$\Phi_2 = \sum_{e=1}^n \int_{\Omega^e} \left[\frac{1}{(1 - \omega^0)} (\mathbf{B}_e^T \boldsymbol{\sigma}_0 \mathbf{N}_\omega) \right] d\Omega \quad (60)$$

$$\Phi_3 = \sum_{e=1}^n \int_{\Omega^e} (\mathbf{B}_e^T \bar{\mathbf{D}} \mathbf{B}_e) d\Omega \quad (61)$$

$$\mathbf{q} = \sum_{e=1}^n \int_{\Omega^e} (\mathbf{N}_u^T d\mathbf{b}) d\Omega + \sum_{e=1}^{n_2} \int_{S^e} (\mathbf{N}_u^T d\bar{\mathbf{p}}) d\Omega \quad (62)$$

$$\mathbf{C}_1 = \sum_{e=1}^n \int_{\Omega^e} (\mathbf{B}_e^T \boldsymbol{\xi}^{(c)}) d\Omega \quad (63)$$

$$\mathbf{U}_1 = \sum_{e=1}^n \int_{\Omega^e} (\mathbf{N}_w^T \boldsymbol{\eta}^{(c)}) d\Omega \quad (64)$$

$$\mathbf{V}_1 = \sum_{e=1}^{n_1} \int_{\Omega^e} \mathbf{I}^{(c)} d\Omega \quad (65)$$

$$\mathbf{W}_1 = \sum_{e=1}^n \int_{\Omega^e} (\mathbf{B}_e^T \boldsymbol{\rho}^{(c)}) d\Omega \quad (66)$$

$$\mathbf{d}_1 = \sum_{e=1}^n \int_{\Omega^e} (\boldsymbol{\xi}^{(c)}) d\Omega \quad (67)$$

$$\mathbf{C}_2 = \sum_{e=1}^n \int_{\Omega^e} (\mathbf{B}_e^T \boldsymbol{\xi}^{(d)}) d\Omega \quad (68)$$

$$\mathbf{U}_2 = \sum_{e=1}^n \int_{\Omega^e} (\mathbf{N}_w^T \boldsymbol{\eta}^{(d)}) d\Omega \quad (69)$$

$$\mathbf{V}_2 = \sum_{e=1}^{n_1} \int_{\Omega^e} \mathbf{I}^{(d)} d\Omega \quad (70)$$

$$\mathbf{W}_2 = \sum_{e=1}^n \int_{\Omega^e} (\mathbf{B}_e^T \boldsymbol{\rho}^{(d)}) d\Omega \quad (71)$$

$$\mathbf{d}_2 = \sum_{e=1}^n \int_{\Omega^e} \boldsymbol{\xi}^{(d)} d\Omega \quad (72)$$

$$\mathbf{C}_3 = \sum_{e=1}^{n_1} \int_{\Omega^e} (\mathbf{B}_e^T \boldsymbol{\xi}^{(f)}) d\Omega \quad (73)$$

$$\mathbf{V}_3 = \sum_{e=1}^{n_1} \int_{\Omega^e} \mathbf{I}^{(f)} d\Omega \quad (74)$$

$$\mathbf{W}_3 = \sum_{e=1}^{n_1} \int_{\Omega^e} (\mathbf{B}_e^T \boldsymbol{\rho}^{(f)}) d\Omega \quad (75)$$

$$\mathbf{d}_3 = \sum_{e=1}^{n_1} \int_{\Omega^e} \boldsymbol{\xi}^{(f)} d\Omega \quad (76)$$

where n is the number of total elements, n_1 is the number of plastic elements, n_2 is the number on the force boundary, the subscript 'e' denotes the element number, $\bar{\mathbf{K}}$ is called the damage-coupled assembled stiffness matrix for the creep problem, and \mathbf{K} is the assembled stiffness matrix of an undamaged body, which is same as that of an elastic problem. It is to be noted that the potential energy functional without considering the damage-coupled effect and plasticity is given by

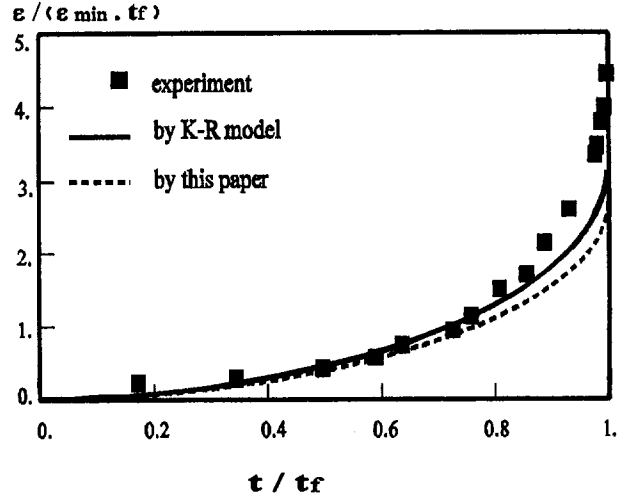


Fig. 2 Creep curve of GH33A alloy at 700°C

$$\Pi(\boldsymbol{\delta}) = \frac{1}{2} \boldsymbol{\delta}^T \mathbf{k} \boldsymbol{\delta} - \boldsymbol{\delta}^T \mathbf{q}, \quad (77)$$

which is the potential energy functional of the elastic structure or body.

Equation (53) expresses the total potential energy of structure or body for damage-coupled creep problem in terms of the nodal displacement $\boldsymbol{\delta}$. By the variational principle expressed by (48), we have

$$\frac{\partial \Pi}{\partial \boldsymbol{\delta}} = 0. \quad (78)$$

By using the expression (53), the above equation can be expressed as

$$\bar{\mathbf{K}} \boldsymbol{\delta} - \Phi_1 \boldsymbol{\lambda}^p - \Phi_2 \boldsymbol{\alpha} - \Phi_3 \boldsymbol{\kappa} - \mathbf{q} = 0. \quad (79)$$

Linking up Eq. (79) with the constraint Eqs. (54)–(57), we can simultaneously solve the unknown variables $\boldsymbol{\delta}$, $\boldsymbol{\alpha}$, $\boldsymbol{\kappa}$, $\boldsymbol{\lambda}^p$, $\boldsymbol{\nu}$ with coupling between them, i.e.,

$$\bar{\mathbf{K}} \boldsymbol{\delta} - \Phi_1 \boldsymbol{\lambda}^p - \Phi_2 \boldsymbol{\alpha} - \Phi_3 \boldsymbol{\kappa} - \mathbf{q} = 0 \quad (80)$$

$$\mathbf{C}_1 \boldsymbol{\delta} + \mathbf{U}_1 \boldsymbol{\alpha} + \mathbf{V}_1 \boldsymbol{\lambda}^p + \mathbf{W}_1 \boldsymbol{\kappa} + \mathbf{d}_1 = 0 \quad (81)$$

$$\mathbf{C}_2 \boldsymbol{\delta} + \mathbf{U}_2 \boldsymbol{\alpha} + \mathbf{V}_2 \boldsymbol{\lambda}^p + \mathbf{W}_2 \boldsymbol{\kappa} + \mathbf{d}_2 = 0 \quad (82)$$

$$\mathbf{C}_3 \boldsymbol{\delta} + \mathbf{V}_3 \boldsymbol{\lambda}^p + \mathbf{W}_3 \boldsymbol{\kappa} + \mathbf{d}_3 + \boldsymbol{\nu} = 0 \quad (83)$$

$$\boldsymbol{\nu}^T \boldsymbol{\lambda}^p = 0, \quad \boldsymbol{\lambda}^p \geq 0, \quad \boldsymbol{\nu} \geq 0. \quad (84)$$

Among these equations, the first four equations are linear and the last one is nonlinear; however, they can be transferred into the linear complementary problem and be solved by using quadratic programming (Bararara, 1979; Zeng, 1990).

7 Experiments and Analysis

7.1 Simple Examples. The following examples are of interest to show the ability of the application to the above numerical method. First, the paper quotes the results of high-temperature creep experiments about GH33A alloy at 700°C (see Liu, 1990, 1991) in which the smooth specimen is submitted to a constant load. We apply the proposed structural analysis principle to carry out the corresponding calculations and analysis which are compared with the results of both experiments and the Kachanov-Rabotnov theory model. Figure 2 gives the creep-

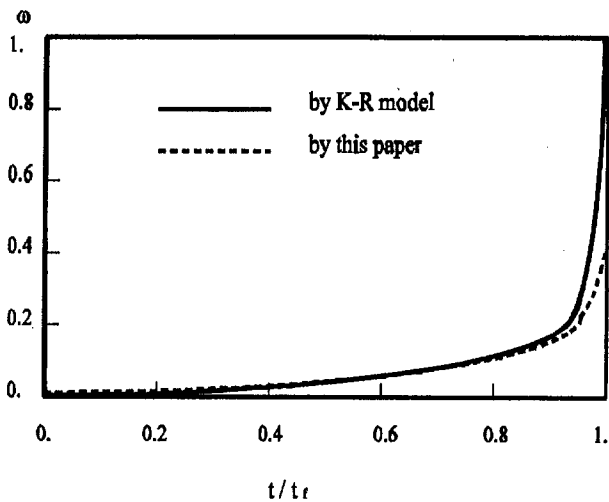


Fig. 3 Damage curve of GH33A alloy at 700°C

time curve of GH33A alloy at 700°C, and Fig. 3 gives the damage behaviour curve.

Another two examples about 2.25Cr-1Mo steel at 550°C and GH36 alloy at 650°C have been carried out with satisfactory results.

7.2 CT Specimen. The paper has also dealt with CT (compact tension) specimen (GH36 alloy) with the complex field problem. The experiment condition is high-temperature creep at 650°C by ASTM standard. The two-dimensional FEM based on the coupling principle of the paper is used to numerically calculate the whole process of damage deterioration of a CT specimen in comparison with results of experiments (see Fig. 4 and Fig. 5).

From the above examples regarding the uniaxial specimen and the CT specimen with a complex damage field problem, it is shown that the coupling principle proposed by this paper is effective to numerically deal with damage-coupled problems.

8 Concluding Remarks

An effort has been made to elucidate some of damage-coupled structural analysis of creep problems and the corresponding framework from the point of view of continuum damage mechanics. Furthermore, the attention has been focused on the numerical variational principle for damage-coupled creep problems that aims at developing a useful means to deal with the

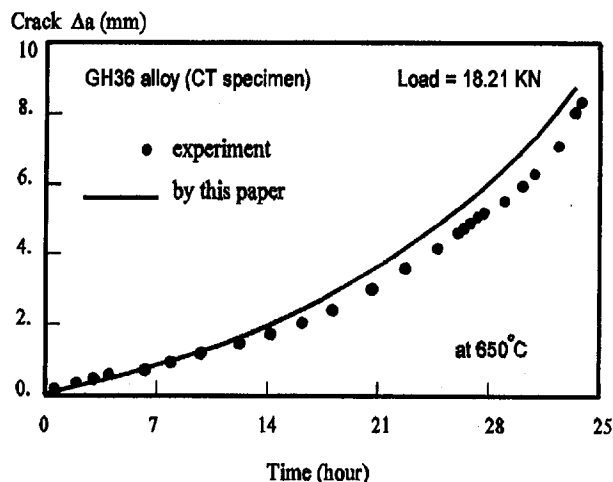


Fig. 4 Crack propagation curve

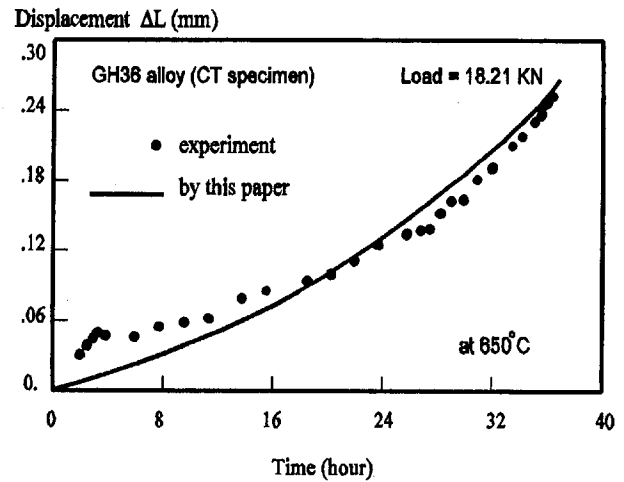


Fig. 5 Displacement curve

complex and nonlinear constitutive relations. The established variational principle can be summarized as follows, in brief:

find du_i or $d\epsilon_{ij}$

$$\text{minimize } \Pi(d\epsilon_{ij}, du_i, d\omega, \lambda^p, \lambda_{ij}^c) \quad (85)$$

subject to

$$\psi^{(f)}(d\epsilon_{ij}, \lambda^p, \lambda_{ij}^c, \nu) = 0 \quad (86)$$

$$\psi_{ij}^{(c)}(d\epsilon_{kl}, d\omega, \lambda^p, \lambda_{kl}^c) = 0 \quad (87)$$

$$\psi^{(d)}(d\epsilon_{ij}, d\omega, \lambda^p, \lambda_{ij}^c) = 0 \quad (88)$$

$$\lambda^p \nu = 0, \quad \lambda^p \geq 0, \quad \nu \geq 0 \quad (89)$$

$$\omega|_{t=0} = 0 \quad (90)$$

$$\lambda_{ij}^c|_{t=0} = 0 \quad (91)$$

where the expressions of Π , $\psi^{(f)}$, $\psi_{ij}^{(c)}$, $\psi^{(d)}$ refer to (48), (29), (32), (38), respectively.

The main contents of the paper and features of the proposed principle may be found as follows:

1 The complete description of creep problem for structural analysis considering damage-coupling effects has been established, strongly aimed at engineering applications.

2 All the constitutive relations of the damage-coupled creep problem are treated in generalized forms with linear equations, except for one (i.e., positive complementary Eq. (89)). Therefore, the principle proposed in the paper is suitable for the general creep problem expressed in Eqs. (12) and (13).

3 The proposed structural principle can be easily approximated by numerical methods (e.g., FEM techniques) in a direct equation-solving way without any iterative procedures for the nonlinear problem. Its implementation of FEM is also discussed in detail.

4 The principle is very simple since the variation operation is carried out only for du_i or $d\epsilon_{ij}$, and λ^p , λ_{ij}^c , $d\omega$ may be regarded as constants during the variation operation, but λ^p , λ_{ij}^c , and $d\omega$ play the important role in connection between the energy functional and the constraint equations.

5 Some examples about high-temperature creep of GH33A alloy at 700°C, 2.25Cr-1Mo steel at 550°C, and GH36 at 650°C are presented to show some applications of the principle.

Acknowledgments

This work was supported by the National Natural Science Foundation of China. The authors would like to thank Prof. Q. Gao for the helpful discussions.

References

- Ashby, M. F., and Dyson, B. F., 1984, "Creep Damage Mechanics and Micro-mechanism," *Proceedings of the 6th International Conference on Fracture*, New Delhi, Vol. 1, pp. 3-30.
- Bararaa, M. S., and Shetty, C. M., 1979, *Nonlinear Programming: Theory and Algorithms*, John Wiley and Sons, New York.
- Benallal, A., Billardon, R., and Lemaitre, J., 1984, "Failure Analysis of Structures by Continuum Damage Mechanics," *Proceedings of the 6th International Conference on Fracture*, New Delhi, Vol. 5, pp. 3669-3676.
- Chaboche, J. L., 1989, "Phenomenological Aspects of Continuum Damage Mechanics," *Theoretical and Applied Mechanics*, P. German et al. eds., Proceedings of ICTAM-17, North-Holland, Amsterdam, pp. 41-56.
- Hayhurst, D. R., et al., 1984, "The Role of Continuum Damage in Creep Crack Growth," *Phil. Trans. Roy. Soc. Lond.*, Vol. A311, pp. 131-158.
- Jacobs, O. L. R., 1974, *Introduction to Control Theory*, Oxford University Press, Oxford, UK.
- Kachanov, L. M., 1958, "The Time to Failure Under Creep Condition," *Izv. Akad. Nauk., SSSR. Tekh. Nauk.*, No. 8, pp. 26-31.
- Krajcinovic, D., and Fonseka, G. U., 1979, "Continuous Damage Theory of Brittle Materials," *ASME JOURNAL OF APPLIED MECHANICS*, Vol. 48, pp. 809-824.
- Lemaitre, J., 1983, "A Three Dimensional Ductile Damage Model Applied to Deep Drawing Forming Limits," *Proceedings of the 4th International Conference on Mechanical Behaviour of Materials*, Vol. 2, pp. 1059-1065.
- Lemaitre, J., 1985, "A Continuous Damage Mechanics Model for Ductile Fracture," *ASME Journal of Engineering Materials and Technology*, Vol. 107, pp. 83-89.
- Lemaitre, J., 1985, "Coupled Elasto-Plasticity and Damage Constitutive Equations," *Comp. Meth. Appl. Mech. Engng.*, Vol. 51, pp. 31-49.
- Lin, Y., 1991, "A Micro-Composite Model of Localization in Creep Damage," *Mechanical Behaviour of Materials-VI*, Jono et al. eds., Proceedings of the ICM-6, Pergamon Press, New York, Vol. 3, pp. 859-864.
- Murakami, S., and Ohno, N., 1980, "A Continuum Theory of Creep and Creep Damage," *Creep in Structures*, A. R. S. Ponter and D. R. Hayhurst, eds., pp. 422-442.
- Rabotnov, Y. M., 1969, *Creep Problems in Structural Members*, North-Holland, Amsterdam.
- Saanouni, K., Chaboche, J. L., and Bathias, C., 1986, "On the Creep Crack Growth Prediction by a Local Approach," *IUTAM Symp. on Mechanics of Damage and Fatigue*, *Journal of Engineering Fracture Mechanics*, Vol. 25, No. 5-6, pp. 677-691.
- Saanouni, K., 1988, "Sur l'analyse de la fissuration des milieux élasto-viscoplastiques par la théorie de l'endommagement continu," Thèse d'Etat, Université de Compiègne.
- Zeng, P., 1990, "A Direct Algorithm for Linear Complimentary Problem of Quadratic Programming," *Proceedings of the Int. Symp. on Approximation, Optimization and Computing*, Elsevier Science Publishers, Amsterdam, The Netherlands, pp. 361-364.
- Zeng, P., and Zhong, W. X., 1991, "The Parametric Variational Principle for Perzyna Model in Viscoplasticity," *Applied Mathematics and Mechanics*, Vol. 12, No. 5, pp. 409-414.
- Zeng, P., 1992, "Computational Damage Mechanics: Concept and Principle," ICTAM-18, Session B-P3, Israel.
- Zhong, W. X., and Zhang, R. L., 1988, "The Parametric Variational Principle for Elastoplasticity," *Acta Mechanica Sinica*, Vol. 4, pp. 134-137.

Measurement of Cyclic Biaxial Elastoplastic Stresses at Notch Roots

C. H. Yang

Associate Professor,
Department of Mechanical Engineering,
Chang Gung College of Medicine
and Technology,
Taiwan

W. N. Sharpe

Department of Mechanical Engineering,
The Johns Hopkins University,
Baltimore, MD 21218-2686
Fellow ASME

A straightforward procedure is demonstrated for measuring local cyclic elastoplastic biaxial stresses at notch roots. First, the biaxial cyclic strains are measured over short gage lengths (150 or 200 micrometers) with a laser-based strain measuring system. Then, cyclic stresses are computed from those measured strains by using an elastoplastic constitutive model. The material selected for this study is HY-80 steel which has a fine grain size and is isotropic. Double-notched specimens were prepared with two different notch geometries: a U-shaped notch with a 4.76 mm radius and a V-shaped notch with a 1.0 mm radius. Two thicknesses, 2.54 and 12.7 mm, were tested for each notch geometry to produce four different amounts of notch constraint. The results of cyclic biaxial strain measurements show good reproducibility. Stress computations based on two different constitutive models were used to compute stresses for the first cycle and a stable cycle. One of the constitutive models is the classical J_2 flow theory and the other is a two-surface cyclic plasticity model. The results computed using these two models show good agreement with each other. The measured stresses show the effect of constraint on the elastoplastic behavior at notch roots under cyclic loading conditions.

1 Introduction

Most engineering components and structures contain notches or other forms of geometrical discontinuities where failures initiate; often these failures are associated with complex loading histories. Designs with high load-to-weight ratios are required to meet economic or operational considerations in many modern applications. These considerations have led to a trend of loading part of the component or structure, generally around geometrical discontinuities, into the inelastic range. Engineering components subject to cyclic inelastic loadings usually have a finite life which is shorter than those subjected to elastic cycling. One purpose of research in low-cycle fatigue is to improve the accuracy in life prediction for components loaded into the inelastic region.

In the last three decades a method known as the local strain approach (Dowling, 1979) has become very useful in low-cycle fatigue life prediction. This approach, based on local stresses and strains, incorporates three major modules: (a) material stress-strain properties, (b) relations between remote loads and local strains, and (c) fatigue damage laws. The first two modules provide the local stress/strain history of a structural component subject to a given loading history. This local stress/strain history is the basis for failure damage calculations. The goal of this research to experimentally investigate the local inelastic response—in particular the stresses—at notch roots subjected to cyclic loading.

The next section reviews previous works and cyclic constitutive models. Materials and specimens used in the experimental studies are described in Section 3. Section 4 shows the results of cyclic strain measurements at the notch roots via an optical technique. Section 5 describes the process of cyclic stress com-

putation based on the measured strains and shows the results of computed stresses. The last section contains the conclusions.

2 Background

Stresses are not directly “measured,” but computed from measured strains through a constitutive model. As pointed out by Sharpe (1992a), only a few cases of elastoplastic stress measurement are found in the literature. Stresses were computed from monotonic tests by Theocaris (1962), Durelli and Sciammarella (1963), and Keil and Benning (1979). A companion-specimen method was employed by Griffith (1948) and Crews (1969) to measure the cyclic elastoplastic stress at notch roots. In the companion-specimen method, local strains were measured at the notch roots. The local strain records were then reproduced on an unnotched companion specimen to determine the stress corresponding to the strain history. The essential assumption in the companion-specimen method is that when the thickness of the specimen is much smaller than the radius of the notch, two of the principal stresses vanish—one normal to the notch surface and the other in the thickness direction. Thus the assumed uniaxial stress state at the notch root can be simulated with a companion specimen undergoing the same strain history as in the notch root.

However, if the thickness-to-radius ratio becomes significant, a biaxial (instead of uniaxial) stress state exists at the notch root and the companion specimen method is not accurate anymore. Griffith's notches had a radius of 50.8 mm and a thickness of 2.30 mm. Crews' specimens had radii of notch roots ranging from 3.10 mm to 42.47 mm and thicknesses around 4 mm. In the latter case, the largest ratio of thickness to radius is 1.3, which could make the assumption of uniaxial stress state at the notch roots suspect. Actually, the thickness-to-radius ratio in the notches in common engineering applications can easily be as high as this value. This points out the need of a more sophisticated scheme for measuring cyclic stresses. One of the solutions is to measure the local in-plane strains at the notch roots and then compute the stress through a constitutive model. However, there are two difficulties in obtaining elastoplastic stresses at the critical locations with this methodology.

Contributed by the Applied Mechanics Division of THE AMERICAN SOCIETY OF MECHANICAL ENGINEERS for publication in the ASME JOURNAL OF APPLIED MECHANICS.

Discussion on this paper should be addressed to the Technical Editor, Prof. Lewis T. Wheeler, Department of Mechanical Engineering, University of Houston, Houston, TX 77204-4792, and will be accepted until four months after final publication of the paper itself in the ASME JOURNAL OF APPLIED MECHANICS.

Manuscript received by the ASME Applied Mechanics Division, May 27, 1993; final revision, April 6, 1994. Associate Technical Editor: L. T. Wheeler.

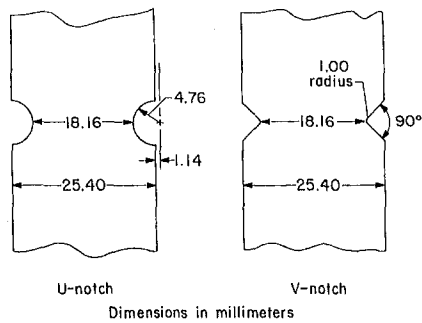


Fig. 1 Dimensions of the two notch geometries

First, as the size of the notch decreases the first part of this scheme—strain measuring—becomes more difficult. Although miniature resistance strain gages have been used, the bonding between gages and specimens can be a problem (Keil and Benning, 1979). A laser-based interferometric optical technique developed by Sharpe and Wang (1991) has been demonstrated to be suitable for measuring local elastoplastic biaxial strains at notch roots under cyclic loadings.

The second difficulty concerns the constitutive model describing cyclic plasticity. During the past three decades, incremental plasticity models have proved to be suitable constitutive relations for describing plastic behavior in metals. These incremental plasticity models can be grouped into two categories. The first group uses a single surface to describe yielding behavior; while the second group uses multiple surfaces. The first group of models are simple and able to describe inelastic behavior under monotonic loadings, but are presumed inadequate for more complex cyclic loading histories. Motivated by this inadequacy, a multisurface model was proposed by Mroz (1967) to accommodate cyclic loading. Due to its computational complexity, Mroz's model was modified into various two-surface models; Krieg (1975), Dafalias and Popov (1976), Lamba and Sidebottom (1978a, b), Tseng and Lee (1983), McDowell (1985), and Ellyin and Xia (1990).

Among the two-surface models, the one proposed by Tseng and Lee (1983), which was motivated by the experimental work of Philips and Lee (1979) and Lamba and Sidebottom (1978a, b), is widely known and can be easily coded for computation. This model is used in this work to calculate cyclic stresses from measured strains.

3 Material and Specimens

The material used for the study of notch root behavior is HY-80 steel. It is a high strength low alloy (HSLA) naval steel used in submarine structures. HY-80 has a fine grain size compared with the gage length of the experimental technique used in this study. The grain size is around $20 \mu\text{m}$ which is only 10 to 13 percent of the gage length. Although local strains are measured over a gage length of 150 or $200 \mu\text{m}$, the average response of 7 to 10 grains are measured instead of individual grain behavior.

Four kinds of notched specimens were tested: thin-U, thin-V, thick-U, and thick-V. Two notch geometries and two thicknesses were used; the geometries are shown in Fig. 1. The "thin" specimens have a thickness of 2.54 mm and the "thick" specimens have a thickness of 12.7 mm. These four kinds of specimen simulate *notch constraints* at the notch roots from a nearly plane stress state at the notch root of a thin-U specimen to a nearly plane-strain state at the notch root of a thick-V specimen.

Local biaxial strains were measured at the center of the root of the notch (not on the flat side of the specimen) using the laser-based technique described in the next section. To quantify the notch constraint, an *effective Poisson's Ratio*, α , is defined as $\alpha = -(\epsilon_{22}/\epsilon_{11})$, where x_1 is along the axial direction of the specimen and x_2 is in the thickness direction. (The effective Poisson's Ratio for plane strain would be zero.) The effective Poisson's Ratio was computed from the measured strains and is 0.26 for the thin-U, 0.19 for the thin-V, 0.17 for the thick-U, and 0.10 for the thick-V geometry.

The material for the specimens was received in block form and first cut into plates using electric discharge machining (EDM). Then, the U-notches were machined using a computer numerically controlled (CNC) milling machine, and the V-notches were cut via EDM. The stress concentration factors obtained from the local strain measurements for those four specimens are 1.96 for thin-U, 2.10 for thick-U, 3.56 for thin-V, and 3.70 for thick-V specimens, respectively. Specimens for stress-strain tests were fabricated in the form of round bars following ASTM standard E606.

4 Strain Measurements

Monotonic and cyclic stress-strain curves for the material were obtained by testing the round specimens in an electrohydraulic test machine. A clip gage with 25.4 mm gage length

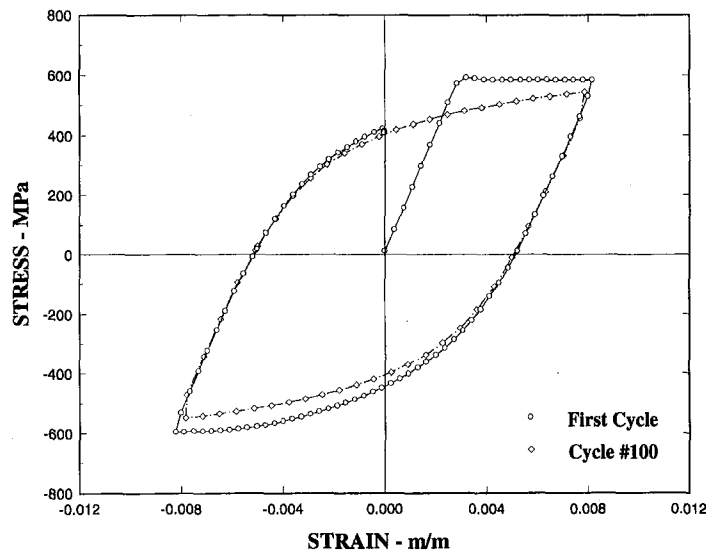


Fig. 2 Monotonic and cyclic stress-strain curve of HY-80 steel

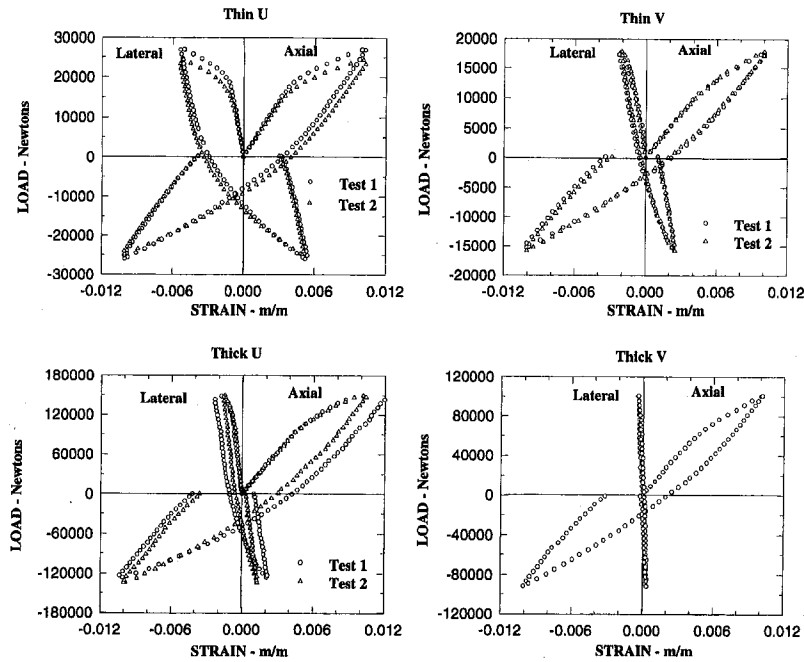


Fig. 3 Results of cyclic biaxial strain measurements at the notch roots of the four kinds of specimens for the first cycle

provided the feedback signal for strain controlled testing. Six specimens were tested to obtain cyclic stress-strain curves, with different strain ranges. All the specimens were cycled until the hysteresis loop became stable; this occurred within 100 cycles. Figure 2 shows a typical stress-strain curve of HY-80, including the first fully reversed cycle and a stable cycle. The strain limits in this example are ± 0.8 percent. Other stress-strain curves are similar, but with strain limits up to ± 1.0 percent. In all cases, the material softened only very slightly under cyclic loading.

A laser-based strain measuring system known as the Interferometric Strain Displacement Gage (ISDG) was used to measure cyclic biaxial elastoplastic strains at notch roots. The principle of the ISDG is simply Young's two-slit interferometric phenomenon, but in reflection rather than transmission. Two indentations are placed in the surface of the specimen with a Vickers microhardness tester. The distance between the two indentations (the gage length) is 150 micrometers for the V-shaped notches and 200 micrometers for the U-shaped notches. When the indents are illuminated with a laser, interference patterns form in space. These fringe patterns move when the distance between indents varies while external load is applied. A computer controlled system monitors the fringe patterns and translates them into strains. The biaxial version of ISDG operates in the same manner, but a third indent is needed to form an "L" shape arrangement. Details of the biaxial ISDG system are discussed in (Sharpe and Wang, 1991).

Cyclic biaxial elastoplastic strains at the center of notch roots were measured with the biaxial ISDG system. The ISDG continuously measured strains from the first cycle until a stable cycle was reached. The first fully reversed elastoplastic cycle used the longitudinal strain measured by the ISDG as the controlling parameter. When the local longitudinal strain reached a preset value, say $+1.0$ percent, the loading was stopped, then followed by unloading until another preset limit, -1.0 percent, was reached. The load then returned to zero, completing the first cycle. Several strain controlled cycles were run after the first cycle, but the rest of the cycles were run in a load-controlled manner for simplicity.

Figures 3 and 4 show the results of cyclic biaxial strain measurements as applied load versus longitudinal and transverse strains measured at the notch roots. Figure 3 is for the first

cycle and Fig. 4 is for a stable cycle—cycle 100. Each of these two figures contains four plots pertaining to results measured for the four kinds of specimens. Except for the thick-V case, replicate tests were run. One notices that the repeatability of the separate tests is in general good. There does exist some discrepancy in the measured strains at the maximum tension load; this is typical in elastoplastic strain measurement (Papirno, 1971).

Note that these tests were performed in the longitudinal strain control mode with limits of ± 1.0 percent. The effect of notch constraint is readily visible in the transverse strain. The notch constraint increases in the order of thin-U (nearly plane stress) \rightarrow thin-V \rightarrow thick-U \rightarrow thick-V (nearly plane strain). The measured transverse strains shown in Figs. 3 and 4 do indicate the trend of decreasing transverse strain as the notch constraint increases. The thick-V specimen is an extreme case, in which the transverse strain almost vanishes. The measured strains are used as inputs for computing stresses through constitutive models.

5 Computation of Cyclic Stresses

Two independent stress computations were performed based on two different constitutive models. The first computation followed the classical J_2 flow theory and treated a cyclic loading event as segments of monotonic loading. The other one is based on a two-surface cyclic plasticity model with a combined isotropic-kinematic hardening yield surface traveling inside a memory surface. These two constitutive models are briefly described in the next section. Then the computation processes, fitting of stress-strain curves and results of the stress computations are discussed.

5.1 Constitutive Models.

5.1.1 J_2 Flow Theory. Under the assumptions of the Mises yield criterion and isotropic hardening, the classical J_2 flow theory provides the following equation for computing stress increments from strain increments:

$$d\sigma_{ij} = 2\mu d\epsilon_{ij} + \lambda \delta_{ij} d\epsilon_{kk} - FS_{ij} S_{mn} d\epsilon_{mn} \quad (1)$$

where

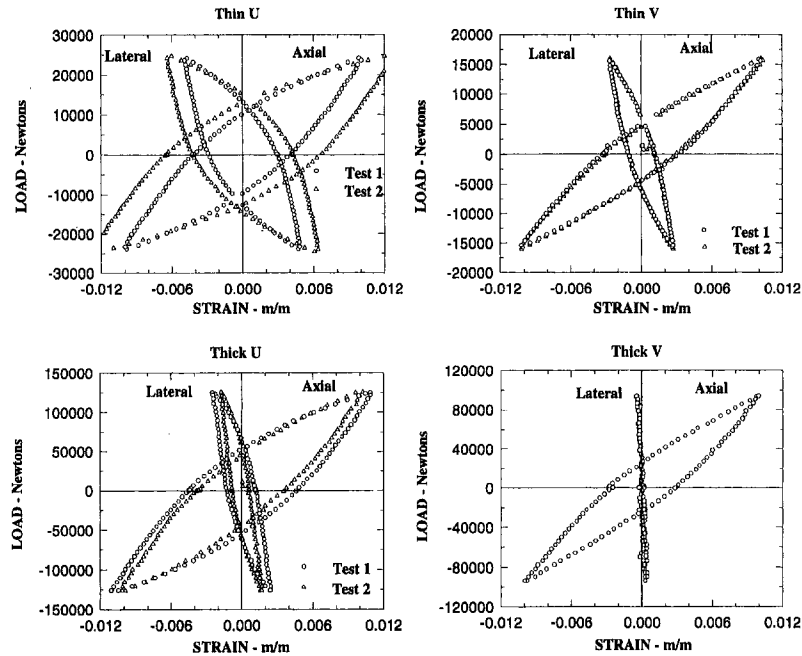


Fig. 4 Results of cyclic biaxial strain measurements at the notch roots of the four kinds of specimens for stable cycle #100

$$F = \frac{18\mu^2}{(2H' + 6\mu)\sigma_e^2} \quad (2)$$

and μ , λ are Lamé constants. $S_{ij} = \sigma_{ij} - (1/3)\sigma_{kk}\delta_{ij}$, and $\sigma_e = ((3/2)S_{ij}S_{ij})^{1/2}$ is the effective stress. The quantity H' is the slope of the uniaxial stress versus plastic strain curve.

Since the stress and strain tensors are symmetric, Eq. (1), has six scalar equations in 12 unknowns: six stress and six strain components. If only principal stresses and strains are considered, the number of equations is reduced to three, while the number of unknowns becomes six. If biaxial in-plane strains can be measured on a surface, where the normal stress component vanishes, Eq. (1) becomes simply a set of three equations with three unknowns— $d\epsilon_3$, $d\sigma_1$, and $d\sigma_2$. Here x_1 is along the axial direction of the specimen, x_2 in the thickness direction, and x_3 normal to the notch surface. One can then rewrite Eq. (1) in the following form for the calculation of stress increments from strain increments:

$$d\epsilon_3 = \frac{(FS_1S_3 - \lambda)d\epsilon_1 + (FS_2S_3 - \lambda)d\epsilon_2}{\lambda + 2\mu - FS_3^2} \quad (3)$$

$$d\sigma_1 = (\lambda + 2\mu - FS_1^2)d\epsilon_1 + (\lambda + 2\mu - FS_1S_2)d\epsilon_2 + (\lambda + 2\mu - FS_1S_3)d\epsilon_3 \quad (4)$$

$$d\sigma_2 = (\lambda + 2\mu - FS_2^2)d\epsilon_2 + (\lambda + 2\mu - FS_1S_2)d\epsilon_1 + (\lambda + 2\mu - FS_2S_3)d\epsilon_3. \quad (5)$$

5.1.2. *Two-Surface Model by Tseng and Lee.* The two-surface model introduces a memory surface which encloses all the initial and the subsequent yield surfaces in the stress space. Cyclic loading events are then described by two surfaces—a

yield surface and a memory surface. The definition of a memory surface is identical to that of a yield surface in the classical theory of plasticity. In general, both the memory surface and the yield surface may deform and translate in the stress space as plastic loading takes place. Mathematically the yield surface, expressed in terms of the isotropic-kinematic hardening rule, is given by

$$f = \frac{3}{2}(S_{ij} - \alpha_{ij})(S_{ij} - \alpha_{ij}) - \kappa^2 = 0 \quad (6)$$

while the memory surface is described by the Von Mises yield function

$$F = \frac{3}{2}S_{ij}S_{ij} - \bar{\kappa}^2 = 0. \quad (7)$$

Here $\alpha_{ij} = \bar{\alpha}_{ij} - (1/3)\alpha_{kk}\delta_{ij}$ is the deviatoric tensor corresponding to the center of the yield surface $\bar{\alpha}$. The parameter κ is the instantaneous size of the yield surface, which is $((3/2)(S_{ij} - \alpha_{ij})(S_{ij} - \alpha_{ij}))^{1/2}$, while $\bar{\kappa}$ is the current size of the memory surface. Since the yield surface has a combined isotropic-kinematic hardening characteristic, it is allowed to deform as well as move inside the memory surface. The motion of the yield surface inside the memory surface is schematically shown in Fig. 5. In this illustration, the tensor space is schematically represented in two-dimensional vector form. The current center of the yield surface is located at \mathbf{O}_y with radius $(2/3)^{1/2}\kappa$; the memory surface has radius $(2/3)^{1/2}\bar{\kappa}$ and is centered at \mathbf{O} .

Hardening rule. According to Fig. 5, the yield surface moves along the segment $\overline{O_yC}$, which has ν as a unit vector:

$$\nu_{ij} = \frac{\frac{2}{3}(\bar{\kappa} - \kappa)\lambda_{ij} - \alpha_{ij}}{|\frac{2}{3}(\bar{\kappa} - \kappa)\lambda - \alpha|} \quad (8)$$

where λ is the unit vector along \overline{OB} , and

Table 1 Stress-strain parameters in Tseng's model

CASES	Part of S-S	h	κ -MPa	$\bar{\kappa}$ -MPa	\bar{H} -MPa
ALL	MONOTONIC	35000	580	600	0
Thin U	UNLOADING	45000	500	1360	4000
Thin-V, Thick-U, Thick-V	UNLOADING	70000	500	1350	2000

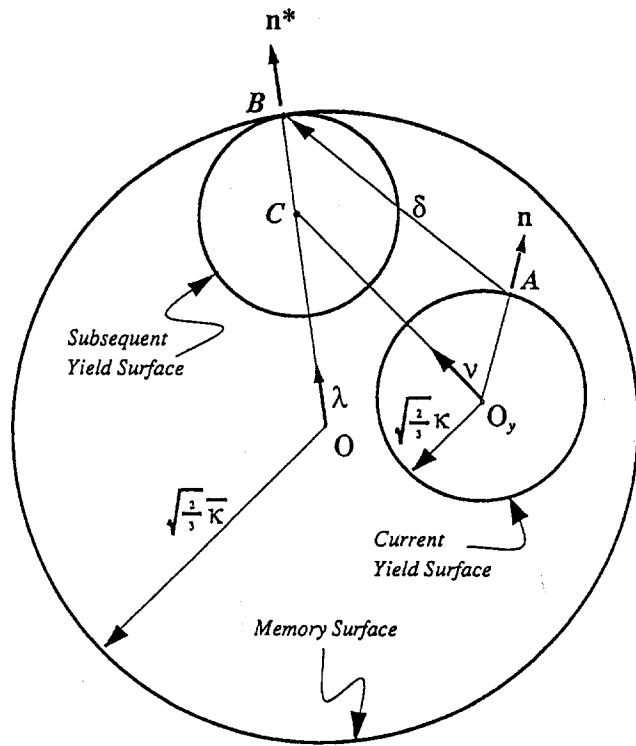


Fig. 5 A schematic showing the motion of the yield surface inside the memory surface in the Tseng-Lee two surface cyclic plasticity model

$$\lambda_{ij} = \frac{S_{ij} + \delta \frac{dS_{ij}}{|dS_{ij}|}}{\left| \mathbf{S} + \delta \frac{d\mathbf{S}}{|d\mathbf{S}|} \right|} \quad (9)$$

where the relative distance δ (with the dimension stress)

between the two surfaces is equal to the segment \overline{AB} and is given by

$$\delta = \frac{-(S_{ij}dS_{ij}) + [(S_{ij}dS_{ij})^2 + (\frac{2}{3}K^2 - |\mathbf{S}|^2)|d\mathbf{S}|^2]^{1/2}}{|d\mathbf{S}|} \quad (10)$$

The magnitude of the incremental movement for the yield surface $|\alpha|$ is determined by using a consistency condition and is given by

$$|\alpha| = \frac{\frac{\partial f}{\partial \mathbf{S}} \cdot d\mathbf{S}}{\frac{\partial f}{\partial d\mathbf{S}} \cdot \nu} \quad (11)$$

Generalized plastic modulus function. The generalized plastic modulus, H , is given by

$$H = \left(1 + h \frac{e}{1 - e} \right) \hat{H} \quad (12)$$

in which h , the shape parameter, can be determined from a cyclic uniaxial stress-strain curve and $e = \delta / \delta_{in}$. Here δ and δ_{in} are the current and initial distance between the load point and memory surface. \hat{H} corresponds to the generalized plastic modulus of the memory surface, i.e., the extreme slope of the stress versus plastic strain curve.

It is shown in Dafalias and Popov (1976) that in the special case of proportional loading $H = \frac{2}{3}H'$, where $H' = d\sigma/de^p$, is the plastic modulus. Since $\hat{H} = \frac{2}{3}H' = \frac{2}{3}d\sigma/de^p$, Eq. (12) represents the differential equation of the nonlinear stress-strain curve. When integrated, Eq. (12) yields a representation for h in terms of δ_{in} and \hat{H} :

$$h = \hat{H} - \frac{\sigma}{\epsilon^p} - \frac{\delta_{in}}{\epsilon^p} \ln \left[1 + \frac{\hat{H}\epsilon^p - \sigma}{\delta_{in}} \right] \quad (13)$$

Equation (13) can be used in a curve-fitting procedure to find the best value of h by choosing points (σ, ϵ^p) on the stress-plastic strain curve.

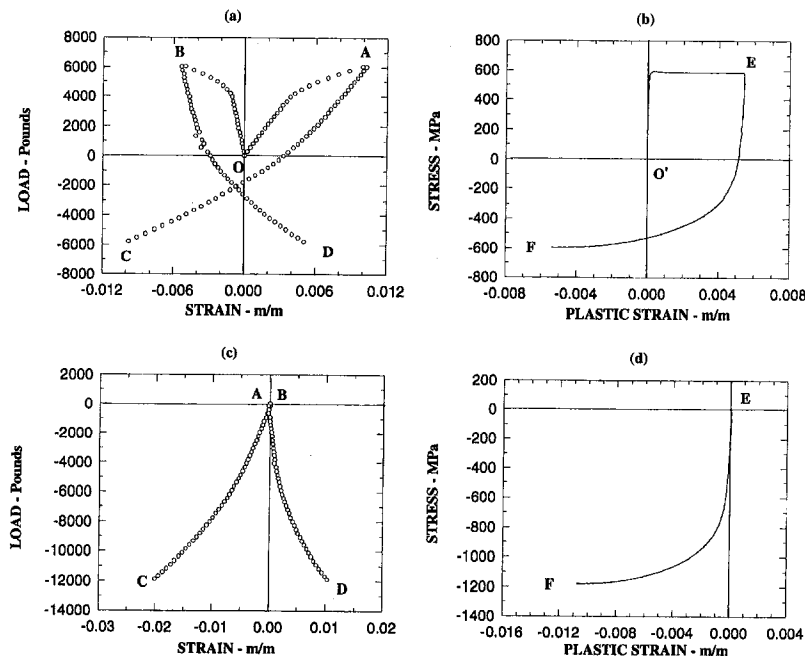


Fig. 6 Figures explaining the process of computing cyclic stresses based on the J_2 flow theory by segmenting the complete cycle into three parts—loading, unloading and reloading; (a) measured biaxial strains, (b) plastic strain-stress curve, (c) shifted unloading part of measured biaxial strains, (d) shifted unloading part of plastic strain-stress curve

Incremental stress-strain relation. The inelastic stress-strain relation can be written as

$$d\sigma_{ij} = D_{ijkl}d\epsilon_{kl} \quad (14)$$

where the fourth-order tensor D_{ijkl} is considered in two cases; first, when the yield surface is moving within the memory surface,

$$D_{ijkl} = \mu(\delta_{ik}\delta_{jl} + \delta_{il}\delta_{jk}) + \lambda\delta_{ij}\delta_{kl} - \frac{1}{\kappa^2} \frac{6\mu^2}{H + 2\mu} (S_{ij} - \alpha_{ij})(S_{kl} - \alpha_{kl}); \quad (15)$$

second, when the yield and memory surface contact at the load point and move together,

$$D_{ijkl} = \mu(\delta_{ik}\delta_{jl} + \delta_{il}\delta_{jk}) + \lambda\delta_{ij}\delta_{kl} - \frac{1}{\bar{\kappa}^2} \frac{6\mu^2}{\bar{H} + 2\mu} (S_{ij})(S_{kl}). \quad (16)$$

On a surface where only principal strains and stresses appear and normal stresses vanish, Eqs. (14) and (15) are reduced to the following form:

$$d\epsilon_3 = \frac{(F_1(S_1 - \alpha_1)(S_3 - \alpha_3) - \lambda)d\epsilon_1 + (F_1(S_2 - \alpha_2)(S_3 - \alpha_3) - \lambda)d\epsilon_2}{\lambda + 2\mu - F_1(S_3 - \alpha_3)^2} \quad (17)$$

$$d\sigma_1 = (\lambda + 2\mu - F_1(S_1 - \alpha_1)^2)d\epsilon_1 + (\lambda + 2\mu - F_1(S_1 - \alpha_1)(S_2 - \alpha_2))d\epsilon_2 + (\lambda + 2\mu - F_1(S_1 - \alpha_1)(S_3 - \alpha_3))d\epsilon_3 \quad (18)$$

$$d\sigma_2 = (\lambda + 2\mu - F_1(S_1 - \alpha_1)(S_2 - \alpha_2))d\epsilon_1 + (\lambda + 2\mu - F_1(S_2 - \alpha_2)^2)d\epsilon_2 + (\lambda + 2\mu - F_1(S_2 - \alpha_2)(S_3 - \alpha_3))d\epsilon_3 \quad (19)$$

where

$$F_1 = \frac{1}{\kappa^2} \frac{6\mu^2}{(H + 2\mu)} \quad (20)$$

while Eqs. (14) and (16) are reduced to

$$d\epsilon_3 = \frac{(F_2S_1S_3 - \lambda)d\epsilon_1 + (F_2S_2S_3 - \lambda)d\epsilon_2}{\lambda + 2\mu - F_2S_3^2} \quad (21)$$

$$d\sigma_1 = (\lambda + 2\mu - F_2S_1^2)d\epsilon_1 + (\lambda + 2\mu - F_2S_1S_2)d\epsilon_2 + (\lambda + 2\mu - F_2S_1S_3)d\epsilon_3 \quad (22)$$

$$d\sigma_2 = (\lambda + 2\mu - F_2S_1S_2)d\epsilon_1 + (\lambda + 2\mu - F_2S_2^2)d\epsilon_2 + (\lambda + 2\mu - F_2S_2S_3)d\epsilon_3 \quad (23)$$

where

$$F_2 = \frac{1}{\bar{\kappa}^2} \frac{6\mu^2}{(\bar{H} + 2\mu)}. \quad (24)$$

Note that in the special case of proportional loading with isotropic hardening, in which $H = (2/3)H' = (2d\sigma/3d\epsilon^p)$ and $\alpha_{ij} = 0$, Eqs. (20) and (24) have the same form as Eq. (2) for the J_2 flow theory. If the special case of pure isotropic hardening is further assumed, Eqs. (17)-(19) and Eqs. (21)-(23) are exactly the same as Eqs. (3)-(5) for the J_2 flow theory.

5.2 Computation of Stresses. The computation of stresses based on J_2 flow theory for monotonic loading has been investigated by Sharpe (1992b). Here it is extended to cyclic loading. Strictly speaking, the classical J_2 flow theory should be used for materials obeying the isotropic hardening rule, which is not the case here. However, one can approximate a cyclic event as many segments of monotonic parts with each of them described by the J_2 flow theory. Figure 6 is used to explain the process of computing cyclic stresses based on the J_2 flow theory by segmenting the complete cycle into three parts—monotonic loading, unloading, and reloading. Figure 6(a) shows the measured biaxial strains and Fig. 6(b) shows the stress versus plastic strain curve used for computing stresses. A method similar to the companion-specimen method employed by Griffith (1948) and Crews (1969) was used to generate the stress-plastic

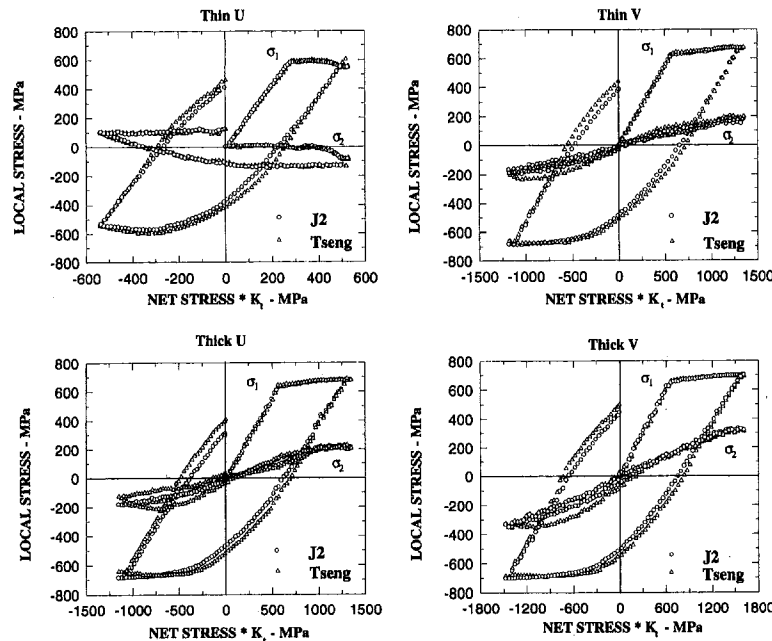


Fig. 7 Results of the computed local biaxial stresses for the first cycle. The abscissa is the net stress multiplied by the appropriate stress concentration factor K_i for each geometry.

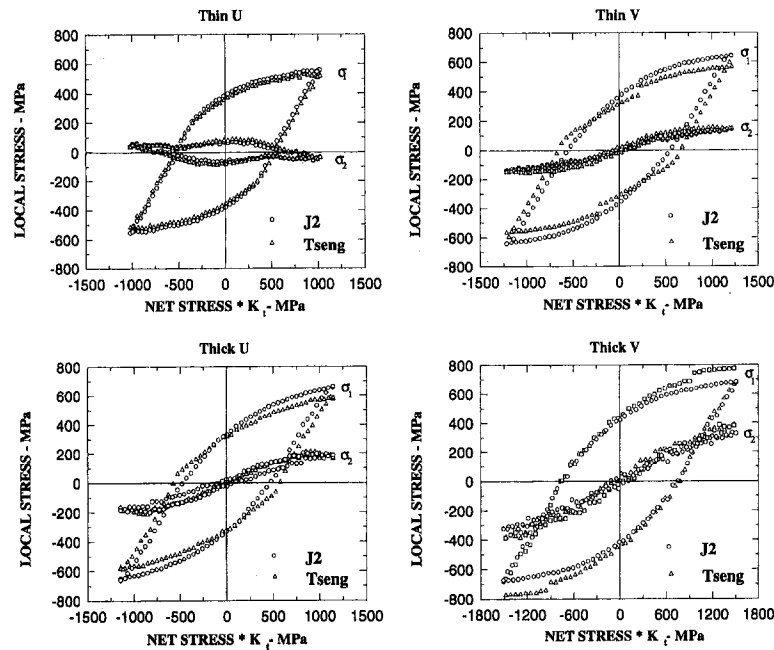


Fig. 8 Results of the computed local biaxial stresses for the stable cycle #100. The abscissa is the net stress multiplied by the appropriate stress concentration factor K_i for each geometry.

strain curve in Fig. 6(b); the plastic strain limits at points E and F in Fig. 6(b) correspond to the total strain limits at points A and C in Fig. 6(a).

The biaxial stresses during initial loading were computed using the biaxial strains OA and OB in Fig. 6(a) along with the stress versus plastic-strain curve O'E in Fig. 6(b) as inputs to Eqs. (2) to (5). The biaxial stresses during unloading and compression loading were computed in a similar manner using AC and BD along with curve EF after the biaxial strains at points A and B had been shifted to the origin along with point E on the stress versus plastic-strain curve; see Figs. 6(c) and 6(d). These biaxial stresses were then added to the final stresses at points A and B in Fig. 6(a). The same process was used to compute the stresses in the reloading part.

The stress computation based on Tseng's model (Tseng and Lee, 1983) incorporates the kinematic and the isotropic hardening feature. In principle, this stress computation does not need to break the cyclic loading event into segments. However, because of the dissimilarity between the loading and unloading parts of the stress-strain curve, it is necessary to process the initial loading part separately from the rest of the loading history. Still, this is an improvement, because no matter how long the loading history is, the whole process contains only two parts—initial loading and subsequent loading.

5.3 Fitting of Stress-Strain Curves. The two different constitutive models employed require different ways of representing the uniaxial material response. $H' = H'(\sigma_e)$, which is the slope of uniaxial stress versus plastic strain; is needed in the J_2 theory, while in Tseng's model four parameters, h , κ , $\bar{\kappa}$, \hat{H} must be determined. A cubic spline fitting technique has been demonstrated by Sharpe (1992b) to work well and is used here to fit the monotonic, unloading and reloading part of the stress versus plastic strain curve.

Determining the four parameters in Tseng's model is simple. First, κ is taken as the initial yielding stress in a stress-strain curve from a uniaxial test. The second parameter, $\bar{\kappa}$, is taken at the maximum stress of the stress-strain curve. \hat{H} is the extreme slope of the stress versus plastic strain. And h is determined using Eq. (13) and a point on the stress-plastic strain curve. These parameters must be determined for both the load-

ing and the unloading stress-strain curves; furthermore, the unloading must begin at a strain equal to the maximum effective plastic strain limit at the root of the notch. This limit is similar for the three more constrained notches. These four parameters, h , κ , $\bar{\kappa}$, \hat{H} , for monotonic loading and unloading are listed in Table 1. These parameters enable the stresses within the plastic region of interest to be predicted within five percent.

5.4 Results of Stress Computation and Discussion. Results of the computed local biaxial stresses are shown in Fig. 7 for the first cycle and Fig. 8 for the stable cycle. Each figure has four plots corresponding to the stresses computed for the four kinds of specimens. Each of the plots shows one set of local biaxial stress histories computed by the J_2 flow theory and one by Tseng's model for the same strain history. Local longitudinal stress (σ_1) and transverse stress (σ_2) are plotted versus a parameter proportional to external loading— $K_i \times$ net stress—where K_i is the elastic stress concentration factor.

Based on the results, several observations can be made.

- It is generally seen in all the plots that stresses computed by the J_2 flow theory and Tseng's model agree very well with each other almost anywhere in the whole loading history.
- The stress measurement demonstrated here is more general than the companion-specimen method which is limited by the notch constraint. Indeed, as shown in both figures, the calculated transverse stress in the case of thin-V, thick-U, and thick-V is significant enough to violate the assumption in the companion specimen method—a uniaxial stress state. However, in the thin-U case, the results support this assumption of uniaxial stress state which is physically expected.
- The notch constraint shows the strongest effect on the transverse stress. In fact, the effect of the notch constraint is to bring the transverse stress “in phase” with the longitudinal stress.
- For the case with least notch constraint—the thin-U case—the local longitudinal stress decreases in the monotonic regime as plasticity prevails. This unusual behavior is confirmed in a finite element analysis (Tregoning, 1992).

6 Conclusions

Biaxial stresses at a notch root can be computed with little difficulty from measured strains, and there is little difference in the stresses obtained by using the simpler J_2 flow theory compared to the more sophisticated Tseng model.

These results quantify the increase in the principal stress in the thickness direction with the increase in the ratio of thickness to root radius. Unless the thickness-to-radius ratio is small, implying plane stress at the notch root, the companion method of measuring stresses is incorrect.

Acknowledgments

The authors appreciate the support of the National Science Foundation under Grant MSM-8702110. The assistance of The Applied Physics Laboratory of The Johns Hopkins University in machining the specimens is greatly appreciated.

References

- Crews, Jr., J. H., 1969, "Elastoplastic Stress-Strain Behavior at Notch Roots in Sheet Specimens Under Constant-Amplitude Loading," NASA TN D-5253.
- Dafalias, Y. F., and Popov, E. P., 1976, "Plastic Internal Variables Formalism in Cyclic Plasticity," ASME JOURNAL OF APPLIED MECHANICS, Vol. 98, pp. 645–651.
- Dowling, N. E., Brose, W. R., and Wilson, W. K., 1979, "Notch Member Fatigue Life Predictions by the Local Strain Approach," *Advances in Engineering*, Vol. 6, Wetzel, ed., pp. 55–84, SAE, Warrendale, PA.
- Durelli, A. J., and Sciammarella, C. A., 1963, "Elastoplastic Stress and Strain Distribution in a Finite Plate with a Circular Hole Subjected to Unidimensional Load," ASME JOURNAL OF APPLIED MECHANICS, Vol. 30, pp. 115–121.
- Ellyin, F., and Xia, Z., 1985, "A Rate-independent Constitutive Model for Transient Non-proportional Loading," *Journal of Mechanics Physics and Solids*, Vol. 11, pp. 411–428.
- Griffith, G. E., 1948, "Experimental Investigation of the Effects of Plastic Flow in a Tension Panel with a Circular Hole," NACA TN 1705.
- Keil, S., and Benning O., 1979, "On the Evaluation of Elasto-Plastic Strains Measured with Strain Gages," *Experimental Mechanics*, Vol. 19, pp. 265–270.
- Krieg, R. D., 1975, "A Practical Two Surface Plasticity Theory," ASME JOURNAL OF APPLIED MECHANICS, Vol. 42, pp. 641–646.
- Lamba, H. S., and Sidebottom, O. M., 1978a, "Cyclic Plasticity for Nonproportional Paths: Part I—Cyclic Hardening, Erasure of Memory, and Subsequent Strain Hardening Experiments," ASME *Journal of Engineering Materials and Technology*, Vol. 100, pp. 96–103.
- Lamba, H. S., and Sidebottom, O. M., 1978b, "Cyclic Plasticity for Nonproportional Paths: Part II—Comparison with Three-Incremental Plasticity Models," ASME *Journal of Engineering Materials and Technology*, Vol. 100, pp. 104–111.
- McDowell, D. L., 1985, "A Two Surface Model for Transient Nonproportional Cyclic Plasticity: Part I—Development of Appropriate Equations," ASME JOURNAL OF APPLIED MECHANICS, Vol. 52, pp. 298–302.
- Mroz, Z., 1967, "An Attempt to Describe the Behavior of Metals Under Cyclic Loads Using a More General Workhardening Model," *Acta Mechanica*, Vol. 7, pp. 199–212.
- Phillips, A., and Lee, C. W., 1979, "Yield Surfaces and Loading Surfaces, Experiments and Recommendations," *International Journal of Solids and Structures*, Vol. 15, pp. 715–729.
- Papirno, R., 1971, "Plastic Stress-Strain History at Notch Roots in Tensile Strips under Monotonic Loading," *Experimental Mechanics*, Vol. 11, pp. 446–452.
- Sharpe, W. N., Jr., and Wang, K. C., 1991, "Evaluation of a Modified Neuber Relation," ASME *Journal of Engineering Materials and Technology*, Vol. 113, pp. 350–353.
- Sharpe, W. N., Jr., 1992a, "On the Measurement of Monotonic Biaxial Elastoplastic Stresses," *Experimental Mechanics*, Vol. 32, pp. 62–67.
- Sharpe, W. N., Jr., 1992b, "Measurement of Monotonic Biaxial Elastoplastic Stresses at Notch Roots," ASME JOURNAL OF APPLIED MECHANICS, Vol. 58, pp. 916–922.
- Theocaris, P. S., 1962, "Experimental Solution of Elastic-Plastic Plane-Stress Problems," *Journal of Mechanics Physics and Solids*, Vol. 37, No. 1, pp. 71–91.
- Tregoning, R. L., 1992, Ph.D. Thesis, The Johns Hopkins University.
- Tseng, N. T., and Lee, G. C., 1983, "Simple Plasticity Model of Two-Surface Type," *ASCE Journal of Engineering Mechanics*, Vol. 109, No. 3, pp. 785–810.

S. A. Matemilola

W. J. Stronge

Mem. ASME.

Department of Engineering,
University of Cambridge,
Trumpington Street,
Cambridge. CB2 1PZ, U.K.

D. Durban

Faculty of Aerospace Engineering,
Technion,
Haifa 32000, Israel

Diffusion Rate for Stress in Orthotropic Materials

Axial rates of diffusion of the symmetrical state of stress caused by equal but opposed normal forces acting on opposite sides of an indefinitely long strip or plate, are examined in the context of orthotropic elastic materials. To obtain the stress components for this boundary value problem, the imposed surface tractions are represented by a Fourier integral. At distances larger than one quarter of the thickness, the normal stress on the middle surface is closely represented by the sum of eigenfunctions for this problem, up to, and including the first complex eigenfunction as well as its conjugate. Each eigenfunction is a product of exponentially decreasing and oscillatory terms. The exponential term is more significant for determining the rate of diffusion of stress in materials with a large ratio of axial to transverse Young's moduli $E_x/E_y \geq 3$; this term shows a strong dependence on the ratio of transverse Young's modulus to shear modulus E_y/G .

1 Introduction

The stress field in an elastic body is governed by elliptic partial differential equations, so stress concentrations as well as discontinuities in stress diffuse with increasing distance from the source. Quantitative measures of the diffusion rate of stress have received considerable attention, mostly in the context of Saint Venant's principle for bodies with self-equilibrating end tractions. Early studies in this regard include those of Toupin (1965) and Knowles (1966), who provided a measure of the stress decay from an end disturbance, using strain energy decay bounds. A more recent study by Durban and Stronge (1992), of an isotropic elastic bar subjected to large initial stretch showed that away from the loaded section, the transverse stress exponentially decreases with increasing distance, at the same rate as the smallest eigenvalue for a self-equilibrating end disturbance. In plane-strain plasticity, symmetric and antisymmetric axial stress distributions in a bar have very different rates of axial decay at any level of initial stretch (Durban and Stronge, 1988). Analysis of a compound circular cylinder with axisymmetric self-equilibrating end loads (Stephen, 1991), has shown that the rate of transfer of axial force from one cylinder to the other is rapid when both the ratio of stiffnesses E_{outer}/E_{inner} , as well as the ratio of diameters d_{outer}/d_{inner} of the cylinders are small.

Particular attention was focused on diffusion of stress in anisotropic materials by Choi and Horgan (1977), and Horgan (1974, 1982, 1989). These investigations obtained lower bounds on the decay rate for axial stress; the bounds depend on elastic properties of the material. For example, for a highly anisotropic rectangular strip of width b , shear modulus G , and axial stiffness E_x , Horgan (1982) concluded that the stress decay rate k , has an asymptotic value $k \approx (2\pi/b)\sqrt{G/E_x}$, as $(G/E_x) \rightarrow 0$. Also, for an axisymmetric problem of a circular cylinder of radius c , with self-equilibrating end loads, $k \approx (3.83/c)\sqrt{(G_r/E_z)}$, as $(E_r/E_z) \rightarrow 0$. Here, z and r refer to the axial and radial directions, respectively, of the cylinder. An extensive review of important results within the framework of

Saint Venant's principle was provided by Horgan and Knowles (1983).

The present study addresses the problem of diffusion rate of a stress perturbation in either a beam or plate which is loaded on the lateral surfaces by a pair of equal but opposed transverse forces. For isotropic materials, Filon (1903) obtained a solution for the stresses in the strip. In the present work, the same problem is examined in the context of anisotropic materials. The imposed surface tractions are represented by a Fourier integral, and an analytical solution is derived for the stress distribution in a beam or plate. The influence of the ratio of Young's moduli E_x/E_y , and that of the transverse Young's modulus to shear modulus E_y/G , on the distribution of normal stress σ_y , along the middle surface is examined under conditions of either plane stress or plane strain. For this boundary value problem, the axial rates of decay are obtained for components of stress; for highly anisotropic materials the rates for different components of stress are distinct.

An important conclusion from the present study is that for this boundary value problem, the lower bound given by Horgan (1982) is representative of the rate of decay for all components of stress only if the material is not too anisotropic. This lower bound is obtained from the smallest eigenvalue of the corresponding eigenfunction problem of a self-equilibrating end load on the strip. The present study reveals that at practical distances from the loaded section, good estimates for the rates of decay of different components of stress lie between those of eigenfunctions for the smallest and the smallest complex eigenvalues. For isotropic materials the smallest eigenvalue is complex, so all components of stress have the same rate of decay. For highly anisotropic materials, however, the smallest eigenvalue is real; in this case the axial rate of decay is not a material property.

2 Plane Deformation of an Orthotropic Body

Consider an orthotropic elastic strip and a Cartesian coordinate system. If the transverse and the axial directions of the strip are taken as the y and x -axes, respectively, the strains are related to the stress components (Lekhnitskii, 1968),

$$\epsilon_x = a_{11}\sigma_x + a_{12}\sigma_y$$

$$\epsilon_y = a_{12}\sigma_x + a_{22}\sigma_y$$

$$\gamma_{xy} = a_{66}\tau_{xy} \quad (1)$$

where in plane stress,

Contributed by the Applied Mechanics Division of THE AMERICAN SOCIETY OF MECHANICAL ENGINEERS for publication in the ASME JOURNAL OF APPLIED MECHANICS.

Discussion on this paper should be addressed to the Technical Editor, Prof. Lewis T. Wheeler, Department of Mechanical Engineering, University of Houston, Houston, TX 77204-4792, and will be accepted until four months after final publication of the paper itself in the ASME JOURNAL OF APPLIED MECHANICS.

Manuscript received by the ASME Applied Mechanics Division, Apr. 28, 1993; final revision, Jan. 31, 1994. Associate Technical Editor: X. Markenscoff.

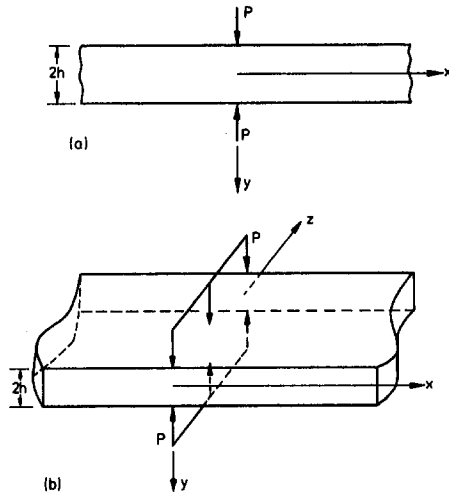


Fig. 1 Orthotropic beam (a), or plate (b) compressed by two equal but opposite collinear normal forces

$$a_{11} = \frac{1}{E_x}, \quad a_{22} = \frac{1}{E_y}, \quad a_{12} = -\frac{\nu_{xy}}{E_x}, \quad a_{66} = \frac{1}{G}, \quad (2)$$

and in plane strain,

$$\begin{aligned} a_{11} &= \frac{1}{E_x^*} \equiv \frac{1}{E_x} \left(1 - \nu_{xz}^2 \frac{E_z}{E_x} \right) \\ a_{22} &= \frac{1}{E_y^*} \equiv \frac{1}{E_y} \left(1 - \nu_{yz}^2 \frac{E_z}{E_y} \right) \\ a_{12} &= \frac{-\nu_{xy}^*}{E_x^*} \equiv -\frac{\nu_{xy}}{E_x} \left(1 + \frac{\nu_{xz}\nu_{yz}}{\nu_{yx}} \frac{E_z}{E_x} \right) \\ a_{66} &= \frac{1}{G^*} \equiv \frac{1}{G}. \end{aligned} \quad (3)$$

In (2) and (3), E_x , E_y , G , and ν_{ij} denote axial Young's modulus, transverse Young's modulus, shear modulus, and Poisson's ratio, respectively. Also, an asterix superscript denotes an effective modulus for plane strain.

We introduce an Airy stress function $\Phi(x, y)$, which is related to stress components by

$$\sigma_x = \Phi_{,yy}, \quad \sigma_y = \Phi_{,xx}, \quad \tau_{xy} = -\Phi_{,xy}. \quad (4)$$

In the absence of body forces, the equilibrium equations for the strip are identically satisfied by Φ . Thus the condition of compatibility for plane stress yields

$$\frac{1}{E_y} \Phi_{,xxxx} + \left(\frac{1}{G} - 2 \frac{\nu_{xy}}{E_x} \right) \Phi_{,xxyy} + \frac{1}{E_x} \Phi_{,yyyy} = 0, \quad (5)$$

while for plane strain

$$\frac{1}{E_y^*} \Phi_{,xxxx} + \left(\frac{1}{G^*} - 2 \frac{\nu_{xy}^*}{E_x^*} \right) \Phi_{,xxyy} + \frac{1}{E_x^*} \Phi_{,yyyy} = 0. \quad (6)$$

In the case of an isotropic material $E_x = E_y = 2(1 + \nu)G = E$, and Eq. (5) is further reduced to the familiar biharmonic equation:

$$\Phi_{,xxxx} + 2\Phi_{,xxyy} + \Phi_{,yyyy} = 0. \quad (7)$$

3 Boundary Value Problem—Opposed Transverse Forces on Strip

Consider an infinite beam with depth $2h$, that is in equilibrium under the action of two equal but opposed normal forces P , acting on the upper and lower edges of the strip at $x = 0$ (Fig. 1(a)). Let dimensionless spatial coordinates be defined as

$$\xi = \frac{x}{h}, \quad \eta = \frac{y}{h}. \quad (8)$$

On the lateral surfaces, the transverse stress $\sigma_y(\xi, \eta)$ and shear stress $\tau_{xy}(\xi, \eta)$ satisfy boundary conditions that can be expressed in Fourier integral form as

$$\begin{aligned} \sigma_y(\xi, \pm 1) &= -\frac{P}{\pi h} \int_0^\infty (\cos \alpha \xi) d\alpha \\ \tau_{xy}(\xi, \pm 1) &= 0, \end{aligned} \quad (9)$$

where α is the Fourier integral parameter.

A stress function of the form

$$\Phi = h \int_0^\infty f(\alpha, \eta) (\cos \alpha \xi) d\alpha \quad (10)$$

can be substituted into (5) and (6) to obtain the explicit form of governing differential equation

$$f'''' - (2\alpha^2 R_1) f'' + (\alpha^4 R_2) f = 0, \quad (11)$$

where $f' \equiv df/d\eta$. For plane stress,

$$R_1 = \frac{E_x E_y}{E_y 2G} - \nu_{xy}, \quad R_2 = \frac{E_x}{E_y}, \quad (12)$$

and for plane strain,

$$R_1 = \frac{E_x^* E_y^*}{E_y^* 2G^*} - \nu_{xy}^*, \quad R_2 = \frac{E_x^*}{E_y^*}. \quad (13)$$

It is assumed that $R_1, R_2 > 0$ for the materials under consideration (for isotropic materials $R_1 = R_2 = 1$). Also, E_x/G is expressed as a product $(E_x/E_y)(E_y/G)$, in order to emphasize the separate roles of the two elastic parameter ratios E_x/E_y and E_y/G , on diffusion of stress in different materials. It follows from Eqs. (11)-(13) that any difference between the behavior of the stress field for plane strain as opposed to plane stress, will be due to a change in value of quantities R_1 and R_2 .

We seek a solution of the form

$$f = e^{\omega \eta} \quad (14)$$

The characteristic equation of (11) is

$$\omega^4 - 2R_1 \omega^2 + R_2 = 0. \quad (15)$$

The symmetry of the problem about the middle surface ($\eta = 0$) suggests that we require only an even solution of $f(\alpha, \eta)$, the arbitrary constants of which can be determined from the boundary conditions (9). The roots of (15) appear in conjugate pairs,

$$\omega = \pm(\Gamma \pm i\Omega), \quad (16)$$

where $\omega^2 = R_1 \pm \sqrt{R_1^2 - R_2}$. Three possibilities exist: (1) real and distinct roots, (2) complex roots, or (3) real repeated roots.

3.1 Real Distinct Roots. The characteristic Eq. (15) has real roots if

$$R_1^2 > R_2 > 0. \quad (17)$$

Most carbon fiber composite materials of practical importance fall into this category. The elastic properties of some typical composite materials are given in Table 1.

The quantity Ω in (16) is complex, and the required roots are

$$\begin{aligned} \omega_1 &= (\Gamma - \Omega) = \Gamma_1 & \omega_2 &= -\Gamma_1 \\ \omega_3 &= (\Gamma + \Omega) = \Gamma_2 & \omega_4 &= -\Gamma_2. \end{aligned} \quad (18)$$

Table 1 Elastic properties for some carbon fiber composite and crystalline materials

Material	E_x (GPa)	E_y (GPa)	E_z (GPa)	G (GPa)	ν_{xy}	ν_{yz}	ν_{zx}
(a) Gr./Ep. composite unidirectional (Choi and Horgan, 1977)	137.93	6.90	6.90	4.13	0.25	0.25	0.01
(b) Gr./Ep. composite $(0^\circ, 45^\circ, 0^\circ, -45^\circ, 0^\circ)_{2z}$ (Calrns, 1991)	93.1	9.7	21.1	4.92	0.3	0.64	0.15
(c) Gr./Ep. composite Quasi-isotropic (Shivakumar <i>et al.</i> , 1985)	50.81	11.78	50.81	4.11	0.25	0.31	0.06
(d) Magnesium crystal (Dahan and Zarka, 1977)	50.76	45.25	45.25	16.56	0.25	0.28	0.35
(e) Zinc crystal (Dahan and Zarka, 1977)	37.88	121.5	121.5	40	0.25	0.08	0.04

The symmetric solution of $f(\alpha, \eta)$ is

$$f(\alpha, \eta) = A_1 \cosh \Gamma_1 \alpha \eta + A_2 \cosh \Gamma_2 \alpha \eta \quad (19)$$

where Γ_1 and Γ_2 are

$$\begin{aligned} \Gamma_1 &= \sqrt{R_1 + \sqrt{R_1^2 - R_2}} \\ \Gamma_2 &= \sqrt{R_1 - \sqrt{R_1^2 - R_2}} \end{aligned} \quad (20)$$

Using $f(\alpha, \eta)$ given by (19), the stress components can be obtained from the stress function (10),

$$\begin{aligned} \sigma_y(\xi, \eta) &= -\frac{\alpha^2}{h} \int_0^\infty (A_1 \cosh \Gamma_1 \alpha \eta + A_2 \cosh \Gamma_2 \alpha \eta) \cos \alpha \xi d\alpha \\ \sigma_x(\xi, \eta) &= \frac{\alpha^2}{h} \int_0^\infty (A_1 \Gamma_1^2 \cosh \Gamma_1 \alpha \eta + A_2 \Gamma_2^2 \cosh \Gamma_2 \alpha \eta) \cos \alpha \xi d\alpha \\ \tau_{xy}(\xi, \eta) &= \frac{\alpha^2}{h} \int_0^\infty (A_1 \Gamma_1 \sinh \Gamma_1 \alpha \eta + A_2 \Gamma_2 \sinh \Gamma_2 \alpha \eta) \sin \alpha \xi d\alpha \end{aligned} \quad (21)$$

Constants A_1 and A_2 are obtained from the boundary conditions (9), to give

$$\begin{aligned} A_1 &= \frac{P}{\pi \alpha^2} \frac{\Gamma_2 \sinh \Gamma_2 \alpha}{\Gamma_2 \sinh \Gamma_2 \alpha \cosh \Gamma_1 \alpha - \Gamma_1 \sinh \Gamma_1 \alpha \cosh \Gamma_2 \alpha} \\ A_2 &= \frac{P}{\pi \alpha^2} \frac{-\Gamma_1 \sinh \Gamma_1 \alpha}{\Gamma_2 \sinh \Gamma_2 \alpha \cosh \Gamma_1 \alpha - \Gamma_1 \sinh \Gamma_1 \alpha \cosh \Gamma_2 \alpha} \end{aligned} \quad (22)$$

3.2 Complex Roots. Equation (15) has complex roots if

$$R_1^2 < R_2. \quad (23)$$

The elastic properties of crystalline zinc (see Table 1) corresponds to this case. Here, the roots are

$$\begin{aligned} \omega_1 &= \Gamma + i\Omega & \omega_2 &= -(\Gamma + i\Omega) \\ \omega_3 &= \Gamma - i\Omega & \omega_4 &= -(\Gamma - i\Omega). \end{aligned} \quad (24)$$

The symmetric solution of $f(\xi, \eta)$ is

$$f(\alpha, \eta)$$

$$= B_1 \cosh \Gamma \alpha \eta \cos \Omega \alpha \eta + B_2 \sinh \Gamma \alpha \eta \sin \Omega \alpha \eta \quad (25)$$

where

$$\begin{aligned} \Gamma &= \frac{1}{\sqrt{2}} \sqrt{\sqrt{R_2} + R_1} \\ \Omega &= \frac{1}{\sqrt{2}} \sqrt{\sqrt{R_2} - R_1} \end{aligned} \quad (26)$$

By substituting (25) into the stress function (10), and with the appropriate differentiation, we arrive at the stress components

$$\begin{aligned} \sigma_y &= -\frac{2\alpha^2}{h} \int_0^\infty (B_1 \cosh \Gamma \alpha \eta \cos \Omega \alpha \eta \\ &\quad + B_2 \sinh \Gamma \alpha \eta \sin \Omega \alpha \eta) \cos \alpha \xi d\alpha \\ \sigma_x &= \frac{2\alpha^2}{h} \int_0^\infty [B_1((\Gamma^2 - \Omega^2) \cosh \Gamma \alpha \eta \cos \Omega \alpha \eta \\ &\quad - 2\Omega \Gamma \sinh \Gamma \alpha \eta \sin \Omega \alpha \eta) \\ &\quad + B_2((\Gamma^2 - \Omega^2) \sinh \Gamma \alpha \eta \sin \Omega \alpha \eta \\ &\quad + 2\Omega \Gamma \cosh \Gamma \alpha \eta \cos \Omega \alpha \eta)] \cos \alpha \xi d\alpha \\ \tau_{xy} &= \frac{2\alpha^2}{h} \int_0^\infty [B_1(\Gamma \sinh \alpha \Gamma \eta \cos \alpha \Gamma \eta \\ &\quad - \Omega \cosh \alpha \Gamma \eta \sin \alpha \Gamma \eta) \\ &\quad + B_2(\Gamma \cosh \alpha \Gamma \eta \sin \alpha \Gamma \eta \\ &\quad + \Omega \sinh \alpha \Gamma \eta \cos \alpha \Gamma \eta)] \sin \alpha \xi d\alpha. \end{aligned} \quad (27)$$

By substituting the boundary conditions (9) into (27), B_1 and B_2 are obtained,

$$\begin{aligned} B_1 &= \frac{P}{\pi \alpha^2} \frac{\Gamma \cosh \Gamma \alpha \sin \Omega \alpha + \Omega \sinh \Gamma \alpha \cos \Omega \alpha}{\Gamma \sin 2\Omega \alpha + \Omega \sinh 2\Gamma \alpha} \\ B_2 &= \frac{P}{\pi \alpha^2} \frac{\Omega \cosh \Gamma \alpha \sin \Omega \alpha - \Gamma \sinh \Gamma \alpha \cos \Omega \alpha}{\Gamma \sin 2\Omega \alpha + \Omega \sinh 2\Gamma \alpha} \end{aligned} \quad (28)$$

3.3 Real Repeated Roots. The subcase of (15) with repeated real roots includes isotropic elastic materials. Real repeated roots occur only if

$$R_1^2 = R_2. \quad (29)$$

In this case the roots are

$$\omega_1 = \omega_3 = \Gamma \quad \omega_2 = \omega_4 = -\Gamma \quad (30)$$

where $\Gamma \equiv \sqrt{R_1}$. The symmetric solution of $f(\xi, \eta)$ is

$$f(\alpha, \eta) = C_1 \cosh \Gamma \alpha \eta + C_2 \eta \sinh \Gamma \alpha \eta. \quad (31)$$

In view of (31) and boundary conditions (9), the stress components are

$$\begin{aligned} \sigma_y(\xi, \eta) &= -\frac{2P}{\pi h} \\ &\quad \times \int_0^\infty \frac{[(\alpha \Gamma \cosh \alpha \Gamma + \sinh \alpha \Gamma) \cosh \alpha \Gamma \eta \\ &\quad - \alpha \Gamma \eta \sinh \alpha \Gamma \sinh \alpha \Gamma \eta]}{\sinh 2\alpha \Gamma + 2\alpha \Gamma} \cos \alpha \xi d\alpha \\ \sigma_x(\xi, \eta) &= \frac{2P}{\pi h} \\ &\quad \times \int_0^\infty \frac{[(\alpha \Gamma \cosh \alpha \Gamma - \sinh \alpha \Gamma) \cosh \alpha \Gamma \eta \\ &\quad - \alpha \Gamma \eta \sinh \alpha \Gamma \sinh \alpha \Gamma \eta]}{\sinh 2\alpha \Gamma + 2\alpha \Gamma} \cos \alpha \xi d\alpha \end{aligned}$$

$$\tau_{xy}(\xi, \eta) = -\frac{2P}{\pi h} \times \int_0^{\infty} \frac{[\alpha\Gamma \cosh \alpha\Gamma \sinh \alpha\Gamma\eta - \alpha\Gamma\eta \sinh \alpha\Gamma \cosh \alpha\Gamma\eta]}{\sinh 2\alpha\Gamma + 2\alpha\Gamma} \sin \alpha\xi d\alpha. \quad (32)$$

For $\Gamma = 1$, (32) reduces to the solution obtained by Filon (1903) for an isotropic material.

4 Eigenfunctions for Boundary Value Problem

Our primary interest is in investigating the longitudinal decay rate for stress in an orthotropic strip or plate. In this section a procedure for obtaining the decay rate of normal stress on the middle surface of the strip is outlined; this is done without recourse to numerical computation of the stress components given by (21) or (27). Returning to Section 3, recall the characteristic Eq. (15)

$$\omega^4 - 2R_1\omega^2 + R_2 = 0. \quad (33)$$

For purely real roots of (33) $\omega_{1,2}(= \pm\Gamma_1)$, $\omega_{3,4}(= \pm\Gamma_2)$, we obtain from (21), the expression for the nondimensional normal stress component on the middle surface $\eta = 0$,

$$-\frac{\pi h}{P} \sigma_y(\xi, 0) = \int_0^{\infty} \frac{\Gamma_2 \sinh \Gamma_2\alpha - \Gamma_1 \sinh \Gamma_1\alpha}{\Gamma_2 \sinh \Gamma_2\alpha \cosh \Gamma_1\alpha - \Gamma_1 \sinh \Gamma_1\alpha \cosh \Gamma_2\alpha} \times \cos \alpha\xi d\alpha. \quad (34)$$

Now, consider the integral

$$I = \int_{-\infty}^{\infty} \frac{\Gamma_2 \sinh \Gamma_2\alpha - \Gamma_1 \sinh \Gamma_1\alpha}{[\Gamma_2 \sinh \Gamma_2\alpha \cosh \Gamma_1\alpha - \Gamma_1 \sinh \Gamma_1\alpha \cosh \Gamma_2\alpha]} \cos \xi\alpha d\alpha. \quad (35)$$

Applying the residue integration method to (35), we have

$$I = \oint \frac{\Gamma_2 \sinh \Gamma_2\mathcal{Z} - \Gamma_1 \sinh \Gamma_1\mathcal{Z}}{\Gamma_2 \sinh \Gamma_2\mathcal{Z} \cosh \Gamma_1\mathcal{Z} - \Gamma_1 \sinh \Gamma_1\mathcal{Z} \cosh \Gamma_2\mathcal{Z}} e^{i\xi\mathcal{Z}} d\mathcal{Z} = 2\pi i \sum [\text{Residues}] \quad (36)$$

where $\mathcal{Z} = \alpha + i\theta$ is a complex variable in the (α, θ) plane. The integral I , is taken counterclockwise along a semicircular path in the upper region of the \mathcal{Z} plane. The path of integration is bounded by the α -axis and $|\mathcal{Z}| = \mathcal{R}$ in the limit as $\mathcal{R} \rightarrow \infty$; this path encloses the poles of the integrand in (35). The poles are given by the roots of

$$\Gamma_2 \tanh \Gamma_2\mathcal{Z} - \Gamma_1 \tanh \Gamma_1\mathcal{Z} = 0. \quad (37)$$

Because the coefficient of $e^{i\xi\mathcal{Z}}$ in (36) is even, the value of I is twice that of the integral in (34). By applying the transformation $\mathcal{Z} = ik$, (37) becomes

$$\Gamma_2 \tan \Gamma_2k - \Gamma_1 \tan \Gamma_1k = 0. \quad (38)$$

Equation (38) is the exact form of eigenvalue equation for exponential axial stress decay in the self-equilibrating end load problem examined by Choi and Horgan (1977), for materials with real eigenvalues for Eq. (15). Thus the eigenvalues (and hence, the eigenfunctions) for the stress function due to opposed transverse forces are entirely equivalent to the eigenvalues for the stress function due to self-equilibrating end disturbance, as previously noted by Durban and Stronge (1992). The poles of (35) in the upper half of the \mathcal{Z} plane are

$$\mathcal{Z}_m = i[\text{Re}(k_m) \pm i\text{Im}(k_m)] \quad (m = 1, 2, \dots), \quad (39)$$

where k_m is the eigenvalue of (38), and has a positive real part. The expression for the first residue reads

$$\text{First Residue} = i \frac{\Gamma_2 \sin \Gamma_2k_1 - \Gamma_1 \sin \Gamma_1k_1}{(\Gamma_2^2 - \Gamma_1^2) \cos \Gamma_1k_1 \cos \Gamma_2k_1} e^{-k_1\xi}. \quad (40)$$

If k_1 is complex the residue (40) also includes the term contributed by the conjugate part \bar{k}_1 . As ξ becomes large the value of I asymptotically approaches

$$\frac{\pi h}{2P} \sigma_y(\xi, 0) \approx \frac{\pi}{2} \frac{\Gamma_2 \sin \Gamma_2k_1 - \Gamma_1 \sin \Gamma_1k_1}{(\Gamma_2^2 - \Gamma_1^2) \cos \Gamma_1k_1 \cos \Gamma_2k_1} e^{-k_1\xi} + \frac{\pi}{2} \frac{\Gamma_2 \sin \Gamma_2\bar{k}_1 - \Gamma_1 \sin \Gamma_1\bar{k}_1}{(\Gamma_2^2 - \Gamma_1^2) \cos \Gamma_1\bar{k}_1 \cos \Gamma_2\bar{k}_1} e^{-\bar{k}_1\xi}. \quad (41)$$

If the roots of (33) are complex, we have

$$\omega_{1,2} = \pm(\Gamma + i\Omega) \quad \omega_{3,4} = \pm(\Gamma - i\Omega). \quad (42)$$

After some algebraic manipulation, the first equation in (27) transforms to

$$-\frac{\pi h}{2P} \sigma_y(\xi, 0) = \int_0^{\infty} \frac{[\Gamma \cosh \Gamma\alpha \sin \Omega\alpha + \Omega \sinh \Gamma\alpha \cos \Omega\alpha]}{\Gamma \sin 2\Omega\alpha + \Omega \sinh 2\Gamma\alpha} \cos \xi\alpha d\alpha \quad (43)$$

In the limiting case of $\Omega = 0$, $\Gamma = 1$, we arrive at the case for an isotropic material, and (43) reduces to

$$-\frac{\pi h}{2P} \sigma_y(\xi, 0) = \int_0^{\infty} \frac{\alpha \cosh \alpha + \sinh \alpha}{\sin 2\alpha + 2\alpha} \cos \xi\alpha d\alpha. \quad (44)$$

This expression is the same as that obtained by Filon (1903). Applying the residue integration procedure to (43), we obtain

$$I = \oint \frac{\Gamma \cosh \Gamma\mathcal{Z} \sin Y\mathcal{Z} + \Omega \sinh \Gamma\mathcal{Z} \cos \Omega\mathcal{Z}}{\Gamma \sin 2\Omega\mathcal{Z} + \Omega \sinh 2\Gamma\mathcal{Z}} e^{i\xi\mathcal{Z}} d\mathcal{Z} = 2\pi i \sum [\text{Residues}] \quad (45)$$

with poles given by roots of the equation

$$\Gamma \sin 2\Omega\mathcal{Z} + \Omega \sinh 2\Gamma\mathcal{Z} = 0. \quad (46)$$

Using the transformation $\mathcal{Z} = ik$, in (46) gives

$$\Gamma \sinh 2\Omega k + \Omega \sin 2\Gamma k = 0. \quad (47)$$

Again, (47) is the eigenvalue equation for exponential stress decay rates in the self-equilibrating end load problem, obtained by Choi and Horgan (1977) for materials with complex roots for (15). If k_1 is the first eigenvalue in the upper half of the \mathcal{Z} plane, and its conjugate is \bar{k}_1 , then, for large values of $k_1\xi$ (43) has an asymptotic value

$$\frac{\pi h}{2P} \sigma_y(\xi, 0) \approx \pi \frac{\Omega \cosh \Omega k_1 \sin \Gamma k_1 + \Gamma \sinh \Omega k_1 \cos \Gamma k_1}{2\Gamma\Omega(\cos 2\Gamma k_1 + \cosh 2\Omega k_1)} e^{-k_1\xi} + \pi \frac{\Omega \cosh \Omega \bar{k}_1 \sin \Gamma \bar{k}_1 + \Gamma \sinh \Omega \bar{k}_1 \cos \Gamma \bar{k}_1}{2\Gamma\Omega(\cos 2\Gamma \bar{k}_1 + \cosh 2\Omega \bar{k}_1)} e^{-\bar{k}_1\xi} \quad (48)$$

For the case of repeated roots of (33), the eigenvalue equation is

$$\sinh 2\Gamma k + 2\Gamma k = 0 \quad (49)$$

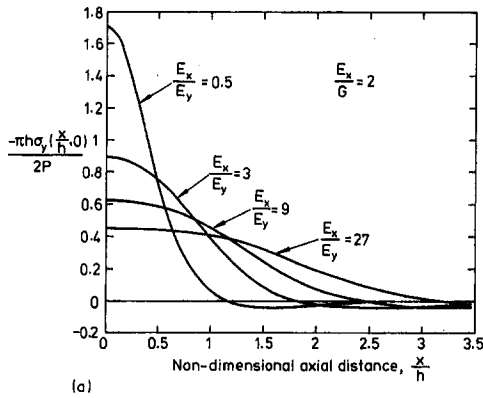


Fig. 2(a)

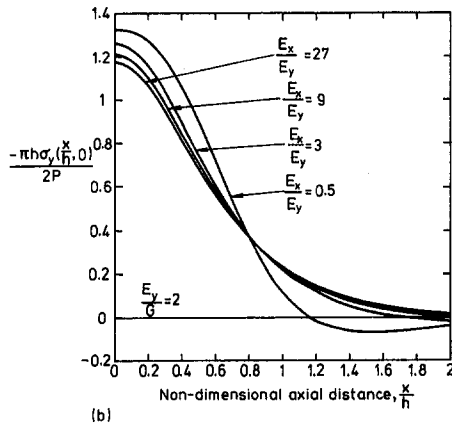


Fig. 2(b)

Fig. 2 Normal stress σ_y on the middle surface ($y/h = 0$) as a function of the ratio of axial to transverse Young's moduli E_x/E_y for (a) ($E_y/G = 2$), and (b) ($E_x/G = 2$). In-plane Poisson's ratio $\nu_{xy} = 0.3$.

where $\Gamma = \sqrt{R_1} = R_2$, and the first eigenvalue is given by

$$\Gamma k_1 = 2.1061 \pm i1.1254. \quad (50)$$

The expression for nondimensional normal stress is obtained from (48), by taking the limiting value of $\Omega = 0$. Thus for repeated roots,

$$\begin{aligned} \frac{\pi h}{2P} \sigma_y(\xi, 0) \approx \pi \frac{k_1 \Gamma \cos \Gamma k_1 + \sin \Gamma k_1}{2\Gamma(1 + \cos 2\Gamma k_1)} e^{-k_1 \xi} \\ + \pi \frac{\bar{k}_1 \Gamma \sin \Gamma \bar{k}_1 + \sin \Gamma \bar{k}_1}{2\Gamma(1 + \cos 2\Gamma \bar{k}_1)} e^{-\bar{k}_1 \xi}. \quad (51) \end{aligned}$$

The special case of an isotropic material where $\Gamma = 1$, in (49), was considered by Durban and Stronge (1992).

5 Eigenfunctions and the Rate of Decay for Stress

The influence of elastic parameter ratios E_x/E_y and E_y/G on the distribution of normal stress σ_y , along the middle surface ($y/h = 0$), is illustrated in Figs. 2 to 3 for plane-stress and plain-strain conditions; these curves were evaluated from Eqs. (21) and (27). Our studies indicate that the normal stress on the middle surface $\sigma_y(x/h, 0)$ is insensitive to the modulus ratio E_x/E_y for values of the ratio of transverse Young's modulus to shear modulus ($E_y/G \gg 1$). However, for constant values of the ratio of axial Young's modulus to shear modulus E_x/G , the

rate of decay of the normal stress on the middle surface $\sigma_y(x/h, 0)$ becomes more rapid as the modulus ratio E_x/E_y becomes smaller.

If the ratio of transverse to shear moduli E_y/G is held constant, for large ratios of axial to transverse Young's moduli E_x/E_y , the rate at which the middle surface stress ($\pi h/2P \sigma_y$) is spread by shear does not significantly change, as shown in Fig. 2(b). However, for small values of the ratio of axial to transverse Young's moduli ($E_x/E_y < 1$), the influence of Poisson's ratio on the distribution of normal stress ($\pi h/2P \sigma_y$) is significant, causing more rapid diffusion of the middle surface stress. It is evident from Figs. 2 that the transverse Young's modulus E_y has a strong influence on the distribution of normal stress on the middle surface. This might be expected from physical reasoning, since in the present problem the applied forces are directed along the y -axis.

Figure 3 shows the distribution of normal stress on the middle surface ($y/h = 0$), for plane stress and plane strain, for crystalline zinc, an isotropic material, a crossply composite (b), as well as a unidirectional composite (a). The plots indicate that the stress distributions for plane stress and plane strain are practically identical. This is because the quantities R_1 and R_2 given by (12) for plane stress, and (13) for plane strain, remain relatively unchanged for all the materials.

6 Comparison of Eigenfunctions and Analytical Solution

The exponential axial diffusion of normal stress on the middle surface is examined in this section, in the context of the eigenfunctions obtained in Section 4; i.e.,

$$\frac{\pi h}{2P} \sigma_y(\xi, 0) = \sum_n \{ \Pi_n e^{-k_n \xi} + \bar{\Pi}_n e^{-\bar{k}_n \xi} \} \quad (52)$$

where tacitly it has been assumed that Π_n and k_n are complex. Let $\bar{\Pi}_n$ be the conjugate of Π_n , and

$$k_n = \beta_n + i\chi_n$$

$$\Pi_n = \varphi_n + i\varrho_n \quad (53)$$

where φ_n , ϱ_n , β_n , and χ_n are real, and β_n and χ_n have positive values. In the region close to the plane of applied forces $\xi = 0$, the diffusion of stress is determined by the sum of exponential terms in (52), which in turn are governed by the real part of the decay rate β_n . The eigenvalue k_n has an imaginary part χ_n , which becomes more important at large distances from the axis of applied forces, where the normal stress is negligibly small.

The axial diffusion of stress can be evaluated on the basis of the eigencomponents (52) of the solution for the boundary value problem. For the materials listed in Table 1, values of decay

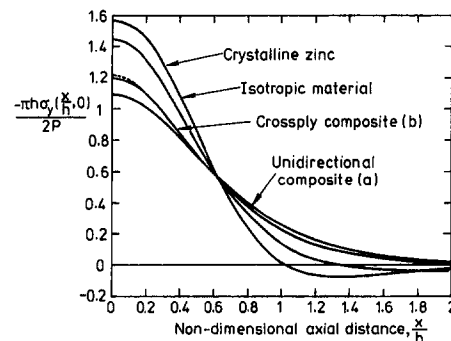


Fig. 3 Normal stress distribution on the middle surface for beams (plane stress) and strips (plane strain) composed of typical orthotropic materials. Curves for plane strain are shown as bold lines, while plane stress are shown as light lines. Middle surface stresses for plane stress and plane strain almost coincide for all the materials.

Table 2 Comparison of elastic parameters and property ratios with eigenvalues for stress function

		Isotropic	Magnesium	Zinc	Composite (a)	Composite (b)	Composite (c)
Material parameters	$\frac{E_x}{E_y}$	2.6	2.73	3.04	1.67	1.97	2.87
	$\frac{E_x}{G}$	2.6	3.06	0.94	33.4	18.92	12.36
	$\frac{E_x}{E_c}$	1.0	1.12	0.31	19.99	9.61	4.31
Roots for elastic field eq. (15)	$\Gamma_1 + i\Omega_1$	1.0	1.417	(0.625 + i0.409)	5.6814	4.2170	3.3893
	$\Gamma_2 + i\Omega_2$	1.0	0.748	(0.625 - i0.409)	0.7870	0.7347	0.6128
Smallest eigenvalues eqs. (38) (47) and (49)	$k = (\beta + i\chi)$	-	-	-	0.5646	-	-
		-	-	-	1.1360	0.7712	0.9625
		-	-	-	1.7773	1.5804	1.9888
		(2.1062 + i1.1254)	(2.1401 + i0.9375)	(2.4755 + i1.9785)	(2.0505 + i0.1521)	(2.1876 + i0.2802)	(2.6207 + i0.3243)

rate k_n ($n = 1, 2, \dots$) taken in the order of increasing real part of the smallest eigenvalues evaluated from (38), are compared in Table 2. We find that except for the composite materials, the first eigenvalue k_1 for all the other materials is complex. The eigencomponent given by each first complex eigenvalue k_1 is an accurate approximation for the stress distribution on the middle surface of the strip, at axial distances that are more than one quarter of the strip or plate thickness ($x/h > 0.5$) away from the line of action of the applied forces. This is illustrated in Fig. 4, where the first eigenfunction for crystalline zinc and an isotropic material are compared with the numerically computed stress distributions.

In the case of a unidirectional fiber composite (a), the fourth eigenvalue k_4 (taken in the order of increasing real part), is the first complex eigenvalue. The eigenfunctions for $k_1, k_2,$ and k_3 (which are all purely real) give a normal stress on the middle surface that is tensile at every section, as illustrated in Fig. 5. The tensile stress field is associated with positive real values of stress amplitude Π (see Table 3), evaluated from (41) for these eigenvalues. On the other hand, the normal stress on the middle surface given by the sum of eigenfunctions for the first complex eigenvalue and its conjugate, is compressive. As shown in Fig. 5(i), the sum of eigencomponents for eigenvalue terms from k_1 up to and including k_4 , as well as its conjugate \bar{k}_4 , gives a stress distribution on the middle surface ($y/h = 0$), which is in close agreement with the numerically computed stress field.

The first and second eigenvalues for both the angle-ply composite (b), as well as quasi-isotropic composite (c), are also

purely real. Similar to the case of a unidirectional fiber composite (a), these eigenvalues give tensile eigencomponents for normal stress at every point along the middle surface; these eigencomponents have real positive values of stress amplitude Π_1, Π_2 , as tabulated in Table 3. For both materials, the sum of eigencomponents for eigenvalues up to, and including the first complex eigenvalue k_3 , as well as its conjugate \bar{k}_3 , gives a close approximation for the stress field on the middle surface ($y/h = 0$), as shown in Figs. 5(ii) and (iii).

Figure 6 relates the number n of purely real or imaginary eigenvalues smaller than the first complex eigenvalue, to the elastic parameter ratios E_x/E_y and E_x/G . The curves indicate the transition regions where there is a change in the number of eigenvalue terms smaller than the first complex eigenvalue. For example, in a region where $n = i$, there are i purely real or imaginary eigenvalue terms smaller than the first complex eigenvalue; i.e., k_{i+1} is the first complex eigenvalue. For a ratio of axial to shear stiffness ($E_x/G = 0.5$), the first eigenvalue k_1 , is always complex, with both the real part β_1 , and the imaginary part χ_1 , having the same value. Below an (E_x/G) ratio of 0.5, the eigenvalues are either purely imaginary or complex, while for values of E_x/G larger than 0.5, the eigenvalues are either purely real or complex. For reference purposes, the elastic moduli ratios for an isotropic material, unidirectional composite (a), crossply composite (b), as well as quasi-isotropic composite (c), are indicated in Fig. 6.

Since the first complex eigenvalue plays an important role in the distribution of this component of stress, it is necessary to have a simple expression for evaluating this quantity. As illustrated in Fig. 2(b), for a ratio of axial to transverse elastic modulus ($E_x/E_y \geq 3$), a further increase in E_x/E_y does not cause any significant change in normal stress distribution. Using the method of least squares, a relation was obtained for the real part of decay rate β , for materials with a ratio of axial to transverse elastic moduli ($E_x/E_y \gg 1$),

$$\text{Re}(k) \approx 1.7 \sqrt{\frac{E_y}{G}} - 0.28. \quad (54)$$

It is worth mentioning that the asymptotic value for rate of decay obtained previously by Choi and Horgan (1977),

$$k \approx \pi \sqrt{\frac{G}{E_x}} \quad (55)$$

gives an estimate for the first eigenvalue rather than the first complex eigenvalue.

Finally, in order to examine whether decay of normal stress on the middle surface $\sigma_y(x)$ is representative of decay rate for all stress components, the rate of decay of the standard deviation δ_x of axial stress variation on cross sections was obtained for

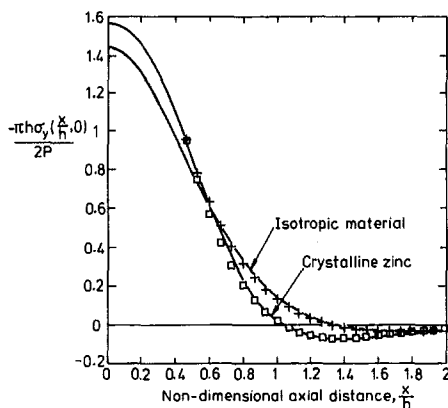
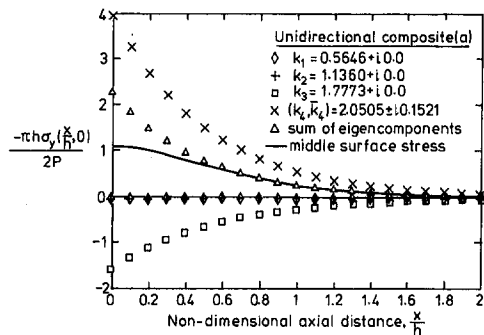
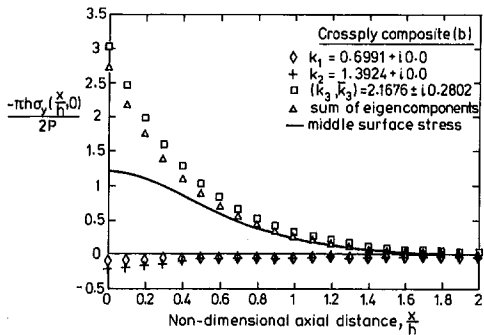


Fig. 4 Comparison of the first eigencomponent (shown in open symbols) along the middle surface, with numerically evaluated stress field (curves) for an isotropic material and crystalline zinc. The smallest eigenvalue for both materials are complex.



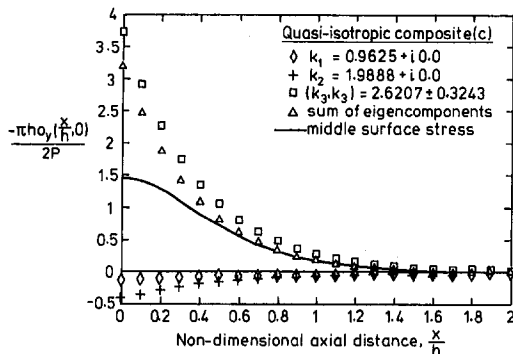
(i)

Fig. 5(i)



(ii)

Fig. 5(ii)



(iii)

Fig. 5(iii)

Fig. 5 Comparison of the sum of eigencomponents for eigenvalue terms up to, and including the first complex eigenvalue, with stress field obtained numerically, for (i) unidirectional fiber composite (a), (ii) crossply composite (b), and (iii) quasi-isotropic composite (c).

a unidirectional composite (a), and an isotropic material. These results were compared with the decay of normal stress on the middle surface $\sigma_y(x, 0)$, the lower bound on decay rate predicted by Choi and Horgan (1977), Eq. (55), and the present estimate for the real part of the first complex eigenvalue Eq. (54). This comparison is shown in Fig. 7, where the stress values have been normalized by the stress magnitude on the axis of applied forces. Figure 7 indicates that the decay of normal stress on the middle surface and that of axial stress variation on different cross sections are not the same. Near the axis of applied forces, the axial stress variation on cross sections decays more rapidly than the normal stress on the middle surface. However, for both stress components the relative magnitudes of decay rates for unidirectional composite (a) and an isotropic material are similar; in both cases, decay is slower in unidirectional composite (a) than in an isotropic material.

Table 3 Amplitude of stress Π_n , from small eigenvalues k_i , for materials in Table 1

	Stress Amplitude $\Pi_n = P_n + i Q_n$ ($n = 1, 2, \dots$), eq. (41)					
	Isotropic	Magnesium	Zinc	Composite (a)	Composite (b)	Composite (c)
1	-	-	-	(0.0250 + i0.0)	-	-
2	-	-	-	(0.0180 + i0.00)	(0.0594 + i0.0)	(0.0816 + i0.0)
3	-	-	-	(1.0178 + i0.0)	(0.1406 + i0.00)	(0.2679 + i0.00)
4	(-1.0- i0.088)	(-1.091- i0.333)	(-0.9674- i0.475)	(-1.2688- i1.1327)	(-0.9636- i0.0894)	(-1.1943- i0.3564)

For a highly anisotropic unidirectional composite (a), it can be noticed that far away from the loaded section, the lower bound on decay rate predicted by Choi and Horgan (1977) is in close agreement with the decay rate of axial stress variation in the strip. This is because Eq. (55) gives an estimate based on the smallest eigenvalue; which is purely real for the unidirectional composite (a). On the other hand, at practical distances from the loaded section the decay rate estimate given by Eq. (54) is in good agreement with the decay rate of normal stress on the middle surface. In the case of an isotropic material where the first eigenvalue is complex, at distances larger than one-half of the strip thickness, there is good agreement between the rate of decay of variations in the distribution of axial stress and the exponential decay predicted by either (54) or Choi and Horgan's (55).

7 Conclusions

Analytical solutions have been presented for stresses in an orthotropic strip or plate, loaded transversely by equal but opposed collinear forces. At distances larger than a quarter of the thickness from the plane of applied forces, the sum of eigenfunctions for eigenvalue terms up to, and including the first complex eigenvalue as well as its conjugate, closely approximates the stress field on the middle surface. The real part of this first complex eigenvalue has a major influence on the exponential decay of normal stress, while the imaginary part governs the sinusoidal variation. In highly anisotropic materials, the smallest eigenvalues are real rather than complex. For boundary value problems involving highly anisotropic materials, the rate

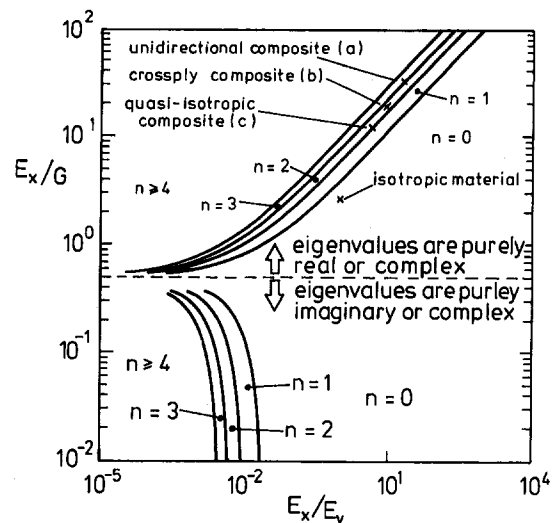


Fig. 6 Effect of elastic parameter ratios E_x/E_y and E_x/G on the number n of purely real or imaginary eigenvalues smaller than the first complex eigenvalue for plane stress ($\nu_{xy} = 0.3$)

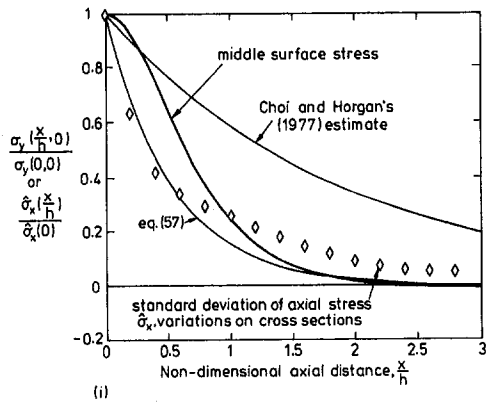


Fig. 7(i)

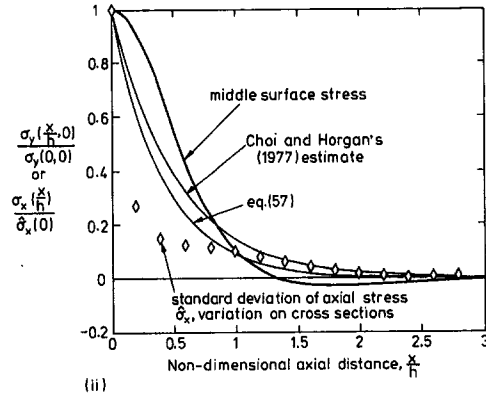


Fig. 7(ii)

Fig. 7 Comparison of the axial decay of standard deviation of axial stress with the decay of middle surface stress as well as exponential decay predicted by Choi and Horgan (1977), as well as Eq. (54), for (i) unidirectional composite (a), and (ii) an isotropic material. Values of stress were normalized by the stress magnitude on the axis of the applied forces.

of decay is not a material property; it differs between various components of stress. Nevertheless, for each component of

stress the rate of decay lies somewhere between the rates given by the first and the first complex eigenvalues.

Acknowledgment

S. A. Matemilola gratefully acknowledges financial support of a research grant from B P International. D. Durban wishes to thank the fund for promotion of research at the Technion.

References

- Cairns, D. S., 1991, "A Simple Elasto-Plastic Contact Law for Composites," *J. Reinforced Plastics & Composites*, Vol. 10, pp. 423-433.
- Choi, I., and Horgan, C. O., 1977, "Saint-Venant's Principle and End Effects in Anisotropic Elasticity," *ASME JOURNAL OF APPLIED MECHANICS*, Vol. 44, pp. 424-430.
- Dahan, M., and Zarka, J., 1977, "Elastic Contact Between a Sphere and a Semi-Infinite Transversely Isotropic Body," *Int. J. Solids & Structures*, Vol. 13, pp. 227-238.
- Durban, D., and Stronge, W. J., 1988, "On the Validity of Saint Venant's Principle in Finite Strain Plasticity," *ASME JOURNAL OF APPLIED MECHANICS*, Vol. 36, pp. 459-476.
- Durban, D., and Stronge, W. J., 1992, "Diffusion of Incremental Loads in Prestrained Bars," *Proc. R. Soc. Lond.*, Vol. A439, pp. 583-600.
- Filon, L. N. G., 1903, "On an Approximate Solution for Bending of a Beam of Rectangular Cross-Section Under any System of Load, with Special Reference to Points of Concentrated or Discontinuous Loading," *Transactions of Royal Society (London)*, Vol. A201, pp. 67-154.
- Horgan, C. O., 1974, "The Axisymmetric End Problem for Transversely Isotropic Circular Cylinders," *Int. J. Solids Structures*, Vol. 10, pp. 837-852.
- Horgan, C. O., 1982, "Saint Venant's End Effects in Composites," *J. Composite Materials*, Vol. 16, pp. 411-422.
- Horgan, C. O., 1989, "Recent Developments Concerning Saint-Venant's Principle: An Update," *ASME Appl. Mech. Rev.*, Vol. 42, pp. 295-303.
- Horgan, C. O., and Knowles, J. K., 1983, "Recent Developments Concerning Saint-Venant's Principle," *Advances in Applied Mechanics*, Vol. 23, pp. 179-267.
- Jones, R. M., 1975, *Mechanics of Composite Materials*, Scripta Book Company, Washington, D.C.
- Knowles, J. K., 1966, "On Saint-Venant's Principle in the Two-Dimensional Linear Theory of Elasticity," *Archive for Rational Mechanics and Analysis*, Vol. 21, pp. 1-22.
- Lekhnitskii, S. G., 1968, *Anisotropic Plates*, translation from Russian Edition, Gordon and Breach, New York.
- Shivakumar, K. N., Elber, W., and Illg, W., 1985, "Prediction of Impact Force and Duration Due to Low-Velocity Impact on Circular Composite Laminates," *ASME JOURNAL OF APPLIED MECHANICS*, Vol. 52, pp. 674-650.
- Stephen, N. G., 1991, "Decay Rates for the Compound Circular Cylinder," *Journal of Strain Analysis*, Vol. 26, No. 4, pp. 215-220.
- Timoshenko, S. P., and Goodier, J. N., 1970, *Theory of Elasticity*, 3rd Ed., McGraw-Hill, New York.
- Toupin, R. A., 1965, "Saint-Venant's Principle," *Archive for Rational Mechanics and Analysis*, Vol. 18, pp. 83-96.

Rotation of a Cylinder in a Casing at Zero Reynolds Number

C. Y. Wang¹

Michigan State University,
East Lansing, MI

A finite solid cylinder rotates inside a larger, fluid-filled cylindrical casing. The Stokes equation is solved by an efficient method using domain decomposition, eigenfunction expansion, and collocation. The resistive torque is found as a function of the geometric parameters. The torque due to the rotation of a finite cylinder in an infinite fluid is extrapolated.

1 Introduction

Due to the advent of micro fluid-mechanical devices such as miniature motors, Stokes or zero Reynolds number flow analyses (e.g., Happel and Brenner, 1986) have become more and more important. Of interest is the rotation of rigid bodies in a viscous fluid. Jeffrey (1915) and Kanwal (1961) used separable orthogonal coordinates and studied the rotation of ellipsoids, lenses, and tori in an infinite fluid. The solution of the rotation of concentric spheres separated by a viscous fluid was presented by Landau and Lifshitz (1959). A sphere rotating inside an infinite cylinder was solved by Brenner and Sonshine (1964) using cylindrical singularities expressed in terms of spherical coordinates and solving the subsequent infinite system of algebraic equations. Kim (1981) used dual integral equations and expansions to solve the rotation of a disk in an infinite cylinder. The problem of a disk in a finite cylindrical casing was studied by Schmieden (1928) using elliptic integrals and numerical methods and more recently by Wang (1992) using an eigenfunction expansion and point match method.

The present paper studies the rotation of a centered, finite cylinder in a larger cylindrical casing. Due to the geometry all aforementioned methods do not apply. We shall use a domain decomposition and matching method perhaps first used by Weil (1951) who studied the Stokes flow into a gap. Other variations of the method include the works of Trogden and Joseph (1982) who solved the flow over a slot and Wang (1993) who investigated the flow through filter slits.

2 Formulation

Figure 1(a) shows the cross section of a cylinder (diameter $2bR$, height $2aR$) rotating with an angular velocity ω inside a larger, fixed casing (diameter $2R$, height $2cR$). For very low Reynolds number, the flow between the cylinders is governed by the Stokes equation

$$\frac{\partial^2 v}{\partial r^2} + \frac{1}{r} \frac{\partial v}{\partial r} - \frac{v}{r^2} + \frac{\partial^2 v}{\partial z^2} = 0 \quad (1)$$

where v is the azimuthal velocity normalized by ωR and all lengths have been normalized by the outer radius R . The boundary conditions are that on the outer casing $v = 0$ and that on the inner cylinder $v = r$.

Since the domain between the two finite cylinders is complex, we partition it into simple regions to be solved separately and then matched along their common boundary. The following two cases are distinguished. If $c \leq 1$ the outer casing is "cake-like" and the domain is decomposed as in Fig. 1(b) (only $\frac{1}{2}$ of the cross section is shown). If $c \geq 1$ the outer casing is "rod-like" and the domain is decomposed as in Fig. 1(c). As we shall see later, such separation decreases the number of necessary collocation points and thus increases numerical efficiency. Since the problem can be solved for any of the two decompositions, there is considerable overlap where both methods are quite efficacious. The distinction according to the value of c is only a useful guideline.

3 $c \leq 1$ Case

For Region 1 in Fig. 1(b) let $v_1(r, z)$ be the solution. Partial boundary conditions are

$$v_1(0, z) = 0 \quad (2)$$

$$v_1(r, 0) = 0 \quad (3)$$

$$v_1(r, c - a) = r. \quad (4)$$

The general solution satisfying Eqs. (1)–(4) is

$$v_1(r, z) = \frac{rz}{c - a} + \sum_{n=1}^{\infty} A_n \sin(\alpha_n z) I_1(\alpha_n r) e^{-\alpha_n b}. \quad (5)$$

The first term on the right-hand side of Eq. (5) satisfies the nonhomogeneous boundary condition; $\alpha_n = n\pi/(c - a)$ are eigenvalues in z ; I_1, K_1 are modified Bessel functions; and A_n are unknown coefficients. Since $I_1(\alpha_n r) \sim \exp(\alpha_n r)$ for large α_n , the exponential factor in Eq. (5) is multiplied such that the coefficients A_n would be of reasonable magnitude. For Region 2 partial boundary conditions for $v_2(r, z)$ are

$$v_2(r, 0) = 0 \quad (6)$$

$$v_2(1, z) = 0 \quad (7)$$

$$\frac{\partial v_2}{\partial z}(r, c) = 0. \quad (8)$$

The general solution is

$$v_2(r, z) = \sum_{n=1}^{\infty} B_n \cos[\beta_n(c - z)] [I_1(\beta_n r) K_1(\beta_n) - I_1(\beta_n) K_1(\beta_n r)] e^{-\beta_n(1-b)}. \quad (9)$$

Here $\beta_n = (n - 1/2)\pi/c$ are eigenvalues in z , and the exponential factor ensures the coefficients B_n are of order unity. The solutions v_1, v_2 are then matched along $r = b$.

$$v_2(b, z) = b \quad c - a < z \leq c \quad (10)$$

$$v_2(b, z) = v_1(b, z) \quad 0 \leq z < c - a \quad (11)$$

¹ Currently at the Institute of Applied Mechanics, National Taiwan University, Taipei 10764, Taiwan, R.O.C.

Contributed by the Applied Mechanics Division of THE AMERICAN SOCIETY OF MECHANICAL ENGINEERS for publication in the ASME JOURNAL OF APPLIED MECHANICS.

Discussion on this paper should be addressed to the Technical Editor, Prof. Lewis T. Wheeler, Department of Mechanical Engineering, University of Houston, Houston, TX 77204-4792, and will be accepted until four months after final publication of the paper itself in the ASME JOURNAL OF APPLIED MECHANICS.

Manuscript received by the ASME Applied Mechanics Division, Oct. 22, 1993; final revision, Mar. 17, 1994. Associate Technical Editor: T. Y. Akylas.

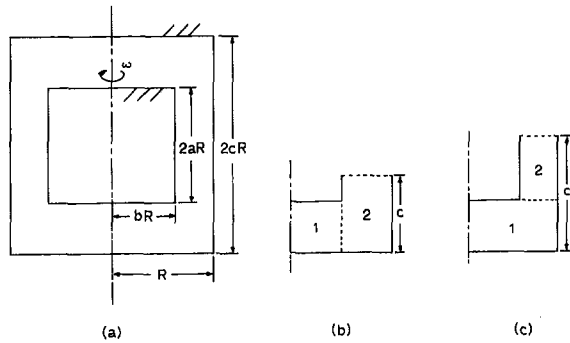


Fig. 1 (a) Axial cross section of a rotating cylinder inside a casing; (b) Partition into Regions for $c < 1$ (only $\frac{1}{4}$ of cross section is shown); (c) Partition into Regions for $c > 1$

$$\frac{\partial v_2}{\partial r}(b, z) = \frac{\partial v_1}{\partial r}(b, z) \quad 0 \leq z < c - a \quad (12)$$

Equations (10)–(12) represent an infinite system of linear equations in the unknowns A_n, B_n . One can of course eliminate a set of unknowns by using Fourier inversion. Since the mixed boundary conditions and thus collocation is unavoidable, there is little advantage in doing so. We truncate B_n to N terms and A_n to $M = \text{Int}[(1 - a/c)N] < N$ terms since v_1 serves a lesser height. Then N uniformly spaced collocation points are chosen

$$z_i = (i - 0.5)c/N \quad i = 1 \text{ to } N. \quad (13)$$

After some work, Eqs. (10)–(12) become

$$\sum_1^N B_n \cos[\beta_n(c - z_i)] [I_1(\beta_n b) K_1(\beta_n) - I_1(\beta_n) K_1(\beta_n b)] e^{-\beta_n(1-b)} = b \quad i = M + 1 \text{ to } N \quad (14)$$

$$\sum_1^N B_n \cos[\beta_n(c - z_i)] \times [I_1(\beta_n b) K_1(\beta_n) - I_1(\beta_n) K_1(\beta_n b)] e^{-\beta_n(1-b)} = \frac{bz_i}{c - a} + \sum_1^M A_n \sin(\alpha_n z_i) I_1(\alpha_n b) e^{-\alpha_n b} \quad i = 1 \text{ to } M \quad (15)$$

$$\sum_1^N B_n \frac{\beta_n}{2} \cos[\beta_n(c - z_i)] \{ [I_0(\beta_n b) + I_2(\beta_n b)] K_1(\beta_n) + [K_0(\beta_n b) + K_2(\beta_n b)] I_1(\beta_n) \} e^{-\beta_n(1-b)} = \frac{z_i}{c - a} + \sum_1^M A_n \frac{\alpha_n}{2} \sin(\alpha_n z_i) [I_0(\alpha_n b) + I_2(\alpha_n b)] e^{-\alpha_n b} \quad i = 1 \text{ to } M. \quad (16)$$

There are $N + M$ equations and $N + M$ unknowns. Figure 2

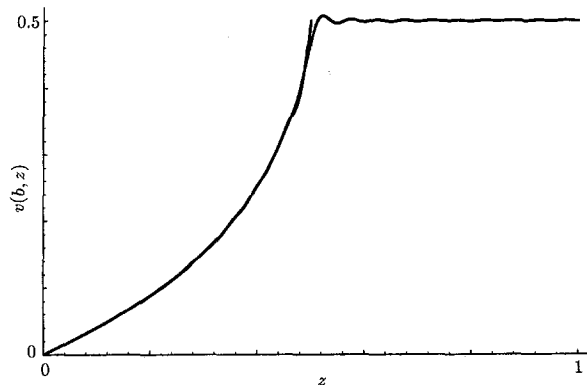


Fig. 2 Matching of $v_2(b, z)$ with b and $v_1(b, z)$, the latter shown only for $0 \leq z < c - a$ ($c = 1, a = b = 0.5, N = 40$)

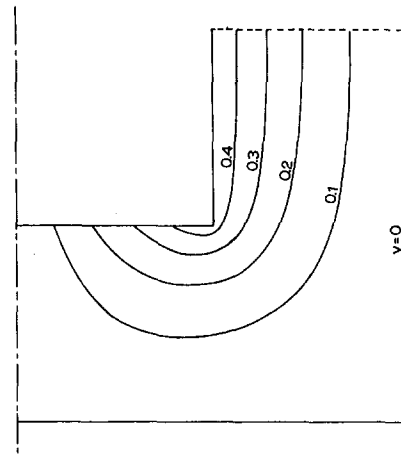


Fig. 3 Constant velocity lines, $c = 1, a = b = 0.5$

shows the match of Eqs. (10), (11) for the case $c = 1, a = b = 0.5$. The error, mostly at the corner $z = c - a$ is about five percent for $N = 40$ and decreases to one percent for $N = 80$. The corresponding constant velocity lines are shown in Fig. 3.

4 $c \geq 1$ Case

From Fig. 1(c) the matching boundary is along $z = c - a$. We seek eigenfunctions in the r direction. Partial boundary conditions for Region 1 are

$$v_1(0, z) = 0 \quad (17)$$

$$v_1(r, 0) = 0 \quad (18)$$

$$v_1(1, z) = 0. \quad (19)$$

The general solution satisfying Eqs. (1), (17)–(19) is

$$v_1(r, z) = \sum_1^{\infty} C_n J_1(\lambda_n r) (e^{\lambda_n(z-c+a)} - e^{-\lambda_n(z+c-a)}) \quad (20)$$

where λ_n are the zeroes of the Bessel function J_1 : 3.83171, 7.0156, 10.1735, the other zeroes are well approximated by (Olver, 1967)

$$\lambda_n = \left(n + \frac{1}{4} \right) \pi - \frac{3}{8(n + 1/4)\pi} \quad n \geq 4. \quad (21)$$

For Region 2 partial boundary conditions are

$$v_2(b, z) = b \quad (22)$$

$$v_2(1, z) = 0 \quad (23)$$

$$\frac{\partial v_2}{\partial z}(r, c) = 0. \quad (24)$$

The general solution is more complicated

$$v_2(r, z) = \frac{1/r - r}{1/b^2 - 1} + \sum_1^{\infty} D_n [J_1(\gamma_n r) Y_1(\gamma_n b) - J_1(\gamma_n b) Y_1(\gamma_n r)] (e^{\gamma_n(z-c-a)} + e^{-\gamma_n(z+c+a)}) \quad (25)$$

Here the first term on the right-hand side of Eq. (25) satisfies the nonhomogeneous boundary condition, J_1, Y_1 are Bessel functions, and γ_n are the eigenvalues of the equation

$$J_1(\gamma) Y_1(\gamma b) - J_1(\gamma b) Y_1(\gamma) = 0. \quad (26)$$

For each given b, γ_n can be obtained from Eq. (26). For large n , an asymptotic solution is highly desirable. Since for large ζ

$$J_1(\zeta) \sim \sqrt{\frac{2}{\pi\zeta}} \left[\cos \xi - \frac{3}{8\zeta} \sin \xi + \dots \right] \quad (27)$$

$$Y_1(\zeta) \sim \sqrt{\frac{2}{\pi\zeta}} \left[\sin \xi + \frac{3}{8\zeta} \cos \xi + \dots \right] \quad (28)$$

where $\xi \equiv \zeta - 3\pi/4$, Eq. (26) gives

$$\begin{aligned} & \left(\cos \xi_1 - \frac{3}{8\gamma} \sin \xi_1 \right) \left(\sin \xi_2 + \frac{3}{8\gamma b} \cos \xi_2 \right) \\ & - \left(\cos \xi_2 - \frac{3}{8\gamma b} \sin \xi_2 \right) \left(\sin \xi_1 + \frac{3}{8\gamma} \cos \xi_1 \right) \\ & = O\left(\frac{1}{\gamma^2}\right) \quad (29) \end{aligned}$$

where $\xi_1 = \gamma - 3\pi/4$, $\xi_2 = \gamma b - 3\pi/4$. Equation (29) simplifies to

$$\begin{aligned} & \sin [\gamma(1-b)] + \frac{3}{8\gamma} \left(1 - \frac{1}{b} \right) \\ & \times \cos [\gamma(1-b)] = O\left(\frac{1}{\gamma^2}\right). \quad (30) \end{aligned}$$

The perturbation solution for large γ is then

$$\gamma_n = \frac{n\pi}{1-b} + \frac{3(1-b)}{8b\pi n} + O(n^{-3}). \quad (31)$$

From Eq. (26) we solved the first ten eigenvalues numerically by bisection and the higher eigenvalues are well represented by Eq. (31). The matching conditions are

$$v_1(r, c-a) = r \quad 0 \leq r < b \quad (32)$$

$$v_1(r, c-a) = v_2(r, c-a) \quad b < r \leq 1 \quad (33)$$

$$\frac{\partial v_1}{\partial z}(r, c-a) = \frac{\partial v_2}{\partial z}(r, c-a) \quad b < r \leq 1. \quad (34)$$

Similar to the $c \leq 1$ case, we truncate C_n to N terms and D_n to $M = \text{Int}[N(1-b)]$ terms. The N collocation points along $z = c-a$ are

$$r_j = (j - 0.5)/N. \quad (35)$$

The $M + N$ linear equations are then

$$\sum_{j=1}^N C_n J_1(\lambda_n r_j) (1 - e^{-2\lambda_n(c-a)}) = r_j \quad j = 1 \text{ to } N - M \quad (36)$$

$$\begin{aligned} & \sum_{j=1}^N C_n J_1(\lambda_n r_j) (1 - e^{-2\lambda_n(c-a)}) \\ & = \frac{1/r_j - r_j}{1/b^2 - 1} + \sum_{j=1}^M D_n [J_1(\gamma_n r_j) Y_1(\gamma_n b) \\ & - J_1(\gamma_n b) Y_1(\gamma_n r_j)] (1 + e^{-2a\gamma_n}) \\ & \quad j = N - M + 1 \text{ to } N \quad (37) \end{aligned}$$

$$\begin{aligned} & \sum_{j=1}^N C_n \lambda_n J_1(\lambda_n r_j) (1 + e^{-2\lambda_n(c-a)}) \\ & = \sum_{j=1}^M D_n \gamma_n [J_1(\gamma_n r_j) Y_1(\gamma_n b) \\ & - J_1(\gamma_n b) Y_1(\gamma_n r_j)] (e^{-2a\gamma_n} - 1) \\ & \quad j = N - M + 1 \text{ to } N. \quad (38) \end{aligned}$$

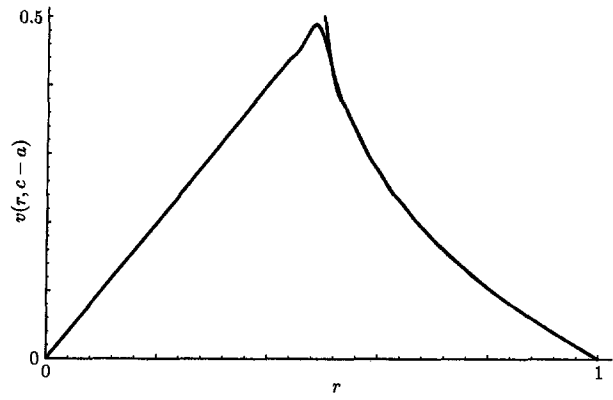


Fig. 4 Match of $v_1(r, c-a)$ with r and $v_2(r, c-a)$, the latter shown only for $b < r \leq 1$ ($c = 1$, $a = 0.5$, $N = 40$)

The match along $z = c-a$ is shown in Fig. 4. The error is similar to that of the $c \leq 1$ case. The constant velocity lines are identical to Fig. 3.

5 Torque

The torque T' induced by the rotation can be integrated from the shear on the casing

$$T \equiv \frac{T'}{4\pi\mu\omega R^3} = -\int_0^c \frac{\partial v}{\partial r}(1, z) dz + \int_0^1 \frac{\partial v}{\partial z}(r, 0) r^2 dr \quad (39)$$

where μ is the viscosity. For the $c \leq 1$ case

$$\begin{aligned} T & = -\int_0^c \frac{\partial v_2}{\partial r}(1, z) dz \\ & + \int_0^b \frac{\partial v_1}{\partial z}(r, 0) r^2 dr + \int_b^1 \frac{\partial v_2}{\partial z}(r, 0) r^2 dr \\ & = \frac{b^4}{4(c-a)} + \sum_1^M A_n b^2 I_2(\alpha_n b) e^{-\alpha_n b} \\ & + \sum_1^N B_n (-1)^n b^2 [I_2(\beta_n b) K_1(\beta_n) \\ & + I_1(\beta_n) K_2(\beta_n b)] e^{-\beta_n(1-b)}. \quad (40) \end{aligned}$$

For the $c \geq 1$ case

$$\begin{aligned} T & = -\int_0^{c-a} \frac{\partial v_1}{\partial r}(1, z) dz \\ & - \int_{c-a}^1 \frac{\partial v_2}{\partial r}(1, z) dz + \int_0^1 \frac{\partial v_1}{\partial z}(r, 0) r^2 dr \\ & = \sum_1^N \frac{C_n}{2} [J_2(\lambda_n) (1 + e^{-\lambda_n(c-a)})^2 - J_0(\lambda_n) (1 - e^{-\lambda_n(c-a)})^2] \\ & + \frac{2a}{1/b^2 - 1} - \sum_1^M D_n [J_0(\gamma_n) Y_1(\gamma_n b) \\ & - J_1(\gamma_n b) Y_0(\gamma_n)] (1 - e^{-2a\gamma_n}). \quad (41) \end{aligned}$$

Since the torque is a function of three geometric parameters a , b , c , we shall present the results only for some specific cases. Figure 5 shows the torque for constant gap width ratio δ , i.e., $b = 1 - \delta$, $a = c - \delta$. The dashed lines are from the linear Couette approximation for small δ . The velocities on the side and bottom (top) are assumed to be $(1-r)/\delta$ and rz/δ , giving a torque of

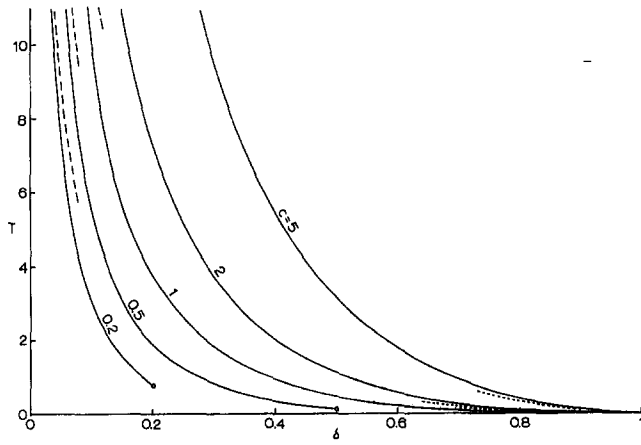


Fig. 5 Torque as a function of gap width δ for constant c . --- Eq. (42), Eq. (43). Circles represent disks.

$$T = \frac{1}{\delta} \left(c + \frac{1}{4} \right). \quad (42)$$

The relative error of Eq. (42) is of order δ , severely restricting the validity of the linear approximation. The torque decreases as δ increases. For $c > 1$ the torque is zero at $\delta = 1$, where the rotating cylinder shrinks to a thin rod. By using the solution of an infinite rod in an unbounded fluid, the torque is approximated by

$$T = 2(1 - \delta)^2(c - \delta) \quad (43)$$

which is shown as dotted lines in Fig. 5. For $c < 1$, the curves terminate at $c = \delta$ whereby the rotating cylinder becomes a disk. Our values compare well with those of Wang (1992).

Results for other combinations of a, b, c can be obtained by the methods outlined in this paper and will not be presented here.

6 Rotating Finite Cylinder in an Infinite Fluid

Consider the case of a finite cylinder rotating between and perpendicular to parallel plates, i.e., $a, b, c \rightarrow 0$ while their ratios remain finite. Let $a/b \equiv \sigma, c/b \equiv \rho, \bar{T} = T'/4\pi\mu\omega(bR)^3$. We expect as $R \rightarrow \infty$ the torque \bar{T} will be a function of σ, ρ only. Given σ, ρ we decrease b until \bar{T} tends to a limit. The accuracy is determined by increasing N (to about 50 for three-figure accuracy). The results are shown in Fig. 6. The torque approaches infinity as $\rho \rightarrow \sigma$. An approximate formula using

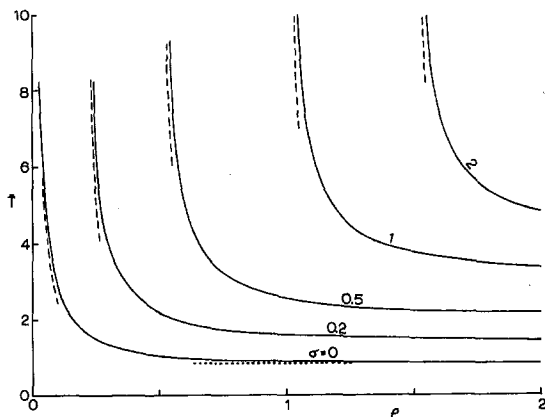


Fig. 6 Torque of a finite cylinder rotating perpendicularly between two parallel plates. --- Eq. (44), Jeffrey's value of $8/3\pi$.

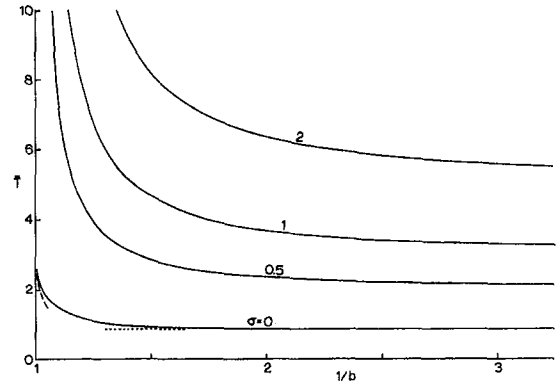


Fig. 7 Torque of a finite cylinder rotating coaxially inside an infinite tube. --- Eq. (46), Jeffrey's value of $8/3\pi$.

linear velocity for top and bottom gaps and the velocity of an infinite rotating cylinder for the sides is

$$\bar{T} = 2\sigma + \frac{1}{4(\rho - \sigma)}. \quad (44)$$

Equation (44) is represented by dashed lines in Fig. 6. For the disk ($\sigma = 0$) the torque for large ρ approaches Jeffrey's (1915) value of $8/3\pi$ for a disk rotating in an infinite fluid.

Next we investigate the case of a finite cylinder rotating inside an infinite coaxial tube. We fix a, b and increase c until \bar{T} tends to a limit. The results are shown in Fig. 7. As $b \rightarrow 1$ the torque is infinite logarithmically. For the disk ($\sigma = 0$) we plotted Kim's (1981) asymptotic formula as $b \rightarrow 1$

$$\bar{T} = \frac{8}{3\pi} \left[-\frac{3}{4} \ln(1 - b) - 0.5818 \right]. \quad (45)$$

Of interest is the torque of a finite cylinder rotating in an unbounded fluid. We can approach this limit by increasing ρ in Fig. 6 or decreasing b in Fig. 7. A better way is to extrapolate using Brenner's (1962) result for a small object rotating on the axis of an infinite tube. In our parameters the formula is

$$\bar{T}(\sigma, b) = \frac{\bar{T}_0(\sigma)}{1 - 0.79682b^3\bar{T}_0(\sigma)/2 + O(b^5)} \quad (46)$$

where \bar{T}_0 is the torque in an infinite fluid. Solving for \bar{T}_0 , we find

$$\bar{T}_0(\sigma) = \frac{\bar{T}(\sigma, b)}{1 + 0.39841b^3\bar{T}(\sigma, b)} + O(b^5). \quad (47)$$

By using Richardson's extrapolation for $b = 0.1, 0.2$, the torque

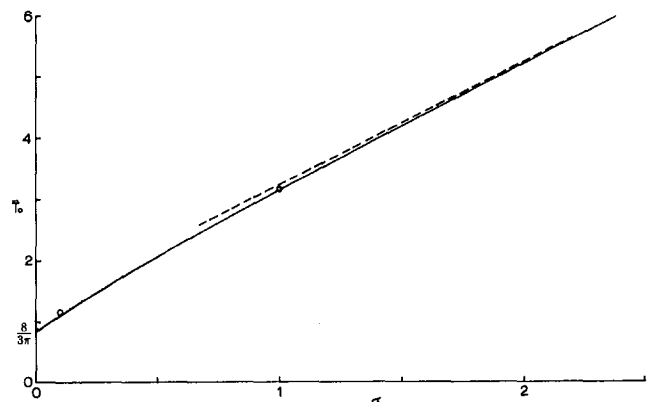


Fig. 8 Torque of a finite cylinder rotating in an infinite fluid. Dashed line is Eq. (48). Circles are from Chan et al. (1986).

\bar{T}_0 due to a finite cylinder rotating in an infinite fluid ($b \rightarrow 0$) is accurately shown in Fig. 8. The asymptote for large σ is found to be

$$\bar{T}_0 \sim 2\sigma + 1.242. \quad (48)$$

Since 2σ is the torque due to an infinite cylinder (per same length) half of the constant in Eq. (48), 0.621, must be the added torque due to the truncation of one end. Chan et al. (1986) used Greens function integrals to obtain the torque of a rotating finite cylinder in an infinite fluid. Their results are slightly higher (e.g., for $\sigma = 10$ they obtained $\bar{T}_0 = 21.306$ as compared to our 21.242).

7 Discussion

The present method is highly efficient in comparison to finite difference or finite element methods. The number of computations is about the square root of that needed for direct numerical integration. The number of collocation points is further minimized by considering separate formulations for $c > 1$ or $c < 1$ and taking the shorter distance for the matching boundary. Also, our torque integrations can be done analytically, further eliminating a source of error.

The rotation of finite coaxial cylinders separated by a viscous fluid is also important in viscometry. One particular problem of interest is the end effect due to the finite length. References to earlier experiments on end effects can be found in, for example, Kobayashi et al. (1991). A theoretical attempt was made by Oka (1960) who used matched eigenfunctions in three contiguous regions. Unfortunately the expression for the corner region is incomplete and his results are in error. Due to the fact that the torque is a function of three geometric parameters a full tabulation of end effects is not attempted in this paper. Our Figs. 5-8 should be extremely useful in the design of rotating cylinders at low Reynolds numbers.

References

- Brenner, H., 1962, "Effect of Finite Boundaries on the Stokes Resistance of an Arbitrary Particle," *Journal of Fluid Mechanics*, Vol. 12, pp. 35-48.
- Brenner, H., and Sonshine, R. M., 1964, "Slow Viscous Rotation of a Sphere in a Circular Cylinder," *Quarterly Journal of Mechanics and Applied Mathematics*, Vol. 17, pp. 55-63.
- Chan, P. C., Leu, R. J., and Zargar, N. H., 1986, "On the solution for the rotational motion of an axisymmetric rigid body at low Reynolds number with application to a finite length cylinder," *Chemical Engineering Communications*, Vol. 49, pp. 145-163.
- Happel, J., and Brenner, H., 1986, *Low Reynolds Number Hydrodynamics*, Martinus Nijhoff, Dordrecht, The Netherlands.
- Jeffrey, G. B., 1915, "On the Steady Rotation of a Solid of Revolution in a Viscous Fluid," *Proceedings of London Mathematical Society*, Section 2, Vol. 14, pp. 327-338.
- Kanwal, R. P., 1961, "Slow Steady Rotation of Axially Symmetric Bodies in a Viscous Fluid," *Journal of Fluid Mechanics*, Vol. 10, pp. 17-24.
- Kim, M. U., 1981, "Slow Rotation of a Disk in a Fluid-Filled Circular Cylinder," *Journal of the Physical Society of Japan*, Vol. 50, pp. 4063-4067.
- Kobayashi, H., Nashima, T., Okamoto, Y., and Kaminaga, F., 1991, "End effect in a coaxial cylindrical viscometer," *Review of Scientific Instruments*, Vol. 62, pp. 2748-2750.
- Landau, L. P., and Lifshitz, E. M., 1959, *Fluid Mechanics*, Addison-Wesley, Reading, MA.
- Oka, S., 1960, "The principles of rheology," *Rheology, Theory and Applications*, F. R. Eirich, ed. Academic Press, New York, Vol. 3, Chapter 2.
- Olver, F. W. J., 1967, "Bessel Functions of Integer Order," *Handbook of Mathematical Functions*, M. Abramowitz and I. A. Stegun, eds., Dover, New York, Chapter 9.
- Schmieden, C., 1928, "Über den Widerstand einer in einer Flüssigkeit rotierenden Scheibe," *Zeitschrift für Angewandete Mathematik und Mechanik*, Vol. 8, pp. 460-479.
- Trogden, S. A., and Joseph, D. D., 1982, "Matched Eigenfunction Expansions for Slow Flow over a Slot," *Journal of Non-Newtonian Mechanics*, Vol. 10, pp. 185-213.
- Wang, C. Y., 1992, "Slow Rotation of a Disc in a Fluid-Filled Casing," *Acta Mechanica*, Vol. 94, pp. 97-103.
- Wang, C. Y., 1993, "Stokes Flow through a Two-Dimensional Filter," *Physics of Fluids-A*, Vol. 5, pp. 1113-1116.
- Weil, H., 1951, "On the Extrusion of a Very Viscous Liquid," *ASME JOURNAL OF APPLIED MECHANICS*, Vol. 18, pp. 267-272.

Three-Dimensional Viscous Flows Between Concentric Cylinders Executing Axially Variable Oscillations: A Hybrid Spectral/Finite Difference Solution

D. Mateescu

M. P. Paidoussis
Fellow ASME.

W.-G. Sim

Department of Mechanical Engineering,
McGill University,
Montreal, Quebec H3A 2K6, Canada

A hybrid spectral/finite difference method is developed in this paper for the analysis of three-dimensional unsteady viscous flows between concentric cylinders subjected to fully developed laminar flow and executing transverse oscillations. This method uses a partial spectral collocation approach, based on spectral expansions of the flow parameters in the transverse coordinates and time, in conjunction with a finite difference discretization of the axial derivatives. The finite difference discretization uses central differencing for the diffusion derivatives and a mixed central-upwind differencing for the convective derivatives, in terms of the local mesh Reynolds number. This mixed scheme can be used with coarser as well as finer axial mesh spacings, enhancing the computational efficiency. The hybrid spectral/finite difference method efficiently reduces the problem to a block-tridiagonal matrix inversion, avoiding the numerical difficulties otherwise encountered in a complete three-dimensional spectral-collocation approach. This method is used to compute the unsteady fluid-dynamic forces, the real and imaginary parts of which are related, respectively, to the added-mass and viscous-damping coefficients. A parametric investigation is conducted to determine the influence of the Reynolds and oscillatory Reynolds (or Stokes) numbers on the axial variation of the real and imaginary components of the unsteady forces. A semi-analytical method is also developed for the validation of the hybrid spectral method, in the absence of previous accurate solutions or experimental results for this problem. Good agreement is found between these very different methods, within the applicability domain of the semi-analytical method.

1 Introduction

The analysis of three-dimensional unsteady viscous flows generated by the transverse oscillations of cylindrical structures conveying annular or axial flows is of particular interest for the study of flow-induced vibrations and instabilities, related to numerous engineering applications (as reviewed by Mulcahy (1980), Chen (1981), Mateescu and Paidoussis (1988), and Paidoussis et al. (1990)). The fluid and cylindrical-structure interaction and the related vibrations and instabilities have been seriously studied by, among others, Au-Yang and co-workers (1976, 1981), Chen and co-workers (1976, 1981), Mulcahy (1980), Hobson (1982), Brennen and Au-Yang (1992), and Mateescu, Paidoussis, and co-workers. Thus, Mateescu and Paidoussis (1985) contributed to the analysis of narrow annular unsteady flows based on potential flow theory; this theory has subsequently been extended by developing simplified flow models to take into account the unsteady viscous effects in laminar and turbulent regimes (Mateescu and Paidoussis, 1987; Ma-

teescu et al., 1989); good agreement was found with the experimental results (Mateescu et al., 1988, 1989).

These theoretical solutions have been used directly for the study of dynamics and stability of a flexible cylinder in a narrow coaxial cylindrical duct subjected to annular flow (Paidoussis et al., 1990). However, despite the success of these simplified solutions, there is obvious need for more accurate formulations based on the unsteady Navier-Stokes equations, applicable to more realistic and complex geometric configurations. In this respect, two computational methods have recently been developed and thoroughly validated, representing efficient solutions for unsteady confined flow with oscillating boundaries: (a) a spectral collocation method (Mateescu et al., 1990, 1994a), and (b) a time-integration method based on a finite difference formulation (Mateescu et al., 1994b). Recently, the spectral collocation method has been used in the analysis of two-dimensional unsteady annular motions between eccentric, infinitely long cylinders in translational oscillations, in the absence of an axial flow (Mateescu et al., 1990, 1994c).

The present analysis is devoted to the study of the three-dimensional unsteady annular flows between concentric cylinders conveying a fully developed laminar axial flow, when the inner cylinder executes axially variable transverse oscillations. In this case, a full-fledged spectral-collocation approach would lead to large fully populated matrices, which might be ill-conditioned and cause numerical difficulties. For this reason, spectral expansions in the transverse coordinates and time are used in

Contributed by the Applied Mechanics Division of THE AMERICAN SOCIETY OF MECHANICAL ENGINEERS for publication in THE ASME JOURNAL OF APPLIED MECHANICS.

Discussion on the paper should be addressed to the Technical Editor, Professor Lewis T. Wheeler, Department of Mechanical Engineering, University of Houston, Houston, TX 77204-4792, and will be accepted until four months after final publication in the paper itself in the ASME JOURNAL OF APPLIED MECHANICS.

Manuscript received by the ASME Applied Mechanics Division, Oct. 256, 1993; final revision, May 4, 1994. Associate Technical Editor: S. A. Berger.

conjunction with a finite difference approach for the discretization of the axial derivatives, using a mixed central-upwind differencing scheme.

In the absence of previous accurate solutions or experimental results for this problem to be used for comparison, a semi-analytical method, which is an extension of an earlier one (Mateescu and Païdoussis, 1987; Païdoussis et al., 1990), is also developed in this paper for validation of the hybrid spectral method. The semi-analytical solution is compared with previous results and to the hybrid spectral solution.

2 Hybrid Spectral Finite Difference Formulations

2.1 Partial Spectral Formulation for Three-Dimensional Unsteady Flows.

Consider two concentric cylinders of radii a and ba (where $b > 1$, Fig. 1(a)) subjected to fully developed laminar annular flow, characterized far upstream by the axial flow velocity $U^*(r) = U_0 U(r)$, where U_0 is the mean axial velocity and $U(r) = 2[(b^2 - 1) \ln r - (r^2 - 1) \ln b]/[(b^2 + 1) \times \ln b - (b^2 - 1)]$ represents the radial profile function of the axial velocity, in which $r = r^*/a$ is the nondimensional radial coordinate relative to the inner cylinder radius.

The central portion of length $l^* = al$ of the outer (or inner) cylinder executes, in the plane $\theta = 0$, axially variable transverse oscillations with respect to the rest of the outer and inner cylinders which are fixed, defined by

$$ae(x, t) = a\epsilon E(x) \cos \omega t = \Re\{a\epsilon E(x) \exp(i\omega t)\}, \quad (1)$$

where $\Re\{ \}$ denotes the real part, ϵ is the nondimensional amplitude relative to the radius a (assumed small), ω the radian frequency of the oscillations, and x the nondimensional axial coordinate (also relative to the inner radius, $x = x^*/a$); $E(x)$ denotes the axial mode of oscillations, represented, for example, by the eigenfunctions of a clamped-clamped beam,

$$E(x) = \sum_{k=0}^N [E_{Tk}(\beta_k x) + E_{Hk}(\beta_k x)], \quad (2)$$

$$E_{Tk}(\beta_k x) = -\cos(\beta_k x) + \sigma_k \sin(\beta_k x),$$

$$E_{Hk}(\beta_k x) = \cosh(\beta_k x) - \sigma_k \sinh(\beta_k x), \quad (3)$$

$$\sigma_k = \frac{\cosh \beta_k l - \cos \beta_k l}{\sinh \beta_k l - \sin \beta_k l}, \quad (4)$$

where $\beta_k l$ are the beam eigenvalues (of a clamped-clamped beam).

For the unsteady viscous incompressible flow generated by the oscillations, the time-dependent Navier-Stokes and continuity equations may be expressed in the cylindrical coordinates ax , ar , and θ in the form

$$\begin{aligned} \frac{\partial u}{\partial t} + \frac{1}{a} \left[(U_0 U + u) \frac{\partial u}{\partial x} + v \frac{\partial (U_0 U + u)}{\partial r} \right. \\ \left. + \frac{w}{r} \frac{\partial u}{\partial \theta} + \frac{1}{\rho} \frac{\partial (P + p)}{\partial x} \right] \\ = \frac{\nu}{a^2} \left[\frac{\partial^2 u}{\partial x^2} + \frac{1}{r} \frac{\partial}{\partial r} \left(r \frac{\partial (U_0 U + u)}{\partial r} \right) + \frac{1}{r^2} \frac{\partial^2 u}{\partial \theta^2} \right], \quad (5) \end{aligned}$$

$$\begin{aligned} \frac{\partial v}{\partial t} + \frac{1}{a} \left[(U_0 U + u) \frac{\partial v}{\partial x} + v \frac{\partial v}{\partial r} + \frac{w}{r} \left(\frac{\partial v}{\partial \theta} - w \right) + \frac{1}{\rho} \frac{\partial p}{\partial r} \right] \\ = \frac{\nu}{a^2} \left[\frac{\partial^2 v}{\partial x^2} + \frac{1}{r} \frac{\partial}{\partial r} \left(r \frac{\partial v}{\partial r} \right) + \frac{1}{r^2} \left(\frac{\partial^2 v}{\partial \theta^2} - v - 2 \frac{\partial w}{\partial \theta} \right) \right], \quad (6) \end{aligned}$$

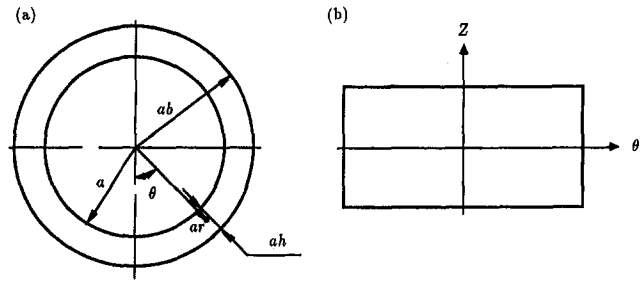


Fig. 1(a) Cross-sectional view of the system under consideration; (b) the associated, transformed, computational domain

$$\begin{aligned} \frac{\partial w}{\partial t} + \frac{1}{a} \left[(U_0 U + u) \frac{\partial w}{\partial x} + v \frac{\partial w}{\partial r} + \frac{w}{r} \left(\frac{\partial w}{\partial \theta} + v \right) + \frac{1}{\rho} \frac{\partial p}{\partial \theta} \right] \\ = \frac{\nu}{a^2} \left[\frac{\partial^2 w}{\partial x^2} + \frac{1}{r} \frac{\partial}{\partial r} \left(r \frac{\partial w}{\partial r} \right) + \frac{1}{r^2} \left(\frac{\partial^2 w}{\partial \theta^2} - w + 2 \frac{\partial v}{\partial \theta} \right) \right], \quad (7) \end{aligned}$$

$$\frac{\partial u}{\partial x} + \frac{1}{r} \left[\frac{\partial}{\partial r} (rv) + \frac{\partial w}{\partial \theta} \right] = 0, \quad (8)$$

where $U_0 U(r)$ and $P(x)$ represent the known steady fluid velocity and pressure field in the fully developed laminar flow undisturbed by the oscillations, and where u , v , w , and p are the axial, radial, and circumferential perturbation velocity components and the unsteady pressure generated by the oscillations and superimposed on the steady flow field [hence $(U_0 U + u)$, v , w and $P(x) + p(x, r, \theta, t)$ are the total velocity components and pressure in the overall unsteady flow]; ν is the kinematic viscosity of the fluid.

These governing equations are subjected to the boundary conditions

$$u = v = w = 0 \quad (9)$$

on the fixed parts of the cylinders and

$$u = 0, \quad v = ae \cos \theta, \quad w = -ae \sin \theta \quad (10)$$

on the oscillating central portion of the inner cylinder, where $e = del/dt = i\omega e(x, t)$. Conditions (10) become approximate boundary conditions, based on the assumption of small-amplitude oscillations, when they are applied at the mean position of the oscillating cylinder, $r = 1$ on a fixed grid, as in this analysis. By considering a truncated Taylor expansion of the fluid velocity in the vicinity of the moving cylinder, one can obtain improved boundary conditions (of second-order accuracy, ϵ^2) on the mean position of the oscillating cylinder [$\mathbf{V}_{\text{meanposition}} = \mathbf{V}_{\text{boundary}} - (ae \cdot \nabla) \mathbf{V}_{\text{boundary}}$] in the form

$$\begin{aligned} u|_{r=1} = -eU_0 \left[\frac{\partial U}{\partial r} \right]_{r=1} \cos \theta, \quad v|_{r=1} = ae \cos \theta, \\ w|_{r=1} = -ae \sin \theta, \quad (11) \end{aligned}$$

where $U_0 [\partial U / \partial r]_{r=1}$ represents the velocity gradient, at the inner wall, of the steady flow in the absence of any oscillations. In these improved boundary conditions, of second-order accuracy in ϵ^2 , only the first condition is different from the approximate one. At higher frequencies, the difference between the fluid-dynamic forces obtained with the two sets of boundary conditions (10) and (11) is rather small, both in amplitude and phase angle (at least for the examples to be discussed); hence, the numerical results given in the following sections are obtained with boundary conditions (10).

For solving this unsteady three-dimensional flow problem, the annular space (ar, θ) at any $x = \text{constant}$ plane is transformed

into a rectangular computational domain (Z, θ) , shown in Fig. 1(b), obtained by the transformation

$$Z = 1 - 2 \frac{r-1}{h}, \quad \theta = \theta, \quad \text{where } h = b - 1. \quad (12)$$

The Navier-Stokes and continuity equations are transformed accordingly. Thus, the first of the Navier-Stokes equations becomes

$$\begin{aligned} \frac{\partial u}{\partial t} + \frac{1}{a} \left[U_0 \left(U \frac{\partial u}{\partial x} - \frac{2}{h} v \frac{\partial U}{\partial Z} \right) + \frac{1}{\rho} \frac{\partial p}{\partial x} \right] \\ = \frac{\nu}{a^2} \left\{ \frac{\partial^2 u}{\partial x^2} + \frac{4}{h^2} \left[\frac{\partial^2 u}{\partial Z^2} - \sqrt{D} \frac{\partial u}{\partial Z} + D \frac{\partial^2 u}{\partial \theta^2} \right] \right\}, \\ D = \frac{h^2}{[2 + (1-Z)h]^2}, \end{aligned} \quad (13)$$

with similar expressions for the other two Navier-Stokes equations, and the continuity equation

$$\frac{\partial u}{\partial x} - \frac{2}{h} \left[\frac{\partial v}{\partial Z} - \sqrt{D} \left(v + \frac{\partial w}{\partial \theta} \right) \right] = 0. \quad (14)$$

In the computational domain, the following partial spectral expansions are considered for the unsteady pressure and velocity components:

$$\begin{aligned} u &= a\omega e^{i\omega t} \sum_{j=0}^m \mathcal{U}_j(x) T_j(Z) \cos \theta, \\ v &= a\omega e^{i\omega t} \sum_{j=0}^m \mathcal{V}_j(x) T_j(Z) \cos \theta, \end{aligned} \quad (15)$$

$$\begin{aligned} w &= a\omega e^{i\omega t} \sum_{j=0}^m \mathcal{W}_j(x) T_j(Z) \sin \theta, \\ p &= \rho a^2 \omega^2 \epsilon e^{i\omega t} \sum_{j=0}^{m-2} \mathcal{P}_j(x) T_j(Z) \cos \theta, \end{aligned} \quad (16)$$

where $T_j(Z)$ represents Chebyshev polynomials of order j and where $\mathcal{U}_j(x)$, $\mathcal{V}_j(x)$, $\mathcal{W}_j(x)$ and $\mathcal{P}_j(x)$ are unspecified functions of x . These semi-spectral expansions are used instead of the full ones, so as to avoid a substantial increase in the size of the full matrix associated with the three-dimensional spectral collocation approach, which might become nearly singular and produce numerical difficulties.

Based on the expansions (15)–(16), the Navier-Stokes and continuity equations can be expressed in the form

$$\begin{aligned} \sum_{j=0}^m \left\{ \mathcal{U}_j''(x) T_j(Z) + \frac{4}{h^2} \mathcal{U}_j(x) [T_j''(Z) - \sqrt{D} T_j'(Z) - D T_j(Z)] \right. \\ \left. - \text{Re} \left[U(Z) \mathcal{U}_j'(x) - \frac{2}{h} \mathcal{V}_j(x) U'(Z) \right] T_j(Z) \right. \\ \left. - i\beta [\mathcal{U}_j(x) - \mathcal{P}_j'(x)] T_j(Z) \right\} = 0, \end{aligned} \quad (17)$$

$$\begin{aligned} \sum_{j=0}^m \left\{ \mathcal{V}_j''(x) T_j(Z) + \frac{4}{h^2} [\mathcal{V}_j(x) (T_j''(Z) - \sqrt{D} T_j'(Z)) \right. \\ \left. - 2D(\mathcal{V}_j(x) - \mathcal{W}_j(x)) T_j(Z)] - \text{Re} U(Z) \mathcal{V}_j'(x) T_j(Z) \right\} = 0, \end{aligned} \quad (18)$$

$$\begin{aligned} - i\beta \left[\mathcal{V}_j(x) T_j(Z) + \frac{2}{h} \mathcal{P}_j(x) T_j'(Z) \right] \Big\} = 0, \quad (18) \\ \sum_{j=0}^m \left\{ \mathcal{W}_j''(x) T_j(Z) + \frac{4}{h^2} [\mathcal{W}_j(x) (T_j''(Z) - \sqrt{D} T_j'(Z)) \right. \\ \left. - 2D(\mathcal{W}_j(x) + \mathcal{V}_j(x)) T_j(Z)] - \text{Re} U(Z) \mathcal{W}_j'(x) T_j(Z) \right. \\ \left. - i\beta \left[\mathcal{W}_j(x) - \sqrt{D} \frac{2}{h} \mathcal{P}_j(x) \right] T_j(Z) \right\} = 0, \end{aligned} \quad (19)$$

$$\begin{aligned} \sum_{j=0}^m \left\{ \mathcal{P}_j''(x) T_j(Z) - \frac{2}{h} [\mathcal{P}_j(x) T_j'(Z) \right. \\ \left. - \sqrt{D} (\mathcal{V}_j(x) - \mathcal{W}_j(x)) T_j(Z)] \right\} = 0, \end{aligned} \quad (20)$$

where $\text{Re} = U_0 a / \nu$ and $\beta = \omega a^2 / \nu$ are the Reynolds number and the oscillatory Reynolds (or Stokes) number, and where $\mathcal{P}_j'(x)$ and $T_j'(Z)$ denotes the derivatives with respect to x and Z , and $U'(Z) = (-2/h)[dU/dr]_{r=1+h(1-Z)/2}$. This system of equations will be discretized using a hybrid finite difference and collocation approach in which the collocation points are defined at various radial levels Z_j , where $J \in \{1, m-1\}$.

2.2 Mixed Finite Differences for the Axial Derivatives.

In order to avoid numerical difficulties caused by a large size of fully populated matrices, encountered in a complete three-dimensional spectral collocation approach, the axial derivatives will be discretized by a finite difference approach. Hence, the physical domain is discretized into a number of grid points $P_{kj}(x_k, r_j)$, obtained at the intersection of planes of constant x_k with cylinders of constant r_j . In the computational domain, the corresponding grid points (x_k, Z_j) form a rectangular grid, where $K \in \{1, n\}$ and $J \in \{1, m-1\}$.

For axial discretization, Eqs. (17)–(20) can be expressed in the general form

$$\mathcal{F}_j''(x) - \text{Re} U(Z) \mathcal{F}_j'(x) + \mathcal{E}_j(x, Z) = 0, \quad (21)$$

where the first two terms, of interest for the axial discretization, represent the diffusion and convection terms associated to $\mathcal{F}_j(x)$, which can successively be $\mathcal{U}_j(x)$, $\mathcal{V}_j(x)$, or $\mathcal{W}_j(x)$. Equation (21) in general form, or the specific Eqs. (17)–(20), have to be discretized at the grid points x_k and Z_j .

The axial discretization of the diffusion and convection terms will be based on a mixed central-upwind finite difference scheme, similar to that introduced by Spalding (1972); hence, these terms in Eq. (21) can be discretized as

$$\begin{aligned} \mathcal{F}_j''(x_k) - \text{Re} U(Z_j) \mathcal{F}_j'(x_k) \\ = a_{K+1,J} \mathcal{F}_{j,K+1} + a_{K-1,J} \mathcal{F}_{j,K-1} - a_{K,J} \mathcal{F}_{j,K}, \end{aligned} \quad (22)$$

where

$$\begin{aligned} a_{K+1,J} &= \frac{2 - (1 + \delta) \text{Re}_{K+1,J}}{\Delta x_{K+1} (\Delta x_K + \Delta x_{K+1})}, \\ a_{K-1,J} &= \frac{2 + (1 - \delta) \text{Re}_{K,J}}{\Delta x_K (\Delta x_K + \Delta x_{K+1})}, \\ a_{K,J} &= a_{K+1,J} + a_{K-1,J}, \\ \text{Re}_{K,J} &= \frac{U_0 U(Z_j) a \Delta x_K}{\nu}, \quad \mathcal{F}_{j,K} = \mathcal{F}_j(x_k), \end{aligned} \quad (23)$$

and where $\text{Re}_{K,J}$ represents the mesh Reynolds number at the grid point (x_k, Z_j) , while δ is 0 or -1 accordingly as $\text{Re}_{K+1,J}$ is smaller or larger than 2.

When $Re_{K+1,J} < 2$, the discretizing Eq. (22) reduces, for $\delta = 0$, to a *central* differencing scheme for both the diffusion and convection terms; this type of discretization accords well with the physical phenomenon and leads to well-converged numerical solutions. However, this mesh Reynolds number requirement is often too restrictive, requiring a very fine grid with a very small axial mesh spacing, which leads to large matrices to be inverted, with negative effects on computational efficiency. This fine-mesh restriction can be relaxed by considering $Re_{K+1,J} > 2$, for which $\delta = -1$ is taken in Eq. (23), in order to prevent the coefficient $a_{K+1,J}$ becoming negative. In this case, Eq. (22) corresponds to an *upwind* differencing scheme for the convective term and *central* differences for the diffusion term; this upwind differencing introduces an artificial dissipation which stabilizes the numerical scheme for higher mesh Reynolds numbers. The mixed central-upwind differencing scheme for the axial derivatives is used in conjunction with a collocation approach in the transverse direction to solve the unsteady viscous flow problem.

2.3 Integrated Finite Difference and Collocation Method of Solution. The mixed finite difference discretization (22) for the axial derivatives and a collocation approach in the radial direction are used to discretize the Navier-Stokes and continuity equations at every grid point (x_K, Z_j) in the form

$$\sum_{j=0}^m [a_{K-1,J} u_{j,K-1} - (a_{K,J} + b_{j,J}^u) u_{j,K} + a_{K+1,J} u_{j,K+1} + c_{j,J}^u v_{j,K}] + \sum_{j=0}^{m-2} [g_{j,J,K-1}^u v_{j,K-1} + g_{j,J,K}^u v_{j,K} + g_{j,J,K+1}^u v_{j,K+1}] = 0, \quad (25)$$

$$\sum_{j=0}^m [a_{K-1,J} v_{j,K-1} - (a_{K,J} + b_{j,J}^v) v_{j,K} + a_{K+1,J} v_{j,K+1} + c_{j,J}^v w_{j,K}] + \sum_{j=0}^{m-2} g_{j,J}^v p_{j,K} = 0, \quad (26)$$

$$\sum_{j=0}^m [a_{K-1,J} w_{j,K-1} - (a_{K,J} + b_{j,J}^w) w_{j,K} + a_{K+1,J} w_{j,K+1} + c_{j,J}^w v_{j,K}] + \sum_{j=0}^{m-2} g_{j,J}^w p_{j,K} = 0, \quad (27)$$

$$\sum_{j=0}^m [d_{j,J,K-1} u_{j,K-1} + d_{j,J,K} u_{j,K} + d_{j,J,K+1} u_{j,K+1} + f_{j,J} v_{j,K} + h_{j,J} w_{j,K}] = 0, \quad (28)$$

where all the coefficients of the unknowns $u_{j,K}$, $v_{j,K}$, $w_{j,K}$, and $p_{j,K}$ are determined from Eq. (17)–(20).

The above equations are subjected to the boundary conditions imposed at the collocation points $(x_K, Z = \pm 1)$, which can be expressed in the form

$$\sum_{j=0}^m u_{j,K} T_j(Z_{fb}) = 0, \quad \sum_{j=0}^m v_{j,K} T_j(Z_{fb}) = 0, \quad \sum_{j=0}^m w_{j,K} T_j(Z_{fb}) = 0, \quad (29)$$

on the fixed parts of the inner cylinder ($Z_{fb} = 1$) and on the outer cylinder ($Z_{fb} = -1$), and

$$\sum_{j=0}^m u_{j,K} T_j(Z_{mb}) = 0, \quad \sum_{j=0}^m v_{j,K} T_j(Z_{mb}) = E(x_K), \quad \sum_{j=0}^m w_{j,K} T_j(Z_{mb}) = -E(x_K), \quad (30)$$

on the moving part of the inner ($Z_{mb} = 1$) cylinder. Equations (25)–(28) applied for $K \in \{1, N\}$ and $J \in \{1, m-1\}$ and the boundary conditions (29)–(30) applied for $K \in \{1, N\}$ together

form an algebraic system of equations, which can be expressed in matrix form as

$$\mathbf{A}\mathcal{F} = \mathcal{B}, \quad (31)$$

where $\mathcal{F} = [u_{j,K}, v_{j,K}, w_{j,K}, p_{j,K}]^T$ represents the vector of the unknown coefficients of the velocity components and unsteady pressure (with $j \in \{0, m\}$ and $K \in \{1, n\}$), \mathcal{B} is the known right-hand side of the equations (nonzero only for the boundary conditions on the oscillating cylinders), and \mathbf{A} is a block-tridiagonal matrix of the system, with the diagonals $C_2, \dots, C_K, \dots, C_n, B_1, \dots, B_K, \dots, B_n$ and $D_1, \dots, D_K, \dots, D_{n-1}$, where C_K, B_K , and D_K are submatrices of order $(4m+2)$ associated with the K th axial grid points.

In confined flows with smooth axial variation of the flow parameters, as is the case in the unsteady problem under consideration, the axial grid spacing may be taken uniformly distributed axially, i.e., $\Delta x_1 = \dots = \Delta x_K = \dots = \Delta x_n = \Delta x$; hence the submatrices simplify to $B_K = B, C_K = C$ and $D_K = D$ for all K , thus substantially reducing the storage requirements for matrix \mathbf{A} .

The numerical solution for the unknown coefficients $u_{j,K}, v_{j,K}, w_{j,K}$, and $p_{j,K}$ is obtained by using an LU decomposition technique.

3 Numerical Results for Unsteady Fluid Dynamic Forces

The unsteady fluid dynamic forces per unit length, acting on the oscillating cylinder at an axial location ax can be calculated, for small amplitude oscillations of the inner cylinder, by

$$F(x, t) = \int_0^{2\pi} a \left[\left(-p + 2 \frac{\mu}{a} \frac{\partial v}{\partial r} \right) \cos \theta - \frac{\mu}{a} \left(\frac{\partial w}{\partial r} + \frac{w}{r} + \frac{1}{r} \frac{\partial v}{\partial \theta} \right) \sin \theta + \frac{\mu}{a} \left(\frac{\partial u}{\partial r} + \frac{\partial v}{\partial x} \right) \frac{\partial e}{\partial x} \right]_{r=1} d\theta, \quad (32)$$

where the last term in the square bracket makes no contribution to the overall force.

This unsteady force can be expressed as

$$F(x, t) = \pi \rho a^3 \omega^2 \epsilon E(l/2) \hat{F}(x) \exp(i\omega t), \quad (33)$$

where the nondimensional fluid dynamic force, $\hat{F}(x)$, in complex form, is

$$\hat{F}(x) = - \sum_{j=0}^m \left\{ \varphi_j(x) + \frac{i}{\beta} \left[\mathcal{W}_j(x) - \mathcal{V}_j(x) + \frac{8}{hc_j} \sum_{q=j+1}^{m-1} q (\mathcal{V}_q(x) - \mathcal{W}_q(x)) \right] \right\}, \quad (34)$$

in which the coefficients c_j are defined as

$$c_0 = 2, \quad c_j = 1 \quad \text{for } j \geq 1. \quad (35)$$

The real and imaginary parts $\hat{F}(x)$ are proportional to the added mass and viscous damping coefficients, C_m and C_v , respectively, in phase and in quadrature with the oscillatory displacement.

Numerical computations have been performed with the hybrid method of Section 2 for oscillations following the first axial mode, $k = 1$ in Eqs. (2)–(4), considering a length-to-radius ratio $l = l^*/a = 15$, for Reynolds numbers and oscillatory Reynolds (Stokes) numbers in the range 0 to 2512 for Re , and 500 to 10000 for β .

First, computations have been performed considering $b = 1.05$, $Re = 3,000$ and $\beta = 5000$, for various values of the axial mesh spacing, $\Delta x/l$, defined for the finite difference part of the

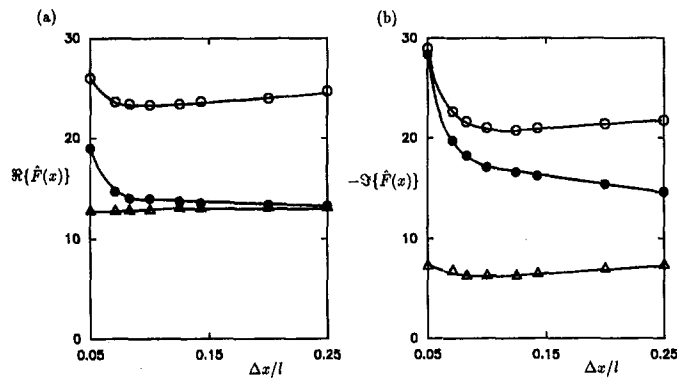


Fig. 2 Variation of (a) the real and (b) the imaginary components of the nondimensional unsteady force, $\hat{F}(x)$, with the axial mesh spacing, $\Delta x/l$, for $b = 1.05$, $l = 15$, $Re = 3000$ and $\beta = 5000$ ($m = 8$) at three axial locations: \bullet —, $x = 0.25 l$; \circ —, $x = 0.50 l$; \triangle —, $x = 0.75 l$

method. The results for $m = 8$ are shown in Fig. 2 for the real and imaginary parts of the nondimensional sectional fluid dynamic forces at several axial locations, ax . It was found that by decreasing the axial mesh spacing, Δx , the results appear to converge for a certain $\Delta x_{\text{optimum}}$, after which they start diverging with a further reduction in Δx . This type of behavior might be caused by truncation errors for coarse axial meshes and by round-off errors for very fine ones. Based on these results, a mesh spacing of $\Delta x/l = 0.1$ was selected for further calculations, which is near the average optimum value.

Typical axial variations of the real and imaginary parts of the nondimensional fluid dynamic force, $\hat{F}(x)$, calculated for $l = 15$, $b = 1.25$, and $\beta = 5000$ are shown in Fig. 3 for $Re = 0$, 1252 and 2512 (in the laminar flow regime). It is found that $\Re\{\hat{F}(x)\}$ is only slightly dependent on Re , as opposed to $\Im\{\hat{F}(x)\}$ which is strongly influenced by it; this affects not only the magnitude of $\Im\{\hat{F}(x)\}$, but also its axial variation, which changes from a symmetric one with respect to the midpoint ($x = l/2$) in the absence of axial flow ($Re = 0$), towards an antisymmetric axial variation for the higher Reynolds numbers.

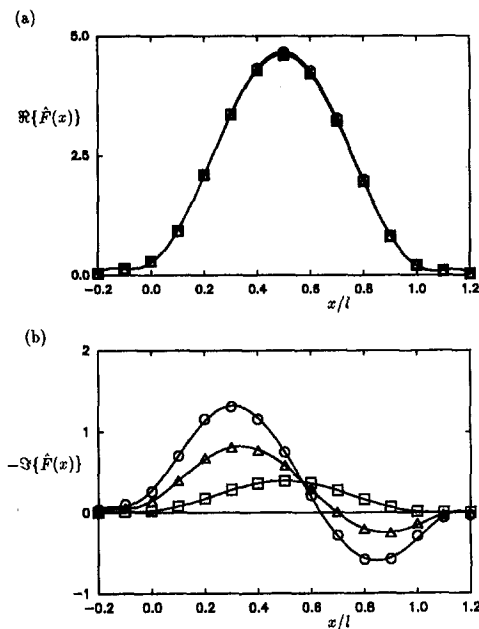


Fig. 3 Influence of the Reynolds number on the axial variation of the real and imaginary components of the nondimensional unsteady force, $\hat{F}(x)$, for $b = 1.25$, $l = 15$ and $\beta = 5000$ ($\Delta x/l = 0.1$) for three values of the Reynolds number: \square —, $Re = 0$; \triangle —, $Re = 1252$; \circ —, $Re = 2512$

The influence of the oscillatory Reynolds number, β , on the axial variations of the real and imaginary parts of $\hat{F}(x)$, is shown in Fig. 4 for $b = 1.25$, and $Re = 1252$ (computed with $\Delta x/l = 0.1$ and $m = 6$). Both the real and imaginary parts of $\hat{F}(x)$ decrease with increasing β ; this effect is much stronger for $\Im\{\hat{F}(x)\}$, which tends to become very small for the higher values of the oscillatory Reynolds number.

4 Comparison With a Semi-analytical Method of Solution

There are few theoretical solutions for three-dimensional unsteady annular viscous flows between oscillating cylinders, and they are mainly based on restrictive assumptions and simplified flow models (e.g., Mateescu and Païdoussis, 1987; Païdoussis et al., 1990). An improvement of this theoretical solution is briefly presented in this section, so as to provide a meaningful comparison for the validation of the hybrid spectral/finite difference solution of Section 2.

4.1 Spectral Solution of Unsteady Potential Flows. As shown in Mateescu and Païdoussis (1987) and Païdoussis (1990), the velocity potential, $\phi(x, r, \theta, t)$, may be expressed as

$$\phi(x, r, \theta, t) = \sum_k \hat{\phi}_k(x, r) \cos \theta e^{i\omega t} \quad (36)$$

where, by separation of variables, the reduced potentials $\hat{\phi}_k(x, r)$ may be expressed in terms of the new coordinate Z obtained by transformation (12) in the form

$$\hat{\phi}_k(x, Z) = f_k(x)F_k(Z). \quad (37)$$

Following the cited references, the reduced potentials can be separated into trigonometric ($q = 1$) and hyperbolic ($q = 2$) components (related to the eigenfunctions of the oscillating beam with fixed ends, see Eqs. (1)–(4)) in the form

$$\hat{\phi}_k(x, Z) = \sum_{q=1}^2 f_{qk}(x)F_{qk}(Z) = \hat{\phi}_{1k}(x, Z) + \hat{\phi}_{2k}(x, Z), \quad (38)$$

where, in the present spectral approach, Chebyshev expansions are used for $F_{qk}(Z)$ in the form

$$\hat{\phi}_{1k}(x, Z) = [A_1 \cos(\beta_k x) + B_1 \sin(\beta_k x)] \sum_{j=0}^m \Phi_{1kj} T_j(Z), \quad (39)$$

$$\hat{\phi}_{2k}(x, Z) = [A_2 \cosh(\beta_k x) + B_2 \sinh(\beta_k x)] \sum_{j=0}^m \Phi_{2kj} T_j(Z). \quad (40)$$

Since $\phi(x, r, \theta, t)$ satisfies the Laplace equation, the following

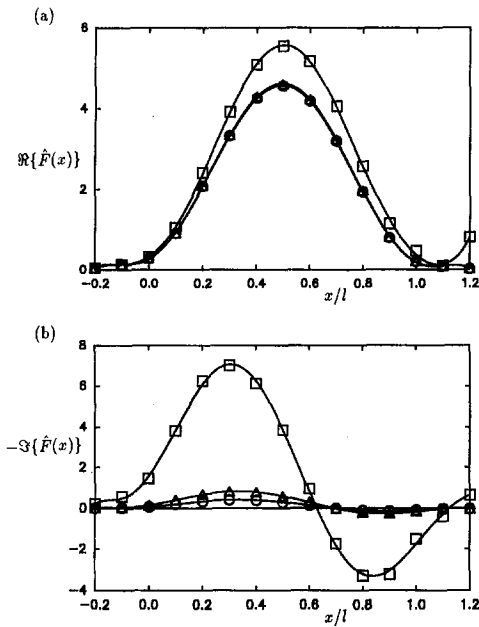


Fig. 4 Influence of the oscillatory Reynolds (or Stokes) number on the axial variation of the real and imaginary components of the nondimensional unsteady force, $\hat{F}(x)$, for $b = 1.25$, $l = 15$ and $Re = 1252$ ($\Delta x/l = 0.1$) for three values of the oscillatory Reynolds number: \square —, $\beta = 500$; \triangle —, $\beta = 5000$; \circ —, $\beta = 10,000$

equations define the trigonometric ($q = 1$) and hyperbolic ($q = 2$) components of the reduced potentials $\phi_{qk}(x, Z)$:

$$\sum_{j=0}^m \{\Phi_{qkj} T_j''(Z) - \sqrt{D} \Phi_{qkj} T_j'(Z) - [D - (-1)^q h^2 \beta_k^2 / 4] \Phi_{qkj} T_j(Z)\} = 0, \quad (41)$$

subject to the boundary conditions

$$\sum_{j=0}^m \Phi_{qkj} T_j'(1) = 1, \quad \sum_{j=0}^m \Phi_{qkj} T_j'(-1) = 0, \quad (42)$$

obtained after the determination of the constants A_q and B_q , given by

$$A_q = (-1)^q (ah/2) [-i\omega + U\sigma_k \beta_k],$$

$$B_q = (ah/2) [(-1)^q i\omega \sigma_k - U\beta_k]. \quad (43)$$

The a priori unknown coefficients Φ_{qkj} are determined from the system of equations obtained by imposing Eq. (41) at $(m - 1)$ collocation points in the radial direction and the boundary conditions (42).

The perturbation pressure in the unsteady potential flow, $p_p = P - P_\infty$, can now be determined from the Bernoulli-Lagrange equation,

$$\frac{\partial \phi}{\partial t} + U \frac{\partial \phi}{\partial x} + \frac{1}{2} (\nabla \phi)^2 + p_p = 0. \quad (44)$$

4.2 Semi-analytical Solution Based on an Approximate Viscous Flow Solution. As shown in Mateescu and Païdoussis (1987), the perturbation pressure for small amplitude oscillations may be expressed as

$$P - P_\infty = p(x, r, \theta, t) = p_v(x, r; \theta, t) + p_p(x, r, \theta, t), \quad (45)$$

where $p_p(x, r, \theta, t)$ is the potential component of the perturbation pressure, calculated as shown in Section 4.1, and $p_v(x, r; \theta, t)$ represents the remainder of the perturbation pressure, associated with viscous effects in a real flow. This remainder pressure and the associated remainder flow-field (u_v, v_v, w_v) are calculated as shown in the cited references—not presented here for brevity. The main difference is that the approximate viscous solution as determined here is based on the exact spectral solution of the unsteady potential flow instead of an approximate potential solution as before.

The unsteady fluid dynamic forces are then determined by integrating the unsteady pressure and the circumferential shear stress acting on the oscillating cylinder.

4.3 Numerical Results and Comparisons. The semi-analytical solutions for the nondimensional forces, $\Re\{\hat{F}(x)\}$ and $\Im\{\hat{F}(x)\}$, are compared first in Fig. 5(a) with the previous solutions based on the method formulated by Mateescu and Païdoussis (1987) and Païdoussis et al. (1990). These results for $l = 15$, $b = 1.1$, $Re = 2000$, and $\beta = 5000$ ($m = 6$), are in reasonably close agreement.

A comparison is shown then in Fig. 5(b) between the semi-analytical solutions and the results obtained with the hybrid

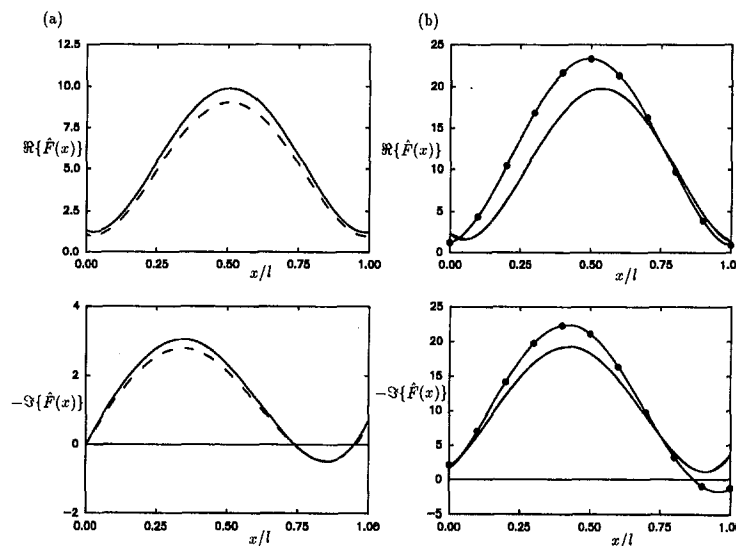


Fig. 5 Axial variations of the real and imaginary components of the nondimensional unsteady force, $\hat{F}(x)$, for $l = 15$, and $\beta = 5000$. (a) Comparison between semi-analytical method (—), and previous analytical results (---) for $b = 1.1$ and $Re = 2000$; (b) Comparison between hybrid spectral method (—●—) and semi-analytical method (—), for $b = 1.05$ and $Re = 3000$.

spectral/finite difference method formulated in Section 2. These results for $l = 15$, $Re = 3000$, $\beta = 5000$, and $b = 1.05$ are compared to the semi-analytical solution being derived for smaller, rather than larger, outer-to-inner radius ratio, b , while the hybrid spectral method has no restrictions in this respect. Reasonably good agreement is found between the two sets of results.

5 Conclusions

A hybrid spectral/finite difference method is developed in this paper for the analysis of three-dimensional unsteady viscous flows between concentric cylinders subjected to a fully developed laminar flow, and generated by axially variable oscillations of the central portion of one of the cylinders. This method uses a partial spectral collocation approach, based on spectral expansions of the unsteady pressure and velocity components in the transverse coordinates and time, in conjunction with a finite-difference approach for the discretization of the axial derivatives. The spectral expansions use Chebyshev polynomials for the radial direction in a computational domain obtained by a coordinate transformation.

A mixed-type finite difference scheme is used for the convective and diffusion axial derivatives. This mixed scheme uses central differences for the diffusion derivatives, but switches from central to upwind differencing for the convective derivatives as the axial mesh Reynolds number is increased. This enhances computational efficiency, by permitting the use of coarser, as well as finer, axial mesh spacings.

The hybrid spectral/finite-difference method efficiently reduces the unsteady problem to the inversion of a block-tridiagonal matrix, avoiding the numerical difficulties and instabilities otherwise encountered in the inversion of a fully populated and possibly ill-conditioned matrix in the case of a fully fledged three-dimensional spectral-collocation approach. A numerical investigation has been conducted to determine an optimum value for the axial mesh spacing, which was then used in subsequent computations.

This hybrid spectral method was used to compute the unsteady fluid dynamic forces acting on the oscillating cylinder, by integrating circumferentially the unsteady pressure and shear stresses; the real and imaginary parts of these forces are related to the added-mass and viscous-damping coefficients, which are required in the study of the dynamics and flow-induced vibrations and instabilities in such systems. The influence of the Reynolds number and of the oscillatory Reynolds (or Stokes) number on the axial variation of the real and imaginary parts of the unsteady forces has been thoroughly investigated in the range of laminar flows.

Finally, a semi-analytical method, representing an improvement over an earlier analytical method (Mateescu and Paï-

doussis, 1987), has also been developed for the validation of the hybrid spectral method. Good agreement has been found between the hybrid spectral method and the semi-analytical method within the domain of applicability of the latter.

References

- Au-Yang, M. K., 1976, "Free Vibration of Fluid-Coupled Coaxial Cylindrical Shells of Different Lengths," *ASME JOURNAL OF APPLIED MECHANICS*, Vol. 43, pp. 480–484.
- Au-Yang, M. K., and Galford, J. E., 1981, "A Structural Priority Approach to Fluid-Structure Interaction Problems," *ASME Journal of Pressure Vessel Technology*, Vol. 103, pp. 142–150.
- Brenneman, B., and Au-Yang, M. K., 1992, "Fluid-Structure Dynamics with a Modal Hybrid Method," *ASME Journal Pressure Vessel Technology*, Vol. 114, pp. 133–138.
- Chen, S. S., Wambsganss, M. W., and Jendrzejczyk, J. A., 1976, "Added Mass and Damping of a Vibrating Rod in Confined Viscous Fluid," *ASME JOURNAL OF APPLIED MECHANICS*, Vol. 43, pp. 325–329.
- Chen, S. S., 1981, "Fluid Damping for Circular Cylindrical Structures," *Nuclear Engineering and Design*, Vol. 63, pp. 81–100.
- Hobson, D. E., 1982, "Fluid-Elastic Instabilities Caused by Flow in an Annulus," *Proceedings of the BNES Third International Conference on Vibration in Nuclear Plant*, Keswick, U.K., pp. 440–463.
- Mateescu, D., and Païdoussis, M. P., 1985, "The Unsteady Potential Flow in an Axially Variable Annulus and its Effects on the Dynamics of the Oscillating Rigid Centreboddy," *ASME Journal of Fluids Engineering*, Vol. 107, pp. 421–427.
- Mateescu, D., and Païdoussis, M. P., 1987, "Unsteady Viscous Effects on the Annular-Flow-Induced Instabilities of a Rigid Cylindrical Body in a Narrow Duct," *Journal of Fluids and Structures*, Vol. 1, pp. 197–215.
- Mateescu, D., Païdoussis, M. P., and Bélanger, F., 1988, "Unsteady Pressure Measurements on an Oscillating Cylinder in Narrow Annular Flow," *Journal of Fluids and Structures*, Vol. 2, pp. 615–628.
- Mateescu, D., Païdoussis, M. P., and Bélanger, F., 1989, "A Theoretical Model Compared with Experiments for the Unsteady Pressure on a Cylinder Oscillating in a Turbulent Annular Flow," *Journal of Sound and Vibration*, Vol. 135, pp. 487–498.
- Mateescu, D., Païdoussis, M. P., and Sim, W.-G., 1990, "CFD Solutions for Steady Viscous and Unsteady Potential Flows Between Eccentric Cylinders," *Proceedings of the ASME International Symposium on Nonsteady Fluid Dynamics*, Toronto, FED-Vol. 92, pp. 235–242.
- Mateescu, D., Païdoussis, M. P., and Bélanger, F., 1991, "Computational Solutions Based on a Finite Difference Formulation for Unsteady Internal Flows," 29th Aerospace Sciences Meeting, Reno, Nevada, AIAA Paper 91-0724.
- Mateescu, D., Païdoussis, M. P., and Sim, W.-G., 1994a, "A Spectral Collocation Method for Confined Unsteady Flows with Oscillating Boundaries," *Journal of Fluids and Structures*, Vol. 8, pp. 157–181.
- Mateescu, D., Païdoussis, M. P., and Bélanger, F., 1994b, "A Time-Integration Method Using Artificial Compressibility for Unsteady Viscous Flows," *Journal of Sound and Vibration*, Vol. 117, pp. 197–203.
- Mateescu, D., Païdoussis, M. P., and Sim, W.-G., 1994c, "Spectral Solutions for Unsteady Annular Flows Between Eccentric Cylinders Induced by Transverse Oscillations," *Journal of Sound and Vibration*, Vol. 117, pp. 635–649.
- Mulcahy, T. M., 1980, "Fluid Forces on Rods Vibrating in Finite Length Annular Regions," *ASME JOURNAL OF APPLIED MECHANICS*, Vol. 47, pp. 234–240.
- Païdoussis, M. P., Mateescu, D., and Sim, W.-G., 1990, "Dynamics and Stability of a Flexible Cylinder in a Narrow Coaxial Cylindrical Duct Subjected to Annular Flow," *ASME JOURNAL OF APPLIED MECHANICS*, Vol. 57, pp. 232–240.
- Spalding, D. B., 1972, "A Novel Finite Difference Formulation for Differential Expressions Involving both First and Second Derivatives," *International Journal for Numerical Methods in Engineering*, Vol. 4, pp. 551–559.

Thermohydrodynamic Analysis of Process-Liquid Hydrostatic Journal Bearings in Turbulent Regime, Part I: The Model and Perturbation Analysis

Zhou Yang

Cummings Engine Company, Inc.
Columbus, IN 47201
Assoc. Mem. ASME

L. San Andres

Assoc. Mem. ASME.

D. W. Childs

Fellow ASME.

Mechanical Engineering Department,
Texas A&M University,
College Station, TX 77843

A bulk-flow thermohydrodynamic (THD) analysis is developed for prediction of the static and dynamic performance characteristics of turbulent-flow, process-liquid, hydrostatic journal bearings (HJBs). Pointwise evaluation of temperature and hence liquid properties is achieved through the solution of the energy equation in the fluid film with insulated boundaries, and justified for fluid film bearings with external pressurization. Fluid inertia within the film lands and at recess edges is preserved in the analysis. Flow turbulence is accounted through turbulence shear parameters based on friction factors derived from Moody's formulae. The effects of fluid compressibility and temperature variation in the bearing recesses are included. Numerical solution and results are presented in the second part of this work and compared with some limited experimental data for a liquid hydrogen (LH₂) bearing.

1 Introduction

There is an increasing interest in the use of process liquid, fluid film bearings in high-performance turbomachinery. Hydrostatic journal bearings (HJBs) are now being used in liquefied natural gas (LNG) pumps, where the working fluid on the bearings is the LNG delivered from the pump, and consequently, overhaul intervals are extended to several times those of LNG pumps supported on conventional ball bearings (Katayama and Okada, 1992). HJBs have also been selected as support elements in future cryogenic high-speed turbomachinery such as the High Pressure Fuel Turbopump (HPFTP) and the High Pressure Oxygen Turbopump (HPOTP) of the Space Shuttle Main Engine (SSME). HJBs, unlike rolling-element bearings, have no apparent DN limit (bore diameter in mm multiplied by journal speed in rpm); therefore, shaft speeds can be allowed to increase to a level more suitable for high operating efficiency with a reduced machinery size and weight. This bearing type has other advantages over conventional rolling-element bearings, such as high radial stiffness, accuracy of positioning, good vibration-damping characteristics, low starting torque, and extremely long life.

Despite their attractive features, HJBs operating at high speeds and with cryogenic liquids are yet not fully understood. The thermophysical properties of cryogenic liquids are strongly dependent on their local state of pressure and temperature. Although process liquids (like LH₂) offer very small viscosities, the trends toward higher rotational speeds and larger pressure differentials, as well as the implementation of intentionally roughened surfaces to improve bearing dynamic stability (Von Pragenau, 1990), provide unique flow characteristics and operating conditions where high levels of turbulence (energy dissipation) may yield

significant thermal effects. Viscous dissipation due to shear motion and pressure extrusion, and heat transfer from or to bearing surfaces can generate significant temperature and viscosity variations within the fluid film and affect pronouncedly the bearing static and dynamic force characteristics. Prediction of bearing performance is then no longer meaningful when based on an isothermal or isoviscous assumption.

Prediction of HJB performance has been commonly based on analysis of the isothermal form of the Reynolds equation (or the Bulk-Flow equations) due to the following considerations. First, conventional HJBs operate at low journal speeds and in the laminar flow regime with low heat generation and hence small temperature variations in the fluid film. Second, the flow of fresh fluid into the film region causes thermal effects in HJBs to be less severe than in hydrodynamic bearings where hot lubricants recirculate in the fluid film region. Third, including thermal effects in HJB analysis greatly increases the analytical complexity. Pointwise evaluation of temperature and viscosity in the fluid film (the thermohydrodynamic or THD theory) requires the solution of the energy equation. The boundary temperatures in the fluid film region are related to the thermal transport in the journal and bearing solids. The coupling of the heat conduction equations in the solids with the governing equations in the fluid film leads to a trial-and-error solution of the liquid/solid interface boundary temperatures. Such a nonlinear iterative problem is costly and may be very sensitive and prone to numerical instabilities.

Reddecliff and Vohr (1969) initially studied HJBs for use in high-pressure cryogenic rocket engine turbopumps. In their analysis, the turbulent model provided by Elrod and Ng (1967) was introduced into the Reynolds equation. The inertia effects at the edges of the recesses were found to change the pressure distribution, which reduced the flow rate but did not affect the total bearing load capacity. The nonlinear fluid advective inertial terms could not be accounted for due to numerical difficulties. Variable fluid properties were treated as linear between those at the supply and discharge pressures, and steady-state predictions were reported to agree well with experimental results. The scatter in the measured recess pressures was attributed to measure-

Contributed by the Applied Mechanics Division of THE AMERICAN SOCIETY OF MECHANICAL ENGINEERS for publication in the ASME JOURNAL OF APPLIED MECHANICS.

Discussion on this paper should be addressed to the Technical Editor, Prof. Lewis T. Wheeler, Department of Mechanical Engineering, University of Houston, Houston, TX 77204-4792, and will be accepted until four months after final publication of the paper itself in the ASME JOURNAL OF APPLIED MECHANICS.

Manuscript received by the ASME Applied Mechanics Division, Feb. 11, 1993; final revision, Apr. 4, 1994. Associate Technical Editor: S. A. Berger.

ment inaccuracies and to variations in bearing clearance caused by temperature differences between the bearing and shaft.

Artiles et al. (1982) presented a numerical solution to the static and dynamic performance characteristics of hydrostatic journal bearings. A turbulent Reynolds equation with constant fluid properties was solved by the column-matrix method, while a Newton-Raphson scheme was implemented for efficient calculation of the recess pressures. Turbulent-to-laminar flow power-loss ratios were reported to be in the range of 25 to 30 for the Reynolds numbers considered. Even though there were neither energy considerations nor thermal effects in the analysis, large temperature rises (up to 24.5°C) in the fluid film were reported for LO₂ bearings, while temperature rises in LH₂ bearings were negligibly small.

Braun et al. (1987) introduced a comprehensive THD analysis for a two-row recess LH₂ hydrostatic journal bearings. On the fluid film region, a variable-properties Reynolds equation was coupled to a two-dimensional energy transport equation. The heat transfer to the bounding solids (shaft and bush) was analyzed in its three-dimensional complexity. Bulk-flow heat-transfer coefficients were used to represent the boundary conditions at the fluid/solid interfaces, and fluid inertia effects were considered only at the pocket's edges with no recess volume-liquid compressibility effects. Braun et al.'s analysis regarded the fluid flow as laminar, although large pressure differentials and rotational speeds were considered in the applications studied. A small temperature increment was found in the fluid film, and thermal effects were shown to be minimal relative to a constant properties liquid model. No conclusions were made as to the effects of heat transfer from the fluid film to the bounding solids. The numerical predictions presented show circumferential flow Reynolds numbers as large as 100,000 with a laminar flow model.

San Andres (1990a, b) introduced a turbulent bulk-flow analysis for prediction of the performance characteristics of orifice-compensated HJBs. Here bulk-flow equations with fluid inertia replace the conventional Reynolds equation, and include recess volume-fluid compressibility effects known to deteriorate the bearing stability characteristics due to pneumatic hammer (San Andres, 1991a). For example, the whirl frequency ratio, an indicator of bearing stability, is predicted to be larger than 0.5 for nonzero recess-fluid compressibility. San Andres (1992a) extended his incompressible liquid model to a barotropic fluid model for analysis of cryogenic liquid HJBs. The variable fluid properties are considered to depend on the local pressure and a mean operating (uniform) temperature. The barotropic label applies to the fluid and not to the complex flow process in the fluid film bearing. Numerical results show the effects of variable properties to be significant for a LH₂ (highly compressible) hydrostatic bearing, but show no significant difference between the two models for a LO₂ bearing.

Yang et al. (1993a) developed a thermohydrodynamic model for analysis of turbulent flow annular seals with process liquids and gases. Fluid inertia, flow turbulence, and actual fluid properties for cryogenics are all considered. Numerical results show that large temperature rises occur in LO₂ seals with significant effects on the fluid properties and the onset of two-phase flow conditions at relatively small values of rotor eccentricity. Seal leakage and torque are lower than those from an isothermal solution (San Andres, 1991b). A difference up to 20 percent was found for the predicted direct stiffness coefficients. The analysis has been shown to correlate well with experimental data and successfully used in the industrial design of annular damping seals (Scharrer et al., 1992a, b).

Heat transfer from fluid film to the bounding surfaces of a cryogenic turbulent-flow annular seal has been studied both analytically and numerically (Yang et al., 1993b). In the full numerical THD analysis, the fluid flow equations in the film are treated by the finite difference method (FDM) while the three-dimensional heat conduction equation in the seal stator is

solved by the boundary element method (BEM). The numerical example of a LO₂ seal shows that there is substantially no difference in the predictions from the full THD analysis and the adiabatic flow approximation. The heat generated in the fluid is carried away mainly by fluid advection due to the large flow rate produced by the imposed high axial pressure gradient in the seal. Heat transfer from the fluid film to the stator (or shaft) is found to be negligible and adiabatic bounding surfaces are shown to be a good assumption for externally pressurized turbulent flows in cryogenic liquid seals.

The unique flow characteristics of cryogenic liquid HJBs determine that fluid inertia, flow turbulence, actual fluid properties, and thermal effects are important for the accurate prediction of the static and dynamic performance characteristics of the bearings. The static characteristics include the film pressure, fluid velocity and temperature fields, mass flow rate, fluid-film forces or bearing load capacity, friction torque, and power dissipation. The dynamic force characteristics refer to the stiffness (K), damping (C), and added mass (M) coefficients required for rotordynamic analysis. These coefficients are defined by the following expression for the bearing forces:

$$\begin{bmatrix} F_x \\ F_y \end{bmatrix} = \begin{bmatrix} F_{x0} \\ F_{y0} \end{bmatrix} - \begin{bmatrix} K_{xx} & K_{xy} \\ K_{yx} & K_{yy} \end{bmatrix} \begin{bmatrix} \Delta X \\ \Delta Y \end{bmatrix} - \begin{bmatrix} C_{xx} & C_{xy} \\ C_{yx} & C_{yy} \end{bmatrix} \begin{bmatrix} \Delta \dot{X} \\ \Delta \dot{Y} \end{bmatrix} - \begin{bmatrix} M_{xx} & M_{xy} \\ M_{yx} & M_{yy} \end{bmatrix} \begin{bmatrix} \Delta \ddot{X} \\ \Delta \ddot{Y} \end{bmatrix}, \quad (1)$$

where (F_{x0} , F_{y0}) are the static fluid film forces at the journal equilibrium position (e_{x0} , e_{y0}); and $\Delta X = \Delta e_x e^{i\tau}$ and $\Delta Y = \Delta e_y e^{i\tau}$ are the components of the journal-center dynamic displacement. The dynamic-force coefficients defined by Eq. (1) are important measures of dynamic bearing force performance since they influence the critical speeds, resonant amplitude response, and rotordynamic stability of a rotor-bearing system.

A bulk-flow thermohydrodynamic (THD) analysis is introduced to determine the static and dynamic performance characteristics for turbulent flow process liquid HJBs. Pointwise evaluation of temperature and hence liquid properties is achieved through the solution of the energy equation in the fluid film with adiabatic journal and bearing surfaces. Flow turbulence is accounted through turbulence shear parameters based on friction factors derived from Moody's formulae. Fluid inertia on film lands and at recess edges are preserved. The effects of fluid compressibility and temperature variation in the recess are included. Cryogenic fluid properties are calculated from standard 32-term state equations (McCarty, 1986).

2 Mathematical Model

The general type of bearing selected as a support element for cryogenic liquid turbopumps is a 360-deg hydrostatic journal bearing, orifice-compensated, with a variable number of feeding recesses or pockets machined in the surface of the bearing (Butner and Murphy, 1986). The flow is confined to the thin annular region between an inner journal of radius (R) rotating at an angular speed (Ω) and a stationary bushing (Fig. 1). The fluid flow is characterized by high levels of turbulence due to the externally imposed large axial pressure drop across the bearing and/or the high journal surface speed.

The problem of calculating the flow and load performance characteristics of HJBs consists basically of determining the pressure, temperature, and flow distribution in the bearing film lands subject to the condition that the flow discharging from each recess through the bearing film lands must equal the flow entering that recess from the supply source through a fixed orifice restrictor.

2.1 Governing Equations for Turbulent Fluid Film Flows. Large pressure gradients typical in low viscosity fluid HJBs cause high axial turbulent flow Reynolds numbers, and the

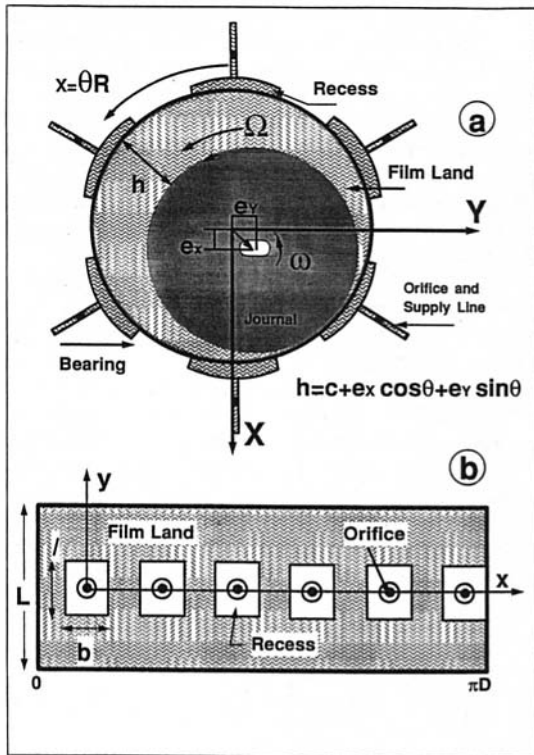


Fig. 1 Geometry of a hydrostatic journal bearing; (a) axial view and coordinate systems, (b) unwrapped bearing surface

effect of turbulent mixing far outweighs molecular diffusivity. In consequence, the temperature rise produced by viscous dissipation tends to be distributed uniformly across the film thickness; hence, temperature gradients in the cross-film coordinate (z) are confined to turbulent flow boundary layers adjacent to the bounding (bearing and journal) surfaces (Suganami and Szeri, 1979; Di Pasquantonio and Sala, 1984). Furthermore, in the absence of regions of reversed flow or recirculation, the fluid velocity field presents the same characteristics as discussed above.

These considerations allow the three-dimensional continuity, momentum, and energy equations to be integrated across the film thickness to determine the two-dimensional bulk-flow governing equations for thin fluid film flows (Yang et al., 1993a):

Continuity Equation.

$$\frac{\partial(\rho H)}{\partial t} + \frac{\partial(\rho H U)}{\partial x} + \frac{\partial(\rho H V)}{\partial y} = 0 \quad (2)$$

Circumferential-Momentum Equation.

$$\frac{\partial(\rho H U)}{\partial t} + \frac{\partial(\rho H U^2)}{\partial x} + \frac{\partial(\rho H U V)}{\partial y} = -H \frac{\partial P}{\partial x} + \tau_{xz}|_0^H \quad (3)$$

Axial-Momentum Equation.

$$\frac{\partial(\rho H V)}{\partial t} + \frac{\partial(\rho H U V)}{\partial x} + \frac{\partial(\rho H V^2)}{\partial y} = -H \frac{\partial P}{\partial y} + \tau_{yz}|_0^H \quad (4)$$

Energy-Transport Equation.

$$C_p \left[\frac{\partial(\rho H T)}{\partial t} + \frac{\partial(\rho H U T)}{\partial x} + \frac{\partial(\rho H V T)}{\partial y} \right] + Q_s = T \beta_t H \left(\frac{\partial P}{\partial t} + U \frac{\partial P}{\partial x} + V \frac{\partial P}{\partial y} \right) + R \Omega \tau_{xz}|_0^H - U \tau_{xz}|_0^H - V \tau_{yz}|_0^H \quad (5)$$

where the circumferential and axial coordinates are denoted by (x) and (y). The bulk-flow primitive variables, velocities (U , V), pressure (P), and temperature (T), are defined as average quantities across the film thickness (H). The density (ρ), viscosity (μ), specific heat (C_p), and volumetric expansion coefficient (β_t) represent the material fluid properties. Q_s denotes the heat flux from the fluid film to the bounding solids.

The wall shear stress differences (τ) in the circumferential and axial directions are based on the bulk-flow turbulence theory in thin film flows (Hirs, 1973; Launder and Leschziner, 1978):

$$\tau_{xz}|_0^H = -\frac{\mu}{H} \left(k_x U - k_j \frac{R \Omega}{2} \right);$$

$$\tau_{yz}|_0^H = -\frac{\mu}{H} (k_y V);$$

$$\tau_{xz}|_0^H = \frac{H}{2} \frac{\partial P}{\partial x} + \frac{\mu}{4H} [U k_B - (U - R \Omega) k_j] \quad (6)$$

where the turbulent shear parameters (k_x , k_y) and (k_j , k_B) are local functions of the Reynolds numbers and friction factors based on Moody's formulae (Massey, 1983; Nelson et al., 1987). The present turbulence model is selected due to its simplicity and ability to represent surface roughness conditions.

The variation of temperature in the axial direction and the energy generated by compression work are retained in the analysis due to the strong influence of the large pressure drop across the bearing. These conditions differentiate the present problem from conventional THD analyses of viscous, incompressible fluids in hydrodynamic journal bearings.

2.2 Governing Equations for Bearing Recess Flows.

The analysis of turbulent flow in a HJB recess is complicated and not yet fully understood. To date, only two-dimensional laminar flow numerical solutions are available for rectangular recesses (see, for example, San Andres and Velthuis, 1992b; Braun et al., 1993). While the actual prediction of flow fields in the recess may give a better description of the recess-edge boundary conditions, the global mass and energy conservation principles at the recess are known to be both efficient and sufficiently accurate in hydrostatic bearings with radial ports (San Andres, 1992a).

Mass Conservation at a Recess. The continuity equation at the recess is defined by the global balance between the flow through the orifice restrictor of effective area (A_0), the recess outflow into the film lands (\dot{M}_r), and the temporal change of fluid mass within the recess volume (∇_r). The fluid external supply pressure is P_s and drops to a value P_r at the recesses. The flow continuity equation at each bearing recess is expressed as

$$A_0 \sqrt{2\rho_r (P_s - P_r)} = \dot{M}_r + \rho_r \frac{\partial \nabla_r}{\partial t} + \rho_r \nabla_r \left(\beta_p \frac{\partial P}{\partial t} - \beta_t \frac{\partial T}{\partial t} \right) \quad (7)$$

where

$$\beta_p = \frac{1}{\rho} \left(\frac{\partial \rho}{\partial P} \right)_T, \quad \beta_t = -\frac{1}{\rho} \left(\frac{\partial \rho}{\partial T} \right)_P \quad (8)$$

are the liquid compressibility factor and volumetric expansion coefficient, respectively, and

$$\dot{M}_r = \int_{\Gamma_r} \rho H (\tilde{U} \cdot \tilde{n}) d\Gamma \quad (9)$$

is the mass flow rate across the recess boundary (Γ_r) into the film lands.

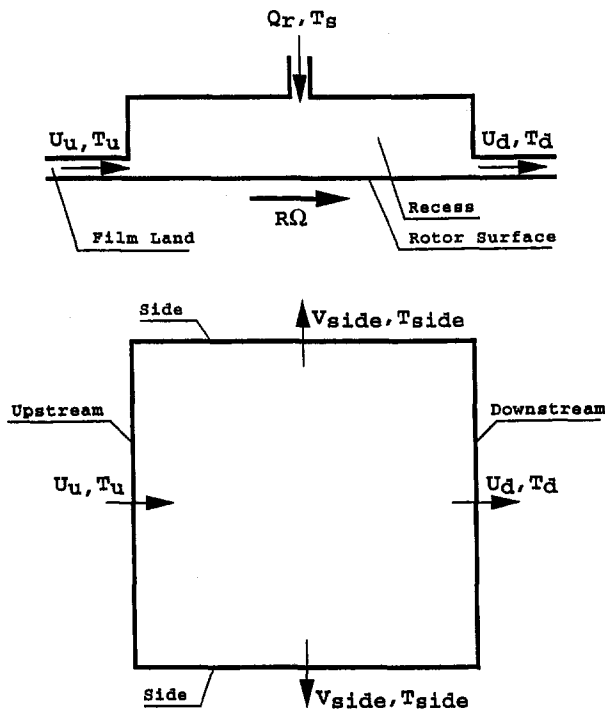


Fig. 2 Conceptual description of global energy balance at a recess

Global Energy Balance Equation at a Recess. The energy-transport phenomenon in a HJB recess is controlled by the following three mechanisms: the carryover of hot fluid from upstream to downstream of the recess, the mixing of cool fluid from the supply source into the recess volume, and the heat generation in the recess volume due to shear dissipation by journal rotation. Energy transport produced by pressure gradients, kinetic energy changes, and heat conduction are negligible due to the uniform recess pressure and the large mass flow rate through the recess. Based on these considerations, a global energy balance equation at the recess is derived, reflecting the heat carryover and mixing effects, and the friction heat generation (dissipation) in the recess (Fig. 2):

$$C_p \frac{\partial(\rho_r T_r)}{\partial t} \nabla_r + C_p (\sum \dot{m}_d T_d + 2 \sum \dot{m}_{side} T_{side}) = C_p (\sum \dot{m}_u T_u + \dot{M}_r T_s) + T_{or} \Omega \quad (10)$$

where

$$T_{or} = \tau_{xz}^H A_r R \quad (11)$$

is the drag torque on the recess area, \dot{M}_r is the total mass flow rate through the supply orifice, ∇_r is the recess volume, and the subscripts "u," "d" and "side" refer to the upstream, downstream, and side edges of a rectangular recess, respectively. The temperatures at the downstream and side edges of the recess are approximately equal to the recess temperature since liquid flows from the orifice to the sides at a large velocity:

$$T_d = T_{side} = T_r = \text{Constant}, \quad (12)$$

while the temperature at the upstream of the recess is given by

$$T_u = \begin{cases} T_r, & \text{if } (\vec{U} \cdot \vec{n}) > 0; \\ \text{Upstream values,} & \text{otherwise.} \end{cases} \quad (13)$$

Recess/Film Entrance Pressure Rise/Drop. For purely hydrostatic operation, a uniform pressure in the recess volume is achieved by deepening the recesses. However, a minimum re-

cess volume is required to avoid a typical pneumatic hammer instability associated to compressible fluids. Design criteria for uniformity of recess pressure and pneumatic hammer instability are given by Redecliff and Vohr (1969) and San Andres (1991a).

For hybrid operation, a pressure rise is produced in the downstream portion of the recess due to the journal rotation (Chaomleffel and Nicholas, 1986). San Andres (1992a) considers this region as a one-dimensional step bearing and adopted Constantinescu et al.'s (1975) model to evaluate the pressure rise just in front of the downstream recess edge. The local acceleration of fluid from the deep recess to the thin film lands causes a sudden pressure drop at the recess edge. The pressure drop at the entrance to the film lands is then modeled by a simple Bernoulli-type relation. Details of the recess-edge pressure equations can be found in the analyses of Artiles et al. (1982) and San Andres (1992a) for incompressible and compressible fluids, respectively.

3 Boundary Conditions

The boundary conditions for the flow variables are expressed as

(a) On the 360-degree extended film land, the pressure, velocity, and temperature fields are continuous and single-valued in the circumferential (x) direction.

(b) At the bearing exit plane ($y = L$), the fluid pressure takes a constant value equal to the discharge or ambient pressure (P_d) for unchoked conditions. The present analysis is limited to subsonic flow conditions over the lands of the HJB.

(c) The axial velocity (V) and the axial gradients (d/dy) of all the flow variables are null at the circumferential center line ($y = 0$) of the bearing if this is axially symmetric and has no journal misalignment. This allows solution of the flow field on only half the bearing. The nonsymmetric bearing case with journal misalignment requires solution over the whole bearing plane.

(d) The recess-edge temperatures and pressures are obtained as described in the previous sections. The velocity vector at the interface with the recess boundary is regarded as normal to the recess edges (Artiles et al., 1982).

(e) At the fluid/journal and the fluid/bearing interfaces, the heat flux to the bounding surfaces Q_s is assumed to be zero. This oversimplification is fully justified by the analysis of Yang et al. (1993b), where the heat transfer from fluid film to the bounding surfaces of a cryogenic turbulent flow annular seal is studied. The numerical example of a LO₂ seal (high temperature rise in the fluid film) shows that there is substantially no difference in the predictions from the full THD analysis and the adiabatic flow approximation. The heat generated in the fluid is carried away mainly by the axial fluid velocity (large flow rate) produced by the imposed high pressure gradient. This assertion also applies to the fluid flow in HJBs due to the similarity in geometry and operating environment.

4 Perturbation Analysis

The inertial coordinate system $\{X, Y\}$ shown in Fig. 1 helps to define the position of the rotating journal. For steady-state operating conditions, the journal center is at the equilibrium position (e_{x0}, e_{y0}), and, superimposed on this, the journal describes motions of small amplitude Δe_x and Δe_y and whirl frequency ω . The film thickness is represented by the real part of the following equation:

$$H = H_0 + e^{i\tau} (\Delta e_x h_x + \Delta e_y h_y) \quad (14)$$

where

$$H_0 = H_0^* + e_{x0} h_x + e_{y0} h_y, \quad \tau = \omega t, \quad \mathbf{i} = \sqrt{-1}, \quad (15)$$

$$h_x = \cos \theta, \quad h_y = \sin \theta, \quad (16)$$

and $H_0^* = c + e_x \cos \theta + e_y \sin \theta$ for uniform radial clearance or, $H_0^* = c(\theta, y)$ is a general function of the axial coordinate for nonuniform clearance bearings (San Andres, 1991b).

For small amplitude motions of the journal, all the bulk-flow variables (P, U, V, T) as well as the fluid properties (ρ, μ, β, C_p) are expressed as the superposition of zeroth and first-order fields representing the steady-state and dynamic motion conditions, respectively. In general,

$$\phi = \phi_0 + e^{i\tau}(\Delta e_x \phi_x + \Delta e_y \phi_y),$$

$$\phi = U, V, P, T, \rho, \mu, \beta, k_x, k_y, \dots, \text{etc.} \quad (17)$$

Substitution of the perturbation variables into the dimensionless governing equations yields the zeroth and first-order flow equations which are omitted here for brevity. A complete description of the analysis is given by San Andres (1993). The bearing static and dynamic force characteristics are evaluated once a solution to the flow equations is obtained. Fluid film forces are calculated by integration of the pressure field over the journal surface. The components of the static equilibrium force are given by

$$F_{i0} = \int_0^L \int_0^{2\pi} P_0 h_i R d\theta dy \quad i = X, Y. \quad (18)$$

The Taylor series expansion of the dynamic forces (Eq. (1)) allows the dynamic force coefficients to be calculated from integration of the first-order complex pressure field (P_j) over the journal surface,

$$K_{ij} - \omega^2 M_{ij} + i\omega C_{ij} = - \int_0^L \int_0^{2\pi} P_j h_i R d\theta dy; \quad i, j = X, Y. \quad (19)$$

From the above equation, the first-order equations need to be solved for at least two different frequencies to obtain the added mass coefficients.

The friction torque is given by integration of the wall shear stress at the journal surface as

$$T_{or} = \int_0^L \int_0^{2\pi R} \tau_{xz}^H dx dy \quad (20)$$

where the wall shear stress at the journal surface τ_{xz}^H is determined from the bulk-flow velocities as given by the third expression on Eq. (6).

5 Summary of the Analysis

The unique flow characteristics of cryogenic liquid bearings determine fluid inertia, flow turbulence, actual fluid properties and thermal effects to be important for the accurate prediction of bearing performance. A bulk-flow thermohydrodynamic (THD) analysis for determination of the static and dynamic performance characteristics of orifice-compensated liquid hydrogen (LH₂) HJBs in the turbulent flow regime is introduced. Turbulence shear parameters in the momentum and energy transport equations are determined in terms of the bulk-flow velocities and friction factors derived from Moody's formula. Pointwise evaluation of temperature and hence liquid properties is achieved through the solution of the energy equation in the fluid film with insulated bounding surfaces. This simplification is justified for cryogenic liquid bearings with large pressure gradients.

Equations for global mass conservation and energy transport are presented at the bearing recesses. Effects of fluid compressibility at the recess volume and the orifice supply line are also included. Fluid inertia at the recess edges is modeled by Bernoulli-type relationships, while a pressure rise due to journal rotation in the downstream portion of the recess is considered as a one-dimensional step-bearing. The energy transport phe-

nomenon in a HJB recess is controlled by the carry over of hot fluid from upstream to downstream of the recess, the mixing of fresh fluid from the supply orifice into the recess volume, and the heat generation in the recess volume due to shear dissipation by journal rotation.

Predictions from the numerical solution are presented on the second part of this paper. Numerical results are compared with limited experimental data available for a liquid hydrogen (LH₂) bearing.

References

- Artiles, A., Walowitz, J., and Shapiro, W., 1982, "Analysis of Hybrid Fluid Film Journal Bearings with Turbulence and Inertia Effects," *Advances in Computer Aided Bearing Design*, ASME Press, ASME, New York.
- Braun, M. J., Wheeler, R. L., III, and Hendricks, R. C., 1987, "A Fully Coupled Variable Properties Thermohydraulic Model for a Cryogenic Hydrostatic Journal Bearing," *ASME Journal of Tribology*, Vol. 109, pp. 405-416.
- Braun, M. J., Don, Q., and Choy, F. K., 1993, "The Effects of a Hydrostatic Pocket Aspect Ratio, and its Supply Orifice Position and Attack Angle on Steady-State Flow Patterns, Pressure and Shear Characteristics," *ASME Journal of Tribology*, Vol. 115, pp. 678-685.
- Butner, M., and Murphy, B., 1986, "SSME Long Life Bearings," NASA Report, CR179455.
- Chaomleffel, J. P., and Nicholas, D., 1986, "Experimental Investigation of Hybrid Journal Bearings," *Tribology International*, Vol. 19, pp. 253-259.
- Constantinescu, V. N., and Galetuse, S., 1975, "Pressure Drop due to Inertia Force in Step Bearings," *ASME Paper*, 75-LUB-34.
- Di Pasquantonio, F., and Sala, P., 1984, "Influence of Thermal Field on the Resistance Law in Turbulent Bearing-Lubrication Theory," *ASME Journal of Tribology*, Vol. 106, pp. 368-376.
- Elrod, Jr, H. G., and Ng, C. W., 1967, "A Theory for Turbulent Fluid Films and Its Application to Bearings," *ASME Journal of Lubrication Technology*, Vol. 89, pp. 346-362.
- Hirs, G. G., 1973, "A Bulk-Flow Theory for Turbulence in Lubricant Films," *ASME Journal of Lubrication Technology*, Vol. 95, pp. 137-146.
- Katayama, T., and Okada, A., 1992, "Liquefied Natural Gas Pump with Hydrostatic Journal Bearings," *Proceedings of the 9th International Pump Users Symposium*, Houston, Texas, pp. 39-50.
- Lauder, B. E., and Leschziner, M., 1978, "Flow in Finite Width Thrust Bearings Including Inertial Effects, I—Laminar Flow, II—Turbulent Flow," *ASME Journal of Lubrication Technology*, Vol. 100, pp. 330-345.
- Massey, B. S., 1983, *Mechanics of Fluids*, Van Nostrand Reinhold (UK) Co. Ltd., Workingham, Berkshire, U.K.
- McCart, R. D., NBS Standard Reference Data Base 12, 1986, "Thermophysical Properties of Fluids, MIPROPS-86," Thermophysics Div., Center for Chemical Engineering, National Bureau of Standards, Colorado.
- Nelson, C. C., and Nguyen, D. T., 1987, "Comparison of Hirs Equation with Moody's Equation for Determining Rotordynamic Coefficients of Annular Pressure Seals," *ASME Journal of Lubrication Technology*, Vol. 109, pp. 144-148.
- Reddelcliff, J. M., and Vohr, J. H., 1969, "Hydrostatic Bearings for Cryogenic Rocket Engine Turbopumps," *ASME Journal of Lubrication Technology*, Vol. 91, pp. 557-575.
- San Andres, L., 1990a, "Turbulent Hybrid Bearings with Fluid Inertia Effects," *ASME Journal of Tribology*, Vol. 112, pp. 699-707.
- San Andres, L., 1990b, "Approximate Analysis of Turbulent Hybrid Bearings: Static and Dynamic Performance for Centered Operation," *ASME Journal of Tribology*, Vol. 112, pp. 692-698.
- San Andres, Luis A., 1991a, "Effect of Fluid Compressibility on the Dynamic Response of Hydrostatic Journal Bearings," *Wear*, Vol. 146, pp. 269-283.
- San Andres, Luis A., 1991b, "Analysis of Variable Fluid Properties, Turbulent Annular Seals," *ASME Journal of Tribology*, Vol. 113, pp. 694-702.
- San Andres, Luis A., 1992a, "Analysis of Turbulent Hydrostatic Bearings with a Barotropic Cryogenic Fluid," *ASME Journal of Tribology*, Vol. 114, pp. 755-765.
- San Andres, L., and Velthuis, J. F. M., 1992b, "Laminar Flow in a Recess of a Hydrostatic Bearing," *STLE Tribology Transactions*, Vol. 35, pp. 738-744.
- San Andres, Luis A., 1993, "Thermohydrodynamic Analysis of Cryogenic Liquid Turbulent Flow Fluid Film Bearings," Annual Research Progress Report to NASA Lewis Research Center, Project NAG3-1434, Dec.
- Scharer, J. K., Hibbs, R. I., and Nolan, S. A., 1992a, "Extending the Life of the SSME HPOTP Through the Use of Annular Hydrostatic Bearings," *AIAA* 92-3401.
- Scharer, J. K., Tellier, J. G., and Hibbs, R. I., 1992b, "Start Transient Testing of an Annular Hydrostatic Bearings in Liquid Oxygen," *AIAA* 92-3404.
- Suganami, T., and Szeri, A. Z., 1979, "A Thermohydrodynamic Analysis of Journal Bearings," *ASME Journal of Lubrication Technology*, Vol. 101, pp. 21-27.
- Von Pragenau, G. L., 1990, "Damping Bearings for Turbomachines," NASA Conference Publication 3092, Vol. II, Advanced Earth-to-Orbit Propulsion Technology, pp. 155-162.
- Yang, Z., San Andres, L., and Childs, D., 1993a, "Thermal Effects in Cryogenic Liquid Annular Seals," *ASME Journal of Tribology*, Vol. 115, pp. 267-284.
- Yang, Z., San Andres, L., and Childs, D., 1993b, "Importance of Heat Transfer from Fluid Film to Stator in Turbulent Annular Seals," *Wear*, Vol. 160, pp. 269-277.

Thermohydrodynamic Analysis of Process-Liquid Hydrostatic Journal Bearings in Turbulent Regime, Part II: Numerical Solution and Results

Zhou Yang

Cummins Engine Company, Inc.
Columbus, IN 47201
Assoc. Mem. ASME

L. San Andres

Assoc. Mem. ASME.

D. W. Childs

Fellow ASME.

Mechanical Engineering Department,
Texas A&M University,
College Station, TX 77843

A finite difference scheme is implemented to solve the nonlinear differential equations describing the turbulent bulk-flow on the film lands of a hydrostatic journal bearing (HJB). A Newton-Raphson scheme is used to update the recess pressures and to satisfy the mass continuity requirement at each bearing recess. Comparisons of numerical predictions from the thermohydrodynamic (THD) model with experimental measurements of mass flow rate, fluid temperature, and static stiffness coefficient from a LH₂ test HJB article show very good agreement. In particular, the exit temperature of the bearing is lower than the supply temperature; i.e., the liquid temperature decreases along the bearing length. Similar values of direct stiffness and damping coefficients are predicted by the adiabatic THD model and other considering isothermal flow characteristics. However, the THD model predicts lower cross-coupled stiffness and whirl frequency ratio (WFR < 0.5). The results show that for the application presented, the LH₂ hydrostatic bearing is more stable than previously thought.

1 Introduction

High rotor speeds, large pressure drops, and intentionally roughened bearing-stator surfaces provide unique flow characteristics on cryogenic liquid hydrostatic journal bearings (HJBs), and determine fluid inertia, flow turbulence, actual fluid properties and thermal effects to be important for the accurate prediction of bearing performance. Within the range of practical cryogenic applications, the material properties of liquid hydrogen (LH₂) depend strongly on both pressure and temperature.

Yang et al. (1995, Part I) introduced a bulk-flow thermohydrodynamic (THD) model for the determination of performance characteristics in process liquid HJBs. Fluid inertia, flow turbulence, and actual fluid properties for cryogenics are considered in the analysis. Boundary conditions at the recess/film entrances (recess edges) are obtained through global mass conservation and energy balance at each bearing recess. Fluid compressibility and temperature variation in the recess volume are also included. A perturbation method is used for calculation of the zeroth and first-order flow equations defining the fluid film bearing steady-state response and dynamic force coefficients, respectively.

Part II complements the analysis of Yang et al. (1995) and discusses the numerical solution to the non linear governing equations. The solution scheme is based on efficient and accurate CFD algorithms and calculates the performance characteristics of single-phase process liquid HJBs at centered and off-centered journal positions. Numerical predictions for mass flow

rate, static stiffness, and operating eccentricity are compared with experimental results from a LH₂ HJB article tested by Butner and Murphy (1986). In addition, the dynamic force coefficients for the same bearing are compared for two different bulk-flow models, namely the adiabatic THD and the isothermal-variable properties models. A discussion on the thermal effects and their significance on the performance of the reference HJB are detailed.

2 Numerical Solution Procedure

The mathematical model of a bulk-flow THD analysis of process liquid HJBs is given in Part I (Yang et al., 1995). The coupling of the nonlinear bulk-flow equations at the film lands with the mass and energy conservation equations for each recess is a complicated problem which can not be solved analytically. A finite difference scheme is implemented to solve the governing equations on the film lands. The procedure is based on the forward marching scheme presented by Launder and Leschziner (1978) and uses the SIMPLEX algorithm of Van Doormaal and Raithby (1984). The SIMPLEX algorithm is well known in the literature, and details on its superior convergence rate, grid refinement sensitivity, and accuracy can be found elsewhere (Van Doormaal and Raithby, 1984, 1985; Jang et al., 1986). The procedure has been adapted by San Andres (1992) to solve isothermal fluid film bearing problems, and extended here for the thermohydrodynamic analysis. The flow domain is discretized into a series of staggered rectangular control volumes for the primitive variables (Patankar, 1980). The velocities are located at points which lie at interfaces midway between the nodes where the pressure is determined. The discrete temperature field shares the same control volumes as the pressure field. The governing equations are integrated on the finite size control volumes to give sets of nonlinear algebraic difference equations with local mass flow conservation for each primitive variable.

The pressure, temperature, and velocity fields on the bearing film lands are determined so that the flow discharging from

Contributed by the Applied Mechanics Division of THE AMERICAN SOCIETY OF MECHANICAL ENGINEERS for publication in the ASME JOURNAL OF APPLIED MECHANICS.

Discussion on this paper should be addressed to the Technical Editor, Prof. Lewis T. Wheeler, Department of Mechanical Engineering, University of Houston, Houston, TX 77204-4792, and will be accepted until four months after final publication of the paper itself in the ASME JOURNAL OF APPLIED MECHANICS.

Manuscript received by the ASME Applied Mechanics Division, Feb. 11, 1993; final revision, Apr. 4, 1994. Associate Technical Editor: S. A. Berger.

each recess through the film lands must equal the flow entering that recess from supply pressure through the orifice restrictor. The Newton-Raphson scheme is used to update the recess pressure and to satisfy the mass continuity requirement at the bearing recesses. For bearing operation at the concentric position, the numerical scheme is at its peak efficiency. Under this condition, the flow fields for only one recess need to be calculated due to symmetry and continuity. Flow fields for the other recesses are then obtained by proper rotations (San Andres, 1990).

Extensive numerical calculations for HJBs with different working fluids show that the numerical algorithm is stable and efficient. Another feature of the algorithm is the small number of grid points required to get grid independent results. In fact, less than two percent difference in the bearing static and dynamic performance characteristics is detected when comparing the results from a 67 by 16 grid (number of circumferential points \times axial points) with those from a 85 by 26 grid for the six-recess LH₂ HJB studied in this paper. Details of the numerical solution procedure are provided by Yang (1992).

3 Results and Discussion

Experimental results for the static and dynamic performance parameters of turbulent flow HJBs are given by Kurtin et al. (1993) and Franchek et al. (1993). Water heated to 55°C is used as the lubricant to achieve comparatively high Reynolds numbers in the test bearings without using cryogenic liquids. The measurements are performed for HJBs of different geometries and at journal speeds ranging from 10,200 to 24,600 rpm and supply pressures from 4 to 7 MPa. Extensive comparisons show a good correlation between the experimental results and the numerical predictions based on the variable properties, bulk-flow model of San Andres (1990, 1992), and also with the present thermohydrodynamic model (Yang, 1992).

Comparisons of numerical predictions with other flow models existing in the literature are given elsewhere. San Andres (1991) presents results for static and dynamic force characteristics on a water HJB and compares calculations with those obtained from the analysis of Artiles et al. (1982). The correlation shows the model of Artiles et al. to be in error with force coefficients offering a nonlinear jump-like response as the journal rotational speed increases. Numerical comparisons with the advanced thermal analysis of Braun et al. (1987) are totally impractical. The numerical predictions presented by Braun et al. refer to a HJB with a circumferential flow Reynolds number as large as 100,000, with the flow being considered as laminar and inertialess.

Numerical predictions from the present THD model are here compared with limited experimental data available from a LH₂ HJB article tested by Butner and Murphy (1986). Dynamic force coefficients are calculated for an adiabatic THD condition and compared with predictions from the isothermal model of San Andres (1992). The experimental measurements include mass flow rate (\dot{M}), exit temperature (T_a), and a stiffness coefficient (K_{xx}) extracted from a statically applied load and mea-

Table 1 Characteristics of LH₂ bearing (Butner and Murphy, 1986)

Bearing characteristics	Dimension
Diameter (D)	75.04 mm (2.954 in.)
Length (L)	35.0 mm (1.38 in.)
No. of recesses (N_{rec})	6
Orifice diameter (d_o)	1.27 mm (0.05 in.)
Rectangular recess ($A_r = b \times l$)	$8.89 \times 11.41 \text{ mm}^2$ ($0.35 \times 0.449 \text{ in.}^2$)
Recess area ratio ($N_{\text{rec}}A_r/(\pi DL)$)	0.1
Recess depth (H_r)	0.2286 mm (0.009 in.)
Nominal clearance (at zero speed) (c_*)	0.05334 mm (0.0021 in.)

Table 2 Operating conditions of LH₂ bearing (fixed radial load) (Butner and Murphy, 1986)

Speed (cpm)	P_s (MPa)	P_a (MPa)	T_s (K)	Load (N)	Clearance c (mm)
0	16.27	2.358	46.7	1801	0.05334
12800	16.14	2.393	45.0	2006	0.05080
25000	16.14	2.468	45.6	2064	0.04570
36400	16.14	2.393	46.1	2046	0.03810

sured journal eccentricity. The objectives of the experimental program of Butner and Murphy were to test hybrid bearings designed to replace ball bearings in the SSME high pressure fuel turbopump (HPFTP), and to provide reliable empirical data to anchor computational models used in hydrostatic bearing design. The hydrostatic bearings were designed with emphasis on maximizing stiffness and damping and minimizing friction torque and flow rate. Table 1 presents the geometry for the six-recess test hydrostatic bearing. The bearing and journal surfaces are regarded as perfectly smooth since no information is available on this aspect. The fixed radial load and concentric operation test conditions are given in Tables 2 and 3, respectively. The bearing was tested at different speeds to 36,400 cpm, a pressure supply (P_s) of 16.3 MPa, two pressure drops ($\Delta P = P_s - P_a$) equal to 6.9 and 13.8 MPa, and a supply temperature around $T_s = 46$ K typical of a cryogenic turbopump environment.

In the experimental procedure and for bearing eccentric operation (Table 2), a fixed radial load ($W \approx 2000$ N) was applied after a steady-state speed and supply pressure conditions were achieved. The measured eccentricity ratio ($\epsilon = e/c$) ranges from 0.1271 to 0.1675 for the design pressure drop of 13.8 MPa. The static stiffness was obtained by dividing the fixed radial load by the corresponding static displacement of the journal. The static displacement of the journal under the fixed load was too large ($\epsilon = 0.433$) for the half design pressure drop ($\Delta P = 6.9$ MPa). At such large journal displacement or eccentricity ratio, the numerical predictions show that some of the flows through the bearing orifices are choked (sonic speed is reached). The present model can not handle choked flows, and therefore, the half design pressure drop case ($\Delta P = 6.9$ MPa) is not presented here. A close examination of the experimental results confirms that the orifice flow in the bearing recess opposite to the load direction is choked. This situation is not desirable in a LH₂ HJB since it will certainly cause a pneumatic hammer instability under dynamic operation. The measurements at 12,000 cpm and $\epsilon = 0.433$ show a recess pressure of 3.692 MPa with an orifice speed of 635 m/s while the fluid sonic speed is equal to 611 m/s.

It is of importance to observe the effect of pressure on the material properties of LH₂. At a supply pressure $P_s = 16.27$ MPa and temperature $T_s = 46.7$ K these are

$$\rho_* = 65.25 \text{ (kg/m}^3\text{)}, \quad \mu_* = 9.55 \times 10^{-6} \text{ (N-s/m}^2\text{)}$$

$$C_{p,*} = 12720 \text{ (J/kg K)}, \quad \beta_{t,*} = 1.18 \times 10^{-2} \text{ (1/K)},$$

Table 3 Operating conditions of LH₂ bearing (concentric case) (Butner and Murphy, 1986)

Speed (cpm)	P_s (MPa)	P_a (MPa)	T_s (K)	c (mm)
10950	16.18	2.406	46.1	0.05091
14040	16.18	2.413	46.1	0.05070
22450	16.19	2.406	46.7	0.04758
26080	16.18	2.413	46.7	0.04565
32520	16.20	2.399	47.2	0.04169
36270	16.18	2.406	47.8	0.03821

Table 4 Empirical parameters for LH₂ bearing

C_d	α	ξ_{xu}	ξ_{xd}	ξ_y
0.90	0.50	0.50	0.50	0.50

while at a discharge pressure $P_a = 2.358$ MPa and supply temperature $T_* = 46.7$ K, the fluid properties are

$$\rho_a = 16.09 \text{ (kg/m}^3\text{)}, \quad \mu_a = 2.96 \times 10^{-6} \text{ (N-s/m}^2\text{)}$$

$$C_{pa} = 17760 \text{ (J/kg K)}, \quad \beta_{ta} = 4.60 \times 10^{-2} \text{ (1/K)}$$

The ratio of properties between discharge to supply conditions is equal to 0.25 for density and 0.31 for viscosity. Note that the fluid operating conditions are well above the critical temperature and pressure for LH₂ given as 32.94 K and 1.284 MPa, respectively. The compressibility factor (β_p) at the recess pressure ($P_r \approx 0.5P_s$) is about $5 \times 10^{-8} \text{ m}^2/\text{N}$ (1/2,900 psi) demonstrating the large compressibility of the liquid in the recess.

The circumferential flow (Re_c) and axial flow (Re_a) Reynolds numbers based on the top journal speed (36,000 cpm) and the largest mass flow rate are equal to

$$Re_c = \rho_* R \Omega c_* / \mu_* = 3.71 \times 10^4$$

$$Re_a = \rho_* V c_* / \mu_* = \dot{M} / (2\pi D \mu_*) \approx 6.11 \times 10^4$$

$$Re_s = \rho_* \omega c_*^2 / \mu_* = 37.65$$

Note that the axial flow Reynolds number is higher than Re_c even though the rotational speed is rather large. For LH₂ HJBs, a high pressure drop across the bearing along with the low viscosity of the working fluid causes an axially dominant flow which is turbulent even at zero rotational speed. The squeeze-film-flow Reynolds number (Re_s) with synchronous whirl frequency ($\omega = \Omega$) is much larger than unity and demonstrates that fluid inertia effects are not negligible in this bearing application.

The empirical parameters for the numerical calculations are given in Table 4. The orifice discharge coefficient (C_d) in Table 4 is determined as the average of the experimentally calculated C_d 's for a hydrostatic water bearing (Franchek et al., 1993; Yang, 1992), and very close to the value reported by Butner and Murphy (1986) from their measurements. The ξ parameters refer to the entrance loss (nonisentropic) coefficients in the axial (y) and circumferential (x) directions, (u) upstream and downstream (d), of the recess edges, respectively. These empirical parameters and the fluid entrance swirl ratio (α) are determined by matching the measured flow rate with a calculated one for the case of 36,400 cpm. The resulting parameters are then used for all other cases.

3.1 Static Performance Characteristics.

Static Stiffness. Figure 1 shows the theoretical and experimental static stiffness as a function of rotational speed. This stiffness as identified from the load versus journal displacement curve increases with increasing rotational speed mainly due to the reduction of the bearing radial clearance from centrifugal growth of the rotating journal. The exception corresponds to the measured data at zero rotational speed. Numerical predictions from both the adiabatic THD and the isothermal models correlate well with the experimental data. The maximum error between the theoretical and experimental results is 10.3 percent. Note that the discrepancy at zero speed (purely hydrostatic operation) is much higher (22.2 percent), but the measured stiffness may be in error since it is larger than the experimental value at 12,800 cpm which has a smaller operating clearance.

Static Load Capacity. Figure 2 shows the journal eccentricity ratio under a fixed radial load ($\approx 2000N$) as a function of increasing rotational speed. The data at zero speed are excluded

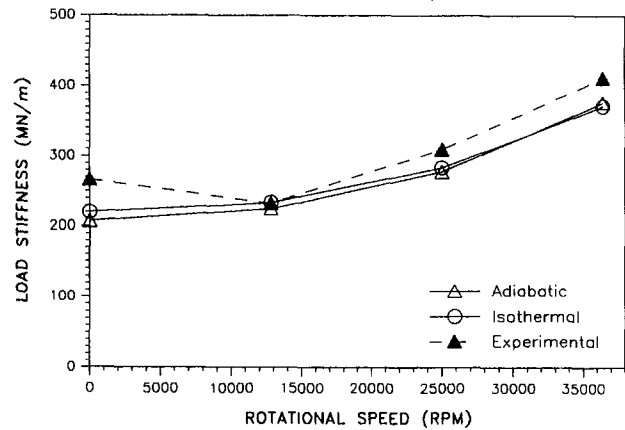


Fig. 1 Static stiffness (K_{xx}) versus rotational speed (fixed load); (LH₂ HJB tested by Butner and Murphy, 1986)

since the experimental radial load for purely hydrostatic operation is different ($\approx 1800N$). The eccentricity ratio decreases with rotational speed, demonstrating that a higher speed provides slightly larger load capacity which is consistent with the behavior of the static stiffness in Fig. 1. The predictions from the adiabatic THD model are better than the isothermal model. The maximum error between the test and prediction is 2.6 percent for the THD model, and eight percent for the constant temperature model.

The measurement of dynamic force coefficients for LH₂ HJBs was not successful due to signal interference by casing resonances as reported by Butner and Murphy (1986). However, the test program did provide valuable static performance characteristics like flow rates and discharge temperatures for concentric operations (Table 3).

Mass Flow Rate. Figure 3 shows the mass flow rate to decrease with journal speed due to a reduction of the operating bearing radial clearance. The contribution of the hydrodynamic effect to the reduction of the mass flow rate with speed is negligible since the viscosity of LH₂ is very small. The numerical predictions from both the adiabatic THD and the isothermal models correlate very well with the experimental measurements.

Exit Temperature. Figure 4 shows a comparison between the measured exit temperature and numerical predictions as the journal speed increases. The supply fluid temperatures obtained from the test data are also presented in the figure to demonstrate the temperature difference across the bearing length. Note particularly that the exit temperatures are lower than the supply

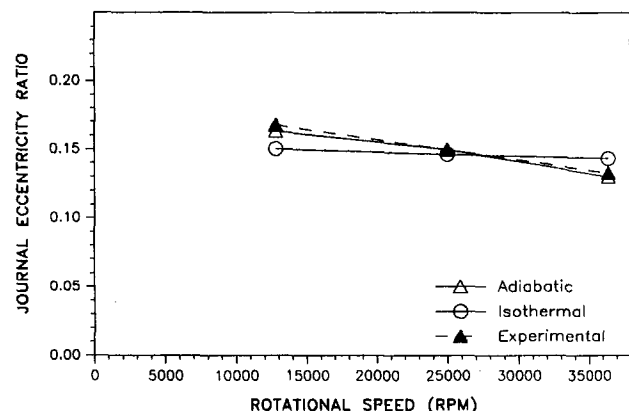


Fig. 2 Eccentricity ratio (ϵ) versus rotational speed (fixed load); (LH₂ HJB tested by Butner and Murphy, 1986)



Fig. 3 Mass flow rate (M) versus rotational speed ($\epsilon = 0$); (LH_2 HJB tested by Butner and Murphy, 1986)

temperatures ($\Delta T = T_{\text{exit}} - T_s \approx -5$ K), which show that the liquid temperature *decreases* instead of increasing along the bearing length. This phenomenon unusual in a liquid bearing is accurately predicted by the THD model and can be explained as follows.

Half of a symmetric HJB (from the circumferential center plane ($y = 0$) to the discharge plane ($y = L/2$)) behaves approximately like an annular pressure seal. Therefore, the examination of temperature variations in an annular seal will, at least conceptually, be helpful in understanding those of a HJB. For an adiabatic flow in a centered pressure annular seal (or a HJB), the temperature difference across the seal length (or half of the bearing length) can be approximated as (Yang, 1993):

$$\Delta T = T_{\text{exit}} - T_s = \frac{T_{\text{or}} \Omega}{C_{pA} \dot{M}} + (1 - \beta_{IA} T_s) \frac{\Delta P}{\rho_A C_{pA}} - \frac{\rho_A (U^2 + V^2) \frac{L}{2}}{2 \rho_A C_{pA}} \quad (1)$$

where

$$\Delta P = \begin{cases} P_s - P_a, & \text{for annular pressure seals;} \\ P_r - P_a, & \text{for hydrostatic bearings} \end{cases} \quad (2)$$

and the subscript "A" represents the average value across the seal/bearing length.

The first term on the right-hand side of Eq. (1) is generated from viscous dissipation by shear friction and is always positive. The second term shows the pressure extrusion which is zero

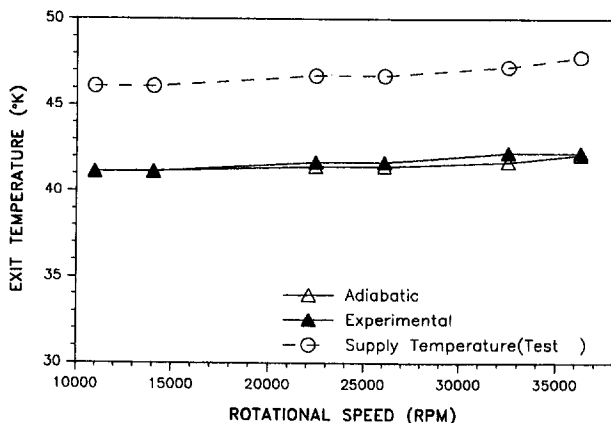


Fig. 4 Exit temperature (T_{exit}) versus rotational speed ($\epsilon = 0$); (LH_2 HJB tested by Butner and Murphy, 1986)

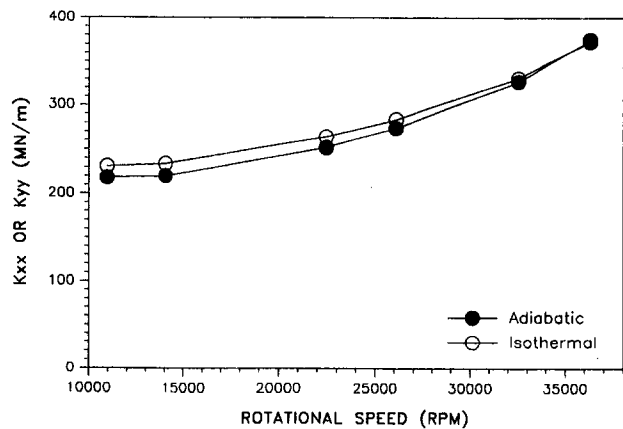


Fig. 5 Direct stiffness (K_{xx}) versus rotational speed ($\epsilon = 0$); (bearing parameters presented in Tables 1 to 3)

for ideal gases ($\beta_{IA} T_s = 1$). The last term is the kinetic energy variation which is generally negative for compressible fluid flows in annular pressure seals or HJBs, since by mass conservation the discharge velocity is larger than the inlet one.

For viscous liquids of low compressibility, such as oils, water, and other conventional lubricants, the viscous dissipation is large, the thermal expansion coefficient is small ($\beta_{IA} T_s < 1$), and the kinetic energy variation is negligible, which always results in a temperature rise across the seal/bearing length by Eq. (1).

For an ideal gas, Eq. (1) usually gives a temperature decrease along the seal/bearing length due to the large kinetic energy variation, small viscous dissipation, and null pressure extrusion work. However, for seals/bearings with roughened surfaces (including labyrinth seals), the gas temperature could increase in the seals/bearings due to the high viscous dissipation and reduced mass flow rate.

Even though liquid hydrogen is highly compressible, its behavior is different from an ideal gas. The properties of an ideal gas, like density and viscosity, are less sensitive to absolute temperature variation than those of liquid hydrogen. Depending on the operating condition (supply temperature and pressure, sump pressure, and rotational speed), the rate of temperature growth across the seal/bearing length could be positive or negative. Usually, the fluid supply temperature is the control parameter. A higher supply temperature offers a lower fluid viscosity and a higher thermal expansion coefficient ($\beta_{IA} T_s > 1$) leading to a temperature decrease across the seal/bearing length, which corresponds to the present bearing test article.

3.1 Dynamic Performance Characteristics. The relevant experimental data from Butner and Murphy (1986) did not provide rotordynamic force coefficients for the bearing configuration tested. The importance of the proper identification of force coefficients can be hardly overlooked. This is an area where detailed testing is needed with cryogenics or appropriate surrogate fluids. Undaunted by the lack of experimental results, the following figures present numerical predictions for the dynamic force coefficients using the adiabatic THD model (solid symbols) and the isothermal model (hollow symbols). Note that at the centered position ($\epsilon = 0$), the dynamic coefficient matrices (Eq. (1), Yang et al., 1995) are

$$\phi_{xx} = \phi_{yy}, \quad \phi_{xy} = -\phi_{yx}, \quad \text{where } \phi = K, C, \text{ or } M. \quad (3)$$

Direct Stiffness Coefficient. Figure 5 shows the direct stiffness coefficients (K_{xx} or K_{yy}) as a function of rotational speed. The increase of the direct stiffness coefficients with rotational speed is caused by the reduction of the radial clearance and it is also illustrated in Fig. 1 where the bearing is operating eccentrically. The isothermal model predicts a higher direct

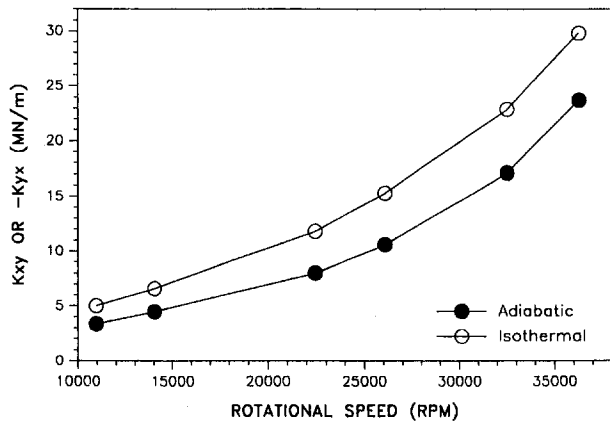


Fig. 6 Cross-coupled stiffness (K_{xy}) versus rotational speed ($\epsilon = 0$); (bearing parameters presented in Tables 1 to 3)

stiffness except at the highest speed (36,270 cpm) where the adiabatic thermal model shows a more pronounced hydrodynamic effect due to the temperature decrease in the bearing and hence the larger fluid viscosity. The maximum difference between the two models is 6.4 percent.

Cross-Coupled Stiffness. Figure 6 illustrates the cross-coupled stiffness coefficients (K_{xy} or $-K_{yx}$) versus rotational speed. The cross-coupled stiffness coefficients increase rapidly with increasing rotational speed. The magnitude of the cross-coupled stiffness coefficients is much smaller than the direct ones showing that the hydrodynamic force component in LH₂ HJBs is small. However, as has been shown before, the bearing stability is a combined effect of the dynamic coefficients, especially the cross-coupled stiffness and the direct damping. The THD model predicts lower cross-coupled stiffness coefficients and hence smaller destabilizing forces in the bearing with a maximum discrepancy of 49.3 percent between the two models. This is surprising since the lower fluid temperature and hence larger viscosity predicted by the THD model should provide a higher cross-coupled stiffness (San Andres, 1992). This result might be explained by the fact that, unlike laminar flows where a rise in viscosity leads directly to a gain of shear force, in a turbulent flow this gain is overshadowed by the simultaneous decrease in the Reynolds number and the turbulent shear gradients at the bearing surfaces.

Direct Damping. Figure 7 shows the direct damping coefficients (C_{xx} or C_{yy}) as a function of rotational speed. The direct damping coefficients increase with rotational speed. The small

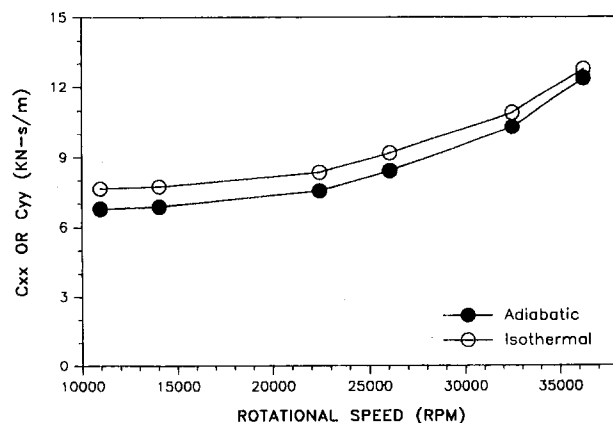


Fig. 7 Direct damping (C_{xx}) versus rotational speed ($\epsilon = 0$); (bearing parameters presented in Tables 1 to 3)

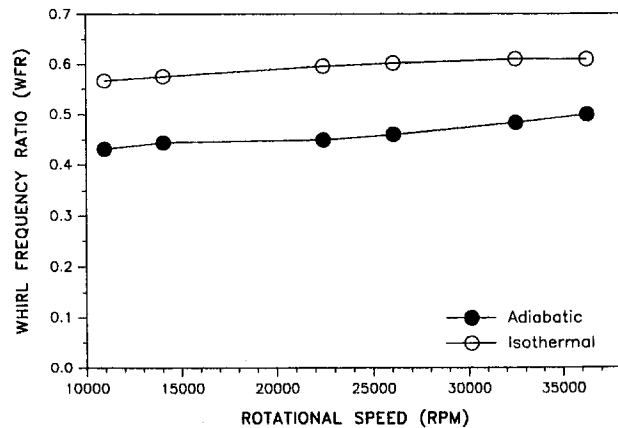


Fig. 8 Whirl frequency ratio versus rotational speed ($\epsilon = 0$); (bearing parameters presented in Tables 1 to 3)

viscosity of LH₂ not only generates small cross-coupled stiffness, but also provides low direct damping when compared to a more viscous liquid such as liquid oxygen (LO₂). Again, the THD model predicts smaller direct damping coefficients. However, the difference for direct damping between the two models (maximum difference: 13 percent) are smaller than that for the cross-coupled stiffness.

Other dynamic force coefficients, such as the cross-coupled damping and the added mass, are very small for this LH₂ bearing geometry and will not influence the bearing dynamic performance. This condition is well known to be valid for light-density liquid and gas bearings and seals.

Whirl Frequency Ratio. The whirl frequency ratio (WFR) is an indicator of bearing stability as it relates in a single expression the effect of destabilizing cross-coupled forces and stabilizing viscous damping forces. A low WFR indicates enhanced ability of a fluid film bearing to safely operate at higher running speeds relative to the first critical speed of the rotor-bearing system. For concentric operation, Fig. 8 shows the whirl frequency ratio (WFR) to increase with the journal rotational speed. The adiabatic THD model predicts lower WFR's than the isothermal model, and asymptotically appears to approach the maximum value of 0.50 at the highest speed (36,270 cpm). The largest difference between the two models is 31.6 percent.

For an incompressible liquid cylindrical bearing with smooth surfaces, the WFR should approach 0.50 at the concentric position (Rowe, 1980). This has been verified by the experimental measurements on hydrostatic water bearings (Franchek et al., 1993). However, the isothermal model of San Andres (1992) also shows that the stability indicator in a HJB is larger than 0.50 for compressible liquids. In general, a higher compressibility ratio (β_{pr}) determines a higher WFR. This conclusion can not be drawn from the results predicted by the THD model, and unfortunately, no experimental data on the stability of LH₂ HJBs is available to date.

4 Conclusions and Recommendations

A bulk-flow thermohydrodynamic (THD) analysis is developed for calculation of the static and dynamic performance characteristics of turbulent flow, process liquid hydrostatic journal bearings (HJBs). A finite difference scheme is implemented to solve the governing equations on the film lands, while the Newton-Raphson scheme is used to update the recess pressures and satisfy the mass continuity requirement at each recess.

Comparisons of numerical predictions from the THD model with experimental measurements of mass flow rate, fluid temperature, and load stiffness coefficient from a LH₂ HJB tested by Butner and Murphy (1986) show very good agreement. In

particular, the exit temperature of the LH₂ HJBs is lower than the supply temperature; i.e., the liquid temperature *decreases* along the bearing length. This phenomenon unusual in a conventional liquid bearing is predicted correctly by the THD model. Both the THD model and an isothermal model predict well the mass flow rate and the stiffness coefficient of the LH₂ HJBs, while the static load capacity is predicted better by the THD model. The orifice-discharge coefficient (C_d) is the major uncertain parameter in the calculation of performance characteristics in orifice-compensated HJBs. For the LH₂ bearing configuration studied, choked flows through the orifice restrictors are not unlikely to occur at journal eccentric operation.

For concentric journal operating conditions, numerical predictions of dynamic force coefficients for the test LH₂ HJB are presented. No experimental data is yet available for the dynamic force coefficients. The adiabatic THD and isothermal flow models predict approximately the same direct stiffness (maximum difference: 6.4 percent) and damping coefficients (maximum difference: 13 percent), while the THD model predicts much lower cross-coupled stiffness (maximum difference: 49.3 percent) and whirl frequency ratio (WFR) (maximum difference: 31.6 percent), and thus, it shows a bearing with better dynamic stability characteristics.

The analysis shows that the variation of temperature (increase or decrease) in a LH₂ HJB is largely dependent on the operating conditions such as supply temperature and pressure, sump pressure, and journal rotational speed. The fluid inlet temperature to the bearing is one of the control parameters. A low supply temperature (lower than the critical temperature: $T_c < 32.9$ K) will make LH₂ behave more like a liquid rather than a gas. Larger supply temperatures may produce choked flows or significant temperature gradients within the bearing. Also, a low supply temperature will keep the state of LH₂ away from the saturation region and hence avoid two-phase flow conditions.

Acknowledgments

The support from Pratt & Whitney and the NASA Center for the Commercial Development of Space is gratefully acknowledged. Also thanks to NASA Lewis Research Center Grant NAG3-1434 for their interest and continued support for this research program. Thanks to Mr. Robert Hendricks from NASA LeRC for his invaluable comments to this work.

References

- Artiles, A., Watlowit, J., and Shapiro, W., 1982, "Analysis of Hybrid Fluid Film Journal Bearings with Turbulence and Inertia Effects," *Advances in Computer Aided Bearing Design*, ASME Press, New York.
- Braun, M. J., Wheeler, R. L. III, and Hendricks, R. C., 1987, "A Fully Coupled Variable Properties Thermohydraulic Model for a Cryogenic Hydrostatic Journal Bearing," *ASME Journal of Tribology*, Vol. 109, pp. 405–416.
- Butner, M., and Murphy, B., 1986, "SSME Long Life Bearings," NASA Report CR 179455.
- Franchek, N., and Childs, D., 1993, "Experimental Test Results for Four High-Speed, High-Pressure, Orifice-Compensated Hybrid Bearings," ASME Paper 93-Trib-24.
- Jang, D. S., Jetli, R., and Acharya, S., 1986, "Comparison of the PISO, SIMPLER, and SIMPLEC algorithms for the Treatment of the Pressure-Velocity Coupling in Steady Flow Problems," *Numerical Heat Transfer*, Vol. 10, pp. 209–228.
- Kurtin, K. A., Childs, D., San Andres, L., and Hale, K., 1993, "Experimental Versus Theoretical Characteristics of a High-Speed Hybrid (Combination Hydrostatic and Hydrodynamic) Bearing," *ASME Journal of Tribology*, Vol. 115, pp. 160–169.
- Lauder, B. E., and Leschziner, M., 1978, "Flow in Finite Width Thrust Bearings Including Inertial Effects, I—Laminar Flow, II—Turbulent Flow," *ASME Journal of Lubrication Technology*, Vol. 100, pp. 330–345.
- Patankar, S. V., 1980, *Numerical Heat Transfer and Fluid Flow*, Hemisphere, New York.
- Rowe, W. B., 1980, "Dynamic and Static Properties of Recessed Hydrostatic Journal Bearing by Small Displacement Analysis," *ASME Journal of Lubrication Technology*, Vol. 102, pp. 71–79.
- San Andres, L., 1990, "Turbulent Hybrid Bearings with Fluid Inertia Effects," *ASME Journal of Tribology*, Vol. 112, pp. 699–707.
- San Andres, L., 1991, "Improved Analysis of High Speed, Turbulent Hybrid Bearings" 4th NASA Conference on Advanced Earth-to-Orbit Propulsion Technology, NASA CP 3092, Vol. 2, May, pp. 414–431.
- San Andres, Luis A., 1992, "Analysis of Turbulent Hydrostatic Bearings with a Barotropic Cryogenic Fluid," *ASME Journal of Tribology*, Vol. 114, pp. 755–765.
- Van Doormaal, J. P., and Raithby, G. D., 1984, "Enhancements of the SIMPLE Method for Predicting Incompressible Fluid Flows," *Numerical Heat Transfer*, Vol. 7, pp. 147–163.
- Van Doormaal, J. P., and Raithby, G. D., 1985, "An Evaluation of the Segregated Approach for Predicting Incompressible Fluid Flow," ASME Paper 85-HT-9.
- Yang, Z., 1992, "Thermohydrodynamic Analysis of Product-Lubricated Hydrostatic Bearings in Turbulent Regime," Ph.D. Dissertation, Texas A&M University, College Station, TX, December.
- Yang, Z., San Andres, L., and Childs, D., 1993, "Thermal Effects in Cryogenic Liquid Annular Seals, Part I: Theory and Approximate Solution; Part II: Numerical Solution and Results," *ASME Journal of Tribology*, Vol. 115, pp. 267–284.
- Yang, Z., San Andres, L., and Childs, D., 1995, "Thermohydrodynamic Analysis of Liquid Hydrostatic Journal Bearings in Turbulent Regime, Part I: The Model and Perturbation Analysis," *ASME JOURNAL OF APPLIED MECHANICS*, Vol. 62, pp. 674–678.

F. Ma

Professor of Applied Mechanics,
Department of Mechanical Engineering,
University of California,
Berkeley, CA 94720
Mem. ASME

T. K. Caughey

Professor of Applied Mechanics and
Hayman Professor of Mechanical
Engineering,
Division of Engineering and
Applied Science,
California Institute of Technology,
Pasadena, CA 91125

Analysis of Linear Nonconservative Vibrations

The coefficients of a linear nonconservative system are arbitrary matrices lacking the usual properties of symmetry and definiteness. Classical modal analysis is extended in this paper so as to apply to systems with nonsymmetric coefficients. The extension utilizes equivalence transformations and does not require conversion of the equations of motion to first-order forms. Compared with the state-space approach, the generalized modal analysis can offer substantial reduction in computational effort and ample physical insight.

1 Introduction

The equation of motion of an n -degree-of-freedom linear nonconservative system can be written as

$$A\ddot{q} + B\dot{q} + Cq = f(t), \quad (1)$$

where A , B , and C are arbitrary square matrices of order n . These coefficient matrices are real, but they need not possess any of the familiar properties of symmetry or definiteness. The Lagrangian coordinate q and the generalized excitation $f(t)$ are n -dimensional vectors. In traditional applications, equations of the above type arise mostly in the area of vehicle dynamics. The use of control devices in structures in recent years, however, has permitted linear nonconservative systems to manifest on a widespread scale. Development of a fast method for the analysis of these systems is thus much deserving.

To be sure, it would be preferable if classical modal analysis could somehow be modified to treat linear nonconservative systems. That might indeed be assumed in some earlier investigations. A literature survey in the testing of aircraft flutter and in the stressing of ship hulls, for example, reveals rather occasional use of terms such as logarithmic decrements, modes, or natural frequencies. But the meanings of these terms are not clear. When does a linear nonconservative system possess classical normal modes? What are the natural frequencies of a nonconservative system? A theoretical basis, on which these concepts can be properly explored, is much desired.

In theory, it is always possible to investigate a linear nonconservative system with the Hamiltonian approach, whereby the second-order Eq. (1) is recast into a first-order system of dimension $2n$. The state-space representation is one such approach. After conversion into a first-order form, a large variety of numerical techniques are then available for subsequent analysis. But the Hamiltonian method has never appealed to engineers. An inordinate amount of computational effort is usually given as a reason. More importantly, there is serious absence of physical insight in tackling a first-order equation recast from the Lagrangian formulation. The reluctance to employ Hamiltonian techniques has led to a predictable observation: engineers routinely invoke a whole array of rather bold approximations to continue to base the analysis of linear nonconservative systems upon the Lagrangian coordinate q .

Contributed by the Applied Mechanics Division of THE AMERICAN SOCIETY OF MECHANICAL ENGINEERS for publication in the ASME JOURNAL OF APPLIED MECHANICS.

Discussion on this paper should be addressed to the Technical Editor, Prof. Lewis T. Wheeler, Department of Mechanical Engineering, University of Houston, Houston, TX 77204-4792, and will be accepted until four months after final publication of the paper itself in the ASME JOURNAL OF APPLIED MECHANICS.

Manuscript received by the ASME Applied Mechanics Division, Aug. 23, 1993; final revision, July 18, 1994. Associate Technical Editor: P. D. Spanos.

Over the years, three systematic techniques have nonetheless emerged for the analysis of linear nonconservative vibrations in Lagrangian coordinates. The first technique, pioneered by Huseyin and Leipholz (1973) as well as Inman (1983), concerns the simultaneous reduction of A , B , and C to symmetric matrices by a common similarity transformation. Necessary and sufficient conditions for the existence of symmetrizing transformations have been given. The second technique involves simultaneous reduction of the coefficient matrices to diagonal forms. Many authors have considered this method, which has direct relevance to classical modal superposition. One simply recalls that modal analysis of a symmetric and positive definite system is a process of diagonalizing two matrices at the same time. When simultaneous diagonalization applies, a linear nonconservative system is completely decoupled. As a result, the system can be regarded as composing of n -independent single-degree-of-freedom systems. Using an idea related to diagonalization, a remarkable study of linear vibrations was reported by Fawzy and Bishop (1976). The third approach concerns the simultaneous reduction of A , B , and C to upper triangular matrices by a common similarity transformation. Necessary and sufficient conditions for the existence of triangularizing transformations have recently been provided by Caughey and Ma (1993). The above three techniques have certainly contributed to the theoretical basis of linear nonconservative vibrations. On a practical side, however, the situation is less satisfactory. An examination of the restrictions involved in these methods reveals that only a small subclass of linear nonconservative systems can indeed be treated.

Were system (1) symmetric and definite, the coefficient of acceleration would be a positive definite mass matrix M , and the coefficients of velocity and displacement would respectively be positive semidefinite damping and stiffness matrices D and K . In this case, Eq. (1) would take the familiar form

$$M\ddot{q} + D\dot{q} + Kq = f(t). \quad (2)$$

The difference between the matrices B and D is sometimes accounted for by gyroscopic forces, and that between C and K by circulatory forces (Müller and Schiehlen, 1985). Hence $B = 0$ implies an undamped nongyroscopic system, and so on. While this type of terminology may not be applicable to controlled linear systems, it will be convenient to adhere to such terminology. The various ways in which control gains can be embedded in the coefficients and the excitation of system (1) are discussed by Soong (1990). Applications in which A is not symmetric are given, for example, by Schmitz (1973) as well as Soom and Kim (1983).

The purpose of this article is to expound a fast method for the analysis of linear nonconservative vibrations. This constructive

method utilizes equivalence transformations in Lagrangian coordinates, and does not involve conversion of the equations of motion to first-order forms. As will be evident, the method represents a direct extension of classical modal analysis. The organization of this article is as follows. In Section 2, it is shown that an undamped nongyroscopic system can be completely decoupled by an equivalence transformation. The meanings of natural frequencies and normal modes will be clarified. Equivalence transformation is applied to a general nonconservative system in Section 3. There, comparison is made with classical modal analysis of viscously damped systems. Two illustrative examples are given in Section 4, in which practical implications of the method are also discussed. A summary of findings is provided in Section 5. The terms, *linear vibrations* and *linear nonconservative systems*, will be used interchangeably in exposition.

2 Undamped Nongyroscopic Vibrations

Consider an undamped nongyroscopic linear system, for which $B = 0$. The equation of motion is

$$A\ddot{q} + C\dot{q} = f(t). \quad (3)$$

This type of systems was elucidated by Huseyin (1978), with particular emphasis on the stability of two subclasses termed pseudoconservative and circulatory systems. Pflüger's column was one of the many illuminating examples discussed at length. The above system can be decoupled if and only if there exist two nonsingular matrices U and V such that VAU , VCU are diagonal. Two square matrices P and Q , related by $P = VQU$, are said to be connected by an equivalence transformation. An equivalence transformation between P and Q preserves the rank of the matrices. If $V = U^{-1}$, the equivalence transformation is called a similarity transformation. In the event that $V = U^T$, the equivalence transformation is a congruence transformation. The classical modal transformation is an example of congruence transformation. A congruence transformation is also a similarity transformation if U is an orthogonal matrix. Equivalence transformations that are neither similarity nor congruence transformations are rarely used in structural analysis. Nevertheless, equivalence transformations are the most general nonsingular linear transformation, and it will be shown that A and C can be diagonalized simultaneously by an equivalence transformation in practically every situation.

Let u be a column vector of order n and α be a scalar constant. If

$$q = ue^{\alpha t} \quad (4)$$

is a homogeneous or complementary solution to Eq. (3), the generalized eigenvalue problem

$$Cu = \lambda Au \quad (5)$$

must be satisfied, where $\lambda = -\alpha^2$. Eigenvalue problems of this kind were traditionally addressed in the abstract theory of matrix pencils. Emphasis was usually placed on symmetric and definite pencils. As a consequence, results applicable to the above eigenvalue problem are scattered and rather incomplete. Most constructive methods for the eigenvalue problem (5) have been summarized by Golub and Van Loan (1989). In what follows, an extension based upon the presentation of Zurmühl and Falk (1984) will be made. Associated with eigenvalue problem (5) is the adjoint eigenvalue problem

$$C^T v = \lambda A^T v. \quad (6)$$

As Eqs. (5) and (6) lead to the same characteristic determinant, the corresponding eigenvalues are identical. But that says nothing about the number of eigenvalues available.

At this point, the two assumptions underlying this investigation must be reviewed. First, it is required that A is nonsingular.

This is a common assumption made in earlier investigations of nonconservative systems. Technically speaking, there is no practical loss of generality in accommodating this assumption. Should the coefficient matrix A be singular, at least one component of the acceleration can be removed from the formulation. A linear nonconservative system is termed degenerate if its coefficient of acceleration A is singular. The eigenvalue problem (5) possesses n eigenvalues if and only if A is nonsingular. Thus, the implicit assumption that a system is not degenerate ensures the existence of a full set of eigenvalues. The second requirement presumes independence of the eigenvectors associated with eigenvalue problem (5). An eigenvalue problem is termed defective if it does not possess a full complement of independent eigenvectors. Experience indicates that an eigenvalue problem (5) possessing physical significance is invariably not defective. And the assumption that there is a full complement of independent eigenvectors can be made without fail in almost every application. A sufficient condition under which problem (5) is not defective is that the eigenvalues be distinct. However, this is only a sufficient and not a necessary condition. In addition, the eigenvalue problem (5) is not defective if and only if its adjoint problem (6) is not defective. Henceforth, without practical loss of generality, it will be assumed that a linear nonconservative system is not degenerate or defective.

Corresponding to each eigenvalue λ_i , an eigenvector u_i can be found such that

$$Cu_i = \lambda_i Au_i. \quad (7)$$

Likewise, a solution to the adjoint eigenvalue problem associated with the eigenvalue λ_j is expressed by

$$C^T v_j = \lambda_j A^T v_j. \quad (8)$$

Note that each column vector u_i or v_j is undetermined to the extent of an arbitrary multiplicative constant. Transpose the above equation to obtain

$$v_j^T C = \lambda_j v_j^T A. \quad (9)$$

Premultiply Eq. (7) by v_j^T and postmultiply Eq. (9) by u_i . It follows by subtraction that

$$(\lambda_i - \lambda_j)v_j^T Au_i = 0. \quad (10)$$

Provided $\lambda_i \neq \lambda_j$, the eigenvectors u_i and v_j are orthogonal, with A playing the role of a weighting matrix. Thus, the two sets of column vectors u_i and v_j are biorthogonal with respect to A if the corresponding eigenvalues are distinct. Extension to include repeated eigenvalues becomes necessary at this stage.

Suppose λ_k is a repeated eigenvalue of multiplicity m . Since the linear system under consideration is not defective, there are m -independent ordinary eigenvectors u_k and m independent adjoint eigenvectors v_k associated with λ_k . These m ordinary eigenvectors u_k are biorthogonal to the other $n - m$ adjoint eigenvectors not connected with λ_k but, in general, are not biorthogonal to v_k . One can biorthogonalize these two sets of eigenvectors by taking them in certain linear combinations, in much the same fashion as an orthogonalization process. The slight difference in procedure may be briefly explained as follows. Let G and H be m -dimensional linear subspaces spanned respectively by u_k and v_k . Choose any vector u_k^1 in G . Generate a vector v_k^1 in H orthogonal to u_k^1 with respect to A . This completes the first step. Next, construct a vector u_k^2 in G which is orthogonal to v_k^1 . Generate a vector v_k^2 in H orthogonal to u_k^1 and u_k^2 . This completes the second step. Clearly, the procedure is inductive. In the i th step, u_k^i is constructed in G such that it is orthogonal to $v_k^1, v_k^2, \dots, v_k^{i-1}$ with respect to A . In addition, v_k^i is generated in H such that it is orthogonal to $u_k^1, u_k^2, \dots, u_k^i$. After m steps, two sets of biorthogonal eigenvectors u_k^i, v_k^i ($i = 1, 2, \dots, m$) are obtained. However, biorthogonalization need not generate unique resultant vectors. An analogous situa-

tion arises in classical modal analysis of symmetric and definite systems. There, positive definiteness of the mass matrix M ensures the system is not inertially degenerate, and symmetry of M and K ensures the system is not defective. In the case of repeated frequencies, the modal matrix can only be obtained by orthogonalizing the independent eigenvectors associated with each repeated frequency (Meirovitch, 1967). Orthogonalization need not produce unique resultant vectors. Should there be a repeated frequency, the modal matrix is not unique. But one modal matrix can be obtained from another through an orthogonal transformation.

Based on the above clarification, a biorthogonality relation between the eigenvectors u_i and v_j holds whether or not there are repeated eigenvalues. Normalization of these eigenvectors leads to

$$v_j^T A u_i = \delta_{ij}, \quad i, j = 1, 2, \dots, n. \quad (11)$$

Note that each eigenvector u_i and its adjoint eigenvector v_i are still determined within an arbitrary multiplicative constant. If the multiplier for u_i is a_i and that for v_i is b_i , the above equation determines only the product $a_i b_i$. In other words, the choice of either a_i or b_i separately is still arbitrary. The above relation implies, in addition, that

$$v_j^T C u_i = \lambda_i \delta_{ij}, \quad i, j = 1, 2, \dots, n. \quad (12)$$

Define the following square matrices of order n by

$$U = [u_1, u_2, \dots, u_n], \quad (13)$$

$$V = [v_1, v_2, \dots, v_n]^T, \quad (14)$$

$$\Lambda = \text{diag} [\lambda_1, \lambda_2, \dots, \lambda_n]. \quad (15)$$

The biorthogonality relations (11) and (12) can now be expressed in a compact form:

$$V A U = I, \quad (16)$$

$$V C U = \Lambda. \quad (17)$$

Let $q = Up$. Equation (3) may be simplified to

$$\ddot{p} + \Lambda p = V f(t), \quad (18)$$

which represents a completely decoupled system. Needless to emphasize, the solution of a decoupled system is immediate. The following statement has been established.

Theorem 1. An undamped nongyroscopic system that is not degenerate or defective can always be decoupled by equivalence transformation.

The decoupling equivalence transformation is defined by two adjoint eigenvalue problems (5) and (6). It will be proved in a subsequent section that any other equivalence transformation that decouples system (3) must be derivable from these eigenvalue problems. As explained earlier, the decoupling transformation is uniquely determined within arbitrary multiplicative constants in the eigenvectors u_i and v_j if the associated eigenvalues are distinct. The complex eigenvectors u_i and v_j may be termed modes and adjoint modes, respectively. In the case of repeated eigenvalues, the decoupling transformation is not unique.

For a symmetric and definite system, Eq. (5) takes the form

$$K u = \lambda M u, \quad (19)$$

leading to classical normal modes and natural frequencies. Due to symmetry of M and K , Eqs. (5) and (6) are identical and solution of only one of them is sufficient. The modes and adjoint modes are equal and $V = U^T$. Thus, *the decoupling equivalence transformation reduces to classical modal transformation if the coefficient matrices possess symmetry and definiteness.* The method of equivalence transformation represents a direct exten-

sion of classical modal analysis, and *the lack of symmetry in a system only approximately doubles the computational effort.*

The meanings of natural frequencies and normal modes of a nonconservative system can now be clarified. According to Theorem 1, it is legitimate to write the equation of an undamped nongyroscopic system in the form (18). For *free vibration*, in which $f(t) = 0$, the coordinate p admits a harmonic solution if and only if $\lambda_i > 0$ ($i = 1, 2, \dots, n$). Let $\lambda_i = \omega_i^2$, where each ω_i is real and positive. A component p_i of the vector p then has the solution

$$p_i = c_i \cos(\omega_i t - \phi_i), \quad i = 1, 2, \dots, n. \quad (20)$$

The real constants c_i and ϕ_i can be identified as amplitude and phase angle. Bearing in mind that $q = Up$, one obtains

$$q = \sum_{i=1}^n c_i u_i \cos(\omega_i t - \phi_i). \quad (21)$$

In an undamped nongyroscopic system, the eigenvectors u_i are generally complex. However, for each real eigenvalue λ_i of the eigenvalue problem (5), the corresponding eigenvector u_i can be chosen to be real. Thus Eq. (21) implies that in harmonic motion with a specified natural frequency ω_i , all components also vibrate with identical phase angle ϕ_i . Amplitudes of vibration of the components are proportional to the magnitudes of elements in u_i . For this reason, each eigenvector u_i determines a mode shape, in analogy to classical modal vibration. The general response in free vibration is then the superposition of n harmonic motions of this kind. Validity of the following statement has therefore been demonstrated.

Theorem 2. All components of an undamped nongyroscopic system can perform harmonic vibration with identical frequency and phase angle if the associated eigenvalue problem (5) possesses positive eigenvalues.

The natural frequencies of free vibration are simply the square roots of these positive eigenvalues. From a strictly mathematical viewpoint, the modes u_i are still not the same as classical normal modes when the corresponding eigenvalues are all positive. Classical normal modes of a symmetric and definite system are orthogonal to each other with respect to the coefficient matrices M and K . By contrast, the modes u_i and adjoint modes v_j of a nonconservative system are biorthogonal with respect to the coefficient matrices A and C . The eigenvalue problem (5) is self-adjoint if and only if $u_i = v_i$ ($i = 1, 2, \dots, n$), with equality determined within an arbitrary multiplicative constant. As a consequence, a linear nonconservative system possesses classical normal modes when the associated eigenvalue problem (5) is self-adjoint with positive eigenvalues. These restrictions are only slightly more general than requiring the system to be symmetric and positive definite. In other words, the use of two sets of adjoint modes u_i and v_j is indeed necessary for treating nonconservative systems.

3 General Nonconservative Vibrations

In classical modal analysis of a viscously damped symmetric system, the modal matrix diagonalizes the mass matrix M and stiffness matrix K but, in general, will not diagonalize the damping matrix D . Caughey and O'Kelly (1965) showed that D can be diagonalized by the modal matrix if and only if $M^{-1}D$ and $M^{-1}K$ commute in multiplication. In other words,

$$D M^{-1} K = K M^{-1} D \quad (22)$$

is a necessary and sufficient condition for the modal transformation to completely decouple a damped symmetric and definite system. Condition (22) is not usually satisfied. A common procedure in this case is to ignore the off-diagonal elements in the transformed damping matrix, especially when these elements are small. This procedure is termed the decoupling approxima-

tion in damping, which allows modal transformation to decouple an entire system. In addition, an iterative scheme can be used to improve the accuracy of approximate solution if the off-diagonal elements in the transformed damping matrix are not small. A discussion of this aspect was given by Udewadia and Esfandiari (1990) as well as Hwang and Ma (1993). Practically speaking, there is no objection to using the decoupling approximation in damping. But, as reviewed by Park et al. (1994), rigorous analysis of errors committed by such an approximation has not been reported in the open literature.

A similar situation arises in the analysis of linear nonconservative vibrations. Referring to Eq. (1), an equivalence transformation diagonalizes A and C . As before, let this equivalence transformation be defined by the two nonsingular matrices U and V . Recall $q = Up$. Equation (1) may be expressed in the form

$$\ddot{p} + VBUp + \Lambda p = Vf(t). \quad (23)$$

The transformed coefficient matrix of velocity VBU is in general not diagonal. That means the entire nonconservative system is not decoupled by equivalence transformation. Clearly, an extension to the decoupling approximation in damping may be proposed. The *decoupling approximation in damping and gyroscopy* states that off-diagonal elements in VBU can be ignored if they are small. This would allow equivalence transformations to completely decouple the subclass of lightly damped and lightly gyroscopic systems. Intuitively, the errors of approximation should be small if the off-diagonal elements in VBU are small. In addition, an iterative scheme, similar to the one for symmetric and definite systems, may be applied to improve the accuracy of approximate solution if the off-diagonal elements in VBU are not small. These approximate techniques have immense practical implications. However, as in classical modal analysis, these are also points of speculation. To continue to dwell upon them would merely be distracting.

It is possible to further refine the method of equivalence transformation. The coefficient matrices A and C in nonconservative vibrations need not have the same divine rights as the symmetric matrices M and K . Sometimes it is more convenient to apply an equivalence transformation to diagonalize A and B instead. Afterwards, the entire system may be decoupled through approximating the transformed coefficient matrix of displacement by a diagonal matrix. This digression will not be pursued. Henceforth, it will be assumed that an equivalence transformation is chosen primarily to diagonalize A and C , in a fashion expounded earlier. An upshot at this stage is the following statement.

Theorem 3. The linear nonconservative system (1) can be decoupled by an equivalence transformation if and only if the matrices $A^{-1}B$ and $A^{-1}C$ commute in multiplication.

In other words, this extension of criterion (22) asserts that

$$BA^{-1}C = CA^{-1}B \quad (24)$$

is a necessary and sufficient condition for an equivalence transformation to completely decouple linear nonconservative vibrations. To prove the above statement, it will be easier if condition (24) is first recast in a more transparent form. From Eq. (16), observe that

$$A^{-1} = UV. \quad (25)$$

Condition (24) is therefore equivalent to

$$BUCV = CUVB. \quad (26)$$

Premultiply the above equation by V and postmultiply by U . This gives

$$VBUCU = VCUVBU. \quad (27)$$

Let $S = VBU$. It follows, on substitution of Eq. (17) into Eq. (27), that

$$SA = \Lambda S. \quad (28)$$

Conditions (24) and (28) are equivalent, satisfaction of one implies satisfaction of the other.

If the equivalence transformation defined by U and V decouples system (1), the matrix VBU must be diagonal. Since diagonal matrices commute in multiplication, condition (28) is satisfied. Condition (24) is therefore also satisfied.

On the other hand, assume that condition (24) is valid. Upon expansion, condition (28) is equivalent to

$$\lambda_j s_{ij} = \lambda_i s_{ij}, \quad i, j = 1, 2, \dots, n, \quad (29)$$

where s_{ij} is the ij th element of S . If all eigenvalues λ_i are distinct, the above equation implies that $s_{ij} = 0$ when $i \neq j$. That means S is diagonal, and the equivalence transformation which diagonalizes A and C decouples the entire system. If some eigenvalues are repeated, then there are only k distinct eigenvalues, with $k < n$. In this case, Eq. (29) implies that S is a block diagonal matrix:

$$S = \text{diag} [S_1, S_2, \dots, S_k]. \quad (30)$$

Each S_i is itself a square matrix whose order coincides with the multiplicity of the eigenvalue with which it associates. Remember that the equivalence transformation which diagonalizes A and C is not unique when there are repeated eigenvalues. In constructing this equivalence transformation through a biorthogonalization process, one can select the modes and adjoint modes so as to render each S_i diagonal. This completes the demonstration that condition (24) is both necessary and sufficient for system (1) to be decoupled by an equivalence transformation.

Confining to symmetric and definite systems, the above demonstration still applies if M , D , and K take the place of A , B , and C . And the necessity and sufficiency of condition (22) are established. In fact, the case of repeated eigenvalues, which was not specifically addressed by Caughey and O'Kelly (1965), can now be given an elegant presentation. Bearing in mind that $V = U^T$ for a symmetric and definite system, it is observed that $S = U^T D U$ must be symmetric. That means each matrix block S_i in Eq. (30) is symmetric. If S is not already diagonal, there exists a block orthogonal matrix

$$W = \text{diag} [W_1, W_2, \dots, W_k] \quad (31)$$

possessing the same block structure as S such that $W_i^T W_i = I$ ($i = 1, 2, \dots, k$), and each $W_i^T S_i W_i$ is diagonal (Horn and Johnson, 1985). Both U and UW possess the properties of a modal matrix. Let UW be selected as the modal matrix. Then $(UW)^T M (UW) = I$, $(UW)^T K (UW) = \Lambda$, and $(UW)^T D (UW)$ is diagonal. This presentation illustrates an additional point: *a proper choice of modal matrix, effected by orthogonal transformation, may be required when there is a repeated eigenvalue.* The last point was only explained in the past through a geometric interpretation of the symmetric eigenvalue problem (19).

Finally, assume that one is solely interested in employing similarity transformations to decouple system (1). As explained by Caughey and Ma (1993), satisfaction of condition (24) will allow a similarity transformation to diagonalize $A^{-1}B$ and $A^{-1}C$ simultaneously, provided each of the two matrices is diagonalizable by similarity transformation.

4 Discussion and Examples

The exposition of simultaneous reduction of matrices to symmetric forms by Inman (1983) provides an inspiring account of linear nonconservative vibrations. This article also draws upon a remarkable study by Fawzy and Bishop (1976). There, under more restrictive assumptions, the authors attempted to derive orthogonality relations involving all three matrices A , B , and C . As a result, their orthogonality relations contained the eigenvalues and became rather impractical. In view of Theorem

3, an equivalence transformation cannot be constructed to diagonalize A , B , and C in every case.

There are three practical implications of the method developed herein. First, this constructive method represents a direct extension of classical modal analysis and only approximately doubles the computational effort required of modal transformation. While the method is exact for an undamped nongyroscopic system, it is necessary to use some type of decoupling approximation for a general nonconservative system. Extensive simulations have indicated that the method is substantially more efficient than the Hamiltonian approach. Reduction in computational effort, particularly in the case of large-scale systems, is indeed very attractive. Second, this method appears to possess *ample physical insight*, more of which has yet to be uncovered. For instance, in the course of establishing Theorem 2, it has been pointed out that the eigenvectors u_i determine the mode shapes. Third, the method of equivalence transformations may be used to streamline computational algorithms based upon the method of weighted residuals. Many numerical techniques in this family of algorithms generate the same type of equations as (1). As an example, the collocation method leads to equations resembling that of an undamped nongyroscopic system. These numerical techniques may be greatly streamlined by utilizing equivalence transformations.

A last and yet theoretically important point is worth emphasizing: any other equivalence transformation that decouples the undamped nongyroscopic system (3) must be derivable from the adjoint eigenvalue problems (5) and (6). In essence, a general theory of decoupling by equivalence transformations has been presented. Suppose an equivalence transformation, defined by two nonsingular matrices X and Y , diagonalizes A and C simultaneously. Without loss of generality, assume that elements in X and Y have been scaled so that

$$YAX = I, \quad (32)$$

$$YCX = Z, \quad (33)$$

where $Z = \text{diag} [z_1, z_2, \dots, z_n]$. Eliminate Y from the above equations to obtain

$$CX = AXZ. \quad (34)$$

If x_i is the i th column of X , then

$$Cx_i = z_i Ax_i. \quad (35)$$

Hence z_i and x_i represent a solution to the eigenvalue problem (5). Likewise, it can be shown that the i th row of Y is a solution to the adjoint eigenvalue problem (6) associated with z_i . It is now clear that a general theory of diagonalization by equivalence transformations has indeed been given. Equivalence transformations are already the most general nonsingular linear transformations. It can therefore be stated that *no nonsingular linear transformation will ever diagonalize A , B , and C simultaneously every time*. Further research to find universal decoupling transformations will not be necessary. Equation (23) is the simplest representation of a linear nonconservative system in Lagrangian coordinate.

Two illustrative examples will be presented. These examples also address some interesting features not previously mentioned. The first example has been used by Meirovitch (1967) in description of the collocation method and the second by Caughey and Ma (1993) in simultaneous reduction of matrices to triangular forms.

Example 1. An undamped nongyroscopic system, whose equation of motion has the form (3), is defined by

$$A = \begin{bmatrix} 0.5740 & 1.3858 & 1.3858 \\ 0.7070 & 0.7070 & -0.7070 \\ 0.4620 & -0.1914 & -0.1914 \end{bmatrix}, \quad (36)$$

$$C = \begin{bmatrix} 1.3748 & 10.9440 & 25.2975 \\ 1.2625 & 2.8770 & -17.4195 \\ 0.7455 & -4.1244 & 0.8625 \end{bmatrix}. \quad (37)$$

Solution of two adjoint eigenvalue problems (5) and (6) yields, after normalization,

$$U = \begin{bmatrix} 1.0000 & 1.0000 & 0.5064 \\ -0.0272 & -1.5441 & -0.6217 \\ -0.0044 & 0.0465 & 1.0000 \end{bmatrix}, \quad (38)$$

$$V = \begin{bmatrix} 0.3310 & 0.5397 & 0.9648 \\ -0.3043 & -0.1872 & 0.6211 \\ 0.4511 & -0.6962 & 0.5164 \end{bmatrix}. \quad (39)$$

With this equivalence transformation, the system is decoupled and can be expressed in the form (18), where

$$\Lambda = \text{diag} [1.8241, 9.5561, 23.5486]. \quad (40)$$

The natural frequencies are simply the square roots of the positive eigenvalues and are 1.35, 3.09 and 4.85 radians per second. Furthermore, the modes u_i make up the columns of U . At each natural frequency, all components of the system can perform harmonic vibration with identical phase angle. Amplitudes of vibration of the components are proportional to the magnitudes of elements in u_i . However, this system still does not possess classical normal modes because the eigenvectors u_i are not orthogonal to each other with respect to A . The adjoint modes v_j constitute the rows of V . In addition to complementing biorthogonality relations, the role of the adjoint modes is to modify the generalized excitation $f(t)$.

The coefficient matrices A and C do not commute in multiplication. For this reason, they cannot be diagonalized at the same time by similarity transformation (Horn and Johnson, 1985). In addition, it can be verified that A and C cannot be reduced simultaneously to symmetric forms by similarity transformation. However, as discussed by Meirovitch (1967), the system under consideration can be decoupled by first reducing it to a simple eigenvalue problem associated with the matrix $C^{-1}A$. Suppose a similarity transformation, defined by a matrix P , is subsequently used to diagonalize $C^{-1}A$. In recasting the equation of motion, it would become necessary to determine the modified excitation $P^{-1}C^{-1}f(t)$. Therefore, implicit or explicit computation of both C^{-1} and P^{-1} as well as their product would be required. It appears that the method of equivalence transformation is more compact and abundant in insight. Clearly, solution by equivalence transformation in this example is substantially more efficient than the state-space approach, which involves conversion of the equation of motion into a first-order form. Computational algorithms that incorporate equivalence transformation will generally economize on both core memory and computing time.

Example 2. A nonconservative system of the form (1) is defined by

$$\begin{bmatrix} 2 & -1 \\ 1 & 0 \end{bmatrix} \begin{bmatrix} \dot{q}_1 \\ \dot{q}_2 \end{bmatrix} + \begin{bmatrix} 1 & 0 \\ 1 & 0 \end{bmatrix} \begin{bmatrix} q_1 \\ q_2 \end{bmatrix} + \begin{bmatrix} 1 & -1 \\ 0 & 0 \end{bmatrix} \begin{bmatrix} q_1 \\ q_2 \end{bmatrix} = \begin{bmatrix} f_1(t) \\ f_2(t) \end{bmatrix}. \quad (41)$$

This system can be reduced to the form (23) by using an equivalence transformation involving

$$U = \begin{bmatrix} 1 & 0 \\ 1 & 1 \end{bmatrix}, \quad V = \begin{bmatrix} 0 & 1 \\ -1 & 1 \end{bmatrix}. \quad (42)$$

Recall $q = Up$. The transformation leads to

$$\begin{bmatrix} \ddot{p}_1 \\ \dot{p}_2 \end{bmatrix} + \begin{bmatrix} 1 & 0 \\ 0 & 0 \end{bmatrix} \begin{bmatrix} \dot{p}_1 \\ \dot{p}_2 \end{bmatrix} + \begin{bmatrix} 0 & 0 \\ 0 & 1 \end{bmatrix} \begin{bmatrix} p_1 \\ p_2 \end{bmatrix} = \begin{bmatrix} f_2(t) \\ f_2(t) - f_1(t) \end{bmatrix}. \quad (43)$$

System (41) has been completely decoupled and, on expansion, gives the more transparent scalar equations:

$$\ddot{p}_1 + \dot{p}_1 = f_2(t), \quad (44)$$

$$\ddot{p}_2 + p_2 = f_2(t) - f_1(t). \quad (45)$$

According to Theorem 3, condition (24) must be satisfied. This can be verified by a simple calculation. Although the coefficient matrices A , B , and C in Eq. (41) can be diagonalized by equivalence transformation, they cannot be diagonalized by similarity transformation. Among other things, A itself is not diagonalizable by similarity transformation because there is only one eigenvector $[1, 1]^T$ associated with the repeated eigenvalue 1. In addition, the coefficient matrices A , B , and C cannot be simultaneously reduced to symmetric forms because A itself is not similar to a real symmetric matrix. If one insists on using similarity transformations, two observations can be made. First, the matrices A , B , and C generate a solvable Lie algebra. As explained by Caughey and Ma (1993), these three matrices can be reduced to upper triangular forms by a common similarity transformation. Second, each of the two matrices

$$A^{-1}B = \begin{bmatrix} 1 & 0 \\ 1 & 0 \end{bmatrix}, \quad A^{-1}C = \begin{bmatrix} 0 & 0 \\ -1 & 1 \end{bmatrix} \quad (46)$$

is diagonalizable by similarity transformation. They can be diagonalized by a common similarity transformation since they commute in multiplication. The diagonalizing similarity transformation is defined by

$$P = \begin{bmatrix} 0 & 1 \\ 1 & 1 \end{bmatrix}. \quad (47)$$

In most applications, the computation of $A^{-1}B$ and $A^{-1}C$ is not advisable. There is no guarantee that these two matrices can be further reduced. An equivalence transformation should simply be applied to diagonalize the coefficient matrices A and C . Afterwards, one can examine the transformed coefficient matrix of velocity VBU to determine if the use of decoupling approximation would require a corrective scheme. From this discussion, the power and generality of equivalence transformation over similarity transformation are clear.

5 Conclusions

Classical modal analysis has been extended so as to apply to linear nonconservative vibrations. The extension utilizes equivalence transformations in Lagrangian coordinates, and does not require conversion of the equations of motion to first-order forms. It is assumed, without practical loss of generality, that a linear nonconservative system is not degenerate or defective. That means the coefficient of acceleration A is nonsingular, and the eigenvalue problem (5) possesses a full complement of independent eigenvectors. The major results, summarized in the following, are applicable for any generalized excitation $f(t)$.

(1) An undamped nongyroscopic system that is not degenerate or defective can always be decoupled by equivalence transformation. Compared with classical modal transformation, the lack of symmetry in a system only approximately doubles the computational effort.

(2) In free vibration, all components of an undamped nongyroscopic system can perform harmonic vibration with identical frequency and phase angle if the associated eigenvalue problem (5) possesses positive eigenvalues. The natural frequencies are simply the square roots of these positive eigenvalues, and the mode shapes can be determined from the corresponding eigenvectors.

(3) The linear nonconservative system (1) can be decoupled by equivalence transformation if and only if the matrices $A^{-1}B$ and $A^{-1}C$ commute in multiplication. Similar to classical

modal analysis of a viscously damped symmetric system, it is often necessary to draw upon the decoupling approximation in damping and gyroscopy for fast solution.

(4) Any decoupling equivalence transformation must be derivable from the adjoint eigenvalue problems (5) and (6). No nonsingular linear transformation will ever diagonalize A , B , and C simultaneously in every case. Equation (23) is the simplest representation of a linear nonconservative system in Lagrangian coordinate.

Compared with the state-space approach, the method expounded herein offers substantial reduction in computational effort and ample physical insight. The method of equivalence transformations is applicable to nonsymmetric systems of any order, just as classical modal analysis is applicable to symmetric systems of arbitrary order. The tremendous power of equivalence transformation reflects its role as mathematically the most general nonsingular linear transformation. In addition, many numerical techniques involve equations resembling those of linear nonconservative vibrations. These numerical algorithms will generally economize on both core memory and computing time if the method of equivalence transformation is incorporated. Among other things, it is hoped that the present paper would point to directions along which further research efforts can be profitably made. It appears feasible, for example, to examine stability and other qualitative features of a nonconservative system with equivalence transformations. Analysis of errors committed by the decoupling approximation in damping and gyroscopy is also worthwhile in a subsequent course of investigation.

Acknowledgments

We would like to thank Prof. W. Schiehlen for highly valuable comments and for hosting the visit of one of us to Germany. Members of the Institut B für Mechanik in Stuttgart, in particular Mr. J. Haug, Prof. H. Hu, Mr. F. Melzer, and Mr. U. Petersen have provided assistance in various ways. This research has been supported in part by the Alexander von Humboldt Foundation and by the National Science Foundation under Grant No. MSS-8657619. Opinions, findings, and conclusions expressed in this paper are those of the authors and do not necessarily reflect the views of the National Science Foundation.

References

- Caughey, T. K., and Ma, F., 1993, "Complex Modes and Solvability of Nonclassical Linear Systems," *ASME JOURNAL OF APPLIED MECHANICS*, Vol. 60, pp. 26–28.
- Caughey, T. K., and O'Kelly, M. E. J., 1965, "Classical Normal Modes in Damped Linear Dynamic Systems," *ASME JOURNAL OF APPLIED MECHANICS*, Vol. 32, pp. 583–588.
- Fawzy, I., and Bishop, R. E. D., 1976, "On the Dynamics of Linear Nonconservative Systems," *Proceedings of the Royal Society of London*, Vol. A352, pp. 25–40.
- Golub, G. H., and Van Loan, C. F., 1989, *Matrix Computations*, 2nd ed., Johns Hopkins University Press, Baltimore, p. 394.
- Horn, R. A., and Johnson, C. R., 1985, *Matrix Analysis*, Cambridge University Press, Cambridge, U.K., pp. 50, 171.
- Huseyin, K., 1978, *Vibrations and Stability of Multiple Parameter Systems*, Noordhoff, Alphen aan den Rijn, The Netherlands, pp. 91, 106, 171.
- Huseyin, K., and Leipholz, H. H. E., 1973, "Divergence Instability of Multiple-Parameter Circulatory Systems," *Quarterly of Applied Mathematics*, Vol. 31, pp. 185–197.
- Hwang, J. H., and Ma, F., 1993, "On the Approximate Solution of Nonclassically Damped Linear Systems," *ASME JOURNAL OF APPLIED MECHANICS*, Vol. 60, pp. 695–701.
- Inman, D. J., 1983, "Dynamics of Asymmetric Nonconservative Systems," *ASME JOURNAL OF APPLIED MECHANICS*, Vol. 50, pp. 199–203.
- Meirovitch, L., 1967, *Analytical Methods in Vibrations*, MacMillan, New York, pp. 89, 239.
- Müller, P. C., and Schiehlen, W. O., 1985, *Linear Vibrations*, Martinus Nijhoff, Dordrecht, The Netherlands, p. 37.

Park, I. W., Kim, J. S., and Ma, F., 1994, "Characteristics of Modal Coupling in Nonclassically Damped Systems under Harmonic Excitation," ASME JOURNAL OF APPLIED MECHANICS, Vol. 61, pp. 77–83.

Schmitz, P. D., 1973, "Normal Mode Solution to the Equations of Motion of a Flexible Airplane," *Journal of Aircraft*, Vol. 10, pp. 318–320.

Soom, A., and Kim, C., 1983, "Roughness-Induced Dynamic Loading at Dry and Boundary-Lubricated Sliding Contacts," ASME *Journal of Lubrication Technology*, Vol. 105, pp. 514–517.

Soong, T. T., 1990, *Active Structural Control: Theory and Practice*, Longman, Essex, U.K., p. 8.

Udwadia, F. E., and Esfandiari, R. S., 1990, "Nonclassically Damped Dynamic Systems: An Iterative Approach," ASME JOURNAL OF APPLIED MECHANICS, Vol. 57, pp. 423–433.

Zurmühl, R., and Falk, S., 1984, *Matrizen und ihre Anwendungen*, Vol. 1, 5th ed., Springer-Verlag, Berlin, p. 180.

On the Inverse Problem of Rectangular Plates Subjected to Elastic Impact, Part I: Method Development and Numerical Verification

Ching-Shih Yen¹

Enboa Wu²

Institute of Applied Mechanics,
National Taiwan University,
Taipei, Taiwan 106, R.O.C.

A method to identify both the impact location and the transverse impact force history from the strain responses at certain points on a rectangular plate is presented. The governing equations of the plate were obtained by applying the Reissner-Mindlin plate theory and the Rayleigh-Ritz method. The strain response was related to the impact force by solving the above equations using the eigenmode expansion method. A mutuality relationship among any pairs of strain responses was used to find the impact location without knowing in advance the impact force history. The force history was subsequently determined after the impact location was identified. The conjugate gradient method was adopted to search for the optimal impact location as well as the force history. Numerical verification was performed using randomly generated impact locations and force histories to simulate impact events. The excellent agreement showed the effectiveness and the validity of the proposed method.

1 Introduction

The dynamic response of a structure subjected to impact is among the most important phenomena of concern in both the analysis and the design stages. For the purpose of evaluation, various loading conditions are usually assumed to simulate service situations. However, what is important in practical applications also relies upon a thorough understanding of the true loading history for a structure under impact in a real service situation. Since it is still impractical to directly sense the impact force as well as the impact location, the development to find another versatile technique is, thus, valuable.

As one of the possible tools used to attack the above problem, the technique to determine the impact force from the impact responses of a structure has been proposed by many researchers. For example, Doyle (1984a, b, 1987a, b) presented his method in a series of papers to determine the impact force for beam and plate types of structures subjected to transverse impact. Strain gages were used in his experiments to sense the strain responses at selected locations on the specimens. The relationship between any measured strain response and the applied force was established based on the classical beam theory (1984a), the Timoshenko beam theory (1984b), and the classical plate theory (1987a, b). Techniques in time domain (1984a) and in frequency domain (1984b, 1987a, b) were then applied to reconstruct the force history. The location at which the force was applied had to be given in advance in his papers. Chang and Sun (1989) proposed a method to recover the dynamic

impact force by using an experimentally generated Green's function along with signal deconvolution. The benefit of their method was that the material, shape, and boundaries of the structure were all accounted for by the experimental Green's functions. Therefore, no governing equations of the structure were needed. This method was recently further improved to explicitly eliminate the Green's function in the deconvolution process (Wu et al., 1995).

Michaels and Pao (1985, 1986) applied a double iterative scheme to solve an inverse source problem for an oblique impact force on an elastic plate when the impact duration was in the order of $10 \mu\text{s}$ so that wave motions very much governed the plate response. A minimum of two receivers were required to sense the wave motions and to recover the oblique force in the time domain. Meanwhile, a modified processing algorithm was developed by Chang and Sachse (1985), who utilized the signals at a single receiver point to reconstruct an extended source in a plate. In Michaels and Pao (1985, 1986), numerical and experimental verifications were performed, respectively, to validate the proposed method, whereas only numerical results were presented in Chang and Sachse (1985). Recently, Zhu and Lu (1991) offered a time-domain method for identifying dynamic loads on a continuous system. The dynamic response at a certain point was expressed by means of the modal superposition method. An integral equation was then established to relate the response to the dynamic load, and the problem of load identification was turned into solving a Volterra integral equation of the first kind. An important factor in their work, and also in Michaels and Pao (1985, 1986) as well as Chang and Sachse (1985), was based on the assumption that the dynamic load was separable in time and spatial space. Discretization of the above integral equation by some interpolation functions could then be possible and led to the solution of the source identification problem.

What is of concern in this paper is to develop a method to identify both the impact location and the force history from the recorded strain responses at certain points on a rectangular plate. These problems were not solved in the aforementioned papers. Although in the field of acoustic emission and seismology a

¹ Presently, Associate Professor of the Department of Mechanical Engineering, Fushin Institute of Technology, Ilan, Taiwan 261 R.O.C.

² Professor, Mem. ASME. To whom all correspondence should be addressed.

Contributed by the Applied Mechanics Division of THE AMERICAN SOCIETY OF MECHANICAL ENGINEERS for publication in the ASME JOURNAL OF APPLIED MECHANICS.

Discussion on this paper should be addressed to the Technical Editor, Prof. Lewis T. Wheeler, Department of Mechanical Engineering, University of Houston, Houston, TX 77204-4792, and will be accepted until four months after final publication of the paper itself in the ASME JOURNAL OF APPLIED MECHANICS.

Manuscript received by the ASME Applied Mechanics Division, Jan. 12, 1993; final revision, May 16, 1994. Associate Technical Editor: M. E. Fournay.

useful technique to detect the source location is the arrival-time difference method (Pao, 1978), this technique is much dependent upon accuracy in determining the absolute or the relative arrival instants of the recorded primary waves. Since the received response signals in a service situation are frequently so noise-contaminated that the absolute or relative arrival instants are difficult to accurately determine, some uncertainties may thus occur. In order to overcome these problems, we develop a mutuality relationship among any pairs of strain responses to find the source location without knowing in advance the impact force history. The force history is then determined after the impact location is identified. In this paper, optimization methods are employed to search for both the impact location and the force history. Numerical verifications using randomly generated impact locations and force histories to simulate impact events are performed to verify the proposed method.

In Part 2 of this investigation, the method is further verified by conducting impact experiments on a rectangular aluminum plate. Also, in addition to the identification of both the impact location and the force history, a method is developed to determine the mass as well as the initial velocity of a striking object by which the impact is induced. Lastly, the inverse problem using incomplete response signals as the given data is investigated.

2 Equations of Motion

Only isotropic plates were considered in this study. The governing equations of motion of the rectangular plate were derived by applying the Reissner-Mindlin plate theory and the Rayleigh-Ritz method (cf., Cairns and Lagace, 1989; Qian and Swanson, 1990). Three independent variables for the displacements are presented by series of products of beam functions as

$$\begin{aligned} u_1(x, y, z, t) &= z\bar{\alpha}(x, y, t) = z \sum_i \sum_j \alpha_{ij}(t) \xi'_i(x) \eta_j(y) \\ u_2(x, y, z, t) &= z\bar{\beta}(x, y, t) = z \sum_i \sum_j \beta_{ij}(t) \xi_i(x) \eta'_j(y) \\ u_3(x, y, z, t) &= w(x, y, t) = \sum_i \sum_j w_{ij}(t) \xi_i(x) \eta_j(y) \quad (1) \end{aligned}$$

where u_1 , u_2 , and u_3 are the displacement components in the x , y , and z directions, respectively; $\xi_i(x)$ and $\eta_j(y)$ are the normal modes of beams under appropriate boundary conditions (Blevins, 1979); α_{ij} , β_{ij} , and w_{ij} are the corresponding modal amplitudes; and ()' denotes a spatial derivative.

Throughout the study in this paper, only thin plates are considered. Thus, the rotary inertia effects is considered to be negligible and the kinetic energy of the plate is given by

$$T = \frac{\rho h}{2} \int_0^b \int_0^a w^2 dx dy \quad (2)$$

where ρ , h , a and b are density, thickness, and in-plane dimensions in the x and y directions of the plate, respectively; and ()' denotes a derivative with respect to time. The potential energy of the plate, which is expressed as the strain energy minus the work done by the load applied in the normal direction of the plate, can be expressed as

$$\begin{aligned} V &= \frac{1}{2} \int_0^b \int_0^a \left\{ D_1 \left[\left(\frac{\partial \bar{\alpha}}{\partial x} \right)^2 + \left(\frac{\partial \bar{\beta}}{\partial y} \right)^2 \right] \right. \\ &\quad \left. + 2D_2 \left(\frac{\partial \bar{\alpha}}{\partial x} \right) \left(\frac{\partial \bar{\beta}}{\partial y} \right) + D_3 \left(\frac{\partial \bar{\beta}}{\partial y} + \frac{\partial \bar{\alpha}}{\partial x} \right)^2 \right\} dx dy \end{aligned}$$

$$\begin{aligned} &+ \frac{\kappa}{2} \int_0^b \int_0^a D_4 \left\{ \left(\bar{\beta} + \frac{\partial w}{\partial y} \right)^2 + \left(\bar{\alpha} + \frac{\partial w}{\partial x} \right)^2 \right\} dx dy \\ &- \int_0^b \int_0^a p(x, y, t) w(x, y, t) dx dy. \quad (3) \end{aligned}$$

Note that

$$\begin{aligned} D_1 &= \frac{Eh^3}{12(1-\nu^2)}, \quad D_2 = \frac{\nu Eh^3}{12(1-\nu^2)} \\ D_3 &= \frac{Eh^3}{24(1+\nu)}, \quad D_4 = \frac{Eh}{2(1+\nu)} \end{aligned}$$

where E and ν are Young's modulus and Poisson's ratio, respectively, and κ is the shearing correction factor. In this study κ was taken as $\frac{5}{6}$. The Lagrangian L , by definition, is given by $T - V$. Consequently, using the Hamilton's principle of

$$\delta \int_{t_1}^{t_2} L dt = 0 \quad (4)$$

three sets of equations of motion of the plate with unknowns α_{ij} , β_{ij} , and w_{ij} can be obtained. They are in the form of

$$\begin{bmatrix} 0 & 0 \\ 0 & M_{22} \end{bmatrix} \begin{Bmatrix} \ddot{q}_1 \\ \ddot{q}_2 \end{Bmatrix} + \begin{bmatrix} K_{11} & K_{12} \\ K_{21} & K_{22} \end{bmatrix} \begin{Bmatrix} q_1 \\ q_2 \end{Bmatrix} = \begin{Bmatrix} 0 \\ P_2 \end{Bmatrix} \quad (5)$$

where $\{q_1\}$ is a column vector containing α_{ij} and β_{ij} , and $\{q_2\}$ is a column vector composed of w_{ij} . The mass matrix $[M_{22}]$ is a diagonal matrix due to the orthogonality characteristics of the beam functions. On the other hand, the components of the stiffness matrix, $[K_{ij}]$, are obtained by integrating the corresponding assumed functions and their derivatives over the plate surface. These integrations can be performed exactly for the functions shown in Eq. (1). A static condensation scheme is then applied to Eq. (5) and results in

$$[M_{22}]\{\ddot{q}_2\} + [K_{22}^*]\{q_2\} = \{P_2\} \quad (6)$$

$$\{q_1\} = -[K_{11}]^{-1}[K_{12}]\{q_2\} \quad (7)$$

and

$$[K_{22}^*] = [K_{22}] - [K_{12}]^T [K_{11}]^{-1} [K_{12}]$$

where ()^T means transpose of the associated matrix. By assuming the time-varying forcing function, $p(x, y, t)$, to be applied transversely at (x_0, y_0) of the plate, the corresponding vector, $\{P_2\}$, on the right-hand side of Eq. (6), can be expressed by

$$\begin{aligned} \{P_2\}^T &= p(t) \{ \xi_1 \eta_1, \xi_1 \eta_2, \dots, \xi_2 \eta_1, \dots \}_{(x_0, y_0)} \\ &= p(t) \{Y\}. \quad (8) \end{aligned}$$

With the above derivation, the dynamic equations of the plate have been obtained in their final form as in Eqs. (6) and (7).

There are many techniques available to solve Eq. (6) for $\{q_2\}$. Among these, the eigenmode expansion method (cf., Craig, 1981) can be used to relate the response to the applied load in an explicit form, and is employed in this study. As shown in the following paragraph, this explicit expression is convenient for the implementation of an inverse problem. Let Eq. (6) be of rank L , and $\omega_1, \omega_2, \dots, \omega_L$ and $\{e_1\}, \{e_2\}, \dots, \{e_L\}$ be, respectively, the eigenvalues and eigenvectors of the associated homogeneous equations; the unknown vector $\{q_2\}$ can be expressed by linear superposition of $\{e_j\}$'s as

$$\{q_2\} = \sum_{j=1}^L a_j \{e_j\} = [X]\{a\}. \quad (9)$$

In the above equation, each a_j is a function of time and can be obtained by solving each of the uncoupled equations as follows:

$$m_j \ddot{a}_j + k_j a_j = p(t) (\{e_j\}^T \{Y\}), \quad j = 1, 2, \dots, L \quad (10)$$

where

$$m_j = \{e_j\}^T [M_{22}] \{e_j\}$$

$$k_j = m_j \omega_j^2.$$

Under the trivial initial conditions, Eq. (10) can easily be solved to obtain

$$a_j(t) = \frac{\{e_j\}^T \{Y\}}{m_j} \int_0^t p(t-\tau) s_j(\tau) d\tau \quad (11)$$

where

$$s_j(t) = \begin{cases} \frac{\sin(\omega_j t)}{\omega_j} & \text{if } \omega_j \neq 0 \\ t & \text{if } \omega_j = 0. \end{cases}$$

Thus, the modal amplitude w_{ij} , contained in vector $\{q_2\}$, can be obtained by using Eq. (9), and the values of α_{ij} and β_{ij} can be determined by substituting the results into Eq. (7). Consequently, the dynamic response of the plate can be expressed in terms of these modal amplitudes. For example, the strain response at a certain point, (x_1, y_1) , on the surface of $z = -h/2$ can be expressed in the form of a convolution integral:

$$\epsilon_{\xi\zeta}(x_1, y_1, h/2, t) = \int_0^t p(t-\tau) G^{(\xi)}(x_1, y_1, \tau; x_0, y_0) d\tau \quad (12)$$

where ξ represents x or y . The Green's function, $G^{(\xi)}(x_1, y_1, \tau; x_0, y_0)$, which means the transient strain response at (x_1, y_1) by a unit impulse force applied at (x_0, y_0) through an elapsed time of length τ , is in the form of

$$G^{(\xi)}(x_1, y_1, t; x_0, y_0) = \frac{h}{2} \sum_{j=1}^L \frac{(\{\Gamma_\xi\}^T [K_{11}]^{-1} [K_{12}] \{e_j\}) (\{e_j\}^T \{Y\})}{m_j} s_j(t) \quad (13)$$

Also,

$$\{\Gamma_x\}^T = \{\xi_1'' \eta_1, \xi_1'' \eta_2, \dots, \xi_1'' \eta_{N_2},$$

$$\xi_2'' \eta_1, \dots, \eta_{N_1}'' \eta_{N_2}, 0, 0, \dots, 0\}_{(x_1, y_1)}$$

$$\{\Gamma_y\}^T = \{0, 0, \dots, 0, \xi_1 \eta_1',$$

$$\xi_1 \eta_2', \dots, \xi_1 \eta_{N_2}', \xi_2 \eta_1', \dots, \xi_{N_1} \eta_{N_2}'\}_{(x_1, y_1)}$$

Note that N_1 and N_2 are the number of beam functions employed in the x and y directions, respectively; $\{\Gamma_\xi\}$ contains $2N_1 N_2$ components; and L is equal to $N_1 N_2$.

Thus, giving the forcing function and the location where the force is applied in Eq. (12), one can find the strain response at any position of the plate. This is called the forward problem. On the other hand, the inverse problem investigated in this paper is to use the impact-induced strain responses at certain points on the plate to recover the impact location as well as the force history. Assuming that there are a total of N (≥ 2) strain responses recorded at (x_1, y_1) , (x_2, y_2) , \dots , (x_N, y_N) , then N equations, each in the form of Eq. (12), can be established. The aforementioned problem is, thus, equivalent to solving these equations for the forcing function, $p(t)$, and the location, $(x_0,$

$y_0)$. To the authors' knowledge, an analytical solution is still not available for such a problem. To search for an approximate numerical solution, the convolution integral in the time domain is discretized here. By separating the whole concerned time period into n equally spaced intervals and by performing necessary manipulations, Eq. (12) is transformed into the following system of algebraic equations:

$$\begin{Bmatrix} r_1 \\ r_2 \\ r_3 \\ \vdots \\ r_n \end{Bmatrix}_{(k)} = \begin{bmatrix} G_1 & & & & \\ G_2 & G_1 & & & \\ G_3 & G_2 & G_1 & & \\ \vdots & \vdots & \vdots & \ddots & \\ G_n & G_{n-1} & G_{n-2} & \cdots & G_1 \end{bmatrix}_{(k)} \begin{Bmatrix} p_1 \\ p_2 \\ p_3 \\ \vdots \\ p_n \end{Bmatrix} \quad (14)$$

or expressed as

$$R_{(k)} = G_{(k)} P \quad k = 1, 2, \dots, N \quad (15)$$

where r_j and p_j are quantities of the strain and the impact force at time $t = j\Delta t$, respectively; Δt is the discretized time interval; and G_j is in the form of Eq. (A3) in the Appendix. The notation (k) indicates the quantity related to the k th sensor. Note that both $R_{(k)}$ and P are n -component vectors, and $G_{(k)}$ is an n by n matrix and is usually ill-conditioned (Rust and Burrus, 1972). All the elements in the upper triangular part of $G_{(k)}$ are zero and are not shown in Eq. (14). The special form of the Green's function matrix reflects the characteristic of the convolution integral.

3 Location Identification

If $k = i$ and $k = j$ are substituted into Eq. (15), the following equations are obtained:

$$R_{(i)} = G_{(i)} P \quad (16a)$$

$$R_{(j)} = G_{(j)} P. \quad (16b)$$

Premultiplying the above two equations by $G_{(j)}$ and $G_{(i)}$, respectively, they become

$$G_{(j)} R_{(i)} = G_{(j)} G_{(i)} P \quad (17a)$$

$$G_{(i)} R_{(j)} = G_{(i)} G_{(j)} P. \quad (17b)$$

Recalling that the convolution integral is commutative, it is easy to prove that

$$G_{(i)} G_{(j)} = G_{(j)} G_{(i)} \quad (18)$$

Thus, a mutuality relationship can be deduced from Eq. (17a), (17b), and (18) as

$$G_{(i)} R_{(j)} = G_{(j)} R_{(i)}. \quad (19)$$

This equation is simple and does not involve the force history vector, P . A similar relationship was obtained by Sachse and Ceranoglu (1979) to get $G_{(2)}$ from a known $G_{(1)}$, and by Doyle (1987a, b), although were in the frequency domain, to find $R_{(2)}$ from a known $R_{(1)}$. In their work, the location where the impact force was applied was assumed to be known.

In this paper, Eq. (19) is now used to find the impact location without actually knowing the impact force history. This is based on the following fact: Given the recorded strain responses and the locations where they are sensed, Eq. (19) is valid only when the Green's functions are evaluated using the accurate position at which the force is applied. As compared to the commonly used arrival-time difference method, this method is more reliable. This is because in the arrival-time difference method the absolute or relative arrival instants of primary waves must be known very accurately, whereas in the present method the whole response histories are used for the purpose of location detection. Thus the arrival times of primary signals are not critical. Espe-

cially when the signals are so noise-contaminated that the arrival instants cannot be clearly recognized, the proposed method is still applicable. The traditional method, however, may fail because it depends solely upon these noisy data at the very beginning stage in an impact event.

However, the complicated form of the Green's function in Eq. (13) forbids that the impact location (x_0, y_0) be determined by an analytical method. In this paper another approach is proposed, which applies the optimization technique to solve this problem approximately. An objective function is defined as

$$F(x, y) = \sum_{i=1}^N \sum_{\substack{j=1 \\ j \neq i}}^N f_{ij} \|G_{(i)}R_{(j)} - G_{(j)}R_{(i)}\|^2 \quad (20)$$

where $\|\bullet\|$ denotes a square norm of the associated vector, and f_{ij} are non-negative weighting factors to be determined. To obtain the impact location is now equivalent to finding the point (x_0, y_0) at which F is minimum. Note that at least two strain gages located asymmetrically with respect to both \bar{x} and \bar{y} axes are needed, where the original of \bar{x} and \bar{y} axes is at the plate center. The weighting factor in Eq. (20) is considered to be necessary because, if (x, y) is located on a plate boundary which is simply supported or fixed, all components of $G_{(j)}$ will be zero. Thus $F = 0$ if f_{ij} are taken to be constant in Eq. (20). As a result, all points at the boundary have minimum values in the optimization problem. Therefore, a suitable weighting factor must be selected to eliminate such a problem. In this paper, it is proposed that

$$f_{ij} = \frac{1}{\|G_{(i)}R_{(j)}\|^2} \quad (21)$$

such that $G_{(i)}R_{(j)}$ is normalized at any location.

There is another difficulty to be resolved because many local minimum locations exist within the plate domain, and what we need is the impact location at which F has the global minimum value. A strategy to resolve this problem is to find any points within the domain of attraction of the global minimum location such that an optimization process starting from these points always converges to this location. Also, if these points are located very near to the global minimum point, an important characteristic in such points is that their F -values are usually much smaller as compared to those corresponding to other points outside the domain of attraction of the global minimum location.

Thus, a simple grid generation scheme is proposed along with the aforementioned method to identify the impact location, i.e., the location at which F has the global minimum value. A typical example for the grid generation procedure is depicted in Fig. 1. By using this scheme, a set of appropriate initial grid points, denoted Generation-1, are selected first over the plate surface, and the corresponding objective functions are calculated. Optimization processes are then performed to search for the global minimum location from a number of grid points which have the smallest F -values among all the grid points calculated. As long as a converged F -value is smaller than a preset constant, the identified impact location is considered to be obtained. Otherwise, grid points belonging to the next generation are chosen and the same procedures proceed again. However, the number of total grid points must also be confined to a certain bound, even when all minima obtained do not satisfy the convergence criterion. This is because the recorded responses in a practical situation may be so noise-contaminated that, even at the real impact location, the corresponding F -value does not satisfy the convergence criterion which is too strictly set. For this latter case, the best solution, which is the one with the smallest F -value among all the obtained minima, is identified as the impact location.

During the optimization process, it is necessary to compute the gradient of the objective function by which the search direc-

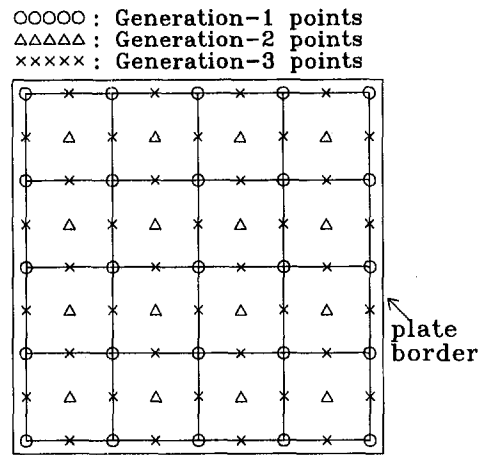


Fig. 1 Schematic of the procedure for grid point generation. In this example, 5 × 5 points were selected in generation-1. In generation-2 and 3, additional 16 and 40 points, respectively, were added.

tion can be determined. A spatial derivative of F can be obtained as

$$\frac{\partial F}{\partial \zeta} = 2 \sum_{i=1}^N \sum_{\substack{j=1 \\ j \neq i}}^N \left[\frac{(G_{(i)}R_{(j)} - G_{(j)}R_{(i)})^T \left(\frac{\partial G_{(i)}}{\partial \zeta} R_{(j)} - \frac{\partial G_{(j)}}{\partial \zeta} R_{(i)} \right)}{\|G_{(i)}R_{(j)}\|^2} - \frac{\|G_{(i)}R_{(j)} - G_{(j)}R_{(i)}\|^2 \left(\frac{\partial G_{(i)}}{\partial \zeta} R_{(j)} \right)^T (G_{(i)}R_{(j)})}{\|G_{(i)}R_{(j)}\|^4} \right] \quad (22)$$

where ζ denotes x or y . In this study the conjugate gradient method (Fletcher, 1964) was adopted to determine the sequential search directions. In general, this method has a faster convergence rate than the well-known steepest descent method. A unidirectional minimization search was then performed to locate the minimum location. In this study this was accomplished by applying a combination of the quadratic interpolation scheme and the bisection method (Fox, 1971).

4 Force Identification

Once the impact location is obtained, the Green's functions for all the recorded responses are also determined. Finding the impact force history is then equivalent to performing deconvolution of Eq. (12) to obtain the unknown forcing function, $p(t)$. The discrete form in Eq. (15), which is obtained from Eq. (12), is used again, and an error function is defined as

$$E = \sum_{j=1}^N \|G_{(j)}P - R_{(j)}\|^2. \quad (23)$$

The subject now turns into finding the forcing function, P , which minimizes E . Here, the conjugate gradient method is also adopted. For a quadratic objective function such as that in Eq. (23), it can be proved that the minimum point is always obtained within n iterations.

One may feel that the objective function defined in Eqs. (20) and (21) can be replaced using the error function in Eq. (23) to locate the impact position. In fact, this was also the authors' initial idea. But notice that the computation time spent in a deconvolution process involving n variables is in the order of n^3 , whereas only an order of n^2 is required for the evaluation

of the objective function defined by Eqs. (20) and (21). This is why the objective function different from that given by Eq. (23) is proposed in this paper to search for the impact location.

5 Numerical Verification

Problems of impact by randomly generated force histories and locations were employed to examine the validity and the effectiveness of the proposed method. A rectangular aluminum plate of $200 \times 200 \times 2$ mm in size was used and was assumed to be fixed at all edges.

The location at which the impact force was applied was randomly generated by letting

$$\begin{aligned} x_0 &= (\text{ran}) \cdot a \\ y_0 &= (\text{ran}) \cdot b \end{aligned} \quad (24)$$

where (x_0, y_0) is the impact location and (ran) is a computer-generated random number, whose range is always between 0.01 and 0.99 in this study. Also, a and b are the plate dimensions in the x and y directions, respectively. The impact force was randomly generated in the following way:

$$p(t) = \begin{cases} \sum_{j=1}^{10} C_j \sin\left(\frac{j\pi t}{T}\right) & \text{for } 0 \leq t \leq T \\ 0 & \text{for } t > T \end{cases} \quad (25)$$

where C_j s are randomly generated real numbers. Without loss of generality, a constant was multiplied by these C_j s such that the maximum value of $p(t)$ was equal to 1000 N. Here, T denotes a chosen time period and was set to be 400 μ s for all the numerical examples. On the loading surface of the plate, three strain gages, which were located at (50, 50), (150, 100) and (50, 150) mm, and were oriented in the x , x , and y directions, respectively, were used to sense the dynamic response from a "forward" calculation; i.e., to obtain the strain responses by multiplying the Green's function matrix by the force history vector at the right-hand side of Eq. (15). A time-step of 2 μ s was used for numerical discretization, and the strain responses at 250 time steps were calculated accordingly.

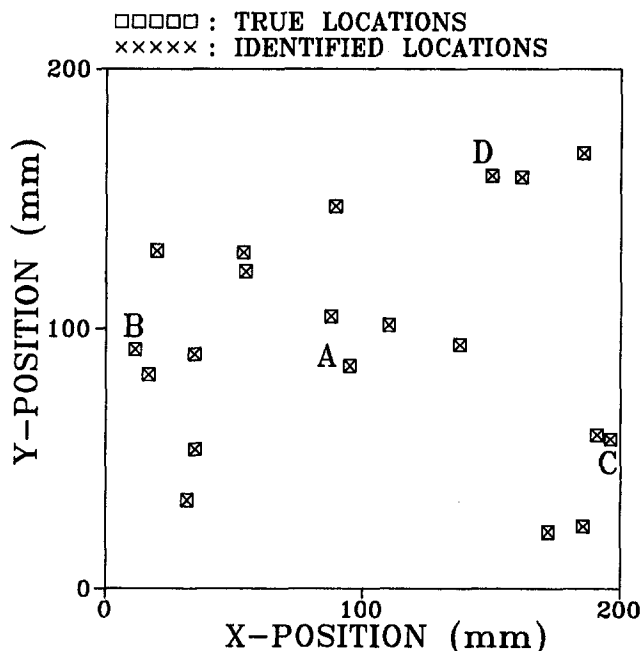


Fig. 2 Comparisons of the identified and the true impact locations for 20 numerical examples

Table 1 A typical optimization process to find the impact location

Numerical Example A		
Optimization process to find the impact location		
No. of unid. search	Temporary min. pt. (mm)	F-value
0	(100.00, 75.250)	0.37289E+01
1	(93.717, 81.676)	0.11412E+01
2	(93.477, 85.915)	0.21694E+00
3	(94.920, 86.000)	0.86594E-02
4	(95.001, 85.619)	0.27910E-09
5	(95.001, 85.619)	0.27910E-09

An inverse problem was then resolved, after the strain responses were obtained, to recover both the impact location and the force history. The Generation-1 grid points were chosen to be $9 \times 9 = 81$ for all examples. According to the procedure depicted in Fig. 1, the number of the additionally generated grid points at consecutive generations, i.e., generation-2, 3, and 4, would be 64, 144, and 256, respectively. Among the grid points of the same generation, three with the smallest objective functions were chosen as the starting points for further optimization searches. In this section, when a converged F -value was less than 0.05, the location corresponding to that F -value was identified as the impact location. Once the impact point was located, Eq. (23) was then used to search for the optimal impact force history. The conjugate gradient method was applied to detect the impact location as well as the force history.

Twenty examples were executed. Table 1 shows a typical example corresponding to "A" in Fig. 2 for locating the impact position using the optimization process. The starting point was at (100.00, 75.250) mm, and the optimal location was at (95.001, 85.619) mm. In Table 1, each temporary minimum point is where the minimal F was located along a sequential search direction. It can be found that the convergence rate was fast. Comparisons between the identified and the true impact locations for all the 20 examples are shown in Fig. 2. Excellent agreements are found. Comparisons of the identified and the true force histories for four typical examples are presented in Fig. 3. One can find that very good agreement was obtained. All other examples not shown in Fig. 3 were almost as good as that of Example A.

The above computations were conducted on a CONVEX C1 computer at the Institute of Applied Mechanics of National Taiwan University. The CPU time required for computing an F -value at a trial location was 0.258 sec, whereas an average of 17.89 sec of CPU time was needed to obtain the force history vector, P , by the deconvolution process. Note that the later is about 69 times longer than the former.

Among the 20 examples executed, the impact locations for 14 examples were identified using starting points belonging to Generation-1. The remaining six examples in which the impact locations were identified used starting points belonging to Generation-2. Also, it was found that the F -value corresponding to the identified impact location was smaller than other local minima by several orders of magnitude for all examples.

The aforementioned method has also been applied to force and location detection on composite laminates. Similar numerical tests were performed and the agreement between the identified and the true results was found to be as good as that shown in this section (Wu and Yen, 1992).

6 Conclusion

The proposed method to identify both the impact location and the transverse impact force history from the strain responses at certain points of a rectangular plate has been presented. It

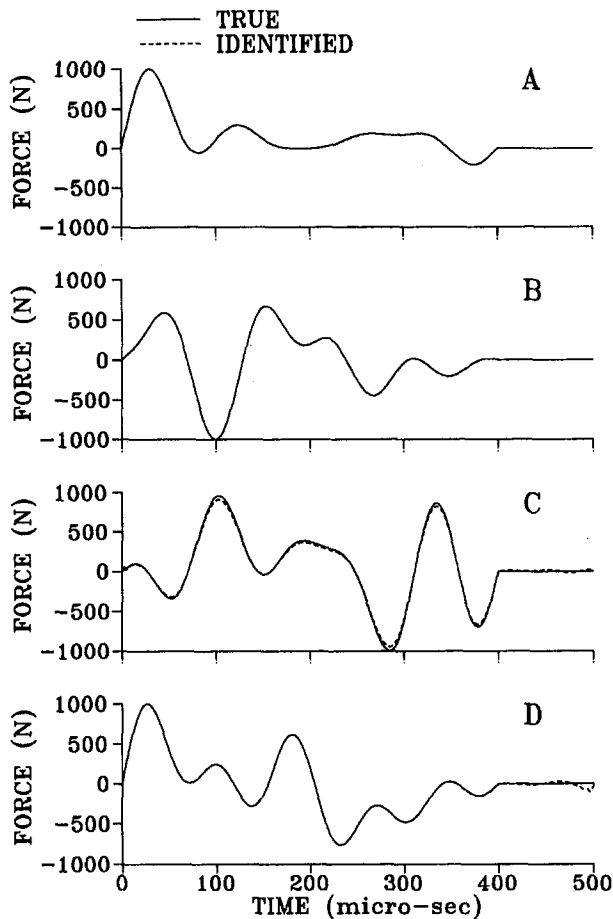


Fig. 3 Comparisons of the identified and the true force history for examples denoted by A, B, C, and D

has been shown by the results of numerical verification that the method is valid and effective. The simple mutuality relationship among any pairs of strain responses can be used to obtain the impact location without actually knowing the impact force history. The impact force history can be obtained subsequently after the impact point is located. The conjugate gradient method has been successfully employed to search for the impact location as well as the force history.

The remaining work of concern is to check the validity of the proposed methods using strain signals from real impact events, which is one of the subjects in Part 2 of this investigation.

Acknowledgments

This paper represents a portion of the doctoral dissertation of the first author written in partial fulfillment of the requirements for the PhD degree at National Taiwan University. This work was also supported by National Science Council of Taiwan, ROC, under Contract Number NSC-82-0405-E-002-086.

Reference

- Blevins, R. D., 1979, *Formulas for Natural Frequency and Mode Shape*, Van Nostrand Reinhold, London.
- Cairns, D. S., and Lagace, P. A., 1989, "Transient Response of Graphite/Epoxy and Kevlar/Epoxy Laminates Subjected to Impact," *AIAA Journal*, Vol. 27, No. 11, pp. 1590–1596.
- Chang, C., and Sachse, W., 1985, "Analysis of Elastic Wave Signals from an Extended Source in a Plate," *Journal of the Acoustical Society of America*, Vol. 77, pp. 1335–1341.
- Chang, C., and Sun, C. T., 1989, "Determining Transverse Impact Force on a Composite Laminate by Signal Deconvolution," *Experimental Mechanics*, Vol. 29, pp. 414–419.

- Craig, R. R., Jr., 1981, *Structure Dynamics*, John Wiley and Sons, New York.
- Doyle, J. F., 1984a, "An Experimental Method for Determining the Dynamic Contact Law," *Experimental Mechanics*, Vol. 24, No. 1, pp. 10–16.
- Doyle, J. F., 1984b, "Further Developments in Determining the Dynamic Contact Law," *Experimental Mechanics*, Vol. 24, No. 4, pp. 265–270.
- Doyle, J. F., 1987a, "Determining the Contact Force during the Transverse Impact of Plates," *Experimental Mechanics*, Vol. 27, No. 1, pp. 68–72.
- Doyle, J. F., 1987b, "Experimentally Determining the Contact Force during the Transverse Impact of an Orthotropic Plate," *Journal of Sound and Vibration*, Vol. 118, No. 3, pp. 441–448.
- Fletcher, R., and Reeves, C. M., 1964, "Function Minimization by Conjugate Gradients," *Computer Journal*, Vol. 7, No. 2, pp. 149–154.
- Fox, R. L., 1971, *Optimization Methods for Engineering Design*, Addison-Wesley.
- Michaels, J. E., and Pao, Y. H., 1985, "Inverse Source Problem for an Oblique Force on an Elastic Plate," *Journal of the Acoustical Society of America*, Vol. 77, pp. 2005–2011.
- Michaels, J. E., and Pao, Y. H., 1986, "Determination of Dynamic Forces from Wave Motion Measurements," *ASME JOURNAL OF APPLIED MECHANICS*, Vol. 53, pp. 61–68.
- Pao, Y. H., 1978, "Theory of Acoustic Emission," *Elastic Waves and Nondestructive Testing of Materials*, ASME AMD Vol. 29, pp. 107–128.
- Qian, Y., and Swanson, S. R., 1990, "A Comparison of Solution Techniques for Impact Response of Composite Plates," *Composite Structures*, Vol. 14, pp. 177–192.
- Rust, B. W., and Burrus, W. R., 1972, *Mathematical Programming and the Numerical Solution of Linear Equations*, Elsevier, New York.
- Sachse, W., and Ceranoglu, A. N., 1979, "Experiments with a Well Characterized Acoustic Emission System," *Ultrasonics International 1979*, Conference Proceedings, IPC Science and Technology Press, Guildford, U.K.
- Wu, E., Tsai, T. D., and Yen, C. S., 1995, "Two Methods for Determining Impact Force History on Elastic Plates," *Experimental Mechanics*, Vol. 35, pp. 11–18.
- Wu, E., and Yen, C. S., 1992, "Detection of Impact Force History and Location on a Laminated Plate," presented at 18th International Congress of Theoretical and Applied Mechanics, Haifa, Israel, Aug. 22–28.
- Zhu, J., and Lu, Z., 1991, "A Time Domain Method for Identifying Dynamic Loads on Continuous Systems," *Journal of Sound and Vibration*, Vol. 148, No. 1, pp. 137–146.

APPENDIX

In this Appendix the derivation of Eq. (14) is given. The time period in Eq. (12) is discretized into n equally spaced intervals. The applied force in each interval is approximated by linear interpolation and expressed as

$$p(\tau) = p_{j-1} + \frac{\tau - t_{j-1}}{t_j - t_{j-1}} (p_j - p_{j-1}) \quad t_{j-1} < \tau < t_j \quad (A1)$$

where

$$t_j = j\Delta t$$

$$p_j = p(t_j)$$

Δt = discretized time interval.

By substituting Eq. (A1) into Eq. (12) and performing integration, one obtains

$$\epsilon_{\zeta\zeta}(x_1, y_1, h/2, t_k) = \sum_{j=1}^k G_{k+1-j}^{(\zeta)} p_j \quad 1 \leq k \leq n \quad (A2)$$

where

$$G_1^{(\zeta)} = \frac{h}{2} \{\Gamma_{\zeta}^T [K_{11}]^{-1} [K_{12}] [X] [T] [X]^T \{Y\} \quad (A3)$$

$$G_{j+1}^{(\zeta)} = \frac{h}{2} \{\Gamma_{\zeta}^T [K_{11}]^{-1} [K_{12}] [X] [S] [X]^T \{Y\} \quad j \geq 1$$

$$[X] = [\{e_1\}, \{e_2\}, \dots, \{e_L\}]$$

$$[T] = \text{Diag} [T(1), T(2), \dots, T(L)]$$

$$[S] = \text{Diag} [S(j, 1), S(j, 2), \dots, S(j, L)].$$

At $\omega_i \neq 0$

$$\left\{ \begin{array}{l} T(i) = \frac{1}{\kappa_i} \left[1 - \frac{\sin(\omega_i \Delta t)}{\omega_i \Delta t} \right] \\ S(j, i) = \frac{1}{\kappa_i \omega_i \Delta t} [-\sin(\omega_i t_{j-1}) + 2 \sin(\omega_i t_j) \\ \quad - \sin(\omega_i t_{j+1})] \end{array} \right.$$

and at $\omega_i = 0$

$$T(i) = (\Delta t)^2 / (6m_i)$$

$$S(j, i) = j(\Delta t)^2 / m_i.$$

In the above, Diag means a diagonal matrix. Writing Eq. (A2) for $k = 1, 2, \dots, n$, a system of equations like that in Eq. (14) is then obtained.

On the Inverse Problem of Rectangular Plates Subjected to Elastic Impact, Part II: Experimental Verification and Further Applications

Ching-Shih Yen¹

Enboa Wu²

Institute of Applied Mechanics,
National Taiwan University,
Taipei, Taiwan 106, ROC

Experimental verification of the method developed in Part I to identify both the impact location and the force history from strain responses on a rectangular plate was performed. Results showed the validity of the method in a real impact event. Also, a method was developed to further identify the initial velocity and the mass of an impactor by which a transverse impact was induced. This was accomplished by solving algebraic equations obtained from the assumption that the lateral displacements of both the impactor and the plate at the impact point were coincident during the contact period. Moreover, the inverse problem using incomplete response signals as the given data was investigated. A procedure to temporarily reconstruct the lost portions of the recorded signals was first presented, and the identification problem could then be solved by similar methods as that used for the complete response signals. Experimental verification was also performed. The agreement between the measured and the identified results was very satisfactory.

1 Introduction

In Part I of this investigation (Yen and Wu, Part I), a method has been developed to identify both the impact location and the transverse impact force history from strain responses on a rectangular plate. Numerical verification of the method was performed by randomly generating the impact locations and the force histories, and then performing forward calculations to obtain the corresponding strain responses. These responses were then used as the input data for the identification purposes. Although the agreement between the true and the identified results was excellent, it is also important to know how reliable the method is when it is applied to a real impact event. That is to include the effects due to background noise, instrumentation limitation, and other operation factors, etc. Therefore, the first goal of this paper is to experimentally verify the method developed in Part I. An instrumented hammer was employed as the impactor to strike a rectangular aluminum plate where three strain gages were taped at different locations and were used to sense the strain responses.

Secondly, in addition to identification of the location and the force history, a method is developed to further determine the initial velocity and the mass of an impactor by which a transverse impact is induced. This is conducted after the location and force history are identified using the methods proposed in Part I. Then, by assuming that the lateral displacements of both the rigid impactor and the plate at the striking point are coinci-

dent during the contact period, simple algebraic equations containing the initial velocity and the mass of the impactor can be obtained. Because the system of equations are always overdetermined, the least-square method can be employed to obtain the solution.

Further, in the service condition of a structure, it is often that the initial stage of the recorded response signals of the structure during impact are missing. A typical situation is due to use of a finite triggering level in a transient recorder, in which such data missing often occurs either because the recorder is without a pretrigger function, or because the pretrigger time is not properly set. Under this circumstance the arrival-time difference method (Pao, 1978) is, in general, no longer applicable to locate the source location. In this paper, methods are developed to overcome this problem. Experiments were also conducted to verify the proposed methods.

For the sake of completeness, some equations used in this paper, which were already developed in Part I, are repeated here.

The equation derived to relate the dynamic strain response to the impact force is given by

$$\begin{Bmatrix} r_1 \\ r_2 \\ r_3 \\ \vdots \\ r_n \end{Bmatrix}_{(k)} = \begin{bmatrix} G_1 & & & & \\ G_2 & G_1 & & & \\ G_3 & G_2 & G_1 & & \\ \vdots & \vdots & \vdots & \ddots & \\ G_n & G_{n-1} & G_{n-2} & \cdots & G_1 \end{bmatrix}_{(k)} \begin{Bmatrix} p_1 \\ p_2 \\ p_3 \\ \vdots \\ p_n \end{Bmatrix} \quad (1)$$

Alternatively, it can be symbolized as

$$R_{(k)} = G_{(k)}P \quad k = 1, 2, \dots, N \quad (2)$$

where the vector on the left-hand side of the above equations represents the strain response; the vector on the right-hand side is the discrete impact force history; and the matrix which relates the former to the latter represents the Green's function. The notation (k) denotes the quantity which belongs to the k th sensor, and the total number of the sensors used for the identification purposes is N .

¹ Presently, Associate Professor of the Department of Mechanical Engineering, Fushin Institute of Technology, Ilan, Taiwan 261, ROC.

² Professor, Mem. ASME. To whom all correspondence should be addressed. Contributed by the Applied Mechanics Division of THE AMERICAN SOCIETY OF MECHANICAL ENGINEERS for publication in the ASME JOURNAL OF APPLIED MECHANICS.

Discussion on this paper should be addressed to the Technical Editor, Prof. Lewis T. Wheeler, Department of Mechanical Engineering, University of Houston, Houston, TX 77204-4792, and will be accepted until four months after final publication of the paper itself in the ASME JOURNAL OF APPLIED MECHANICS.

Manuscript received by the ASME Applied Mechanics Division, Jan. 12, 1993; final revision, May 16, 1994. Associate Technical Editor: M. E. Fourny.

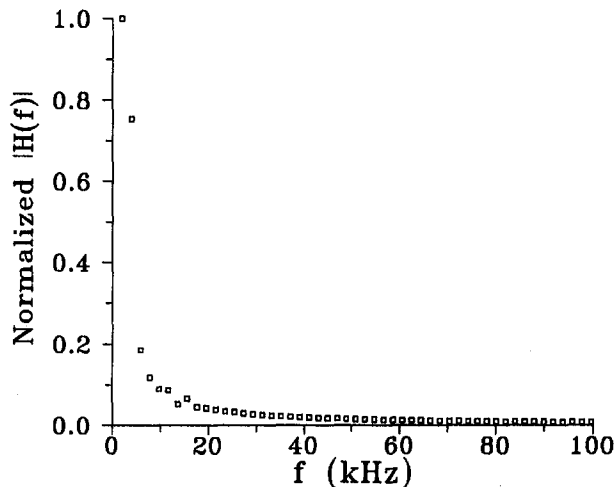


Fig. 1 Energy spectrum of a typical strain response, G2, of Experiment-1. A hammer was used as the impactor.

The objective function used to find the impact location is defined by

$$F = \sum_{i=1}^N \sum_{j=1, j \neq i}^N \frac{1}{\|G_{(i)}R_{(j)}\|^2} \|G_{(i)}R_{(j)} - G_{(j)}R_{(i)}\|^2. \quad (3)$$

The location at which the value of F is minimum corresponds to the impact point. The work to find the point where F is minimum is accomplished by the proposed grid generation scheme and the conjugate gradient method, as described in Part 1 of this investigation.

The objective function defined to find the impact force history is given by

$$E = \sum_{j=1}^N \|G_{(j)}P - R_{(j)}\|^2. \quad (4)$$

The optimal force history is obtained once the P , which minimizes the objective function, is found. In Part 1, this work is accomplished by the conjugate gradient method. Whereas in this part, the gradient projection method (Rosen, 1960; Fox, 1971), which can confine the impact force in the unilateral compressive direction, is employed to obtain the force history when response data from a real impact event are used.

2 Experimental Verification

Experiments using a 6061-T6 aluminum plate as the target were performed to examine the validity of the methods developed in Part 1 of this investigation. The Young's modulus, Poisson's ratio and the density of the plate were $E = 70$ Gpa, $\nu = 0.3$ and $\rho = 2700$ kg/m³, respectively. The target had dimensions of 141 mm \times 141 mm \times 2 mm, and was hung from two light strings at two corners to simulate the free boundary condition. On the loading surface, three strain gages (KYOWA KFG-2-350-C1-11) were taped to measure the dynamic strain responses, which were then recorded by an oscilloscope (Nicolet Company, System 460). The orientations and locations (in mm) of the three gages were $\epsilon_{xx}(40.5, 40.5)$, $\epsilon_{xx}(90.5, 70.5)$, and $\epsilon_{yy}(40.5, 100.5)$, respectively. The impact force was exerted at the target by an instrumented hammer (PCB Piezotronics Company, 086B01 SN6445, sensitivity 10.9 mV/Newton), which contained a force transducer to measure the impact force directly. The hammer had a flat head of 3 mm in diameter and the impact force exerted by this hammer was approximated as a point load.

Eight impact tests were performed. The recorded strain responses were then used to identify both the impact location and

the force history. To know how many modes must be included in the eigenmode expansion, the response signals can always be analyzed by using the fast Fourier transform method to obtain the frequency content. For example, the recorded strain response for the gage at (90.5, 70.5) mm in the first example was analyzed using an FFT program provided by Press et al. (1989). The result is shown in Fig. 1. It can be found that most of the spectrum energy was distributed in the frequencies lower than 50 kHz. Thus, the first 14 \times 14 vibration modes of the plate were employed in the computation, and the highest natural frequency was 74.95 kHz. A time-step of 4 μ s was used for the time domain discretization.

Initially, as that used in Part 1, the conjugate gradient method was applied to search for both the impact location and the optimal force history. A comparison between the identified and the measured impact force history for Example 1 is shown in Fig. 2(a). One can find that the identified results oscillate about the measured history. Negative impact force, i.e., tensile contact force between the impactor and the target, was even obtained in certain periods, which is not physically permitted in this study. As compared with the numerical results obtained in Part 1, this was mainly due to noise contained in the recorded response signals. Because the recorded response signals are always contaminated with noise to some degree, this situation was encountered in most of the identified results. In order to confine the identified force history in the unilateral compressive direction, a constrained optimization algorithm using the gradient projection method was adopted to find the optimal force history. The only constraint imposed on the optimization search was that the impact force had not to be in tension. As shown in Fig. 2(b), one can find that more reasonable results were obtained. Therefore, for all the experimental cases conducted in this study, the conjugate gradient method was used to search

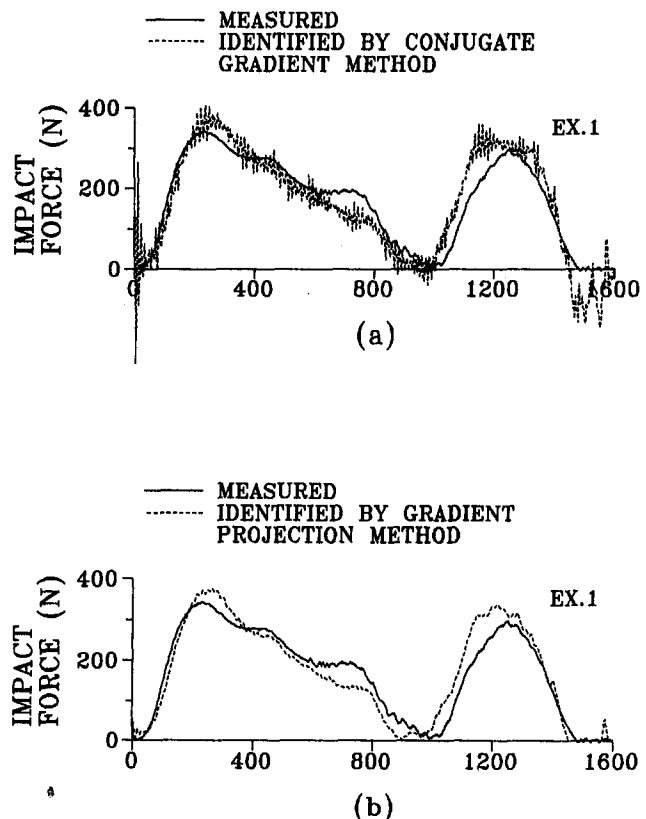


Fig. 2 The identified force history obtained by (a) the conjugate gradient method, and (b) the gradient projection method. The solid curves represent the measured forces.

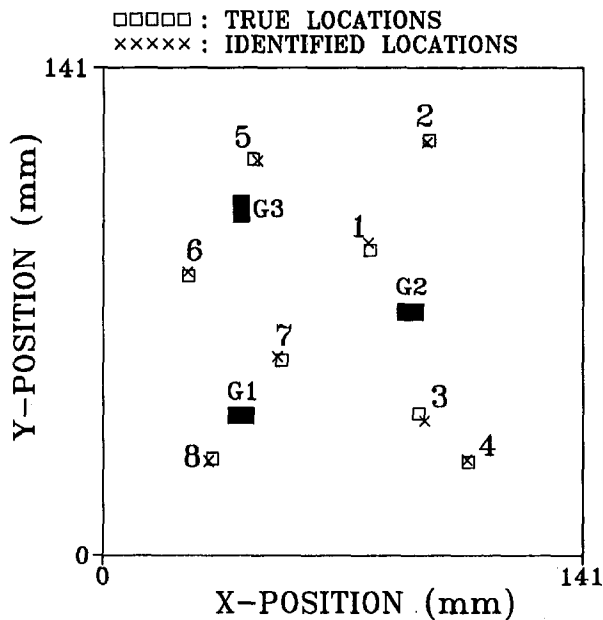


Fig. 3 Comparisons of the identified and the true impact locations for the eight examples using a hammer as the impactor. Also shown is arrangement of the strain gages for G1: $\epsilon_{xx}(40.5, 40.5)$ mm, G2: $\epsilon_{xx}(90.5, 70.5)$ mm, and G3: $\epsilon_{yy}(40.5, 100.5)$ mm.

for the impact location, and the gradient projection method was applied to identify the optimal force histories.

Comparisons of the identified and the measured impact locations for all the eight examples are shown in Fig. 3. Also shown in this figure is the arrangement of the strain gages. It can be found that good agreements were obtained. The largest deviation was 2.77 mm, which corresponded to Example 3. This value was still smaller than the 3 mm diameter of the hammer head. Comparisons of the identified and the measured impact force histories are presented in Fig. 4. The results were satisfactory for all examples. Therefore, the developed method is considered reliable for the impact location and force history detections in a real impact event.

In the above calculations, the initial grid points for detection of the impact location was 9×9 . Three grid points of the same generation corresponding to the smallest objective functions were chosen as the starting points for further optimization search. The corresponding F -values at the identified impact locations were between 0.112 (for Example 2) and 0.0178 (for Example 8). The F -values at all other local minima obtained were found to be greater than 2.0 for all examples. Therefore, there were at least one order-of-magnitude differences between the global and the local minima. In this study, an F -value smaller than 0.2 was set as the convergence criterion. Among the eight examples executed, only Example 5 used the starting point belonging to Generation-2 grid points to find the impact location. All other examples used only Generation-1 grid points. Thus, the method to find the impact location was considered to be simple and effective in real impact situations.

In this study, all received signals were only scaled by their corresponding physical units. Neither of these signals were processed by any filters, nor were the environmental noises handled with special care.

3 Identification of Mass and Velocity of a Projectile

It is well known that when a structure is hit by a foreign object, the impact force history is strongly affected by the mass and the striking velocity of the impactor. Conversely, this also reveals that the impact force history must contain the informa-

tion about what the mass and the striking velocity should be to cause such an impact event. In this section, the latter subject is investigated.

For a rigid impactor of mass, M , and at an initial velocity, v_0 , striking on a structure, the displacement, $s(t)$, can be expressed by

$$s(t) = s_0 + v_0 t - \frac{1}{M} \int_0^t (t - \tau) p(\tau) d\tau \quad (5)$$

where s_0 is the initial displacement and $p(\tau)$ is the impact force exerted on the impactor. If we let the instant displacement at the impact point of the plate be $w(t)$, which is obtained through forward calculation by exerting the identified impact force at the identified impact location, then, by assuming that the lateral displacements of both the impact point of the plate and the impactor are coincident during the contact period, the following equation can be obtained:

$$w(t) = s(t) = s_0 + v_0 t - \frac{1}{M} \int_0^t (t - \tau) p(\tau) d\tau \quad (6)$$

provided that the time, t , is within the contact period. Intuitively,

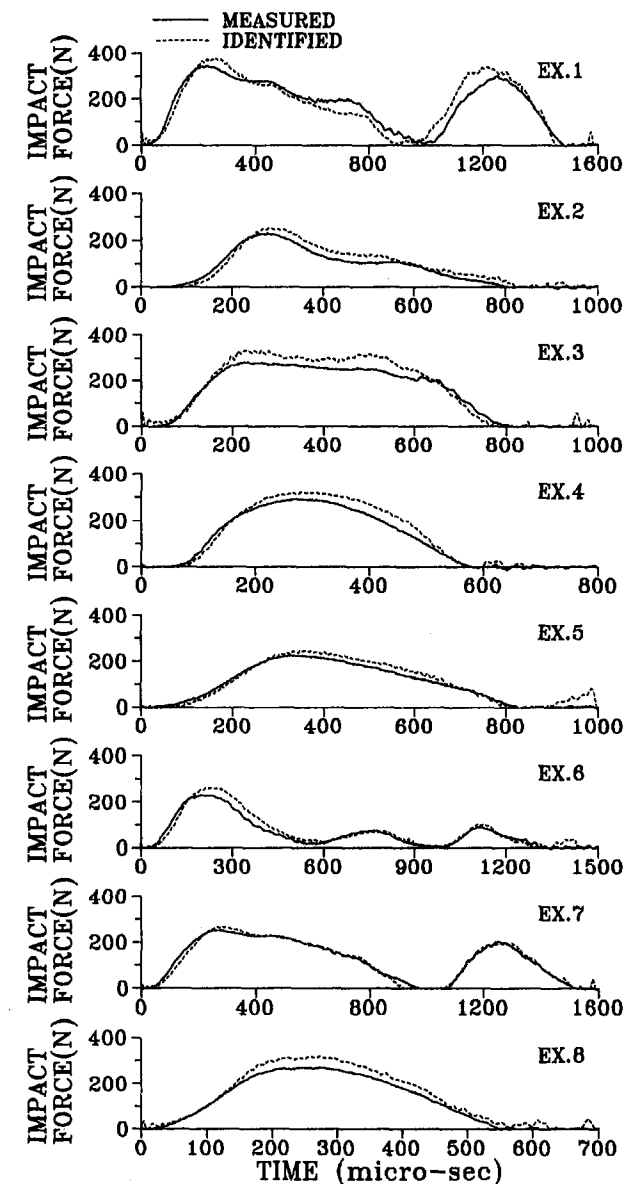


Fig. 4 Comparisons of the identified and the measured force histories for the eight examples using a hammer as the impactor

we may think that the initial displacement of the plate is zero, and s_0 should also be zero if the instant for the onset of contact is set to be $t = 0$. However, the response signals in a real impact event are usually recorded using a transient recorder with a pretrigger device, i.e., the response signals might be recorded from some instant before impact occurs. This was also the case in this study. Thus, the time $t = 0$ determined using pretriggering was actually before the onset of contact. Typical and obvious results can be found from the corresponding force histories in Fig. 4 for Examples 2, 4, and 5. Thus, the initial displacement of the impactor, s_0 , in Eq. (6), is the displacement before the onset of contact and shall be a negative value. In this study, in addition to v_0 and M , s_0 is treated as the third unknown. Note also that the identified impact force before the occurrence of impact might not be zero in this study, which was due to the existence of noise and the approximation involved in numerical calculation, as also exemplified in Fig. 4 for Examples 1, 3, and 8.

Suppose that during the contact period there are discrete time instants, $t_k = k\Delta t$, for $k = n_1, \dots, n_2$. Then, there are $(n_2 - n_1 + 1)$ equations, each in the form of Eq. (6), available to solving for the three unknowns of s_0 , v_0 , and M . Since the force, $p(\tau)$ in Eq. (6), is the identified impact force obtained in discrete form, and its distribution is approximated by linear interpolation in each time interval, the integral can easily be evaluated. By performing integration in each time interval and summing the results, Eq. (6) can be reduced to

$$w_k = s_0 + v_0 k \Delta t - \frac{\Delta t^2}{6M} \sum_{j=1}^k [(3k - 3j + 2)p_{j-1} + (3k - 3j + 1)p_j] \quad n_1 \leq k \leq n_2 \quad (7)$$

where w_k is the magnitude of w at time $t = k\Delta t$. Because the system of equations obtained are always overdetermined, these unknowns can be solved by applying the least-square method.

Two experiments were conducted. The experimental setup was similar to that in Section 2 except that the target was struck by a pendulum, instead of by a hammer. The pendulum was composed of a steel rod hung at two appropriate locations by two pairs of light strings. Each pair of strings were arranged in a V-shape to prevent the rod from yaw motion. The rod had a hemispherical head of 12.7 mm in diameter. An accelerometer

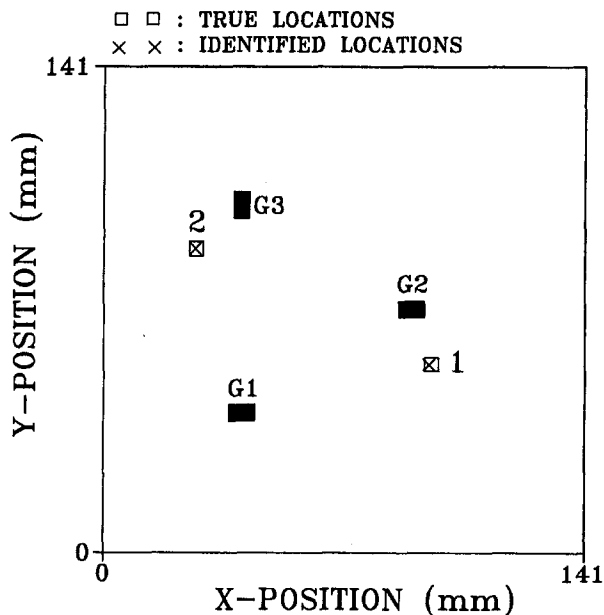


Fig. 5 Comparisons of the identified and the true impact locations for two examples using a projectile as the impactor

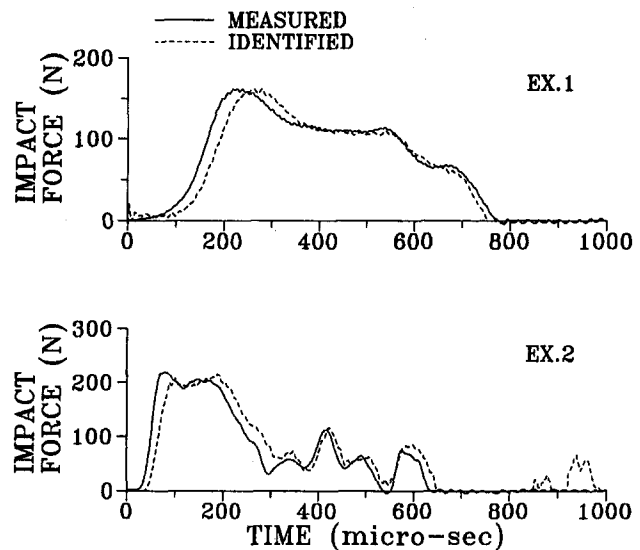


Fig. 6 Comparisons of the identified and the measured force histories for the two examples using a projectile as the impactor

(PCB Piezotronics company, 303A02 SN23823, sensitivity 11.6 mv/g) was screwed at the tail of the rod to measure the acceleration history of the impactor. Under the approximation that the steel impactor was rigid, the impact force could be obtained by multiplying the acceleration of the impactor by its mass. The arrangement of the strain gages was the same as before.

Comparisons of the identified and the measured impact locations as well as the impact force histories are shown in Figs. 5 and 6, respectively. One can find that very good agreements were obtained, especially for the location identification. The identified impact forces in Fig. 6 were then used to find the displacement responses at the identified impact locations. The displacements obtained are shown in Fig. 7 for both test cases. A time-step of $4 \mu s$ was used in the above numerical calculation. Then, the force and displacement data in the time intervals between 200 to 700 μs and 100 to 500 μs , respectively, were applied to find the masses, initial velocities, and initial displacements for these two tests. The time intervals taken in the above calculation were based on a conservative estimation that contact

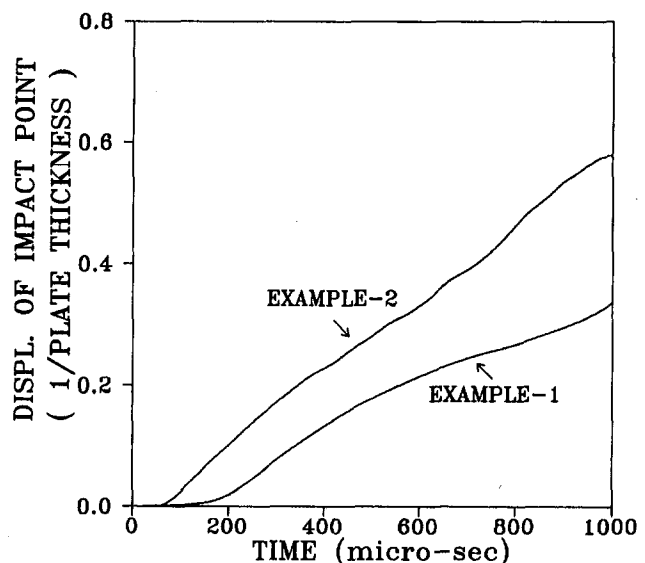


Fig. 7 Displacement histories at the identified impact locations for the two examples using a projectile as the impactor

Table 1 Identified mass and initial velocity of the projectile

Identified mass and initial velocity:

Example	Mass (g)			Initial Velocity (m/sec)		
	true	identified	error	true	identified	error
1.	64.4	69.6	+8.1%	1.58	1.46	-7.6%
2.	64.4	59.0	-8.4%	1.79	1.92	+7.3%

between the impactor and the target was sure to happen during these intervals. The computation results are listed in Table 1. Also shown in this table are the true values. The errors were found to be less than nine percent for both the identified masses and initial velocities in both cases. The results were considered to be satisfactory.

4 Identification Using Incomplete Response Signals

Force Identification. When the impact location is known a priori and only the impact force is of interest, the method is very simple. If the recorded signals from r_1 to r_m ($m < n$) in Eq. (1) are lost, there are only $(n - m)$ equations; whereas the unknown discrete force variables are still P_1 to P_n . Equation (1) is not solvable if the plate response from only one gage is used. However, if there are N gages used, and if

$$N(n - m) \geq n \tag{8}$$

holds, the objective function defined in Eq. (4) can still be applied to identify the impact force history, except that the total available equations are now $N(n - m)$. The optimization method used in the preceding sections can thus be applied to find the optimal force history. Because the procedure is very similar to that for the complete plate responses, no example is illustrated.

Location and Force Identification. When both the impact location and the force history are to be identified, the problem becomes more complicated. Recalling that the objective function in Eq. (3) has to be evaluated for complete response signals of $R_{(i)}$ and $R_{(j)}$, $i, j = 1, \dots, N$, this equation can not be used

directly when the first m discrete signals recorded from plate motion are missing. To overcome this problem, the lost signals are first temporarily "reconstructed." The grid points based on the method illustrated in Part 1 of this investigation are still used as the trial impact locations. The "impact force history," which is assumed to be applied at each of the grid points, is then recovered by the method illustrated in the above subsection. The corresponding lost response signals can then be computed from a forward calculation once this impact force history is obtained. Consequently, the objective function, F , in Eq. (3) can be evaluated because the response signals are now complete. Since in this way, the lost signals may not be reconstructed at the true impact location, the objection function, F , obtained corresponding to each grid point is in general not the same as that associated with the complete response signals. However, this does not influence the search of the true impact location since the global minimum value of F will still be obtained when the lost signals are reconstructed at the true impact location.

But it is valuable to note that the computation time in the deconvolution process to find the force history is in the order of n^3 . Thus, this method may soon become infeasible when the total number of the discrete signals is large. However, because the lost signals at the beginning stage in an impact event are usually of a short period and because multiple gages are used, one only needs to recover the force of sufficient duration so that the corresponding lost response signals can be reconstructed. For example, if the strain signals obtained from N gages at the time t_1 to t_m are missing, it is only required to identify the force history using the signals at time t_{m+1} to t_{m+k} as long as the following inequality holds:

$$Nk \geq m + k. \tag{9}$$

Thus, the corresponding discrete impact force history, p_i , $i = 1, \dots, m + k$, which acts at each trial grid point, can be obtained through deconvolution and, subsequently, the corresponding lost response signals can be reconstructed from forward calculation. By using this method, the computation time for deconvoluting Eq. (4) can be much reduced.

The above procedures are executed at all grid points such that the objective function, F , defined in Eq. (3) can be evaluated accordingly. Then, again, a number of grid points belonging to the same generation, which have the smallest objective functions, are chosen as the starting points for the subsequently optimal location search. In the search process, the lost strain

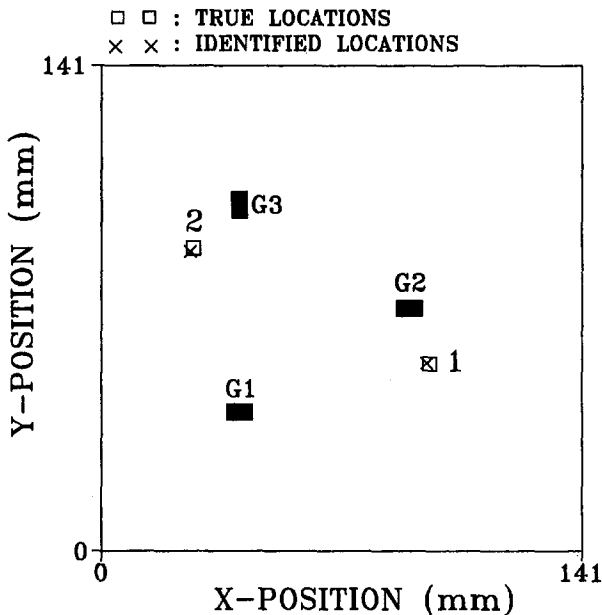


Fig. 8 Comparisons of the identified and the true impact locations for the two examples using a projectile as the impactor when the first 400 μ s response signals are missing

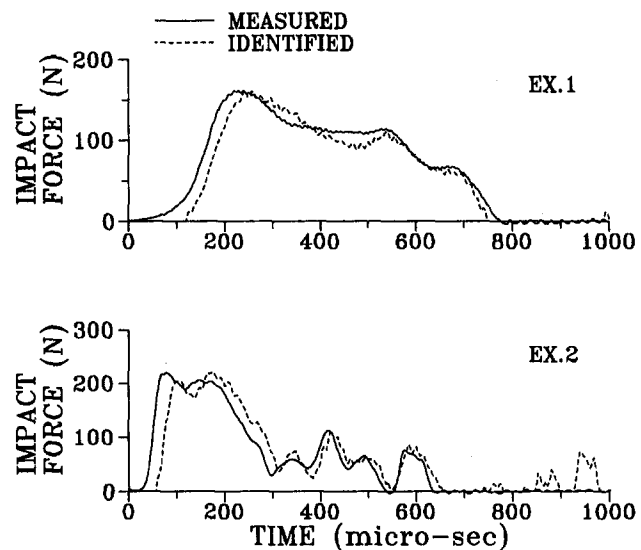


Fig. 9 Comparisons of the identified and the true force histories for the two examples using a projectile as the impactor when the first 400 μ s response signals are missing

Table 2 Identified mass and initial velocity of the projectile when the first 400 μs signals are missing

Identified mass and initial velocity:

Example	Mass (g)			Initial Velocity (m/sec)		
	true	identified	error	true	identified	error
1.	64.4	61.1	-5.1%	1.58	1.47	-7.0%
2.	64.4	65.9	+2.3%	1.79	1.82	+1.7%

signals are also reconstructed by the same way until the optimal impact location is identified. Then, the impact force can be determined using the same method as that illustrated in the preceding subsection.

Experimental Verification. To verify the proposed method, strain signals from the same experiments as that used in Section 3, i.e., an aluminum plate struck by a steel projectile, were used again. The complete strain signals lasted 1000 μs . Assuming that the strain signals in the first 400 μs were lost, the value of m was equal to 100 because the time-step used was 4 μs . Thus, m in Eq. (9) could be taken as 75 when three gages were used. This was considered suitable because $3 \times 75 > 100 + 75$. The number of initial grid points employed for locating the impact point was still 9×9 . Comparisons of the identified and the measured impact locations as well as the force histories are shown in Figs. 8 and 9, respectively. It can be found that the agreement was nearly as good as that with complete strain response signals. Identification of the mass and initial velocity of the projectile was also conducted. These values are presented in Table 2. Again, very satisfactory results were obtained. It may also be interesting to calculate the "identified strain response" for each strain sensor by using the identified

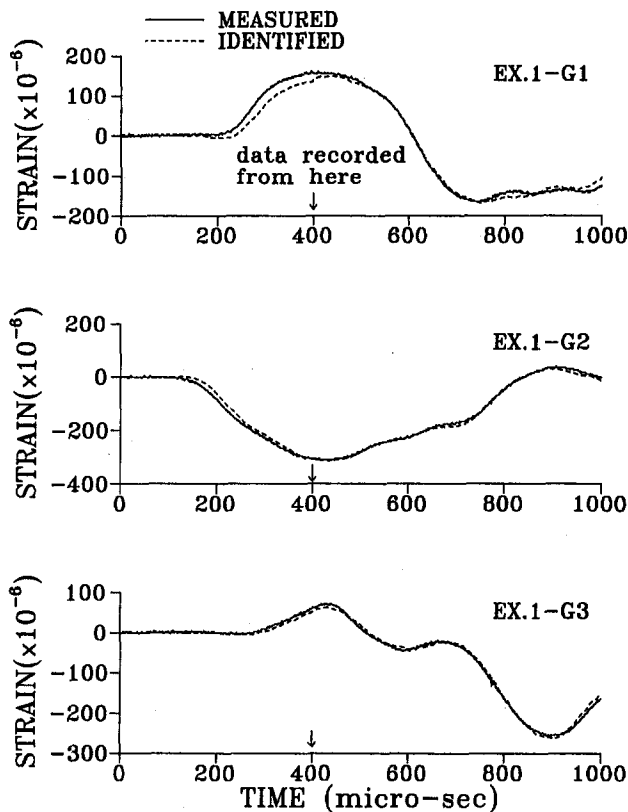


Fig. 10 Comparisons of the identified and the measured strain responses for the first example using a projectile as the impactor when the first 400 μs response signals are missing

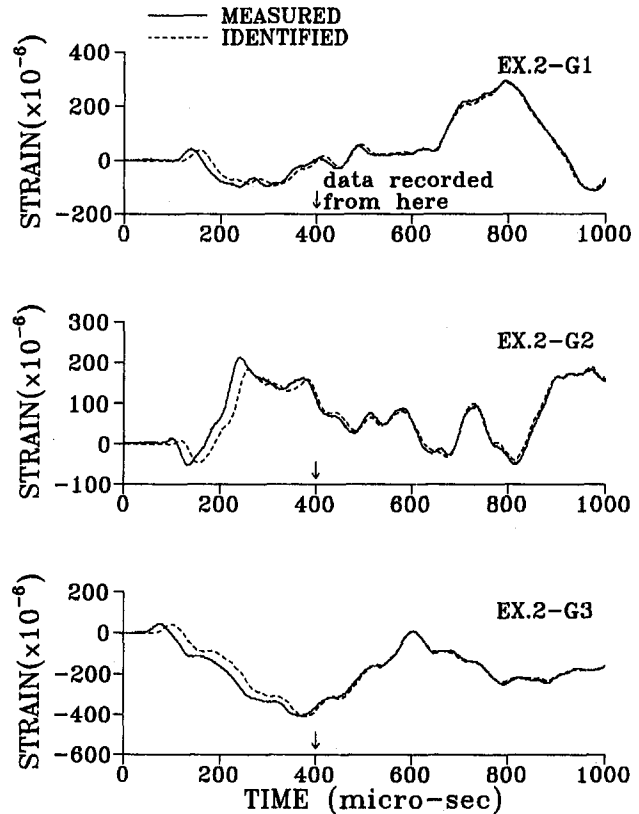


Fig. 11 Comparisons of the identified and the measured strain responses for the second example using a projectile as the impactor when the first 400 μs response signals are missing

force history as the applied load, and then to compare the results with the corresponding measured curves, of which the first 40 percent of the data were assumed to be missing. Figures 10 and 11 show such comparisons. One can find that the lost response signals were reconstructed fairly well. Although not shown in this paper, similar good results were also obtained when incomplete strain signals were used to identify the impact location and the force history, and to reconstruct the lost strain histories for the eight examples shown in Section 2, i.e., an aluminum plate struck by a hammer (Yen, 1992). Further, this method was extended to identify the impact forces exerted at multiple locations on a laminated plate when part of the recorded strain data were missing (Wu et al., 1994).

In the above calculation, the total computation time to obtain an objective function, F , when the strain histories in the first 400 μs were missing was approximately 5.12 sec; whereas only 0.254 sec was required for the case with complete strain histories. The former was about 20 times longer than the latter. This comparison also shows that additional cost is required in solving the problem with incomplete signals. However, it is still reasonable.

5 Conclusion

The method to identify the impact location and the force history from strain responses on a rectangular plate has been further verified by impact experiments. This method was also successfully extended to identify the mass and the initial velocity of an impactor by which the transverse impact was induced. Furthermore, in a situation when the recorded response signals are incomplete, a procedure has been proposed to temporarily reconstruct the lost signals such that the methods used for complete response signals are still applicable. This method has also been verified experimentally. The identified impact location,

force history, as well as the initial velocity and mass of the impactor all agreed very well with the measured results.

It is noted that if the strain histories are replaced by different dynamic responses of the plate, e.g., lateral displacements or velocities, all the proposed methods can still be applicable without further modification. Thus the proposed method is considered to be general.

Acknowledgments

This paper represents a portion of the doctoral dissertation of the first author written in partial fulfillment of the requirements for the Ph.D. degree at National Taiwan University. This work was also supported by National Science Council of Taiwan, ROC, under Contract Number NSC-82-0405-E-002-086.

References

- Fox, R. L., 1971, *Optimization Methods for Engineering Design*, Addison-Wesley.
- Pao, Y. H., 1978, "Theory of Acoustic Emission," *Elastic Waves and Nondestructive Testing of Materials*, ASME AMD Vol. 29, pp. 107–128.
- Press, W. H., Flannery, B. P., Teukolsky, S. A., and Vetterling, W. T., 1986, *Numerical Recipes*, Cambridge University Press, Cambridge, U.K.
- Rosen, J. B., 1960, "The Gradient Projection Method for Nonlinear Programming, Part 1," *Journal of the Society for Industrial and Applied Mathematics*, Vol. 8, pp. 181–217.
- Wu, E., Yeh, J. C., and Yen, C. S., 1994, "Identification of Impact Forces at Multiple Locations on Laminated Plates," *AIAA Journal*, Vol. 32, No. 12, pp. 2433–2439.
- Yen, C. S., 1992, "On the Forward and Inverse Problems of Plates Subjected to Elastic Impact," Ph.D. dissertation, National Taiwan University, (in Chinese).
-

force history, as well as the initial velocity and mass of the impactor all agreed very well with the measured results.

It is noted that if the strain histories are replaced by different dynamic responses of the plate, e.g., lateral displacements or velocities, all the proposed methods can still be applicable without further modification. Thus the proposed method is considered to be general.

Acknowledgments

This paper represents a portion of the doctoral dissertation of the first author written in partial fulfillment of the requirements for the Ph.D. degree at National Taiwan University. This work was also supported by National Science Council of Taiwan, ROC, under Contract Number NSC-82-0405-E-002-086.

References

- Fox, R. L., 1971, *Optimization Methods for Engineering Design*, Addison-Wesley.
- Pao, Y. H., 1978, "Theory of Acoustic Emission," *Elastic Waves and Nondestructive Testing of Materials*, ASME AMD Vol. 29, pp. 107-128.
- Press, W. H., Flannery, B. P., Teukolsky, S. A., and Vetterling, W. T., 1986, *Numerical Recipes*, Cambridge University Press, Cambridge, U.K.
- Rosen, J. B., 1960, "The Gradient Projection Method for Nonlinear Programming, Part 1," *Journal of the Society for Industrial and Applied Mathematics*, Vol. 8, pp. 181-217.
- Wu, E., Yeh, J. C., and Yen, C. S., 1994, "Identification of Impact Forces at Multiple Locations on Laminated Plates," *AIAA Journal*, Vol. 32, No. 12, pp. 2433-2439.
- Yen, C. S., 1992, "On the Forward and Inverse Problems of Plates Subjected to Elastic Impact," Ph.D. dissertation, National Taiwan University, (in Chinese).

ERRATA

Errata on "Antiplane Elastic Wave Scattering From a Curved Randomly Rough Crack" by A. Boström, P.-Å. Jansson and P. Olsson, published in the Dec. 1994 issue of ASME JOURNAL OF APPLIED MECHANICS, Vol. 61, pp. 835-842.

On page 839, on the second lines of Eqs. (44) and (46), the factor $im\pi\varphi_0^2/2$ should be replaced by $im\pi\varphi_0^2/4$.

On page 840, left column, eighth line from the bottom, $1/(2ka)$ should be replaced by $1/(2k^2\lambda_c^2)$.

A programming error has been discovered which affect all curves corresponding to rough cracks in Figs. 2-4 as well as Table 1. Furthermore, the curves in Figs. 2(a)-(d) should be replaced by their mirror images with respect to the vertical axes, while the curves in Figs. 4(a)-(b) should be replaced by their mirror images with respect to the horizontal axes. Two examples of the corrected plots are shown below. The interested reader is referred to the authors for a corrected version of the complete paper.

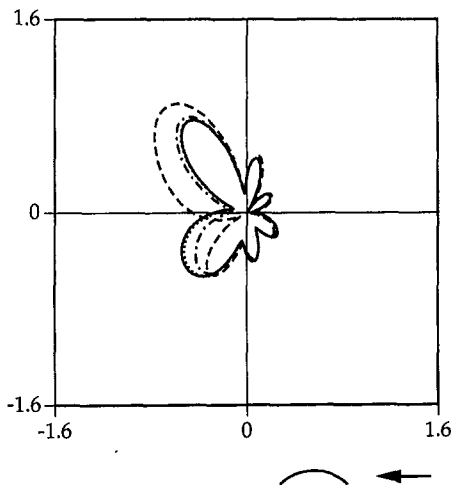


Fig. 2(d) Polar plot of the scattered far-field amplitude versus the scattering angle for $\alpha = 90$ deg, $ka = 10$, $\lambda_c/a = 0.2$, and for $\epsilon = 0$ (—), $\epsilon = 0.02$ (·····), $\epsilon = 0.05$ (- · - · -), $\epsilon = 0.1$ (----)

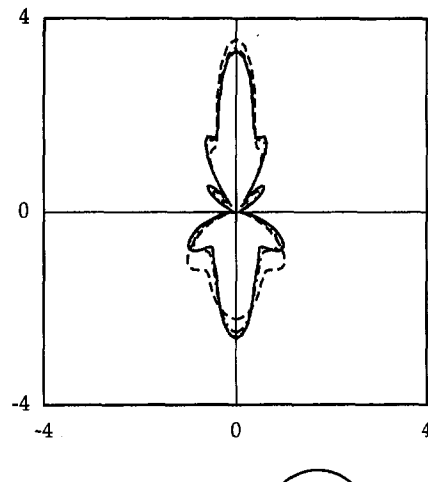


Fig. 4(b) Polar plot of the back-scattered far-field amplitude versus the angle of incidence for $ka = 10$, $\lambda_c/a = 0.1$, and for $\epsilon = 0$ (—), $\epsilon = 0.02$ (·····), $\epsilon = 0.05$ (- · - · -), $\epsilon = 0.1$ (----)

Free Vibration of a Class of Homogeneous Isotropic Solids

P. G. Young

S. M. Dickinson¹

Department of Mechanical Engineering,
The University of Western Ontario,
London, ON N6A 5B9, Canada

A Ritz approach, with simple polynomials as trial functions, is used to obtain the natural frequencies of vibration of a class of solids. Each solid is modeled by means of a segment which is described in terms of Cartesian coordinates and is bounded by the yz, zx, and xy orthogonal coordinate planes as well as by a fourth curved surface, which is defined by a polynomial expression in the coordinates x, y, and z. By exploiting symmetry, a number of three-dimensional solids previously considered in the open literature are treated, including a sphere, a cylinder and a parallelepiped. The versatility of the approach is then demonstrated by considering several solids of greater geometric complexity, including an ellipsoid, an elliptical cylinder, and a cone.

1 Introduction

A survey of the literature on the free vibration of solids reveals that the preponderance of the work has been concerned with spheres, cylinders, and parallelepipeds. Among the works on the free vibration of spheres are those by Lamb (1882), Chree (1889), Sato and Usami (1962a,b), and Lapwood and Usami (1981). Examples of the works on solid cylinders include those by Hutchinson (1967), Armenakas, Gazis, and Herrmann (1969), Gladwell and Vijay (1975), and McMahan (1970). Rectangular parallelepipeds have been studied by Fromme and Leissa (1970), Leissa and Zhang (1983), Hutchinson and Zilmer (1983), Leissa and Jacob (1986), and McGee (1992), among others.

Solids of other geometries have received less attention in the literature. Examples of such solids are the truncated quadrangular pyramid treated by Irie, Yamada, and Tagawa (1987), and the truncated triangular prism and cone considered by Narita (1990).

In the present work, a Ritz approach with simple algebraic polynomials as trial functions is used to study the vibration of a class of solids. Each solid may be modeled by means of a segment which sits in one octant and is bounded by the three orthogonal coordinate planes $x = 0$, $y = 0$, and $z = 0$, and by a fourth curved surface describable by a polynomial function in x , y , and z . By treating any or all of the three coordinate planes as planes of symmetry, a wide variety of geometries may be treated.

2 Analytical Approach

Consider an isotropic solid or segment of solid bounded by the orthogonal planes $x = 0$, $y = 0$, and $z = 0$ and by a fourth curved surface described by the equation

$$f(x, y, z) = \left(\frac{x}{a}\right)^p + \left(\frac{y}{b}\right)^q + \left(\frac{z}{c}\right)^r - 1 = 0, \quad (1)$$

where p , q , and r are arbitrary real positive numbers.

For the free vibration problem, simple harmonic motion at radian frequency ω is assumed. The displacements u , v , and w

in the x , y , and z directions, respectively, have amplitudes U , V , and W , which can be expressed as

$$\begin{aligned} U(x, y, z) &= \sum \sum \sum A_{ijk} x^{i+l_x^U} y^{j+l_y^U} z^{k+l_z^U}, \\ V(x, y, z) &= \sum \sum \sum B_{ijk} x^{i+l_x^V} y^{j+l_y^V} z^{k+l_z^V}, \\ W(x, y, z) &= \sum \sum \sum C_{ijk} x^{i+l_x^W} y^{j+l_y^W} z^{k+l_z^W}, \end{aligned} \quad (2)$$

where A_{ijk} , B_{ijk} , and C_{ijk} are as yet undetermined linear coefficients. The index l_x^U depends upon the restraints placed on the U displacement on the surface $x = 0$ and takes the value 0 for no restraint ($U \neq 0$) and 1 for full restraint ($U = 0$). Similarly, indices l_y^U and l_z^U depend upon the restraints imposed upon V and W in the $x = 0$ plane, and indices l_x^V , l_y^V , and l_z^V , l_x^W , l_y^W , and l_z^W depend upon the restraints in the $y = 0$ and $z = 0$ planes, respectively. The displacement series given can also be used to model problems exhibiting symmetry of geometry and boundary conditions about one or more of the planes given by $x = 0$, $y = 0$, and $z = 0$. This is done by choosing values of indices l to apply appropriate boundary conditions on the plane(s) of symmetry to model symmetric (S) modes (zero displacement normal to plane, nonzero displacements in-plane) and antisymmetric (A) modes (nonzero displacement normal to plane, zero displacements in-plane) about particular planes.

The maximum strain energy of the solid V_{\max} can be expressed in terms of the normal strains ϵ_x , ϵ_y , and ϵ_z in the x , y , and z directions, respectively, and the shear strains γ_{xy} , γ_{yz} , and γ_{zx} (Leissa and Zhang, 1983), which are in turn expressible in terms of derivatives of U , V and W . The maximum strain energy T_{\max} is directly expressible in terms of U , V , and W .

Finally, the trial function series (2) are substituted into the energy expressions and the Lagrangian functional $L_{\max} = (T_{\max} - V_{\max})$ is minimized with respect to the undetermined coefficients A_{ijk} , B_{ijk} , and C_{ijk} to yield a set of equations in a standard eigenvalue form.

3 Numerical Results

In all cases treated, the frequency parameter reported is $\Omega = \omega a \sqrt{\rho/G}$ and the same number of terms has been used in each of the displacement series for U , V , and W , as well as in all three coordinate directions x , y , and z , and is referred to as $N \times N \times N$ in the text and the tables. Also, in all but one case, the sphere, the Poisson ratio, has been taken as 0.3 and, unless otherwise stated, all surfaces of each solid are taken as free. In any of the computations where the exponent ∞ appears, it was approximated by using the very high value of 10^{12} .

The first problem treated is that of the free vibration of a sphere, for which an exact solution in terms of Bessel functions

¹ To whom correspondence should be addressed.

Contributed by the Applied Mechanics Division of THE AMERICAN SOCIETY OF MECHANICAL ENGINEERS for publication in the ASME JOURNAL OF APPLIED MECHANICS.

Discussion on this paper should be addressed to the Technical Editor, Prof. Lewis T. Wheeler, Department of Mechanical Engineering, University of Houston, Houston, TX 77204-4792, and will be accepted until four months after final publication of the paper itself in the ASME JOURNAL OF APPLIED MECHANICS.

Manuscript received by the ASME Applied Mechanics Division, Apr. 12, 1993; final revision, Nov. 20, 1993. Associate Technical Editor: F. Y. M. Wan.

Table 1 Frequency parameters Ω for a solid sphere of radius a . Poisson's ratio $\nu = 0.25$.

Number of Terms NxNxN	Mode type				
	SSA 1 AAA 1,2 $1T_2$	SSS 1,2 SAA 1 $1S_2$	SSA 2 $2S_1$	SSS 3 SAA 2,3 $1T_3$	SSA 3,4 AAA 3 $1S_3$
4x4x4	2.501	2.640	3.4251	3.865	3.916
5x5x5	2.501	2.640	3.4247	3.865	3.916
6x6x6	2.501	2.640	3.4245	3.865	3.916
7x7x7	2.501	2.640	3.4245*	3.865	3.916
	SSS 4 $1S_0$	SSS 5,6 SAA 4 $2S_2$	SSS 7-9 SAA 5,6 $1S_4$	SSA 5,6 AAA 4-6 $1T_4$	SAA 7 $2T_1$
4x4x4	4.440	4.867	5.017	5.096	5.778
5x5x5	4.440	4.866	5.011	5.095	5.766
6x6x6	4.440	4.865	5.009	5.095	5.764
7x7x7	4.440	4.865	5.009	5.095	5.763
	SSA 7-9 AAA 7,8 $1S_5$	SAA 8-10 SSS 10,11 $1T_5$	SSA 10,11 AAA 9 $2S_3$	SSA 12 $2S_1$	SSS 12-15 SAA 11-13 $1S_6$
4x4x4	6.048	6.275	6.463	6.944	7.141
5x5x5	6.034	6.267	6.455	6.779	7.030
6x6x6	6.033	6.266	6.454	6.774	7.024
7x7x7	6.033	6.266	6.454	6.771	7.023

* Value given by Sato and Usami (1962a) is 3.424

of the first kind is possible, and for which exact natural frequencies and mode shapes have been computed by Sato and Usami (1962a, 1962b) by using a value of 0.25 for the Poisson ratio. In this case, only $\frac{1}{8}$ th of the sphere is modeled and the curved surface is described by $f(x, y, z) = (x/a)^2 + (y/a)^2 + (z/a)^2 - 1 = 0$. Of the eight possible sets of symmetry conditions, only four are distinct cases, namely SSS, AAA, one of SAA, ASA, AAS, and one of SSA, SAS, ASS, where the first, second, and third letters refer to the symmetry conditions applied on the $x = 0$, $y = 0$, and $z = 0$ planes, respectively. In Table 1, the first 15 nonzero natural frequency parameters Ω are given, for a Poisson ratio of 0.25, as computed by using the present approach with increasing number of terms in the displacement series, from which it may be seen that the rate of convergence of the solution is very rapid. The results obtained by using $7 \times 7 \times 7$ terms in the series agree to the number of figures given with the values obtained by Sato and Usami (1962a) from the exact solution, with the exception of the third mode, which, when rounded to four decimal figures, differs in the last decimal place as can be seen in the table. In Table 1 the frequency parameters are identified not only by their symmetry class, but also as $1T_n$ or $1S_n$, referring to the i th mode of the n th harmonic

Table 2 Frequency parameters Ω for a solid cylinder of circular cross section

Mode Type	AAA 1	AAA 2 SSA 1 $n = 2$	SAS 1 $n = 1$	SAA 1 $n = 1$	SSS 1 $n = 0$	SSS 2 AAS 1 $n = 2$
Ω	1.570796	1.978	1.994	2.151	2.326	2.338
	1.570796*	(1.993)	(1.996)	(2.151)	(2.326)	(2.360)
Mode Type	SSS 3 AAS 2 $n = 2$	SAS 2 $n = 1$	SSA 2 $n = 0$	SSS 4 $n = 0$	AAS 3	SSA 3 AAA 3 $n = 2$
Ω	2.488	2.802	2.872	3.067	3.141593	3.192
	(2.503)	(2.814)	(2.872)	(3.068)	3.141593	(3.218)

() Results by Gladwell and Vijay (1975)

* Exact results from torsion theory $\pi/2, \pi$

Table 3 Frequency parameters Ω for a cone

B.C. on Base	Mode type				
FREE	SS 1/AA 1	SS 2	SA 1	SA 2	SS 3/AA 2
	1.768	2.639	2.728	2.975	3.103
	SS 4/AA 3	SA 3	AA 4	SS 5	SA 4
	3.607	3.650	3.858	4.023	4.236
CLAMPED	SA 1	AA 1	SS 1	SA 2	SS 2/AA 2
	2.106	2.883	3.486	3.946	4.378
	SA 3	SS 3/AA 3	AA 4	SA 4	SA 5
	4.932	5.419	5.444	5.695	5.829

of toroidal (T) or spheroidal (S) vibration as was done in Sato and Usami (1962a, 1962b).

The second problem considered is the vibration of a solid cylinder of length $2a$ and of radius a . Again only $\frac{1}{8}$ th of the cylinder is modeled, with the portion of the cylinder lying in the first octant being described by $f(x, y, z) = (x/a)^2 + (y/a)^2 + (z/a)^2 - 1 = 0$. A total of six sets of symmetry conditions are considered, namely SSS, AAA, SSA, AAS, one of SAS or ASS, and one of SAA or ASA. The first 12 nonzero frequency parameters Ω are given in Table 2 together with results obtained by Gladwell and Vijay (1975) by using a finite element approach. The symmetry class and the circumferential wave number n corresponding to each frequency is also given in Table 2. The present results reported were obtained by using both $6 \times 6 \times 6$ and $8 \times 8 \times 8$ terms in each of the displacement series U, V , and W and were identical to the number of figures given; it is reasonable to assume that the solution had converged and that the values are exact to the number of figures given. The first and the 11th nonzero frequency parameters obtained by using the present method were not reported by Gladwell and Vijay and correspond to the first and second pure torsional modes for which the exact solution may be obtained from elementary torsional vibration theory.

The third problem treated is that of a cone of circular cross section and of height-to-base radius ratio c/a equal to 1 and either free or clamped at the base which lies on the $z = 0$ plane. This is modeled by using one quarter of the cone with the curved face being described by $f(x, y, z) = (x/a)^2 + (y/a)^2 + (z/a)^2 - 1 = 0$. Of the four possible symmetry cases, only three are distinct, namely SS, AA and one of SA or AS. The lowest ten nonzero frequency parameters Ω are given in Table 3 as computed by using $7 \times 7 \times 7$ terms in the displacement series for a cone with a clamped base ($U = V = W = 0$) and for a cone with a free base. A convergence study performed suggested that the frequency parameters have converged to the number of figures given.

The fourth problem treated is that of an ellipsoid with semi-axes ratios $a/b = 1/2$ and $a/c = 1/3$ and is modeled by using only $\frac{1}{8}$ th of the solid with the curved surface being described by $f(x, y, z) = (x/a)^2 + (y/2a)^2 + (z/3a)^2 - 1 = 0$. The lowest 18 nonzero frequency parameters Ω are given in Table 4 as computed by using $7 \times 7 \times 7$ terms in the series. Again, a

Table 4 Frequency parameters Ω for an ellipsoid

Mode Type	ASS 1	AAA 1	SAS 1	ASA 1	SSS 1	AAS 1
Ω	0.5666	0.6626	0.8551	1.038	1.060	1.110
Mode Type	SAA 1	ASS 2	ASS 3	SSA 1	SAA 2	AAA 2
Ω	1.152	1.222	1.503	1.514	1.515	1.547
Mode Type	ASA 2	SSS 2	SAS2	SSA 2	AAS 2	SSS 3
Ω	1.571	1.593	1.671	1.709	1.807	1.911

Table 5 Frequency parameters Ω for a solid cylinder of elliptical cross section

Mode Type	AAA 1	SAS 1	ASS 1	ASA 1	SAS 2	AAS 1
Ω	1.202	1.513	2.030	2.184	2.199	2.265
Mode Type	SSS 1	SSA 1	SAA 1	SSS 2	SAA 2	SSS 3
Ω	2.365	2.372	2.473	2.708	2.912	3.070
Mode Type	AAA 2	AAS 2	ASS 2	SAS 3	SSA 2	AAA 3
Ω	3.144	3.363	3.412	3.427	3.443	3.733

convergence study, not given here, suggested that the natural frequency parameters had converged to four significant figures.

The fifth problem treated is that of the free vibration of a solid cylinder of elliptical cross section of major to minor semi-axis ratio $a/b = 2$ and of major semi-axis to length ratio $a/2c = 0.5$. Again, this case is modeled by using $\frac{1}{8}$ th of the cylinder with the curved surface being given by $f(x, y, z) = (x/a)^2 + (2y/a)^2 + (z/a)^\infty - 1 = 0$. The lowest 18 frequency parameters Ω , as computed by using $7 \times 7 \times 7$ terms in the series, are given in Table 5. Again, accuracy to the number of figures given was determined through a convergence study.

The sixth and last problem treated is that of the free vibration of a class of solids, an example of which is illustrated in Fig. 1. Each solid is fully clamped on the surface defined by $z = 0$ and is symmetrical about the planes $x = 0$ and $y = 0$, hence only $\frac{1}{4}$ of the solid need be considered. The free surface is defined by the equation $f(x, y, z) = (x/a)^\infty + (y/a)^p + (z/a)^p - 1 = 0$, for $p = \frac{2}{3}, 1, \frac{3}{2}, 2, 3$, and ∞ . The lowest three frequency parameters Ω for each of the four classes of symmetry are given in Table 6, as computed by using $7 \times 7 \times 7$ terms in the series. A convergence study, not presented here, suggested that the values given are accurate to within three significant figures.

4 Concluding Remarks

The Ritz method with simple algebraic polynomials as trial functions has been applied to the problem of the free vibration of a number of solids of different geometries and very accurate natural frequencies have been obtained. It should be noted that the polynomial trial function series described by Eqs. (2) form a mathematically complete set of functions and hence convergence of the Ritz method to the exact frequencies is guaranteed as the number of terms in each series tends to infinity. Furthermore, by virtue of the Ritz procedure, the numerical natural frequencies computed are always upper bounds. It should be

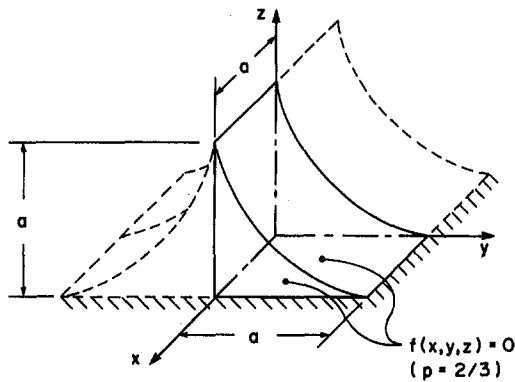


Fig. 1 Prismatic solid

Table 6 Frequency parameters Ω for the class of solids shown in Fig. 1

Exponent p	Mode type					
	SS			AA		
	1	2	3	1	2	3
2/3	3.160	4.293	4.607	2.461	3.365	3.888
1	2.856	3.588	3.965	2.371	3.576	4.267
3/2	2.685	3.195	3.614	2.104	3.154	3.964
2	2.605	3.007	3.445	1.928	2.868	3.731
3	2.529	2.820	3.250	1.740	2.576	3.460
10 ¹²	2.367	2.513	2.891	1.475	2.181	3.072
Exponent p	SA			AS		
	1	2	3	1	2	3
	2/3	2.367	4.238	4.795	2.355	2.828
1	1.928	3.559	4.282	2.169	2.937	3.918
3/2	1.686	3.178	3.899	1.880	2.786	3.660
2	1.577	2.999	3.566	1.706	2.694	3.475
3	1.473	2.816	3.216	1.537	2.603	3.240
10 ¹²	1.334	2.465	2.842	1.334	2.465	2.842

cautioned that, as with most series solutions in which polynomials are used, if too many terms are retained in the deflection series, the resulting matrices can become ill-conditioned, the eigenvalue solving routines then failing to yield meaningful results.

References

Armenakas, A. E., Gazis, D. C., and Herrmann, G., 1969, *Free vibrations of circular cylindrical shells*, Pergamon Press, New York.

Chree, C., 1889, "The equations of an isotropic elastic solid in polar and cylindrical coordinates, their solution and application," *Transactions of the Cambridge Philosophical Society*, Vol. 14, pp. 250-369.

Fromme, J. A., and Leissa, A. W., 1970, "Free vibration of the rectangular parallelepiped," *The Journal of the Acoustical Society of America*, Vol. 48, pp. 290-298.

Gladwell, G. M. L., and Vijay, D. K., 1975, "Natural frequencies of free finite-length circular cylinders," *Journal of Sound and Vibration*, Vol. 42, pp. 387-397.

Hutchinson, J. R., 1967, "Axisymmetric vibrations of a solid elastic cylinder encased in a rigid container," *The Journal of the Acoustical Society of America*, Vol. 42, pp. 398-402.

Hutchinson, J. R., and Zillmer, S. D., 1983, "Vibration of a free rectangular parallelepiped," *ASME JOURNAL OF APPLIED MECHANICS*, Vol. 50, pp. 123-130.

Irie, T., Yamada, G., and Tagawa, Y., 1987, "Three-dimensional vibration analysis of a truncated quadrangular pyramid," *ASME JOURNAL OF APPLIED MECHANICS*, Vol. 54, pp. 115-120.

Lamb, H., 1882, "On the vibrations of an elastic sphere," *Proceedings of the London Mathematical Society*, Vol. 13, pp. 189-212.

Lapwood, E. R., and Usami, T., 1981, *Free Oscillations of The Earth*, Cambridge University Press, Cambridge, U.K.

Leissa, A. W., and Jacob, K. I., 1986, "Three-dimensional vibrations of twisted cantilevered parallelepipeds," *ASME JOURNAL OF APPLIED MECHANICS*, Vol. 53, pp. 614-618.

Leissa, A. W., and Zhang, Z., 1983, "On the three-dimensional vibrations of the cantilevered rectangular parallelepiped," *The Journal of the Acoustical Society of America*, Vol. 73, pp. 2013-2021.

McGee, O. G., 1992, "On the three-dimensional vibration analysis of simultaneously skewed and twisted cantilevered parallelepipeds," *International Journal for Numerical Methods in Engineering*, Vol. 33, pp. 1383-1411.

McMahon, G. W., 1970, "Finite difference analysis of the vibrations of solid cylinders," *The Journal of the Acoustical Society of America*, Vol. 48, pp. 307-312.

Narita, Y., 1990, "Three-dimensional vibration analysis of arbitrarily shaped elastic bodies by plane approximation," *Nippon Kikai Gakkai Ronbunshu (Transactions of the Japan Society of Mechanical Engineers)*, Vol. 56, pp. 1125-1129, (in Japanese).

Sato, Y., and Usami, T., 1962a, "Basic study on the oscillation of a homogeneous elastic sphere; Part I, Frequency of the free oscillations," *Geophysics Magazine*, Vol. 31, pp. 15-24.

Sato, Y., and Usami, T., 1962b, "Basic study on the oscillation of a homogeneous elastic sphere; Part II, Distribution of displacement," *Geophysics Magazine*, Vol. 31, pp. 25-47.

Toeplitz Jacobian Matrix for Nonlinear Periodic Vibration

A. Y. T. Leung
Reader.

T. Ge
Research Student.

Department of Civil and Structural
Engineering,
University of Hong Kong,
Pokfulam Road,
Hong Kong, R.O.C.

The main difference between a linear system and a nonlinear system is in the non-uniqueness of solutions manifested by the singular Jacobian matrix. It is important to be able to express the Jacobian accurately, completely, and efficiently in an algorithm to analyze a nonlinear system. For periodic response, the incremental harmonic balance (IHB) method is widely used. The existing IHB methods, however, requiring double summations to form the Jacobian matrix, are often extremely time-consuming when higher order harmonic terms are retained to fulfill the completeness requirement. A new algorithm to compute the Jacobian is to be introduced with the application of fast Fourier transforms (FFT) and Toeplitz formulation. The resulting Jacobian matrix is constructed explicitly by three vectors in terms of the current Fourier coefficients of response, depending respectively on the synchronizing mass, damping, and stiffness functions. The part of the Jacobian matrix depending on the nonlinear stiffness is actually a Toeplitz matrix. A Toeplitz matrix is a matrix whose k, r position depends only on their difference $k-r$. The other parts of the Jacobian matrix depending on the nonlinear mass and damping are Toeplitz matrices modified by diagonal matrices. If the synchronizing mass is normalized in the beginning, we need only two real vectors to construct the Toeplitz Jacobian matrix (TJM), which can be treated in one complex fast Fourier transforms. The present method of TJM is found to be superior in both computation time and storage than all existing IHB methods due to the simplified explicit analytical form and the use of FFT.

1 Introduction

The application of the incremental harmonic balance method (IHB) to the analysis of nonlinear oscillations has become well recognized. Various exact steady-state solutions have been established for a number of strongly nonlinear discrete and continuous systems (Lau et al., 1981, 1982; Pierre et al., 1985). The IHB have been illustrated to be more effective than perturbation methods in analyzing the systems with large nonlinearities and more efficient than direct numerical integration methods in performing parametric studies (Leung and Fung, 1988). Recently, fast Fourier transformations (FFT) algorithm has been used to facilitate algebraic manipulations that lead to a more general IHB procedure. This procedure will permit more complicated forms of nonlinear functions, such as dry friction damping (Pierre et al., 1985) and piece-wise linear restoring spring (Kim and Noah, 1991). The method of IHB has been treated as a general numerical method for seeking periodic solution of nonlinear differential equations. However, there are some drawbacks found in the existing IHB methods. For example, as pointed out by Cameron and Griffin (1989) etc., to include higher order harmonic terms for accurate solution the numerical iteration of IHB is tedious and may not be more efficient than that of direct numerical integrations, i.e., the Runge-Kutta method. An alternative computation strategy to execute the harmonic balance was first reported by Ling and Wu (1987) in the fast Galerkin method (FG) and later by Cameron and Griffin (1989) in the alternating frequency/time method (AFT). By means of fast Fourier transform (FFT) and inverse fast Fourier transform (IFFT) algorithms, the methods include the inter-

active manipulations between the time and frequency domain as to employ the computation conveniences on each domain. This strategy circumvents the tedious processing of the Jacobian matrix in IHB and is proved useful to accelerate the computation of simple nonlinear problems by Ling and Wu (1988) and Cameron and Griffin (1989). Since the Jacobian is estimated by finite differences, only the secant iterative methods can be adapted. Consequently, the convergent rate in the iteration is decreased and the energy conservation properties of IHB method are lost so that the location of the bifurcation or singular points and that the post bifurcation solutions cannot be accurately determined (Iooss and Joseph, 1980).

To improve the IHB approach on both aspects, the present paper introduces a new computational algorithm that leads to a Toeplitz formulation of the Jacobian matrix. The method substantially reduces the amount of computational work while conserves the energy in the iterations. Based on the Galerkin averaging theory and discrete Fourier transformation (Brigham, 1974), we provide an explicit formula for the Jacobian matrix. A path-following method is also incorporated in the algorithm to ensure the effectiveness and robustness in handling complex nonlinear phenomenon. The procedure provided in this paper is extended to a subharmonic response of a multiple DOF system with general forms of nonlinearities.

2 Formulation

Consider a nonlinear oscillators governed by the equation

$$u'' + N(u, u', \omega, \lambda, t) = 0, \quad (1)$$

where ω, t are the linear fundamental frequency and the time scale, respectively, prime represents d/dt , and $N(\cdot)$ is a nonlinear time-dependent function of displacement u , velocity u' , fundamental frequency ω , and system parameter λ . A nondimensional time change $\tau = \omega t$ is preferable in seeking the periodic solutions. This leads to a nondimensional time-dependent equation,

$$f(\tau) = \omega^2 \ddot{u} + N(u, \dot{u}, \omega, \lambda, \tau) = 0, \quad (2)$$

where the upper dot indicates a derivative with respect to τ .

Contributed by the Applied Mechanics Division of THE AMERICAN SOCIETY OF MECHANICAL ENGINEERS for publication in the ASME JOURNAL OF APPLIED MECHANICS.

Discussion on this paper should be addressed to the Technical Editor, Prof. Lewis T. Wheeler, Department of Mechanical Engineering, University of Houston, Houston, TX 77204-4792, and will be accepted until four months after final publication of the paper itself in the ASME JOURNAL OF APPLIED MECHANICS.

Manuscript received by the ASME Applied Mechanics Division, July 14, 1993; final revision, Mar. 4, 1994. Associate Technical Editor: W. K. Liu.

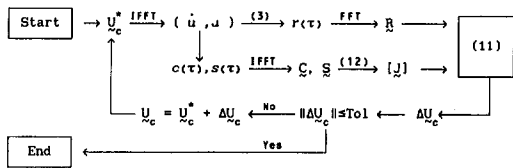


Fig. 1 Flow chart for Newtonian iteration (* represents the unbalanced state)

Table 1 Comparison of the numbers of multiplication

Method	Number of Multiplications
Direct IHB	$11M(2N+1)^2$
Present	$11(2N+1)^2 + 2M \log_2 M$

The corresponding first-order incremental forms of Eq. (2) is then obtained by the substitutions $\omega = \omega_0 + \Delta\omega$, $\lambda = \lambda_0 + \Delta\lambda$, $u = u_0 + \Delta u$,

$$\omega_0^2 \Delta \ddot{u} + \omega_0 \left. \frac{\partial N}{\partial \dot{u}} \right|_0 \Delta \dot{u} + \left. \frac{\partial N}{\partial u} \right|_0 \Delta u = \gamma(\tau) \quad (3)$$

where, Δu , $\Delta \dot{u}$, $\Delta \ddot{u}$ are small increments of displacement, velocity, acceleration with respect to τ , respectively; the subscript zero refers to an approximated known state and $\gamma(\tau)$ is a residual function. In general, while incrementing from a known solution to the next, a predictor-and-corrector procedure can be used and the residual function is evaluated by

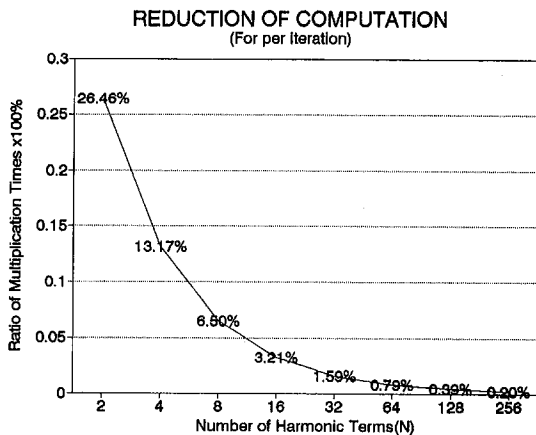


Fig. 2 Percentage of computing times (TJM/IHB \times 100 percent)

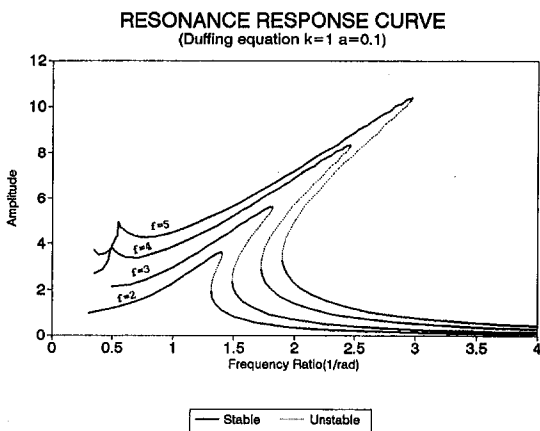


Fig. 3 Frequency response curves

Table 2 Numerical comparison of TJM versus IHB

(for step length 0.4 and residual tolerance 1.e-6)

No. of Step	Frequency Ratio ω (1/rad)	1st Order Amplitude	Number of Iterations I and CPU - times T				
			IHB method (a)		Present Method (b)		
			I_a	T_a	I_b	T_b	T_b/T_a
0	1.000000	3.935953	12	5.65	5	0.49	8.67%
1	1.173276	4.343391	12	6.21	4	0.55	8.86%
2	1.302025	4.676480	16	8.18	5	0.66	8.06%
3	1.419599	5.000948	18	9.18	5	0.61	6.64%
4	1.528153	5.315249	22	11.15	5	0.61	5.47%
5	1.628985	5.617792	29	14.67	5	0.65	4.43%
6	1.722977	5.907414	36	18.07	5	0.66	3.65%
7	1.810760	6.183333	42	21.09	5	0.66	3.13%
8	1.892812	6.445093	46	23.01	5	0.61	2.65%
9	1.969521	6.692505	49	24.49	5	0.61	2.49%
Total Running Time			2:46.48		0:06.21		3.67%

Table 3 Stability points along a solution path (Fig. 2)

f	Stability	Property	η	λ
0.000000	1x1T stable			
0.461353	1x1T unstable	Fold		
0.228323	1x1T stable			
2.395560	2x1T stable	Symmetric Breaking		
3.291727	2x1T unstable	Fold		
3.257349	2x1T stable			
5.387085	4x2T stable	Period 2 Bifurcation	2.9915	3.41
6.264048	8x4T stable	Period 4 Bifurcation	0.8769	4.39
6.443806	16x8T stable	Period 8 Bifurcation	0.1998	4.56
6.483227	32x16T stable	Period 16 Bifurcation	0.0394	

η — distance between period double bifurcation points

λ — ratio of distance

$$\gamma(\tau) = \begin{cases} - \left[2\omega_0 \ddot{u}_0 + \left. \frac{\partial N}{\partial \omega} \right|_0 \right] \Delta\omega \\ - \left[\left. \frac{\partial N}{\partial \lambda} \right|_0 \right] \Delta\lambda \quad \text{predictor} \\ - [\omega_0^2 \ddot{u}_0 + N(u_0, \dot{u}_0, \omega_0, \lambda_0, \tau)] \\ = -f_0(\tau) \quad \text{corrector.} \end{cases} \quad (4a)$$

$$(4b)$$

Here, $\Delta\omega$ and $\Delta\lambda$ are the active increments of fundamental frequency and system control parameter, respectively. In the predictor phase, Eq. (3) can also be expressed as a time-varying coefficient equation

$$\omega_0^2 \Delta \ddot{u} + \omega_0 c(\tau) \Delta \dot{u} + s(\tau) \Delta u = \gamma(\tau) \quad (5)$$

where $c(\tau)$, $s(\tau)$ are the synchronizing damping and stiffness

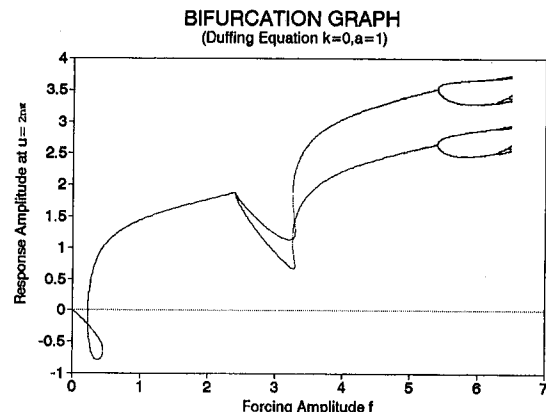


Fig. 4 Bifurcation diagram

PHASE DIAGRAM
($f=6.0, w=1.0$ lower)

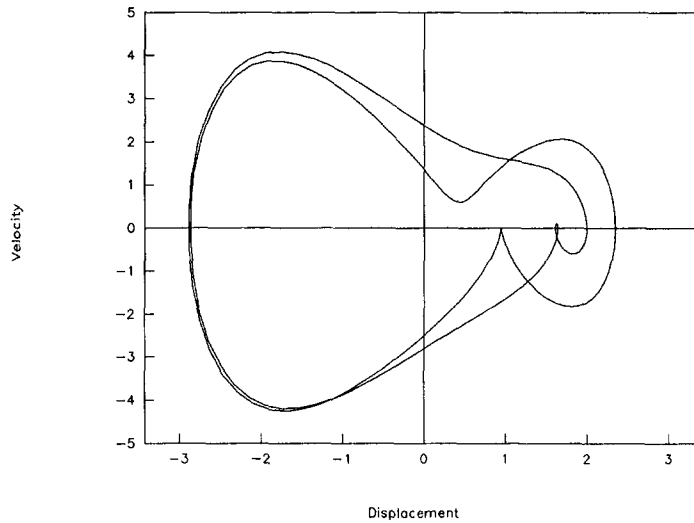


Fig. 5(a) Phase diagram at $f = 6.0$ (lower branch)

functions, respectively, and the synchronizing mass has been normalized,

$$c(\tau) = \left. \frac{\partial N}{\partial \dot{u}} \right|_0 \quad \text{and} \quad s(\tau) = \left. \frac{\partial N}{\partial u} \right|_0. \quad (6)$$

An approximated steady-state periodic solution of Eq. (2) is expressed by the truncated Fourier series with complex coefficients U_r ,

$$u(\tau) = \sum_{r=-N}^N U_r \exp(ir\tau) \quad (7)$$

whose increment is assumed to be

$$\Delta u = \sum_{r=-N}^N \Delta U_r \exp(ir\tau) \quad \text{where} \quad i = \sqrt{-1} \quad (8)$$

Here, the integer N must be large enough to accommodate the higher order harmonic solutions. Substitution of Eq. (8) into Eq. (5) leads to

$$\sum_{r=-N}^N [s(\tau) - r^2\omega_0^2 + ir\omega_0c(\tau)] \Delta U_r \exp(ir\tau) = \gamma(\tau). \quad (9)$$

After applying the inverse discrete Fourier transformation to the time-varying Eq. (9), we have the following period-averaged equation:

$$\sum_{q=0}^{M-1} \sum_{r=-N}^N \left[s\left(\frac{2\pi q}{M}\right) - r^2\omega_0^2 + ir\omega_0c\left(\frac{2\pi q}{M}\right) \right] \times \Delta U_r \exp\left[\frac{-i2\pi q(k-r)}{M}\right] = \sum_{q=0}^{M-1} \gamma\left(\frac{2\pi q}{M}\right) \exp\left(\frac{-i2\pi qk}{M}\right) = R_k \quad (10)$$

TIME HISTORY
($f=6.0, w=1.0$ lower)

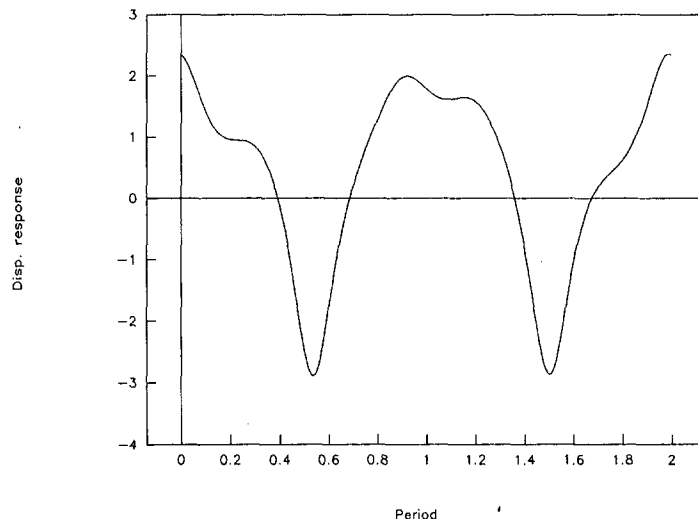


Fig. 5(b) Time history at $f = 6.0$ (lower branch)

PHASE DIAGRAM

($f=6.0, w=1.0$ upper)

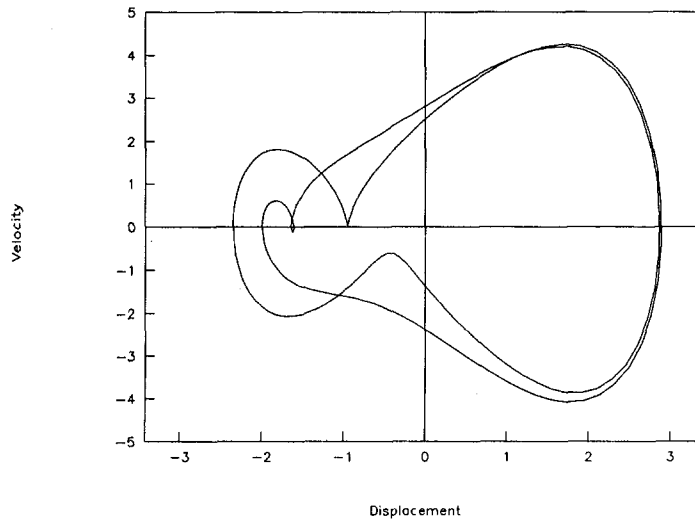


Fig. 5(c) Phase diagram at $f = 6.0$ (upper branch)

$$k = -N, \dots, 0, \dots, N$$

$$q = 0, 1, \dots, M - 1$$

where M is the total number of discrete points per period and should be taken as $M \geq 2N + 1$ to avoid the *aliasing distortion* occurring in the discretization.

Exchanging the order of the inner and outer summations in Eq. (10), we put the incremental Eq. (3) in the frequency domain,

$$[\mathbf{J}]\{\Delta \mathbf{U}_c\} = \{\mathbf{R}\} \quad (11)$$

where $\{\Delta \mathbf{U}_c\} = [\Delta U_{-N}, \dots, \Delta U_0, \dots, \Delta U_N]^T$ is the unknown frequency incremental vector, $\{\mathbf{R}\}$ is the residual vector, and $[\mathbf{J}]$ is the Jacobian matrix used in the Newton-Raphson iteration, whose components are given by

$$J_{kr} = S(k - r) - r^2 \omega_0^2 \delta(k - r) + ir \omega_0 C(k - r) \quad (12)$$

in which $\delta(\cdot)$, $S(\cdot)$, and $C(\cdot)$ are given by Eqs. (13)-(15), respectively, and r, k denote the row and column numbers

corresponding to the location of the element in the Jacobian matrix. In Eq. (12), the resulting Jacobian matrix is constructed explicitly by three convolution vectors $\delta(\cdot)$, $C(\cdot)$, and $S(\cdot)$ in terms of the current Fourier coefficients of response, depending, respectively, on the synchronizing mass, damping, and stiffness functions. Therefore, the part of the Jacobian matrix depending on the nonlinear stiffness is actually a Toeplitz matrix. The other parts of the Jacobian matrix depending on the nonlinear mass and damping are Toeplitz matrices modified by diagonal matrices. If the synchronizing mass is normalized in the beginning, we need only two real convolution vectors to construct the Toeplitz Jacobian matrix (TJM), which can be treated within one complex fast Fourier transformation. The evaluating process can be further accelerated by mean of the efficient use of the FFT techniques. Apparently, $\delta(\cdot)$ can be feasibly treated as the Dirac's delta function

$$\delta(k - r) = \begin{cases} 1 & k = r \\ 0 & \text{otherwise} \end{cases} \quad (13)$$

TIME HISTORY

($f=6.0, w=1.0$ upper)

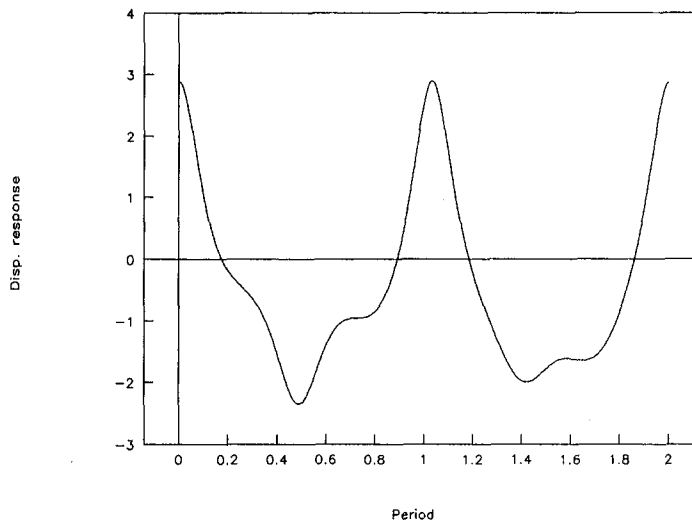


Fig. 5(d) Time history at $f = 6.0$ (upper branch)

PHASE DIAGRAM

($f=6.46, w=1.0$)

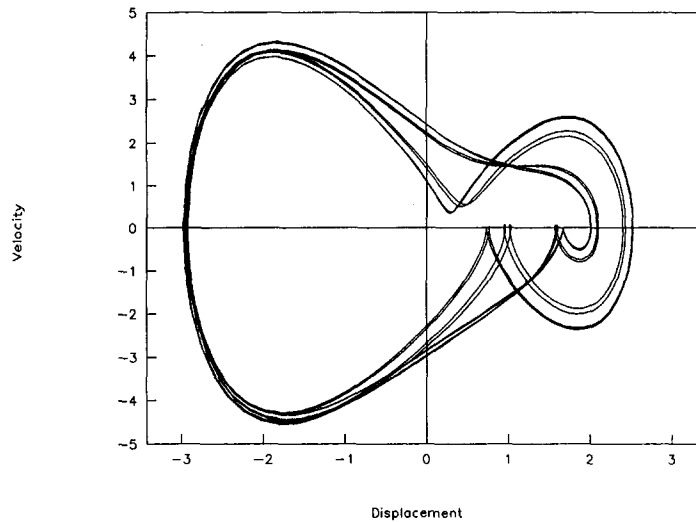


Fig. 6(a) Phase diagram at $f = 6.46$ (lower branch)

and $S(\cdot)$, $C(\cdot)$ as modal damping and stiffness functions, respectively, which can be transformed directly from their synchronizing time-dependent functions $s(\cdot)$ and $c(\cdot)$ in Eq. (6) through a standard FFT algorithm,

$$S(p) = \sum_{q=0}^{M-1} s\left(\frac{2\pi q}{M}\right) \exp\left(\frac{-i2\pi qp}{M}\right) \quad (14)$$

$$C(p) = \sum_{q=0}^{M-1} c\left(\frac{2\pi q}{M}\right) \exp\left(\frac{-i2\pi qp}{M}\right). \quad (15)$$

Here p refers to the index of the convolution sequences used by the Toeplitz matrices, $p = k - r$. Moreover, since $s(\cdot)$ and $c(\cdot)$ are evaluated discretely at a set of finite M time-dependent points, the related functions $S(\cdot)$ and $C(\cdot)$ may also be determined within the M discrete points on frequency domain. Therefore, in case the index $r - k$ in Eq. (12) exceeds the range, p

$\in \mathbb{N}[0, M - 1]$, their values can also be evaluated by shifting the period,

$$p = \text{mod}\left(\frac{M + k - r}{M}\right). \quad (16)$$

Thus, once $S(p)$ and $C(p)$ are obtained by inverse fast Fourier transforms in Eqs. (14), (15), the whole Jacobian matrix is readily available according to a simple algebraic relations described in Eq. (12). The resultant linear algebraic Eq. (11) can be solved by any standard solver. Its solution is then transformed back into time domain again by Eq. (8) to evaluate the nonlinear function $N(\cdot)$ and to update the residual function $\gamma(\tau)$ for the next iteration. The iteration goes until the residuals become sufficient small. A flow chart for the Newtonian iteration is given in Fig. 1.

It is also advantageous to write Eq. (11) in real form, because only $(2N + 1)$ real variables, instead of $(2N + 1)$ complex ones are needed. The reduction is possible because U_k and U_{-k}

PHASE DIAGRAM

($f=6.46, w=1.0$ upper)

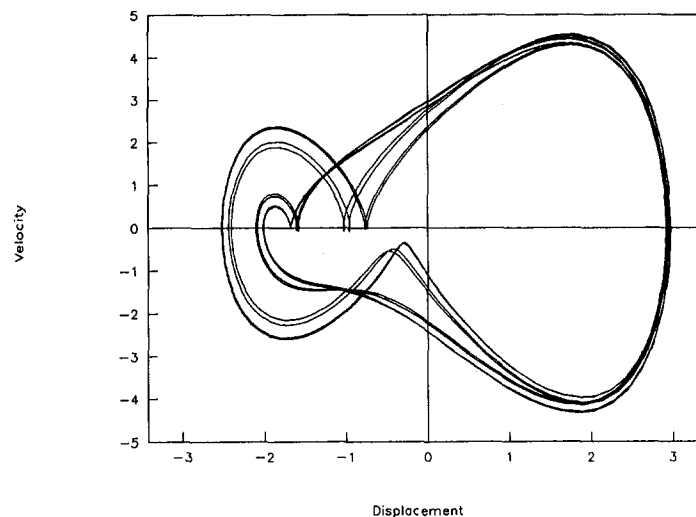


Fig. 6(b) Time history at $f = 6.46$ (lower branch)

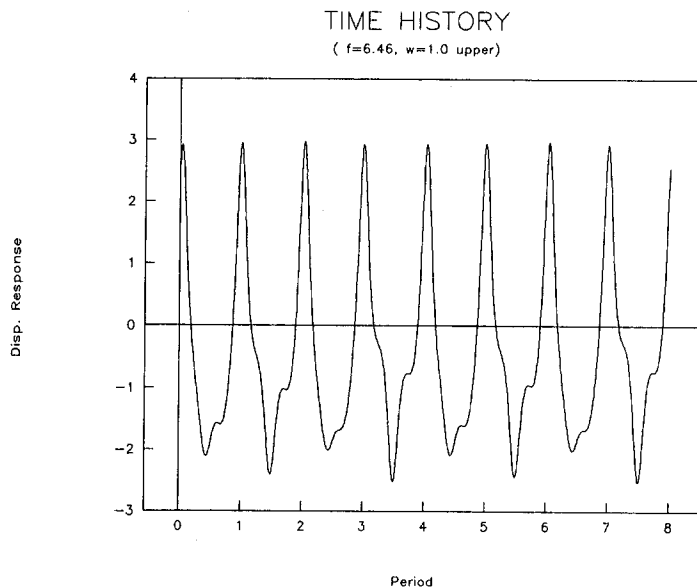


Fig. 6(c) Phase diagram at $f = 6.46$ (upper branch)

are complex conjugates. Assuming the original $f(\tau)$ presented in Eq. (2) be expanded simultaneously by a real and a complex discrete Fourier series, we have

$$f\left(\frac{2\pi q}{M}\right) = \sum_{r=-N}^{+N} F_r \exp\left(\frac{i2\pi qr}{M}\right) \\ = \frac{G_0}{2} + \sum_{r=1}^N G_r \cos\left(\frac{2\pi qr}{M}\right) + H_r \sin\left(\frac{2\pi qr}{M}\right) \\ q = 0, \dots, M-1. \quad (17)$$

Substituting the identity relation

$$\exp(i\vartheta) = \cos \vartheta + i \sin \vartheta \quad (18) \quad \text{therefore,}$$

we have

$$G_r = F_r + F_{-r} \quad (19a)$$

$$H_r = i(F_r - F_{-r}) \quad (19b)$$

$$G_r, H_r \in \mathbb{R}^{2n+1} \text{ and } F_r \in \mathbb{C}^{2n+1}$$

$$r = 0, 1, \dots, N.$$

Meanwhile, if the solution $u(\tau)$ is similarly presented,

$$u\left(\frac{2\pi q}{M}\right) = \sum_{r=-N}^{+N} C_r \exp\left(\frac{i2\pi qr}{M}\right) \\ = \frac{A_0}{2} + \sum_{r=1}^N A_r \cos\left(\frac{2\pi qr}{M}\right) + B_r \sin\left(\frac{2\pi qr}{M}\right) \\ q = 0, \dots, M-1 \quad (20)$$

$$q = 0, \dots, M-1 \quad (20)$$

$$C_r = \frac{1}{2}(A_r - iB_r) \quad (21a)$$

$$C_{-r} = \frac{1}{2}(A_r + iB_r) \quad (21b)$$

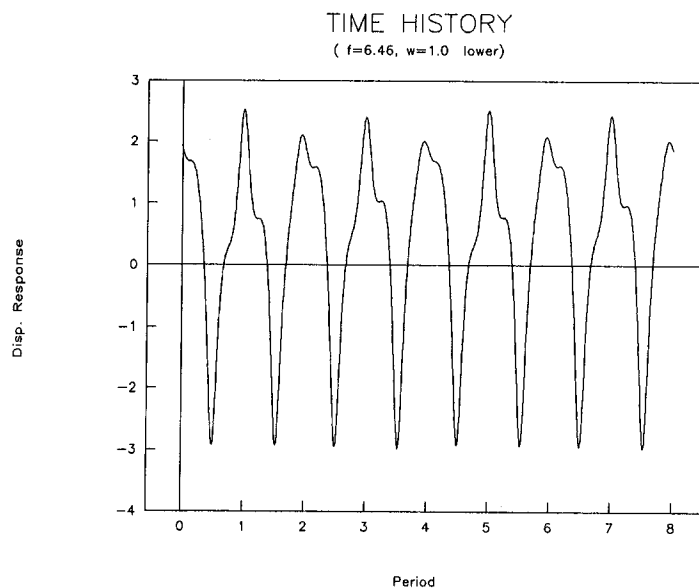


Fig. 6(d) Time history at $f = 6.46$ (upper branch)

$$A_r, B_r \in \mathbb{R} \text{ and } C_r \in \mathbb{R}$$

$$r = 0, 1, \dots, N.$$

Concurrently, the trigonometric coefficients of the residual function $\gamma(\tau)$ can be evaluated through the same substitutions

$$\begin{aligned} \gamma\left(\frac{2\pi q}{M}\right) &= \sum_{r=-N}^{+N} R_r \exp\left(\frac{-i2\pi qr}{M}\right) \\ &= \frac{R_{co}}{2} + \sum_{r=1}^N R_{cr} \cos\left(\frac{2\pi qr}{M}\right) - R_{sr} \sin\left(\frac{2\pi qr}{M}\right) \end{aligned} \quad (22)$$

$$q = 0, \dots, M-1$$

$$\begin{aligned} R_{cr} &= R_r + R_{-r} \\ &= \sum_{q=0}^{M-1} \gamma\left(\frac{2\pi q}{M}\right) \left[\exp\left(\frac{i2\pi qk}{M}\right) + \exp\left(\frac{-i2\pi qk}{M}\right) \right] \\ &= 2 \sum_{q=0}^{M-1} \gamma\left(\frac{2\pi q}{M}\right) \cos\left(\frac{2\pi qk}{M}\right) \end{aligned} \quad (23a)$$

$$R_{sr} = i(R_r - R_{-r}) = 2 \sum_{q=0}^{M-1} \gamma\left(\frac{2\pi q}{M}\right) \sin\left(\frac{2\pi qk}{M}\right). \quad (23b)$$

If the solution vector in the real incremental equations is arranged according to the order $\{\Delta \mathbf{U}\} = [\Delta A_0, \Delta A_1, \dots, \Delta A_N, \Delta B_1, \dots, \Delta B_N]^T$, the real form incremental equation can be written as

$$\begin{pmatrix} \mathbf{K}^{11} & \mathbf{K}^{12} \\ \mathbf{K}^{21} & \mathbf{K}^{22} \end{pmatrix} \{\Delta \mathbf{U}\} = \begin{Bmatrix} \mathbf{R}_{cr} \\ \mathbf{R}_{sr} \end{Bmatrix}. \quad (24)$$

From Eqs. (17), (18), (19), (20), (21), the real Jacobian matrix $[\mathbf{K}]$ can then be generated from Eq. (12) by the chain rule of differentiation

$$\begin{aligned} K_{kr}^{11} &= \frac{\partial G_k}{\partial A_r} = \frac{\partial G_k}{\partial F_k} \frac{\partial F_k}{\partial C_r} \frac{\partial C_r}{\partial A_r} + \frac{\partial G_k}{\partial F_k} \frac{\partial F_k}{\partial C_{-r}} \frac{\partial C_{-r}}{\partial A_{-r}} \\ &\quad + \frac{\partial G_k}{\partial F_{-k}} \frac{\partial F_{-k}}{\partial C_r} \frac{\partial C_r}{\partial A_r} + \frac{\partial G_k}{\partial F_{-k}} \frac{\partial F_{-k}}{\partial C_{-r}} \frac{\partial C_{-r}}{\partial A_{-r}} \\ &= \frac{1}{2} [J_{k,r} + J_{k,-r} + J_{-k,r} + J_{-k,-r}] \\ &\quad k = 0, \dots, N, \quad r = 0, \dots, N. \end{aligned} \quad (25a)$$

Similarly, we have

$$\begin{aligned} K_{kr}^{12} &= \frac{\partial G_k}{\partial B_r} = \frac{i}{2} [-J_{k,r} + J_{k,-r} - J_{-k,r} + J_{-k,-r}] \\ &\quad k = 0, \dots, N, \quad r = 1, \dots, N \end{aligned} \quad (25b)$$

$$\begin{aligned} K_{kr}^{21} &= \frac{\partial H_k}{\partial A_r} = \frac{i}{2} [J_{k,r} + J_{k,-r} - J_{-k,r} - J_{-k,-r}] \\ &\quad k = 1, \dots, N, \quad r = 0, \dots, N \end{aligned} \quad (25c)$$

$$\begin{aligned} K_{kr}^{22} &= \frac{\partial H_k}{\partial B_r} = \frac{1}{2} [J_{k,r} - J_{k,-r} - J_{-k,r} + J_{-k,-r}] \\ &\quad k = 1, \dots, N, \quad r = 1, \dots, N \end{aligned} \quad (25d)$$

where $J_{k,r}, J_{k,-r}, J_{-k,r}, J_{-k,-r}$ represent the corresponding elements in the complex Jacobian matrix. In summary,

$$\begin{pmatrix} K_{kr}^{11} \\ K_{kr}^{12} \\ K_{kr}^{21} \\ K_{kr}^{22} \end{pmatrix} = \begin{bmatrix} 0.5 & 0.5 & 0.5 & 0.5 \\ -i/2 & i/2 & -i/2 & i/2 \\ i/2 & i/2 & -i/2 & -i/2 \\ 0.5 & -0.5 & -0.5 & 0.5 \end{bmatrix} \begin{pmatrix} J_{k,r} \\ J_{k,-r} \\ J_{-k,r} \\ J_{-k,-r} \end{pmatrix}. \quad (26)$$

3 Continuous Method

An adaptive arc-length parameterization scheme is implemented to perform the path-following calculation as smoothly as possible. Suppose one advances the solution curve with a prescribed step value ρ , the auxiliary spherical surface of radius ρ will travel in \mathbb{R}^{2N+2} space and if there are intersections with the solution curves contained in original Eq. (2) the moving spherical surface will generate a sequence of points along these curves. The equation of the auxiliary surface is usually expressed as an arc-length constraint

$$g(\mathbf{U}, \xi) - \rho = 0 \quad (27a)$$

where ρ is the prescribed arc length of the solution curve and $g(\mathbf{U}, \xi)$ takes the role of path function that may be described by

$$g(\mathbf{U}, \xi) = [\partial \mathbf{U} / \partial \rho]^T \{\Delta \mathbf{U}\} + (\partial \xi / \partial \rho) (\Delta \xi) \quad (27b)$$

where $\Delta \xi$ represents the control parameter which can be either $\Delta \omega$ or $\Delta \lambda$ in Eq. (4), $\{\Delta \mathbf{U}\}$ is the unknown increment vector. The incremental Eq. (24) becomes

$$[\mathbf{K}]\{\Delta \mathbf{U}\} = \{\Phi\} \Delta \xi + \{\Delta \mathbf{R}_f\} \quad (28)$$

where $\{\Phi\}$ indicates the tangent vector along the solution curve. $\{\Delta \mathbf{R}_f\}$ is the residual vector related to $f(\tau)$. Therefore, together with Eq. (27b), we obtain the extended set of equations

$$\begin{bmatrix} \mathbf{K} & -\Phi^T \\ \partial \mathbf{U} / \partial \rho & \partial \xi / \partial \rho \end{bmatrix} \begin{bmatrix} \Delta \mathbf{U} \\ \Delta \xi \end{bmatrix} = \begin{bmatrix} \Delta \mathbf{R}_f \\ \rho - g_0 \end{bmatrix} \quad (29)$$

or

$$[\mathbf{K}_r]\{\Delta \mathbf{X}\} = \{\Delta \mathbf{P}\} \quad (30)$$

where g_0 refers to the approximated path function evaluated at the former iterating step; $\rho - g_0$ defines the searching direction on solution curve along which the solution errors existing in the initial approximation tends to be eliminated to the certain tolerant level (Rik, 1984). The properties of the solution points can be determined by (i) the determinant of Jacobian matrix including the subharmonic terms and (ii) the eigenvalues of the transition matrix in Floquet-Liapunov theory (Leung and Fung, 1989; Leung and Ge, 1992). For example, if $\det [K]$ and $\det [K_r]$ pass through zero simultaneously while one of the eigenvalues increase through positive one, the point is identified as a symmetry breaking or period $1T$ bifurcation point. If $\det [K]$ and $\det [K_r]$ pass through zero simultaneously while one of the eigenvalues decreases through negative one, the point is identified as a period double bifurcation point. And if $\det [K]$ pass through zero while the sign of $\det [K_r]$ remain unchanged, a fold point is encountered with one of its eigenvalues growing through positive unit.

4 Verification

To justify the formulas given in Section 2, we further compared them with the published results. Substituting Eq. (12) into (25a) gives

$$\begin{aligned} K_{kr}^{11} &= \frac{1}{2} [S(r-k) - r^2 \omega_0^2 \delta(r-k) + ir \omega_0 C(r-k) \\ &\quad + S(-r-k) - r^2 \omega_0^2 \delta(-r-k) - ir \omega_0 C(-r-k) \\ &\quad + S(r+k) - r^2 \omega_0^2 \delta(r+k) + ir \omega_0 C(r+k) \end{aligned}$$

$$+ S(-r+k) - r^2\omega_0^2\delta(-r+k) - ir\omega_0 C(-r+k)]. \quad (31)$$

Assuming $p = r - k$ or $p = r + k$, we apply the identity relation (18) to simplify Eq. (31),

$$S(p) + S(-p) = \sum_{q=0}^{M-1} s\left(\frac{2\pi q}{M}\right) \times \left[\exp\left(\frac{i2\pi qp}{M}\right) + \exp\left(\frac{-i2\pi qp}{M}\right) \right] = 2 \sum_{q=0}^{M-1} s\left(\frac{2\pi q}{M}\right) \cos\left(\frac{2\pi qp}{M}\right) \quad (32a)$$

$$iC(p) - iC(-p) = i \sum_{q=0}^{M-1} c\left(\frac{2\pi q}{M}\right) \times \left[\exp\left(\frac{i2\pi qp}{M}\right) - \exp\left(\frac{-i2\pi qp}{M}\right) \right] = -2 \sum_{q=0}^{M-1} c\left(\frac{2\pi q}{M}\right) \sin\left(\frac{2\pi qp}{M}\right) \quad (32b)$$

$$\delta(p) + \delta(-p) = \sum_{q=0}^{M-1} \left[\exp\left(\frac{i2\pi qp}{M}\right) + \exp\left(\frac{-i2\pi qp}{M}\right) \right] = 2 \sum_{q=0}^{M-1} \cos\left(\frac{2\pi qp}{M}\right) \quad (32c)$$

$r, k = 0, \dots, N.$

By the following trigonometric simplifications

$$\cos\left[\frac{2\pi q(r-k)}{M}\right] + \cos\left[\frac{2\pi q(r+k)}{M}\right] = 2 \cos\left(\frac{2\pi qk}{M}\right) \cos\left(\frac{2\pi qr}{M}\right) \quad (33a)$$

$$\sin\left[\frac{2\pi q(r-k)}{M}\right] + \sin\left[\frac{2\pi q(r+k)}{M}\right] = 2 \cos\left(\frac{2\pi qk}{M}\right) \sin\left(\frac{2\pi qr}{M}\right) \quad (33b)$$

we obtain

$$K_{kr}^{11} = 2 \sum_{q=0}^{M-1} \left[s\left(\frac{2\pi q}{M}\right) \cos\left(\frac{2\pi qr}{M}\right) - c\left(\frac{2\pi q}{M}\right) r\omega_0 \times \sin\left(\frac{2\pi qr}{M}\right) - r^2\omega_0^2 \cos\left(\frac{2\pi qr}{M}\right) \right] \cos\left(\frac{2\pi qk}{M}\right). \quad (34a)$$

Similarly,

$$K_{kr}^{12} = 2 \sum_{q=0}^{M-1} \left[s\left(\frac{2\pi q}{M}\right) \sin\left(\frac{2\pi qr}{M}\right) + c\left(\frac{2\pi q}{M}\right) r\omega_0 \times \cos\left(\frac{2\pi qr}{M}\right) - r^2\omega_0^2 \sin\left(\frac{2\pi qr}{M}\right) \right] \cos\left(\frac{2\pi qk}{M}\right) \quad (34b)$$

$$K_{kr}^{21} = 2 \sum_{q=0}^{M-1} \left[s\left(\frac{2\pi q}{M}\right) \cos\left(\frac{2\pi qr}{M}\right) - c\left(\frac{2\pi q}{M}\right) r\omega_0 \times \sin\left(\frac{2\pi qr}{M}\right) - r^2\omega_0^2 \cos\left(\frac{2\pi qr}{M}\right) \right] \sin\left(\frac{2\pi qk}{M}\right) \quad (34c)$$

$$K_{kr}^{22} = 2 \sum_{q=0}^{M-1} \left[s\left(\frac{2\pi q}{M}\right) \sin\left(\frac{2\pi qr}{M}\right) + c\left(\frac{2\pi q}{M}\right) r\omega_0 \times \cos\left(\frac{2\pi qr}{M}\right) - r^2\omega_0^2 \sin\left(\frac{2\pi qr}{M}\right) \right] \sin\left(\frac{2\pi qk}{M}\right). \quad (34d)$$

The factor 2 in Eqs. (34) and (23) can be canceled from both sides of Eq. (24). Therefore, the real Jacobian matrix generated in the present method are exactly the same as the result discretized from the Ferri's formulae (Ferri, 1983). However, the reduction of computational works at each Newtonian iteration is significant as tabulated in Table 1 and depicted in Fig. 2. The computer storage requirement is much reduced as we can construct the Jacobian in Eq. (12) using two Toeplitz sequences $S(k-r)$ and $C(k-r)$ only. The accuracy of the Newtonian iterations is also greatly enhanced at the vicinity of singular points. It is possible because the round-off errors in digital computation decrease with the significant reduction of the numerical multiplications involved.

5 Illustrative Examples

Consider the Duffing equation under harmonic forcing function of period $T = 2\nu\omega\pi$, $u'' + 2\mu u' + ku + \alpha u^3 = f \cos \omega t$, where μ, k, α, f are the damping, linear stiffness, cubic stiffness coefficients, and forcing amplitude, respectively, ν is the order of subharmonics considered.

(i) **Cyclic fold.** Consider the case when $\mu = 0.1, k = 1, \alpha = 0.1, \nu = 1$ are fixed values, and f is taken as 2, 3, 4, 5, respectively. As we slowly vary the remaining control parameter ω from 1 to 3 incrementally, it is found that two limit cycles of different stability coexist for certain values of the control parameter. They approach one another as we vary the control parameter ω , Fig. 3. The dotted lines represent the unstable solutions which are not observable physically. At fold points, the stable solutions collide and disappear out of the immediate neighborhood associating with the so-called jump phenomenon or hysteresis. The Jacobian in incremental Eq. (24) was evaluated by both approaches; the TJM formula, Eqs. (25a-d), and the IHB formula, Eqs. (30a-d). We compare the numerical performance of the both the IHB and the present TJM methods for the construction of the resonance response diagram, Fig. 3, for $f = 5$. We tabulate the information in constructing the response diagram between $1 < \omega < 2$, where the transition is smooth, in Table 2 for step arc-length $\rho = 0.4$ and residual tolerance 10^{-6} . I_a and T_a are the number of iterations and the computing time required (by a 486 DX-50 IBM compatible computer) in each step for method (a), IHB, and I_b and T_b for method (b), TJM, respectively. It is shown that IHB requires more iterations to achieve the same accuracy and each iteration requires more computation than the TJM method. In the range $2 < \omega < 2.5$, the arc-length step $\rho = 0.4$ is too large for IHB, although it can be handled by TJM comfortably. In addition, the storage requirement is very favorable for TJM because the Jacobian is constructed by two Toeplitz matrices only. The fourth order Runge-Kutta method is also applied in the range $1 < \omega < 2$ for comparison purpose. It needs 16'87" (averaged) CPU-time to reach one at rest initial conditions.

(ii) **Period-Double Cascade.** A sequence of n period-doubling bifurcation is computed and a set of stable limit cycles with $\nu = 2^n$ is finally obtained when the other system parameters

Table 4 Comparison of CPU times

ν	TERMS	PRESENT METHOD	R. K. Method	
			Regular P.T	Singular P.T(f)
1	21	00:00.44	00:18.13	03:23.44(2.395561)
2	41	00:10.10	00:22.19	21:35.15(5.387086)
4	81	00:16.75	00:25.98	06:53.76(6.264049)
8	161	00:50.41	00:48.90	03:03.83(6.443807)

are defined as $\mu = 0.1$, $k = 0$, $\alpha = 1$, $\omega = 1$, and f is varying incrementally from zero to seven. The stability points along the solution path are tabulated in Table 3. With the application of analytical Jacobian when the additional bifurcated subharmonic components are taken into account, the location of singularity as well as the continuation along the second branch are computed by the inverse iteration without trial and error (Leung and Fung, 1989) (Fig. 4). The ratios of distance of the period double bifurcation points λ_i , as mentioned by many nonlinear dynamics textbook, are found to have a trend to approach the universal Feigenbaum number of 4.67. (Table 3). On the other hand, after the symmetry breaking, the two asymmetric period double cascades coexist in the upper and the lower branch. Fig. 5(a)–(d) exhibit the coexisted upper and lower periodic orbits of period $2T$, where the phase diagrams and time histories are drawn, respectively. Figure 6(a)–(d) show the period $8T$ bifurcation existed. The harmonic terms used for numerical computation is up to $20\nu + 1$ and the ideal numbers of iteration are expected to be 4. Under such circumstances, in Table 4, comparisons are made between TJM and Runge-Kutta methods on the amount of computational work. It is found that at the vicinity of stability points, the convergent rate of Runge-Kutta method is very slow.

6 Conclusion

We have described an efficient TJM algorithm for implementing the incremental harmonic balance to nonlinear oscillations. Significant improvements to the existing IHB on efficiency and

convergency have been illustrated. On the other hand, it is worth mentioned that, the amount of analytical work involved in the proposed algorithm is just about the same as those in numerical integration; however, their efficiencies are different in many orders of magnitude especially at the vicinity of the stability points.

Acknowledgment

The research is supported by the Research Grant Council of Hong Kong.

References

- Brigham, E. O., 1974, *The Fast Fourier Transformation*, Prentice-Hall, Englewood Cliffs, NJ.
- Cameron, T. M., and Griffin, J. H., 1989, "An Alternating Frequency/Time Domain Method for Calculating the Steady-State Response of Nonlinear Dynamic Systems," *ASME JOURNAL OF APPLIED MECHANICS*, Vol. 56, pp. 149–154.
- Ferri, A. A., 1986, "On the Equivalence of the Incremental Harmonic Balance Method and the Harmonic Balance-Newton Raphason Method," *ASME JOURNAL OF APPLIED MECHANICS*, Vol. 53, pp. 455–457.
- Iooss, G., and Joseph, D. D., 1980, *Elementary Stability and Bifurcation Theory*, Springer-Verlag, New York.
- Kim, Y. B., and Noah, S. T., 1991, "Stability and Bifurcation Analysis of Oscillators With Piecewise-Linear Characteristic: A General Approach," *ASME JOURNAL OF APPLIED MECHANICS*, Vol. 58, pp. 545–553.
- Lau, S. L., and Cheung, Y. K., 1981, "Amplitude Incremental Variational Principle for Nonlinear Vibration of Elastic Systems," *ASME JOURNAL OF APPLIED MECHANICS*, Vol. 48, pp. 959–964.
- Lau, S. L., Cheung, Y. K., and Wu, S. Y., 1982, "Variable Parameter Incrementation Method for Dynamics Instability of Linear and Nonlinear System," *ASME JOURNAL OF APPLIED MECHANICS*, Vol. 49, pp. 849–853.
- Leung, A. Y. T., and Fung, T. C., 1989, "Construction of Chaotic Regions," *Journal of Sound and Vibration*, Vol. 131, pp. 445–455.
- Leung, A. Y. T., and Ge, T., 1992, "Multi-Harmonic Branch Switching method for Nonlinear Oscillations," *Microcomputers in Civil Engineering*, submitted for publication.
- Ling, F. H., and Wu, X. X., 1987, "Fast Galerkin Method and Its Application to Determine Periodic Solutions of Non-linear Oscillators," *Int. J. Non-Linear Mechanics*, Vol. 22, No. 2, pp. 89–98.
- Pierre, C., Ferri, A. A., and Dowell, E. H., 1985, Multi-Harmonic Analysis of Dry Friction Damped Systems Using an Incremental Harmonic Balance Method, *ASME JOURNAL OF APPLIED MECHANICS*, Vol. 52, pp. 958–964.
- Riks, E., 1984, "Bifurcation and Stability: A Numerical Approach," *Innovative Methods for Nonlinear Problems*, W. K. Liu et al., eds., Pineridge Press, Swansea, U.K.

K. M. Liew
Director,
Mem. ASME.

K. C. Hung
Teaching Assistant.

M. K. Lim
Associate Professor.

School of Mechanical and
Production Engineering,
Nanyang Technological University,
Nanyang Avenue,
Singapore 639798

Vibration of Stress-Free Hollow Cylinders of Arbitrary Cross Section

A three-dimensional elasticity solution to the vibrations of stress-free hollow cylinders of arbitrary cross section is presented. The natural frequencies and deformed mode shapes of these cylinders are obtained via a three-dimensional displacement-based energy formulation. The technique is applied specifically to the parametric investigation of hollow cylinders of different cross sections and sizes. It is found that the cross-sectional property of the cylinder has significant effects on the normal mode responses, particularly, on the transverse bending modes. By varying the length-to-width ratio of these elastic cylinders, interesting results demonstrating the dependence of frequencies on the length of the cylinder have been concluded.

1 Introduction

The free vibrations of isotropic elastic solid cylinders with traction-free surfaces have been investigated by several researchers over the last few decades. A large proportion of these works, however, is concerned with the axisymmetric modes of vibration. McNiven and Perry (1962) and Rumerman and Raynor (1971) have presented frequency solutions to free cylinders of infinite length. Hutchinson (1971), on the other hand, presented results for the axisymmetric vibrations of a free finite-length solid cylinder. Later, Hutchinson (1980) expanded his earlier formulation (Hutchinson, 1971) and solved the general three-dimensional vibrations of a solid cylinder which includes the nonaxisymmetric vibration modes. A recent study by Liew et al. (1995) on the vibration of three-dimensional elastic solids also includes the results for a short, solid square cylinder with stress-free surfaces. A remarkable benchmark experimental data for stress-free circular cylinders was reported by McMahon (1964). To date, many pioneering works in this topic, however, are limited to only solid cylinders. Results for cylinders with a deep cavity are virtually nonexistent. Very often in engineering practice, cylindrical elastic solids are created with deep cavities to reduce their weight, provide access, and to cut down on production costs. A proper three-dimensional free-vibration study on these hollow cylinders will, therefore, be useful to many branches of engineering.

The present work proposes an energy-based solution approach to the free-vibration analysis of arbitrarily shaped elastic hollow cylinders. The method is developed based on a global three-dimensional elasticity energy principle with polynomial-based displacement shape functions. The functions are expressed in the forms of truncated series of one and two-dimensional orthogonal polynomials. The one-dimensional longitudinal function is employed to account for the boundary conditions at both ends. On the other hand, the two-dimensional surface function is uniquely constructed to satisfy the essential geometric boundary conditions of the internal and external walls of the cylinder.

Contributed by the Applied Mechanics Division of THE AMERICAN SOCIETY OF MECHANICAL ENGINEERS for publication in the ASME JOURNAL OF APPLIED MECHANICS.

Discussion on this paper should be addressed to the Technical Editor, Prof. Lewis T. Wheeler, Department of Mechanical Engineering, University of Houston, Houston, TX 77204-4792, and will be accepted until four months after final publication of the paper itself in the ASME JOURNAL OF APPLIED MECHANICS.

Manuscript received by the ASME Applied Mechanics Division, Nov. 15, 1993; final revision, Aug. 18, 1994. Associate Technical Editor: F. Y. M. Wan.

In this study, we focus on stress-free symmetric hollow cylinders with arbitrary cross section. By considering the symmetry inherent in the problem, the natural vibration of the elastic solids can be categorized into four distinct symmetry classes. Frequency parameters have been found for hollow cylinders with different cross section properties and sizes. The accuracy of the results is validated through direct comparisons with the existing three-dimensional elasticity solutions and experimental data. For the first time, vivid three-dimensional vibration mode shapes of these hollow cylinders are presented which serve to enhance our understanding on the physics of vibration of this kind.

2 Three-Dimensional Elasticity Solutions

Consider a hollow cylinder of finite length L as shown in Fig. 1. The cross section is assumed to be arbitrary. The outer and inner characteristic dimensions of the cross section are denoted by a_0 and a_i , respectively. The orientation of the cylinder is defined on a Cartesian coordinate system (x_1, x_2, x_3) . At a general point, the spatial displacement may be resolved into u_1, u_2 (lateral) and u_3 (longitudinal) components, respectively.

2.1 Truncated Double Polynomial Series. For an elastic solid undergoing linear, small-strain, simple harmonic vibratory motion, the displacement components have the general forms,

$$u_i(x_1, x_2, x_3, t) = U_i(x_1, x_2, x_3) \sin \omega t; \quad i = 1, 2, 3 \quad (1)$$

where ω and t denote the angular frequency and time, respectively. The displacement amplitude function, $U_i(x_1, x_2, x_3)$, for each displacement component assumes the form of a truncated double polynomial series in one and two dimensions. It is expressed as follows:

$$U_i(x_1, x_2, x_3) = \sum_{m=1}^M \sum_{n=1}^N C_{mn}^i \phi_m(x_1, x_2) \psi_n(x_3); \quad i = 1, 2, 3. \quad (2)$$

The two-dimensional polynomials, $\phi_m(x_1, x_2)$ dictate the lateral surface variations of each displacement component. The one-dimensional polynomials $\psi_n(x_3)$, on the other hand, approximate the displacement variations in the longitudinal direction. These polynomials have been used in the authors' earlier work (Liew, et al., 1993).

2.2 Treatment of Free Wall Conditions. Considering a cylinder with free-wall conditions, the corresponding boundary conditions at the inner and outer walls are

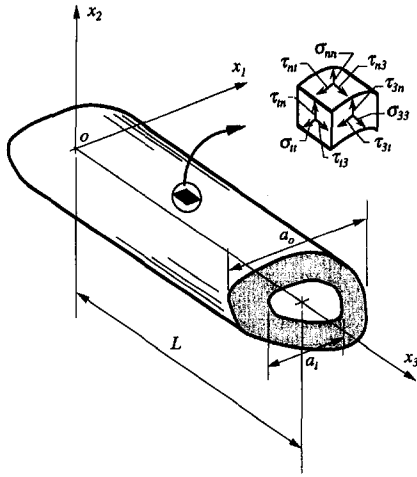


Fig. 1 Geometry and dimensions of an arbitrarily shaped hollow cylinder

$$\sigma_{nn} = \tau_{nt} = \tau_{t3} = 0 \quad (3)$$

where n and t are the coordinate normal and tangent to the wall boundary. σ_{nn} is the normal stress, τ_{nt} and τ_{t3} are the shearing stresses. For a cylinder with symmetric cross section, the deflection mode shapes can be divided into four symmetry classes. They are the doubly symmetry modes (SS), symmetry-antisymmetry modes (SA), symmetry-antisymmetry modes (AS) and doubly antisymmetry modes (AA) about the x_1x_3 and x_2x_3 planes, respectively. At each symmetry class, the basic functions chosen are given in Table 1. It should be noted that in the Ritz procedure, it is sufficient to satisfy the essential boundary conditions. In the minimization process, Eq. (3) is satisfied only approximately.

In this study, both ends of the hollow cylinder are assumed to be free from stresses. The stress-free boundary conditions are defined as

$$\sigma_{33} = \tau_{3n} = \tau_{t3} = 0. \quad (4)$$

The following basic functions satisfy the geometric boundary conditions of a cylinder with stress-free ends:

$${}^i\psi_1(x_3) = 1.0; i = 1, 2, 3. \quad (5)$$

2.3 Energy Functional in a Three-Dimensional Space.

For a linear, small-strain vibratory motion, the strain energy of an elastic solid can be expressed as

$$V = \frac{1}{2} \iiint_V \sigma^T \epsilon dV \quad (6)$$

where $\epsilon = \{\epsilon_{ij}; i, j = 1, 2, 3\}$ and $\sigma = \{\sigma_{ij}; i, j = 1, 2, 3\}$ are the strain and stress tensors, respectively.

The constitutive relation between the stress and strain is given by

$$\sigma = \mathbf{D}\epsilon. \quad (7)$$

The elasticity matrix \mathbf{D} for isotropic material is given by

$$\mathbf{D} = \begin{bmatrix} d_{11} & d_{12} & d_{13} & 0 & 0 & 0 \\ d_{12} & d_{22} & d_{23} & 0 & 0 & 0 \\ d_{13} & d_{23} & d_{33} & 0 & 0 & 0 \\ 0 & 0 & 0 & d_{44} & 0 & 0 \\ 0 & 0 & 0 & 0 & d_{55} & 0 \\ 0 & 0 & 0 & 0 & 0 & d_{66} \end{bmatrix} \quad (8)$$

and

$$d_{kk} = \frac{(1 - \nu)E}{(1 + \nu)(1 - 2\nu)}; k = 1, 2, 3 \quad (9a)$$

$$d_{12} = \frac{\nu E}{(1 + \nu)(1 - 2\nu)}; d_{12} = d_{13} = d_{23} \quad (9b)$$

$$d_{ll} = \frac{E}{1 + \nu}; l = 4, 5, 6 \quad (9c)$$

where E is the Young's modulus and ν is the Poisson ratio.

The kinetic energy for free vibration is defined as

$$T = \frac{\rho}{2} \iiint_V \sum_{i=1}^3 \dot{u}_i^2 dV \quad (10)$$

in which u_i ; $i = 1, 2, 3$ are the periodic displacement components. The symbol ρ denotes the mass density per unit volume. The volumetric integrations in Eqs. (6) and (10) are performed over the volume of the cylinder which excludes the deep cavity.

An instantaneous energy functional consisting of the strain and kinetic energies can be defined as

$$\Pi = V - T. \quad (11)$$

2.4 The Eigenvalue Matrix of a Hollow Cylinder. By eliminating the periodic components and replacing the spatial displacements with the displacement amplitude functions defined in Eq. (2) into Eq. (11) gives the maximum energy functional of the hollow cylinder:

$$\Pi_{\max} = V_{\max} - T_{\max}. \quad (12)$$

This is minimized with respect to the undetermined coefficients by setting

$$\frac{\partial \Pi_{\max}}{\partial C_{mn}^i} = 0; i = 1, 2, 3. \quad (13)$$

The resulting eigenvalue matrix has the following form:

$$\left(\begin{bmatrix} \mathbf{k}^{11} & \mathbf{k}^{12} & \mathbf{k}^{13} \\ & \mathbf{k}^{22} & \mathbf{k}^{23} \\ \text{Sym} & & \mathbf{k}^{33} \end{bmatrix} - \lambda^2 \begin{bmatrix} \mathbf{m}^{11} & 0 & 0 \\ & \mathbf{m}^{22} & 0 \\ \text{Sym} & & \mathbf{m}^{33} \end{bmatrix} \right) \begin{Bmatrix} C^1 \\ C^2 \\ C^3 \end{Bmatrix} = \begin{Bmatrix} 0 \\ 0 \\ 0 \end{Bmatrix}. \quad (14)$$

The explicit form of the respective elements in the stiffness and mass matrices are given as follows:

$$k_{mjnk}^{11} = \frac{1 - \nu}{(1 - 2\nu)} (\mathbf{E}_{mj}^{1010} \mathbf{F}_{nk}^{00})_{11} + \frac{1}{2} (\mathbf{E}_{mj}^{0101} \mathbf{F}_{nk}^{00})_{11} + \frac{1}{2} \left(\frac{a_0}{L} \right)^2 (\mathbf{E}_{mj}^{0000} \mathbf{F}_{nk}^{11})_{11} \quad (15a)$$

$$k_{mjnk}^{12} = \frac{\nu}{1 - 2\nu} (\mathbf{E}_{mj}^{1001} \mathbf{F}_{nk}^{00})_{12} + \frac{1}{2} (\mathbf{E}_{mj}^{0100} \mathbf{F}_{nk}^{00})_{12} \quad (15b)$$

Table 1 Basic two-dimensional surface functions used in each symmetry class of vibration

Symmetry class	Two-dimensional surface function		
	${}^1\phi_1(x_1, x_2)$	${}^2\phi_1(x_1, x_2)$	${}^3\phi_1(x_1, x_2)$
SS	x_1	x_2	1
SA	x_1x_2	1	x_2
AS	1	x_1x_2	x_1
AA	x_2	x_1	x_1x_2

Table 2 Convergence of frequency parameters, $\lambda = \omega a_0 \sqrt{\rho/E}$, for stress-free hollow cylinders with symmetric cross sections (inner-to-outer characteristic dimension, $a_i/a_o = 0.5$; length-to-width ratio, $L/a_o = 5.0$; $\nu = 0.3$)

Order of polynomials	Symmetry Classes and Mode Sequence Number								
	SS-1	SS-2	SS-3	SA-1†	SA-2†	SA-3†	AA-1	AA-2	AA-3
(a.) Solid cylinder with an annular cross section									
$p=6, q=5$	0.6267	1.2349	1.2390	0.2218	0.6243	1.1781	0.3898	0.7822	1.2349
$p=6, q=7$	0.6265	1.2326	1.2363	0.2203	0.5119	0.8495	0.3897	0.7793	1.1692
$p=6, q=8$	0.6265	1.2319	1.2360	0.2203	0.5083	0.8347	0.3897	0.7793	1.1692
$p=6, q=9$	0.6265	1.2319	1.2360	0.2203	0.5082	0.8343	0.3897	0.7793	1.1692
(b.) Square cylinder with a deep circular cavity									
$p=6, q=5$	0.6261	1.2389	1.2577	0.2435	0.6580	1.1964	0.3566	0.7157	1.2093
$p=6, q=7$	0.6260	1.2344	1.2560	0.2419	0.5453	0.9015	0.3565	0.7128	1.0693
$p=6, q=8$	0.6260	1.2344	1.2555	0.2419	0.5417	0.8730	0.3565	0.7128	1.0689
$p=6, q=9$	0.6260	1.2344	1.2555	0.2419	0.5416	0.8729	0.3565	0.7128	1.0689
(c.) Square cylinder with a deep square cavity									
$p=6, q=5$	0.6260	1.1327	1.1517	0.2466	0.5564	1.1717	0.3559	0.7142	1.0001
$p=6, q=7$	0.6258	1.1319	1.1483	0.2450	0.5464	0.8818	0.3557	0.7112	0.9975
$p=6, q=8$	0.6258	1.1315	1.1483	0.2450	0.5427	0.8676	0.3557	0.7112	0.9971
$p=6, q=9$	0.6258	1.1315	1.1483	0.2450	0.5426	0.8673	0.3557	0.7112	0.9971

†For symmetrical cross sections, the symmetry-antisymmetry (SA) modes and the antisymmetry-symmetry (AS) modes have the same frequency values.

$$k_{mjnk}^{13} = \left(\frac{a_0}{L}\right) \left\{ \frac{\nu}{(1-2\nu)} (\mathbf{E}_{mj}^{1000} \mathbf{F}_{nk}^{01})_{13} + \frac{1}{2} (\mathbf{E}_{mj}^{0010} \mathbf{F}_{nk}^{10})_{13} \right\} \quad (15c)$$

$$k_{mjnk}^{22} = \frac{1-\nu}{(1-2\nu)} (\mathbf{E}_{mj}^{0101} \mathbf{F}_{nk}^{00})_{22} + \frac{1}{2} (\mathbf{E}_{mj}^{1010} \mathbf{F}_{nk}^{10})_{22} \quad (15d)$$

$$k_{mjnk}^{23} = \left(\frac{a_0}{L}\right) \left\{ \frac{\nu}{(1-2\nu)} (\mathbf{E}_{mj}^{0010} \mathbf{F}_{nk}^{01})_{23} + (\mathbf{E}_{mj}^{0001} \mathbf{F}_{nk}^{10})_{23} \right\} \quad (15e)$$

$$k_{mjnk}^{33} = \left(\frac{a_0}{L}\right)^2 \left\{ \frac{1-\nu}{(1-2\nu)} (\mathbf{E}_{mj}^{0000} \mathbf{F}_{nk}^{11})_{33} + \frac{1}{2} (\mathbf{E}_{mj}^{0101} \mathbf{F}_{nk}^{00})_{33} \right\} + \frac{1}{2} (\mathbf{E}_{mj}^{0101} \mathbf{F}_{nk}^{00})_{33} \quad (15f)$$

and

$$m_{mjnk}^{11} = (1+\nu) (\mathbf{E}_{mj}^{0000} \mathbf{F}_{nk}^{00})_{11} \quad (15g)$$

$$m_{mjnk}^{22} = (1+\nu) (\mathbf{E}_{mj}^{0000} \mathbf{F}_{nk}^{00})_{22} \quad (15h)$$

$$m_{mjnk}^{33} = (1+\nu) (\mathbf{E}_{mj}^{0000} \mathbf{F}_{nk}^{00})_{33} \quad (15i)$$

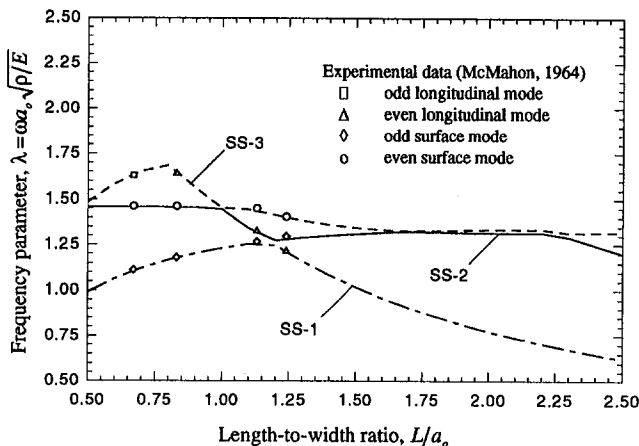


Fig. 2 Plot of first three lowest doubly symmetry (SS) modes for a stress-free solid circular cylinder at different length ($\nu = 0.294$)

where

$$(\mathbf{E}_{mj}^{defg})_{\alpha\beta} = \iint_A \left[\frac{\partial^{d+e} \{ {}^\alpha \phi_m(\bar{x}_1, \bar{x}_2) \}}{\partial \bar{x}_1^d \partial \bar{x}_2^e} \right] \times \left[\frac{\partial^{f+g} \{ {}^\beta \phi_j(\bar{x}_1, \bar{x}_2) \}}{\partial \bar{x}_1^f \partial \bar{x}_2^g} \right] d\bar{x}_1 d\bar{x}_2 \quad (16a)$$

$$(\mathbf{F}_{nk}^{rs})_{\alpha\beta} = \int_{-0.5}^{0.5} \left[\frac{\partial^r \{ {}^\alpha \psi_n(\bar{x}_3) \}}{\partial \bar{x}_3^r} \right] \left[\frac{\partial^s \{ {}^\beta \psi_k(\bar{x}_3) \}}{\partial \bar{x}_3^s} \right] d\bar{x}_3 \quad (16b)$$

in which $m, j = 1, 2, \dots [(p+1)(p+2)/2]$, $n, k = 1, 2, \dots q$ and $\alpha, \beta = 1, 2, \text{ and } 3$. The normalized variables, \bar{x}_1, \bar{x}_2 , and \bar{x}_3 are defined as

$$\bar{x}_1 = \frac{x_1}{a_0}; \bar{x}_2 = \frac{x_2}{a_0} \quad \text{and} \quad \bar{x}_3 = \frac{x_3}{L} \quad (17)$$

Finally, by solving the eigenvalue equation defined in Eq. (14) yields the eigenvalues of the hollow cylinder:

$$\lambda = \omega a_0 \sqrt{\rho/E} \quad (18)$$

3 Normal Modes of Hollow Cylinders

Frequency solutions for hollow cylinders of various cross sections have been obtained from the present formulation. In this study we focus only on three practical cases to illustrate the method. These cases are: (1) a hollow cylinder with annular cross section; (2) a square cylinder with a deep circular cavity; and (3) a square cylinder with a deep square cavity.

3.1 Convergence Characteristics. To ascertain the reliability of the present formulation, comprehensive convergence studies have been carried out for hollow cylinders of different

Table 3 Comparison of transverse vibration frequency parameters, $\lambda = \omega a_0 \sqrt{\rho/E}$, for a stress-free circular solid cylinder at different length-to-width ratios

Mode	Source of results	Length-to-width ratio, L/a					
		1.0	1.25	2.0	2.50	5.0	10.0
SA-1	Hutchinson	2.47324	1.86902	0.95960	0.67752	0.20444	0.05524
	Present 3-D	2.47308	1.86876	0.95950	0.67740	0.20412	0.05454
		(0.006)†	(0.014)	(0.010)	(0.018)	(0.157)	(1.283)
SA-2	Hutchinson	2.66806	2.40800	1.77520	1.38064	0.49476	0.14476
	Present 3-D	2.66794	2.40782	1.77508	1.38052	0.49452	0.14410
		(0.004)	(0.007)	(0.007)	(0.009)	(0.049)	(0.458)
SA-3	Hutchinson	-	-	2.59376	2.10542	0.84590	0.26804
	Present 3-D	3.47491	2.68794	2.59400	2.10596	0.84654	0.26778
		-	-	(-0.009)	(-0.026)	(0.076)	(0.097)

†Figure in parenthesis denotes the discrepancy in %.

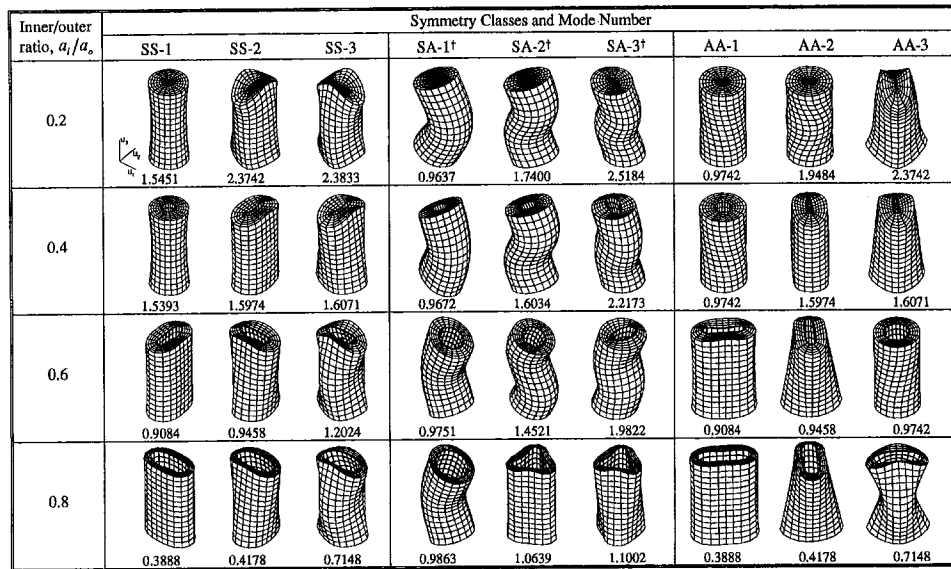


Fig. 3 Vibration mode shapes of an annular hollow cylinder at different inner-to-outer characteristic dimensions, a_i/a_o and $L/a_o = 2.0$ (†deformed geometries for the symmetry-antisymmetry (SA) modes are equivalent to the antisymmetry-symmetry (AS) modes in this case)

cross-sectional shapes. Table 2 shows the rate of convergence of the frequency parameters, $\lambda = \omega a_o \sqrt{\rho/E}$, at each symmetry class of vibration. The inner-to-outer characteristic dimension, a_i/a_o , and the length to width ratio, L/a_o , of these cylinders are fixed at 0.5 and 5.0, respectively. The degree, p , of the polynomial in the lateral surface function and the number of terms, q , for the longitudinal function are varied in different steps to show the relative effects on the convergence rate. It is observed that $p = 6$ is required to approximate the surface variations in a doubly connected domain. By increasing the number of terms, q , used in the longitudinal direction, significant improvement on the convergence rate is achieved. It is also deduced that the cross sections of the hollow cylinder has very little effect on the convergence rate. From the above numerical experiment, it is deduced that fairly accurate frequency results can be obtained with admissible functions of $p = 6$ and $q = 9$ in each displacement component.

3.2 Comparison of Results.

3.2.1 Experimental Benchmark Data. The first reported experimental results on free vibration of stress-free cylindrical solids are attributed to McMahon (1964). He examined the natural frequencies and mode shapes for cylinders of different sizes and presented a very comprehensive set of frequency data. Both aluminium and steel materials have been used in his fabrication of these cylindrical solids.

In this section, we compared the present predicted solutions with the benchmark data of McMahon (1964) for steel solid cylinders with length varying in the range of $0.5 \leq L/a_o \leq 2.50$. The frequency spectral of the first three lowest doubly symmetry (SS) modes is presented in Fig. 2. McMahon (1964) devised a different characterization of the vibration modes for the solid cylinder. The present doubly symmetry modes fall into the set of results presented for circumferential order of zero and

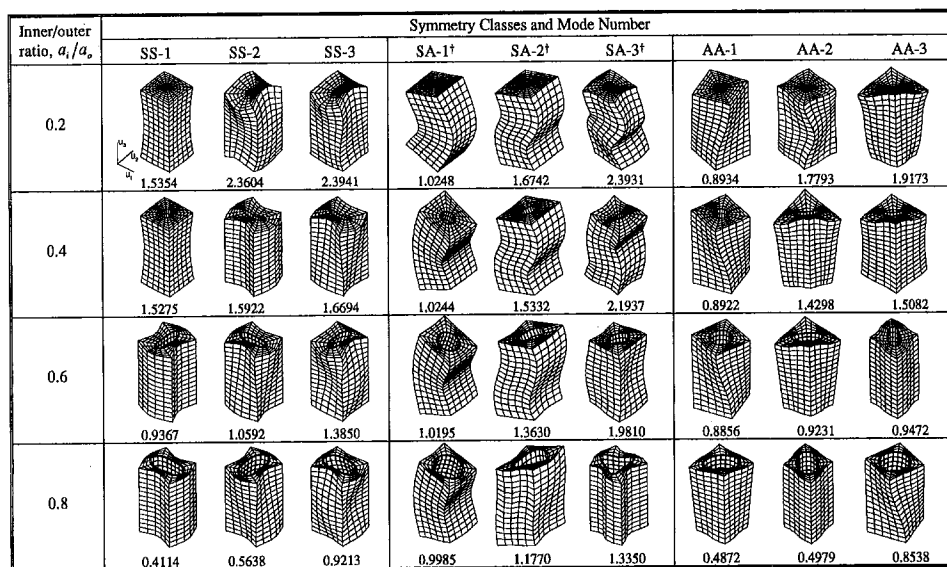


Fig. 4 Vibration mode shapes of a square cylinder with a deep circular cavity at different inner-to-outer characteristic dimensions, a_i/a_o and $L/a_o = 2.0$ (†deformed geometries for the symmetry-antisymmetry (SA) modes are equivalent to the antisymmetry-symmetry (AS) modes in this case)

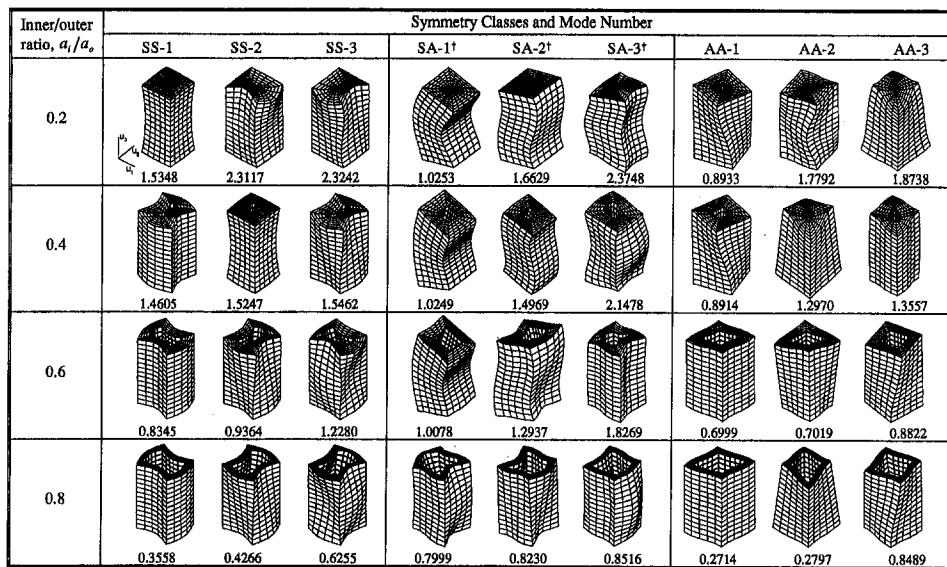


Fig. 5 Vibration mode shapes of a square cylinder with a deep square cavity at different inner-to-outer characteristic dimensions, a_i/a_o and $L/a_o = 2.0$ (†deformed geometries for the symmetry-antisymmetry (SA) modes are equivalent to the antisymmetry-symmetry (AS) modes in this case)

two in his experimental work. The symbols in Fig. 2 denotes the experimental points reproduced from the work of McMahon (1964). The Poisson ratio used for the computation is taken as $\nu = 0.293$ (which corresponds to steel material). The terms odd and even used in this figure describe antisymmetry and symmetry motions about the longitudinal direction of the cylinder, respectively.

From the figure, it is evident that the present predictions are in excellent agreement with the experimental results. In addition, it is interesting to note that the odd longitudinal rod mode (denoted by triangle) passes gradually from SS-3 to SS-2 and finally merges with the fundamental doubly symmetry (SS-1) mode. Similar mode crossings of this nature are also observed for the odd and even surface modes.

3.2.2 Three-Dimensional Analytical Results. The frequency results for stress free hollow cylinders of arbitrary cross section are very limited in the literature. To enable comparison with the existing three-dimensional solutions, we have computed the frequency parameters, $\lambda = \omega a_o \sqrt{\rho/E}$, for a stress-free elastic solid circular cylinder treated earlier by Hutchinson (1981). Table 3 compares the first three frequency parameters of the symmetry-antisymmetry (SA) modes with the analytical solutions of Hutchinson (1981). Excellent agreement is found for all the length-to-width ratios. The percentage of discrepancy between both methods is found to be well within 1.0 percent except for the SA-1 mode at a length-to-width ratio of 10.0 which produces a maximum discrepancy of 1.3 percent.

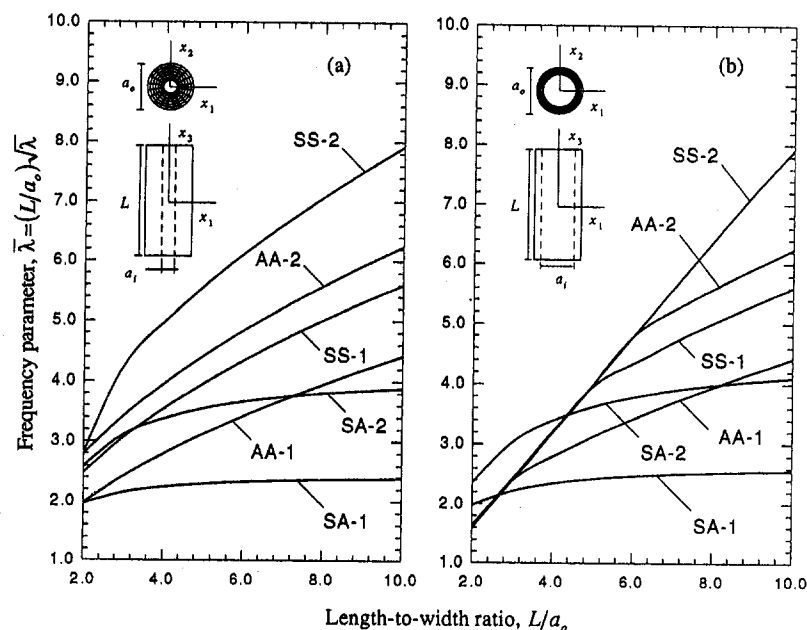


Fig. 6 Plots of frequency parameters $\bar{\lambda} = (L/a_o)\lambda$ versus length-to-width ratio, L/a_o , for a stress-free hollow cylinder with an annular cross section; (a) $a_i/a_o = 0.3$ and (b) $a_i/a_o = 0.7$

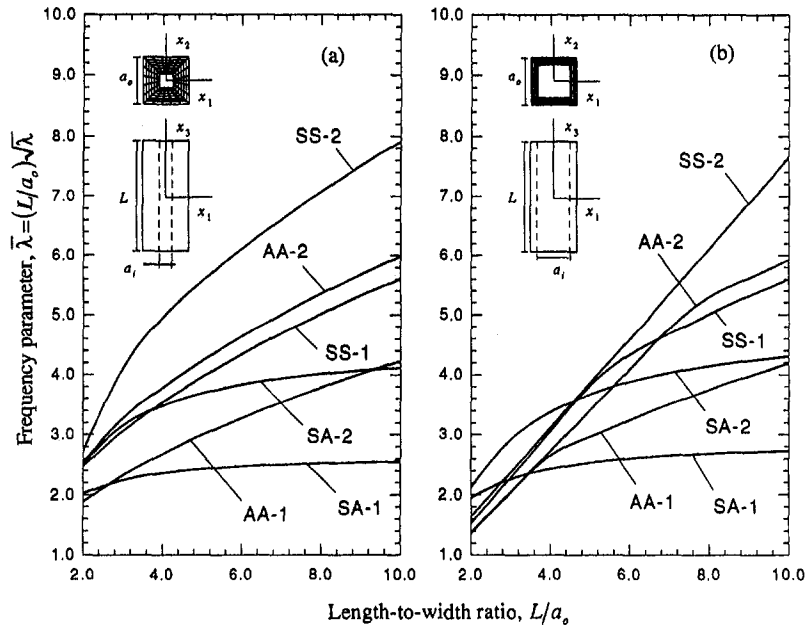


Fig. 7 Plots of frequency parameters $\bar{\lambda} = (L/a_0)\sqrt{\lambda}$ versus length-to-width ratio, L/a_0 , for a stress-free square hollow cylinder with a deep square cavity; (a) $a_i/a_0 = 0.3$ and (b) $a_i/a_0 = 0.7$

3.3 Vibration Frequencies and Mode Shapes. In this section, the natural frequencies and mode shapes of different hollow cylinders are presented. Figures 3 to 5 show the deformed geometries of the stress-free hollow cylinders of finite length ($L/a_0 = 2.0$) with different cross sections.

For the annular hollow cylinder depicted in Fig. 3, it is observed that the natural frequencies and deformed mode shapes change significantly as the inner-to-outer characteristic dimension, a_i/a_0 of the cross section varies. The fundamental doubly symmetry (SS) and doubly antisymmetry (AA) modes at $a_i/a_0 = 0.2$ exhibit extensional and torsional motions, respectively. As the wall thickness decreases (with higher value of a_i/a_0), however, it is found that the fundamental modes in these two symmetry classes become dominated by the circumferential motions. At $a_i/a_0 = 0.8$, it is further noticed that the first three doubly symmetry (SS) and the doubly antisymmetry (AA) modes are equivalent in mode shapes and frequencies. For the symmetry-antisymmetry modes (SA), the transverse bending motion continue to dominate the fundamental frequency for the range of a_i/a_0 considered in this study. As a_i/a_0 increases to 0.8, it is observed that the second and third symmetry-antisymmetry modes change to circumferential motions of order two.

Figures 4 and 5 show the deformed mode shapes of a square cylinder with a deep circular or square cavity, respectively. Again, it is found that as the wall thickness decreases, the extensional and torsional modes of the cylinder tend to occur at a much higher mode number. The circumferential modes begin to dominate the lower vibration spectrum as a_i/a_0 increases. In general, it can be deduced that as the wall thickness reduces (corresponds to a higher a_i/a_0 ratio), the frequency of vibration decreases proportionally. A cross examination of these figures further reveals that for the same inner-to-outer characteristic dimension ratio, a_i/a_0 , the square cylinder with a deep square cavity possesses the lowest natural frequencies at all symmetry classes.

3.4 Parametric Investigation. To investigate further on the influence of the inner-to-outer characteristic dimension ratio, a_i/a_0 , and the length-to-width ratio, L/a_0 , upon the natural frequencies, the computed results are presented in Figs. 6 and

7. The frequency parameter, used in these figures has been redefined as

$$\bar{\lambda} = (L/a_0)\sqrt{\lambda}. \quad (19)$$

The ratios, a_i/a_0 , are taken as 0.3 and 0.7 in this investigation. The first two modes at each symmetry class are presented. By increasing the length-to-width ratio of the cylinder, it is found that the frequency parameter, $\bar{\lambda}$, increases monotonically. The variation is most steep for the SS and AA modes. On the other hand, the frequency variations with respect to ratio, L/a_0 , for the SA modes (which correspond to transverse vibratory motions about the x_1 and x_2 directions) are more gradual and as the length increases further, these modes converge asymptotically to the elementary beam solutions. Several mode crossings are found in the frequency diagrams for both the square and circular hollow cylinders. The mode crossing is caused mainly by the lowering of the frequency parameters in the symmetry-antisymmetry (SA) modes following the increases in the length of the cylinder.

It is interesting to note that for the annular hollow cylinder at $a_i/a_0 = 0.7$, the doubly symmetry and doubly antisymmetry modes are closely coupled in the range of $2.0 \leq L/a_0 < 4.5$.

4 Conclusions

An in-depth exposition of the free vibration characteristics of hollow cylinders is presented. In this work, we focused on the free vibration studies of cylinders with free-wall conditions and traction-free boundaries at both ends. For the first time, vibration frequencies and deformed mode shapes for various stress free hollow cylinders were presented in a systematic manner. The deformed mode shape diagrams showed very interesting mode changing phenomena as the basic geometric parameters of the cylinder varies. Particularly, the occurrence of circumferential modes at the lower frequencies as the wall thickness of the cylinder decreases. The effects of wall thickness and length-to-width ratio on the overall dynamic behaviour of these cylinders have been investigated via frequency plots. It is noted that frequency crossings are commonly encountered as the length-to-width ratio increases. It is concluded that the square

hollow cylinder with a square cavity has the highest bending stiffness while the cylinder with an annular cross section possesses the highest torsional stiffness as compared to cylinders of other shapes.

References

- Hutchinson, J. R., 1971, "Axisymmetric Vibrations of a Free Finite-Length Rod," *Journal of the Acoustical Society of America*, Vol. 51, pp. 233-240.
- Hutchinson, J. R., 1980, "Vibrations of Solid Cylinders," *ASME JOURNAL OF APPLIED MECHANICS*, Vol. 47, pp. 901-907.
- Hutchinson, J. R., 1981, "Transverse Vibrations of Beams: Exact Versus Approximate Solutions," *ASME JOURNAL OF APPLIED MECHANICS*, Vol. 48, pp. 923-928.
- Liew, K. M., Hung, K. C., and Lim, M. K., 1993, "A Continuum Three-Dimensional Vibration Analysis of Thick Rectangular Plates," *International Journal of Solids and Structures*, Vol. 30, pp. 3357-3379.
- Liew, K. M., Hung, K. C., and Lim, M. K., 1995, "Free Vibration Studies on Stress-Free Three-Dimensional Elastic Solids," *ASME JOURNAL OF APPLIED MECHANICS*, Vol. 62, pp. 159-165.
- McMahon, G. W., 1964, "Experimental Study of the Vibrations of Solid, Isotropic Elastic Cylinders," *Journal of the Acoustical Society of America*, Vol. 38, pp. 85-92.
- McNiven, H. D., and Perry, D. C., 1962, "Axially Symmetric Waves in Finite, Elastic Rods," *Journal of the Acoustical Society of America*, Vol. 34, pp. 433-437.
- Rumerman, M., and Raynor, S., 1971, "Natural Frequencies of Finite Circular Cylinders in Axially Symmetric Longitudinal Vibration," *Journal of Sound and Vibration*, Vol. 15, pp. 529-543.
-

Three-Dimensional Rigid-Body Collisions With Multiple Contact Points

D. B. Marghitu
Graduate Assistant.

Y. Hurmuzlu
Associate Professor.

Mechanical Engineering Department,
Southern Methodist University,
Dallas, TX 75275

This article deals with three-dimensional collisions of rigid, kinematic chains with an external surface while in contact with other surfaces. We concentrate on a special class of kinematic chain problems where there are multiple contact points during the impact process. A differential formulation based algorithm is used to obtain solutions that utilize the kinematic, kinetic, and the energetic definitions of the coefficient of restitution. Planar and spatial collisions of a three-link chain with two contact points are numerically studied to compare the outcomes predicted by each approach. Particular emphasis is placed on the relation between the post and pre-impact energies, slippage and rebounds at the contact points, and differences among planar and nearly planar three-dimensional solutions.

1 Introduction

In rigid-body mechanics, a basic assumption is that the configuration of the rigid bodies are held constant in the analysis of the collision process, with no significant change in mass and moments of inertia. Furthermore, it is customarily assumed that each body exerts an impulsive force on the other at a common point of contact. The duration of the contact is assumed to be negligible in the time scale of the motion before or after the impact. Therefore, positions of the rigid bodies are held constant in the analysis of the collision process. Analytical solutions (obtaining post-impact velocities in terms of pre-impact velocities) of rigid-body collision problems are formulated in terms of two principles: Newton's law of motion and Coulomb's law of friction. In addition, the solutions require the knowledge of two constants: coefficient of friction and coefficient of restitution.

The original definition of the coefficient of restitution is due to Newton (1686), who established that the ratio of the rebound and incidence velocities of two colliding particles (or small spheres) in the normal direction is constant, and inherently tied to the material properties of the colliding bodies. Today, this definition is called the kinematic definition of the coefficient of restitution. Newton's experiments did not consider cases where there was a relative tangential velocity at the contact point. Poisson (1817) hypothesized that the coefficient of restitution was the ratio of the normal restitution impulse to the compression impulse at the contact point (the kinetic definition of the coefficient of restitution). He also pointed out that there were several possible tangential motions that may arise at the contact point during the collision period. With the help of his co-worker (Morin, 1855), he proved that Coulomb's friction model can be used to relate the normal and tangential contact forces. Routh (1860) developed a graphical method to solve planar impact problems of rough, inelastic bodies. His method brought solution to collisions where the slip between the colliding bodies changes direction during impact (Poisson listed this as a possible case but did not provide a solution method). These develop-

ments lead to Whittaker's (1904) method of solution of impact with friction, which is fundamentally different that its predecessors and can be extended to three dimensions. Whittaker's method combines Newton's definition of the coefficient of restitution and Poisson's definition of the phases of collision and yields algebraic equations, which can be easily solved for the post-impact velocities. Although this approach does not properly treat the contact forces when the slip direction changes during collision, it has been widely accepted as the standard method that is being taught today in undergraduate engineering education.

Kane and Levinson (1985) showed that Whittaker's approach may predict erroneous energy results in rigid-body problems when friction is present. This observation sparked an intense effort geared toward resolving the energy inconsistencies in the classical solution of collision problems. An important contribution to the solution of rigid-body collision problems was made in Keller (1986). Keller revisited Routh's graphical method and formulated a three-dimensional differential approach that resolved the energy paradox by using the kinetic definition of the coefficient of restitution. The proposed solution method was based on the differential formulation of collision problems and allowed the utilization of various definitions for the coefficient of restitution using the same solution scheme (Stronge, 1990). An important recent contribution to the area was the definition of a new coefficient of restitution (the energetic definition) by Stronge based on the internal dissipation hypothesis (Stronge, 1990). This new definition resolved the arguable (Smith, 1991) inconsistencies in energy losses predicted by the kinetic definition. Subsequently, Brach (1992) bridged the gap among the algebraic and differential solution methods for planar collision problems by proposing and algebraic scheme that yields the same outcome as the differential schemes.

In the present article we study a rarely addressed class of three-dimensional collision problems in the light of recent developments in the area. These type of impacts arise in applications that involve multibody systems such as walking machines and space structures (Hurmuzlu, 1993). We study three-dimensional collisions of kinematic chains with external surfaces that take place through multiple contact points. This class of problems was considered in Hurmuzlu and Chang (1992). They formulated an algebraic solution of impacts of planar multibody system with two contact points based on the kinematic formulation of the coefficient restitution (with an energy correction scheme proposed in Brach, 1989). Here a three-dimensional solution scheme based on the differential formulation of impact

Contributed by the Applied Mechanics Division of THE AMERICAN SOCIETY OF MECHANICAL ENGINEERS for publication in the ASME JOURNAL OF APPLIED MECHANICS.

Discussion on this paper should be addressed to the Technical Editor, Prof. Lewis T. Wheeler, Department of Mechanical Engineering, University of Houston, Houston, TX 77204-4792, and will be accepted until four months after final publication of the paper itself in the ASME JOURNAL OF APPLIED MECHANICS.

Manuscript received by the ASME Applied Mechanics Division, Oct. 4, 1993; final revision, Mar. 21, 1994. Associate Technical Editor: E. J. Haug, Jr.

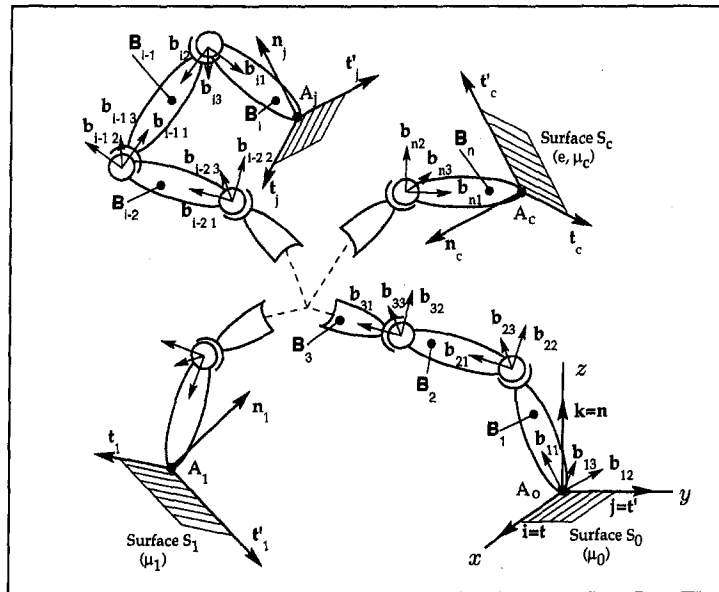


Fig. 1 Spatial kinematic chain with multiple contact points

equations that incorporates the three definitions of the coefficient of restitution is presented. Unlike the planar cases, the equations of motion are nonlinear and algebraic formulations cannot be used to solve the problem when Coulomb's law is used to model the frictional effects.

In the ensuing article we first define the impacting system and the related coordinate frames. Then, we develop the differential equations that govern the impulsive motion. Subsequently, we present a procedure to solve the collision problem using the three definitions of the coefficient of restitution. Finally, we use a simplified three-link chain with two contact points to numerically study the effect of choosing a particular coefficient of restitution on the predicted post-impact conditions. We specially focus on the relation between the post and pre-impact energies, slippage, and rebounds at the contact points, and differences among planar and nearly planar three-dimensional solutions.

2 Problem Statement, Coordinate Systems, and Variable Definitions

Consider the n interconnected rigid links B_1, \dots, B_n (Fig. 1). The end A_c of the chain collides with the surface S_c . Prior to impact, $k + 1$ free ends of the chain are resting on the surfaces S_j . The collision at A_c may lead to several consequences depending on the initial conditions, the coefficients of friction among the surfaces and the chain (here we assume isotropic surfaces with a coefficient of friction μ_j at the contact point A_j), and the coefficient of restitution e at A_c . The impulsive forces generated at the collision point are assumed to be instantaneously transmitted through the chain without any dissipative losses. We further consider that the contacts with external surfaces occur only at the free ends of the chain. In addition, we assume that the contacts at the noncolliding ends are perfectly rigid contacts (i.e., no restitution or energy loss). The motion of an end point during the collision at any given contact point can be specified by one of the following three cases:

- I The end is slipping along surface while interacting with it in the normal direction.
- II The end is not slipping along but interacting with it in the normal direction.
- III The end is not interacting with the surface.

In addition, an end may undergo a sequence of motions during the collision period that can be presented by a combination of these three cases. Interaction in this article denotes that a particular end exerts a normal force on the contact surface. This normal force results in a tangential dry friction force which is proportional to the normal force (Coulomb's model). It is worthwhile to note that other possible modes of interaction such as tangential restitution has been considered by previous investigators. In this article the primary mode of tangential interaction is assumed to be through dry friction.

Now we describe the coordinate systems that are used to describe the motion of the chain in the three-dimensional space. The link B_1 has three rotational and three translational degrees-of-freedom. Each body $B_i, i = 2, 3, \dots, n$ has spherical joints, and therefore has three relative degrees-of-freedom with respect to the body B_{i-1} . Let $R[\mathbf{i}, \mathbf{j}, \mathbf{k}]$ define a fixed inertial reference frame and R_i a set of reference frames attached to bodies B_i as depicted in Fig. 1. Without loss of generality, the R coordinate axes are aligned with the plane surface S_0 . We express by $\mathbf{b}_{i1}, \mathbf{b}_{i2},$ and \mathbf{b}_{i3} ($i = 1, 2, \dots, n$) the corresponding mutually perpendicular unit vectors along the axis of R_i . Let \mathbf{n}_j be the unit vector of the normal to the surface S_j and directed from S_j into the contacting link. Let \mathbf{t}_j and \mathbf{t}'_j be unit vectors in the common tangent plane to the surface S_j and the contacting link satisfying $\mathbf{n}_j = \mathbf{t}_j \times \mathbf{t}'_j$.

The orientation of each body with respect to its lower adjacent body is defined through Euler's angles $\phi_{i1}, \phi_{i2},$ and ϕ_{i3} where $i = 1, \dots, n$. The relative translations of body B_1 is given by $\alpha_1, \alpha_2,$ and α_3 . The generalized coordinates for the system can be expressed as the $(3n + 3) \times 1$ dimensional vector

$$\mathbf{q} = \{\alpha_1, \alpha_2, \alpha_3, \phi_{11}, \phi_{12}, \phi_{13}, \dots, \phi_{n1}, \phi_{n2}, \phi_{n3}\}^T \quad (1)$$

The unit vectors of an axis frame of a body can be expressed as a linear combination of the unit vectors of the axis frame of an adjacent body as

$$\begin{bmatrix} \mathbf{b}_{i1} \\ \mathbf{b}_{i2} \\ \mathbf{b}_{i3} \end{bmatrix} = \mathbf{S}_{i-1} \begin{bmatrix} \mathbf{b}_{i-11} \\ \mathbf{b}_{i-12} \\ \mathbf{b}_{i-13} \end{bmatrix} \quad (2)$$

where

$$S_{ii-1} = \begin{bmatrix} c\phi_{i2}c\phi_{i3} & c\phi_{i1}s\phi_{i3} + s\phi_{i1}c\phi_{i2}c\phi_{i3} & s\phi_{i3}s\phi_{i1} - c\phi_{i1}s\phi_{i2}c\phi_{i3} \\ -c\phi_{i2}s\phi_{i3} & c\phi_{i1}c\phi_{i3} - s\phi_{i1}s\phi_{i2}s\phi_{i3} & s\phi_{i1}s\phi_{i3} + c\phi_{i1}s\phi_{i2}s\phi_{i3} \\ s\phi_{i2} & -s\phi_{i1}c\phi_{i2} & c\phi_{i1}c\phi_{i2} \end{bmatrix}$$

in which the symbols $c = \cos$ and $s = \sin$. The angular velocity of B_i in R can be written as

$$\boldsymbol{\omega}_i = \{u_{i1}, u_{i2}, u_{i3}\}^T \quad (3)$$

and the $(3n + 3) \times 1$ dimensional vector of generalized speeds is given by

$$\mathbf{u} = \{u_1, u_2, u_3, u_{11}, u_{12}, u_{13}, \dots, u_{n1}, u_{n2}, u_{n3}\}^T \quad (4)$$

where $u_1 = \dot{\alpha}_1$, $u_2 = \dot{\alpha}_2$, and $u_3 = \dot{\alpha}_3$. The velocity of the A_j end is

$$\mathbf{v}_j = \mathbf{v}'_j + v'_j \mathbf{n}_j \quad (j = 0, 1, \dots, k, c) \quad (5)$$

where v'_j is the normal and $\mathbf{v}'_j = v'_j \mathbf{t}_j + v'_j \mathbf{t}'_j$ is the tangential velocity. The $1 \times (3k + 6)$ vector of contact forces is given by

$$\mathbf{F} = \{F'_0, F''_0, F^n_0, \dots, F'_k, F''_k, F^n_k, F'_c, F''_c, F^n_c\}^T \quad (6)$$

where, F^n_j is the normal contact force and $\mathbf{F}'_j = F'_j \mathbf{t}_j + F''_j \mathbf{t}'_j$ is the tangential contact force. The impulses at the contact points are obtained by integrating Eq. (6) with respect to time, which gives

$$\boldsymbol{\tau} = \begin{bmatrix} \tau'_0 \\ \tau''_0 \\ \tau^n_0 \\ \vdots \\ \tau'_k \\ \tau''_k \\ \tau^n_k \\ \vdots \\ \tau'_c \\ \tau''_c \\ \tau^n_c \end{bmatrix} = \begin{bmatrix} \int_0^\eta F'_0 d\eta \\ \int_0^\eta F''_0 d\eta \\ \int_0^\eta F^n_0 d\eta \\ \vdots \\ \int_0^\eta F'_k d\eta \\ \int_0^\eta F''_k d\eta \\ \int_0^\eta F^n_k d\eta \\ \vdots \\ \int_0^\eta F'_c d\eta \\ \int_0^\eta F''_c d\eta \\ \int_0^\eta F^n_c d\eta \end{bmatrix} \quad (7)$$

where

$$\boldsymbol{\tau}_j = \boldsymbol{\tau}'_j + \boldsymbol{\tau}''_j \mathbf{n}_j \quad (j = 0, 1, \dots, k, c) \quad (8)$$

with τ^n_j the normal impulse and $\boldsymbol{\tau}'_j = \tau'_j \mathbf{t}_j + \tau''_j \mathbf{t}'_j$ the tangential impulse. We have denoted with η the time variable since t is used as a tangential coordinate.

3 Equations of Motion

3.1 Equations of the Impulsive Motion. In this article we use Kane's formalism (Kane and Levinson, 1985) to derive the equations of motion, because this is a minimally laborious method and can be easily implemented by using symbolic manipulation programs. Accordingly, the total kinetic energy of

the rigid multibody system moving in the reference frame R is specified by

$$K = K_{tr} + K_{rot} = K(\mathbf{q}, \mathbf{u}) \quad (9)$$

where K_{tr} denotes the kinetic energy due to the translation and is given by

$$K_{tr} = \frac{1}{2} \sum_{i=1}^n m_i \mathbf{v}_{Gi} \cdot \mathbf{v}_{Gi} \quad (10)$$

Here, the mass of the rigid link B_i is m_i and \mathbf{v}_{Gi} expresses the velocity of center mass of B_i in R . The kinetic energy due to the rotation is given by K_{rot} and defined as

$$K_{rot} = \frac{1}{2} \sum_{i=1}^n \boldsymbol{\omega}_i \cdot \mathbf{I}_i \cdot \boldsymbol{\omega}_i \quad (11)$$

where \mathbf{I}_i is the central inertia dyadic of the member B_i . The generalized active forces in R are given by

$$\mathcal{F}_r = \sum_{j=0}^k \frac{\partial \mathbf{v}_j}{\partial \mathbf{u}_r} \cdot \mathbf{F}_j + \frac{\partial \mathbf{v}_c}{\partial \mathbf{u}_r} \cdot \mathbf{F}_c \quad \text{and} \quad \mathcal{F}_{ir} = \sum_{j=0}^k \frac{\partial \mathbf{v}_j}{\partial \mathbf{u}_{ir}} \cdot \mathbf{F}_j + \frac{\partial \mathbf{v}_c}{\partial \mathbf{u}_{ir}} \cdot \mathbf{F}_c \quad (r = 1, 2, 3; i = 1, 2, \dots, n) \quad (12)$$

where \mathbf{v}_j and \mathbf{v}_c are the velocities of A_j and A_c in R . For collision, however, an integrated form of equations can be written as

$$\frac{d}{d\eta} \frac{\partial K}{\partial \mathbf{u}_r} = \mathcal{F}_r \quad \text{and} \quad \frac{d}{d\eta} \frac{\partial K}{\partial \mathbf{u}_{ir}} = \mathcal{F}_{ir} \quad (r = 1, 2, 3; i = 1, 2, \dots, n). \quad (13)$$

Equation (13) establishes a relationship between the time derivative of the generalized velocity vector \mathbf{u} and the force vector \mathbf{F} , which leads to the matrix form

$$\mathbf{M}(\mathbf{q}) \dot{\mathbf{u}} = \mathbf{D}(\mathbf{q}, \boldsymbol{\theta}) \mathbf{F} \quad (14)$$

where $\mathbf{M}(\mathbf{q})$ is the $(3n + 3) \times (3n + 3)$ mass matrix; $\mathbf{D}(\mathbf{q}, \boldsymbol{\theta})$ is a $(3n + 3) \times (3k + 6)$ matrix that depends on pre-impact positions and inclination angles of the contact surfaces; and $\boldsymbol{\theta}$ is the vector of S_j surface inclination angles, which is given by the direction cosines of the surface normal \mathbf{n}_j .

3.2 Equations of Motion With Contact Constraints.

The linear velocities and accelerations of the points of the chain contacting the external surfaces can be related to the generalized velocity and acceleration vector by using kinematic relations. The general forms (the exact form depends on the structure of the chain) of these relationships can be written as

$$\mathbf{v} = \begin{bmatrix} 1 & 1 & 1 & \mathbf{0} \\ \mathbf{H}_1(\mathbf{q}) \end{bmatrix} \mathbf{u} \quad (15)$$

and

$$\mathbf{a} = \begin{bmatrix} 1 & 1 & 1 & \mathbf{0} \\ \mathbf{H}_1(\mathbf{q}) \end{bmatrix} \dot{\mathbf{u}} + \begin{bmatrix} \mathbf{0} \\ \mathbf{H}_2(\mathbf{q}, \mathbf{u}) \end{bmatrix} \quad (16)$$

where

$$\mathbf{a} = \{a'_0, a'_0, a''_0, \dots, a'_k, a'_k, a''_k, a'_c, a'_c, a''_c\}^T \quad (17)$$

is the $(3k + 6) \times 1$ acceleration vector. Combining Eqs. (14) and (16) yields

$$\mathbf{a} = \begin{bmatrix} \mathbf{0} \\ \mathbf{H}_2(\mathbf{q}, \mathbf{u}) \end{bmatrix} + \begin{bmatrix} 1 & 1 & 1 & 0 \\ \mathbf{H}_1(\mathbf{q}) \end{bmatrix} \mathbf{M}(\mathbf{q})^{-1} \mathbf{D}(\mathbf{q}, \boldsymbol{\theta}) \mathbf{F} \quad (18)$$

Elimination of the nonimpulsive terms (i.e., $\mathbf{H}_2(\mathbf{q}, \mathbf{u})$) from this equation gives

$$\mathbf{a} = \frac{d\mathbf{v}}{d\eta} = \begin{bmatrix} 1 & 1 & 1 & 0 \\ \mathbf{H}_1(\mathbf{q}) \end{bmatrix} \mathbf{M}(\mathbf{q})^{-1} \mathbf{D}(\mathbf{q}, \boldsymbol{\theta}) \mathbf{F} = \boldsymbol{\Gamma}(\mathbf{q}, \boldsymbol{\theta}) \mathbf{F} \quad (19)$$

where \mathbf{v} is the velocity vector of the contact points of the chain with the surfaces S_i and $\boldsymbol{\Gamma}(\mathbf{q}, \boldsymbol{\theta})$ is a constant $(3k + 6) \times (3k + 6)$ matrix that depends on the pre-impact positions and inclination angles of the contact surfaces.

Additional constraint equations can be written by considering the relative motions of the contacting ends with respect to the external surfaces. For the three possible cases of the end point motions that were listed in Section 2, the following equations can be written:

I A_j is slipping with interaction in the normal direction:

$$F_j^t = -\mu_j \cos(\xi_j) F_j^n, \quad F_j^r = -\mu_j \sin(\xi_j) F_j^n \quad \text{and} \quad \dot{v}_j^n = v_j^n = 0$$

with

$$\xi_j = \arctan(v_j^t/v_j^n) \quad (j \in \mathbf{J} \subset \{0, 1, \dots, k, c\}). \quad (20)$$

Note that we are assuming isotropic contact surfaces, and therefore, using the same coefficient of friction for the two tangential directions. Also, in this article we assume that deformations occur only at the collision point A_c . Therefore, at the other points when the end contacts the surface it is assumed that its normal velocity is zero.

II A_j is not slipping but interacts with the surface:

$$\dot{v}_j = v_j = \mathbf{0} \quad \text{subject to} \quad |\mathbf{F}_j^t/F_j^n| \leq \mu_j \quad (j \in \mathbf{J} \subset \{0, 1, \dots, k, c\}). \quad (21)$$

III A_j does not interact with the surface:

$$\mathbf{F}_j = \mathbf{0} \quad (j \in \mathbf{J} \subset \{0, 1, \dots, k\}). \quad (22)$$

Note that during collision $F_c^n \neq 0$, since the impact occurs at A_c .

The $3n + 3$ differential equations that are given in Eq. (19) include $3k + 6$ unknown contact forces on the right-hand side. Having specified the constraint equations that correspond to the various possibilities at the contacting ends, one can get $3k + 5$ additional relationships using Eqs. (20) through (22). The general form of the constraint equations for all contacting ends can be written as

$$\boldsymbol{\Lambda}_1 \dot{\mathbf{v}} = \mathbf{0}, \quad (23)$$

$$\boldsymbol{\Lambda}_2 \begin{bmatrix} \mathbf{F}^t \\ \mathbf{F}^n \end{bmatrix} = \mathbf{0}, \quad (24)$$

and

$$\boldsymbol{\Lambda}_3 \mathbf{F}^t = \boldsymbol{\Lambda}_4(\mathbf{v}) \dot{\mathbf{F}}^n + \boldsymbol{\Lambda}_5(\mathbf{v}) F_c^n \quad (25)$$

where, the force vector is partitioned as,

$$\mathbf{F}^t = \{F'_0, F'_0, \dots, F'_k, F'_k, F'_c, F'_c\}^T$$

$$\dot{\mathbf{F}}^n = \{F''_0, \dots, F''_k\}^T$$

also, $\boldsymbol{\Lambda}_1$ is an $l_1 \times (3n + 3)$ ($l_1 =$ number of ends in category I + $3 \times$ number of ends in category II) matrix with elements that are equal to one or zero, $\boldsymbol{\Lambda}_2$ is an $l_2 \times (3k + 5)$ ($l_2 = 3 \times$ number of ends in category III) matrix with elements that are equal to one or zero, $\boldsymbol{\Lambda}_3$ is an $l_3 \times (2k + 2)$ ($l_3 = 2 \times$ number of ends in category I) matrix with elements that are equal to one or zero, and $\boldsymbol{\Lambda}_4$ and $\boldsymbol{\Lambda}_5$ are $l_3 \times (2k + 2)$ and $l_3 \times 1$ matrices that are nonlinear functions of the velocity vector (the dependence on velocity is due to the ξ_j terms in Eq. (20)). Equations (23), (24), (25), and (19) can be combined to obtain

$$d\mathbf{v}/d\eta = F_c^n \boldsymbol{\Pi}(\mathbf{v}, \mathbf{q}, \boldsymbol{\theta}). \quad (26)$$

Now we will replace the independent variable t , with the normal impulse at A_c , $\tau \equiv \tau_c^n$. For this purpose we use the last rows of the vectors in Eq. (7) to obtain

$$\frac{d}{d\eta} = F_c^n \frac{d}{d\tau}. \quad (27)$$

Dividing Eq. (26) by F_c^n and using Eq. (27) yields

$$d\mathbf{v}/d\tau = \boldsymbol{\Pi}(\mathbf{v}, \mathbf{q}, \boldsymbol{\theta}). \quad (28)$$

Here we can observe that the differential equations are nonlinear functions of the velocities. This occurs only in three-dimensional problems. Therefore, algebraic formulations that depend on the kinetic, kinematic, or energetic definitions of the coefficients of restitution are only possible for planar cases. Perhaps, this is also the reason that Routh's graphical method cannot be extended to three-dimensional cases.

3.3 Slipping Conditions for the Contacting Ends.

During collision, the relative motion of a contacting end that is interacting with the respective surface may change from one case to another (e.g., originally the end may be slipping in a particular direction, it may stop and/or slip in another direction). The following two cases are possible:

I A_j is slipping initially (i.e., $\mathbf{v}_j^t(\tau_0) \neq \mathbf{0}$) and stops slipping. The normal impulse at A_c when end j stops slipping is defined as τ_j^{**} with $\mathbf{v}_j^t(\tau_j^{**}) = \mathbf{0}$.

II A_j starts slipping when it is not slipping initially (i.e., $\mathbf{v}_j^t(\tau_0) = \mathbf{0}$). Slippage at a specific end happens when the friction condition in Eq. (21) is violated.

3.4 Interaction Conditions for the Contacting Ends.

Another factor that should be considered is the motion of the contacting ends (excluding A_c) in the normal directions. For example, an end that is initially interacting with the surface separates during collision and attaches again. Accordingly, we list the following possibilities for the respective cases enumerated earlier (section 3.2) in the article:

I and II A_j stops interacting with the surface when the normal acceleration becomes positive as a result of a case change at any of the contacting ends (i.e., $a_j^n > 0$). In the absence of such changes A_j will not detach from the surface S_j until the end of collision.

III A_j is not interacting with the surface and initially the normal velocity is directed away from the surface (i.e., $v_j^n(\tau_0) > 0$). Interaction reoccurs at A_j when this velocity vanishes. The normal impulse at A_c when end j begins interacting with surface S_j is defined as τ_j^{**} with $v_j^n(\tau_j^{**}) = 0$.

4 Solution of the Impact Problem

In this section we present a procedure to calculate the post-impact velocity vector $\mathbf{u}(\tau_f)$ given the pre-impact velocity vector $\mathbf{u}(0)$. The procedure is centered around the solution of the

set of nonlinear differential equations given in Eq. (28). Yet, the structure of the right-hand sides of these equations depends on the conditions at the contacting ends (i.e., on the matrices Λ_i). As stated earlier, during collision, a contacting end may slip along the surface while interacting with it in the normal direction (other possible cases are listed in Sections 3.3 and 3.4). A change in the relative motion of one contacting end in the chain requires the modification of the differential equations. Here we will develop a procedure that automatically detects such changes and implements the necessary modifications to differential equations to produce consistent results.

Starting from a set of pre-impact conditions, the problem is solved in incremental stages. A unique set of equations that reflects the conditions which have to be satisfied at the contacting ends are used in each stage. An important factor that should be reminded to the reader, is that, we use the normal impulse τ at the colliding end, A_c , as the independent variable in the differential equations. This convenient transformation of variable, which was introduced in Keller (1986), is particularly useful in tracking the continuous changes in the generalized velocities during collision. Furthermore, formulation in terms of the normal collision impulse allows the implementation of various definitions of coefficients of restitution with relative ease. This can be realized by first determining the normal impulse at the end of the compression phase or the onset of the restitution phase. The restitution phase starts when the normal velocity at A_c vanishes during the collision. We define the normal impulse at A_c that marks the beginning of the restitution phase by τ^\dagger with $v_c^n(\tau^\dagger) = 0$. The value of the normal impulse at A_c at the end of the restitution phase (i.e., end of the collision) τ_f depends on the definition that is used for the coefficient of restitution. Computation of τ_f for each definition can be specified as follows:

1 *Kinematic Coefficient of Restitution:*

$$v_c^n(\tau_f^{(1)}) = -e v_c^n(0). \quad (29)$$

2 *Kinetic Coefficient of Restitution:*

$$\tau_f^{(2)} = (e + 1)\tau^\dagger. \quad (30)$$

3 *Energetic Coefficient of Restitution:* The work done by the normal force at the impact point is

$$\Delta W^n = - \int F_c^n v_c^n dt = - \int v_c^n(\tau) d\tau. \quad (31)$$

From the energetic definition of the coefficient of restitution (Stronge, 1990) we obtain $\tau_f^{(3)}$

$$\int_{\tau^\dagger}^{\tau_f^{(3)}} v_c^n(\tau) d\tau = -e^2 \int_0^{\tau^\dagger} v_c^n(\tau) d\tau. \quad (32)$$

The overall solution procedure of the collision can be outlined by the following steps:

1 Set $\tau_{ir} = 0$, $\tau(0) = \mathbf{0}$, $\Delta W^n(0) = 0$ and compute $\mathbf{v}(0)$ as function of $\mathbf{u}(0)$.

2 Define an initially empty set L_c , which includes the contact points where the chain interacts with the respective contact surfaces. Add A_c to the list L_c (interaction is always present at A_c). Thus, L_c can be written as

$$L_c = \{A_j, A_c | \tau_j^n \neq 0, v_c^n(\tau_{ir}) < 0 (j = 0, 1, \dots, k)\}.$$

3 Set $\mathbf{F}_j^i = \mathbf{0}$ and $F_j^n = 0 \forall A_j \notin L_c$. Create a new set L_s that includes the contact points $A_j \in L_c$ having zero tangential velocities ($\mathbf{v}_j^t(\tau_{ir}) = \mathbf{0}$) at τ_{ir} but slip for $\tau > \tau_{ir}$. This set is initially empty and is given by

$$L_s = \{A_j \in L_c | \mathbf{v}_j^t(\tau_{ir}) = \mathbf{0} \text{ and } \mathbf{v}_j^t(\tau) \neq \mathbf{0} \forall \tau > \tau_{ir}\}.$$

4 Set $F_j^i = -\mu_j \cos [\xi_j^a(\tau_{ir})] F_j^n$ and $F_j^i = -\mu_j \sin [\xi_j^a(\tau_{ir})] F_j^n \forall A_j \in L_c \setminus L_s$.

5 Set $F_j^i = -\mu_j \cos [\xi_j^a(\tau_{ir})] F_j^n$ and $F_j^i = -\mu_j \sin [\xi_j^a(\tau_{ir})] F_j^n \forall A_j \in L_s$.

6 Set $\mathbf{a}_j^i = \mathbf{0}$ for the remaining points in L_c .

7 Set $a_j^n = 0 \forall A_i \in L_c$.

8 Applying the relations formulated in steps 3, 4, 5, 6, and 7 solve Eq. (19) for \mathbf{a} and \mathbf{F} in terms of F_c^n .

9 Compute the force ratios $\mu_j^a = |\mathbf{F}_j^i / F_j^n|$ (note that, the ratios $|\mathbf{F}_j^i / F_j^n|$ do not depend on F_c^n) at the contact points that are bracketed in step 6. Calculate the slip angle $\xi_j^a = \arctan [F_j^i / F_j^n]$. If all $\mu_j^a < \mu_j$ continue to the following step. Otherwise, add the point A_j to L_s where $\mu_j^a = \max [\mu_{j_1}^a, \dots, \mu_{j_l}^a]$, such that $\mu_{j_1}^a > \mu_{j_1}, \dots, \mu_{j_l}^a > \mu_{j_l}$. Then, go to step 5.

10 Check if all $a_j^n \geq 0$ for $A_j \notin L_c$ and $v_j^t(\tau_{ir}) = 0$, if true proceed to the next step. Otherwise, append A_j to the list L_c , where $a_j^n = \max [|a_{j_1}^n|, \dots, |a_{j_m}^n|]$, such that $a_{j_1}^n, \dots, a_{j_m}^n < 0$. Then, go to step 3.

11 Having determined the conditions at the contacting ends, construct the matrices Λ_i and prepare the differential equations given in Eq. (28).

12 Calculate τ_j^* for all slipping ends including A_c and compute τ_j^{**} for all noninteracting ends. Compute τ^\dagger , the normal impulse at A_c when the normal velocity at this point vanishes (end of the compression phase). Computation of τ_j^{**} and τ^\dagger is confounded by the nonlinear form of the differential equations. One would normally solve the differential equations to obtain the velocities in terms of τ and set

$$\mathbf{v}_j^t(\tau_j^{**}) = 0 \quad (33)$$

to solve for τ_j^{**} . Here, the solution $\mathbf{v}(\tau)$ can only be obtained numerically. Thus, the root finding process should be combined with the numerical integration process to obtain the roots of Eq. (33). In the present study, we realized this by using the package MathematicaTM, and obtained the solution of the differential equations in the form of interpolating polynomials of τ . Then the polynomials were used to numerically compute the roots of the equations.

13 Set $\tau_{\text{new}} = \min [\tau^\dagger, \tau_0^*, \dots, \tau_k^*, \tau_c^*, \tau_0^{**}, \dots, \tau_k^{**}]$ subject to $\tau_{\text{new}} > \tau_{ir}$. Compute $\mathbf{v}(\tau_{\text{new}})$, $\mathbf{u}(\tau_{\text{new}})$, and $\Delta W^n(\tau_{\text{new}})$. Let $\tau_{ir} = \tau_{\text{new}}$. If $\tau_{\text{new}} \neq \tau^\dagger$ go to step 2, otherwise proceed to the next step.

14 Set $\Delta W^n(\tau^\dagger) = \Delta W^n(\tau_{\text{new}})$ and $\Delta W^n(\tau_{\text{new}}) = 0$, and go to step 2. Henceforth, in step 12 do not compute τ^\dagger , instead when using:

- (1) the kinematic definition calculate $\tau_f^{(1)}$ from Eq. (29).
- (2) the kinetic definition calculate $\tau_f^{(2)}$ from Eq. (30).
- (3) the energetic definition calculate $\tau_f^{(3)}$ from Eq. (32).

Then, carry out the computations of 13 with $\tau_f^{(i)}$ instead of τ^\dagger , skip this step and proceed to the next step.

15 The solution of the problem is given by the vector of the generalized velocities that was obtained in step 13.

This procedure is based on the presumption that at the onset of each stage there are no interactions at the contacting ends except at A_c . Therefore, in step 2 the list of contacting ends L_c contains only this point. Then, in step 10, the ends that interact with the external surfaces are sequentially appended to this list. Each time a contact point appended to L_c , the slippage is checked again for all interacting points in step 9. Once the motions of the all of the ends are resolved (the loop that is bracketed by steps 2 and 10), the equations of motion are set in step 11. The equations are integrated until a case change in the contacting occurs. If no case changes are detected, the integration is carried out until the end of the compression or restitution phase.

5 Application

In this section we present the application of the solution procedure to the impact problem of a three link chain with two

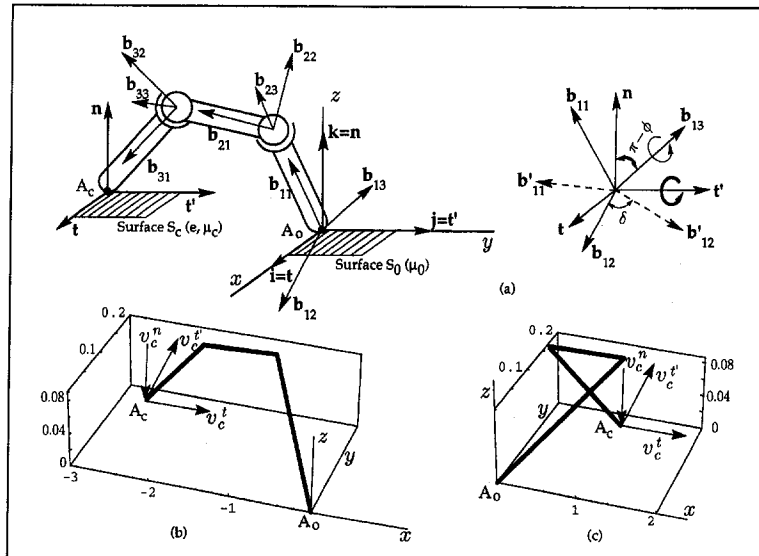


Fig. 2(a) Three-link chain with two contact points; (b) stick diagram for $\delta = 10^\circ$ and $\phi = 5^\circ$; (c) stick diagram for $\delta = 10^\circ$ and $\phi = 175^\circ$

contact points (Fig. 2). The contact surfaces are horizontal, and the chain includes slender members (each with a length of 1 m and mass of 1 kg) that are connected with spherical joints. In the analysis that follows, we seek to study three aspects of multicontact chain collision problems using the simplified model.

i Effect of the Slip Reversal at A_c on Two and Three-Dimensional Solutions. To conduct a numerical analysis we started with planar pre-impact configurations and then gradually perturbed the coordinates to observe the difference among planar and three-dimensional solutions. Accordingly, the generalized coordinate vector at the instant of impact was selected as

$$\mathbf{q} = \{0, 0, 0, \phi_{11}, \phi_{12}, \phi_{13}, \phi_{21}, \phi_{22}, \phi_{23}, \phi_{31}, \phi_{32}, \phi_{33}\}^T \\ = \{0, 0, 0, 0, \pi - \phi, \delta, 0, \phi, \delta, 0, \phi, \delta\}^T$$

where ϕ was the configuration and δ was the perturbation parameter. The configuration of the chain at impact was gradually varied from a completely extended ($\phi = 0$ deg) to a completely collapsed position ($\phi = 180$ deg), whereas the chain was planar for $\delta = 0$ deg and three-dimensional for $\delta \neq 0$ deg (see Fig. 2). The pre-impact generalized speed vector was selected as

$$\mathbf{u}(0) = \{0, 0, 0, 0, -0.1, 0, 0, -0.2, 0, 0, 0.3, 0\}^T \frac{\text{rad}}{s}$$

This particular selection ensured that the velocity of the colliding end was directed toward the surface prior to collision for all configurations. In addition, the coefficients of friction and restitution were selected as $\mu_0 = \mu_c = 0.5$ and $e = 0.9$, respectively.

The results indicated that kinematic definition of the coefficient of restitution leads to paradoxical energy outcomes when the tangential velocity of the colliding end stopped slipping during the impact (see the energy and velocity plots in Fig. 3). This behavior was observed for planar and three-dimensional solutions. On the other hand, when the tangential velocity of the colliding continued slipping in the same direction ($109 \text{ deg} \leq \phi \leq 180 \text{ deg}$), three definitions of the coefficient of restitution lead to identical outcomes. The energy loss plots revealed further discrepancies among various results obtained by using the three definitions of coefficient of restitution. When the slip at the colliding end stopped during compression ($0 \text{ deg} \leq \phi < 75 \text{ deg}$ and $\tau_c^* < \tau^+$), kinematic definition lead to the lowest and kinetic definition lead the highest energy losses. When the

slip stopped at the maximum compression ($\phi = 75 \text{ deg}$ and $\tau_c^* = \tau^+$), all definitions gave the same results. Yet, when the slip stopped in the restitution phase ($75 \text{ deg} < \phi < 109 \text{ deg}$ and $\tau_c^* > \tau^+$), the kinematic definition lead to the highest and the kinetic definition lead to the lowest energy losses.

Next we focused on the difference among planar and three-dimensional solutions. This characterization is important because in many applications the collision may be approximated as a planar event (an attractive option given the simplicity of planar solutions). Yet practically every real problem is three dimensional. We observed that for small perturbations (up to $\delta = 10$ deg), the difference among the planar and three-dimensional results were insignificant. In this case it appeared that assumption of planar collisions can be justified for nearly two-dimensional collisions.

ii Effect of Slip at the Noncolliding End. When slip reversal occurred at the colliding end, the solutions that were obtained by using the three definitions of the coefficient of restitution lead to different results. Then one interesting aspect of the present problem was the effect of slip reversals at the noncolliding end A_0 , on the solutions obtained using the three definitions of the coefficient of restitution.

We selected the following pre-impact generalized coordinate and velocity vectors to study the problem:

$$\mathbf{q} = \{0, 0, 0, 0, \pi - \phi, \delta, 0, \phi, \delta, 0, 3\pi/2 - \phi, \delta\}^T$$

and

$$\mathbf{u}(0) = \left\{ 0.02 \frac{m}{s}, 0, 0, 0, -0.1 \frac{\text{rad}}{s}, \right.$$

$$\left. 0, 0, -0.2 \frac{\text{rad}}{s}, 0, 0, -0.3 \frac{\text{rad}}{s}, 0 \right\}^T$$

To simplify the analysis we kept the problem planar by letting $\delta = 0$ deg. The results computed for $90 \text{ deg} \leq \phi \leq 180 \text{ deg}$ (see Fig. 4) revealed that solutions obtained for the three definitions of the coefficient of restitution differed only when the slippage in the colliding end reversed or stopped during the collision period. As we observed from the shaded regions of Fig. 4, when slip reversal was only present of the noncolliding end the solutions were identical. Thus, we concluded that the changes in the slip direction at noncolliding ends did not change

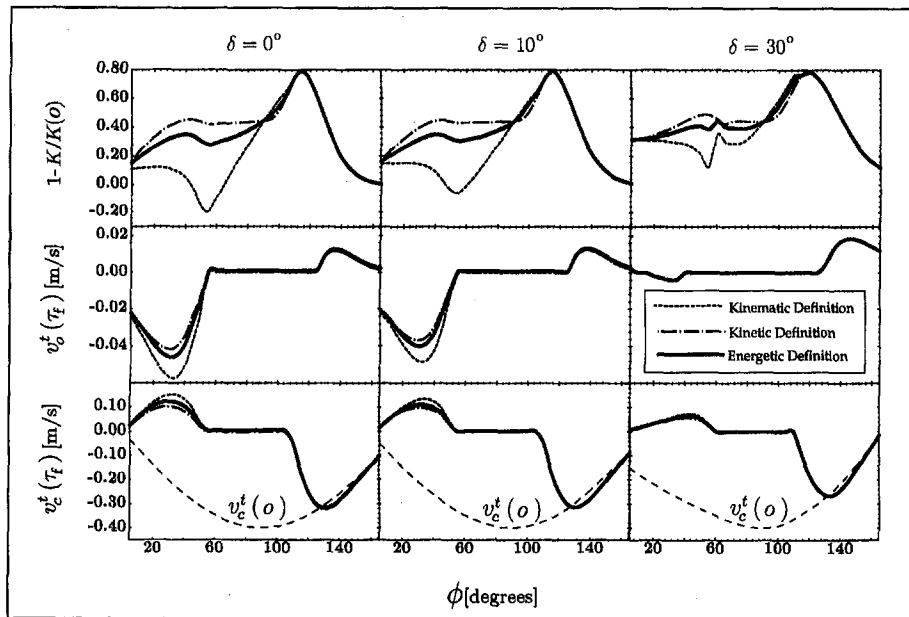


Fig. 3 Energy loss, tangential velocity in t direction at A_o , and tangential velocity in t direction at A_c .

the results obtained by using different definitions of the coefficient of restitution.

iii *Rebounds at the Noncolliding End.* Finally, we studied the rebounds at the noncolliding end. We considered the results obtained for the following pre-impact conditions:

$$\mathbf{q} = \{0, 0, 0, 0, \pi - \phi, \delta, 0, \phi, \delta, 0, 3\pi/2 - \phi, \delta\}^T$$

and

$$\mathbf{u}(0) = \{0, 0, 0, 0, -0.1, 0, 0, -0.2, 0, 0, -0.3, 0\}^T \frac{\text{rad}}{\text{s}}$$

The numerical analyses were conducted for $90 \text{ deg} < \phi < 180 \text{ deg}$ and $\delta = 0 \text{ deg}, 10 \text{ deg}, \text{ and } 30 \text{ deg}$. We considered the

rebound velocities and normal impulses at the end A_o (see Fig. 5). With the exception of the shaded interval, either the rebound velocity or the normal impulse was zero for any given collision. Two transition regions regarding the rebounds at the noncolliding end, A_o were observed. The first transition ($\phi \approx 101 \text{ deg}$) occurred through a single point where the normal rebound velocity and impulse were simultaneously equal to zero. The rebound without interaction was observed for $\phi < 101 \text{ deg}$ and interaction without rebound was observed for $\phi > 101 \text{ deg}$. During the second transition (the shaded interval), however, an intermediate region was observed such that the chain rebounded after it interacted with the surface ($159 \text{ deg} \leq \phi < 168 \text{ deg}$). The main difference between the two transitions were the slip conditions at A_o during collision. For the former case, the noncolliding end did not slip when interacting with the surface. For the latter case, however, the end was slipping when it was interacting with the surface.

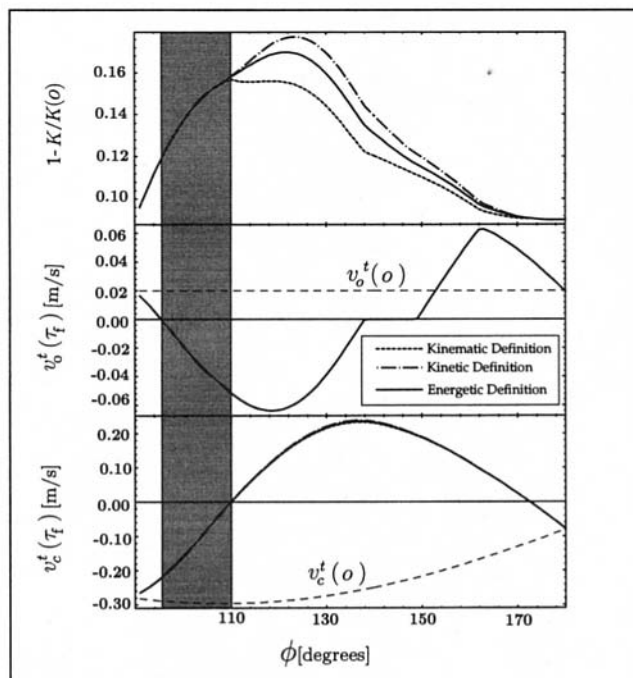


Fig. 4 Energy loss, tangential velocity at A_o , and tangential at A_c .

6 Conclusion

This paper considers the multicontact, rigid-body collisions of spatial, kinematic chains in the presence of friction. The solution techniques are based on the differential formulation of the equations of impact. Full details of a procedure to solve three-dimensional, multicontact collision problems are presented. The procedure can be used to solve the problem by utilizing the kinematic (Newton, 1686), kinetic (Poisson, 1817), and the energetic (Stronge 1990) definitions of the coefficient of restitution.

The numerical results of the collisions of a three link chain, with two contact points were utilized to investigate several aspects of the solutions obtained using the three definitions of the coefficient of restitution. We observed that the kinematic definition lead to paradoxical results regarding energy loss during collision (energy gain as a result of collision). This behavior was present in planar and spatial solutions. We also observed that the energy loss predicted by the energetic definition of the coefficient of restitution always lied between the losses predicted by the other two definitions. One notable aspect of the results was that the three definitions lead to identical results when the colliding end slipped continuously during collision or when it stopped slipping at the instant of maximum compression. Furthermore, the kinetic definition predicted the greatest

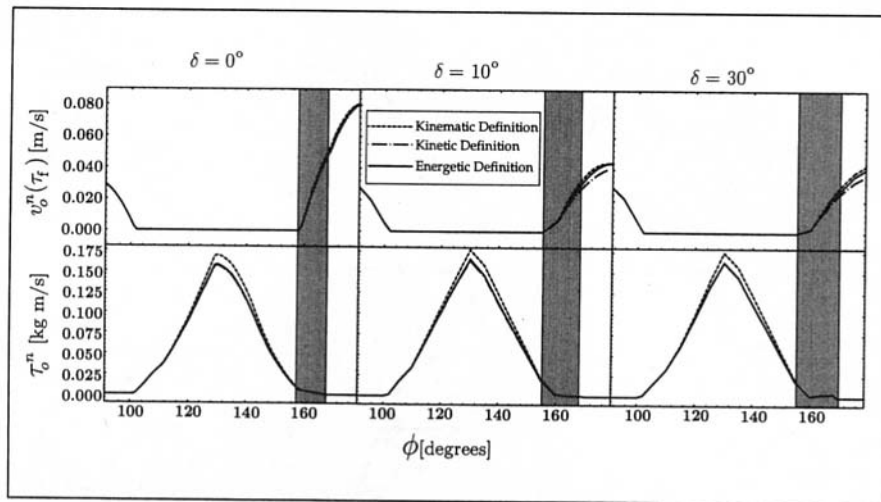


Fig. 5 Rebounds at A_o , rebound velocity, and normal impulse

energy losses when the slip stopped during compression and the least energy losses when the slip stopped during the restitution phase.

The slip conditions at the noncolliding end did not cause the solutions obtained by the three definitions of coefficient restitution to differ. Yet the slippage at this end was the primary determinant in the transitions that occurred from a rebounding to a nonrebounding configuration at the noncolliding end. When the end did not slip, we observed that there is convergence point where the end does not rebound and does not interact with surface (i.e., zero normal velocity and zero normal impulse). When the end slipped, the transition occurred over an interval where the end rebounds with interaction with the surface (i.e., nonzero normal velocity and nonzero normal impulse). If the brief occurrence of the latter type of transition regions was overlooked, we might have concluded that the proposed solutions methods generally predicted that the rebound at the noncolliding end only occurs without interaction with the surface. When the end rebounds, however, it attains a velocity that is directed away from the contact surface at the onset of collision and never interacts with it during the entire impact period.

Acknowledgment

This material is based upon work supported by the National Science Foundation Grant No. MSS-9203097. Any opinions, findings, and conclusions or recommendations expressed in this

material are those of the authors and do not necessarily reflect the views of the National Science Foundation.

References

- Amirouche, F. M. L., 1992, *Computational Methods in Multibody Dynamics*, Prentice-Hall, Englewood Cliffs, New Jersey.
- Brach, R. M., 1989, "Rigid Body Collisions," *ASME JOURNAL OF APPLIED MECHANICS*, Vol. 56, pp. 133-138.
- Brach, R. M., 1992, "Classical Planar Impact Theory and the Tip Impact of a Slender Rod," by the *International Journal of Impact Engineering*, accepted for publication.
- Hurmuzlu, Y., 1993, "Dynamics of Bipedal Gait: Part I-Objective Functions and the Contact Event of a Planar Five-Link Biped," *ASME JOURNAL OF APPLIED MECHANICS*, Vol. 60, pp. 331-336.
- Hurmuzlu, Y., and Chang, T., 1992, "Rigid Body Collisions of a Special Class of Planar Kinematic Chains," *IEEE Transaction in System, Man, and Cybernetics*, Vol. 22, No. 5, pp. 964-971.
- Kane, T. R., and Levinson, D. A., 1985, *Dynamics: Theory and Applications*, McGraw-Hill, New York.
- Keller, J. B., 1986, "Impact with Friction," *ASME JOURNAL OF APPLIED MECHANICS*, Vol. 53, pp. 1-4.
- Morin, A., 1855, *Notions fondamentales de mécanique*, Hachette, Paris.
- Newton, I., 1686, *Philosophiae naturalis principia mathematica*, Reg. Soc. Praeses, London.
- Poisson, S. D., 1817, *Mechanics*, Longmans, London.
- Routh, E. J., 1860, *Dynamics of a System of Rigid Bodies*, Macmillan and Co., London.
- Smith, C. E., 1991, "Predicting Rebounds Using Rigid-Body Dynamics," *ASME JOURNAL OF APPLIED MECHANICS*, Vol. 58, pp. 754-758.
- Stronge, W. J., 1990, "Rigid Body Collisions with Friction," *Proceedings of Royal Society, London*, Vol. A431, pp. 169-181.
- Whittaker, E. T., 1904, *A Treatise on the Analytical Dynamics of Particles and Rigid Bodies*, Cambridge University Press, Cambridge, U.K.

A Finite Elastoplastic Constitutive Formulation With New Co-rotational Stress-Rate and Strain-Hardening Rule

Z. Xia

F. Ellyin

Mem. ASME.

Department of Mechanical Engineering,
University of Alberta,
Edmonton, AB T6G 2G8, Canada

A constitutive model for finite elastoplastic deformations is presented. This model incorporates two novel features: first, a strain-hardening law that is applicable to complex loading paths and histories; and second, an objective stress-rate measure that is based on the spin of an orthogonal triad of material unit vectors which instantaneously coincides with the principal directions of the stress tensor. Problems of shear superposed on triaxial tension, cyclic shear deformation, and biaxial nonproportional loading are studied. It is shown that realistic predictions for the aforementioned problems are obtained by using the proposed constitutive model.

1 Introduction

Metals exhibit a rather complex elastoplastic behavior under different loading paths or histories. The classical isotropic or kinematic-hardening models are not sufficient to properly describe the observed material behavior. Consequently, a number of elastoplastic constitutive models have been proposed in recent years. They include so-called unified models (viscoplastic models): Miller (1976), Krempl et al. (1986), Chaboche (1989), and Moosbrugger and McDowell (1990); and two- or multi-surface models: Mroz (1967), Dafalias and Popov (1976), McDowell (1985), and Ellyin and Xia (1989), among others. However, most of these models are formulated within the assumption of infinitesimal strains.

In the case of finite elastoplastic constitutive theories, there are some disagreements among various investigators on a number of important issues. A comprehensive review regarding these issues and the state of finite plasticity, up to its date of publication, is given by Naghdi (1990). It contains a list of major contributors in the field and, due to space limitation, they are not repeated herein. It is not the purpose of the present paper to discuss general issues such as the suitable decomposition of the total strain rate, etc., which are amply discussed elsewhere, e.g., see Naghdi (1990) for further references. Instead, the objective of this paper is to extend in a straightforward manner, a recently developed elastoplastic constitutive model for small deformations to the *finite* deformation range. This can be achieved because most of the basic ideas and features of a small deformation theory can be extended to the finite deformation range with proper care. The proposed model incorporates two recent contributions by the authors: a comprehensive strain-hardening law applicable to complex loading path and histories, Ellyin and Xia (1989), and an objective stress-rate, Xia and Ellyin (1993). The latter provides a more realistic prediction for problems involving dominant shear stress or shear deformations. The model is developed mainly for polycrystalline metals in which relatively small elastic deformation takes place and von Mises yield condition is assumed to hold.

Contributed by the Applied Mechanics Division of THE AMERICAN SOCIETY OF MECHANICAL ENGINEERS for publication in the ASME JOURNAL OF APPLIED MECHANICS.

Discussion on this paper should be addressed to the Technical Editor, Professor Lewis T. Wheeler, Department of Mechanical Engineering, University of Houston, Houston, TX 77204-4792 and will be accepted until four months after final publication of the paper itself in the ASME JOURNAL OF APPLIED MECHANICS.

Manuscript received by the ASME Applied Mechanics Division, Nov. 2, 1993; final revision, May 10, 1994. Associate Technical Editor: J. W. Rudnicki.

After a general description of the model in Section 2, three types of problems are considered: (a) shear superposed on triaxial tension, (b) cyclic shear deformation, and (c) biaxial nonproportional loading. The proposed constitutive model furnishes satisfactory predictions for these examples. This prompts us to recommend the use of the proposed model for practical engineering problems.

2.1 General Form of the Constitutive Equation. The present model is formulated in the Eulerian reference frame, i.e., the constitutive relation has the basic form

$$\dot{\tau}^* = f(\mathbf{D}, \tau) \quad (1)$$

where \mathbf{D} is the spatial strain rate, which is defined as the symmetric part of the velocity gradient, τ is the Kirchhoff stress, and $\dot{\tau}^*$ is an objective measure of the stress rate.

Two types of hypersurfaces are introduced in the Kirchhoff stress space, a yield surface and a stress memory surface,

$$\phi_y = f(\tau - \alpha) - q^2 = 0 \quad (2)$$

$$\phi_m = f(\tau - \beta) - R^2 = 0. \quad (3)$$

In the above, α and q specify the center and radius of the yield surface. The size of the stress memory, R , is determined by the maximum equivalent stress level experienced by the material during its previous loading history, i.e., $R = \tau_{eq,max}$. The equivalent stress is defined as $\tau_{eq} = [3/2 s : s]^{1/2}$, where s is the deviatoric part of τ . β is the center of the memory surface, which will be discussed in Subsection 2.3.

By introducing the stress memory surface, two types of plastic loading are distinguished (see Fig. 1(a)). The first type is called monotonic loading (ML), in which the stress memory surface expands with the movement of the yield surface and the two surfaces remain tangent to each other at the current loading point (Fig. 1(a), path AB). The second type is termed plastic reloading (RL). After an elastic unloading (Fig. 1(a), path BC) plastic deformation takes place again. In this case, however, the current loading point is inside the stress memory surface and the size of the stress memory surface does not change during this loading stage (Fig. 1(a), path CD). When the current stress point touches the memory surface and moves it through the expansion, we incorporate the latter stage into the ML case.

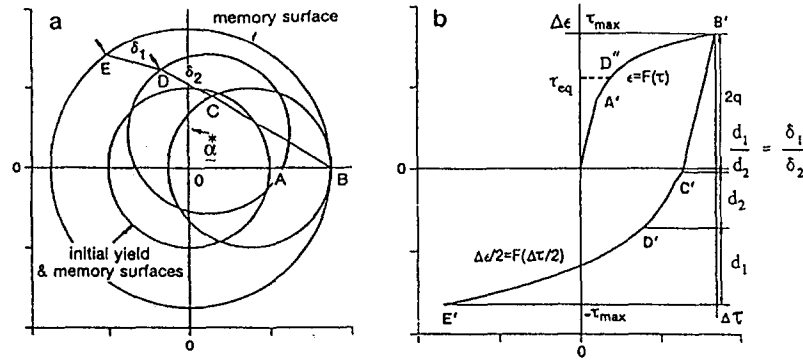


Fig. 1 Yield surface, stress memory surface and two types of plastic loading. Loading path O-A-B-C-D. For A-B, monotonic loading; for C-D plastic reloading. At point D, α^* is parallel to DE. The tangent modulus at this instant is calculated at point D' of the unloading branch, or D'' on the uniaxial curve.

It is assumed that the spatial strain rate can be decomposed into elastic and plastic parts,¹ i.e.,

$$\mathbf{D} = \mathbf{D}^e + \mathbf{D}^p. \quad (4)$$

The elastic strain rate is related to the objective stress rate by the generalized Hooke's law, and the plastic strain rate is obtained from an associated flow rule related to the von Mises yield surface $3J_2 = 3/2 \bar{s} : \bar{s}$, thus we obtain,

$$\mathbf{D} = \frac{1}{E} [(1 + \nu) \dot{\bar{\tau}} - \nu (\text{tr } \dot{\bar{\tau}}) \mathbf{1}] + \frac{9}{4q^2} \left(\frac{1}{E_t} - \frac{1}{E} \right) (\dot{\bar{\tau}} : \bar{s}) \bar{s} \quad (5)$$

where E , ν are the elastic constants, \bar{s} is the deviatoric part of $\bar{\tau} = \tau - \alpha$, and E_t is the tangent modulus. The method of determining the tangent modulus will be described later. The inverse form of Eq. (5) can be obtained after some algebraic manipulation, yielding

$$\dot{\bar{\tau}} = \frac{E}{1 + \nu} \left[\mathbf{D} + \frac{\nu}{1 - 2\nu} (\text{tr } \mathbf{D}) \mathbf{1} - \frac{9}{2q^2} \frac{E - E_t}{3E + (2\nu - 1)E_t} (\mathbf{D} : \bar{s}) \bar{s} \right], \quad (6)$$

which is in the form of Eq. (1).

2.2 Evolution Rule of the Yield Surface. The evolution rule of the yield surface is different for the two plastic loading cases.

For the ML case, a Ziegler-type (1959) rule is adopted,

$$\dot{\alpha}^* = \dot{\mu}(\tau - \alpha). \quad (7)$$

For the RL case, a Mroz-type (1967) rule is used,

$$\dot{\alpha}^* = \dot{\mu}(\tau^m - \tau) \quad (8)$$

where τ^m is a point E, found on the stress memory surface, whose exterior normal is parallel to the outward normal at the current stress point D, (see Fig. 1(a)). By using the consistency condition, $\dot{\phi}_y = 0$ and one of the Eqs. (7) or (8), the scalar $\dot{\mu}$ can be determined.

2.3 Determination of the Center of Stress Memory Surface, β . As mentioned above, in the ML case, the stress memory surface should be tangent to the yield surface at the current

stress point. To satisfy this condition, the β is determined from the following equations:

$$\begin{cases} \left. \frac{\partial f(\tau - \alpha)}{\partial \tau} \right|_{\tau=\tau'} = \lambda \left. \frac{\partial f(\tau - \beta)}{\partial \tau} \right|_{\tau=\tau'}, \\ f(\tau' - \alpha) = q^2, \\ f(\tau' - \beta) = R^2, \end{cases} \quad (9)$$

where τ' is the current stress point. It is to be noted that for a proportional loading and within the small deformation range, $\beta = 0$, i.e., the stress memory surface is an isotropic one. However, for nonproportional loading or in the large deformation case, the stress memory surface may become anisotropic, i.e., $\beta \neq 0$ (see Section 4.2). Condition (9) is applied to the ML loading case only. For the RL loading case, the stress memory surface (R and β) does not change since the current stress point is inside the memory surface.

2.4 Description of Transient Hardening in the Cyclic Loading. Experimental data indicate that the transient-hardening behavior of metals is usually reflected in two ways: one is in the change of the size of the yield surface, q , and the other is in the change of the tangent modulus, E_t . Both changes can be represented by the evolution of the uniaxial Kirchhoff stress-logarithmic strain curve. As shown in Fig. 2, we can imagine that the uniaxial curve evolves from a virgin state to a saturated

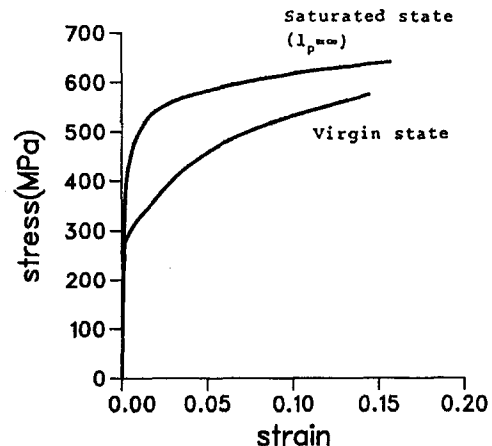


Fig. 2 Uniaxial curve evolving from a virgin state to a saturated state with increasing l_p

¹ This type of decomposition is preferable in comparison to other forms, e.g., that of deformation gradient $\mathbf{F} = \mathbf{F}^e \mathbf{F}^p$; see Naghdi (1990) for further discussion.

state with increasing accumulated plastic strain, l_p , which can be defined as

$$l_p = \int \left[\frac{2}{3} \mathbf{D}^p : \mathbf{D}^p \right]^{1/2} . \quad (10)$$

Assuming an exponential function form for the evolution of the uniaxial curve, we can write the following equations:

$$\begin{cases} \frac{\partial q}{\partial l_p} = k(q_{st} - q), \\ \frac{\partial E_t}{\partial l_p} = k(E_{t,st} - E_t), \end{cases} \quad (11)$$

where q_{st} , $E_{t,st}$ are the saturated values of q and E_t , which are determined from the saturated uniaxial curve. The initial values q_0 , $E_{t,0}$ are determined from the virgin uniaxial curve. Equation (11) is applied for both ML and RL cases.

To describe the additional hardening in the nonproportional cyclic loading, a strain memory surface in the Lagrangian strain space has been introduced in the model. Since this type of behavior is not studied in the examples chosen in the present paper (Sections 3–5), its description is omitted herein. Interested readers are encouraged to consult Ellyin and Xia (1989, 1991).

2.5 Determination of the Tangent Modulus. The calculation of the tangent modulus, E_t , is also different for the two types of plastic loading. In the ML case, E_t is directly defined as a function of the equivalent stress τ_{eq} and the function relation is obtained from the current uniaxial stress-strain curve. In the RL case, we can find a ratio in the stress space (see Fig. 1(a)), $r = \delta_1/\delta_2$, where δ_1 is the distance measured from the loading point D, to the point E on the memory surface, and δ_2 is the distance from the point of the onset of the plastic flow C, to the point D. For every ratio r , a corresponding point on the uniaxial unloading branch can be found (see Fig. 1(b)). Masing's (1926) assumption is used which states that the uniaxial unloading stress-strain branch can be described by the equation $\Delta\epsilon = 2F(\Delta\tau/2)$, which is the magnification of the curve, $\epsilon = F(\tau)$, by a factor of two (see Fig. 1(b)). The current tangent modulus can then be calculated from the uniaxial stress-strain curve.

2.6 Objective Stress Rate. In extending a small deformation theory to a finite deformation, an objective rate of stress tensor should be adopted instead of its material derivative. The most popular rate measure used in the past has been the Jaumann rate. However, Dienes (1979), Nagtegaal and de Jong (1982) showed that the Jaumann rate furnishes an unrealistic oscillatory response in simple shear deformation for a hypoelastic or a kinematically hardening plastic material model. Attempts have been made since then to find an alternative objective stress rate which provides a more realistic prediction *without* changing the basic form of constitutive equations for the material investigated; see for example Xia and Ellyin (1993) for a list of references. These alternative stress rates have provided a monotonically increasing solution for the simple shear problem with prescribed deformation condition. However, when the problem of prescribed shear stress with or without superposed triaxial normal stresses (see Section 3) is considered, one finds that the Jaumann rate, as well as other proposed rates, still furnish physically unrealistic solutions for this example.

Recently, an objective stress rate has been proposed by Xia and Ellyin (1993), in the form of

$$\dot{\boldsymbol{\tau}} = \dot{\boldsymbol{\tau}} + \boldsymbol{\tau}\dot{\mathbf{W}} - \dot{\mathbf{W}}\boldsymbol{\tau}, \quad (12)$$

in which a dot represents the material rate, and

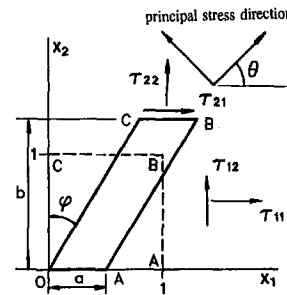


Fig. 3 Undeformed and deformed state of a unit block. Note that the principal stress direction is not changed for the stress-controlled shear superposed on triaxial tension provided the applied stress components increase proportionally.

$$\dot{\mathbf{W}} = \mathbf{W} + (\mathbf{D}\boldsymbol{\tau} - \boldsymbol{\tau}\mathbf{D})/(\xi\tau_{eq}), \quad (13)$$

where \mathbf{W} is the antisymmetric part of the velocity gradient, or the spin, and ξ is a constant. The present stress rate, based on the spin of a material triad that coincides momentarily with principal stress axes, accounts for the general stress state in a weighted average sense that emphasizes the contributions of the dominant principal stress. Detailed discussion and derivation of Eq. (13) is given in Xia and Ellyin (1993). It has been brought to our attention by a reviewer that the second term of the right side of Eq. (13) could be envisaged as a special case of a general representation of skew-symmetric tensor-valued isotropic function with two tensor variables, introduced by Dafalias (1985b, Eq. (27)), which was first derived mathematically by Wang (1970, Table II) in the form of

$$\begin{aligned} \eta_1(\mathbf{a}\boldsymbol{\sigma} - \boldsymbol{\sigma}\mathbf{a}) + \eta_2(\mathbf{a}^2\boldsymbol{\sigma} - \boldsymbol{\sigma}\mathbf{a}^2) + \eta_3(\mathbf{a}\boldsymbol{\sigma}^2 - \boldsymbol{\sigma}^2\mathbf{a}) \\ + \eta_4(\mathbf{a}\boldsymbol{\sigma}\mathbf{a}^2 - \mathbf{a}^2\boldsymbol{\sigma}\mathbf{a}) + \eta_5(\boldsymbol{\sigma}\mathbf{a}\boldsymbol{\sigma}^2 - \boldsymbol{\sigma}^2\mathbf{a}\boldsymbol{\sigma}). \end{aligned} \quad (14)$$

In Dafalias' work (1985a, b), the plastic spin is further defined by the first term of the above equation and by choosing $\mathbf{a} = \boldsymbol{\alpha}$, $\boldsymbol{\sigma} = \mathbf{s} - \boldsymbol{\alpha}$, where \mathbf{s} , $\boldsymbol{\alpha}$ are deviatoric stress and back stress tensors. In the present work, $\mathbf{a} = \mathbf{D}$ and $\boldsymbol{\sigma} = \boldsymbol{\tau}$. In addition, our derivation of Eqs. (12)-(13) was not based on the concept of plastic spin.

3 Stress-Controlled Shear Superposed on Triaxial Normal Stresses

The stress-controlled simple shear or "unconstrained shear" was studied by a few researchers (see Lee and Weithermer, 1983; Paulun and Pecherski, 1985; Harren et al. 1989). In the following, we will study the more general problems of stress-controlled shear with the superposed triaxial normal stresses.

Consider a body whose configuration in the reference state is a unit block, Fig. 3. Let the block be subjected to a homogeneous stress state τ_{11} , τ_{22} , τ_{33} and $\tau_{12} = \tau_{21}$. With an additional constraint condition that the point O is fixed and line OA does not rotate. The corresponding homogeneous deformation state can be assumed to be

$$\begin{cases} x_1 = a(X_1 + eX_2) \\ x_2 = bX_2 \\ x_3 = cX_3 \end{cases} \quad (15)$$

where X_i and x_i denote the coordinates of material points in the undeformed and deformed states, respectively. Suppose that the applied stress components increase proportionally, i.e., τ_{11}/τ_{12} , τ_{22}/τ_{12} and τ_{33}/τ_{12} keep constant. Thus, the direction of the principal stress is fixed (see Fig. 3) since

$$\tan 2\theta = \frac{2\tau_{12}}{\tau_{11} - \tau_{22}} = \text{const.} \quad (16)$$

where θ is the angle measured from the x_1 -axis. The initially

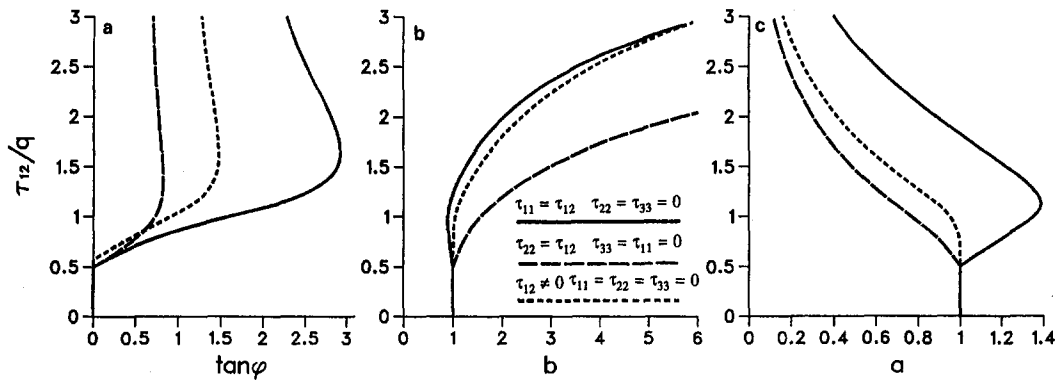


Fig. 4 Stress-controlled shear superposed on triaxial tension. (a) τ_{12} versus $\tan \phi$, (b) τ_{12} versus b , (c) τ_{12} versus a (see Fig. 3 for notation).

vertical faces of the block, OC, BA, will rotate under the action of the fixed direction stress. However, physical intuition leads us to believe that this rotation may tend toward a limiting value under a monotonically increasing but fixed directional stress. Let us first consider an elastic solution of the problem. For an arbitrary isotropic elastic material, compressible or incompressible, linear or nonlinear, Wineman and Gandhi (1984) have obtained a universal relation for the present problem expressed as

$$\frac{\tau_{11} - \tau_{22}}{\tau_{12}} = \frac{a^2/b^2 + \tan^2 \phi - 1}{\tan \phi} \quad (17)$$

By comparing Eqs. (16) and (17), one would find that if the ratio a/b tends to zero with increasing applied stress, then the rotation ϕ will have a limit value of $\pi/2 - \theta$, i.e., the initially vertical faces OC, BA will eventually align themselves with the principal stress direction.

Next we consider an elastoplastic material. For a monotonic proportional loading (without unloading), we would expect to observe a somewhat similar response to that of the path-independent elastic material. Based on the deformation mode, Eq. (15), the constitutive equations (5), (7), (12), and (13), a set of eight differential equations for the variables $a, b, c, e, \alpha_{11}, \alpha_{22}, \alpha_{33}$, and α_{12} can be derived. They are not produced here due to space limitation. Numerical integration was carried out to obtain solution for the posed problem. For the sake of simplicity, q and E_t are assumed to be constant (bilinear kinematic-hardening material). The material constants are taken to be

$$E = 10^5 \text{ MPa}, \quad \nu = 0.25, \quad q = 207 \text{ MPa},$$

$$E_t = 310 \text{ MPa}, \quad \xi = 2/\sqrt{3}.$$

Three combinations of loading are considered:

- (i) $\tau_{11} = \tau_{12} \neq 0, \tau_{22} = \tau_{33} = 0,$
- (ii) $\tau_{12} \neq 0, \tau_{11} = \tau_{22} = \tau_{33} = 0,$
- (iii) $\tau_{22} = \tau_{12} \neq 0, \tau_{33} = \tau_{11} = 0.$

The results for all three cases are displayed in Fig. 4. It is to be noted that in all three cases, the principal stress directions are fixed in $\theta_i = 31.7, 45, 58.3$ deg, respectively. The results show that the rotation of the vertical surfaces OC or AB, that is the angle ϕ tends towards a limiting value. This value for all cases is exactly equal to $\phi_i = 90 - \theta_i$ deg. This implies that at the limit, $b \rightarrow \infty, a \rightarrow 0$, and the unit block will deform into a slender bar along the principal stress direction. Thus we obtain the same trend as the arbitrary isotropic elastic materials. Further numerical experiments indicate the following interesting features of the solution:

- (a) For any other combination of stress components, the

limit value of ϕ is always equal to $90 - \theta$ deg as long as the constant ξ is taken to be $2/\sqrt{3}$.

- (b) The limit value of ϕ is only dependent on the constant ξ , a change in other material constants (E, ν, E_t, q) does not change the limit value. With different value of ξ , the limiting value will vary proportionally. Furthermore, even if the value ξ changes first and following that asymptotically reaches a fixed value, the limit of ϕ is only dependent on the latter fixed value.

A constant value of $\xi = 2/\sqrt{3}$ will be used for all the examples in Sections 3-5 in order to obtain the same limiting value of ϕ as for the arbitrary isotropic elastic materials. However, to obtain a better fit to experimental data, it is still possible to adjust the value of ξ for different stages of the large deformation or for different materials.

A comparative study is also carried out by using other proposed objective stress rates for the same problem. For example, the prediction for the case (ii) (pure shear stress) by other objective rates is shown in Fig. 5. For the Jaumann rate it is found that when loading increases to $\tau_{12}/q \approx 1.05$, an instability occurs and the value of $\tan \phi$ drastically reduces to zero. The result by using Dafalias rate (1985a) ($\mathbf{W} = \mathbf{W} + \rho(\mathbf{D}\boldsymbol{\alpha} - \boldsymbol{\alpha}\mathbf{D}), \rho = 0.5/\text{tr}[(\mathbf{D}\boldsymbol{\alpha} - \boldsymbol{\alpha}\mathbf{D})^2]$) is close to our result up to $\tau_{12}/q = 3$. When the loading is increased further, the Dafalias' rate, as well as other proposed rates, predicts an increasing $\tan \phi$ to infinity, whereas only the present rate predicts a limited value of $\tan \phi = 1$.

For other combinations of shear stress and normal stress, the trend is the same. For the Jaumann rate an instability occurs when loading increases to a certain value. For other proposed rates, the value of $\tan \phi$ tends to infinity as the shear stress τ_{12} becomes large, irrespective of the combination of stress

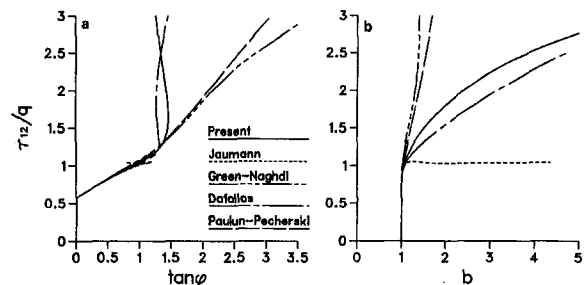


Fig. 5 Comparison of predicted results for unconstrained shear by various proposed objective stress-rates. (a) τ_{12} versus $\tan \phi$, (b) τ_{12} versus b .

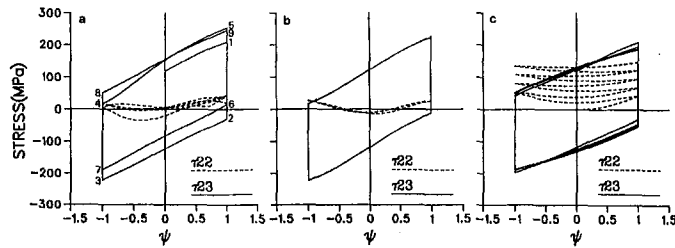


Fig. 6 Stress responses for constrained cyclic shear; (a) first two cycles by the present model, (b) stabilized response by the present model, (c) result by using classical Ziegler hardening rule. No stabilized response is obtained by the latter.

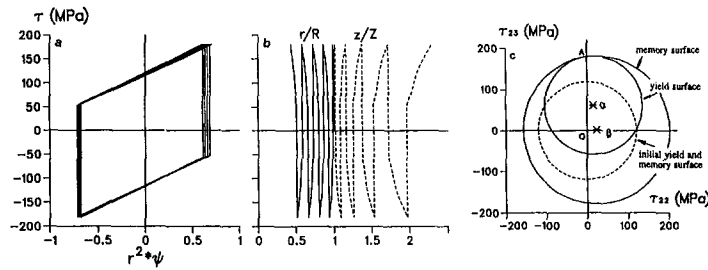


Fig. 7 Deformation response for unconstrained cyclic shear by the present model. (a) $r^2\psi$ versus τ ; (b) r/R versus τ , and z/Z versus τ ; (c) relative position of the yield and memory surfaces. The deformation response does not stabilize—the swift effect is not reversible.

components. This implies that the vertical surface of the cube always rotates 90 deg and the block collapses onto the (X_1, X_3) -plane under the action of monotonically increasing stress with any fixed principal direction, θ (see Fig. 3). From the physical intuition, and the aforementioned results for the isotropic elastic material models, it follows that the predictions of other proposed rates are inappropriate in this case.

Reliable experimental data for the stress controlled shear to a large enough shear strain are limited. Such tests are usually performed on thin-walled tubes, and to avoid buckling, the shear strain cannot reach a high value. In this respect the experimental investigations on large deformation by Bell (1983, 1990) are worth noting. For the sake of comparison, we choose one of his simple twist tests on aluminum tubes with the largest shear strain (see Bell, 1990, Table 1). The measured values of α , δ , and γ (corresponding to a , b , and $\tan \phi$ in our formulation) are 0.9963, 1.000, and 0.250, respectively. Based on the polar decomposition of the deformation gradient $\mathbf{F} = \mathbf{R}\mathbf{V}$, the rigid-body rotation of principal axes and the trace of \mathbf{V} are

$$\psi = \arctan [-\alpha\gamma/(\alpha + \delta)] = -7.1119 \text{ deg,}$$

$$\text{tr } \mathbf{V} = \alpha + (\alpha + \delta) \sec \psi = 3.0081.$$

Our calculated results by using the above chosen material constants are: $a = 0.998575$, $b = 1.00143$, $\tan \phi = 0.249996$, $\psi = -7.11484$ deg and $\text{tr } \mathbf{V} = 3.01410$. If only these numbers are compared then one would conclude that the predictions of the present model are quite good. However, the problem is that the shear deformation of the test is still not large enough to distinguish between different constitutive models. For example, if we use the conventional Jaumann rate ($\xi = \infty$ in Eq. 13), the calculated results are $a = 0.998558$, $b = 1.00144$, $\tan \phi = 0.250001$, $\psi = -7.11488$ deg, and $\text{tr } \mathbf{V} = 3.014074$. Thus the difference between the two co-rotational rates (as well as most of the other proposed formulations) cannot be evaluated at shear strain of the order reported in Bell's experiments.

4 Response of a Thin-Walled Cylindrical Tube Subjected to Cyclic Torsional Loading

Two types of applied cyclic loading are considered. The first type is constrained shear, i.e., deformation of the thin-walled tube is controlled by

$$r = R, \quad \theta = \Theta + \psi(t)Z, \quad z = Z \quad (18)$$

where $\psi(t) = \psi_a \cos t$, and R , Θ , Z and r , θ , z are cylindrical polar coordinates of a material point in the undeformed and deformed configurations, respectively. The second type of loading is termed unconstrained shear, for which only a pair of cyclic shear stress, $\tau = \tau_a \cos t$, is applied at two ends of the tube, and there is no constraint in the longitudinal and radial directions.

4.1 Constrained Cyclic Shear. By using Eq. (18) and constitutive Eqs. (6)-(8), (12), and (13), it is found that $\tau_{22} = -\tau_{33}$, $\alpha_{22} = -\alpha_{33}$, and $\tau_{11} = \tau_{12} = \tau_{13} = \alpha_{11} = \alpha_{12} = \alpha_{13} = 0$, when loading from a virgin state. There are four differential equations for τ_{22} , τ_{23} , α_{22} , and α_{23} with respect to variable ψ .

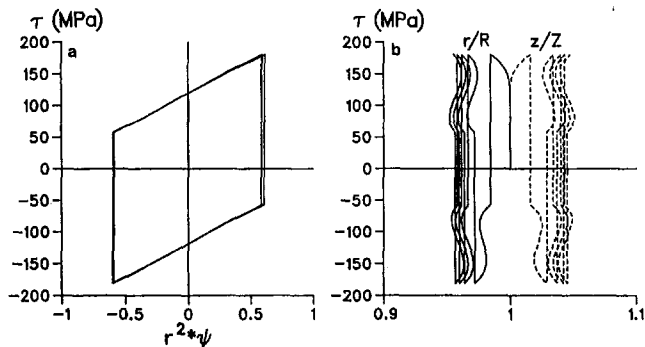


Fig. 8 Deformation response for unconstrained cyclic shear by the classical Ziegler's hardening rule. (a) $r^2\psi$ versus τ , (b) r/R versus τ , and z/Z versus τ . The amplitude of shear strain decreases after each reversal of shear stress.

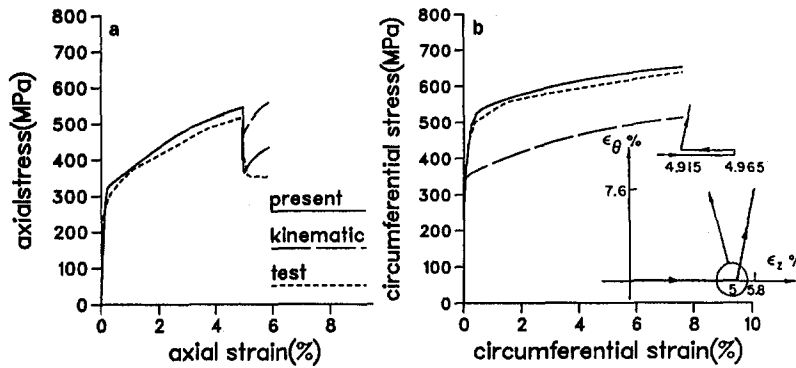


Fig. 9 Biaxial nonproportional loading—tested and predicted results

They are not produced here due to space limitation. The numerical results shown in Fig. 6 are for a tube with a mean radius $R = 1$, subjected to a cyclic twist with $\psi = 1 \cdot \cos t$, having the same material constants as that of the example in Section 3. It is seen that the stress response (shear stress τ_{23} and circumferential stress τ_{22} and longitudinal stress τ_{33}) reaches a stabilized state after the first two cycles. This is because the equivalent stress reaches its maximum value after one and a quarter cycles at point 5 (Fig. 6(a)), thereafter the yield surface moves inside the stress memory surface and a stable cyclic response is obtained due to the evolution rule for the RL case, Eq. (8). The predicted result using only Ziegler's (1959) kinematic hardening rule, Eq. (7), which does not distinguish between the monotonic and reloading cases, is shown in Fig. 6(c). It is to be noted that the stress response does not reach a stable state, especially for τ_{22} and τ_{33} .

4.2 Unconstrained Cyclic Shear. The following deformation mode is assumed for this stress-controlled cyclic loading, $\tau = \tau_a \cos t$:

$$r = f[R, \psi(t)], \quad \theta = \Theta + \psi(t)Z, \quad z = \lambda[\psi(t)]Z. \quad (19)$$

Again, substituting (19) into the constitutive Eqs. (6)-(8), (12), (13) we find that $\alpha_{22} = -\alpha_{33}$, $\alpha_{11} = \alpha_{12} = \alpha_{13} = 0$, and $\dot{r}/r = -\dot{\lambda}/\lambda$, when loading from a virgin state. The deformation is isochoric, that is the thickness of the thin-walled tube does not change and the value of rz keeps constant during the loading history. Four differential equations for r , ψ , α_{22} , and α_{23} with respect to variable τ are obtained. The numerical results with $\tau_a = 180$ MPa and the same material constants as the previous example are shown in Fig. 7.

It is seen that with the constant applied stress amplitude, the deformation response cannot reach a cyclically stable state. Amplitude of the shear strain, $r^2\psi$ (it corresponds to the $\tan \phi$ in the examples of Section 3) increases after each reversal of

the shear stress (Fig. 7(a)). The r decreases and the z increases all the time regardless of the shear stress reversal (Fig. 7(b)). This implies that the Swift effect is not reversible. Such a response is to be expected. We twist two tubes in opposite directions (clockwise and counterclockwise), physically the response will not differ if the material properties are the same in these two opposite directions. Figure 7(c) shows the relative position of the yield and memory surfaces at the instance of $\tau_{23} = \tau_a$ when loading from the virgin state. It is seen that due to the large deformation, the component α_{22} is no longer zero. To keep the yield surface tangent to the memory surface at the loading point $(0, \tau_a)$, the coordinates of the centre of the memory surface (β_{22}, β_{23}) must have certain nonzero values. For the sake of comparison, the predicted results by using only Ziegler's hardening rule are shown in Fig. 8. The range of $r^2\psi$ decreases after each reversal of the shear stress. The r values do not monotonically decrease in each half cycle.

To the best of our knowledge, no experimental results are available for large cyclic torsional deformation to compare with the above predictions. However, comparing the predicted response by two different hardening rules, it is seen that the present model predicts more reasonable results.

5 Nonproportional Biaxial Loading

To compare the predictions with the experimental data, we use two biaxial nonproportional loading test results taken from El-Rafei (1980). These tests were performed on thin-walled tubular specimens of C1026 steel. The loading paths for the two tests are shown in the insets of Figs. 9 and 10. Our predicted results are based on the initial uniaxial curve and saturated uniaxial curve as shown in Fig. 2. From these curves interpolation tables relating the tangent modulus, E_t , to the equivalent stress, τ_{eq} , are obtained. Other material constants are taken to be

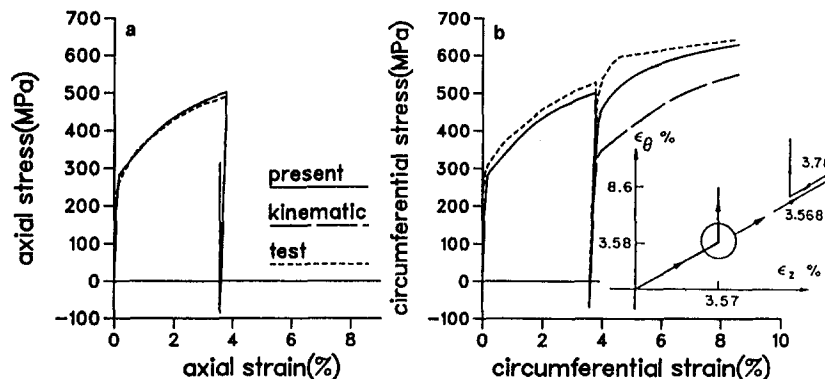


Fig. 10 Biaxial nonproportional loading—tested and predicted results

$$E = 2.1 \times 10^5 \text{ MPa}, \quad \nu = 0.29, \quad q_o = 175 \text{ MPa},$$

$$q_{st} = 275 \text{ MPa}, \quad \beta = 10.$$

The predicted results by the present model, as well as that of Ziegler's kinematical hardening, are shown in Figs. 9 and 10. It is seen that predictions by the present model are closer to the experimental results, especially for the reloading path following the elastic unloading.

At this stage there are no suitable finite deformation experimental data with complex loading paths available; thus further advantages of the proposed hardening model have not been fully demonstrated. Interested readers are referred to Ellyin and Xia (1989, 1991) where examples are provided with various loading paths and histories within the small strain ranges.

6 Conclusions

A constitutive model is formulated for finite elastoplastic deformation. The model incorporates two novel features, viz. a comprehensive hardening law applicable to complex loading paths and histories, and an objective stress-rate measure which provides more realistic responses for problems involving dominant shear stress or shear deformation. The predicted results for problems of shear superposed on triaxial tension (Section 3) shows the superiority of the proposed objective stress rate, whereas the problems of cyclic shear deformation of tubes and biaxial nonproportional loading (Sections 4 and 5) demonstrate the advantages of the hardening law. These examples indicate that the present constitutive model can be used to solve other engineering problems with confidence.

7 Acknowledgment

We gratefully acknowledge the support provided by the Natural Sciences and Engineering Research Council of Canada.

References

- Bell, J. F., 1983, "Continuum Plasticity at Finite Strain for Stress Path of Arbitrary Composition and Direction," *Archive for Rational Mechanics and Analysis*, Vol. 84, pp. 139–170.
- Bell, J. F., 1990, "Material Objectivity in an Experimentally Based Incremental Theory of Large Finite Plastic Strain," *International Journal of Plasticity*, Vol. 6, pp. 293–314.
- Chaboche, J. L., 1989, "Constitutive Equations for Cyclic Plasticity and Cyclic Viscoplasticity," *International Journal of Plasticity*, Vol. 5, pp. 247–302.
- Dafalias, Y. F., 1985a, "A Missing Link in the Macroscopic Constitutive Formulation of Large Plastic Deformation," *Plasticity Today, Modelling, Methods and Application*, A. Sawczuk and G. Bianchi, eds., Elsevier, London, pp. 135–151.
- Dafalias, Y. F., 1985b, "The Plastic Spin," *ASME JOURNAL OF APPLIED MECHANICS*, Vol. 52, pp. 865–871.

- Dafalias, Y. F., and Popov, E. P., 1976, "Plastic Internal Variables Formalism of Cyclic Plasticity," *ASME JOURNAL OF APPLIED MECHANICS*, Vol. 43, pp. 645–651.
- Dienes, J. K., 1979, "On the Analysis of Rotation and Stress Rate in Deforming Bodies," *Acta Mechanica*, Vol. 32, pp. 217–232.
- El-Rafei, A. M., 1980, "Etude experimentale et comparative des aciers ecourissables soumis a des deformation finies," M.Sc. thesis, IV-258, Université de Sherbrooke, Sherbrooke, PQ, Canada.
- Ellyin, F., and Xia, Z., 1989, "A Rate-Independent Constitutive Model for Transient Nonproportional Loading," *Journal of Mechanics and Physics of Solids*, Vol. 37, pp. 71–91.
- Ellyin, F., and Xia, Z., 1991, "A Rate-Dependent Inelastic Constitutive Model—Part I: Elastic-Plastic Flow," *ASME Journal of Engineering Materials and Technology*, Vol. 113, pp. 314–323.
- Green, A. E., and Naghdi, P. M., 1965, "A General Theory of an Elastic-Plastic Continuum," *Archive for Rational Mechanics and Analysis*, Vol. 18, pp. 251–281.
- Harren, S., Lowe, T. C., Asaro, R. J., and Needleman, A., 1989, "Analysis of Large-Strain Shear in Rate-Dependent Face-Centred Cubic Polycrystals: Correlation of Micro- and Macromechanics," *Philosophical Transactions of Royal Society of London*, Vol. A328, pp. 493–500.
- Krempl, E., McMahon, J. J., and Yao, D., 1986, "Viscoplasticity Based on Overstress with a Differential Growth Law for the Equilibrium Stress," *Mechanics of Materials*, Vol. 5, pp. 35–48.
- Lee, E. H., and Wertheimer, T. B., 1983, "Deformation Analysis of Simple Shear Loading with Anisotropic Hardening in Finite Deformation Plasticity," *Recent Developments in Computing Methods for Nonlinear Solids and Structural Mechanics*, ASME Applied Mechanics Div. Symp., June 20–22, pp. 297–310.
- Masing, G., 1926, "Eigenspannungen und Verfestigung beim Messing," *Proceedings of 2nd International Congress of Applied Mechanics*, Zurich, pp. 332–335.
- McDowell, D. L., 1985, "A Two Surface Model for Transient Nonproportional Cyclic Plasticity: Part I—Development of Appropriate Equations; Part II—Comparison of Theory with Experiments," *ASME JOURNAL OF APPLIED MECHANICS*, Vol. 52, pp. 298–308.
- Miller, A. K., 1976, "An Inelastic Constitutive Model for Monotonic, Cyclic and Creep Deformation: Part I—Equations Development and Analytical Procedures," *ASME Journal of Engineering Materials and Technology*, Vol. 99, pp. 97–105.
- Moosbrugger, J. C., and McDowell, D. L., 1990, "A Rate-Dependent Bounding Surface Model with a Generalized Image Point for Cyclic Nonproportional Viscoplasticity," *Journal of Mechanics and Physics of Solids*, Vol. 38, pp. 627–656.
- Mroz, Z., 1967, "An Attempt to Describe the Behaviour of Metals under Cyclic Loads Using a More General Work Hardening Model," *Acta Mechanica*, Vol. 7, pp. 199–212.
- Nagtegaal, J. C., and de Jong, J. E., 1982, "Some Aspects of Non-Isotropic Work-Hardening in Finite Strain Plasticity," *Proceedings of the Workshop on Plasticity of Metals at Finite Strain: Theory, Experiment and Computation*, E. H. Lee and R. L. Mallet, eds., R.P.I., Troy, NY, pp. 65–102.
- Paulun, J. E., and Pecherski, R. B., 1985, "Study of Corotational Rates for Kinematic Hardening in Finite Deformation Plasticity," *Archives of Mechanics*, Vol. 37, pp. 661–667.
- Wang, C. C., 1970, "A New Representation Theorem for Isotropic Functions: An Answer to Professor G. F. Smith's Criticism of My Paper on Representations for Isotropic Functions," *Archive for Rational Mechanics and Analysis*, Vol. 36, pp. 198–223.
- Wineman, A., and Gandhi, M., 1984, "On Local and Global Universal Relations in Elasticity," *Journal of Elasticity*, Vol. 14, pp. 97–102.
- Xia, Z., and Ellyin, F., 1993, "A Stress Rate Measure for Finite Elastic Plastic Deformation," *Acta Mechanica*, Vol. 98, pp. 1–14.
- Ziegler, H., 1959, "A Modification of Prager's Hardening Rule," *Quarterly Journal of Applied Mathematics*, Vol. 17, pp. 55–65.

Partitioning the Parameter Space According to Different Behaviors During Three-Dimensional Impacts

V. Bhatt

J. Koechling

Sibley School of Mechanical
and Aerospace Engineering,
Cornell University,
Ithaca, NY 14853-7501

The equations of motion that define three-dimensional rigid-body impact with finite friction and restitution cannot be solved in a closed form. Previous work has shown that for general shapes and initial conditions, the direction of sliding velocity keeps changing continuously throughout the duration of impact. The flow patterns defined by the trace of the sliding velocity can be classified into a finite number of qualitatively distinct physical behavior. We identify three dimensionless parameters that completely specify the sliding behavior, and determine regions in this parameter space that correspond to each of the different flow patterns. The qualitative behavior during impact can now be determined based on the region which contains the parameters for a given impact configuration. The analysis is also used to study the sensitivity of the sliding behavior to changes in shape or configuration of the body and to rule out the occurrence of certain ambiguities in the post-sticking behavior during impact.

1 Introduction

Routh (1877) first suggested a general rigid-body impact model that incorporated finite friction and restitution. He obtained a "closed-form" geometric solution for the case of a laminar body constrained to move in a plane. In extending Routh's model to the case of three-dimensional impact, Batlle and Condomines (1991), Stronge (1993), and Bhatt and Koechling (1993a, 1993b) have variously shown that for general shapes and initial conditions, the equations of motion do not have a closed-form solution, and need to be numerically integrated.

Bhatt and Koechling (1994a, 1994b) study the qualitative behavior of the contact velocity during impact, by looking at the flow associated with the differential equations defining the velocity components. They analyze the flow in the tangent velocity space, and identify all possible qualitative sliding behavior during impact. The *invariant directions* lie along

the fixed points of the differential equations, and the direction of flow on them heavily influences the global sliding behavior. Finer details of the flow like the local maxima and minima also lie along constant directions which are called the *flow change directions*. Both the invariant and the flow change directions are obtained as real roots of quartics, and are therefore finite in number. By considering all combinations of the number of invariant directions, the sign of flow along them, and the number of flow change directions, every possible qualitative flow pattern for the sliding velocity can be enumerated.

We identify the mass parameters at the point of impact with the qualitative flow patterns for sliding velocity presented in Bhatt and Koechling (1994b). Three independent nondimensional parameters suffice to uniquely define the governing equations and consequently the flow patterns. By mapping each point in this parameter space to a flow pattern, the problem of determining the sliding behavior a priori can be reduced to the much simpler problem of finding the region which contains the contact parameters for a given impact configuration.

We define three separate partitions of the parameter space. The first is based on the number of invariant directions, the second on the number of invariant directions with flow directed outward, and the third according to the number of flow change directions.

By analyzing the coefficients of the quartic for invariant directions, we show that there always exist two or four invariant directions for the flow. A partition of the parameter space is defined by the surface on which the number of

Contributed by the Applied Mechanics Division of THE AMERICAN SOCIETY OF MECHANICAL ENGINEERS for presentation at the Joint Applied Mechanics and Materials Summer Annual Meeting of the ASME, Los Angeles, CA, June 28-30, 1995.

Discussion on this paper should be addressed to the Technical Editor, Professor Lewis T. Wheeler, Department of Mechanical Engineering, University of Houston, Houston, TX 77204-4792, and will be accepted until four months after final publication of the paper itself in the ASME JOURNAL OF APPLIED MECHANICS.

Manuscript received by the ASME Applied Mechanics Division, Dec. 20, 1993; final revision, Aug. 26, 1994. Associate Technical Editor: E. J. Haug, Jr.

Paper No. 95-APM-8.

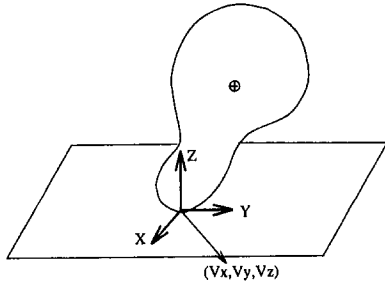


Fig. 1 Coordinate system for the rigid body. The x and y -axes are chosen to eliminate the cross-coupling term a_{12} in the tangential direction.

invariant directions change from two to four, and we determine the algebraic expression for it. The global flow behavior is influenced by the direction of flow on the invariant directions, which can be either towards or away from the point of sticking. There can only be zero or one invariant directions with the flow directed outward, and the second surface of partition in the parameter space differentiates between these two cases. There can be four, two, or zero flow change directions, and the third surface of partition defines regions in the parameter space corresponding to each of these cases.

Since the qualitative nature of the sliding velocity flow is uniquely defined by the number of invariant directions, invariant directions with outflow, and the flow change directions; by intersecting the three surfaces of partition defined above, we can divide the parameter space into regions with a one-to-one correspondence with the flow patterns. Boundaries between these regions correspond to a transition between flow patterns and represent the "bifurcation surfaces."

Given a rigid body and its impact configuration, we can find the dimensionless parameters which identify it with a unique sliding behavior during impact. Sensitivity of the sliding behavior to changes in the mass distribution, or configuration, depends on the proximity of the mass parameters to the bifurcation surfaces.

2 Flow in the Tangent Velocity Space

In previous work Bhatt and Koechling (1994a, 1994b) identified the possible behavior of the sliding velocity during impact. Some relevant points from those articles are recapitulated here.

2.1 Defining the Flow. Figure 1 shows the coordinate system for the impact problem. The z -axis defines the common normal to the impacting surfaces, and the x and y axes define the common tangent plane. The impulse-momentum change law which governs the impact process is $\Delta\hat{\mathbf{V}} = \mathbf{M}^{-1}\Delta\hat{\mathbf{P}}$, where $\hat{\mathbf{V}}$ is the velocity vector, $\hat{\mathbf{P}}$ the impulses, and \mathbf{M}^{-1} the inverse inertia tensor, at the point of contact. Since the choice of orientation of the x and y -axes is arbitrary, we can choose them such that there is no coupling between the components of $\hat{\mathbf{V}}$ and $\hat{\mathbf{P}}$ along those two axes. If $\text{Rot}(z, \theta)$ is the matrix that rotates the coordinate system by θ about the z -axis, we get

$$\Delta\mathbf{V} = \mathbf{A}^{-1}\Delta\mathbf{P} \quad (1)$$

$$\Delta\mathbf{V} = \text{Rot}(z, \theta)\Delta\hat{\mathbf{V}} \quad \Delta\mathbf{P} = \text{Rot}(z, \theta)\Delta\hat{\mathbf{P}}$$

$$\mathbf{A}^{-1} = \text{Rot}(z, \theta)\mathbf{M}^{-1}\text{Rot}(z, \theta)^T.$$

If a_{ij} are the elements of \mathbf{A}^{-1} and m_{ij} the elements of \mathbf{M}^{-1} ,

$$a_{12} = (m_{11} - m_{22}) \cos \theta \sin \theta + m_{12} \cos^2 \theta - m_{21} \sin^2 \theta.$$

To remove the coupling along the tangent axes, we need $a_{12} = 0$, which is satisfied if

$$\theta = \frac{1}{2} \text{atan} \left(\frac{2m_{12}}{(m_{22} - m_{11})} \right) + q \frac{\pi}{2} \quad (2)$$

where q is an integer, and we use the symmetry of \mathbf{M} to set $m_{12} = m_{21}$. In the transformed coordinates, the impulse-momentum relation for the sliding velocity are

$$\begin{aligned} v_x &= v_{x0} + a_{11}P_x + a_{13}P_z \\ v_y &= v_{y0} + a_{22}P_y + a_{23}P_z \end{aligned} \quad (3)$$

where v_x, v_y is the relative sliding velocity and P_x, P_y, P_z the net accumulated impulse at the point of contact. The subscript 0 refers to the initial value of the contact velocity.

Using Coulomb's law with a friction coefficient of μ , and the rescaling $d\tau = (\mu / \sqrt{v_x^2 + v_y^2}) dP_z$,

$$\frac{dP_x}{d\tau} = -v_x \quad \frac{dP_y}{d\tau} = -v_y. \quad (4)$$

If we express the sliding velocity in polar coordinates, $v_r = \sqrt{v_x^2 + v_y^2}$ and $v_\theta = \text{atan}(v_y/v_x)$, and differentiate Eq. (3) with respect to τ , we get the following flow equations:

$$\begin{aligned} \frac{dv_r}{d\tau} &= v_r \left(-a_{11} \cos^2 v_\theta - a_{22} \sin^2 v_\theta \right. \\ &\quad \left. + \frac{a_{13}}{\mu} \cos v_\theta + \frac{a_{23}}{\mu} \sin v_\theta \right) \end{aligned} \quad (5)$$

$$\frac{dv_\theta}{d\tau} = (a_{11} - a_{22}) \cos v_\theta \sin v_\theta + \frac{a_{23}}{\mu} \cos v_\theta - \frac{a_{13}}{\mu} \sin v_\theta. \quad (6)$$

2.2 Identifying the Parameter Space. The coefficients $a_{11}, a_{22}, a_{13}/\mu$, and a_{23}/μ in Eqs. (5)–(6) determine the behavior of the sliding velocity. If we rescale the independent variable τ to τ' , such that $d\tau' = (a_{13}/\mu)d\tau$,

$$\frac{dv_r}{d\tau'} = v_r (-\lambda \cos^2 v_\theta - \phi \sin^2 v_\theta + \cos v_\theta + \delta \sin v_\theta) \equiv f \quad (7)$$

$$\frac{dv_\theta}{d\tau'} = (\lambda - \phi) \cos v_\theta \sin v_\theta + \delta \cos v_\theta - \sin v_\theta \equiv g \quad (8)$$

$$\delta = \frac{a_{23}}{a_{13}} \quad \lambda = \frac{\mu a_{11}}{a_{13}} \quad \phi = \frac{\mu a_{22}}{a_{13}}.$$

δ, λ, ϕ are dimensionless parameters that now define the flow, and consequently the sliding behavior. This three-dimensional parameter space is enough to capture all possible behavior for the tangent velocity.

If $a_{13} = 0$, we can rotate the tangential axes by $\pi/2$ (increment q by 1 in Eq. (2)), interchanging the x and y -axes and consequently the magnitudes of a_{13} and a_{23} . For the case when $a_{13} = a_{23} = 0$, every direction is invariant and the problem reduces to the planar form.

a_{11} and a_{22} are always positive, and therefore λ and ϕ are either both positive or both negative depending on the sign of a_{13} . δ can be either positive or negative. Therefore, for real bodies, parameters in only four of the octants of the parameter space are possible. A change in the sign of δ reflects the flow about the $v_\theta = 0$ line. The change in sign for both λ and ϕ is equivalent to a reflection about the $v_r = 0$ point. Due to these symmetry properties, the positive octant of the parameter space can be reflected about $v_r = 0$ and $v_\theta = 0$ to define the other three octants where the parameters for real bodies can lie.

Table 1 The possible flow patterns and the corresponding properties of the flow

Case	Invariant directions	Flow Change directions	No. of Saddles	No. of Nodes	No. of Separatrix	In Flow direction	Out flow direction
0 a	4	4	4	0	2	2	2
1 a, b	4	4, 2	3	1	2	3	1
2 a, b, c	4	4, 2, 0	2	2	2	4	0
3 a, b	2	4, 2	2	0	1	1	1
4 a, b, c	2	4, 2, 0	1	1	1	2	0

We can further restrict the region in the parameter space that we need to analyze by assuming that $|a_{23}| < |a_{13}|$. If this is not true, we can rotate the x and y -axes by $\pi/2$, effectively interchanging a_{13} and a_{23} . The solution behavior over the whole parameter space is therefore reflected in

$$\lambda \geq 0, \quad \phi \geq 0, \quad 1 \geq \delta \geq 0. \quad (9)$$

2.3 Invariant Directions. The invariant directions (\tilde{v}_θ) are solution curves for the flow along which v_θ does not change. They are obtained as real roots of $dv_\theta/d\tau' = g = 0$ in Eq. (8). The resulting trigonometric equation can be written as an algebraic quartic by substituting $\alpha = \tan \tilde{v}_\theta$.

$$\alpha^4 - 2\delta\alpha^3 + (1 + \delta^2 - (\lambda - \phi)^2)\alpha^2 - 2\delta\alpha + \delta^2 = 0 \quad (10)$$

$$\text{sign}\left(\frac{-(\lambda - \phi)\alpha}{\delta - \alpha}\right) = \text{sign}(\cos \tilde{v}_\theta) \quad (11)$$

2.4 Flow Change Directions. At the flow change directions (\hat{v}_θ), the radial component of the flow changes sign. By setting $dv_r/d\tau' = f = 0$ in Eq. (7), we get the following quartic in $\beta = \tan \hat{v}_\theta$, whose real roots give the flow change directions.

$$(\delta^2 - \phi^2)\beta^4 + 2\delta\beta^3 + (1 + \delta^2 - 2\lambda\phi)\beta^2 + 2\delta\beta + (1 - \lambda^2) = 0 \quad (12)$$

$$\text{sign}\left(\frac{\lambda + \phi\beta^2}{1 + \delta\beta}\right) = \text{sign}(\cos \hat{v}_\theta) \quad (13)$$

2.5 Possible Flow Patterns. Based on the number of invariant directions and flow change directions, the possible flow patterns can be determined according to Table 1 and Fig. 2 (Bhatt and Koechling, 1994b). The global behavior is dependent on the number of invariant directions and the sign of flow along them, and is given by the cases 0–4. The number of flow change directions (4, 2, or 0), define the local maxima and minima for the flow, resulting in up to three subcases (a, b, or c, respectively). In Section 4.1, we show that case 0 cannot occur for any set of real parameters.

3 Regions With Different Number of Invariant Directions

Since the invariant directions are determined by the real roots of the quartic in Eq. (10), they can be zero, two, or four in number. The number of invariant directions changes at points in the parameter space which correspond to a double root of this quartic, the condition for which can be algebraically determined to get the surface of partition in the parameter space.

To determine the boundary between different number of invariant directions, we assume that Eq. (10) has a double root at p_0 , and $a \pm ib$ are the other two roots. If b is real, the double root corresponds to a transition between zero and

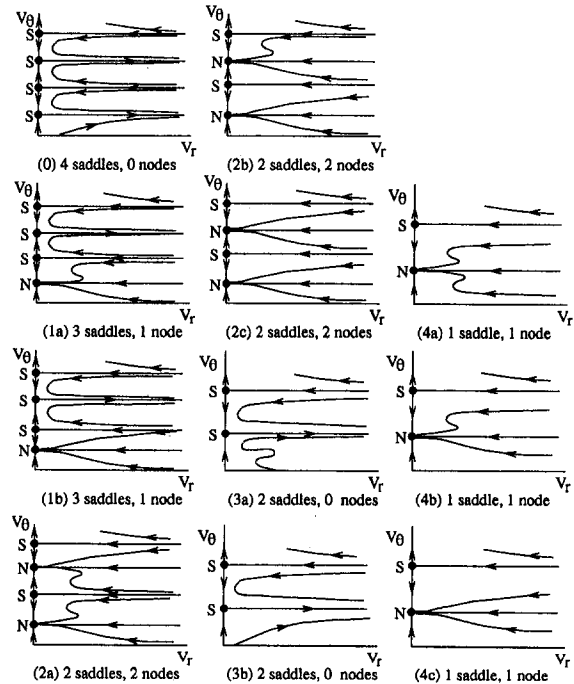


Fig. 2 The possible flow patterns for the tangential velocity

two real roots, otherwise it gives the boundary between regions with two and four real roots (or invariant directions).

In Appendix A we show that there is only one surface that corresponds to a double root of the quartic for invariant directions.

$$(\lambda - \phi)^2 = (\delta^{2/3} + 1)^3 \quad (14)$$

On this surface $\delta = -p_0^3$ and $b^2 = -p_0^2(1 + p_0^2 + p_0^4)$, which means that b is imaginary and therefore the surface forms a boundary between regions with two and four invariant directions. The case of zero invariant directions does not exist. Figure 3 shows this partition in the parameter space. Since the boundary depends only on δ and $|\lambda - \phi|$, it can be captured on a two-dimensional plane. Expressed algebraically,

$$\text{for 4 invariant directions: } |\lambda - \phi| > (\delta^{2/3} + 1)^{3/2}$$

$$\text{for 2 invariant directions: } |\lambda - \phi| < (\delta^{2/3} + 1)^{3/2}. \quad (15)$$

4 Invariant Directions With Outward Flow

From Fig. 2 we know that there can be at most two invariant directions with the flow directed away from the point of sticking. The direction of flow on an invariant direction changes when a flow change direction coincides with an invariant direction. This happens for \tilde{v}_θ values such that $f(\tilde{v}_\theta) = g(\tilde{v}_\theta) = 0$. Appendix B shows that this happens when \tilde{v}_θ satisfies

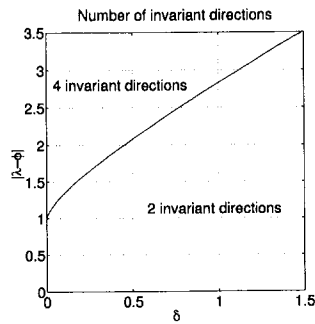


Fig. 3 Partition of the parameter space into regions with different number of invariant directions. The space is two-dimensional since only δ and $|\lambda - \phi|$ affect the number of real roots. We do not have the case where there are 0 invariant directions.

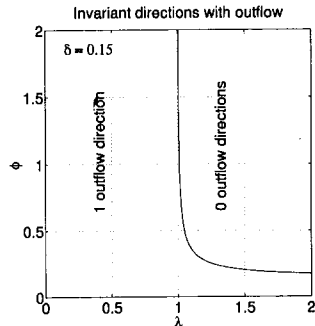


Fig. 4 Partition of the parameter space into regions with different number of invariant directions with outward flow. The figure shows a slice of the parameter space at $\delta = 0.15$.

$$\cos \check{\nu}_\theta = \frac{1}{\lambda} \quad \sin \check{\nu}_\theta = \frac{\delta}{\phi} \quad (16)$$

Equation (16) is a valid solution only on the surface in the parameter space where the trigonometric identity $\sin^2 \check{\nu}_\theta + \cos^2 \check{\nu}_\theta = 1$ is satisfied. This gives the following boundary in the parameter space on which the number of invariant directions with outflow changes.

$$\left(\frac{1}{\lambda}\right)^2 + \left(\frac{\delta}{\phi}\right)^2 = 1 \Rightarrow \lambda = \frac{\phi}{\sqrt{\phi^2 - \delta^2}} \quad (17)$$

The surface of partition exists only for $\phi > \delta$, and its asymptotes are

$$\text{as } \phi \rightarrow \infty, \quad \lambda \rightarrow 1 \quad \text{as } \lambda \rightarrow \infty, \quad \phi \rightarrow \delta.$$

Table 1 states that the flow can be directed outward on zero, one, or two invariant directions. However, there is only one surface of partition between regions with different number of invariant directions with outward flow, and therefore only two of these three cases are possible.

To find out which two of the three cases exist, consider the line $\lambda = \phi$, for which there are two invariant directions given by $\cos \nu_\theta = \pm 1/\sqrt{1 + \delta^2}$ and $\sin \nu_\theta = \pm \delta/\sqrt{1 + \delta^2}$. From Eq. (7), the sign of flow along them is given by the sign of $-\lambda \pm \sqrt{1 + \delta^2}$.

For $\lambda < \sqrt{1 + \delta^2}$ the flow is outward along one of the invariant directions, while for $\lambda > \sqrt{1 + \delta^2}$ it is radially inward along both. Since the boundary of partition (Eq. (17)) on this line is at $\lambda = \phi = \sqrt{1 + \delta^2}$, it has regions with either zero or one outflow direction on either side of it (Fig. 4). Therefore, the case with two invariant directions with outflow (Case 0 in Table 1) does not exist.

$$\text{For 0 invariant directions with outflow: } \lambda > \frac{\phi}{\sqrt{\phi^2 - \delta^2}}.$$

For 1 invariant direction with outflow:

$$\lambda < \frac{\phi}{\sqrt{\phi^2 - \delta^2}} \text{ or } \phi < \delta. \quad (18)$$

4.1 Resumption of Sliding. If the flow reaches the point of sticking, the condition for the instantaneous resumption of sliding is given by (Bhatt and Koechling, 1994b)

$$\frac{a_{13}^2 a_{22}^2 + a_{23}^2 a_{11}^2}{a_{11}^2 a_{22}^2} > \mu^2 \Rightarrow \frac{1}{\lambda^2} + \frac{\delta^2}{\phi^2} > 1$$

$$\Rightarrow \lambda < \frac{\phi}{\sqrt{\phi^2 - \delta^2}} \text{ or } \delta > \phi. \quad (19)$$

Since sliding resumes along an invariant direction on which the flow is directed outward, there would be ambiguities if there were zero or two such invariant directions when the conditions for the resumption of sliding are satisfied. From Eqs. (18) and (19), we see that the condition for resumption of sliding automatically ensures that there is always one and only one invariant direction with outflow, and therefore no ambiguities arise.

5 Different Number of Flow Change Directions

The flow change directions are given by the roots of the quartic in Eq. (12). Using a development similar to that used to get the partition for invariant directions in Section 3, we look for the surface in the parameter space that corresponds to a double root of the quartic. This surface forms the boundary between regions with different number of flow change directions. Appendix C shows that the equation for this surface of partition is

$$16(\phi^2 - \delta^2)\lambda^4 - 8\phi(4\phi^2 - 4\delta^2 + 1)\lambda^3 + (16\phi^4 - 8\delta^2\phi^2 - 8\phi^2 - 8\delta^4 + 20\delta^2 + 1)\lambda^2 - 2\phi(4\delta^2\phi^2 - 16\phi^2 - 4\delta^4 + 19\delta^2 - 4)\lambda - (16\phi^4 - \delta^4\phi^2 - 20\delta^2\phi^2 + 8\phi^2 + (\delta^2 + 1)^3) = 0. \quad (20)$$

The surface of partition defined by Eq. (20) is illustrated for different constant δ slices in Fig. 5. The boundary between regions with 0 and 2 flow change directions has the following asymptotic behavior:

$$\text{as } \phi \rightarrow \infty, \quad \lambda \rightarrow 1; \quad \text{as } \lambda \rightarrow \infty, \quad \phi \rightarrow \delta;$$

and lies inside the region with 0 invariant direction with outflow defined by Eq. (18).

The boundary between two and four flow change directions defines the "triangular" region which becomes smaller as δ increases from 0. The value of δ_c for which the region with four flow change directions disappears for all $1 \geq \delta > \delta_c$, can be calculated by noting that at $\delta = \delta_c$, there is a double root $\lambda = \lambda_c$ for $\phi = 0$ in Eq. (20):

$$16\delta_c^2\lambda_c^4 + (8\delta_c^4 - 20\delta_c^2 - 1)\lambda_c^2 + (\delta_c^2 + 1)^3 = 0 \\ \Rightarrow \delta_c = \frac{1}{\sqrt{8}}, \quad \lambda_c = \frac{3\sqrt{3}}{4\sqrt{2}}.$$

Therefore, for $1 > \delta > (1/\sqrt{8})$, the region with four flow change directions does not exist.

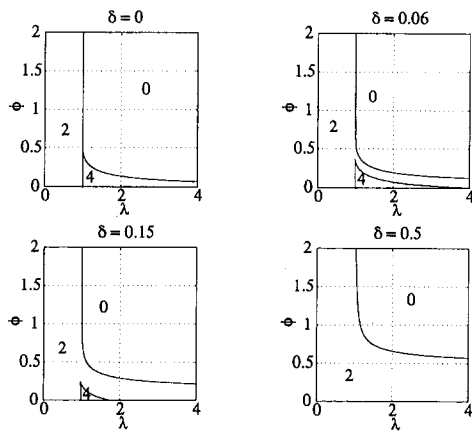


Fig. 5 Partition of the parameter space, at different values of δ , according to the number of flow change directions. For values of $\delta < (1/\sqrt{8})$, there are regions with 0, 2, and 4 flow change directions. For $\delta > (1/\sqrt{8})$, only regions with 0 or 2 flow change directions exist. The numbers on the plot correspond to the number of flow change directions.

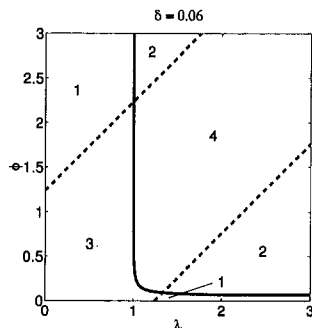


Fig. 6 Partition of the parameter space based on the global asymptotic behavior of the flow. The numbers in each region correspond to the cases in Table 1. At the solid curve, the number of invariant directions with outflow changes. The dashed line is the boundary between different number of invariant directions.

6 Partitioning the Parameter Space

The flow patterns are uniquely defined by the number of invariant directions, invariant directions with outflow, and the flow change directions (Table 1). In the preceding sections, we have defined partitions of the parameter space based on each of the three criteria. The regions in the parameter space defined by these partitions can now be intersected to get a partition of the parameter space according to the flow patterns.

The asymptotic behavior of the flow depends only on the number of invariant directions and the sign of flow along them (Cases 1–4 in Table 1). By intersecting the regions for different number of invariant directions defined by Eq. (15), and the invariant directions with outward flow defined by Eq. (18), we find a first level partition of the parameter space based on the asymptotic flow behavior. Figure 6 shows this partition for $\delta = 0.06$ slice in the parameter space.

Each of the regions in Fig. 6 can be subclassified according to the number of flow change directions. The flow change directions define the local maxima and minima, and add further information about the structure of the flow to the asymptotic flow behavior. Depending on whether there are four, two or zero flow change directions, each of the cases 1–4 are subclassified with the labels a, b, or c, respectively (Table 1). Figure 7 illustrates how the regions in Fig. 6 are divided into subclasses by intersecting them with the partition based on the flow change directions (defined by Eq. (20)

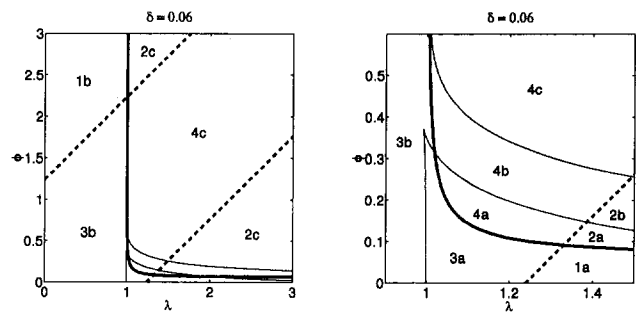


Fig. 7 Subpartition of the regions shown in Fig. 6. The thick dashed and solid lines are the boundaries between different number of invariant directions and invariant directions with outflow, respectively. The thin curves are the boundaries for different number of flow change directions. The figure on the right shows the details of the partition structure.

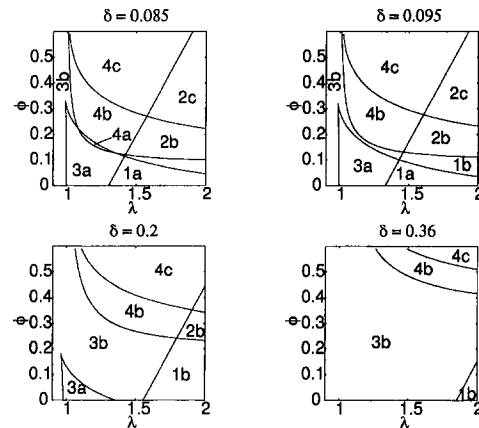


Fig. 8 Partition of the parameter space at various values of δ , showing the successive disappearance of regions 2a, 4a, 1a, 3a.

and shown for the $\delta = 0.06$ slice in Fig. 5). For the value of $\delta = 0.06$, all the ten possible flow patterns exist.

As δ is increased from 0, the region with four flow change directions shrinks until it disappears for $\delta_c > (1/\sqrt{8})$. After this limit, cases 1a, 2a, 3a, and 4a are not possible. The sequence in which these regions disappear is, 2a at $\delta = \sqrt{37 + 21\sqrt{3} - 3^3 \sqrt{299\sqrt{3}} + 518} = 0.08255$, 4a at $\delta = (5\sqrt{5} - 11)/2 = 0.09017$, 1a at $\delta = 0.17653$, and 3a at $\delta = (1/\sqrt{8}) = 0.35355$. Except for the limit of 1a, which involves solving a quintic in δ , the other limits can be solved for symbolically. Figure 8 shows the successive disappearance of these regions as δ is increased.

6.1 Bifurcation Surfaces. Each surface of partition in the parameter space represents the transition of one flow pattern into another. This happens at the point of coincidence of two invariant directions, or two flow change directions, or an invariant direction and a flow change direction. Transitions between regions that share a common surface represents one of the preceding degeneracies. Transitions between regions that share only a curve represent two, and for regions that share only a vertex represents the simultaneous existence of all three degeneracies. The flow patterns are structurally stable as long as the parameters, after taking uncertainties into account, are clear of these degeneracies.

7 Discussion and Conclusion

The trace of the sliding velocity at the contact point

defines flow patterns that show the evolution of impact. We identify three dimensional parameters (which are functions of the system inertia, orientation, and contact friction) that govern the defining equations for the sliding behavior of the contact point. A partition of this parameter space into regions that correspond to each of the possible sliding velocity flow patterns is then obtained. By doing so, we reduce the problem of determining the qualitative sliding behavior to the much simpler problem of determining which region of the parameter space the given set of contact parameters lie in.

Apart from simplifying the procedure for determining the flow patterns, the analysis can be used to study the sensitivity of the flow patterns to small changes in the mass parameters, impact orientation, or contact friction. As long as any potential error in determining the dimensionless parameter space is clear of any boundaries ("bifurcation surfaces"), small changes will not affect the overall flow pattern. The analysis is also used to rule out the existence of ambiguities in the direction of the initial sliding velocity, when sliding resumes after instantaneous sticking.

Using the results presented in this article, any general three-dimensional rigid-body impact problem with finite friction can be reduced to three dimensionless parameters, and the qualitative behavior determined using simple algebraic inequalities.

References

- Battle, J. A., and Condomines, A. B., 1991, "Rough Collisions in Multibody Systems," *Mech. Mach. Theory*, Vol. 26, No. 6, pp. 565-577.
- Bhatt, V., and Koechling, J. C., 1993a, "Investigations into Three Dimensional Impacts of Rigid Bodies," *Proceedings of the 14th Canadian Congress of Applied Mechanics*, June 1993, pp. 785-786.
- Bhatt, V., and Koechling, J. C., 1993b, "Modeling 3D Frictional Rigid Body Impact: Dealing with Degenerate Singularities," *Proceedings of the IASTED International Conference on Modeling and Simulation*, M. H. Hamza, ed., May, pp. 5-8.
- Bhatt, V., and Koechling, J. C., 1994a, "Classifying Dynamic Behavior during Three Dimensional Frictional Rigid Body Impact," *Proceedings of the IEEE International Conference on Robotics and Automation*, May, pp. 2342-2348.
- Bhatt, V., and Koechling, J. C., 1994b, "Three-Dimensional Frictional Rigid Body Impact," *ASME JOURNAL OF APPLIED MECHANICS*, to be published.
- Routh, E. J., 1877, *An Elementary Treatise on the Dynamics of a System of Rigid Bodies*, 3rd ed., MacMillan and Co., London, U.K.
- Stronge, W. J., 1993, "Swerve During Impact of Rough Rigid Bodies," *ASME JOURNAL OF APPLIED MECHANICS*, to be published.

APPENDIX A

Double Roots of the Invariant Direction Quartic

To look for double roots of the quartic in Eq. (10), let us assume that the double root is p_0 and the other two roots of the quartic are $a \pm ib$. The form of the quartic corresponding to this double root is

$$\alpha^4 + (-2p_0 - 2a)\alpha^3 + (p_0^2 + 4ap_0 + b^2 + a^2)\alpha^2 + (-2ap_0^2 - 2b^2p_0 - 2a^2p_0)\alpha + (b^2p_0^2 + a^2p_0^2) = 0.$$

Comparing the coefficients with those of the quartic for the invariant directions (10), we get

$$-2p_0 - 2a = -2\delta$$

$$b^2p_0^2 + a^2p_0^2 = \delta^2$$

$$p_0^2 + 4ap_0 + b^2 + a^2 = 1 + \delta^2 - (\lambda - \phi)^2$$

$$-2ap_0^2 - 2b^2p_0 - 2a^2p_0 = -2\delta.$$

Substituting $a = \delta - p_0$ from the first equation into the other three,

$$b^2 = 1 + 2p_0^2 - 2\delta p_0 - (\lambda - \phi)^2 \quad (21)$$

$$b^2 = \frac{\delta}{p_0}(1 + p_0^2 - \delta p_0) \quad (22)$$

$$b^2 = \frac{1}{p_0^2}(\delta^2 + 2\delta p_0^3 - \delta^2 p_0^2 - p_0^4). \quad (23)$$

Equating the right-hand sides of Eqs. (22) and (23),

$$\delta^2 + \delta(p_0^3 - p_0) - p_0^4 = 0 \Rightarrow \delta = p_0 \text{ or } \delta = -p_0^3. \quad (24)$$

Equating the right-hand sides of Eqs. (21) and (22),

$$2p_0^3 - 3\delta p_0^2 + p_0(1 + \delta^2 - (\lambda - \phi)^2) - \delta = 0. \quad (25)$$

If we substitute for the value of p_0 from Eq. (24) in (25), we get the curve in the parameter space on which double roots exist and which forms the boundary of the regions with different number of invariant directions.

$$\begin{aligned} \delta = p_0 \quad \delta = -p_0^3 \\ -(\lambda - \phi)^2 \delta = 0 \quad p_0^6 + 3p_0^4 + 3p_0^2 + 1 - (\lambda - \phi)^2 = 0 \\ \delta = 0 \text{ or } (\lambda - \phi) = 0 \quad (\lambda - \phi)^2 = (\delta^{2/3} + 1)^3 \text{ (boundaries)} \end{aligned} \quad (26)$$

Even though the boundaries $\delta = 0$ and $\lambda - \phi = 0$, for $\delta = p_0$ represent a "double root" for Eq. (10), they do not represent the coincidence of invariant directions. This occurs because the same α represents two different flow directions that are π radian apart. To disambiguate these, we have to consider Eq. (11) in conjunction with Eq. (10). We can then show that on "boundaries" associated with $\delta = p_0$, there is no double root. This agrees with our observation that the parameter space is symmetric under a change in sign of δ or both λ and ϕ , and therefore, $\delta = 0$ and $\lambda - \phi = 0$ cannot have different number of invariant directions across them.

APPENDIX B

Coinciding Flow Change and Invariant Directions

If the invariant and flow change directions coincide along some direction, \check{v}_θ , then $f(\check{v}_\theta) = g(\check{v}_\theta) = 0$ in Eqs. (7) and (8). Treating $\cos \check{v}_\theta$ and $\sin \check{v}_\theta$ as independent variables, we can solve the two equations simultaneously for four sets of $\cos \check{v}_\theta$ and $\sin \check{v}_\theta$:

$$\begin{aligned} \cos \check{v}_\theta = \sin \check{v}_\theta = 0 \quad \cos \check{v}_\theta = \frac{-1 \pm i\delta}{\phi - \lambda} \sin \check{v}_\theta = \frac{\delta \pm i}{\phi - \lambda} \\ \cos \check{v}_\theta = \frac{1}{\lambda} \sin \check{v}_\theta = \frac{\delta}{\phi} \end{aligned}$$

The first three sets give $\sin^2 \check{v}_\theta + \cos^2 \check{v}_\theta = 0$, and therefore do not constitute a solution for real \check{v}_θ . The only direction along which the invariant and flow change directions coincide is given by $\cos \check{v}_\theta = 1/\lambda$ and $\sin \check{v}_\theta = \delta/\phi$ at the points in the parameter space where the trigonometric identity $\sin^2 \check{v}_\theta + \cos^2 \check{v}_\theta = 1$ is satisfied.

APPENDIX C

Double Roots for the Flow Change Direction Quartic

Following the development for finding the boundaries for invariant directions in Appendix A, we look for the double

root of Eq. (12). The equations for the flow change direction that correspond to Eqs. (21)–(23) are

$$b^2 = \frac{1 + \delta^2 - 2\lambda\phi + 2p_0\delta}{\delta^2 - \phi^2} + 2p_0^2 - \left(\frac{\delta}{\delta^2 - \phi^2}\right)^2 \quad (27)$$

$$b^2 = -\frac{\delta/p_0 + p_0\delta}{\delta^2 - \phi^2} - \left(\frac{\delta}{\delta^2 - \phi^2}\right)^2 \quad (28)$$

$$b^2 = \frac{(1 - \lambda^2)/p_0^2 - 2\delta p_0}{\delta^2 - \phi^2} - p_0^2 - \left(\frac{\delta}{\delta^2 - \phi^2}\right)^2 \quad (29)$$

Equating the right-hand sides of (27) and (28) we get (30), and Eqs. (27) and (29) give (31)

$$2(\delta^2 - \phi^2)p_0^3 + 3\delta p_0^2 + (1 + \delta^2 - 2\lambda\phi)p_0 + \delta = 0 \quad (30)$$

$$3(\delta^3 - \phi^2)p_0^4 + 4\delta p_0^3 + (1 + \delta^2 - 2\lambda\phi)p_0^2 + (\lambda^2 - 1) = 0. \quad (31)$$

Taking $(6(\delta^2 - \phi^2)p_0 - \delta) \times$ Eq. (30) and subtracting $4(\delta^2 - \phi^2) \times$ Eq. (31), we get the following quadratic that can be symbolically solved to get the value of p_0 ,

$$((4\lambda\phi - 2\delta^2 + 1)(\phi^2 - \delta^2) - 3\phi^2)p_0^2 + (2\delta\lambda\phi + 5\delta^3 - 6\delta\phi^2 - \delta)p_0 + 4(\lambda^2 - 1)(\phi^2 - \delta^2) - \delta^2 = 0. \quad (32)$$

We can solve Eq. (32) for p_0 and substitute the value in Eq. (30). If we take the resulting expression, rationalize it, and factorize symbolically using MACSYMA (symbolic algebra package), we get the following equation for the boundary of the region with different number of flow change directions:

$$16(\phi^2 - \delta^2)\lambda^4 - 8\phi(4\phi^2 - 4\delta^2 + 1)\lambda^3 + (16\phi^4 - 8\delta^2\phi^2 - 8\phi^2 - 8\delta^4 + 20\delta^2 + 1)\lambda^2 - 2\phi(4\delta^2\phi^2 - 16\phi^2 - 4\delta^4 + 19\delta^2 - 4)\lambda - (16\phi^4 - \delta^4\phi^2 - 20\delta^2\phi^2 + 8\phi^2 + (\delta^2 + 1)^3) = 0.$$

A General Formulation of the Theory of Wire Ropes

Wei Jiang

Mechanical Engineering Department,
Florida International University,
Miami, FL 33199

This paper presents a general formulation of the nonlinear and linear analysis of wire ropes. In the formulation, wires, strands, and wire ropes are all considered as a kind of identical structure characterized by seven stiffness and deformation constants, and as such they can be used, in the same way, as component elements in some layered general structures. Based on such a point of view, the general formulation thus developed can be used to analyze wire ropes of various complex cross sections, and to analyze simple wire strands as well.

1 Introduction

A wire rope is a structure made up of layers of strands wrapped helically around a central straight strand core, while a strand is a structure made up of layers of helical wires wound around a central core of a straight wire. Therefore, in a wire rope, only the central wire core of the core strand is straight. The outer wires of the core strand and the central core wires of all other strands are single helices, while remaining wires in outer strands take on the forms of a double helix.

The stress and strain analysis of wire ropes was once considered too complex to be dealt with by the theory of elasticity (Suslov, 1936), and therefore, various assumptions were made regarding the number and types of the loads acting on each wire in the strand in order to obtain a solution. For example, in a paper by Hall (1951), assumption was made that all rope loads were equally distributed among the individual wires and only the axial force in each wire was considered. Hruska (1951, 1952, and 1953) also assumed that the wires in the strand were subjected to simple tension only, and then tried to estimate the magnitude of the radial force and the resultant end moment of the strand. Hruska's work was extended by Leissa (1959) and by Starkey and Cress (1959) to take the contact stresses between the wires into consideration. Then, Phillips and Costello (1973) introduced a new point of view in examining the stresses in the wire ropes. They regarded the strand as a collection of helical wire springs, and used Love's general theory of the bending and twisting of thin rods and spiral springs (Love, 1927) to solve strand problems, so that most of the assumptions made or implied previously can be removed. While considerable progress has been made in the development of various theories of wire rope, most investigations have been concentrated on strands of single helical wires, only a few dealing with wire rope with complex cross sections (Velinsky et al., 1984; Phillips and Costello, 1985; for example). One of the difficulties involved in the wire rope analysis is that it no longer can be considered as a collection of helical wires. First of all, most wires in the wire rope are double helices. Secondly, there are so many wires with different geometric and physical parameters involved that the conventional analysis method, analyzing the wires one by one, turns out to be too complex. This paper presents a simple and well-organized approach to circumvent such difficulties. As is previously mentioned, a strand is a struc-

ture composed of layers of helical wires, while a wire rope is a structure composed of layers of helical strands. Thus, the frame structure of the strand and the wire rope is in fact identical. The difference consists only in the components which construct the frame structure. That is, if we take a single-layered or multilayered strand and then replace its basic components, the wires, with strands or even wire ropes of any structure, we obtain a wire rope with various complex cross sections. Based on such a point of view, a general formulation is developed in this paper for layered structures with generalized components characterized by seven stiffness and deformation constants. By specifying these constants, various strand and wire rope problems can be solved as special cases.

2 The General Formulation of a Layered Structure

Consider a structure which is composed of a central straight core wound around by n layers of surrounding helical components. It is assumed that a typical surrounding layer in the structure, say the layer i , is made of m_i components of identical cross section, which is symmetric with respect to a series of axes, and these components are symmetrically arranged in the structure cross section with identical helix radius r_i . It is further assumed that under a wrench load, the frictional forces between the surrounding components and the central core can be neglected and that after deformation the components take the shape of another helix. Under these assumptions, the structure can be regarded as a collection of helical components, and Love's theory can be used in analysis. Obviously, if the components are wires, the structure considered is a wire strand. If the components are wire strands, the structure becomes a wire rope.

Consider a single helical component in the i layer. As is shown in Fig. 1, the resultant forces and moments on a cross section consist of a tensile force T_i , a binormal shear force N_i , a binormal bending moment G_i , and a torsional couple H_i , while along the central line of the component acts distributed contact force X_i . These resultants and the contact force should satisfy the equilibrium condition (Phillips and Costello, 1973):

$$\begin{cases} T_i \bar{\kappa}_i - N_i \bar{\tau}_i + X_i = 0 \\ H_i \bar{\kappa}_i - G_i \bar{\tau}_i - N_i = 0 \end{cases} \quad (1)$$

where $\bar{\kappa}_i$ and $\bar{\tau}_i$ are the curvature and the twist of the deformed component central line.

The initial curvature and twist are determined by the helix radius r_i and the helical angle α_i of the component. Let k_i be the tangent of the helical angle:

$$k_i = \tan \alpha_i. \quad (2)$$

Contributed by the Applied Mechanics Division of THE AMERICAN SOCIETY OF MECHANICAL ENGINEERS for publication in the ASME JOURNAL OF APPLIED MECHANICS.

Discussion on this paper should be addressed to the Technical Editor, Prof. Lewis T. Wheeler, Department of Mechanical Engineering, University of Houston, Houston, TX 77204-4792, and will be accepted until four months after final publication of the paper itself in the ASME JOURNAL OF APPLIED MECHANICS.

Manuscript received by the ASME Applied Mechanics Division, Dec. 6, 1993; final revision, May 10, 1994. Associate Technical Editor: W. K. Liu.

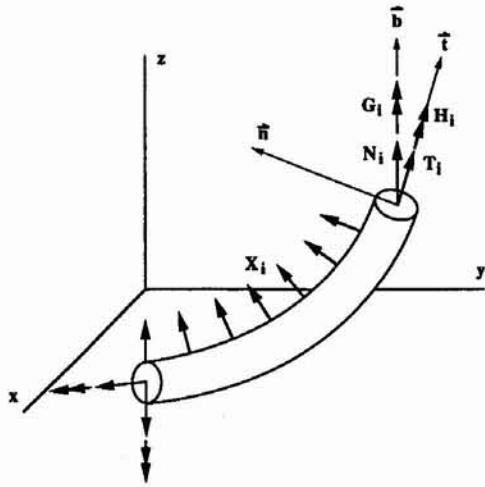


Fig. 1 Resultants and contact force that act on a component

Then

$$\begin{cases} \kappa_i = \frac{1}{r_i(1+k_i^2)} \\ \tau_i = \frac{k_i}{r_i(1+k_i^2)} \end{cases} \quad (3)$$

The deformed curvature $\bar{\kappa}_i$ and twist $\bar{\tau}_i$ can be found from the deformed helix radius \bar{r}_i and helical angle $\bar{\alpha}_i$ similarly.

The deformation of the component is characterized by the increments $\Delta\kappa_i$ and $\Delta\tau_i$ of the curvature and twist, and the axial strain ξ_i ,

$$\xi_i = \frac{\Delta l_i}{l_i} \quad (4)$$

where l_i is the length of the component. We assume in the analysis that the radial strain of the cross section, ζ_i , and the resultants of the component can be expressed in terms of the strains as follows:

$$\zeta_i = -(p_i\xi_i + q_i\Delta\tau_i) \quad (5)$$

$$T_i = a_i\xi_i + b_i\Delta\tau_i \quad (6)$$

$$H_i = c_i\xi_i + d_i\Delta\tau_i \quad (7)$$

$$G_i = A_i\Delta\kappa_i \quad (8)$$

where a_i, b_i, c_i, d_i , and A_i are stiffness constants, while p_i and q_i are lateral deformation coefficients of the component. These seven constants will be specified later.

Investigation shows that the increments $\Delta\kappa_i$ and $\Delta\tau_i$ are not parameters convenient in the general formulation of the problem. Therefore, instead of these two increments, we introduce two component strains as follows:

$$\begin{cases} e_i = \frac{\Delta\left(\frac{h}{l_i}\right)}{\frac{h}{l_i}} \\ \chi_i = \frac{\Delta\left(\frac{\theta}{l_i}\right)}{\frac{\theta}{l_i}} \end{cases} \quad (9)$$

where h and θ are the height and the twist angle of the structure, and therefore, are the height and twist angle of all the components. In terms of these two strains, we can find the geometric parameters of the deformed component:

$$\begin{cases} \bar{k}_i = \frac{k_i(1+e_i)}{\sqrt{1-k_i^2e_i(2+e_i)}} \\ \bar{r}_i = \frac{r_i\sqrt{1-k_i^2e_i(2+e_i)}}{1+\chi_i} \end{cases} \quad (10)$$

$$\begin{cases} \bar{\kappa}_i = \kappa_i(1+\chi_i)\sqrt{1-k_i^2e_i(2+e_i)} \\ \bar{\tau}_i = \tau_i(1+e_i)(1+\chi_i) \end{cases} \quad (11)$$

and consequently, by Eqs. (1) and (6)–(8):

$$\begin{cases} T_i = a_i\xi_i + b_i\tau_i(e_i + \chi_i + e_i\chi_i) \\ N_i = \kappa_i(1+\chi_i)\{[c_i\xi_i + d_i\tau_i(e_i + \chi_i + e_i\chi_i)] \\ \sqrt{1-k_i^2e_i(2+e_i)} - A_i\tau_i(1+e_i) \\ [(1+\chi_i)\sqrt{1-k_i^2e_i(2+e_i)} - 1]\} \end{cases} \quad (12)$$

$$\begin{cases} G_i = A_i\kappa_i[(1+\chi_i)\sqrt{1-k_i^2e_i(2+e_i)} - 1] \\ H_i = c_i\xi_i + d_i\tau_i(e_i + \chi_i + e_i\chi_i) \end{cases} \quad (13)$$

$$\begin{aligned} X_i = & -\kappa_i(1+\chi_i)\sqrt{1-k_i^2e_i(2+e_i)} \\ & \times \left\{ [a_i - c_i\tau_i(1+e_i)(1+\chi_i)]\xi_i \right. \\ & + \tau_i(e_i + \chi_i + e_i\chi_i)[b_i - d_i\tau_i(1+e_i)(1+\chi_i)] \\ & + A_i\tau_i^2(1+e_i)^2(1+\chi_i) \left[(1+\chi_i) \right. \\ & \left. \left. - \frac{1}{\sqrt{1-k_i^2e_i(2+e_i)}} \right] \right\} \quad (14) \end{aligned}$$

To keep the component in the shape of a helix, the end force and torque are needed, and they are

$$\begin{cases} F_i = \frac{1}{\sqrt{1+\bar{k}_i^2}} (\bar{k}_i T_i + N_i) \\ M_i = \frac{1}{\sqrt{1+\bar{k}_i^2}} [(\bar{k}_i H_i + G_i) + \bar{r}_i(T_i - \bar{k}_i N_i)] \end{cases} \quad (15)$$

or

$$\left\{ \begin{aligned}
F_i &= \sqrt{1 - \frac{k_i^2(1+e_i)^2}{1+k_i^2}} \left\{ \left[\frac{a_i k_i(1+e_i)}{\sqrt{1-k_i^2 e_i(2+e_i)}} + c_i \kappa_i(1+\chi_i) \sqrt{1-k_i^2 e_i(2+e_i)} \right] \xi_i \right. \\
&\quad + \tau_i(e_i + \chi_i + e_i \chi_i) \left[\frac{b_i k_i(1+e_i)}{\sqrt{1-k_i^2 e_i(2+e_i)}} + d_i \kappa_i(1+\chi_i) \sqrt{1-k_i^2 e_i(2+e_i)} \right] \\
&\quad \left. - A_i \tau_i \kappa_i(1+e_i)(1+\chi_i)[(1+\chi_i) \sqrt{1-k_i^2 e_i(2+e_i)} - 1] \right\} \\
M_i &= \sqrt{1 - \frac{k_i^2(1+e_i)^2}{1+k_i^2}} \left\{ \left[\frac{a_i r_i \sqrt{1-k_i^2 e_i(2+e_i)}}{1+\chi_i} + \frac{c_i k_i^3(1+e_i)^3}{(1+k_i^2) \sqrt{1-k_i^2 e_i(2+e_i)}} \right] \xi_i \right. \\
&\quad + \tau_i(e_i + \chi_i + e_i \chi_i) \left[\frac{b_i r_i \sqrt{1-k_i^2 e_i(2+e_i)}}{1+\chi_i} + \frac{d_i k_i^3(1+e_i)^3}{(1+k_i^2) \sqrt{1-k_i^2 e_i(2+e_i)}} \right] \\
&\quad \left. + A_i \kappa_i \left[1 + \frac{k_i^2(1+e_i)^2}{1+k_i^2} \right] [(1+\chi_i) \sqrt{1-k_i^2 e_i(2+e_i)} - 1] \right\}
\end{aligned} \right. \quad (16)$$

if use is made of Eqs. (12) and (13).

Equation (16) represents the force-strain relationships of a helical component. The central core is a special component, because it is straight. The force-strain relationships of the central core will be expressed as

$$\begin{cases} F_0 = F_0(\epsilon, \phi) \\ M_0 = M_0(\epsilon, \phi) \end{cases} \quad (17)$$

where $F_0(\epsilon, \phi)$ and $M_0(\epsilon, \phi)$ are known functions, which will be discussed in the following section, and ϵ and ϕ are the axial and rotational strains of the central core, and thus are the axial and rotational strains of the structure due to deformation compatibility conditions:

$$\begin{cases} \epsilon = \frac{\Delta h}{h} \\ \phi = \frac{\Delta \theta}{h} \end{cases} \quad (18)$$

The force and torque applied on the structure are the resultants of all the forces and torques carried by the central core and the components. Suppose that the structure is composed of n layers and that in each layer there are m_i components. Then, by Eqs. (16) and (17), the resultants:

$$\left\{ \begin{aligned}
F &= F_0(\epsilon, \phi) \\
&\quad + \sum_{i=1}^n m_i \sqrt{1 - \frac{k_i^2(1+e_i)^2}{1+k_i^2}} \left\{ \left[\frac{a_i k_i(1+e_i)}{\sqrt{1-k_i^2 e_i(2+e_i)}} + c_i \kappa_i(1+\chi_i) \sqrt{1-k_i^2 e_i(2+e_i)} \right] \xi_i \right. \\
&\quad + \tau_i(e_i + \chi_i + e_i \chi_i) \left[\frac{b_i k_i(1+e_i)}{\sqrt{1-k_i^2 e_i(2+e_i)}} + d_i \kappa_i(1+\chi_i) \sqrt{1-k_i^2 e_i(2+e_i)} \right] \\
&\quad \left. - A_i \tau_i \kappa_i(1+e_i)(1+\chi_i)[(1+\chi_i) \sqrt{1-k_i^2 e_i(2+e_i)} - 1] \right\} \\
M &= M_0(\epsilon, \phi) \\
&\quad + \sum_{i=1}^n m_i \sqrt{1 - \frac{k_i^2(1+e_i)^2}{1+k_i^2}} \left\{ \left[\frac{a_i r_i \sqrt{1-k_i^2 e_i(2+e_i)}}{1+\chi_i} + \frac{c_i k_i^3(1+e_i)^3}{(1+k_i^2) \sqrt{1-k_i^2 e_i(2+e_i)}} \right] \xi_i \right. \\
&\quad + \tau_i(e_i + \chi_i + e_i \chi_i) \left[\frac{b_i r_i \sqrt{1-k_i^2 e_i(2+e_i)}}{1+\chi_i} + \frac{d_i k_i^3(1+e_i)^3}{(1+k_i^2) \sqrt{1-k_i^2 e_i(2+e_i)}} \right] \\
&\quad \left. + A_i \kappa_i \left[1 + \frac{k_i^2(1+e_i)^2}{1+k_i^2} \right] [(1+\chi_i) \sqrt{1-k_i^2 e_i(2+e_i)} - 1] \right\}.
\end{aligned} \right. \quad (19)$$

It is seen that the resultant force and torque are functions of $3n + 2$ strains, that is, functions of the two structure strains (ϵ, ϕ) and $3n$ component strains (ξ_i, e_i, χ_i), $i = 1, 2, \dots, n$. To solve the problem, therefore, we need to find $3n$ compatibility conditions.

There are two kinds of compatibility conditions that the central core and the components have to meet. First, the axial and rotational deformations of the central core and the helical components should be the same so that the structure can deform as a whole. By Eqs. (9) and (18), this requirement yields $2n$ compatibility equations which establish relationships between the structure strains and the component strains:

$$\begin{cases} \epsilon = e_i + (1+e_i)\xi_i \\ \phi = \frac{1}{k_i r_i} [\chi_i + (1+\chi_i)\xi_i] \quad i = 1, 2, \dots, n. \end{cases} \quad (20)$$

Secondly, on a cross section, all the layers should contact each other during the deformation. This requirement leads to n compatibility conditions between the component strains. Different from the first kind of compatibility conditions, these n conditions rely on the lay structures.

For simplicity, the cross section of a component is assumed to be circular in the following analysis, and two kinds of lay

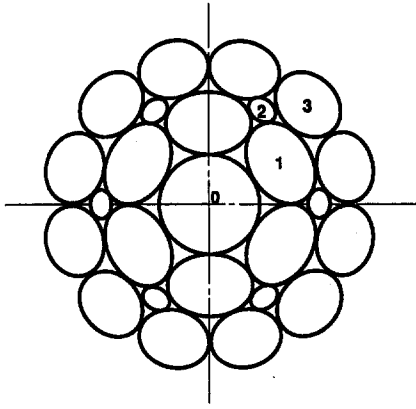


Fig. 2 Close-packed lay

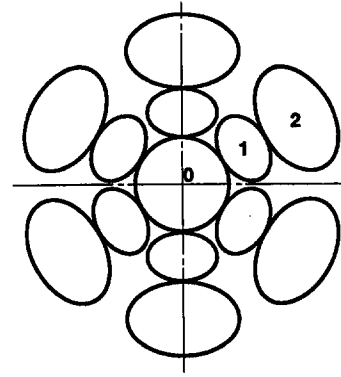


Fig. 3 Resting lay

structure, the close-packed layer and the resting layer, will be discussed.

Close-packed layer is a layer structure where components in the layer are closely packed so that the helix radius of the components assumes a least possible value (Fig. 2). As a result, any component in a close-packed layer will contact two components in the layer beneath it, or conversely, two components in this layer will contact only one component in the inner layer. Whether or not the components in the same layer contact each other is irrelevant in this definition. The only exception is the first layer where the components should touch each other to form a minimal helix radius. For the close-packed layer, the helix radii can be found as

$$\begin{cases} r_1 = \frac{R_1}{k_1} \sqrt{k_1^2 + (1 + k_1^2) \cot^2 \frac{\pi}{m_1}} \\ r_i = r_{i-1} \cos \frac{\pi}{m_i} + \sqrt{(R_{i-1} + R_i)^2 - r_{i-1}^2 \sin^2 \frac{\pi}{m_i}} \end{cases} \quad i = 2, 3, \dots, n. \quad (21)$$

The helix radii after the deformation are expressed similarly. Then, one can find the radial and axial strains of the components,

A layer is called resting, if the component in this layer contacts only one component in the layer beneath it and vice versa, and the centers of these two contact components are located on one radius (Fig. 3). Contrary to the close-packed layer, the resting layer will form a maximal helix radius. For the resting layer, the helix radii are

$$\begin{cases} r_1 = R_0 + R_1 \\ r_i = r_{i-1} + R_{i-1} + R_i \quad i = 2, 3, \dots, n \end{cases} \quad (24)$$

and the radial and axial strains of the component can be found as

$$\begin{cases} \zeta_1 = \frac{r_1(1 + e_1)}{1 + \chi_1} \sqrt{\frac{1 - k_1^2 e_1(2 + e_1)}{r_1^2 + R_1^2 e_1(2 + e_1)}} - 1 \\ \zeta_i = \frac{1}{R_i} \left\{ \left[\frac{r_i \sqrt{1 - k_i^2 e_i(2 + e_i)}}{1 + \chi_i} - \frac{r_{i-1} \sqrt{1 - k_{i-1}^2 e_{i-1}(2 + e_{i-1})}}{1 + \chi_{i-1}} \right]^2 \right. \\ \left. + \frac{(R_i + R_{i-1})^2 - (r_i - r_{i-1})^2}{(1 + \chi_{i-1})(1 + \chi_i)} \sqrt{[1 - k_{i-1}^2 e_{i-1}(2 + e_{i-1})][1 - k_i^2 e_i(2 + e_i)]} \right\}^{1/2} - \frac{R_{i-1}}{R_i} (1 + \zeta_{i-1}) - 1 \end{cases} \quad i = 2, 3, \dots, n \quad (22)$$

$$\begin{cases} \xi_1 = \frac{1}{p_1} \left[1 - q_1 \tau_1 (e_1 + \chi_1 + e_1 \chi_1) - \frac{r_1(1 + e_1)}{1 + \chi_1} \sqrt{\frac{1 - k_1^2 e_1(2 + e_1)}{r_1^2 + R_1^2 e_1(2 + e_1)}} \right] \\ \xi_i = \frac{1}{p_i} \left\{ 1 + \frac{R_{i-1}}{R_i} [1 - p_{i-1} \xi_{i-1} - q_{i-1} \tau_{i-1} (e_{i-1} + \chi_{i-1} + e_{i-1} \chi_{i-1})] - q_i \tau_i (e_i + \chi_i + e_i \chi_i) \right. \\ \left. - \frac{1}{R_i} \left[\left(\frac{r_i \sqrt{1 - k_i^2 e_i(2 + e_i)}}{1 + \chi_i} - \frac{r_{i-1} \sqrt{1 - k_{i-1}^2 e_{i-1}(2 + e_{i-1})}}{1 + \chi_{i-1}} \right)^2 \right. \right. \\ \left. \left. + \frac{(R_i + R_{i-1})^2 - (r_i - r_{i-1})^2}{(1 + \chi_{i-1})(1 + \chi_i)} \sqrt{[1 - k_{i-1}^2 e_{i-1}(2 + e_{i-1})][1 - k_i^2 e_i(2 + e_i)]} \right]^{1/2} \right\} \quad i = 2, 3, \dots, n. \end{cases} \quad (23)$$

$$\left\{ \begin{aligned} \zeta_1 &= \frac{1}{R_1} \left[\frac{r_1 \sqrt{1 - k_1^2 e_1 (2 + e_1)}}{1 + \chi_1} - R_0 (1 + \zeta_0) \right] - 1 \\ \zeta_i &= \frac{1}{R_i} \left[\frac{r_i \sqrt{1 - k_i^2 e_i (2 + e_i)}}{1 + \chi_i} - \frac{r_{i-1} \sqrt{1 - k_{i-1}^2 e_{i-1} (2 + e_{i-1})}}{1 + \chi_{i-1}} - R_{i-1} (1 + \zeta_{i-1}) \right] - 1 \quad i = 2, 3, \dots, n \end{aligned} \right. \quad (25)$$

$$\left\{ \begin{aligned} \xi_1 &= \frac{k_1 r_1}{k_1 r_1 [R_0 p_0 (1 + e_1) + R_1 p_1] + R_0 q_0 (1 + \chi_1)} \left\{ r_1 \left[1 - \frac{\sqrt{1 - k_1^2 e_1 (2 + e_1)}}{1 + \chi_1} \right] \right. \\ &\quad \left. - (R_0 p_0 + R_1 q_1 \tau_1) e_1 - \left(\frac{R_0 q_0}{k_1 r_1} + R_1 q_1 \tau_1 \right) \chi_1 - R_1 q_1 \tau_1 e_1 \chi_1 \right\} \\ \xi_i &= \frac{1}{p_i} \left\{ 1 + \frac{R_{i-1}}{R_i} [1 - p_{i-1} \xi_{i-1} - q_{i-1} \tau_{i-1} (e_{i-1} + \chi_{i-1} + e_{i-1} \chi_{i-1})] \right. \\ &\quad \left. - q_i \tau_i (e_i + \chi_i + e_i \chi_i) - \frac{1}{R_i} \left[\frac{r_i \sqrt{1 - k_i^2 e_i (2 + e_i)}}{1 + \chi_i} - \frac{r_{i-1} \sqrt{1 - k_{i-1}^2 e_{i-1} (2 + e_{i-1})}}{1 + \chi_{i-1}} \right] \right\} \quad i = 2, 3, \dots, n. \end{aligned} \right. \quad (26)$$

Note that different layers can have different lay structures in the structure.

Now the force-component strain relationships, Eq. (19), together with $3n$ compatibility conditions, Eqs. (20) and (23), or Eqs. (20) and (26), form $3n + 2$ equations with respect to two force resultants, (F, M) , and $3n + 2$ strains, (ϵ, ϕ) and (ξ_i, e_i, χ_i) , $i = 1, 2, \dots, n$. If any of the following sets, (F, M) , (ϵ, ϕ) , (F, ϕ) , or (M, ϵ) , is given, these equations can be solved to give all the unknown quantities, and the problem is solved. For convenience, we will use the following notations

$$\left\{ \begin{aligned} F &= F(\epsilon, \phi) \\ M &= M(\epsilon, \phi) \end{aligned} \right. \quad (27)$$

to represent the above $3n + 2$ equations. The two functions, $F(\epsilon, \phi)$ and $M(\epsilon, \phi)$, in Eq. (27) represent the nonlinear force-strain relationships of the structure.

$$\left\{ \begin{aligned} \zeta_i &= -[q_i \tau_i + (p_i - 2q_i \tau_i) \lambda_i] \epsilon \\ &\quad - [k_i r_i q_i \tau_i + (p_i - 2q_i \tau_i) \mu_i] \phi \\ \xi_i &= \lambda_i \epsilon + \mu_i \phi \end{aligned} \right. \quad (28)$$

$$\left\{ \begin{aligned} e_i &= (1 - \lambda_i) \epsilon - \mu_i \phi \\ \chi_i &= -\lambda_i \epsilon + (k_i r_i - \mu_i) \phi \end{aligned} \right. \quad (29)$$

where, for close-packed lay:

$$\left\{ \begin{aligned} \lambda_1 &= -\frac{1 - k_1^2 - R_1^2 / r_1^2 + q_1 \tau_1}{k_1^2 + R_1^2 / r_1^2 + p_1 - 2q_1 \tau_1} \\ \mu_1 &= \frac{k_1 r_1 (1 - q_1 \tau_1)}{k_1^2 + R_1^2 / r_1^2 + p_1 - 2q_1 \tau_1} \end{aligned} \right. \quad (30)$$

$$\left\{ \begin{aligned} \lambda_i &= \frac{\kappa_i}{f_i + R_i \kappa_i (p_i - 2q_i \tau_i)} \left\{ [(k_i^2 r_i f_i - R_i q_i \tau_i) - (k_{i-1}^2 r_{i-1} g_i + R_{i-1} q_{i-1} \tau_{i-1})] \right. \\ &\quad \left. - \left[R_{i-1} (p_{i-1} - 2q_{i-1} \tau_{i-1}) - \frac{g_i}{\kappa_{i-1}} \right] \lambda_{i-1} \right\} \\ \mu_i &= \frac{\kappa_i}{f_i + R_i \kappa_i (p_i - 2q_i \tau_i)} \left\{ [k_i r_i (f_i r_i - R_i q_i \tau_i) - k_{i-1} r_{i-1} (g_i r_{i-1} + R_{i-1} q_{i-1} \tau_{i-1})] \right. \\ &\quad \left. - \left[R_{i-1} (p_{i-1} - 2q_{i-1} \tau_{i-1}) - \frac{g_i}{\kappa_{i-1}} \right] \mu_{i-1} \right\} \quad i = 2, 3, \dots, n \end{aligned} \right. \quad (31)$$

3 Linear Theory

If the strains are small so that the nonlinear terms can be neglected in comparison with the first-order terms, the compatibility conditions, Eqs. (20), (22), (23), (25), and (26) can be linearized to give component strains in terms of the structure strains:

in which

$$\left\{ \begin{aligned} f_i &= \frac{(r_i^2 - r_{i-1}^2) + (R_i + R_{i-1})^2}{2(R_i + R_{i-1})r_i} \\ g_i &= \frac{(r_i^2 - r_{i-1}^2) - (R_i + R_{i-1})^2}{2(R_i + R_{i-1})r_{i-1}} \end{aligned} \right. \quad (32)$$

and for resting lay:

$$\left\{ \begin{aligned} \lambda_i &= \frac{\kappa_i}{1 + R_i \kappa_i (p_i - 2q_i \tau_i)} (k_i^2 r_i - R_0 q_0 - R_i q_i \tau_i) \\ \mu_i &= \frac{\kappa_i}{1 + R_i \kappa_i (p_i - 2q_i \tau_i)} [k_i r_i (r_i - R_i q_i \tau_i) - R_0 q_0] \end{aligned} \right. \quad (33)$$

$$X_i = -\tau_i \kappa_i \left\{ \left[b_i - (d_i + A_i k_i^2) \tau_i \right. \right. \\ \left. \left. + \left(\frac{a_i}{\tau_i} - 2b_i - c_i + 2d_i \tau_i - A_i \tau_i (1 - k_i^2) \right) \lambda_i \right] \epsilon \right. \\ \left. + \left[k_i r_i (b_i - (d_i - A_i) \tau_i) + \left(\frac{a_i}{\tau_i} - 2b_i - c_i \right. \right. \right.$$

$$\left\{ \begin{aligned} \lambda_i &= \frac{\kappa_i}{1 + R_i \kappa_i (p_i - 2q_i \tau_i)} \left\{ [(k_i^2 r_i - R_i q_i \tau_i) - (k_{i-1}^2 r_{i-1} + R_{i-1} q_{i-1} \tau_{i-1})] \right. \\ &\quad \left. - \left[R_{i-1} (p_{i-1} - 2q_{i-1} \tau_{i-1}) - \frac{1}{\kappa_{i-1}} \right] \lambda_{i-1} \right\} \\ \mu_i &= \frac{\kappa_i}{1 + R_i \kappa_i (p_i - 2q_i \tau_i)} \left\{ [k_i r_i (r_i - R_i q_i \tau_i) - k_{i-1} r_{i-1} (r_{i-1} + R_{i-1} q_{i-1} \tau_{i-1})] \right. \\ &\quad \left. - \left[R_{i-1} (p_{i-1} - 2q_{i-1} \tau_{i-1}) - \frac{1}{\kappa_{i-1}} \right] \mu_{i-1} \right\} \quad i = 2, 3, \dots, n. \end{aligned} \right. \quad (34)$$

As a result, Eqs. (12), (13), and (14) can also be linearized and expressed directly in terms of the structure strains

$$\left\{ \begin{aligned} T_i &= [b_i \tau_i + (a_i - 2b_i \tau_i) \lambda_i] \epsilon \\ &\quad + [k_i r_i b_i \tau_i + (a_i - 2b_i \tau_i) \mu_i] \phi \\ N_i &= \tau_i \kappa_i \left\{ \left[(d_i + A_i k_i^2) \right. \right. \\ &\quad \left. \left. + \left(\frac{c_i}{\tau_i} - 2d_i + A_i (1 - k_i^2) \right) \lambda_i \right] \epsilon \right. \\ &\quad \left. + \left[k_i r_i (d_i - A_i) \right. \right. \\ &\quad \left. \left. + \left(\frac{c_i}{\tau_i} - 2d_i + A_i (1 - k_i^2) \right) \mu_i \right] \phi \right\} \end{aligned} \right. \quad (35)$$

Then, Eq. (19) yields the linear force-strain relationship

$$\left\{ \begin{aligned} F &= a\epsilon + b\phi \\ M &= c\epsilon + d\phi \end{aligned} \right. \quad (38)$$

where a , b , c , and d are the extensional-torsional stiffness constants of the structure

$$\left\{ \begin{aligned} a &= a_0 + \sum_{i=1}^n \frac{m_i \tau_i}{\sqrt{1 + k_i^2}} \left\{ [b_i k_i + (d_i + A_i k_i^2) \kappa_i] + \left[\frac{a_i}{\kappa_i} - 2b_i k_i + \frac{c_i}{k_i} - 2d_i \kappa_i + A_i (1 - k_i^2) \kappa_i \right] \lambda_i \right\} \\ b &= b_0 + \sum_{i=1}^n \frac{m_i \tau_i}{\sqrt{1 + k_i^2}} \left\{ k_i r_i [b_i k_i + (d_i - A_i) \kappa_i] + \left[\frac{a_i}{\kappa_i} - 2b_i k_i + \frac{c_i}{k_i} - 2d_i \kappa_i + A_i (1 - k_i^2) \kappa_i \right] \mu_i \right\} \\ c &= c_0 + \sum_{i=1}^n \frac{m_i r_i}{\sqrt{1 + k_i^2}} \left\{ \tau_i [b_i + d_i k_i^2 \tau_i - A_i (1 + 2k_i^2) \tau_i] \right. \\ &\quad \left. + [a_i - 2b_i \tau_i + (c_i - 2d_i \tau_i) k_i^2 \tau_i - A_i (1 - k_i^2) (1 + 2k_i^2) \kappa_i^2] \lambda_i \right\} \\ d &= d_0 + \sum_{i=1}^n \frac{m_i r_i}{\sqrt{1 + k_i^2}} \left\{ k_i r_i [b_i \tau_i + d_i k_i^2 \tau_i^2 + A_i (1 + 2k_i^2) \kappa_i^2] \right. \\ &\quad \left. + [a_i - 2b_i \tau_i + (c_i - 2d_i \tau_i) k_i^2 \tau_i - A_i (1 - k_i^2) (1 + 2k_i^2) \kappa_i^2] \mu_i \right\}. \end{aligned} \right. \quad (39)$$

$$\left\{ \begin{aligned} G_i &= -A_i \kappa_i \left\{ [k_i^2 + (1 - k_i^2) \lambda_i] \epsilon \right. \\ &\quad \left. - [k_i r_i - (1 - k_i^2) \mu_i] \phi \right\} \\ H_i &= [d_i \tau_i + (c_i - 2d_i \tau_i) \lambda_i] \epsilon \\ &\quad + [k_i r_i d_i \tau_i + (c_i - 2d_i \tau_i) \mu_i] \phi \end{aligned} \right. \quad (36)$$

In Eq. (39), a_0 , b_0 , c_0 , and d_0 are the extensional-torsional stiffness constants of the central core.

Note that in the analysis if we assume that the cross section of the structure can be taken as a circle which encloses all the helical component layers, the radius R of the structure cross

section will be the sum of the helix radius r_n and the radius R_n of the outermost component:

$$R = r_n + R_n \quad (40)$$

Then, the radial strain of the structure can be found as

$$\zeta = \frac{\Delta R}{R} = -(p\epsilon + q\phi) \quad (41)$$

where

$$\left\{ \begin{array}{l} p = \frac{1}{R} \left\{ (k_n^2 r_n + R_n q_n \tau_n) \right. \\ \left. + \left[R_n (p_n - 2q_n \tau_n) - \frac{1}{\kappa_n} \right] \lambda_n \right\} \\ q = \frac{1}{R} \left\{ k_n r_n (r_n + R_n q_n \tau_n) \right. \\ \left. + \left[R_n (p_n - 2q_n \tau_n) - \frac{1}{\kappa_n} \right] \mu_n \right\} \end{array} \right. \quad (42)$$

In the above development, we considered a general structure made up of n layers of helical components. The components can be of any structure, as long as they are characterized by seven stiffness and deformation constants: a_i , b_i , c_i , d_i , A_i , p_i , and q_i , as are shown in Eqs. (5)-(8). It is interesting to see that the linear theory yields six similar constants a , b , c , d , p , and q to characterize the general structure considered. Therefore, if the bending stiffness of the general structure is defined, it can also be used as components in a more generalized structure. It is based on such a fact that a general formulation of the wire rope problems can be achieved.

Costello (1977) studied the bending of a helical spring and then assumed that the bending stiffness of a cable was the sum of the stiffness of the component wires, the interaction between the component wires being neglected. Following the same line, we assume the bending stiffness of the general structure to be

4 Strands

If the components of the general structure are wires, the structure becomes a strand. The seven characteristic constants are

$$\left\{ \begin{array}{l} a_i = \pi E_i R_i^2 \\ b_i = 0 \\ c_i = 0 \\ d_i = \frac{\pi E_i R_i^4}{4(1 + \nu_i)} \end{array} \right. \quad (44)$$

$$A_i = \frac{\pi E_i R_i^4}{4} \quad (45)$$

and

$$\left\{ \begin{array}{l} p_i = \nu_i \\ q_i = 0 \end{array} \right. \quad (46)$$

The nonlinear force-strain relationships can be expressed as

$$\left\{ \begin{array}{l} F_s = F_s(\epsilon, \phi) \\ M_s = M_s(\epsilon, \phi) \end{array} \right. \quad (47)$$

which indicate the following $3n + 2$ equations:

$$\left\{ \begin{array}{l} F = \pi E_0 R_0^2 \epsilon + \sum_{i=1}^n \frac{m_i \pi E_i R_i^4 \tau_i \kappa_i}{4\sqrt{1+k_i^2}} \left\{ \frac{4(1+e_i)}{R_i^2 \kappa_i^2} \xi_i \right. \\ \left. + (1+\chi_i) \left[(1+e_i) - \left(1 + \frac{\nu_i(e_i + \chi_i + e_i \chi_i)}{1+\nu_i} \right) \sqrt{1-k_i^2 e_i(2+e_i)} \right] \sqrt{1-k_i^2 e_i(2+e_i)} \right\} \\ M = \frac{\pi E_0 R_0^4}{4(1+\nu_0)} \phi + \sum_{i=1}^n \frac{m_i \pi E_i R_i^4 \kappa_i}{4(1+k_i^2)^{3/2}} \left\{ \frac{4}{R_i^2 \kappa_i^2} \frac{1-k_i^2 e_i(2+e_i)}{1+\chi_i} \xi_i \right. \\ \left. + [1+k_i^2(2+2e_i+e_i^2)][(1+\chi_i)\sqrt{1-k_i^2 e_i(2+e_i)} - 1] \sqrt{1-k_i^2 e_i(2+e_i)} \right. \\ \left. + \frac{k_i^4}{1+\nu_i} (1+e_i)^3 (e_i + \chi_i + e_i \chi_i) \right\} \end{array} \right. \quad (48)$$

$$A = \sum_{i=0}^n \frac{2m_i A_i k_i \sqrt{1+k_i^2}}{(2+\nu_i) + 2k_i^2} \quad (43)$$

We can now discuss the strand and wire rope problems, based on the general formulation obtained.

$$\left\{ \begin{array}{l} \epsilon = e_i + (1+e_i)\xi_i \\ \phi = \frac{1}{k_i r_i} [\chi_i + (1+\chi_i)\xi_i] \quad i = 1, 2, \dots, n \end{array} \right. \quad (49)$$

$$\left\{ \begin{aligned} \xi_1 &= \frac{1}{\nu_1} \left[1 - \frac{r_1(1+e_1)}{1+\chi_1} \sqrt{\frac{1-k_1^2 e_1(2+e_1)}{r_1^2 + R_1^2 e_1(2+e_1)}} \right] \\ \xi_i &= \frac{1}{\nu_i R_i} \left\{ R_i + R_{i-1}(1 - \nu_{i-1} \xi_{i-1}) - \left[\frac{r_i \sqrt{1-k_i^2 e_i(2+e_i)}}{1+\chi_i} - \frac{r_{i-1} \sqrt{1-k_{i-1}^2 e_{i-1}(2+e_{i-1})}}{1+\chi_{i-1}} \right]^2 \right. \\ &\quad \left. + \frac{(R_i + R_{i-1})^2 - (r_i - r_{i-1})^2}{(1+\chi_{i-1})(1+\chi_i)} \sqrt{[1-k_{i-1}^2 e_{i-1}(2+e_{i-1})][1-k_i^2 e_i(2+e_i)]} \right]^{1/2} \end{aligned} \right\} \quad i = 1, 2, \dots, n \quad (50)$$

for close-packed lay, and

$$\left\{ \begin{aligned} \xi_1 &= \frac{r_1}{\nu_0 R_0(1+e_1) + \nu_1 R_1} \left[1 - \frac{\nu_0 R_0}{r_1} e_1 - \frac{1}{1+\chi_1} \sqrt{1-k_1^2 e_1(2+e_1)} \right], \\ \xi_i &= \frac{1}{\nu_i R_i} \left[R_i + R_{i-1}(1 - \nu_{i-1} \xi_{i-1}) - \frac{r_i \sqrt{1-k_i^2 e_i(2+e_i)}}{1+\chi_i} + \frac{r_{i-1} \sqrt{1-k_{i-1}^2 e_{i-1}(2+e_{i-1})}}{1+\chi_{i-1}} \right] \end{aligned} \right\} \quad i = 1, 2, \dots, n \quad (51)$$

for resting lay.

The linear theory yields

$$\left\{ \begin{aligned} F_s &= a_s \epsilon + b_s \phi \\ M_s &= c_s \epsilon + d_s \phi \end{aligned} \right. \quad (52) \quad \left\{ \begin{aligned} \lambda_1 &= \frac{1}{1+k_1^2 + \nu_1 R_1/r_1} \left(k_1^2 - \frac{\nu_0 R_0}{r_1} \right) \\ \mu_1 &= \frac{k_1 r_1}{1+k_1^2 + \nu_1 R_1/r_1} \end{aligned} \right. \quad (56)$$

where

$$\left\{ \begin{aligned} a_s &= \pi E_0 R_0^2 + \sum_{i=1}^n \frac{m_i \pi E_i R_i^4 \tau_i \kappa_i}{4\sqrt{1+k_i^2}} \left[\left(\frac{1}{1+\nu_i} + k_i^2 \right) - \left(\frac{1-\nu_i}{1+\nu_i} + k_i^2 - \frac{4}{R_i^2 \kappa_i^2} \right) \lambda_i \right] \\ b_s &= -\sum_{i=1}^n \frac{m_i \pi E_i R_i^4 \tau_i \kappa_i}{4\sqrt{1+k_i^2}} \left[\frac{\nu_i}{1+\nu_i} k_i r_i + \left(\frac{1-\nu_i}{1+\nu_i} + k_i^2 - \frac{4}{R_i^2 \kappa_i^2} \right) \mu_i \right] \\ c_s &= -\sum_{i=1}^n \frac{m_i \pi E_i R_i^4 \kappa_i}{4(1+k_i^2)^{3/2}} \left[\left(1 + \frac{1+2\nu_i}{1+\nu_i} k_i^2 \right) k_i^2 + \left(1 + k_i^2 - \frac{2\nu_i}{1+\nu_i} k_i^2 - \frac{4}{R_i^2 \kappa_i^2} \right) \lambda_i \right] \\ d_s &= \frac{\pi E_0 R_0^4}{4(1+\nu_0)} + \sum_{i=1}^n \frac{m_i \pi E_i R_i^4 \kappa_i}{4(1+k_i^2)^{3/2}} \left[\left(1 + 2k_i^2 + \frac{1}{1+\nu_i} k_i^4 \right) k_i r_i - \left(1 + k_i^2 - \frac{2\nu_i}{1+\nu_i} k_i^2 - \frac{4}{R_i^2 \kappa_i^2} \right) \mu_i \right] \end{aligned} \right. \quad (53)$$

in which

$$\left\{ \begin{aligned} \lambda_1 &= -\frac{1}{\nu_1 + k_1^2 + R_1^2/r_1^2} \left(1 - k_1^2 - \frac{R_1^2}{r_1^2} \right) \\ \mu_1 &= \frac{k_1 r_1}{\nu_1 + k_1^2 + R_1^2/r_1^2} \end{aligned} \right. \quad (54)$$

$$\left\{ \begin{aligned} \lambda_i &= \frac{\kappa_i}{f_i + \nu_i R_i \kappa_i} \left[(k_i^2 r_i f_i - k_{i-1}^2 r_{i-1} g_i) \right. \\ &\quad \left. - \left(\nu_{i-1} R_{i-1} - \frac{g_i}{\kappa_{i-1}} \right) \lambda_{i-1} \right] \\ \mu_i &= \frac{\kappa_i}{f_i + \nu_i R_i \kappa_i} \left[(k_i r_i^2 f_i - k_{i-1} r_{i-1}^2 g_i) \right. \\ &\quad \left. - \left(\nu_{i-1} R_{i-1} - \frac{g_i}{\kappa_{i-1}} \right) \lambda_{i-1} \right] \end{aligned} \right\} \quad i = 1, 2, \dots, n \quad (55)$$

for close-packed lay, while

$$\left\{ \begin{aligned} \lambda_i &= \frac{\kappa_i}{1 + \nu_i R_i \kappa_i} \left[(k_i^2 r_i - k_{i-1}^2 r_{i-1}) \right. \\ &\quad \left. - \left(\nu_{i-1} R_{i-1} - \frac{1}{\kappa_{i-1}} \right) \lambda_{i-1} \right] \\ \mu_i &= \frac{\kappa_i}{1 + \nu_i R_i \kappa_i} \left[(k_i r_i^2 - k_{i-1} r_{i-1}^2) \right. \\ &\quad \left. - \left(\nu_{i-1} R_{i-1} - \frac{1}{\kappa_{i-1}} \right) \lambda_{i-1} \right] \end{aligned} \right. \quad (57)$$

for resting lay.

The radial deformation coefficients and the bending stiffness of the strain can be found from Eqs. (42) and (43):

$$\left\{ \begin{aligned} p_s &= \frac{r_n}{R} \left[k_n^2 - \left(1 + k_n^2 - \frac{\nu_n R_n}{r_n} \right) \lambda_n \right] \\ q_s &= \frac{r_n}{R} \left[k_n r_n - \left(1 + k_n^2 - \frac{\nu_n R_n}{r_n} \right) \mu_n \right] \end{aligned} \right. \quad (58)$$

$$A_s = \sum_{i=0}^n \frac{m_i \pi E_i R_i^4 k_i \sqrt{1 + k_i^2}}{2[(2 + \nu_i) + 2k_i^2]} \quad (59)$$

5 Wire Ropes

If the components of the general structure are strands, the structure becomes a wire rope. In the case of large deformation, the force-strain relationships of the central strand are represented by Eq. (47), where the subscript s should now be considered as a variable representing the layer number of the wire rope. Therefore, for the central strand, we can write

$$\begin{cases} F_0 = F_0(\epsilon, \phi) \\ M_0 = M_0(\epsilon, \phi) \end{cases} \quad (60)$$

For the surrounding helical strands, the axial and rotational strains are ξ_s and $\Delta\tau_s$, which are usually small. Therefore, the surrounding helical strands can be characterized by the linear theory, that is by the seven constants, $a_s, b_s, c_s, d_s, A_s, p_s,$ and q_s , found from Eqs. (53), (58), and (59). Note that the strands in different layers can have different structures. In other words, these seven constants should first be determined for all the component strands, and the wire rope problem can be solved using the general formulation previously obtained.

A general program has been developed to solve various wire rope problems. The core of this program is a subroutine which makes use of the formulation derived in this paper and yields the nonlinear solutions and the seven characteristic constants of a general structure. Following the input information, the program starts by analyzing the component strands one layer after the other to find, using the subroutine, the characteristic constants of all the component strands. After that, a call of the subroutine again solves the wire rope problem. Note that a wire rope is also characterized by seven constants, by Eqs. (39), (42), and (43). Therefore, wire ropes can also be used as components in more complex structures, and the problems can be solved similarly.

6 Conclusions

The difficulty with the wire rope analysis is that there are many wires with different geometric and physical parameters involved that even numbering the wires can be complicated. The conventional method, analyzing the wires one by one, turns out to be too complex and inconvenient for computer pro-

gramming. This paper points out that the wire, the strand, and the wire rope can be considered as a kind of identical structure in the analysis, only with different values of stiffness and deformation constants. In this way, if we consider a general structure, which is composed of a central core and layers of surrounding helical components, and then choose any wires, strands, or even wire ropes to be its component elements, we can create a wire rope structure of any possible cross section, and the wire rope thus formed can be solved using the same general formulation.

Because of the complexity of the problem, a program is required in the analysis. In the case of a strand structure, the seven stiffness and deformation constants of the component wires are readily known, and the program solves the strand problem directly. In the case of a wire rope structure, the seven stiffness and deformation constants of all the component strands need to be determined first, using the program, based on the seven stiffness and deformation constants of the component wires of these component strands. Then, the wire rope can be considered as a generalized strand, and solved similarly. In this way, various strand and wire rope problems can be attacked with one general formulation and one program. The advantages of the presented approach are self-evident.

References

- Costello, G. A., 1977, "Large Deflection of Helical Spring due to Bending," *ASCE Journal of Engineering Mechanics*, Vol. 103, No. EM3, 481-487.
- Costello, G. A., and Sinha, S. K., 1977, "Static Behavior of Wire Rope," *ASCE Journal of Engineering Mechanics*, Vol. 103, No. EM6, 1011-1022.
- Hall, H. M., 1951, "Stresses in Small Wire Ropes," *Wire and Wire Products*, Vol. 26, pp. 228, 257-259.
- Hruska, F. H., 1951, "Calculations of Stresses in Wire Rope," *Wire and Wire Products*, Vol. 26, pp. 766-767, 799-801.
- Hruska, F. H., 1952, "Radial Forces in Wire Ropes," *Wire and Wire Products*, Vol. 27, pp. 459-463.
- Hruska, F. H., 1953, "Tangential Forces in Wire Ropes," *Wire and Wire Products*, Vol. 28, 455-460.
- Leissa, A. W., 1959, "Contact Stresses in Wire Ropes," *Wire and Wire Products*, Vol. 34, pp. 307-314, 372-373.
- Love, A. E. H., 1927, *A Treatise on the Mathematical Theory of Elasticity*, 4th ed., Dover, New York.
- Phillips, J. W., and Costello, G. A., 1973, "Contact Stresses in Twisted Wire Cables," *ASCE Journal of Engineering Mechanics*, Vol. 99, No. 2, 331-341.
- Phillips, J. W., and Costello, G. A., 1985, "Analysis of Wire Ropes with Internal-Wire-Rope Cores," *ASME JOURNAL OF APPLIED MECHANICS*, Vol. 52, 510-516.
- Suslov, B. M., 1936, "On the Modulus of Elasticity of Wire Ropes," *Wire and Wire Products*, Vol. 11, pp. 176-182.
- Velinsky, S. A., Anderson, G. L., and Costello, G. A., 1984, "Wire Rope with Complex Cross Sections," *ASCE Journal of Engineering Mechanics*, Vol. 110, No. 3, 380-391.

Dynamic Formulation for Geometrically Exact Sandwich Beams and One-Dimensional Plates¹

Loc Vu-Quoc
Mem. ASME.

I. K. Ebcioğlu

Department of Aerospace Engineering,
Mechanics and Engineering Science,
University of Florida,
Gainesville, FL 32611

A new theory of sandwich beams/one-dimensional plates is presented with finite rotations and shear allowed in each layer. The layers, variable in number from one to three, need not have the same thickness and the same length, thus allowing for ply drop-off. Restricting to planar deformation, the cross section has a motion identical to that of a multibody system that consists of rigid links connected by hinges. Large deformation and large overall motion are accommodated, with the beam dynamics referred directly to an inertial frame. An important approximated theory is developed from the general nonlinear equations. The classical linear theory is recovered by consistent linearization.

1 Introduction

Multilayered structures have widespread applications in engineering. Laminated composite structures, initially developed for use in the aerospace industry, have played an increasingly important role in robotics and machine systems that require high operating speed. The low weight and high stiffness offered by laminated composite structures help reduce the power consumption, increase the ratio of payload/self-weight, and would contribute to improve the accuracy in the motion characteristics and the reduction in the level of acoustic emission of these systems. It is shown from computer simulations with experimental corroboration that the low weight/stiffness ratio of laminated composites is essential for obtaining high performance in slider-crank and four-bar linkage systems (Sung et al., 1986; Thompson and Sung, 1986). More recently, considerable attention has been given to a class of smart structures with embedded piezoelectric layers as sensors and actuators (see, e.g., Evseichik, 1989; Tzou, 1989) or interferometric optical fiber sensors (see, e.g., Sirkis, 1993) for monitoring the strain level and for vibration control. Large overall motion of multilayered structures can be found in robot arms or space structures with embedded sensors/actuators. Yet another example of multilayered structures can be found in the damping of structural vibration by the use of viscoelastic constrained layers (e.g., Alberts, 1993; Dubbelday, 1993; Rao, 1993).

Several formulations to model the dynamic response of multilayered structures have been proposed (see, e.g., Yu, 1989). Particularly for sandwich structures, an account of the classical formulations (among other topics) is given in Plantema (1966). The bending stiffness of the core layer was often neglected; only shear is accounted for. The transverse shear effects of the outer layers were first considered in Yu (1959), who was also the first to employ the hypothesis of continuous piecewise linear deformed sandwich cross section (Toledano and Murakami,

1987). Most formulations so far have incorporated the geometric nonlinearity as higher-order deformation (see the review paper by Chia, 1988), and are not suitable for problems that include the large overall motion such as the slider-crank mechanism or the four-bar linkage systems. On the other hand, formulations proposed for studying the large overall motion of laminated composite structures in general bypass the kinematic description of the deformation in different layers to use the classical single-layer Euler-Bernoulli beam theory, and make use of a constitutive law which is a weighted average of the constitutive laws of the layers (see, e.g., Thompson, 1987).

We propose here a new theory of geometrically exact sandwich beams,² also applicable to one-dimensional plates, accounting for bending stiffness and shear deformation in all layers. In the present work, each layer can have arbitrary thickness, with no a priori assumption made on the distribution of mass over the layer cross section. The deformed cross section is piecewise linear, and admits finite rotations in the layer cross sections. The continuity of the displacement field at the layer interfaces is enforced. The beam deformation being restricted to be planar, the motion of a typical cross section is the same as that of a *multibody system* consisted of three (planar) rigid links, connected to each other by hinges, and moving in the plane *without* any a priori restriction on the magnitude of motion.³ With the kinematics of its deformation described by exact, fully nonlinear expressions, the formulation of this multirigid/flexible-body system can be employed to model problems involving large deformation in very flexible multilayered structures, and/or large overall motion as typified by the large rotation maneuvers of flexible composite robot arms or satellite appendages with embedded layers of sensors and actuators.

With the dynamics of motion referred directly to the inertial frame—bypassing the need for a floating reference frame as employed, e.g., in Thompson and Sung (1986)—the resulting equations of motion are fully nonlinear. Of particular interest is the case where the core layer admits finite rotation (thus large deformation and/or large overall motion), but rotations in the outer layers are infinitesimal *relative* to the core layer rotation.⁴

¹This paper is dedicated to Professor Robert L. Taylor of U. C. Berkeley on the occasion of his 60th birthday.

Contributed by the Applied Mechanics Division of THE AMERICAN SOCIETY OF MECHANICAL ENGINEERS for publication in the ASME JOURNAL OF APPLIED MECHANICS.

Discussion on this paper should be addressed to the Technical Editor, Prof. Lewis T. Wheeler, Department of Mechanical Engineering, University of Houston, Houston, TX 77204-4792, and will be accepted until four months after final publication of the paper itself in the ASME JOURNAL OF APPLIED MECHANICS.

Manuscript received by the ASME Applied Mechanics Division, Nov. 5, 1993; final revision, Apr. 1, 1994. Associate Technical Editor: J. N. Reddy.

²For backgrounds on the theoretical and computational formulation of single-layer geometrically-exact beams, the reader is referred to, e.g., Simo & Vu-Quoc (1986), Vu-Quoc (1986), Simo & Vu-Quoc (1991).

³See Figure 2.2 and Kamman & Huston (1984) for the dynamic formulation of a chain of rigid links.

⁴This situation is closely related to, but not exactly the same as, the one in Danielson & Hodges (1988), where the (single-layer) beam cross section deforms

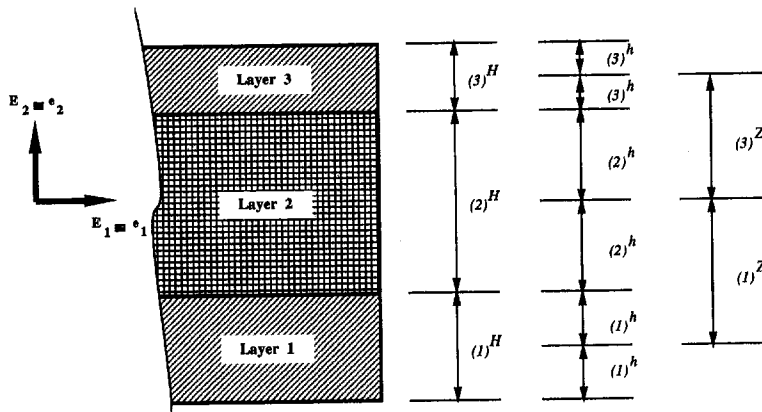


Fig. 1 Sandwich beam/one-dimensional plate. Profile of a sandwich structure. The layer thicknesses and the position of the layer midpoints are indicated.

Such cases can be found in flexible multilayered structures performing large overall motion (but not large deformation), e.g., robot arms. For this case, the nonlinear approximated equations of motion are consistently deduced from the fully nonlinear equations. Finally, we obtain the linear equations of motion in the case where all rotations are infinitesimal, and of the same order. These linear equations include those obtained in Yu (1959) as a particular case. The present result is more general in that we do not make the a priori assumption of zero axial motion as in Yu (1959).

The beam can admit a variable number of layers from one to three, with the number of unknown kinematic quantities varying from three to five. In the case of a single layer, we recover the equations of motion in Simo and Vu-Quoc (1986). In addition, the length of each layer can be arbitrary; such is the case of an important class of multilayered structures having *ply drop-off*. The computational formulation and numerical simulations, with application to multilayered beams with *ply drop-off* are given in Vu-Quoc and Deng (1995).

2 Kinematics of Deformation

Shown in Fig. 1 is the profile of a sandwich beam with three layers: The bottom layer (1), the core layer (2), and the top layer (3). Each layer may have a different thickness. The thickness of layer (l)—for $l = 1, 2, 3$ —is denoted by $(l)H := 2(l)h$.

The material configuration is defined by means of the material basis vectors $\{\mathbf{E}_1, \mathbf{E}_2\}$, with the associated coordinates (X^1, X^2) . The undeformed beam lies along the X^1 axis. The spatial configuration is defined by the basis vectors $\{\mathbf{e}_1, \mathbf{e}_2\}$, with \mathbf{e}_3 normal to the previous two vectors according to the right-hand rule. For convenience, it is often chosen such that $\mathbf{E}_\alpha \equiv \mathbf{e}_\alpha$ for $\alpha = 1, 2$. The time parameter is denoted by $t \in \mathbb{R}^+$, with $\mathbb{R}^+ := [0, +\infty[$. Let $\mathcal{L} =]0, L[$ denote the interval, with the axial coordinate X^1 , covering the length of the undeformed beam, and \mathcal{U} the interval, with the transverse coordinate X^2 , representing cross section of the sandwich beam. Let $\hat{\Omega} = \mathcal{L} \times \mathcal{U} \subset \mathbb{R}^2$ denote the domain of the undeformed beam. We define $(l)\mathcal{U} :=](l)Z - (l)h, (l)Z + (l)h[$ as the cross section of layer (l), where $(l)Z$ designates the X^2 -coordinate of the midpoint of layer (l).⁵ Setting the origin of coordinate X^2 to coincide with the midpoint of core layer (2) (see Fig. 1), we have $(1)Z = -(1)h + (2)h$, $(2)Z = 0$, and $(3)Z = (2)h + (3)h$; also $\mathcal{U} = \cup (l)\mathcal{U} =]-(1)H + (2)h, (2)h + (3)H[$. With the domain of layer (l) denoted by $(l)\Omega := \mathcal{L} \times (l)\mathcal{U}$, we have $\hat{\Omega} = \cup_l (l)\Omega$.

smoothly due to warping and without the presence of any "hinges" as in sandwich beams.

⁵ Open intervals are written as $]a, b[$.

⁶ The midpoint of a layer cross section coincides with its centroid when the mass distribution is symmetric within the layer cross section.

The deformation map for layer (l), denoted by $(l)\Phi: (l)\Omega \times \mathbb{R}^+ \rightarrow \mathbb{R}^2$ is described as follows: A material point⁷ $X^\alpha \mathbf{E}_\alpha$ in layer (l) is mapped to a spatial point $(l)\Phi(X^1, X^2, t) \in \mathbb{R}^2$ defined by

$$(l)\Phi(X^1, X^2, t) := (l)\Phi_0(X^1, t) + (X^2 - (l)Z)(l)\mathbf{t}_2(X^1, t), \quad (2.1)$$

for $X^1 \in \mathcal{L}$, and $X^2 \in (l)\mathcal{U}$, and for $l = 1, 2, 3$. In (2.1), $(l)\Phi_0: \mathcal{L} \times \mathbb{R}^+ \rightarrow \mathbb{R}^2$ is the deformation map of the centroidal line of layer (l). Describing the orientation of the cross section of layer (l) is a set of orthonormal basis vectors $\{(l)\mathbf{t}_1, (l)\mathbf{t}_2\}$ attached to that cross section, such that $(l)\mathbf{t}_\alpha(X^1, 0) \equiv \mathbf{e}_\alpha$, for $\alpha = 1, 2$, at time $t = 0$.

The motion of the cross section is that of a multibody system consisting of a chain of three rigid links connected by hinges as shown in Fig. 2, with $(l)\Phi_0$ being the position of the centroid of link (layer) (l). The following kinematic constraint equations express $(1)\Phi_0$ and $(3)\Phi_0$ in terms of $(2)\Phi_0$, which is chosen as a principal unknown function

$$(1)\Phi_0 = (2)\Phi_0 - (1)h(1)\mathbf{t}_2 - (2)h(2)\mathbf{t}_2, \quad (2.2)$$

$$(3)\Phi_0 = (2)\Phi_0 + (2)h(2)\mathbf{t}_2 + (3)h(3)\mathbf{t}_2, \quad (2.3)$$

and satisfy the continuity conditions across layer boundaries

$$(l)\Phi(X^1, (l)Z + (l)h, t) = (l+1)\Phi(X^1, (l+1)Z - (l+1)h, t), \quad (2.4)$$

for $l = 1, 2$ and for all $X^1 \in \mathcal{L}$ and $t \in \mathbb{R}^+$.

Let $S \equiv X^1$, and $\mathbf{u}(S, t) = u^\alpha(S, t)\mathbf{e}_\alpha$ be the displacement vector of the material point $S \in \mathcal{L}$ on the undeformed line of centroids, then

$$(2)\Phi_0 := [S + u^1(S, t)]\mathbf{e}_1 + u^2(S, t)\mathbf{e}_2. \quad (2.5)$$

Let $(l)\theta(S, t)$ be the rotation angle of the cross section of layer (l), then

$$(l)\mathbf{t}_\alpha(S, t) = (l)\mathbf{\Lambda}(S, t)\mathbf{E}_\alpha, \quad (2.6)$$

$$(l)\mathbf{\Lambda} = (l)\Lambda_\beta^\alpha \mathbf{e}_\alpha \otimes \mathbf{E}^\beta,$$

$$[(l)\Lambda_\beta^\alpha] := \begin{bmatrix} \cos (l)\theta & -\sin (l)\theta \\ \sin (l)\theta & \cos (l)\theta \end{bmatrix}, \quad (2.7)$$

where $(l)\mathbf{\Lambda}$ is an orthogonal two-point tensor, whose matrix of components with respect to the basis $\mathbf{e}_\alpha \otimes \mathbf{E}^\beta$ is denoted by

⁷ Summation convention on repeated indices applies, with Greek indices taking values in $\{1, 2\}$.

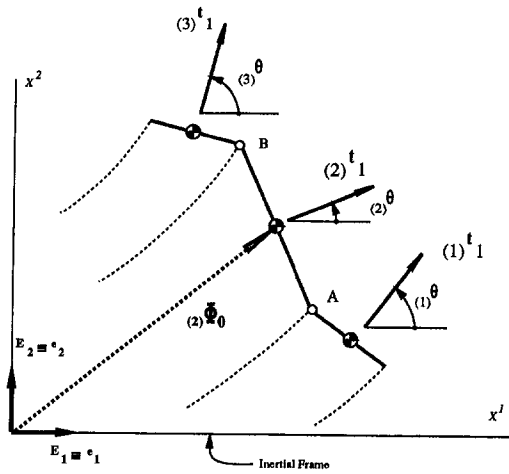


Fig. 2 Multibody dynamics. Motion of cross section as a chain of rigid links. For clarity, the basis vectors ${}_{(l)}\mathbf{t}_2$ for layers $l = 1, 2, 3$ are not drawn.

$[\Lambda_{\beta}^{\alpha}]$, where in ${}_{(l)}\Lambda_{\beta}^{\alpha}$, the superscript α denotes the row index and the subscript β the column index. Since we are using Cartesian coordinates, it follows that $\mathbf{E}^{\alpha} \equiv \mathbf{E}_{\alpha}$. Thus, from (2.6)–(2.7) we have ${}_{(l)}\mathbf{t}_{\alpha} = {}_{(l)}\Lambda_{\alpha}^{\beta} \mathbf{e}_{\beta}$ (see, e.g., Marsden and Hughes, 1983; Vu-Quoc, 1986).

The five principal unknown functions of (S, t) for a three-layer sandwich structure are the following kinematic quantities: $u^1, u^2, {}_{(1)}\theta, {}_{(2)}\theta$, and ${}_{(3)}\theta$. Using (2.2)–(2.3), and (2.5)–(2.7), we can relate the deformation maps ${}_{(l)}\Phi$ of the three layers ($l = 1, 2, 3$) to the above five principal unknown functions.

3 Equations of Motion

3.1 Power of Contact and Assigned Forces/Couples.

The mechanical power of contact forces/couples in a three-layer sandwich structure is given by

$$\mathcal{P}_c := \sum_{l=1}^3 \int_{\ell} [{}_{(l)}\mathbf{n} \cdot {}_{(l)}\boldsymbol{\gamma} + {}_{(l)}m_{(l)}\dot{\theta}, s] dS, \quad (3.1)$$

where ${}_{(l)}\mathbf{n} = {}_{(l)}n^{\alpha} \mathbf{e}_{\alpha}$ is the resultant contact (internal) force for layer (l) , ${}_{(l)}m$ the resultant contact couple with respect to the centroid of the layer (l) cross section, whereas ${}_{(l)}\boldsymbol{\gamma}$ and ${}_{(l)}\theta, s$ are the strain measures conjugated to ${}_{(l)}\mathbf{n}$ and ${}_{(l)}m$, respectively (see Simo and Vu-Quoc (1986) for the single-layer case). In (3.1), the overhead dot “ $\dot{\cdot}$ ” designates time differentiation, whereas the overhead symbol “ ${}^{[l]}\cdot$ ” designates the time differentiation of a vector quantity, say, \mathbf{v} , expressed in the cross-section basis $\{{}_{(l)}\mathbf{t}_1, {}_{(l)}\mathbf{t}_2\}$ of layer (l) while keeping *this* basis fixed in the following sense:

$${}_{(l)}\dot{\mathbf{t}}_{\alpha} \equiv 0, \quad \text{and} \quad \mathbf{v} = v^{\alpha} {}_{(l)}\mathbf{t}_{\alpha} \Rightarrow \dot{\mathbf{v}} := \dot{v}^{\alpha} {}_{(l)}\mathbf{t}_{\alpha}. \quad (3.2)$$

Note that $\dot{\mathbf{v}}$ can be re-expressed in the basis $\{\mathbf{e}_1, \mathbf{e}_2\}$ using (2.6)–(2.7). Using (3.2), the objective rates of the spatial strains for each layer $l = 1, 2, 3$ are given by

$${}_{(l)}\boldsymbol{\gamma} := \frac{\partial {}_{(l)}\Phi_0}{\partial S} - {}_{(l)}\mathbf{t}_1 \Rightarrow {}_{(l)}\boldsymbol{\gamma} = \left(\frac{\partial {}_{(l)}\Phi_0}{\partial S} \right)^{[l]} =: {}_{(l)}\Phi_{0,S}^{[l]}, \quad (3.3)$$

where we have made use of (3.2), and the subscript “ S ” designates a differentiation with respect to S (see Simo and Vu-Quoc (1986) for the single-layer case). We record below some expressions for the rates of the basis vectors $\{{}_{(l)}\mathbf{t}_1, {}_{(l)}\mathbf{t}_2\}$ which will be used frequently later

$${}_{(l)}\dot{\mathbf{t}}_{1,S} = {}_{(l)}\dot{\theta}_{,S} {}_{(l)}\mathbf{t}_2, \quad {}_{(l)}\dot{\mathbf{t}}_{2,S} = -{}_{(l)}\dot{\theta}_{,S} {}_{(l)}\mathbf{t}_1, \quad (3.4)$$

$${}_{(2)}\dot{\mathbf{t}}_1 = \dot{\psi}_{21} {}_{(2)}\mathbf{t}_2, \quad {}_{(2)}\dot{\mathbf{t}}_2 = -\dot{\psi}_{21} {}_{(2)}\mathbf{t}_1,$$

$$\text{with } \psi_{21} := {}_{(2)}\theta - {}_{(1)}\theta. \quad (3.5)$$

Note that the case for $l = 2$ in (3.5) is trivial, and corresponds to the definition of the special time differentiation in (3.2). We want to express the strain rates in (3.3) in terms of the five principal unknown functions. From (3.3), (2.2)–(2.3), and (3.4)–(3.5), the expressions for ${}_{(l)}\boldsymbol{\gamma}$ can be written as follows:

$${}_{(1)}\boldsymbol{\gamma} = {}_{(2)}\Phi_{0,S}^{[1]} + {}_{(1)}h_{(1)}\dot{\theta}_{,S} {}_{(1)}\mathbf{t}_1 + {}_{(2)}h_{(2)}\dot{\theta}_{,S} {}_{(2)}\mathbf{t}_1 + {}_{(2)}h_{(2)}\theta_{,S}\dot{\psi}_{21} {}_{(2)}\mathbf{t}_2, \quad (3.6)$$

$${}_{(3)}\boldsymbol{\gamma} = {}_{(2)}\Phi_{0,S}^{[3]} - {}_{(2)}h_{(2)}\dot{\theta}_{,S} {}_{(2)}\mathbf{t}_1 - {}_{(2)}h_{(2)}\theta_{,S}\dot{\psi}_{23} {}_{(2)}\mathbf{t}_2 - {}_{(3)}h_{(3)}\dot{\theta}_{,S} {}_{(3)}\mathbf{t}_1. \quad (3.7)$$

Remark 3.1. In arriving at (3.6)–(3.7), the order of differentiation as shown in the definition (3.3)₂—space first, time after—must be observed, lest we would obtain incorrect results, which are different from (3.6)–(3.7). The reason for this non-commutativity is that the time differentiation $(\dot{\cdot})^{[l]}$ is *not* the total time derivative, and thus does not commute with the spatial derivative $d(\cdot)/dS$. ■

Next using (2.5)–(2.7) with $\mathbf{E}_{\alpha} = \mathbf{e}_{\alpha}$, and (3.4)–(3.5), it can be shown that

$${}_{(2)}\Phi_{0,S}^{[1]} = [\dot{u}_{,S}^1 + u_{,S}^2 {}_{(1)}\dot{\theta}] \mathbf{e}_1 + [\dot{u}_{,S}^2 - (1 + u_{,S}^1) {}_{(1)}\dot{\theta}] \mathbf{e}_2. \quad (3.8)$$

With the aid of formulae (3.3), (3.6), (3.8), and (2.6)–(2.7), the strain rates ${}_{(l)}\boldsymbol{\gamma}$ (for $l = 1, 2, 3$) can now be related to the five principal unknown functions. Next we want to arrange the terms in the expression for the power \mathcal{P}_c as factors of the time rate of the five principal unknown functions $\dot{u}^1, \dot{u}^2, {}_{(1)}\dot{\theta}, {}_{(2)}\dot{\theta}$, and ${}_{(3)}\dot{\theta}$. We first note that

$$u_{,S}^2 {}_{(1)}n^1 - (1 + u_{,S}^1) {}_{(1)}n^2 = -[{}_{(2)}\Phi_{0,S} \times {}_{(1)}\mathbf{n}] \cdot \mathbf{e}_3. \quad (3.9)$$

We also introduce the following definition:

$$\hat{\mathbf{n}} := \sum_{l=1}^3 {}_{(l)}\mathbf{n}, \quad (3.10)$$

where $\hat{\mathbf{n}}$ represents the resultant contact force on the cross section. After performing an integration by parts with respect to S , we obtain the following expression for the power of contact forces and contact couples

$$\begin{aligned} \mathcal{P}_c = & - \int_{\ell} \hat{\mathbf{n}}_S \cdot \dot{\mathbf{u}} dS + [\hat{\mathbf{n}} \cdot \dot{\mathbf{u}}]_{S=0}^{S=L} - \int_{\ell} \{ {}_{(1)}m_S \\ & + [{}_{(2)}\Phi_{0,S} \times {}_{(1)}\mathbf{n}] \cdot \mathbf{e}_3 + {}_{(1)}h_{(1)}(\mathbf{n} \cdot {}_{(1)}\mathbf{t}_1)_S \\ & + {}_{(2)}h_{(2)}\theta_{,S}(\mathbf{n} \cdot {}_{(2)}\mathbf{t}_2) \} {}_{(1)}\dot{\theta} dS \\ & + [\{ {}_{(1)}m + {}_{(1)}h_{(1)}(\mathbf{n} \cdot {}_{(1)}\mathbf{t}_1) \} {}_{(1)}\dot{\theta}]_{S=0}^{S=L} \\ & - \int_{\ell} \{ {}_{(2)}m_S + [{}_{(2)}\Phi_{0,S} \times {}_{(2)}\mathbf{n}] \cdot \mathbf{e}_3 \\ & + {}_{(2)}h_{(1)}(\mathbf{n}_S - {}_{(3)}\mathbf{n}_S) \cdot {}_{(2)}\mathbf{t}_1 \} {}_{(2)}\dot{\theta} dS \\ & + [\{ {}_{(2)}m + {}_{(2)}h_{(1)}(\mathbf{n} - {}_{(3)}\mathbf{n}) \cdot {}_{(2)}\mathbf{t}_1 \} {}_{(2)}\dot{\theta}]_{S=0}^{S=L} \\ & - \int_{\ell} \{ {}_{(3)}m_S + [{}_{(2)}\Phi_{0,S} \times {}_{(3)}\mathbf{n}] \cdot \mathbf{e}_3 \\ & - {}_{(2)}h_{(2)}\theta_{,S}({}_{(3)}\mathbf{n} \cdot {}_{(2)}\mathbf{t}_2) - {}_{(3)}h_{(3)}(\mathbf{n} \cdot {}_{(3)}\mathbf{t}_1)_S \} {}_{(3)}\dot{\theta} dS \\ & + [\{ {}_{(3)}m - {}_{(3)}h_{(3)}(\mathbf{n} \cdot {}_{(3)}\mathbf{t}_1) \} {}_{(3)}\dot{\theta}]_{S=0}^{S=L}. \end{aligned} \quad (3.11)$$

A geometric interpretation of the moment term $[{}_{(2)}h_{(1)}\mathbf{n} -$

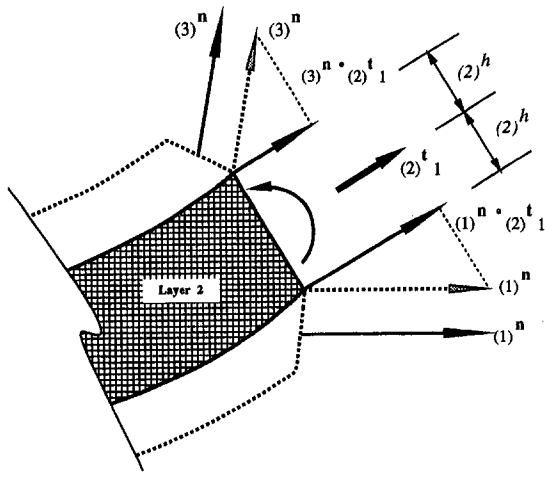


Fig. 3 Sandwich beams/one-dimensional plates. Geometric interpretation of the moment $[(2)h(1)\mathbf{n} - (3)\mathbf{n}] \cdot (2)\mathbf{t}_1$ at the extremities of layer (2)—see the third boundary term in Eq. (3.11).

$(3)\mathbf{n} \cdot (2)\mathbf{t}_1$ at the extremities of the core layer (2)—i.e., the third boundary term in (3.11)—is given in Fig. 3; similar interpretations can be made for the moment terms $[(1)h(1)\mathbf{n} \cdot (1)\mathbf{t}_1]$ and $[(3)h(3)\mathbf{n} \cdot (3)\mathbf{t}_1]$ for layers (1) and (3), respectively.

Let $\bar{\mathbf{n}}(S, t)$ be the resultant assigned forces for all layers, and $(l)\bar{\mathbf{M}}(S, t)$ the resultant assigned couple associated with layer (l). The power due to assigned forces/couples for a three-layer sandwich structure is given by

$$\mathcal{P}_a := \int_t \{ \bar{\mathbf{n}} \cdot \dot{\mathbf{u}} + \sum_{l=1}^3 (l)\bar{\mathbf{M}}(l)\dot{\theta} \} dS + [\bar{\mathbf{n}} \cdot \dot{\mathbf{u}} + \sum_{l=1}^3 (l)\bar{\mathbf{M}}(l)\dot{\theta}]_{S=0}^{S=L}, \quad (3.12)$$

where the moments $(l)\bar{\mathbf{M}}$ have a special meaning (different than that of $(l)m$) to be defined shortly.

3.2 Rate of Kinetic Energy. Let $(l)\rho$ denote the mass per unit volume⁸ in layer (l). Then the kinetic energy \mathcal{K} and its rate are

$$\mathcal{K} := \frac{1}{2} \sum_{l=1}^3 \int_{(l)\Omega} (l)\rho (l)\dot{\Phi} \cdot (l)\dot{\Phi} d\Omega \Rightarrow \frac{d}{dt} \mathcal{K} = \sum_{l=1}^3 \int_{(l)\Omega} (l)\rho (l)\ddot{\Phi} \cdot (l)\dot{\Phi} d\Omega. \quad (3.13)$$

Using (2.1) and the kinematic constraint Eqs. (2.2)–(2.3), the deformation maps $(l)\Phi$ (for $l = 1, 2, 3$) can be expressed in terms of the principal unknown functions $(2)\Phi_0$, $(1)\theta$, $(2)\theta$, $(3)\theta$. One can then derive the expression for the rate of the kinetic energy in terms of the rates of the five principal unknown functions. The time rates of $(l)\Phi$ involve the time rates of the basis vector $(l)\mathbf{t}_2$, which are recorded as follows:

$$(l)\dot{\mathbf{t}}_2 = -(l)\dot{\theta} (l)\mathbf{t}_1, \quad (l)\ddot{\mathbf{t}}_2 = -[(l)\ddot{\theta} (l)\mathbf{t}_1 + (l)\dot{\theta}^2 (l)\mathbf{t}_2]. \quad (3.14)$$

It is convenient for the evaluation of the rate of the kinetic energy to introduce the following definitions. Combining (2.1) and (2.2)–(2.3), we have

$$(l)\dot{\Phi} = (l)\dot{\varphi} + X^2 (l)\dot{\mathbf{t}}_2, \quad \text{for } l = 1, 2, 3, \quad (3.15)$$

$$(1)\dot{\varphi} := (2)\dot{\Phi}_0 + (2)h(1)\dot{\mathbf{t}}_2 - (2)\dot{\mathbf{t}}_2, \quad (3.16)$$

$$(2)\dot{\varphi} := (2)\dot{\Phi}_0, \quad (3.17)$$

$$(3)\dot{\varphi} := (2)\dot{\Phi}_0 + (2)h(2)\dot{\mathbf{t}}_2 - (3)\dot{\mathbf{t}}_2. \quad (3.18)$$

The rate of the kinetic energy (3.13) is then written as

$$\begin{aligned} \frac{d}{dt} \mathcal{K} &= \int_t \left\{ \sum_{l=1}^3 \int_{(l)\Omega} (l)\rho (l)\dot{\varphi} + X^2 (l)\dot{\mathbf{t}}_2 \right. \\ &\quad \left. \cdot (l)\dot{\varphi} + X^2 (l)\dot{\mathbf{t}}_2 \right\} dX^2 \\ &= \sum_{l=1}^3 \int_t \{ (l)A_\rho^0 (l)\dot{\varphi} \cdot (l)\dot{\varphi} + (l)A_\rho^1 [(l)\dot{\varphi} \cdot (l)\dot{\mathbf{t}}_2 + (l)\dot{\mathbf{t}}_2 \cdot (l)\dot{\varphi}] \\ &\quad + (l)A_\rho^2 (l)\dot{\mathbf{t}}_2 \cdot (l)\dot{\mathbf{t}}_2 \} dS, \quad (3.19) \end{aligned}$$

where we have made use of the following definition

$$(l)A_\rho^k := \int_{(l)\Omega} (l)\rho (X^2)^k dX^2, \quad \text{for } k = 0, 1, 2. \quad (3.20)$$

For layer (l), $(l)A_\rho^0$ is the mass per unit undeformed length, whereas $(l)A_\rho^1$ is the mass moment of area, and $(l)A_\rho^2$ the mass moment of inertia, of the layer cross section $(l)\Omega$ with respect to the midpoint of the core layer (2). Assumptions are made neither on the layer thickness, nor on the distribution of mass in each layer. For a symmetric distribution of mass in each layer cross section, $(l)A_\rho^1 = (l)Z(l)A_\rho^0$ (in particular, $(2)A_\rho^1 = 0$); however, for a general distribution of mass, $(l)A_\rho^1 \neq (l)Z(l)A_\rho^0$.

The expressions for $(l)\dot{\varphi}$ and for $(l)\dot{\Phi}$ can be readily obtained from (3.15)–(3.18), (2.5), and (3.14). First, it follows from (2.5) and (3.17) that

$$(2)\dot{\varphi} = (2)\dot{\Phi}_0 = \dot{\mathbf{u}}, \quad \text{and} \quad (2)\dot{\Phi} = (2)\dot{\Phi}_0 = \dot{\mathbf{u}}. \quad (3.21)$$

Next, using (3.15)–(3.18), we can regroup the terms in (3.19) as factors of the time rates $\dot{\mathbf{u}}$, $(1)\dot{\mathbf{t}}_2$, $(2)\dot{\mathbf{t}}_2$, $(3)\dot{\mathbf{t}}_2$ as follows:

$$\begin{aligned} \frac{d}{dt} \mathcal{K} &= \int_t \left[\sum_{l=1}^3 \{ (l)A_\rho^0 (l)\dot{\varphi} + (l)A_\rho^1 (l)\dot{\mathbf{t}}_2 \} \cdot \dot{\mathbf{u}} \right. \\ &\quad + \{ (1)A_\rho^0 (2)h(1)\dot{\varphi} + (1)A_\rho^1 (1)\dot{\varphi} + (2)h(1)\dot{\mathbf{t}}_2 \} \\ &\quad + (1)A_\rho^2 (1)\dot{\mathbf{t}}_2 \} \cdot (1)\dot{\mathbf{t}}_2 + \{ (2)h(-1)A_\rho^0 (1)\dot{\varphi} \\ &\quad + (3)A_\rho^0 (3)\dot{\varphi} \} + (-2)h(1)A_\rho^1 (1)\dot{\mathbf{t}}_2 + (2)A_\rho^1 (2)\dot{\varphi} \\ &\quad + (2)h(3)A_\rho^1 (3)\dot{\mathbf{t}}_2 + (2)A_\rho^2 (2)\dot{\mathbf{t}}_2 \} \cdot (2)\dot{\mathbf{t}}_2 \\ &\quad + \{ (-3)A_\rho^0 (2)h(3)\dot{\varphi} + (3)A_\rho^1 (3)\dot{\varphi} - (2)h(3)\dot{\mathbf{t}}_2 \} \\ &\quad \left. + (3)A_\rho^2 (3)\dot{\mathbf{t}}_2 \} \cdot (3)\dot{\mathbf{t}}_2 \right] dS, \quad (3.22) \end{aligned}$$

which, by using (3.14)₁, can be recast into the following form:

$$\frac{d}{dt} \mathcal{K} = \int_t [\mathbf{f} \cdot \dot{\mathbf{u}} + \sum_{l=1}^3 (l)C(l)\dot{\theta}] dS. \quad (3.23)$$

We record below results that will help to arrive at the expressions for the inertia force and the couples $(l)C$:

$$(l)\mathbf{t}_\alpha \cdot (l)\mathbf{t}_\beta = \delta_{\alpha\beta}, \quad \mathbf{e}_1 \cdot (l)\mathbf{t}_1 = \cos (l)\theta, \quad (3.24)$$

$$\mathbf{e}_2 \cdot (l)\mathbf{t}_1 = \sin (l)\theta, \quad (3.24)$$

$$(2)\mathbf{t}_1 \cdot (l)\mathbf{t}_1 = (l)\mathbf{t}_1 \cdot (2)\mathbf{t}_1 = \cos \psi_{2l}, \quad (3.25)$$

$$-(2)\mathbf{t}_2 \cdot (l)\mathbf{t}_1 = (l)\mathbf{t}_2 \cdot (2)\mathbf{t}_1 = \sin \psi_{2l}, \quad (3.26)$$

with $\delta_{\alpha\beta}$ being the Kronecker delta, and for $l = 1, 2, 3$. Using (3.24)–(3.26), one obtains⁹

$$\dot{\mathbf{u}} \cdot (l)\mathbf{t}_1 = (\dot{u}^1 \cos (l)\theta + \dot{u}^2 \sin (l)\theta), \quad (3.27)$$

$$(l)\dot{\mathbf{t}}_2 \cdot (l)\mathbf{t}_1 = -(l)\dot{\theta}, \quad (3.28)$$

⁸ The mass density $(l)\rho$ is assumed constant in time.

⁹ Recall that $\psi_{2l} := (2)\theta - (l)\theta$ as defined in (3.5).

$${}_{(1)}\ddot{\mathbf{t}}_2 \cdot {}_{(2)}\mathbf{t}_1 = -[{}_{(1)}\ddot{\theta} \cos \psi_{2l} + ({}_{(1)}\dot{\theta})^2 \sin \psi_{2l}], \quad (3.29)$$

$${}_{(2)}\ddot{\mathbf{t}}_2 \cdot {}_{(1)}\mathbf{t}_1 = -[{}_{(2)}\ddot{\theta} \cos \psi_{2l} - ({}_{(2)}\dot{\theta})^2 \sin \psi_{2l}], \quad (3.30)$$

for $l = 1, 2, 3$. From the expressions for ${}_{(l)}\varphi$ in (3.15)–(3.18) together with (2.5), we arrive at the expression for the inertia force \mathbf{f} from the first term of (3.22)

$$\begin{aligned} \mathbf{f} &= \sum_{l=1}^3 \{ {}_{(l)}A_\rho^0 {}_{(l)}\ddot{\varphi} + {}_{(l)}A_\rho^1 {}_{(l)}\ddot{\mathbf{t}}_2 \} \\ &= \left(\sum_{l=1}^3 {}_{(l)}A_\rho^0 \right) \ddot{\mathbf{u}} + [{}_{(2)}h_{(1)}A_\rho^0 + {}_{(1)}A_\rho^1] {}_{(1)}\ddot{\mathbf{t}}_2 \\ &\quad + [-{}_{(2)}h_{(1)}A_\rho^0 + {}_{(2)}A_\rho^1 + {}_{(2)}h_{(3)}A_\rho^0] {}_{(2)}\ddot{\mathbf{t}}_2 \\ &\quad - [{}_{(2)}h_{(3)}A_\rho^0 - {}_{(3)}A_\rho^1] {}_{(3)}\ddot{\mathbf{t}}_2. \end{aligned} \quad (3.31)$$

The expressions for the inertia couple ${}_{(l)}C$, for $l = 1, 2, 3$ follow from the use of (3.14)₁, the definitions (3.16)–(3.18), and (2.5) in the last three terms of (3.22)

$${}_{(1)}C = [({}_{(2)}h)^2 {}_{(1)}A_\rho^0 + 2({}_{(2)}h_{(1)}A_\rho^1 + {}_{(1)}A_\rho^2)] {}_{(1)}\ddot{\theta} - [{}_{(2)}h_{(1)}A_\rho^0 + {}_{(1)}A_\rho^1] (\ddot{\mathbf{u}} - {}_{(2)}h_{(2)}\ddot{\mathbf{t}}_2) \cdot {}_{(1)}\mathbf{t}_1, \quad (3.32)$$

$$\begin{aligned} {}_{(2)}C &= [({}_{(2)}h)^2 {}_{(1)}A_\rho^0 + {}_{(2)}A_\rho^2 + ({}_{(2)}h)^2 {}_{(3)}A_\rho^0] {}_{(2)}\ddot{\theta} \\ &\quad + [{}_{(2)}h_{(1)}A_\rho^0 - {}_{(2)}A_\rho^1 - {}_{(2)}h_{(3)}A_\rho^0] (\ddot{\mathbf{u}} \cdot {}_{(2)}\mathbf{t}_1) \\ &\quad + {}_{(2)}h [{}_{(2)}h_{(1)}A_\rho^0 + {}_{(1)}A_\rho^1] ({}_{(1)}\ddot{\mathbf{t}}_2 \cdot {}_{(2)}\mathbf{t}_1) \\ &\quad + {}_{(2)}h [{}_{(2)}h_{(3)}A_\rho^0 - {}_{(3)}A_\rho^1] ({}_{(3)}\ddot{\mathbf{t}}_2 \cdot {}_{(2)}\mathbf{t}_1), \end{aligned} \quad (3.33)$$

$${}_{(3)}C = [({}_{(2)}h)^2 {}_{(3)}A_\rho^0 - 2({}_{(2)}h_{(3)}A_\rho^1 + {}_{(3)}A_\rho^2)] {}_{(3)}\ddot{\theta} + [{}_{(2)}h_{(3)}A_\rho^0 - {}_{(3)}A_\rho^1] (\ddot{\mathbf{u}} + {}_{(2)}h_{(2)}\ddot{\mathbf{t}}_2) \cdot {}_{(3)}\mathbf{t}_1. \quad (3.34)$$

One can recast the expressions in (3.31)–(3.34) in terms of the five principal unknown functions u^1 , u^2 , ${}_{(1)}\theta$, ${}_{(2)}\theta$, ${}_{(3)}\theta$, using (3.14)₂ and (3.27)–(3.30).

3.3 Balance of Power: Equations of Motion. We are now ready to employ the balance of (i) the power of assigned forces/couples and (ii) the combined rate of kinetic energy and power of contact forces/couples

$$\frac{d}{dt} \mathcal{K} + \mathcal{P}_\sigma = \mathcal{P}_a, \quad (3.35)$$

for all admissible rates $\dot{\mathbf{u}}$, ${}_{(1)}\dot{\theta}$, ${}_{(2)}\dot{\theta}$, ${}_{(3)}\dot{\theta}$. It follows from (3.23), (3.11), and (3.12) that the equations of motion for a three-layer sandwich structure are given by

$$\hat{\mathbf{n}}_S + \hat{\mathbf{n}} = \mathbf{f}, \quad (3.36)$$

$${}_{(1)}m_{,S} + [{}_{(2)}\Phi_{0,S} \times ({}_{(1)}\mathbf{n}) \cdot \mathbf{e}_3 + {}_{(1)}h_{(1)}(\mathbf{n} \cdot {}_{(1)}\mathbf{t}_1)_{,S} + {}_{(2)}h_{(2)}\theta_{,S}({}_{(1)}\mathbf{n} \cdot {}_{(2)}\mathbf{t}_2) + {}_{(1)}\bar{\mathcal{M}}] = {}_{(1)}C, \quad (3.37)$$

$${}_{(2)}m_{,S} + [{}_{(2)}\Phi_{0,S} \times ({}_{(2)}\mathbf{n}) \cdot \mathbf{e}_3 + {}_{(2)}h_{(1)}(\mathbf{n}_{,S} - ({}_{(3)}\mathbf{n}_{,S}) \cdot {}_{(2)}\mathbf{t}_1) + {}_{(2)}\bar{\mathcal{M}}] = {}_{(2)}C, \quad (3.38)$$

$${}_{(3)}m_{,S} + [{}_{(2)}\Phi_{0,S} \times ({}_{(3)}\mathbf{n}) \cdot \mathbf{e}_3 - {}_{(2)}h_{(2)}\theta_{,S}({}_{(3)}\mathbf{n} \cdot {}_{(2)}\mathbf{t}_2) - {}_{(3)}h_{(3)}(\mathbf{n} \cdot {}_{(3)}\mathbf{t}_1)_{,S} + {}_{(3)}\bar{\mathcal{M}}] = {}_{(3)}C, \quad (3.39)$$

and the boundary conditions at $S = 0$ and $S = L$ are

$$\hat{\mathbf{n}} = \bar{\mathbf{n}}, \quad (3.40)$$

$${}_{(1)}m + {}_{(1)}h_{(1)}(\mathbf{n} \cdot {}_{(1)}\mathbf{t}_1) = {}_{(1)}\bar{\mathcal{M}}, \quad (3.41)$$

$${}_{(2)}m + {}_{(2)}h_{(1)}(\mathbf{n} - ({}_{(3)}\mathbf{n}) \cdot {}_{(2)}\mathbf{t}_1) = {}_{(2)}\bar{\mathcal{M}}, \quad (3.42)$$

$${}_{(3)}m - {}_{(3)}h_{(3)}(\mathbf{n} \cdot {}_{(3)}\mathbf{t}_1) = {}_{(3)}\bar{\mathcal{M}}. \quad (3.43)$$

Relation (3.41) suggests that the assigned couple ${}_{(1)}\bar{\mathcal{M}}$ is effectively the resultant couple of the assigned forces in layer (1)

with respect to hinge A shown in Fig. 2. Similarly, ${}_{(3)}\bar{\mathcal{M}}$ is the resultant assigned couple in layer (3) with respect to hinge B in Fig. 2. The assigned couple ${}_{(2)}\bar{\mathcal{M}}$ with respect to the midpoint of core layer (2) is interpreted in the same manner as shown in Fig. 3. In fact, by defining the layer internal moments ${}_{(l)}\bar{\mathcal{M}}$ in a similar manner as in (3.41)–(3.43), one obtains an alternative form for the balance of angular momenta (3.37)–(3.39).¹⁰

Global balance of angular momentum equation. Note that the third term in (3.38) has an equivalent form

$$\begin{aligned} ({}_{(1)}\mathbf{n}_{,S} - ({}_{(3)}\mathbf{n}_{,S}) \cdot {}_{(2)}\mathbf{t}_1) \cdot ({}_{(2)}\mathbf{t}_1) &= [({}_{(1)}\mathbf{n} - ({}_{(3)}\mathbf{n}) \cdot {}_{(2)}\mathbf{t}_1)_{,S} \\ &\quad - ({}_{(2)}\theta_{,S}({}_{(1)}\mathbf{n} - ({}_{(3)}\mathbf{n}) \cdot {}_{(2)}\mathbf{t}_2)], \end{aligned} \quad (3.44)$$

where we have made use of (3.4)₁. We introduce the definition of the resultant moment of layer (l) with respect to the midpoint of the core layer (2) denoted by ${}_{(l/2)}m$ as follows:

$${}_{(1/2)}m := {}_{(1)}m + {}_{(1)}\mathbf{n} \cdot ({}_{(1)}h_{(1)}\mathbf{t}_1 + {}_{(2)}h_{(2)}\mathbf{t}_1), \quad (3.45)$$

$${}_{(2/2)}m := {}_{(2)}m, \quad (3.46)$$

$${}_{(3/2)}m := {}_{(3)}m - ({}_{(3)}\mathbf{n} \cdot ({}_{(2)}h_{(2)}\mathbf{t}_1 + {}_{(3)}h_{(3)}\mathbf{t}_1)), \quad (3.47)$$

and

$$\hat{m} := \sum_{l=1}^3 {}_{(l/2)}m, \quad \bar{m} := \sum_{l=1}^3 {}_{(l)}\bar{\mathcal{M}}, \quad \hat{C} := \sum_{l=1}^3 {}_{(l)}C, \quad (3.48)$$

which stand for the *resultant contact couple*, *resultant assigned couple*, and *resultant inertia couple* with respect to the midpoint of core layer (2), respectively. Using (3.44) in (3.38), then adding (3.37)–(3.39) together, we arrive at the global balance of angular momentum equation

$$\hat{m}_{,S} + [{}_{(2)}\Phi_{0,S} \times \hat{\mathbf{n}}] \cdot \mathbf{e}_3 + \bar{m} = \hat{C} \quad (3.49)$$

after making use of definitions (3.10) and (3.48).

Remark 3.2. It should be emphasized that the present theory remains valid for multilayered structures with an arbitrary number of layers (anywhere between one and three). In case of one layer, the equations are the same as those in Simo and Vu-Quoc (1986), which constitute a particular case.¹¹ In addition, the present theory can accommodate the important case of multilayered structures with ply drop-off. These points are clearly discussed in Vu-Quoc and Deng (1995), where we present the computational formulation and the numerical results for the present theory. ■

4 Constitutive Laws

We define the material contact force ${}_{(l)}\mathbf{N}$ and the material strain measure ${}_{(l)}\Gamma$ pertaining to layer (l) as follows:

$${}_{(l)}\mathbf{N} = {}_{(l)}N^\alpha \mathbf{E}_\alpha, \quad {}_{(l)}\mathbf{N} := {}_{(l)}\Lambda^T {}_{(l)}\mathbf{n}, \quad (4.1)$$

$${}_{(l)}\Gamma = {}_{(l)}\Gamma^\alpha \mathbf{E}_\alpha, \quad {}_{(l)}\Gamma := {}_{(l)}\Lambda^T {}_{(l)}\boldsymbol{\gamma}, \quad (4.2)$$

where the orthogonal two-point tensor ${}_{(l)}\Lambda$ had been defined in (2.6)–(2.7), and ${}_{(l)}\mathbf{n}$ and ${}_{(l)}\boldsymbol{\gamma}$ are the spatial contact force and spatial strain measure, respectively. For layer (l), we employ the constitutive relations¹²

$$\begin{aligned} {}_{(l)}\mathbf{N} &= {}_{(l)}\mathbf{D}({}_{(l)}\Gamma), \quad {}_{(l)}\mathbf{D} = {}_{(l)}D_\beta^\alpha \mathbf{E}_\alpha \otimes \mathbf{E}^\beta, \\ {}_{(l)}m &= {}_{(l)}D_3^3 {}_{(l)}\theta_{,S}, \end{aligned} \quad (4.3)$$

¹⁰ See Vu-Quoc and Ebcioglu (1993) for more details.

¹¹ See Vu-Quoc and Ebcioglu (1993) for more details.

¹² See, e.g., Chadwick (1976) or Marsden and Hughes (1983) for the tensor notation and rules of calculation. The matrix $[{}_{(l)}D_j^i] \in \mathbb{R}^{3 \times 3}$ in (4.4)–(4.5) has the representative element ${}_{(l)}D_j^i$ with the upper index i designates the row index, and the lower index j the column index.

$$[{}_{(l)}D_j^i] := \begin{bmatrix} {}_{(l)}EA & 0 & 0 \\ 0 & {}_{(l)}GA_s & 0 \\ 0 & 0 & {}_{(l)}EI \end{bmatrix} \in \mathbb{R}^{3 \times 3}, \quad (4.4)$$

or

$$[{}_{(l)}D_j^i] := \begin{bmatrix} \frac{2{}_{(l)}E_{(l)}h}{1 - {}_{(l)}\nu^2} & 0 & 0 \\ 0 & {}_{(l)}GA_s & 0 \\ 0 & 0 & \frac{2{}_{(l)}E_{(l)}h^3}{3(1 - {}_{(l)}\nu^2)} \end{bmatrix} \in \mathbb{R}^{3 \times 3}, \quad (4.5)$$

where for beams, ${}_{(l)}EA$, ${}_{(l)}GA_s$, and ${}_{(l)}EI$ denote the extensional stiffness, shear stiffness, and bending stiffness of layer (l) , respectively, whereas for plates, ${}_{(l)}E$ and ${}_{(l)}\nu$ are Young's modulus and Poisson's ratio of layer l . The effects of stretching, shearing, and bending are uncoupled in the above constitutive relations (4.3)–(4.5) as a result of choosing ${}_{(l)}\Phi_0$ to be the deformation map of the centroidal line of layer (l) .¹³ Of particular usefulness is the relation between the spatial contact force ${}_{(l)}\mathbf{n}$ and the five principal unknown functions u^1 , u^2 , ${}_{(1)}\theta$, ${}_{(2)}\theta$, and ${}_{(3)}\theta$ given by

$${}_{(l)}\mathbf{n} = {}_{(l)}\mathbf{A} {}_{(l)}\mathbf{D} {}_{(l)}\mathbf{A}^T {}_{(l)}\boldsymbol{\gamma}, \quad (4.6)$$

which are obtained from (4.1) and (4.3). The expressions for ${}_{(l)}\boldsymbol{\gamma}$, for $l = 1, 2, 3$, in terms of the five principal unknown functions are obtained from using definition (3.3)₁, together with the kinematic constraint equations (2.2)–(2.3), and relations (2.6)–(2.7) and (3.4). Finally, we recall, however, Remark 3.2 on the variable number of layers and the case of ply drop-off in multilayered structures accommodated by the present theory.

5 Approximated Equations of Motion

5.1 Infinitesimal Relative Rotations in Outer Layers.

In this section, the rotation ${}_{(2)}\theta$ of the core layer (2) remains finite, but the rotations of the outer layers (1) and (3) are assumed to be small relative to the core rotation ${}_{(2)}\theta$, i.e.,

$$|\psi_{2l}| = |{}_{(2)}\theta - {}_{(l)}\theta| \ll 1, \quad \cos \psi_{2l} \approx 1, \quad \sin \psi_{2l} \approx \psi_{2l}. \quad (5.1)$$

Also we shall assume that¹⁴

$${}_{(l)}\theta_{,s} \approx {}_{(2)}\theta_{,s}, \quad {}_{(l)}\dot{\theta} \approx {}_{(2)}\dot{\theta}, \quad {}_{(l)}\ddot{\theta} \approx {}_{(2)}\ddot{\theta}. \quad (5.2)$$

The five principal unknown functions are now u^1 , u^2 , ${}_{(2)}\theta$, ψ_{21} , and ψ_{23} . It follows from (5.1) that

$$\cos {}_{(l)}\theta = \cos ({}_{(2)}\theta - \psi_{2l}) \approx \cos {}_{(2)}\theta + \psi_{2l} \sin {}_{(2)}\theta, \quad (5.3)$$

$$\sin {}_{(l)}\theta = \sin ({}_{(2)}\theta - \psi_{2l}) \approx \sin {}_{(2)}\theta - \psi_{2l} \cos {}_{(2)}\theta, \quad (5.4)$$

and

$${}_{(l)}\mathbf{A} \approx [\mathcal{I} - \check{\boldsymbol{\psi}}_{2l}] {}_{(2)}\mathbf{A}, \quad \check{\boldsymbol{\psi}}_{2l} = \{\check{\psi}_{2l}\}_{\beta}^{\alpha} \mathbf{e}_{\alpha} \otimes \mathbf{e}^{\beta}, \quad (5.5)$$

$$[\{\check{\psi}_{2l}\}_{\beta}^{\alpha}] := \begin{bmatrix} 0 & -\psi_{2l} \\ \psi_{2l} & 0 \end{bmatrix},$$

$${}_{(l)}\mathbf{t}_{\alpha} \approx [\mathcal{I} - \check{\boldsymbol{\psi}}_{2l}] {}_{(2)}\mathbf{t}_{\alpha}, \quad (5.6)$$

¹³ i.e., we are restricting to the case where the centroid of a layer cross section coincides with the midpoint of that cross section.

¹⁴ It is important to realize that in general (5.2)₂ does not imply (5.2)₃, if the approximation is to remain consistent. Such case has been clearly illustrated in Vu-Quoc and Olsson (1993) (See Eqs. (2.3ab) and Remark 2.2 in the latter reference).

where \mathcal{I} designates the identity two-tensor $\mathcal{I} := \delta_{\beta}^{\alpha} \mathbf{e}_{\alpha} \otimes \mathbf{e}^{\beta}$ with δ_{β}^{α} being the Kronecker delta, and $\{\check{\psi}_{2l}\}_{\beta}^{\alpha}$ designates the component of the tensor $\check{\boldsymbol{\psi}}_{2l}$ along the basis tensor $\mathbf{e}_{\alpha} \otimes \mathbf{e}^{\beta}$. The approximation (5.6) will be used in (3.37)–(3.39) to obtain the approximated stiffness operators (left-hand sides) of the moment equations. Application of (2.2)–(2.3), (3.4)₂, and (3.3)₁ in (4.2)₂ yields the nonlinear expressions for the material strain measures

$${}_{(l)}\boldsymbol{\Gamma} = {}_{(l)}\mathbf{A}^T {}_{(l)}\boldsymbol{\Phi}_{0,s} - \mathbf{E}_1, \quad \text{for } l = 1, 2, 3, \quad (5.7)$$

$${}_{(1)}\boldsymbol{\Gamma} = {}_{(1)}\mathbf{A}^T [{}_{(2)}\boldsymbol{\Phi}_{0,s} + {}_{(2)}h {}_{(2)}\theta_{,s} {}_{(2)}\mathbf{t}_1] + ({}_{(1)}h {}_{(1)}\theta_{,s} - 1) \mathbf{E}_1, \quad (5.8)$$

$${}_{(3)}\boldsymbol{\Gamma} = {}_{(3)}\mathbf{A}^T [{}_{(2)}\boldsymbol{\Phi}_{0,s} - {}_{(2)}h {}_{(2)}\theta_{,s} {}_{(2)}\mathbf{t}_1] - ({}_{(3)}h {}_{(3)}\theta_{,s} + 1) \mathbf{E}_1, \quad (5.9)$$

which then lead to their approximated expressions by using (5.5)₁, (5.2)₁, and by noting the skew-symmetry $\check{\boldsymbol{\psi}}_{2l}^T = -\check{\boldsymbol{\psi}}_{2l}$,

$${}_{(1)}\boldsymbol{\Gamma} \approx {}_{(2)}\mathbf{A}^T [\mathcal{I} + \check{\boldsymbol{\psi}}_{21}] [{}_{(2)}\boldsymbol{\Phi}_{0,s} + {}_{(2)}h {}_{(2)}\theta_{,s} {}_{(2)}\mathbf{t}_1] + ({}_{(1)}h {}_{(2)}\theta_{,s} - 1) \mathbf{E}_1 =: {}_{(1)}\check{\boldsymbol{\Gamma}}, \quad (5.10)$$

$${}_{(3)}\boldsymbol{\Gamma} \approx {}_{(2)}\mathbf{A}^T [\mathcal{I} + \check{\boldsymbol{\psi}}_{23}] [{}_{(2)}\boldsymbol{\Phi}_{0,s} - {}_{(2)}h {}_{(2)}\theta_{,s} {}_{(2)}\mathbf{t}_1] - ({}_{(3)}h {}_{(2)}\theta_{,s} + 1) \mathbf{E}_1 =: {}_{(3)}\check{\boldsymbol{\Gamma}}. \quad (5.11)$$

The approximated constitutive laws (4.6) and (4.3)–(4.5) now take the following form:

$${}_{(l)}\mathbf{n} \approx [\mathcal{I} - \check{\boldsymbol{\psi}}_{2l}] {}_{(2)}\mathbf{A} {}_{(l)}\mathbf{D} {}_{(l)}\check{\boldsymbol{\Gamma}}, \quad (5.12)$$

$${}_{(l)}\mathbf{m} \approx {}_{(l)}EI {}_{(2)}\theta_{,s}. \quad (5.13)$$

Relations (5.12)–(5.13) are intended for the outer layers (1) and (3). If one introduces, however, the identity ${}_{(2)}\check{\boldsymbol{\Gamma}} \equiv {}_{(2)}\boldsymbol{\Gamma}$, then expressions (5.12)–(5.13) are also valid for the core layer (2) since $\psi_{22} = 0$; hence, the approximation in (5.12)–(5.13) becomes exact equality for the core layer (2). It is now easy to obtain the approximated stiffness operators (left-hand sides) of the equations of motion (3.36)–(3.39) by using the above approximations for the layer resultant forces/couples.

Remark 5.1. Note the consistent approximation in (5.3)–(5.4): The approximation (5.1) is only applied *after* the expansion of the trigonometric functions in (5.3)–(5.4). Also the results as in (5.10)–(5.11), had approximation been introduced first in ${}_{(l)}\boldsymbol{\gamma}$ to obtain

$${}_{(1)}\boldsymbol{\gamma} \approx {}_{(2)}\boldsymbol{\Phi}_{0,s} + [({}_{(1)}h {}_{(2)}\theta_{,s} - 1) [\mathcal{I} - \check{\boldsymbol{\psi}}_{21}] + {}_{(2)}h {}_{(2)}\theta_{,s} \mathcal{I}] {}_{(2)}\mathbf{t}_1 =: {}_{(1)}\check{\boldsymbol{\gamma}}, \quad (5.14)$$

$${}_{(3)}\boldsymbol{\gamma} \approx {}_{(2)}\boldsymbol{\Phi}_{0,s} - [({}_{(3)}h {}_{(2)}\theta_{,s} + 1) [\mathcal{I} - \check{\boldsymbol{\psi}}_{23}] + {}_{(2)}h {}_{(2)}\theta_{,s} \mathcal{I}] {}_{(2)}\mathbf{t}_1 =: {}_{(3)}\check{\boldsymbol{\gamma}}, \quad (5.15)$$

which were then used to obtain an approximation for ${}_{(l)}\boldsymbol{\Gamma}$ with the aid of (5.5)₁, i.e., ${}_{(2)}\mathbf{A}^T [\mathcal{I} + \check{\boldsymbol{\psi}}_{2l}] {}_{(l)}\check{\boldsymbol{\gamma}}$; such result is not consistent with the expressions for ${}_{(1)}\boldsymbol{\Gamma}$ and ${}_{(3)}\boldsymbol{\Gamma}$ in (5.10)–(5.11). ■

We now turn our attention to the inertia terms, and consider first the inertia force \mathbf{f} in (3.31). Using (5.6) in (3.14)₂, together with the approximation (5.2), we have

$${}_{(l)}\ddot{\mathbf{t}}_2 \approx -[\mathcal{I} - \check{\boldsymbol{\psi}}_{2l}] [{}_{(2)}\ddot{\theta} {}_{(2)}\mathbf{t}_1 + ({}_{(2)}\dot{\theta})^2 {}_{(2)}\mathbf{t}_2] = [\mathcal{I} - \check{\boldsymbol{\psi}}_{2l}] {}_{(2)}\ddot{\mathbf{t}}_2, \quad (5.16)$$

which then leads to the approximated inertia force

$$\mathbf{f} \approx \widehat{A}_\rho^0 \ddot{\mathbf{u}} + [A_\rho^1 \mathcal{F} - {}_{(2)}h_{(1)}A_\rho^0 + {}_{(1)}A_\rho^1] \ddot{\psi}_{21} + [{}_{(2)}h_{(3)}A_\rho^0 - {}_{(3)}A_\rho^1] \ddot{\psi}_{23} {}_{(2)}\mathbf{t}_2, \quad (5.17)$$

where \widehat{A}_ρ^k is defined as follows:

$$\widehat{A}_\rho^k := \sum_{l=1}^3 {}_{(l)}A_\rho^k. \quad (5.18)$$

Next we look at the approximated inertia couples. As a result of (5.1)–(5.2), the relations (3.27)–(3.30) are approximated by

$$\ddot{\mathbf{u}} \cdot {}_{(l)}\mathbf{t}_1 \approx \ddot{\mathbf{u}} \cdot [{}_{(2)}\mathbf{t}_1 - \psi_{2l(2)}\mathbf{t}_2], \quad (5.19)$$

$${}_{(l)}\ddot{\mathbf{t}}_2 \cdot {}_{(l)}\mathbf{t}_1 \approx -{}_{(2)}\ddot{\theta}, \quad (5.20)$$

$${}_{(l)}\ddot{\mathbf{t}}_2 \cdot {}_{(2)}\mathbf{t}_1 \approx -[{}_{(l)}\ddot{\theta} + ({}_{(l)}\dot{\theta})^2 \psi_{2l}], \quad (5.21)$$

$${}_{(2)}\ddot{\mathbf{t}}_2 \cdot {}_{(l)}\mathbf{t}_1 \approx -[{}_{(2)}\ddot{\theta} - ({}_{(2)}\dot{\theta})^2 \psi_{2l}]. \quad (5.22)$$

Application of (5.2)₃ and (5.19)–(5.22) in (3.32)–(3.34) yields the following approximated inertia couples:

$${}_{(1)}C \approx [{}_{(2)}h_{(1)}A_\rho^1 + {}_{(1)}A_\rho^2] {}_{(2)}\ddot{\theta} - [{}_{(2)}h_{(1)}A_\rho^0 + {}_{(1)}A_\rho^1] [\ddot{\mathbf{u}} \cdot {}_{(1)}\mathbf{t}_1 - {}_{(2)}h_{(2)}(\dot{\theta})^2 \psi_{21}], \quad (5.23)$$

$${}_{(2)}C \approx [-{}_{(2)}h_{(1)}A_\rho^1 + {}_{(2)}A_\rho^2 + {}_{(2)}h_{(3)}A_\rho^1] {}_{(2)}\ddot{\theta} + [{}_{(2)}h_{(1)}A_\rho^0 - {}_{(2)}A_\rho^1 - {}_{(2)}h_{(3)}A_\rho^0] (\ddot{\mathbf{u}} \cdot {}_{(2)}\mathbf{t}_1) - {}_{(2)}h [{}_{(2)}h_{(1)}A_\rho^0 + {}_{(1)}A_\rho^1] ({}_{(2)}\dot{\theta})^2 \psi_{21} - {}_{(2)}h [{}_{(2)}h_{(3)}A_\rho^0 - {}_{(3)}A_\rho^1] ({}_{(2)}\dot{\theta})^2 \psi_{23}, \quad (5.24)$$

$${}_{(3)}C \approx [-{}_{(2)}h_{(3)}A_\rho^1 + {}_{(3)}A_\rho^2] {}_{(2)}\ddot{\theta} + [{}_{(2)}h_{(3)}A_\rho^0 - {}_{(1)}A_\rho^1] [\ddot{\mathbf{u}} \cdot {}_{(3)}\mathbf{t}_1 + {}_{(2)}h_{(2)}(\dot{\theta})^2 \psi_{23}]. \quad (5.25)$$

Clearly, to express (5.23)–(5.25) completely in terms of the five unknown functions u^1 , u^2 , ${}_{(2)}\theta$, ψ_{21} , and ψ_{23} , we need to use (5.19) and (2.6)–(2.7).

Remark 5.2. For a symmetric sandwich beam such that

$${}_{(1)}A_\rho^0 = {}_{(3)}A_\rho^0, \quad {}_{(1)}A_\rho^1 = -{}_{(3)}A_\rho^1, \quad {}_{(2)}A_\rho^1 = 0, \quad (5.26)$$

the inertia force \mathbf{f} and inertia couple ${}_{(2)}C$ can be significantly simplified; see Vu-Quoc and Ebcioğlu (1993) for more details. ■

5.2 All Infinitesimal Rotations: Linearized Equations.

In this section, all rotations angles are assumed small such that $|\theta_l| \ll 1$, $\cos \theta_l \approx 1$, and $\sin \theta_l \approx \theta_l$, for $l = 1, 2, 3$. The five principal unknown functions are the usual u^1 , u^2 , ${}_{(1)}\theta$, ${}_{(2)}\theta$, and ${}_{(3)}\theta$. We will neglect all nonlinear terms, and retain only the linear terms in a consistent manner. Thus using

$${}_{(l)}\mathbf{A}^T {}_{(2)}\theta_{,S} {}_{(2)}\mathbf{t}_1 \approx {}_{(2)}\theta_{,S} \mathbf{E}_1, \quad (5.27)$$

$${}_{(l)}\mathbf{A}^T {}_{(2)}\Phi_{0,S} \approx [1 + u_{,S}^1] \mathbf{E}_1 + [-{}_{(l)}\theta + u_{,S}^2] \mathbf{E}_2, \quad (5.28)$$

in expressions (5.7)–(5.9) for ${}_{(l)}\Gamma = {}_{(l)}\Gamma^\alpha \mathbf{E}_\alpha$, we obtain

$${}_{(1)}\Gamma \approx [u_{,S}^1 + {}_{(1)}h_{(1)}\theta_{,S} + {}_{(2)}h_{(2)}\theta_{,S}] \mathbf{E}_1 + [-{}_{(1)}\theta + u_{,S}^2] \mathbf{E}_2 =: {}_{(1)}\check{\Gamma}, \quad (5.29)$$

$${}_{(2)}\Gamma \approx [u_{,S}^1 \mathbf{E}_1 + [-{}_{(2)}\theta + u_{,S}^2] \mathbf{E}_2] =: {}_{(2)}\check{\Gamma}, \quad (5.30)$$

$${}_{(3)}\Gamma \approx [u_{,S}^1 - {}_{(2)}h_{(2)}\theta_{,S} - {}_{(3)}h_{(3)}\theta_{,S}] \mathbf{E}_1 + [-{}_{(3)}\theta + u_{,S}^2] \mathbf{E}_2 =: {}_{(3)}\check{\Gamma}. \quad (5.31)$$

Since the expressions for ${}_{(l)}\check{\Gamma}$, for $l = 1, 2, 3$, contain only the five principal unknown functions and their derivatives, and since

we neglect all nonlinear terms in this section, it follows from (4.6) that

$${}_{(l)}\mathbf{n} \approx {}_{(l)}\mathbf{D} {}_{(l)}\check{\Gamma}. \quad (5.32)$$

The constitutive law for the moment ${}_{(l)}m$ remains identical to (4.3)₃.

It follows from (3.14)₂ that ${}_{(l)}\check{\mathbf{t}}_2 \approx -{}_{(l)}\ddot{\theta} \mathbf{e}_1$; it is then easy to obtain the linearization of the inertia force \mathbf{f} given in (3.31), which we omit here. The equation of balance of linear momentum has identical form as that in (3.36).

Remark 5.3. For a symmetric sandwich beam such that (5.26) holds, the linearized inertia force is approximated by

$$\mathbf{f} \approx \widehat{A}_\rho^0 \ddot{\mathbf{u}} + [{}_{(2)}h_{(1)}A_\rho^0 + {}_{(1)}A_\rho^1] ({}_{(3)}\ddot{\theta} - {}_{(1)}\ddot{\theta}) \mathbf{e}_1. \quad (5.33)$$

Clearly, if it is assumed that ${}_{(1)}\theta = {}_{(3)}\theta$ as in Yu (1959), then

$$(5.33) \text{ simply becomes } {}^{15} \mathbf{f} \approx \widehat{A}_\rho^0 \ddot{\mathbf{u}}. \quad \blacksquare$$

Next, consider the equations for balance of angular momentum (3.37)–(3.39). Using the following approximations,

$${}_{(2)}\Phi_{0,S} \times {}_{(l)}\mathbf{n} \approx {}_{(l)}n^2, \quad (5.34)$$

$$({}_{(l)}\mathbf{n} \cdot {}_{(l)}\mathbf{t}_1)_{,S} \approx {}_{(l)}n_{,S}^1, \quad (5.35)$$

$$({}_{(1)}\mathbf{n}_{,S} - {}_{(3)}\mathbf{n}_{,S}) \cdot {}_{(2)}\mathbf{t}_1 \approx {}_{(1)}n_{,S}^1 - {}_{(3)}n_{,S}^1, \quad (5.36)$$

and neglecting all nonlinear terms in the stiffness operators, we obtain the linearized equations of balance of angular momentum

$${}_{(1)}m_{,S} + {}_{(1)}n^2 + {}_{(1)}h_{(1)}n_{,S}^1 + {}_{(1)}\overline{M} = {}_{(1)}\check{C}, \quad (5.37)$$

$${}_{(2)}m_{,S} + {}_{(2)}n^2 + {}_{(2)}h_{(1)}n_{,S}^1 - {}_{(3)}n_{,S}^1 + {}_{(2)}\overline{M} = {}_{(2)}\check{C}, \quad (5.38)$$

$${}_{(3)}m_{,S} + {}_{(3)}n^2 - {}_{(3)}h_{(3)}n_{,S}^1 + {}_{(3)}\overline{M} = {}_{(3)}\check{C}, \quad (5.39)$$

where ${}_{(l)}\check{C}$ are the linearized inertia couples to be discussed below. The approximated expressions corresponding to (3.27), (3.29), and (3.30) are

$$\ddot{\mathbf{u}} \cdot {}_{(l)}\mathbf{t}_1 \approx \ddot{u}^1, \quad (5.40)$$

$${}_{(l)}\ddot{\mathbf{t}}_2 \cdot {}_{(2)}\mathbf{t}_1 \approx -{}_{(l)}\ddot{\theta}, \quad (5.41)$$

$${}_{(2)}\ddot{\mathbf{t}}_2 \cdot {}_{(l)}\mathbf{t}_1 \approx -{}_{(2)}\ddot{\theta}. \quad (5.42)$$

Using (5.40)–(5.42) in (3.32)–(3.34), we obtain

$${}_{(1)}\check{C} := [({}_{(2)}h)^2 {}_{(1)}A_\rho^0 + 2 {}_{(2)}h_{(1)}A_\rho^1 + {}_{(1)}A_\rho^2] {}_{(1)}\ddot{\theta} - [{}_{(2)}h_{(1)}A_\rho^0 + {}_{(1)}A_\rho^1] [\ddot{u}^1 + {}_{(2)}h_{(2)}\ddot{\theta}] \approx {}_{(1)}C, \quad (5.43)$$

$${}_{(2)}\check{C} := [({}_{(2)}h)^2 {}_{(1)}A_\rho^0 + {}_{(2)}A_\rho^2 + ({}_{(2)}h)^2 {}_{(3)}A_\rho^0] {}_{(2)}\ddot{\theta} + [{}_{(2)}h_{(1)}A_\rho^0 - {}_{(2)}A_\rho^1 - {}_{(2)}h_{(3)}A_\rho^0] \ddot{u}^1 - {}_{(2)}h [{}_{(2)}h_{(1)}A_\rho^0 + {}_{(1)}A_\rho^1] {}_{(1)}\ddot{\theta} - {}_{(2)}h [{}_{(2)}h_{(3)}A_\rho^0 - {}_{(3)}A_\rho^1] {}_{(3)}\ddot{\theta} \approx {}_{(2)}C, \quad (5.44)$$

$${}_{(3)}\check{C} := [({}_{(2)}h)^2 {}_{(3)}A_\rho^0 - 2 {}_{(2)}h_{(3)}A_\rho^1 + {}_{(3)}A_\rho^2] {}_{(3)}\ddot{\theta} + [{}_{(2)}h_{(3)}A_\rho^0 - {}_{(3)}A_\rho^1] [\ddot{u}^1 - {}_{(2)}h_{(2)}\ddot{\theta}] \approx {}_{(3)}C. \quad (5.45)$$

Remark 5.4. If we further assume that ${}_{(1)}\theta = {}_{(3)}\theta$ and consider symmetric sandwich cross section such that (5.26) holds as in Yu (1959), the inertia couple ${}_{(2)}\check{C}$ in (5.44) becomes

$${}_{(2)}\check{C} = [2({}_{(2)}h)^2 {}_{(1)}A_\rho^0 + {}_{(2)}A_\rho^2] {}_{(2)}\ddot{\theta} - 2 {}_{(2)}h [{}_{(2)}h_{(1)}A_\rho^0 + {}_{(1)}A_\rho^1] {}_{(1)}\ddot{\theta}. \quad (5.46)$$

¹⁵ And the linearized equation of balance of linear momentum for the shear force n^2 agrees with equation (13) in Yu (1959).

Equation of motion (5.38) for the core layer (2)—together (5.46)—is identically the same as Eq. (11) in Yu (1959).¹⁶

We emphasize, however, that the absence of the acceleration \ddot{u}^1 in (5.46) is a result of the symmetry—in both geometry and mass distribution—of the cross section; this symmetry reduces to zero the multiplicative factor of \ddot{u}^1 in (5.44). That $u^1 \neq 0$ —and therefore $\ddot{u}^1 \neq 0$ —in our formulation stands in contrast to the assumption $u^1 \equiv 0$ introduced at the outset as in Yu (1959).¹⁷ Consequently, the above results for ${}_{(1)}\tilde{C}$ —relations (5.43)–(5.45) and (5.46)—which indicate a clear coupling with the axial motion u^1 even for symmetric cross section, are exact.

On the other hand, it can be seen easily from (5.43) and (5.45) that

$${}_{(1)}\tilde{C} + {}_{(3)}\tilde{C} = 2[{}_{(2)}h]{}_{(1)}A_p^0 + 2{}_{(2)}h{}_{(1)}A_p^1 + {}_{(1)}A_p^2]{}_{(1)}\ddot{\theta} - 2{}_{(2)}h[{}_{(2)}h{}_{(1)}A_p^0 + {}_{(1)}A_p^1]{}_{(2)}\ddot{\theta} \quad (5.47)$$

does not depend on \ddot{u}^1 , and hence the inertia couple of the global moment equation in the sense defined in (3.49),

$$\tilde{C} := \sum_{i=1}^3 {}_{(i)}\tilde{C} = 2[{}_{(2)}h{}_{(1)}A_p^1 + {}_{(1)}A_p^2]{}_{(1)}\ddot{\theta} + [-2{}_{(2)}h{}_{(1)}A_p^1 + {}_{(2)}A_p^2]{}_{(2)}\ddot{\theta} \quad (5.48)$$

is also uncoupled with the axial motion u^1 . Recall from Remark 5.3 that under the assumption of symmetric cross section and ${}_{(1)}\theta = {}_{(3)}\theta$, the inertia force \mathbf{f} is uncoupled with the rotations—even in the case of finite core rotation ${}_{(2)}\theta$. This remark suggests that the set of equations of motion having complete uncoupled inertia forces and couples, and *without* having to assume $u^1 = 0$, comprises equations (i) (3.36) with inertia force $\mathbf{f} = \hat{A}_p^0 \ddot{\mathbf{u}}$, (ii) (5.38) with inertia couple (5.46), and (iii-a) the sum of (5.37) and (5.39) (i.e., layer (1) and layer (3)) with inertia couple (5.47), or (iii-b) the sum of (5.37)–(5.39) (global moment equations for all three layers) with inertia couple (5.48).¹⁸ ■

6 Closure

We have successfully formulated a Galerkin projection of the equations developed herein; this formulation and the numerical results are presented in Vu-Quoc and Deng (1995), where also discussed is the analysis of the important class of structures with variable number of layers and with ply drop-off. For shell structures, a formulation for geometrically exact multilayered shells using the methodology employed above can be found in Vu-Quoc and Ebcioğlu (1995).

Acknowledgments

The research is supported by a grant from the National Science Foundation. This support is appreciated. The authors also thank Mr. H. Deng for his comments on the formulation.

¹⁶ To facilitate the comparison for the reader, we first note that the sign convention for the moment employed in Yu (1959) is the reverse of ours and that of Plantema (1966). Also, the relationship between our notation and the one in Yu (1959) is as follows: ${}_{(1)}A_p^0 = \rho_2 h_2$, ${}_{(1)}A_p^1 = -\rho_2 [h^2 - (h_1)^2]/2$, ${}_{(2)}A_p^2 = \rho_1 (h_1)^3/3$, ${}_{(2)}\theta = \psi_1$, and ${}_{(1)}\theta = {}_{(3)}\theta = \psi_2$.

¹⁷ See Eq. (3)₁ in Yu (1959).

¹⁸ The resulting global moment (iii-b) is identical to Eq. (10) in Yu (1959).

References

- Alberts, T. E., 1993, "Dynamic Analysis to Evaluate Viscoelastic Passive Damping Augmentation for the Space Shuttle Remote Manipulator System," *ASME Journal of Dynamic Systems, Measurements, and Control*, Vol. 114, pp. 468–475.
- Chadwick, P., 1976, *Continuum Mechanics*, John Wiley and Sons, New York.
- Chia, C., 1988, "Geometrically nonlinear behavior of composite plates: A review," *ASME Applied Mechanics Review*, Vol. 41, pp. 439–450.
- Danielson, D. A., and Hodges, D. H., 1988, "A Beam Theory for Large Global Rotation, Moderate Local Rotation, and Small Strain," *ASME JOURNAL OF APPLIED MECHANICS*, Vol. 55, pp. 179–184.
- Dubbelday, P. S., 1993, "Constrained-layer damping analysis for extensional waves in infinite, fluid-loaded plates," *The Journal of the Acoustical Society of America*, Vol. 93, pp. 1927–1935.
- Evschik, Y. B., 1989, "Equations of vibrations of multilayer piezoceramic shells with tangential polarization," *Soviet Applied Mechanics*, Vol. 24, No. 8, pp. 758–763.
- Kamman, J. W., and Huston, R. L., 1984, "Dynamics of Constrained Multibody Systems," *ASME JOURNAL OF APPLIED MECHANICS*, Vol. 51, pp. 889–903.
- Marsden, J. E., and Hughes, T. J. R., 1983, *Mathematical Foundations of Elasticity*, Prentice-Hall, Englewood Cliffs, NJ.
- Plantema, J., 1966, *Sandwich Construction*, John Wiley and Sons, New York.
- Rao, M. D., 1993, "Dynamic analysis and design of laminated composite beams with multiple damping layers," *AIAA Journal*, Vol. 31, pp. 736–745.
- Simo, J. C., and Vu-Quoc, L., 1986, "On the dynamics of flexible beams under large overall motions—The plane case: Parts I and II," *ASME JOURNAL OF APPLIED MECHANICS*, Vol. 53, pp. 849–863.
- Simo, J. C., and Vu-Quoc, L., 1991, "A geometrically-exact beam model incorporating torsion shear and torsion warping deformation," *International Journal of Solids and Structures*, Vol. 27, pp. 371–393.
- Sirkis, J. S., 1993, "Unified approach to phase-strain-temperature models for smart structure interferometric optical fiber sensors: Applications," *Optical Engineering*, Vol. 32, pp. 762–773.
- Sung, C. K., Thompson, B. S., Crowley, P., and Cuccio, J., 1986, "An experimental study to demonstrate the superior response characteristics of mechanisms constructed with composite laminates," *Mechanism and Machine Theory*, Vol. 21, No. 2, pp. 109–119.
- Thompson, B. S., 1987, "Composite laminate components for robotic and machine systems: Research issues in design," *ASME Applied Mechanics Review*, Vol. 40, pp. 1545–1552.
- Thompson, B. S., and Sung, C. K., 1986, "An analytical and experimental investigation of high-speed mechanisms fabricated with composite laminates," *Journal of Sound and Vibration*, Vol. 111, pp. 399–428.
- Toledano, A., and Murakami, H., 1987, "A Composite Plate Theory for Arbitrary Laminate Configurations," *ASME JOURNAL OF APPLIED MECHANICS*, Vol. 54, 181–189.
- Tzou, H. S., 1989, "Theoretical analysis of a multi-layered thin shell coupled with piezoelectric shell actuators for distributed vibration controls," *Journal of Sound and Vibration*, Vol. 132, pp. 433–450.
- Vu-Quoc, L., 1986, "Dynamics of Flexible Structures Performing Large Overall Motions: A Geometrically-Nonlinear Approach," PhD thesis, University of California at Berkeley, Berkeley, CA; Electronics Research Laboratory, Memorandum No. UCB/ERL M86/36.
- Vu-Quoc, L., and Deng, H., 1995, "Galerkin Projection for Geometrically-Exact Multilayered Beams Allowing for Ply Drop-Off," *ASME JOURNAL OF APPLIED MECHANICS*, Vol. 62, pp. 479–488.
- Vu-Quoc, L., and Ebcioğlu, I. K., 1993, "Dynamic formulation for flexible multibody geometrically exact sandwich beams/1-D plates," Technical Report AeMES-TR-93-3-02, Aerospace Engineering, Mechanics and Engineering Science, University of Florida, Gainesville, FL.
- Vu-Quoc, L., and Ebcioğlu, I. K., 1995, "Formulation of equations of motion for multilayered geometrically-exact shells accommodating large deformation and large overall motions," to be submitted.
- Vu-Quoc, L., and Olsson, M., 1993, "High-Speed Vehicle Models Based on a New Concept of Vehicle/Structure Interaction Component. Part I: Formulation," *ASME Journal of Dynamic Systems, Measurements, and Control*, Vol. 115, pp. 140–147.
- Yu, Y., 1959, "A New Theory of Elastic Sandwich Plates: One Dimensional Case," *ASME JOURNAL OF APPLIED MECHANICS*, Vol. 26, 415–421.
- Yu, Y., 1989, "Dynamics and vibration of layered plates and shells—A perspective from sandwiches to laminated composites," in *AIAA/ASCE/AHS/ASC 30th Structures, Structural Dynamics, and Materials Conference*, Mobile, AL, Vol. 4.

On the Instability Mechanisms of a Disk Rotating Close to a Rigid Surface¹

F. Y. Huang
Research Assistant,
Assoc. Mem. ASME.

C. D. Mote
FANUC Chair of Mechanical Systems,
and Vice Chancellor,
Fellow ASME.

Department of Mechanical Engineering,
University of California,
Berkeley, CA 94720

The instability mechanisms of a rotating disk, coupled to a rigid surface through a viscous fluid film at the interface, are investigated analytically. The fluid in the film is driven circumferentially by the viscous shear, and it flows outwards radially under centrifugal forces. The circumferential flow component creates an equivalent viscous damping rotating at one half the disk rotation speed. This film damping dissipates all backward traveling waves where the undamped wave speeds are greater than one half the disk rotation speed. The radial flow component creates a nonsymmetric stiffness in the disk-film system that energizes any wave mode at rotation speeds above its flutter speed. Instabilities in the disk-film system are of two types. A rotating damping instability is caused by the rotating film damping at rotation speeds above a critical value that is less than the flutter speed. A combination instability is caused by the combined effect of the film stiffness and damping at rotation speeds above a threshold that is greater than the flutter speed. The maximum rotation speed of stable disk vibration is bounded above by the lowest onset speed of rotating damping instability. This speed limit is predicted for two wall enclosure designs. The maximum stable rotation speed of a 5.25-inch diameter flexible, memory disk, separated from a rigid surface by a viscous air film, is shown to be more than 15 times greater than the maximum speed of the disk without the air film.

1 Introduction

The stability of a spinning disk remains a research topic of great interest because of the development of computer memory disks. The strong demands for high data access rates and high reliability require small transverse vibration of the disk at high rotation speeds. Transverse instability of the disk can be excited by a "sliding" transverse follower like the read/write head in a computer disk drive. Modeling this sliding force as either a constant or a spring-mass-dashpot suggests that the disk vibration is stable only at rotation speeds lower than the critical speed (Mote, 1970; Iwan and Stahl, 1973; Iwan and Moeller, 1976; Shen and Mote, 1991).

The critical speed is the lowest speed at which the propagation speed of a backward traveling circumferential wave mode equals the disk rotational speed. Moreover, D'Angelo and Mote (1993) showed that a single rotating disk, without an imposed transverse force, can be excited aerodynamically to moderate amplitude at supercritical speed and to large amplitude at speeds above a flutter onset speed that is much larger than the critical speed.

Although the surrounding air can energize the disk, it can also stabilize disk vibration if the enclosure is designed properly. Yasuda and Kaneko (1987) found in experiments that a membrane-like disk can operate in a stable manner at speeds much greater than the critical speed if it rotates very close to a rigid plane. Disk flutter did not occur in their experiments. A viscous fluid film, formed in the 0.1 mm gap between the disk and the plane, can stiffen the disk and dissipate vibration energy. The coupled system of the viscous film and disk was first investigated by Pelech and Shapiro (1964). They found the equilibrium film thickness is approximately proportional to $r^{-2/3}$ at high rotation speeds. Recently, the static, coupled system problem has been studied by Bogy and Talke (1978), Greenberg (1978), Adams (1980), Carpino and Domoto (1988), and others.

Adams (1987) predicted the maximum speed limit of the coupled system through calculation of the disk critical speed. He represented the effect of the film on the disk by a distributed linear spring with stiffness dependent on radius.

¹The authors would like to thank the National Science Foundation, Computer Mechanics Laboratory, and the author's industrial sponsors for their support and interest in this work.

Contributed by the Applied Mechanics Division of THE AMERICAN SOCIETY OF MECHANICAL ENGINEERS for presentation at the Joint Applied Mechanics and Materials Summer Meeting of the ASME, Los Angeles, CA, June 28-30, 1995.

Discussion on this paper should be addressed to the Technical Editor, Professor Lewis T. Wheeler, Department of Mechanical Engineering, University of Houston, Houston, TX 77204-4792, and will be accepted until four months after final publication of the paper itself in the JOURNAL OF APPLIED MECHANICS.

Manuscript received by the ASME Applied Mechanics Division, Feb. 21, 1994; final revision, Oct. 31, 1994. Associate Technical Editor: T. R. Akylas.

Paper No. 95-APM-9.

The nonsymmetric stiffness and the rotating damping generated in the viscous film were not modeled. Yasuda and Kaneko (1987) showed experimentally that the peak to peak vibration amplitude of the disk decreases as disk rotation speed increases and as the initial film thickness decreases. However, no theoretical analysis or physical explanation were provided.

Hosaka and Crandall (1992) first dealt with this subject theoretically. They used a single-mode approximation to estimate the maximum stable operating speed of the disk. The single-mode analysis reduced the disk-film system to one homogeneous linear algebraic equation, which has a form identical to the characteristic equation governing wave propagation of an axially moving beam subjected to axially moving damping. In their beam-damping model, the film coupling is equivalent to combination of an elastic foundation and a moving damping. The moving damping can energize the system under certain conditions. The onset speed of instability predicted was close to the speed obtained from more accurate numerical procedures. They neglected the film stiffness and calculated a lower bound to the maximum stable rotation speed. The instability they observed is called the rotating damping instability in this paper.

Huang and Mote (1995a) concluded that the viscous fluid in a thin film between two translating surfaces can be modeled as damping translating at the mean flow speed in the film, and that this translating damping does not dissipate energy at all times. It will be shown here that the mechanics of the film between the disk and the rigid surface, where the circumferential mean flow in the film creates a force equivalent to a rotating, viscous damping, is similar to that in Huang and Mote (1995a). Huang and Mote (1995b) showed that stability of a rotating disk under rotating, positive-definite damping can be predicted using the wave speeds in the undamped disk (termed the *undamped wave speeds* in the sequel). Vibration energy in a backward, circumferentially propagating wave is dissipated by the rotating damping until the speed of the damping relative to the disk exceeds the undamped wave speed. The terms "backward" and "wave speed" in the above statement, and in the sequel, characterize the propagation direction and speed of a wave when observed from the disk reference.

This paper presents an analytical investigation of instability mechanisms in the coupled film-disk system. A modified Reynolds equation, governing the fluid film response, is derived that includes contribution of the fluid centrifugal inertia. The static pressure in the film, induced by disk rotation, is used to predict the disk equilibrium shape. The dynamic pressure in the film, induced by disk vibration, couples the film and disk. The mechanics of the film and the instability mechanisms of the film-disk system are identified. The circumferential flow component in the film creates an equivalent positive-definite damping, and the radial flow component creates nonsymmetric stiffness. Two types of instability are observed: rotating damping instability is caused by film damping which underpins the observation in Hosaka and Crandall (1992); and combination instability is caused by the combined effect of nonsymmetric film stiffness and film damping. Because the static problem has been investigated thoroughly (Benson and Takahashi, 1991), two particular film designs are investigated where the equilibrium shape of the disk is flat.

2 Modeling

Consider a vibrating, flexible, circular disk rotating close to a stationary, rigid surface as shown in Fig. 1. Air flows freely into, or out of, the gap between the disk and the rigid wall at both the disk inner radius through the clearance between the hub and the wall and the outer rim. The film thickness

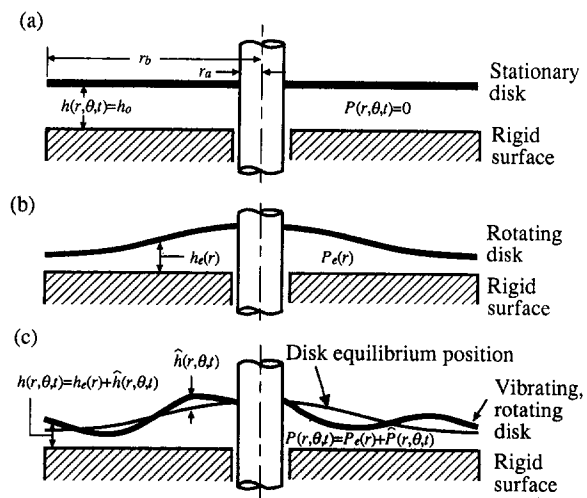


Fig. 1 Schematics of a disk rotating close to a rigid surface, and three states of the coupled disk-film system. (a) stationary state S_0 : the disk is neither rotating nor vibrating; (b) equilibrium state S_e : the disk rotates without vibration; (c) perturbed state S_p : the disk vibrates while rotating.

between the two surfaces, $h(r, \theta, t)$, is sufficiently small that the viscous forces in the film dominate all fluid inertial forces, except the centrifugal inertial force which is of central importance to the flow in the film at high speeds. Figure 1(a) depicts the stationary state S_0 where the disk neither rotates nor vibrates. The film thickness is h_0 (constant), and the film pressure is ambient. When the disk rotates at a constant speed Ω without vibration, the equilibrium pressure $P_e(r)$, generated by the flow under disk rotation, deforms the disk into an equilibrium shape with film thickness $h_e(r)$. This equilibrium state S_e is shown in Fig. 1(b). When perturbed from S_e , the disk vibrates transversely with amplitude $\hat{h}(r, \theta, t)$ measured from $h_e(r)$, and the corresponding film pressure variation $\hat{P}(r, \theta, t)$ is the deviation from $P_e(r)$ (see Fig. 1(c)). $\hat{P}(r, \theta, t)$ couples dynamically the film and the disk.

The fluid film model is developed under the assumptions: (i) the fluid is Newtonian, and the flow is laminar and incompressible; (ii) the viscosity is constant, and thermal effects are neglected; (iii) the no slip condition is satisfied on both surfaces; (iv) all fluid inertial forces, except the centrifugal forces, are negligible compared to the viscous forces; (v) film pressure variations across film thickness are negligible compared to variations in the in-plane.

Assumptions (iv) and (v) are deduced from the orders of magnitude of terms in the Navier-Stokes equations in cylindrical coordinates when the modified Reynolds number ($Re = \rho\Omega h_0^2/\mu$, where ρ and μ are density and viscosity of air) is much smaller than one (Walowit and Anno, 1975). The centrifugal forces energize secondary flow in the radial direction, especially at high speeds. This flow will be shown to have major effect on disk vibration. Under the above assumptions the Navier-Stokes equations reduce to

$$-\rho \frac{v_\theta^2}{r} = -\frac{\partial P}{\partial r} + \mu \frac{\partial^2 v_r}{\partial z^2} \quad (1a)$$

$$0 = -\frac{\partial P}{\partial \theta} + \mu \frac{\partial^2 v_\theta}{\partial z^2} \quad (1b)$$

$$0 = \frac{\partial P}{\partial z} \quad (1c)$$

and the continuity equation is

² θ is a space-fixed coordinate.

$$\frac{1}{r} \frac{\partial}{\partial r} (rv_r) + \frac{1}{r} \frac{\partial v_\theta}{\partial \theta} + \frac{\partial v_z}{\partial z} = 0 \quad (2)$$

where $P(r, \theta, t) = P_e(r) + \hat{P}(r, \theta, t)$ is pressure in the film, and v_r , v_θ , and v_z are velocity components in the radial, circumferential, and transverse directions. The boundary conditions of the fluid film are

$$v_r = 0, \quad v_\theta = r\Omega, \quad v_z = \frac{\partial h}{\partial t} + \Omega \frac{\partial h}{\partial \theta} \quad \text{at } z = h \quad (3a)$$

$$v_r = 0, \quad v_\theta = 0, \quad v_z = 0 \quad \text{at } z = 0 \quad (3b)$$

$$P = 0, \quad \text{at } r = r_a, r_b. \quad (3c)$$

The disk is modeled as a classical rotating plate under distributed film pressure,

$$\rho_d H \left(\frac{\partial^2 h}{\partial t^2} + 2\Omega \frac{\partial^2 h}{\partial \theta \partial t} + \Omega^2 \frac{\partial^2 h}{\partial \theta^2} \right) + K_\Omega[h] = P(r, \theta, t), \quad (4)$$

where ρ_d and H are mass density and thickness of the disk, and K_Ω is the stiffness operator representing both bending and membrane stress components. The boundary conditions for the disk are clamped at the inner radius and free at the outer radius.

2.1 Equilibrium State. The axisymmetric equilibrium state is obtained by substituting $P = P_e(r)$, $h = h_e(r)$ and $\partial(\cdot)/\partial\theta = \partial(\cdot)/\partial t = 0$ into (1)–(4) and the disk boundary conditions, and by following the procedure used in Pelech and Shapiro (1964). Then

$$P_e(r) = \frac{3}{20} \rho \Omega^2 \left[(r^2 - r_a^2) - \frac{(r_b^2 - r_a^2)}{\int_{r_a}^{r_b} \frac{1}{rh_e^3} dr} \int_{r_a}^r \frac{1}{rh_e^3} dr \right] \quad (5)$$

and h_e can be obtained by solving (5) and (4) simultaneously.

2.2 Perturbed State. When the film-disk system is perturbed from equilibrium,

$$v_r = v_{re} + \hat{v}_r, \quad v_\theta = v_{\theta e} + \hat{v}_\theta, \quad P = P_e + \hat{P}, \quad h = h_e + \hat{h} \quad (6)$$

where $|\hat{\cdot}|$ is much smaller than $|\cdot|_e$. Equations (1a, b, c) become

$$-2\rho \frac{v_{\theta e} \hat{v}_\theta}{r} = -\frac{\partial \hat{P}}{\partial r} + \mu \frac{\partial^2 \hat{v}_r}{\partial z^2} \quad (7a)$$

$$0 = -\frac{\partial \hat{P}}{\partial \theta} + \mu \frac{\partial^2 \hat{v}_\theta}{\partial z^2} \quad (7b)$$

$$0 = \frac{\partial \hat{P}}{\partial z} \quad (7c)$$

where terms of higher order in the perturbation are neglected. Application of boundary perturbation to (3a, b, c) and neglect of higher order terms leads to boundary conditions for the perturbed variables

$$\hat{v}_r = -\frac{\hat{h} h_e}{2\mu} \left(\frac{\partial P_e}{\partial r} - \frac{\rho \Omega^2 r}{2} \right), \quad \hat{v}_\theta = -r\Omega \frac{\hat{h}}{h_e}, \quad \text{at } z = h_e \quad (8a)$$

$$\hat{v}_r = 0 \quad \hat{v}_\theta = 0 \quad \text{at } z = 0 \quad (8b)$$

$$\hat{P} = 0 \quad \text{at } r = r_a, r_b. \quad (8c)$$

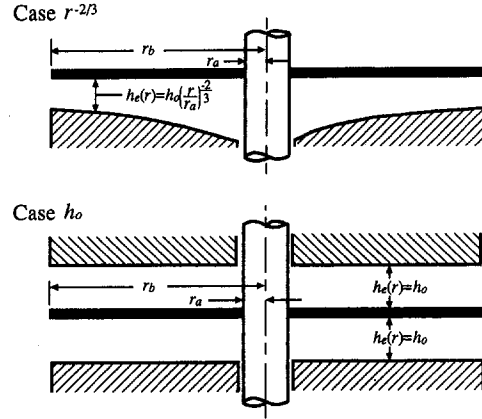


Fig. 2 Schematic of the coupled disk-film systems for two flat disk cases. The equilibrium state for both cases is a flat surface regardless of the rotation speed.

Explicit expressions of \hat{v}_r and \hat{v}_θ can be obtained in terms of \hat{P} , \hat{h} and their derivatives through integration of (7a, b) in the z -direction subject to (7c) and (8a, b). Integration of (2) from $z = 0$ to $z = h_e + \hat{h}$, and neglect of higher order terms, leads to

$$\frac{1}{r} \frac{\partial}{\partial r} \left(\int_0^{h_e + \hat{h}} r \hat{v}_r dz \right) + \frac{1}{r} \frac{\partial}{\partial \theta} \left(\int_0^{h_e + \hat{h}} \hat{v}_\theta dz \right) + \Omega \frac{\partial \hat{h}}{\partial \theta} + \frac{\partial \hat{h}}{\partial t} = 0 \quad (9)$$

where (3a, b) have been used. Substitution of the explicit expressions of \hat{v}_r and \hat{v}_θ into (9) leads to a partial differential equation in \hat{P} and \hat{h}

$$\begin{aligned} & \frac{1}{12\mu} \nabla \cdot (h_e^3 \nabla \hat{P}) + \frac{\rho \Omega}{120\mu^2} \frac{1}{r} \frac{\partial}{\partial r} \left(h_e^5 \frac{\partial \hat{P}}{\partial \theta} \right) \\ &= -\frac{1}{4\mu} \frac{1}{r} \frac{\partial}{\partial r} \left(rh_e^2 \frac{\partial P_e}{\partial r} \hat{h} \right) + \frac{3\rho \Omega^2}{40\mu} \frac{1}{r} \frac{\partial (r^2 h_e^2 \hat{h})}{\partial r} \\ & \quad + \frac{\Omega}{2} \frac{\partial \hat{h}}{\partial \theta} + \frac{\partial \hat{h}}{\partial t}. \quad (10) \end{aligned}$$

Substitution of $P = P_e + \hat{P}$ and $h = h_e + \hat{h}$ into (4) gives

$$\rho_d H \left(\frac{\partial^2 \hat{h}}{\partial t^2} + 2\Omega \frac{\partial^2 \hat{h}}{\partial \theta \partial t} + \Omega^2 \frac{\partial^2 \hat{h}}{\partial \theta^2} \right) + K_\Omega[\hat{h}] = \hat{P}(r, \theta, t). \quad (11)$$

Equations (10) and (11), plus the disk and film boundary conditions, govern the response of the coupled system shown in Fig. 1.

2.3 Two Flat Disk Cases. The h_e and P_e normally depend on Ω and can be obtained only through numerical analysis (Adams, 1980). To examine the instability mechanisms and sidestep the equilibrium calculation, we study two cases shown in Fig. 2 whose equilibria are flat regardless of Ω . Case $r^{-2/3}$ is a disk rotating close to a rigid wall whose shape gives h_e proportional to $r^{-2/3}$ and $h_0 = h_e(r_a)$; and Case h_0 is a disk rotating midway between two flat, parallel, rigid walls with equal and uniform separation (h_0) from both walls.

Case $r^{-2/3}$. Equation (5) shows $P_e = 0$ when $h_e = h_0$ (r/r_a)^{-2/3} and the equilibrium of the disk is flat for all Ω . Substitution of P_e and h_e and introduction of dimensionless variables

$$\xi = \frac{r}{r_b}, \tau = \tilde{\Omega} t, u = \frac{\hat{h}}{h_0}, \omega = \frac{\Omega}{\tilde{\Omega}}, q = \frac{\hat{P}}{\rho_d H h_0 \tilde{\Omega}^2} \quad (12)$$

where $\tilde{\Omega}$ is the unit of rotation speed, into (10) and (11), leads to

$$\frac{\partial^2 u}{\partial \tau^2} + 2\omega \frac{\partial^2 u}{\partial \theta \partial \tau} + \omega^2 \frac{\partial^2 u}{\partial \theta^2} + \bar{D} \nabla^4 u - \omega^2 \left[\frac{1}{\xi} \frac{\partial}{\partial \xi} \left(\xi \bar{\sigma}_{\xi\xi} \frac{\partial u}{\partial \xi} \right) + \frac{\bar{\sigma}_{\theta\theta}}{\xi^2} \frac{\partial^2 u}{\partial \theta^2} \right] = q \quad (13)$$

$$\nabla \cdot (\tilde{h}_e^3 \nabla q) + \frac{\text{Re}}{10} \frac{1}{\xi} \frac{\partial}{\partial \xi} \left(\tilde{h}_e^5 \frac{\partial q}{\partial \xi} \right) = f \frac{1}{\xi} \frac{\partial}{\partial \xi} (\xi^2 \tilde{h}_e^2 u) + a \left(\frac{\partial u}{\partial \tau} + \frac{\omega}{2} \frac{\partial u}{\partial \theta} \right) \quad (14)$$

The bending and membrane stress contributions to disk stiffness are expressed explicitly, and

$$\begin{aligned} \bar{\sigma}_{\xi\xi} &= \frac{3 + \nu}{8} \left(\frac{\gamma}{\xi^2} + (1 - \gamma) - \xi^2 \right), \\ \bar{\sigma}_{\theta\theta} &= \frac{3 + \nu}{8} \left(-\frac{\gamma}{\xi^2} + (1 - \gamma) - \frac{1 + 3\nu}{3 + \nu} \xi^2 \right), \\ \gamma &= \frac{1 - \frac{1 + \nu}{3 + \nu} c^2}{1 + \frac{1 + \nu}{1 - \nu} c^2} \quad \bar{D} = \frac{EH^2}{12(1 - \nu^2) \rho_d \tilde{\Omega}^2 r_b^4}, \\ a &= 12 \frac{r_b^2 \mu}{h_0^3 \rho_d H \tilde{\Omega}}, \quad f = \frac{9}{10} \frac{\rho r_b^2}{\rho_d H h_0} \omega^2, \quad \tilde{h}_e = \left(\frac{\xi}{c} \right)^{-2/3} \end{aligned}$$

E , ν , and $c = r_a/r_b$ are Young's modulus, Poisson's ratio, and clamping ratio of the disk; and $\omega^2 \bar{\sigma}_{\xi\xi}$, $\omega^2 \bar{\sigma}_{\theta\theta}$, and \bar{D} are dimensionless radial and circumferential membrane stresses; and disk flexural rigidity. a and f are measures of film damping and stiffness (which will be defined in Section 3). The boundary conditions on the disk displacement and the film pressure are

$$q = u = \frac{\partial u}{\partial \xi} = 0 \quad \text{at } \xi = c \quad (15a)$$

$$q = \frac{\partial^2 u}{\partial \xi^2} + \nu \left(\frac{\partial u}{\partial \xi} + \frac{\partial^2 u}{\partial \theta^2} \right) = \frac{\partial}{\partial \xi} (\nabla^2 u) + (1 - \nu) \frac{\partial^2}{\partial \theta^2} \left(\frac{\partial u}{\partial \xi} - u \right) = 0 \quad \text{at } \xi = 1. \quad (15b)$$

Case h_0 . Symmetry of the disk enclosure requires the disk to remain flat at one equilibrium state regardless of Ω . After calculating the resultant pressure in both fluid films, the dimensionless disk equation is represented by (13) and the dimensionless film equation is

$$\nabla^2 q + \frac{\text{Re}}{10} \frac{1}{\xi} \frac{\partial^2 q}{\partial \xi \partial \theta} = e \frac{1}{\xi} \frac{\partial u}{\partial \xi} + 2a \left(\frac{\partial u}{\partial \tau} + \frac{\omega}{2} \frac{\partial u}{\partial \theta} \right) \quad (16)$$

where $e = \frac{9}{10} \frac{\rho r_b^2 (1 - c^2)}{(-\ln c) \rho_d H h_0} \omega^2$ is a measure of film stiffness.

3 Instability Mechanisms

Equations (10), (14), and (16) can be represented by

$$\left(L + \frac{\text{Re}}{10} \tilde{L} \right) [q] = F_s[u] + F_d \left[\frac{\partial u}{\partial \tau} + \frac{\omega}{2} \frac{\partial u}{\partial \theta} \right] \quad (17)$$

where $L + (\text{Re}/10)\tilde{L}$ is a fluid operator, L being negative-definite, F_s is a nonsymmetric operator, and F_d is positive definite. Because $\text{Re}/10 \ll 1$ and L dominates $\text{Re}/10 \tilde{L}$, we neglect $\text{Re}/10 \tilde{L}$ in the fluid operator, and decompose q into q_s and q_{rd}

$$L[q_s] = F_s[u], \quad L[q_{rd}] = F_d \left[\frac{\partial u}{\partial \tau} + \frac{\omega}{2} \frac{\partial u}{\partial \theta} \right] \quad (18)$$

Variables q_s and q_{rd} are functionals of u , $q_s = Q_s[u]$ and $q_{rd} = Q_d [\partial u/\partial \tau + (\omega/2) (\partial u/\partial \theta)]$, and (13) becomes

$$\frac{\partial^2 u}{\partial \tau^2} + 2\omega \frac{\partial^2 u}{\partial \theta \partial \tau} + \omega^2 \frac{\partial^2 u}{\partial \theta^2} + \bar{D} \nabla^4 u - \omega^2 \left[\frac{1}{\xi} \frac{\partial}{\partial \xi} \left(\xi \bar{\sigma}_{\xi\xi} \frac{\partial u}{\partial \xi} \right) + \frac{\bar{\sigma}_{\theta\theta}}{\xi^2} \frac{\partial^2 u}{\partial \theta^2} \right] - Q_s[u] - Q_d \left[\frac{\partial u}{\partial \tau} + \frac{\omega}{2} \frac{\partial u}{\partial \theta} \right] = 0. \quad (19)$$

$-Q_s$ is a nonsymmetric operator, and $-Q_s[u]$ represents nonsymmetric stiffness emanating from the film. Equations (11), (14), and (16) show that the film stiffness is proportional to $\rho \omega^2$, and f for Case $r^{-2/3}$ (e for Case h_0) is a measure of the film stiffness. $-Q_d$ is a positive-definite operator (for proof see Appendix), and $-Q_d [\partial u/\partial \tau + (\omega/2) (\partial u/\partial \theta)]$ represents rotating damping resulting from the film. Equations (11), (14), and (16) show that the magnitude of the film damping is proportional to a , and the rotation speed of the film damping is always one half the disk rotation speed.

According to Huang and Mote (1995b), stability of a rotating disk under rotating, positive-definite damping can be predicted through the wave speeds in the undamped disk. The rotating damping will energize a backward traveling wave when its speed relative to the disk exceeds the undamped wave speed. Therefore, the wave speeds in the undamped (19) are determined from

$$\frac{\partial^2 u}{\partial \tau^2} + 2\omega \frac{\partial^2 u}{\partial \theta \partial \tau} + \omega^2 \frac{\partial^2 u}{\partial \theta^2} + \bar{D} \nabla^4 u - \omega^2 \left[\frac{1}{\xi} \frac{\partial}{\partial \xi} \left(\xi \bar{\sigma}_{\xi\xi} \frac{\partial u}{\partial \xi} \right) + \frac{\bar{\sigma}_{\theta\theta}}{\xi^2} \frac{\partial^2 u}{\partial \theta^2} \right] - Q_s[u] = 0 \quad (20)$$

plus the boundary conditions. Because the film stiffness $-Q_s[u]$ is not positive definite, flutter can occur. Figure 3 illustrates three characteristic patterns of wave speed and exponential decay/growth rate showing how the film stiffness affects wave modes of a particular disk. The membrane stresses generated by the rotation of the disk are equated to zero in Fig. 3 so that the film stiffness $Q_s[u]$ is the only ω dependent term affecting wave speeds³ in the undamped system. The film stiffness increases the speeds of wave modes without increasing energy in the wave with increasing disk rotation speed (i.e., increasing system stiffness) until flutter occurs at flutter speeds ($\Omega_a^{(f)}$, $\Omega_b^{(f)}$, $\Omega_c^{(f)}$). The film stiffness neither energizes nor dissipates vibration in a mode at rotation speeds less than the flutter speed. The dash line indicates the difference in speeds between the film damping and the disk. It intersects the wave speed loci in the pre-flutter region (mode M_a), in the post-flutter region (mode M_b), and not at all (mode M_c) for some modes. Mode M_a becomes unstable at speeds higher than $\Omega_a^{(rd)}$, because at those speeds the film damping energizes the mode. The instability of this

³It should be noted that the "wave speed" in this paper is the propagation speed of a wave observed on the disk. The inertial disk acceleration $\partial^2 u/\partial \tau^2 + 2\omega (\partial^2 u/\partial \theta \partial \tau) + \omega^2 (u/\partial \theta^2)$ makes propagation speeds of waves observed in a stationary reference dependence on Ω , but does not affect on propagation speeds of waves observed in the disk reference.

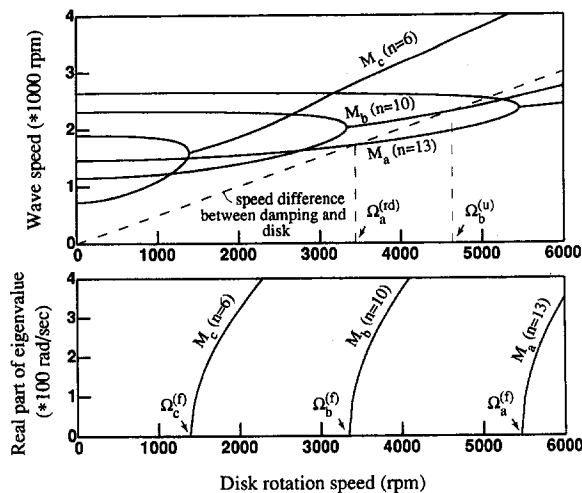


Fig. 3 Three characteristic relationships of wave speeds and real parts of eigenvalues of the Case $r^{-2/3}$ disk under the nonsymmetric film stiffness with the film damping neglected. Nodal diameter numbers n are given in the parentheses. The dash line intersects the wave speed loci in the pre-flutter region (mode M_a), in the post-flutter region (mode M_b), and not at all (mode M_c). Membrane stresses in the disk stiffness are neglected.

type is termed the *rotating damping instability*. This type of instability is equivalent to the instability observed in Hosaka and Crandall (1992). The rotating damping instability can be predicted from wave speeds in the undamped system described by (20). The film stiffness energizes modes M_b and M_c at speeds above $\Omega_b^{(f)}$ and $\Omega_c^{(f)}$. However, the film damping may simultaneously dissipate vibration energy in these modes and render them stable. Therefore, the flutter speeds serve as a lower bond for the stability boundary of these modes, and *do not* indicate mode instability. For mode M_b , both film stiffness and film damping energize the mode at speeds higher than $\Omega_b^{(u)}$ (which serves as an upper bond for the stability boundary of mode M_b). Instability in mode M_b occurs at speeds above an onset speed $\Omega_b^{(c)}$ ($\Omega_b^{(f)} < \Omega_b^{(c)} < \Omega_b^{(u)}$). Though the upper and lower bonds for $\Omega_b^{(c)}$ can be located through the wave speeds in the undamped system described by (20), the identification of the instability relies on the exponential decay/growth rates of vibration modes in the coupled film-disk system described by (19). The instability of this type is termed the *combination instability*, because it is caused by the combined effect of the nonsymmetric film stiffness and rotating film damping.

4 Numerical Technique

The coordinate transformation, $\Theta = \theta - \omega\tau$, fixing the coordinate system to the disk, and assumption of a nodal diameter mode $u = R_n(\xi)e^{in\theta}e^{\lambda_n\tau}$, reduces (20) to an uncoupled set of one dimensional eigenvalue problems

$$\lambda_n^2 R_n + B_n[R_n] + \omega^2 S_n[R_n] - \omega^2 Q_{s,n}[R_n] = 0 \quad n = 0, \pm 1, \pm 2, \dots \pm \infty \quad (21)$$

where n represents the nodal diameter number, and B_n , $\omega^2 S_n$ and $\omega^2 Q_{s,n}$ are operators describing the bending and membrane stress components of the disk stiffness and the nonsymmetric film stiffness for the n nodal diameter mode. The boundary conditions on $R_n(\xi)$ are obtained through substitution of the assumed nodal diameter mode into (15a,b). The Galerkin method is used to calculate the eigensolutions of (21). $R_n(\xi)$ is approximated by $R_n(\xi) \approx \sum_{m=1}^{m_0} d_{mn} \phi_{mn}(\xi)$, where d_{mn} are constants to be determined and $\phi_{mn}(\xi)$ are polynomials in ξ . The trial functions ($\hat{\phi}_{mn}(\xi)$)

for the film pressure can be obtained explicitly⁴ from $L[\hat{\phi}_{mn}e^{in\theta}] = F_s[\phi_{mn}e^{in\theta}]$ described in (18). Each $\phi_{mn}(\xi)$ is a seven-term polynomial satisfying the six homogeneous boundary conditions in (15a, b).

The eigenvalues ($\lambda_n = \alpha_n + i\beta_n$, where α_n and β_n are real) of (21) are computed repetitively with specified ω increasing from zero. α_n is zero when ω is small; the flutter speed ($\omega_n^{(f)}$) is the disk rotation speed first resulting in nonzero α_n . The undamped wave speed of the n nodal diameter wave mode is $v_n = |\beta_n/n|$. When ω is small, v_n is always larger than $\omega/2$, the difference in speeds between the damping and the disk. If $v_n = \omega/2$ in the pre-flutter region, say at $\omega = \omega_n^{(rd)}$, then the rotating damping instability occurs for $\omega \geq \omega_n^{(rd)}$. If $v_n = \omega/2$ in the post-flutter region, say at $\omega = \omega_n^{(u)}$, then the combination instability occurs at speeds above an onset speed $\omega_n^{(c)}$ between $\omega_n^{(f)}$ and $\omega_n^{(u)}$. The exact prediction of $\omega_n^{(c)}$ can only be located through the real parts of eigenvalues of the dual eigenvalue problem to (19). We use the approximate eigenfunction $R_n(\xi)e^{in\theta}$, obtained from the above calculation, as a trial function and apply the one-term Galerkin method to compute the eigenvalues of the dual eigenvalue problem to (19).

Because the maximum stable rotation speed of the disk is the lowest $\omega_n^{(rd)}$ for all n (this will be shown later), a more efficient method to compute $\omega_n^{(rd)}$ without computation of λ_n is suggested. Because $\omega_n^{(rd)}$ is obtained through the condition that $\lambda_n = in\omega/2$ at $\omega = \omega_n^{(rd)}$, at the onset speed of the rotating damping instability $\lambda_n = in\omega_n^{(rd)}$. Substitution of $\lambda_n = in\omega_n/2$ and $\omega = \omega_n$ into (20) leads to

$$\omega_n^2 \left(-\frac{n^4}{2} R_n + S_n[R_n] - Q_{s,n}[R_n] \right) + B_n[R_n] = 0 \quad n = 0, \pm 1, \pm 2, \dots \pm \infty \quad (22)$$

Equation (22) is an eigenvalue problem where the eigenvalue ω_n^2 predicts the onset speed of the rotating damping instability in the n nodal diameter mode. ω_n real indicates that a rotating damping instability exists in this mode and $\omega_n^{(rd)} = \omega_n$. Real ω_n may not exist for all n , because, as described in Section 3, the nonsymmetric film stiffness causes flutter in some modes at lower speeds while their undamped wave speeds are always higher than $\omega/2$ in the pre-flutter region. Rotating damping instability does not occur in these modes, and the instability in these modes, if it exists, is a combination instability.

5 Results and Discussion

When the disk rotates close to a rigid wall, the viscous fluid between the disk and the rigid surface has a circumferential mean flow component rotating at one half the disk speed. This mean flow produces an effect equivalent to a rotating, viscous damping. The damping force is proportional to viscosity. A radial, secondary flow is generated by the centrifugal forces, and the radial flow is proportional to the fluid density and the square of the disk rotation speed. Therefore, by examining (18) and the associated operators L , F_s , and F_d in (10), (14), and (16), q_{rd} results from the circumferential mean flow and q_s from the radial, secondary flow. $-q_{rd}$ is positive-definite damping rotating at $\omega/2$. $-q_s$ is nonsymmetric stiffness and its magnitude is proportional to $\rho\omega^2$.

The specifications of the disk investigated in the paper are: $E = 3.48$ GPa, $\rho_d = 1420$ kg/m³, $H = 0.1$ mm, $r_b = 70$

⁴Though q_s is represented by a functional $Q_s[u]$, the explicit expression for Q_s is not found. However, if the trial functions for the radial mode shape of u ($R_n(\xi)$) are polynomials, the close-form trial function for the radial mode shape of q_s are obtained explicitly from (18) through term by term integration. This is an advantage gained by use of polynomials as trial functions.

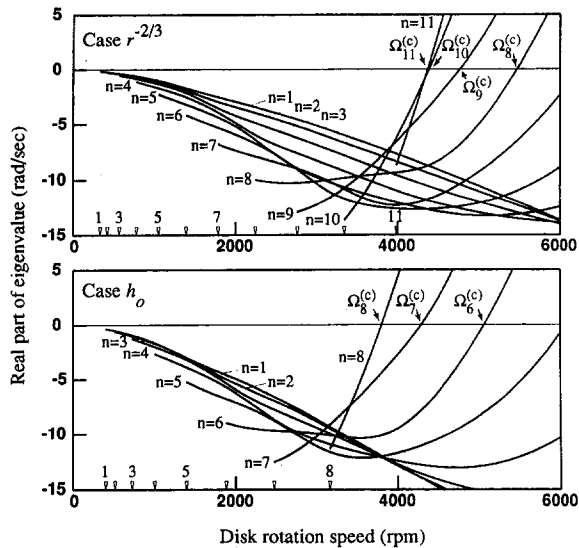


Fig. 4 Real parts of eigenvalues of the coupled film-disk system in the post-flutter regions when the film damping is modeled. The individual flutter speeds are denoted by ∇ , and the nodal diameter number by n . Combination instability occurs for positive real parts. Membrane stresses in the disk stiffness are neglected.

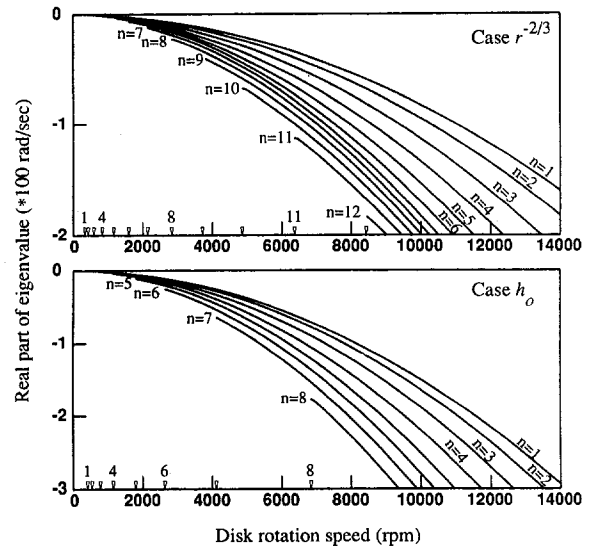


Fig. 6 Real parts of eigenvalues of the coupled film-disk system in the post-flutter regions when the film damping is modeled. The individual flutter speeds are denoted by ∇ and the nodal diameter number by n . Membrane stresses in the disk stiffness are modeled.

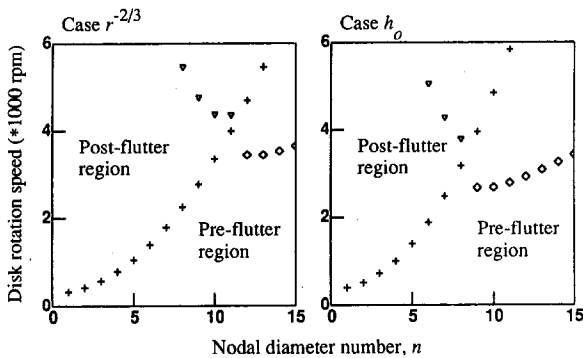


Fig. 5 Prediction of stability of modes of different nodal diameter number (n). The flutter speed (+) divides the speed space into pre-flutter and post-flutter regions, but does not indicate mode instability. A mode becomes unstable at speeds above the onset speed of rotating damping instability (\diamond), which exists only in the pre-flutter region, or above the onset speed of combination instability (∇), which exists only in the post-flutter region. Membrane stresses in the disk stiffness are neglected.

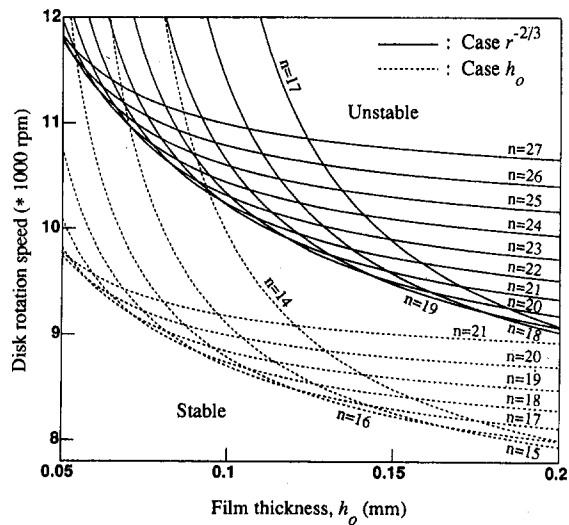
mm, $\nu = 0.3$, and $c = 0.3$. The disk model is similar to a 5.25-in. floppy memory disk. The critical speed of the disk, when not coupled to the rigid surface through the boundary film, is 532 rpm. The fluid is air and $h_0 = 0.1$ mm. When studying the effect of a specific parameter on disk stability, only that parameter is changed in the calculation.

When membrane stresses in the disk are neglected, the film stiffness is the only ω -dependent term in (21). Figure 3 shows the film stiffness effect on wave modes ($n = 6, 10, 13$) in the undamped system at different ω for Case $r^{-2/3}$. Analogous wave speed and real part of eigenvalue loci are obtained for Case h_0 . The onset speed of the rotating damping instability in a mode exists when the disk speed equals two times the undamped wave speed of the mode in the pre-flutter region (like $\Omega_a^{(rd)}$ in Fig. 3). Figure 4 shows the real part of eigenvalues of wave modes, with $-q_{rd}$ included, in the post-flutter regions. They are calculated from their individual flutter speeds $\Omega_n^{(f)}$, and all real parts remain negative at speeds above their flutter speeds. The combination instability occurs when the real part of eigenvalue is positive, and its onset speed is $\Omega_n^{(c)}$. Figure 5 shows instabilities of modes with different nodal diameter number for

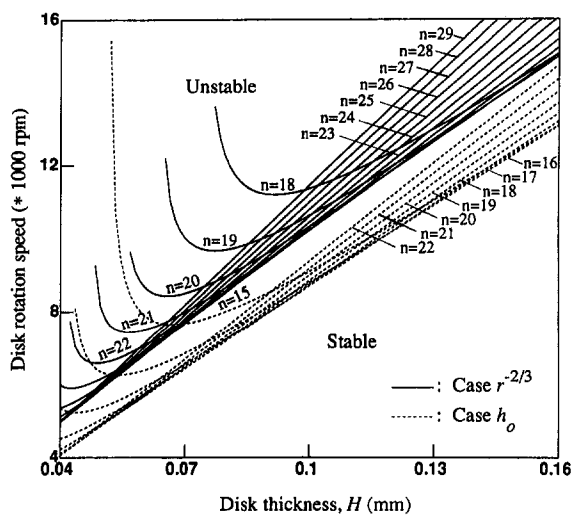
Cases $r^{-2/3}$ and h_0 . A mode is stable only at speeds lower than both the onset speed of rotating damping instability and the onset speed of combination instability. It should be noted again that the flutter speed does not predict disk instability. Figure 5 also shows that rotating damping instability occurs only in modes with large n , and that combination instability occurs only in a few modes and at speeds higher than the speed first producing rotating damping instability.

When membrane stresses caused by disk rotation are modeled, undamped wave speeds increase substantially with increasing disk rotation speed, and that wave modes with wave speeds equal one half the disk speed exists only in the pre-flutter region for modes with a very large number of nodal diameters. Figure 6 shows the real parts of eigenvalues of wave modes, with rotating damping $-q_{rd}$ included. The real parts decrease substantially from the flutter speed as disk rotation speed increases. This may explain the decrease in peak to peak vibration amplitude reported in Yasuda and Kaneko (1987) as disk rotation speed increases. Combination instability does not occur here. A mode is stable only at speeds lower than the onset speed of rotating damping instability. The disk is stable iff every mode is stable. After calculating the onset speeds of instability for each mode, the maximum stable disk rotation speed is 10,167 rpm (8,692 rpm) for Case $r^{-2/3}$ (Case h_0). This speed first produces rotating damping instability in the $n = 21$ ($= 17$) nodal diameter wave mode, and it is about 19 (16) times the critical speed of the disk without coupling to the rigid wall through the fluid film. The maximum stable disk rotation speed in both cases is much larger than the operation speed of a typical rigid disk drive (3,600 rpm). The trends in the real parts of eigenvalues in Fig. 6 indicate that combination instability is unlikely to occur when disk membrane stresses are included in the model of most disks. In calculations of combination instability for different disk and film properties, the combination instability has never been observed at speeds lower than the lowest onset speed of rotating damping instability. Therefore, (22) is used in the next paragraph to calculate $\omega_n^{(rd)}$ without computation of λ_n to predict the effects of the disk and film properties on disk stability.

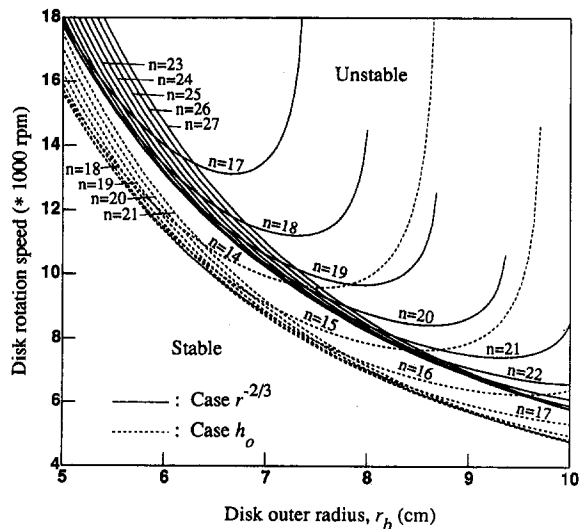
The rotation speed of film damping relative to the disk is always one half the disk rotation speed. Therefore, increasing the onset speed of rotating damping instability requires increasing the undamped wave speeds in the disk. The stiffness



(a)



(b)



(c)

Fig. 7 Onset speeds of rotating damping instability for modes of nodal diameter number (n) as a function of (a) film thickness (h_o), (b) disk thickness (H), and (c) disk outer radius (r_b). The disk is stable only at speeds lower than the lowest onset speed. Membrane stresses in the disk stiffness are modeled.

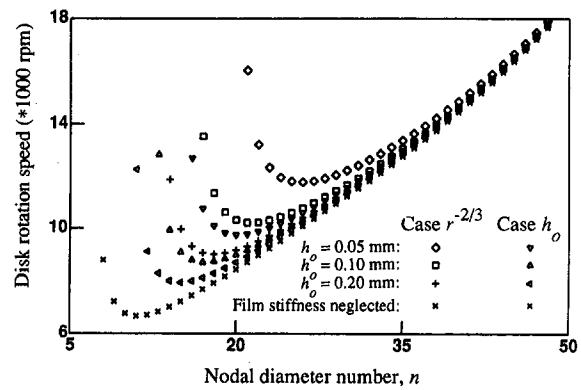


Fig. 8 Onset speeds of rotating damping instability for modes under different film thickness (h_o) and when the film stiffness ($-q_s$) is equated to zero. Membrane stresses in the disk stiffness are modeled.

in the coupled, undamped system has contributions from the bending and membrane stress stiffnesses in the disk and the film stiffness. Figures 7(a-c) show the onset speeds of the rotating damping instability for Cases $r^{-2/3}$ and h_o . The stable rotation speed of the disk is bounded above by the lowest onset speed of the rotating damping instability. Figure 7(a) shows that, as h_o increases from 0.05 mm to 0.2 mm, the maximum stable disk rotation speed decreases from 11,783 rpm in Case $r^{-2/3}$ (9,749 rpm in Case h_o) to 9,022 rpm (7,943 rpm), and the nodal diameter number of the first unstable mode changes from 26 (20) to 18 (15). It can be shown from (14) and (16) that decreasing h_o increases only the magnitude of q_s , thereby stiffening the disk. Figure 8 gives the onset speeds of rotating damping instability in the disk with the film stiffness modeled for different h_o and with the film stiffness equated to zero. It shows that the film stiffness has little effect on the onset speeds of rotating damping instability in modes with $n > 30$. When n is large, $\partial(\)/\partial\theta$ dominates $\partial(\)/\partial\xi$ in L . Therefore, in (18) $L \approx \partial^2/\partial\theta^2$ for Case h_o , and in (21) $\omega^2 Q_{s;n}[R_n] \approx (e/n^2)(1/\xi)(\partial R_n/\partial\xi)$. When n is large, the effect of q_s on modes with n nodal diameters is approximately proportional to n^{-2} . Similar reasoning and conclusions follow for Case $r^{-2/3}$.

Increasing H increases the disk bending stiffness and decreases the film stiffness. Increasing r_b decreases the disk bending stiffness and increases the film stiffness. When n is large, the disk bending stiffness $B_n[R_n]$ in (21) is approximately proportional to n^4 , and therefore dominates the film stiffness. This explains why the maximum stable rotation speed of the disk increases as H increases in Fig. 7(b) and as r_b decreases in Fig. 7(c).

The models for Cases $r^{-2/3}$ and h_o are described by (19) with film effects producing nonsymmetric stiffness and rotating damping. Because the coupled system in the single flat wall case, modeled by (10) and (11), can also be represented by (19), the same instability mechanisms as seen in Cases $r^{-2/3}$ and h_o will result. The results of Case $r^{-2/3}$ can be used to approximate the responses of the single flat wall case, because the equilibrium film thickness in the single flat wall case is approximately proportional to $r^{-2/3}$ at high rotation speeds (Pelech and Shapiro, 1964). Because increasing disk stiffness increases the maximum stable rotation speed, increasing disk thickness, Young's modulus and clamping ratio, or decreasing disk density and outer radius all move a disk design toward stability at higher speeds. Decreasing h_o and increasing fluid density also increase the maximum stable rotation speed by increasing the film stiffness. Increasing inlet flow rate, or fluid pressure at the inner radius, increases the film stiffness and as a consequence the maximum stable rotation speed. Increasing flow resistance at the inlet or

outlet will attenuate the radial flow and should reduce the maximum stable rotation speed. These observations are deduced from the instability mechanisms rather than calculation of disk response. The findings provide a plausible explanation for some of the phenomena reported by Yasuda and Kaneko (1987).

6 Conclusions

1 In the rotating disk coupled to a thin viscous fluid film, the fluid in the film rotates circumferentially under viscous fluid forces, and a secondary flow, that moves radially outwards, is generated due to the centrifugal forces. The circumferential mean flow creates an equivalent positive-definite damping rotating at one half the disk rotation speed. The radial, secondary flow creates a nonsymmetric stiffness in the disk-film system.

2 The nonsymmetric film stiffness stiffens the disk, but can energize wave modes at speeds higher than their flutter speeds. The rotating film damping dissipates energy from each wave mode until the disk speed exceeds twice its undamped wave speed. At rotation speeds less than the flutter speed, the film damping can cause rotating damping instability, which agrees with the observation in Hosaka and Crandall (1992). At rotation speeds greater than the flutter speed, the combined effect of the film damping and film stiffness can cause combination instability.

3 Rotating damping instability occurs only in modes with a large nodal diameter number. Combination instability occurs only in a few modes when disk membrane stresses are neglected or insignificant, and is unlikely to occur in a rotating disk where membrane stresses are modeled. Combination instability does not occur at speeds lower than the lowest onset speed of rotating damping instability.

4 The maximum speed of stable operation of the disk is the lowest onset speed of rotating damping instability. Increasing disk stiffness (increasing disk thickness or decreasing disk outer radius) and increasing film stiffness (decreasing film thickness or increasing radial flow) increase the maximum rotation speed of stable operation.

5 The effect of the film stiffness on increasing undamped wave speeds of modes with large n is approximately proportional to n^{-2} . The onset speeds of rotating damping instability in modes of a larger nodal diameter number are virtually independent of film stiffness.

6 When $h_0 = 0.1$ mm, the maximum stable operation speed of a 5.25-in. flexible memory disk is about 19 times its critical speed (without the viscous film) when it rotates close to a wall whose shape gives $h_e(r) = h_0(r/r_a)^{-2/3}$, and 16 times if it rotates midway between two flat, parallel walls. The exponential decay rates of modes with small nodal diameter number increase substantially as the disk rotation speed increases.

References

- Adams, G. G., 1980, "Analysis of the Flexible Disk/Head Interface," *ASME Journal of Lubrication Technology*, Vol. 102, pp. 86-90.
 Adams, G. G., 1987, "Critical Speeds for a Flexible Spinning Disk," *International Journal of Mechanical Science*, Vol. 29, No. 29, pp. 525-531.

Benson, R. C., and Takahashi, T. T., 1991, "Mechanics of Flexible Disks in Magnetic Recording," *ASME Advances in Information Storage Systems*, Vol. 1, pp. 15-35.

Bogy, D. B., and Talke, F. E., 1978, "Steady Axisymmetric Solutions for Pressurized Rotating Disk Packs," *IBM Journal of Research and Development*, Vol. 22, No. 2, pp. 179-184.

Carpino, M., and Domoto, G. A., 1988, "Axisymmetric Solution of a Flexible Disk Rotating near a Rigid Surface," *ASME Journal of Tribology*, Vol. 110, pp. 674-677.

D'Angelo, C., III, and Mote, C. D., Jr., 1993, "Aerodynamically Excited Vibration and Flutter of a Thin Disk Rotating at Supercritical Speed," *Journal of Sound and Vibration*, Vol. 168, No. 1, pp. 1-15.

Greenberg, H. J., 1978, "Flexible Disk-Read/Write Head Interface," *IEEE Transactions of Magnetics*, Vol. MAG-14, No. 5, pp. 336-338.

Hosaka, H., and Crandall, S. H., 1992, "Self-Excited Vibrations of a Flexible Disk Rotating on an Air Film Above a Flat Surface," *Acta Mechanica Supplementum*, Vol. 3, pp. 115-127.

Huang, F. Y., and Mote, C. D., Jr., 1995a, "On the Translating Damping Caused by a Thin Viscous Fluid Layer Between a Translating String and a Translating Rigid Surface," *Journal of Sound and Vibration*, Vol. 181, No. 2, pp. 251-260.

Huang, F. Y., and Mote, C. D., Jr., 1995b, "Mathematical Prediction of Stability of a Spinning Disk Under a Rotating, Arbitrarily Large Damping Force," *ASME Journal of Vibration and Acoustics*, in press.

Iwan, W. D., and Moeller, T. L., 1976, "The Stability of a Spinning Elastic Disk With a Transverse Load System," *ASME JOURNAL OF APPLIED MECHANICS*, Vol. 43, pp. 485-490.

Iwan, W. D., and Stahl, K. J., 1973, "The Response of an Elastic Disk With a Moving Mass System," *ASME JOURNAL OF APPLIED MECHANICS*, Vol. 40, pp. 445-451.

Mote, C. D., Jr., 1970, "Stability of Circular Plate Subjected to Moving Loads," *Journal of the Franklin Institute*, Vol. 290, No. 4, pp. 329-333.

Pelech, I., and Shapiro, A. H., 1964, "Flexible Disk Rotating on a Gas Film Next to a Wall," *ASME JOURNAL OF APPLIED MECHANICS*, Vol. 31, pp. 577-584.

Shen, I. Y., and Mote, C. D., Jr., 1991, "On the Mechanisms of Instability of a Circular Plate Under a Rotating Spring-Mass-Dashpot System," *Journal of Sound and Vibration*, Vol. 148, pp. 307-318.

Walowitz, J. A., and Anno, J. N., 1975, *Modern Developments in Lubrication Mechanics*, John Wiley and Sons, New York, pp. 12-59.

Yasuda, K., and Kaneko, R., 1987, "R/W Experiment Using High-Speed Flexible Disk," *IEEE Translation Journal on Magnetics in Japan*, Vol. TJMJ-2, pp. 580-588.

APPENDIX

The Appendix shows that the film damping operator, $-Q_d$, is positive-definite. The theory in Huang and Mote (1995b), that predicts the onset speed of disk instability due to rotating damping, pertains to positive-definite $-Q_d$.

Let

$$\tilde{q} = Q_d[\tilde{u}]. \quad (A1)$$

From (18) and the expression F_d in (10), (14), and (16)

$$L[\tilde{q}] = F_d[\tilde{u}] = \tilde{a}\tilde{u} \quad (A2)$$

where \tilde{a} is a positive constant. Therefore,

$$\langle \tilde{u}, -Q_d[\tilde{u}] \rangle = \langle \frac{L[\tilde{q}]}{\tilde{a}}, -q \rangle = \frac{\langle L[\tilde{q}], \tilde{q} \rangle}{-\tilde{a}} \quad (A3)$$

where $\langle w, v \rangle = \int_0^{2\pi} \int_0^1 w\bar{v} \xi d\xi d\theta$, and overbar denotes complex conjugate here. Because L is a negative-definite operator

$$\langle \tilde{u}, -Q_d[\tilde{u}] \rangle > 0 \quad \text{for all } \tilde{u} \neq 0. \quad (A4)$$

Equilibrium Displacement and Stress Distribution in a Two-Dimensional, Axially Moving Web Under Transverse Loading

C. C. Lin

Senior Advisory Development Engineer,
Seagate Technology,
915 Disc Drive,
Scotts Valley, CA 95067
Assoc. Mem. ASME.

C. D. Mote, Jr.

Vice Chancellor and FANUC Chair
in Mechanical Systems,
Department of Mechanical Engineering,
University of California,
Berkeley, CA 94720
Fellow ASME.

Von Karman nonlinear plate equations are modified to describe the motion of a wide, axially moving web with small flexural stiffness under transverse loading. The model can represent a paper web or plastic sheet under some conditions. Closed-form solutions to two nonlinear, coupled equations governing the transverse displacement and stress function probably do not exist. The transverse forces arising from the bending stiffness are much smaller than those arising from the applied axial tension except near the edges of the web. This opens the possibility that boundary layer and singular perturbation theories can be used to model the bending forces near the edges of the web when determining the equilibrium solution and stress distribution. The present analysis is applied to two examples: (I) a web deflecting under its own uniformly distributed weight; (II) a web deflecting under a transverse load whose distribution is described by the product of sine functions in the axial and width directions. Membrane theory and linear plate theory solutions are used to characterize the importance of the web deformation solutions.

Introduction

The deflection of a web with small flexural stiffness subjected to transverse loading is often large compared to its thickness. The weight of a web and the aerodynamic forces are notable transverse loadings on the unsupported span of the web. The membrane stresses induced by large deflection are usually significant to web response and can not be neglected. Depending on the intensity of the shear, or compressive stresses developed, the web may wrinkle (Lin and Mote, in press). Wrinkling degrades the web quality, increases defects, or can lead to its breakage. To predict web deflection and stresses, the coupling between them must be modeled. The equilibrium solution provides the deflection and the state of the membrane stresses required for study of web stability and wrinkling.

Membrane and linear plate theories do not model the membrane stresses arising from the curvature of the web and are realistic only for small amplitude transverse response. In this paper, von Karman nonlinear plate theory (von Karman, 1910) is modified to include the inertial forces resulting from longitudinal transport of the axially moving web. The coupling between the large amplitude deflection and the membrane stresses is also modeled.

Reissner (1912) first analyzed boundary layers of bending stiffness effects near the edges of thin shells. Later, boundary layer and perturbation theories have been used to solve different engineering problems. Fung and Wittrick (1955) developed nonlinear boundary layers along the free edges of a thin plate to predict large deflection under uniform bending. Triantafyllou and Triantafyllou (1991) used a bending stiffness boundary layer at the free end of a hanging string while predicting the

natural responses. Renshaw (1992) included bending stiffness boundary layers at the inner and outer edges of a rotating membrane-like disk while examining stability of the disk. In this analysis, the transverse forces arising from the bending stiffness of the web are assumed much smaller than those arising from the applied, uniform, axial tension except near the four edges of the web. This permits use of boundary layer and singular perturbation theories to model the bending forces near the edges of the web for prediction of the equilibrium displacement and stress distribution.

The purpose of this paper is to predict the large amplitude equilibrium displacement and stress distribution of a two dimensional, axially moving web under smooth transverse loading. The exact solutions, satisfying the two nonlinear, coupled equations governing the transverse displacement and stress function, probably cannot be determined in closed form. The bending stiffness of the web is small and can be modeled as a perturbation parameter. Singular perturbation and boundary layer theories lead to a useful analytical representation of the equilibrium solution. The outer solution is developed at the middle of the web and the inner solutions are developed in the boundary layers. A uniform approximation of the deflection is obtained by summing the outer and inner solutions, and then subtracting the matching solutions. This analysis is applied to two examples: (I) equilibrium of the web under its own uniformly distributed weight; (II) equilibrium of the web under a transverse load whose distribution is described by the product of sine functions in the axial and width directions. Inclusion of the boundary layers at the free edges increases the predicted deflection at the free edges and decreases slightly the predicted deflection at the middle of the web. Depending on the bending stiffness and the web curvature, the deflection predicted by this analysis can be quite different from that predicted by either membrane theory or linear plate theory.

Formulation

The equations governing the transverse motion and the membrane stress field of the axially moving web in Fig. 1 are

Contributed by the Applied Mechanics Division of THE AMERICAN SOCIETY OF MECHANICAL ENGINEERS for publication in the ASME JOURNAL OF APPLIED MECHANICS.

Discussion on this paper should be addressed to the Technical Editor, Prof. Lewis T. Wheeler, Department of Mechanical Engineering, University of Houston, Houston, TX 77204-4792, and will be accepted until four months after final publication of the paper itself in the ASME JOURNAL OF APPLIED MECHANICS.

Manuscript received by the ASME Applied Mechanics Division, Nov. 3, 1993; final revision, Apr. 15, 1994. Associate Technical Editor: W. K. Liu.

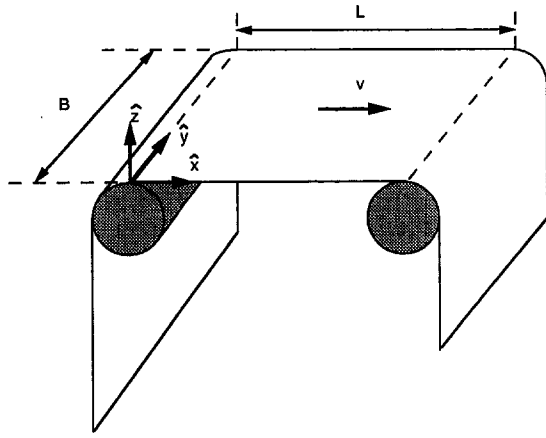


Fig. 1 Axially moving web

$$\rho(\hat{w}_{tt} + 2v\hat{w}_{xt} + v^2\hat{w}_{xx}) - \hat{F}_{,yy}\hat{w}_{,xx} - F_{,xx}\hat{w}_{,yy} + 2F_{,xy}\hat{w}_{,xy} + D(\hat{w}_{,xxxx} + 2\hat{w}_{,xxyy} + \hat{w}_{,yyyy}) = \hat{P} \quad (1)$$

and

$$\hat{F}_{,xxxx} + 2\hat{F}_{,xxyy} + \hat{F}_{,yyyy} = Eh[(\hat{w}_{,xy})^2 - (\hat{w}_{,xx})(\hat{w}_{,yy})]. \quad (2)$$

These equations are derived from von Karman nonlinear plate theory (von Karman, 1910) modified to include the inertial forces resulting from longitudinal transport of the web. $\hat{w}(\hat{x}, \hat{y}, \hat{t})$ denotes the transverse displacement, $D = Eh^3/[12(1 - \nu^2)]$, E is Young's modulus, ρ is mass density, ν is Poisson's ratio, h is thickness, T is constant longitudinal tension applied at the boundaries, $\hat{F}(\hat{x}, \hat{y}, \hat{t})$ is the stress function, $\hat{P}(\hat{x}, \hat{y}, \hat{t})$ is the (smooth) transverse loading, and v is constant axial transport speed. The material properties are uniform and constant. Transforming to dimensionless variables, (1) and (2) become

$$w_{,tt} + 2Cw_{,xt} + C^2w_{,xx} - L[w, F] + \epsilon\nabla^4w = P \quad (3)$$

and

$$\nabla^4F = -6(1 - \nu^2)\epsilon L[w, w]. \quad (4)$$

The dimensionless parameters are

$$w = \frac{\hat{w}}{h}; \quad x = \frac{\hat{x}}{L}; \quad y = \frac{\hat{y}}{L}; \quad (5)$$

$$F = \frac{\hat{F}}{TL^2}; \quad P = \frac{\hat{P}L^2}{Th}; \quad t = \hat{t}\left(\frac{T}{\rho L^2}\right)^{1/2}; \quad (6)$$

and the dimensionless constants are

$$\epsilon = \frac{D}{TL^2}; \quad C = \frac{v}{\left(\frac{T}{\rho}\right)^{1/2}}; \quad (7)$$

$$\eta = \frac{B}{L}; \quad \beta^2 = (1 - C^2) > 0. \quad (8)$$

The stiffness ratio, ϵ , is a small nondimensional ratio of the flexural stiffness to the stiffness derived from the applied axial tension. C is the constant, non-negative ratio of the transport speed to the propagation speed of a transverse wave in a string. η is the ratio of the width to the length of the web. β^2 is introduced to simplify the presentation of the equation of motion. We consider the web transported at subcritical speed, $\beta^2 = (1 - C^2) > 0$. The biharmonic operator ∇^4 and the bilinear operator L are

$$\nabla^4\gamma = \gamma_{,xxxx} + 2\gamma_{,xxyy} + \gamma_{,yyyy} \quad (9)$$

$$L[\gamma, \delta] = \gamma_{,xx}\delta_{,yy} - 2\gamma_{,xy}\delta_{,xy} + \gamma_{,yy}\delta_{,xx}. \quad (10)$$

The boundary conditions on the free edges at $y = 0, y = \eta$ are

$$[w_{,yyy} + (2 - \nu)w_{,cxy}] = 0 \quad (11)$$

$$[w_{,yy} + \nu w_{,cx}] = 0 \quad (12)$$

$$F_{,xx} = 0 \quad (13)$$

$$F_{,xy} = 0 \quad (14)$$

and on the loosely clamped edges (Chia, 1980) at $x = 0, x = 1$ are

$$w = 0 \quad (15)$$

$$w_{,x} = 0 \quad (16)$$

$$F_{,yy} = 1 \quad (17)$$

$$F_{,xy} = 0. \quad (18)$$

Method of Solution

The equilibrium solutions in (3) and (4) satisfy

$$C^2w_{,xx} - L[w, F] + \epsilon\nabla^4w = P \quad (19)$$

and

$$\nabla^4F = -6(1 - \nu^2)\epsilon L[w, w]. \quad (20)$$

Closed-form solutions to the coupled, nonlinear Eqs. (11)–(20) are not known. The ϵ multiplies the highest derivative, bending stiffness term in (19) and the nonlinear coupling of transverse displacement to membrane stresses in (20). With ϵ as a small perturbation parameter, (11)–(20) form a coupled, singular perturbation problem. As $\epsilon \rightarrow 0$, the problem becomes linear and uncoupled. Boundary layers for w exist near the four edges of the web because (19) decreases to a second-order equation as $\epsilon \rightarrow 0$. F has no boundary layer in this model because the order of (20) is unchanged as $\epsilon \rightarrow 0$. Figure 2 shows schematically the regions of the outer and inner expansions. The outer solution, governed by linear equations, is developed in the central part of the web away from the edges. The inner solution is developed in the boundary layer where bending effects are significant. The outer and the inner solutions are matched asymptotically in the matching region. The stiffness terms from the applied axial tension, membrane stress, and flexural rigidity are of the same order of magnitude when the width of the boundary layer at the clamped edges is $\epsilon^{1/2}$. Thus, they form a dominant balance and the distinguished limits of the boundary layers at the clamped ends are $\epsilon^{1/2}$ (Bender and Orszag, 1978). Similarly, the width of the boundary layer at free ends is $\epsilon^{1/4}$.

Expansion of the stress function F has the form

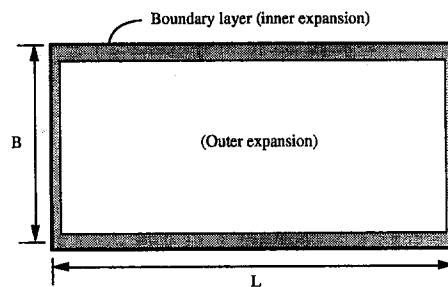


Fig. 2 Rectangular web and boundary layer. The width of the boundary layer at the clamped edges is of order $\epsilon^{1/2}$ and that at the free edges is of order $\epsilon^{1/4}$.

$$F = F_0 + \epsilon^{1/2}F_1 + \epsilon F_2 + \dots, \quad (21) \quad F = F_0 + \epsilon[F_2(0, y) + F_{2,x}(0, y)(x - 0)$$

and the outer expansion of w is

$$w = w_0 + \epsilon^{1/2}w_1 + \epsilon w_2 + \dots \quad (22) \quad + \frac{1}{2}F_{2,xx}(0, y)(x - 0)^2 + \dots] + \dots \quad (36)$$

Substitution of (21) and (22) into (20) and collection of balances of like order gives a sequence of equations governing F_j ,

$$\nabla^4 F_0 = 0 \quad (23)$$

$$\nabla^4 F_1 = 0 \quad (24)$$

$$\nabla^4 F_2 = -6(1 - \nu^2)L[w_0, w_0] \quad (25)$$

⋮

The solutions to (23) and (24), satisfying the boundary conditions, are

$$F_0 = \frac{1}{2}y^2 \quad (26)$$

$$F_1 = 0. \quad (27)$$

F_2 can be predicted from (25) and boundary conditions when w_0 is known. The method of Yamaki (1961) is modified to determine F_2 (Appendix A). Substitution of (21), (22), (26), and (27) into (19) and collection of balances of like order gives a sequence of equations governing w_j ,

$$-\beta^2 w_{0,xx} = P \quad (28)$$

$$-\beta^2 w_{1,xx} = 0 \quad (29)$$

$$-\beta^2 w_{2,xx} - L[w_0, F_2] + \nabla^4 w_0 = 0 \quad (30)$$

⋮

If the bending effects and the membrane stresses arising from the curvature of the web are neglected, (19) reduces to

$$-\beta^2 w_{,xx} = P, \quad (31)$$

which is the membrane solution w_0 described by (28). The boundary conditions for the outer expansion are the conditions of asymptotic matching with the inner solutions (Bender and Orszag, 1978).

Asymptotic Matching Conditions

The inner variables $X, \bar{X}, Y,$ and \bar{Y} inside the boundary layers at $x = 0, x = 1, y = 0,$ and $y = \eta$ are

$$X = \frac{x}{\epsilon^{1/2}}; \quad \bar{X} = \frac{(1-x)}{\epsilon^{1/2}}; \quad (32)$$

$$Y = \frac{y}{\epsilon^{1/4}}; \quad \bar{Y} = \frac{(\eta-y)}{\epsilon^{1/4}}. \quad (33)$$

Overbars relate to the inner expansion of w at $x = 1$ or at $y = \eta$.

(i) Near $x = 0$: The inner expansion near $x = 0$ has the form

$$w = W_0(X, y) + \epsilon^{1/2}W_1(X, y) + \epsilon W_2(X, y) + \dots, \quad (34)$$

and the outer expansion (22) near $x = 0$ becomes

$$w = w_0(0, y) + \epsilon^{1/2}[Xw_{0,x}(0, y) + w_1(0, y)] \\ + \epsilon[\frac{1}{2}X^2w_{0,xx}(0, y) + Xw_{1,x}(0, y) + w_2(0, y)] \\ + \dots \quad (35)$$

Asymptotic matching of (34) and (35) is undertaken term by term in the limits $x \rightarrow 0$ and $X \rightarrow \infty$. Taylor expansions of the stress function and loading about $x = 0$ are

Substitution of (26), (34), (36), and (37) into (19) yields equations governing $W_0, W_1,$ and W_2 . The boundary conditions on W_j at $x = 0$ are found by substituting (34) into (15) and (16). With W_j determined, w in (34) becomes

$$w = \epsilon^{1/2}[A_1(y)(e^{-\beta X} + \beta X - 1)] \\ + \epsilon\left[A_2(y)(e^{-\beta X} + \beta X - 1) - \frac{P(0, y)}{2\beta^2}X^2\right] + \dots \quad (38)$$

Note that $W_0 \equiv 0$ and

$$A_1(y) = \frac{w_{0,x}(0, y)}{\beta}; \quad A_2(y) = \frac{w_{1,x}(0, y)}{\beta}. \quad (39)$$

The asymptotic matching conditions near $x = 0$ are

$$w_0(0, y) = 0; \quad w_1(0, y) = -\frac{w_{0,x}(0, y)}{\beta}; \\ w_2(0, y) = -\frac{w_{1,x}(0, y)}{\beta}. \quad (40)$$

(ii) Near $x = 1$: The inner solution of w near $x = 1$ is

$$w = \epsilon^{1/2}[\bar{A}_1(y)(e^{-\beta \bar{X}} + \beta \bar{X} - 1)] \\ + \epsilon\left[\bar{A}_2(y)(e^{-\beta \bar{X}} + \beta \bar{X} - 1) - \frac{P(1, y)}{2\beta^2}\bar{X}^2\right] \\ + \dots, \quad (41)$$

where

$$\bar{A}_1(y) = -\frac{w_{0,x}(1, y)}{\beta}; \quad \bar{A}_2(y) = -\frac{w_{1,x}(1, y)}{\beta} \quad (42)$$

and the asymptotic matching conditions near $x = 1$ are

$$w_0(1, y) = 0; \quad w_1(1, y) = \frac{w_{0,x}(1, y)}{\beta}; \\ w_2(1, y) = \frac{w_{1,x}(1, y)}{\beta}. \quad (43)$$

(iii) Near $y = 0$: The inner expansion of w near $y = 0$ has the form

$$w = U_0(x, Y) + \epsilon^{1/4}U_1(x, Y) + \epsilon^{1/2}U_2(x, Y) \\ + \epsilon^{3/4}U_3(x, Y) + \epsilon U_4(x, Y) + \dots, \quad (44)$$

and the outer solution (22) near $y = 0$ becomes

$$w = w_0(x, 0) + \epsilon^{1/4}[Yw_{0,y}(x, 0)] \\ + \epsilon^{1/2}[\frac{1}{2}Y^2w_{0,yy}(x, 0) + w_1(x, 0)] \\ + \epsilon^{3/4}[\frac{1}{6}Y^3w_{0,yyy}(x, 0) + Yw_{1,y}(x, 0)] \\ + \epsilon[\frac{1}{24}Y^4w_{0,yyyy}(x, 0) + \frac{1}{2}Y^2w_{1,yy}(x, 0) \\ + w_2(x, 0)] + \dots \quad (45)$$

The Taylor expansions of the stress function and loading about $y = 0$ are

$$F = F_0 + \epsilon[F_2(x, 0) + F_{2,y}(x, 0)(y - 0) + \frac{1}{2}F_{2,yy}(x, 0)(y - 0)^2 + \dots] + \dots \quad (46)$$

$$P = P(x, 0) + P_y(x, 0)(y - 0) + \frac{1}{2}P_{yy}(x, 0)(y - 0)^2 + \dots \quad (47)$$

Substitution of (26), (44), (46), and (47) into (19) yields equations governing U_0, \dots, U_4 . Boundary conditions on U_j at $Y = 0$ are found by substituting (44) into (11) and (12). With U_j determined, w in (44) becomes

$$w = [w_0(x, 0)] + \epsilon^{1/4}[Yw_{0,y}(x, 0)] + \epsilon^{1/2}[\frac{1}{2}Y^2w_{0,yy}(x, 0) + w_1(x, 0) + \sum_{n=1}^{\infty} I_n G_1(x, Y)] + \epsilon^{3/4}[\frac{1}{6}Y^3w_{0,yyy}(x, 0) + Yw_{1,y}(x, 0) + \sum_{n=1}^{\infty} J_n G_2(x, Y)] + \epsilon[\frac{1}{24}Y^4w_{0,yyyy}(x, 0) + \frac{1}{2}Y^2w_{1,yy}(x, 0) + w_2(x, 0) + \sum_{n=1}^{\infty} K_n G_1(x, Y)] + \dots \quad (48)$$

The expressions of $I_n, J_n, K_n, G_1,$ and G_2 are listed in Appendix B.

Matching can be accomplished if $w_j(x, 0)$ ($j = 0, 1,$ and 2) is of order 1. Thus, the asymptotic matching conditions near $y = 0$ are

$$w_0(x, 0) \sim O(1); \quad w_1(x, 0) \sim O(1); \quad w_2(x, 0) \sim O(1). \quad (49)$$

(iv) Near $y = \eta$: The inner solution of w near $y = \eta$ is

$$w = [w_0(x, \eta)] + \epsilon^{1/4}[-\bar{Y}w_{0,y}(x, \eta)] + \epsilon^{1/2}[\frac{1}{2}\bar{Y}^2w_{0,yy}(x, \eta) + w_1(x, \eta) + \sum_{n=1}^{\infty} \bar{I}_n G_1(x, \bar{Y})] + \epsilon^{3/4}[-\frac{1}{6}\bar{Y}^3w_{0,yyy}(x, \eta) - \bar{Y}w_{1,y}(x, \eta) + \sum_{n=1}^{\infty} \bar{J}_n G_2(x, \bar{Y})] + \epsilon[\frac{1}{24}\bar{Y}^4w_{0,yyyy}(x, \eta) + \frac{1}{2}\bar{Y}^2w_{1,yy}(x, \eta) + w_2(x, \eta) + \sum_{n=1}^{\infty} \bar{K}_n G_1(x, \bar{Y})] + \dots \quad (50)$$

The expressions of $\bar{I}_n, \bar{J}_n,$ and \bar{K}_n are listed in Appendix B.

The asymptotic matching conditions near $y = \eta$ are

$$w_0(x, \eta) \sim O(1); \quad w_1(x, \eta) \sim O(1); \quad w_2(x, \eta) \sim O(1). \quad (51)$$

Uniform Approximation

A uniform approximation for transverse displacement is

$$w = w_0(x, y) + \epsilon^{1/2}w_1(x, y) + \epsilon w_2(x, y) + H_1(X, y) + \bar{H}_1(\bar{X}, y) + H_2(x, Y) + \bar{H}_2(x, \bar{Y}), \quad (52)$$

where H_i and \bar{H}_i ($i = 1,$ and 2) are listed in Appendix B. The outer solutions $w_j(x, y)$ ($j = 0, 1,$ and 2) satisfy (28)–(30), and the asymptotic matching conditions (40), (43), (49), and (51). The solution in (52) is carried out to order ϵ where the coupling of membrane stresses and flexural stiffness appears. It is obtained by summing the outer solution (22) and the inner solutions (38), (41), (48), and (50), and then subtracting the matching solutions (Bender and Orszag, 1978). The matching

solutions are determined from the inner solutions with $X \rightarrow \infty, \bar{X} \rightarrow \infty, Y \rightarrow \infty,$ and $\bar{Y} \rightarrow \infty$. The effects of the bending stiffness in the boundary layers on the deflection are assessed through $H_1, \bar{H}_1, H_2,$ and \bar{H}_2 . The effects of membrane stresses on the deflection are represented in w_2 .

Results and Discussion

A principal benefit of the singular perturbation solution is the analytical clarity of the coupling between the deflection and the membrane stresses. The solution to order ϵ represents this coupling. Higher-order solutions are possible though a substantial increase in effort is required.

This analysis is meaningful for ϵ less than 10^{-2} and for the boundary layer width not extending to the middle of the web. The range of ϵ , typical for paper webs, is 10^{-5} to 10^{-3} . For example, one paper web product of James River Corporation gives $\epsilon = 1.58 \times 10^{-4}$ ($E = 5 \times 10^9$ N/m², $\rho = 0.04$ Kg/m², $T = 55$ N/m, $\nu = 0.3, L = 1.194$ m, $B = 0.597$ m, $h = 0.3$ mm). In this case, the width of the boundary layer at the clamped edges ($\epsilon^{1/2}$) is of order 0.01 and that at the free edges ($\epsilon^{1/4}$) is of order 0.1. The solution herein is representative of this paper web response. A band saw, used to cut timber, can yield $\epsilon = 1.127$, ($E = 2 \times 10^{11}$ N/m², $T = 4 \times 10^4$ N/m, $\nu = 0.3, L = 1.0$ m, $B = 0.25$ m, $h = 0.0135$ m). In this case, ϵ is not sufficiently small for application of this analysis.

When the curvature of the web is large, membrane stretching, described by $-6(1 - \nu^2)\epsilon L[w, w]$ in (20), can be relatively large. The analysis herein requires $\min\{|w^*_{,xy}|^{-2}, |w^*_{,xx}w^*_{,yy}|^{-1}\} \gg \epsilon$ which ensures that F has no boundary layer (w^* is the outer solution, and both $|w^*_{,xy}|^{-2}$ and $|w^*_{,xx}w^*_{,yy}|^{-1}$ are evaluated at the four edges of the web).

As tension decreases and/or flexural stiffness increases, the stiffness ratio ϵ increases and the width of the boundary layer increases. As ϵ increases, the effects of the bending stiffness in the boundary layers on the deflection, entering through $H_1, \bar{H}_1, H_2,$ and \bar{H}_2 in (52), increases.

Consider two illustrative examples. In loading I, a paper web is loaded by its own uniform weight, where the web weight ranges from $P = 5$ to 50 . In loading II, a paper web is under the transverse loading $P = P_c \sin(\pi x) \sin(\pi y)$, where P_c is a constant. Figure 3(a) shows the deflection under loading I with $P = 5, \epsilon = 10^{-3}, \nu = 0.3, C = 0.8,$ and $\eta = 1$. The transverse displacement is symmetric to the midpoint of the span and is larger at the free edges than at the middle of the web. Inclusion of the boundary layers at the free edges increases the predicted deflection at the free edges and decreases slightly the predicted deflection at the middle of the web. The transverse displacement is only slightly y -dependent. Thus, w_y and $\epsilon L[w, w]$ in (20) are small. The effect of web curvature on membrane stresses is negligible in loading I. Figure 3(b) shows the deflection under loading II with $P_c = 15, \epsilon = 10^{-4}, \nu = 0.3, C = 0.8,$ and $\eta = 1$. Membrane stretching, $-6(1 - \nu^2)\epsilon L[w, w]$ in (20), is of order 1 and is not negligible. The coupling between the membrane stresses and the large-amplitude deflection is significant.

Figure 4 shows the stress distribution (from (21)) in the web under loading II with $P_c = 15, \epsilon = 10^{-4}, \nu = 0.3, C = 0.8,$ and $\eta = 1$. The normal stress in the width direction ($\sigma_{yy} = F_{,yy}$) is shown in Fig. 4(a). Compressive stresses exist at the clamped ends. Figure 4(b) shows the normal stress in the axial direction ($\sigma_{xx} = F_{,yy}$) which results from the applied axial tension and the curvature of the web. Depending on the intensity of the width compression developed in the web, the web can wrinkle (Lin and Mote, in press).

The deflection of the web at $y = 0.5$ under loading II with $P_c = 15, \epsilon = 10^{-4}, \nu = 0.3, \eta = 1,$ and different axial transport speeds is shown in Fig. 5. The deflection of the equilibrium increases as the axial transport speed increases. The effective stiffness from the applied axial tension and axial transport

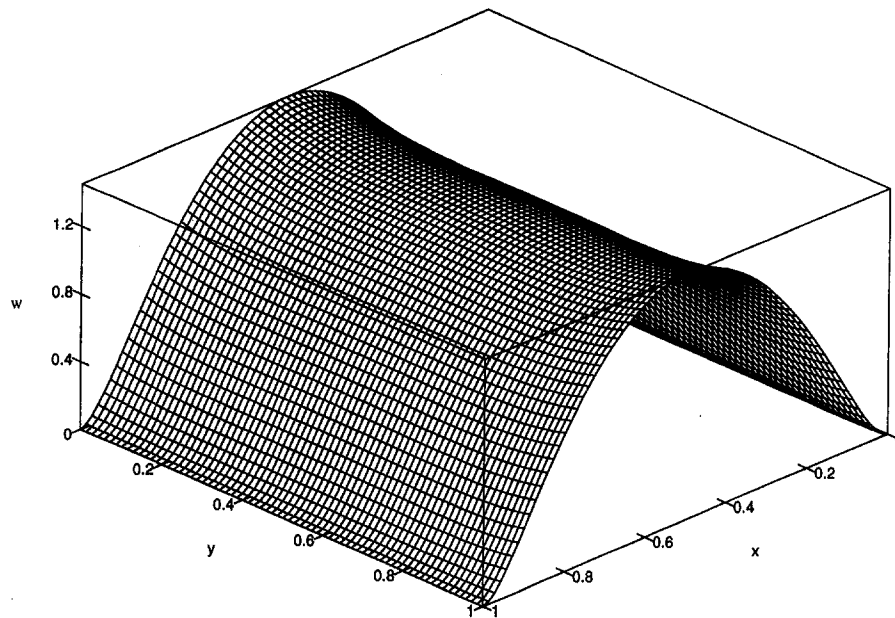


Fig. 3(a)

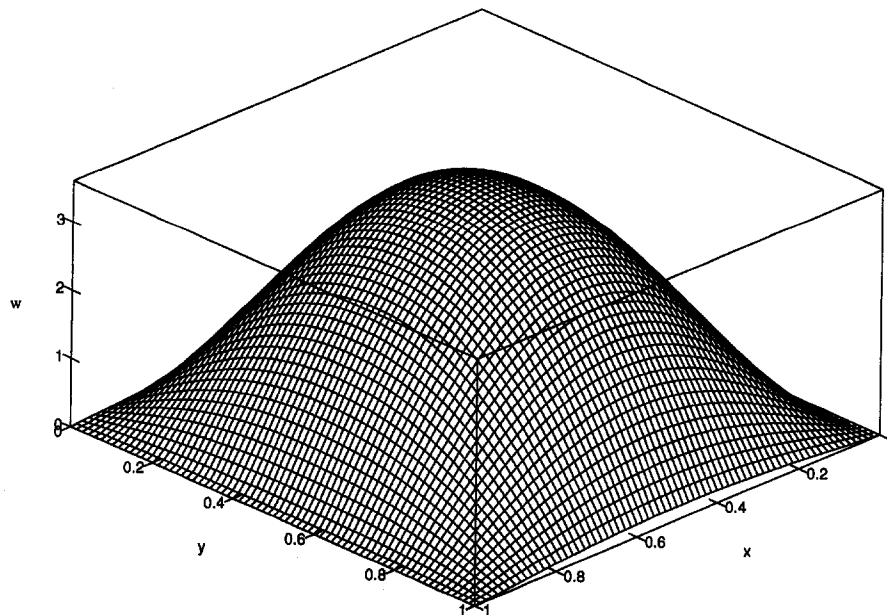


Fig. 3(b)

Fig. 3 (a) The deflection under loading I with $P = 5$, $\epsilon = 10^{-3}$, $\nu = 0.3$, $C = 0.8$, and $\eta = 1$; (b) the deflection under loading II with $P_c = 15$, $\epsilon = 10^{-4}$, $\nu = 0.3$, $C = 0.8$, and $\eta = 1$

speed, determined from $\beta^2 = (1 - C^2)$, decreases as the axial transport speed increases. The web deflection increases under the smaller effective stiffness β^2 .

The deflection at the midpoint of the web under loading II with $\epsilon = 10^{-4}$, $\nu = 0.3$, $C = 0.8$, and $\eta = 1$ is shown in Fig. 6. Membrane and linear plate theories do not model the membrane stresses arising from the curvature of the web and therefore often overestimate the deflection at the midpoint of the web. The effects of the membrane stresses on the web deflection can be assessed by the nonlinear plate theory. The relationship between deflection and transverse load P_c is not linear for $P_c > 7$.

The leading order approximation to w is $w_0(x, y)$, the deflection predicted by the membrane model. The effects of bending and membrane stresses enter through the perturbation terms in

(52). If the stress function depends on the applied, uniform, axial tension only ($F = F_0 = \frac{1}{2}y^2$ in (26) and $F_2 = 0$ in (30)), w in (52) reduces to the deflection predicted by a linear plate model.

Depending on ϵ and the web curvature, w predicted by (52) can be quite different from that predicted by membrane or linear plate theories. Consider a web deflected under loading II. Introduce two dimensionless parameters,

$$\zeta_1 = \frac{\epsilon^{1/2}\pi}{\beta}; \quad \zeta_2 = \frac{3(1 - \nu^2)\epsilon(P_c)^2}{\pi^2\beta^6}. \quad (53)$$

Here, ζ_1 is the ratio of the half-order term, $\epsilon^{1/2}w_1$, to the zero-order term, w_0 in (52) evaluated at the midpoint of the web. The half-order and other higher-order terms in (52) are negligi-

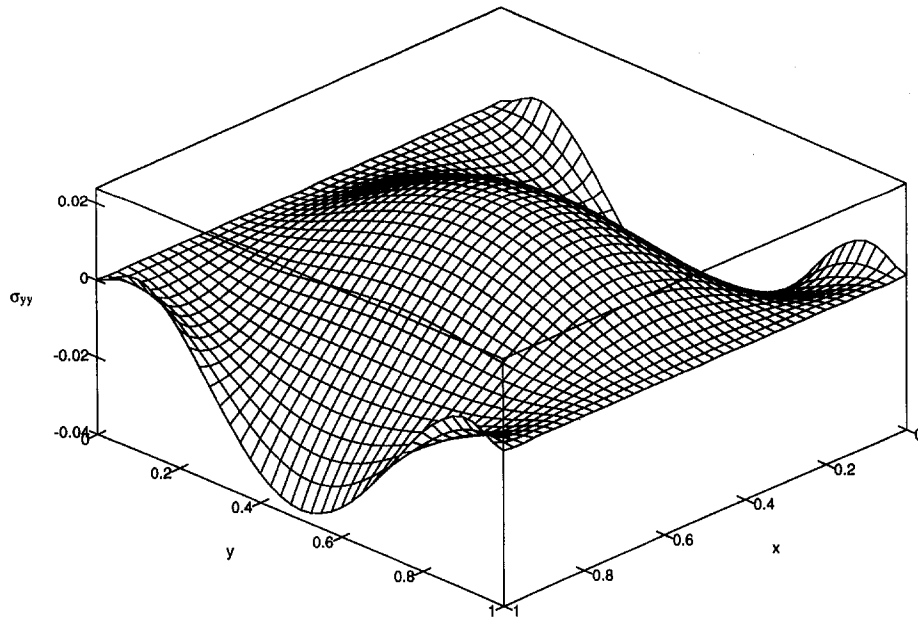


Fig. 4(a)

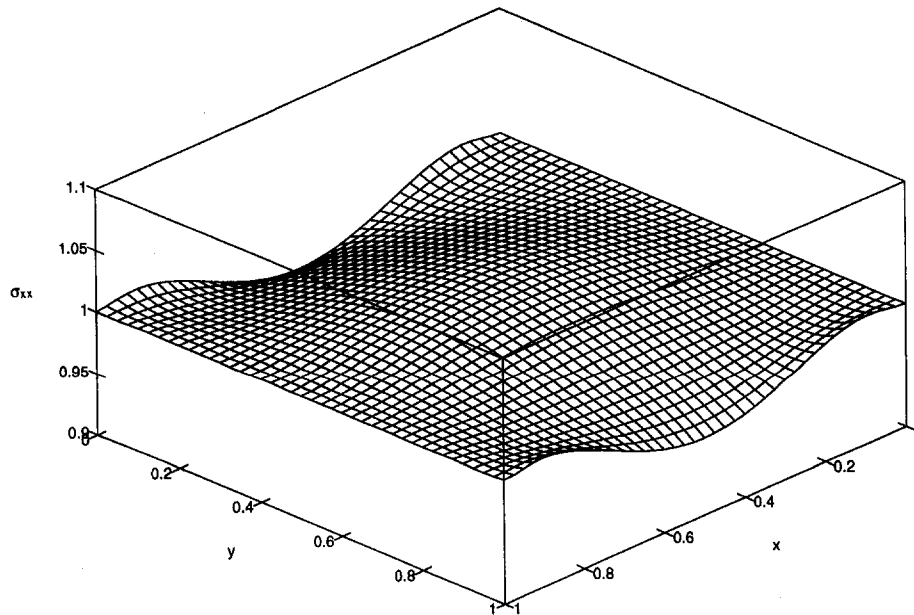


Fig. 4(b)

Fig. 4 The stress distribution in the web under loading II with $P_c = 15$, $\epsilon = 10^{-4}$, $\nu = 0.3$, $C = 0.8$, and $\eta = 1$; (a) the normal stress in the width direction ($\sigma_{yy} = F_{,yy}$), (b) the normal stress in the axial direction ($\sigma_{xx} = F_{,xx}$) which results from the applied axial tension and the membrane stresses arising from the curvature of the paper web

ble when ζ_1 is small. Thus, the membrane theory is representative of the web response for small ζ_1 , say $\zeta_1 < 0.02$. ζ_2 is the ratio of the maximum stiffness due to membrane stretching to the effective stiffness β^2 . The membrane stresses induced from the curvature of the web are negligible when ζ_2 is small. Thus, the linear plate theory is applicable to the web response for small ζ_2 , say $\zeta_2 < 0.02$. The effects of bending and membrane stresses arising from the web curvature on deflection are significant when ζ_1 and ζ_2 are not small, say $\zeta_1 > 0.02$, and $\zeta_2 > 0.02$.

For example, consider the webs under loading II with $P_c = 5$, $C = 0.8$, and different stiffness ratios. Both ζ_1 and ζ_2 are less than 0.02 for ϵ less than 10^{-5} . The membrane or the linear

plate models are both representative of the web deflection. With ϵ in the range 10^{-4} to 10^{-3} , both ζ_1 and ζ_2 are of order 0.1. The membrane theory overestimates the deflection at the midpoint of the span between 8 percent and 58 percent and the linear plate theory overestimates that deflection between 1 percent and 15 percent.

Conclusions

The equilibrium displacement and stress distribution in a two dimensional, axially moving web under transverse loading have been predicted through singular perturbation and boundary layer theories. The conclusions of this analysis are the following:

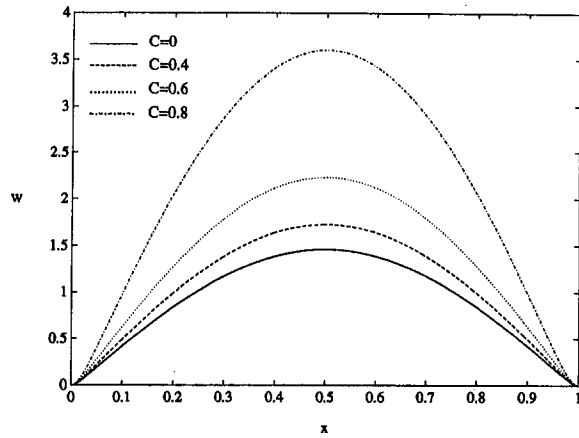


Fig. 5 The deflection of the web at $y = 0.5$ under loading II with $P_c = 15$, $\epsilon = 10^{-4}$, $\nu = 0.3$, $\eta = 1$, and different axial transport speeds

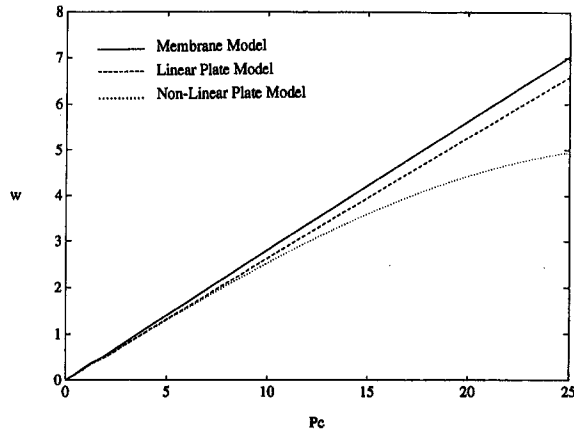


Fig. 6 The deflection at the midpoint of the web under loading II with $\epsilon = 10^{-4}$, $\nu = 0.3$, $C = 0.8$, and $\eta = 1$

(1) The predictions of deflection and membrane stress distribution at equilibrium are valid for a web with stiffness ratio ϵ less than 10^{-2} .

(2) The singular perturbation and boundary layer theory solution is applicable to prediction of paper web deflection and membrane stress distribution because the stiffness ratio ϵ falls between 10^{-5} and 10^{-3} .

(3) A principal benefit of this analysis is the easy assessment of the contribution of membrane stresses to the predicted transverse deflection of a web.

(4) The width of the boundary layer, or matching region, is of order $\epsilon^{1/2}$ at the clamped edges and is of order $\epsilon^{1/4}$ at the free edges.

(5) Compression and shear may be developed in the web under distributed loading. The width compression and shear can wrinkle the web (Lin and Mote, in press).

(6) The boundary layers at the free edges increase the predicted deflection at the free edges and slightly decrease the predicted deflection at the middle of the web.

(7) The web deflection increases as the axial transport speed increases. The effective stiffness β^2 in (8) decreases as the axial transport speed increases. The deflection of the equilibrium increases under the smaller effective stiffness β^2 .

(8) The membrane model and the linear plate model are realistic for small amplitude transverse response only. They often overestimate the deflection in the middle of the web and do not model the membrane stresses arising from its curvature. The two dimensionless parameters ζ_1 and ζ_2 in (53) are used to estimate the magnitude of the effects of bending and membrane

stresses on deflection. With $\zeta_1 > 0.02$ or $\zeta_2 > 0.02$, a plate theory coupling membrane and flexural stiffness effects should be used to model the system.

Acknowledgment

The authors would like to thank the James River Corporation and the TAPPI Research Foundation for their support and interest in this work.

References

- Bender, C. M., and Orszag, S. A., 1978, *Advanced Mathematical Methods for Scientists and Engineers*, McGraw-Hill, New York, pp. 426–446.
- Chia, C. Y., 1980, *Nonlinear Analysis of Plates*, McGraw-Hill, New York, p. 38.
- Fung, Y. C., and Wittrick, W. H., 1955, "A Boundary-Layer Phenomenon in the Large Deflection of Thin Plates," *Quarterly Journal of Mechanics and Applied Mathematics*, Vol. 8, pp. 191–210.
- Lin, C. C., and Mote, C. D. Jr., 1995, "The Wrinkling of Thin, Flat, Rectangular Webs," *ASME JOURNAL OF APPLIED MECHANICS*, in press.
- Reissner, H., 1912, "Spannungen in Kugelschalen-(Kuppeln)," *Festschrift Mueller-Breslau*, Leipzig, pp. 181.
- Renshaw, A. A., 1992, "Perturbation and Stability Theories for Flexible Rotating Disks," Ph.D. Dissertation, Dept. of Mechanical Engineering, University of California, Berkeley, pp. 11–41.
- Triantafyllou, M. S., and Triantafyllou, G. S., 1991, "The Paradox of the Hanging String: An Explanation Using Singular Perturbations," *Journal of Sound and Vibration*, Vol. 148, pp. 343–351.
- von Karman, T., 1910, "Festigkeitsprobleme im Maschinenbau," *Encyklopaedie der Mathematischen Wissenschaften*, Vol. IV₄, p. 349.
- Yamaki, N., 1961, "Influence of Large Amplitudes on Flexural Vibrations of Elastic Plates," *ZAMM*, Vol. 41, pp. 501–510.

APPENDIX A

Method to Solve F_2

Find a particular solution F_2^p satisfying (25) and zero shear stress boundary conditions. Then, F_2 has the form

$$F_2 = F_2^p + F_2^H, \quad (A1)$$

where

$$F_2^H = \sum_{n=1}^{\infty} B_n \left\{ -[\sinh(n\pi\eta) + n\pi\eta] \cosh(n\pi y) - [1 - \cos(n\pi\eta)] \sinh(n\pi y) + [n\pi - n\pi \cosh(n\pi\eta)] y \cosh(n\pi y) + [n\pi \sinh(n\pi\eta)] y \sinh(n\pi y) \right\} \cos(n\pi x) + \tilde{B}_n \left\{ -\left[\sinh\left(\frac{n\pi}{\eta}\right) + \frac{n\pi}{\eta} \right] \cosh\left(\frac{n\pi}{\eta} x\right) - \left[1 - \cos\left(\frac{n\pi}{\eta}\right) \right] \sinh\left(\frac{n\pi}{\eta} x\right) + \left[\frac{n\pi}{\eta} - \frac{n\pi}{\eta} \cosh\left(\frac{n\pi}{\eta}\right) \right] x \cosh\left(\frac{n\pi}{\eta} x\right) + \left[\frac{n\pi}{\eta} \sinh\left(\frac{n\pi}{\eta}\right) \right] x \sinh\left(\frac{n\pi}{\eta} x\right) \right\} \cos\left(\frac{n\pi}{\eta} y\right). \quad (A2)$$

F_2^H is a homogeneous solution of F_2 with zero shear stress along the boundaries. Constants B_n and \tilde{B}_n are determined to satisfy (13) and (17).

APPENDIX B

List of Functions and Constants

$$H_1(X, y) = \epsilon^{1/2} A_1 e^{-\beta X} + \epsilon A_2 e^{-\beta X} \quad (B1)$$

$$\bar{H}_1(\bar{X}, y) = \epsilon^{1/2} \bar{A}_1 e^{-\beta \bar{X}} + \epsilon \bar{A}_2 e^{-\beta \bar{X}} \quad (B2)$$

$$H_2(x, Y) = \epsilon^{1/2} \left(\sum_{n=1}^{\infty} I_n G_1(x, Y) \right) + \epsilon^{3/4} \left(\sum_{n=1}^{\infty} J_n G_2(x, Y) \right) + \epsilon \left(\sum_{n=1}^{\infty} K_n G_1(x, Y) \right) \quad (\text{B3})$$

$$\bar{H}_2(x, \bar{Y}) = \epsilon^{1/2} \left(\sum_{n=1}^{\infty} \bar{I}_n G_1(x, \bar{Y}) \right) + \epsilon^{3/4} \left(\sum_{n=1}^{\infty} \bar{J}_n G_2(x, \bar{Y}) \right) + \epsilon \left(\sum_{n=1}^{\infty} \bar{K}_n G_1(x, \bar{Y}) \right) \quad (\text{B4})$$

$$A_1(y) = \frac{w_{0,x}(0, y)}{\beta}; \quad \bar{A}_1(y) = -\frac{w_{0,x}(1, y)}{\beta} \quad (\text{B5})$$

$$A_2(y) = \frac{w_{1,x}(0, y)}{\beta}; \quad \bar{A}_2(y) = -\frac{w_{1,x}(1, y)}{\beta} \quad (\text{B6})$$

$$I_n = 2 \int_0^1 - (w_{0,yy}(x, 0) + \nu w_{0,xx}(x, 0)) \sin(n\pi x) dx \quad (\text{B7})$$

$$J_n = 2 \int_0^1 - (w_{0,yyy}(x, 0) + (2 - \nu) w_{0,xyy}(x, 0)) \sin(n\pi x) dx \quad (\text{B8})$$

$$K_n = 2 \int_0^1 - (w_{1,yy}(x, 0) + \nu w_{1,xx}(x, 0)) \sin(n\pi x) dx \quad (\text{B9})$$

$$\bar{I}_n = 2 \int_0^1 - (w_{0,yy}(x, \eta) + \nu w_{0,xx}(x, \eta)) \sin(n\pi x) dx \quad (\text{B10})$$

$$\bar{J}_n = 2 \int_0^1 (w_{0,yyy}(x, \eta) + (2 - \nu) w_{0,xyy}(x, \eta)) \sin(n\pi x) dx \quad (\text{B11})$$

$$\bar{K}_n = 2 \int_0^1 - (w_{1,yy}(x, \eta) + \nu w_{1,xx}(x, \eta)) \sin(n\pi x) dx \quad (\text{B12})$$

$$G_1(x, Y) = (\beta n \pi)^{-1} \sin(n\pi x) \exp \left[- \left(\frac{\beta n \pi}{2} \right)^{1/2} Y \right] \times \left[\cos \left(\left(\frac{\beta n \pi}{2} \right)^{1/2} Y \right) - \sin \left(\left(\frac{\beta n \pi}{2} \right)^{1/2} Y \right) \right] \quad (\text{B13})$$

$$G_2(x, Y) = \sqrt{2} (\beta n \pi)^{-3/2} \sin(n\pi x) \times \exp \left[- \left(\frac{\beta n \pi}{2} \right)^{1/2} Y \right] \cos \left(\left(\frac{\beta n \pi}{2} \right)^{1/2} Y \right) \quad (\text{B14})$$

Anisotropic Yield Surfaces Based on Elastic Projection Operators

H. L. Schreyer
Fellow ASME.

Q. H. Zuo

Department of Mechanical Engineering,
University of New Mexico,
Albuquerque, NM 87131

Although most materials are anisotropic to some extent, most yield surfaces are either chosen to be isotropic or to be a smooth anisotropic surface with no connection to the elastic anisotropic features. Here, the elastic projection operators obtained from the spectral decomposition of the elasticity tensor are used to define anisotropic yield surfaces with a yield surface defined for each of the projection operators. The advantages of the approach are (1) plastic deformation modes are associated with the elastic anisotropic behavior, (2) the spectral decomposition of the tangent tensor is readily available for a bifurcation analysis, (3) the composite yield surface has vertices which are thought to be important for predicting plastic buckling, and (4) the contributions to plastic deformations from each yield surface are uncoupled. The result is a theory that is actually quite simple but yet reflects some of the observed features for materials to yield in specific modes.

1 Introduction

Many, if not all, materials exhibit anisotropic behavior, especially if large deformations occur in the plastic regime. The assumption of isotropy is useful for simplifying an elastic-plastic analysis but in order to predict physical phenomena, it is often necessary to introduce an anisotropic yield criterion which is often based solely on experimental evidence. More often than not, such experimental evidence is not available and the form of the yield surface is postulated. Here, it is assumed that the anisotropy of the elastic response, no matter how slight, provides evidence of anisotropy in the plastic regime. Projection operators obtained from the spectral decomposition of the anisotropic elasticity tensor are used to define yield surfaces whose composition provides a single yield surface with vertices. In addition to simplicity, the resulting theory has other features which may prove useful in correlating theoretical predictions with experimental data.

With a generalization from the von Mises criterion, Hill (1948) provided a quadratic yield function to handle orthotropic plasticity. The yield function has been and continues to be widely used although it was later realized that the functional form could not adequately represent some materials (Mellor, 1982). Suggestions for improvement have been primarily confined to modifying Hill's function by changing the exponent on stress components to different integer and noninteger values with several typical examples given in the literature (Gotoh, 1977; Parmar and Mellor, 1978; Hill, 1979; Zhou, 1990; Montheillet et al., 1991). Hill (1990, 1993) has recently placed these contributions in perspective and has proposed his own improved version with particular emphasis on applications to textured sheets and convenience of use as reflected by relatively few material parameters that are easily determined, and by algebraic convenience. In all of this work no attempt is made to relate the anisotropic plastic properties with the underlying anisotropic structure of elasticity.

Contributed by the Applied Mechanics Division of THE AMERICAN SOCIETY OF MECHANICAL ENGINEERS for publication in the ASME JOURNAL OF APPLIED MECHANICS.

Discussion on this paper should be addressed to the Technical Editor, Prof. Lewis T. Wheeler, Department of Mechanical Engineering, University of Houston, Houston, TX 77204-4792, and will be accepted until four months after final publication of the paper itself in the ASME JOURNAL OF APPLIED MECHANICS.

Manuscript received by the ASME Applied Mechanics Division, Jan. 7, 1994; final revision, May 7, 1994. Associate Technical Editor: R. Abeyaratne.

Recently, several papers (Mehrabadi and Cowin, 1990; Saidegh and Cowin, 1991; Sutcliffe, 1992) have elegantly provided spectral decompositions of the fourth-order elasticity tensor. In addition to providing mathematical representations, these authors have suggested that such decompositions may prove to be useful for developing anisotropic plasticity theories. We explore the manifestations of such a suggestion under the assumptions that each mode acts independently and that the flow rule is associated. The result is a yield surface composed of piecewise flat surfaces so that vertices arise automatically. The presence of vertices has been deemed important, for example, in connection with the plastic buckling of structures (Needleman and Tvergaard, 1982).

The proposed theory is intended for the macroscopic representation of materials, not necessarily metals, for which elastic anisotropic properties might be available but for which little experimental data exist in the plastic regime. The resulting theory is algebraically simple and there are only a few material parameters. Therefore, the desirable attributes enunciated by Hill are retained but with a fundamentally different approach in which anisotropic elastic features are used to suggest the appropriate form of the anisotropic yield function. The proposed theory also provides a particularly simple expression for the tangent tensor so that statements concerning the nature of plastic modes and the potential for a discontinuous bifurcation are easily obtained.

2 Elastic Projection Operators

Consider a material governed by linear elasticity. Then the constitutive equation relating the stress, \mathbf{s} , and strain, \mathbf{e} , is

$$\mathbf{s} = \mathbf{E} : \mathbf{e}. \quad (1)$$

All elastic properties including material symmetries are described by the fourth-order elasticity tensor, \mathbf{E} , which is assumed here to satisfy both the minor and major symmetry conditions.

The eigenproblem for this tensor is

$$\mathbf{E} : \mathbf{N} = \lambda \mathbf{N} \quad (2)$$

in which λ denotes the eigenvalue and the second-order tensor, \mathbf{N} , the eigentensor which we choose to normalize such that $\mathbf{N} : \mathbf{N} = 1$. If \mathbf{E} satisfies major symmetry, then the eigenvalues are real and for each distinct eigenvalue, λ_i , the corresponding

eigentensor, \mathbf{N}_i , is perpendicular to all other eigentensors. The combined property of orthonormality is summarized in the relation

$$\mathbf{N}_i : \mathbf{N}_j = \delta_{ij} \quad i, j = 1, \dots, 6 \quad (3)$$

in which δ_{ij} denotes the Kronecker delta. Assume temporarily that all eigenvalues are distinct which corresponds to six pieces of information about \mathbf{E} (six independent material parameters). Because of normality five parameters are required to obtain \mathbf{N}_1 . Then with the use of normality and orthogonality, four additional pieces of information are needed to define \mathbf{N}_2 . It follows in a similar manner that three, two, one, and zero pieces of information are required to obtain \mathbf{N}_3 , \mathbf{N}_4 , \mathbf{N}_5 , and \mathbf{N}_6 , respectively. The maximum number of independent material parameters is therefore 21 which is the number of independent components of \mathbf{E} for general anisotropy.

Associated with each eigentensor is the following projection operator:

$$\mathbf{P}_i = \mathbf{N}_i \otimes \mathbf{N}_i \quad i = 1, \dots, 6. \quad (4)$$

In this relation and in subsequent equations, the usual summation convention of repeated indices is not used. By definition, the operators span the space of symmetric fourth-order tensors, are orthogonal, and therefore satisfy

$$\sum_{i=1}^6 \mathbf{P}_i = \mathbf{I} \quad \mathbf{P}_i : \mathbf{P}_j = \delta_{ij} \mathbf{P}_i \quad i, j = 1, \dots, 6 \quad (5)$$

in which \mathbf{I} denotes the symmetric fourth-order identity tensor. The spectral decomposition of \mathbf{E} and its inverse (provided an eigenvalue is not zero) are

$$\mathbf{E} = \sum_{i=1}^6 \lambda_i \mathbf{P}_i \quad \mathbf{E}^{-1} = \sum_{i=1}^6 \frac{1}{\lambda_i} \mathbf{P}_i \quad (6)$$

According to Mehrabadi and Cowin (1990) this result is already embodied in the work of Kelvin who quite appropriately called, λ_i , the principal elasticities of the material. In a similar fashion one might consider \mathbf{N}_i to be the principal elastic modes.

If symmetries exist, the eigenvalues are not all distinct and the derivation of the projection operators is not quite as straightforward. Let K denote the number of distinct eigenvalues, a minimum of two for isotropic materials to a maximum of six for completely anisotropic materials. Luehr and Rubin (1990) derived a general expression for the independent projection operators for second-order tensors. The theory is directly applicable to fourth-order tensors so that for any K the projection operators are

$$\mathbf{P}_i = \left[\prod_{j=1, \dots, K(j \neq i)} (\lambda_i - \lambda_j) \right]^{-1} \prod_{j=1, \dots, K(j \neq i)} (\mathbf{E} - \lambda_j \mathbf{I}) \quad i = 1, \dots, K. \quad (7)$$

The spectral decomposition of (6) becomes a sum from 1 to K instead of 1 to 6.

Each projection operator will have an eigenvalue of one with multiplicity identical to that associated with the corresponding eigenvalue of the elasticity tensor. The other eigenvalues are zero. Using orthogonality, one can construct the eigentensors, \mathbf{N}_i , which span the space complementary to the null space of \mathbf{P}_i . The null space of \mathbf{P}_i is spanned by the eigentensors of the other projection operators with eigenvalues of one. In principle then, one can find the six eigentensors, \mathbf{N}_i , and the K projection operators.

The linear constitutive relation can now be expressed as follows:

$$\mathbf{s} = \sum_{i=1}^K \lambda_i \mathbf{P}_i : \mathbf{e}. \quad (8)$$

Define projected stress and strain tensors as follows:

$$\mathbf{s}_i = \mathbf{P}_i : \mathbf{s} \quad \mathbf{e}_i = \mathbf{P}_i : \mathbf{e} \quad (9)$$

with the consequence that

$$\mathbf{s} = \sum_{i=1}^K \mathbf{s}_i \quad \mathbf{e} = \sum_{i=1}^K \mathbf{e}_i. \quad (10)$$

The projected stresses and strains satisfy the orthogonality relation

$$\mathbf{s}_i : \mathbf{s}_j = \delta_{ij} \bar{s}_i^2 \quad \bar{s}_i^2 = \mathbf{s}_i : \mathbf{s}_i \quad (11a)$$

$$\mathbf{e}_i : \mathbf{e}_j = \delta_{ij} \bar{e}_i^2 \quad \bar{e}_i^2 = \mathbf{e}_i : \mathbf{e}_i. \quad (11b)$$

Operate on each term in (8) with the projection \mathbf{P}_j and use the orthonormal relation (5) to obtain an alternative form of the constitutive equation as

$$\mathbf{s}_i = \lambda_i \mathbf{e}_i \quad i = 1, \dots, K, \quad (12)$$

i.e., the projected stress and strain are directly related through the corresponding eigenvalue of the elasticity tensor and are uncoupled from other projected stress and strain tensors. This relation was stated by Mehrabadi and Cowin (1990) as property B . It follows that the invariants of each projected stress and strain are related by

$$\begin{aligned} \text{tr } \mathbf{s}_i &= \lambda_i \text{tr } \mathbf{e}_i \quad \mathbf{s}_i : \mathbf{s}_i = (\lambda_i)^2 \mathbf{e}_i : \mathbf{e}_i \\ \text{tr } (\mathbf{s}_i \cdot \mathbf{s}_i \cdot \mathbf{s}_i) &= (\lambda_i)^3 \text{tr } (\mathbf{e}_i \cdot \mathbf{e}_i \cdot \mathbf{e}_i) \end{aligned} \quad (13)$$

In a similar fashion, twice the strain energy density is

$$\mathbf{e} : \mathbf{E} : \mathbf{e} = \sum_{i=1}^K \lambda_i \bar{e}_i^2 = \sum_{i=1}^K \frac{1}{\lambda_i} \bar{s}_i^2. \quad (14)$$

It follows immediately that the maximum and minimum eigenvalues can be used to obtain upper and lower bounds, respectively, on the strain energy density (Mehrabadi et al., 1993). The last term involving invariants of the projected stress suggest yield criteria based on energy analogous to the von Mises criterion (Sutcliffe, 1992). Such criteria will be developed later.

3 Symmetries

3.1 Isotropy. Complete isotropy is characterized by two distinct eigenvalues, and therefore from (7)

$$\mathbf{P}_1 = \frac{\mathbf{E} - \lambda_2 \mathbf{I}}{\lambda_1 - \lambda_2} \quad \mathbf{P}_2 = \frac{\mathbf{E} - \lambda_1 \mathbf{I}}{\lambda_2 - \lambda_1}. \quad (15)$$

Once the eigenvalues are known, then so are the projection operators, i.e., there are only two independent material parameters. This representation is equivalent to the usual form $\mathbf{E} = \lambda \mathbf{I} \otimes \mathbf{I} + 2G \mathbf{I}$ in which λ and G denote the Lamé parameters and \mathbf{I} the two-dimensional identity tensor. It follows that $\lambda_1 = 3\lambda + 2G$ and $\lambda_2 = 2G$. It is more common to label the eigenvalues as $3B$ (distinct) and $2G$ (multiplicity 5) where B and G are the bulk and shear modulus, respectively. The corresponding projection operators are the spherical and deviatoric projections:

$$\mathbf{P}^{sp} = \frac{1}{3} \mathbf{I} \otimes \mathbf{I} \quad \mathbf{P}^d = \mathbf{I} - \mathbf{P}^{sp} \quad (16)$$

so that, if \mathbf{s} denotes the stress tensor, P the mean pressure, \mathbf{s}^{sp} the spherical part of the stress tensor, and \mathbf{s}^d the stress deviator, it follows that

$$\mathbf{s} = \mathbf{s}^{sp} + \mathbf{s}^d \quad \mathbf{s}^{sp} = \mathbf{P}^{sp} : \mathbf{s} = -P \mathbf{I} \quad \mathbf{s}^d = \mathbf{P}^d : \mathbf{s} \quad (17)$$

3.2 Cubic Symmetry. Cubic symmetry exists if the elasticity tensor has three distinct eigenvalues, and the eigentensors are independent of material parameters and satisfy a particular relationship concerning multiplicity to be given next. Specifically, the elasticity tensor becomes

$$\mathbf{E} = \lambda_1 \mathbf{P}_1 + \lambda_2 \mathbf{P}_2 + \lambda_3 \mathbf{P}_3 \quad (18)$$

and the projection operators are

$$\begin{aligned} \mathbf{P}_1 &= \mathbf{N}_1 \otimes \mathbf{N}_1 \\ \mathbf{P}_2 &= \mathbf{N}_2 \otimes \mathbf{N}_2 + \mathbf{N}_3 \otimes \mathbf{N}_3 \\ \mathbf{P}_3 &= \mathbf{N}_4 \otimes \mathbf{N}_4 + \mathbf{N}_5 \otimes \mathbf{N}_5 + \mathbf{N}_6 \otimes \mathbf{N}_6 \end{aligned} \quad (19)$$

which indicates that the eigenvalues λ_1 , λ_2 , and λ_3 have multiplicities of 1, 2, and 3, respectively. Suppose a rectangular Cartesian coordinate system is chosen such that the associated base vectors coincide with the principle directions of \mathbf{N}_1 (also of \mathbf{N}_2 and \mathbf{N}_3). Then in this coordinate system the eigentensors display the following components:

$$\begin{aligned} \mathbf{N}_1 &\Rightarrow \frac{1}{\sqrt{3}} \begin{bmatrix} 1 & 0 & 0 \\ 0 & 1 & 0 \\ 0 & 0 & 1 \end{bmatrix} & \mathbf{N}_2 &\Rightarrow \frac{1}{\sqrt{2}} \begin{bmatrix} 0 & 0 & 0 \\ 0 & 1 & 0 \\ 0 & 0 & -1 \end{bmatrix} \\ \mathbf{N}_3 &\Rightarrow \frac{1}{\sqrt{6}} \begin{bmatrix} -2 & 0 & 0 \\ 0 & 1 & 0 \\ 0 & 0 & 1 \end{bmatrix} & \mathbf{N}_4 &\Rightarrow \frac{1}{\sqrt{2}} \begin{bmatrix} 0 & 0 & 0 \\ 0 & 0 & 1 \\ 0 & 1 & 0 \end{bmatrix} \\ \mathbf{N}_5 &\Rightarrow \frac{1}{\sqrt{2}} \begin{bmatrix} 0 & 0 & 1 \\ 0 & 0 & 0 \\ 1 & 0 & 0 \end{bmatrix} & \mathbf{N}_6 &\Rightarrow \frac{1}{\sqrt{2}} \begin{bmatrix} 0 & 1 & 0 \\ 1 & 0 & 0 \\ 0 & 0 & 0 \end{bmatrix} \end{aligned} \quad (20)$$

The first projection operator remains identical with the spherical projection, a property not found in materials with less symmetry. The eigenvectors of the first three eigentensors of \mathbf{E} , namely, \mathbf{N}_1 , \mathbf{N}_2 , and \mathbf{N}_3 are identical although the eigenvalues are not. The eigenvalues for the last three eigentensors \mathbf{N}_4 , \mathbf{N}_5 , and \mathbf{N}_6 are identical but the eigenvectors are not identical and differ from the first set. Each eigenvector of the last set is obtained by a 45 deg rotation about one of the eigenvectors in the first set.

For ease of representing detailed components, we convert to a fairly standard matrix notation (Sadegh and Cowin, 1991). Collect the components of the stress and strain tensor into vectors with six components as follows:

$$\begin{aligned} \{\sigma\}^T &= \{\sigma_{11}, \sigma_{22}, \sigma_{33}, \sqrt{2}\sigma_{23}, \sqrt{2}\sigma_{31}, \sqrt{2}\sigma_{12}\}^T \\ \{e\}^T &= \{e_{11}, e_{22}, e_{33}, \sqrt{2}e_{23}, \sqrt{2}e_{31}, \sqrt{2}e_{12}\}^T \end{aligned} \quad (21)$$

in which the superscript "T" denotes the transpose. The factor $\sqrt{2}$ is used so that the 2-norm is preserved:

$$\{\sigma\}^T \{\sigma\} = \boldsymbol{\sigma} : \boldsymbol{\sigma} \quad (22)$$

Then the constitutive relation becomes

$$\{\sigma\} = [C]\{e\} \quad (23)$$

For cubic symmetry and the choice of coordinate system (material coordinates) defined previously, the elasticity matrix becomes

$$[C] = \begin{bmatrix} C_{11} & C_{12} & C_{12} & 0 & 0 & 0 \\ & C_{11} & C_{12} & 0 & 0 & 0 \\ & & C_{11} & 0 & 0 & 0 \\ & & & 2C_{44} & 0 & 0 \\ & & & & 2C_{44} & 0 \\ & & & & & 2C_{44} \end{bmatrix}_{\text{sym}} \quad (24)$$

in which the three independent material parameters are

$$\begin{aligned} C_{11} &= E_{1111} = E_{2222} = E_{3333} \\ C_{12} &= E_{1122} = E_{1133} = E_{2233} \\ C_{44} &= E_{2323} = E_{3131} = E_{1212} \end{aligned} \quad (25)$$

If we return to the spectral decomposition of the elasticity tensor, the eigenvalues are (Sutcliffe, 1992)

$$\lambda_1 = C_{11} + 2C_{12} \quad \lambda_2 = C_{11} - C_{12} \quad \lambda_3 = 2C_{44} \quad (26)$$

If $C_{44} = (C_{11} - C_{12})/2$, then $\lambda_3 = \lambda_2$ and cubic symmetry degenerates to isotropy. Since the first projection operator is identical with the spherical projection, the sum of the other two projection operators span the deviatoric space, i.e.,

$$\mathbf{P}_2 + \mathbf{P}_3 = \mathbf{P}^d \quad (27)$$

3.3 Tetragonal (6) Symmetry. Although cubic symmetry is a special case of tetragonal (6) symmetry, the treatment of cubic symmetry was given first so that essential ideas could be presented in a simple context. Here, we give only those aspects which are different from those given previously.

The elasticity matrix for tetragonal (6) symmetry displays six independent material parameters:

$$[C] = \begin{bmatrix} C_{11} & C_{12} & C_{12} & 0 & 0 & 0 \\ & C_{22} & C_{23} & 0 & 0 & 0 \\ & & C_{22} & 0 & 0 & 0 \\ & & & 2C_{44} & 0 & 0 \\ & & & & 2C_{66} & 0 \\ & & & & & 2C_{66} \end{bmatrix}_{\text{sym}} \quad (28)$$

The spectral decomposition of the elasticity tensor

$$\begin{aligned} \mathbf{E} &= \lambda_1 \mathbf{N}_1^* \otimes \mathbf{N}_1^* + \lambda_2 \mathbf{N}_2 \otimes \mathbf{N}_2 + \lambda_3 \mathbf{N}_3^* \otimes \mathbf{N}_3^* \\ &+ \lambda_4 \mathbf{N}_4 \otimes \mathbf{N}_4 + \lambda_5 (\mathbf{N}_5 \otimes \mathbf{N}_5 + \mathbf{N}_6 \otimes \mathbf{N}_6) \end{aligned} \quad (29)$$

displays five independent eigenvalues with one of multiplicity two. The projection operators are implicitly defined as the coefficients of the eigenvalues. The eigentensors are identical to those obtained for cubic symmetry with the following exceptions:

$$\begin{aligned} \mathbf{N}_1^* &\Rightarrow \frac{1}{\sqrt{2 + \alpha^2}} \begin{bmatrix} \alpha & 0 & 0 \\ 0 & 1 & 0 \\ 0 & 0 & 1 \end{bmatrix} \\ \mathbf{N}_3^* &\Rightarrow \frac{1}{\sqrt{2 + \beta^2}} \begin{bmatrix} \beta & 0 & 0 \\ 0 & 1 & 0 \\ 0 & 0 & 1 \end{bmatrix} \end{aligned} \quad (30)$$

while the eigenvalues are

$$\begin{aligned} \lambda_1 &= \frac{1}{2}[(C_{11} + C_{22} + C_{23}) + \sqrt{(C_{11} - C_{22} - C_{23})^2 + 8(C_{12})^2}] \\ \lambda_3 &= \frac{1}{2}[(C_{11} + C_{22} + C_{23}) - \sqrt{(C_{11} - C_{22} - C_{23})^2 + 8(C_{12})^2}] \\ \lambda_2 &= C_{22} - C_{23} \\ \lambda_4 &= 2C_{44} \\ \lambda_5 &= 2C_{66} \text{ (multiplicity two)}. \end{aligned} \quad (31)$$

Here, components of two of the eigentensors depend on the material parameters as follows:

$$\alpha = \frac{2C_{12}}{\lambda_1 - C_{11}} \quad \beta = \frac{2C_{12}}{\lambda_3 - C_{11}} \quad (32)$$

Note that $\alpha\beta = -2$. For cubic symmetry, $C_{22} = C_{11}$, $C_{23} = C_{12}$, and $C_{66} = C_{44}$ which infers that $\alpha = 1$, $\beta = -2$, $\mathbf{N}_1^* = \mathbf{N}_1$, and $\mathbf{N}_3^* = \mathbf{N}_3$.

Transverse symmetry, or hexagonal (5) symmetry, can be viewed as a special case of tetragonal (6) symmetry with $2C_{44} = C_{22} - C_{23}$. The result is that $\lambda_4 = \lambda_2$ and the elasticity tensor exhibits two eigenvalues of multiplicity two:

$$\mathbf{E} = \lambda_1 \mathbf{N}_1^* \otimes \mathbf{N}_1^* + \lambda_2 (\mathbf{N}_2 \otimes \mathbf{N}_2 + \mathbf{N}_4 \otimes \mathbf{N}_4) + \lambda_3 \mathbf{N}_3^* \otimes \mathbf{N}_3^* + \lambda_5 (\mathbf{N}_5 \otimes \mathbf{N}_5 + \mathbf{N}_6 \otimes \mathbf{N}_6) \quad (33)$$

in which \mathbf{N}_1^* and \mathbf{N}_3^* continue to be defined by (30). Note that cubic symmetry is not a subset of transverse isotropy.

Another important symmetry class for noncrystalline materials is that of orthotropy. However, the solution of a cubic equation is required to obtain the eigenvalues of the elasticity tensor. The eigentensors \mathbf{N}_i , with $i = 1, 2$, and 3 , retain the diagonal form but all nonzero entries depend on the material parameters. Since the algebra is rather complex (Mehrabadi and Cowin, 1990), the development has not been included.

4 Plasticity

4.1 Formulation. Consider small deformation so the strain rate, $\dot{\mathbf{e}}$, can be decomposed into elastic and plastic parts as follows:

$$\dot{\mathbf{e}} = \dot{\mathbf{e}}^e + \dot{\mathbf{e}}^p. \quad (34)$$

The stress rate consists of a map of the elastic strain rate:

$$\dot{\mathbf{s}} = \mathbf{E} : \dot{\mathbf{e}}^e. \quad (35)$$

The plastic strain is obtained from an evolution equation, to be given later, in terms of a monotonically increasing parameter, t .

Assume that the elastic projection operators are implicitly describing preferred modes of deformation. For each projection define a projected total and plastic strain rate:

$$\dot{\mathbf{e}}_i = \mathbf{P}_i : \dot{\mathbf{e}} \quad \dot{\mathbf{e}}_i^p = \mathbf{P}_i : \dot{\mathbf{e}}^p. \quad (36)$$

For each mode, define a plastic strain-path invariant

$$\bar{\epsilon}_i = \int (\dot{\mathbf{e}}_i^p : \dot{\mathbf{e}}_i^p)^{1/2} dt \quad (37)$$

and a yield function

$$f_i = \frac{1}{2}(\bar{\epsilon}_i)^2 - \frac{1}{2}(H_i)^2 \quad (38)$$

such that $f_i > 0$ is not allowed and $f_i < 0$ denotes an elastic state. Yielding in a particular mode occurs only when $f_i = 0$. Each function, H_i , may remain constant (perfect plasticity), increase (strain hardening) or decrease (strain softening). To experimentally determine each H_i , a stress path must be followed that activates only mode i . Particular examples are given later.

The contributions from each mode to the plastic strain and to the hardening function are obtained from evolution equations of the form:

$$\dot{\mathbf{e}}_i^p = \omega_i \mathbf{m}_i \quad \dot{H}_i = \omega_i h_i \quad (39)$$

in which ω_i is a monotonically increasing parameter associated with mode i . Conventional formulations are obtained if \mathbf{m}_i is a function of the projected stress \mathbf{s}_i , and h_i is a function of the plastic strain invariant, $\bar{\epsilon}_i$. The consistency condition, $\dot{f}_i = 0$, yields

$$\mathbf{s}_i : \dot{\mathbf{s}}_i - H_i \dot{H}_i = 0. \quad (40)$$

If associated evolution equations for plastic strain are chosen, then

$$\mathbf{m}_i = \mathbf{s}_i. \quad (41)$$

Consider the rate form of the elastic constitutive equation

$$\dot{\mathbf{s}} = \mathbf{E} : \dot{\mathbf{e}}^e = \mathbf{E} : (\dot{\mathbf{e}} - \dot{\mathbf{e}}^p). \quad (42)$$

Apply the projection operator, \mathbf{P}_i , to each term to obtain

$$\dot{\mathbf{s}}_i = \lambda_i (\dot{\mathbf{e}}_i - \dot{\mathbf{e}}_i^p). \quad (43)$$

Substitute (39), (41), and (43) in (40):

$$\lambda_i \mathbf{s}_i : \dot{\mathbf{e}}_i - \omega_i \lambda_i (\mathbf{s}_i : \mathbf{s}_i) - \omega_i H_i h_i = 0. \quad (44)$$

The result is an uncoupled equation for each evolution parameter ω_i :

$$\omega_i = \frac{\lambda_i \mathbf{s}_i : \dot{\mathbf{e}}_i}{\lambda_i (\bar{\epsilon}_i)^2 + H_i h_i} \quad i = 1, \dots, K \quad (45)$$

Koiter (1953) provided a formulation for satisfying simultaneously a set of yield conditions used to define a composite yield surface. In effect, the result is a set of algebraic equations for determining ω_i . Here, by defining yield functions based on the elastic projection operators and with associated flow rules, the set of equations becomes decoupled so that algorithms used for single surfaces can be carried over with very little modification to the present case even though the composite surface is described with the use of several yield functions.

For an associated flow rule, (41) indicates that the plastic strain rate is proportional to the projected stress, \mathbf{s}_i . If a projection operator is of the form (4), then

$$\mathbf{s}_i = (\mathbf{N}_i : \mathbf{s}) \mathbf{N}_i \quad (46)$$

which infers that the eigentensor, \mathbf{N}_i , describes the "mode" of plastic deformation.

4.2 Tangent Tensor. An investigation of material stability requires the tangent tensor, \mathbf{T} , defined such that

$$\dot{\mathbf{s}} = \mathbf{T} : \dot{\mathbf{e}} \quad (47)$$

The derivation of the expression for \mathbf{T} follows from the following equivalent forms of (42):

$$\begin{aligned} \dot{\mathbf{s}} &= \mathbf{E} : \dot{\mathbf{e}} - \mathbf{E} : \sum_{i=1}^K \dot{\mathbf{e}}_i^p \\ &= \mathbf{E} : \dot{\mathbf{e}} - \mathbf{E} : \sum_{i=1}^K \omega_i \mathbf{s}_i \end{aligned} \quad (48)$$

Because of the orthonormal property of the projection operator

$$\mathbf{E} : \mathbf{s}_i = \sum_{j=1}^K \lambda_j \mathbf{P}_j : \mathbf{P}_j : \mathbf{s} = \lambda_i \mathbf{s}_i, \quad (49)$$

it follows immediately when (45) and (49) are substituted in (48) that

$$\mathbf{T} = \mathbf{E} - \sum_{i=1}^K \frac{(\lambda_i)^2 \mathbf{s}_i \otimes \mathbf{s}_i}{\lambda_i (\bar{\epsilon}_i)^2 + H_i h_i}. \quad (50)$$

Consider the result when the strain rate is assumed to be proportional to a projected stress. When \mathbf{T} operates on a projected stress, and with the use of orthogonality of modes, the result is

$$\mathbf{T} : \mathbf{s}_i = \Lambda_i \mathbf{s}_i \quad \Lambda_i \equiv \lambda_i - \frac{(\lambda_i)^2 (\bar{\epsilon}_i)^2}{\lambda_i (\bar{\epsilon}_i)^2 + H_i h_i} \quad (51)$$

i.e., \mathbf{s}_i is an eigentensor of \mathbf{T} with eigenvalue Λ_i .

Care must be taken because (51) provides the eigenpair for only those modes for which plasticity is activated. For those modes not activated, the eigenvalues and eigentensors of the tangent tensor are identical to those of the elasticity tensor.

If a plasticity mode is activated, then an alternative form for the eigenvalue is

$$\Lambda_i = \frac{\lambda_i H_i h_i}{\lambda_i (\bar{\epsilon}_i)^2 + H_i h_i} = \frac{\lambda_i h_i}{\lambda_i H_i + h_i} \quad (52)$$

in which the second equality is obtained with the use of (38) and $f_i = 0$. The eigenvalue is zero (a limit point) if the evolution

function, h_i , is zero and material instability based on Drucker's criterion is satisfied.

One of the characteristics of a strain rate tensor associated with a discontinuous bifurcation is that one of its eigenvalues is zero, and the other two are of opposite sign (Neilsen and Schreyer, 1993). This feature is labeled the "pzn" property (for positive, zero, and negative). The complete criteria for the appearance of a discontinuous bifurcation are that s_i satisfy the pzn criterion, and $\Lambda_i \leq 0$. Therefore, Drucker's criterion is a necessary precursor to a discontinuous bifurcation.

4.3 Plasticity for Isotropic Materials. For isotropic elasticity, suppose the first mode is identified with the spherical projection, i.e.,

$$\mathbf{P}_1 = \mathbf{P}^{sp} \quad \mathbf{P}_2 = \mathbf{P}^d \quad (53)$$

so that

$$\begin{aligned} \bar{s}_1^2 &= \mathbf{s}^{sp} : \mathbf{s}^{sp} = \frac{1}{3}[s_{11} + s_{22} + s_{33}]^2 = 3P^2 \\ \bar{s}_2^2 &= \mathbf{s}^d : \mathbf{s}^d = \frac{1}{3}[(s_{11} - s_{22})^2 + (s_{22} - s_{33})^2 \\ &\quad + (s_{33} - s_{11})^2 + 6(s_{12})^2 + 6(s_{23})^2 + 6(s_{31})^2] \quad (54) \end{aligned}$$

in which P denotes the mean pressure. Suppose H_1 is set so high that the first mode is never activated. Then the remaining yield function from (38) is

$$f_2 = \frac{1}{2}(\bar{s}_2)^2 - \frac{1}{2}(H_2)^2. \quad (55)$$

The plastic strain rate is proportional to the stress deviator and the result is the classical von Mises formulation.

If only the second mode is activated, then

$$\begin{aligned} \Lambda_1 &= \lambda_1 = 3B \\ \Lambda_2 &= \frac{2Gh_2}{2GH_2 + h_2}. \quad (56) \end{aligned}$$

The corresponding eigentensor of \mathbf{T} is \mathbf{s}^d so a discontinuous bifurcation does not occur unless the eigenvalues of \mathbf{s}^d satisfy the pzn criterion and $h_2 \leq 0$ (Neilsen and Schreyer, 1993).

4.4 Plasticity for Materials With Cubic Symmetry. Now there is a potential for three yield surfaces involving the following "effective" stresses:

$$\begin{aligned} \bar{s}_1^2 &= 3P^2 \\ \bar{s}_2^2 &= \mathbf{s}_2 : \mathbf{s}_2 = \frac{1}{3}[(s_{11} - s_{22})^2 + (s_{22} - s_{33})^2 + (s_{33} - s_{11})^2] \\ \bar{s}_3^2 &= \mathbf{s}_3 : \mathbf{s}_3 = 2[(s_{12})^2 + (s_{23})^2 + (s_{31})^2] \quad (57) \end{aligned}$$

The first is again associated with the spherical projection. If experimental data indicate plastic incompressibility, then the corresponding hardening function need only be set to a large constant value to delete the spherical mode. The other two effective stresses indicate that the deviatoric space has been split into two subspaces with the result that the von Mises yield surface is replaced with two surfaces. If the principal axes of stress coincide with the material axes, or if all the normal components of stress are zero, then the yield surface is no different from the isotropic case. However, for other situations, the third effective stress may become significant and the predicted response will differ from isotropic plasticity.

Two experimental paths are necessary to determine the hardening functions for the deviatoric space. As examples, a uniaxial stress path to determine H_2 and a path involving only a shear stress component to determine H_3 are sufficient provided both paths are prescribed in the material symmetry axes.

The third mode identified with \mathbf{P}_3 defined in (19) and (20) represents a sum of three stress states corresponding to shear in each of the coordinate planes. There is no preference of one

case over the other so yield can occur at the same level of shear stress in any plane. Furthermore, hardening caused by a shear excursion in one plane is automatically reflected in the other two planes. The pzn criterion is satisfied if any one of the shear stresses is nonzero.

The second mode can be considered a sum of two stress states. If, for example, the stress has components proportional to \mathbf{N}_2 , then the plastic strain rate is also proportional to \mathbf{N}_2 and is of the pzn type. This mode corresponds to shear on planes defined by $x^* - x_1$ where x^* is in the $x_2 - x_3$ plane oriented at an angle of 45 deg to either the x_2 or x_3 material axes. Because the choice of \mathbf{N}_2 and \mathbf{N}_3 is not unique (although \mathbf{P}_2 is unique), shear on planes $y^* - x_2$ and $z^* - x_3$ is also possible where y^* and z^* are oriented at 45 deg to either coordinate in the $x_1 - x_3$ and $x_1 - x_2$ planes, respectively. The yield stress for this mode can be different from the yield stress associated with the third mode. If the stress is proportional to \mathbf{N}_3 , a plastic strain rate can be obtained that is not of the pzn type.

Overall, the dominant modes of plastic response suggested by the projection operators are pure shear on the planes described by the material axes and shear on the planes oriented at 45 deg to the material symmetry planes.

4.5 Plasticity for Materials With Tetragonal (6) Symmetry. Now the structure is much richer with the possibility of five active yield functions and modes of plastic deformation as defined by the projection operators implied in (29) and (30):

$$\begin{aligned} \bar{s}_1^2 &= \mathbf{s}_1 : \mathbf{s}_1 = \frac{1}{(2 + \alpha^2)} [\alpha s_{11} + s_{22} + s_{33}]^2 \\ \bar{s}_2^2 &= \mathbf{s}_2 : \mathbf{s}_2 = \frac{1}{2}(s_{22} - s_{33})^2 \\ \bar{s}_3^2 &= \mathbf{s}_3 : \mathbf{s}_3 = \frac{1}{(2 + \beta^2)} [\beta s_{11} + s_{22} + s_{33}]^2 \\ \bar{s}_4^2 &= \mathbf{s}_4 : \mathbf{s}_4 = 2(s_{23})^2 \\ \bar{s}_5^2 &= \mathbf{s}_5 : \mathbf{s}_5 = 2(s_{12})^2 + 2(s_{31})^2. \quad (58) \end{aligned}$$

Now the first mode is not purely spherical and the third mode is not pure shear at 45 deg. The second mode represents shear on the $x_2 - x_3$ material coordinate planes. The fifth mode represents shear on the $x_1 - x_2$ and $x_1 - x_3$ material coordinate planes with identical shear stresses so that hardening in one case affects the other. The fourth mode singles out shear in the $x_2 - x_3$ material coordinate plane and is independent of the shear associated with the second mode. Furthermore, the second, fourth, and fifth mode each satisfy the pzn condition.

Special care must be taken to prescribe a path to activate a single mode to determine a hardening function. For example, a path with $s_{22} = -s_{33}$ and all other stress components zero activates only the second mode. To activate only the third mode, the experimental path that must be followed is defined by zero shear components, $s_{22} = s_{33}$ and $s_{11} = -2s_{22}/\alpha$ to eliminate contributions to the second and first modes, respectively. Paths to determine hardening functions for the remaining modes are defined in a similar manner.

For transverse isotropy, or hexagonal (5) symmetry, the second and fourth modes combine into a single mode and the new effective stress becomes

$$\bar{s}_2^*{}^2 = \mathbf{s}_2 : \mathbf{s}_2 + \mathbf{s}_4 : \mathbf{s}_4 = \frac{1}{2}(s_{22} - s_{33})^2 + 2(s_{23})^2, \quad (59)$$

which implies that any shear yield stress in the $x_2 - x_3$ plane is perceived equally.

For plasticity associated with cubic symmetry, transverse isotropy, and tetragonal (6) symmetry, there are certain modes for which the pzn condition is always satisfied. For these cases, a discontinuous bifurcation occurs if the corresponding eigenvalue of the tangent tensor is zero or negative. The physical

manifestation of a discontinuous bifurcation can be an apparent brittle failure once a peak stress is reached, even for a displacement controlled test, so knowledge of these properties of the tangent tensor is important for interpreting experimental data.

4.6 Volumetric Plastic Strain. Many metallic materials display plastic incompressibility. For isotropic and cubic symmetry, \mathbf{N}_1 is always the spherical mode. For tetragonal (6) symmetry and transverse isotropy, if α is close to unity, then \mathbf{N}_1^* in (30) represents a spherical mode to a high degree of accuracy. Sutcliffe (1992) gives data which indicate $\alpha = 1.008$ for indium and $\alpha = 0.91$ for tin, both of which are tetragonal (6) metals, and $\alpha = 0.96$ for magnesium which is in the transverse isotropy class. As mentioned previously, plastic incompressibility can be invoked by choosing a large value for H_1 . For metals with cubic symmetry (e.g., Cu and Al) α is automatically one. If α is not close to one and experimental data indicate plastic incompressibility, modifications must be made to project out the spherical parts from the first and third modes, \mathbf{N}_1^* and \mathbf{N}_3^* , respectively. However, the projected modes are not independent. Alternatively, one can define a new deviatoric projection operator, \mathbf{P}_3^* by enforcing orthogonality with \mathbf{P}_2 , \mathbf{P}_4 , and \mathbf{P}_5 and the spherical projection operator. The result is that four modes exist in the deviatoric space and the procedure outlined above can be invoked. A similar approach for transverse isotropy yields three projection operators in the deviatoric space. Orthotropic symmetry provides three projection operators with a spherical part so the approach for developing the appropriate deviatoric projection operators is not so transparent.

On the other hand, there are materials such as foams ($\alpha = 1.8$) that exhibit considerable volumetric plastic strain. Then hardening functions can be introduced for each mode without the need for deleting the effects of the spherical mode.

5 Summary

For each projection operator obtained from the elasticity tensor, a yield function is defined in a manner completely analogous to that of von Mises plasticity. Experimental data are necessary to define the hardening function associated with each yield surface. The lower bound formed from the union of these surfaces provides a single yield surface with vertices. If an associated flow rule is used, then the evolution equations for projected plastic strains and hardening functions for each mode become uncoupled. Also the projection operators associated with the fourth-order tangent stiffness tensor are similar to those identified from the elasticity tensor. The result is that material instability based on the Drucker criterion or on a discontinuous bifurcation mode can be easily performed. Based on physical observations, each mode can reflect individually strain hardening, perfect plasticity or strain softening. The overall simplicity of the model also makes it feasible for numerical calculations.

If an elastic material is only slightly anisotropic, the assumption of isotropy is usually made with good justification to simplify the analysis. However, the slight elastic anisotropy is all

that is needed to define projection operators which may prove to be quite important in the plasticity regime. Even though for certain materials in manufacturing processes the elastic behavior is essentially isotropic, the plastic response is quite anisotropic. The use of the theory provided here would provide an approach for an appropriate explanation and theory.

It is also believed these projections could be applied profitably to the areas of kinematic hardening, continuum damage mechanics, and anisotropic heat conduction.

Acknowledgment

This research was supported in part by Grant No. MSS 9203747 from the National Science Foundation to the University of New Mexico.

References

- Gotoh, M., 1977, "A theory of plastic anisotropy based on a yield function of fourth order (plane stress state)-I," *International Journal of Mechanical Sciences*, Vol. 19, pp. 505-512.
- Hill, R., 1948, "A theory of yielding and plastic flow of anisotropic metals," *Proceedings of the Royal Society of London*, Vol. A193, pp. 281-297.
- Hill, R., 1979, "Theoretical plasticity of textured aggregates," *Mathematics Proceedings of the Cambridge Philosophical Society*, Vol. 85, pp. 179-191.
- Hill, R., 1990, "Constitutive modelling of orthotropic plasticity in sheet metals," *Journal of the Mechanics and Physics of Solids*, Vol. 38, No. 3, pp. 405-417.
- Hill, R., 1993, "A user-friendly theory of orthotropic plasticity in sheet metals," *International Journal of Mechanical Sciences*, Vol. 35, No. 1, pp. 19-25.
- Koiter, W. T., 1953, "Stress-Strain Relations, Uniqueness and Variational Theorems for Elastic-Plastic Materials with a Singular Yield Surface," *Quarterly of Applied Mathematics*, Vol. 11, pp. 350-354.
- Luehr, C. P., and Rubin, M. B., 1990, "The significance of projection operators in the spectral representation of symmetric second order tensors," *Computer Methods in Applied Mechanics and Engineering*, Vol. 84, pp. 243-246.
- Mehrabadi, M. M., and Cowin, S. C., 1990, "Eigensensors of linear anisotropic elastic materials," *Quarterly Journal of Mechanics and Applied Mathematics*, Vol. 43, Pt. 1, pp. 15-41.
- Mehrabadi, M. M., Cowin, S. C., and Horgan, C. O., 1993, "Strain energy density bounds for linear anisotropic elastic materials," *Journal of Elasticity*, Vol. 30, pp. 191-196.
- Mellor, P. B., 1982, "Experimental studies of plastic anisotropy in metal sheet," *Mechanics of Solids: The Rodney Hill 60th Anniversary Volume*, H. G. Hopkins and M. J. Sewell eds., Pergamon Press, Oxford, U.K., pp. 383-415.
- Montheillet, F., Jonas, J. J., and Benferrah, M., 1991, "Development of anisotropy during the cold rolling of aluminum sheet," *International Journal of Mechanical Sciences*, Vol. 33, No. 3, pp. 197-209.
- Needleman, A., and Tvergaard, V., 1982, "Aspects of plastic postbuckling behavior," *Mechanics of Solids: The Rodney Hill 60th Anniversary Volume*, H. G. Hopkins and M. J. Sewell eds., Pergamon Press, Oxford, U.K., pp. 453-498.
- Neilsen, M. K., and Schreyer, H. L., 1993, "Bifurcations in Elastic-Plastic Materials," *The International Journal of Solids and Structures*, Vol. 30, No. 4, pp. 521-544.
- Parmar, A., and Mellor, P. B., 1978, "Plastic expansion of a circular hole in sheet metal subjected to biaxial tensile stress," *International Journal of Mechanical Sciences*, Vol. 20, pp. 707-720.
- Sadegh, A. M., and Cowin, S. C., 1991, "The Proportional Anisotropic Elastic Invariants," *ASME JOURNAL OF APPLIED MECHANICS*, Vol. 58, pp. 50-57.
- Sutcliffe, S., 1992, "Spectral Decomposition of the Elasticity Tensor," *ASME JOURNAL OF APPLIED MECHANICS*, Vol. 59, pp. 762-773.
- Woodthorpe, J., and Pearce, R., 1970, "The anomalous behavior of aluminum sheet under balanced biaxial tension," *International Journal of Mechanical Sciences*, Vol. 12, pp. 341-347.
- Zhou, W., 1990, "A new non-quadratic orthotropic yield criterion," *International Journal of Mechanical Sciences*, Vol. 32, No. 6, pp. 513-520.

Analytical Expressions for the Relaxation Moduli of Linear Viscoelastic Composites With Periodic Microstructure

R. Luciano¹

University of Cassino,
via Zamosh 43,
Cassino, Italy

E. J. Barbero

West Virginia University,
Morgantown, WV 26506-6106,
Assoc. Mem. ASME.

In this paper the viscoelastostatic problem of composite materials with periodic microstructure is studied. The matrix is assumed linear viscoelastic and the fibers elastic. The correspondence principle in viscoelasticity is applied and the problem in the Laplace domain is solved by using the Fourier series technique and assuming the Laplace transform of the homogenization eigenstrain piecewise constant in the space. Formulas for the Laplace transform of the relaxation functions of the composite are obtained in terms of the properties of the matrix and the fibers and in function of nine triple series which take into account the geometry of the inclusions. The inversion to the time domain of the relaxation and the creep functions of composites reinforced by long fibers is carried out analytically when the four-parameter model is used to represent the viscoelastic behavior of the matrix. Finally, comparisons with experimental results are presented.

Introduction

A large number of micromechanical models have been developed to estimate the elastic properties of composite materials (see Christensen, 1990; Mura, 1987; Nemat Nasser and Hori, 1993). However, few theoretical and experimental results are available in the field of viscoelastic behavior of heterogeneous media.

The first micromechanical model used to evaluate the macroscopic viscoelastic properties of fiber-reinforced materials was the cylinder assemblage model proposed by Hashin (1965, 1966), where the analogy between the elastic and the viscoelastic relaxation moduli of heterogeneous materials with identical phase geometry was presented. This analogy is known as the correspondence principle (Christensen, 1979) and many authors applied it. For example, Christensen (1969) proposed an approximate formula for the effective complex shear modulus in the case of materials with two viscoelastic phases by using the composite sphere model.

Laws and McLaughlin (1978) estimated the viscoelastic creep compliances of several composites by applying the self-consistent method. They used Stieltjes convolution integrals to formulate the problem in the Carson domain and a numerical inversion method to obtain the solution in the time domain. Yancey and Pindera (1990) estimated the creep response of unidirectional composites with linear viscoelastic matrices and elastic fibers by applying the micromechanical model proposed by Aboudi (1991) to obtain the Laplace transform of the effective viscoelastic moduli. Then, they used Bellman's numerical method for the inversion to the time domain. For different geometry of the inclusions, Wang and Weng (1992) adopted the Eshelby-Mori-Tanaka method (Mori and Tanaka, 1973) in order to obtain the overall linear viscoelastic properties of the corresponding composite material.

Finally, it is possible to conclude that many micromechanical models applied for the analysis of the elastic behavior of composites have been extended to the viscoelastic case. However, no theory has been developed for linear viscoelastic solids with periodic microstructure, even though many results are available for the elastic case (Nemat-Nasser and Taya, 1981, 1986; Nemat-Nasser et al., 1982; Nemat-Nasser and Hori, 1993). For this reason, in the present paper, close-form expressions in the Laplace domain for the coefficients of the linear viscoelastic relaxation tensor of composite materials with periodically distributed elastic inclusions and linear viscoelastic matrix are proposed. Moreover, the inversion to the time domain is carried out *analytically* for composites reinforced by long fibers and when the viscoelastic behavior of the matrix can be represented by a four-parameter model.

¹Visiting Assistant Professor, Department of Mechanical and Aerospace Engineering, West Virginia University, Morgantown, WV 25606-6106.

Contributed by the Applied Mechanics Division of THE AMERICAN SOCIETY OF MECHANICAL ENGINEERS for presentation at the Joint Applied Mechanics and Materials Summer Meeting of the ASME, Los Angeles, CA, June 28-30, 1995.

Discussion on this paper should be addressed to the Technical Editor, Professor Lewis T. Wheeler, Department of Mechanical Engineering, University of Houston, Houston, TX 77204-4702, and will be accepted until four months after final publication of the paper itself in the ASME JOURNAL OF APPLIED MECHANICS.

Manuscript received by the ASME Applied Mechanics Division, Mar. 16, 1994; final revision, Dec. 2, 1994. Associate Technical Editor: G. J. Drorak.

Paper No. 95-APM-10.

More complex creep behaviour of the matrix requires numerical inversion to the time domain (Barbero and Luciano 1995). Finally, comparisons with available experimental data obtained by Skudra and Auzukalns (1973) are presented.

Viscoelastic Constitutive Equations

The constitutive equations of a linear viscoelastic isotropic material can be expressed in the time domain in the following way:

$$\sigma(t) = I^{(2)} \int_{-\alpha}^t \lambda(t - \tau) \text{tr} \dot{\epsilon}(\tau) d\tau + 2 \int_{-\alpha}^t \mu(t - \tau) \dot{\epsilon}(\tau) d\tau, \quad (1)$$

where $\sigma(t)$ and $\epsilon(t)$ are the stress and strain tensor, $\lambda(t)$ and $\mu(t)$ are the two stress-relaxation functions, the dot indicates the differentiation with respect to time, and $I^{(2)}$ denotes the identity second-order tensor.

The inverse relations of Eq. (1) can be written in terms of the creep functions $\theta(t)$ and $\zeta(t)$ as

$$\epsilon(t) = I^{(2)} \int_{-\alpha}^t \theta(t - \tau) \text{tr} \dot{\sigma}(\tau) d\tau + 2 \int_{-\alpha}^t \zeta(t - \tau) \dot{\sigma}(\tau) d\tau. \quad (2)$$

Let us assume that the relaxation and the creep functions are smooth functions (Gurtin and Sternberg, 1962) and denote the Laplace transform of a function $f(t)$ as

$$\tilde{f}(s) = \int_0^{\alpha} f(t) \exp(-st) dt, \quad (3)$$

then the Eqs. (1) and (2) can be expressed in the Laplace domain as

$$\tilde{\sigma}(s) = s\tilde{\lambda}(s) \text{tr} \tilde{\epsilon}(s) I^{(2)} + 2s\tilde{\mu}(s) \tilde{\epsilon}(s) = s\tilde{L}(s) \tilde{\epsilon}(s), \quad (4)$$

$$\tilde{\epsilon}(s) = s\tilde{\theta}(s) \text{tr} \tilde{\sigma}(s) I^{(2)} + 2s\tilde{\zeta}(s) \tilde{\sigma}(s) = s\tilde{M}(s) \tilde{\sigma}(s), \quad (5)$$

where the Laplace transform of the creep compliance $\tilde{M}(s)$ and the relaxation tensor $\tilde{L}(s)$ satisfy the following relation:

$$\tilde{M}(s) = \frac{1}{s^2} \tilde{L}(s)^{-1}. \quad (6)$$

The Poisson ratio in the transformed domain ν^{TD} is written in terms of $\tilde{\lambda}(s)$ and $\tilde{\mu}(s)$ as

$$\nu^{TD} = \tilde{\lambda}(s) / 2(\tilde{\lambda}(s) + \tilde{\mu}(s)). \quad (7)$$

For simplicity, and consistently with earlier work (Aboudi, 1991; Wang and Weng, 1992), only the set of linear viscoelastic materials whose Poisson ratio remains constant in the course of the deformation (i.e., $\nu(t) = \nu = \nu^{TD}$) will be considered. However, the Poisson ratio of the fibers can be different of that of the matrix.

Periodic Eigenstrain in the Laplace Domain

Suppose that an infinitely extended linearly viscoelastic solid is represented by an assembly of unit cells and let each cell D be a parallelepiped with dimensions a_j in the directions of the coordinate axes x_j where $j = 1, 2, 3$ (see Fig. 1) and let V be its volume. Then, let us denote with Ω the part of D occupied by the inclusions, with $D - \Omega$ the part of D occupied by the matrix, and with v_f be the volume fraction of Ω . The constitutive equations of the linear viscoelastic matrix in the Laplace domain can be written by using Eq. (4) as

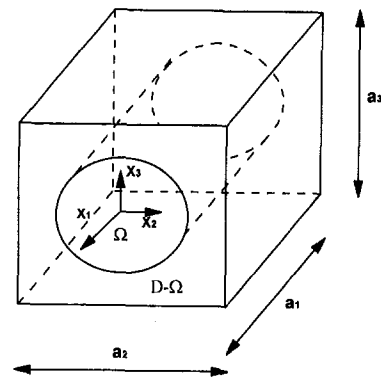


Fig. 1 Geometry of the unit cell D

$$\tilde{\sigma}(s, x) = s\tilde{L}(s) \tilde{\epsilon}(s, x) \text{ in } D - \Omega, \quad (8)$$

while the elastic inclusion is represented as

$$\tilde{\sigma}(s, x) = sL'(s) \tilde{\epsilon}(s, x) = L' \epsilon(s, x) \text{ in } \Omega, \quad (9)$$

and L' is the elastic stiffness tensor of the inclusion. In order to simulate the inclusions inside the body, the equivalent eigenstrain method will be used (see Mura, 1987; Nemat Nasser and Hori, 1993). The idea is to apply an eigenstrain on the homogeneous solid to obtain the equivalence between the stress in the homogeneous material and the heterogeneous one. Then, consider the Laplace transform of the homogenization eigenstrain $\tilde{\epsilon}^*(s, x)$ which must be periodic in x for the particular geometry of the problem and different from zero only in Ω . By using this technique, the inclusion problem is reduced to a viscoelastostatic problem of an homogeneous solid subject to a suitable periodic eigenstrain $\tilde{\epsilon}^*(s, x)$.

Next, by using the correspondence principle for linear viscoelastic solids (see Christensen, 1979; Aboudi, 1991), the relation between the eigenstrain and the strain inside Ω will be introduced in the Laplace domain. Since the material is linear viscoelastic, the Laplace transform of the actual stress tensor $\tilde{\sigma}(s, x)$ inside the unit cell can be expressed in terms of $\tilde{\epsilon}^*(s, x)$ and the Laplace transform of the actual strain tensor $\tilde{\epsilon}(s, x)$ in the following way:

$$\tilde{\sigma}(s, x) = s\tilde{L}(s) (\tilde{\epsilon}(s, x) - \tilde{\epsilon}^*(s, x)) \text{ for } x \in D, \quad (10)$$

while Eq. (8) is valid in $D - \Omega$. Then, assuming the body forces equal to zero, the tensor $\tilde{\sigma}(s, x)$ must satisfy the following equilibrium conditions:

$$\text{div} \tilde{\sigma}(s, x) = 0 \text{ for } x \in D, \quad (11)$$

where div denotes the divergence of a tensor field.

Since the object of this paper is the analysis of composite materials with periodic microstructure, the eigenstrain $\tilde{\epsilon}(s, x)$ simulates the presence of the periodic inclusions. Furthermore, in a solid with periodic microstructure, the boundary conditions of the unit cell D are governed by the periodicity in x of the microstructure and are satisfied by expanding the displacements and the eigenstrain or their Laplace transforms ($\tilde{\mathbf{u}}(s, x)$ and $\tilde{\epsilon}^*(s, x)$) in the following Fourier series representation:

$$\tilde{\mathbf{u}}(s, x) = \sum_{\xi}^{\pm\infty} \tilde{\mathbf{u}}(s, \xi) \exp(i\xi x), \quad (12)$$

$$\tilde{\epsilon}(s, x) = \text{sym}(\nabla \tilde{\mathbf{u}}(s, x)) = \sum_{\xi}^{\pm\infty} \tilde{\epsilon}(s, \xi) \exp(i\xi x), \quad (13)$$

$$\tilde{\epsilon}^*(s, x) = \sum_{\xi}^{\pm\infty} \tilde{\epsilon}^*(s, \xi) \exp(i\xi x), \quad (14)$$

where $\xi = \{\xi_1, \xi_2, \xi_3\}$ with $\xi_j = 2\pi n_j/a_j$ ($n_j = 0, \pm 1, \pm 2, \dots, j$ not summed, $j = 1, 2, 3$), $i = \sqrt{-1}$ and

$$\bar{\mathbf{u}}(s, \xi) = \frac{1}{V} \int_D \bar{\mathbf{u}}(s, x) \exp(-i\xi x) dx, \quad (15)$$

$$\bar{\tilde{\epsilon}}(s, \xi) = \frac{i}{2} [\xi \otimes \bar{\mathbf{u}}(s, x) + \bar{\mathbf{u}}(s, \xi) \otimes \xi], \quad (16)$$

$$\bar{\tilde{\epsilon}}^*(s, \xi) = \frac{1}{V} \int_D \tilde{\epsilon}^*(s, x) \exp(-i\xi x) dx. \quad (17)$$

Combining Eq. (10) and Eq. (11) gives

$$\text{div}(s\tilde{L}(s)(\bar{\tilde{\epsilon}}(s, x) - \bar{\tilde{\epsilon}}^*(s, x))) = 0 \text{ in } D. \quad (18)$$

Then, by Eqs. (13), (16), and (14) in Eq. (18), the following expressions are obtained:

$$-\xi \cdot \tilde{L}(s)(\xi \otimes \bar{\mathbf{u}}(s, \xi)) = i\xi \cdot \tilde{L}(s)\bar{\tilde{\epsilon}}^*(s, \xi) \quad \text{for every } \xi \neq 0, \quad (19)$$

where the symbols \otimes and \cdot represent the outer and the inner product, respectively (Spiegel 1959). Thus, since $\tilde{L}(s)$ represents the Laplace transform of the viscoelastic relaxation tensor of the matrix, the coefficients $\bar{\mathbf{u}}(s, \xi)$ are obtained uniquely in terms of the $\bar{\tilde{\epsilon}}^*(s, \xi)$ in the following way:

$$\bar{\mathbf{u}}(s, \xi) = -i(\xi \cdot \tilde{L}(s) \cdot \xi)^{-1} \cdot \xi \cdot \tilde{L}(s)\bar{\tilde{\epsilon}}^*(s, \xi) \quad \text{for every } \xi \neq 0, \quad (20)$$

and from Eq. (16), the Fourier coefficients of the corresponding strain are

$$\bar{\tilde{\epsilon}}(s, \xi) = \text{sym}(\xi \otimes (\xi \cdot \tilde{L}(s) \cdot \xi)^{-1} \otimes \xi) : \tilde{L}(s)\bar{\tilde{\epsilon}}^*(s, \xi) \quad \text{for every } \xi \neq 0. \quad (21)$$

Finally denoting

$$P(s, \xi) = \text{sym}(\xi \otimes (\xi \cdot \tilde{L}(s) \cdot \xi)^{-1} \otimes \xi), \quad (22)$$

the actual strain inside the inclusion from Eq. (21) using Eqs. (13) and (17) is

$$\bar{\tilde{\epsilon}}(s, x) = \frac{1}{V} \sum_{\xi}^{\pm\infty'} P(s, \xi) : \tilde{L}(s) \int_D \tilde{\epsilon}^*(s, x') \times \exp(-i\xi(x' - x)) dx' \quad (23)$$

where a prime on the sum indicates that $\xi = 0$ is excluded in the summation.

Since the aim of this work is to obtain the overall viscoelastic properties, the exact expression of the strain tensor $\bar{\tilde{\epsilon}}(s, x)$ is not necessary. Only its volume average on Ω denoted by $\overline{\bar{\tilde{\epsilon}}(s)} = 1/V_{\Omega} \int_{\Omega} \bar{\tilde{\epsilon}}(s, x) dx$ is needed,

$$\overline{\bar{\tilde{\epsilon}}(s)} = \frac{1}{V} \sum_{\xi}^{\pm\infty'} P(s, \xi) : \tilde{L}(s) \left(\frac{g_0(\xi)}{V_{\Omega}} \right) \int_D \tilde{\epsilon}^*(s, x') \times \exp(-i\xi x') dx', \quad (24)$$

where V_{Ω} is the volume of the inclusion and

$$g_0(\xi) = \int_{\Omega} \exp(i\xi x) dx. \quad (25)$$

In a periodic microstructure, the equivalent eigenstrain is not constant in Ω . However, in order to solve the problem analytically, an approximation of Eq. (24) is introduced using a constant $\bar{\tilde{\epsilon}}^*(s, x)$. While it is possible to use a polynomial approximation for the eigenstrain, the differences between

the two approaches have been shown to be small in the elastic case (Nemat-Nasser and Taya, 1981). Then, replacing $\tilde{\epsilon}^*(s, x)$ with its volume average $\bar{\tilde{\epsilon}}^*(s)$, Eq. (24) becomes

$$\overline{\bar{\tilde{\epsilon}}(s)} = \frac{1}{V} \sum_{\xi}^{\pm\infty'} P(s, \xi) : \tilde{L}(s) \left(\frac{g_0(\xi)g_0(-\xi)}{V_{\Omega}} \right) \overline{\bar{\tilde{\epsilon}}^*(s)}, \quad (26)$$

or

$$\bar{\tilde{\epsilon}}(s) = \nu_f \sum_{\xi}^{\pm\infty'} \left(\frac{g_0(\xi)}{V_{\Omega}} \right) \left(\frac{g_0(-\xi)}{V_{\Omega}} \right) P(s, \xi) : \tilde{L}(s) : \overline{\bar{\tilde{\epsilon}}^*(s)}, \quad (27)$$

and by denoting

$$t(\xi) = \nu_f \left(\frac{g_0(\xi)}{V_{\Omega}} \right) \left(\frac{g_0(-\xi)}{V_{\Omega}} \right), \quad (28)$$

and

$$P(s) = \sum_{\xi}^{\pm\infty'} t(\xi) P(s, \xi), \quad (29)$$

the following expression holds:

$$\overline{\bar{\tilde{\epsilon}}(s)} = P(s) : \tilde{L}(s) : \overline{\bar{\tilde{\epsilon}}^*(s)}. \quad (30)$$

Note that Eq. (30) represents the relation between the volume average of the strain inside $\Omega(\bar{\tilde{\epsilon}}(s))$ and the volume average of the applied eigenstrain ($\overline{\bar{\tilde{\epsilon}}^*(s)}$) in the transformed domain.

Overall Linear Viscoelastic Relaxation Tensor

In order to obtain the homogenization eigenstrain which simulates the presence of the periodic inclusions inside the body, let us consider an applied average strain tensor with Laplace transform $\bar{\tilde{\epsilon}}_0(s)$. Under this condition, the Laplace transform of the average stress in the inclusion is

$$\sigma_{\text{het}}(s) = s\tilde{L}'(s) : (\bar{\tilde{\epsilon}}_0(s) + P(s) : \tilde{L}(s) : \overline{\bar{\tilde{\epsilon}}^*(s)}), \quad (31)$$

where σ_{het} indicates the stress in the heterogeneous material. In the equivalent homogeneous solid, the Laplace transform of the average stress σ_{hom} is

$$\sigma_{\text{hom}}(s) = s\tilde{L}(s) : (\bar{\tilde{\epsilon}}_0(s) + (P(s) : \tilde{L}(s) - I^{(4)}) : \overline{\bar{\tilde{\epsilon}}^*(s)}). \quad (32)$$

Then, by imposing the equivalence between the stress in the homogeneous material σ_{hom} and the heterogeneous one σ_{het} (equivalent eigenstrain method), the following average consistency condition in the Laplace domain is obtained (see Nemat-Nasser and Hori, 1990, for the elastic case):

$$\tilde{L}'(s) : (\bar{\tilde{\epsilon}}_0(s) + P(s) : \tilde{L}(s) : \overline{\bar{\tilde{\epsilon}}^*(s)}) = \tilde{L}(s) : (\bar{\tilde{\epsilon}}_0(s) + (P(s) : \tilde{L}(s) - I^{(4)}) : \overline{\bar{\tilde{\epsilon}}^*(s)}), \quad (33)$$

where L' is the elastic tensor of the inclusion and $I^{(4)}$ is the identity fourth-order tensor. Observe that the tensor $P(s)$ takes into account the geometry of the inclusion and can be evaluated once and for all. Then from Eq. (33), the equivalent average volume eigenstrain $\bar{\tilde{\epsilon}}^*(s)$ can be solved in terms of the tensors $\tilde{L}'(s)$, $\tilde{L}(s)$, $P(s)$, and $\bar{\tilde{\epsilon}}_0$ for every s as

$$\bar{\tilde{\epsilon}}^*(s) = \left[\left((\tilde{L}'(s) - \tilde{L}(s))^{-1} - P(s) \right) \tilde{L}(s) \right]^{-1} \bar{\tilde{\epsilon}}_0(s). \quad (34)$$

Furthermore, using the linear constitutive equation in the Laplace domain, the Laplace transform of the uniform over-

all stress $\bar{\sigma}_0(s)$ in the unit cell is

$$s\tilde{L}^*(s):\bar{\epsilon}_0(s) = s\tilde{L}(s):(\bar{\epsilon}_0(s) - \nu_f \bar{\epsilon}^*(s)), \quad (35)$$

where $\tilde{L}^*(s)$ is the overall relaxation tensor of the composite material. By using Eq. (34) and noting that $\bar{\epsilon}_0(s)$ is arbitrary, the following expression of $\tilde{L}^*(s)$ is obtained:

$$s\tilde{L}(s) = s\tilde{L}(s) - \nu_f \left((\tilde{L}(s) - \tilde{L}(s))^{-1} - P(s) \right)^{-1}. \quad (36)$$

In particular, if the matrix is isotropic, denoting by $\bar{\xi} = \xi/|\xi|$, the tensor $P(s)$ is (Mura, 1987; Nemat-Nasser and Hori, 1990)

$$P(s) = \frac{1}{\tilde{\mu}_0(s)} \sum_{\xi}^{\pm\infty'} t(\xi) \left(\text{sym}(\bar{\xi} \otimes I^{(2)} \otimes \bar{\xi}) - \frac{1}{2(1-\nu_0)} (\bar{\xi} \otimes \bar{\xi} \otimes \bar{\xi} \otimes \bar{\xi}) \right), \quad (37)$$

where $\mu_0(s)$ and ν_0 are the Laplace transform of the shear modulus and the Poisson ratio of the matrix, respectively. Hence, when the matrix and the inclusion are both isotropic, Eq. (36) can be written:

$$s\tilde{L}^*(s) = s\tilde{\lambda}_0(s)I^{(2)} \otimes I^{(2)} + 2s\tilde{\mu}_0(s)I^{(4)} - \nu_f \left[(s\tilde{\lambda}_0(s) - \lambda_1)I^{(2)} \otimes I^{(2)} + 2(s\tilde{\mu}_0(s) - \mu_1)I^{(4)} \right]^{-1} + \frac{1}{s\tilde{\mu}_0(s)} \sum_{\xi}^{\pm\infty'} t(\xi) \left(\text{sym}(\bar{\xi} \otimes I^{(2)} \otimes \bar{\xi}) - \frac{1}{2(1-\nu_0)} (\bar{\xi} \otimes \bar{\xi} \otimes \bar{\xi} \otimes \bar{\xi}) \right) \Bigg]^{-1}, \quad (38)$$

where $\tilde{\mu}_0(s)$, $\tilde{\lambda}_0(s)$, μ_1 , and λ_1 are the Laplace transform of the Lamé constants of the matrix and the Lamé constants of the inclusion, respectively. Then, defining the following series S_l (with $l = 1$ to 9) as

$$S_1 = \sum_{\xi}^{\pm\infty'} t(\xi) \bar{\xi}_1^2, S_2 = \sum_{\xi}^{\pm\infty'} t(\xi) \bar{\xi}_2^2, S_3 = \sum_{\xi}^{\pm\infty'} t(\xi) \bar{\xi}_3^2, S_4 = \sum_{\xi}^{\pm\infty'} t(\xi) \bar{\xi}_1^4, S_5 = \sum_{\xi}^{\pm\infty'} t(\xi) \bar{\xi}_2^4, S_6 = \sum_{\xi}^{\pm\infty'} t(\xi) \bar{\xi}_3^4, S_7 = \sum_{\xi}^{\pm\infty'} t(\xi) \bar{\xi}_2^2 \bar{\xi}_3^2, S_8 = \sum_{\xi}^{\pm\infty'} t(\xi) \bar{\xi}_1^2 \bar{\xi}_3^2, S_9 = \sum_{\xi}^{\pm\infty'} t(\xi) \bar{\xi}_1^2 \bar{\xi}_2^2, \quad (39)$$

the final expressions of the nonzero components of the tensor $L^*(s)$ can be written in the following way:

$$s\tilde{L}_{11}^*(s) = \hat{\lambda}_0 + 2\hat{\mu}L_0 - \nu_f \left(\frac{S_3S_2}{\hat{\mu}_0^2} - \frac{S_5S_3 + S_6S_2}{\hat{\mu}_0^2g} - \frac{a(S_2 + S_3)}{2\hat{\mu}_0c} + \frac{S_6S_5 - S_7^2}{\hat{\mu}_0^2g^2} + \frac{a(S_5 + S_6) + 2bS_7}{2\hat{\mu}_0gc} + \frac{a^2 - b^2}{4c^2} \right) / D$$

$$s\tilde{L}_{12}^*(s) = \hat{\lambda}_0 + \nu_f \left(\left(-\frac{S_9}{\hat{\mu}_0^2g} + \frac{b}{2c\hat{\mu}_0} \right) S_3 + \frac{S_9S_6 - S_8S_7}{\hat{\mu}_0^2g^2} - \frac{b(S_6 - S_7) - bS_8 - aS_9}{2c\hat{\mu}_0g} - \frac{ba + b^2}{4c^2} \right) / D$$

$$s\tilde{L}_{13}^*(s) = \hat{\lambda}_0 - \nu_f \left(\left(-\frac{S_8}{\hat{\mu}_0^2g} + \frac{b}{2c\hat{\mu}_0} \right) S_2 - \frac{S_8S_5 - S_9S_7}{\hat{\mu}_0^2g^2} + \frac{b(S_5 - S_7) - aS_8 - bS_9}{2c\hat{\mu}_0g} + \frac{ab + b^2}{4c^2} \right) / D$$

$$s\tilde{L}_{22}^*(s) = \hat{\lambda}_0 + 2\hat{\mu}L_0 - \nu_f \left(\frac{S_3S_1}{\hat{\mu}_0^2} - \frac{S_4S_3 + S_6S_1}{\hat{\mu}_0^2g} - \frac{a(S_1 + S_3)}{2\hat{\mu}_0c} + \frac{S_6S_4 - S_8^2}{\hat{\mu}_0^2g^2} + \frac{a(S_4 + S_6) + 2bS_8}{2\hat{\mu}_0gc} + \frac{a^2 - b^2}{4c^2} \right) / D$$

$$s\tilde{L}_{33}^*(s) = \hat{\lambda}_0 + 2\hat{\mu}_0 - \nu_f \left(\frac{S_2S_1}{\hat{\mu}_0^2} - \frac{S_4S_2 + S_5S_1}{\hat{\mu}_0^2g} - \frac{a(S_1 + S_2)}{2\hat{\mu}_0c} + \frac{S_5S_4 - S_9^2}{\hat{\mu}_0^2g^2} + \frac{a(S_5 + S_4) + 2bS_9}{2\hat{\mu}_0gc} + \frac{a^2 - b^2}{4c^2} \right) / D$$

$$s\tilde{L}_{23}^*(s) = \hat{\lambda}_0 + \nu_f \left(\left(-\frac{S_7}{\hat{\mu}_0^2g} + \frac{b}{2c\hat{\mu}_0} \right) S_1 + \frac{S_7S_4 - S_9S_8}{\hat{\mu}_0^2g^2} - \frac{b(S_4 - S_8 - S_9) - aS_7}{2c\hat{\mu}_0g} - \frac{ab + b^2}{4c^2} \right) / D$$

$$s\tilde{L}_{44}^*(s) = \hat{\mu}_0 - \nu_f \left(-\frac{S_2}{\hat{\mu}_0} - \frac{S_3}{\hat{\mu}_0} + (\hat{\mu}_0 - \mu_1)^{-1} + \frac{4S_7}{\hat{\mu}_0(2 - 2\nu_0)} \right)^{-1}$$

$$s\tilde{L}_{55}^*(s) = \hat{\mu}_0 - \nu_f \left(-\frac{S_1}{\hat{\mu}_0} - \frac{S_3}{\hat{\mu}_0} + (\hat{\mu}_0 - \mu_1)^{-1} + \frac{4S_8}{\hat{\mu}_0(2 - 2\nu_0)} \right)^{-1}$$

$$s\tilde{L}_{66}^*(s) = \hat{\mu}_0 - \nu_f \left(-\frac{S_1}{\hat{\mu}_0} - \frac{S_2}{\hat{\mu}_0} + (\hat{\mu}_0 - \mu_1)^{-1} + \frac{4S_9}{\hat{\mu}_0(2 - 2\nu_0)} \right)^{-1}, \quad (40)$$

where

$$\begin{aligned}
D = & -\frac{S_3 S_2 S_1}{\hat{\mu}_0^3} + \frac{(S_6 S_2 + S_6 S_2 + S_6 S_2) S_1}{\hat{\mu}_0^3 g} \\
& + \frac{a(S_1 S_2 + (S_1 + S_2) S_3)}{2\hat{\mu}_0^2 c} + \frac{(S_5 S_4 - S_7^2) S_1 + (S_6 S_4 + S_8^2) S_2 + (S_5 S_4 + S_9^2) S_3}{\hat{\mu}_0^3 g^2} \\
& - \frac{(aS_5 + aS_6 + 2bS_7^2) S_1 + (aS_4 + aS_6 + 2bS_8^2) S_2 + (aS_4 + aS_5 + 2bS_9^2) S_3}{2\hat{\mu}_0^2 g c} \\
& + \frac{(b^2 - a^2)}{4\hat{\mu}_0 c^2} (S_1 + S_2 + S_3) + \frac{(S_5 S_6 - S_7^2) S_4 - S_8^2 S_5 - S_9^2 S_6 - 2S_8 S_9 S_7}{\hat{\mu}_0^3 g^3} \\
& + \frac{(aS_5 + aS_6 + 2bS_7) S_4 - (aS_7 + 2bS_8 + 2bS_9) S_7 + (2bS_5 - aS_8 + 2bS_9) S_8}{2\hat{\mu}_0^2 g^2 c} \\
& + \frac{-aS_9^2 + (2bS_9 + aS_5) S_6}{2\hat{\mu}_0^2 g^2 c} + \frac{a(aS_4 + aS_5 + aS_6 + 2(bS_7 + bS_8 + bS_9))}{4\hat{\mu}_0 g c^2} \\
& + \frac{d(2(S_7 + S_8 + S_9) - (S_4 + S_5 + S_6))}{4} + \frac{a^3 - 3ab^2 - 2b^3}{8c^3}, \quad (41)
\end{aligned}$$

and

$$\begin{aligned}
a &= \mu_1 - \hat{\mu}_0 - 2\mu_1 \nu_0 + 2\hat{\nu}_0 \nu_1 \\
b &= -\hat{\mu}_0 \nu_0 + \mu_1 \nu_1 + 2\hat{\mu}_0 \nu_0 \nu_1 - 2\mu_1 \nu_0 \nu_1 \\
c &= (\hat{\mu}_0 - \mu_1)(-\hat{\mu}_0 + \mu_1 - \hat{\mu}_0 \nu_0 - 2\mu_1 \nu_0 \\
&\quad + 2\hat{\mu}_0 \nu_1 + \mu_1 \nu_1 + 2\hat{\mu}_0 \nu_0 \nu_1 - 2\mu_1 \nu_0 \nu_1) \\
d &= b^2 / (\hat{\mu}_0 g c^2) \\
g &= (2 - 2\nu_0) \quad (42)
\end{aligned}$$

where $\hat{\mu}_0 = s\tilde{\mu}_0(s)$, $\hat{\lambda}_0 = s\tilde{\lambda}(s)$ and the series S_i are given by Nemat-Nasser et al. (1982) and Iwakuma and Nemat-Nasser (1983) for several geometries of the inclusions.

Unidirectional Composite

For composite material reinforced by long circular cylindrical fibers, five series are different from zero and only three are independent (Nemat-Nasser et al., 1982). If the fibers are aligned with the x_1 , then

$$\begin{aligned}
S_1 &= S_4 = S_8 = S_9 = 0 \\
S_2 &= S_3, S_5 = S_6. \quad (43)
\end{aligned}$$

Therefore, Eqs. (40) to (42) became

$$\begin{aligned}
s\tilde{L}_{11}^*(s) &= \hat{\lambda}_0 + 2\hat{\mu}L_0 - \nu_f \left[\frac{S_3^2}{\hat{\mu}_0^2} - \frac{S_6 S_3}{\hat{\mu}_0^2 g} - \frac{aS_3}{\hat{\mu}_0 c} \right. \\
&\quad \left. + \frac{S_6^2 - S_7^2}{\hat{\mu}_0^2 g^2} + \frac{aS_6 + bS_7}{\hat{\mu}_0 g c} + \frac{a^2 - b^2}{4c^2} \right] / D
\end{aligned}$$

$$s\tilde{L}_{12}^*(s) = \hat{\lambda}_0 + \nu_f b \left[\frac{S_3}{2c\hat{\mu}_0} - \frac{S_6 - S_7}{2c\hat{\mu}_0 g} - \frac{a + b}{4c^2} \right] / D$$

$$s\tilde{L}_{23}^*(s) = \tilde{\lambda}_0 + \nu_f \left[\frac{aS_7}{2\hat{\mu}_0 g c} + \frac{ba + b^2}{4c^2} t \right] / D$$

$$s\tilde{L}_{22}^*(s) = \hat{\lambda}_0 + 2\hat{\mu}_0 - \nu_f \left[-\frac{aS_3}{2\hat{\mu}_0 c} + \frac{aS_6}{2\hat{\mu}_0 g c} + \frac{a^2 - b^2}{4c^2} \right] / D$$

$$\begin{aligned}
s\tilde{L}_{44}^*(s) &= \hat{\mu}_0 - \nu_f \left[\frac{2S_3}{\hat{\mu}_0^2} + (\hat{\mu}_0 - \mu_1)^{-1} + \frac{4S_7}{\hat{\mu}_0(2 - 2\nu_0)} \right]^{-1} \\
s\tilde{L}_{66}^*(s) &= \hat{\mu}_0 - \nu_f \left[-\frac{S_3}{\hat{\mu}_0} + (\hat{\mu}_0 - \mu_1)^{-1} \right]^{-1}, \quad (44)
\end{aligned}$$

where

$$\begin{aligned}
D &= \frac{aS_3^2}{2\hat{\mu}_0^2 c} - \frac{aS_6 S_3}{\hat{\mu}_0^2 g c} + \frac{a(S_6^2 - S_7^2)}{2\hat{\mu}_0^2 g^2 c} + \frac{S_3(b^2 - a^2)}{2\hat{\mu}_0 c^2} \\
&\quad + \frac{S_6(a^2 - b^2) + S_7(ab + b^2)}{2\hat{\mu}_0 g c^2} + \frac{(a^3 - 2b^3 - 3ab^2)}{8c^3}, \quad (45)
\end{aligned}$$

and

$$\begin{aligned}
a &= \mu_1 - \hat{\mu}_0 - 2\mu_1 \nu_0 + 2\hat{\mu}_0 \nu_1 \\
b &= -\hat{\mu}_0 \nu_0 + \mu_1 \nu_1 + 2\hat{\mu}_0 \nu_0 \nu_1 - 2\mu_1 \nu_0 \nu_1 \\
c &= (\hat{\mu}_0 - \mu_1)(-\hat{\mu}_0 + \mu_1 - \hat{\mu}_0 \nu_0 - 2\mu_1 \nu_0 + 2\hat{\mu}_0 \nu_1 \\
&\quad + \mu_1 \nu_1 + 2\hat{\mu}_0 \nu_0 \nu_1 - 2\mu_1 \nu_0 \nu_1) \\
g &= (2 - 2\nu_0). \quad (46)
\end{aligned}$$

The series S_3 , S_6 , S_7 are given by Nemat-Nasser et al. (1982) for several values of the volume fraction of the inclusions. However, the data can be fitted with the following parabolic expressions using a least-square method (Luciano and Barbero 1994):

$$\begin{aligned}
S_3 &= 0.49247 - 0.47603\nu_f - 0.02748\nu_f^2 \\
S_6 &= 0.36844 - 0.14944\nu_f - 0.27152\nu_f^2 \\
S_7 &= 0.12346 - 0.32035\nu_f + 0.23517\nu_f^2. \quad (47)
\end{aligned}$$

Relaxation Tensor in the Time Domain

The viscoelastic behavior of the matrix material is obtained from creep or relaxation tests. A creep test provides the strain as a function of time $\epsilon(t)$ for a fixed stress level. The matrix is said to be linearly viscoelastic if the creep

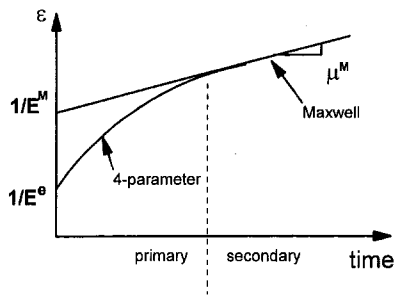


Fig. 2 Representation of creep data

compliance $M(t)$ is independent of the stress level. In this case, it is possible to write:

$$\epsilon(t) = M(t)\sigma.$$

A relaxation tests provides the stress as a function of time $\sigma(t)$ for constant applied strain, as

$$\sigma(t) = L(t)\epsilon.$$

High-temperature secondary (steady-state) creep data of metals (used in metal matrix composites) are commonly approximated by the Maxwell model (Flugge, 1967). The creep compliance of the Maxwell model, which is a series spring dash-pot system, is

$$M(t) = \frac{1}{E^M} + \frac{t}{\mu^M},$$

where μ^M is the slope of the secondary creep data (Fig. 2) and E^M represents both the elastic modulus E^e and the effect of all primary creep deformations lumped at time $t = 0$. The four-parameter model is used when a better representation of the primary creep data is desired. The four-parameter model has been used also by several authors (Skundra and Auzukalns 1973, Yancey 1990) to represent the viscoelastic behavior of polymer matrices. The model is obtained by adding a Kelvin model (also called Voigt model, which is a parallel spring dash-pot system (Flungge, 1967)) in series to the Maxwell model. The resulting creep compliance is

$$M(t) = \frac{1}{E^e} + \frac{t}{\mu^M} + \frac{1}{E^V} \left(1 - \exp\left(-\frac{tE^V}{\mu^V}\right) \right), \quad (48)$$

where $E^e \neq E^M$ (see Fig. 2). The effective relaxation modulus \hat{E} is obtained from the creep compliance using the following relationship:

$$s\hat{L}(s)s\tilde{M}(s) = \hat{L}\tilde{M} = 1.$$

Then, from Eq. (48), the effective relaxation modulus is obtained as

$$\hat{E}_0 = \frac{E^e\eta^M(E^V + \eta^V s)}{E^e E^V + (E^V\eta^M + E^e(\eta^V + \eta^M))s + \eta^V\eta^M s^2}. \quad (49)$$

The Lamé' properties are obtained from Eq. (49) as

$$\hat{\lambda}_0 = \frac{\hat{E}_0\nu_0}{(1 + \nu_0)(1 - 2\nu_0)} \quad (50)$$

$$\hat{\mu}_0 = \frac{\hat{E}_0}{2(1 + \nu_0)}. \quad (51)$$

Introducing these properties into Eq. (45), the coefficients of the relaxation tensor are obtained as rational functions of the Laplace variable s . The order of the polynomial in the

denominator is larger than the numerator's for all the coefficients in the relaxation tensor.

After substitution of the four parameters in Eq. (49) by numerical values, the expressions of the coefficients can be easily back-transformed analytically into the time domain by standard techniques (Ogatha, 1987). Therefore, each of the coefficients of the relaxation tensor in the time domain is given by a finite sum of exponential terms with real coefficients and real-time constants.

Transversely Isotropic Material

Because of the particular geometry of the microstructure (a square array of cylinders, see Fig. 1) used to obtain Eq. (47), the relaxation tensor $L^*(t)$ for unidirectional composite represents an orthotropic material with square symmetry. In the case considered in the previous section, the directions x_2 and x_3 are equivalent and the relaxation tensor is unchanged by a rotation about x_1 of $n\pi/2$ ($n = 0, \pm 1, \pm 2, \dots$). This implies that only six components are required to describe completely the tensor.

In order to obtain a transversely isotropic relaxation tensor $C^*(t)$, equivalent in average sense to the relaxation tensor with square symmetry, the averaging procedure proposed by Aboudi (1991) is used. Then, the following expressions are obtained explicitly in terms of the coefficients of the tensor $L^*(t)$ described in the previous section:

$$\begin{aligned} C_{11}^*(t) &= L_{11}^*(t) \\ C_{12}^*(t) &= L_{12}^*(t) \\ C_{22}^*(t) &= \frac{3}{4}L_{22}^*(t) + \frac{1}{4}L_{23}^*(t) + \frac{1}{2}L_{66}^*(t) \\ C_{23}^*(t) &= \frac{1}{4}L_{22}^*(t) + \frac{3}{4}L_{23}^*(t) - \frac{1}{2}L_{66}^*(t) \\ C_{44}^*(t) &= L_{44}^*(t) \\ C_{66}^*(t) &= \frac{1}{2}(L_{22}^*(t) - L_{23}^*(t)). \end{aligned} \quad (52)$$

Comparisons With Experimental Results

Comparisons with experimental results are presented in this section. Skudra and Auzukalns (1973) measured the creep response $\epsilon(t) = \epsilon_{11}(t)$ of a glass fiber-reinforced composite with a fiber concentration $\nu_f = 0.54$ at three levels of tensile stress ($\sigma = \sigma_{11} = 529$ MPa, 441 MPa and 337 MPa). They represented the viscoelastic behavior of the ED-6 resin with the four-parameter model, using the following set of material constants: $E^e = 3.27$ GPa, $\eta^M = 8000$ GPa*hr, $E^V = 1.8$ GPa, $\eta^V = 300$ GPa*hr and $\nu_0 = 0.38$. On the other hand, the elastic properties of the glass fibers are $\nu_1 = 0.21$ and $E = 68.67$ GPa.

The analytical expressions in the time domain of the coefficients of $C^*(t)$ are obtained back transforming analytically Eqs. (44) after substituting Eq. (50) and (51),

$$\begin{aligned} C_{11}^*(t) &= 37.081 - 0.000000000378e^{-0.0186t} \\ &\quad + 0.00000000324e^{-0.01765t} + 1.790e^{-0.01548t} \\ &\quad - 0.000000001973e^{-0.00014875684943196t} \\ &\quad + 0.00000000164e^{-0.000144t} + 1.1068e^{-0.00013470t} \\ &\quad - 0.6017e^{-0.0086t}\sinh(0.00851t) \\ &\quad + 1.929e^{-0.008654t}\cosh(0.008511t) \end{aligned}$$

$$C_{22}^*(t) = 1.232e^{-0.015t} + 0.803e^{-0.000132t} - 9.937 \times 10^{-11}e^{-0.018630t} - 4.59 \times 10^{-11}e^{-0.001487t} - 0.356e^{-0.00831t} \sinh(0.00817t) + 1.2594e^{-0.00831t} \cosh(0.00817t) + 3.737e^{-0.0001347t} - 6.211 \times 10^{-11}e^{0.0001487t} + 0.000000001749e^{-0.000144t} + 0.000000003044e^{-0.01765t} + 6.045e^{-0.01548t} - 0.317e^{-0.00865t} \sinh(0.008511t) + 1.0177e^{-0.00865t} \cosh(0.008511t)$$

$$C_{12}^*(t) = 0.0000000002623e^{-0.01863t} + 0.00000000318e^{-0.01765t} + 3.289e^{-0.01548t} + 0.000000001133096783e^{-0.0001485t} + 0.0000000001633e^{-0.00014495t} + 2.033826619e^{-0.0001347t} - 0.1745e^{-0.00865t} \sinh(0.00851t) + 0.5595e^{-0.00865t} \cosh(0.00851t)$$

$$C_{23}^*(t) = -1.232e^{-0.015t} - 0.803e^{-0.000132t} + 9.93 \times 10^{-11}e^{-0.01863t} + 4.599 \times 10^{-11}e^{0.0001487t} + 0.356e^{-0.00831t} \sinh(0.00817t) - 1.259e^{-0.00831t} \cosh(0.00817t) + 3.737e^{-0.000134t} - 6.211 \times 10^{-11}e^{-0.0001487t} + 0.00000000174e^{-0.000144t} + 0.000000003044e^{-0.0176t} + 6.0450e^{-0.01548t} - 0.1418e^{-0.00865t} \sinh(0.00851t) + 0.454e^{-0.0086t} \cosh(0.00851t)$$

$$C_{44}^*(t) = 1.232e^{-0.015t} + 0.803e^{-0.000132} - 9.937 \times 10^{-11}e^{-0.0186t} - 4.599 \times 10^{-11}e^{-0.000148t} - 0.356e^{-0.00831t} \sinh(0.00817t) + 1.259e^{-0.00831t} \cosh(0.00817t) - 0.0877e^{-0.00865t} \sinh(0.00851t) + 0.2815e^{-0.00865t} \cosh(0.00851t)$$

$$C_{66}^*(t) = -0.1112e^{-0.00865t} \sinh(0.00851t) + 0.3566e^{-0.00865t} \cosh(0.00851t) - 0.7964e^{-0.00795t} \sinh(0.00781t) + 3.189e^{-0.00795t} \cosh(0.00781t)$$

A typical plot of a coefficient of the equivalent transversely isotropic relaxation tensor $C^*(t)$ is shown in Fig. 3 for several values of the fiber volume fraction. Comparisons of the predicted strain with the experimental data from Skudra and Auzukalns (1973) are shown in Fig. 4.

Conclusions

Analytical expressions for the Laplace transform of the relaxation tensor of composite material with general type of elastic inclusions or voids with periodic microstructure and linear viscoelastic matrix are presented. The Laplace transforms of the relaxation moduli are inverted analytically to the time domain for the case of long fiber-reinforced composites and when a four-parameter model is used to represent the viscoelastic behavior of the matrix. It is worth noting that good agreement with available experimental data is obtained.

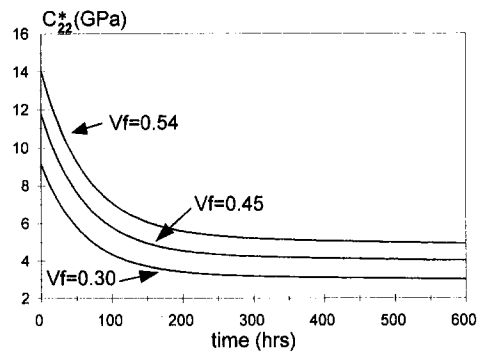


Fig. 3 Coefficient $C_{22}^*(t)$ of the relaxation tensor

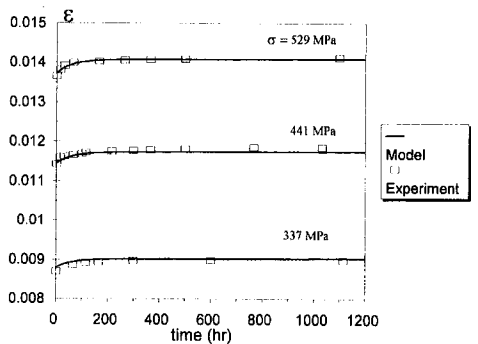


Fig. 4 Comparison with experimental results of axial creep response

The interaction effects between the constituents and the geometry of the inclusions are fully accounted.

Acknowledgments

This work was supported by the Italian National Council of Research (CNR) and the Constructed Facilities Center (CFC) at West Virginia University.

References

Aboudi, J., 1991, *Mechanics of Composite Materials*, Elsevier Science Publishers, The Netherlands.

Barbero, E. J., and Luciano, R., 1995, "Micromechanical Formulas for the Relaxation Tensor of Linear Viscoelastic Composites with Transversely Isotropic Fibers," *I. J. Solids and Structures*, Vol. 32, No. 13, pp. 1859-1872.

Christensen, R. M., 1969, "Viscoelastic Properties of Heterogeneous Media," *J. Mech. Phys. Solids*, Vol. 17, pp. 23-41.

Christensen, R. M., 1979, *Mechanics of Composite Materials*, John Wiley and Sons, New York, p. 288.

Christensen, R. M., 1990, "A Critical Evaluation for a Class of Micromechanics Models," *J. Mech. Phys. Solids*, Vol. 38, No. 3, pp. 379-404.

Flügge, W., 1967, *Viscoelasticity*, Blaisdell Publishing, Waltham, MA.

Gurtin, M. E., and Sternberg, E., 1962, "On the Linear Theory of Viscoelasticity," *Archives for Rational Mechanics and Analysis*, Vol. 11, p. 291.

Hashin, Z., 1965, "Viscoelastic Behavior of Heterogeneous Media," *ASME JOURNAL OF APPLIED MECHANICS*, Vol. 29, Vol. 32, pp. 630-636.

Hashin, Z., 1966, "Viscoelastic Fiber Reinforced Materials," *AIAA Journal*, Vol. 4, pp. 1411-1417.

Iwakuma, T., and Nemat-Nasser, S., 1983, "Composites with Periodic Microstructure," *Comput. and Struct.*, Vol. 16, No. 1-4, pp. 13-19.

Laws, N., and McLaughlin, J. R., 1978, "Self-Consistent Estimates for the Viscoelastic Creep Compliances of Composites Materials," *Proceedings of the Royal Society, London*, Vol. 39, pp. 627-649.

Luciano, R., and Barbero, J. E., 1994, "Formulas for the Stiffness of Composites with Periodic Microstructure," *Int. J. Solids and Structures*, Vol. 31, No. 21, pp. 2933-2944.

Mori, T., and Tanaka, K., 1973, "Average Stress in Matrix and Average Elastic Energy of Materials with Misfitting Inclusions," *Acta Metall.*, Vol. 21, pp. 571-574.

Mura, T., 1987, *Micromechanics of Defects in Solids*, 2nd ed., rev., Martinus Nijhoff, Dordrecht, The Netherlands.

Nemat-Nasser, S., and Hori, M., 1993, *Micromechanics: Overall Properties of Heterogeneous Solids*, Elsevier Science Publishers, The Netherlands.

Nemat-Nasser, S., Iwakuma, T., and Hejazi, M., 1982, "On Composites with Periodic Structure," *Mech. of Materials*, Vol. 1, pp. 239-267.

Nemat-Nasser, S., and Taya, M., 1981, "On Effective Moduli of an Elastic Body Containing Periodically Distributed Voids," *Q. Appl. Math.*, Vol. 39, pp. 43-59.

Nemat-Nasser, S., and Taya, M., 1986 "On Effective Moduli of an Elastic Body Containing Periodically Distributed Voids: Comments and Corrections," *Q. Appl. Math.*, Vol. 43, pp. 187-188.

Ogatha, K., 1987, *Discrete-Time Control System*, Prentice-Hall, Englewood Cliffs, NJ.

Skundra, A. M., and Auzukalns, Y. V., 1973, "Creep and Long-Time Strength of Unidirectional Reinforced Plastics in Compression," *Polymer Mechanics*, Vol. 6, No. 5, pp. 718-722.

Spiegel, M. R., 1959, *Vector Analysis*, (Schaum's outline series), McGraw-Hill, New York.

Wang, Y. M., and Weng, G. J., 1992, "The Influence of Inclusion Shape on the Overall Viscoelastic Behavior of Composites," *ASME JOURNAL OF APPLIED MECHANICS*, Vol. 59, pp. 510-518.

Yancey, R. N., and Pindera, M. J., 1990, "Micromechanical Analysis of the Creep Response of Unidirectional Composites," *ASME Journal of Engineering Materials and Technology*, Vol. 112, pp. 157-163.

The Role of Temperature in the Entanglement Kinetics of a Polymer Melt

R. S. Jeyaseelan

Rheology Research Laboratory,
Mechanical Engineering Department,
Texas A&M University,
College Station, TX 77843-3123

A. J. Giacomin¹

Department of Mechanical Engineering,
University of Wisconsin,
1513 University Avenue,
Madison, WI 53706-1572
Mem. ASME

Large-amplitude oscillatory shear (LAOS) experiments were conducted at different temperatures on a molten low-density polyethylene standard, designated IUPAC LDPE X. Jeyaseelan et al. (1993) have successfully employed a simplification of transient network theory to describe the LAOS behavior of this polymer melt, at 150°C. The transient network is described by two kinetic rate constants, one for the formation of entanglements due to Brownian motion (k_1), and another for the destruction of entanglements (k_2) due to the imposed deformation. Upon comparison of the predictions of this transient network theory with the measured LAOS behavior of this polymer, we find that the kinetic rate constants k_1 and k_2 are invariant in the range of temperatures examined (150 to 190°C). The temperature dependence of departures from linear viscoelasticity is fully accounted for in the equilibrium entanglement kinetics.

Introduction

Most polymer processing operations subject polymer melts to large and rapid deformations, which elicit nonlinear viscoelastic behavior in the material. To evaluate the stress distribution arising in polymer processing operations, we must therefore employ a valid nonlinear viscoelastic constitutive equation. Furthermore, most polymer processing operations impose large spatial and temporal thermal gradients in the molten polymer, requiring nonisothermal analyses. It has been shown that large errors can arise due to restriction to isothermal analysis in the numerical simulation of polymer processing operations (Nikoleris and Darby, 1989; Luo and Tanner, 1985; Gupta and Metzner, 1982). This is due to the strong dependence of constitutive model parameters on temperature.

It is well known that the linear viscoelastic properties, $G'(\omega)$ and $G''(\omega)$, of most polymer melts in small amplitude oscillatory shear at different temperatures, can be shifted to obtain temperature invariant master curves (Dealy and Wissbrun, 1990). Matsumoto et al. (1973) have studied the LAOS behavior of dispersions of spherical particles in a concentrated polymer solution. For these materials they measured the frequency dependence of the Fourier coefficients of the shear stress response given by

$$\sigma(t) = G'_1 \gamma_0 \sin(\omega t) + G''_1 \gamma_0 \cos(\omega t) - G'_3 \gamma_0^3 \sin(3\omega t) - G''_3 \gamma_0^3 \cos(3\omega t) + \dots \quad (1)$$

where γ_0 is the strain amplitude and ω is the frequency. For fixed strain amplitudes they found that curves of $G'_1(\omega)$, $G''_1(\omega)$, $G'_3(\omega)$, and $G''_3(\omega)$, can also be shifted to yield temperature invariant curves, in the same manner as the linear viscoelastic properties, $G'(\omega)$ and $G''(\omega)$. While the data reduction technique (Matsumoto et al., 1973) enables one to obtain temperature invariant forms for the Fourier coefficients in (1),

determining the effect of γ_0 on these properties requires the use of a specific constitutive equation.

In step shear, departures from linearity are normally reported in terms of the nonlinear relaxation modulus:

$$G(t, \gamma) = h(\gamma)G(t) \quad (2)$$

where γ is the step strain amplitude and $h(\gamma)$ is called the damping function. For melts, the measured damping functions are normally independent of temperature (Dealy and Wissbrun, 1991).

Interestingly, reptation theory with independent alignment also predicts that the damping function will be independent of temperature. However, the specific function predicted by this theory

$$h(\gamma) = \frac{1}{1 + 0.22\gamma^2} \quad (3)$$

is rarely approached by polymer melts.

In this work, we chose LAOS for studying nonlinear viscoelasticity since the strain amplitude and the frequency can be independently controlled. We can therefore separately investigate the effect of temperature on strain and frequency dependent nonlinearity.

In this paper we explore the temperature dependence of a nonlinear viscoelastic theory (Jeyaseelan et al., 1993), which has been particularly successful in describing polymer melt rheology in the most frequently occurring stress state in polymer processing operations, that of shear. This theory employs a structure-dependent relaxation spectrum proposed by Acerno et al. (1976), with a kinetic rate expression developed by Liu et al. (1984). The ability of this theory to model the creation and destruction of molecular entanglements is explored for different conditions of γ_0 , ω and temperature, in LAOS. The use of a sliding plate rheometer incorporating a shear stress transducer allows us to experimentally observe the temperature dependence of the nonlinear viscoelastic behavior of a molten polymer, up to a large strain amplitude, $\gamma_0 = 10$.

A Valid Nonlinear Viscoelastic Constitutive Theory

Various nonlinear viscoelastic constitutive equations have been proposed for polymer melts, and their validity in describing commercial polymer melts can be readily discerned by rheological experiments which invoke nonlinear viscoelastic behav-

¹To whom all correspondence should be addressed.

Contributed by the Applied Mechanics Division of THE AMERICAN SOCIETY OF MECHANICAL ENGINEERS for publication in the ASME JOURNAL OF APPLIED MECHANICS.

Discussion on this paper should be addressed to the Technical Editor, Prof. Lewis T. Wheeler, Department of Mechanical Engineering, University of Houston, Houston, TX 77204-4792, and will be accepted until four months after final publication of the paper itself in the ASME JOURNAL OF APPLIED MECHANICS.

Manuscript received by the ASME Applied Mechanics Division, Sept. 13, 1993; final revision, Apr. 19, 1994. Associate Technical Editor: I. M. Daniel.

ior in the material. It has been shown that a constitutive theory based on the concept of a transient entanglement network (Acierno et al., 1976) can accurately describe the steady shear and the LAOS behavior of molten LDPE and linear low-density polyethylene (LLDPE) (Jeyaseelan et al., 1993). The same constitutive theory is capable of describing the LAOS behavior of seven polymer melts, including high-density polyethylene (HDPE) (Giacomin and Jeyaseelan, 1993a). Comparing the predictions of this theory in shear stress growth and biaxial shear with the published experimental data (Meisser, 1984; Hürlimann, 1991), it has been concluded that this theory accurately describes the behavior of molten LDPE and polyisobutylene in these flows also (Giacomin and Jeyaseelan, 1993b). We therefore conclude that this theory provides a valid description of the nonlinear viscoelastic behavior of polymer melts in shear.

This constitutive theory can be expressed as (Acierno et al., 1976)

$$\boldsymbol{\tau} = \sum_i \boldsymbol{\tau}^i \quad (4)$$

$$\frac{\boldsymbol{\tau}^i}{G_i} + \lambda_i \frac{\delta}{\delta t} \left[\frac{\boldsymbol{\tau}^i}{G_i} \right] = 2\lambda_i \mathbf{D} \quad (5)$$

The transience in the structure is imparted by the flow-field-dependent scalar structural parameters, x_i , which are defined as the ratios of the present number of entanglements per molecule to the number of entanglements per molecule at equilibrium in the i th relaxation mode.

The transient relaxation times and moduli depart from their equilibrium values by (Acierno et al., 1976)

$$\lambda_i = \lambda_{0i} x_i^{1.4} \quad (6)$$

$$G_i = G_{0i} x_i \quad (7)$$

where λ_{0i} and G_{0i} are the relaxation time and modulus of the i th spectral element at equilibrium. The contravariant derivative in (3) is evaluated as

$$\begin{aligned} \frac{\delta}{\delta t} \left[\frac{\boldsymbol{\tau}^i}{G_i} \right] &= \frac{1}{G_i} \frac{d\boldsymbol{\tau}^i}{dt} - \frac{1}{G_i^2} \frac{dG_i}{dt} \boldsymbol{\tau}^i - \frac{1}{G_i} (\nabla v \cdot \boldsymbol{\tau}^i + \boldsymbol{\tau}^i \cdot \nabla v^T). \quad (8) \end{aligned}$$

A special case of the model originally proposed by Liu et al. (1981), the simplified Liu kinetic rate equation (Jeyaseelan et al., 1993), describes the kinetics of the entanglement network (simplified Liu model):

$$\frac{dx_i}{dt} = k_1 \frac{1 - x_i}{\lambda_i} - k_2 x_i [\Pi(\mathbf{D})]^{1/2} \quad (9)$$

The parameter k_1 is the kinetic rate constant for the creation of entanglements in the material due to Brownian motion. The parameter k_2 is the kinetic rate constant for the destruction of entanglements due to the imposed flow field. Larger values of k_1 represent a greater tendency for the material to return to equilibrium following a given nonlinear deformation. Larger values of k_2 reflect a greater ability of an imposed deformation to destroy entanglements and cause increased nonlinearity in the arising stresses.

The constitutive theory described herein possesses a set of N pairs of linear viscoelastic parameters (G_{0i} , λ_{0i}) and two nonlinear viscoelastic parameters, k_1 and k_2 . In the event that the imposed deformation is mild, the network of entanglements in the material is unaffected, and $x_i = 1$. This limit corresponds to the predictions of linear viscoelasticity, described by the generalized Maxwell model. The temperature dependence of the linear viscoelastic parameters (G_{0i} , λ_{0i}) can be treated in the context of linear viscoelasticity for thermo-rheologically simple materials (Tanner, 1985).

Large-Amplitude Oscillatory Shear

When there is no slip at the walls, the imposed shear strain in LAOS is

$$\gamma(t) = \gamma_0 \sin(\omega t), \quad (10)$$

and the shear rate is

$$\dot{\gamma}(t) = \gamma_0 \omega \cos(\omega t). \quad (11)$$

The steady-state nonlinear shear stress response for an isotropic fluid with a fading memory is given by a Fourier series containing only odd harmonics:

$$\sigma(t) = \sum_{\substack{j=1 \\ \text{odd}}}^{\infty} \sigma_j \sin(j\omega t + \delta_j). \quad (12)$$

To evaluate the aforementioned constitutive theory in LAOS, Eqs. (4) through (9) and (11) are solved simultaneously, using a fifth- and sixth-order Runge-Kutta-Verner method (Verner, 1977). It has been suggested that shear stress versus shear rate loops represent the most useful manner of studying the LAOS behavior of polymer melts (Tee and Dealy, 1975). We therefore make the comparison of model predictions with the data in like manner.

The Fourier coefficients in (1) are easily obtained from those in (12) using

$$G'_j = \frac{\sigma_j}{\gamma_0^j} \cos(\delta_j) \quad (13)$$

and

$$G''_j = \frac{\sigma_j}{\gamma_0^j} \sin(\delta_j). \quad (14)$$

Experimental Technique

IUPAC LDPE X is a standard low-density polyethylene which has been extensively used in rheological experiments (Tanner, 1985). A MTS Direct Shear Rheometer incorporating a shear stress transducer was used in this study. This is a commercial version of a sliding plate rheometer incorporating a shear stress transducer (Giacomin et al., 1989). Use of the shear stress transducer eliminates errors caused by thermal degradation and flow-field distortion at the free boundary of the sample.

The gap thickness that was used in the sliding plate rheometer was 1.0 mm. The samples were compression molded to 50 mm \times 125 mm \times 1.25 mm. LAOS experiments were conducted on this material at five different temperatures, ranging from 150 to 190°C. The experiments were conducted at two frequencies, π and 2π rad/s. Measurements were made at strain amplitudes ranging from three to ten.

The initial transients in the shear stress typically fade in less than four cycles. 128 data points were collected per cycle for four cycles, commencing with the seventh cycle. A discrete Fourier transform (DFT) was used to obtain the amplitude of each harmonic of the shear stress response, defined in (9). The phase differences δ_j were determined by comparing the DFT of the measured shear stress with the DFT of the measured plate displacement.

$G'(\omega)$ and $G''(\omega)$ data were obtained for this material at 150, 170, and 190°C from small-amplitude oscillatory shear experiments using a cone and plate rheometer. From these measurements, the discrete relaxation spectra shown in Table 1 were calculated using the method of linear regression with regularization (Orbey and Dealy, 1991).

Results and Discussion

Figures 1 through 4 are plots of σ_j and δ_j as functions of temperature, for different conditions of strain amplitude and

Table 1 Discrete relaxation spectrum for IUPAC LDPE X calculated using the method of linear regression with regularization, following Orbey and Dealy (1991)

λ_{oi} (s)	G_{oi} (Pa) 150°C	G_{oi} (Pa) 170°C	G_{oi} (Pa) 190°C
0.000015	18494	24673	17861
0.00015	167046	227418	109827
0.0015	116903	90938	80583
0.015	47206	37154	30227
0.15	20158	15112	11445
1.5	6598	4673	3291
15.0	1582	924	571
150.0	207	106	39

frequency. In all these plots, the severity of the conditions of oscillation increase upwards from the lowest curve. The curves with the filled symbols represent experiments conducted at a frequency of 2π rad/s, and the curves with unfilled symbols represent experiments at a frequency of π rad/s. Curves with diamonds, triangles, and circles represent experiments conducted at strain amplitudes of 3, 7, and 10, respectively. Figure 1 shows the dependence of the stress amplitude of the first harmonic, on temperature. σ_1 decreases monotonically with temperature, rapidly at lower temperatures and more gradually at higher temperatures. Also clear from this figure is that shapes of the family of curves are virtually identical, suggesting that the qualitative effect of temperature on σ_1 is the same for the conditions of oscillation studied here. The family of curves shown in Fig. 2 are the loss angles of the first harmonic δ_1 corresponding to the curves in Fig. 1. We note here that, in contrast to Fig. 1, the curves do not have the same shapes. Figures 3 and 4 are plots of the stress amplitudes and the phase angles of the third harmonic, for the same conditions of oscillation as the curves in Figs. 1 and 2. In Fig. 3 we observe that for the less severe conditions (the two curves at the bottom) σ_3 is virtually unaffected by temperature, whereas for the more severe conditions, there is a monotonic decrease with temperature, for lower temperatures, and a tendency to reach a steady value at higher temperatures. The reason for the curious depres-

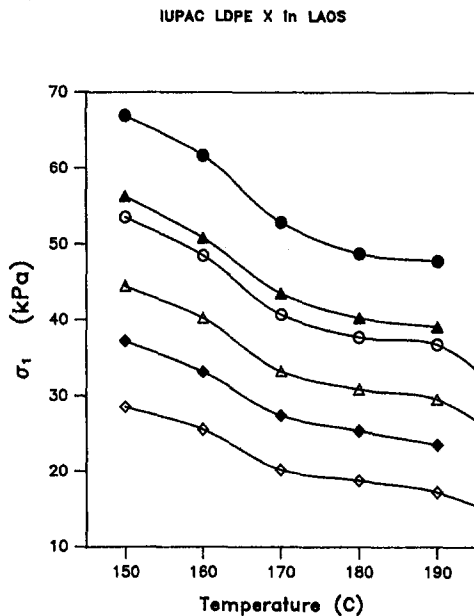


Fig. 1 The dependence of σ_1 on temperature, measured for IUPAC LDPE X in LAOS. Curves with filled symbols represent measurements at $\omega = 2\pi$ rad/s and those with unfilled symbols represent measurements at $\omega = \pi$ rad/s. Measurements for $\gamma_0 = 3, 7,$ and 10 are represented as diamonds, triangles, and circles, respectively.

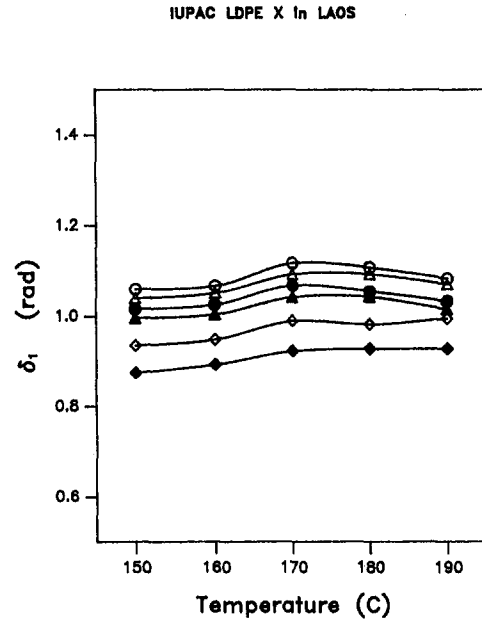


Fig. 2 The dependence of δ_1 on temperature, measured for IUPAC LDPE X in LAOS. Curves with filled symbols represent measurements at $\omega = 2\pi$ rad/s and those with unfilled symbols represent measurements at $\omega = \pi$ rad/s. Measurements for $\gamma_0 = 3, 7,$ and 10 are represented as diamonds, triangles, and circles, respectively.

sion in the phase angle of the third harmonic, δ_3 for the less severe conditions, around 170°C , is not known. For the more severe conditions we see that δ_3 is nearly unaffected by temperature in this range.

In the order of increasing severity of oscillation conditions, Figs. 5 through 7 compare the shear stress versus shear rate loop predicted by the transient network theory discussed in this paper, with the experimental data for IUPAC LDPE X at 190°C . The conditions in Fig. 5 are $\gamma_0 = 3$ and $\omega = \pi$ rad/s. The kinetic rate constants used are $k_1 = 3.4$ and $k_2 = 1.3$. Figure 5

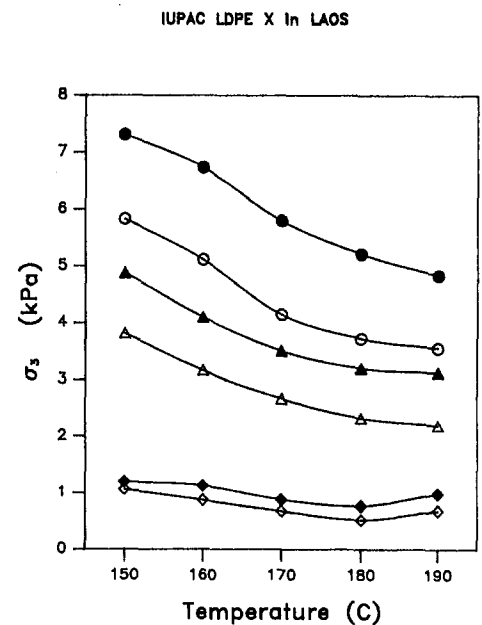


Fig. 3 The dependence of σ_3 on temperature, measured for IUPAC LDPE X in LAOS. Curves with filled symbols represent measurements at $\omega = 2\pi$ rad/s and those with unfilled symbols represent measurements at $\omega = \pi$ rad/s. Measurements for $\gamma_0 = 3, 7,$ and 10 are represented as diamonds, triangles and circles, respectively.

IUPAC LDPE X in LAOS

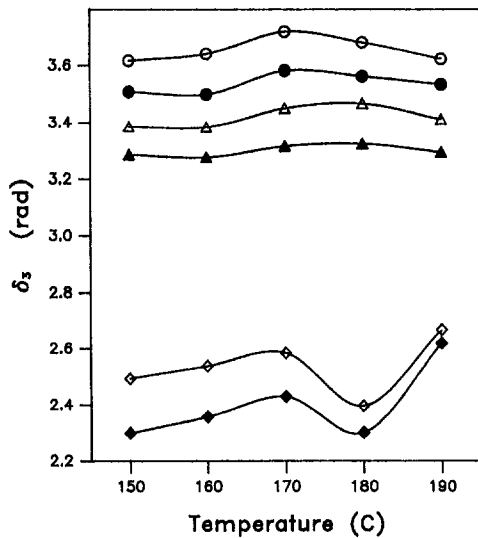


Fig. 4 The dependence of δ_s on temperature, measured for IUPAC LDPE X in LAOS. Curves with filled symbols represent measurements at $\omega = 2\pi$ rad/s and those with unfilled symbols represent measurements at $\omega = \pi$ rad/s. Measurements for $\gamma_0 = 3, 7,$ and 10 are represented as diamonds, triangles, and circles, respectively.

shows that the theory is in excellent agreement with the data, regarding the overall stress amplitude, the shape, and the area of the loop. Upon increasing the strain amplitude to 7, for the same frequency as in Fig. 5, Fig. 6 shows that the theory predicts the right shape and area of the loop, and nearly the same overall stress amplitude. For the very severe condition ($\gamma_0 = 10$ and $\omega = 2\pi$ rad/s) shown in Fig. 7, the model predictions are in slight disagreement with the data, regarding the shape of the loop and the overall stress amplitude. The area of the predicted and the experimental loops are in reasonable agreement.

IUPAC LDPE X at 190 C

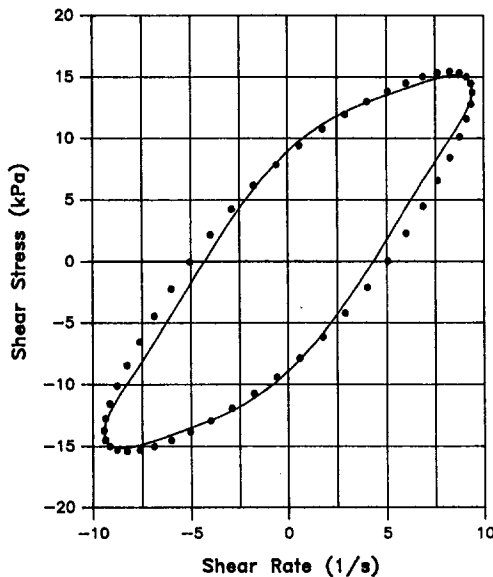


Fig. 5 Comparison of the experimentally obtained shear stress versus shear rate loop (circles) for IUPAC LDPE X at 190°C in LAOS, with the predictions of the simplified Liu model (solid loop) with $k_1 = 3.4$ and $k_2 = 1.3$. The strain amplitude is three and the frequency is π rad/s.

IUPAC LDPE X at 190 C

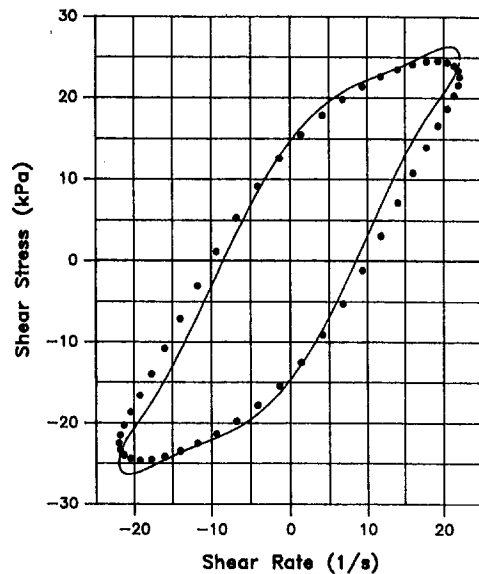


Fig. 6 Comparison of the experimentally obtained shear stress versus shear rate loop (circles) for IUPAC LDPE X at 190°C in LAOS, with the predictions of the simplified Liu model (solid loop) with $k_1 = 3.4$ and $k_2 = 1.3$. The strain amplitude is seven and the frequency is π rad/s.

Figures 8 and 9 compare the predictions of the theory with the data, at temperatures of 170°C and 150°C at the same conditions of strain amplitude and frequency as in Fig. 5. The parameters k_1 and k_2 are the same as in Fig. 5. The excellent agreement shown in Figs. 8 and 9 reveals that the parameters k_1 and k_2 are unaltered by temperature. Figures 10 and 11 compare the predictions of the theory with experiments, at temperatures of 170°C and 150°C at the same conditions of strain amplitude and frequency as in Fig. 6. The parameters k_1 and k_2 are the same as in the previous figures. We note that the comparisons made in Figs. 10 and 11 are virtually identical to that in Fig.

IUPAC LDPE X at 190 C

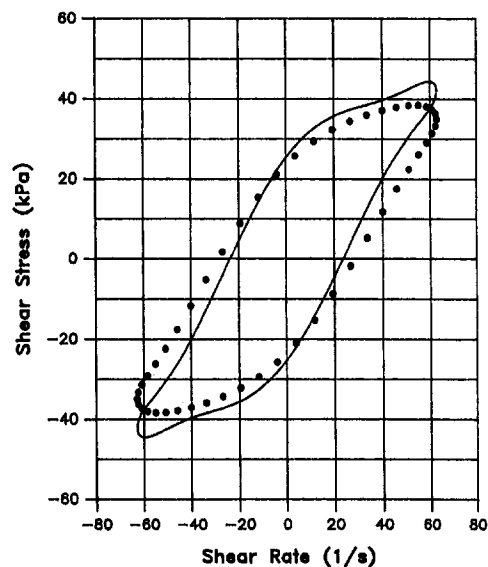


Fig. 7 Comparison of the experimentally obtained shear stress versus shear rate loop (circles) for IUPAC LDPE X at 190°C in LAOS, with the predictions of the simplified Liu model (solid loop) with $k_1 = 3.4$ and $k_2 = 1.3$. The strain amplitude is ten and the frequency is 2π rad/s.

IUPAC LDPE X at 170 C

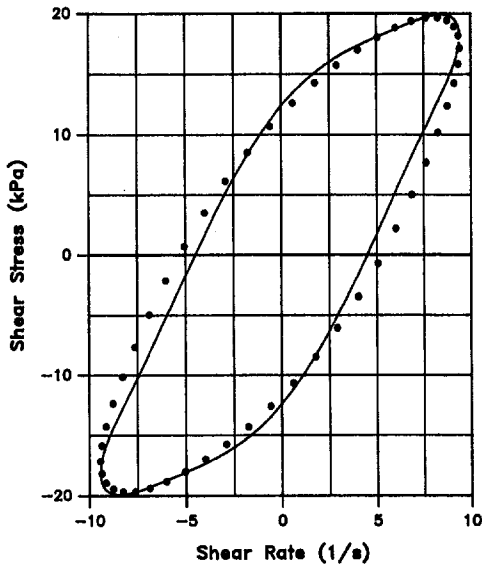


Fig. 8 Comparison of the experimentally obtained shear stress versus shear rate loop (circles) for IUPAC LDPE X at 170°C in LAOS, with the predictions of the simplified Liu model (solid loop) with $k_1 = 3.4$ and $k_2 = 1.3$. The strain amplitude is three and the frequency is π rad/s.

IUPAC LDPE X at 170 C

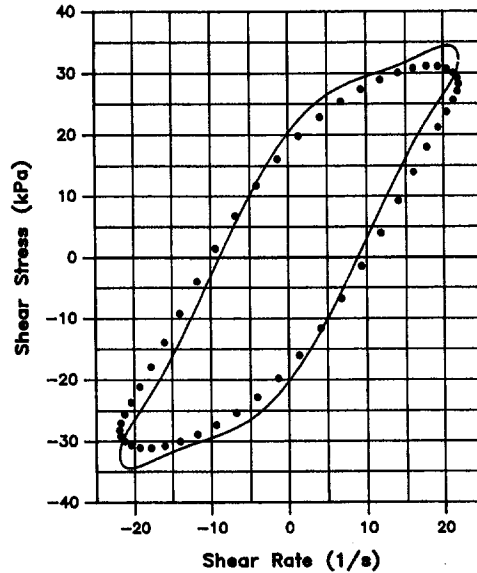


Fig. 10 Comparison of the experimentally obtained shear stress versus shear rate loop (circles) for IUPAC LDPE X at 170°C in LAOS, with the predictions of the simplified Liu model (solid loop) with $k_1 = 3.4$ and $k_2 = 1.3$. The strain amplitude is seven and the frequency is π rad/s.

6, again suggesting that the parameters k_1 and k_2 are independent of temperature.

Mewis and Denn (1983) have criticized (9) by arguing that the dependence of the structural parameters (x_i) on the rate of deformation tensor precludes a proper reduction to linear viscoelastic behavior in the high-frequency limit. They have also suggested the replacement of $\Pi(\mathbf{D})$ in the kinetic rate equation by $[(\text{tr}(\boldsymbol{\tau}'))/(2G_1)]$ as a remedy (Mewis-Denn model)

$$\frac{dx_i}{dt} = k_1 \frac{1 - x_i}{\lambda_i} - k_2 x_i \left[\frac{\text{tr}(\boldsymbol{\tau}')} {2G_1} \right]^{1/2} \quad (15)$$

In oscillatory shear over many decades of strain amplitudes and frequencies we therefore compare the predictions of (9) with those of (15) with identical model parameters. The predictions were obtained over six decades of strain amplitude and for the frequencies between 5 and 100000 Hz, and are plotted in Figs. 12–15.

Figures 12 and 13 are curves of σ_1 predicted by (15) and (9), respectively, with frequency increasing from the lowest curve to the topmost. In Fig. 12, the solutions for the four highest frequencies differ by less than a pen-width. No nonlinearity is seen in this figure. Figure 13 shows that above a strain

IUPAC LDPE X at 150 C

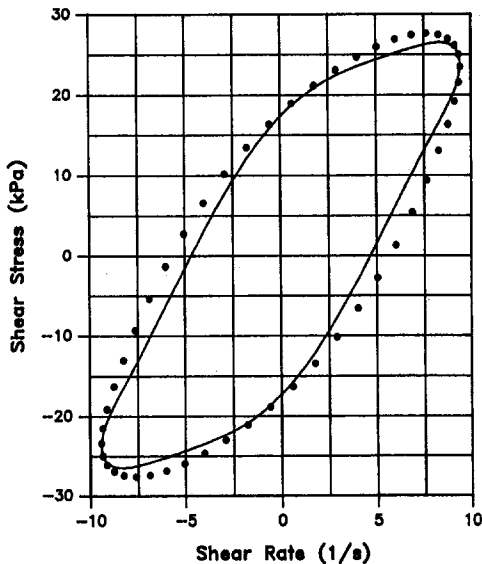


Fig. 9 Comparison of the experimentally obtained shear stress versus shear rate loop (circles) for IUPAC LDPE X at 150°C in LAOS, with the predictions of the simplified Liu model (solid loop) with $k_1 = 3.4$ and $k_2 = 1.3$. The strain amplitude is three and the frequency is π rad/s.

IUPAC LDPE X at 150 C

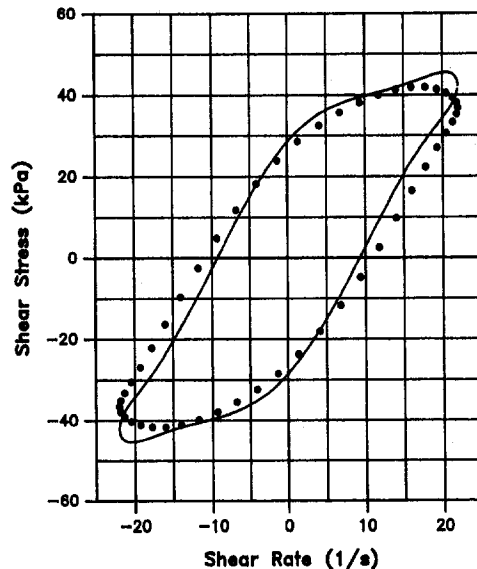


Fig. 11 Comparison of the experimentally obtained shear stress versus shear rate loop (circles) for IUPAC LDPE X at 150°C in LAOS, with the predictions of the simplified Liu model (solid loop) with $k_1 = 3.4$ and $k_2 = 1.3$. The strain amplitude is seven and the frequency is π rad/s.

IUPAC LDPE X at 150 C, In LAOS

$k_1 = 3.4 \quad k_2 = 1.3$

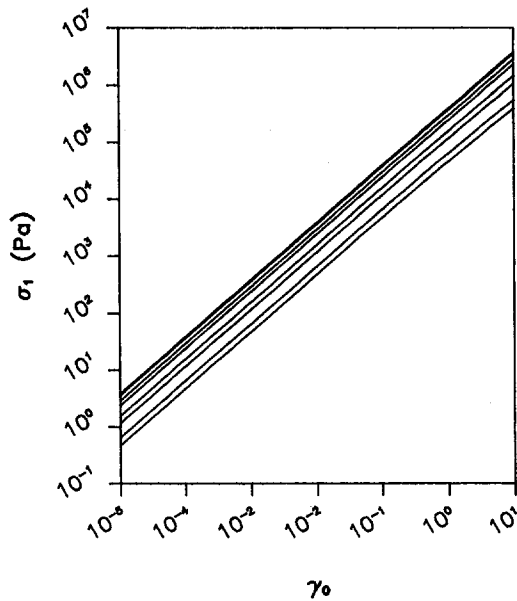


Fig. 12 Prediction of σ_1 by the Mewis-Denn model for IUPAC LDPE X at 150°C in oscillatory shear. From bottom to top, the curves are for frequencies 5, 10, 50, 100, 500, 1000, 5000, 10000, 50000, and 100000 Hz. The curves for the four highest frequencies differ by less than a pen-width.

amplitude of about 0.01, σ_1 becomes dependent on γ_0 indicating nonlinearity.

Figures 14 and 15 are predictions of δ_1 by (15) and (9), respectively, with frequency increasing from the uppermost curve to the lowest. Nonlinear behavior is indicated by a dependence of δ_1 on γ_0 . Figure 14 shows that the predictions for the

IUPAC LDPE X at 150 C, In LAOS

$k_1 = 3.4 \quad k_2 = 1.3$

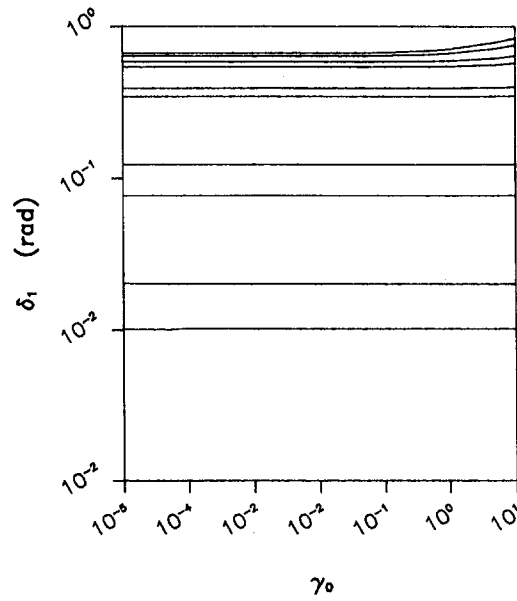


Fig. 14 Prediction of δ_1 by the Mewis-Denn model for IUPAC LDPE X at 150°C in oscillatory shear. The frequencies are the same as in Fig. 12.

six higher frequencies are linear, even up to a strain amplitude of ten. Figure 15 shows that (9) predicts increasing nonlinearity with increasing frequency, which is physically more realistic, despite the nonmonotonicity in the curves for the higher frequencies. It therefore appears that the Liu kinetic model provides an adequate description of polymer melts in both LAOS, and also reasonably describes the reduction to linear viscoelastic behavior.

IUPAC LDPE X at 150 C, In LAOS

$k_1 = 3.4 \quad k_2 = 1.3$

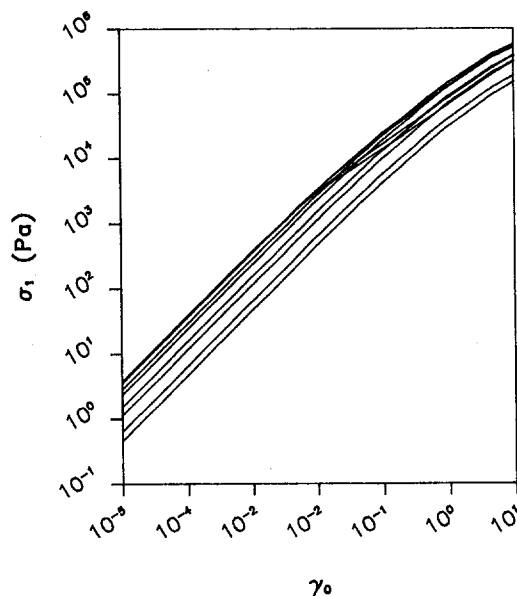


Fig. 13 Prediction of σ_1 by the simplified Liu model for IUPAC LDPE X at 150°C in oscillatory shear. The frequencies are the same as in Fig. 12.

IUPAC LDPE X at 150 C, In LAOS

$k_1 = 3.4 \quad k_2 = 1.3$

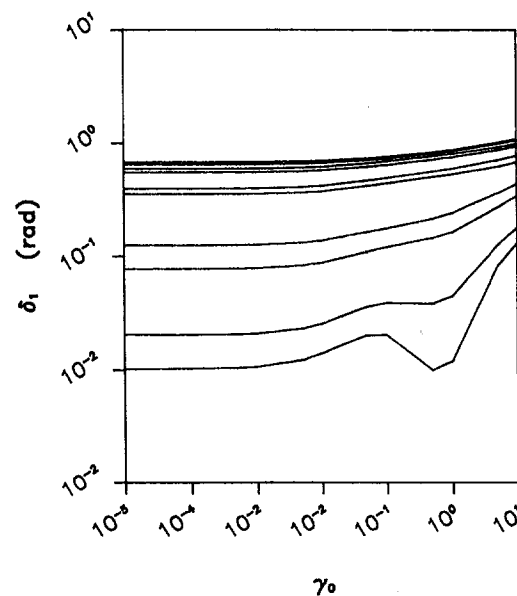


Fig. 15 Prediction of δ_1 by the simplified Liu model for IUPAC LDPE X at 150°C in oscillatory shear. The frequencies are the same as in Fig. 12.

of IUPAC LDPE X In Large Amplitude Oscillatory Shear

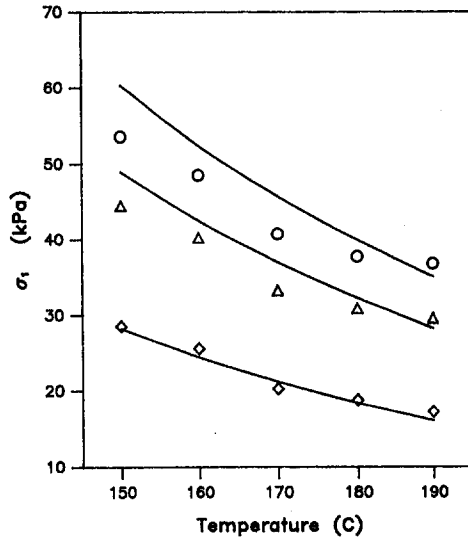


Fig. 16 Comparison of the prediction of the simplified Liu model for the dependence of σ_1 on temperature, for IUPAC LDPE X in LAOS. The markers represent the same data in in Fig. 1.

For the data at the lower frequency in Figs. 1–4, Figs. 16–19 compare the predictions of transient network theory with the simplified Liu kinetic rate Eq. (9). We judge these fits to be reasonably accurate. The significant discrepancy in the prediction for the lowest strain amplitude data in Fig. 19 is due to very weak nonlinearity. The utility of the Liu model to describe polymer melt LAOS for other materials and a wider range of conditions is also demonstrated in Giacomini and Jeyaseelan (1993b).

A popular class of integral constitutive models which recovers (2) in step shear has been studied extensively. Called separa-

of IUPAC LDPE X In Large Amplitude Oscillatory Shear

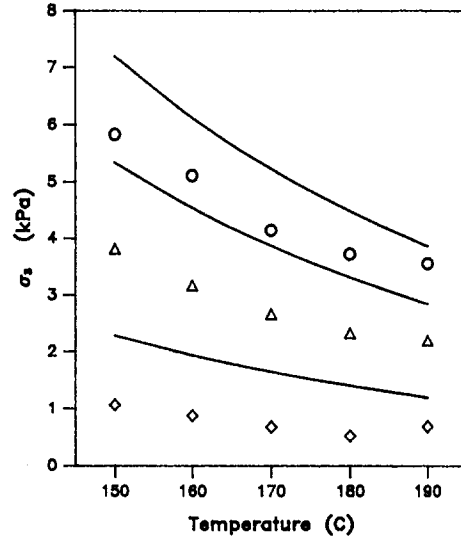


Fig. 18 Comparison of the prediction of the simplified Liu model for the dependence of σ_3 on temperature, for IUPAC LDPE X in LAOS. The markers represent the same data in in Fig. 3.

ble BKZ models (Wagner, 1976), Giacomini and coworkers have shown that they are inaccurate in LAOS except at low frequencies (Giacomini et al., 1993). This is why the results of the present work cannot be interpreted in terms of the nonlinear damping function.

Conclusion

Transient network theory can adequately describe the large amplitude oscillatory shear behavior of molten LDPE, over a range of temperatures. The kinetic rate constants in the simpli-

of IUPAC LDPE X In Large Amplitude Oscillatory Shear

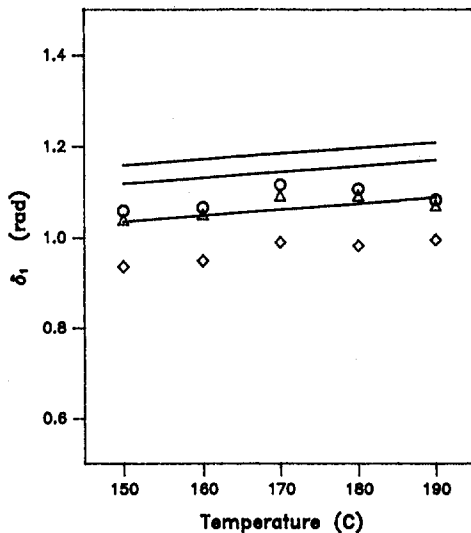


Fig. 17 Comparison of the prediction of the simplified Liu model for the dependence of δ_1 on temperature, for IUPAC LDPE X in LAOS. The markers represent the same data in in Fig. 2.

of IUPAC LDPE X In Large Amplitude Oscillatory Shear

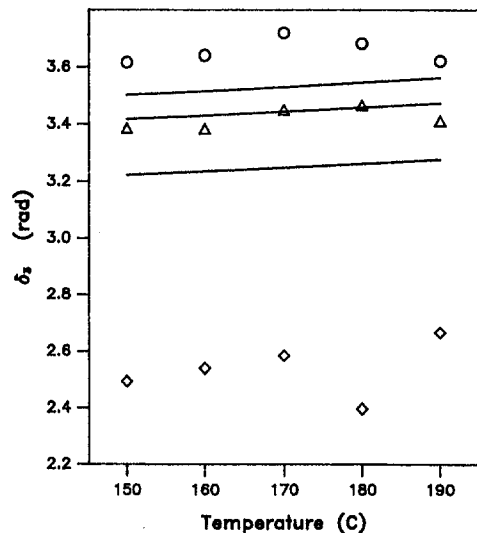


Fig. 19 Comparison of the prediction of the simplified Liu model for the dependence of δ_3 on temperature, for IUPAC LDPE X in LAOS. The markers represent the same data in in Fig. 4.

fied Liu model are invariant with temperature over the temperature range 150–190°C. This does not mean that departures from linear viscoelasticity do not depend on temperature. It does mean that the temperature dependence of these departures is properly accounted for by λ_{0i} in the thermal motion term of the kinetic rate equation. In this way, the temperature dependence of departures from linear viscoelasticity is fully accounted for in the equilibrium entanglement kinetics.

Acknowledgment

We are grateful for the small amplitude oscillatory shear measurements which were made by Dr. Rajen Patel of the Dow Chemical Company. The authors acknowledge the financial support of the Advanced Research Program of the State of Texas. The support of the Computing and Information Services of Texas A&M University was invaluable.

References

Acierno, D., La Mantia, F. P., Marrucci, G., and Titomanlio, G., 1976, "A Non-linear Viscoelastic Model with Structure-Dependent Relaxation Times I. Basic Formulation," *Journal of Non-Newtonian Fluid Mechanics*, Vol. 1, pp. 125–146.

Dealy, J. M., and Wissbrun, K. F., 1990, *Melt Rheology and its Role in Plastics Processing: Theory and Applications*, Van Nostrand Reinhold, New York.

Giacomin, A. J., and Jeyaseelan, R. S., 1995a, "A Constitutive Theory for Polyolefins in Large Amplitude Oscillatory Shear," *Polymer Engineering and Science*, Vol. 35, pp. 768–777.

Giacomin, A. J., and Jeyaseelan, R. S., 1995b, "Polymer Melt Anisotropy in Biaxial Shear," *Journal of Rheology*, Vol. 39, pp. 267–283.

Giacomin, A. J., Samurkas, T., and Dealy, J. M., 1989, "A Novel Sliding Plate Rheometer for Molten Plastics," *Polymer Engineering and Science*, Vol. 29, pp. 499–504.

Giacomin, A. J., Jeyaseelan, R. S., Samurkas, T., and Dealy, J. M., 1993, "Validity of Separable BKZ Model for Large Amplitude Oscillatory Shear," *Journal of Rheology*, Vol. 37, pp. 811–826.

Gupta, R. K., and Metzner, A. B., 1982, "Modelling of Nonisothermal Polymer Processes," *Journal of Rheology*, Vol. 26, pp. 181–198.

Hürlimann, H. P., 1991, "A Multidirectional Shear Rheometer for Polymer Melts," *Rheologica Acta*, Vol. 30, pp. 480–490.

Jeyaseelan, R. S., Giacomin, A. J., and Oakley, J. G., 1993, "Simplification of Network Theory for Polymer Melts in Nonlinear Oscillatory Shear," *AICHE Journal*, Vol. 39, pp. 846–854.

Larson, R. G., 1988, *Constitutive Equations for Polymer Melts and Solutions*, Butterworths, Boston.

Liu, T. Y., Soong, D. S., and Williams, M. C., 1984, "Transient and Steady Rheology of Polydisperse Entangled Melts. Predictions of a Kinetic Network Model and Data Comparisons," *Journal of Polymer Science*, Vol. 22, pp. 1561–1587.

Luo, X-L., and Tanner, R. I., 1985, "A Computer Study of Film Blowing," *Polymer Engineering and Science*, Vol. 25, pp. 620–629.

Matsumoto, T., Segawa, Y., Warashina, Y., and Onogi, S., 1973, "Nonlinear Behavior of Viscoelastic Materials II: The Method of Analysis and Temperature Dependence of Nonlinear Viscoelastic Functions," *Transactions of The Society of Rheology*, Vol. 17, pp. 47–62.

Meißner, J., 1984, "Polymer Melt Rheology—A Challenge for the Polymer Scientist and Engineer," *Pure and Applied Chemistry*, Vol. 56, pp. 369–384.

Mewis, J., and Denn, M. M., 1983, "Constitutive Equations based on the Transient Network Concept," *Journal of Non-Newtonian Fluid Mechanics*, Vol. 12, pp. 69–83.

Nikoleris, T., and Darby, R., 1989, "Numerical Simulation of the Non-Isothermal Flow of a Nonlinear Viscoelastic Fluid in a Rectangular Channel," *Journal of Non-Newtonian Fluid Mechanics*, Vol. 31, pp. 193–207.

Orbey, N., and Dealy, J. M., 1991, "Determination of the Relaxation Spectrum from Oscillatory Shear Data," *Journal of Rheology*, Vol. 35, pp. 1035–1049.

Tanner, R. I., 1985, *Engineering Rheology*, Oxford University Press, New York.

Tee, T. T., and Dealy, J. M., 1975, "Nonlinear Viscoelasticity of Polymer Melts," *Transactions of The Society of Rheology*, Vol. 19, pp. 595–615.

Verner, J. H., 1977, "Explicit Runge-Kutta Methods with Estimates of the Local Truncation Error," *SIAM Journal on Numerical Analysis*, Vol. 15, pp. 772–790.

Wagner, M. H., 1976, "Analysis of Time-Dependent Non-Linear Stress-Growth Data for Shear and Elongational Flow of a Low-Density Branched Polyethylene Melt," *Rheologica Acta*, Vol. 15, pp. 136.

P. Yu

P. S. Wong

P. W. International, Inc.
2655 Kingsway,
Vancouver, BC V5H 5H4
Canada

F. Kaempffer

Engineering and Technical
Services Department,
B. C. Hydro,
6911 Southpoint Drive,
Burnaby, BC V3N 4X8
Canada

Tension of Conductor Under Concentrated Loads

A common difficulty in the analysis and design of transmission and distribution lines is to determine a conductor's tension and its static profile under concentrated loads. For relatively small concentrated loads (such as detuning pendulums on transmission lines), approximation methods may give good predictions. For large concentrated loads (such as fallen trees on distribution lines), however, exact solutions must be found. This paper presents methodologies to compute conductor tension and static profile in three-dimensional space using both approximate and exact solution procedures under concentrated loads with different boundary conditions. Practical engineering examples from galloping control of transmission lines and mechanical coordination of distribution lines are given to demonstrate the applicability of the theory.

1 Introduction

A necessary step in designing an electrical transmission line or distribution line is to compute the line component loads and the static profile. One important component load is the conductor tension because most of the other component loads and the static profile are related to it. These computations depend heavily upon environmental conditions which produce external forces on the line such as wind load and ice load. External loads are usually approximated as a distributed force on a line component (such as the conductor) so that closed-form solutions for tension and static profile can be obtained to greatly simplify the computation. However, in certain situations, the line has concentrated loads. One example is the detuning pendulum, an anti-galloping control device (Havard et al., 1985), which is attached to a transmission line or distribution line. The new conductor tension and the new static profile due to the detuning pendulums need to be calculated for new line design and line maintenance, because field measurements are impractical and may cause service interruptions. Another example of a concentrated load is a tree falling onto an overhead distribution line during a storm. In situations where the tree load exceeds the structural strength of the line, the calculation method developed for small concentrated loads (such as detuning pendulums) is not applicable. A large tree plus wind load can be up to 30 times heavier than the weight of a conductor span, whereas the total weight of a span's detuning pendulums is only up to 20 percent of that of a conductor span. Thus, an approach to calculate the conductor tension and static profile for large concentrated loads is desirable to aid in determining which components of a power line are most likely to fail. Ideally the structures should be designed with a component failure hierarchy (or "mechanical coordination") such that the most likely components to fail are also the easiest to repair.

Both an approximation formula and an exact solution procedure were considered by Irvine (1981) for a conductor structure in a two dimensional (longitudinal and vertical) space. For the approximation formula, a closed form of the tension increase is found from a third-degree polynomial of one variable (tension

increase), which makes it easy to use in practice. However, this formula is only valid for a single vertical concentrated load with the assumptions that the static profile of the conductor without the concentrated load is parabolic and both ends of the cable are fixed. For the exact solution procedure, on the other hand, Irvine gave the solution formulae for multiple vertical concentrated masses with fixed boundary conditions, but they require information on the unstrained cable length which is usually unavailable in practice.

In this paper, both approximation and exact solution formulae are generalized for a three-dimensional (longitudinal, vertical, and transversal) space, which is closer to the reality where the transversal (horizontal) displacement (due to wind load, for example) cannot be neglected. The approximation formulas are generalized to compute the conductor tension and static profile for multiple inclined concentrated loads with different boundary conditions. For the exact solution, using an approach developed recently to calculate the unstrained length of a conductor (Wong and Yu, 1993), a comprehensive procedure is developed to compute exact solutions for conductor tension and static profile in three-dimensional space with various boundary conditions. However, when very large concentrated loads are encountered, an approximation to the exact solution by neglecting the concentrated loads may be acceptable, and the formulae become simpler. This approximation solution is also presented in this paper. Two practical examples, one from galloping control of transmission lines and the other from mechanical coordination of distribution lines, are presented to illustrate the applicability of the theory.

2 Formulation

A span of a typical conductor line is shown in Fig. 1 where x , y , and z indicate the coordinates along longitudinal, vertical, and horizontal directions, respectively. s' is the Lagrangian coordinate under both distributed and concentrated loads and indicates a reference distance from the left end of the span. The concentrated loads are denoted by F_i , $i = 1, 2, \dots, n$, each of which deviates from the vertical coordinate by an angle θ_i .

2.1 Approximate Solution for Small Concentrated Loads. In order to compute the tension change due to concentrated loads, the first step is to find the solution of the static profile of the conductor without concentrated load.

Static Profile Without Concentrated Loads. The static profile without concentrated loads may be described by the following differential equations:

Contributed by the Applied Mechanics Division of THE AMERICAN SOCIETY OF MECHANICAL ENGINEERS for publication in the ASME JOURNAL OF APPLIED MECHANICS.

Discussion on this paper should be addressed to the Technical Editor, Prof. Lewis T. Wheeler, Department of Mechanical Engineering, University of Houston, Houston, TX 77204-4792, and will be accepted until four months after final publication of the paper itself in the ASME JOURNAL OF APPLIED MECHANICS.

Manuscript received by the ASME Applied Mechanics Division, Dec. 20, 1993; final revision, May 18, 1994. Associate Technical Editor: J. N. Reddy.

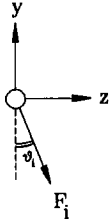
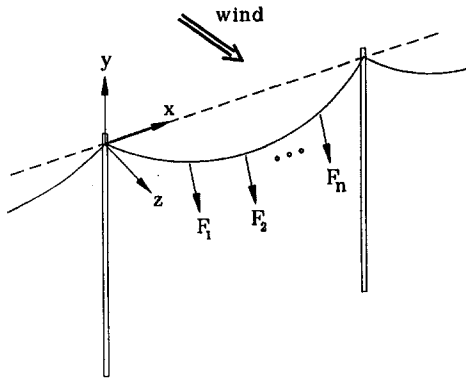


Fig. 1 Static profile of a conductor span

$$\frac{d}{ds} \left(T \frac{dx}{ds} \right) = 0 \quad (1)$$

$$\frac{d}{ds} \left(T \frac{dy_1}{ds} \right) = -Q_y \quad (2)$$

$$\frac{d}{ds} \left(T \frac{dz_1}{ds} \right) = -Q_z \quad (3)$$

where s is the Lagrangian coordinate along the conductor without concentrated loads (but under the distributed load). T is a function of s , representing the tension of the conductor. Q_y and Q_z are the vertical and horizontal loads, respectively, per unit length which are assumed spatially uniform along the span. Q_y includes the conductor weight, wind load and ice load, etc., while Q_z usually consists of wind load only. The boundary conditions are given by

$$\begin{aligned} y_1(0) &= y_{10}, & y_1(L_x) &= y_{1L_x} \\ z_1(0) &= z_{10}, & z_1(L_x) &= z_{1L_x} \end{aligned} \quad (4)$$

where L_x is the span length. These boundary values may be found from the static loads by using a stress analysis. The solutions of (1) to (3) are given by

$$T = H(ds/dx) \quad (5)$$

where H is a constant representing the horizontal component of conductor tension, and

$$\begin{aligned} y_1(x) &= y_{10} - B(Q_z/Q^2)x + 2HQ_y\sqrt{Q^2 + B^2}/Q^3 \\ &\quad \times \sinh [(Q/2H)x] \sinh [(Q/2H)(2D - x)] \\ z_1(x) &= (Q_z/Q_y)y_1(x) + (Bx + C)/Q_y \end{aligned} \quad (6)$$

Here,

$$\begin{aligned} Q &= \sqrt{Q_y^2 + Q_z^2} \\ B &= [Q_y(z_{1L_x} - z_{10}) - Q_z(y_{1L_x} - y_{10})] \\ C &= Q_y z_{10} - Q_z y_{10} \end{aligned}$$

$$\begin{aligned} D &= \frac{L_x}{2} + \left(\frac{H}{Q} \right) \\ &\quad \times \sinh^{-1} \left[\left(\frac{Q}{2H} \right) \frac{Q_y(y_{1L_x} - y_{10}) + Q_z(z_{1L_x} - z_{10})}{\sqrt{Q^2 + B^2} \sinh (QL_x/2H)} \right] \end{aligned} \quad (7)$$

The solution of s is found by integrating $ds/dx = [1 + (dy_1/dx)^2 + (dz_1/dx)^2]^{1/2}$ as

$$\begin{aligned} s(x) &= 2H\sqrt{Q^2 + B^2}/Q^2 \sinh [(Q/2H)x] \\ &\quad \times \cosh [(Q/2H)(2D - x)]. \end{aligned} \quad (8)$$

Therefore, given H , Q_y , Q_z and the boundary conditions, the static profile can be determined from (6)–(8). The span length, L , equals $s(L_x)$. Setting $Q_z = y_{10} = z_{10} = y_{1L_x} = z_{1L_x} = 0$ in (6)–(8) leads to the solutions given by Irvine (1981).

Tension Increase and New Static Profile. Next, suppose that the tension increase due to concentrated loads is expressed as τ , and that u , y_2 , and z_2 are additional displacements produced by the inclined concentrated loads along longitudinal, vertical, and horizontal directions, respectively. The new static profile can be described by

$$\frac{d}{ds} \left[(T + \tau) \left(\frac{dx}{ds} + \frac{du}{ds} \right) \right] = 0 \quad (9)$$

$$\begin{aligned} \frac{d}{ds} \left[(T + \tau) \left(\frac{dy_1}{ds} + \frac{dy_2}{ds} \right) \right] \\ = -Q_y + \sum_{i=1}^n F_i \cos \theta_i \delta(s - s_i) \end{aligned} \quad (10)$$

$$\begin{aligned} \frac{d}{ds} \left[(T + \tau) \left(\frac{dz_1}{ds} + \frac{dz_2}{ds} \right) \right] \\ = -Q_z - \sum_{i=1}^n F_i \sin \theta_i \delta(s - s_i) \end{aligned} \quad (11)$$

$$\tau = AE \left(\frac{ds'}{ds} - 1 \right) \quad (12)$$

where $\delta(s - s_i) = 1$ (or 0) if $s = s_i$ ($s \neq s_i$), AE (A is the cross-sectional area of the conductor and E is the Young's modulus) is the axial rigidity of the conductor without concentrated loads, and s' indicates the new Lagrangian coordinate under both distributed and concentrated loads.

It is not possible to obtain a general analytic solution from (9) to (12). However, if the additional conductor displacement along the longitudinal direction due to the small concentrated loads is assumed to be small compared to the original displacement due to the distributed loads Q_y and Q_z (i.e., $du/ds \approx 0$ compared with dx/ds), then (9) becomes $(T + \tau)(dx/ds) = H + h$ which, by using (5), results in

$$\tau = h(ds/dx) \quad (13)$$

where h is a constant. It should be noted here that the horizontal component, H , of the conductor tension under the distributed load only is not the same as that given in (5) because the boundary conditions are now different from the case without concentrated load. However, it can be shown that if the difference of the end movements along all the three directions (e.g., $u(L_x) - u(0)$) are sufficiently small, the change in H is negligible.

Now, with the aid of (2), (3), (5), and (13), (10) and (11) can be rewritten with boundary conditions as

$$\begin{aligned} \frac{d}{dx} \left[(H + h) \frac{dy_{2i}}{dx} + h \frac{dy_{1i}}{dx} \right] = 0 \\ (x_i < x < x_{i+1}, i = 0, 1, 2, \dots, n) \end{aligned}$$

$$y_{2i}(x_i) = y_{2i-1}(x_i) \quad \text{and} \quad \frac{dy_{2i}(x_i)}{dx} - \frac{dy_{2i-1}(x_i)}{dx} \\ = \frac{1}{H+h} F_i \cos \theta_i \quad (i = 0, 1, 2, \dots, n) \quad (14)$$

and

$$\frac{d}{dx} \left[(H+h) \frac{dz_{2i}}{dx} + h \frac{dz_1}{dx} \right] = 0 \\ (x_i < x < x_{i+1}, i = 0, 1, 2, \dots, n)$$

$$z_{2i}(x_i) = z_{2i-1}(x_i) \quad \text{and} \quad \frac{dz_{2i}(x_i)}{dx} - \frac{dz_{2i-1}(x_i)}{dx} \\ = -\frac{1}{H+h} F_i \sin \theta_i \quad (i = 0, 1, 2, \dots, n), \quad (15)$$

respectively, where, as in the case without concentrated loads, boundary conditions $y_{20}(0)$, $y_{2n}(L_x)$, $z_{20}(0)$, and $z_{2n}(L_x)$ are not necessarily zero. The solutions of (14) and (15) are given by

$$y_{2i}(x) = -[hy_1 - (c_i x + e_i)]/(H+h) \\ z_{2i}(x) = -[hz_1 - (d_i x + f_i)]/(H+h) \quad (16)$$

where

$$c_i = c_{i1} h + c_{i0}, \quad d_i = d_{i1} h + d_{i0}$$

$$c_{i1} = [y_{2n}(L_x) - y_{20}(0) + y_{1L_x} - y_{10}]/L_x$$

$$c_{i0} = \frac{1}{L_x} [y_{2n}(L_x) - y_{20}(0)] \\ + \sum_{k=1}^n \left(\frac{x_k}{L_x} - 1 \right) F_k \cos \theta_k + \sum_{k=0}^i F_k \cos \theta_k$$

$$d_{i1} = [z_{2n}(L_x) - z_{20}(0) + z_{1L_x} - z_{10}]/L_x$$

$$d_{i0} = \frac{1}{L_x} [z_{2n}(L_x) - z_{20}(0)] \\ - \sum_{k=1}^n \left(\frac{x_k}{L_x} - 1 \right) F_k \sin \theta_k - \sum_{k=0}^i F_k \sin \theta_k$$

$$e_i = Hy_{20}(0) + h[y_{20}(0) + y_{10}] - \sum_{k=0}^i x_k F_k \cos \theta_k$$

$$f_i = Hz_{20}(0) + h[z_{20}(0) + z_{10}] + \sum_{k=0}^i x_k F_k \sin \theta_k \quad (17)$$

for $i = 1, 2, \dots, n$. Here, $F_0 \equiv 0$, introduced for convenience. The new static profile can be found as $y(x) = y_1 + y_2 = [Hy_1 + (c_i x + e_i)]/(H+h)$ and $z(x) = z_1 + z_2 = [Hz_1 + (d_i x + f_i)]/(H+h)$ if the tension change, h , is known.

h can be derived from (12) as follows: First, (12) can be approximated as

$$\frac{\tau}{AE} \approx \frac{ds'^2 - ds^2}{2ds^2} = \frac{du}{ds} \frac{dx}{ds} + \frac{dy_1}{ds} \frac{dy_2}{ds} + \frac{dz_1}{ds} \frac{dz_2}{ds} \\ + \frac{1}{2} \left[\left(\frac{du}{ds} \right)^2 + \left(\frac{dy_2}{ds} \right)^2 + \left(\frac{dz_2}{ds} \right)^2 \right]. \quad (18)$$

Then, combining (13) and (18) and integrating the resulting equation from 0 to L_x yields a third-degree polynomial of h

$$(h/H)^3 + a(h/H)^2 + b(h/H) - c = 0 \quad (19)$$

in which

$$a = 2 + \frac{1}{24} \lambda^2 + \left(\frac{AE}{HL_e} \right) [u(0) - u(L_x)] \\ + \frac{1}{2} \left(\frac{AE}{H^3 L_e} \right) \sum_{i=1}^n (c_{i1}^2 + d_{i1}^2)(x_{i+1} - x_i) \\ b = 1 + \frac{1}{12} \lambda^2 + 2 \left(\frac{AE}{HL_e} \right) [u(0) - u(L_x)] \\ + \left(\frac{AE}{H^3 L_e} \right) \sum_{i=1}^n \{ (c_{i1} c_{i0} + d_{i1} d_{i0})(x_{i+1} - x_i) \\ + H c_{i1} [y_1(x_{i+1}) - y_1(x_i)] + H d_{i1} [z_1(x_{i+1}) - z_1(x_i)] \} \\ c = \left(\frac{AE}{H^3 L_e} \right) \left\{ \frac{1}{2} \sum_{i=0}^n (c_i^2 + d_i^2)(x_{i+1} - x_i) \right. \\ \left. + H \sum_{i=0}^n c_{i0} [y_1(x_{i+1}) - y_1(x_i)] + H \sum_{i=0}^n d_{i0} \right. \\ \left. \times [z_1(x_{i+1}) - z_1(x_i)] \right\} - \left(\frac{AE}{HL_e} \right) [u(0) - u(L_x)] \quad (20)$$

where $y_1(x_i)$ and $z_1(x_i)$ are given in (6), and

$$L_e = \int_0^{L_x} \left(\frac{ds}{dx} \right)^3 dx \\ = \frac{2H\sqrt{Q^2 + B^2}}{Q} \sinh \left(\frac{Q}{H} D \right) \left[1 + \frac{1}{3} \sinh^2 \left(\frac{Q}{H} D \right) \right] \\ \lambda^2 = 6 \left(\frac{AE}{HL_e} \right) \left\{ \left(1 + \frac{B^2}{Q^2} \right) \left(\frac{H}{2Q} \right) \left[\sinh \left(\frac{2Q}{H} (L_x - D) \right) \right. \right. \\ \left. \left. + \sinh \left(\frac{2Q}{H} D \right) \right] - \left(1 - \frac{B^2}{Q^2} \right) L_x \right\}. \quad (21)$$

Given H , L_x , Q_y , and Q_z , the tension increase h can be found in a closed form from the third-degree polynomial (19) if $u(0)$ and $u(L_x)$ are known. How to find $u(0)$ and $u(L_x)$ is discussed in Section 2.3. If the boundary conditions are zero along all the directions, then all the three coefficients a , b , and c are positive because $0 \leq \theta_i \leq 90$ deg, therefore, the polynomial (19) has only one positive root.

It is noted that the formulae given by Irvine (1981) for one vertical concentrated load without horizontal displacement can be deduced directly from (17), (19)-(21) by simply setting $n = 1$, $Q_z = \theta_1 = 0$, boundary conditions to zero, and approximating L_e , λ^2 and $y_1(x_i)$ up to second-order terms.

2.2 Exact Solution for Large Concentrated Loads. Suppose that the Lagrange's coordinate of the unstretched conductor is denoted by s whereas the stretched conductor is given by s' , as shown in Fig. 2. It should be noted here that the definition of s is different from that given in Section 2.1. Then, the static profile of the stretched conductor may be described by

$$\frac{d}{ds} \left(T' \frac{dx}{ds'} \right) = 0$$

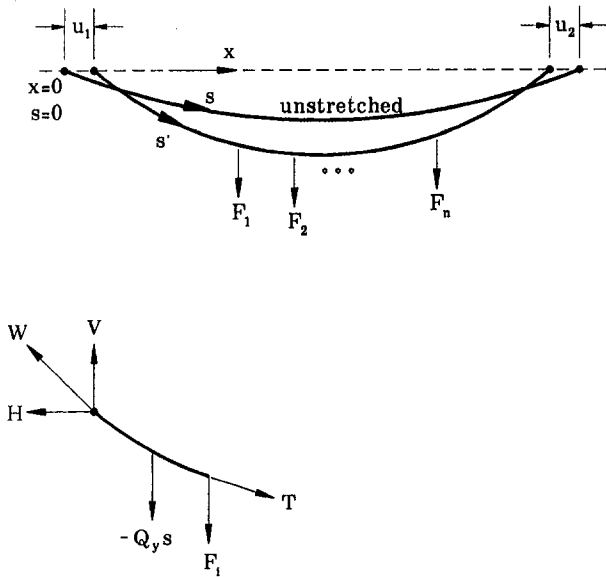


Fig. 2 Conductor under concentrated loads

$$\frac{d}{ds} \left(T' \frac{dy}{ds'} \right) = -Q_y + \sum_{i=1}^n F_i \cos \theta_i \delta(s - s_i)$$

$$\frac{d}{ds} \left(T' \frac{dz}{ds'} \right) = -Q_z - \sum_{i=1}^n F_i \sin \theta_i \delta(s - s_i) \quad (22)$$

and

$$T' = A_0 E \left(\frac{ds'}{ds} - 1 \right) \quad (23)$$

where T' is the tension of the stretched conductor under both distributed and concentrated loads and $A_0 E$ is the axial rigidity of unstrained profile (A_0 can be approximated by A and therefore A will be used in the following sections). To find the exact tension of a conductor under concentrated loads, the original unstretched conductor length of one span has to be found first.

Unstretched Conductor Length. Given H , Q_y , and Q_z , the unstretched conductor length, L_0 , can be found by solving (22) and (23) without the terms of the concentrated loads. First, one can find from (22) the following solutions $T(dx/ds') = H$, $T(dy/ds') = -Q_y(s - L_0/2)$, $T(dz/ds') = -Q_z(s - L_0/2)$ and $T = [H^2 + Q^2(s - L_0/2)^2]^{1/2}$ and then, combine these solutions, with the aid of (23), to yield

$$\frac{dx}{ds} = \frac{dx}{ds'} \frac{ds'}{ds} = \left(\frac{H}{T} \right) \left(\frac{T}{AE} + 1 \right)$$

$$= \frac{H}{AE} + \left[1 + \left(\frac{Q}{H} \right)^2 \left(s - \frac{1}{2} L_0 \right)^2 \right]^{-1/2} \quad (24)$$

which, in turn, results in

$$x(s) = (H/AE)s + (H/Q) \{ \sinh^{-1} (QL_0/2H) + \sinh^{-1} [(Q/H)(s - L_0/2)] \} \quad (25)$$

where the boundary condition $x(0)$ has been used. Next, use the boundary condition $x(L_x) = L_x$ to find

$$L_0 = (2H/Q) \sinh [(Q/2H)(L_x - HL_0/AE)] \quad (26)$$

from which L_0 can be solved simply by numerical iteration. Moreover, if the sag of the conductor line is also known, then L_0 can be found without knowing the distributed load Q by using equation

$$\text{Sag} = (H/Q) [\cosh (QL_x/2H) - 1], \quad (27)$$

and solving this equation together with (26) by eliminating Q .

New Tension and Static Profile. Integrating (22) results in

$$T'_i \frac{dx_i}{ds'} = H'$$

$$T'_i \frac{dy_i}{ds'} = -V - Q_y s + \sum_{k=0}^i F_k \cos \theta_k$$

$$T'_i \frac{dz_i}{ds'} = W - Q_z s - \sum_{k=0}^i F_k \sin \theta_k \quad (28)$$

for $s_i < s < s_{i+1}$, $i = 0, 1, 2, \dots, n$, with boundary conditions

$$x_0(0) = u(0), \quad x_n(L_x) = L_x + u(L_x), \quad x_i(s_i) = x_{i-1}(s_i)$$

$$y_i(s_i) = y_{i-1}(s_i) \quad \text{and} \quad z_i(s_i) = z_{i-1}(s_i) \quad (29)$$

where $i = 1, 2, \dots, n$. Boundary conditions $y_0(0)$, $y_n(L_x)$, $z_0(0)$, and $z_n(L_x)$ are not necessarily zero. H' is the unknown horizontal tension component of the stretched conductor; V and W represent the vertical and horizontal reactions, respectively, at the left support end; $u(0)$ and $u(L_x)$ are additional end displacements of the stretched conductor along the longitudinal direction under the distributed and concentrated loads (see Fig. 2). The following equation can be directly obtained from (28) with the aid of $(dx_i/ds')^2 + (dy_i/ds')^2 + (dz_i/ds')^2 = 1$:

$$T'_i = Q \sqrt{(s + a_i)^2 + b_i^2} \quad (30)$$

where

$$a_i = [Q_y(V - E_i) - Q_z(W - G_i)]/Q^2$$

$$b_i = \{ Q^2 H'^2 + [Q_y(V - E_i) + Q_z(W - G_i)]^2 \}^{1/2} / Q^2$$

$$E_i = \sum_{k=0}^i F_k \cos \theta_k \quad \text{and} \quad G_i = \sum_{k=0}^i F_k \sin \theta_k \quad (31)$$

for $i = 0, 1, 2, \dots, n$. Employing (23), (28), (29) and the relation

$$\frac{dx_i}{ds} = \frac{dx_i}{ds'} \frac{ds'}{ds} = \frac{H'}{AE} + \left(\frac{H'}{Q} \right) [(s + a_i)^2 + b_i^2]^{-1/2} \quad (32)$$

one can find

$$x_i(s) = (H'/AE)s + (H'/Q) \sinh^{-1} [(s + a_i)/b_i] + \bar{x}_i$$

$$(s_i < s < s_{i+1}, i = 0, 1, \dots, n) \quad (33)$$

where

$$\bar{x}_0 = u(0) - (H'/Q) \sinh^{-1} (a_0/b_0)$$

$$\bar{x}_i = \bar{x}_{i-1} + (H'/Q) \{ \sinh^{-1} [(s_i + a_{i-1})/b_{i-1}] - \sinh^{-1} [(s_i + a_i)/b_i] \}, \quad (i = 1, 2, \dots, n) \quad (34)$$

in which the boundary condition $x_0(0) = u(0)$ has been used. Similarly, $y_i(s)$ is given by

$$y_i(s) = -[Q_y s/2 + (V - E_i)]s/AE$$

$$- \{ (V - E_i - Q_y a_i) \sinh^{-1} [(s + a_i)/b_i] + Q_y \sqrt{(s + a_i)^2 + b_i^2} \} / Q + \bar{y}_i$$

$$(s_i < s < s_{i+1}, i = 0, 1, \dots, n)$$

$$\bar{y}_0 = [(V - E_0 - Q_y a_0) \sinh^{-1} (a_0/b_0) + Q_y \sqrt{a_0^2 + b_0^2}] / Q + y_0(0)$$

$$\begin{aligned} \bar{y}_i &= \bar{y}_{i-1} - (E_i - E_{i-1})s_i/AE \\ &+ \{(V - E_i - Q_y a_i) \sinh^{-1} [(s_i + a_i)/b_i] \\ &- (V - E_{i-1} - Q_y a_{i-1}) \sinh^{-1} [(s_i + a_{i-1})/b_{i-1}]\}/Q \\ &+ [\sqrt{(s_i + a_i)^2 + b_i^2} - \sqrt{(s_i + a_{i-1})^2 + b_{i-1}^2}]Q_y/Q \\ &(i = 1, 2, \dots, n). \quad (35) \end{aligned}$$

$z_i(s)$ and \bar{z}_i can be obtained from (35) by substituting Q_y , V , E_i , and $y_0(0)$ with Q_z , $-W$, $-G_i$ and $z_0(0)$, respectively. The expressions $x_i(s)$, $y_i(s)$, and $z_i(s)$ describe the static profile under both distributed and concentrated loads if H' , V and W are known.

Next, applying the boundary conditions $x_n(L_0) = L_x + u(L_x)$, $y_n(L_0)$ and $z_n(L_0)$ to the static solutions produces the following equations:

$$\begin{aligned} 0 &= \left[u(0) - u(L_x) - L_x + \left(\frac{H'}{AE} \right) L_0 \right] \left(\frac{Q}{H'} \right) \\ &+ \sum_{i=1}^{n+1} \sinh^{-1} \left(\frac{s_i + a_{i-1}}{b_{i-1}} \right) - \sum_{i=0}^n \sinh^{-1} \left(\frac{s_i + a_i}{b_i} \right) \quad (36) \end{aligned}$$

$$\begin{aligned} 0 &= \frac{1}{AE} [(Q_z V + Q_y W) L_0 \\ &- \sum_{i=1}^n (L_0 - s_i) F_i (Q_z \cos \theta_i + Q_y \sin \theta_i)] \\ &+ \frac{1}{Q} \left\{ \sum_{i=1}^{n+1} [Q_z (V - E_{i-1}) + Q_y (W - G_{i-1})] \right. \\ &\times \sinh^{-1} \left(\frac{s_i + a_{i-1}}{b_{i-1}} \right) - \sum_{i=0}^n [Q_z (V - E_i) \\ &+ Q_y (W - G_i)] \sinh^{-1} \left(\frac{s_i + a_i}{b_i} \right) \left. \right\} \\ &+ Q_z [y_n(L_0) - y_0(0)] - Q_y [z_n(L_0) - z_0(0)] \quad (37) \end{aligned}$$

and

$$\begin{aligned} 0 &= \frac{1}{AE} \left[\left(\frac{1}{2} Q^2 L_0 + Q_y V - Q_z W \right) L_0 \right. \\ &- \sum_{i=1}^n (L_0 - s_i) F_i (Q_y \cos \theta_i - Q_z \sin \theta_i) \left. \right] \\ &+ Q \left[\sum_{i=1}^{n+1} \sqrt{(s_i + a_{i-1})^2 + b_{i-1}^2} - \sum_{i=0}^n \sqrt{(s_i + a_i)^2 + b_i^2} \right] \\ &+ Q_y [y_n(L_0) - y_0(0)] + Q_z [z_n(L_0) - z_0(0)] \quad (38) \end{aligned}$$

where the identity $Q_y(V - E_i) - Q_z(W - G_i) - Q^2 a_i \equiv 0$ ($i = 0, 1, 2, \dots, n$) has been used. Now, the unknown variables H' , V , and W can be solved numerically (e.g., by using Newton-Raphson method) from (36)–(38) if $u(0)$ and $u(L_x)$ are known.

2.3 Approximate Solution for Very Large Concentrated Loads. When the concentrated loads are very large compared to the distributed loads (e.g., their ratio is over 200 percent), then an approximation solution may be found from the results presented in the previous section by neglecting the distributed loads (i.e., letting $Q_y = Q_z = 0$). Thus, the procedure becomes simpler and the formulae of (36)–(38) are reduced to

$$0 = [u(0) - u(L_x) - L_x] + \sum_{i=0}^n (s_{i+1} - s_i) \Psi_i$$

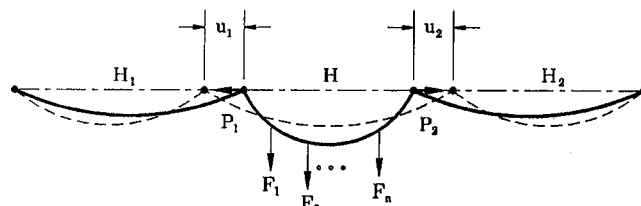


Fig. 3(a)

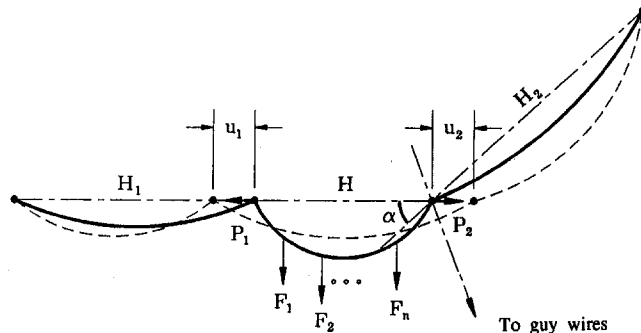


Fig. 3(b)

Fig. 3 Boundary conditions; (a) tangent line, (b) angle line

$$\begin{aligned} 0 &= [y_n(L_0) - y_0(0)] + \sum_{i=0}^n (V - E_i)(s_{i+1} - s_i) \Psi_i \\ 0 &= [z_n(L_0) - z_0(0)] - \sum_{i=0}^n (W - G_i)(s_{i+1} - s_i) \Psi_i, \quad (39) \end{aligned}$$

where $\Psi_i = 1/AE + [H'^2 + (V - E_i)^2 + (W - G_i)^2]^{-1/2}$. Although (39) is much simpler than (36)–(38), a numerical iteration scheme is still needed to solve the nonlinear coupled equations. Having found V , W , and H' , then

$$\begin{aligned} T'_i(s) &= \sqrt{H'^2 + (V - E_i)^2 + (W - G_i)^2} \\ y_i(s) &= \Psi_i (-V + E_i) s + \bar{y}_i \\ \bar{y}_i &= \bar{y}_{i-1} - (E_i - E_{i-1}) \Psi_i + V/T'_i - V/T'_{i-1} \\ &(i = 1, 2, \dots, n) \text{ and } \bar{y}_0 = y_0(0) \\ z_i(s) &= \Psi_i (W - G_i) s + \bar{z}_i \\ \bar{z}_i &= \bar{z}_{i-1} + (G_i - G_{i-1}) \Psi_i - W/T'_i + W/T'_{i-1} \\ &(i = 1, 2, \dots, n) \text{ and } \bar{z}_0 = z_0(0) \quad (40) \end{aligned}$$

for $s_i < s < s_{i+1}$, $i = 0, 1, \dots, n$. It is noted that the tension, T'_i , is now approximated by piecewise constants whereas $y_i(s)$ and $z_i(s)$ are approximated by piecewise linear functions of s .

2.4 Boundary Conditions. To solve for h in Section 2.1 or H' in Section 2.2 (or Section 2.3), either the displacements $u(0)$ and $u(L_x)$, or their relations to other variables are needed. As shown in Fig. 3, the adjacent spans' horizontal components of tension and displacements are denoted by H'_i and u_i , $i = 1, 2$, respectively. Thus, $u_1 = u(0)$ and $u_2 = -u(L_x)$. Furthermore, the relationship between the force P_i and displacement u_i can be found as follows. For a transmission line having supporting towers, the end support components are usually suspension insulator springs and the Hooke's law can be employed to establish a linear approximation

$$P_i = \beta u_i \quad i = 1, 2 \quad (41)$$

where β is the spring constant. For a distribution line, the force

P_i is directly produced by the bending of the supporting poles due to the unbalanced tensions of the adjacent conductor spans. The relation between the force and deflection (bending displacement) can be described as $P_i = -ku_i$ if the pole is treated as elastic material. Here k is called the modulus and the minus sign indicates that the force acts at the opposite direction of the deflection (Salvadori and Schwarz, 1954). Constant k is usually obtained from bending strength tests and can be found from many industrial product manuals (e.g., CSA, 1990). Therefore, Eq. (41) can be used as a general formula. Note that the special case $u_i = 0$, $i = 1, 2$ (i.e., $u(0) = u(L_x) = 0$) implies that the equations given in Section 2.1 (Section 2.2 or Section 2.3) are sufficient for solving $h(H', V, \text{ and } W)$. There are two general cases: tangent line (including dead end) and angle line.

Case 1: Tangent Line. Suppose that the adjacent spans' length are given by $L_x^{(1)}$ and $L_x^{(2)}$, respectively, and the unstrained conductor lengths are obtained from Eq. (26) as $L_0^{(1)}$ and $L_0^{(2)}$, respectively. Then equation (25) yields

$$L_x^{(i)} + u_i = (H'_i/AE)L_0^{(i)} + (2H'_i/Q) \sinh^{-1}(QL_0^{(i)}/2H'_i), \quad i = 1, 2. \quad (42)$$

From Fig. 3(a) it is seen that

$$H' = H'_i + P_i, \quad i = 1, 2. \quad (43)$$

Combining (41)-(43) gives

$$L_x^{(i)} + u_i = (H' - \beta u_i) \times \{L_0^{(i)}/AE + (2/Q) \sinh^{-1}[QL_0^{(i)}/2(H' - \beta u_i)]\}, \quad i = 1, 2. \quad (44)$$

For the exact solution procedure given in Section 2.2 (or approximation in Section 2.3), the above two equations (or one equation if one of u_i equals 0) can now be directly added to (36)-(38) (or (39)), and H', V, W , and u_i can be solved simultaneously by numerical iteration. For the approximate solution procedure given in Section 2.1, note that $H' = H + h$ and that an approximate solution of u_i from (44) is required. This approximation is given by

$$u_i = [L_0^{(i)}h + (AE + H)L_0^{(i)} - AEL_x^{(i)}]/[AE + \beta L_0^{(i)}] \quad (45)$$

and hence

$$u(0) - u(L_x) = u_1 + u_2 = (dh + Hf)L_e/AE$$

$$d = \sum_{i=1}^2 \frac{L_0^{(i)}/L_e}{1 + \beta L_0^{(i)}/AE}$$

$$f = \sum_{i=1}^2 \frac{(AE/H)(L_0^{(i)} - L_x^{(i)})/L_e + L_0^{(i)}/L_e}{1 + \beta L_0^{(i)}/AE} \quad (46)$$

Then, the coefficients, a, b , and c , of the third-degree polynomial of h can be obtained from (20) if λ^2 and the coefficient of the first term of c are divided by $(1 + d)$, and the term, $(AE/HL_e)[u(0) - u(L_x)]$, is replaced by $f/(1 + d)$.

Case 2: Angle Line. It can be seen from Fig. 3(b) that at the supporting end of the angle line, the balance of the resultant forces along the direction perpendicular to guy wires results in

$$H' \cos(\alpha/2) = (H'_2 + P_2 - Q_x) \cos(\alpha/2), \quad \text{i.e., } H' = H'_2 + P_2 - Q_x, \quad (47)$$

where Q_x is the wind load contributed from the angle line due to the wind perpendicular to the central span. Q_x is along the longitudinal direction of the angle line, given by

$$Q_x = Q_z L_x \sin \alpha. \quad (48)$$

The formulae given for Case 1, however, can be employed here

Table 1 Properties of lines

	Transmission line	Distribution line		
L_x (m)	125.000	100.000		
H (kN)	15.000	2.190		
A (mm ²)	402.900	33.600		
E (kN/mm ²)	63.358	80.000		
M (kg/m)	1.663	0.136		
Q_y (N/m)	-16.714	-1.334		
Q_z (N/m)	1.756	3.080		
Detuning pendulum		Fallen tree		
F_i (kg)	14.000	Tree	Branch of tree	
θ_i (deg)	0.000	F_v (kg)	600	80
X_i/L_x	1/4, 5/12, 1/3	F_h (kg)	200	30
		θ (deg)	45	45
		X/L_x	1/2	1/4

again provided that (44) is modified so that $(H' - \beta u_2)$ and Q_z (included in Q) are replaced by $(H' - \beta u_2 + Q_x)$ and $Q_z \cos \alpha$, respectively.

3 Practical Applications

The formulae derived in previous sections are applied to practical examples. One example is chosen from the galloping control of transmission lines by using detuning pendulums (Harvard et al., 1985) and the other one is chosen from the mechanical coordination of distribution lines hit by fallen trees (Wong and Yu, 1993). The main focus is on the conductor's tension, length, and static profile.

3.1 Detuning Pendulum. Galloping is a low-frequency, high-amplitude oscillation which can occur on an iced electrical transmission line in a steady side wind. The inability to prevent galloping can lead to severe disruptions in the electrical supply and even a cascading collapse of a line's supporting towers. This problem has been observed since at least the 1930's and research on galloping control has been conducted extensively during the past two decades in North America, Europe, and Japan (Harvard et al., 1985). While a broad range of control devices were considered, the major one tested in North America is the detuning pendulum (Harvard, 1981). It consists of a mass suspended below and rigidly clamped to the conductor. The detuning pendulum is an economical control device and can provide trouble-free service once installed because it has no moving parts. Hence, many North American utilities have been using and still prefer to use it in galloping control of transmission lines. However, the installation of detuning pendulums alters the load distribution of the conductor and therefore, changes the conductor's tension as well as the static profile.

The relative parameters of the transmission line and detuning pendulum are listed in Table 1. The line is assumed to have an iced shape C11 (CEA, 1992) plus a side wind of 10 m/s. The effect of ice load and wind load has been included in A, Q_y , and Q_z . Three identical detuning pendulums are assumed to be vertically installed on one span of the line. Moreover, it is assumed that the adjacent spans are treated in the same way, i.e., $u(0) = u(L_x) = 0$. Both the approximation and exact solution of the static profile are shown in Fig. 4 with main parameters given in Table 2 where T_M, Y_M , and Z_M represent maximum conductor tension, maximum vertical, and horizontal displacements, respectively. Here, the notations (S) and (L) represent the approximation methods for Small and Large concentrated loads, respectively. It clearly indicates that the approximation excellently agrees with the exact solution. This is because the concentrated load is small compared to the conductor's weight (the ratio of the total weight of three detuning pendulums to the total iced conductor's weight of one span is about 20 percent).

3.2 Fallen Tree. Trees inevitably fall onto overhead distribution lines during storm conditions in heavily treed areas. Because it is not environmentally acceptable to remove all po-

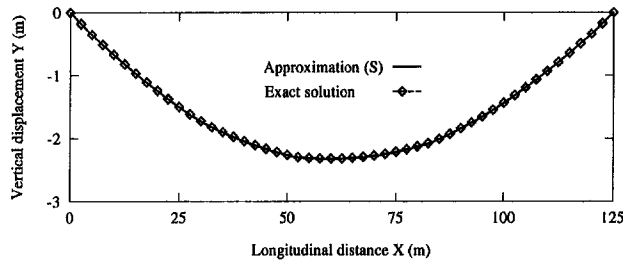


Fig. 4(a)

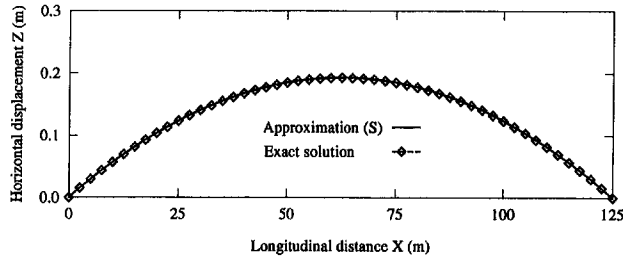


Fig. 4(b)

Fig. 4 Static profile of line with detuning pendulums; (a) vertical direction, (b) horizontal direction

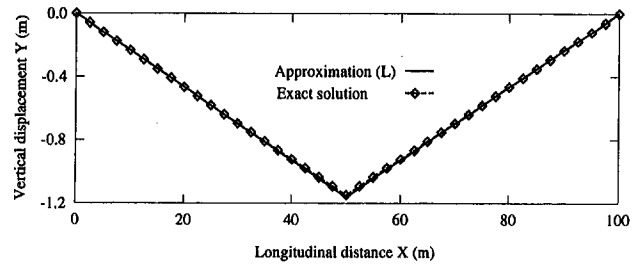


Fig. 5(a)

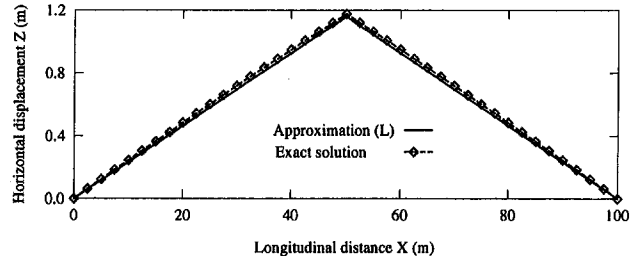


Fig. 5(b)

Fig. 5 Static profile of line with fallen tree at center; (a) vertical direction, (b) horizontal direction

tential danger trees adjacent to distribution lines, the line should be designed so that the component most likely to fail mechanically is also the one that can be repaired with minimum cost and time. This leads to mechanical coordination studies for new line designs as well as the improvement of existing lines. Such a study first requires the computation of component loads due to fallen trees. A tree falling onto the conductor will increase the conductor tension and the tension increase will be transferred to other components of the distribution line including the pole and associated hardware. The new loads for these components can be calculated using basic principles of mechanics on the static profile. The properties of the distribution line are given in Table 1. Also given in this table are data for the case of a whole small tree and the case of a tree branch. The load from a fallen tree consists of two parts, namely the weight of the tree, F_V (vertical) and the wind load on the tree, F_H (horizontal). (The details for estimating these two loads can be found from the report (Wong and Yu, 1993).) The static profiles computed by using the approximation method and the exact solution procedure are given in Fig. 5 for a small tree and in Fig. 6 for a tree branch. The main parameters of the static profile are listed in Table 2.

Figure 5 presents the exact solution with the approximation (L) only because the approximation (S) is inapplicable for this case due to the ratio of concentrated load to distributed load being very large. It is shown that this approximation (L) method produces results which agree well with the exact solution (with error less than two percent) and they are indeed piecewise linear functions (i.e., straight lines). For the case of a typical #2 ACSR conductor branch line, the ultimate tension strength (UTS) of the line is 12.40 kN (Wong and Yu, 1993) and this is much less than the maximum conductor tension caused by the fallen

tree case (73.10 kN, see Table 2). Both the approximation and exact results indicate that the line will fail (e.g., the conductor, the pole or other structural component will break). For the tree branch case, on the other hand, both the two approximations as well as the exact solution are demonstrated in Fig. 6 for a complete comparison. It is seen that the discrepancy between the approximation (S) results and the exact solution is very large. The vertical displacement given by approximation (L) seems a reasonable approximation (the largest error is about 15 percent appearing at 65 m from the left end support) whereas the horizontal approximation cannot be accepted (the largest error > 58 percent). Moreover, the exact solution yields an increase in tension of about 58 percent and 21 percent compared to approximations (S) and (L), respectively. The exact solution

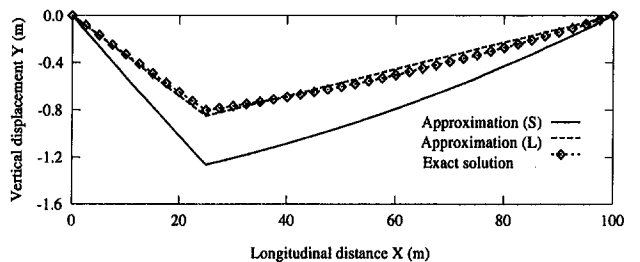


Fig. 6(a)

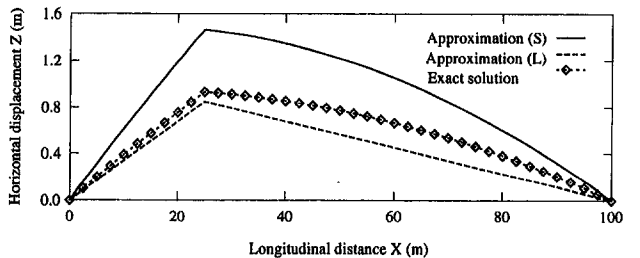


Fig. 6(b)

Fig. 6 Static profile of line with tree branch at quarter point; (a) vertical direction, (b) horizontal direction

Table 2 Main parameters of static profiles

Case	Method	L (m)	H' (kN)	T_M^V (kN)	Y_M (m)	Z_M (m)
Detuning pendulum	(I)	125.12	17.73	17.80	2.33	0.19
	(II)	125.10	17.79	17.84	2.32	0.19
Fallen tree	(II)	100.02	70.84	70.88	1.16	1.16
	(III)	100.03	73.06	73.10	1.15	1.18
Branch of tree	(I)	100.09	8.01	8.04	1.26	1.47
	(II)	100.01	10.43	10.44	0.85	0.85
	(III)	100.02	12.62	12.63	0.80	0.93

indicates that the conductor will break while both approximation results suggest that the line will remain in service. The approximation (S) method failed in this case because the load of the tree branch is relatively large (the ratio of the tree branch's weight to the distributed load is about $\frac{1}{3}$) and located at one point, compared to the case of detuning pendulum where 20 percent concentrated load is distributed to three positions. The approximation (L) method failed, however, due to the neglect of the distributed loads, Q_y and Q_z , which are large, compared to the concentrated loads, especially in the horizontal direction. It is interesting to note from Fig. 6 that the static profile is flat with a ratio of sag to span length of less than $\frac{1}{60}$. For such a low conductor sag, the approximation (S) method should produce very good results for distributed loads only (Irvine, 1981), but this method cannot achieve a reasonable approximation for relatively large concentrated loads.

4 Conclusions

Two approximation and one exact solution methods have been developed to compute conductor tension and static profile under distributed and multiple concentrated loads. Formulae are given explicitly in three-dimensional space with different boundary conditions. The applications to two practical engineering examples show that the approximation (S) approach gives very accurate results for relatively small concentrated

loads and the approximation (L) method produces excellent responses for very large concentrated loads, but the exact solution procedure must be used if concentrated loads are comparable to the distributed loads. It is further shown that the approximation (S) method, which is usually employed for a flat line (a sag to span length ratio of less than 1:8) with only distributed loads, does not provide reasonable results if large concentrated loads are superimposed, and the exact solution procedure must be used. However, the approximation (L) method may be used applied to the exact solution if the concentrated loads are very large.

References

- CEA, 1992, "Modelling of Conductor Galloping," *Canadian Electrical Association*, Technical Report, No. 321 T 672, Montreal, Quebec, Canada.
- CSA Standard, 1990, "Wood Utility Poles and Reinforcing Stubs," *CAN/CSA-015-90*.
- Havard, D. G., 1981, "EPRI Research Program RP-1095, Galloping Control by Detuning, Progress Report No. 4," *Ontario Hydro Progress Report*, No. 4, Ontario, Canada.
- Havard, D. G., Pon, C. J., and Pohlman, J. C., 1985, "Field Evaluation of Galloping Control for Single and Bundle Conductor Lines," *CEA Conductor Vibration Workshop*, Montreal, Canada.
- Irvine, H. M., 1981, *Cable Structures*, MIT Press, Cambridge, U.K.
- Salvadori, M. G., and Schwarz, R. J., 1954, *Differential Equations in Engineering Problems*, Prentice-Hall, Englewood Cliffs, NJ.
- Wong, P. S., and Yu, P., 1993, "Mechanical Coordination of Overhead Distribution Line," *Distribution Technical Services Dept's Report*, B. C. Hydro, Vancouver, Canada.

A Brief Note is a short paper that presents a specific solution of technical interest in mechanics but which does not necessarily contain new general methods or results. A Brief Note should not exceed 1500 words *or equivalent* (a typical one-column figure or table is equivalent to 250 words; a one line equation to 30 words). Brief Notes will be subject to the usual review procedures prior to publication. After approval such Notes will be published as soon as possible. The Notes should be submitted to the Technical Editor of the JOURNAL OF APPLIED MECHANICS. Discussions on the Brief Notes should be addressed to the Editorial Department, ASME, United Engineering Center, 345 East 47th Street, New York, N. Y. 10017, or to the Technical Editor of the JOURNAL OF APPLIED MECHANICS. Discussions on Brief Notes appearing in this issue will be accepted until two months after publication. Readers who need more time to prepare a Discussion should request an extension of the deadline from the Editorial Department.

Thermal Stresses in a Multilayered Anisotropic Medium With Interface Thermal Resistance

T. C. Chen^{1,3} and H. I. Jang^{2,3}

This note is concerned with thermoelastic analysis of a multilayered anisotropic medium under the state of generalized plane deformation with interlayer thermal contact resistance. The powerful flexibility/stiffness matrix method is adopted here to obtain the complete solution of the entire layered medium by introducing the thermal and mechanical boundary and layer interface conditions including interlayer imperfect thermal contact conditions. As a numerical illustration, the effects of interlayer thermal resistance on the distributions of temperatures and thermal stresses in a laminated anisotropic slab subjected to a uniform surface temperature rise are presented.

Introduction

When two layers of a multilayered composite media are brought into contact, an imperfect junction may exist. The flexibility/stiffness matrix method is one of the existing efficient analytical approaches for treating this kind of problem from the viewpoints of both physical interpretation and saving computer time. Choi and Thangjitham (1991, 1992) studied the steady-state thermo-elasticity problem and obtained the distributions of temperature and thermal stresses in a laminated anisotropic slab subjected to a uniform surface temperature rise by this method. The objective of this study is to further extend the flexibility/stiffness method to the steady-state thermo-elasticity problem of a multilayered anisotropic medium in consideration of the constant interlayer thermal contact resistance.

¹ Associate Professor.

² Graduate Student.

³ Department of Mechanical Engineering, National Cheng Kung University, Tainan, Taiwan, R.O.C.

Contributed by the Applied Mechanics Division of THE AMERICAN SOCIETY OF MECHANICAL ENGINEERS for publication in the ASME JOURNAL OF APPLIED MECHANICS. Manuscript received by the ASME Applied Mechanics Division, Nov. 22, 1993; final revision, Oct. 20, 1994. Associate Technical Editor: M. Taya.

Analysis

A layered slab (Fig. 1) composed of N fiber-reinforced layers is considered in this study. The detailed formulation of matrix equations and solution procedures can be found in the paper by Thangjitham and Choi (1991). In this note we only put emphasis on the flexibility matrix formulation of a heat conduction problem pertaining to interlayer thermal contact resistance.

For an imperfectly bonded N -layer medium with interlayer thermal resistance subjected to arbitrary temperature variations on the bounding surfaces, the following thermal boundary and interface conditions are prescribed:

$$\bar{T}_1^+ = \bar{T}_U \quad (1a)$$

$$\bar{q}_k^- = \bar{q}_{k+1}^+, \quad \bar{q}_k^- = \frac{1}{R_k} (\bar{T}_{k+1}^+ - \bar{T}_k^-),$$

$$k = 1, 2, \dots, (N - 1) \quad (1b, c)$$

$$\bar{T}_N^- = \bar{T}_L \quad (1d)$$

where R_k is the interlayer thermal contact resistance, which is defined as the reciprocal of interlayer thermal conductance h between the k th and $(k + 1)$ th layers, i.e., $R_k = 1/h$. For a perfect bonded interface, R_k is equal null, and the temperature distribution becomes continuous between two adjacent surfaces, i.e., $\bar{T}_k^- = \bar{T}_{k+1}^+$. $\bar{T}_U(s)$ and $\bar{T}_L(s)$ represent the transformed temperatures on the upper (+) and lower (-) surfaces of the medium, respectively.

By denoting $\bar{q}_1 = \bar{q}_1^+$ and $\bar{q}_{N+1} = \bar{q}_N^-$ the transverse heat fluxes on the upper and lower bounding surfaces of the medium, respectively, and $\bar{q}_{k+1} = \bar{q}_k^- = \bar{q}_{k+1}^+$, $k = 1, 2, \dots, (N - 1)$, the common interfacial transverse heat fluxes between the k th and $(k + 1)$ th layers, the successive applications of the conditions in Eqs. (1a)–(1d) lead to the global flexibility equations for the N -layer medium written as

$$F_{11}^1 \bar{q}_1 + F_{12}^1 \bar{q}_2 = \bar{T}_U \quad (2a)$$

$$F_{12}^k \bar{q}_k + (F_{22}^k + F_{11}^{k+1} - R_k) \bar{q}_{k+1} + F_{12}^{k+1} \bar{q}_{k+2} = 0$$

$$k = 1, 2, \dots, (N - 1) \quad (2b)$$

$$F_{12}^N \bar{q}_N + F_{22}^N \bar{q}_{N+1} = -\bar{T}_L \quad (2c)$$

In matrix form, the above system of algebraic equations can be expressed as

$$F \bar{q} = \bar{T} \quad (3)$$

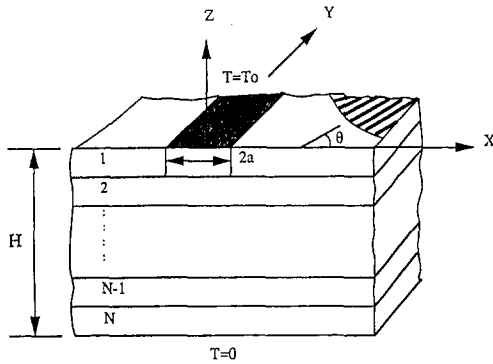


Fig. 1 Configuration and local coordinate for a k th layer of an N -layer anisotropic medium.

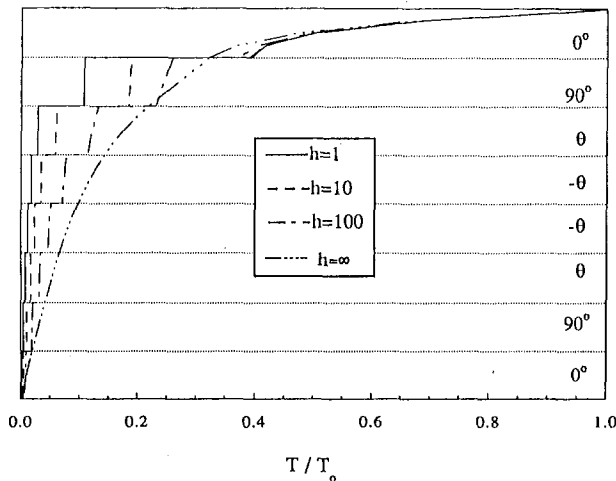


Fig. 2 Temperature distribution T with interface thermal resistance for $\theta = 60$ deg

where \mathbf{F} is the banded and symmetric global flexibility matrix, $\bar{\mathbf{q}}(s)$ is the global vector containing the unknown interfacial transverse heat fluxes, i.e., $\{\bar{q}_1 \bar{q}_2 \dots \bar{q}_{N+1}\}$, and $\bar{\mathbf{T}}(s)$ is the vector containing the transformed surface temperature and zero elements.

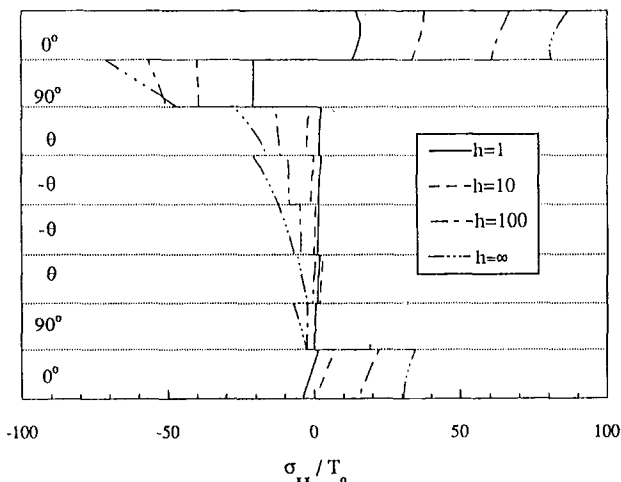


Fig. 3 Thermal stress σ_{xx} distribution interface thermal resistance for $\theta = 60$ deg

Numerical Examples and Discussions

The same numerical example analyzed in the paper by Thangjitham and Choi (1991) is enumerated again in this article. Figures 2–3 show the distributions of temperature T and the stress σ_{xx} through the thickness at $x = 0$ with fiber angle $\theta = 60$ deg for various interface thermal contact conductance, respectively. It can be seen that the temperature distributions are not continuous as expected between two adjacent layers. These discontinuities in temperature between two adjacent layers increase as the values of interface thermal contact conductance are decreased. Moreover, all the solutions without interlayer thermal contact resistance (i.e., $R = 0$ or $h = \infty$) shown here, which are the special cases of the present study, agree completely with the results shown in the literature (Thangjitham and Choi, 1991). By the way, the computation time was around one minute for each case of steady state by using a personal computer with a 486-33 processor.

Acknowledgments

This work was supported by the National Science Council of Taiwan, R.O.C. (Grant No. NSC 83-0401-E006-099).

References

- Thangjitham, S., and Choi, H. J., 1991, "Thermal Stresses in a Multilayered Anisotropic Medium," *ASME JOURNAL OF APPLIED MECHANICS*, Vol. 58, pp. 1021–1027.
- Choi, H. J., and Thangjitham, S., 1992, "Thermal Induced Local Effects in Laminated Composite," *Journal of Thermal Stresses*, Vol. 15, pp. 311–327.

Packing Characterization of Granular Composite Media in Two Dimensions

G. J. Filatovs⁴

1 Introduction

Coverage processes of planar assemblies of hard (impenetrable) disks have been used as geometric analogues for a variety of composite media. Characterizing their packing arrangement is of relevance to a wide range of mechanical, physical, and transport properties, particularly in light of recent efforts to embody stochasticity into micromechanics formulations (for a recent overview see Ostoja-Starzewski, 1993). Such assemblies are not amenable to direct analytic approaches; exploration of their statistical phenomena rests largely on computer and experimental simulation. There is a scarcity of systematic exploration, particularly at high densities, and of incorporation of loading geometry and dynamic variables such as friction. While the literature has shown attempts to statistically characterize actual composite microstructures, the usefulness of these rests on the identification of reference states and bounds determined under controlled conditions.

This note summarizes an experimental simulation of two-phase fibrous composites modeled (in the sense of Hashin,

⁴ Department of Mechanical Engineering, North Carolina A&T State University, Greensboro, NC 27411.

Contributed by the Applied Mechanics Division of THE AMERICAN SOCIETY OF MECHANICAL ENGINEERS for publication in the *ASME JOURNAL OF APPLIED MECHANICS*. Manuscript received by the ASME Applied Mechanics Division, Feb. 7, 1994; final revision, Mar. 4, 1995. Associate Technical Editor: J. T. Jenkins.

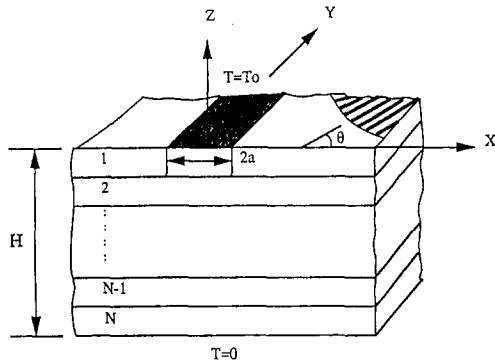


Fig. 1 Configuration and local coordinate for a k th layer of an N -layer anisotropic medium.

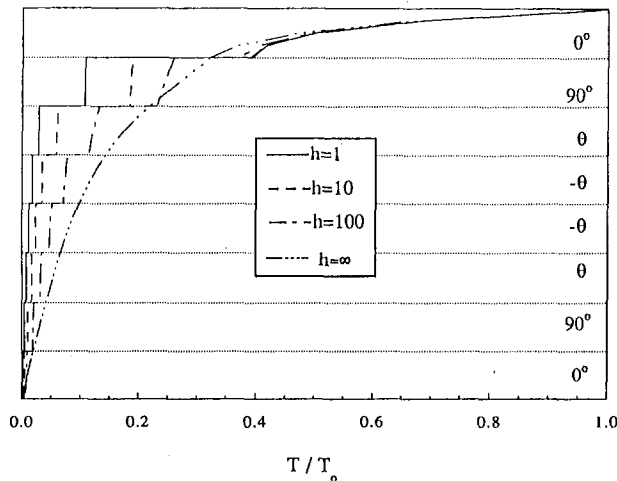


Fig. 2 Temperature distribution T with interface thermal resistance for $\theta = 60$ deg

where \mathbf{F} is the banded and symmetric global flexibility matrix, $\bar{\mathbf{q}}(s)$ is the global vector containing the unknown interfacial transverse heat fluxes, i.e., $\{\bar{q}_1 \bar{q}_2 \dots \bar{q}_{N+1}\}$, and $\bar{\mathbf{T}}(s)$ is the vector containing the transformed surface temperature and zero elements.

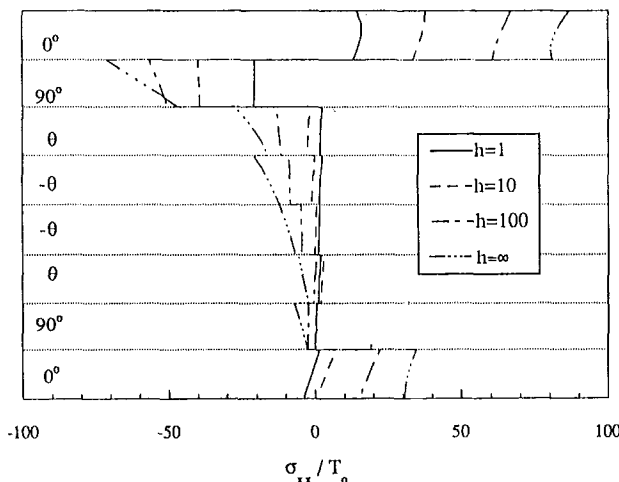


Fig. 3 Thermal stress σ_{xx} distribution interface thermal resistance for $\theta = 60$ deg

Numerical Examples and Discussions

The same numerical example analyzed in the paper by Thangjitham and Choi (1991) is enumerated again in this article. Figures 2–3 show the distributions of temperature T and the stress σ_{xx} through the thickness at $x = 0$ with fiber angle $\theta = 60$ deg for various interface thermal contact conductance, respectively. It can be seen that the temperature distributions are not continuous as expected between two adjacent layers. These discontinuities in temperature between two adjacent layers increase as the values of interface thermal contact conductance are decreased. Moreover, all the solutions without inter-layer thermal contact resistance (i.e., $R = 0$ or $h = \infty$) shown here, which are the special cases of the present study, agree completely with the results shown in the literature (Thangjitham and Choi, 1991). By the way, the computation time was around one minute for each case of steady state by using a personal computer with a 486-33 processor.

Acknowledgments

This work was supported by the National Science Council of Taiwan, R.O.C. (Grant No. NSC 83-0401-E006-099).

References

- Thangjitham, S., and Choi, H. J., 1991, "Thermal Stresses in a Multilayered Anisotropic Medium," *ASME JOURNAL OF APPLIED MECHANICS*, Vol. 58, pp. 1021–1027.
- Choi, H. J., and Thangjitham, S., 1992, "Thermal Induced Local Effects in Laminated Composite," *Journal of Thermal Stresses*, Vol. 15, pp. 311–327.

Packing Characterization of Granular Composite Media in Two Dimensions

G. J. Filatovs⁴

1 Introduction

Coverage processes of planar assemblies of hard (impenetrable) disks have been used as geometric analogues for a variety of composite media. Characterizing their packing arrangement is of relevance to a wide range of mechanical, physical, and transport properties, particularly in light of recent efforts to embody stochasticity into micromechanics formulations (for a recent overview see Ostoja-Starzewski, 1993). Such assemblies are not amenable to direct analytic approaches; exploration of their statistical phenomena rests largely on computer and experimental simulation. There is a scarcity of systematic exploration, particularly at high densities, and of incorporation of loading geometry and dynamic variables such as friction. While the literature has shown attempts to statistically characterize actual composite microstructures, the usefulness of these rests on the identification of reference states and bounds determined under controlled conditions.

This note summarizes an experimental simulation of two-phase fibrous composites modeled (in the sense of Hashin,

⁴ Department of Mechanical Engineering, North Carolina A&T State University, Greensboro, NC 27411.

Contributed by the Applied Mechanics Division of THE AMERICAN SOCIETY OF MECHANICAL ENGINEERS for publication in the *ASME JOURNAL OF APPLIED MECHANICS*. Manuscript received by the ASME Applied Mechanics Division, Feb. 7, 1994; final revision, Mar. 4, 1995. Associate Technical Editor: J. T. Jenkins.


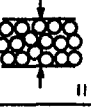
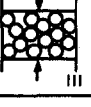
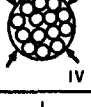
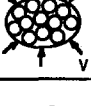
EDGE LOADING	SIMULATION CONDITIONS	PACKING DENSITY	
	RANDOMLY PLACED AND REPLACED IF OVERLAPPING	0.54	
	SMOOTH DISCS TEMPLATE WALLS FOR CASES II AND III	0.76 ANISOTROPY AT 45° DIRECTIONS WHEN DISCS "FLOW"	
	DISC SURFACE SMOOTH	0.82	0.76
	DISC SURFACE ROUGH	0.74	0.71
	DISC ROTATION FREE		
	DISC ROTATION CONSTRAINED		
	SMOOTH WALLS AND DISCS	0.78	
	2:1 ELLIPSE SMOOTH WALLS AND DISCS	0.82 ANISOTROPY AT 45° TO ELLIPSE AXES	

Fig. 1 Summary of simulation conditions and results

1983) by an array of parallel cylinders and represented here in a planar transverse cut as equidiameter hard disks. High density compacts were generated using varied edge loading and inter-disk conditions and examined for configurational statistics and quantities such as packing density (ρ), coordination number (η), and anisotropy.

2 Simulation and Analysis

Simulation was mechanically realized through edge loading an array of disks on a glass plate placed on a digitizing scanner. The edge and disk materials were Teflon; to study the effect of inter-disk friction a set of disks was roughened by sandblasting (raising the coefficient of friction from approximately 0.05 to 0.15) and one set used wires to constrain rotation. 500, 10.00 mm-diameter, 3 mm-thick disks were used with a sampling window of approximately 150 × 150 mm. Twenty trials were made for each configuration with scans made at various stages of compaction.

Loading was accomplished through smooth and simulated random edges (template walls), the latter prompted by early trials in which smooth walls for some cases nucleated large ordered regions. Figure 1 contains schematics of the loading configurations, which were intended to approximate some of the conditions encountered in processing of fibrous composites. In case I disks were dropped onto an adhesive covered glass plate, and either stuck to the adhesive or were blocked by other disks and were redropped. Otherwise, the starting arrangement was placed by hand ($\rho \approx 0.3$) and in most cases loaded to the point of negligible further increase in ρ .

Exploratory data analysis was conducted by examining the point processes created from the disc center coordinates. Methods included grid sampling (Miles, 1978), reduced second-order measures such as the reduced K -function and its L -transform (Cressie, 1991a), and a directional distribution function (Stoyan et al., 1987) to investigate anisotropy. In determining ρ the toroid edge correction was used.

3 Results and Discussion

The compressive edge loading initially induced inward ρ gradients because compaction occurs by disk-disk interaction

and accommodation. At $\rho \approx 0.67$ continuous load paths were formed throughout the arrays and resulted in a threshold in the compaction force. Continuation of loading increased ρ to the limit given in Fig. 1 for each loading case. Using the method of Cressie (1991b) the arrays for cases I, III, and IV were found to be thinned (inhibited) Poisson-process variates i.e., mutually independent and random. Cases II and V also displayed anisotropy, discussion of which is forthcoming.

In random packing, changes in ρ alter the local symmetry. This link was quantified by obtaining the mean values of η from the distributions of touching nearest neighbors as a function of ρ ; actual contacts were difficult to determine and approaches within 0.30 mm were admitted. It was found that

$$\eta = 7.8 \rho - 2.1, \quad \eta \pm 0.2, \quad 0.67 \leq \rho \leq 0.82 \quad (1)$$

the uncertainty stemming from the difficulty of assigning group membership at such high values of ρ . For the smooth disk, unconstrained conditions of cases III and V, $\Delta\eta/\Delta\rho$ showed a large increase above $\rho = 0.82$, with η rapidly approaching 6, through the formation of ordered hexagonal close packed (hcp) regions. The 0.82 value is therefore the highest planar density for the random state.

Table 1 compares of the present results to representative literature values of the two statistically distinguishable states which appear to have correspondence in the literature but were determined through diverse approaches. The present work is apparently the only experimental determination of the first state, which results from the random sequential placement of disks with no subsequent disk motion, and contains few touching disks. While topologically important and applicable to physical situations such as percolation this state is unrealistic for actual composites. It is, however, amenable to computer simulation; the differences in Table 1 most likely reflect differences in computer algorithms. The situation is reversed in the second state, termed random dense packing (ρ_{rdp}) in which experimental simulations predominate because large scale, collective disk interactions and movement are more difficult to computer simulate. The range of values likely arise in the manner exemplified by the varied disk conditions of case III. There, rearrangement of assemblies into higher densities was hindered by friction and restriction of rotation (as in a tow structure), while it was difficult to avoid formation of hcp regions in the smooth, unconstrained disk condition. These ordered regions also most likely contribute to the disagreement among the literature values for ρ_{rdp} , as the degree of contaminating ordering will vary.

Case IV resulted in lower ρ values because equidirectional loading reduced disk motion. Case V, with shear-inducing unbalanced loading, promoted disk motion which raised ρ . This unequal loading also resulted in slight anisotropy, which was much more evident in case II. There, once a maximum of $\rho =$

Table 1 Selected literature values for random packing density

Packing Density	Simulation Method	Reference
LOOSE PACKING		
0.50	Computer	Finegold and Donnell,1979
0.54	Experimental	Present Work
0.55	Computer	Smith and Torquato,1988
0.56	Computer	Lotwick,1982
DENSE PACKING		
0.81	Experimental	Stillinger et al.,1964
0.82	Experimental	Present work
0.82	Analytic	Berryman,1983
0.83	Experimental	Quickenden and Tan,1974
0.89	Experimental	Shahinpoor,1980

0.76 was reached (and loading continued), the process entered a flow regime which imparted a 23 percent increase in linear density in a prevailing direction 45 degrees to the flow direction. No state corresponding to the 0.89 value of Table 1 was observed.

In summary, the baseline simulated disk/fiber structures were essentially random configurations. Compaction occurred by collective accommodation and rearrangement, the degree of which depended on the factors of inter-disk friction, severity and anisotropy of compaction, and constraint of rotation. The ρ_{rdp} value was not easily realized and for ordinarily fabricated fibrous composites the $\rho = 0.71 - 0.76$ range of cases II and III appears to represent realistic upper bounds; higher values require more severe compaction conditions than expected in usual processing. The $\rho = 0.54$ state arises from a static process and shows minimum disk touching, while the $0.67 \leq \rho \leq 0.82$ range displays largely contiguous arrays. Antithetically, for the second, $(1-\rho)$ phase, in this latter range there is no interconnection and thus no permeability. Flow through the medium requires connected pathways which can be formed by lowering of ρ or creation of underdispersion through ordered clustering. In modeling, the implications of the considerable deviation in local symmetry from the square or *hcp* packing customarily assumed for representative volume elements and the relationship which obtains between η and ρ given by (1) should be recognized.

Acknowledgment

The work reported in this paper was supported by grant No. NAG3-1432 from NASA Lewis Research Center.

References

- Berryman, J. G., 1983, "Random close packing of hard spheres and disks," *Physical Review A*, Vol. 27, No. 2, pp. 1053-1061.
- Cressie, N., 1991, *Statistics for Spatial Data*, Wiley-Interscience, New York, (a) pp. 631-650, 669-673, (b) 689-693.
- Finogold, H. L., and Donnell, J. T., 1979, "Maximum density of random packing of membrane particles," *Nature*, Vol. 278, pp. 443-445.
- Hashin, Z., 1983, "Analysis of Composite Materials—A Survey," *ASME JOURNAL OF APPLIED MECHANICS*, Vol. 50, No. 3, pp. 481-505.
- Lotwick, H. W., 1982, "Simulation of Some Spatial Hard Core Models, and the Complete Packing Problem," *Journal of Statistical Computing and Simulation*, Vol. 15, pp. 295-314.
- Ostojic-Starzewski, M., 1993, "Micromechanics as a basis of stochastic finite elements and differences: An overview," *Applied Mechanics Review*, Vol. 46, No. 11, Part 2, pp. S136-147.
- Quickenden, T. E., and Tan, G. K., 1974, "Random Packing in Two Dimensions and the Structure of Monolayers," *Journal of Colloid and Interface Science*, Vol. 48, No. 3, pp. 382-393.
- Shahinpoor, M., 1980, "Statistical Mechanical Considerations of the Random Packing of Granular Materials," *Powder Technology*, Vol. 25, pp. 163-176.
- Stoyan, D., Kendall, W. S., and Mecke, J., 1987, *Stochastic Geometry and Its Applications*, John Wiley, Chichester, pp. 117-148.
- Smith, P., and Torquato, S., 1988, "Computer Simulation Results for the Two-Point Probability Function for Composite Media," *Journal of Computational Physics*, Vol. 76, pp. 176-191.
- Stillinger, F. H., DiMarzio, E. A., and Kornegay, R. L., 1964, "Systematic approach to explanation of the rigid disk phase transition," *Journal of Chemical Physics*, Vol. 40, pp. 1564-1576.

Elastic Buckling of a Circular Disk due to Internal Membrane Forces

W.-Y Shih,^{5,8} L. Kudryavtsev,^{6,8} and K. K. Wang^{7,8}

Residual internal stresses often remain in materials after thermal-mechanical processes. Considerable deformation, such as elastic buckling, may result from such stresses. Some cases of circular-plate buckling due to internal membrane forces are analyzed in this work. The internal membrane-force field is introduced with a nonuniform radial temperature distribution in the disk. Detailed analysis is performed and critical buckling criteria are tabulated for some specific sets of parameters. Although the membrane force in the plate is axially symmetric, symmetry breaking is found at buckling. When the temperature is higher at the disk center, the first buckling mode is dome-shaped, which maintains the polar symmetry. The mode of buckling, however, changes to a saddle shape when the radial temperature distribution is reversed.

1 Introduction

During material processing, residual (internal) stresses often arise as a result of noneven cooling or nonuniform plastic deformation. Such residual stresses can sometimes cause buckling

of the product. The onset of elastic buckling in a circular disk due to internal membrane forces is discussed in this paper.

Internal stresses of volumetric origin can be conveniently represented in terms of thermal stresses since treatments on thermal stresses are readily available (Boley and Weiner, 1960). We consider a circular plate that is stress-free when it is at a uniform temperature. Introducing a radial temperature distribution results in an axially symmetric internal plane-stress field in the absence of external load and constraint. The homogeneous system of the circular plate is analyzed in detail using the method of Frobenius. Buckling criteria are obtained in terms of thermal loading, with critical thermal loadings being tabulated for some specific temperature profiles and deformation modes. We conclude with some observations.

2 The Planar Thermal Stress

Consider the temperature distribution in the disk to be

$$T(m, r) = T_0 \left(\frac{r}{a} \right)^m + \text{constant}, \quad (1)$$

where a is the radius of the disk and r is the radial distance from the disk center. The constant m is a positive integer. Since the disk is stress-free under a uniform temperature field, the "constant" in the temperature distribution (1) is ignored in what follows.

The plane-stress state of a thin plate can be described (Boley and Weiner, 1960) in terms of an Airy stress function φ which satisfies

$$\nabla^4 \varphi + \alpha E \nabla^2 T = 0, \quad (2)$$

where α is the coefficient of linear thermal expansion. The stress components are: $\sigma_{rr} \equiv (\varphi_{,r}/r) + (\varphi_{,00}/r^2)$, $\sigma_{\theta\theta} \equiv \varphi_{,rr}$ and $\sigma_{r\theta} \equiv -(\varphi_{,\theta}/r)_{,r}$. For a disk free of boundary traction, Eq. (2) can be easily integrated for the temperature distribution in Eq. (1). The resulting planar stress-tensor components are

$$\sigma_{rr} = \left(\frac{\alpha E T_0}{m+2} \right) (1 - \rho^m), \quad (3)$$

⁵ Postdoctoral Research Associate.

⁶ Postdoctoral Research Associate, currently at Parametric Technologies, Inc.

⁷ Professor, Fellow ASME.

⁸ Sibley School of Mechanical and Aerospace Engineering, Cornell University, Ithaca, NY 14853.

Contributed by the Applied Mechanical Division of THE AMERICAN SOCIETY OF MECHANICAL ENGINEERS for publication in the ASME JOURNAL OF APPLIED MECHANICS. Manuscript received by the ASME Applied Mechanics Division, June 27, 1994; final revision, Dec. 13, 1994. Associate Technical Editor: W. K. Liu.

0.76 was reached (and loading continued), the process entered a flow regime which imparted a 23 percent increase in linear density in a prevailing direction 45 degrees to the flow direction. No state corresponding to the 0.89 value of Table 1 was observed.

In summary, the baseline simulated disk/fiber structures were essentially random configurations. Compaction occurred by collective accommodation and rearrangement, the degree of which depended on the factors of inter-disk friction, severity and anisotropy of compaction, and constraint of rotation. The ρ_{rdp} value was not easily realized and for ordinarily fabricated fibrous composites the $\rho = 0.71 - 0.76$ range of cases II and III appears to represent realistic upper bounds; higher values require more severe compaction conditions than expected in usual processing. The $\rho = 0.54$ state arises from a static process and shows minimum disk touching, while the $0.67 \leq \rho \leq 0.82$ range displays largely contiguous arrays. Antithetically, for the second, $(1-\rho)$ phase, in this latter range there is no interconnection and thus no permeability. Flow through the medium requires connected pathways which can be formed by lowering of ρ or creation of underdispersion through ordered clustering. In modeling, the implications of the considerable deviation in local symmetry from the square or *hcp* packing customarily assumed for representative volume elements and the relationship which obtains between η and ρ given by (1) should be recognized.

Acknowledgment

The work reported in this paper was supported by grant No. NAG3-1432 from NASA Lewis Research Center.

References

- Berryman, J. G., 1983, "Random close packing of hard spheres and disks," *Physical Review A*, Vol. 27, No. 2, pp. 1053-1061.
- Cressie, N., 1991, *Statistics for Spatial Data*, Wiley-Interscience, New York, (a) pp. 631-650, 669-673, (b) 689-693.
- Finogold, H. L., and Donnell, J. T., 1979, "Maximum density of random placing of membrane particles," *Nature*, Vol. 278, pp. 443-445.
- Hashin, Z., 1983, "Analysis of Composite Materials—A Survey," *ASME JOURNAL OF APPLIED MECHANICS*, Vol. 50, No. 3, pp. 481-505.
- Lotwick, H. W., 1982, "Simulation of Some Spatial Hard Core Models, and the Complete Packing Problem," *Journal of Statistical Computing and Simulation*, Vol. 15, pp. 295-314.
- Ostojic-Starzewski, M., 1993, "Micromechanics as a basis of stochastic finite elements and differences: An overview," *Applied Mechanics Review*, Vol. 46, No. 11, Part 2, pp. S136-147.
- Quickenden, T. E., and Tan, G. K., 1974, "Random Packing in Two Dimensions and the Structure of Monolayers," *Journal of Colloid and Interface Science*, Vol. 48, No. 3, pp. 382-393.
- Shahinpoor, M., 1980, "Statistical Mechanical Considerations of the Random Packing of Granular Materials," *Powder Technology*, Vol. 25, pp. 163-176.
- Stoyan, D., Kendall, W. S., and Mecke, J., 1987, *Stochastic Geometry and Its Applications*, John Wiley, Chichester, pp. 117-148.
- Smith, P., and Torquato, S., 1988, "Computer Simulation Results for the Two-Point Probability Function for Composite Media," *Journal of Computational Physics*, Vol. 76, pp. 176-191.
- Stillinger, F. H., DiMarzio, E. A., and Kornegay, R. L., 1964, "Systematic approach to explanation of the rigid disk phase transition," *Journal of Chemical Physics*, Vol. 40, pp. 1564-1576.

Elastic Buckling of a Circular Disk due to Internal Membrane Forces

W.-Y Shih,^{5,8} L. Kudryavtsev,^{6,8} and K. K. Wang^{7,8}

Residual internal stresses often remain in materials after thermal-mechanical processes. Considerable deformation, such as elastic buckling, may result from such stresses. Some cases of circular-plate buckling due to internal membrane forces are analyzed in this work. The internal membrane-force field is introduced with a nonuniform radial temperature distribution in the disk. Detailed analysis is performed and critical buckling criteria are tabulated for some specific sets of parameters. Although the membrane force in the plate is axially symmetric, symmetry breaking is found at buckling. When the temperature is higher at the disk center, the first buckling mode is dome-shaped, which maintains the polar symmetry. The mode of buckling, however, changes to a saddle shape when the radial temperature distribution is reversed.

1 Introduction

During material processing, residual (internal) stresses often arise as a result of noneven cooling or nonuniform plastic deformation. Such residual stresses can sometimes cause buckling

of the product. The onset of elastic buckling in a circular disk due to internal membrane forces is discussed in this paper.

Internal stresses of volumetric origin can be conveniently represented in terms of thermal stresses since treatments on thermal stresses are readily available (Boley and Weiner, 1960). We consider a circular plate that is stress-free when it is at a uniform temperature. Introducing a radial temperature distribution results in an axially symmetric internal plane-stress field in the absence of external load and constraint. The homogeneous system of the circular plate is analyzed in detail using the method of Frobenius. Buckling criteria are obtained in terms of thermal loading, with critical thermal loadings being tabulated for some specific temperature profiles and deformation modes. We conclude with some observations.

2 The Planar Thermal Stress

Consider the temperature distribution in the disk to be

$$T(m, r) = T_0 \left(\frac{r}{a} \right)^m + \text{constant}, \quad (1)$$

where a is the radius of the disk and r is the radial distance from the disk center. The constant m is a positive integer. Since the disk is stress-free under a uniform temperature field, the "constant" in the temperature distribution (1) is ignored in what follows.

The plane-stress state of a thin plate can be described (Boley and Weiner, 1960) in terms of an Airy stress function φ which satisfies

$$\nabla^4 \varphi + \alpha E \nabla^2 T = 0, \quad (2)$$

where α is the coefficient of linear thermal expansion. The stress components are: $\sigma_{rr} \equiv (\varphi_r/r) + (\varphi_{\theta\theta}/r^2)$, $\sigma_{\theta\theta} \equiv \varphi_{,rr}$ and $\sigma_{r\theta} \equiv -(\varphi_{,\theta}/r)_{,r}$. For a disk free of boundary traction, Eq. (2) can be easily integrated for the temperature distribution in Eq. (1). The resulting planar stress-tensor components are

$$\sigma_{rr} = \left(\frac{\alpha E T_0}{m+2} \right) (1 - \rho^m), \quad (3)$$

⁵ Postdoctoral Research Associate.

⁶ Postdoctoral Research Associate, currently at Parametric Technologies, Inc.

⁷ Professor, Fellow ASME.

⁸ Sibley School of Mechanical and Aerospace Engineering, Cornell University, Ithaca, NY 14853.

Contributed by the Applied Mechanical Division of THE AMERICAN SOCIETY OF MECHANICAL ENGINEERS for publication in the ASME JOURNAL OF APPLIED MECHANICS. Manuscript received by the ASME Applied Mechanics Division, June 27, 1994; final revision, Dec. 13, 1994. Associate Technical Editor: W. K. Liu.

$$\sigma_{r,\theta} = 0, \tag{4}$$

for zero bending moment and

$$\sigma_{\theta\theta} = \left(\frac{\alpha E T_0}{m+2} \right) [1 - (m+1)\rho^m], \tag{5}$$

where $\rho \equiv r/a$. The membrane-force tensor \mathbf{N} is simply the product of the planar stress-tensor $\boldsymbol{\sigma}$ and the plate thickness h . We define $g_{rr}(\rho) \equiv (1 - \rho^m)$ and $g_{\theta\theta}(\rho) \equiv [1 - (m+1)\rho^m]$ for later use.

3 Modal Analysis of the Plate

With a nonzero membrane-force field, the torque equilibrium of the plate can be shown as

$$D\nabla\nabla^2 w + \mathbf{Q} - \mathbf{N} \cdot \nabla w = 0, \tag{6}$$

where $D = Eh^3/12(1 - \nu^2)$, ν is the Poisson's ratio, w is the out-of-plane displacement, and \mathbf{Q} is the shear force in the plate cross sections. Note that $\nabla \cdot \mathbf{N} = 0$ for the force equilibrium in the plane; and $\nabla \cdot \mathbf{Q} = -q$ for the force equilibrium in the out-of-plane direction, where q is the distributed out-of-plane force. The plate equation (Timoshenko and Woinowsky-Krieger, 1959)

$$D\nabla^4 w - \mathbf{N} : \nabla\nabla w = q \tag{7}$$

is obtained by taking the divergence of Eq. (6).

The deflection w and the lateral loading q can be expressed as the sums of their respective Fourier modes, i.e.,

$$w(\rho, \theta) = a \sum_{n=0}^{\infty} S_n(\rho) e^{in\theta}, \quad q(\rho, \theta) = \sum_{n=0}^{\infty} q_n(\rho) e^{in\theta}.$$

By replacing w and q with their n th mode in Eq. (8), individual modes can be treated separately and the azimuthal (θ) dependence can be factored out in the process. This leads to an ordinary differential equation for the n th mode:

$$\left(\frac{d^2}{d\rho^2} + \frac{1}{\rho} \frac{d}{d\rho} - \frac{n^2}{\rho^2} \right)^2 S_n(\rho) - \lambda \left[g_{rr}(\rho) S_n''(\rho) + g_{\theta\theta}(\rho) \left(\frac{S_n'(\rho)}{\rho} - \frac{n^2 S_n(\rho)}{\rho^2} \right) \right] = \frac{a^4 q_n}{D}, \tag{8}$$

where

$$\lambda = \left[\frac{12(1 - \nu^2)\alpha T_0}{m+2} \right] \left(\frac{a}{h} \right)^2 \tag{9}$$

measures the strength of the thermal loading.

When elastic buckling due to the thermal loading alone is concerned, $q_n = 0$ and the governing Eq. (8) becomes homogeneous. The corresponding free-edge boundary conditions are

$$S_n''(1) + \nu[S_n'(1) - n^2 S_n(1)] = 0 \tag{10}$$

$$S_n'''(1) + S_n''(1) - S_n'(1) - n^2[(2 - \nu)S_n'(1) - (3 - \nu)S_n(1)] = 0 \tag{11}$$

for zero shear force along the outer edge. The continuity and smoothness at the center requires

$$S_n(0) = 0 \tag{12}$$

and

$$S_n'(0) = 0, \tag{13}$$

respectively. The linear homogeneous system, Eq. (8) with $q_n = 0$ and Eqs. (10)–(13), has only the trivial solution $S_n \equiv 0$ except for a set of discrete eigenvalues of λ . The non-trivial solutions for $S_n(\rho)$ at these special λ 's correspond to the buckling modes of the disk.

4 The Formal Solution

The method of Frobenius can be applied to obtain the complementary solutions for Eq. (8). Let the solutions for S_n assume the following form:

$$S_n(\rho) = \rho^s \sum_{j=0}^{\infty} c_j \rho^j, \tag{14}$$

and substitute this into Eq. (8) for $S_n(\rho)$. After organizing terms according to the exponents of ρ , the allowable values for s are found to be

$$s_1, s_2, s_3, s_4 = (n+2), n, (-n+2), -n. \tag{15}$$

In addition, $c_1 = 0$ in all cases. It can be shown that only $s = n+2$ and $s = n$ lead to valid independent power-series complementary solutions to Eq. (8). The remaining two complementary solutions to Eq. (8) can be obtained by using a standard procedure (e.g., Hildebrand, 1976, Chap. 4). They are, however, singular and correspond to unbounded shear forces at the center.

The regular power-series solutions derived with $s = n+2$ and $s = n$ thus constitute the complete solution for the full disk under thermal loading alone. We shall call these two regular power-series solutions u_{n1} and u_{n2} for later references, where

$$u_{n1}(\rho) = \rho^{n+2} \left(1 + \sum_{j=2}^{\infty} a_j \rho^j \right) \tag{16}$$

and

$$u_{n2}(\rho) = \rho^n \left(1 + \sum_{j=2}^{\infty} b_j \rho^j \right). \tag{17}$$

The recursion formula is given by

$$a_{i+2} = \begin{cases} \frac{\lambda a_i}{(i+2)(2n+i+2)} & \text{for } 0 \leq i \leq (m-1) \\ \lambda \left[\frac{a_i}{(i+2)(2n+i+2)} + \frac{m(n^2+n+i) - i(2n+i)}{i(i+2)(2n+i)(2n+i+2)} a_{i-m} \right] & \text{for } m \leq i \end{cases} \tag{18}$$

where $a_0 = 1$ and $a_1 = 0$, as indicated in Eq. (16). Replacing a_i with b_i in Eq. (18) gives the recursion relation for the coefficients of u_{n2} .

With the exceptions of $n = 0$ and $n = 1$, u_{n1} and u_{n2} automatically satisfy the continuity and smooth conditions (12) and (13) at the disk center. The complete solution $S_n(\rho)$ is thus a linear combination of $u_{n1}(\rho)$ and $u_{n2}(\rho)$:

$$S_n(\rho) = Au_{n1}(\rho) + Bu_{n2}(\rho). \quad (19)$$

One needs simply to meet the homogeneous moment and shear-force boundary conditions with eigenvalues of λ and suitable B/A 's to get the non-trivial solutions for the buckled disk.

5 Exceptions

The complementary solutions $u_0 = 1$ and $u_1 = \rho$ represent rigid-body translation and rotation, respectively, regardless the value of λ . They are not of interest and need to be removed in the particular solution (19).

$n = 0$. For this axially symmetric case, B in Eq. (19) has to be zero so that the boundary condition (12) is satisfied. It may seem to be a problem how $S_0(\rho)$ alone,

$$S_0(\rho) = Au_{01}(\rho) = A\rho^2(1 + \sum_{j=2}^{\infty} a_j\rho^j), \quad (20)$$

could satisfy both outer boundary conditions (10) and (11) with $A \neq 0$. Consider a concentric portion of the disk that has a radius of ρ . Its out-of-plane force equilibrium equation $2\pi\rho Q_r(\rho) = -2\pi a \int_0^\rho \rho' q_0(\rho') d\rho' = 0$, can be simplified using the r -component of Eq. (6):

$$\frac{d}{d\rho} \left[\frac{1}{\rho} \frac{d}{d\rho} \left(\rho \frac{dS_0}{d\rho} \right) \right] - \lambda g_{rr}(\rho) \left(\frac{dS_0}{d\rho} \right) = 0, \quad (21)$$

which in turn reduces to the zero-shear-force boundary condition (11) at $\rho = 1$. Since the solution S_0 always satisfies this force equilibrium condition, it is clear that only the bending-moment boundary condition (10) remains to be satisfied by the eigenvalues of λ for non-trivial S_0 to exist.

$n = 1$. Similar to the previous case, B must be zero in Eq. (19) so that the boundary condition (13) is satisfied. We again have only one variable λ in the solution $S_1 = Au_{11}$ to satisfy both boundary conditions (10) and (11) at buckling. Consider the torque \mathbf{T} on the same concentric portion of the disk. Let T_1 and T_2 be the components of \mathbf{T} along the axis directions of a Cartesian system. Recognizing that $N_{r\theta} = 0$, we have

$$T_1 = a\rho \int_0^{2\pi} d\theta (-M_{rr} \sin \theta + M_{r\theta} \cos \theta + Q_r a \rho \sin \theta - N_{rr} w \sin \theta) \quad (22)$$

and

$$T_2 = a\rho \int_0^{2\pi} d\theta (M_{rr} \cos \theta + M_{r\theta} \sin \theta - Q_r a \rho \cos \theta + N_{rr} w \cos \theta). \quad (23)$$

The shear-force component Q_r and the bending/twisting moments M_{rr} , $M_{r\theta}$ can be expressed in terms of w using the r -component of Eq. (6) and the Kirchoff kinematic assumptions for plates. Substituting $aS_n(\rho)e^{in\theta}$ for w in the torque-equilibrium equations, $T_1 = 0$ and $T_2 = 0$, it can be shown that only $n = 1$ results in a non-trivial identity:

$$S_1'''(\rho) - \frac{3S_1'(\rho)}{\rho^2} + \frac{3S_1(\rho)}{\rho^3} - \lambda g_{rr}(\rho) \left[S_1'(\rho) - \frac{S_1(\rho)}{\rho} \right] = 0. \quad (24)$$

Table 1 Lowest eigenvalues (λ_{cr}) of λ for thermal buckling when the Poisson's ratio is 0.3. The cases of $m = 1, 2$ and 3 indicate a radial temperature distribution that is linear, quadratic, and cubic, respectively.

n	m = 1		m = 2		m = 3	
	$T_0 < 0$	$T_0 > 0$	$T_0 < 0$	$T_0 > 0$	$T_0 < 0$	$T_0 > 0$
0	-15.52		-9.829		-7.935	
1	-49.70		-31.22		-25.07	
2	-138.0	11.84	-76.29	7.234	-57.08	5.697
3	-299.0	22.26	-153.6	13.06	-109.1	9.993
4	-504.7	35.22	-255.3	20.19	-178.6	15.17

At $\rho = 1$, Eq. (24) becomes identical to the difference between boundary conditions (10) and (11). Hence, only one of these two boundary conditions needs to be used in solving for the eigenvalues of λ when $n = 1$.

6 The Eigenvalues

The eigenvalues for λ are obtained numerically using u_{n1} and u_{n2} constructed with the recursion formula (18) and the boundary conditions (10) and (11). When $n = 0$ and 1, only u_{n1} and the bending-moment boundary condition (10) are needed.

Listed in Table 1 are some of the smallest eigenvalues of λ , λ_{cr} , for the internal membrane-force states considered and $\nu = 0.3$. We shall focus on the lowest eigenvalue in each column since they are of most practical importance.⁹

Analogous to a circular disk under radial compression, the buckled disk maintains the polar symmetry ($n = 0$) for $T_0 < 0$ and has the dome shape. A saddle shape with $n = 2$, however, occurs as the first buckling mode when T_0 is positive. There is no analogue to an externally loaded disk.

It is seen that the critical value of λ , λ_{cr} , decreases as the value of m increases. The critical center-to-edge temperature difference, $|T_{0,cr}| = [(m + 2)/12(1 - \nu^2)\alpha](h/a)^2|\lambda_{cr}|$, however, varies slowly with the value of m . It is curious to note that the value of $|T_{0,cr}|$ drops less than 20 percent from $m = 1$ to $m = 2$ and is practically the same for $m = 2$ and $m = 3$. The critical values of λ for $\nu = 0.2, 0.4$ and 0.5 show the same behavior. Since buckling is sensitive to structural imperfections and material inhomogeneity, the change of $T_{0,cr}$ due to changes in the detailed temperature distribution can be regarded as insignificant. For practical purposes, approximating the temperature distribution linearly might be sufficient.

7 Conclusions

We have presented some examples of circular-disk buckling due to internal membrane-force fields. The analysis gives the thresholds for different buckling modes in terms of the critical thermal-loading parameter $T_{0,cr}$. Only the dome and saddle-shaped buckling modes are of physical significance. The saddle-shaped buckling mode due to an axially symmetric loading in a full disk presents an interesting case of symmetry breaking not seen when only external loading is involved. It is also found that the buckling threshold $T_{0,cr}$ is only weakly dependent on the detailed temperature distribution for both modes.

⁹ It can be proved based on minimum potential energy that no positive eigenvalue for λ exists for $n = 0$ and non-negative σ_{rr} distribution. In the case of $n = 1$, root-search up to 500 for λ_{cr} found nothing. It is speculated that positive λ_{cr} may only exist in some odd internal membrane-force states. The proof in the $n = 0$ case is not shown here for brevity.

8 Acknowledgment

The authors would like to thank Prof. T. Healey and Dr. C. A. Hieber for their helpful discussions. The work has been supported by the Cornell Injection Molding Program, an industrial consortium.

References

- Boley, B. A., and Weiner, J. H., 1960, *Theory of Thermal Stresses*, John Wiley and Sons, New York.
- Hildebrand, F. B., 1976, *Advanced Calculus for Applications*, 2nd ed., Prentice-Hall, Englewood Cliffs, NJ.
- Timoshenko, S. P., and Woinowsky-Krieger, S., 1959, *Theory of Plates and Shells*, 2nd ed., McGraw-Hill, New York.

A Numerical Investigation of the Elastothermodynamic Damping of Fiber-Reinforced Metal-Matrix Composites

K. B. Milligan¹⁰ and V. K. Kinra¹¹

Introduction

A problem of current interest to the composites community is the calculation of elastothermodynamic damping (ETD) in continuous fiber-reinforced metal-matrix composites (MMCs). As a first step in that direction, we recently reported an exact solution for ETD of a continuous fiber of circular cross-section embedded in a concentric matrix (Milligan and Kinra, 1994); this model will be referred to as the circular matrix model (CMM). The CMM suffers from several limitations; for example, the heat conduction is confined to only one (the radial) direction. Also, using the CMM with a fixed radius (i.e., a fixed volume fraction, V_f), one cannot fill the entire space. We cannot use the composite cylinders (static) model of Hashin and Rosen (1964) where a continuous gradation of the fiber radius is used. In our (dynamic) model the damping is frequency dependent, and, therefore, we must use fibers of a fixed radius. Moreover, using the CMM we cannot estimate the effect of randomness in fiber distribution on the ETD. Addressing these limitations in the CMM is the objective of the present work.

Recently we developed a numerical technique for calculating ETD for a variety of planar problems where the heat conduction may occur in both in-plane directions (Milligan, 1994). Using this technique, we present a numerical solution to a more realistic model of a MMC: a circular fiber embedded in a square matrix; for brevity, we will refer to it as the square matrix model (SMM). It is obvious that we can fill the entire space using SMM representative volume elements (RVEs). For identical fiber size and volume fraction, we will compare the results of the CMM and SMM. We will also examine — to a first

¹⁰ United States Air Force, Wright Laboratory, Armament Directorate, Eglin Air Force Base, FL 32542-6810, Assoc. Mem. ASME.

¹¹ General Dynamics Professor, Center for Mechanics of Composites and Department of Aerospace Engineering, College Station, TX 77843-3141, Fellow ASME.

Contributed by the Applied Mechanics Division of THE AMERICAN SOCIETY OF MECHANICAL ENGINEERS for publication in the ASME JOURNAL OF APPLIED MECHANICS. Manuscript received by the ASME Applied Mechanics Division, Aug. 29, 1994; final revision, Mar. 3, 1995. Associate Technical Editor: J. T. Jenkins.

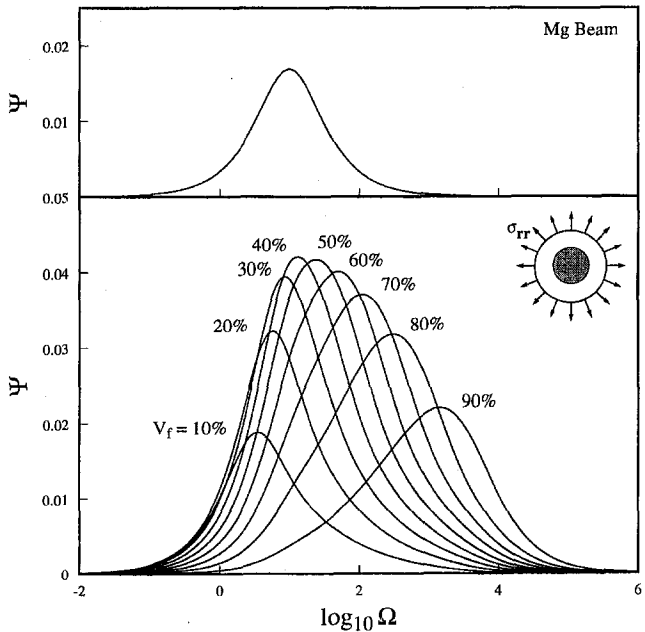


Fig. 1 The volume-averaged damping of a fiber-reinforced metal-matrix composite using the circular matrix model for the SiC/Mg material combination under uniform radial load. $T_o = 300$ K.

approximation — the effect of a random distribution of fibers on ETD.

Analytical Results: Circular Matrix Model

We define a normalized frequency $\Omega = \omega \rho c a^2 / k$ where ρ , c , and k are the density, specific heat per unit mass, and thermal conductivity, respectively, of the fiber; ω is the frequency of vibration of the loading; and a is the fiber radius. Let Ψ be the volume-averaged specific damping capacity. For a SiC fiber in a magnesium matrix subjected to a uniform radial loading, we reported Ψ versus Ω for the CMM for $0 \leq \Omega \leq 20$ (Milligan and Kinra, 1994). For a later comparison with the numerical results for the SMM, we begin by presenting in Fig. 1 a plot of Ψ versus Ω over a much broader range of frequencies (see Table 1 for the elastothermodynamic properties of these materials). By way of comparison, the damping for a magnesium beam in pure bending is also shown (Kinra and Milligan, 1994); the total beam height was taken to be $2a$. A peak damping of about four percent is achieved over a broad range of volume fractions (30 percent $\leq V_f \leq 60$ percent). An observation of great practical use is that a significant damping is obtained over a broad range of frequencies. Unlike the beam damping, the CMM damping is not symmetric about its peak value. The frequency at which Ψ attains a maximum increases by an order of magnitude as V_f increases.

Numerical Results: Square Matrix Model

In the present context we consider only the plane-strain condition and the SiC/Mg material combination. Due to the symmetry of the problem, it is necessary to model only one quarter of the fiber/matrix region. Calculations were carried out for three

Table 1 Elastothermodynamic properties of constituent materials

Material	ρ (10^3 kg/m ³)	E (GPa)	k (J/s-m-K)	c (J/kg-K)	α (10^{-6} /K)
Mg	1.74	44	154	1030	27.1
SiC	3.26	460	90.0	1330	4.3

$\nu = 0.333$ for each material

8 Acknowledgment

The authors would like to thank Prof. T. Healey and Dr. C. A. Hieber for their helpful discussions. The work has been supported by the Cornell Injection Molding Program, an industrial consortium.

References

- Boley, B. A., and Weiner, J. H., 1960, *Theory of Thermal Stresses*, John Wiley and Sons, New York.
- Hildebrand, F. B., 1976, *Advanced Calculus for Applications*, 2nd ed., Prentice-Hall, Englewood Cliffs, NJ.
- Timoshenko, S. P., and Woinowsky-Krieger, S., 1959, *Theory of Plates and Shells*, 2nd ed., McGraw-Hill, New York.

A Numerical Investigation of the Elastothermodynamic Damping of Fiber-Reinforced Metal-Matrix Composites

K. B. Milligan¹⁰ and V. K. Kinra¹¹

Introduction

A problem of current interest to the composites community is the calculation of elastothermodynamic damping (ETD) in continuous fiber-reinforced metal-matrix composites (MMCs). As a first step in that direction, we recently reported an exact solution for ETD of a continuous fiber of circular cross-section embedded in a concentric matrix (Milligan and Kinra, 1994); this model will be referred to as the circular matrix model (CMM). The CMM suffers from several limitations; for example, the heat conduction is confined to only one (the radial) direction. Also, using the CMM with a fixed radius (i.e., a fixed volume fraction, V_f), one cannot fill the entire space. We cannot use the composite cylinders (static) model of Hashin and Rosen (1964) where a continuous gradation of the fiber radius is used. In our (dynamic) model the damping is frequency dependent, and, therefore, we must use fibers of a fixed radius. Moreover, using the CMM we cannot estimate the effect of randomness in fiber distribution on the ETD. Addressing these limitations in the CMM is the objective of the present work.

Recently we developed a numerical technique for calculating ETD for a variety of planar problems where the heat conduction may occur in both in-plane directions (Milligan, 1994). Using this technique, we present a numerical solution to a more realistic model of a MMC: a circular fiber embedded in a square matrix; for brevity, we will refer to it as the square matrix model (SMM). It is obvious that we can fill the entire space using SMM representative volume elements (RVEs). For identical fiber size and volume fraction, we will compare the results of the CMM and SMM. We will also examine — to a first

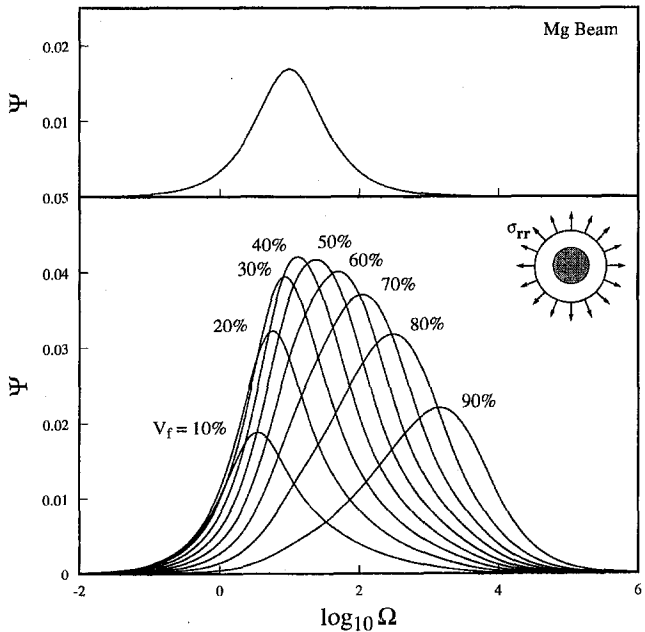


Fig. 1 The volume-averaged damping of a fiber-reinforced metal-matrix composite using the circular matrix model for the SiC/Mg material combination under uniform radial load. $T_o = 300$ K.

approximation — the effect of a random distribution of fibers on ETD.

Analytical Results: Circular Matrix Model

We define a normalized frequency $\Omega = \omega \rho c a^2 / k$ where ρ , c , and k are the density, specific heat per unit mass, and thermal conductivity, respectively, of the fiber; ω is the frequency of vibration of the loading; and a is the fiber radius. Let Ψ be the volume-averaged specific damping capacity. For a SiC fiber in a magnesium matrix subjected to a uniform radial loading, we reported Ψ versus Ω for the CMM for $0 \leq \Omega \leq 20$ (Milligan and Kinra, 1994). For a later comparison with the numerical results for the SMM, we begin by presenting in Fig. 1 a plot of Ψ versus Ω over a much broader range of frequencies (see Table 1 for the elastothermodynamic properties of these materials). By way of comparison, the damping for a magnesium beam in pure bending is also shown (Kinra and Milligan, 1994); the total beam height was taken to be $2a$. A peak damping of about four percent is achieved over a broad range of volume fractions (30 percent $\leq V_f \leq 60$ percent). An observation of great practical use is that a significant damping is obtained over a broad range of frequencies. Unlike the beam damping, the CMM damping is not symmetric about its peak value. The frequency at which Ψ attains a maximum increases by an order of magnitude as V_f increases.

Numerical Results: Square Matrix Model

In the present context we consider only the plane-strain condition and the SiC/Mg material combination. Due to the symmetry of the problem, it is necessary to model only one quarter of the fiber/matrix region. Calculations were carried out for three

Table 1 Elastothermodynamic properties of constituent materials

Material	ρ (10^3 kg/m ³)	E (GPa)	k (J/s-m-K)	c (J/kg-K)	α (10^{-6} /K)
Mg	1.74	44	154	1030	27.1
SiC	3.26	460	90.0	1330	4.3

$\nu = 0.333$ for each material

¹⁰ United States Air Force, Wright Laboratory, Armament Directorate, Eglin Air Force Base, FL 32542-6810, Assoc. Mem. ASME.

¹¹ General Dynamics Professor, Center for Mechanics of Composites and Department of Aerospace Engineering, College Station, TX 77843-3141, Fellow ASME.

Contributed by the Applied Mechanics Division of THE AMERICAN SOCIETY OF MECHANICAL ENGINEERS for publication in the ASME JOURNAL OF APPLIED MECHANICS. Manuscript received by the ASME Applied Mechanics Division, Aug. 29, 1994; final revision, Mar. 3, 1995. Associate Technical Editor: J. T. Jenkins.

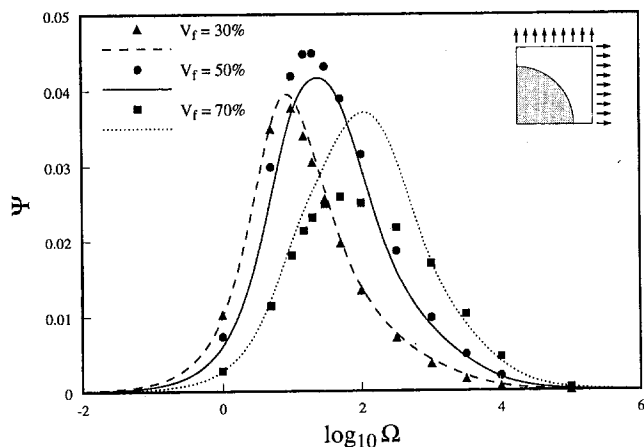


Fig. 2 A comparison of the radial load case for the circular matrix model with the biaxial case for the square matrix model: the volume-averaged damping as a function of normalized frequency for the SiC/Mg material combination. $T_o = 300$ K.

representative volume fractions of fibers: $V_f = 30$ percent, 50 percent, and 70 percent. First we consider the RVE subjected to a homogeneous, biaxial boundary displacement perpendicular to the square boundary. The numerical results for the SMM (discrete points) are compared with the CMM (continuous lines) in Fig. 2. For $V_f \leq 50$ percent the agreement is considered very good. At the higher volume fraction, $V_f = 70$ percent, the agreement is good except near the peak.

Although the SMM is superior to the CMM in that using a square RVE one can fill the entire space, an obvious drawback is that the resulting fiber arrangement is a periodic square array. In most MMCs the fibers are distributed in a fairly random manner. As a first step in understanding the influence of random fiber distribution on Ψ , we consider one row of square RVEs in which pairs of adjacent fibers are shifted toward one another by an equal amount c (see Fig. 3). It is obvious that after this transformation, the RVE boundaries still remain adiabatic. Let $\delta = c/b$, and let $\Psi_{\delta=0}$ be the damping when the fibers are not shifted ($\delta = 0$). In Fig. 4 we have plotted $\Psi/\Psi_{\delta=0}$ versus δ for $V_f = 50$ percent and 70 percent. The effect of the fiber shift on the overall damping is considered to be negligibly small for most engineering applications. (The fibers in the neighboring RVEs contact each other when $\delta = 1 - (4V_f/\pi)^{1/2}$.) We conclude that for all practical purposes, the effect of random distribution of fibers on Ψ may be neglected.

Our attention so far has been confined to biaxial loading. We now consider the SMM subjected to a uniaxial loading, in particular, to a homogeneous, uniaxial boundary displacement perpendicular to the square boundary. The damping, Ψ , is plotted in Fig. 5. The discrete numerical results have been joined by smooth spline curve fits for visual clarity. Note that Ψ for

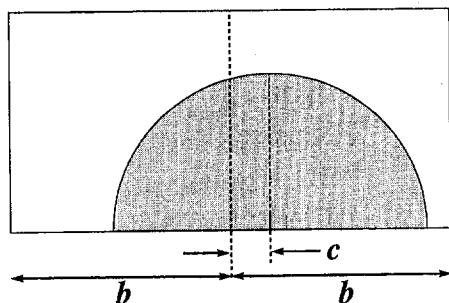


Fig. 3 The fiber/matrix representative volume element for the nonuniform distribution of fibers.

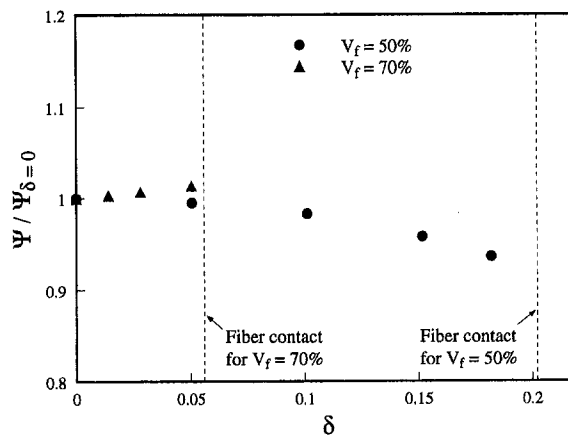


Fig. 4 The effect of nonuniform fiber distribution on the damping for the SiC/Mg material combination under biaxial loading for $\Omega = 20$. $T_o = 300$ K.

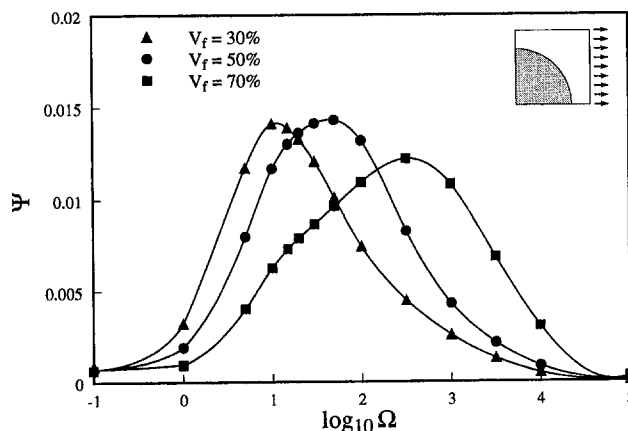


Fig. 5 The uniaxial case for the square matrix model: the volume-averaged damping as a function of normalized frequency for the SiC/Mg material combination. $T_o = 300$ K.

biaxial loading is roughly three times larger than that for the uniaxial loading. Elsewhere (Bishop and Kinra, 1994) it has been shown that the ETD for a plate subjected to biaxial bending is about three times higher than the ETD for a beam subjected to uniaxial bending. The essential physics for the two cases is identical (i.e., higher hydrostatic stress for the case of biaxial loading); therefore, for brevity, the detailed discussion given by Bishop and Kinra (1994) will not be repeated here.

Conclusions

For biaxial loading the closed form solution presented by the authors for elastothermodynamic damping in continuous fiber-reinforced metal-matrix composites (Milligan and Kinra, 1994) is an adequate engineering approximation for $V_f \leq 50$ percent. For higher V_f the CMM overpredicts the damping near its peak. For uniaxial loading, the damping is significantly smaller (about one-third) than that for biaxial loading as expected. A random versus a periodic distribution of fibers in the composite has very little effect on the damping.

Acknowledgments

This research is supported by the Office of Naval Research through Grant Number N00014-90-J-1130 to Texas A&M University, College Station, TX. The continued and keen interest

BRIEF NOTES

taken by the program manager, Dr. L. Kabacoff, in the evolution of this work is gratefully acknowledged.

References

Bishop, J. E., and Kinra, V. K., 1994, "Elastothermodynamic Damping in Composite Plates," *Proceedings of the 1994 ASME International Mechanical Engineering Congress and Exposition*, accepted for publication.

Hashin, Z., and Rosen, B. W., 1964, "The Elastic Moduli of Fiber-Reinforced Materials," *ASME JOURNAL OF APPLIED MECHANICS*, Vol. 31, No. 1, pp. 223-232.

Kinra, V. K., and Milligan, K. B., 1994, "A Second-Law Analysis of Thermoelastic Damping," *ASME JOURNAL OF APPLIED MECHANICS*, Vol. 61, No. 1, pp. 71-76.

Milligan, K. B., and Kinra, V. K., 1994, "Elastothermodynamic Damping of Fiber-Reinforced Metal-Matrix Composites," *ASME JOURNAL OF APPLIED MECHANICS*, accepted for publication.

Milligan, K. B., 1994, "A Second-Law Analysis of Elastothermodynamic Damping," Ph.D. Dissertation, Texas A&M University, College Station, TX.

Vibrations of Solid Cylinders Revisited

J. R. Hutchinson¹²

This brief note is a revisit to my previous paper on this subject, Hutchinson (1980). The reason for this revisit is three-fold:

- to correct an error in the plots shown for the circumferential order four.
- to extend the range of the graphical data shown in the original paper.
- to consider modes of higher circumferential order.

In the referenced paper the solution of the governing three-dimensional equations of linear elasticity together with appropriate boundary conditions is found by forming three series of exact solutions of the governing equations which also identically satisfy three of the boundary conditions. The remaining three boundary conditions are satisfied by orthogonalization on the boundary. The solution process leads to a matrix eigenvalue problem with the order of the matrix being the number of the terms in one of the series.

Solutions are split into "even" and "odd" functions. The even functions are defined as those that have the radial and tangential displacements as even functions of the axial coordinate and the axial displacement as an odd function of the axial coordinate. For example, for small thickness to diameter ratio the odd modes are the plate bending modes. The parameters in the problem are the frequency parameter, the height-to-diameter ratio, the circumferential order, and Poisson's ratio. The dimensionless frequency parameter is the frequency times the radius divided by the shear wave velocity.

¹² Civil and Environmental Engineering Department, University of California, Davis, CA 95616. Life Mem. ASME.

Contributed by the Applied Mechanics Division of THE AMERICAN SOCIETY OF MECHANICAL ENGINEERS for publication in the *ASME JOURNAL OF APPLIED MECHANICS*. Manuscript received by the ASME Applied Mechanics Division, Oct. 25, 1994; final revision, Mar. 28, 1995. Associate Technical Editor: T. R. Akylas.

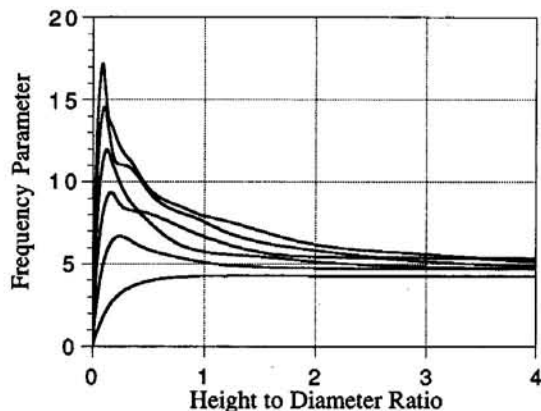


Fig. 1 Frequency spectra for odd modes of circumferential order four

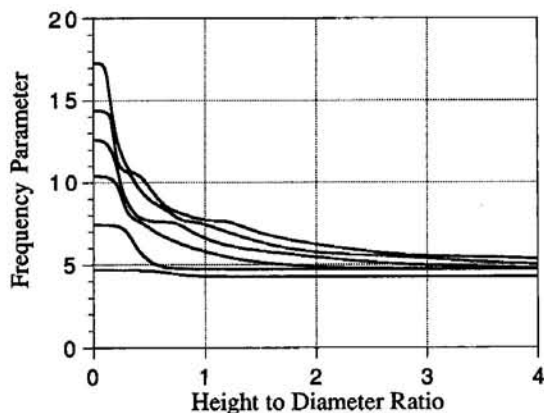


Fig. 2 Frequency spectra for even modes of circumferential order four

In the previous paper there was an error in the plots for circumferential order four. The error was caused by a defective subroutine for computation of the modified Bessel Functions. The subroutine gave correct answers for circumferential order of zero, one, and two. It had the potential of causing problems for circumferential order three, but did not cause any trouble in the range considered. For circumferential order four, however, it caused a number of false roots to be predicted. The errant subroutine has been replaced and the program works well for all cases tried.

Results were found for the six lowest frequencies corresponding to both the even and odd modes, for height-to-diameter

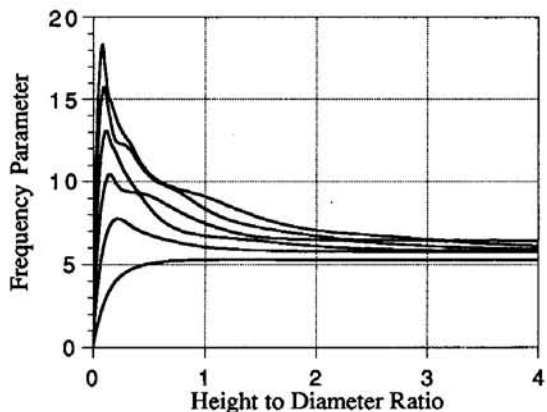


Fig. 3 Frequency spectra for odd modes of circumferential order five

BRIEF NOTES

taken by the program manager, Dr. L. Kabacoff, in the evolution of this work is gratefully acknowledged.

References

Bishop, J. E., and Kinra, V. K., 1994, "Elastothermodynamic Damping in Composite Plates," *Proceedings of the 1994 ASME International Mechanical Engineering Congress and Exposition*, accepted for publication.

Hashin, Z., and Rosen, B. W., 1964, "The Elastic Moduli of Fiber-Reinforced Materials," *ASME JOURNAL OF APPLIED MECHANICS*, Vol. 31, No. 1, pp. 223-232.

Kinra, V. K., and Milligan, K. B., 1994, "A Second-Law Analysis of Thermoelastic Damping," *ASME JOURNAL OF APPLIED MECHANICS*, Vol. 61, No. 1, pp. 71-76.

Milligan, K. B., and Kinra, V. K., 1994, "Elastothermodynamic Damping of Fiber-Reinforced Metal-Matrix Composites," *ASME JOURNAL OF APPLIED MECHANICS*, accepted for publication.

Milligan, K. B., 1994, "A Second-Law Analysis of Elastothermodynamic Damping," Ph.D. Dissertation, Texas A&M University, College Station, TX.

Vibrations of Solid Cylinders Revisited

J. R. Hutchinson¹²

This brief note is a revisit to my previous paper on this subject, Hutchinson (1980). The reason for this revisit is three-fold:

- to correct an error in the plots shown for the circumferential order four.
- to extend the range of the graphical data shown in the original paper.
- to consider modes of higher circumferential order.

In the referenced paper the solution of the governing three-dimensional equations of linear elasticity together with appropriate boundary conditions is found by forming three series of exact solutions of the governing equations which also identically satisfy three of the boundary conditions. The remaining three boundary conditions are satisfied by orthogonalization on the boundary. The solution process leads to a matrix eigenvalue problem with the order of the matrix being the number of the terms in one of the series.

Solutions are split into "even" and "odd" functions. The even functions are defined as those that have the radial and tangential displacements as even functions of the axial coordinate and the axial displacement as an odd function of the axial coordinate. For example, for small thickness to diameter ratio the odd modes are the plate bending modes. The parameters in the problem are the frequency parameter, the height-to-diameter ratio, the circumferential order, and Poisson's ratio. The dimensionless frequency parameter is the frequency times the radius divided by the shear wave velocity.

¹² Civil and Environmental Engineering Department, University of California, Davis, CA 95616. Life Mem. ASME.

Contributed by the Applied Mechanics Division of THE AMERICAN SOCIETY OF MECHANICAL ENGINEERS for publication in the *ASME JOURNAL OF APPLIED MECHANICS*. Manuscript received by the ASME Applied Mechanics Division, Oct. 25, 1994; final revision, Mar. 28, 1995. Associate Technical Editor: T. R. Akylas.

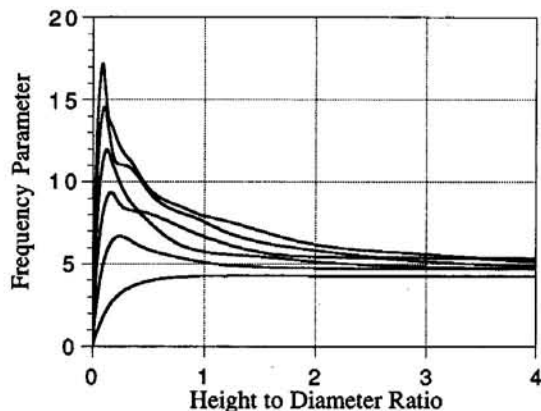


Fig. 1 Frequency spectra for odd modes of circumferential order four

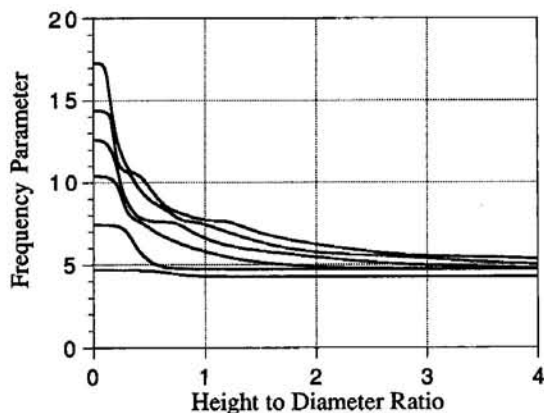


Fig. 2 Frequency spectra for even modes of circumferential order four

In the previous paper there was an error in the plots for circumferential order four. The error was caused by a defective subroutine for computation of the modified Bessel Functions. The subroutine gave correct answers for circumferential order of zero, one, and two. It had the potential of causing problems for circumferential order three, but did not cause any trouble in the range considered. For circumferential order four, however, it caused a number of false roots to be predicted. The errant subroutine has been replaced and the program works well for all cases tried.

Results were found for the six lowest frequencies corresponding to both the even and odd modes, for height-to-diameter

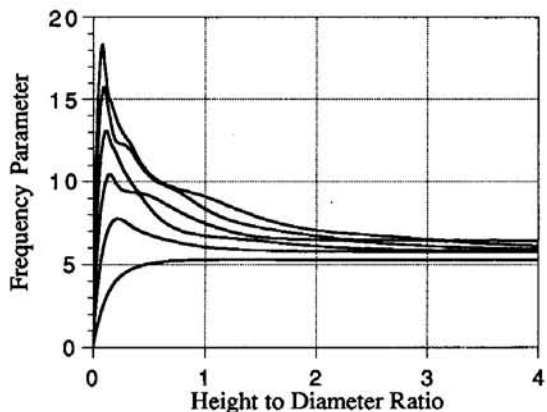


Fig. 3 Frequency spectra for odd modes of circumferential order five

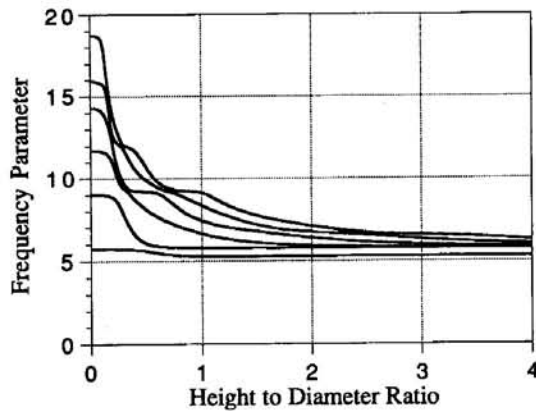


Fig. 4 Frequency spectra for even modes of circumferential order five

On Young's Modulus for Anisotropic Media

P. Boulanger¹³ and M. Hayes¹⁴

If a piece of homogeneous anisotropic elastic material is subject to simple tension along a direction \mathbf{n} for which Young's modulus $E(\mathbf{n})$ is an extremum, then the corresponding strain field is coaxial with the simple tension stress field. An appropriate set of rectangular cartesian coordinate axes may be introduced such that three of the elastic compliances are zero. In this coordinate system the displacement field may be written explicitly and corresponds to a pure homogeneous deformation.

1 Introduction

Within the context of linearized elasticity theory let the constitutive equation for a homogeneous anisotropic elastic material be

$$e_{ij} = S_{ijkl}t_{kl}, \quad (1)$$

where e_{ij} are strain components, S_{ijkl} are the compliances, assumed to be constant and to have the symmetries

$$S_{ijkl} = S_{jikl} = S_{ijlk} = S_{klij}, \quad (2)$$

and t_{kl} are the stress components.

Let

$$t_{ij} = Tn_i n_j, \quad n_i n_i = 1, \quad (3)$$

where T is a constant. This corresponds to simple tension of amount T in the direction \mathbf{n} . Then

$$e_{ij} = TS_{ijkl}n_k n_l \quad (4)$$

¹³ Département de Mathématique, Université Libre de Bruxelles, Campus Plaine C.P.218/1, 1050 Bruxelles, Belgium.

¹⁴ Department of Mathematical Physics, University College Dublin, Belfield, Dublin 4, Ireland.

Contributed by the Applied Mechanics Division of THE AMERICAN SOCIETY OF MECHANICAL ENGINEERS for publication in the ASME JOURNAL OF APPLIED MECHANICS. Manuscript received and accepted by the ASME Applied Mechanics Division, Nov. 21, 1994. Associate Technical Editor: X. Markenscoff.

ratios from zero to four, and circumferential wave numbers from zero to nine. Since the previous results for circumferential order zero to three were correctly shown and because results for circumferential order four through nine are similar, only the plots for circumferential order four and five are shown (Figs. 1–4). These plots are for a Poisson's ratio of 0.300, however, the effect of Poisson's ratio is slight for the modes of circumferential order four and five. A Poisson's ratio of 0.250 produces frequency parameters which are between 0.0 percent and 3.2 percent lower than for a Poisson's ratio of 0.300. A Poisson's ratio of 0.350 produces frequency parameters which are between 0.0 percent and 3.5 percent higher than for a Poisson's ratio of 0.300. For height-to-diameter ratios greater than about 1.25, the discrepancy is less than one percent. The frequency spectra curves for this range of Poisson's ratio are almost identical in shape.

Reference

Hutchinson, J. R., 1980, "Vibrations of Solid Cylinders," ASME JOURNAL OF APPLIED MECHANICS, Vol. 47, pp. 901–907.

and $e(\mathbf{n}) = e_{ij}n_i n_j$, the change in length per unit initial length of an element along \mathbf{n} in the undeformed state, is given by

$$e(\mathbf{n}) = e_{ij}n_i n_j = TS_{ijkl}n_i n_j n_k n_l. \quad (5)$$

Young's modulus $E(\mathbf{n})$, defined by $T = E(\mathbf{n})e(\mathbf{n})$, is given by (Love, 1927; Sirotine and Chaskolskaia, 1984)

$$E(\mathbf{n}) = 1/(S_{ijkl}n_i n_j n_k n_l). \quad (6)$$

The strain-energy density per unit mass W is given by

$$2W = t_{ij}e_{ij}. \quad (7)$$

It is assumed that W is positive. In the present case

$$2W = Te(\mathbf{n}) = T^2/E(\mathbf{n}) \quad (8)$$

so that $E(\mathbf{n}) > 0$. It may be noted for a given tension T , that the energy density W is maximum for a direction \mathbf{n} when the Young's modulus $E(\mathbf{n})$ is least and W is minimum for a direction \mathbf{n} for which $E(\mathbf{n})$ is greatest.

2 Extrema of $E(\mathbf{n})$

In order to determine those directions \mathbf{n} for which $E(\mathbf{n})$ is an extremum we write

$$E(\mathbf{n}) = \frac{1}{S_{ijkl}n_i n_j n_k n_l} + 2\lambda(n_j n_j - 1), \quad (9)$$

where λ is a Lagrange multiplier. Differentiating (9) with respect to n_p , equating to zero and using the symmetries (2), gives

$$E(\mathbf{n})S_{ijkl}n_j n_k n_l = n_i. \quad (10)$$

Equation (10) has a similar structure to the equation determining those directions \mathbf{n} for which a purely longitudinal wave may propagate (Fedorov, 1968; Kolodner, 1966; Truesdell, 1966). It possesses at least two solutions.

3 Displacement Field

Without loss of generality we assume that a direction \mathbf{n} for which (10) has a solution is along Ox_3 . Thus $n_i = \delta_{i3}$ and

$$t_{ij} = T\delta_{i3}\delta_{j3}, \quad e_{ij} = TS_{ij33}. \quad (11)$$

From (10)

$$E(\mathbf{n})S_{i333} = \delta_{i3}, \quad (12)$$

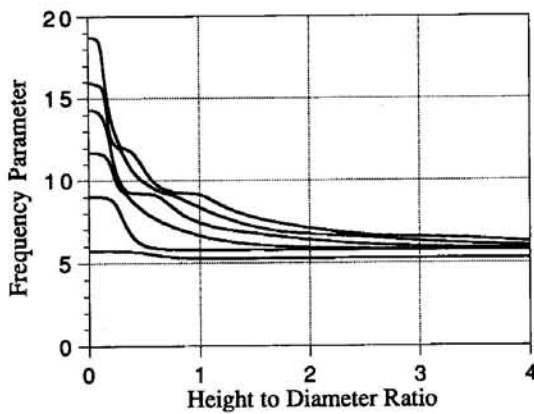


Fig. 4 Frequency spectra for even modes of circumferential order five

On Young's Modulus for Anisotropic Media

P. Boulanger¹³ and M. Hayes¹⁴

If a piece of homogeneous anisotropic elastic material is subject to simple tension along a direction \mathbf{n} for which Young's modulus $E(\mathbf{n})$ is an extremum, then the corresponding strain field is coaxial with the simple tension stress field. An appropriate set of rectangular cartesian coordinate axes may be introduced such that three of the elastic compliances are zero. In this coordinate system the displacement field may be written explicitly and corresponds to a pure homogeneous deformation.

1 Introduction

Within the context of linearized elasticity theory let the constitutive equation for a homogeneous anisotropic elastic material be

$$e_{ij} = S_{ijkl}t_{kl}, \quad (1)$$

where e_{ij} are strain components, S_{ijkl} are the compliances, assumed to be constant and to have the symmetries

$$S_{ijkl} = S_{jikl} = S_{ijlk} = S_{klij}, \quad (2)$$

and t_{kl} are the stress components.

Let

$$t_{ij} = Tn_i n_j, \quad n_i n_i = 1, \quad (3)$$

where T is a constant. This corresponds to simple tension of amount T in the direction \mathbf{n} . Then

$$e_{ij} = TS_{ijkl}n_k n_l \quad (4)$$

¹³ Département de Mathématique, Université Libre de Bruxelles, Campus Plaine C.P.218/1, 1050 Bruxelles, Belgium.

¹⁴ Department of Mathematical Physics, University College Dublin, Belfield, Dublin 4, Ireland.

Contributed by the Applied Mechanical Division of THE AMERICAN SOCIETY OF MECHANICAL ENGINEERS for publication in the ASME JOURNAL OF APPLIED MECHANICS. Manuscript received and accepted by the ASME Applied Mechanics Division, Nov. 21, 1994. Associate Technical Editor: X. Markenscoff.

ratios from zero to four, and circumferential wave numbers from zero to nine. Since the previous results for circumferential order zero to three were correctly shown and because results for circumferential order four through nine are similar, only the plots for circumferential order four and five are shown (Figs. 1–4). These plots are for a Poisson's ratio of 0.300, however, the effect of Poisson's ratio is slight for the modes of circumferential order four and five. A Poisson's ratio of 0.250 produces frequency parameters which are between 0.0 percent and 3.2 percent lower than for a Poisson's ratio of 0.300. A Poisson's ratio of 0.350 produces frequency parameters which are between 0.0 percent and 3.5 percent higher than for a Poisson's ratio of 0.300. For height-to-diameter ratios greater than about 1.25, the discrepancy is less than one percent. The frequency spectra curves for this range of Poisson's ratio are almost identical in shape.

Reference

Hutchinson, J. R., 1980, "Vibrations of Solid Cylinders," ASME JOURNAL OF APPLIED MECHANICS, Vol. 47, pp. 901–907.

and $e(\mathbf{n}) = e_{ij}n_i n_j$, the change in length per unit initial length of an element along \mathbf{n} in the undeformed state, is given by

$$e(\mathbf{n}) = e_{ij}n_i n_j = TS_{ijkl}n_i n_j n_k n_l. \quad (5)$$

Young's modulus $E(\mathbf{n})$, defined by $T = E(\mathbf{n})e(\mathbf{n})$, is given by (Love, 1927; Sirotine and Chaskolskaia, 1984)

$$E(\mathbf{n}) = 1/(S_{ijkl}n_i n_j n_k n_l). \quad (6)$$

The strain-energy density per unit mass W is given by

$$2W = t_{ij}e_{ij}. \quad (7)$$

It is assumed that W is positive. In the present case

$$2W = Te(\mathbf{n}) = T^2/E(\mathbf{n}) \quad (8)$$

so that $E(\mathbf{n}) > 0$. It may be noted for a given tension T , that the energy density W is maximum for a direction \mathbf{n} when the Young's modulus $E(\mathbf{n})$ is least and W is minimum for a direction \mathbf{n} for which $E(\mathbf{n})$ is greatest.

2 Extrema of $E(\mathbf{n})$

In order to determine those directions \mathbf{n} for which $E(\mathbf{n})$ is an extremum we write

$$E(\mathbf{n}) = \frac{1}{S_{ijkl}n_i n_j n_k n_l} + 2\lambda(n_j n_j - 1), \quad (9)$$

where λ is a Lagrange multiplier. Differentiating (9) with respect to n_p , equating to zero and using the symmetries (2), gives

$$E(\mathbf{n})S_{ijkl}n_j n_k n_l = n_i. \quad (10)$$

Equation (10) has a similar structure to the equation determining those directions \mathbf{n} for which a purely longitudinal wave may propagate (Fedorov, 1968; Kolodner, 1966; Truesdell, 1966). It possesses at least two solutions.

3 Displacement Field

Without loss of generality we assume that a direction \mathbf{n} for which (10) has a solution is along Ox_3 . Thus $n_i = \delta_{i3}$ and

$$t_{ij} = T\delta_{i3}\delta_{j3}, \quad e_{ij} = TS_{ij33}. \quad (11)$$

From (10)

$$E(\mathbf{n})S_{i333} = \delta_{i3}, \quad (12)$$

BRIEF NOTES

and hence

$$S_{1333} = 0, \quad S_{2333} = 0. \quad (13)$$

Then, from (11),

$$e_{13} = e_{23} = 0. \quad (14)$$

It follows that the strain tensor \mathbf{e} , with components e_{ij} , is coaxial with the stress tensor \mathbf{t} , with components t_{ij} . Indeed, the principal axes of \mathbf{e} are along \mathbf{n} and two orthogonal directions, in the x_1x_2 -plane, which depend upon the values of e_{11} , e_{22} , e_{12} . These axes are also principal axes of \mathbf{t} — but not conversely, because the principal axes of \mathbf{t} are along \mathbf{n} and two arbitrary directions in the x_1x_2 -plane.

A new set of rectangular cartesian axes $Ox'_1x'_2x'_3$ is now introduced. These are chosen to be the principal axes of \mathbf{e} and are obtained by rotating the set $Ox_1x_2x_3$ about Ox_3 through an angle θ given by (Norris, 1989)

$$\tan 2\theta = \frac{2S_{3312}}{S_{3311} - S_{3322}}, \quad (15)$$

so that

$$\begin{aligned} x'_3 &= x_3, \\ x'_1 &= x_1 \cos \theta + x_2 \sin \theta, \\ x'_2 &= -x_1 \sin \theta + x_2 \cos \theta. \end{aligned} \quad (16)$$

In the new system

$$S'_{3312} = 0. \quad (17)$$

Also, using (13),

$$S'_{3313} = S'_{3323} = 0. \quad (18)$$

Thus three of the compliances are zero in the $Ox'_1x'_2x'_3$ system. Hence

$$e'_{12} = e'_{13} = e'_{23} = 0, \quad (19)$$

$$e'_{11} = TS'_{1133}, \quad e'_{22} = TS'_{2233}, \quad e'_{33} = TS'_{3333}, \quad (20)$$

Thus, ignoring rigid-body deformations, it follows that the displacement components u'_i in the $Ox'_1x'_2x'_3$ system are given by the pure homogeneous deformation

$$u'_1 = TS'_{1133}x'_1, \quad u'_2 = TS'_{2233}x'_2, \quad u'_3 = TS'_{3333}x'_3. \quad (21)$$

References

- Fedorov, F. I., 1968, *Theory of elastic waves in crystals* (translated by J. E. S. Bradley), Plenum Press, New York, Chapter 3 pp. 101–102.
- Kolodner, I., 1966, "Existence of longitudinal waves in anisotropic media," *Journal of the Acoustical Society of America*, Vol. 40, pp. 730–731.
- Love, A. E. H., 1927, *Mathematical theory of elasticity*, 4th ed., Cambridge University Press, Cambridge, U.K., pp. 107–108.
- Norris, A., 1989, "On the acoustic determination of the elastic moduli of anisotropic solids and acoustic conditions for the existence of symmetry planes," *Quarterly Journal of Mechanics and Applied Mathematics*, Vol. 42, pp. 413–426.
- Sirotine, Y., and Chaskolskaia, M., 1984, *Fondements de la physique des cristaux*, Editors MIR, Moscou, pp. 179–183.
- Truesdell, C., 1966, "Existence of longitudinal waves," *Journal of the Acoustical Society of America*, Vol. 40, pp. 729–730.

On Kinematical Conditions for Steady Motions of Strings and Rods

T. R. Nordenholz^{15,17} and O. M. O'Reilly^{16,17}

Introduction

The purpose of this note is to establish the necessity and sufficiency of a representation for particular motions of rod-like bodies which are modeled as directed curves. These motions are defined by three conditions and are referred to here as steady. The result is valid for a body modeled using an arbitrary number of deformable directors. Although the result includes strings as a special case,¹⁸ we find it convenient to establish the result for strings first. The representation is useful for formulating boundary value problems for drawn rods.

The vast majority of studies on steady motions of strings and rods have used an inextensible constrained rod theory or an inextensible string theory. For theories of this type, the position vector \mathbf{r} of a material point during a steady motion has the representation

$$\mathbf{r} = \mathbf{r}(\theta, t) = \mathbf{F}(\theta + ct), \quad (1)$$

where the convected coordinate θ uniquely identifies a material

point, c is the constant speed of the material point as it moves along a fixed space curve C and $\theta + ct$ may be conveniently identified as the arc-length parameter of C (cf., e.g., Cohen and Epstein (1994) or Wickert and Mote (1990)). For these particular constrained theories, the representation (1) is regarded as classical. For nonlinearly elastic strings it is easy to see that a representation of the form (1) represents a steady motion of the string and this has motivated several successful semi-inverse type analyses (cf., e.g., Healey and Papadopoulos (1990) or O'Reilly and Varadi (1995)). However, it is not clear exactly what class of motions is encompassed by representations of the form (1). We will show that motions of the form (1) are necessarily steady motions, as defined by Green and Laws (1968, section 4), for rod-like bodies which are modeled using a string or directed theory. In other words, a representation of the form (1) encompasses all steady motions as defined by Green and Laws.

The reader is referred to the review article by Naghdi (1982) for relevant background information and references on directed theories of rods. Further details, pertaining to constrained rod theories, are contained in Naghdi and Rubin (1984).

Strings

A string is modeled as a deformable material curve \mathcal{L} whose motion is specified by a vector valued function $\mathbf{r} = \mathbf{r}(\theta, t)$. This function uniquely identifies the location of a material point at a given instant t , where the material point is uniquely identified by the convected coordinate θ . For future purposes we define a fixed space curve C which has the parametric representation

$$\mathbf{m} = \mathbf{m}(\xi) = x(\xi)\mathbf{e}_x + y(\xi)\mathbf{e}_y + z(\xi)\mathbf{e}_z, \quad (2)$$

where ξ is a suitably chosen coordinate which uniquely identifies points on C .

The motion of interest is assumed to satisfy three conditions:

¹⁵ Graduate Student.

¹⁶ Assistant Professor. Assoc. Mem. ASME.

¹⁷ Department of Mechanical Engineering, University of California at Berkeley, Berkeley, CA 94720-1740.

¹⁸ We recall that a string theory can be obtained as a special case of directed rod theory by, among others, omitting the director fields.

Contributed by the Applied Mechanics Division of THE AMERICAN SOCIETY OF MECHANICAL ENGINEERS for publication in the ASME JOURNAL OF APPLIED MECHANICS. Manuscript received by the ASME Applied Mechanics Division, Nov. 21, 1994; final revision, Mar. 27, 1995. Associate Technical Editor: S. W. Shaw.

BRIEF NOTES

and hence

$$S_{1333} = 0, \quad S_{2333} = 0. \quad (13)$$

Then, from (11),

$$e_{13} = e_{23} = 0. \quad (14)$$

It follows that the strain tensor \mathbf{e} , with components e_{ij} , is coaxial with the stress tensor \mathbf{t} , with components t_{ij} . Indeed, the principal axes of \mathbf{e} are along \mathbf{n} and two orthogonal directions, in the x_1x_2 -plane, which depend upon the values of e_{11} , e_{22} , e_{12} . These axes are also principal axes of \mathbf{t} — but not conversely, because the principal axes of \mathbf{t} are along \mathbf{n} and two arbitrary directions in the x_1x_2 -plane.

A new set of rectangular cartesian axes $Ox'_1x'_2x'_3$ is now introduced. These are chosen to be the principal axes of \mathbf{e} and are obtained by rotating the set $Ox_1x_2x_3$ about Ox_3 through an angle θ given by (Norris, 1989)

$$\tan 2\theta = \frac{2S_{3312}}{S_{3311} - S_{3322}}, \quad (15)$$

so that

$$\begin{aligned} x'_3 &= x_3, \\ x'_1 &= x_1 \cos \theta + x_2 \sin \theta, \\ x'_2 &= -x_1 \sin \theta + x_2 \cos \theta. \end{aligned} \quad (16)$$

In the new system

$$S'_{3312} = 0. \quad (17)$$

Also, using (13),

$$S'_{3313} = S'_{3323} = 0. \quad (18)$$

Thus three of the compliances are zero in the $Ox'_1x'_2x'_3$ system. Hence

$$e'_{12} = e'_{13} = e'_{23} = 0, \quad (19)$$

$$e'_{11} = TS'_{1133}, \quad e'_{22} = TS'_{2233}, \quad e'_{33} = TS'_{3333}, \quad (20)$$

Thus, ignoring rigid-body deformations, it follows that the displacement components u'_i in the $Ox'_1x'_2x'_3$ system are given by the pure homogeneous deformation

$$u'_1 = TS'_{1133}x'_1, \quad u'_2 = TS'_{2233}x'_2, \quad u'_3 = TS'_{3333}x'_3. \quad (21)$$

References

- Fedorov, F. I., 1968, *Theory of elastic waves in crystals* (translated by J. E. S. Bradley), Plenum Press, New York, Chapter 3 pp. 101–102.
- Kolodner, I., 1966, "Existence of longitudinal waves in anisotropic media," *Journal of the Acoustical Society of America*, Vol. 40, pp. 730–731.
- Love, A. E. H., 1927, *Mathematical theory of elasticity*, 4th ed., Cambridge University Press, Cambridge, U.K., pp. 107–108.
- Norris, A., 1989, "On the acoustic determination of the elastic moduli of anisotropic solids and acoustic conditions for the existence of symmetry planes," *Quarterly Journal of Mechanics and Applied Mathematics*, Vol. 42, pp. 413–426.
- Sirotine, Y., and Chaskolskaia, M., 1984, *Fondements de la physique des cristaux*, Editors MIR, Moscou, pp. 179–183.
- Truesdell, C., 1966, "Existence of longitudinal waves," *Journal of the Acoustical Society of America*, Vol. 40, pp. 729–730.

On Kinematical Conditions for Steady Motions of Strings and Rods

T. R. Nordenholz^{15,17} and O. M. O'Reilly^{16,17}

Introduction

The purpose of this note is to establish the necessity and sufficiency of a representation for particular motions of rod-like bodies which are modeled as directed curves. These motions are defined by three conditions and are referred to here as steady. The result is valid for a body modeled using an arbitrary number of deformable directors. Although the result includes strings as a special case,¹⁸ we find it convenient to establish the result for strings first. The representation is useful for formulating boundary value problems for drawn rods.

The vast majority of studies on steady motions of strings and rods have used an inextensible constrained rod theory or an inextensible string theory. For theories of this type, the position vector \mathbf{r} of a material point during a steady motion has the representation

$$\mathbf{r} = \mathbf{r}(\theta, t) = \mathbf{F}(\theta + ct), \quad (1)$$

where the convected coordinate θ uniquely identifies a material

point, c is the constant speed of the material point as it moves along a fixed space curve C and $\theta + ct$ may be conveniently identified as the arc-length parameter of C (cf., e.g., Cohen and Epstein (1994) or Wickert and Mote (1990)). For these particular constrained theories, the representation (1) is regarded as classical. For nonlinearly elastic strings it is easy to see that a representation of the form (1) represents a steady motion of the string and this has motivated several successful semi-inverse type analyses (cf., e.g., Healey and Papadopoulos (1990) or O'Reilly and Varadi (1995)). However, it is not clear exactly what class of motions is encompassed by representations of the form (1). We will show that motions of the form (1) are necessarily steady motions, as defined by Green and Laws (1968, section 4), for rod-like bodies which are modeled using a string or directed theory. In other words, a representation of the form (1) encompasses all steady motions as defined by Green and Laws.

The reader is referred to the review article by Naghdi (1982) for relevant background information and references on directed theories of rods. Further details, pertaining to constrained rod theories, are contained in Naghdi and Rubin (1984).

Strings

A string is modeled as a deformable material curve \mathcal{L} whose motion is specified by a vector valued function $\mathbf{r} = \mathbf{r}(\theta, t)$. This function uniquely identifies the location of a material point at a given instant t , where the material point is uniquely identified by the convected coordinate θ . For future purposes we define a fixed space curve C which has the parametric representation

$$\mathbf{m} = \mathbf{m}(\xi) = x(\xi)\mathbf{e}_x + y(\xi)\mathbf{e}_y + z(\xi)\mathbf{e}_z, \quad (2)$$

where ξ is a suitably chosen coordinate which uniquely identifies points on C .

The motion of interest is assumed to satisfy three conditions:

¹⁵ Graduate Student.

¹⁶ Assistant Professor. Assoc. Mem. ASME.

¹⁷ Department of Mechanical Engineering, University of California at Berkeley, Berkeley, CA 94720-1740.

¹⁸ We recall that a string theory can be obtained as a special case of directed rod theory by, among others, omitting the director fields.

Contributed by the Applied Mechanics Division of THE AMERICAN SOCIETY OF MECHANICAL ENGINEERS for publication in the ASME JOURNAL OF APPLIED MECHANICS. Manuscript received by the ASME Applied Mechanics Division, Nov. 21, 1994; final revision, Mar. 27, 1995. Associate Technical Editor: S. W. Shaw.

- (i) The material curve \mathcal{L} moves along a fixed curve C .
- (ii) The velocity vector \mathbf{v} of a material point of \mathcal{L} is a function of ξ only.
- (iii) The vector $\partial \mathbf{r} / \partial \theta$ is a function of ξ only.

As in Green and Laws (1968), a steady motion of \mathcal{L} is defined by conditions (i)-(iii).

It was noted by Green and Laws that steady motions in the sense used here do not encompass all three-dimensional steady motions as defined by Truesdell and Toupin (1960, section 67), for instance. In this respect, it is illustrative to consider a motion which is steady in the three-dimensional sense but which is not steady in the sense used here. Suppose an infinitely long string is being stretched during the motion

$$\mathbf{r}(\theta, t) = \theta e^{\lambda t} \mathbf{e}_x = \xi \mathbf{e}_x, \quad \lambda > 0. \quad (3)$$

Clearly

$$\mathbf{v} = \mathbf{v}(\xi) = \lambda \xi \mathbf{e}_x, \quad \frac{\partial \mathbf{r}}{\partial \theta} = e^{\lambda t} \mathbf{e}_x, \quad (4)$$

and this motion satisfies conditions (i)-(ii) but not (iii).

With the preliminaries aside, we now establish the desired result for strings. In the course of the proof, the necessary and sufficient functional relationship between θ and ξ for a motion of \mathcal{L} which satisfies conditions (i)-(iii) will be established.

Theorem 1: A motion of a material curve is steady if and only if the position vector \mathbf{r} has the following representations:

$$\mathbf{r} = \mathbf{r}(\theta, t) = \bar{\mathbf{r}}(\theta + ct), \quad (5)$$

where c is a constant.

Proof: We first prove the necessary part of the assertion. Condition (i) and (2) imply that

$$\mathbf{r} = \mathbf{r}(\theta, t) = \mathbf{m} = \mathbf{m}(\xi). \quad (6)$$

This relation and our earlier comments on $\mathbf{r}(\theta, t)$ and $\mathbf{m}(\xi)$ imply the existence of a function $\xi = \xi(\theta, t)$ which at each instant t is invertible: $\theta = \hat{\theta}(\xi, t)$. This permits a different representation for the function \mathbf{r} :

$$\mathbf{r} = \mathbf{r}(\theta, t) = \mathbf{r}(\hat{\theta}(\xi, t), t) = \bar{\mathbf{r}}(\xi). \quad (7)$$

Using (7), we obtain an expression for the velocity of a material point:

$$\mathbf{v} = \frac{\partial \mathbf{r}}{\partial t}(\theta, t) = \frac{\partial \bar{\mathbf{r}}}{\partial \xi} \frac{\partial \xi}{\partial t}(\theta, t) = \tilde{\mathbf{v}}(\xi, t). \quad (8)$$

Imposing condition (ii) on (8), we obtain the relation

$$\frac{\partial \tilde{\mathbf{v}}}{\partial t}(\theta, t) = g_1(\xi). \quad (9)$$

In parallel with the establishment of (9), the restrictions imposed by condition (iii) on (7) are now considered. With the assistance of (7), we first note that

$$\frac{\partial \mathbf{r}}{\partial \theta}(\theta, t) = \frac{\partial \bar{\mathbf{r}}}{\partial \xi} \frac{\partial \xi}{\partial \theta}(\theta, t). \quad (10)$$

Imposing condition (iii), it follows from (10) that

$$\frac{\partial \tilde{\mathbf{v}}}{\partial \theta}(\theta, t) = g_2(\xi). \quad (11)$$

It should be noted for future purposes that the invertibility of ξ implies that $g_2(\xi) \neq 0$.

We next determine the combined consequences of conditions (ii)-(iii) on ξ . First we integrate (11):

$$f(\xi) = \int_{\xi_0}^{\xi} \frac{du}{g_2(u)} = \theta + h(t), \quad (12)$$

where we have subsumed any arbitrary constants into the functions f and h . After noting from (12) that f is invertible, it follows that

$$\xi = \tilde{\xi}(\theta + h(t)). \quad (13)$$

To consider the additional restrictions placed on (13) by condition (ii), we first differentiate (13) with respect to t and then use (12):

$$\frac{\partial \xi}{\partial t} = \tilde{\xi}'(f(\xi)) \frac{dh}{dt}(t), \quad (14)$$

where ' denotes the derivative of $\tilde{\xi}$ with respect to its argument. However from (9), (14) is necessarily independent of t , and hence

$$\frac{dh}{dt} = c, \quad (15)$$

where c is a constant. After combining (13) and (15), it is easy to see that $\xi = \tilde{\xi}(\theta + ct)$. The proof of necessity is completed by substituting this final functional form of ξ into (7) and appropriately redefining $\bar{\mathbf{r}}(\xi)$.

To establish the sufficiency part of the assertion, we first note that (5) implies condition (i) automatically. The remaining conditions, (ii) and (iii), follow trivially.

Rods

We now consider a rod-like body which is modeled using a directed or Cosserat curve. A directed curve is a material curve \mathcal{L} to which a set of N deformable vectors $\mathbf{d}_i = \mathbf{d}_i(\theta, t)$, $i = 1, \dots, N$, at each point θ are defined (cf., e.g., Naghdi, 1982). To establish the desired result for steady motions of a directed curve, it suffices to supplement condition (iii) for the steady motion of the string with the stipulations that the N directors \mathbf{d}_i are functions of ξ only. We note that these conditions are identical to those used by Green and Laws (1968, section 4). The desired result is established with some obvious modifications to the previous proof and is now stated without proof.

Theorem 2: A motion of a directed curve is steady if and only if the position vector \mathbf{r} and the N directors \mathbf{d}_i have the following representations:

$$\begin{aligned} \mathbf{r} &= \mathbf{r}(\theta, t) = \bar{\mathbf{r}}(\theta + ct), \\ \mathbf{d}_i &= \mathbf{d}_i(\theta, t) = \bar{\mathbf{d}}_i(\theta + ct), \end{aligned} \quad (16)$$

where c is a constant.

We note that the parameter c depends on the particular steady motion of interest and the parameterization θ of \mathcal{L} . In general, c is not equal to the speed of the material point.

Acknowledgment

The authors are grateful to Prof. J. Casey for some helpful comments on an earlier version of this work.

References

- Cohen, H., and Epstein, M., 1994, "On a Class of Planar Motions of Flexible Rods," *ASME JOURNAL OF APPLIED MECHANICS*, Vol. 61, pp. 206-208.
- Green, A. E., and Laws, N., 1968, "Ideal Fluid Jets," *International Journal of Engineering Science*, Vol. 6, pp. 317-328.
- Healey, T. J., and Papadopoulos, J. N., 1990, "Steady Axial Motions of Strings," *ASME JOURNAL OF APPLIED MECHANICS*, Vol. 57, pp. 785-787.
- Naghdi, P. M., 1982, "Finite Deformation of Elastic Rods and Shells," *Proceedings of the IUTAM Symposium on Finite Elasticity, Bethlehem PA 1980*.

(edited by D. E. Carlson, and R. T. Shield, eds., Martinus Nijhoff, The Hague, pp. 47-103.

Naghdi, P. M., and Rubin, M. B., 1984, "Constrained Theories of Rods," *Journal of Elasticity*, Vol. 14, pp. 343-361.

O'Reilly, O. M., and Varadi, P., 1995, "Elastic Equilibria of Translating Cables," *Acta Mechanica*, Vol. 108, pp. 189-206.

Truesdell, C., and Toupin, R. A., 1960, "The Classical Field Theories," *S. Flügge's Handbuch der Physik*, Vol. III/1, Springer-Verlag, Berlin, pp. 226-902.

Wickert, J. A., and Mote, C. D., Jr., 1990, "Classical Vibration Analysis of Axially Moving Continua," *ASME JOURNAL OF APPLIED MECHANICS*, Vol. 57, pp. 738-744.

The Shear Center Problem for Nonlinear Material Behavior

E. Reissner¹⁹

In what follows we reconsider a method proposed in Reissner (1992) to generalize the linear-theory determination of shear center coordinates for prismatic beams on the basis of a mixed boundary value problem of three-dimensional elasticity involving prescribed in-plane rigid-body end-displacements $u = U + y\Theta$ and $v = V - x\Theta$, in accordance with Reissner and Tsai (1972), as it has meanwhile been found that the earlier proposal needed to be modified.

With the formulation of the problem and with the notation essentially as in Reissner and Tsai (1972) the question is how to generalize the linear-theory shear center formulas

$$x_s = C_{\Theta Q}/C_{\Theta T}, \quad y_s = -C_{\Theta P}/C_{\Theta T}, \quad (1)$$

which result upon introducing into the third of the three inverted load deflection relations for bending and twisting of end-loaded cantilevers

$$U = C_{UP}P + C_{UQ}Q + C_{UT}T, \quad V = \dots, \\ \Theta = C_{\Theta P}P + C_{\Theta Q}Q + C_{\Theta T}T, \quad (2)$$

the stipulation that the condition

$$\Theta = 0, \quad T = Py_s - Qx_s, \quad (3)$$

be satisfied *identically* in P and Q .

The corresponding nonlinear problem is how to determine shear center coordinates

$$x_s = x_s(P, Q), \quad y_s = y_s(P, Q) \quad (4)$$

for the case that we have in place of (2)

$$U = f_U(P, Q, T), \quad V = f_V(P, Q, T), \\ \Theta = f_{\Theta}(P, Q, T) \quad (5)$$

Evidently, the statement that

$$f_{\Theta}[P, Q, (Py_s - Qx_s)] = 0 \quad (6)$$

identically in P and Q , which is consistent with (2) and (3), does not permit a determination of x_s and y_s as functions of P and Q .

The proposal in Eqs. (18)-(20) of Reissner (1992) was to associate (6) with a requirement that additionally

$$f_{\Theta}\{P + \Delta P, Q + \Delta Q, [(P + \Delta P)(y_s + \Delta y_s) - (Q + \Delta Q)(x_s + \Delta x_s)]\} = 0 \quad (7)$$

identically in terms of infinitesimal ΔP and ΔQ . Equation (7) and (6), were found to lead to two first-order partial differential equations for x_s and y_s which, it should have been seen at the time, do not allow a determination of x_s and y_s as functions of P and Q .

It is now proposed that the appropriate generalization of (3), in place of (7), should have been the less restrictive requirement that

$$f_{\Theta}[P + \Delta P, Q + \Delta Q, (P + \Delta P)y_s - (Q + \Delta Q)x_s] = 0 \quad (8)$$

identically in ΔP and ΔQ . Equation (8) in conjunction with (6) gives the two relations

$$\frac{\partial f_{\Theta}}{\partial P} + y_s \frac{\partial f_{\Theta}}{\partial (Py_s - Qx_s)} = 0, \quad (9a)$$

$$\frac{\partial f_{\Theta}}{\partial Q} - x_s \frac{\partial f_{\Theta}}{\partial (Py_s - Qx_s)} = 0. \quad (9b)$$

These do not involve derivatives of x_s and y_s , but do require the solution of two simultaneous in general *nonlinear* equations for x_s and y_s .

For an explicit example consider a case with

$$f_{\Theta}(P, Q, T) = C_P P + C_Q Q + C_T T + \frac{1}{3} D_T T^3. \quad (10)$$

The introduction of (10) into (9) gives as equations for x_s and y_s

$$C_P + [C_T + D_T(Py_s - Qx_s)^2]y_s = 0, \quad (11a)$$

$$C_Q - [C_T + D_T(Py_s - Qx_s)^2]x_s = 0 \quad (11b)$$

which may be transformed into the decoupled cubic problem

$$C_Q - C_T x_s - \frac{D_T}{C_Q^2} (PC_P + QC_Q)^2 x_s^3 = 0, \quad (12a)$$

$$\frac{y_s}{x_s} = -\frac{C_P}{C_Q}. \quad (12b)$$

The contents of (12) imply that for small P and Q

$$x_s \approx \frac{C_Q}{C_T} - \frac{D_T C_Q}{C_T^4} (C_P P + C_Q Q)^2 \quad (13a)$$

$$y_s \approx -\frac{C_P}{C_T} + \frac{D_T C_P}{C_T^4} (C_P P + C_Q Q)^2. \quad (13b)$$

It turns out that the necessity of having to solve two simultaneous nonlinear equations for x_s and y_s , may be avoided by determining these quantities as functions of the prescribed rigid end translations U and V in place of the resulting end forces P and Q . With load displacement relations

$$P = f_P(U, V), \quad Q = f_Q(U, V), \quad T = f_T(U, V) \quad (14)$$

where $\Theta = 0$ at the outset, one condition for the determination of $x_s(U, V)$ and $y_s(U, V)$ will be, in accordance with (3),

$$f_P(U, V)y_s - f_Q(U, V)x_s = f_T(U, V). \quad (15)$$

In analogy to the step from (6) to (8) it is now stipulated, as a second condition, that

$$f_P(U + \Delta U, V + \Delta V)y_s - f_Q(U + \Delta U, V + \Delta V)x_s \\ = f_T(U + \Delta U, V + \Delta V) \quad (16)$$

¹⁹ Department of Applied Mechanics and Engineering Sciences, University of California, San Diego, CA 92023-0411. Honorary Mem. ASME.

Contributed by the Applied Mechanics Division of THE AMERICAN SOCIETY OF MECHANICAL ENGINEERS for publication in the ASME JOURNAL OF APPLIED MECHANICS. Manuscript received and accepted by the ASME Applied Mechanics Division, Feb. 2, 1995. Associate Technical Editor: W. K. Liu.

(edited by D. E. Carlson, and R. T. Shield, eds., Martinus Nijhoff, The Hague, pp. 47-103.

Naghdi, P. M., and Rubin, M. B., 1984, "Constrained Theories of Rods," *Journal of Elasticity*, Vol. 14, pp. 343-361.

O'Reilly, O. M., and Varadi, P., 1995, "Elastic Equilibria of Translating Cables," *Acta Mechanica*, Vol. 108, pp. 189-206.

Truesdell, C., and Toupin, R. A., 1960, "The Classical Field Theories," *S. Flügge's Handbuch der Physik*, Vol. III/1, Springer-Verlag, Berlin, pp. 226-902.

Wickert, J. A., and Mote, C. D., Jr., 1990, "Classical Vibration Analysis of Axially Moving Continua," *ASME JOURNAL OF APPLIED MECHANICS*, Vol. 57, pp. 738-744.

The Shear Center Problem for Nonlinear Material Behavior

E. Reissner¹⁹

In what follows we reconsider a method proposed in Reissner (1992) to generalize the linear-theory determination of shear center coordinates for prismatic beams on the basis of a mixed boundary value problem of three-dimensional elasticity involving prescribed in-plane rigid-body end-displacements $u = U + y\Theta$ and $v = V - x\Theta$, in accordance with Reissner and Tsai (1972), as it has meanwhile been found that the earlier proposal needed to be modified.

With the formulation of the problem and with the notation essentially as in Reissner and Tsai (1972) the question is how to generalize the linear-theory shear center formulas

$$x_s = C_{\Theta Q}/C_{\Theta T}, \quad y_s = -C_{\Theta P}/C_{\Theta T}, \quad (1)$$

which result upon introducing into the third of the three inverted load deflection relations for bending and twisting of end-loaded cantilevers

$$U = C_{UP}P + C_{UQ}Q + C_{UT}T, \quad V = \dots, \\ \Theta = C_{\Theta P}P + C_{\Theta Q}Q + C_{\Theta T}T, \quad (2)$$

the stipulation that the condition

$$\Theta = 0, \quad T = Py_s - Qx_s, \quad (3)$$

be satisfied *identically* in P and Q .

The corresponding nonlinear problem is how to determine shear center coordinates

$$x_s = x_s(P, Q), \quad y_s = y_s(P, Q) \quad (4)$$

for the case that we have in place of (2)

$$U = f_U(P, Q, T), \quad V = f_V(P, Q, T), \\ \Theta = f_{\Theta}(P, Q, T) \quad (5)$$

Evidently, the statement that

$$f_{\Theta}[P, Q, (Py_s - Qx_s)] = 0 \quad (6)$$

identically in P and Q , which is consistent with (2) and (3), does not permit a determination of x_s and y_s as functions of P and Q .

The proposal in Eqs. (18)-(20) of Reissner (1992) was to associate (6) with a requirement that additionally

$$f_{\Theta}\{P + \Delta P, Q + \Delta Q, [(P + \Delta P)(y_s + \Delta y_s) - (Q + \Delta Q)(x_s + \Delta x_s)]\} = 0 \quad (7)$$

identically in terms of infinitesimal ΔP and ΔQ . Equation (7) and (6), were found to lead to two first-order partial differential equations for x_s and y_s which, it should have been seen at the time, do not allow a determination of x_s and y_s as functions of P and Q .

It is now proposed that the appropriate generalization of (3), in place of (7), should have been the less restrictive requirement that

$$f_{\Theta}[P + \Delta P, Q + \Delta Q, (P + \Delta P)y_s - (Q + \Delta Q)x_s] = 0 \quad (8)$$

identically in ΔP and ΔQ . Equation (8) in conjunction with (6) gives the two relations

$$\frac{\partial f_{\Theta}}{\partial P} + y_s \frac{\partial f_{\Theta}}{\partial (Py_s - Qx_s)} = 0, \quad (9a)$$

$$\frac{\partial f_{\Theta}}{\partial Q} - x_s \frac{\partial f_{\Theta}}{\partial (Py_s - Qx_s)} = 0. \quad (9b)$$

These do not involve derivatives of x_s and y_s , but do require the solution of two simultaneous in general *nonlinear* equations for x_s and y_s .

For an explicit example consider a case with

$$f_{\Theta}(P, Q, T) = C_P P + C_Q Q + C_T T + \frac{1}{3} D_T T^3. \quad (10)$$

The introduction of (10) into (9) gives as equations for x_s and y_s

$$C_P + [C_T + D_T(Py_s - Qx_s)^2]y_s = 0, \quad (11a)$$

$$C_Q - [C_T + D_T(Py_s - Qx_s)^2]x_s = 0 \quad (11b)$$

which may be transformed into the decoupled cubic problem

$$C_Q - C_T x_s - \frac{D_T}{C_Q^2} (PC_P + QC_Q)^2 x_s^3 = 0, \quad (12a)$$

$$\frac{y_s}{x_s} = -\frac{C_P}{C_Q}. \quad (12b)$$

The contents of (12) imply that for small P and Q

$$x_s \approx \frac{C_Q}{C_T} - \frac{D_T C_Q}{C_T^4} (C_P P + C_Q Q)^2 \quad (13a)$$

$$y_s \approx -\frac{C_P}{C_T} + \frac{D_T C_P}{C_T^4} (C_P P + C_Q Q)^2. \quad (13b)$$

It turns out that the necessity of having to solve two simultaneous nonlinear equations for x_s and y_s , may be avoided by determining these quantities as functions of the prescribed rigid end translations U and V in place of the resulting end forces P and Q . With load displacement relations

$$P = f_P(U, V), \quad Q = f_Q(U, V), \quad T = f_T(U, V) \quad (14)$$

where $\Theta = 0$ at the outset, one condition for the determination of $x_s(U, V)$ and $y_s(U, V)$ will be, in accordance with (3),

$$f_P(U, V)y_s - f_Q(U, V)x_s = f_T(U, V). \quad (15)$$

In analogy to the step from (6) to (8) it is now stipulated, as a second condition, that

$$f_P(U + \Delta U, V + \Delta V)y_s - f_Q(U + \Delta U, V + \Delta V)x_s = f_T(U + \Delta U, V + \Delta V) \quad (16)$$

¹⁹ Department of Applied Mechanics and Engineering Sciences, University of California, San Diego, CA 92023-0411. Honorary Mem. ASME.

Contributed by the Applied Mechanics Division of THE AMERICAN SOCIETY OF MECHANICAL ENGINEERS for publication in the ASME JOURNAL OF APPLIED MECHANICS. Manuscript received and accepted by the ASME Applied Mechanics Division, Feb. 2, 1995. Associate Technical Editor: W. K. Liu.

identically in terms of ΔU and ΔV . From (15) and (16) follows as a system of two simultaneous linear equations for the determination of x_s and y_s

$$\frac{\partial f_P}{\partial U} y_s - \frac{\partial f_Q}{\partial U} x_s = \frac{\partial f_T}{\partial U}, \quad \frac{\partial f_P}{\partial V} y_s - \frac{\partial f_Q}{\partial V} x_s = \frac{\partial f_T}{\partial V} \quad (17)$$

with the linear-theory relations in terms of stiffness coefficients

$$K_{PU}y_s - K_{QU}x_s = K_{TU}, \quad K_{PV}y_s - K_{QV}x_s = K_{TV}, \quad (18)$$

in Reissner (1979) as a special case.

The fact that the consequences of (17) are consistent with the consequences of (9) may be seen as follows. An introduction of x_s and y_s from (9) into (17) gives as consistency conditions the two relations

$$\frac{\partial f_P}{\partial U} \frac{\partial f_\Theta}{\partial P} + \frac{\partial f_Q}{\partial U} \frac{\partial f_\Theta}{\partial Q} + \frac{\partial f_T}{\partial U} \frac{\partial f_\Theta}{\partial T} = 0 \quad (19a)$$

$$\frac{\partial f_P}{\partial V} \frac{\partial f_\Theta}{\partial P} + \frac{\partial f_Q}{\partial V} \frac{\partial f_\Theta}{\partial Q} + \frac{\partial f_T}{\partial V} \frac{\partial f_\Theta}{\partial T} = 0. \quad (19b)$$

Seeing that (19a,b) does in fact hold follows as a consequence

of (5) and (14), in conjunction with the stipulation $\Theta = 0$, and the stipulation that

$$\begin{aligned} \nabla \Theta = 0 &= \frac{\partial f_\Theta}{\partial P} \Delta P + \frac{\partial f_\Theta}{\partial Q} \Delta Q + \frac{\partial f_\Theta}{\partial T} \Delta T \\ &= \frac{\partial f_\Theta}{\partial P} \left(\frac{\partial f_P}{\partial U} \Delta U + \frac{\partial f_P}{\partial V} \Delta V \right) + \dots \quad (20) \end{aligned}$$

should hold identically in ΔU and ΔV .

Remark. Use of the deflection-load relations (2), in place of load-deflection relations $P = K_{PU}U + K_{PV}V + K_{P\Theta}\Theta$, etc., for the linear-theory problem was a consequence of the explicit form of (1) in place of the implicit form (9). In the nonlinear range the generalization (17) of Eq. (18) is clearly preferable to the generalization (9) of Eq. (1).

References

- Reissner, E., 1992, "On Some Ramifications of the Center of Shear Problem," *Zeitschrift für Angewandte Mathematik und Mechanik*, Vol. 72, pp. 315–319.
- Reissner, E., and Tsai, W. T., 1972, "On the Determination of the Centers of Twist and of Shear for Cylindrical Shell Beams," *ASME JOURNAL OF APPLIED MECHANICS*, Vol. 39, pp. 1098–1102.
- Reissner, E., 1979, "Some Considerations of the Problem of Torsion and Flexure of Prismatic Beams," *Intern. J. Solids and Structures*, Vol. 15, pp. 41–53.

Pressure Vessel Design: Concepts and Principles, edited by J. Spence and A. S. Tooth. E & FN Spon (Chapman & Hall), New York, 1994. 491 pages. Price: \$119.95.

REVIEWED BY C. W. BERT¹

This book consists of 12 chapters, three of which were authored by Professor Spence, and the others by various specialists.

The emphasis is on design of pressure vessels including plastic design concepts (Chapter 3), design by rule and design by

analysis (Chapter 4), design of nozzles and branch connections (Chapter 6), design of dished ends (Chapter 7), design for external pressure (Chapter 8), design of tubesheets (Chapter 10), design of flanges (Chapter 11). Chapter 5 deals with local loads and supports, Chapter 9 is concerned with fatigue aspects. The final chapter addresses progress toward a European standard for design of pressure vessels.

The book is well illustrated and adequately referenced and indexed. It is recommended for design engineers concerned with the design of practical pressure vessels of homogeneous, isotropic materials. It is especially recommended to those concerned with British and European design practices and standards. Unfortunately, it does not address vessels constructed of composite materials, although it does include some information on design of ring-stiffened shells.

¹Perkinson Chair, School of Aerospace and Mechanical Engineering, The University of Oklahoma, Norman, OK 73019-0601. Fellow ASME.